INELASTIC STRENGTH BEHAVIOR OF HORIZONTALLY CURVED COMPOSITE I-GIRDER BRIDGE STRUCTURAL SYSTEMS

VOLUME I, II

A Thesis
Presented to
The Academic Faculty

By

Se-Kwon Jung

In Partial Fulfillment
Of the Requirements for the Degree
Doctor of Philosophy in the
School of Civil and Environmental Engineering

Georgia Institute of Technology

August 2006

INELASTIC STRENGTH BEHAVIOR OF HORIZONTALLY CURVED COMPOSITE I-GIRDER BRIDGE STRUCTURAL SYSTEMS

Approved by:

Dr. Donald W. White, Advisor
School of Civil and Environmental Engineering
Georgia Institute of Technology

Dr. Rami Haj-Ali
School of Civil and Environmental Engineering
Georgia Institute of Technology

Dr. Roberto T. Leon
School of Civil and Environmental Engineering
Georgia Institute of Technology

Dr. Kenneth M. Will
School of Civil and Environmental Engineering
Georgia Institute of Technology

Dr. Olivier Bauchau
School of Aerospace Engineering
Georgia Institute of Technology

Date Approved: July 10, 2006

For my parents Young-Tae Jung and Jung-Sook Seo,

my wife Eun-Jung, my two daughters Seo-Hyun and Jae-In,

my brother Il-Kwon and my sister Kyung-Ran.

My great sources of dream, happiness and strength.

ACKNOWLEDGEMENTS

The author wishes to thank his advisor, Dr. Donald W. White, for his guidance, encouragement, patience and support during the course of this study. Heartfelt appreciation is also extended to the committee members, Dr. Roberto T. Leon, Dr. Kenneth M. Will, Dr. Rami Haj-Ali and Dr. Olivier Bauchau, for their valuable comments and revisions.

Financial support provided by the Federal Highway Administration (FHWA) and the Professional Service Industries (PSI), Inc. is gratefully acknowledged. In addition, the author would like to thank the following personnel at PSI, Inc., BSDI, Inc. and the FHWA Turner-Fairbank Highway Research Center for their help through the project: Dr. Beshah Fassil, Michael Grubb, Dr. William Wright and Paul Fuchs.

Deep thanks also go to the author's fellow colleagues at the Georgia Institute of Technology for providing a stimulating and fun environment in which to learn and grow.

The author wishes to thank his wife, Eun-Jung, and his two daughters, Seo-Hyun and Jae-In, for their endless patience, support and love that they provided through many difficult times. The author would have never achieved his goals without their being an integral part of his life. Love and appreciation also go to the author's parents-in-law.

Very special thanks go to the author's brother Il-Kwon and sister Kyung-Ran for their support and words of encouragement. Most of all, deep thanks and love go out to the author's parents, Young-Tae Jung and Jung-Sook Seo, for their unconditional love, sacrifice and support through good times and bad. To them the author dedicates this thesis.

TABLE OF CONTENTS

LIST OF TABLES

Table Page

LIST OF FIGURES

Figure Page

Figure Page

Figure Page

Figure Page

Figure Page

Figure Page

Figure Page

Figure Page

Figure Page

Figure Page

SUMMARY

This research investigates the strength behavior of horizontally curved composite I-girder bridge structural systems, and the representation of this behavior by the AASHTO (2004b) LRFD provisions. The primary focus is on the design of a representative curved composite I-girder bridge tested at the FHWA Turner-Fairbank Highway Research Center, interpretation of the results from the testing of this bridge, including correlation with extensive linear and nonlinear finite element analysis solutions, and parametric extension of the test results using finite element models similar to those validated against the physical tests. These studies support the potential liberalization of the AASHTO (2004b) provisions by the use of a plastic moment based resistance, reduced by flange lateral bending effects, for composite I-girders in positive bending.

INELASTIC STRENGTH BEHAVIOR OF HORIZONTALLY CURVED COMPOSITE I-GIRDER BRIDGE STRUCTURAL SYSTEMS

VOLUME I

By

Se-Kwon Jung

CHAPTER 1

INTRODUCTION

1.1 Background

Horizontally curved steel I-girder bridges have been used increasingly in the United States and internationally due to their functional and aesthetical advantages. These advantages include (Hall et al. 1999):

- Smooth rather than chorded geometry
- Simpler and more uniform construction details
- Longer continuous-spans and corresponding benefits including reduced substructure costs and fewer expansion joints and bearing details
- Ease of satisfaction of predetermined roadway alignments and tight geometric restrictions.

A 1991 survey conducted by SSRC Task Group 14 indicated that curved bridges represented 20 to 25 percent of the annual U.S. market for new steel bridge construction. Information from a recent informal survey of several major U.S. fabricators (McEleney 2004) indicates that the current percentage is likely to be higher.

Because of their inherent three-dimensional response, the analysis, design and construction of horizontally curved steel I-girder bridges are quite challenging. Due to the horizontal curvature, the bridge and its component members are subjected to coupled torsion and bending. Furthermore, due to the horizontal curvature, horizontal deflections and reactions can be important in addition to vertical deflections and reactions. The interaction among curved girders in the bridge cross-section is typically larger than

among straight bridges without skewed supports. Also, curved I-girders typically are not stable until they are connected together by cross-frames. As such, the cross-frames participate as essential (primary) components. Lastly, the slab, which AASHTO (2004b) requires to be composite with curved steel I-girders, plays an important part in distributing the applied loads as well as resisting the overall torsion and bending.

In 1992, the Federal Highway Administration (FHWA) initiated the Curved Steel Bridge Research Project (CSBRP) to conduct fundamental research into the behavior and strength of curved bridge structural systems and their components. The aim of this project is the development of more rational analysis and design procedures for horizontally curved steel bridge structures. The CSBRP has been conducted in three main phases: an erection study phase, a component strength study phase and a composite bridge study phase. The erection study phase addressed the elastic response and locked-in forces in several curved bridge configurations during progressive construction stages. The component strength study phase focused on the ultimate strength and the associated behavior of bare steel I-girder components subjected to uniform major-axis bending, major-axis bending combined with high shear, and high shear combined with relatively low major-axis bending. Figure 1.1.1 shows an overall view of one of the uniform major-axis bending tests. The three-girder bridge shown in the photo served as the test frame. The test components were bolted into the outside girder of the test frame, and the entire structure was loaded until failure occurred in the test segment. Eight components were tested in uniform major-axis bending and four components were tested in major-axis bending combined with high shear. Zureick et al. (2000) conducted experimental studies at the Georgia Institute of Technology to examine the shear (high shear low moment)

behavior and strength of four full-scale curved steel I-girders. Figure 1.1.2 shows an overall view of one of the shear tests.

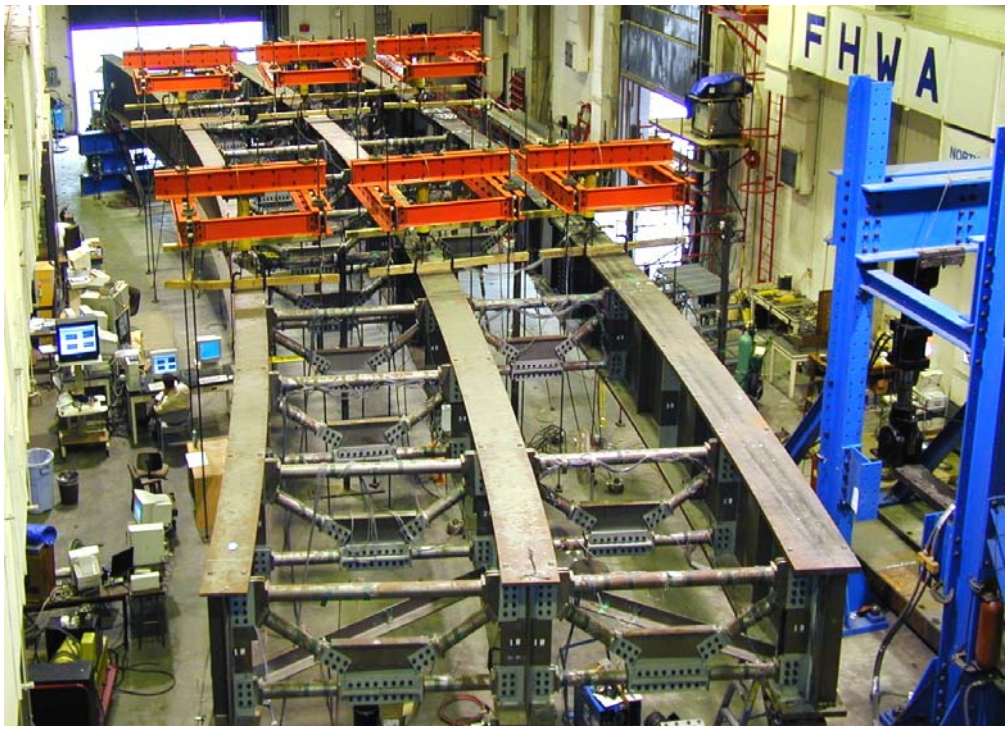

Figure 1.1.1. Overall view of uniform major-axis bending test, courtesy of FHWA.

The last phase of the CSBRP, of which this research is a part, centers on the experimental testing of a representative horizontally curved composite I-girder bridge designed in accordance with the AASHTO (2004b) LRFD Specifications. The major objective of this research is the examination of system and component responses under noncomposite dead load, composite live load and ultimate loading. The overall geometry of the steel superstructure in the test bridge is similar to that of the test frame for the component tests in Phase II. However, three new steel I-girders were designed and fabricated for the composite bridge tests, and the spacing between the cross-frames was

increased relative to that used in the Phase II component tests. The original cross-frames from the component tests were re-used in the composite test bridge. Figure 1.1.3 shows a perspective view of the steel superstructure for the composite test bridge prior to shear stud installation and deck placement.

Figure 1.1.2. Overall view of shear test.

The research presented in this dissertation focuses on the design of the composite test bridge, interpretation of the results from the physical testing of this bridge, including correlation with extensive linear and nonlinear finite element analysis solutions, and parametric extension of the test results using finite element models similar to those validated against the physical tests. The majority of the finite element analysis solutions were conducted prior to the physical testing and were used in the planning of the physical

tests. Emphasis is placed on the representation of the strength behavior by the AASHTO (2004b) LRFD provisions.

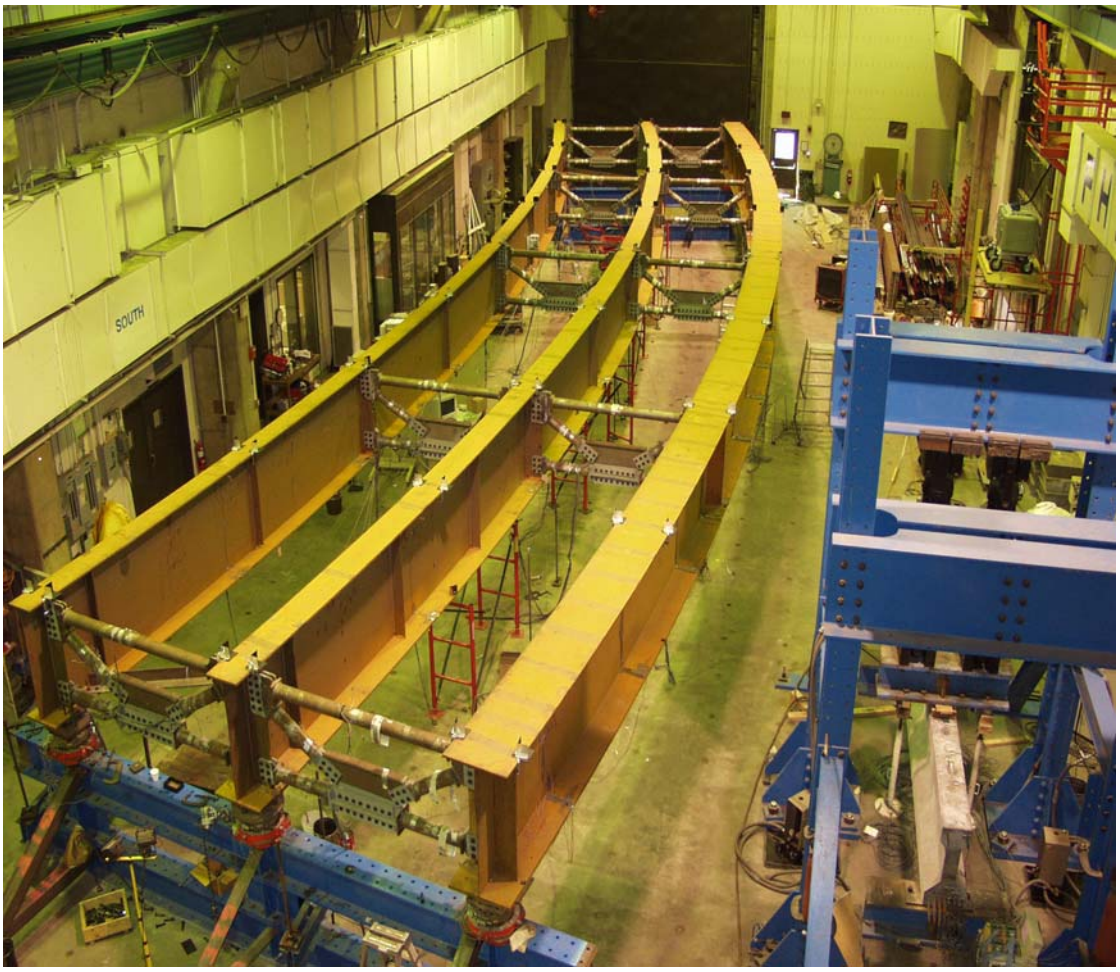

Figure 1.1.3. Overall view of the steel superstructure of the composite test bridge, courtesy of FHWA.

1.2 Motivation

1.2.1 Ultimate Strength Behavior of Curved Composite I-Girder Bridges

Although substantial prior research has been conducted, no physical tests have been performed prior to the CSBRP Phase III study to investigate the maximum strength behavior of horizontally curved composite I-girder bridge systems. Hall et al. (1999) state:

> " **The behavior of curved composite I-girder bridges at ultimate load has not been investigated analytically or experimentally. The reserve capacity of these bridges is unknown. It is likely that curved-girder bridges fail in a manner different from tangent girder bridges due to their larger torsion and the associated load shifting upon yielding. The bracing members in curved-girder bridges are treated as primary members because of their importance. However, the true behavior of these members in curved composite bridges has not been adequately investigated."**
>
> **"The behavior of curved bridges near ultimate load is unknown. Thus, the excess capacity of these bridges for load beyond design levels is not defined. If a stringer in a straight-girder bridge fails, the remaining girders in the bridge cross-section are fully effective. This assumption cannot be safely made with all curved-girder bridges."**
>
> **"The failure mechanism of a curved bridge needs to be defined. Tests of full-scale bridges to failure are needed."**

Hall et al. (1999) indicate that most of the prior research concerning curved composite I-girder bridges was focused on the strength and behavior of individual girders.

Brennan and Mandel (1979) investigated the overall system behavior of complete curved bridge systems using a scale-model bridge. In this research, a scale of 1:6.667 was utilized for a two-span continuous horizontally curved I-girder bridge. The bridge was subjected to service live loading. The test bridge responses, e.g., deflections and stresses, were converted to prototype bridge responses through the application of similitude, and were found to correlate well with analysis predictions. In addition,

several other researchers have investigated the in-service responses of actual curved bridges subjected to construction loads (Pulver 1996) and traffic loads (Kissane and Beal 1972, Galambos et al. 2000, McElwain et al. 2000, Womack and Halling 2001, Domalik et al. 2006 and Krzmarzick and Hajjar 2006).

Despite the considerable contributions of prior research to the understanding of curved bridge behavior, these efforts are somewhat limited in identifying the complete ultimate strength response of curved I-girder bridges.

1.2.2 AASHTO (2004) Specifications for Design of Curved I-Girder Bridges

The newly adopted AASHTO (2004b) Specifications provide unified I-girder resistance equations termed the "one-third rule." These equations address the design for combined major-axis bending and flange lateral bending in all types of straight and curved I-girders. In general, the resistance equations in these provisions may be written in terms of stresses as

$$f_{bu} + \frac{1}{3} f_{\ell} \le \phi_f F_n \tag{1.1}$$

where f_{bu} and f_{ℓ} are the elastically-computed flange major-axis and lateral bending stresses respectively, and $\phi_f F_n$ is the factored flexural resistance in terms of the flange major-axis bending stress for $f_{\ell} = 0$. Also, they may be written in the form

$$M_u + \frac{1}{3} S_x f_{\ell} \le \phi_f M_n \tag{1.2}$$

in terms of the major-axis bending moments M_u and the factored major-axis bending resistances $\phi_f M_n$, where S_x is the elastic section modulus to the flange under consideration. White and Grubb (2005) summarize the background and usage of these equations, and provide references to more detailed research reports and papers on their development.

Although Eqs. (1.1) and (1.2) are conceptually equivalent, since Eq. (1.2) can be obtained by multiplying each of the terms in Eq. (1.1) by S_x, their implementations in AASHTO (2004b) differ. The term $\phi_f F_n$ in Eq. (1.1) is generally taken less than or equal to $\phi_f F_{yf}$ whereas $\phi_f M_n$ in Eq. (1.2) is equal to the factored plastic moment in many cases. For typical bridge I-girders in negative bending, the use of Eq. (1.1) is a simplification that does not involve any significant economic penalty for spans greater than about 30 m (100 ft). This is due to the fact that economical welded I-girders required for these spans tend to have highly noncompact or slender webs. However, for curved bridges, the AASHTO (2004b) provisions restrict the design of *all* I-section members to Eq. (1.1), including composite I-section members in positive bending. That is, although the background research on component member responses supports the use of more liberal resistance equations, the Engineer is not allowed to utilize I-girder major-axis bending resistances in excess of $\phi_f F_n - f_\ell/3$, with the maximum value of $\phi_f F_n$ being $\phi_f F_y$. This restriction is due to the limited understanding of the influence of member yielding on the system response of curved I-girder bridges. Curved bridge system studies are needed to investigate this behavior.

1.2.3 State-of-the-Art Analysis Capabilities for Curved I-Girder Bridges

The application of state-of-the-art refined finite element tools to understand the load-deflection and maximum strength behavior of complete horizontally curved I-girder bridge systems has been limited, both for consideration of constructability and strength during construction, as well as for consideration of the service performance and strength in the final constructed condition. Regarding this issue, Hall et al. (1999) state:

> **"New analysis tools, particularly finite element computer programs, are now available that permit detailed analyses of both structural elements and entire structures. These analysis tools have not been adequately applied to horizontally curved beam bridges. Field instrumentation of curved bridges carried out by several researchers over the past 20 years remains unexplored with the newest analysis tools."**

> **"Even the most refined methods have limitations and assumptions that remain unexplored. … There is a great need to quantify the reliability of various analysis methods and to explore how and when each method might be best applied. It is well known that all V-load analyses are not the same. It is less well known that all 3D finite element analyses do not provide the same results. Application of the methods needs to be studied and compared to field measurements."**

Simplified analysis tools such as grid analysis typically are believed to often provide a reasonable prediction for ordinary bridge systems. However, the behavior of curved bridge structural systems is sufficiently complex such that simplified analysis tools cannot always capture the major characteristics of the system response. For example, elastic analyses and physical tests for the CSBRP Phase III test bridge design show that the webs of the girders deform in the out-of-plane direction when the bridge is subjected to live loads. It is important to consider the influence of the web distortional deformations on the behavior and strength. Unfortunately, this kind of behavior cannot be studied rigorously using beam theory.

Another example is the calculation of the second order elastic lateral bending stresses in girder compression flanges when a bridge is subject to noncomposite construction loading. In the AASHTO (2004b) Specifications, it is explicitly stated that engineers must consider the second order amplification of the lateral bending stress in checking girder strengths, by using a simple amplification formula or second order analysis. The commentary of AASHTO (2004b) indicates that the amplification factor equation for the flange lateral bending stresses is intended as a conservative approximation. In many cases, particularly under final constructed conditions, the second-order amplification will be small and this conservatism is inconsequential. However, in some bridge systems, and particularly under some construction loadings (e.g., eccentric bracket loads on exterior girders), this amplification may be large. In these cases, a refined second-order analysis can provide substantive benefits by allowing more accurate, typically smaller, estimates of the flange lateral bending.

Computationally, shell FEA representation of bridge components was prohibitively expensive in the past, requiring a large amount of memory and storage space, high-end computer systems and extensive pre- and post-processing effort. However, rapid development of computer hardware and software is enabling large-scale finite element simulation to be conducted efficiently on personal computers.

1.3 Problem Statement and Research Approach

This study investigates the ultimate strength and the associated inelastic behavior of horizontally curved composite I-girder bridge systems under various loading stages: dead load, noncomposite construction load and composite live load. The primary focus is on the ultimate strength of composite bridge systems and the associated behavior of their

individual curved composite I-girders. However, bridge system and component responses during construction are also targeted. The ultimate goal is to evaluate the ability of the AASHTO (2004b) LRFD Specifications to represent the system and component strength behavior of composite curved I-girder bridges.

In this research, refined three dimensional FEA models are developed and applied for the elastic design-analysis as well as linear elastic, geometric nonlinear and full nonlinear FEA simulation of curved I-girder bridges. The design of the composite test bridge, as well as the design of several variations on the test bridge considered in parametric FEA studies, is accomplished with the extensive use of refined finite element models. The full nonlinear analyses involve the simulation of the dead load effects on the noncomposite structure, followed consecutively by simulation of the effect of slab shrinkage strains and then the effects of the applied loads on the composite structure in a single continuous process.

First, this study focuses on the design of the full-scale horizontally curved composite test bridge. It then provides a synthesis and assessment of the experimental results and corresponding full nonlinear FEA predictions for the test bridge. The experimental results are used to verify the predicted behavior and the accuracy of the finite element models, and in turn, the finite element models provide confirmation of the measured test results.

The test bridge of course provides a detailed assessment of only one representative structure. With the help of carefully developed full nonlinear finite element analysis models similar to those calibrated against the experimental test results, parametric studies

are performed for a number of variations on the test bridge to extend the physical test results.

The composite test bridge and other bridge configurations studied by FEA are targeted at providing the necessary understanding to potentially allow use of the Eq. (1.2) format with $\phi_f M_n$ near or equal to $\phi_f M_p$ for curved composite I-girders in positive bending. Equation (1.2) with $\phi_f M_n = \phi_f M_p$ is referred to in this work as the M_p-based 1/3 rule.

1.4 Research Scope

The research presented in this dissertation involves five key tasks. The definition of each task and a synopsis of the corresponding research issues are presented below.

1.4.1 Design of the Test Bridge

As mentioned above, Phase III of the CSBRP has involved the experimental testing of a full-scale horizontally curved composite bridge at the FHWA Turner-Fairbank Highway Research Center. The composite test bridge is the first of its kind designed in accordance with the AASHTO (2004b) LRFD Specifications. These Specifications employ a unified approach for consideration of combined major-axis bending and flange lateral bending from any source in either tangent or curved I-girder bridges.

The second chapter of this dissertation is concerned with the analysis of the above test bridge using several approximate and refined three dimensional FEA models, and the corresponding design of the test bridge according to the AASHTO (2004b) LRFD Specifications. Both first- and second-order elastic analyses are performed for the non-composite dead and construction loads, while the response of the bridge under composite live load is analyzed using a first-order elastic analysis. The bridge responses such as

the flange stresses and girder deflections are checked against the requirements stipulated in AASHTO (2004b). The test bridge incorporates a number of key attributes pertaining to horizontally curved composite I-girder bridges. Briefly, these attributes are as follows:

- Only three internal cross-frames are employed, giving a subtended angle between the cross-frames of $L_b/R=0.1125$, which is slightly greater than the maximum limit of 0.10 in AASHTO(2004b).
- The web slenderness D/t_w varies from 133 to 149. These values are close to the AASHTO(2004b) limit of 150 for straight and curved transversely-stiffened web panels.
- The maximum stiffener spacing, d_o, is approximately equal to 3D (three times the girder web depth). This spacing is significantly larger than would be allowed in the prior AASHTO (2003) guide specifications given the test bridge geometry.
- The compression flange slenderness ratio $b_{fc}/2t_{fc}$ for the outermost girder is close to the maximum $b_f/2t_f$ of 12 permitted by AASHTO(2004b).
- A hybrid HPS 70W bottom flange is utilized for the outside girder. The prior AASHTO (2003) guide specifications disallow hybrid curved I-girders.
- The outside and middle girders are sized close to the AASHTO(2004b) strength limits
- The nominal width of the inside girder's top flange is equal to 12 in, giving $L_b/b_f = 21.5$ and $L_l/b_f = 86$. The latter of these ratios is equal to the AASHTO (2004b) suggested limits on the length-to-flange width of a shipping piece.

The test bridge is a simply-supported non-skewed structure. Consideration of support skew as well as consideration of negative bending response associated with continuity effects in continuous-span structures are addressed in the FEA parametric studies outlined in Section 1.4.4.

1.4.2 Full Nonlinear FEA of the Test Bridge

As noted earlier, the major objective of Phase III of the CSBRP is to investigate the ultimate strength behavior of the composite test bridge. A major focus of this dissertation is to provide a refined full nonlinear FEA assessment of this bridge. It has been indicated that despite a rapid development of three-dimensional analysis capabilities, refined analysis tools have not been actively applied to the analysis of curved composite bridges. The author is not aware of any prior attempts to analyze the ultimate capacity of a complete composite curved I-girder bridge structural system.

The third chapter of this dissertation addresses the detailed full nonlinear FEA modeling of the test bridge. Chapters 4 and 5 provide extensive synthesis and interpretation of experimental results and comparisons to corresponding full nonlinear FEA predictions for a number of the test bridge component responses. The primary focus of these chapters is on the maximum strength behavior of the composite test bridge at the M_p-based 1/3 rule load level on the outermost girder, G3. Key topics addressed are:

- Effects of inelasticity on the overall bridge response, particularly on the extent of load shedding or load redistribution,
- Concrete deck failure mode,
- Deformations and forces within the cross-frame members,
- Top and bottom flange behavior in terms of stresses and displacements,

- Effects of inelasticity on the flange lateral bending responses, particularly at the cross-frame locations,
- Web distortion effects on the ultimate capacity of the test bridge,
- Behavior of intermediate transverse stiffeners, and
- Overall failure mechanism of the bridge system.

1.4.3 Overall Assessment of the Test Bridge Responses

FEA internal moments and shear forces are obtained by making cuts and considering the resulting free body diagrams from the full nonlinear FEA solutions. These cuts are made at various locations along the girder lengths. Global equilibrium is evaluated by comparing the combined girder and slab internal forces at specific bridge cross-sections with corresponding static free body diagrams. In addition, because of the apparent accuracy of the M_p-based 1/3 rule in characterizing the useful capacity of the bridge system, the degree of nonlinearity in the internal force variations (relative to the elastic response) is assessed at the M_p-based 1/3 rule strength level for the outermost composite girder G3.

1.4.4 Parametric FEA Studies

Although the test bridge incorporates a number of key attributes pertaining to horizontally curved composite I-girder bridge structural systems, it lacks other important physical attributes that may have a significant influence on the strength behavior of these types of structures. Therefore, the base test bridge FEA model is utilized as a starting point for parametric FEA investigations into the strength behavior of other curved I-girder bridge systems. This is accomplished by systematically modifying selected

parameters of the test bridge. The following is a brief summary of each of the bridge systems considered in the parametric studies:

- ***Case 1: Identical structure to the test bridge, detailed for Total Dead Load Fit (TDLF).*** The composite test bridge was detailed and erected for No-Load Fit (NLF). No-Load Fit (NLF) is a detailing method where the girders are cambered vertically to offset the dead load deflections and the cross-frames are detailed to connect to the girders in their cambered no-load geometry without inducing any locked-in stresses due to fit up. Bridges that are detailed for NLF and have a concrete slab that is cast in one stage may be analyzed for the self-weight of the steel plus the weight of the slab by simply turning on gravity for the full superstructure model. However, since the cross-frames are detailed to fit to the girders with the girder webs plumb in their ideal cambered no-load configuration, the girder webs generally will not be plumb under the steel dead load or the final total dead load.

  Total Dead Load Fit (TDLF) is a detailing method where the girders are cambered vertically to offset the dead load deflections, but the cross-frames are detailed to connect to the girders in a targeted web-plumb total dead load position (with the estimated vertical displacements due to the deflections under the steel self-weight plus the weight of the concrete deck taken out of the initial camber). In bridges detailed for TDLF, internal forces are locked into the system due to the incompatibility of the cross-frame and girder geometries in the no-load geometry. This lack of fit induces a twist in the girders that offsets the torsional rotations due

to the dead loads. In Case 1, the test bridge is detailed for TDLF. This allows the relative impact of the NLF and TDLF detailing methods to be assessed.

- ***Case 2: Homogeneous section for the outermost girder, G3.*** The outermost girder of the composite test bridge (G3) is designed as a hybrid section with HPS 70W for its bottom flange. It is important to note that the use of hybrid curved I-girders was not allowed in the previous AASHTO (2003) Guide Specifications. In Case 2, the bottom flange of the outermost girder is replaced by a Grade 50 steel flange, thereby giving the girder a homogeneous cross-section. Since the shape factor M_p/M_y of a homogeneous I-girder is generally larger than that of a comparable hybrid I-girder, the impact of girder flexural designs using the M_p-based 1/3 rule potentially can be larger for homogeneous girders than for hybrid ones.
- ***Case 3: Cross-frame spacing, L_b, set to 0.075R.*** The subtended angle between the cross-frames (L_b/R) within the composite test bridge is slightly above the limit of 0.1 allowed by the AASHTO (2004b) Specifications. In Case 3, the cross-frame spacing is adjusted to a more realistic value. Five internal cross-frames are used rather than the three internal cross-frames in the physical test bridge. This gives an $L_b/R = 0.075$ and results in a cross-frame spacing of 15 ft on the middle girder (G2) (the corresponding L_b on the outside girder (G3) is slightly larger and the L_b on the inside girder (G1) is slightly smaller). This case is intended to investigate the strength behavior of the composite test bridge with a more realistic cross-frame spacing than used in the physical composite test bridge.

- ***Case 4: Skewed supports (maximum skew angle of 20 degrees), cross-frames normal to girder axes.*** This is the first case of three skewed bridges studied in this work. In Case 4, the two end bearing lines are aligned parallel to each other with a maximum skew angle at one end set to 20 degrees. However, the intermediate cross-frames are kept normal to the girder axes as in the base composite test bridge configuration. The AASHTO (2004b) Specifications state that cross-frames can be either normal to the girder axis or parallel to skewed bearing lines for skew angles up to 20 degrees. This case aims to provide insight into potential changes in the strength behavior due to a mild skew angle at the support locations.
- ***Case 5: Skewed cross-frames and supports (maximum skew angle of 20 degrees).*** This is the second case of three skewed bridges studied in this research. Similar to the first case, the two support lines are aligned parallel to each other with the maximum skew angle at one of the bearing lines set to 20 degrees. In addition, the cross-frames are installed parallel to the bearing lines.
- ***Case 6: Skewed supports (maximum skew angle of 60 degrees).*** This is the last case of three skewed bridges considered in this study. Unlike the first two skewed bridges, which have relatively mild skew angles, this bridge involves an extreme skew angle of 60 degrees at one of the bearing lines. The cross-frames are kept normal to the girder axes, as required by the AASHTO (2004b) Specifications when the skew angle exceeds 20 degrees.
- ***Case 7: Three-lane bridge.*** The base composite test bridge has only three I-girders, and the slab width barely accommodates two traffic lanes. This is due to

the physical constraints placed on the test bridge geometry such that it could be built within the laboratory. In Case 7, the slab width is increased to accommodate three traffic lanes, and four steel I-girders are employed. This case is intended to investigate the strength behavior of a bridge with a wider cross-section and a larger number of girders than the base composite test bridge.

- ***Case 8: Yielding and failure of critical cross-frame members.*** The test bridge cross-frame members were sized such that they remained elastic at the ultimate load capacity of the test bridge. One of the major concerns relating to the system strength behavior of curved bridges is the possibility that the loss of a critically-loaded cross-frame member may lead to a catastrophic failure of the overall bridge system. This concern is largely based on the assumption that the forces released from a failed cross-frame member cannot be redistributed to other less critically-loaded adjacent cross-frame members or girders. In order to address this concern, the following four failure scenarios are considered in Case 8:

  i) First, the critically-loaded bottom chord of the midspan cross-frame between G2 and G3 is sized just to resist the factored member forces obtained from the elastic design-analysis at the Strength I load level. In other words, the design compressive resistance of the bottom chord is exceeded for loads above the governing Strength I load level. However, in this scenario, this member is assumed to yield in compression when its strength condition is reached (i.e., no shedding of any of its compressive load to the adjacent components).

ii) The second scenario assumes that the bottom chord of the midspan cross-frame between G2 and G3 fails catastrophically at its design resistance such that it suddenly loses all of its load-carrying capacity. That is, the bottom chord is effectively removed from the analysis model. The main focus in scenarios (i) and (ii) is on the load redistribution after the yielding or complete loss of the most critically-loaded cross-frame bottom chord.

iii) The third scenario simulates the fracture (pseudo-statically) of the tension diagonal in the cross-frame connected to G3 at the midspan of the test bridge.

iv) Lastly, the fourth scenario assumes that both the bottom chord and the tension diagonal of the midspan cross-frame between G2 and G3 fail catastrophically at their design resistances such that they suddenly lose all their load-carrying capacities.

- ***Case 9: Fixed-end bridge systems.*** All of the above cases are simply-supported structures. Two fixed-end bridge systems are studied in Case 9 to investigate the behavior of continuous-span structures. To limit the changes to the base test bridge configuration to a minimum and to simplify the interpretation of the test results, an ideal assumption is invoked that the girder ends are fully restrained. This case allows important key attributes typical of the strength behavior of continuous-span structures to be investigated. The first fixed-end bridge is designed using a prismatic steel section along the entire span-length. This results in the positive moment region having significant reserve strength at the elastic design limit of the structure (i.e., the girder sizes are governed by the AASHTO (2004b) requirements in the negative moment regions). The second design

utilizes a transition to a smaller cross-section in the positive moment region such that the maximum design ratios are close to 1.0 in both regions.

1.5 Description of the Composite Test Bridge

Figure 1.5.1 shows the girder cross-section, bridge cross-section and plan views of the composite test bridge. The test bridge has a conventional cast-in-place concrete deck. It consists of three prismatic I-girders spaced radially at 2.625 m (8.75 ft). The measured flange and web dimensions are detailed in Figures 1.5.1a through c. The radius of curvature is 57.375 m (191.25 ft) for the inside girder (G1), 60.0 m (200 ft) for the middle girder (G2), and 62.625 m (208.75 ft) for the outside girder (G3). The span of G2 is 27.0 m (90.0 ft) measured along its arc length. Temporary bottom struts are attached to the bottom flanges to prevent relative longitudinal movement of the girders during the construction of the slab.

The bridge slab is a 200 mm (8.0 in) thick cast-in-place concrete slab (average measured thickness of 202 mm (8.06 in) with only a minor variation in thickness over the slab area). The slab has 75 mm (3.0 in) haunches and 0.90 m (3.0 ft) overhangs. Wood forms are used for the concrete casting, to simplify the interpretation of the slab responses, with the primary focus being placed on the actions of the slab as part of the overall bridge structural system in this research. The forms are attached to the I-girders by a typical strap detail, the flexibility of which precludes any significant lateral restraint of the top flanges during the placement of the slab.

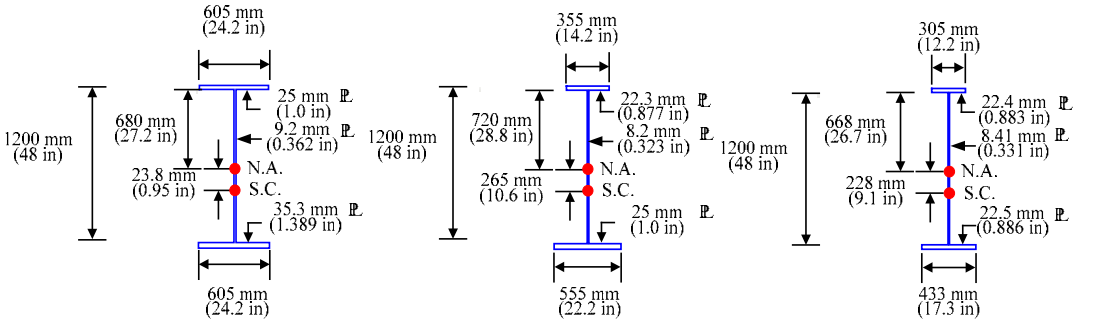

(a) G3 cross-section (b) G2 cross-section (c) G1 cross-section

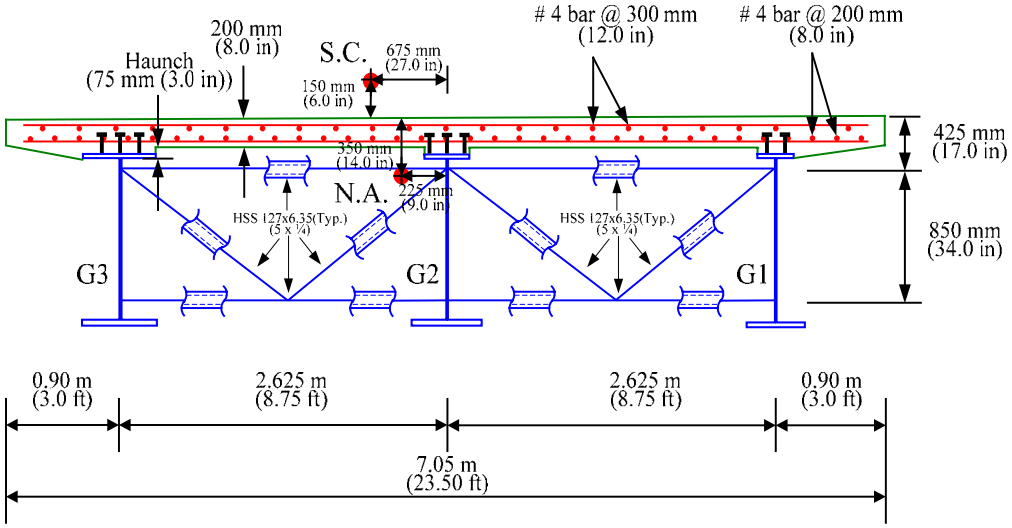

(d) Bridge cross-section

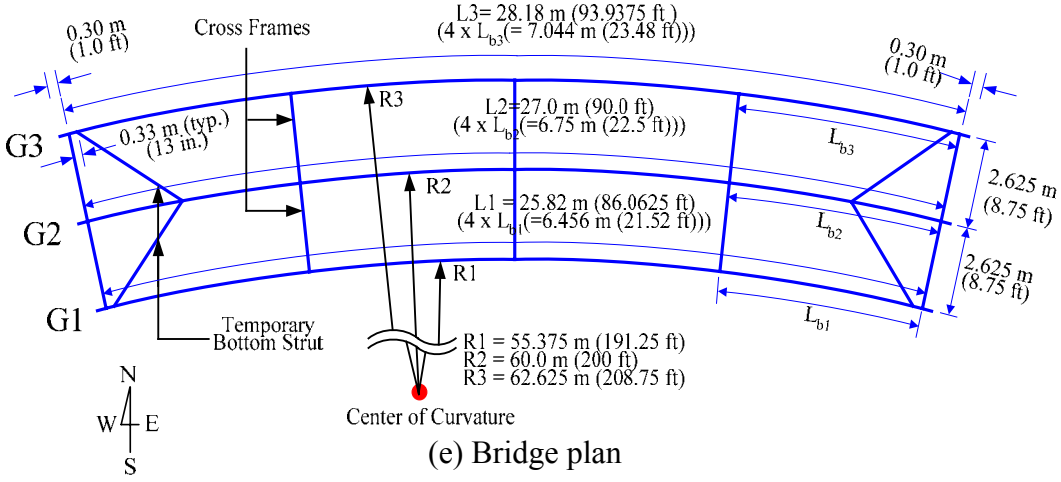

(e) Bridge plan

Figure 1.5.1. Composite test bridge geometry.

Table 1.5.1 presents the measured average girder dimensions and key dimensional properties. Table 1.5.2 provides measured average dimensions for the bearing stiffeners, transverse stiffeners and connection plates.

The composite test bridge is designed at the following extremes relative to the AASHTO (2004b and 2003) provisions:

- There are only three internal cross frames within the span of the test bridge, resulting in a cross frame spacing of 6.75 m (22.5 ft) along G2 and a subtended angle between the cross-frames of L_b/R=0.1125 (or 6.45 degrees). The maximum L_b/R permitted by AASHTO (2004b) is 0.10 for a completed bridge system. This is a practical upper limit suggested originally by McManus (1971) based on ASCE (1971). The cross-frame forces and I-girder lateral bending stresses tend to be rather large in practical configurations with L_b/R values beyond these limits.
- The nominal width of the top flange of G1 is 300 mm (12.0 in). Combined with the wide cross-frame spacing discussed above, this results in an L_b/b_f of 21.5 for this girder. The maximum value of L_b/b_f allowed for curved I-girders in the AASHTO (2003) Guide Specification is 25. AASHTO (2004b) requires that L_b must be smaller than L_r, the smallest unbraced length at which the elastic lateral-torsional buckling strength equations govern the base flexural resistance. For typical I-girders, L_b/b_f is close to 25 when $L_b = L_r$. In general, members with $L_b > L_r$ tend to have larger second-order amplification of flange lateral bending stresses. The 300 mm (12.0 in) wide top flange on G1 also gives $L_l/b_f = 4L_b/b_f = 86$ (where L_1 is the total span length of girder G1), which is close to the AASHTO (2004b) recommended maximum limit for a shipping piece.

Table 1.5.1. Measured average girder dimensions and key dimensional properties.

Girder	$b_{fc} \times t_{fc} + D \times t_w + b_{ft} \times t_{ft}$ mm (in)	Area mm^2 (in^2)	R[1] m (ft)	L[1] m (ft)	L_b[1] m (ft)	L_b/b_{fc}	L_b/b_{ft}
G3	605 × 25 + 1200 × 9.0 + 605 × 35.3 (24.2 × 1.0 + 48.0 × 0.36 + 24.2 × 1.39)	46580 (72.20)	62.625 (208.75)	28.18 (93.94)	7.0455 (23.485)	11.74	11.74
G2	355 × 22.0 + 1200 × 8.0 + 555 × 25 (14.2 × 0.877 + 48.0 × 0.32 + 22.2 × 1.0)	32370 (50.18)	60.0 (200)	27.0 (90)	6.75 (22.5)	19.29	12.27
G1	305 × 22.0 + 1200 × 8.4 + 433 × 22.1 (12.2 × 0.883 + 48.1 × 0.33 + 17.3 × 0.886)	27080 (41.98)	57.375 (191.25)	25.82 (86.06)	6.4545 (21.515)	21.52	15.19

(1) Nominal dimensions are used for the radius of curvature, girder length and unbraced length.

Table 1.5.2. Measured average stiffener dimensions

Stiffener		G1			G2			G3		
		height mm (in)	width mm (in)	thick. mm (in)	height mm (in)	width mm (in)	thick. mm (in)	height mm (in)	width mm (in)	thick. mm (in)
Bearing stiffeners	Outside web panel	1200 (48.0)	180 (7.0)	19 (0.74)	1216 (47.88)	225 (9.0)	19 (0.74)	1200 (48.0)	225 (9.0)	25 (1.0)
	Inside web panel	1200 (48.0)	130 (5.1)	19 (0.75)	1214 (47.81)	225 (9.0)	25 (1.0)	1200 (48.0)	225 (9.0)	25 (1.0)
Intermediate stiffeners		1175 (47.0)	115 (4.5)	16 (0.63)	1200 (48.0)	140 (5.5)	16 (0.63)	1175 (47.0)	150 (6.0)	16 (0.62)
Connection plates	Outside web panel	1200 (48.0)	180 (7.0)	16 (0.62)	1200 (48.0)	225 (9.0)	21 (0.82)	1200 (48.0)	225 (9.0)	21 (0.82)
	Inside web panel	1200 (48.0)	125 (5.0)	16 (0.62)	1215 (47.85)	225 (9.0)	21 (0.83)	1200 (48.0)	225 (9.0)	21 (0.82)

- The slenderness ratio of the I-girder webs (D/t_w) ranges from 133 to 149. This is close to the AASHTO (2004b) limit of 150 for straight and curved transversely-stiffened web panels and exceeds the limits specified for curved webs in AASHTO (2003). Also, the maximum stiffener spacing d_o is approximately 3D. This is the maximum limit for the stiffener spacing in transversely-stiffened straight and curved girders in AASHTO (2004b). This limit is a considerable liberalization relative to AASHTO (2003). AASHTO (2003) requires $d_o \leq D$ when the radius R is less than or equal to 210 m (700 ft). The shear strength design of the girders requires a stiffener spacing of $d_o/D = 1$, 1.7, and 2.4 near the end supports of G3, G2, and G1, respectively. However, $d_o/D = 3$ is sufficient near the midspan of these girders according to the AASHTO (2004b) rules. A spacing of $d_o = 0.5D$ is used in the end panels to ensure anchorage of the shear tension field.

- The compression flange slenderness ratio $b_{fc}/2t_{fc}$ is 12.1 for G3. This is close to the maximum $b_f/2t_f$ of 12 permitted by AASHTO (2004b) for curved and straight I-girders and is somewhat larger than the corresponding limits in AASHTO (2003). The AASHTO (2004b) limit of $b_f/2t_f = 12$ is a practical upper bound intended to ensure that the flanges will not distort excessively when welded to the web. The CSBRP studies on component behavior indicate that the resistances of straight and curved noncompact-flange I-girders are predicted accurately to conservatively and there is no significant adverse effect on the ductility by using $b_{fc}/2t_{fc}$ values up to this limit (e.g., see White and Grubb (2005)). For a given flange area, the use of larger $b_f/2t_f$ values (up to $b_f/2t_f = 12$) may be more economical in some cases, since the resulting flange lateral bending section modulus is larger.

- HPS 70W material is used for the bottom flange of G3, whereas the web and top flange of G3 are composed of Grade 50 steel. AASHTO (2003) prohibits the use of hybrid construction due to the limited testing of curved hybrid girders. Conversely, the AASHTO (2004b) provisions allow curved hybrid girders based on the fact that: (1) the elastic service load stresses tend to be smaller and (2) the inelastic deformations at strength load levels are not significantly different in hybrid-girder webs compared to homogeneous-girder webs where the web is composed of the higher-strength flange material.
- Girders G2 and G3 are sized close to the AASHTO (2004b) strength limits

1.6 Testing of the Composite Test Bridge

A large number of the considerations in the composite bridge test can be discussed succinctly by focusing on the sequence of tests applied to the structure. The testing started with the measurement of responses during erection of the structural steel. The following single erection sequence was employed. First, as illustrated in Figure 1.6.1, the girders were blocked in their ideal unstressed condition on the laboratory floor. Next, the cross-frames were positioned, and holes were drilled in the girder connection plates such that the girders and cross-frames fitted together in the ideal no-load geometry without inducing any internal stresses in the system. Girders G1 and G2 were then assembled as a pair, and the G1-G2 assembly was lifted into position on the bearings as shown in Figure 1.6.2. Subsequently, G3 was positioned on its bearings and was attached to the G1-G2 assembly as shown in Figure 1.6.3.

It should be noted that mechanistically, the composite test bridge structure is a conservative elastic system under its steel and concrete dead load. Its final dead load state is nominally independent of the fabrication and erection processes (within the limits of connection tolerances between the girders and cross-frames). Nominally, there are no locked-in stresses in the test bridge due to the detailing and fit-up of the components. Furthermore, the slab was cast in one continuous stage over a period of about four hours with the laboratory doors open and the ambient temperature in the lab between 50 and 60 ºF.

Figure 1.6.1. Steel erection sequence 1 – the girders blocked in their ideal unstressed condition on the laboratory floor, courtesy of FHWA.

Figure 1.6.2. Steel erection sequence 2 – the paired G1 and G2 assembly lifted into position on the bearings, courtesy of FHWA.

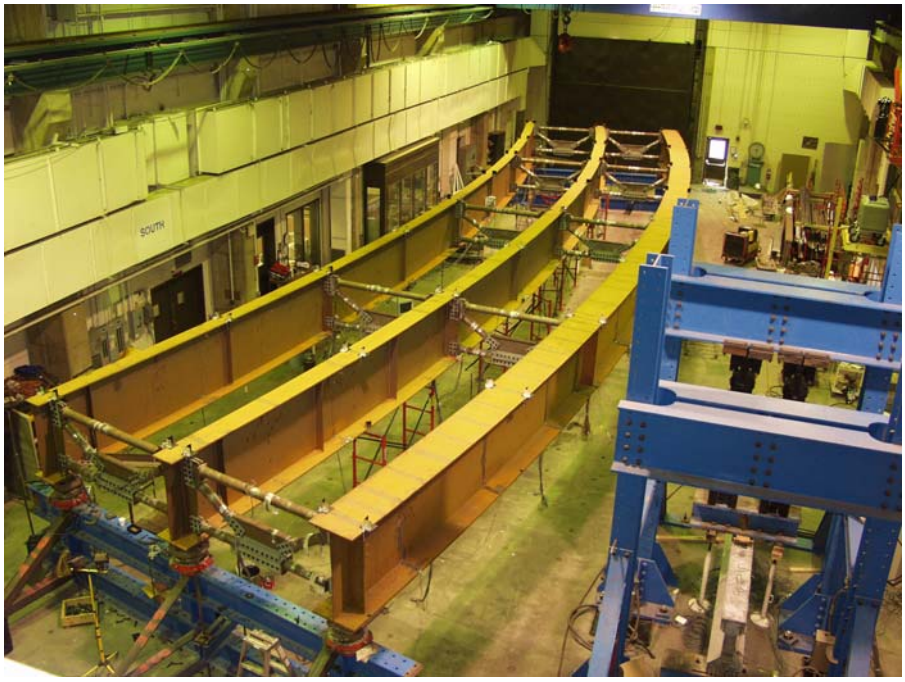

Figure 1.6.3. Steel erection sequence 3 - G3 lifted into its desired position and attached to the G1-G2 assembly, courtesy of FHWA.

The above fabrication and erection scenario represents a typical procedure selected in practice whenever the bridge size and geometry permits. The girders are detailed with their webs plumb in the no-load geometry and with vertical cambers that compensate for the dead load deflections. Furthermore, the connections are detailed for fit up in the ideal no-load position. The bridge cross-section and the girders twist into an out-of-plumb geometry due to the effect of the dead weight of the structure and the horizontal curvature. The resulting out-of-plumbness of the webs in the final dead load position is often inconsequential[1]. Chang (2006) addresses the simulation of complete steel erection and slab casting sequences for general curved I-girder bridge structures.

Subsequent to the completion of the steel superstructure, the test bridge was subjected to several loadings in its noncomposite condition: (1) Point loads were applied at various positions along the steel I-girders to determine influence lines for the bare steel superstructure. (2) A group of loads was applied to G2 and G3 to simulate a combined major-axis and flange lateral bending stress condition approximately equal to 0.90 F_y at the midspan of G3. (3) The above loadings were applied at a smaller level of total stress while additional concentrated loads are applied eccentrically to girder G3 to simulate the effect of eccentric bracket loads on the exterior girders.

At this stage, wood forms were installed to support the concrete casting. It should be noted that the formwork was a significant contributor to the noncomposite dead load stresses during construction. The slab was cast in a single continuous operation (approximately four hours) starting at one end of the bridge and working toward the opposite end. Displacements and strains were monitored throughout the bridge structural

[1] For some bridge geometries, the web out-of-plumbness may be larger than desired, or radial movements may result in problems with roadway alignment. In these cases, measures must be taken to achieve tolerances on the final deflected bridge geometry. Chang (2006) provides further discussion of these issues.

system during the concrete casting and were sequenced with video of the casting process. The weight of the construction equipment was insignificant compared to the other dead loads. The concrete was pumped into position on the slab, and a small vibrating screed was used for placing the concrete. Also, the displacements and strains were monitored subsequently during the curing of the slab, capturing the strains in the slab and in the structural steel due to concrete shrinkage. The long-term composite dead load on the structure was effectively zero, and therefore the concrete creep strains were insignificant. The wood forms were stripped from the bridge at approximately 28 days after the slab casting. Figure 1.6.4 shows an end view of the composite test bridge at this time.

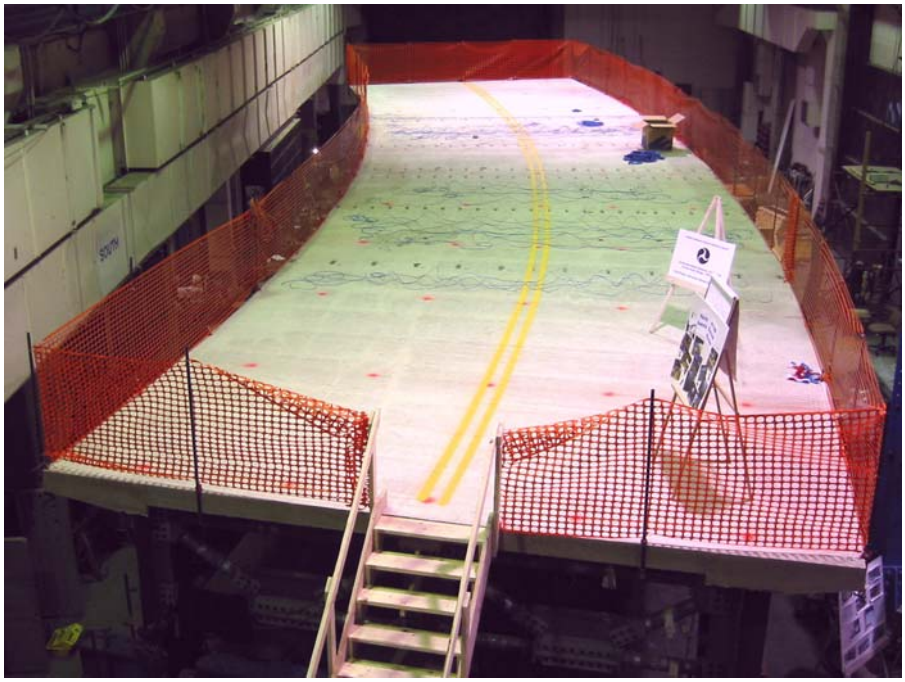

Figure 1.6.4. End view of the composite test bridge with the wood forms stripped at approximately 28 days after the slab casting, courtesy of FHWA.

After the slab gained its 28 day strength, additional testing sequences were applied. These sequences are subdivided into the following four major tests:

- Test 1: 16 kip (71 kN) concentrated loads were applied on a grid over the slab as shown in Figure 1.6.5 to determine influence surfaces.

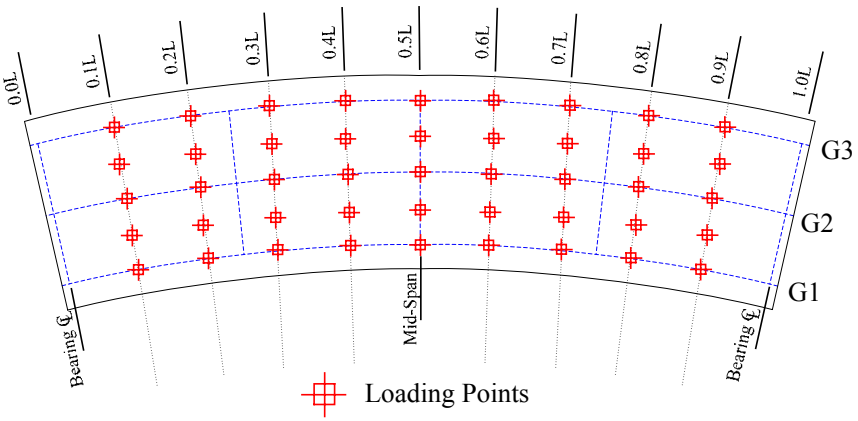

Figure 1.6.5. Grid of loading points on the test bridge slab used to generate influence surfaces.

- Test 2: A group of loads was applied simulating the effects of a single design truck plus a lane load on the outside of the bridge for maximum flexural effects on G3 as shown in Figures 1.6.6 and 1.6.7. The maximum load level corresponded approximately to 90 percent of the AASHTO (2004b) STRENGTH I live load. This loading was halted when the total reactions on the inside girder G1 effectively reached zero and G1 started to lift off of its supports. It is important to note that the uplift does not occur under the total factored AASHTO design load. The statics of the test loading was slightly more severe than the strength loading condition, resulting in the uplift on G1 during this stage of the testing.

Figure 1.6.6. Composite test bridge with loading fixtures for Test 2**,** courtesy of FHWA.

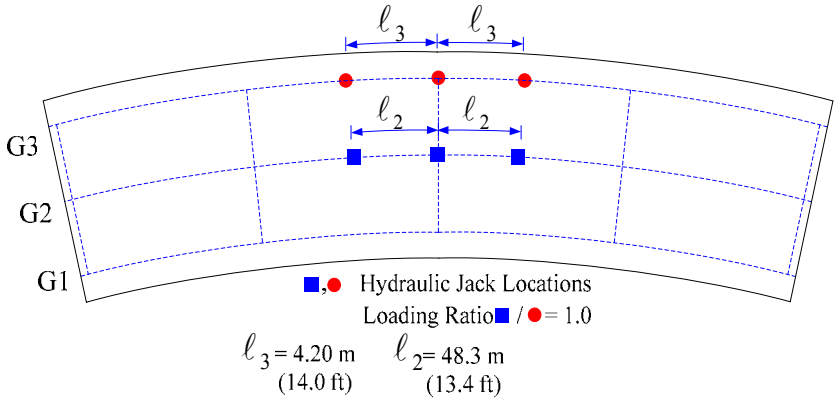

Figure 1.6.7. Six hydraulic jacks positioned on the outside lane of the test bridge slab for Test 2, corresponding approximately to a single AASHTO design vehicle plus lane load.

- Test 3: A similar loading was placed on the bridge simulating the AASHTO loading for maximum flexural effects on G1 as shown in Figures 1.6.8 and 1.6.9. Again, the maximum load level corresponded approximately to 90 percent of the AASHTO (2004b) STRENGTH I live load. This loading was halted just prior to the onset of yielding on G1 (note that the design of G1 was governed by limits

other than strength, but the use of Eq. (1.1) is based on the development of some yielding at strength load levels).

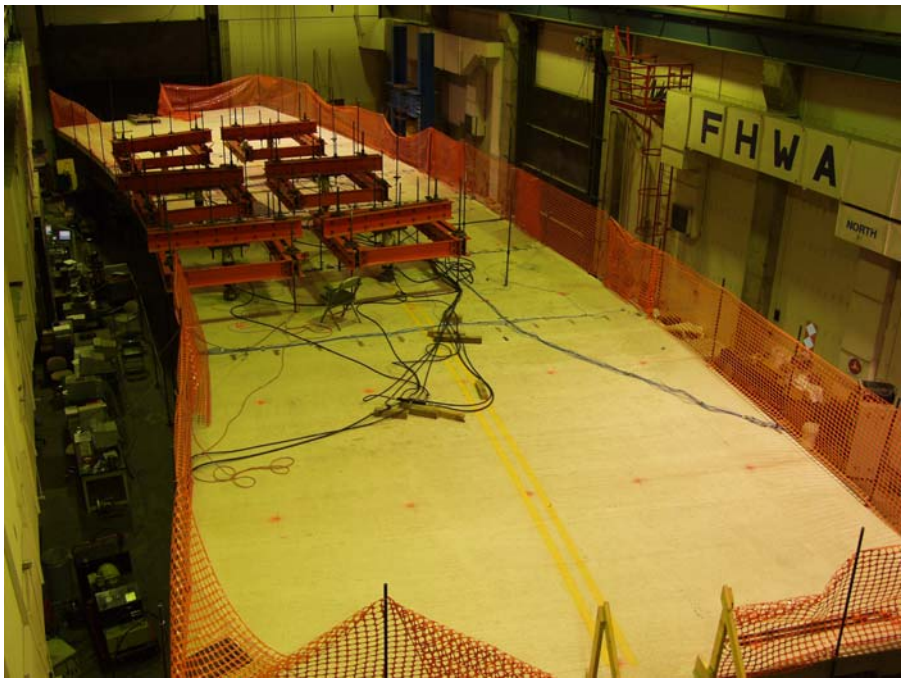

Figure 1.6.8. Composite test bridge with loading fixtures for Test 3, courtesy of FHWA

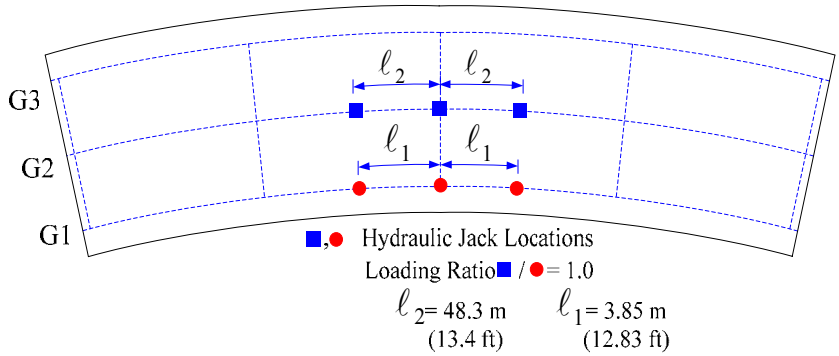

Figure 1.6.9. Six hydraulic jacks positioned on the inside lane of the test bridge slab for Test 3, corresponding approximately to a single AASHTO design vehicle plus lane load.

- Tests 4a and 4b: A group of loads was placed on the bridge that simulated the effects of two design trucks aligned side-by-side at the middle of the bridge plus two lanes as shown in Figures 1.6.10 and 1.6.11. This AASHTO loading governs the flexural strength design of G3; a similar loading governs for G2. Test 4a focused on the cyclic loading of the test bridge at several load levels defined in relation to the AASHTO (2004b) design provisions. Test 4b involved the final monotonic loading of the test bridge to its ultimate load capacity. The loading scheme shown in Figures 1.6.10 and 1.6.11 was used for each these tests.

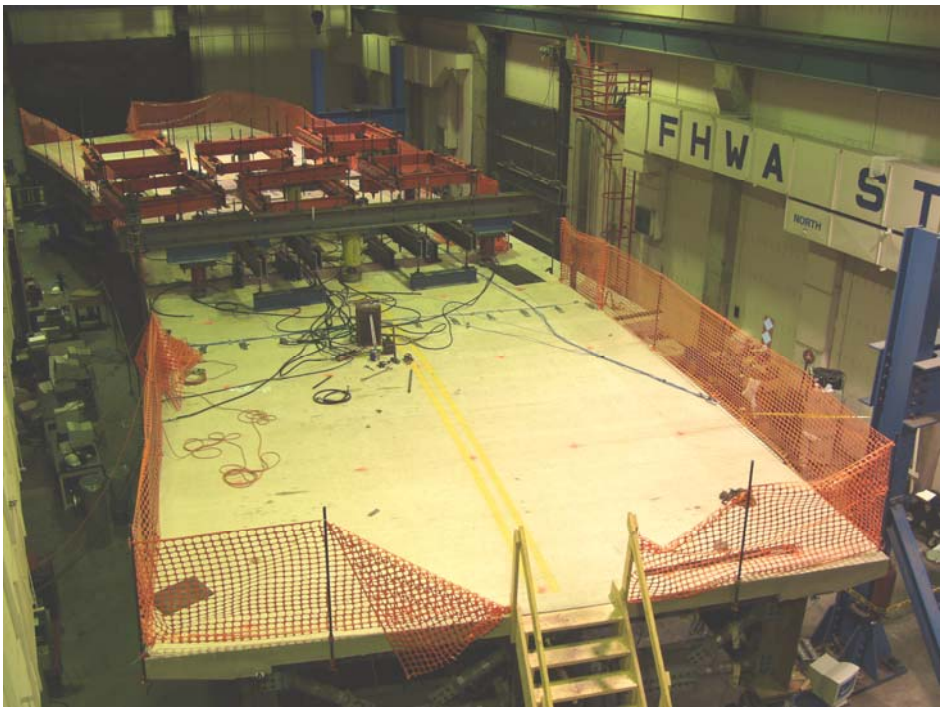

Figure 1.6.10. Composite test bridge with loading fixtures for the cyclic loading and ultimate load capacity tests, Tests 4a and 4b, courtesy of FHWA.

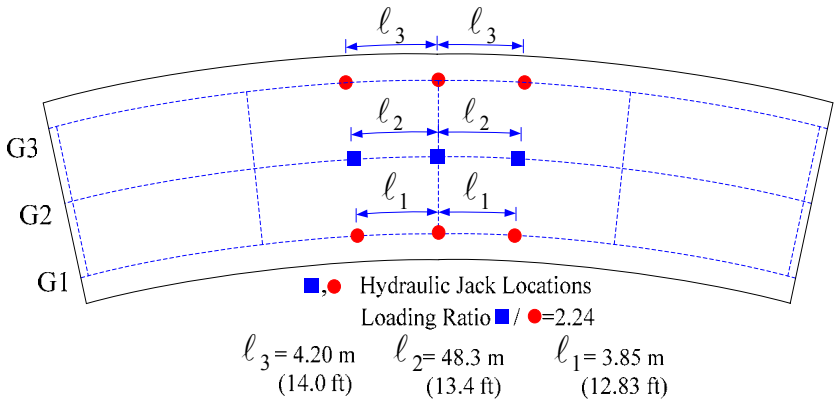

Figure 1.6.11. Nine hydraulic jacks positioned on both the inside and outside lanes of the test bridge slab for Tests 4a and 4b, corresponding approximately to two AASHTO design vehicles plus lane loads.

The above loadings in Tests 2 and 3 were applied repeatedly to the structure to investigate whether any progressive deformations occurred. The loads were also repeated in Test 4a, but in this case, they were repeated at various increasing levels up to a total load larger than can be potentially justified based on the M_p-based 1/3 rule for G3. The testing sequence was completed at the end of the repeated loading cycles by increasing the loads monotonically in Test 4b until a final ultimate strength condition was achieved.

An extensive array of instrumentation was installed to monitor the responses during the above testing sequences. For the final composite bridge configuration, there were 1344 channels of resistance strain gages as well as 80 channels of vibrating wire gages. G3 had the most extensive instrumentation to monitor its web and flange deformations due to general major-axis and flange lateral bending as well as plate bending (e.g., web bend buckling, shear buckling, and general bulging and distortion due to torsional loadings). Also, several of G3's transverse stiffeners were gauged. Two lines of longitudinal rebar and concrete gages were placed across the full width of the slab near the midspan of the bridge, and additional lines were also placed at the 1/4, 3/8, 5/8 and

3/4 span locations. Line gages were also placed in the slab at various positions to measure radial slab strains. Thirty deflection potentiometers were used to monitor vertical and radial deflections, 15 tilt meters were installed to measure rotations, and 15 LVDT's were installed to measure longitudinal, radial and vertical displacements of the slab relative to the girders. The total reactions were monitored via load cells at the bearing locations. In addition, a laser scanning system was employed to map the displacements of G3's web. Finally, a system of 20 channel fiber optic strain gages was installed in the slab for the purposes of evaluating its potential, and thermal and photoelastic stress analysis systems were employed for interpreting detailed responses of the girder webs. The above instrumentation was targeted at measurements not only pertaining to the ultimate strength of the bridge system, but also at quantifying the behavior at service and fatigue load levels.

This dissertation focuses on synthesis and assessment of the composite bridge test measurements, including comparison to refined finite element analysis predictions. Further information about the composite bridge construction and testing can be found in Wright and Beshah (2006) and Beshah (2006).

1.7 Organization

Chapter 2 addresses the elastic analysis and design of the composite test bridge. A brief introduction to the unified AASHTO (2004b) flexural resistance equations used in the design of the composite test bridge is provided first. Secondly, this chapter focuses on the finite element modeling approaches utilized for the elastic analysis and design of the test bridge. The noncomposite and composite girder elastic responses obtained from

the first- and second-order analyses are summarized. This is followed by detailed discussions of the test bridge component designs.

Chapter 3 presents key additional considerations necessary for the full nonlinear FEA simulation of the composite test bridge. These include loading schemes, measured stress-strain curves and corresponding representations utilized in the material models. This chapter also evaluates the composite action between the steel I-girders and the bridge concrete slab and discusses how potential interface flexibility affects the overall strength behavior of the composite test bridge. Next, other modeling considerations including the effects of residual stresses, the influence of concrete creep and shrinkage and the effects of geometric imperfections are presented along with their modeling treatments in the full nonlinear FEA solutions. The full nonlinear FEA analyses are executed in a single continuous process to simulate the dead load effects on the noncomposite structure, followed by the influence of slab shrinkage strains and finally the effects of applied loads on the composite structure.

Chapter 4 presents various measured bridge responses, along with the corresponding FEA solutions, to assess the state of the bridge at several stages of the construction and subsequently after each of the repeated loading tests. First, measured no-load camber values for the three test bridge girders are presented first and are compared to corresponding nominal cambers specified in the engineering drawings. Then, the bridge dead load responses at the end of steel erection are presented. The overall girder reactions, deflections and flange major-axis and lateral bending stresses are discussed. This is followed by a discussion of the bridge responses at the end of the concrete casting operations and a comparison to corresponding FEA solutions. Next, the results of Tests 2

and 3 are provided and compared to corresponding FEA solutions. Emphasis is placed on the effects of these two tests on the response of the test bridge in Tests 4a and 4b. Finally, this chapter focuses on the bridge responses obtained during the repeated loading cycles in Test 4a. The implications of the repeated loading on the subsequent ultimate load test (Test 4b) responses are discussed.

In Chapter 5, the results from the ultimate loading test of the composite test bridge (Test 4b) are assessed, including correlation with extensive linear and nonlinear finite element analysis solutions. The overall bridge deformations, vertical and radial deflections at midspan, cross-section deformations and overall girder end reactions are presented first. This is followed by a detailed discussion of various component responses. These responses include major-axis and lateral bending strains in the steel sections, equivalent plastic strains on the steel sections, radial and longitudinal slab stresses and corresponding strains, damage evolution in the slab concrete, crack patterns in the slab, cross-frame member forces and behavior of intermediate transverse stiffeners. This chapter then closes with a discussion of the force transfer mechanisms among the test bridge girders for the noncomposite dead load and composite live load configurations. This is accomplished by looking at FEA internal moment and shear force diagrams at the end of the concrete casting operations and at a few significant load levels during the ultimate live load test. In particular, the implications at the M_p-based 1/3 rule load level on G3 are studied.

Chapter 6 presents the results of the parametric FEA studies of other curved I-girder bridge systems. A total of 10 parametric FEA cases are considered to evaluate the system ultimate strength behavior. These cases are outlined in Section 1.4.4.

Chapter 7 provides a summary of this research as well as key observations made in the study. This chapter closes by identifying future research needs.

Appendix A provides detailed test bridge responses obtained from the first- and second-order elastic design-analyses for the noncomposite and composite configurations. The presentation focuses on the girder major-axis and lateral bending stress variations along the normalized length of each girder. Appendix B presents the girder flexural design, web shear design, bearing stiffener design, connection plate design, cross-frame member design and shear connector design calculations, closing with a succinct summary of key design checks. Appendix C presents additional detailed results of the repeated loading studies from Test 4a not shown in Chapter 4. Measured and predicted midspan slab longitudinal strain variations across the bridge cross-section are provided at various significant load levels. In addition, measured and predicted girder major-axis and lateral bending strains are compared, followed by an assessment of the relative slip displacements measured at the ends of the composite girders in the longitudinal direction and the radial slip displacements measured at the midspan of G3. Appendix D presents additional detailed results of the final monotonic loading test of Test 4b not shown in Chapter 5. Measured and predicted member axial force variations in the bottom chord, diagonals and top chord of each cross-frame are provided first. This is followed by detailed relative slip displacements measured at the ends of the composite girders for the longitudinal direction and the radial slip displacements measured at the midspan of G3. Finally, Appendix E provides the detailed derivation of a new kinematic definition for a multi-point constraint (MPC) between the girder flange and slab nodes.

CHAPTER 2

ELASTIC ANALYSIS AND DESIGN OF THE TEST BRIDGE

2.1 Overview

The design of the composite test bridge is performed in accordance with the newly adopted AASTHO (2004b) Specifications. The most important feature of the new AASHTO provisions is the implementation of unified resistance equations applicable to both curved and straight bridge girders. The composite test bridge studied in this research is designed to investigate the behavior at a number of the limits of the new Specifications.

The analytical models used to calculate the elastic bridge responses are constructed using the finite element software ABAQUS 6.4-1 (HKS 2004). The general-purpose displacement-based four-node shell element, S4R, is used to model the girder webs and bridge slab while the two-node beam element, B31, is used to model girder flanges, stiffeners and connection plates. This approach captures the influence of web distortion and general three-dimensional slab actions on the bridge response, while providing substantial economies with respect to modeling of the flange, stiffener and connection plates. For these latter components, distortion of the cross-section tends to be small. Even local buckling type deformations of these components are captured accurately via the beam element torsional deformations. The S4R shell element is a large strain shell element based on an exact geometric description of the large rotation kinematics. This element allows for transverse shear deformation, but the Kirchhoff thin shell assumption is enforced numerically as the shell thickness decreases (HKS 2004). Five integration

points are used through the thickness of the shell elements for steel plates, and nine integrations points are used for the shell representation of the slab. The B31 beam element is based on Reissner-Mindlin beam theory, and thus accounts for transverse shear deformation similar to the S4R shell element. Five integration points are used in both directions through the rectangular cross-section of the component plates in the B31 element. For the elastic analysis of the test bridge, both the steel and the concrete are modeled as isotropic elastic materials. B31 beam elements and the T31 truss element are utilized to model the cross-frame members for the bridge analysis.

The numerical solution provided by the finite element models tends toward the exact solution, for a given structural idealization, with increasing mesh density. However, high mesh refinement can significantly increase the solution time. Preliminary studies by the author indicated that sixteen shell elements through the depth of the web and 32 elements across the width of the bridge slab yield converged solutions. The number of elements in the direction of the girder length is set to maintain an element aspect ratio of approximately one in the web panels as well as in the bridge slab. A multi-point constraint is utilized at the interface between the steel girders and the concrete slab, to accommodate an abrupt transition from a finer finite element discretization for the steel I-girders to a coarser discretization for the concrete slab.

Section 2.2 first provides a brief introduction to the AASHTO (2004b) resistance equations used in the flexural design of the composite test bridge. Section 2.3 then focuses on the detailed finite element modeling approaches utilized for the elastic analysis and design of the test bridge. In Section 2.4, results of noncomposite and composite girder elastic responses obtained from first- and second-order analyses are

presented. Finally, details of the various test bridge component designs are summarized in Section 2.5. These include the girder flexural design, cross-frame member design, shear stud design, web shear design, intermediate stiffener design, bearing stiffener design and connection plate design.

2.2 AASHTO (2004b) Flexural Resistance Equations

In general, the girder flexural resistance per (AASHTO 2004b) can be expressed in terms of elastic major-axis and lateral bending stresses as :

$$f_{bu} + \frac{1}{3} f_{\ell} = \phi_f F_n \tag{2.1}$$

where $\phi_f = 1$ is the resistance factor for flexure, f_{bu} is the flange stress calculated without consideration of flange lateral bending, f_{ℓ} is the flange lateral bending stress, and F_n is the nominal flexural resistance of the flange.

Equation (2.1) can be derived by considering one of the flanges of an I-girder subjected to combined major-axis and lateral bending. The lateral moment in the flange is related to the elastically-computed flange lateral bending stress, f_{ℓ}, by the equation

$$M_{\ell} = \frac{f_{\ell} b_f^2 t_f}{6} \tag{2.2}$$

If the flange behaves compactly, it can develop the strengths associated with the idealized fully plastic stress distribution shown in Figure 2.2.1. Within this idealized fully plastic stress distribution, the lateral moment is generated by the strips of width c at the tips of the flange, and the remaining width of the flange ($b_f - 2c$) develops the flange

force associated with the major-axis bending moment. By equating the elastic flange force due to major-axis bending, $f_{bu} b_f t_f$, to this fully plastic flange force, $F_y (b_f - 2c) t_f$, the elastically-computed major-axis bending stress associated with the flange plastic strength may be expressed as

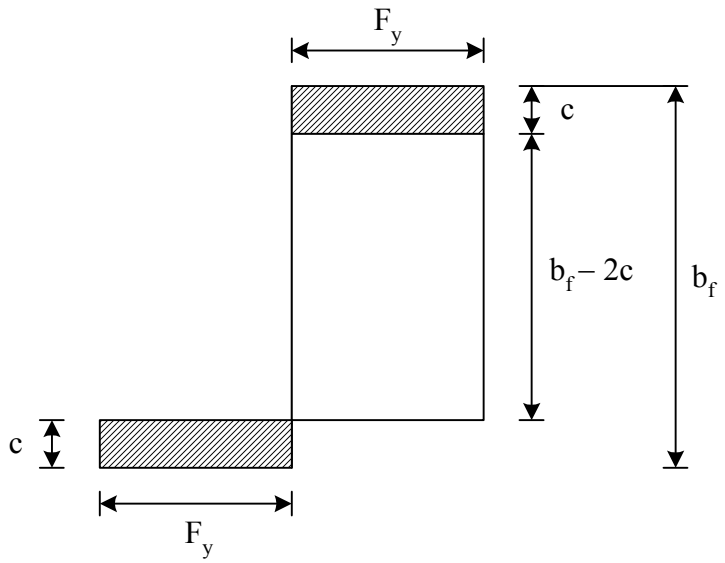

Figure 2.2.1. Idealized plastic stress distribution in a flange due to lateral and major-axis bending.

$$f_{bu} = F_y \frac{b_f - 2c}{b_f} \tag{2.3}$$

Similarly, by equating the right-hand side of Eq. (2.2) to the flange lateral bending moment associated with Figure 2.2.1, one obtains

$$\frac{f_\ell b_f^2 t_f}{6} = F_y c\, t_f (b_f - c) \tag{2.4}$$

This quadratic equation can be solved for the width c shown in Figure 2.2.1 to obtain

$$c = \frac{b_f}{2}\left(1 - \sqrt{1 - \frac{2}{3}\frac{f_\ell}{F_y}}\right) \tag{2.5}$$

Finally, by substituting Eq. (2.5) into Eq. (2.3), an expression for the elastically-computed flange major-axis bending stress (f_{bu}) associated with the plastic strength of the flange is obtained as a function of the elastically-computed lateral bending stress at the flange tips (f_ℓ) as

$$f_{bu} = F_y\sqrt{1 - \frac{2}{3}\frac{f_\ell}{F_y}} \tag{2.6}$$

For the practical design of bridge I girders, where the elastic stress f_ℓ is generally much smaller than F_y, e.g., $f_\ell \leq 0.6\ F_y$, Eq. (2.6) is accurately approximated by the following simple linear equation

$$f_{bu} = F_y - \frac{1}{3}f_\ell \tag{2.7}$$

Figure 2.2.2 compares the exact flange plastic strength (Eq. 2.6) and the stress-based one-third rule (Eq. 2.7) for a section with a base flange strength of $f_{bu} = F_y$. One can observe that the one-third rule equation closely approximates the analytical flange plastic strength although the prediction becomes slightly optimistic near the limit of $0.6\ F_y$. Eq. (2.7) is extended to address the influence of general member yielding and stability limit states on the maximum strength by changing F_y to $\phi_f F_n$, thus giving Eq. (2.1). This approximation is based on extensive comparisons to numerical and experimental results for girder strengths (White et al. 2001). For straight bridges, AASHTO (2004b) applies Eq. (2.1) to

slender-web noncomposite members, slender-web composite members in negative bending and noncompact composite members in positive bending, in Eq. (2.7). However, for curved bridges, AASHTO (2004b) applies Eq. (2.7) to all types of I-girders.

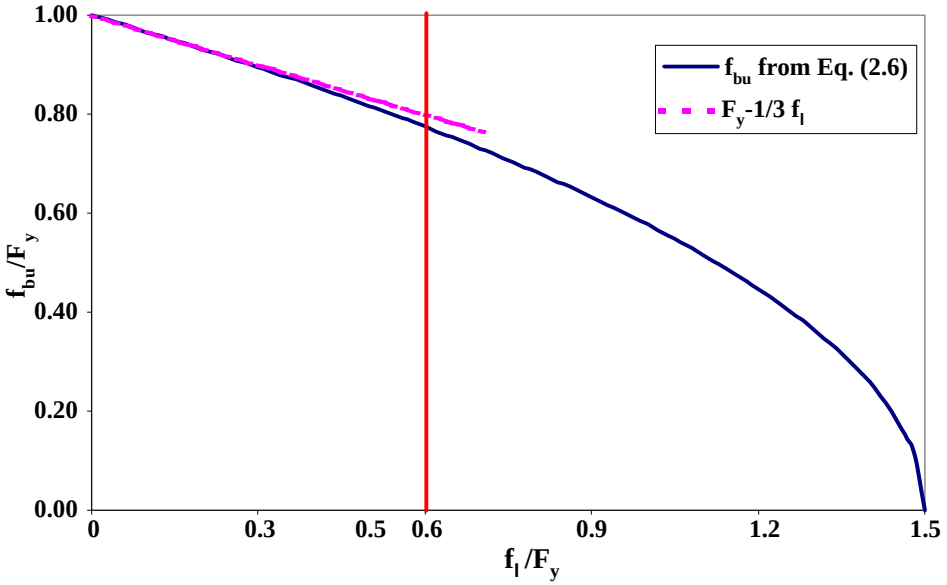

Figure 2.2.2. Comparison of the "exact" flange plastic strength and the stress-based one-third rule for a section with a base flange strength of $f_{bu} = F_y$.

Equation (2.2) considers only the theoretical plastic strength of an isolated flange. However, the web also provides a minor but significant contribution to the flexural resistance in general. The corresponding fully-plastic strength of a compact I-section subjected to combined major-axis and flange lateral bending can be approximated by

$$M_u + \frac{1}{3} f_\ell S_x = M_p \tag{2.8}$$

This equation is derived for a compact section that can develop its fully plastic strength. That is, the strength reduction is not considered due to local flange or lateral-torsional buckling. However, based on curve fitting to analytical, numerical and experimental

results, Eq. (2.8) is extended to noncomposite members and composite members in negative bending with compact or noncompact webs, and to compact composite sections in positive bending, by changing M_p to $\phi_f M_n$. The resulting girder flexural strengths per (AASHTO 2004b) are

$$M_u + \frac{1}{3} f_\ell S_x \le \phi_f M_n \tag{2.9}$$

where M_u is the member major-axis bending moment, f_ℓ is the flange lateral bending stress, S_x is the elastic section modulus about the major-axis of the section to the flange under consideration, taken generally as $M_{yf}/F_{yf,}$ and $\phi_f M_n$ is the factored flexural resistance in terms of the member major-axis bending moment. White and Grubb (2004) summarize the background and usage of these equations, termed the "one-third rule," and provide references to more detailed research reports and papers on their development. As noted in Section 1.2.2, AASHTO (2004b) presently does not allow the use of Eq. (2.9) for curved I-girder bridges, due to the lack of extensive information on the implications of the larger extent of girder yielding on bridge system responses at the Strength limit states.

Similar to the amplification of internal bending moments in beam-column members, the flange lateral bending stresses in curved or straight I-girders are amplified due to stability effects. AASHTO (2004b) provides the following simple lateral bending amplification equation to account in an approximate fashion for these second-order effects:

$$f_\ell = \left(\frac{0.85}{1 - \frac{f_{bu}}{F_{cr}}} \right) f_{l1} \geq f_{l1} \tag{2.10}$$

where $f_{\ell 1}$ is the first-order compression-flange lateral bending stress at the section under consideration, f_{bu} is the largest value of the compressive stress in the flange under consideration without consideration of flange lateral bending, and F_{cr} is the elastic lateral torsional buckling stress for the flange under consideration. In some cases (i.e., some construction conditions with larger unsupported lengths), this amplification formula tends to be significantly conservative. In these situations, the Engineer may wish to consider a direct geometric nonlinear analysis to more accurately determine the second-order effects within the superstructure.

The term $\phi_f F_n$ in Eq. (2.1) is generally less than or equal to $\phi_f F_{yf}$ whereas $\phi_f M_n$ in Eq. (2.9) is equal to the factored plastic moment in many cases. However, for curved bridges, the AASHTO (2004b) provisions restrict the design of *all* I-section members to Eq. (2.1). This restriction is due to a limited understanding of the influence of the member yielding necessary to develop larger I-girder strengths on the system response of curved I-girder bridges (specifically, the inelastic redistribution which may occur prior to reaching the critical strength limit and the impact of this redistribution on the validity of the internal forces and moments obtained from a linear elastic analysis). The test bridge, and other bridge configurations studied parametrically as part of this research, are targeted at providing the necessary understanding to potentially allow the use of Eq. (2.9) with $\phi_f M_n$ up to $\phi_f M_p$ where applicable in both curved and straight I-girder bridges.

2.3 Elastic FEA Modeling of the Test Bridge

2.3.1 FEA Discretization

Figure 2.3.1 shows a typical finite element model utilized for this study. The measured dimensions are used for the section dimensions of the I-girders while nominal dimensions are used for the overall girder geometries such as radius of curvature and length of each girder. The finite element model of the test bridge is constructed using the ABAQUS 6.4.1 analysis system (HKS 2004).

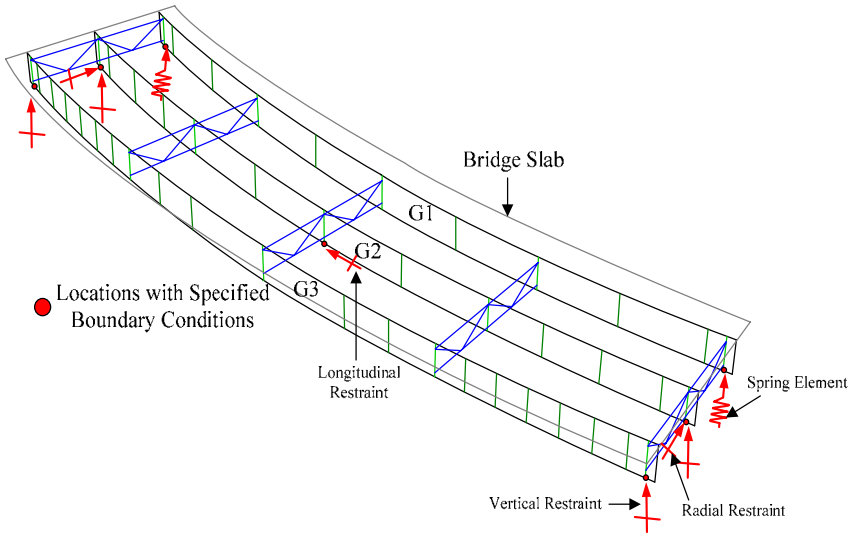

Figure 2.3.1. Perspective view of overall bridge FEA model with specified boundary conditions.

Sixteen elements are used through the depth of the web in all the girders. The number of elements along the girder length is selected such that the aspect ratio of each shell element is close to one. The girder webs and the concrete deck are modeled using the S4R element, a 4-node quadrilateral displacement-based shell element with one-point integration In the through thickness direction of the shell elements, five integration points are used for the steel I-girders and nine integration points are used for the concrete

deck. More integration points are recommended for the concrete deck since the progressive failure of the concrete section cannot be adequately captured with a smaller number of integration points through the thickness (HKS 2004). Figure 2.3.1 also shows specified boundary conditions used in the FEA model. Section 2.3.3 discusses these boundary conditions in detail.

Figure 2.3.2 shows a cross-section schematic of the bridge FEA model. The overhangs are represented by rectangular sections with the average thickness of the physical tapered slab thickness at these locations (see Figure 1.5.1). The remainder of the concrete slab is represented by a series of rectangular sections.

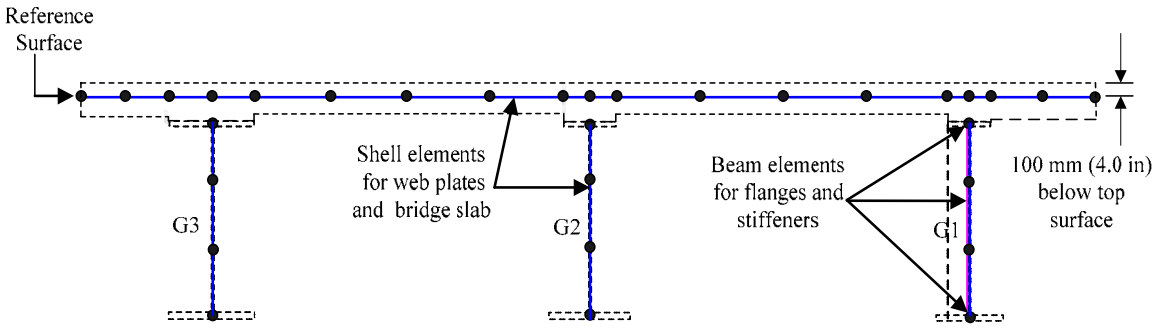

Figure 2.3.2. Cross section schematic of bridge FEA model.

The majority of these rectangular sections have a nominal thickness of 8 in. The sections just above the girder top flanges have slightly larger thicknesses due to the girder haunches as shown in Figure 2.3.2. The reference surface where element nodes are located is positioned 100 mm (4.0 in) below the slab top surface across the deck, and the centroidal location of the concrete deck is defined in relation to this reference surface. The nodal offset option is used within the shell element definitions to offset the element nodes from the mid-thickness of the elements.

A coarser finite element grid is used generally for the modeling of the concrete slab. Thirty-two shell elements are used across the total slab width and the number of shell elements in the slab along the bridge length is set such that the element aspect ratio is approximately equal to one. The mesh density in the slab in the length direction is one-half that used in the I-girders. The ABAQUS beam-type multi-point constraint is used to accommodate this transition between the girder and slab finite element discretizations.

Two node beam elements (B31) are used to model the top and bottom flanges of each girder and the transverse stiffeners (the bearing stiffeners, cross frame connection plates and intermediate transverse stiffeners). Except for the bearing stiffeners and the transverse stiffeners used as connection plates to tie individual steel girders to cross frames, the intermediate transverse stiffeners are omitted from the FEA models for elastic design analysis. This is due to the fact that the intermediate transverse stiffeners typically do not have sufficient strength to elastically restrain the bottom flange lateral movement. That is, they are not able to transfer the torsional restraint from the bridge slab at the top flange down to the level of the bottom flange without yielding in transverse bending prior to reaching the Strength load levels. In fact, preliminary full nonlinear FEA studies indicated that a plastic hinge may be formed in lateral bending at the top of the transverse stiffeners at Strength load levels. Therefore, by neglecting the intermediate transverse stiffeners in the design-analysis models, a conservative design of the I-girders is ensured with respect to this issue. However, the intermediate transverse stiffeners are included in the subsequent full nonlinear FEA models. Other modeling changes made to the elastic FEA models for the purpose of conducting full nonlinear analyses are discussed in Chapter 3. The top chord and diagonal members of the cross-frames are represented by

T31 truss elements. B31 beam elements are used to model the bottom chords of the cross-frames such that the FEA model of these components is stable in the direction normal to the plane of the cross-frames.

2.3.2 Interface Modeling between Concrete Slab and Steel Girders

A beam-type multi-point constraint (MPC) is used to connect the top flange nodes of the steel girders to the test bridge slab nodes unless noted otherwise, modeling ideal full composite action between the test bridge slab and the steel I-girders. It should be noted that with the use of the beam-type MPC for the composite action, there is no consideration of relative bond slip at the interface region and stud deformation, not to mention the behavior of surrounding concrete material. This may seem to be an overly idealized modeling approach for the interface region. However, since the number of shear studs used in the test bridge is governed by fatigue design criteria instead of strength design criteria, the degree of restraint provided by the shear studs is sufficiently large such that the relative slip at the interface region between the concrete and steel is very small at the AASHTO strength design loading conditions. Therefore, the beam-type MPC can be considered to be representative of the composite action in the composite test bridge and appropriate for usual design applications. Nevertheless, there is a possibility that the shear studs may experience some inelastic deformation due to the gradual loss of structural integrity at significantly higher loads levels than the design load levels, as in the case of the ultimate load test of the composite test bridge. This concern is addressed in detail in Section 3.5 by investigating detailed load-slip response of the kinds of shear studs used in the composite test bridge, as well as a few modeling approaches and their influence on the overall strength behavior of the test bridge.

2.3.3 Displacement Boundary Conditions

The physical test setup of the composite test bridge consisted of placing each of the three bridge girders on two steel pedestals located at a distance of 26.25 m (86.0625 ft) for G1, 27.45 m (90 ft) for G2 and 28.65 m (93.9375 ft) for G3, from center to center along the curved members. Figure 2.3.3 shows the schematic of the physical boundary conditions at each of the six bearings at the end supports of the test bridge girders.

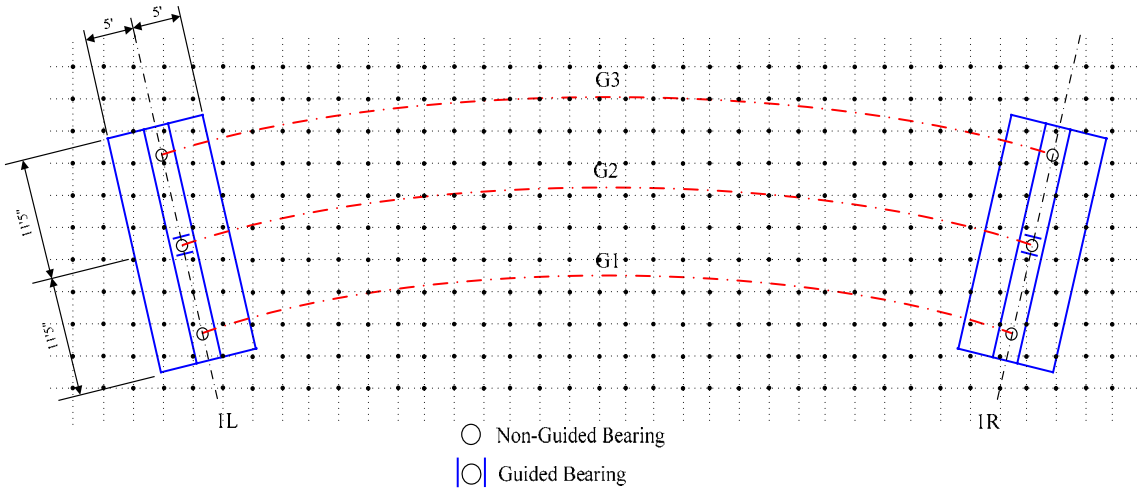

Figure 2.3.3. Plan view of support structure, courtesy of FHWA.

The rationale behind the choice of this set of boundary conditions is that they provide the minimum amount of horizontal restraint to the bridge while still maintaining equilibrium (Grubb and Hall 1998). The bearings at the ends of G1 and G3 provide vertical support only, since they are non-guided bearings intended to allow free translation of the girder in tangential and radial directions, as well as the rotation of the girder about all three axes, at both ends. Conversely, the bearings at the ends of G2 are guided tangentially, providing radial restraint on the bridge. Similar to the end bearings of G1 and G3, free rotation of all girders about all three axes is permitted.

In order to accommodate large loads and significant rotations at the bearings, spherical expansion bearing assemblies are used for the test bridge girders. The spherical bearings consist of woven PTFE (Teflon) either bonded or mechanically fastened to a steel plate with a concave spherical surface. This plate then mates with a solid stainless steel plate with a convex spherical surface. The PTFE provides a low friction interface and the mating spherical surfaces allow for rotation about any axis. To provide freedom of translation, a 16-gage stainless steel sheet is seal welded around its entire periphery to the sole plate that is placed on top of each bearing. The stainless steel mates with PTFE bonded to the flat top of the steel concave plate to allow the bearing to translate freely. The guides to prevent translation in the radial or tangential direction are integral with the sole plate. That is, the sole plate is recessed directly above the bearing to allow translation of the bearing in the desired direction and to prevent translation of the bearing in the orthogonal direction. Figure 2.3.4 shows the girder bearing details.

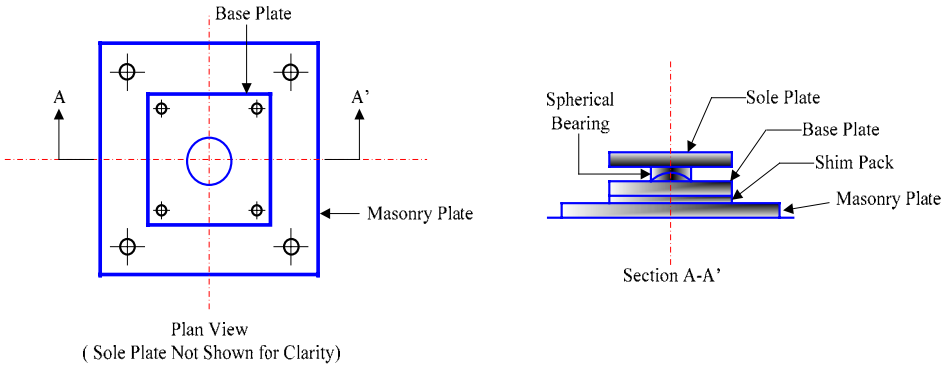

Figure 2.3.4. Girder bearing details used in the support structure.

Along with the spherical bearings, a special three-directional load cell was bolted to the pedestal and placed directly under the spherical bearings, with the center of the load button coinciding with the center of the web-flange juncture. Figure 2.3.5 shows a

schematic of a bearing assembly that consists of a load cell, non-guided spherical bearing, and a Teflon pad. This bearing arrangement allows measurement of vertical reactions, as well as small radial and tangential reactions at the support. Figures 2.3.6 and 2.3.7 show the instrumented bearing assemblies for G2 and G3, respectively.

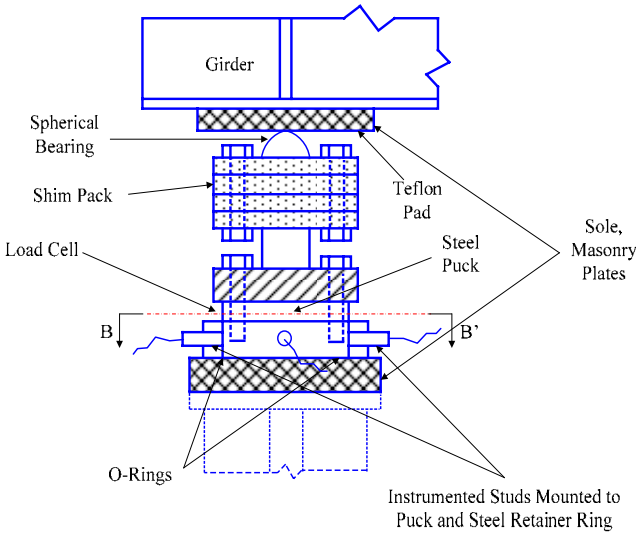

(a) Schematic of bearing assembly

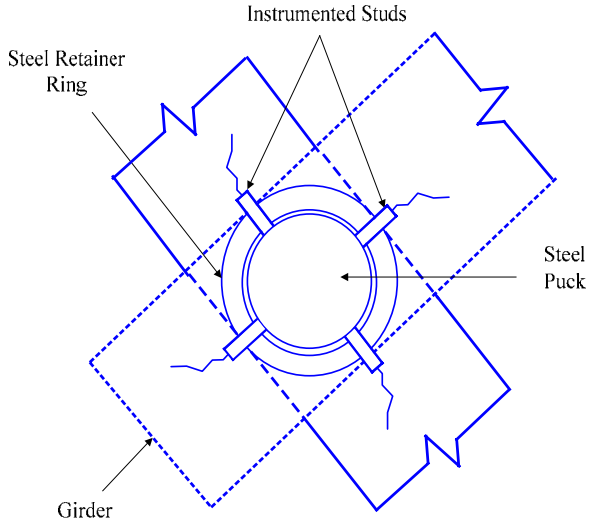

(b) Section B-B'

Figure 2.3.5. Schematic of bearing assembly that consists of a load cell, non-guided spherical bearing, and a Teflon pad, courtesy of FHWA.

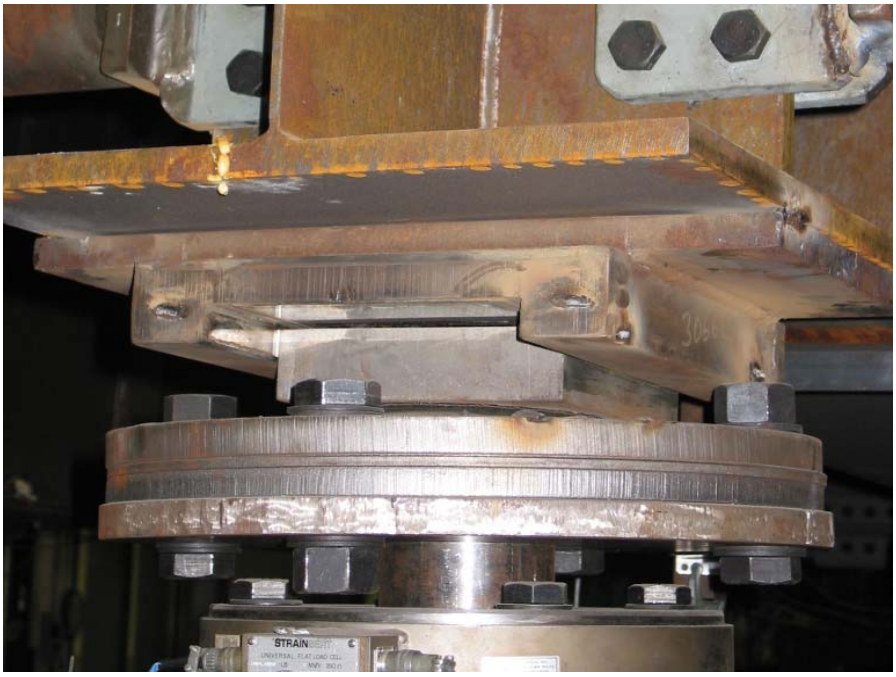

Figure 2.3.6. Guided bearing assembly arranged at the supports of the middle girder, G2, to provide radial restraints, courtesy of FHWA.

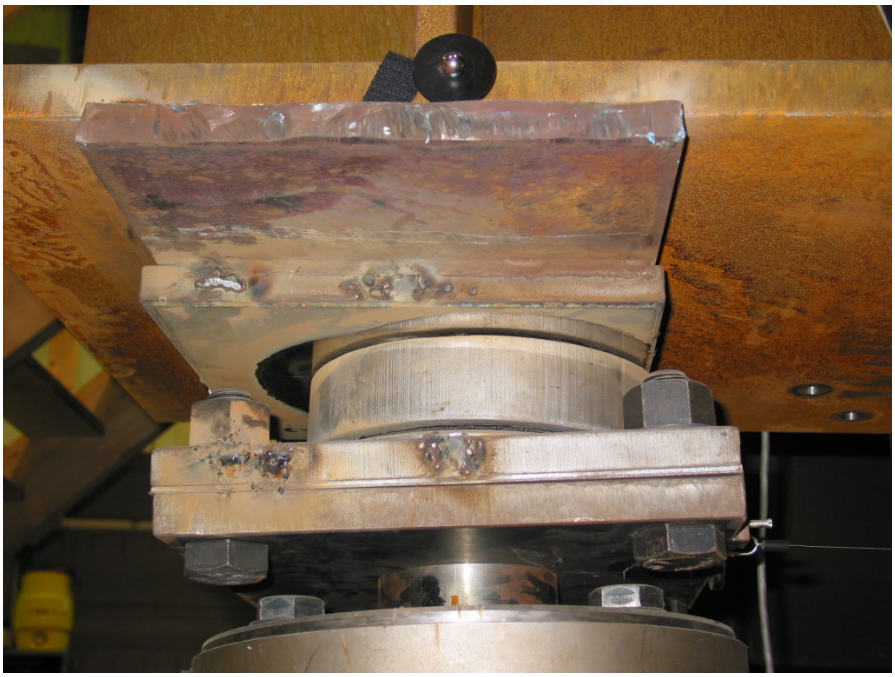

Figure 2.3.7. Non-guided bearing assembly arranged at the support of the outside girder, G3, to allow for free translation, courtesy of FHWA.

In the finite element analysis, the vertical supports at the G3 ends are modeled by restraining the displacements in the vertical direction (see Figure 2.3.1). That is, an ideal roller support is specified, and the girder is free to move along the longitudinal and tangential directions at this location. However, the vertical supports at the G1 ends are modeled as the vertical restraints represented by spring elements with a large elastic stiffness in compression and zero stiffness for net tension. That is, the vertical supports at the G1 girder ends are assumed to be rigid in compressive contact over the full area of the bearing plate, but uplift is allowed at any locations of the bottom flange that would tend to lift off of the bearing plate due to the deformations of the girder. This modeling consideration is important to account for a possible uplift of this girder during the test.

Since G2 has guided spherical bearings aligned in the tangential direction, ideal radial restraints are specified at these support locations in addition to the vertical restraints. The G2 ends are free to move in the longitudinal direction. Finally, there is no specific tangential restraint offered in the experimental setup. To maintain the symmetry of bridge geometry and applied loads, a tangential (longitudinal) restraint is provided at the midspan bottom flange of G2 to prevent rigid body motion in the longitudinal direction in the analysis model (see Figure 2.3.1).

2.3.4 Material Properties

Table 2.3.1 provides a summary of measured material properties used for the design analysis of the test bridge and the design check of the test bridge components. All the bridge responses and design checks presented subsequently are based upon the measured section dimensions and elastic material properties obtained from the bridge test.

Table 2.3.1. Measured material properties used for the bridge response from the elastic bridge FEA and design checks (Beshah 2006).

Concrete†	f'_c MPa (ksi)	33.86 (4.914)
	E_c †† MPa (ksi)	22,790 (4,034)
Steel	F_y	400 MPa (58 ksi) for all top and bottom flanges of bridge I-girders, 441 MPa (64 ksi) for all web panel of the bridge I-girders, with exception of bottom flange of G3
		496 MPa (72 ksi), bottom flange of G3
		503 MPa (73 ksi), cross-frame members
	E_s	204 GPa (29,590 ksi) for elastic design analysis, 200 GPa (29,000 ksi) for design check of the bridge I-girders, with exception of cross-frame members
		207 GPa (30,000 ksi), cross-frame members
Re-bar	F_y MPa (ksi)	413 (60)
	E GPa (ksi)	200 (29,000)

† : The compressive strength is based on six cylinder tests (150 mm (6 in) × 300 mm (12 in)) cured under standard laboratory conditions and tested at a specified rate of loading at 298 days of age.

†† : The elastic modulus of concrete is obtained based on the measured concrete strength as $E_c = 1820\sqrt{f'_c}$ (ksi).

2.3.5 Noncomposite Construction Loads

For unshored construction of composite bridges, the steel superstructure alone must resist the noncomposite construction loads such as the self weight of the steel superstructure and weights of forms, steel reinforcement, wet concrete and construction equipment, assuming that wet concrete and formwork do not contribute any stiffness and strength to the bridge system during concrete casting. In the analysis model, the self weight of the steel girders is based on the density of the steel (taken as 7833 kg/m^3

(0.283 lb/in^3)) and the section profile dimensions. To represent the weight of cross-frames, the measured total weight of each cross-frame, 422 kg (937 lbs), is applied at the ends of top chord of each cross-frame. This is because the weight of miscellaneous attachments such as gusset plates and connecting bolts as shown in Figure 2.3.8 constitutes a significant portion of the total weight of each cross-frame and can be not included properly in the FEA model, unless they are modeled explicitly.

Uniformly distributed line loads are applied to the top flange of the girders to represent the weight of the forms, reinforcement, wet concrete, and construction equipment. These loads are calculated based on the tributary width of each girder across the bridge cross-section. The tributary widths are 2.25 m (7.375 ft) for G1 and G3 and 2.67 m (8.75 ft) for G2.

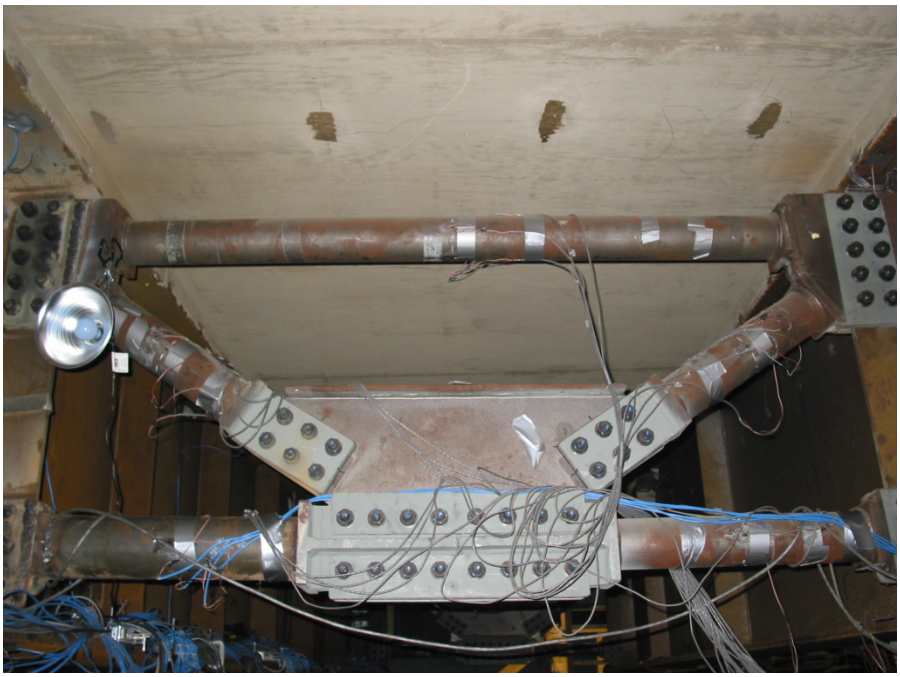

Figure 2.3.8. Instrumented midspan cross-frame attached to G3, courtesy of FHWA.

The magnitudes of the distributed loads applied to the bridge FEA model are as follows:

- Concrete slab: total weight = 940 kN (211.3 kips)

  1) The density of reinforced concrete in the bridge slab is taken as 23.81 kN/m^3 (151.6 pcf). The concrete weight per unit area in the interior slab, based on a uniform thickness of 200 mm (8 in), is 0.2 m × 23.81 kN/m^3 = 4,762 Pa (8 in × 151.6 pcf / 12 in = 101.1 psf)

  2) The concrete weight per unit slab area in the overhangs, based on an average slab thickness of 238 mm (9.5 in), is 0.238 m × 23.81 kN/m^3 = 5,655 Pa (9.5 in × 151.6 pcf / 12 in = 120 psf)

  3) The concrete weight per unit slab area of the 75 mm (3 in) concrete haunches, based on average top flange width and a 22 mm (7/8 in) top flange, is 0.053 m × 0.425 m × 23.81 kN/m^3 ≅ 536 N/m (2.125 in / 12 in × 17 in / 12 in × 151.6 pcf ≅ 40 lbs/ft)

- Formwork: total weight = 87.54 kN (19.68 kips)

  Form weight per unit slab area: 87.54 kN / 201 m^2 = 435 Pa (9.1 psf)

- Reinforcement: total weight = 40 kN (8.98 kips)

  Reinforcement weight per slab unit area: 40 kN / 201 m^2 = 200 Pa (4.1 psf)

- Construction equipment: Although the construction equipment used during the concrete placement may have significant loading effects in some cases, it was found that the effect of the equipment used in the construction of the test bridge on the test bridge responses was very small. Therefore, the weight of the construction equipments is neglected in the design-analysis. This assumption is

also justified for the test bridge because it is a simple span with end abutments aligned in the radial direction

Therefore, the magnitude of uniformly distributed line loads associated with the forms, reinforcement, wet concrete and construction equipment is taken as 12,250 N/m (70.0 lb/in) for G3 and G1 and 13,650 N/m (78.0 lb/in) for G2.

In addition to the weight of the above structural components, bridge structures in service typically must support additional composite dead loads from a future wearing surface, concrete barriers, utilities, etc.. However, since these components are not included in the test bridge, the weights of these components are not considered in this work.

Figure 2.3.9 shows overhang brackets attached to the outside girder (G3) prior to the concrete casting operations. The purpose of these brackets is to resist the weight of formwork and wet concrete until concrete is cured enough to develop a desired strength. The torques from the overhang brackets on the exterior girders are idealized as a uniformly distributed torque of 5,797 Pa × 0.915 m / 2 × 0.915 m = 7,953 N-m / m (121 psf × 3 ft / 2 × 3 ft = 546 ft-lb/ft) applied to G1 and G3 in a fashion that makes the top flange of these girders deflect toward the edge of the slab. This is converted to two equivalent horizontal line loads of 7,953 N-m/m (546 ft-lb/ft) / 0.915 m (3 ft, assumed depth to the bottom of the overhang brackets) = 2,651 N/m (182 lb/ft). The top line load is applied at the top flange, and the bottom one is applied laterally to the web at 0.915 m (3 ft) below the top flange, which simulates the potential effect of the overhang brackets framing into the webs of the exterior girders. The beneficial effects of the eccentric

bracket loads are not included when calculating the design lateral bending stresses in G1 under the construction loadings.

Figure 2.3.9. Overhang brackets attached to the outside girder (G3) prior to concrete casting operation, courtesy of FHWA.

In summary, Figure 2.3.10 shows a schematic illustrating the cross-section view of the noncomposite bridge FEA model subjected to uniformly distributed line loads from the wet concrete plus forms and reinforcing steel, equal and opposite horizontal line loads on G1 and G3 that are statically equivalent to the overhang torques, and concentrated forces representing the cross-frame weights. In addition to these loads, the self-weight of all the girder flanges, webs, stiffeners and connection plates are included in the analysis model via the weight density of the steel and the section dimensions. The applied eccentric bracket loads tend to increase the lateral bending stresses in the flanges of G3,

producing more conservative girder responses than when the eccentric bracket loads are not considered. Conversely, the eccentric bracket loads applied to G1 decrease the lateral bending stresses in the flanges of G1, resulting in less critical responses than when the bracket loads are not considered in the analysis model. Zero long-term composite dead loads are considered in the design of the test bridge. All of the bridge dead loads are assumed to be supported by the noncomposite steel superstructure. All the subsequent composite loads are assumed to be applied to the short-term composite cross-sections

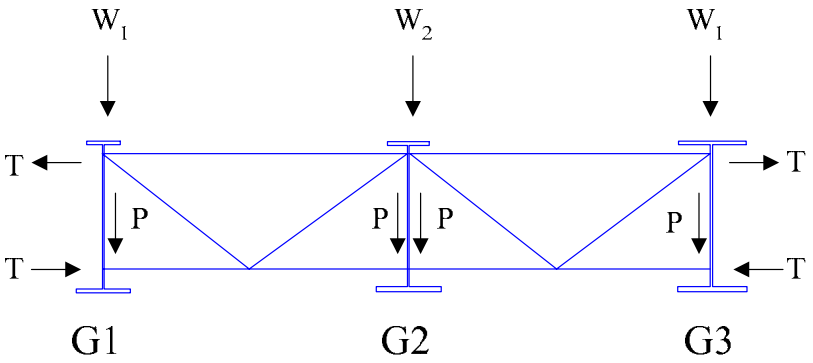

W_1,W_2 : Uniformly distributed noncomposite construction loads based on girder tributary width due to wet concrete + forms + reinforcement
T : Equivalent horizontal force associated with overhang torque
P : Concentrated force associated with cross-frame weight

Figure 2.3.10. Cross-section view of the noncomposite bridge FEA model subjected to construction loads as well as eccentric bracket loads (future wearing surface, concrete barrier and utilities are not included).

2.3.6 Design Live Loads for Flexure – Design Truck Load + Design Lane Load

The AASHTO design live load model consists of two different loads: the design truck load and the design lane load as shown in Figure 2.3.11a. The design truck, termed HL-93, is a model load that resembles a typical semi-trailer truck as shown in Figure 2.3.11b. The front axle is 35 kN (8 kips), located 4300 mm (14 ft) behind the drive axle is 142 kN

(32 kips), and the rear trailer axle is 142 kN (32 kips) and is positioned at a variable distance ranging from 4300 (14 ft) to 9000 mm (29.3 ft).

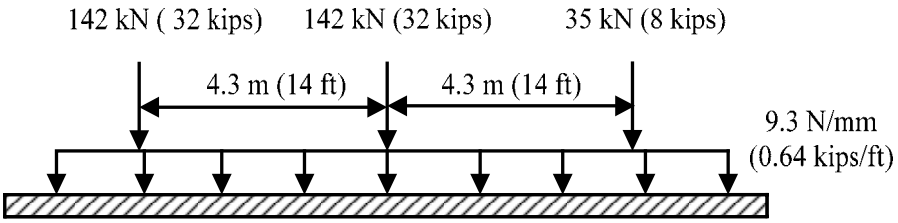

(a) lane load + design truck load

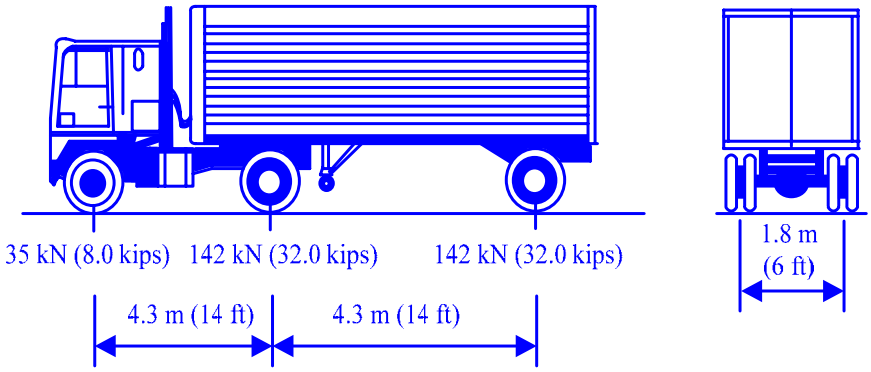

(b) characteristics of the design truck (HL-93)

Figure 2.3.11. AASHTO design live loads.

The design lane load is a uniformly distributed load of 9.3 kN/m (0.64 kips/ft) and is assumed to occupy a region 3000 mm (10 ft) transversely. The load effects of the design truck are applied simultaneously with the load effects of the design lane load. It is important to recognize that these loads are not designed to model any specific single vehicle or combination of vehicles, but rather a spectra of loads and their associated load effects.

In general, the placement of the live loads that gives a particular maximum load effect may not be obvious. This placement can be determined by using the influence surface for

a particular force or moment in combination with the prescribed loadings to establish the load positions. However, for the test bridge, the placement of the live loads that causes the maximum flexural effects at the girder midspan locations and the maximum shear effects at the girder ends can be easily established by inspection. For example, the maximum flexural effects at the girder midspan can be obtained by placing the lane load over the full length of the bridge and by placing the drive axle of the design truck at the midspan. Increasing the distance between the rear axles spreads the load and decreases the load effect in all cases for the test bridge. Thus, the smallest value of 4.3 m (14 ft) for the variable axle spacing is used in all the test bridge calculations.

The above critical load placement is used to determine the load effects for design of the test bridge girders. In lieu of a simple line girder analysis, refined three-dimensional FEA models are used to obtain the elastic stresses needed for the design of the test bridge girders. The following presentations of the live load calcluations focuses on the loading positions that produce the largest flexural effects within the girders, as well as the largest forces within the critical cross-frame located at the outside girder, G3, and at the middle of the bridge.

The curb is assumed to be located at 0.305 m (1 ft) inside of the edge of the slab. Typical parapets would be wider than this; nevertheless, this dimension is considered to be a reasonable small width allowance for the parapets. This assumption leads to the required consideration of two design lanes, each of width 3.28 m (10.75 ft). In what follows, the number of trucks and specific positions of truck wheel loads in the transverse direction of the test bridge are presented for the maximum loading effects on each girder.

Figures 2.3.12 and 2.3.13 illustrate the wheel load positions for two design trucks and the lane load positions for the maximum flexural loading effects on G3. Figure 2.3.12 shows that two AASHTO HL-93 trucks are positioned side-by-side with the second axle (the drive axle) of the vehicles located at the midspan of the test bridge, 4.3 m (14 ft) spacing between all the axles, and wheel transverse spacing = 1.83 m (6 ft).

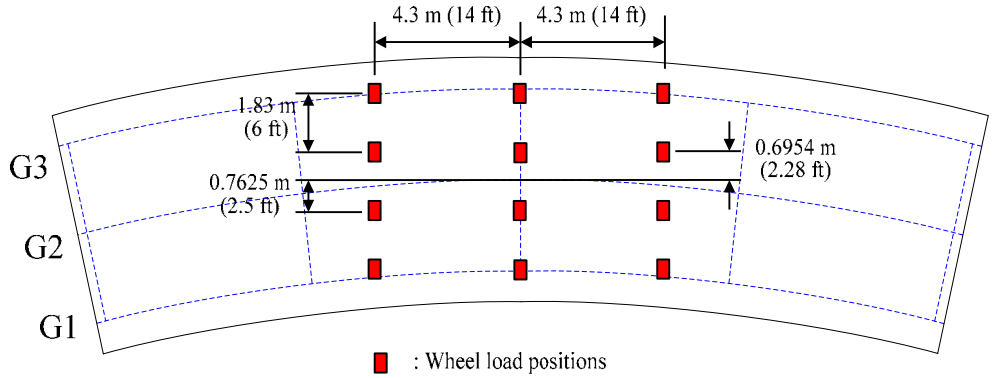

Figure 2.3.12. Wheel load positions associated with two design trucks inducing the maximum loading effects on the outside girder (G3) (Dynamic allowance factor 1.33 is included, but multiple presence factor is not included in this scheme).

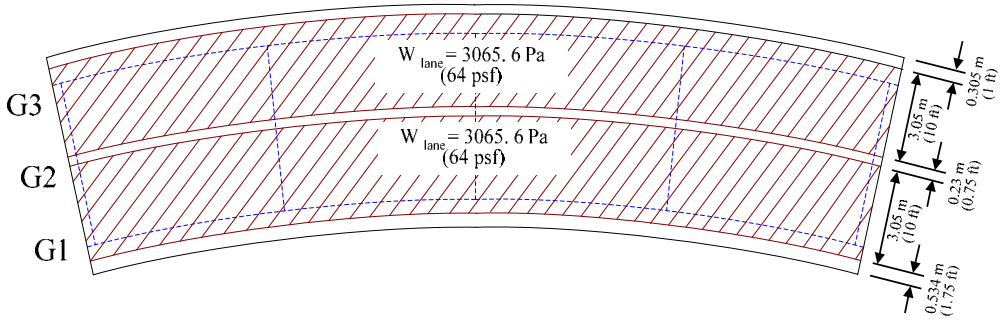

Figure 2.3.13. Lane load position associated with two design trucks inducing the maximum loading effects on the outside girder (G3) (Dynamic allowance factor 1.33 and multiple presence factor are not included in this scheme).

The front and back outside wheels of the outer truck are positioned on top of G3 (0.61 m (2 ft) inside of the "curb" in the radial direction). This positions the middle outside

wheel of the outer truck at 0.753 m (2.47 ft) inside of the curb at the bridge midspan, or 0.143 m (0.47 ft) inside of G3. The front and back outside wheels of the inside truck are positioned at 0.61 m (2 ft) radially inside of the outside edge of its design lane, which is directly over G2. This position of the middle outside wheel of the inside truck is at 0.762 m (2.50 ft) inside of G2. The lane loads of 9.3 kN/m (0.64 kips/ft) are uniformly distributed over a 3.05 m (10 ft) radial width within each design lane as shown in Figure 2.3.13, i.e., a uniform pressure of 3066 Pa (64 psf) is applied over a 3.05 m (10 ft) radial width within each design lane. The outside edge of the lane loads is positioned at the outside edge of the corresponding design lanes.

For the maximum flexural loading effects on G2, it is found that the AASHTO live load model is nearly the same as that for G3 for this bridge. The only differences are:

- The outside design vehicle is moved inward toward the center of curvature of the bridge such that the inside wheel of its middle axle (located at the midspan of the bridge) is positioned at 0.61 m (2 ft) outside of the edge of the design lane (at G2) as shown in Figure 2.3.14. The net inward movement of the design vehicle is only 0.085 m (0.28 ft) from that associated with the maximum loading effects on G3. This reduces the net torsional reaction from the design vehicles at the ends of the bridge by approximately 3 percent.
- The outside lane load is moved to the inside edge of this lane as shown in Figure 2.3.15. That is, the area over which the uniform pressure of 3066 Pa (64 psf) is applied is moved 0.23 m (0.75 ft) inward toward the center of curvature of the bridge from that associated with the maximum loading effects on G3. This reduces the net

torsional reaction from the lane loading at the ends of the bridge by approximately 10 percent. It changes the maximum flexure on G2 by a smaller percent.

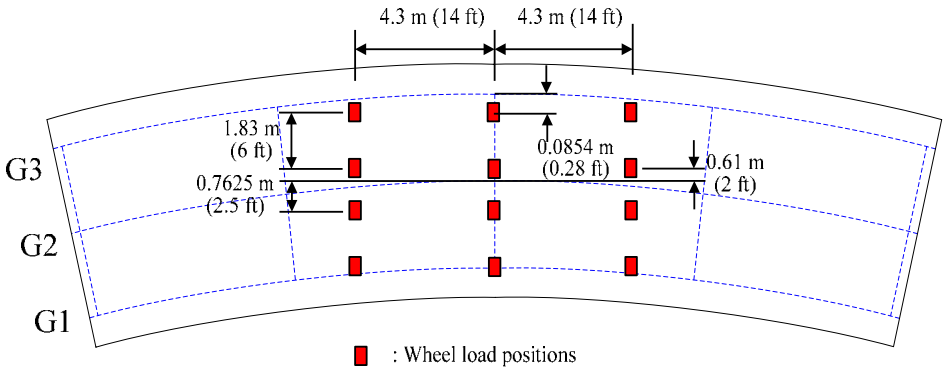

Figure 2.3.14. Wheel load positions associated with two design trucks inducing the maximum loading effects on the outside girder (G2) (Dynamic allowance factor 1.33 is included, but multiple presence factor is not included in this scheme).

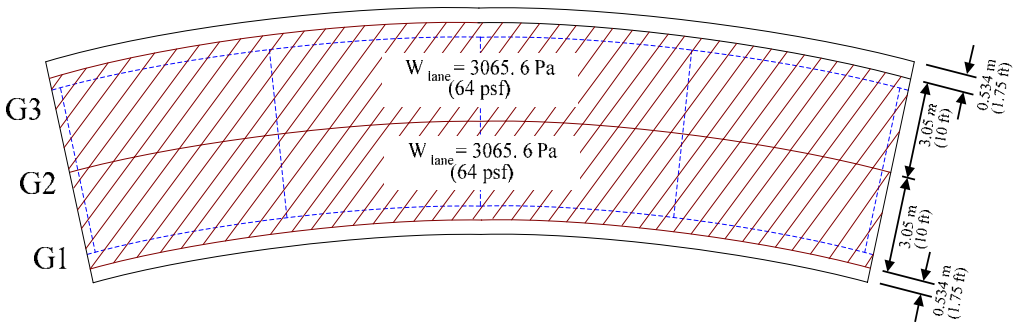

Figure 2.3.15. Lane load position associated with two design trucks inducing the maximum loading effects on the outside girder (G2) (Dynamic allowance factor 1.33 and multiple presence factor are not included in this scheme).

Because of the above small differences between the loadings for the maximum live load effect on G3 and G2, the loading for G3 is used to design both G3 and G2.

Figures 2.3.16 and 2.3.17 illustrate the wheel load positions for a single design truck and lane load positions for the maximum flexural loading effects on G1. Figure 2.3.16 shows that one AASHTO HL-93 truck is used with the inside wheel at its middle axle

positioned at 0.61 m (2 ft) outside of the inside curb, i.e., this wheel load is located directly over G1 at the midspan of the bridge. The other wheels of the design truck are positioned symmetrically about the midspan of the bridge, at 4.27 m (14 ft) axle spacing and 1.83 m (6 ft) transverse wheel spacing.

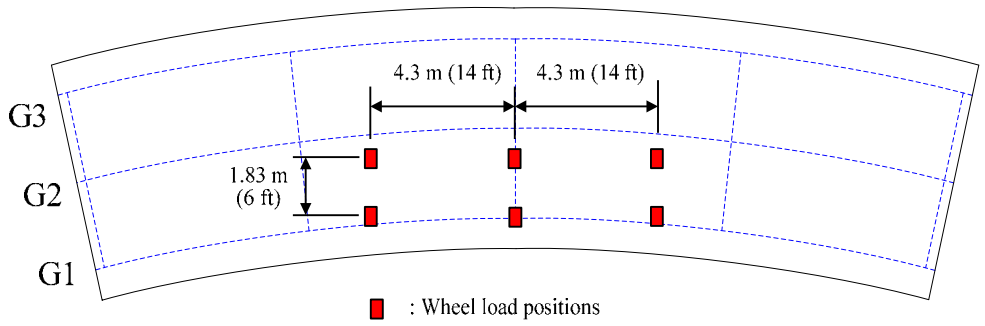

Figure 2.3.16. Wheel load positions associated with a single design truck inducing the maximum loading effects on the outside girder (G1) (Dynamic allowance factor 1.33 and multiple presence factor of 1.2 are included in this scheme).

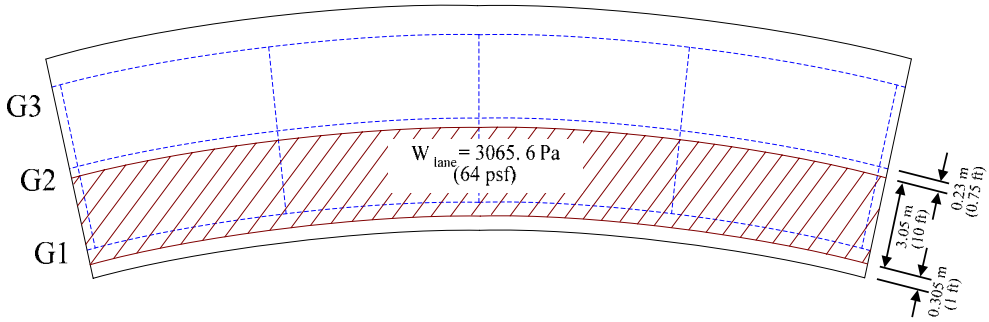

Figure 2.3.17. Lane load position associated with a single design truck inducing the maximum loading effects on girder G1 (Dynamic allowance factor 1.33 and multiple presence factor of 1.2 are not included in this scheme).

A single lane load of 9.3 kN/m (0.64 kips/ft), uniformly distributed over a 3.05 m (10 ft) radial width within the inside design lane as shown in Figure 2.3.17, i.e., uniform pressure of 3066 Pa (64 psf) is applied over a 3.05 m (10 ft) radial width within the inside

design lane. The inside edge of this loading is placed at the edge of the inside curb, i.e., 0.305 m (1 ft) radially inside the inside edge of the slab.

A dynamic allowance of 1.33 is applied to all the design truck loadings. The dynamic allowance is not applied to the lane load portion of the AASHTO live load model. For the case of the two design loadings side-by-side (used for design of G3 and G2), a multiple presence factor of 1.0 is used. For the case of the single truck plus lane loading on the inside design lane, a multiple presence factor of 1.2 is employed. A load factor of 1.75 is applied to the live loads for Strength I design per AASHTO LRFD (2004b). For the Strength I checks, these load effects, applied to the composite bridge, are combined with the noncomposite dead load effects multiplied by a load factor of 1.25. Load factors of 1.3 and 1.0 are applied to the live load and to the noncomposite dead load for checking Service II conditions. For checking of live load deflections, the two side-by-side design vehicles are placed on the bridge for the maximum effect on G3 as described above, with zero lane loads. A dynamic allowance of 1.33 is included with these loads. For checking of live load deflections on G1, the single design truck is placed for maximum effect on G1 as described above, with zero lane load. A dynamic allowance of 1.33 and a multiple presence factor of 1.2 are applied to this load.

In summary, two loading schemes are used for the live load analysis of the test bridge. One is for the case in which the maximum loading effects are expected in girder G1 and the other case is for the maximum effects for girder G2 and G3. The exact locations for the maximum effects on G2 and G3 are slightly different, but the difference is found to be very small. Thus, the loading scheme for the maximum effects on girder G3 is also utilized to approximately obtain the maximum loading for G2.

2.3.7. Braking Forces

In the calculation of braking force, it is assumed that the design truck is moving at a velocity of 90 km/h (56 mph) = 25 m/s (82 ft/s) (and a braking distance of 122,000 mm (400 ft). The resulting braking force is taken as 25 % of the axle weights of the design trucks in all lanes. Therefore, the braking force, F_B, transmitted to the deck is

$$F_B = bW = 0.25W \tag{2.11}$$

where b is the fraction of the weight that is applied to model the braking force and W is the weight of the vehicle.

Preliminary analyses indicate that the effects of braking forces on the bridge response are negligible. Thus, the braking forces are not included in the analysis and design of the test bridge.

2.3.8. Effects of Centrifugal Force and Superelevation

In the design of a horizontally curved bridge, the centrifugal force is a radial force, applied to the live load a given distance above the deck, which is transferred through the wheels of the vehicle to the deck. Because the radial force is applied above the deck, the force causes an overturning moment. Thus, the centrifugal force causes an increase in the vertical wheel loads toward the outside of the bridge and a decrease in the wheel loads toward the inside of the bridge.

As a truck moves along a curvilinear path, its change in direction requires a centrifugal acceleration. The associated centrifugal force, F_r, is defined in the AASHTO specifications as

$$F_r = CW = \frac{4}{3}(\frac{v^2}{Rg})W \tag{2.12}$$

where C is a fraction of the vehicular weight, W is the weight of the vehicle, v is the highway design speed (m/s), R is radius of curvature of traffic lane (m), and g is the gravitational acceleration (9.807 m/s^2).

For a given radius of curvature, a maximum design speed can be found in the Green Book (AASHTO 2004c). The calculated maximum design speeds are 43 km/h (26.7 mph) and 44 km/h (27.3 mph) for the inside and outside lanes, respectively, on the test bridge. Substitution of a given velocity, radius of curvature and gravitational acceleration into Eq. (2.12) yields factors of 0.332 and 0.333 for the inside and outside lanes, respectively. For the sake of simplicity and convenience, 0.33 is used for both the inside and outside lanes in the analysis and design of the test bridge.

If the superelevation of the bridge is significant, the Engineer needs to consider its effects for the case with no centrifugal force effects included, since the superelevation will cause an increase in the vertical wheel loads toward the inside of the bridge and a decrease in the vertical wheel loads toward the outside of the bridge. Also, in general, the superelevation can have an influence on distribution of horizontal reactions. However, according to the provisions of Guide Specifications for Horizontally Curved Bridges (1993), the effect of superelevation can be neglected for superelevation angles between 0 and 10 percent. Also, the test bridge does not contain any superelevation. Therefore, the effect of superelevation is not considered in the subsequent analyses of the test bridge.

2.4 Elastic Analysis of the Test Bridge

The elastic analysis of the test bridge is conducted according to the AASHTO (2004b) constructability, Service II and Strength I requirements. Separate analyses are conducted for the different noncomposite dead loads and the composite live loads, and the resulting stresses and deflections are superposed. For the noncomposite dead loads, geometric nonlinear (second-order) as well as linear elastic (first-order) analyses are conducted. For each of the composite live loads described in Section 2.3.6, the case with centrifugal force effects included is compared to the case with no centrifugal force effects included, and the worst case is selected for the design.

Intermediate transverse stiffeners are not included in the model for the elastic design-analysis. This is due to the fact that intermediate transverse stiffeners generally are not sufficient to develop the torsional restraint from the slab under ultimate strength loading conditions without forming plastic hinges at their tops. By neglecting the intermediate transverse stiffeners in the design-analysis, a conservative design of the I-girders is ensured relative to this consideration. The intermediate transverse stiffeners are included in the subsequent full nonlinear FEA analyses of the system behavior.

2.4.1 Results of the Noncomposite Dead Load Analysis

Figure 2.4.1 presents typical factored lateral and major axis bending stresses in the bottom flange of the test bridge girders that are obtained from the noncomposite analysis. It is interesting to note that the peak elastic flange lateral bending stresses are localized around the cross-frame positions. Figure 2.4.1 also shows that the maximum lateral and major-axis bending stresses occur at the midspan of the bridge.

Tables 2.4.1 and 2.4.2 give the factored maximum major-axis and lateral bending stresses induced in the top and bottom flanges of the bridge girders. A load factor of 1.25 is used for Table 2.4.1 and 1.5 for Table 2.4.2. The results of the first- and second-order analysis are presented side by side for each girder to check the effects of geometric nonlinearity on the girder responses. Generally, except for the bottom flange lateral bending stresses, none of the stresses are affected significantly by the geometric nonlinearity. In fact, the results of the second-order analyses in some cases are slightly smaller than those of the first-order analysis. In contrast, the bottom flange lateral bending stresses are modestly increased for all the girders, with a maximum increase of 20 percent in Table 2.4.1 and 24 percent in Table 2.4.2 for the G1 lateral bending stresses. Detailed major-axis and lateral bending stresses for the test bridge girders are presented in Appendix A.

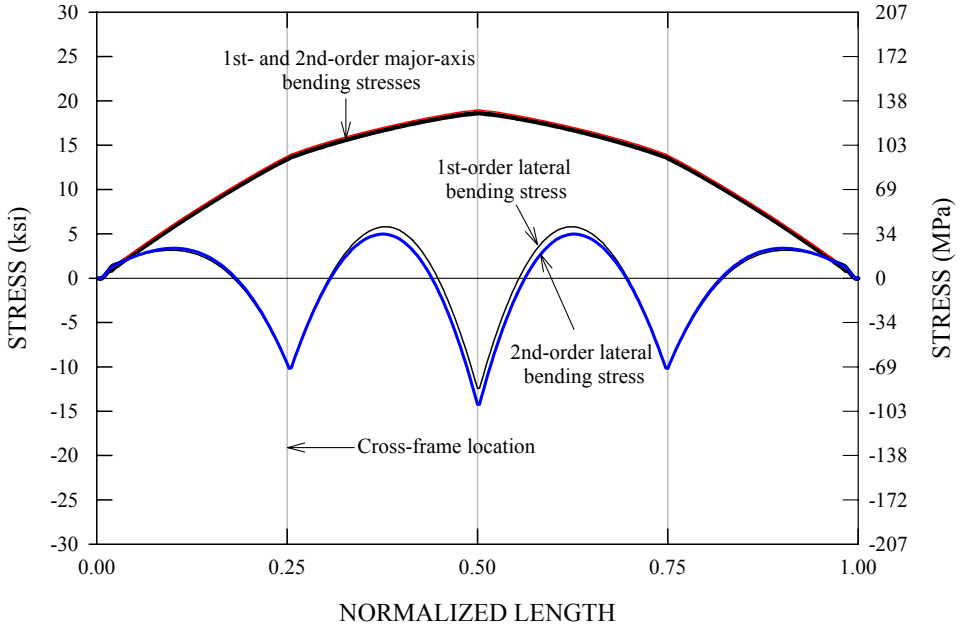

Figure 2.4.1. Typical first- and second-order major-axis and lateral bending stresses along girder length due to noncomposite construction loads.

Table 2.4.1. Factored maximum top and bottom flange stresses relating to Strength I load combination (construction load factor = 1.25).

Flange	Stress	G1†			G2††			G3††		
		1st-order	2nd-order	2nd/1st	1st-order	2nd-order	2nd/1st	1st-order	2nd-order	2nd/1st
Top flange	f_{bc} MPa (ksi)	48.5 (7.03)	45.9 (6.65)	0.95	109 (15.8)	109 (15.8)	1.0	168 (24.3)	170 (24.7)	1.01
	$f_{\ell c}$ MPa (ksi)	62.1 (9.01)	57.0 (8.27)	0.92	133 (19.3)	142 (20.6)	1.06	110 (15.9)	107 (15.5)	0.99
Bottom flange	f_{bt} MPa (ksi)	36.5 (5.30)	33.9 (4.92)	0.93	74.1 (10.7)	72.7 (10.5)	0.98	129 (18.7)	132 (19.1)	1.02
	$f_{\ell t}$ MPa (ksi)	37.3 (5.41)	45.3 (6.57)	1.21	60 (8.7)	66 (9.6)	1.11	91.3 (13.3)	104 (15.1)	1.14

† : Eccentric bracket load *not* included in the analysis model

†† : Eccentric bracket load included in the analysis model

Table 2.4.2. Factored maximum top and bottom flange stresses relating to Strength IV load combination (construction load factor = 1.50). - governs

Flange	Stress	G1†			G2††			G3††		
		1st-order	2nd-order	2nd/ 1st	1st-order	2nd-order	2nd/ 1st	1st-order	2nd-order	2nd/ 1st
Top flange	f_{bc} MPa (ksi)	58.2 (8.44)	54.1 (7.84)	0.93	131 (19.0)	127 (18.4)	0.97	201 (29.2)	199 (28.8)	0.99
	$f_{\ell c}$ MPa (ksi)	74.5 (10.8)	67.6 (9.81)	0.91	160 (23.2)	168 (24.4)	1.05	131 (19.0)	125 (18.1)	0.95
Bottom flange	f_{bt} MPa (ksi)	43.9 (6.36)	39.9 (5.78)	0.91	88.9 (12.9)	84.8 (12.3)	0.95	155 (22.5)	154 (22.3)	0.99
	$f_{\ell t}$ MPa (ksi)	44.8 (6.49)	55.4 (8.03)	1.24	71.6 (10.4)	78.7 (11.4)	1.10	110 (15.9)	124 (18.1)	1.14

† : The bracket load is *not* included in the analysis model

†† : The bracket load is included in the analysis model

It is important to recognize that the level of mesh refinement required for obtaining converged solutions is different for major-axis and lateral bending stresses. In general, a denser mesh is necessary to obtain the converged lateral bending stresses at the cross-frame locations. This is particularly true of the lateral bending stresses at the cross-frame locations where there is a sharp peak. In case of the composite test bridge, it is found that the number of elements along the length required to obtain the converged lateral bending stresses at the cross-frame locations is twice the number required to obtain the converged major-axis bending stresses.

In addition to the design analyses of the test bridge subjected to factored noncomposite loads, a separate analysis was performed for the bridge subjected to nominal dead loads and noncomposite construction loads without load factors. The purpose of this analysis is to predict overall deflections for the bridge girders and to determine necessary cambers so that the bridge girders are level after the completion of erection. Figure 2.4.2 shows a perspective view of deformed shape of the test bridge model obtained from the second-order analysis under steel self weight + wet concrete + formwork. The bare steel bridge model has a maximum deflection of 113.9 mm (4.484 in) at the mid span of girder G3 as shown in the contours for the vertical (axis 3) deflection. The maximum deflection in the second-order analysis is slightly larger than that of the first-order analysis. The ratio of the second-order to the first-order deflection is 1.023. Based on this result, girder G3 was cambered by 125 mm (5 in) at its midspan.

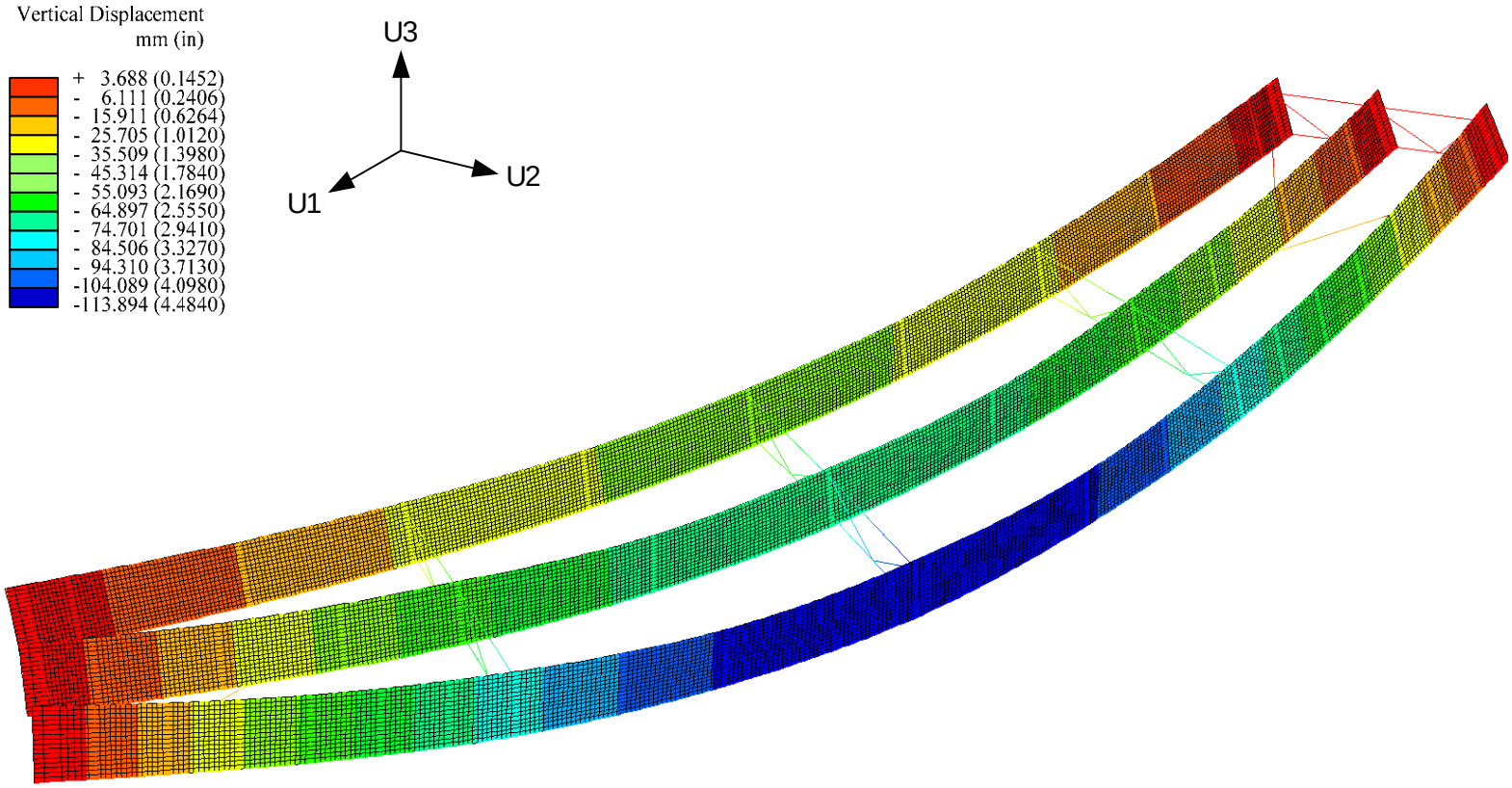

Figure 2.4.2. Perspective view of deformed shape from the second-order analysis due to nominal steel self weight + wet concrete+forms, with contours of vertical (axis 3) deflection (displacements amplified 23 times).

2.4.2 Results of the Composite Live Load Analysis

Only the results of linear elastic (first-order) analyses are presented in this section, since geometric nonlinearity tends to have an insignificant effect on the live load response of completed composite I-girder bridges. Tables 2.4.3 and 2.4.4 present the maximum major-axis and lateral bending stresses induced in the top and bottom flanges of G2 and G3 due to the lane load and two design trucks, respectively. The dynamic allowance factor of 1.33 is included in the results of Table 2.4.4. For the analysis of design truck load, two different cases are considered. One case includes the effects of centrifugal forces whereas the other case does not. Of the two, the case producing the largest lateral and major-axis bending stresses is used for the results reported in Table 2.4.4. Table 2.4.4 indicates that the maximum response on G2 occurs when the effects of centrifugal forces are not included in the analysis model. In contrast, the maximum response on G3 occurs when the centrifugal forces are considered.

Table 2.4.3. Nominal (unfactored) top and bottom flange stresses for G2 and G3, due to lane load.

Flange	Stress	G2	G3
Bottom flange	f_{bt} MPa (ksi)	21.3 (3.09)	30.3 (4.39)
	$f_{\ell t}$ MPa (ksi)	14.8 (2.14)	19.2 (2.79)
Top flange	f_{bc} MPa (ksi)	2.69 (0.39)	4.41 (0.64)
	$f_{\ell c}$ MPa (ksi)	8.34 (1.21)	5.17 (0.75)

Table 2.4.4. Nominal (unfactored) top and bottom flange stresses for G2 and G3, due to design truck load, 1.33 dynamic allowance included.

Flange	Stress	G2†	G3††
Bottom flange	f_{bt} MPa (ksi)	60.2 (8.73)	90.8 (13.2)
	$f_{\ell t}$ MPa (ksi)	41.7 (6.05)	55.2 (8.00)
Top flange	f_{bc} MPa (ksi)	5.79 (0.84)	11.5 (1.66)
	$f_{\ell c}$ MPa (ksi)	21.7 (3.15)	13.2 (1.92)

† : The effects of centrifugal forces are *not* included in the analysis
†† : The effects of centrifugal forces are included in the analysis

Tables 2.4.5 and 2.4.6 present the maximum major-axis and lateral bending stresses occurring in the flanges of G1 due to the governing AASHTO live load, which consists of a lane load (Figure 2.3.16) and a single truck (Figure 2.3.17), respectively. A multiple presence factor of 1.2 is included in the calculation of the girder responses reported in both tables. In addition, it should be noted that the dynamic allowance factor of 1.33 is included in the results of Table 2.4.6.

Table 2.4.5. Nominal (unfactored) top and bottom flange stresses for girder G1, including multiple presence factor of 1.2 due to lane load.

Flange	Stress	G1
Bottom flange	f_{bt} MPa (ksi)	19.7 (2.85)
	$f_{\ell t}$ MPa (ksi)	21.3 (3.09)
Top flange	f_{bc} MPa (ksi)	1.10 (0.16)
	$f_{\ell c}$ MPa (ksi)	1.59 (0.23)

Table 2.4.6. Nominal (unfactored) top and bottom flange stresses for girder G1, including dynamic allowance of 1.33 due to design truck loading and multiple presence factor of 1.2.

Flange	Stress	G1†
Bottom flange	f_{bt} MPa (ksi)	56.5 (8.19)
	$f_{\ell t}$ MPa (ksi)	59.7 (8.66)
Top flange	f_{bc} MPa (ksi)	2.48 (0.36)
	$f_{\ell c}$ MPa (ksi)	3.65 (0.53)

† : The effects of centrifugal forces are *not* included in the analysis

Figures 2.4.3 and 2.4.4 show a contour plot of vertical deflections on the test bridge slab and a perspective view of the deformed geometry due to two lanes loaded by nominal (unfactored) distributed lane loads for maximum effect on G3. The slab is not shown in Figure 2.4.4 in order to focus on the displacements within the steel girders. The maximum vertical deflection occurs at the edge of the slab outside of G3 (17.25 mm (0.691 in)). This is slightly larger than the maximum vertical displacement on G3 (15.5 mm (0.622 in)).

Figures 2.4.5 and 2.4.6 provide a contour plot of vertical deflections on the test bridge slab and a perspective view of displaced geometry due to two HL-93 AASHTO design trucks (nominal loads with dynamic allowance of 1.33 included), positioned side-by-side, for the maximum flexural effect on G3. The effects of centrifugal forces are not included in these plots. Again, the maximum vertical deflection occurs at the edge of the slab outside of G3 (40.8 mm (1.63 in)), which is slightly larger than the maximum vertical displacement on G3 (37.0 mm (1.48 in)).

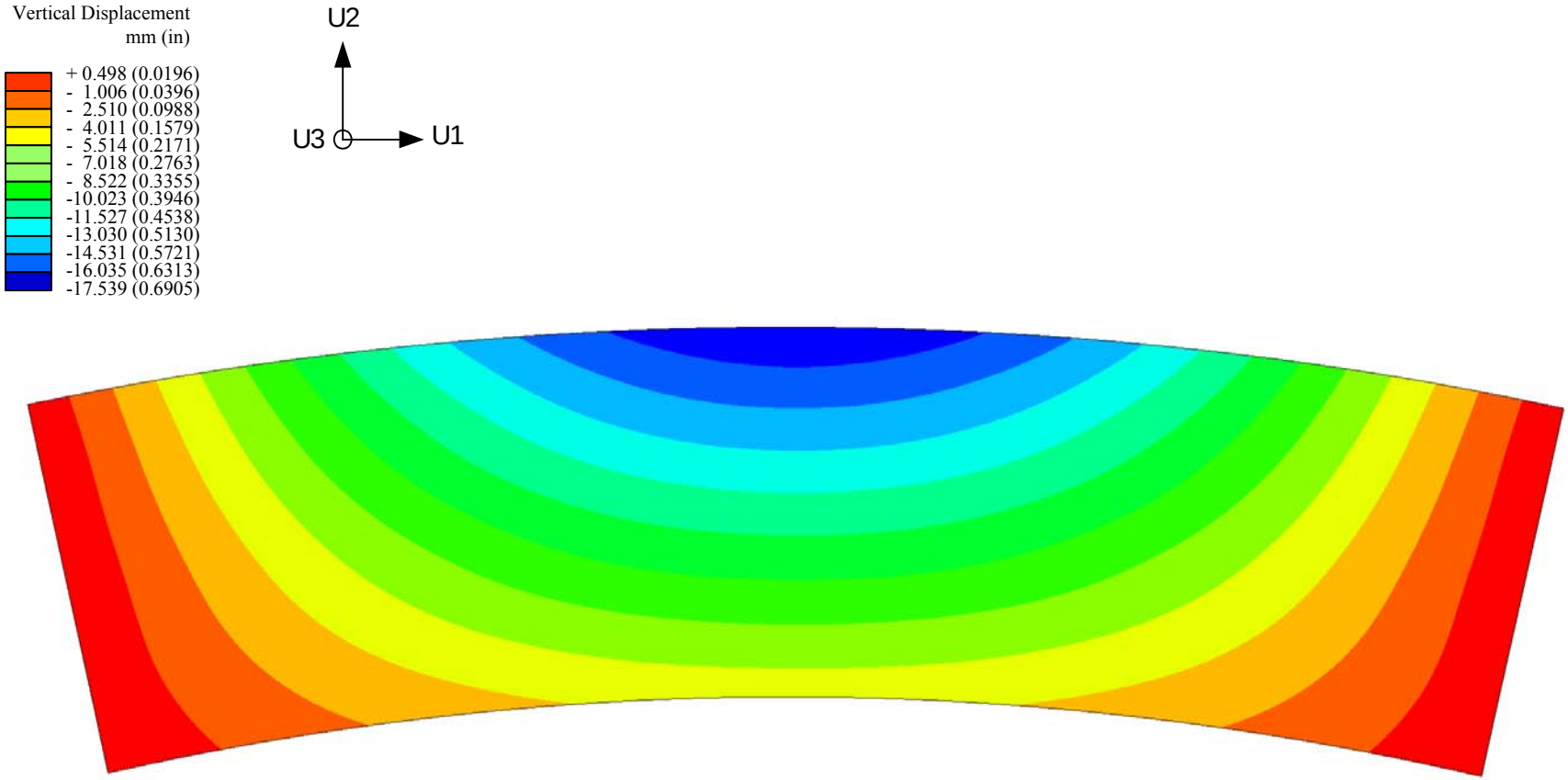

Figure 2.4.3. Contours of vertical deflections on slab due to two lanes loaded by nominal (unfactored) distributed lane loads for the maximum effects on G3.

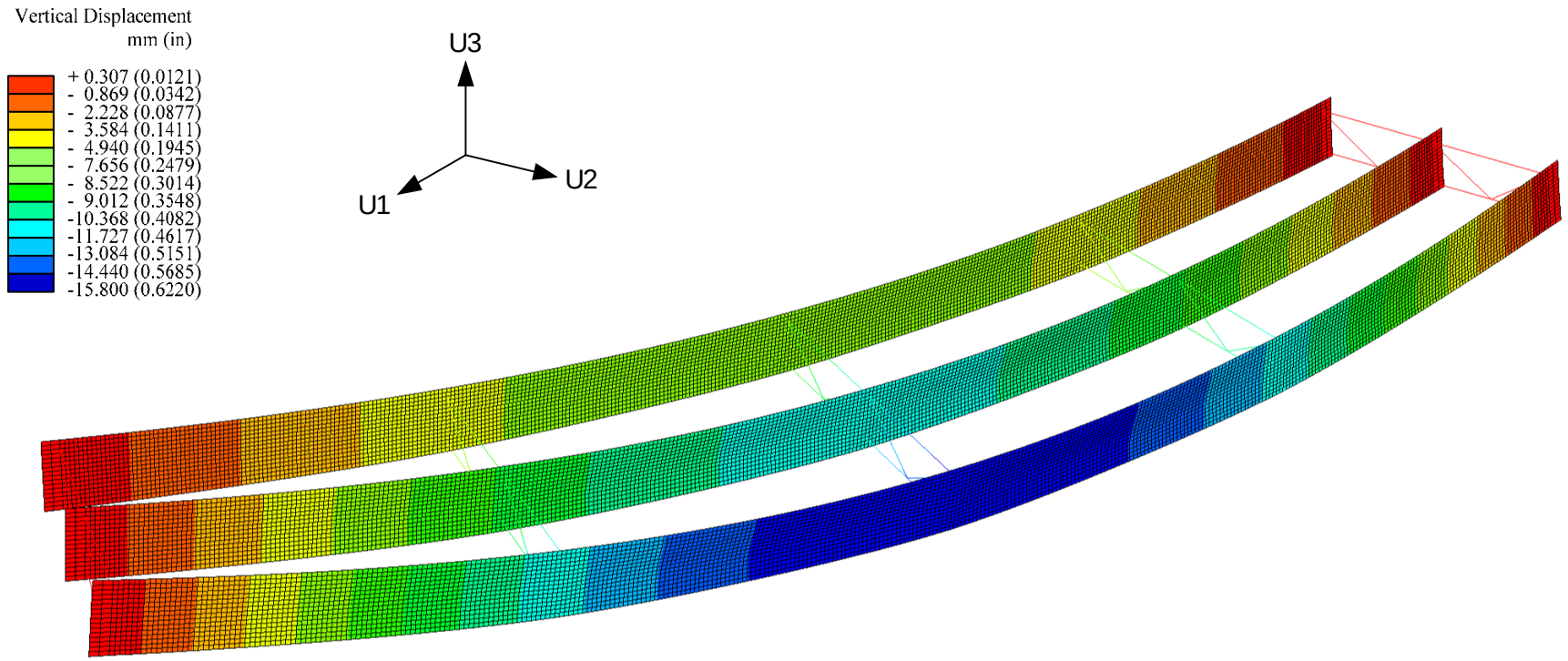

Figure 2.4.4. Perspective view of displaced geometry due to two lanes loaded by nominal (unfactored) distributed lane loads for maximum effect on G3, with contours of vertical (axis 3) deflection (displacements amplified 170 times). This figure does not show the slab in order to focus on the displacements within the steel girders.

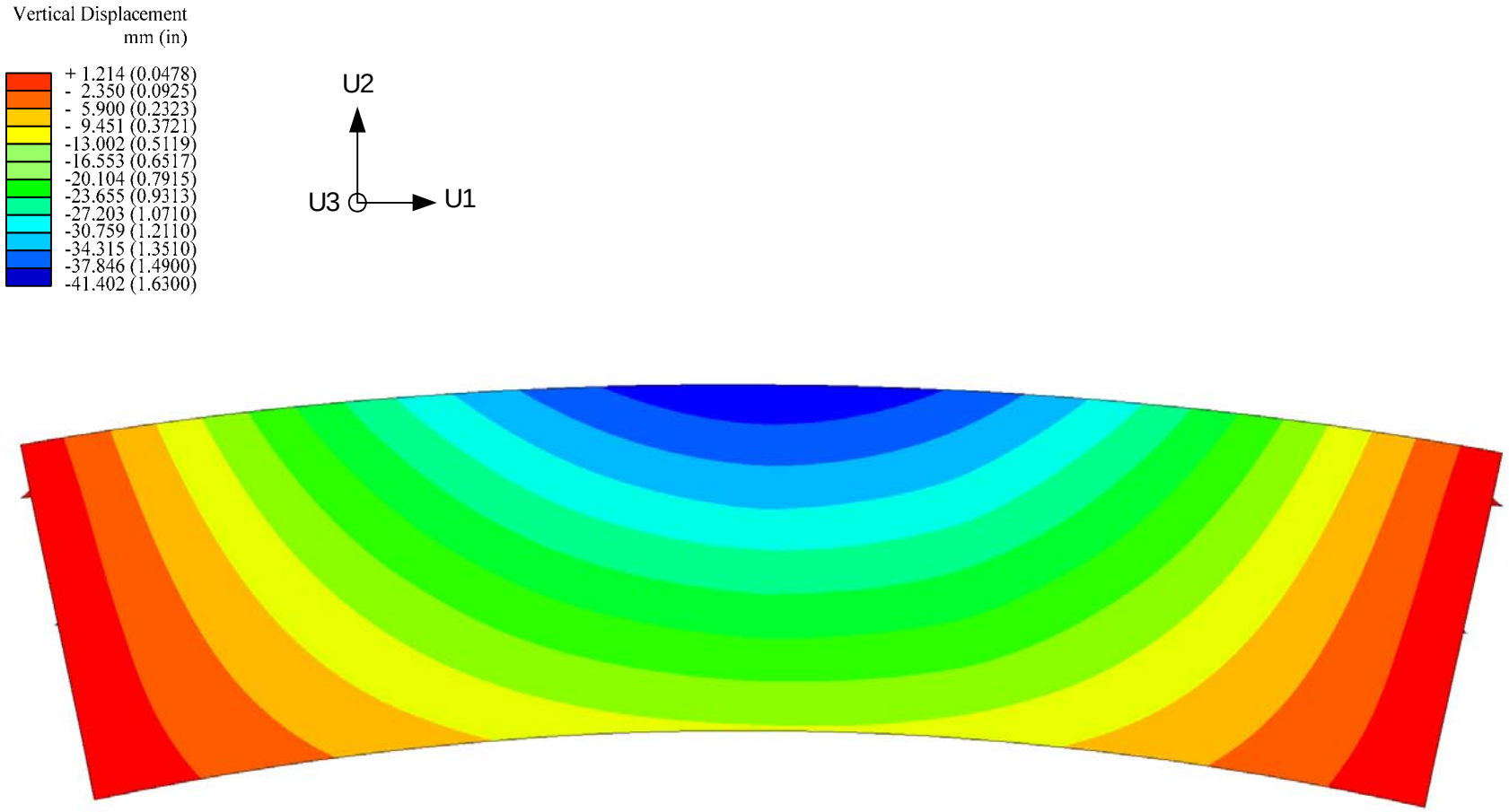

Figure 2.4.5. Contours of vertical deflections on slab due to two HL-93 AASHTO design trucks (nominal loads with dynamic allowance of 1.33 included), positioned side-by-side without the effects of centrifugal force, for the maximum effects on G3.

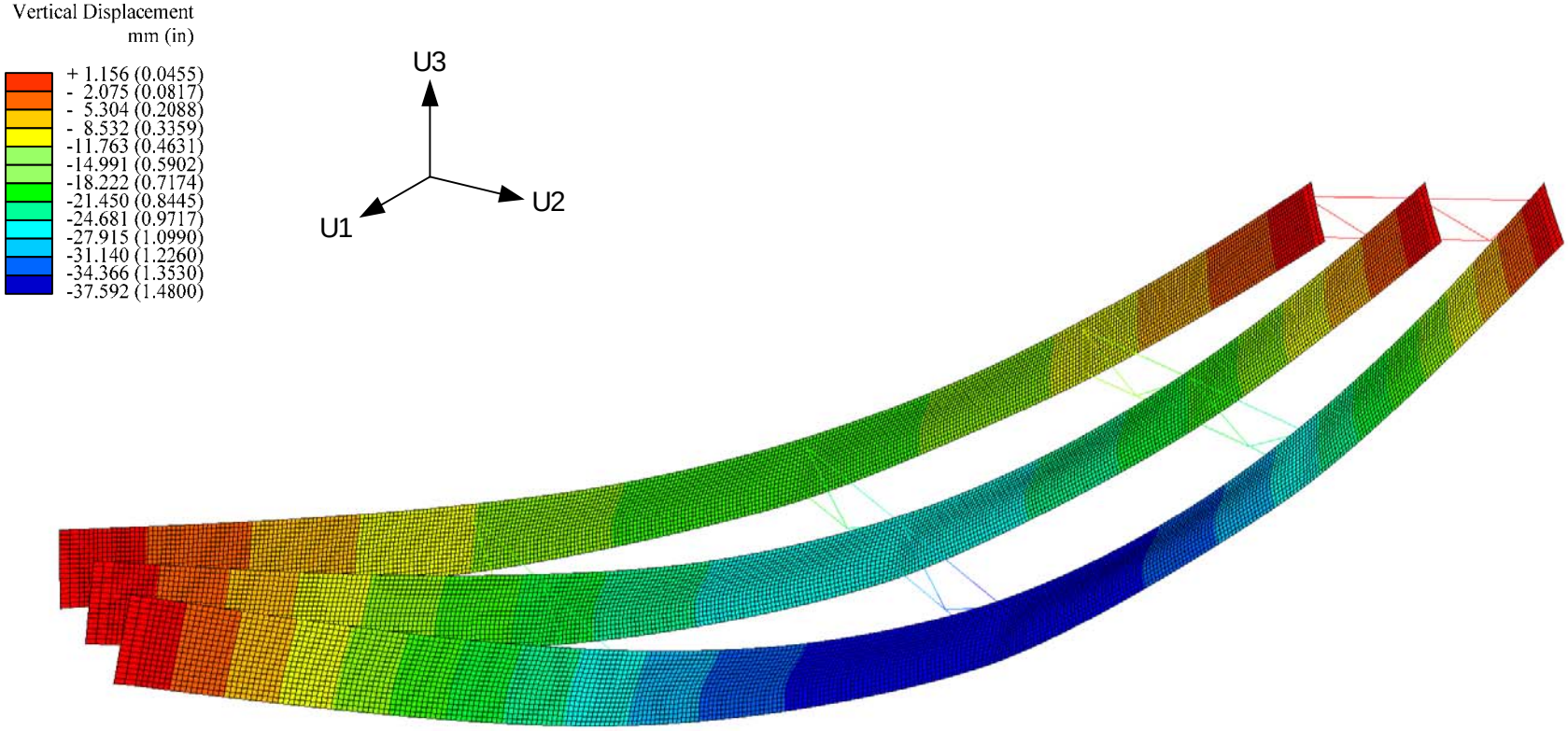

Figure 2.4.6. Perspective view of displaced geometry due to two HL-93 AASHTO design trucks (nominal loads with dynamic allowance of 1.33 included), positioned side-by-side without the effects of centrifugal force, for the maximum effects on G3, with contours of vertical (axis 3) deflection (displacements amplified 100 times). This figure does not show the slab in order to focus on the displacements within the steel girders.

Conversely, Figures 2.4.7 and 2.4.8 show a contour plot of vertical deflection on the test bridge slab and a perspective view of displaced geometry due the same two truck loading scheme, but with the effects of centrifugal forces considered in the FEA model. The maximum vertical deflections are 50 mm (2.0 in) at the edge of the slab outside of G3 and 44 mm (1.76 in) at the midspan of G3.

Figures 2.4.9 and 2.4.10 show a contour plot of vertical deflections on the test bridge slab and a perspective view of displaced geometry due to a single lane loaded by nominal (unfactored) distributed lane load (including a multiple presence factor of 1.2) for the maximum effect on G1. Contrary to the results of the loading scheme causing the maximum loading effects on G2 and G3, the maximum vertical deflection occurs at the edge of the slab outside of G1 (6.70 mm (0.268 in)). This displacement is slightly larger than the maximum vertical displacement on G1 (6.25 mm (0.25 in)).

Figures 2.4.11 and 2.4.12 provide a contour plot of vertical deflections on the test bridge slab and a perspective view of displaced geometry due to a single HL- 93 AASHTO design truck (nominal load with dynamic allowance of 1.33 included, multiple presence factor of 1.2 included) for maximum effect on G1, with the effects of centrifugal forces not considered. In contrast to the previous loading case involving two HL-93 AASHTO design truck loads, the maximum vertical deflection occurs at the edge of the slab outside of G1 (17 mm (0.68 in)), which is larger than the maximum vertical displacement on G1 (16 mm (0.64 in)).

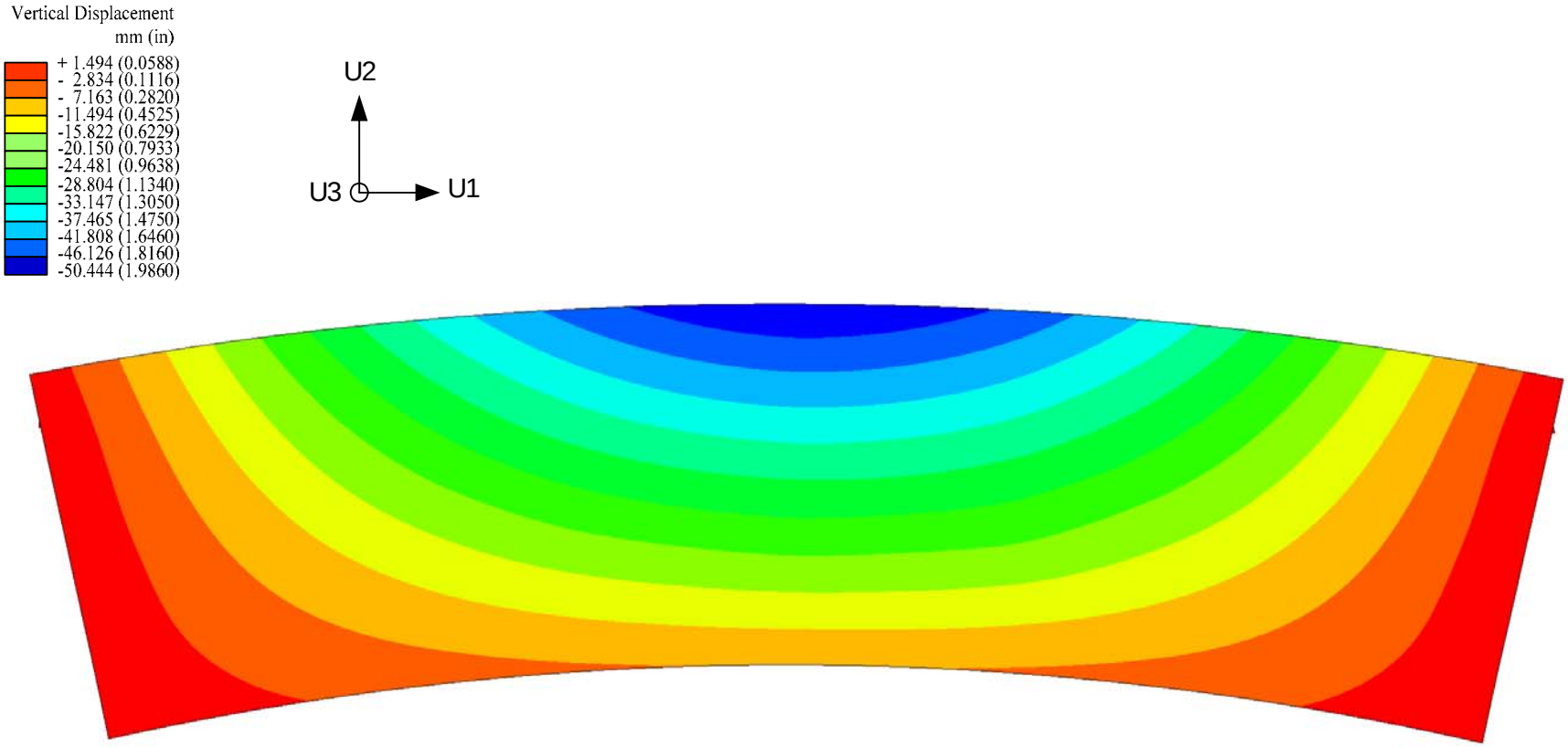

Figure 2.4.7. Contours of vertical deflections on slab due to two HL-93 AASHTO design trucks (nominal loads with dynamic allowance of 1.33 included), positioned side-by-side with the effects of centrifugal forces, for the maximum effects on G3, with the effects of centrifugal forces.

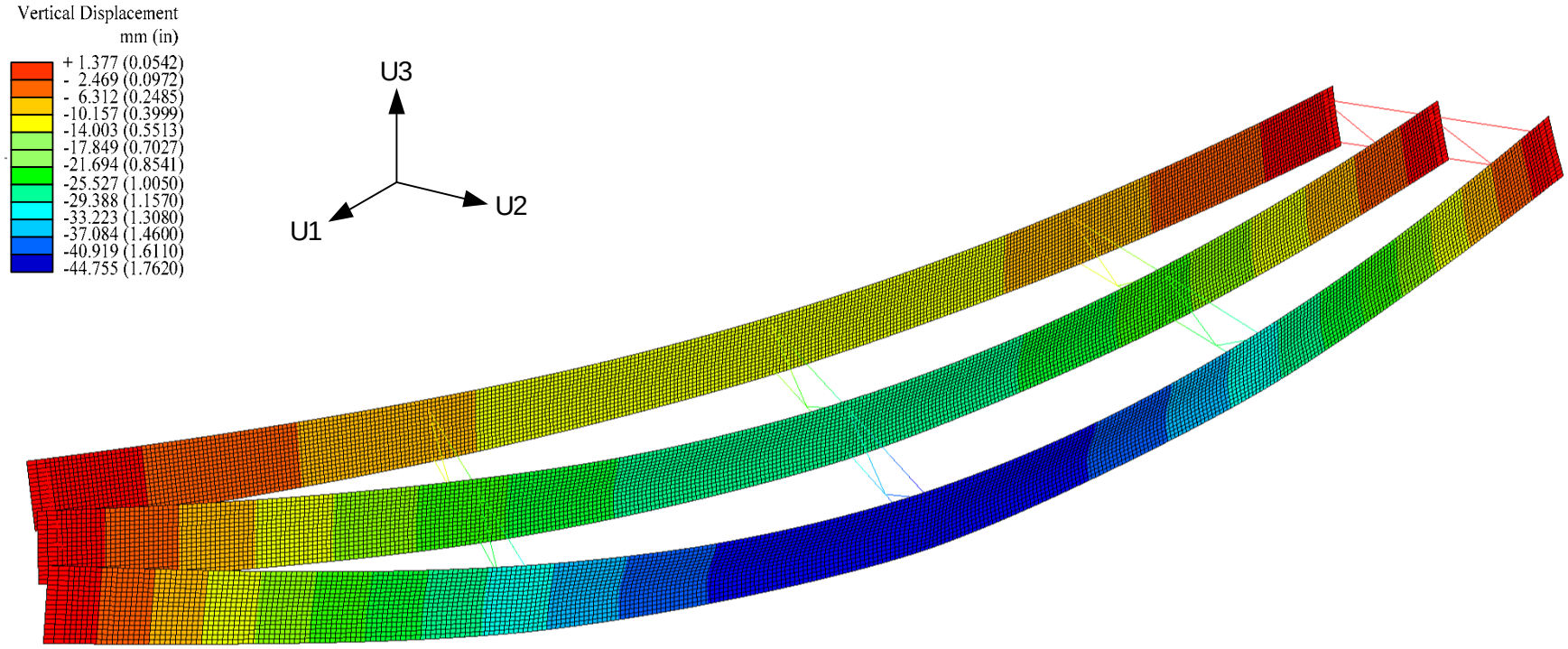

Figure 2.4.8. Perspective view of displaced geometry due to two HL-93 AASHTO design trucks (nominal loads with dynamic allowance of 1.33 included), positioned side-by-side with the effects of centrifugal forces, for the maximum effects on G3, with contours of vertical (axis 3) deflection (displacements amplified 70 times). This figure does not show the slab in order to focus on the displacements within the steel girders.

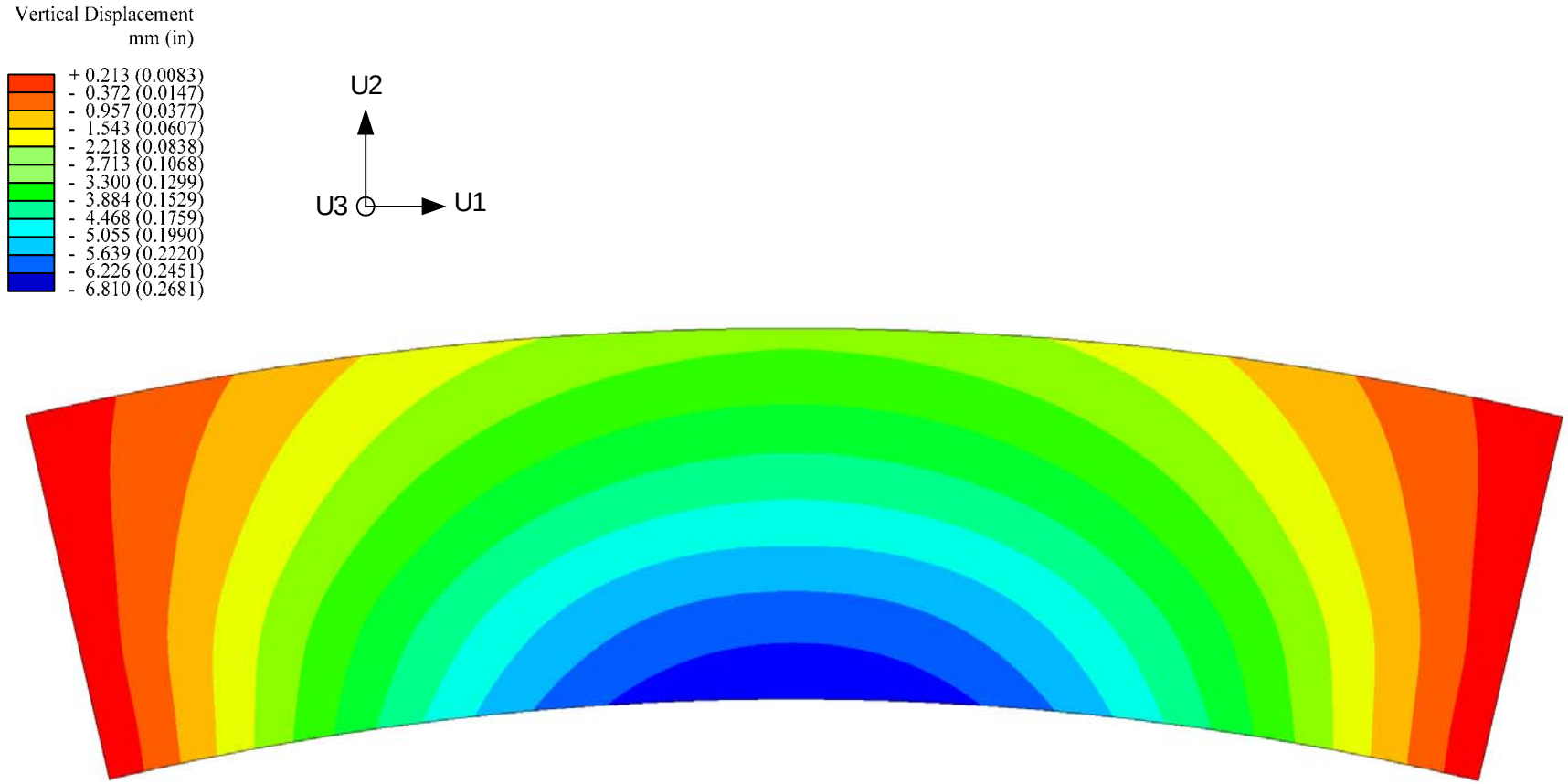

Figure 2.4.9. Contours of vertical deflections on slab due to a single lane loaded by nominal (unfactored) distributed lane load (including multiple presence factor of 1.2) for the maximum effects on G1.

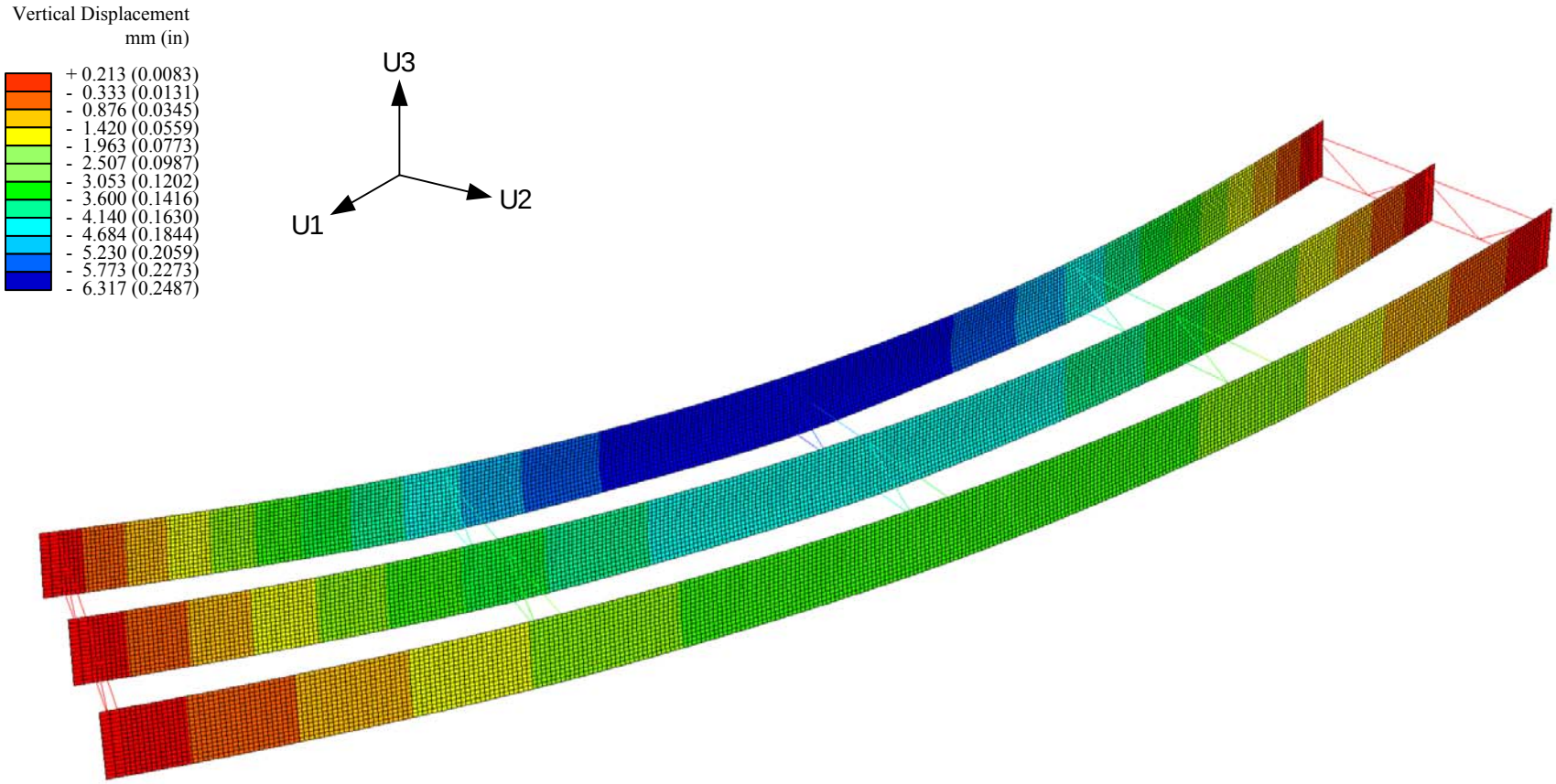

Figure 2.4.10. Perspective view of displaced geometry due to a single lane loaded by nominal (unfactored) distributed lane loads (including multiple presence factor of 1.2) for maximum effect on G1, with contours of vertical (axis 3) deflection (displacements amplified 100 times). This figure does not show the slab in order to focus on the displacements within the steel girders.

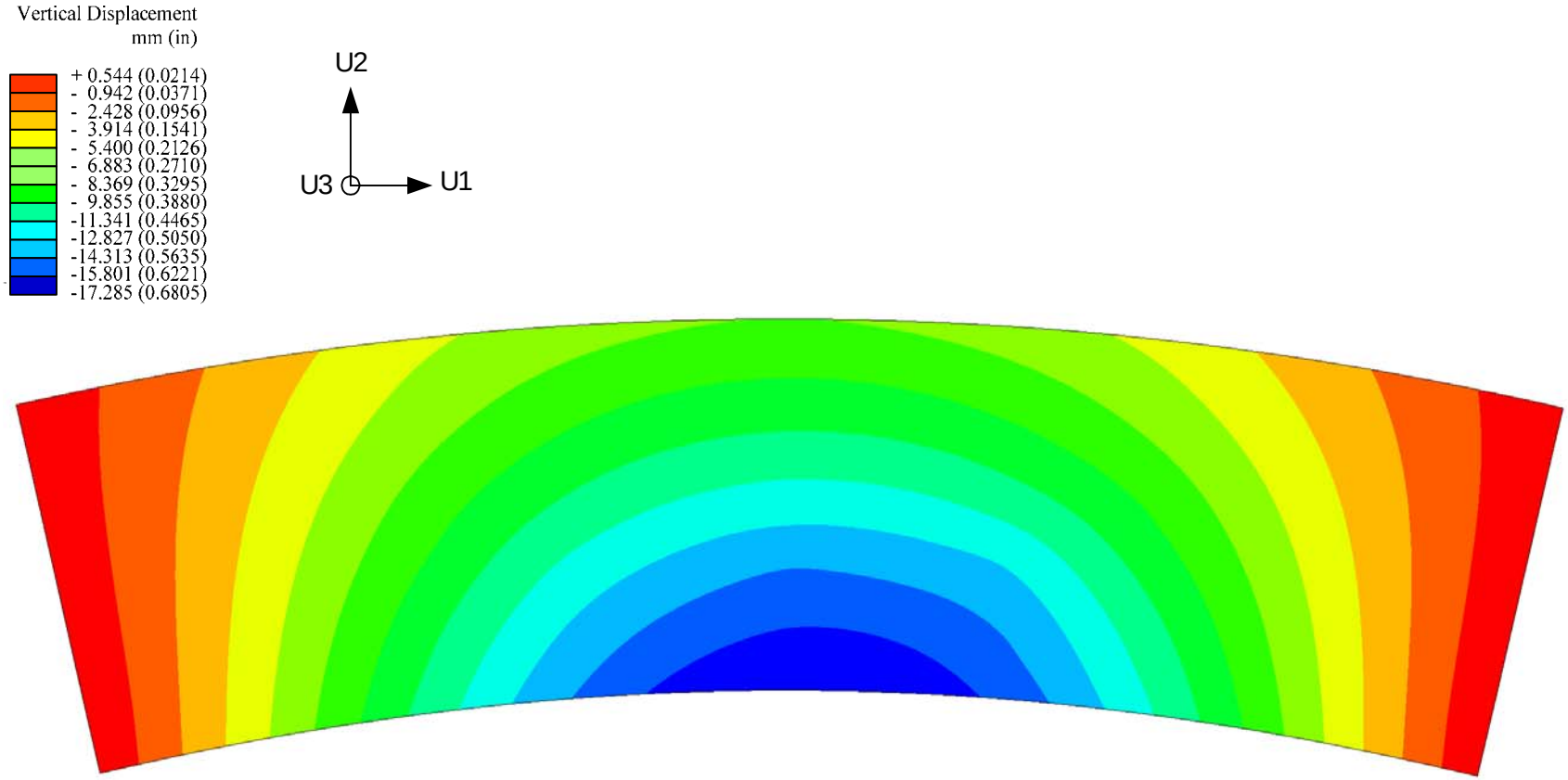

Figure 2.4.11. Contours of vertical deflections on slab due to a single HL-93 AASHTO design truck (nominal loads with dynamic allowance of 1.33 (including multiple presence factor of 1.2)), positioned for the maximum effects on G1 without the effects of centrifugal force.

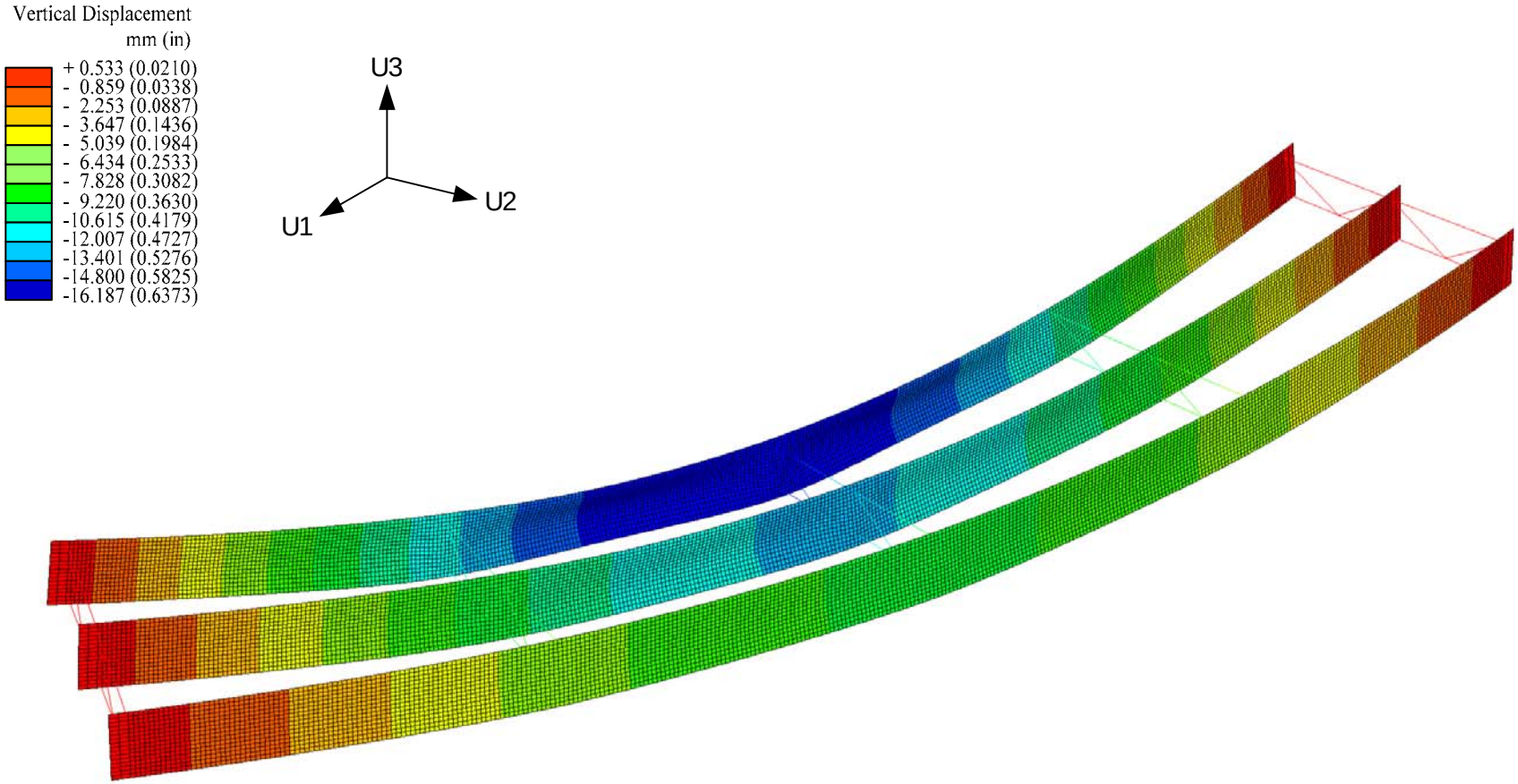

Figure 2.4.12. Perspective view of displaced geometry due to a single HL-93 AASHTO design truck (nominal load with dynamic allowance of 1.33 included, multiple presence factor of 1.2 included) without the effects of centrifugal force, with contours of the vertical (axis 3) deflection(displacements amplified 100 times). This figure does not show the slab in order to focus on the displacements within the steel girders.

2.5 Test Bridge Component Design

The design of the Phase II testing frame by Grubb and Hall, outlined in (FHWA 2001), was used as a starting point for the analysis and design iterations considered in this work. That is, the overall geometry of the girders (span length and radius of curvature) was set based on the original test frame.

The design of bridge I-girders entails two load combinations for the strength limit state check, STRENGTH I and STRENGTH IV, and one load combination for the service limit state check, SERVICE II. STRENGTH I is associated with the normal vehicular use of the bridge without wind. The STRENGTH IV combination involves very high dead load to live load force effect ratios. SERVICE II is a load combination relating only to steel structures and is intended to control permanent deflections due to vehicular live load. The above load combinations are:

- STRENGTH I: $1.25 \times DC + 1.75 \times (LL+CE) \times (1.0+IM) + 1.00 \times FR$
- STRENGTH IV: $1.50 \times DC + 1.00 \times FR$, and
- SERVICE II: $1.00 \times DC + 1.30 \times (LL+CE) \times (1.0+IM) + 1.00 \times FR$

where DC = dead load of structural components and nonstructural attachments, LL = vehicular live load, CE = vehicular centrifugal force, FR = friction force and IM = vehicular dynamic load allowance. The friction forces were taken equal to zero for the test bridge design. The calculation of the other forces is discussed in the previous sections.

Other load combinations relating to fatigue and fracture limit states may control the design rather than the strength and service limit states, but they are not considered in this work since the focus is placed on the study of strength and service load behavior of a bridge that was critical for strength. In the case of the strength limit check, two load

combinations are used to generate the factored responses for the bridge girders from the noncomposite and live load analyses. The load combination producing the larger girder response of the two is selected and used for the strength limit check.

For the constructability check of the test bridge girders under noncomposite loads, it turns out that STRENGTH IV is more critical than STRENGTH I. In contrast, STRENGTH I governs the design check of the girders for the final composite bridge configuration. Therefore, only the design results of STRENGTH IV for the noncomposite bridge configuration and STRENGTH I for the completed bridge are presented in the subsequent sections. The factored maximum bottom (tension) flange stresses due to noncomposite loads, used for combination with the live load stresses in STRENGTH I, do not include the effects of the torsion on exterior girders from the overhangs. This is because the eccentric bracket loads are removed prior to the application of the live loads. Also, it is important to note that all the original design calculations were based on the nominal section dimensions and material properties. However, the results presented in the subsequent sections are based on the measured material properties and test bridge geometry measurements. This allows for a more direct assessment of the AASHTO resistance limits versus the results from the refined finite element analyses and from the experimental testing. The measured material strengths are generally higher than the nominal material properties assumed in the initial design, and the measured section dimensions are larger than the nominal section dimensions. Therefore, the resulting design check ratios are generally smaller than corresponding original values.

2.5.1 Girder Flexural Design

The AASHTO (2004b) constructability checks are governed by nominal first-yielding of the top flange of G3 under the STRENGTH IV condition. Table 2.5.1 presents the constructability checks for the test bridge steel I-girders. The top flange check for all three girders is controlled by yielding limit, and corresponding design unity checks for the total factored noncomposite loads on the full steel superstructure (the ratios of the factored computed quantity from the analysis to the corresponding factored resistance) are 0.31, 0.75, and 0.81 for G1, G2, and G3, respectively.

Table 2.5.1. Unity checks, constructability relating to Strength IV per AASHTO (2004b).

Girder		f_b MPa (ksi)	f_ℓ MPa (ksi)	Design unity checks		
				Stress limit $f_\ell / 0.6F_y$	Strength $(f_b + 1/3\ f_\ell) / \phi_f F_n$	Yielding $(f_b + f_\ell) / \phi_f F_y$
G1	Top Flange	54.0 (7.84)	67.6 (9.81)	0.29	0.25	0.31
	Bottom Flange	39.9 (5.78)	55.4 (8.03)	0.23	·	0.24
G2	Top Flange	127.1 (18.44)	168.3 (24.43)	0.71	0.54	0.75
	Bottom Flange	84.81 (12.30)	78.67 (11.41)	0.33	·	0.41
G3	Top Flange	198.9 (28.84)	125.1 (18.14)	0.52	0.72	0.81
	Bottom Flange	155.0 (22.33)	124.4 (18.05)	0.42	·	0.56

Comparing the ratios for G2 and G3 and that for G1, it may seem that the top flange of G1 is oversized. However, this is mainly due to the fact that the sizing of the G1 top

flange is governed by the suggested AASHTO limit on the length of the shipping piece rather than stresses induced by external loading applied during the construction stage. In conjunction with the flange proportion limits specified in Article 6.10.2.2, the following guideline is suggested to establish a minimum required top flange width in positive flexure regions of composite girders:

$$b_{fc} \geq \frac{L}{85} \tag{2.13}$$

where b_{fc} = full width of the compression flange (in) and L = length of the girder shipping piece (in). Accordingly, G1 needs to have a minimum of 304 mm (12.15 in) for the width of its top flange, based on its total length.

The STRENGTH I condition for two design trucks side-by-side, positioned toward to the outside of their traffic lanes, with centrifugal forces and dynamic load allowance included, their middle axles located at the bridge midspan, plus two lanes fully loaded, governs the flexural design of G3. Table 2.5.2 presents the results of Strength I check for the steel girders. The strength ratio for this loading condition is 0.82 relative to Eq. (2.1). The flexural design of G2 is governed by a similar loading with the truck and lane load moved slightly toward the center of curvature in the outside line. The G2 strength ratio is 0.68 for the above critical G3 loading. The strength check for G1 is governed by STRENGTH I with a single design truck plus lane on the inside of the bridge, but its strength ratio is relatively low (0.57). As noted previously, the size of G1 is governed by other AASHTO (2004b) limits. Regarding the check of the lateral bending stress limit, $f_{\ell} \leq 0.6F_y$, the design unity checks are 0.78, 0.69, and 0.80 for G1, G2, and G3, respectively.

The maximum vertical deflection at the top flange of G3 due to two design trucks, side-by-side, positioned for maximum effect (unfactored loads but including centrifugal force effects and a dynamic allowance of 1.33), is 44 mm (1.76 in). This is slightly higher than $L_3/800$ = 35.3 mm (1.41 in), but is judged to be acceptable by the author.

Table 2.5.2. Unity checks, Strength I for composite section.

Girder		f_b MPa (ksi)	f_ℓ MPa (ksi)	$(f_\ell)/(0.6F_y)$	$(f_b + 1/3\, f_\ell)/(\phi_f F_n)$
G1	Top Flange	52.1 (7.56)	0	NA	0.13
	Bottom Flange	167.1 (24.24)	187.1 (27.13)	0.78	0.57
G2	Top Flange	123.4 (17.90)	0	NA	0.31
	Bottom Flange	215.3 (31.23)	164.8 (23.90)	0.69	0.68
G3	Top Flange	197.7 (28.67)	0	NA	0.50
	Bottom Flange	343.7 (49.85)	235.3 (34.12)	0.80	0.82

The AASHTO Specifications include four different service limit state load combinations, SERVICE I, II, III and IV, which are intended to cover different design situations. Of these four limit states, only the Service II check is relevant to the test bridge and is used to restrict the stresses that occur under regular service conditions. This limit state is intended to control yielding (permanent deflection) under a potential overload condition. Table 2.5.3 presents the Service II check for the steel girders. All three I-girders easily satisfy the SERVICE II check.

Table 2.5.3. Unity checks, Service II.

Girder		f_{bt}† MPa (ksi)	$(f_{bt})/(0.95R_hF_{yt})$
G1	Top Flange	41.4 (6.00)	0.11
	Bottom Flange	126.2 (18.30)	0.33
G2	Top Flange	97.91 (14.20)	0.26
	Bottom Flange	164.1 (23.80)	0.43
G3	Top Flange	156.7 (22.73)	0.41
	Bottom Flange	262.8 (38.12)	0.56

† : The factored maximum bottom (tension) flange stresses due to noncomposite loads that are used for combination with live load stresses in STRENGTH I do not include the effects of torsion on exterior girders from overhangs.

2.5.2 Cross-Frame Member Design

The cross-frame members in curved bridges are major load-resisting structural components. As such, the design of cross-frame members in curved bridges should be based on the forces directly obtained from structural analysis. For the test bridge, the cross-frames from the bending component test frame were re-used as long as they remained elastic during the ultimate load test of the composite test bridge. All the cross-frame members in the original test frame are 125 mm (5.0 in) outside diameter steel tubes with 6.25 mm (¼ in) wall thickness. The bottom chord of the cross-frames is centered at 200 mm (8.0 in) above the bottom of the web and top chord in centered at 150 mm (6.0 in) below the top of the web. It should be noted that the use of angle or T sections

typically used for cross-frame members in bridge construction was ruled out due to the difficulty in instrumenting these types of members to determine their axial strain and thereby estimate their axial force. However, the axial load-deflection behavior of comparable angle or T-sections would be essentially the same as that of the tubes as long as a strength limit state were not reached on the cross-frame members. If this fact were not true, it would not be appropriate to model cross-frames using truss elements for overall structural analysis of a bridge system.

Preliminary full nonlinear FEA studies indicated that the cross-frames from the previous component bending test would remain elastic during the ultimate load test, with the exception of the cross-frame members marked in Figure 2.5.1. These members were anticipated to experience significant yielding unless they were reinforced. Therefore, these members were strengthened by splitting and welding larger tubes around the outside of the original tube members to ensure that these sections would remain elastic. This was done just prior to final loading of the composite test bridge to its ultimate capacity. In addition, the double-shear bolted connections shown in Figure 2.5.2 are reinforced by welding the perimeter of gusset plates in contact with the connection plate to transfer the larger cross-frame member forces at the ultimate capacity of the bridge.

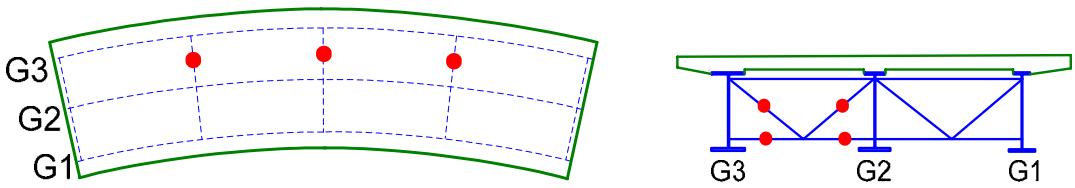

Figure 2.5.1. Cross-frames strengthened with tubes of larger diameters.

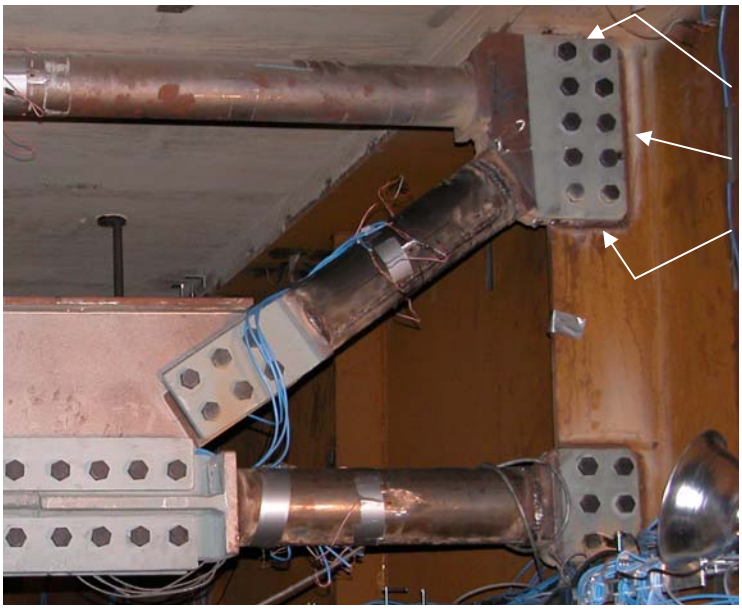

Figure 2.5.2. Welding around the gusset plates in contact with the connection plate to the outside girder, G3, courtesy of FHWA.

2.5.2.1 Sensitivity of Cross-Frame Member Forces to Member Area Changes

As mentioned above, the cross-frame members in curved I-girder bridges should be sized based on actual member forces obtained from structural analysis, since they are major force-resisting structural components. In sharp contrast with straight bridges, the system strength behavior of curved bridges can be influenced significantly by the strength of the cross-frame members. Furthermore, it is important to question the load redistribution capabilities of curved I-girder bridges after some of the cross-frame members have reached their strength limit states. In this regard, the importance of having good estimates for the cross-frame member forces cannot be overemphasized.

Curved bridges with widely-spaced cross-frames, such as the composite test bridge, involve much heavier cross-frame members due to higher axial force demands than other bridge configurations with closer cross-frame spacing. For some curved bridges with

wider cross-frame spacing, the stiffness of the cross-frames can be substantial such that axial forces coming into the cross-frame members might be insensitive to changes in the member areas relative to areas needed to resist the design forces. However, for other curved bridges with more closely-spaced cross-frames, and with the cross-frame member forces reduced accordingly, the sizing of the cross-frame members results in lighter member sizes. As a result, the cross-frames may have substantially smaller stiffness in some cases. It may be possible for the stiffness of the cross-frames in these kinds of bridge systems to reach a point where the axial forces in the cross-frame members are sensitive to changes in the member areas.

In order to investigate this potential sensitivity in the cross-frame member forces due to the changes of cross-frame member areas and due to cross-frame spacing, the area of the cross-frame members is systematically modified for two bridge configurations: (1) the test bridge configuration, which has a relatively wide cross-frame spacing, producing a subtended angle of $L_b/R = 0.1125$ (this subtended angle is slightly beyond the limit of 0.1 specified by AASHTO (2004b)) and (2) the test bridge geometry, but using a more reasonable cross-frame spacing of 4.572 m (15 ft) with a subtended angle of $L_b/R = 0.075$. Other potential variations in bridge geometries (girder dimensions, radius of curvature and slab dimensions) and material properties (concrete elastic modulus) are judged to have smaller effects on the member forces than the member areas and the subtended angle, L_b/R, and are held constant in this study. Also, it is assumed that the same cross-section is used for all the cross-frame members unless noted otherwise. This might be done for simplicity in detailing and fabrication and is a reasonable assumption for moderate length bridges such as the composite test bridge. Finally, the member areas of

all the cross-frame tube members are changed systematically by setting the diameter of the tube to 125 mm (5 in) and varying its thickness. For each case, separate noncomposite construction and composite live load analyses are performed, and factored cross-frame member forces are obtained, using the Strength I load combination: 1.25DC+1.75LL. The composite live load analysis uses the two-truck two-lane AASHTO live load model that induces the maximum flexural effects on the outside girder, G3.

Figure 2.5.3 shows the factored axial force for the bottom chord of the midspan cross-frame attached to girder G3 versus the cross-frame member areas. It is of interest to note that the noncomposite dead load contributions remain relatively constant at 489 kN (110 kips) over a range of the member areas as indicated by the dashed-dotted line. In fact, there is no significant reduction in the noncomposite dead load cross-frame member forces with reduction in member area until the member areas are less than about 0.64 cm^2 (0.1 in^2). Figure 2.5.3 also shows that the total factored cross-frame member forces due to noncomposite dead plus composite live load in the test bridge, increase gradually with increasing member area. However, an area of 24.1 cm^2 (3.73 in^2) is required for the bottom chord to satisfy the AASHTO Strength I requirements. Coincidently, this is the member area for a 5 × ½ tube member taken for the original cross-frames used during Phase II test. The variation in the member force for areas larger than this value is relatively minor. The total forces vary from about 877 kN (197 kips) when the members are sized exactly for the strength requirements to an asymptote at about (966 kN) (217 kips) for increasing member areas. Therefore, at least for the composite test bridge, any

variation in the cross-frame member areas that satisfies the Strength limit state requirements does not cause any significant change in the cross-frame member forces.

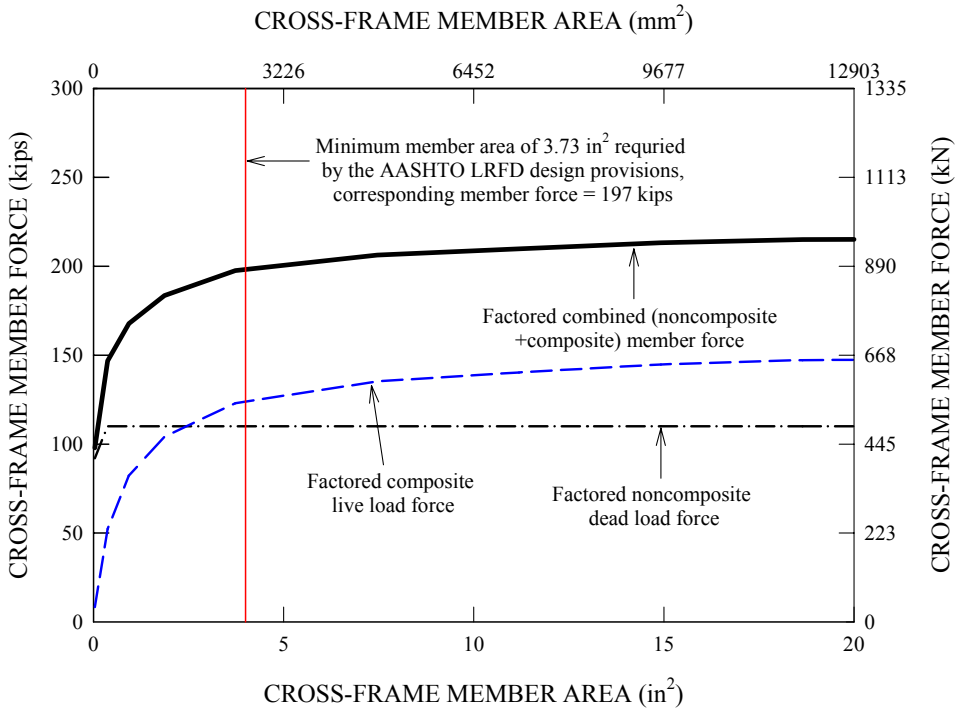

Figure 2.5.3. Test bridge - factored axial member force variations with respect to member area changes for the outside bottom chord of the midspan cross-frame attached to the outermost girder, G3.

Based on the resulting factored member forces, the cross-frame members are checked for their capacities using the AASHTO (2004b) Specifications for steel hollow structural sections (HSS). The bottom chord of the midspan cross-frame can be treated conceptually as a simply-supported column subjected to two axial forces as shown in Figure 2.5.4: P_1, the axial force at the end corresponding to the end of the bottom chord meeting the middle girder, G2, and P_2, the other axial force applied at the middle of the member corresponding to the juncture where two cross-frame diagonals meet the bottom chord.

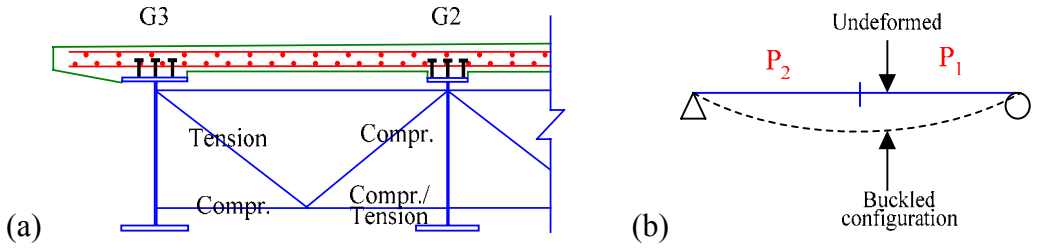

Figure 2.5.4. (a) Elevation view of the midspan cross-frame attached to the outside girder, G3, with possible force states (tension/compression) for the factored member forces and (b) schematic treatment of the bottom chord as a simply-supported column subjected to two axial forces along the length.

The effective-length factor for the chord buckling normal to the plane of the cross-frame may be approximated from the two forces P_1 and P_2, as follows:

$$K = 0.75 + 0.25(P_1 / P_2)$$

where $P_2 < P_1$ (Timoshenko and Gere 1961). In the original development of this equation, two compressive forces only were considered. However, the SSRC Guide (Galambos 1998) extends this equation to the case in which one of the two forces is in tension. As the member area is increased, the ratio of two compressive forces decreases. Accordingly, resulting effective length factors gradually decrease from 0.72 to 0.83. It turns out that the effective length factor is approximately equal to 0.75 for the case with a member area of 24.1 cm^2 (3.73 in^2).

It should be noted that the areas required would be greater if the members were other than tube sections, due to the lesser efficiency of other cross-section types for transmitting the axial force. In general, smaller member forces are induced in the cross-frame diagonal members than in bottom chord members. Correspondingly, the diagonal members are typically sized using smaller member areas than the cross-frame bottom

chords. In order to address the potential influence of smaller cross-frame diagonal members in considering the sensitivity of the cross-frame member forces to cross-frame member area changes, two types of cross-frames are considered below. The first type uses a single tube cross-section with an area equal to 24.1 cm^2 (3.73 in^2) for all the cross-frame members, the case that just satisfies the strength requirements for the critical bottom chord member in the above developments. The resulting factored total member forces are 877 kN (197kips) and 534 kN (120 kips) for the bottom chord and diagonal members, respectively. These member forces bring the design unity checks to 1.0 for the bottom chord and 0.5 for the diagonal member. The second type of cross-frame uses tube members with an area equal to 24.1 cm^2 (3.73 in^2) and 12.1 cm^2 (1.865 in^2) for the top and bottom chords and for the diagonal members, respectively. These areas give design strength ratios that are close to 1.0 for both the bottom chords and the compression diagonal members. It can be seen that only the half member area used for the bottom chord is necessary for resisting the factored member force in the diagonal member. The corresponding factored total member axial forces are 850 kN (191 kips) and 498 kN (112 kips) for the bottom chord and diagonal members, respectively. It is interesting to note that the cross-frame member forces for the second case are reduced from those for the first case by only 4 percent and 7 percent for the bottom chord and diagonal members, respectively. The use of smaller areas for the diagonal members causes a slight reduction in the overall stiffness of the bridge system, in turn increasing the girder deflections slightly. In fact, the G3 bottom flange midspan vertical deflection is increased from 1.58 in to 1.60 in for the composite bridge configuration and from 5.08 in to 5.13 in for the noncomposite bridge configuration. Nonetheless, it is important to note that the factored

member forces for the second case are only slightly less than those for the first case. This indicates that the influence of using the smaller member sizes for the diagonal members on the cross-frame member forces is minor for the test bridge. Therefore, the use of a single tube member cross-section for all the cross-frame members is justified.

As noted above, the L_b/R ratio for the composite test bridge is beyond the design limit allowed by the current AASHTO Specifications. One may argue that the induced cross-frame member forces can be much larger than those observed in typical bridges with smaller cross-frame spacing, and the corresponding cross-frame member sizes must be much heavier than realistic cross-frame members. In other words, the cross-frame forces for the bridge with more reasonable and closer cross-frame spacing may be more sensitive to member area changes than the bridges with wider cross-frame spacing. To study the effects of more realistic cross-frame spacing on the cross-frame member forces, the spacing between the cross-frames within the composite test bridge is modified such that the L_b is equal to 0.075R instead of 0.1125R. Figure 2.5.5 presents a plan view of the bare steel girder configuration for the composite test bridge after the above modification.

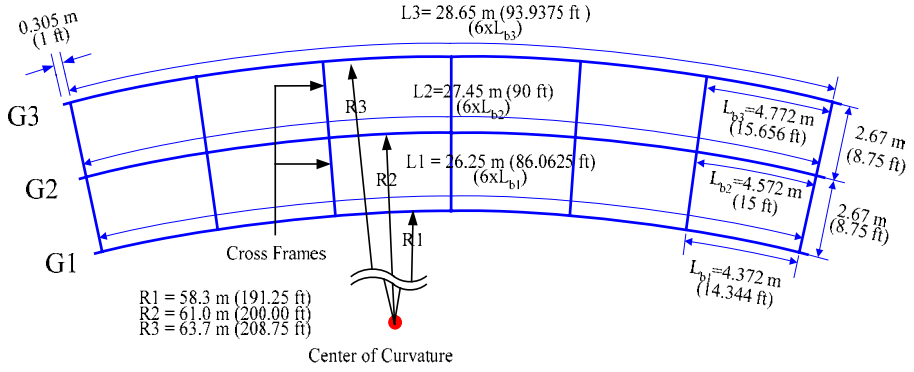

Figure 2.5.5. Plan view of the bare steel girder configuration for the composite test bridge with the spacing between the cross-frames on G2 set to 4.57 m (15 ft) instead of 6.86 m (22.5 ft).

Figure 2.5.6 shows the resulting factored axial member forces for the bottom chord of the midspan cross-frame attached to girder G3 versus the member areas (equal areas assumed for each member). As expected, it can be seen that magnitudes of the member forces coming into the bottom chord member are smaller than those observed for the composite test bridge. However, the overall characteristics of the member force variations are otherwise essentially identical to those for the original test bridge cross-frame member forces (see Figure 2.5.3).

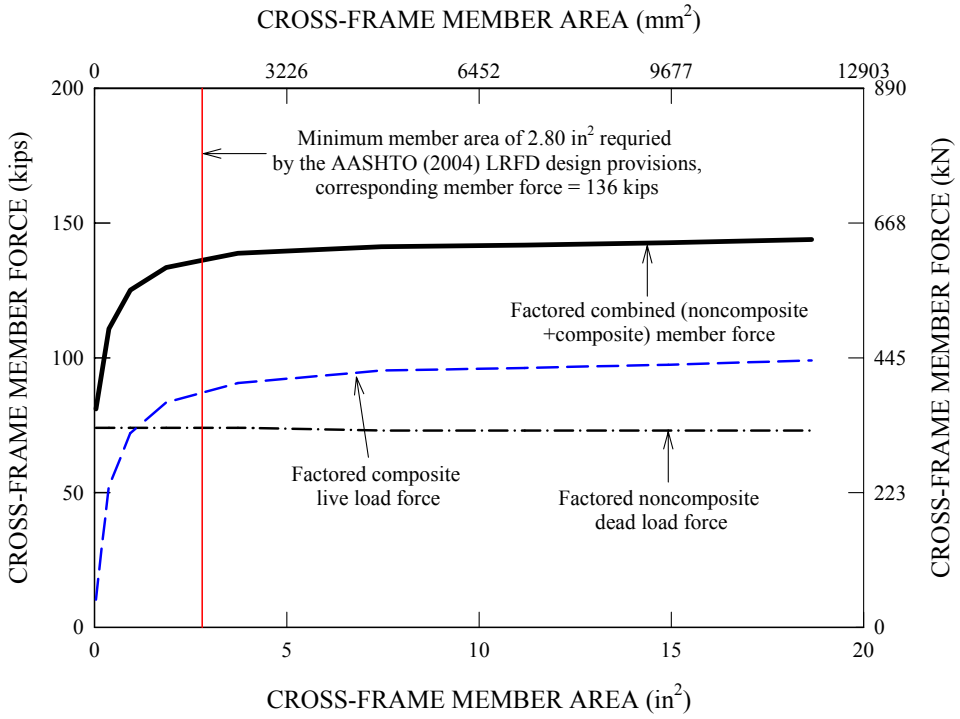

Figure 2.5.6. Test bridge geometry with the L_b/R ratio equal to 0.075 - factored axial member force variations with respect to member area changes for the outside bottom chord of the midspan cross-frame attached to the outermost girder, G3.

The vertical solid line in Figure 2.5.6 indicates the minimum member area of 18.1 cm^2 (2.80 in^2) necessary for the cross-frame members to satisfy the AASHTO Strength I check. Similar to the previous solution, the cross-frame member force at this minimum

member area is not significantly different from the member force of 640.54 kN (144 kips) obtained in the limit of much larger member areas

Based on the above findings, it can be concluded that the axial forces in the cross-frame members are not sensitive to the cross-frame member areas, at least for the bridge configurations considered in this study, as long as the cross-frame members satisfy the AASHTO (2004b) strength requirements. For other types of structural members (e.g. double angles or tee sections) typically used for cross-frame members in curved bridges, the same conclusion can be drawn without loss of generality since the required member areas for these types of structural members are generally larger than those of tube members (the tubes are structurally more efficient sections for struts).

2.5.3 Shear Stud Design

In order to provide the resistance to interface shear between the concrete slab and the steel section, stud shear connectors are provided. According to Article 6.10.10.1.4 in AASHTO (2004b), the height of shear studs is selected as 150 mm (6.0 in). The diameter of the studs is determined from Article 6.10.10.1 as 18.75 mm (0.75 in). The number of shear studs per cross-section, spaced at 150 mm (6.0 in) across the width of the flanges, is 3 for girder G2 and G3 and 2 for girder G2. The pitch of the shear connectors is selected such both the AASHTO fatigue and strength limit state checks are satisfied. The resulting pitch of the shear connectors is taken as 150 mm (6.0 in) for each of the three girders. It should be noted that in determining the pitch, both longitudinal and radial loadings are considered based on the AASHTO provisions. Figure 2.5.7 shows the studs welded on the top flanges of the girders in the test bridge prior to the installation of the slab reinforcement.

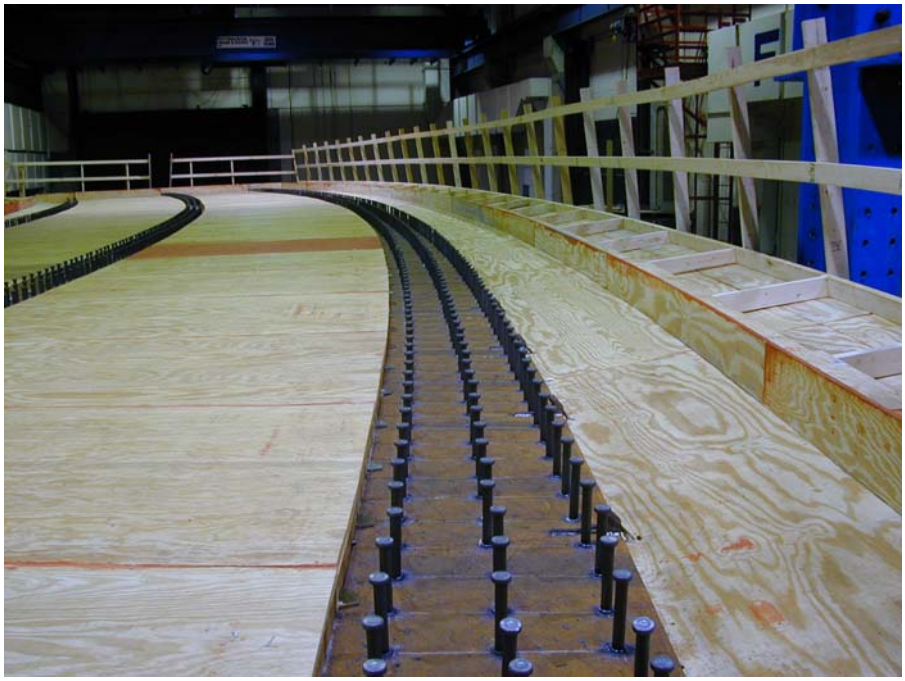

Figure 2.5.7. Shear studs welded on the top flanges of the girders in the test bridge, courtesy of FHWA.

2.5.4 Bridge Slab Design

The slab of the test bridge is designed by the provisions of Article 9.7.2 of the AASHTO (2004b) Specifications, which provides an empirical design methodology based on the concept of internal arching action. However, the empirical design may be used only if certain design conditions are satisfied. The relevant requirements are as follows:

- Cross-frames or diaphragms are used throughout the cross-section at the line of support.
- The supporting girders are steel and/ or concrete
- The deck is fully cast-in-place and water cured

- The deck is of uniform depth, except for haunches at girder flanges and other local thickening
- The ratio of the effective length to design depth does not exceed 18.0 and is not less than 6.0
- The core depth of the slab is not less than 100 mm (4 in)
- The effective length, as specified in Article 9.7.2.3, does not exceed 4100 mm (13.5 ft)
- The minimum depth of the slab is not less than 175 mm (7 in), excluding a sacrificial wearing surface where applicable
- There is an overhang beyond the centerline of the outside girder of at least 5.0 times the depth of the slab; this condition is satisfied if the overhang is at least 3.0 times the depth of the slab and a structurally continuous concrete barrier is made composite with the overhang
- The specified 28-day strength of the deck concrete is not less than 28.0 MPa (4.0 ksi)
- The deck is made composite with the supporting structural components

The test bridge slab meets all the above design requirements necessary for the application of the empirical design method, assuming that a structurally continuous barrier would be eventually made composite with the overhang (the overhang beyond the outside girder is 36 in, which is 4.5 times the depth of the slab).

The empirical design requires that four layers of isotropic reinforcement shall be provided and the minimum amount of reinforcement shall be 0.570 mm^2/mm (0.27 in^2/ft)

of steel for each bottom layer and be 0.380 mm^2/mm (0.18 in^2/ft) of steel for each top layer. The size and spacing of the slab reinforcing steel bares are as follows:

- Top bars: #4 bars @ 300 mm (12.0 in) center-to-center, both directions, centerline of transverse bars at 68.8 mm (2.75 in) below top of slab, centerline of longitudinal bars at 81.3 mm (3.25 in) below top of slab. This gives an area of 0.422 mm^2/mm (0.20 in^2/ft), which is greater than the minimum required 0.380 mm^2/mm (0.18 in^2/ft) in both directions for empirical design.
- Bottom bars: # 4 bars @ 200 mm (8.0 in), center-to-center, both directions, centerline of longitudinal bars at 159 mm (6.25 in) below top of slab, centerline of transverse bars at 169 mm (6.75 in) below top of slab. This gives an area of 0.633 mm^2/mm (0.30 in^2/ft), which is greater than the minimum required 0.570 mm^2/mm (0.27 in^2/ft) in both directions for empirical design.

Figure 2.5.8 shows a schematic illustrating the size and spacing of reinforcement in the bridge slab. Figure 2.5.9 shows the top and bottom layers of reinforcement installed in the bridge slab prior to the concrete casting operations.

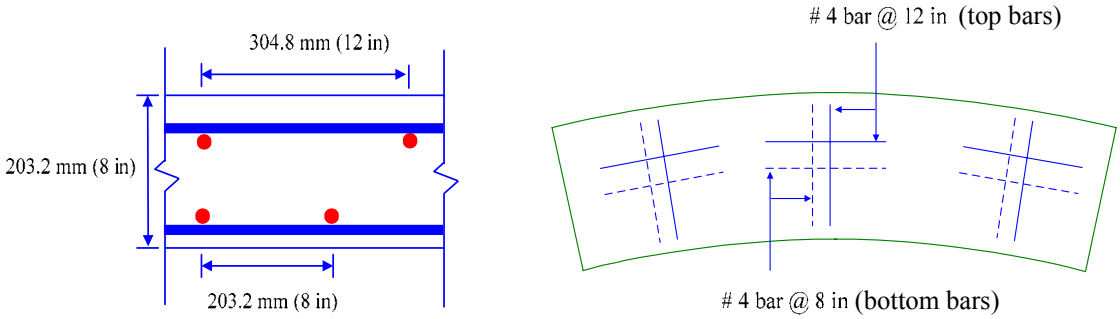

(a) cross-section view (b) plan view

Figure 2.5.8. Reinforcement schedule in the bridge slab.

Figure 2.5.9. Top and bottom layers of reinforcements installed in the bridge slab prior to concrete casting operation, courtesy of FHWA.

2.5.5 Web Shear Design and Design of Transverse Stiffeners

The web shear force envelopes for the three bridge girders are generated under the Strength I condition through a simple estimate of the influence coefficients for the design truck wheel load positions. Figures 2.5.10 through 2.5.12 provide the resulting shear envelopes for the three girders. The web shear design is based on the unified AASHTO LRFD (2004b) provisions, which use Basler's tension field action shear resistance equations for the design of both straight and curved I-girder bridges. The rationale behind this direct extension is based on recent research studies (Lee and Yoo 1999; White et al. 2001; Zureick et al. 2002; Jung and White 2006; White and Barker 2004).

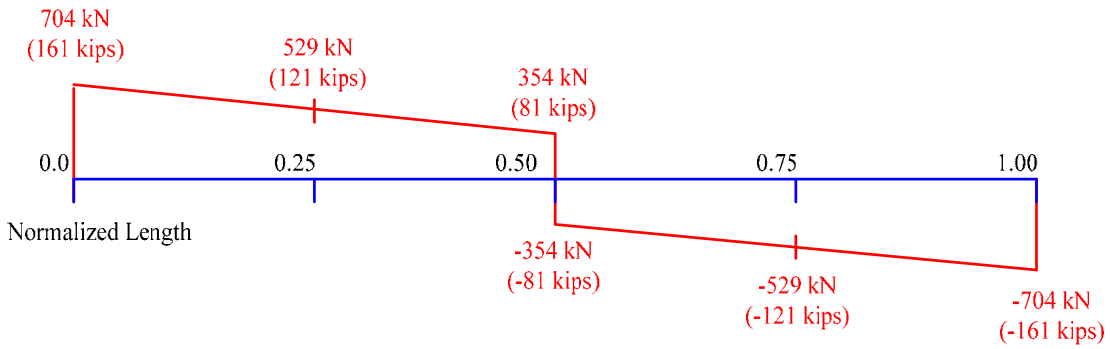

Figure 2.5.10. G1 - design shear envelope due to factored loads (1.25 × Dead load + 1.75 × Lane Load +1.75 × Truck Load × IM).

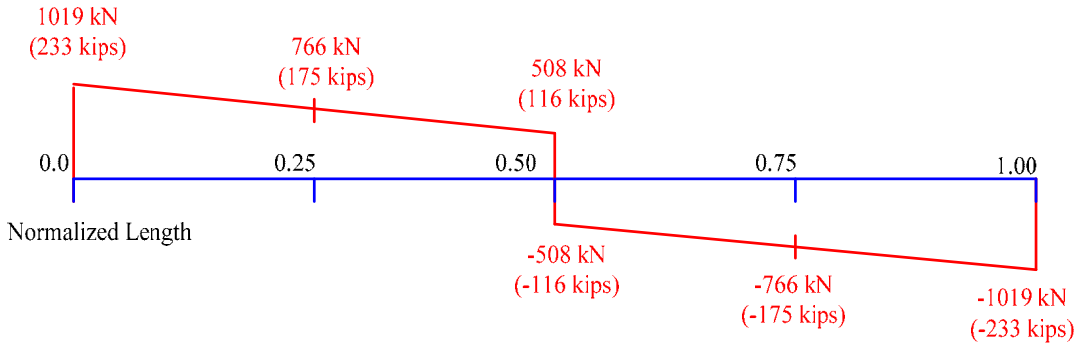

Figure 2.5.11. G2 - design shear envelope due to factored loads (1.25 × Dead load + 1.75 × Lane Load +1.75 × Truck Load × IM).

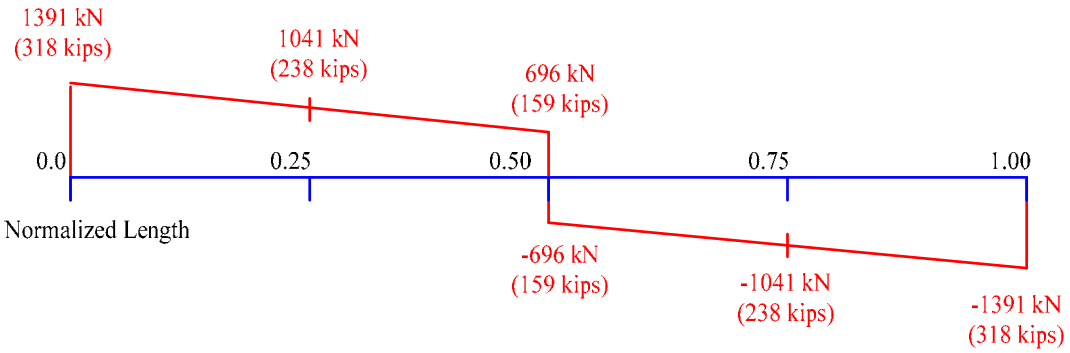

Figure 2.5.12. G3 - design shear envelope due to factored loads (1.25 × Dead load + 1.75 × Lane Load +1.75 × Truck Load × IM).

These studies have demonstrated that there is some reduction in the maximum shear strength of transversely stiffened I-girders due to horizontal curvature. However, this reduction is small and may be neglected within the following limits:

- $d_o/D \leq 3$,
- $D/t_w \leq 160$, and
- $L_b/R \leq 0.1$ in the final constructed configuration

At certain locations along the girder lengths, intermediate transverse stiffeners are needed to develop adequate shear capacity. The unified AASHTO (2004b) provisions for the design of transverse stiffeners in straight and curved I-girders are based on two criteria: (1) a moment of inertia requirement developed to ensure that the stiffener is able to maintain a line of zero lateral deflection at the web shear buckling load, and (2) for webs that are designed including tension-field action, an area requirement based on an estimate of the in-plane forces transmitted by the post-buckled web plate to the transverse stiffeners, for the stiffeners and the tension diagonals of the web panels to act as a Pratt truss in resisting shear forces larger than the web shear buckling load. Interestingly, as demonstrated by various independent research studies (Horne and Grayson 1983; Rahal and Harding 1990a, 1990b and 1991; Stanway et al. 1993 and 1996; Xie 2000; Lee et al. 2002 and 2003), at least for webs with a slenderness up to about $D/t_w = 250$, the stiffeners are loaded predominantly by bending induced by their restraint of web lateral deflections at the shear strength limit state, not by in-plane tension field forces. This indicates that the stiffener moment of inertia and/or section modulus is a more important design parameter than the stiffener area. That is, the area requirement is not relevant to the design of transverse stiffeners.

At the time of design of the transverse stiffeners in the composite test bridge, stiffener rigidity requirements necessary for adequate post-buckling strength of the curved I-girders were not established. Therefore, the transverse stiffeners were resized to have a

flexural rigidity of six times that required in the AASHTO (2004b) LFRD provisions, based on Lee and Yoo's(1999) recommendations for straight I-girder bridges. This is intended to ensure that each girder can develop its post-buckling shear resistance. Also, the transverse stiffeners are preferred to be compact under uniform compression, although the AASHTO (2004b) LRFD specification does not require this. This is to ensure that the transverse stiffeners are not affected by local buckling failures due to their cantilever action and plastic hinging at their tops associated with web distortion in the composite bridge at ultimate load levels.

For all the transverse stiffeners, the nominal thickness is selected as 5/8 in and the nominal width of outstanding leg is 113 mm (4.5 in), 138 mm (5.5 in), and 150 mm (6.0 in) for girders G1, G2, and G3, respectively. Figures 2.5.13 through 2.5.15 show the resulting schematic layouts for the locations of bearing stiffeners, transverse stiffeners, and connection plates for girders G1, G2, and G3, respectively. The transverse stiffeners on the east side of the midspan are cut short of the tension bottom flange.

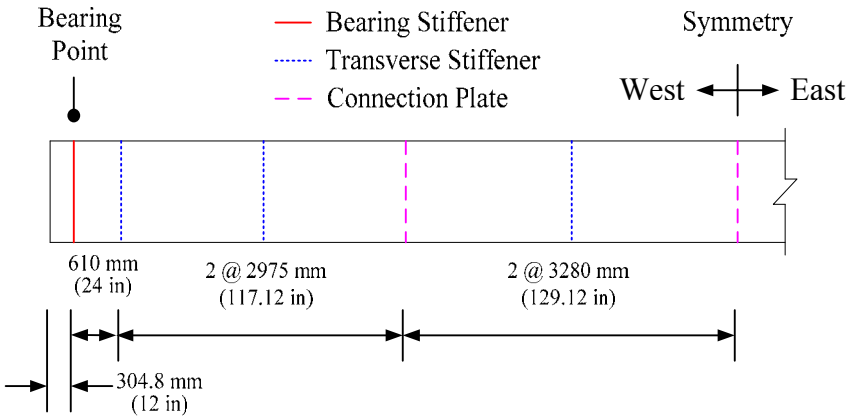

Figure 2.5.13. G1 – location layout for bearing stiffeners, transverse stiffeners and connection plates.

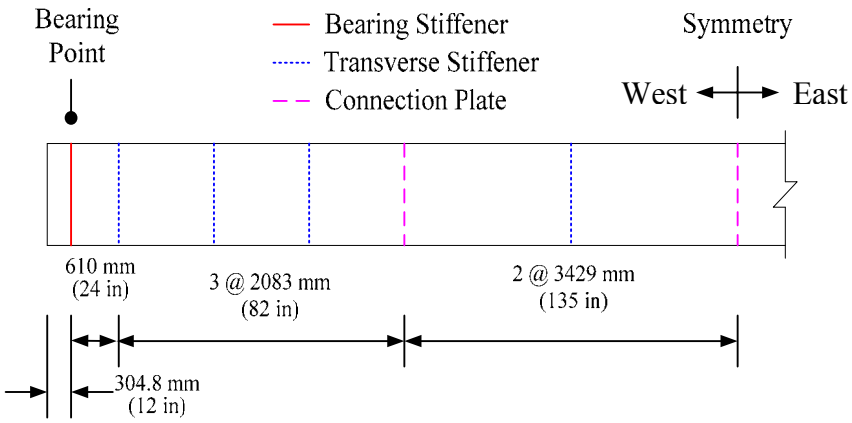

Figure 2.5.14. G2 – location layout for bearing stiffeners, transverse stiffeners and connection plates.

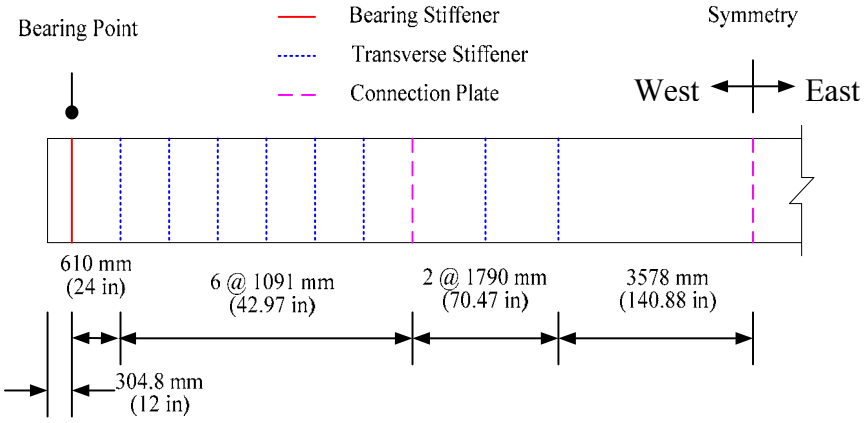

Figure 2.5.15. G3 – location layout for bearing stiffeners, transverse stiffeners and connection plates.

Recently, Kim and White (2004) investigated the behavior of one- and two-sided intermediate transverse stiffeners in straight and horizontally curved steel I-girders by refined finite element analysis, and arrived at new recommendations for the design of transverse stiffeners in straight and curved I-girder bridges. The recommended equation for the design of transverse stiffeners in all types of curved and straight bridge I-girders defines the minimum stiffener moment of inertia needed for development of the web shear post-buckling strength as follows:

$$I_t \geq \frac{bD^3 J}{1.4\left[\frac{Ek}{F_{yw}}\right]^{1.5} \rho_t^{0.75}} \tag{2.11}$$

where b = the smaller of d_o and D (in.),

d_o = the smaller of the adjacent web panel widths (in.),

I_t = moment of inertia of the transverse stiffener taken about the edge in contact with the web for single stiffeners and about the mid-thickness of the web for stiffener pairs (in.^{4}),

J = stiffener bending rigidity constant,

= $\frac{2.5}{(d_o / D)^2} - 2.0 \geq 0.5$

K = shear-buckling coefficient,

= $5 + \frac{5}{(d_o / D)^2}$

ρ_t = the larger of F_{yw}/F_{crs} and 1.0,

F_{crs} = local buckling stress for the stiffener (ksi), and

= $\frac{0.31E}{(b_t / t_p)^2} \leq F_{ys}$

F_{ys} = specified minimum yield strength of the stiffener (ksi)

Eq. (2.11) provides an accurate to somewhat conservative stiffener sizes relative to refined FEA solutions for straight and curved I-girders and all values of D/t_w permitted by the AASTHO (2004b) Specifications (Kim and White 2004). The AASHTO Interim provisions have been updated to include this equation, and the transverse stiffener area requirements have been removed for both straight and curved girders. For girders with single-sided stiffeners as with the test bridge transverse stiffeners, Eq. (2.11) typically gives somewhat smaller single-sided stiffeners compared to the area requirement in

previous specifications at $V_u = \phi_v V_n$. It turns out that the test bridge transverse stiffeners have a moment of inertia that is over four times the minimum moment of inertia using the Eq (2.11). Therefore, the moment of inertia is large enough such that the test bridge girders can develop their web shear post-buckling resistance associated with tension-field action.

2.5.6 Bearing Stiffener Design

The same bearing stiffeners as in the bending component test frame are used with the exception of the exterior face of girder G1. This facilitates the re-use of the existing cross frames. The nominal stiffener dimensions are:

- 25 mm (1.0 in) × 225 mm (9.0 in) (girder G3) on both sides of web
- 25 mm (1.0 in) × 225 mm (9.0 in) (girder G2) on both sides of web
- 18.75 mm (0.75 in) × 175 mm (7.0 in) on inside (girder G1) and 18.75 mm (0.75 in) × 125 mm (5.0 in) on outside of girder G1

The bearing stiffeners are checked against slenderness limit, bearing resistance requirement and axial resistance requirement of AASHTO Article 6.10.11.

2.5.7 Connection Plate Design

The same connection plates as in the bending component test frame are used except on the facia of G1. The nominal dimensions of these plates are:

- 225 mm (9.0 in) × 20.3 mm (13/16 in) both sides for G2 and G3

- 175 mm (7.0 in) × 15.63 mm (5/8 in) on inside (girder G1) and 125 mm (5.0 in) × 15.6 mm (5/8 in) on outside of G1

The connection plates are checked for the transfer of a radial component of the bottom flange force and the web force below the bottom chord of the cross-frame up to the bottom chord. The critical cross-section is located at the bottom chord of the cross-frames.

CHAPTER 3

FULL NONLINEAR FEA MODELING

3.1 Overview

The overall attributes of the full nonlinear FEA bridge models developed in this work are in many ways identical to those of the elastic bridge FEA model described in Chapter 2. However, a number of changes must be made to the elastic bridge FEA models to conduct an ultimate load test simulation. A J2 plasticity model (incremental flow theory) with a multi-linear isotropic hardening rule is utilized for steel and a plastic-damage model (coupled damage elastoplasticity theory) is used for concrete. Intermediate transverse stiffeners attached to physical girder webs to increase girder shear capacities are modeled explicitly in the full nonlinear models. These components are not included in the elastic design-analysis models to avoid including potentially false elastic restraints that these elements may provide to the lateral bending of the girder bottom flanges (if plastic hinging occurs at the top of these elements at maximum strength load levels). In addition, the steel reinforcement in the concrete slab is incorporated into the full nonlinear analysis models using a smeared approach. Top and bottom layers of the reinforcement are positioned in the shell element representation of the slab.

The cross-frame members utilized in the elastic design-analysis of the composite test bridge all have the same member area of 24.1 cm^2 (3.73 in^2). An early full nonlinear FEA indicated that most of the cross-frame members with this area would remain elastic during the ultimate load test. However, this analysis indicated that the bottom chords and diagonals of the mid- and quarter-span cross-frames attached to the outermost girder G3

would be yielded. Since the major goal of this study is to investigate the overall system strength of the test bridge, local yielding or failure of the cross-frame members should be prevented. Thus, the cross-frame members expected to yield were reinforced by increasing the original member area. This modification, which was made just prior to the physical ultimate load test (Test 4b, see Section 1.6) ensured that all the cross-frame members behave elastically through the entire experimental testing procedures. Separate studies not reported in this dissertation indicated that the additional area of the reinforced members did not cause any significant change in the elastic response of the composite test bridge. More general studies of the influence of cross-frame areas on the bridge responses are provided in Section 2.5.2.1.

Additional important modeling considerations for the full nonlinear FEA solutions are described in the following sections. Section 3.2 explains the loading schemes selected for Tests 2 to 4, which are approximately statically equivalent to the AASTHO live load models used for elastic design-analysis. Next, Section 3.3 reports the measured material properties for the concrete and steel along with their multi-linear representations incorporated into full nonlinear FEA models. In Section 3.4, the nonlinear material models for steel and concrete used in the full nonlinear FEA simulations are detailed with the necessary input parameters. In Section 3.5, the composite action between the steel I-girders and concrete slab is discussed with a focus on how different models of the interface affect the overall strength behavior of the composite test bridge. In Sections 3.6 through 3.8, other modeling considerations including the effects of residual stresses, the influence of geometric imperfections and the effects of concrete shrinkage are presented. This is followed by a description of the full nonlinear FEA procedures. The full

nonlinear analyses are executed in a single continuous process to simulate the dead load effects on the noncomposite structure, followed by the effects of slab shrinkage strains and then the effects of the applied loads on the composite structure.

3.2 Loading Schemes

The AASHTO live load models used in the design-analysis of the test bridge are modified to simpler loading setups in the actual composite bridge testing. These setups are approximately statically equivalent to the AASHTO design live load models. These simpler loading schemes are also utilized for the full nonlinear FEA simulation of the test bridge subjected to different loading configurations.

The full nonlinear FEA of the test bridge conducted in this study focuses on the last three testing sequences, Tests 2 through 4 (see Section 1.6). In what follows, the loading schemes employed in these three test sequences are explained in detail. First, the Test 2 loading scheme involves a group of six hydraulic jack loads positioned at the midspan on the outside lane of the test bridge, directly above the middle and outside girders G2 and G3, as shown in Figure 3.2.1. The ratio of the loads on G2 to the loads on G3 is maintained equal to one throughout the testing. This loading scheme is approximately equivalent to the AASHTO live load model that consists of a single design truck plus a lane load on the outside of the bridge for the maximum flexural effects on G3.

Similarly, the Test 3 loading scheme also involves a group of six hydraulic jack loads, but they are positioned at the midspan on the inside lane of the test bridge, directly above the inside and middle girders G1 and G2, as shown in Figure 3.2.2. The ratio of the loads on G1 to the loads on G2 is also maintained equal to one throughout this testing sequence.

This loading scheme approximates the single-truck plus single-lane AASHTO live load model that induces the maximum flexural effects on G1.

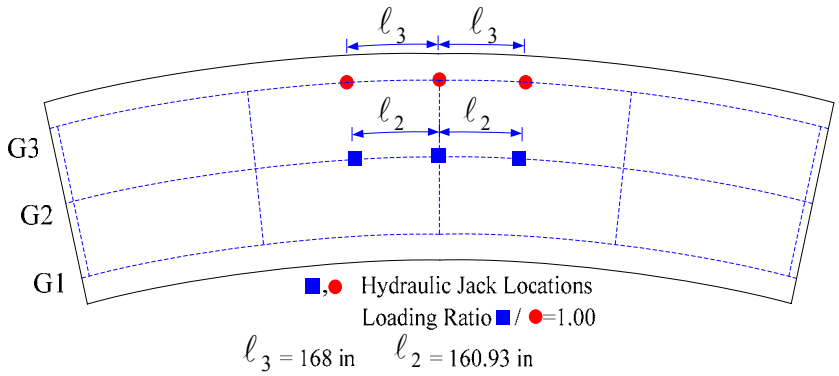

Figure 3.2.1. Test 2 loading scheme with six hydraulic jacks positioned at the midspan on the outside lane, approximately equivalent to the single–truck plus single-lane AASHTO design live load model inducing the maximum flexural effects on G3.

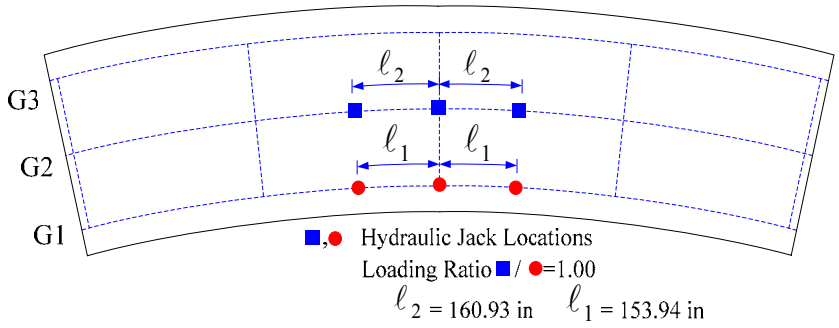

Figure 3.2.2. Test 3 loading scheme with six hydraulic jacks positioned at the midspan on the inside lane, approximately equivalent to the single-truck plus single-lane AASHTO design live load model inducing the maximum flexural effects on G1.

Next, as shown in Figure 3.2.3, the Test 4 loading scheme involves a set of nine hydraulic jack loads positioned at the midspan directly above all three girders. Contrary to the first two loading schemes for Tests 2 and 3, the magnitude of each of the loads is not the same in this setup. The loads applied on the middle girder are 2.24 times the loads applied to the inside and outside girders. This loading scheme is approximately

statically equivalent to the AASHTO live load model that consists of two design trucks aligned side-by-side at the middle of the test bridge slab plus two design lane loads, inducing the maximum flexural effects on G3.

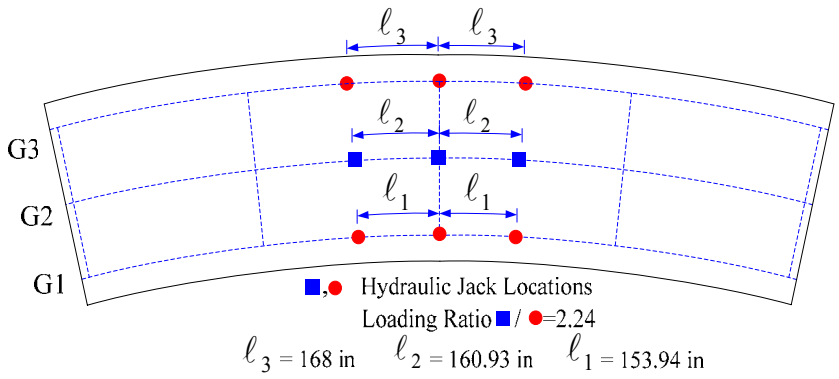

Figure 3.2.3. Test 4 loading scheme with nine hydraulic jacks positioned at the midspan on all three girders, approximately equivalent to the two-truck plus two-lane AASHTO design live load model inducing the maximum flexural effects on G3.

In what follows, the derivation of Test 4 loading scheme from the base AASHTO live load model is presented. The base loading scheme used for this maximum strength test is the AASHTO live load configuration causing the maximum bending effects on girder G3. The wheel load locations for the two design trucks in this loading scheme are shown in Figure 2.3.12 and the lane load locations are shown in Figure 2.3.13. The reader is referred to Section 2.3.6 for a complete description of these loadings. A dynamic allowance of 1.33 and a live load factor of 1.75 are applied to these truck loads. Furthermore, a multiple presence factor of 1.0 is used since there are two design lanes. This gives a total applied load of 1490 kN (335 kips) due to the AASHTO design vehicles. The dynamic allowance of 1.33 is not applied to the lane loads, but the live load factor of 1.75 is applied. The total applied load is equal to 907 kN (204 kips) due to

the two AASHTO lane loads. The total factored load causing the maximum bending effects on girder G3 is therefore 1490 kN (335 kips) + 907 kN (204 kips) = 2398 kN (539 kips).

In order to simplify the loading for the maximum strength test, and to reduce the localized actions within the slab in the vicinity of the load points, the alternate loading scheme shown in Figure 3.2.3 is used. This alternate loading scheme has the following attributes:

- The six wheel loads closest to girder G2 are grouped together into three loads applied directly over the top of this girder.
- The wheel loads near girders G1 and G3 are relocated to points directly over these girders.
- The loads on girders G1 and G3 are converted to three equal loads, rather than using the smaller wheel load associated with the front axle of the design vehicle and the larger loads associated with the two rear axles. These loads are indicated by the solid circles in Figure 3.2.3.
- The loads on girder G2 are also converted to three equal loads, indicated by the solid rectangles in Figure 3.2.3. Furthermore, the magnitude of these loads is taken as 2.24 times that of the circles, where 2.24 is the ratio of the cylinder areas of the hydraulic jacks used at these locations to that of the hydraulic jacks on G1 and G3.
- All of the above loads were applied over an area approximately equal to the AASHTO (2004) wheel load patch dimensions. In the FEA model, these concentrated loads are modeled as a line load over the top of the girders with a length equal to the corresponding wheel load dimension specified by AASHTO (2004b).

3.3 Material Properties

3.3.1 Stress-Strain Responses for Steel Girders

A total of seven steel plates of Grade 50 material and one steel plate of HPS70 material were used for fabricating the girders. The top and bottom flanges for girder G1 and the top flange for girder G2 were cut-curved from the same 2,400 mm × 21,600 mm (8.0 ft × 72.0 ft) Grade 50 steel plate. The bottom flange for girder G2 and the top flange for girder G3 were cut-curved from another 2,400 mm × 22,500 mm (8.0 ft × 75.0 ft) Grade 50 plate. The bottom flange for girder G3 was cut-curved from the 1,800 mm × 15,900 mm (6.0 ft × 53.0 ft) HPS70 plate. The web of girder G1 was cut from two steel plates, 1,560 mm × 20,580 mm (5.2 ft × 68.6 ft) and 1,530 mm × 19,080 mm (5.1 ft × 63.6 ft). The web of girder G2 was cut from two steel plates, 1,590 mm × 21,600 mm (5.3 ft × 72.0 ft) and 1,530 mm × 19,080 mm (5.1 ft × 63.6 ft). Finally, the web of girder G3 was cut from two steel plates, 1,620 mm × 23,100 mm (5.4 ft × 77.0 ft) and 1,530 mm × 19,080 mm (5.1 ft × 63.6 ft).

Table 3.3.1 summarizes the following mean values of key stress-strain data determined from tension coupons taken from the above plates: the modulus of elasticity E, the static yield F_y, the strain hardening modulus E_{st}, the strain at the onset of strain hardening e_{st}, the ultimate tensile strength F_u, and the strain at ultimate e_u.

The average E for all of the tension specimens is 204 GPa (29590 ksi) with a coefficient of variation of 2.3 percent. It is likely that the small differences in elastic moduli for the different plate tests are partly due to measurement errors. Furthermore, more exacting test procedures are necessary for reliable determination of the elastic modulus (ASTM 1997).

Table 3.3.1. Average engineering stress-strain data from the tension coupon tests (Beshah 2006).

Girders	Coupon Location	N	E GPa (ksi)	Static F_y MPa (ksi)	E_{st} GPa (ksi)	ε_{st} (%)	F_u MPa (ksi)	ε_u (%)
Girder G1	Web[(1)]	12	203.5 (29,520)	437.3 (63.43)	3.52 (510)	1.60	589.1 (85.44)	12.18
	Flanges (Top and Bottom)	6	204.4 (29,650)	396.9 (57.56)	4.08 (592)	1.18	564.3 (81.85)	12.36
Girder G2	Web[(1)]	12	206.0 (29,870)	436.3 (63.28)	3.30 (479)	1.61	582.5 (84.49)	12.41
	Top Flange	6	204.4 (29,650)	394.8 (57.56)	4.08 (592)	1.18	564.3 (81.85)	12.36
	Bottom Flange	6	210.9 (30,590)	400.4 (58.07)	4.37 (634)	1.00	577.9 (83.82)	12.04
Girder G3	Web[(1)]	12	203.4 (29,500)	438.7 (63.63)	3.25 (471)	1.72	582.9 (84.55)	12.28
	Top Flange	6	203.7 (29,550)	400.4 (58.07)	4.37 (634)	1.00	577.9 (83.82)	12.04
	Bottom Flange	6	197.5 (28,650)	491.7 (71.31)	2.78 (403)	1.29	621.3 (90.12)	10.71

[(1)]- The material properties for the girder webs are taken as the average properties of the two steel plates from which they are fabricated.

Therefore one value is selected for Young's modulus to represent all of the tests. The average value determined from the full set of the tension coupon tests is certainly reasonable, and thus this value is selected for the analysis studies in this research. The dispersion in the other stress-strain values is also relatively small. Therefore the average engineering stress-strain properties from all the coupons corresponding to each of the individual girder flanges and webs are utilized as the base for the steel stress-strain representations.

Since the S4R element in ABAQUS is based on a large strain formulation, true stress and true stain must be used when defining the material stress-strain response. However, the material test results are expressed in terms of engineering (or nominal) stress and strain. Therefore, this engineering stress-strain data is converted to true stress-strain using the following formulas (HKS 2004):

$$\sigma = \sigma_{nom}(1 + \varepsilon_{nom}) \tag{3.1}$$

$$\varepsilon = \ln(1 + \varepsilon_{nom}) \tag{3.2}$$

where σ is true stress, σ_{nom} is engineering (nominal) stress, ε is true strain, and ε_{nom} is engineering (nominal) strain.

Figures 3.3.1 and 3.3.2 show two representative multi-linear stress-strain curves used within the analysis models. The procedures used to obtain the multi-linear curves are as follows. The curves are based on four points obtained from the average engineering stress-strain data. The first point is the initial yield point of the material, and therefore has a plastic strain value of zero. The second point is defined at the onset of strain hardening (e_{st}, F_y) as defined in (Zureick et al. 2002). The third point is arbitrarily selected at a total engineering stress of $F_y + 2/3\ (F_u - F_y)$. The engineering strain corresponding to this point is determined as $e_{st} + 2/3\ (F_u - F_y) / E_{st}$. The fourth point is defined at the ultimate tensile stress on the engineering stress-strain curve. The four anchor points for the multilinear true stress-strain curves are obtained by applying Eqs. (3.1) and (3.2) to the above four points. The true stress is assumed to be constant for strains larger than that associated with the last point, although this magnitude of strain is not reached in any of the finite element analyses. Tables 3.3.2 through 3.3.7 present the specific stress-strain data for each of the component plates.

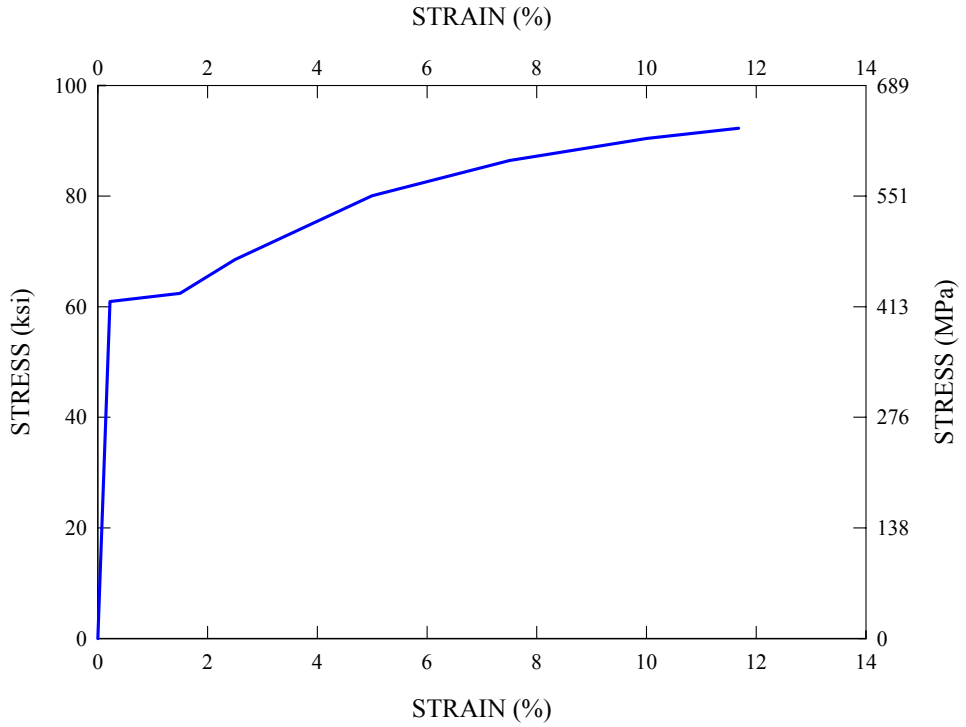

Figure 3.3.1. True stress-strain response for the flanges of girder G1 (Grade 50).

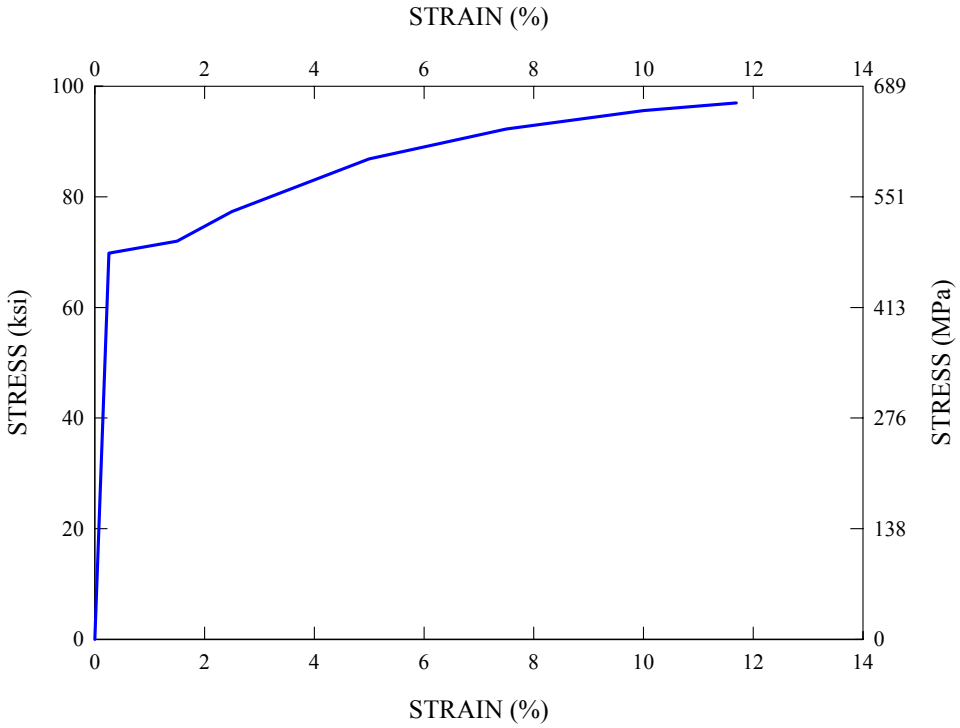

Figure 3.3.2. True stress-strain response for the bottom flange of girder G3 (Grade 70).

Table 3.3.2. Data points for multilinear stress-strain response for the flanges of girder G1 and the top flange of girder G2 (Beshah 2006).

Point	Nominal Stress MPa (ksi)	Nominal Strain (%)	True Stress MPa (ksi)	True Strain (%)
Yielding	396.9 (57.56)	0.20	398.5 (57.79)	0.20
Onset of strain hardening	396.9 (57.56)	1.18	401.5 (58.23)	1.12
Intermediate strain hardening	508.5 (73.75)	3.92	528.4 (76.64)	3.84
Ultimate strength	571.2 (82.85)	15.6	634.0 (91.96)	11.65

Table 3.3.3. Data points for multilinear stress-strain response for the web of girder G1 (Beshah 2006).

Point	Nominal Stress MPa (ksi)	Nominal Strain (%)	True Stress MPa (ksi)	True Strain (%)
Yielding	437.3 (63.43)	0.23	439.2 (63.70)	0.23
Onset of strain hardening	437.3 (63.43)	1.60	444.4 (64.45)	1.58
Intermediate strain hardening	538.5 (78.10)	4.47	562.6 (81.60)	4.37
Ultimate strength	589.1 (85.44)	12.18	660.8 (95.84)	11.49

Table 3.3.4. Data points for multilinear stress-strain response for the bottom flange of girder G2 and the top flange of girder G3 (Beshah 2006).

Point	Nominal Stress MPa (ksi)	Nominal Strain (%)	True Stress MPa (ksi)	True Strain (%)
Yielding	400.4 (58.07)	0.20	401.9 (58.29)	0.20
Onset of strain hardening	400.4 (58.07)	1.00	404.4 (58.65)	0.998
Intermediate strain hardening	518.7 (75.23)	3.71	537.9 (78.02)	3.64
Ultimate strength	577.9 (83.82)	12.04	647.5 (93.91)	11.37

Table 3.3.5. Data points for multilinear stress-strain response for the web of girder G2 (Beshah 2006).

Point	Nominal Stress MPa (ksi)	Nominal Strain (%)	True Stress MPa (ksi)	True Strain (%)
Yielding	436.3 (63.28)	0.22	438.2 (63.55)	0.22
Onset of strain hardening	436.3 (63.28)	1.61	443.3 (64.30)	1.60
Intermediate strain hardening	533.8 (77.42)	4.57	558.1 (80.95)	4.46
Ultimate strength	582.5 (84.49)	12.41	654.8 (94.97)	11.70

Table 3.3.6. Data points for multilinear stress-strain response for the bottom flange of girder G3 (Beshah 2006).

Point	Nominal Stress MPa (ksi)	Nominal Strain (%)	True Stress MPa (ksi)	True Strain (%)
Yielding	491. 7 (71.31)	0.26	493.9 (71.63)	0.26
Onset of strain hardening	491.7 (71.31)	1.30	518.7 (75.23)	1.28
Intermediate strain hardening	578.1 (83.85)	4.41	603.6 (87.54)	4.31
Ultimate strength	621.4 (90.12)	10.71	687.9 (99.77)	10.18

Table 3.3.7. Data points for multilinear stress-strain response for the web of girder G3 (Beshah 2006).

Point	Nominal Stress MPa (ksi)	Nominal Strain (%)	True Stress MPa (ksi)	True Strain (%)
Yielding	438.7 (63.63)	0.23	440.5 (63.89)	0.23
Onset of strain hardening	438.7 (63.63)	1.72	446.2 (64.72)	1.71
Intermediate strain hardening	534.9 (77.58)	4.68	566.8 (82.21)	4.58
Ultimate strength	583.0 (84.55)	12.28	654.6 (94.94)	11.58

3.3.2 Stress-Strain Responses for Cross-Frame Members and Slab Reinforcing Steel

The material used for the cross frame members is taken from the stub column measurements taken in the Phase I bridge erection study by Linzell (2000). A summary of the properties reported by Linzell (2000) is shown in Table 3.3.8. The corresponding stress-strain curves are shown in Figures 3.3.3 through 3.3.5.

Table 3.3.8**.** Cross frame member material properties from stub column tests (Linzell 2000).

Specimen	Meas. Avg. Tube Thickness mm (in)	Prop. Limit Stress MPa (ksi)	Yield Stress MPa (ksi)	Modulus of Elasticity GPa (ksi)	Strain Hardening Modulus GPa (ksi)
SC1	3.25 (0.128)	324 (47.0)	510 (74.0)	207 (30000)	5.52 (800)
SC2	3.28 (0.129)	317 (46.0)	503 (73.0)	207 (30000)	4.83 (700)
SC3	6.43 (0.253)	413 (60.0)	552 (80.0)	202 (29268)	5.52 (800)

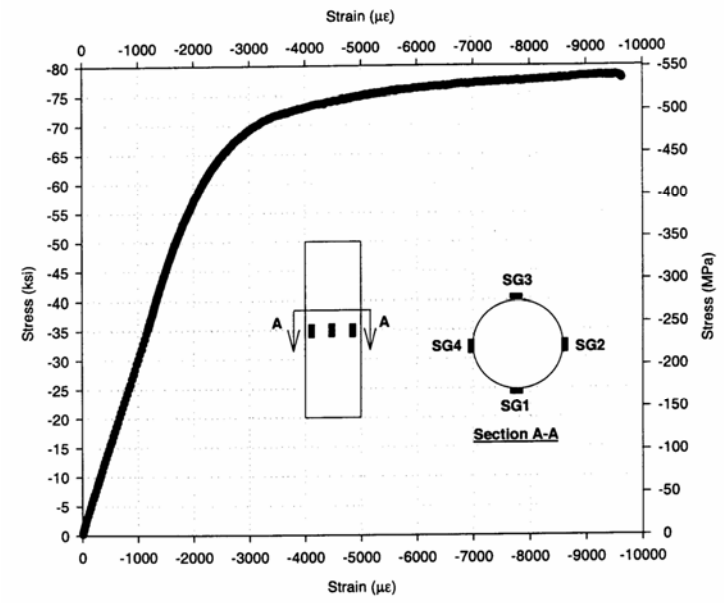

Figure 3.3.3. Stub column test SC1, stress vs. average strain (Linzell 2000).

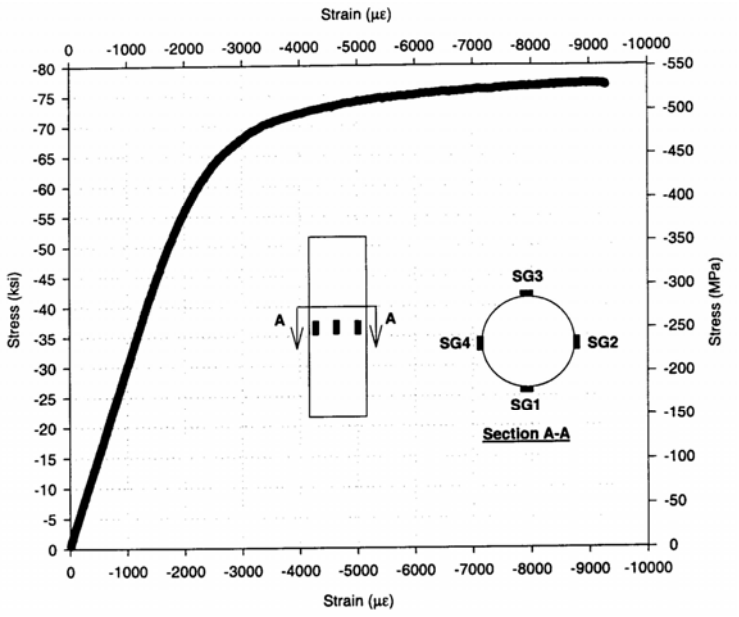

Figure 3.3.4. Stub column test SC2, stress vs. average strain (Linzell 2000).

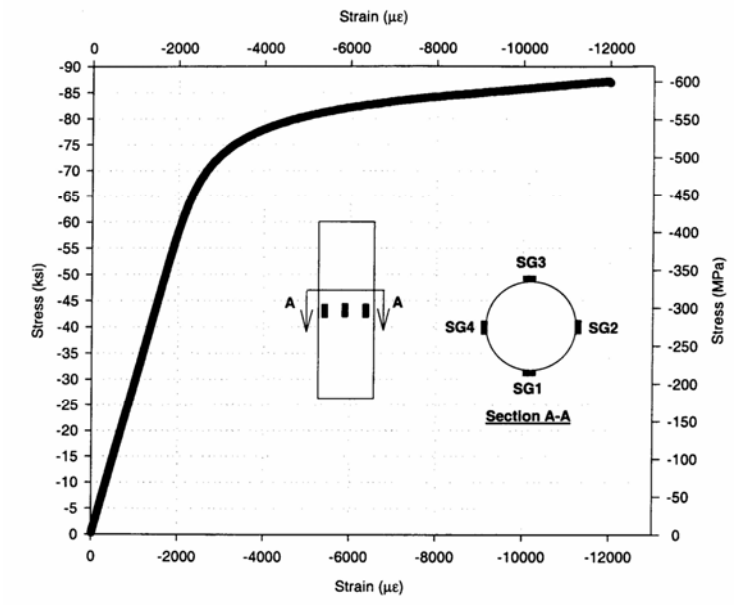

Figure 3.3.5. Stub column test SC3, stress vs. average strain (Linzell 2000).

Since the stub column SC2 has the lowest yield strength of the three columns, the results of SC2 are selected to construct a tri-linear stress-strain relationship for the cross-

frame members. A summary of the resulting stress-strain response is presented in Table 3.3.9 and the corresponding multi-linear stress-strain curve is shown in Figure 3.3.6.

Table 3.3.9. Data points for bilinear stress-strain response of cross frame members.

Point	Nominal Stress MPa (ksi)	Nominal Strain (%)	True Stress MPa (ksi)	True Strain (%)
Yielding	503 (73.0)	0.24	505 (73.2)	0.239
Ultimate strength	538 (78.0)	0.94	545 (79)	0.936

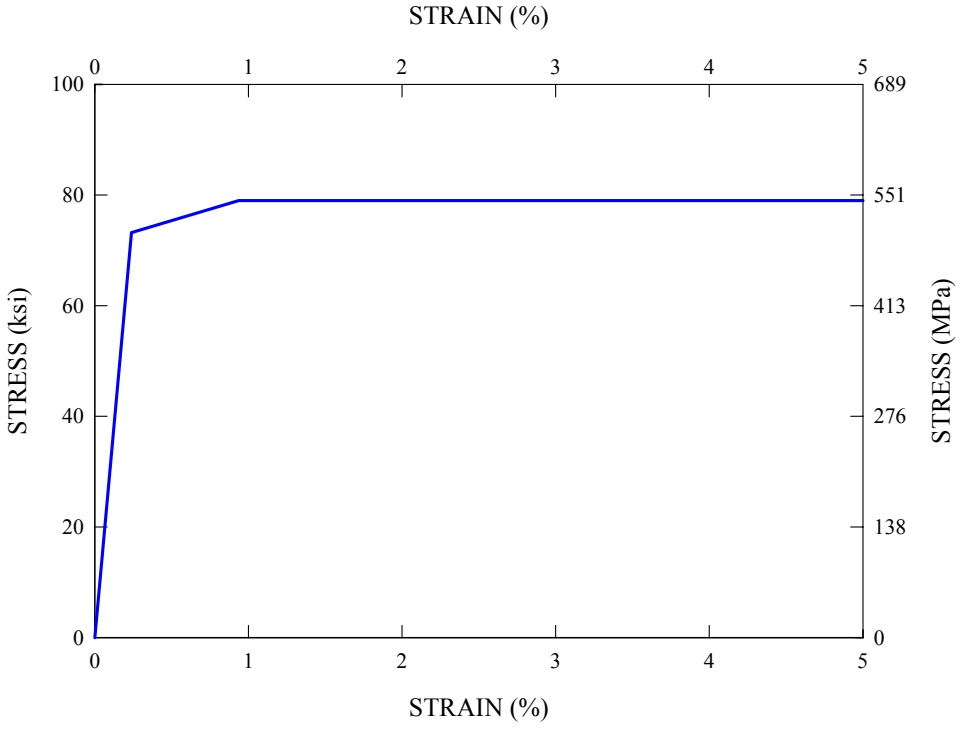

Figure 3.3.6. Typical true stress-strain response for cross-frame members.

For the slab reinforcing steel, an elastic-perfectly plastic stress-strain response with a nominal yield strength of 60 ksi is assumed.

3.3.3 Stress-Strain Responses for Concrete

3.3.3.1 Compressive Strength

Figure 3.3.7 shows the measured concrete compressive stress-strain curves based on six 298-day cylinder tests. Figure 3.3.8 presents the average compressive stress-strain response of these concrete cylinders. The average strength is 33.58 MPa (4.870 ksi) with a coefficient of variation of 2.85 percent. The corresponding strain is 0.03968 mm/mm (0.001562 in/in). Most concrete constitutive models used for FEA have been developed using plasticity concepts. Because of this fact, an initial yield surface must be defined in the material model. However, it is not easy to obtain a well-defined yield surface for brittle materials such as concrete and rock. In this research, the initial yield stress is based on the definition of the elastic modulus in ACI 318-02.

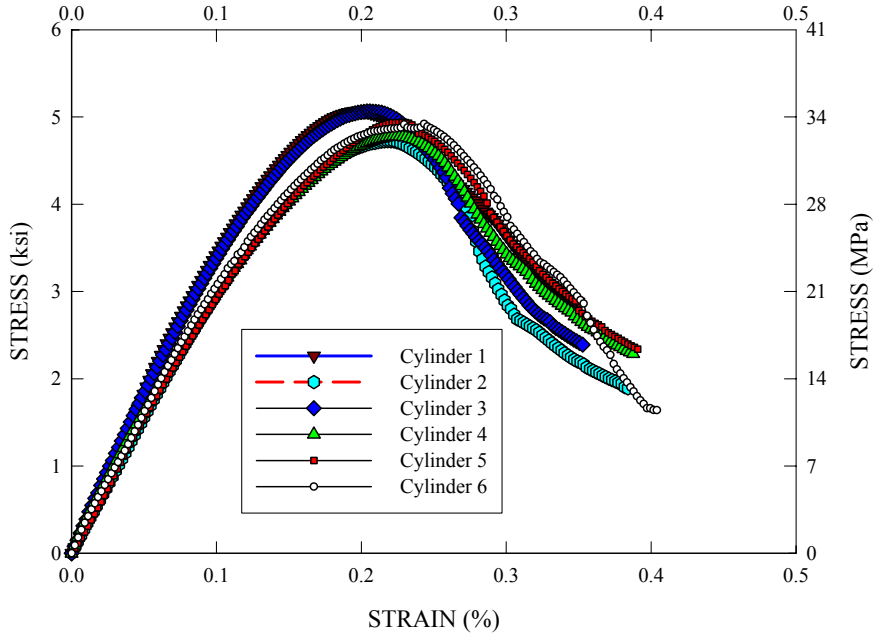

Figure 3.3.7. Measured concrete compressive stress-strain curves based on six 298-day cylinder tests (Beshah 2006).

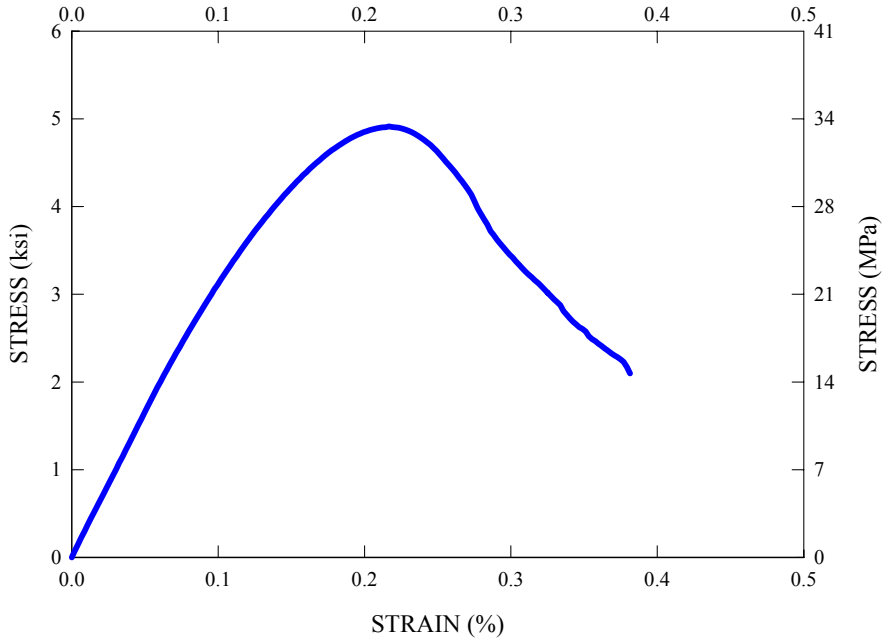

Figure 3.3.8. Measured average compressive stress-strain response of concrete based on six 298-day cylinder tests.

The commentary for Section 8.5 of ACI 318-02 states that elastic modulus of concrete, E_c, is defined as the slope of the line drawn from a stress of zero to a compressive stress of $0.45f_c'$. In this context, the yield stress of the concrete is defined as $0.45f_c' = 15.11$ MPa (2.192 ksi).

Figure 3.3.9 shows the complete multi-linear representation of the measured concrete stress-strain response used within the analysis models. The procedures used to obtain the multi-linear curves are as follows. The curves are based on nine points obtained from the average engineering stress-strain data. The first point is the initial yield point of the material as defined above. The second point is arbitrarily defined at a total engineering stress of $(0.45f_c' + f_c')/2$. The third to seventh points are defined around the peak stress. The fifth point is defined at the ultimate compressive stress on the engineering stress-strain curve. The third and fourth points are arbitrarily defined before the peak

compressive stress while the sixth and seventh points are defined after the peak compressive stress. These four data points near the peak stress are intended to better represent a smooth transition from the strain hardening branch to strain softening branch. The eighth point is selected at the point where there is a slight but distinct slope change in the descending branch. Lastly, the ninth point is defined at the end of the measured stress-strain curve.

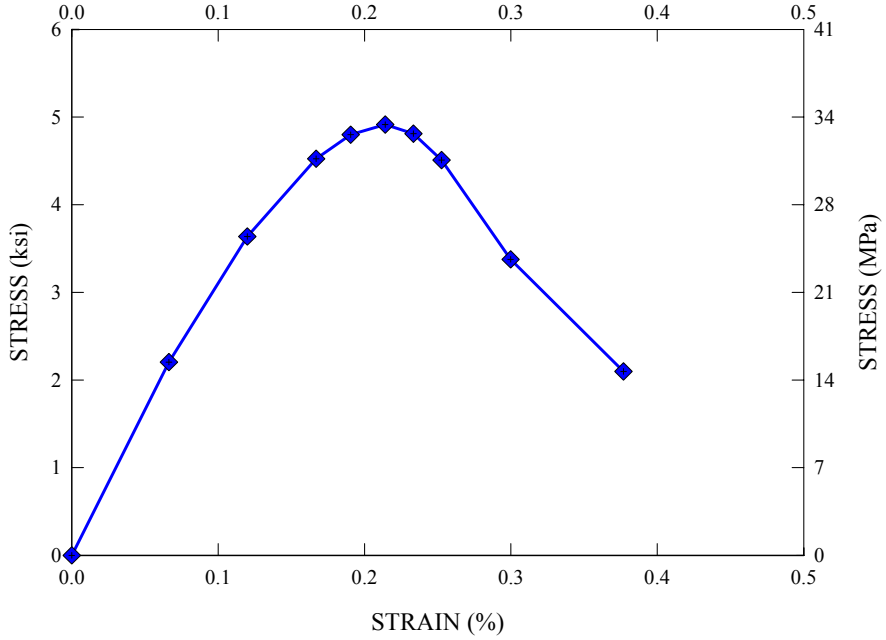

Figure 3.3.9. Multi-linear representation of measured average concrete compression stress-strain response used for the full nonlinear FEA of the test bridge.

3.3.3.2 Tensile Strength

Of a number of methods available for tension testing of concrete, the most commonly used methods are the split-cylinder test and the modulus of rupture test. Due to the fact that the bridge slab is expected to experience predominantly a state of plane stress, the split-cylinder test is considered more appropriate than the modulus of rupture test for determining the tensile strength of the concrete in this research. The strength obtained

from the modulus of rupture test, f_r, is used in design practice typically for members subjected to bending. The modulus of rupture generally has a higher value than the tensile splitting strength.

A total of six 298-day concrete cylinders were tested for the tensile splitting strength (Beshah 2006). The reported average value, f_{ct}, is 3.45 MPa (0.501 ksi) with a coefficient of variation of 6.85 percent. The corresponding strain is 0.03968 mm/mm (0.001562 in/in). The descending branch is constructed from the Barcelona model (Lubliner et al. 1989; Oller et al. 1990), based on the damage value from the cyclic tension tests by Yankelevsky and Reinhardt (1987) obtained at a stress value of $f_{ct}/2$ = 1.72 MPa (0.250 ksi). Figure 3.3.10 shows the assumed multi-linear representation of tension stress-strain response of the slab concrete. The detailed calculations are presented in the next section.

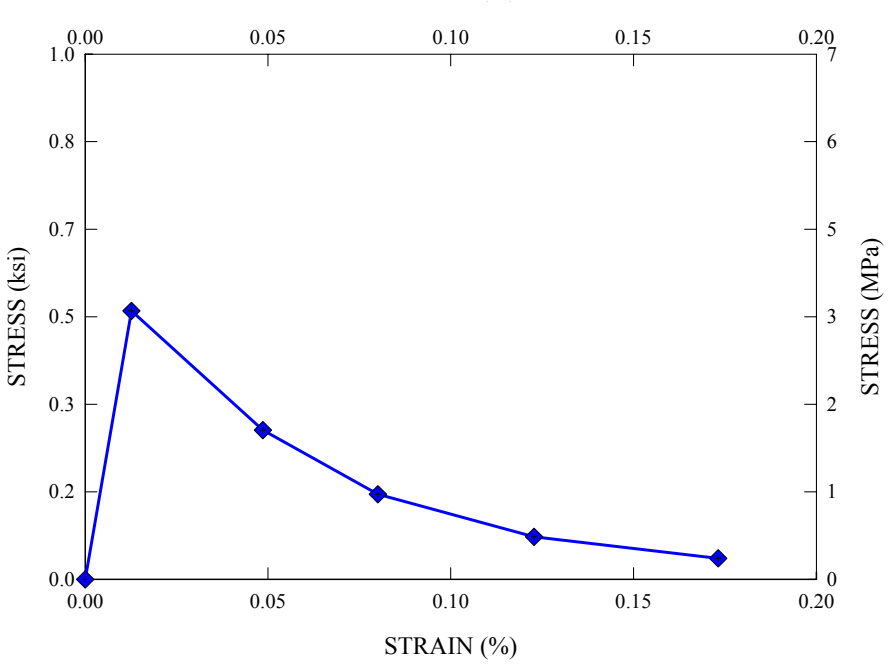

Figure 3.3.10. Multi-linear representation of concrete tension stress-strain response used for the full nonlinear FEA of the test bridge, based on six 298-day split-cylinder tests (Beshah 2006).

3.4 Material Models

3.4.1 J2-Plasticity for Steel

J2-plasticity (von Mises yield criterion) and multi-linear isotropic hardening associated with the true-stress true-strain curves discussed in Section 3.3.1 are assumed for the steel material.

3.4.2 Plastic-Damage Constitutive Model for Concrete

The concrete constitutive model selected for the full nonlinear FEA of the test bridge is the *Concrete Damaged Plasticity* model formulated by Lee et al. (1999). This continuum damage mechanics model is based on the concepts of fracture-energy-based damage and corresponding stiffness degradation. Two damage variables, one for tensile damage and the other for compressive damage, and a yield function with several hardening variables are introduced to account for different damage states.

Constitutive Relationships

In the incremental theory of plasticity, the strain tensor, ε, is decomposed into the elastic part, ε^e, and the plastic part, ε^p , which is given by

$$\varepsilon = \varepsilon^e + \varepsilon^p \tag{3.3a}$$

$$\varepsilon^e = \upsilon^{-1} : \sigma \tag{3.3b}$$

where the elastic stiffness υ is a rank-four tensor, and σ is the stress tensor. Since the effective stress $\overline{\sigma}$ is defined with the undamaged elastic stiffness from Eq. (3.3), it becomes

$$\overline{\sigma} = \upsilon_o : (\varepsilon - \varepsilon^p) \tag{3.4}$$

where υ_o is the initial elastic stiffness tensor. Scalar degradation damage, such that $\upsilon = (1-D)\upsilon_o E$ is assumed in many cases. Accordingly, the stress is factored into effective stress and stiffness degradation parts:

$$\sigma = (1-D)\bar{\sigma} \tag{3.5}$$

$$= (1-D)\upsilon_o : (\varepsilon - \varepsilon^p)$$

The plastic strain rate is evaluated by the flow rule, which is defined by a scalar plastic potential function, Φ. Given a plastic potential in the effective stress space, the plastic strain is given by

$$\dot{\varepsilon}^p = \dot{\lambda}\nabla_\sigma \Phi(\bar{\sigma}) \tag{3.6}$$

where $\dot{\lambda}$ is a non-negative function referred to as the plastic consistency parameter. In contrast with metals, a non-associative flow rule is necessary to obtain the proper dilatancy exhibited by frictional materials. A Drucker-Prager-type function is used as the plastic potential function:

$$\Phi = \|a\| + \alpha_p I_1 \tag{3.7}$$

where, I_1 =tr($\bar{\sigma}$), and $\|a\| = \sqrt{a:a}$ denotes the norm of the deviatoric effective stress, *a*. The parameter α_p is chosen to give the proper dilatancy for concrete. The plastic strain rate is obtained from Eqs. (3.6) and (3.7):

$$\dot{\varepsilon}^p = \dot{\lambda}\left(\frac{a}{\|a\|} + \alpha_p r\right) \tag{3.8}$$

Another internal variable, other than the plastic strain, is needed to represent the damage states. The damage variable, κ, is assumed to be the only necessary state variable. Its evolution is expressed as

$$\dot{\kappa} = \dot{\lambda}(\bar{\sigma}, \kappa) \tag{3.9}$$

For modeling of the cyclic behavior of concrete, which has very different tensile and compressive yield strengths, it is necessary to use two cohesion variables in the yield function: c_t, a tensile cohesion variable, and c_c, a compressive cohesion variable. The yield function in the Barcelona model, which only includes isotropic hardening, is modified to include two cohesion variables:

$$F(\bar{\sigma}, \kappa) = \frac{1}{1-\alpha}\left[\alpha I_1 + \sqrt{3J_2} + \beta(\kappa)\langle \hat{\sigma}_{\max} \rangle\right] - c(\kappa) \tag{3.10}$$

where $\hat{\sigma}_{\max}$ denotes the algebraically maximum principal stress, and α is a parameter determined by the initial shape of the yield function. The evolution of the yield function is determined by defining β, which is a constant in the Barcelona model, and the cohesion parameter, c, such that

$$\beta = \frac{c_c(\kappa)}{c_t(\kappa)}(1-\alpha) - (1+\alpha) \tag{3.11}$$

$$c = c_c(\kappa) \tag{3.12}$$

Figure 3.4.1 shows the initial shape of the yield surface, $F(\bar{\sigma}, h) = 0$, in the principal stress space for plane stress. In Figure 3.4.1, β_o and c_o denote β and c, respectively at the undamaged initial state.

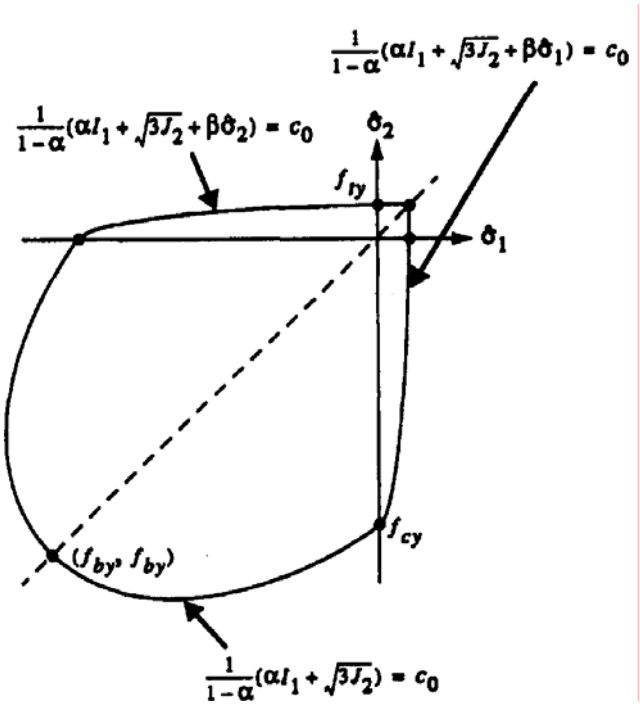

Figure 3.4.1. Lubliner (1989) yield function in plane stress space.

Evolution of Damage

To model the different damage states for tensile and compressive loading, both κ_t and κ_c are used as independent damage variables, and κ is defined as

$$\kappa = \begin{bmatrix} \kappa_t \\ \kappa_c \end{bmatrix} \tag{3.13}$$

The evolution equations for the hardening and degradation variables are obtained by factoring the uniaxial stress strength function, $f_\aleph = f_\aleph(\kappa_\aleph)$, such that

$$f_\aleph = (1 - D_\aleph)\overline{f_\aleph} \tag{3.14}$$

where $\aleph \in \{t, c\}$ is a state variable defined such that the state is uniaxial tension if $\aleph$ is t and uniaxial compression if $\aleph$ is c. Accordingly, the effective stress $\overline{\sigma_\aleph}$ and degradation variable $D_\aleph$ are defined as functions of $\kappa_\aleph$:

$$\overline{\sigma_\aleph} = \overline{f_\aleph}(\kappa_\aleph) \tag{3.15a}$$

$$D_\aleph = D_\aleph(\kappa_\aleph) \tag{3.15b}$$

in which $0 \le D_\aleph < 1$ and $\dot{D}_\aleph \ge 0$. The relation in Eq. (15a) describes the evolution of the cohesion variable used in the yield function, and Eq. (15b) defines the degradation damage as a function of the damage variable.

The damage evolution for a uniaxial state is defined based on the dissipated plastic energy, which can be written for quasi-brittle materials as

$$\dot{\kappa}_\aleph = \frac{1}{g_\aleph} f_\aleph(\kappa_\aleph)\dot{\varepsilon}^p \tag{3.16}$$

where $g_\aleph$ is the energy capacity per unit volume of the material. To obtain objective results at the structural level, the crack bandwidth along which the energy is dissipated is specified as a material property as $g_\aleph = G_\aleph / l_\aleph$ where $G_\aleph$ is the fracture energy in the uniaxial state and its counterpart in the uniaxial compressive state, and $l_\aleph$ is the characteristic length representing the crack bandwidth.

The evolution equations in Eq. (3.16) can be generalized for multiaxial cases in the form of

$$\dot{\kappa} = \dot{\lambda}\hat{t}(\hat{\bar{\sigma}}, \kappa) \tag{3.17}$$

where $\hat{t} = q(\hat{\bar{\sigma}}, \kappa) \cdot \nabla_{\hat{\bar{\sigma}}} G(\hat{\bar{\sigma}})$. Equation (3.17) is the specific form of evolution for the damage variables in Eq. (3.7) in terms of the effective stress and damage variables themselves.

Stiffness Degradation and Crack Opening/Closing

The experimental cyclic tests of concrete demonstrate that the degradation of stiffness from microcracking occurs in tension and compression, and that it becomes more significant as the strain increases. The mechanism of stiffness degradation under cyclic loading is complicated because of the opening and closing of microcracks. The crack opening/closing behavior can be modeled as elastic stiffness recovery during elastic unloading from a tensile state to a compressive state. The degradation damage variable defined in Eq. (3.15b) is modified by a multiplicative parameter, $0 < s < 1$, on D_t:

$$D = 1 - (1 - D_c(\kappa))(1 - sD_t(\kappa)) \tag{3.18}$$

The parameter $s = s(r(\hat{\bar{\sigma}}))$ represents stiffness recovery because r is a weight function of the effective stress, which ranges from 0.0 in pure compression to 1.0 in pure tension. Substituting Eq. (3.18) into Eq. (3.5) gives the total stress:

$$\sigma = 1 - (1 - D_c(\kappa))(1 - sD_t(\kappa))\upsilon_o : (\varepsilon - \varepsilon^p) \tag{3.19}$$

After a large amount of microcracking, the crack opening and closing mechanism becomes similar to discrete cracking, which can not represented by the classical approach of inelastic strain evolution. A modified evolution relation is used to simulate large crack opening and the closing/reopening process for the idealized continuum. It can be assumed that the microcracks join to form a discrete crack if $\kappa_t \geq \kappa_{cr}$, where κ_{cr} is an empirical value near unity. At that tensile damage level, the evolution of the plastic

strain caused by the tensile damage is stopped and the plastic strain rate is defined by an intermediate effective stress $\tilde{\sigma}$:

$$\tilde{\sigma} = \upsilon_o : (\varepsilon - \tilde{\varepsilon}^p) \in \{\tilde{\sigma} \big| F(\tilde{\sigma}, \kappa) \le 0\} \tag{3.20a}$$

$$\dot{\tilde{\varepsilon}}^p = \dot{\lambda} \nabla_{\tilde{\sigma}} \Phi(\tilde{\sigma}) \tag{3.20b}$$

$$\bar{\sigma} = \upsilon_o : (\varepsilon - \varepsilon^p) \tag{3.20c}$$

$$\dot{\varepsilon}^p = (1 - r(\hat{\tilde{\sigma}})) \dot{\lambda} \dot{\tilde{\varepsilon}}^p \tag{3.20d}$$

With the relations in Eq. (3.20), the degradation variable in Eq. (3.18) is redefined as

$$D = 1 - (1 - D_c(\kappa))(1 - sD_t(\kappa))(1 - sD_{cr}) \tag{3.21}$$

where $0 \le D_{cr} < 1$ is an additional degradation variable and determined by the Kuhn-Tucker-type loading/unloading conditions such that

$$\dot{D}_{cr} \ge 0 \tag{3.22a}$$

$$\dot{D}_{cr} F((1 - D_{cr})\bar{\sigma}, \kappa) = 0 \tag{3.22b}$$

$$F((1 - D_{cr})\bar{\sigma}, \kappa) \le 0 \tag{3.22c}$$

During continued loading

$(\dot{D}_{cr} > 0), F((1 - D_{cr})\bar{\sigma}, \kappa) = (1 - D_{cr})(F(\sigma, \kappa) + c_c) - c_c = 0$ which leads to

$$D_{cr} = 1 - \frac{c_c}{(F(\bar{\sigma}, \kappa) + c_c)} \tag{3.23}$$

It is noted that $(F(\bar{\sigma}, \kappa) + c_c)$ is a first-degree homogeneous function with respect to $\bar{\sigma}$.

Thermodynamic consistency of the model including the new degradation variable can be ensured by redefining ω in the generalized Helmholtz free energy rate

$\dot{\Psi} = \dot{e} - \omega\sigma : \dot{\varepsilon} - \rho\dot{\eta}\theta - \rho\eta\dot{\theta}$, in which e is the internal energy per unit volume, ρ is the density, η is the entropy per unit mass and θ is the thermodynamic temperature, from Lee and Fenves (1998), as

$$\omega = 1 - (1 - \omega_1)(1 - \omega_2) \tag{3.24}$$

where $\omega_1 = (1 - s)D_t / (1 - sD_t)$ and $\omega_2 = (1 - s)D_{cr} / (1 - sD_{cr})$. It is noted that $0 \le \omega < 1$ because $0 \le \omega_1$, $\omega_2 < 1$. The relationship between the Helmholtz free energy and the total potential energy function of an undamaged material, Ψ_o, is defined as $\Psi = (1 - \tilde{d})\Psi_o$, in which $\tilde{d} = 1 - (1 - D_c)(1 - D_t)(1 - D_{cr})$. Because $\dot{\tilde{d}} \ge 0$, and it can be assumed that $(\partial\Psi_o / \partial\kappa) \cdot \dot{\kappa} \le 0$ as shown in Lee and Fenves (1998), thermodynamic consistency of the present model is obtained by introducing Ψ_o such that $\partial\Psi_o / \partial\varepsilon^e = \upsilon_o : \varepsilon^e$. This leads to the relation

$$\sigma = \frac{(1 - \tilde{d})}{(1 - \omega_1)(1 - \omega_2)} \frac{\partial\Psi_o}{\partial\varepsilon^e} \tag{3.25}$$

which is identical to Eq. (3.5) using Eq. (3.21)

Rate-Dependent Regularization

Two well-known viscoplastic models used for regularization are the Perzyna model and the Duvaut-Lions model. The Duvaut-Lions model is more appropriate for the regularization of rate-independent plastic-damage models, because the Perzyna model fails to converge to the rate-independent model in some cases. In the original Duvaut-Lions model, the inelastic strain rate, $\dot{\varepsilon}^i$, is defined as

$$\dot{\varepsilon}^i = \frac{1}{\mu}\upsilon^{-1} : (\sigma - \sigma^*) \tag{3.26}$$

where σ^* denotes the projection of the stress, σ, onto a yield surface, and μ, which is called the viscosity parameter, represents the relaxation time of the viscoplastic system. The original Duvaut-Lions model can be generalized for any backbone model, regardless of the existence of the projection on a yield surface, by defining σ^* to be the stress of the rate-independent backbone model for the current strain ε.

Using the cyclic plastic-damage model as the backbone model, Eq. (3.26) is rewritten as

$$\dot{\varepsilon}^i = \frac{1}{\mu}\upsilon^{-1} : (\sigma - (1-D)\overline{\sigma}) \tag{3.27}$$

where $\overline{\sigma}$ is the effective stress, which is evaluated in the rate-independent backbone model. The stress-strain relation is

$$\sigma = \upsilon : (\varepsilon - \varepsilon^i) \tag{3.28a}$$

$$\upsilon = (1-D)\upsilon_o \tag{3.28b}$$

With Eqs. (3.5) and (3.28), the inelastic strain rate in Eq. (3.27) becomes

$$\dot{\varepsilon}^i = \frac{1}{\mu}(\varepsilon^p - \varepsilon^i) \tag{3.29}$$

Similarly, a rate-dependent degradation damage variable D is defined such that

$$\dot{D} = \frac{1}{\mu}(\overline{D} - D) \tag{3.30}$$

where $\overline{D}$ is the degradation damage variable defined in the rate-independent model, which is described earlier.

Equations (3.28)-(3.30) constitute the viscoplastic model based on the rate-independent backbone model. To show this model gives a unique solution in the incremental sense, consider two admissible stress rate fields:

$$\begin{aligned} \Delta\dot{\sigma} &= \Delta(\upsilon : (\dot{\varepsilon} - \dot{\varepsilon}^i)) - \Delta(\dot{D}\upsilon_o : (\dot{\varepsilon} - \dot{\varepsilon}^i)) \\ &= \upsilon : \Delta\dot{\varepsilon} - \upsilon : \Delta\dot{\varepsilon}^i - \Delta(\dot{D})\upsilon_o : (\dot{\varepsilon} - \dot{\varepsilon}^i) \\ &= \upsilon : \Delta\dot{\varepsilon} \end{aligned} \tag{3.31}$$

where Δ denotes a difference between two admissible fields. In Eq. (3.31), the differences between the two possible inelastic rates and degradation rates vanish, because they are determined by the current values in Eqs. (3.29) and (3.30). Since υ is a positive-definite tensor, Eq. (3.31) gives

$$\Delta\dot{\sigma} : \Delta\dot{\varepsilon} = \Delta\dot{\varepsilon} : \upsilon : \Delta\dot{\varepsilon} > 0 \tag{3.32}$$

unless $\Delta\dot{\varepsilon} = 0$ or $\Delta\dot{\sigma} = 0$. Therefore, the incremental uniqueness criterion is satisfied, which implies that the incremental stress field is unique in the model.

Calibration with Experimental Data

The following tests are needed to determine the required material constants for the concrete damaged plasticity model:

(1) Separate monotonic uniaxial compression and tension tests. The uniaxial stress-plastic strain is determined from the stress-strain curve of these tests by subtracting the elastic strain, given by the current stress divided by the undamaged elastic modulus E_c, from the total strain.

(2) Separate uniaxial cyclic compression and cyclic tension tests. These tests are necessary to determine the elastic stiffness degradation as a function of the inelastic strain. The elastic stiffness degradation is used to calculate the value of the corresponding damage variables as a function of the inelastic strain. The elastic stiffness for a given level of plastic strain is determined by the slope of a line between the unloading point and the intersection of the unloading stress-strain curve with the strain axis. The calculation of the damage variables is discussed subsequently.

The uniaxial stress and the value of the damage variables corresponding to each inelastic strain are input to the concrete damaged plasticity model to define the general constitutive response.

Figure 3.4.2 shows a typical uniaxial cyclic compressive stress-strain response of concrete. It can be seen that the elastic stiffness decreases with increasing strains. The stiffness degradation is caused by internal damage such as microvoids and microcracks.

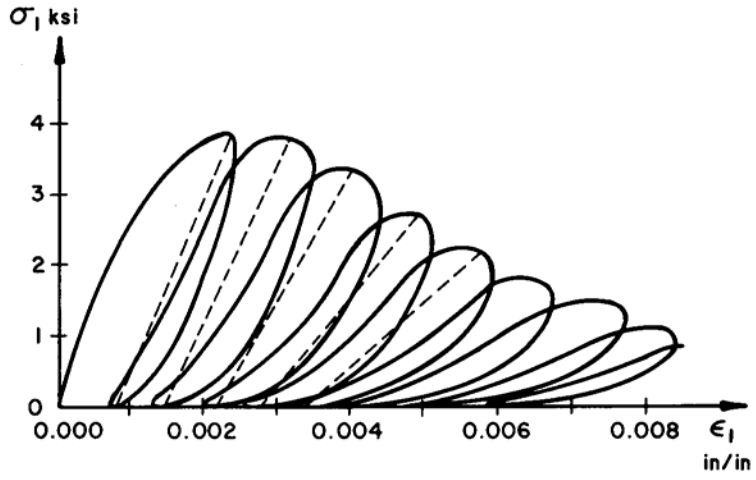

Figure 3.4.2. Typical uniaxial stress-strain curve of a concrete subject to cyclic compressive loading (Sinha et al. 1964).

The above cyclic tests require a special setup and are not as simple to perform as ordinary monotonic uniaxial tests. Also, since the concrete slab in the test bridge is loaded to failure predominantly in monotonic compression, the degradation in the elastic stiffness and the corresponding damage variables are only a secondary consideration. In this study, the damage variables are calculated based on prior experimental results (Sinha et al. 1964, Karsan and Jirsa 1969, Okamoto 1976 and Tanigawa 1979) and a proposed theoretical model explained below.

Damage variable calculation

In the damaged plasticity model, the evolution of the internal state variables is based on the damaged state of the material, which is expressed as the effective stress versus the corresponding damage state variable.

Considering a uniaxial tensile or compressive stress state, the state variable $\aleph \in \{t, c\}$ is introduced ($\aleph = t$ for uniaxial tension and $\aleph = c$ for uniaxial compression). The stress state is assumed to be a function of the plastic strain. The damage in quasi-brittle materials can be defined by evaluating the dissipated fracture energy required to generate microcracks. In the Barcelona model (Lubliner et al. 1989; Oller et al. 1990), one scalar damage variable represents the combination of tensile and compressive damage. Lee et al. (1999) extends this idea by introducing two independent damage variables, one for tensile damage and the other for compressive damage. Each variable is factored into the effective-stress response and the stiffness degradation response. That is, the uniaxial strength functions are factored into the degradation damage and effective-stress responses as follows:

$$f_t = f_t(\kappa_t) \;;\; f_c = f_c(\kappa_c) \tag{3.33a}$$

$$f_t = \left[1 - D_t(\kappa_t)\right]\bar{f}_t(\kappa_t)\,;\, f_c = \left[1 - D_c(\kappa_c)\right]\bar{f}_c(\kappa_c) \tag{3.33b}$$

In the Barcelona model, the relationship between the uniaxial stress, denoted by $\sigma_{\aleph}$, and the corresponding scalar plastic strain, denoted by ε^p, is taken as

$$\sigma_{\aleph} = f_{\aleph 0}\left[(1 + a_{\aleph})\exp(-b_{\aleph}\varepsilon^p) - a_{\aleph}\exp(-2b_{\aleph}\varepsilon^p)\right] \tag{3.34}$$

where $f_{\aleph 0}$=initial yield stress, defined as the maximum stress without damage. and $a_{\aleph}$ and $b_{\aleph}$ are material constants. Note that $a_{\aleph} > 1$ implies initial hardening, while $a_{\aleph} < 1$ implies softening immediately after yielding. The function in Eq. (3.33) is factored by assuming that the degradation takes an exponential form

$$1 - D_{\aleph} = \exp(-d_{\aleph}\varepsilon^p) \tag{3.35}$$

where d_{κ} is a material constant. Then, the effective stress is given by

$$\bar{\sigma}_{\aleph} = f_{\aleph 0}\left[(1 + a_{\aleph})(\exp(-b_{\aleph}\varepsilon^p))^{1-(d_{\aleph}/b_{\aleph})} - a_{\aleph}(\exp(-2b_{\aleph}\varepsilon^p))^{2-(d_{\aleph}/b_{\aleph})}\right]$$

The uniaxial version of the damage variable, denoted by $0 \le \kappa_{\aleph} \le 1$, is defined as

$$\kappa_{\aleph} = \frac{1}{g_{\aleph}}\int_0^{\varepsilon^p} \sigma_{\aleph}(\varepsilon^p)d\varepsilon^p \tag{3.36}$$

where

$$g_{\aleph} = \int_0^{\infty} \sigma_{\aleph}(\varepsilon^p)d\varepsilon^p \tag{3.37}$$

The quantity $g_{\aleph}$ is the dissipated energy density during the entire process of mircocracking. Because the capacity for the dissipated energy per unit volume cannot be

given as a material property, $g_{\aleph}$ must be derived from other known material properties such as the fracture energy. Assuming that the fracture energy in the uniaxial tensile state $G_{\aleph}$ and its counterpart in the uniaxial compressive state are given as a material properties, $g_{\aleph}$ is the specific fracture energy normalized by the localization zone size, also referred to as the characteristic length $l_{\aleph}$. This gives $g_{\aleph} = G_{\aleph} / l_{\aleph}$ (Lubliner et al. 1989; Oliver 1989). To maintain objective results at the structural level, $l_{\aleph}$ must be an objective value or assumed as a material property.

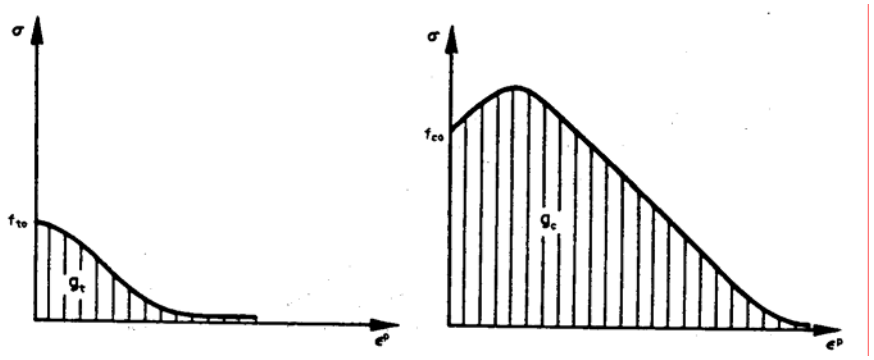

(a) (b)

Figure 3.4.3. Uniaxial curves(stress-plastic strain): (a) tension; (b) compression.

By substitution of (3.34) into (3.37), the relationship between the constants is obtained

$$g_{\aleph} = \frac{f_{\aleph o}}{b_{\aleph}}(1 + \frac{a_{\aleph}}{2}) \tag{3.38}$$

Combining (3.34) and (3.36) gives the uniaxial stress in terms of $\kappa_{\aleph}$

$$\sigma_{\aleph} = f_{\aleph}(\kappa_{\aleph}) \tag{3.39a}$$

$$\sigma_{\aleph} = \frac{f_{\aleph 0}}{a_{\aleph}}\left[(1+a_{\aleph})\sqrt{\phi_{\aleph}(\kappa_{\aleph})} - \phi_{\aleph}(\kappa_{\aleph})\right] \tag{3.39b}$$

where $\phi_{\aleph}(\kappa_{\aleph}) = 1 + a_{\aleph}(2+a_{\aleph})\kappa_{\aleph}$. Similarly, the effective stress and the degradation damage variable are written in terms of $\kappa_{\aleph}$ as

$$\bar{\sigma}_{\aleph} = \bar{f}_{\aleph}(\kappa_{\aleph})$$

$$\bar{\sigma}_{\aleph} = f_{\aleph 0}\left[(\frac{1}{a_{\aleph}})(1+a_{\aleph} - \sqrt{\phi_{\aleph}(\kappa_{\aleph})})\right]^{1-(d_{\aleph}/b_{\aleph})}\sqrt{\phi_{\aleph}(\kappa_{\aleph})} \tag{3.40}$$

$$D_{\aleph} = 1 - \left[(\frac{1}{a_{\aleph}})(1+a_{\aleph} - \sqrt{\phi_{\aleph}(\kappa_{\aleph})})\right]^{(d_{\aleph}/b_{\aleph})} \tag{3.41}$$

The ratio $d_{\aleph}/b_{\aleph}$ can be evaluated by specifying the degradation values in each uniaxial state. To perform the calibration for compressive cases, it is assumed that a value of the elastic stiffness degradation $\widetilde{D}_c$ can be obtained from experiments at the maximum compressive stress. If κ_c' is the compressive damage value at which the effective uniaxial function $\bar{f}_c$ is at its maximum absolute value, it follows from (3.39) that

$$\sqrt{\phi(\kappa_c')} = \frac{1+a_c}{2} \tag{3.42}$$

By substituting (3.42) into (3.41)

$$\widetilde{D}_c = 1 - \left[(\frac{1}{a_c})(1+a_c - \sqrt{\frac{1+a_c}{2}})\right]^{(d_c/b_c)}$$

which leads to the following relation between d_c/b_c and $\widetilde{D}_c$:

$$\frac{d_c}{b_c} = \frac{\log(1-\widetilde{D}_c)}{\log(\frac{1+a_c}{2a_c})}$$

For the tensile case, a different approach is used because the stiffness degradation at the maximum tensile stress usually is assumed to be zero. Assuming that the degradation value in a uniaxial state, denoted by $\widetilde{D}_t$, is given at $\sigma_t = f_{t0}/2$, then from (3.39)

$$\sqrt{\phi(\kappa_t)} = \frac{1+a_t+\sqrt{1+a_t^2}}{2} \tag{3.43}$$

Substitution of (3.43) into (3.41) gives

$$\frac{d_t}{b_t} = \frac{\log(1-\widetilde{D}_t)}{\log[(1+a_t)-\sqrt{1+a_t^2}]-\log(2a_t)} \tag{3.44}$$

Because a_t is not a material property that can be measured explicitly, it is convenient to evaluate a_t as a function of d_t/b_t and $\widetilde{D}_t$ such that

$$a_t = \frac{[2(1-\widetilde{D}_t)^{b_t/d_t}-1]}{2(1-\widetilde{D}_t)^{b_t/d_t}[(1-\widetilde{D}_t)^{b_t/d_t}-1]} \tag{3.45}$$

In the case of the uniaxial compression test, for which a_c is larger than 1, a_c can be obtained in terms of the ratio of the initial yield stress (f_{c0}) to the maximum compressive stress(f_{cm}) as follows:

$$a_c = 2(f_{cm}/f_{co})-1+2\sqrt{(f_{cm}/f_{co})^2-(f_{cm}/f_{co})} \tag{3.46}$$

With a_c obtained, the stress beyond the initial yield stress can be expressed in terms of compressive damage variable

$$\sigma_c = \frac{f_{c0}}{a_c}\left[(1+a_c)\sqrt{\phi_c(\kappa_c)} - \phi_c(\kappa_c)\right] \tag{3.39b}$$

where $\phi_c(\kappa_c) = 1 + a_c(2+a_c)\kappa_c$.

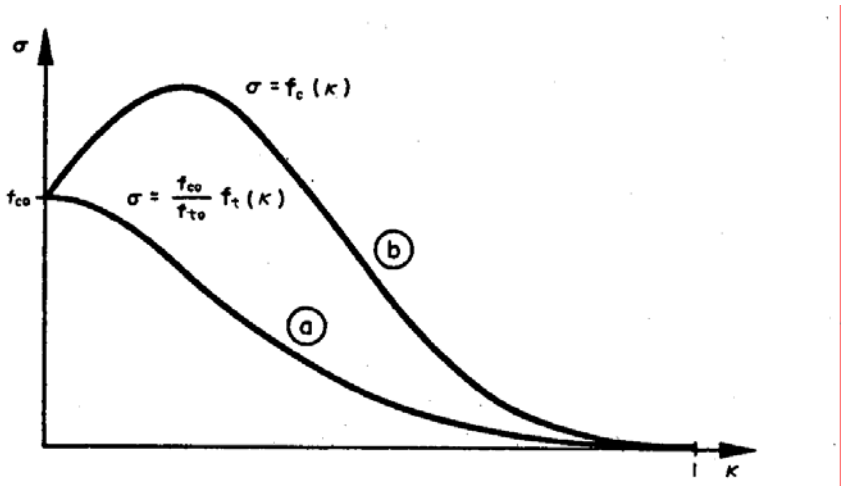

Figure 3.4.4. Uniaxial stress-damage curves : (a) tension; (b) compression.

In the case of the uniaxial compression test, the damage variables for the data points used for multi-linear representation of the concrete stress-strain response are calculated first using the proposed stress function, once a_c is obtained as explained in the above, and the corresponding stiffness degradation parameters are obtained using Eq. (3.41). Table 3.4.1 tabulates the compressive stress data versus the associated values for the damage variable and elastic stiffness degradation for the slab concrete in this research.

Table 3.4.1. Compressive stress and corresponding damage and elastic stiffness degradation variables.

Compressive Stress MPa (ksi)	Damage Variable, κ_c	Elastic Stiffness Degradation, D_c
15.11 (2.192)	0	0
29.00 (4.206)	0.0844	0.0924
33.12 (4.804)	0.1831	0.1649
33.58 (4.870)	0.2304	0.1957
32.30 (4.684)	0.3451	0.2663
28.10 (4.075)	0.4836	0.3500
24.28 (3.522)	0.5747	0.4073
20.58 (2.985)	0.6517	0.4590
18.06 (2.620)	0.7001	0.4938
16.18 (2.347)	0.7347	0.5203
13.91 (2.018)	0.7751	0.5533

Unlike the compressive damage variables, there is no way to calculate a_t without experimental results. As recommended by Lee et al. (1999), one must determine at least one damage variable point from an experiment, i.e., the value of the damage variable for a given total strain from a cyclic test. Therefore, the tension damage variables are calculated based on the cyclic tension test by Yankelevsky and Reinhardt (1987). The tensile strength reported in this test is 3.45 MPa (0.50 ksi). This is approximately the same as that of the concrete used in the test bridge construction. The resulting calculation is shown in Table 3.4.2.

Table 3.4.2. Tensile stress and the corresponding damage and elastic stiffness degradation variables.

Tensile Stress MPa (ksi)	Damage Variable, κ_t	Elastic Stiffness Degradation, D_t
3.454 (0.5010)	0	0
3.078 (0.4464)	0.1204	0.2249
2.798 (0.4058)	0.2342	0.4037
2.519 (0.3653)	0.3325	0.5357
2.239 (0.3247)	0.4217	0.6399
1.959 (0.2841)	0.5047	0.7246
1.679 (0.2435)	0.5833	0.7946
1.399 (0.2029)	0.6584	0.8525
1.119 (0.1623)	0.7307	0.9001
0.8400 (0.1218)	0.8007	0.9386
0.560 (0.0812)	0.8688	0.9685

3.5 Modeling of Composite Action

Composite bridge I-girders are generally designed based on full composite action. Although some amount of restraint is provided by bond and friction forces developed between the concrete slab and the steel I-girders, these forces are not sufficient to develop substantial composite action. Mechanical shear connectors are welded to the girder top flanges to develop the composite action. Figure 3.5.1 shows an idealized section with a headed shear connector welded to a girder top flange.

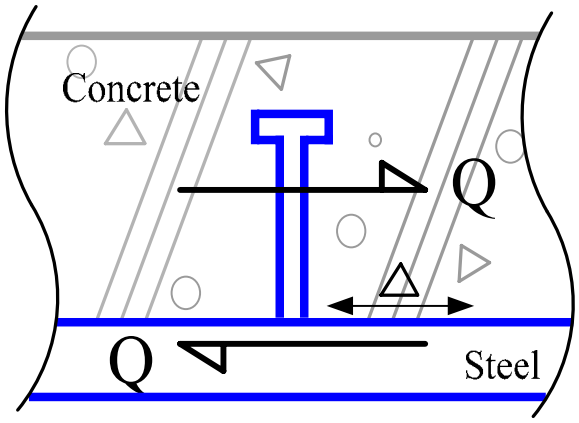

Figure 3.5.1. Relative slip, Δ, due to applied shear force, Q.

The shear transfer between the concrete slab and the steel I-girder is complex, since the shear connector deforms under applied loads and the concrete which surrounds it is also a deformable medium. The amount of deformation a shear connector undergoes is dependent on factors such as its own shape and size. Also, relative slip (Δ) occurs at the concrete-steel interface as the shear force (Q) increases, as illustrated in Figure 3.5.1. In this case, bond and friction resistances are important factors that determine the magnitude of shear force at which a relative slip begins between the slab and the bridge girder. In

general, the amount of relative slip is predominantly a function of the strength of concrete that surrounds the shear connectors. Ollgaard et al. (1971) developed the following equation for the shear load per shear connector versus the relative slip:

$$Q = \frac{2}{5} Q_u (1 - e^{-18\Delta}) \tag{3.47}$$

where Q = applied shear load per shear connector, kips

Q_u = ultimate shear load per shear connector, kips

= $0.5 A_s \sqrt{f_c' \, E_c}$

A_s = cross-sectional area of stud, in^2

= $\pi d_s^2 / 4$

f_c' = 28-day compressive strength of concrete, ksi

E_c = modulus of elasticity of concrete, ksi

= $1746\sqrt{f_c'}$

Δ = average relative slip, in

Figure 3.5.2 shows the nonlinear relationship between the applied shear and the relative slip for the shear connectors used in the composite test bridge, based on Eq. (3.47). The maximum shear force that can be resisted by each shear connector is approximately 133 kN (30 kips) with a corresponding relative slip of 3.18 mm (0.125 in).

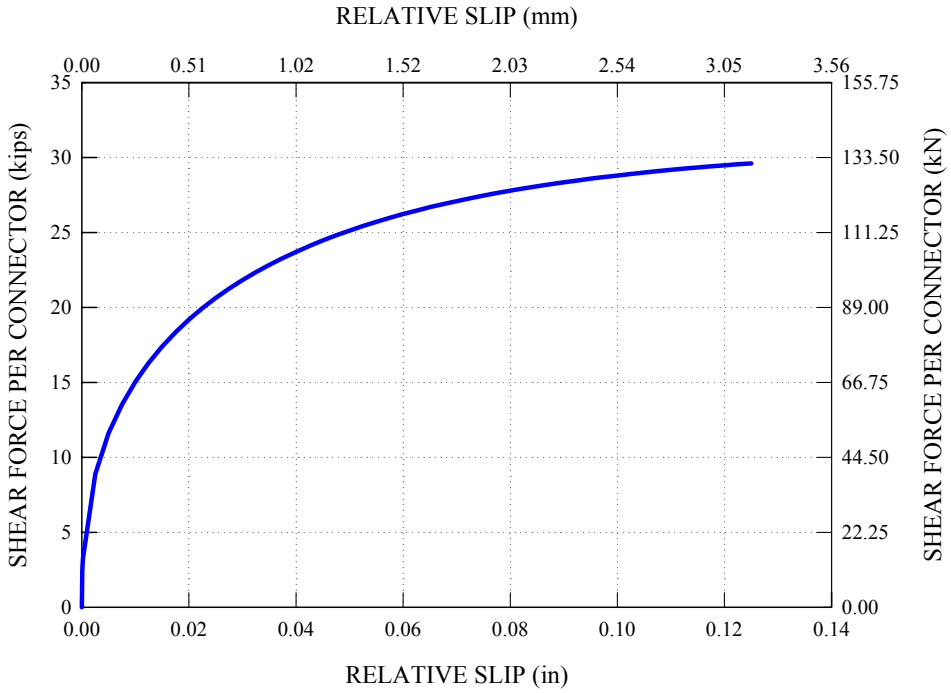

Figure 3.5.2. Applied shear force vs. average relative slip response for one of the shear connectors used in the composite test bridge slab.

Two modeling approaches are considered in this research for the composite action described above. The first one is to map the shear connector response expressed in Eq. (3.47) into the force-displacement response of discrete nonlinear spring elements. This type of modeling approach is economical computationally and appropriate for large-scale composite structures such as the composite test bridge. In the second modeling approach, it is assumed that there is no relative slip in the concrete-steel interface region and a beam-type multi-point constraint (MPC) is used as described in Chapter 2. This basically connects the top flange nodes of the steel girders to the test bridge slab nodes. This modeling approach is popular in research and design due to its simplicity. Furthermore, it gives an accurate prediction of experimental test results in many cases. Nonetheless,

one should not lose sight of the fact that the analysis results based on this modeling approach are always upper-bound solutions relative to the actual physical response.

The composite test bridge model with the Beam MPC approach is labeled Case A. As discussed earlier, the number of shear connectors was selected based on consideration of fatigue strength limit states. As a result, the level of shear resistance provided by shear connectors in the composite test bridge slab is substantially larger than that associated with the strength limit states. Therefore, the Beam MPC can be considered as a reasonable choice for the simulation of the composite action in the composite test bridge. This approach is expected to closely represent the physical behavior of the bridge up to load levels that are significantly higher than design load levels, or even over the entire range of loading up the ultimate capacity of the system.

In contrast with Case A, the other model, labeled Case B, explicitly models the interface flexibility in the full nonlinear FEA of the test bridge. Instead of a refined modeling approach involving detailed slip resistance contributions from various factors to the composite action, the modeling approach taken in Case B combines the effects of bond and friction force, flexibility of the shear studs and the response of concrete in a single phenomenological load-slip response curve. To this end, the shear-slip response relation suggested by Ollgaard et al. (1971) is utilized to define the nonlinear shear-slip response. Furthermore, the nonlinear rotational spring and the rigid bar shown in Figure 3.5.3 are used at each location of the shear studs along the girder lengths to model the shear-slip response of the connectors.

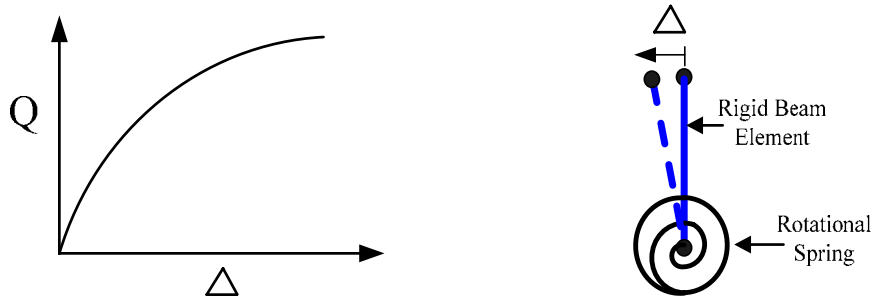

Figure 3.5.3. Mapping of the applied shear-slip response of interface region in composite section to the rigid bar-spring arrangement.

Figure 3.5.4 illustrates how this rigid bar-spring arrangement is implemented in the full nonlinear FEA models of the composite test bridge. The above model is somewhat limited in simulating repeated loading tests, since it cannot represent slip residuals associated with a gradual accumulation of damage throughout the loading history. Particularly when it comes to the simulation of Test 4, Case A may not be sufficient, since the connectors are subjected to high applied load levels that may cause inelastic behavior at the concrete-steel interface.

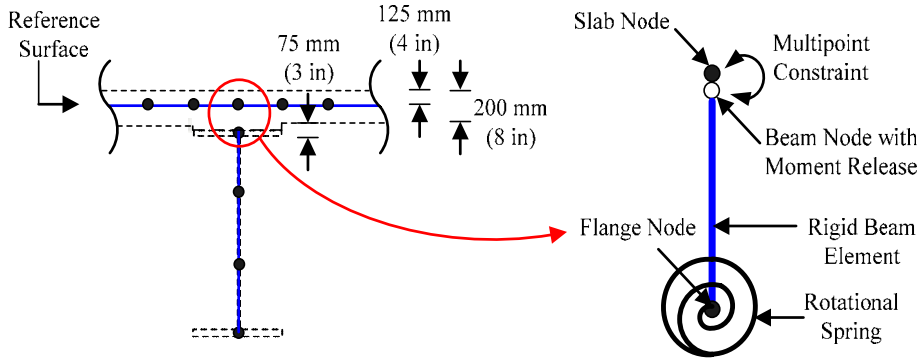

Figure 3.5.4. Rigid bar-spring arrangement within the full nonlinear FEA model for the composite test bridge.

In order to address this concern, two preliminary analyses using both Cases A and B were performed for the simulation of Test 4. Figure 3.5.5 compares the resulting total applied load-vertical displacements at midspan for the bottom flange of the outside girder, G3, obtained from these two cases. It can be seen that the two displacement curves are in a good agreement, although there is a small deviation between the two curves at higher load levels. At a total applied load of 5680 kN (1277 kips) and 510 mm (20 in) vertical deflection, Case B indicates an additional vertical deflection of only 4.1 cm (1.6 in) relative to the deflection in Case A. Therefore, in subsequent simulations, the composite action between the bridge slab and the girder top flanges is modeled by using the Beam MPC.

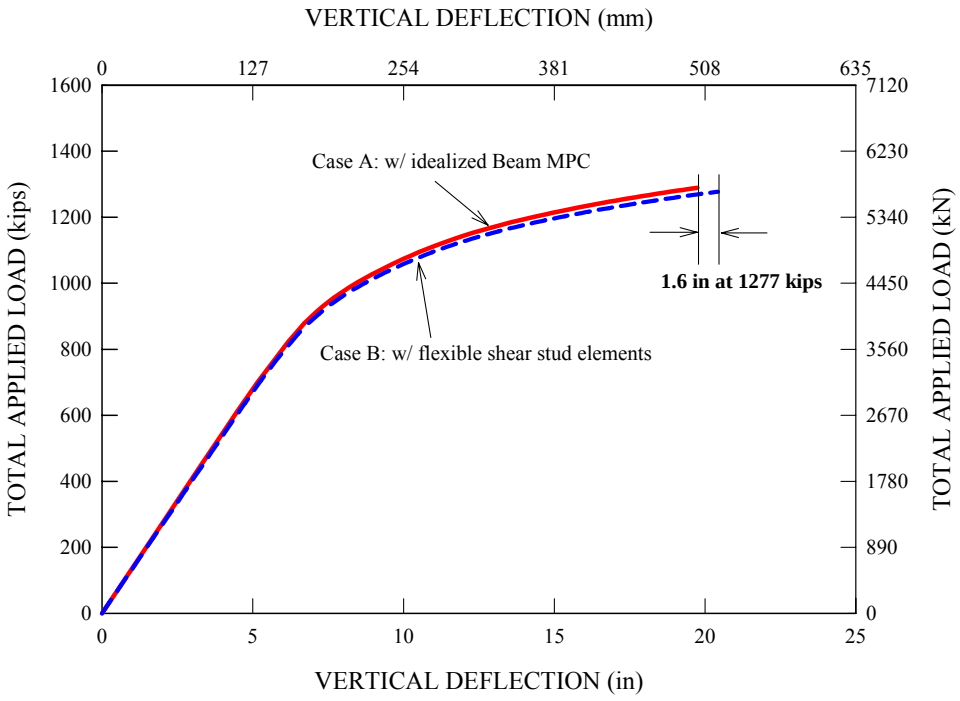

Figure 3.5.5. Comparison of load-deflection responses between Model A using the multi-point constraint (MPC) and Model B using explicit stud elements for modeling the composite action between the concrete slab and the girder top flanges.

3.6 Effects of Residual Stresses

In general, residual stresses can have a significant effect on the stability, strength and load-deflection response of steel structures. The existence of residual stresses causes inelastic behavior at levels of applied load smaller than that associated with the nominal elastic stresses reaching the first yield.

The ECCS Manual on Stability of Steel Structures (ECCS 1976) provides a number of simple equations for estimating residual stresses. These equations reflect the two primary causes of longitudinal residual stresses in welded I-girders:

- flame cutting
- welding of the flanges to the web.

Residual stresses due to heat curving are not considered in the present research. Also, transverse normal residual stresses in the web due to welding of the stiffeners are not considered.

In ECCS (1976), the residual stresses at the web-flange junctures and at the flange tips are taken as constant tensile values equal to the yield stress over narrow strips of the plates representing the heat affected zones. A smaller constant self-equilibrating compression stress is assumed within the other regions of the plates. ECCS (1976) specifies the width of the equivalent yielded rectangular tension block for a plate that is flame-cut as

$$c_f = \frac{1100\sqrt{t}}{F_y} \tag{3.53}$$

where t is the plate thickness in mm and F_y is the plate yield stress in MPa. In case of the outermost girder, G3, in the composite test bridge, Eq. (3.53) gives $c_f = 14.0$ mm

(0.591 in) and 13.0 mm (0.511 in) for the top and bottom flanges and 7.566 mm (0.298 in) for the web edges, based on measured thicknesses of t_{tf} = 25.4 mm (1.001 in), t_{bf} = 35.3 mm (1.389 in) and t_w = 9.2 mm (0.362 in), and measured F_y values of 400 MPa (58 ksi), 493 MPa (71.5 ksi), 441 MPa (64 ksi) for the top and bottom flanges and web, respectively.

In addition, based on the assumption of continuous single-pass fillet welds between the web and the flanges, the resulting widths of the tension block on each side of the welds to the flange plates and at the top and bottom edges of the web plate are given by

$$c_w = \frac{12000 p A_w}{F_y \Sigma t} \tag{3.54}$$

where p is the process efficiency factor, which depends on the welding process adopted and is equal to 0.90 for submerged arc welding, A_w is the cross-section area of the added weld metal in mm^2, and Σt is the sum of the plate thicknesses meeting at the weld in mm. The width c_w is assumed to be the same within the web and flange plates, even if these plate thicknesses are significantly different as is the case with most welded I-girders. The term Σt accounts for each direction in which heat is dissipated away from the weld within the connected plates.

Single-pass submerged arc fillet welds are assumed to be applied consecutively on each side of the web in this research. The size of these welds is taken as 7.94 mm (5/16 in). Based on the measured t and F_y values for the flanges and web of G3, Eq. (3.54) gives c_w = 17.3 mm (0.682 in) for the top flange and the web top edge while it gives c_w = 13.0 mm (0.512 in) for the bottom flange and the web bottom edge.

The combined effect of the two fillet welds on the web plate needs to be considered. If these welds were applied simultaneously, the net effect on the web can be estimated by using the total area of the two welds for A_w in Eq. (3.54). However, based on the assumption that these welds are made consecutively, the following equation from ECCS (1976) may be used:

$$c_n = c_w \cdot n^{1/4} \tag{3.55a}$$

where n is the number of consecutive welds, equal to two in this case. Therefore, the tension block widths due to the two consecutively placed web-to-flange fillet welds are obtained as c_n = 21.0 mm (0.827 in) and 15.5 mm (0.610 in) at the web top and bottom edges of G3.

Also, the effect of welding on the previously flame-cut edges of the webs does not result in the algebraic sum of the tension block widths since the weld heat tends to relieve the tension block stress caused by the cutting. ECCS (1976) suggests that the final tension block width (c_{fw}) can be calculated as

$$c_{fw} = \left(c_f^{\,4} + c_w^{\,4}\right)^{1/4} \tag{3.55b}$$

where c_f is the tension block width due to flame-cutting alone and c_w is the tension block width due to welding alone. Therefore, if c_w is taken as c_n = 21.0 mm (0.827 in), and c_f is taken as 7.566 mm (0.298 in) from Eq. (3.53), Eq. (3.55) gives c_{fw} = 21.0 mm (0.827 in) as the tension block width at each edge of the web plate.

For a web that is fillet welded on each side to the flange plates, ECCS (1976) proposes that the effective value of the flange tension block width on each side of the centerline of the web-flange juncture should be taken as

$$c_2 = c_w + 0.5t_w \quad \text{for} \quad t_w \leq 2c_w \tag{3.56}$$

where c_w is the corresponding tension block width for each weld alone. That is, when $t_w \leq 2c_w$, the effects of the two web-to-flange welds on the residual stresses within the flange plate are assumed to be interdependent. This condition is satisfied for the test bridge girders considered in this work. Therefore, taking c_w = 19.0 mm (0.748 in), and using the measured web thickness for t_w, a value of 24.0 mm (0.945 in) is obtained for c_2 on girder G3. It should be noted that in the limit that t_w approaches zero, one would expect that c_2 should be equal to the value given by Eq. (3.54) using the combined area of both of the fillet welds, if the welds are made simultaneously. Equation (3.56) with c_w calculated from Eq. (3.54) using the area of the individual welds appears to be a reasonable approximation for cases where the welds are made consecutively. In the view of the author, Eq. (3.56) should be used with c_w calculated from Eq. (3.54) using the combined area of the two welds if the welds between the web and the flange are placed simultaneously. Given the above tension block widths c_f and $2c_2$ at the edges and interior of the flange plates, and c_{fw} at the edges of the web plate (see Figure 3.6.1), the smaller constant self-equilibrating compressive stress within the majority of the plate areas is calculated based on equilibrium in the longitudinal direction in each of the plates. That is, the residual stresses are assumed to be self-equilibrating within each of the plates that make up the cross-section. Also, it should be noted that the residual compression induced at the flange tips due to the welding of the flanges to the web is neglected; the residual tension at the flange tips is still assumed as F_{yf} within the width c_f. The corresponding residual compression in the flanges of G3, based on the measured flange widths, is F_{rcf} = $0.20F_{yf}$ and $0.125F_{yf}$ for the top and bottom flanges ,where F_{yf} is the corresponding

measured yield strength. Similarly, the residual compression within the web based on the measured web depth is $F_{rcw} = 0.0371F_{yw}$, where F_{yw} is the measured web yield strength. The corresponding residual stress distributions are given in Figure 3.6.2. Similar residual stress blocks are calculated for the other two girders, G1 and G2. The resulting residual stress distributions are also presented in Figure 3.6.2.

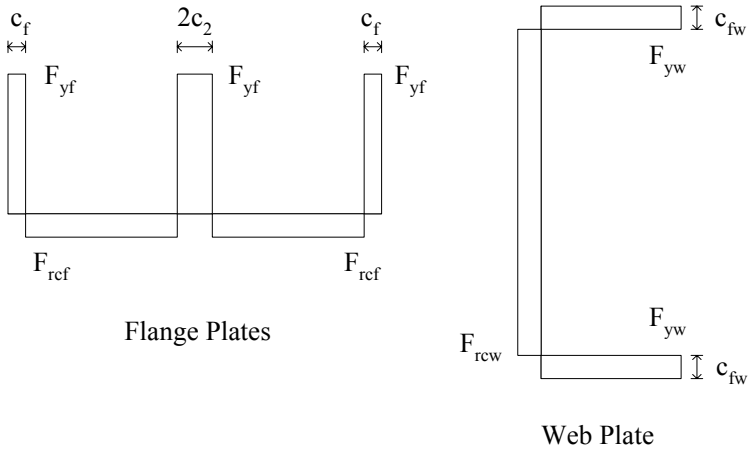

Figure 3.6.1. Idealized residual stress distribution in flange and web plates due to flame cutting and welding (ECCS 1976).

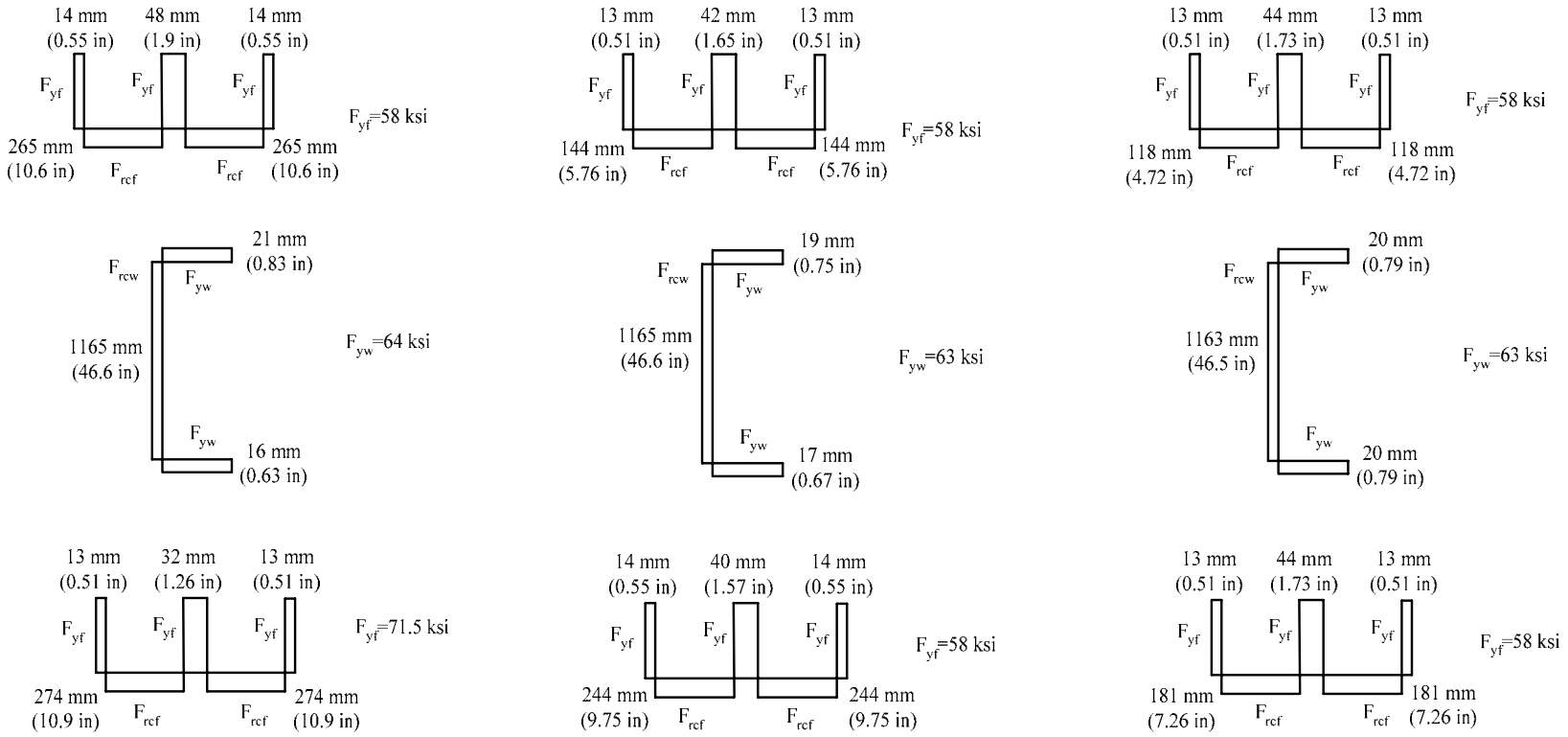

(a) G3 (b) G2 (c) G1

Figure 3.6.2. Idealized residual stress distributions in the top and bottom flanges and web plates of the test bridge girders due to flame cutting and welding (ECCS 1976).

As described earlier in Chapter 2, the base full nonlinear FEA model of the composite test bridge involves beam elements used to model the top and bottom flanges of the test bridge girders. Since ABAQUS does not provide the capability of defining initial residual stresses in its beam elements, the base bridge FEA model can not be used to investigate the effects of residual stresses on the strength behavior of the composite test bridge. Also, ABAQUS assumes that the transverse shear behavior of the B31 element is linear elastic with a fixed modulus and, thus, independent of the response of the beam section to axial stretch and bending.

Therefore, a FEA model with top and bottom flanges represented by four-node shell elements is developed. This way, the residual stresses calculated above can be introduced at the Gauss integration points of the shell elements. This FEA model without residual stresses in the bridge girders also allows the study of the implications of the beam representation of the girder flanges utilized in the base FEA models of the test bridge.

For the S4R shell finite element used in this research, a one point Gauss integration rule is employed in each element. Eight elements are used through the width of the top and bottom flanges while 16 elements are used through the depth of the web. Therefore, there are eight integration points across the width of both the top and bottom flanges and twenty integration points through the depth of the web. The width of the tension blocks is generally narrower than the width of an individual finite element. Therefore, in each of the flange elements that have residual stresses both in tension and compression, the total residual longitudinal force is calculated and then divided by the cross-section area associated with the element to obtain the statically equivalent average residual stress.

This stress is then specified at the single integration point in these elements. In the elements at the top and bottom of the web, which have residual stresses both in tension and compression, the net average residual stress is calculated such that the residual compression in the other 14 web elements is equilibrated. Figure 3.6.3 illustrates the resulting Gauss point residual stresses used within the FEA models.

Figure 3.6.4 gives the load-vertical deflection curves at the G3 bottom flange at midspan for two versions of a new bridge FEA model with a shell representation of girder flanges, labeled Model B, (Model B with and without residual stresses) and the base bridge FEA model with a beam representation of girder flanges, labeled Model A. The full nonlinear analysis procedures used in these three cases are detailed in Section 3.8. The selected loading scheme for these cases is the one used for Test 4 as shown Figure 3.2.3. Comparing the load-deflection responses between Model A and Model B *without residual stresses*, one can observe that the response of Model A is essentially the same as that of Model B without residual stresses up to the proportional limit. Furthermore, it should be noted that the response of Model A is closely matched by that of Model B without residual stresses even in the nonlinear part of the deflection curves, although Model B without residual stresses is slightly softer than Model A in this region. In other words, the girder flanges respond according to beam kinematics in both the elastic and nonlinear regions and the shear stress effects in the flanges are small. Therefore, a beam representation of the girder flanges is a reasonable modeling approach. This significantly reduces the computing time. Therefore, in cases where the modeling of residual stresses is not important, the base modeling approach using shell elements for web and beam elements for flanges is a reasonable choice (the modeling of the residual

stresses is of greater importance for composite I-girders in negative bending, since the residual stresses can have a significant influence on the inelastic stability behavior.

Figure 3.6.4 also provides the deflection response for Model B with residual stresses. Comparing the deflection responses for Model B with and without stresses, one can see that these two curves are virtually identical to each other. They are slightly different in the nonlinear part of the curves. In fact, it is interesting to note that the curve for the case without residual stresses is slightly higher than that of the other case with residual stresses, but still less than the response of the base bridge FEA model, or Model A. However, for all practical purposes, these two curves can be considered to match each other. Therefore, for simply-supported composite structures such as the composite test bridge, it appears that the effects of residual stresses can be generally disregarded.

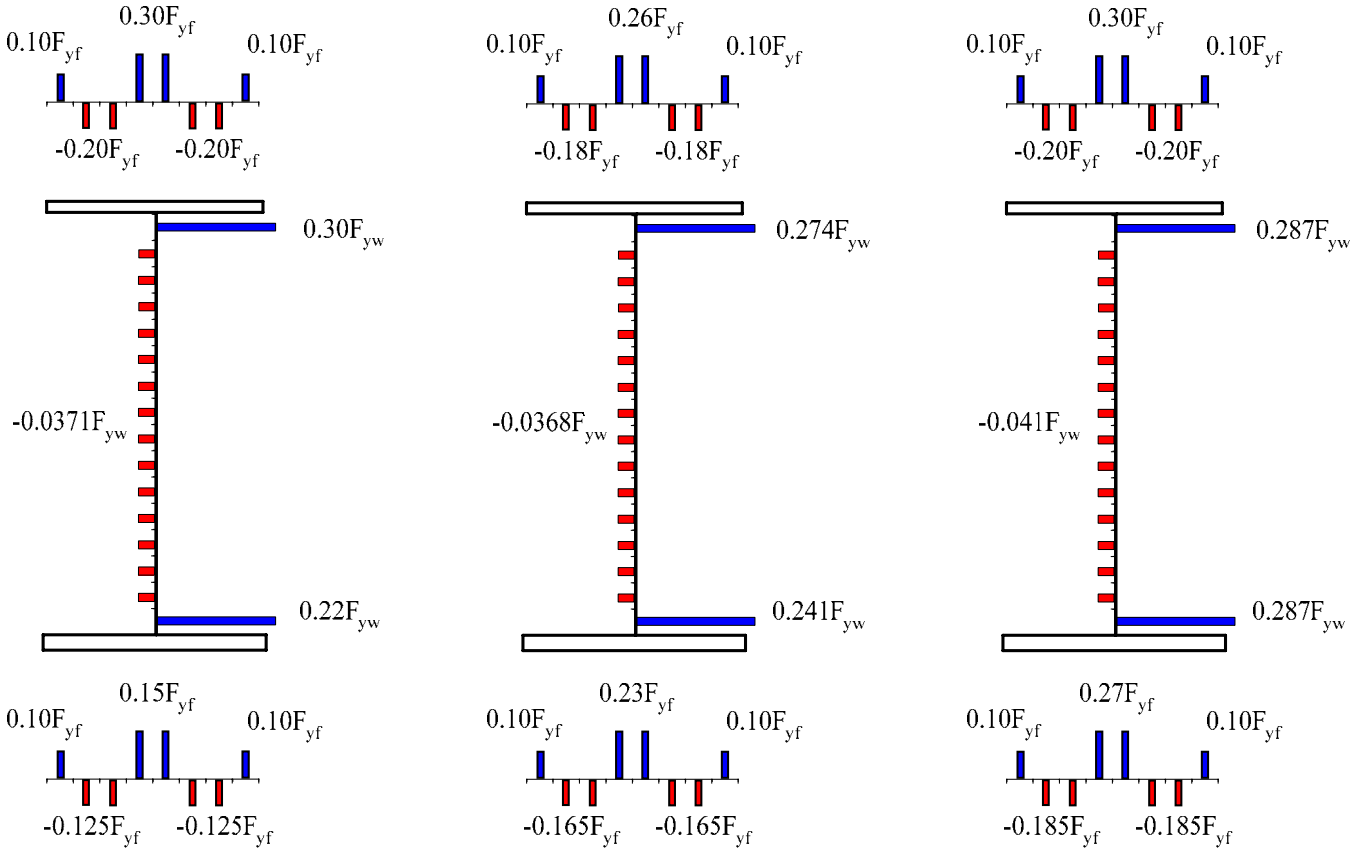

(a) G3 (b) G2 (c) G1

Figure 3.6.3. Gauss point residual stresses used for the test bridge girders, based on flame cutting and consecutive placement of 7.93 mm (5/16 in) web-to-flange fillet welds.

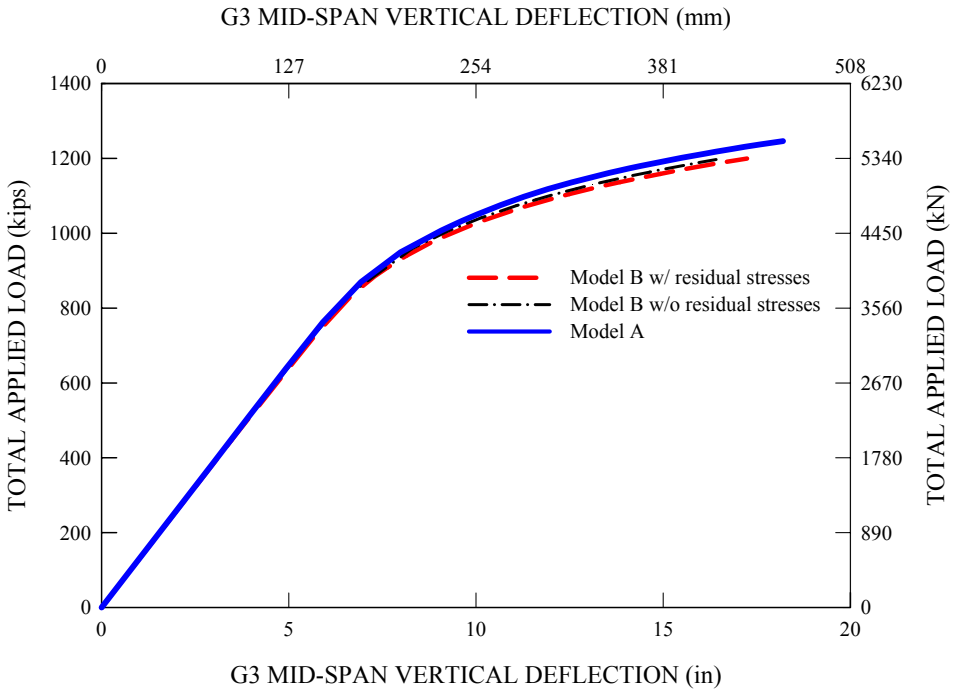

Figure 3.6.4. Load-vertical deflection curves at G3 bottom flange midspan for two versions of a new bridge FEA model with a shell representation of girder flanges, labeled Model B, (i.e. Model B with and without residual stresses) and the base bridge FEA model with a beam representation of girder flanges, labeled Model A.

3.7 Effects of Concrete Shrinkage

After the placement of the slab, the concrete strains were continuously monitored for 298 days. Since the steel superstructure alone resisted the total dead load, it appears that there were negligible strains associated with sustained stress, or creep. Therefore, the majority of the concrete strains are believed to be caused by concrete shrinkage.

Figure 3.7.1 shows locations of concrete vibrating wire gauge lines that were aligned longitudinally (L2, L9, L10 and L17) and radially (2L, L7, L12 and 2R) on the slab. Figures 3.7.2 through 3.7.9 show the average longitudinal and radial concrete strains over time at these gauge locations. It can be seen that the test bridge slab predominantly develops compressive strains due to shrinkage. The compressive shrinkage strains

monotonically increase up to 150 days after the concrete casting operation and then stabilize with small additional strain changes in the remaining days of measurement. For example, the radial strain at the gauge line L7 reaches the final strain values of 393 $\mu\varepsilon$ and 387 $\mu\varepsilon$ for the outside and inside portions of the test bridge slab, respectively, as shown in Figure 3.7.4. Along with these strains, similar final strains at other gauge locations are summarized in Figure 3.7.10. One can observe that the strains at the inside and outside portions of the test bridge slab have a similar magnitude at the same gauge location, with the exception of the gauge line L2. Furthermore, it can be seen that the final radial strains obtained from Figures 3.7.3, 3.8.4, 3.7.7 and 3.7.8 are generally larger than the final longitudinal strains obtained from Figures 3.7.2, 3.7.5, 3.7.6 and 3.7.9. That is, the magnitude of the average of the radial strains reported in Figure 3.7.10 is 350 $\mu\varepsilon$, which is almost twice that of the longitudinal counterpart, 182 $\mu\varepsilon$. This appears to be due to the higher restraint provided by the test bridge girders in the longitudinal direction than in the radial direction.

In general, concrete creep and shrinkage are time-dependent phenomena and closely related each other. Their numerical treatment requires sophisticated rheological models to represent the general deformation behavior and flow of materials under stress. This brings the problem of interest to the time domain. However, detailed time-dependent strain variations are not a focus of this research, but the net effect of these strains on the strength behavior of the composite test bridge is a consideration. Therefore, the two representative average longitudinal and radial strains mentioned above are directly induced in the slab portion of the full nonlinear FEA bridge model using initial stresses. It is important to note that this approximate treatment of the slab shrinkage strains is an

iterative process by nature since the steel girders tend to restrain the concrete shrinkage. That is, arbitrarily chosen initial stresses are updated until resulting longitudinal and radial strains are approximately equal to the measured data. The net effect of these shrinkage strains is manifested by additional downward deflections of the test bridge girders. For example, it is predicted that the G3 experiences an additional deflection of 0.5 in at midspan due to the above concrete shrinkage strains.

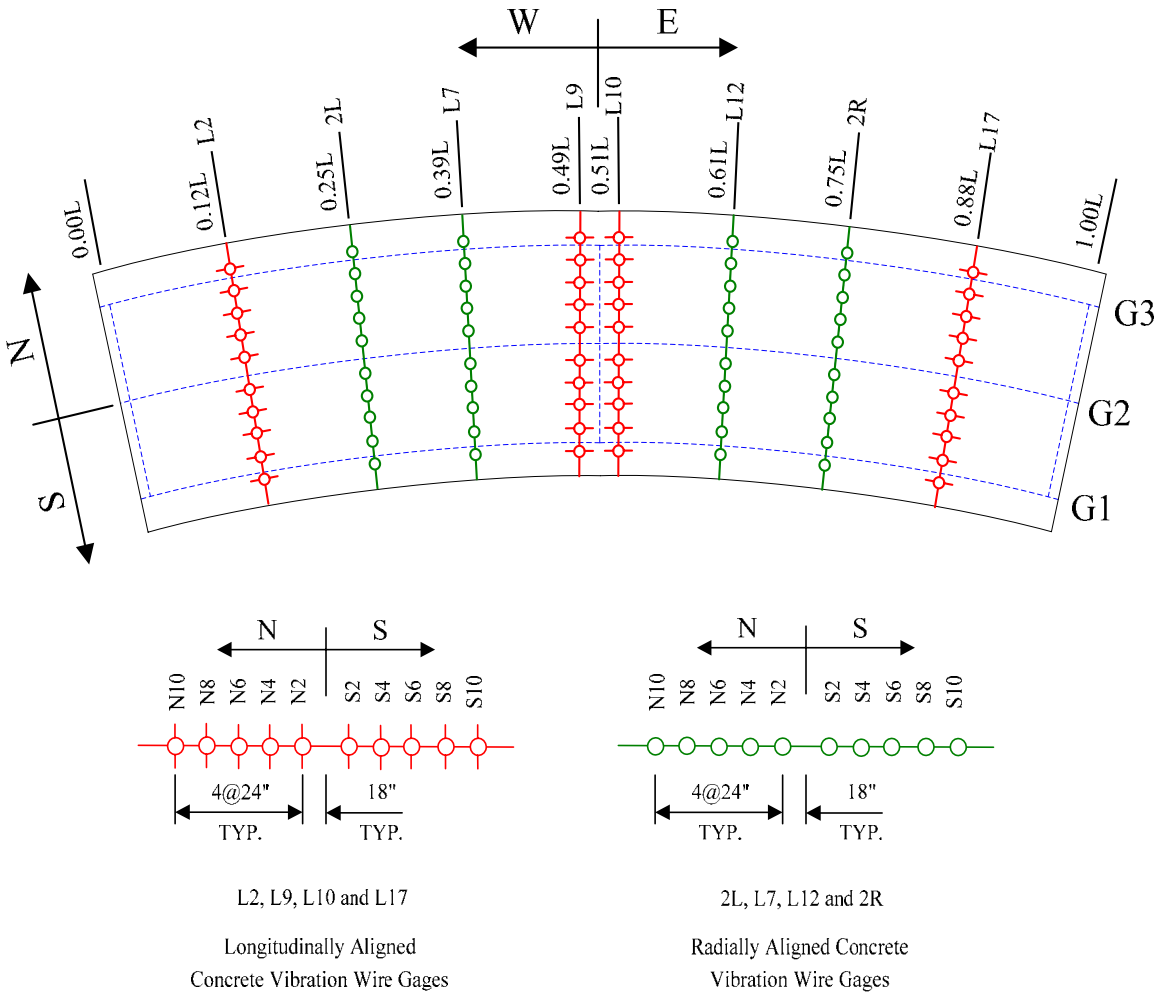

Figure 3.7.1. Locations of concrete vibrating wire gauge lines aligned longitudinally (L2, L9, L10 and L17) and radially (2L, L7, L12 and 2R) on the test bridge slab.

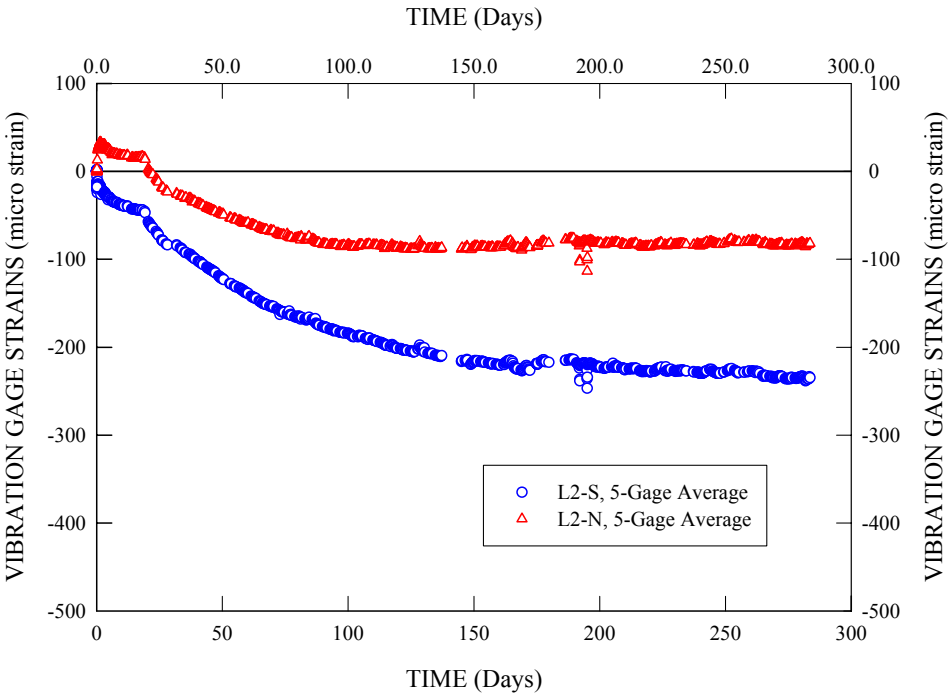

Figure 3.7.2. Average longitudinal concrete strain variations over time due to shrinkage at gage line L2 (Beshah 2006).

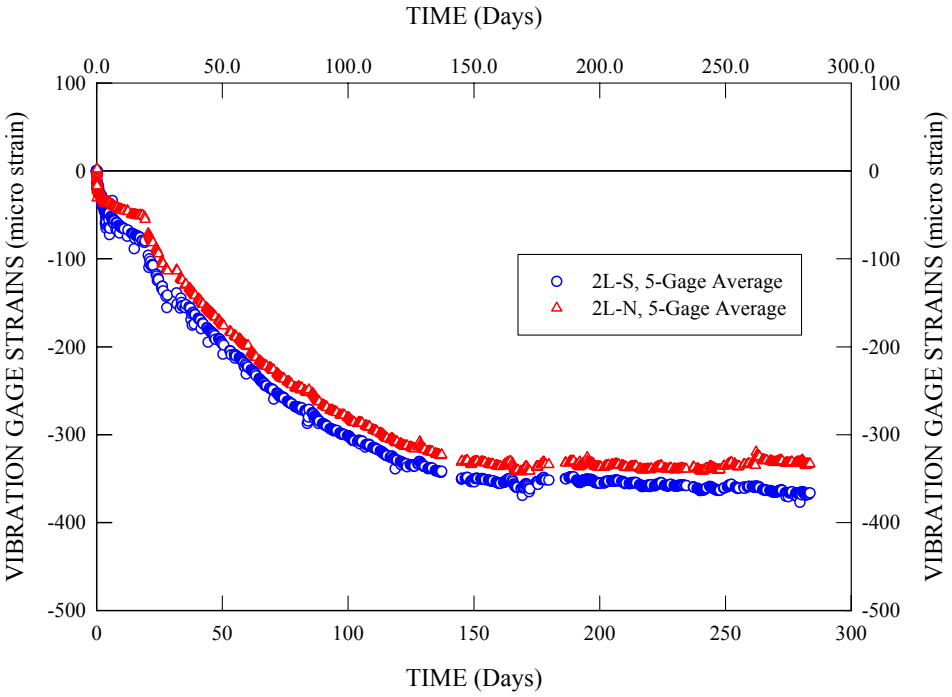

Figure 3.7.3. Average radial concrete strain variations over time due to shrinkage at gage line 2L (Beshah 2006).

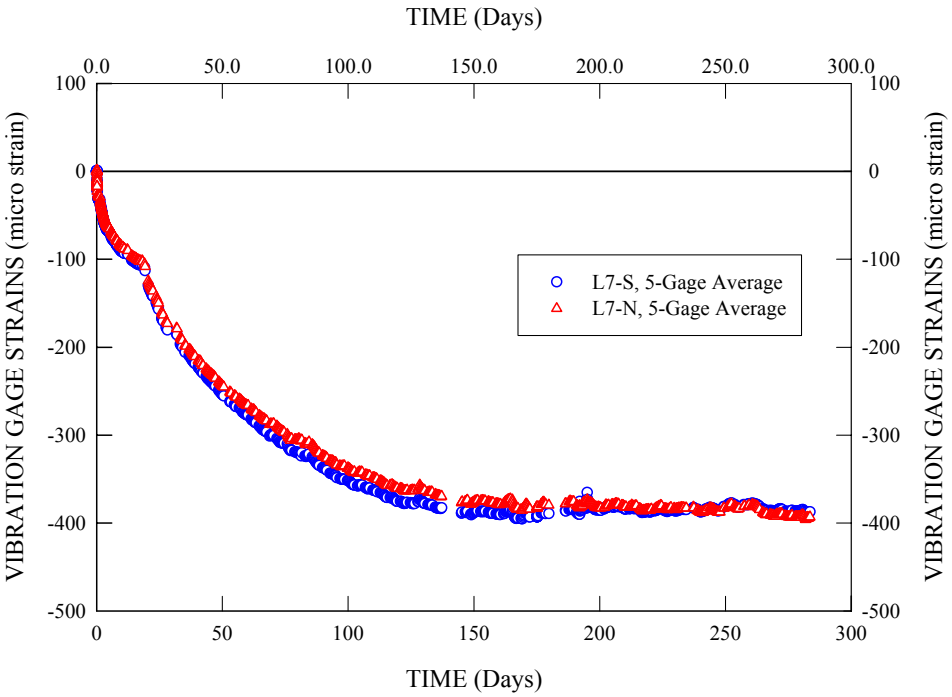

Figure 3.7.4. Average radial concrete strain variations over time due to shrinkage at gage line L7 (Beshah 2006).

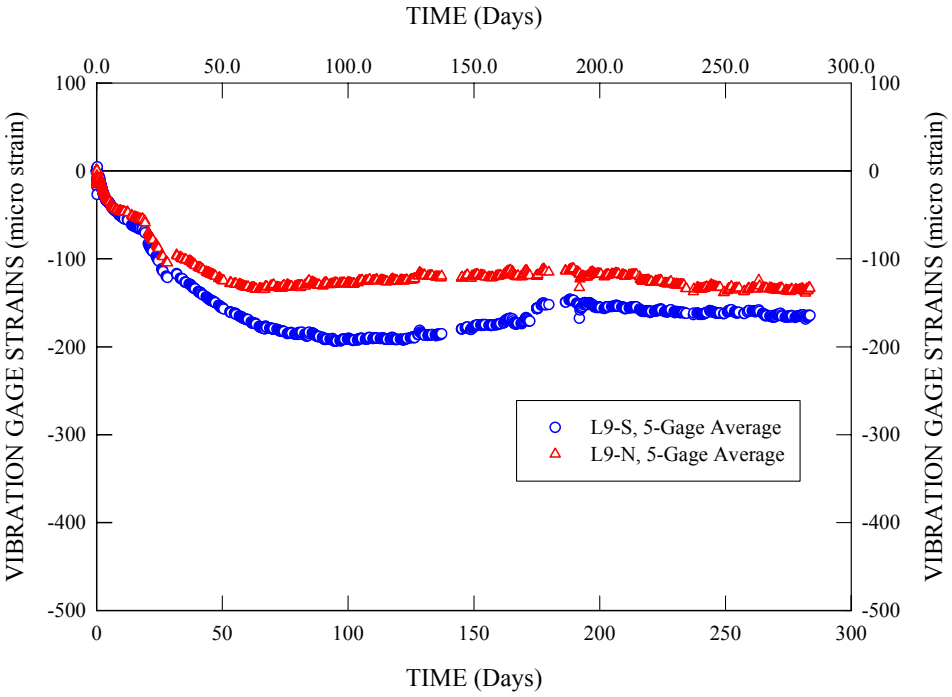

Figure 3.7.5. Average longitudinal concrete strain variations over time due to shrinkage at gage line L9 (Beshah 2006).

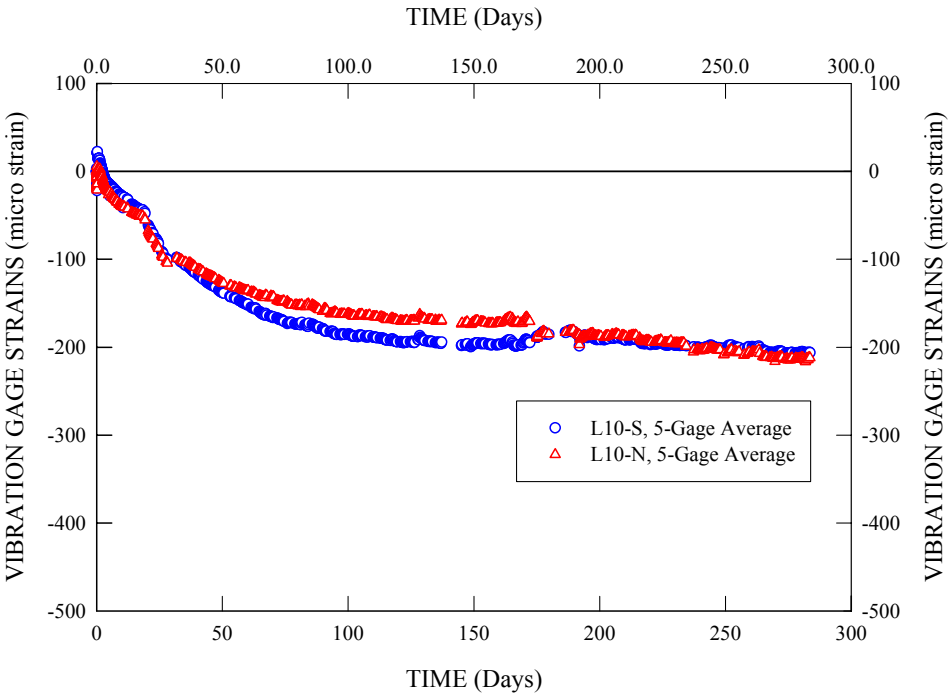

Figure 3.7.6. Average longitudinal concrete strain variations over time due to shrinkage at gage line L10 (Beshah 2006).

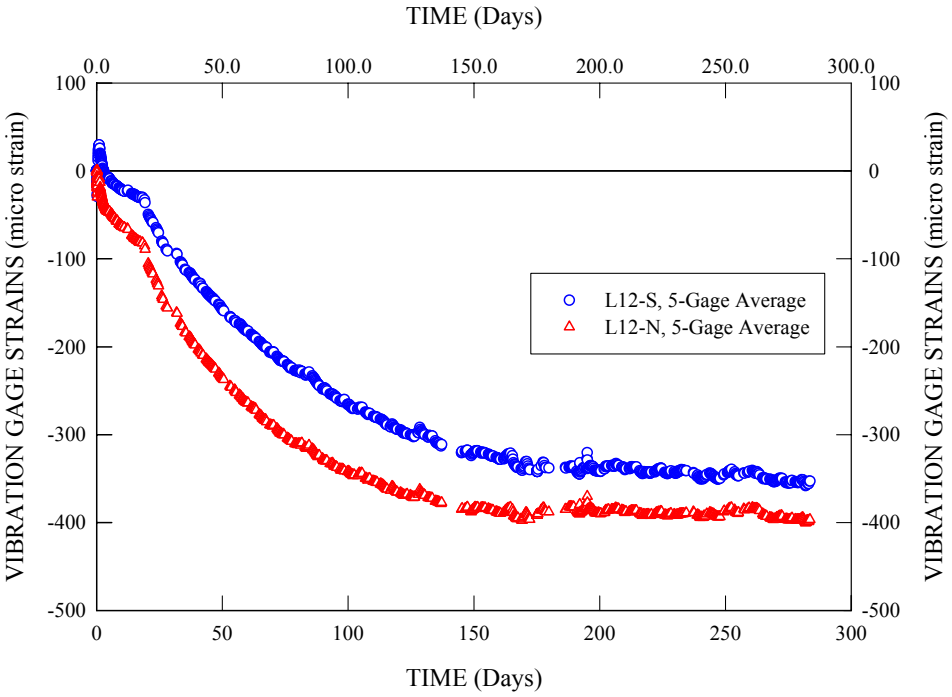

Figure 3.7.7. Average radial concrete strain variations over time due to shrinkage at gage line L12 (Beshah 2006).

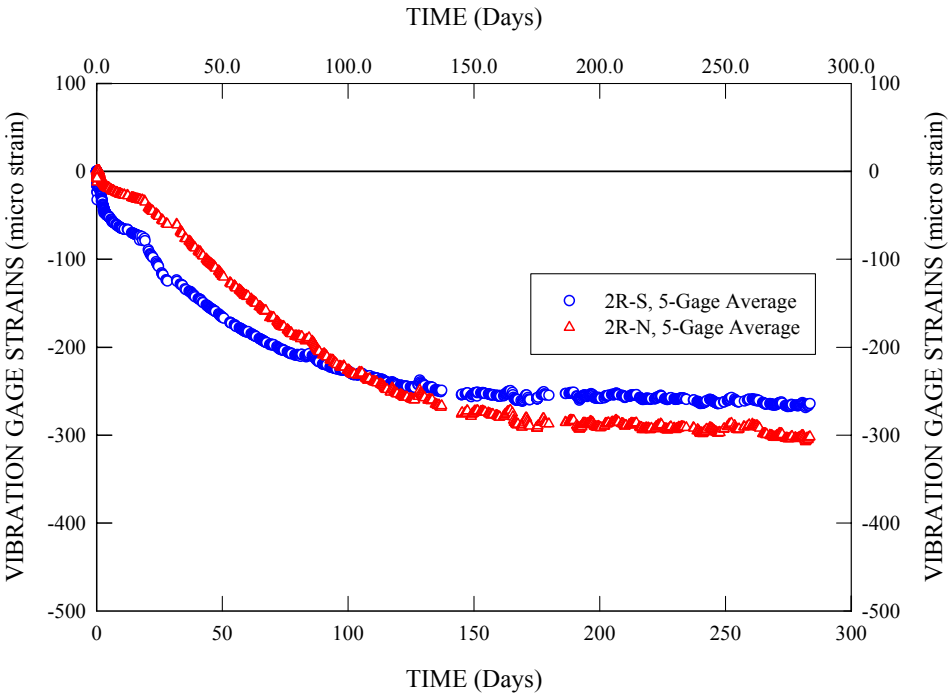

Figure 3.7.8. Average radial concrete strain variations over time due to shrinkage at gage line 2R (Beshah 2006).

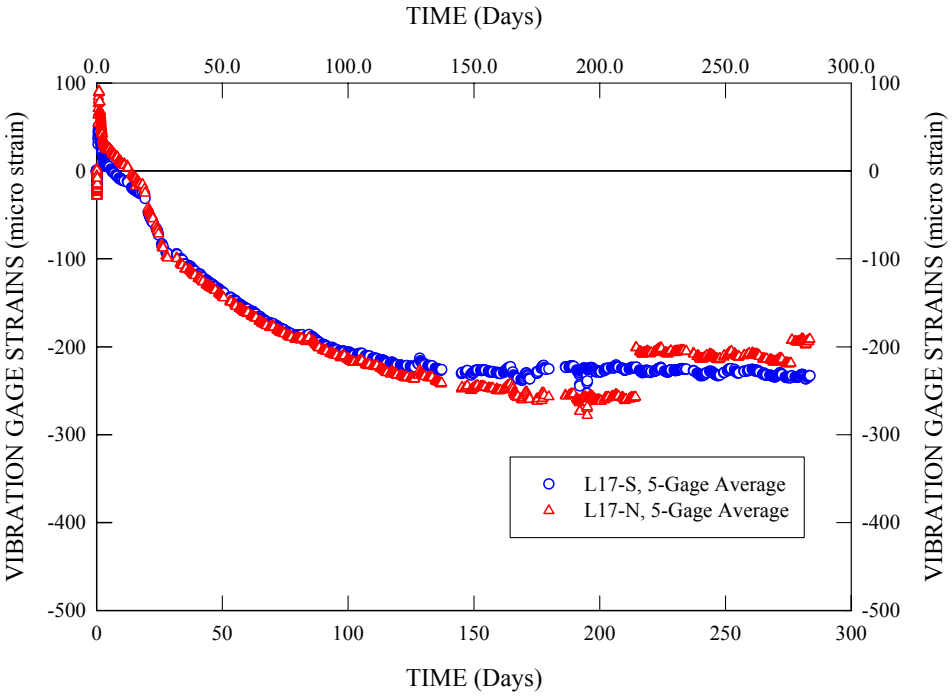

Figure 3.7.9. Average longitudinal concrete strain variations over time due to shrinkage at gage line L17 (Beshah 2006).

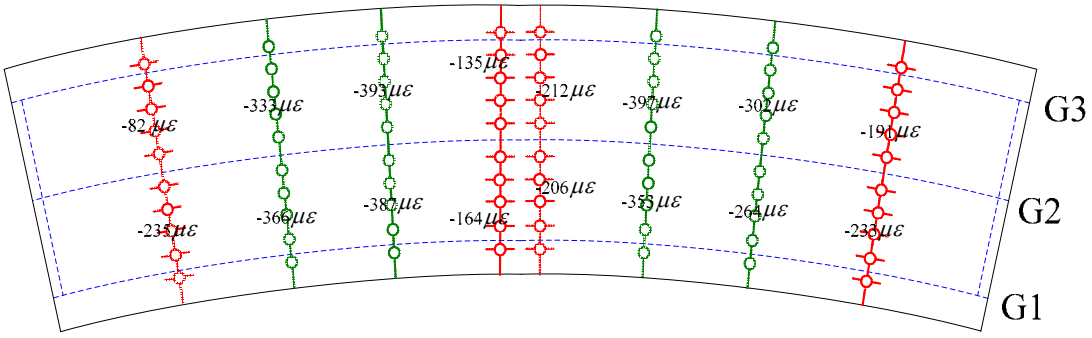

Figure 3.7.10. Average longitudinal and radial concrete strains due to shrinkage at 298 days after concrete casting.

3.8 Full Nonlinear FEA Procedures

The full nonlinear FEA closely follows the complete sequence adopted for the test bridge construction as well as the experimental testing procedures conducted on the composite test bridge: erection of the steel, construction of the forms for casting of the concrete slab, casting of the slab, strength and stiffness gain of the slab concrete such that the bridge acts compositely, removal of forms, slab shrinkage, and the application of hydraulic jack loads to the composite system. For elastic analysis and design, if the composite bridge behavior is assumed to be geometrically linear and elastic, the total stresses and deflections can be obtained by superposing the live load analysis results with the total dead-load deflections and stresses. However, superposition is not valid for determining inelastic response. Also, it is desired to capture the influence of any geometric nonlinearity on the maximum strength of the test bridge. The physical characteristics of the test bridge and the corresponding full nonlinear FEA modeling of these characteristics are addressed in the following steps:

Step 1: Generation of the Complete FEA Model. First, a complete FEA model of the bridge system is generated, including every component in the bridge upon the completion of the construction.

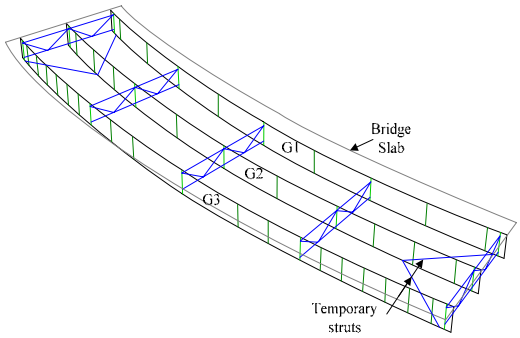

Figure 3.8.1. Step 1 - FEA model upon the completion of construction.

Step 2: Erection of the Steel. The concrete slab is removed from the FEA model using the "CHANGE MODEL" command, leaving the model of the steel superstructure at the end of the steel erection. The analysis then starts by "turning on" the self-weight of the steel superstructure.

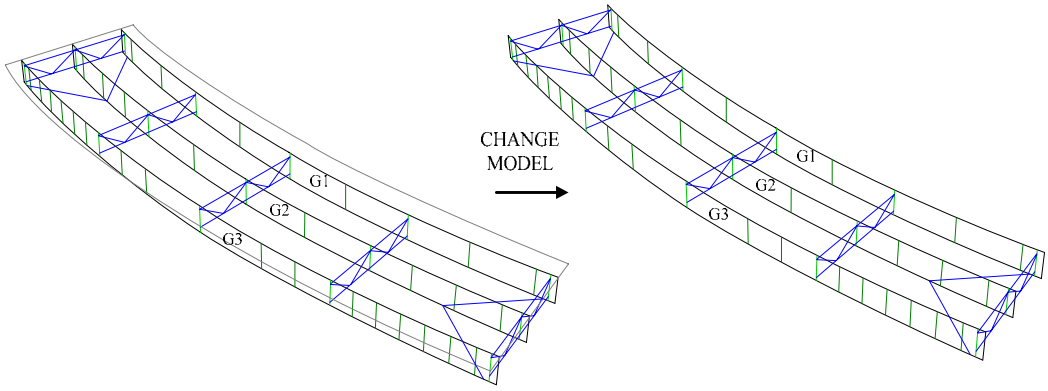

Figure 3.8.2. Step 2 - Noncomposite FEA model.

It should be noted that the steel erection sequence is not explicitly modeled in this study. It does not need to be modeled if the only goal is to estimate the final deformations and stresses at the end of the erection process. The reasons why the erection sequence does not need to be explicitly modeled are as follows:

- If it is assumed that the geometric tolerances are small such that the effect of any deviations from the ideal connection locations and the connection and component geometries may be neglected, if the no-load geometry of all the components is independent of the construction process, and if it is assumed that all the structural components are maintained in their elastic state during the erection process, then the solution for the final erected state of the structure is unique. Given these conditions, which are satisfied by the composite test bridge, the erection history does not influence the deflections and stresses within this final state.

- Geometric nonlinearity in the structural system does not influence the uniqueness of the analysis solution. Within the above stated limits, the structural system is conservative and elastic. If second-order effects are significant, a geometric nonlinear analysis is necessary of course in order to capture these effects.

If different components of the structure are detailed such that the structure would not fit together in its no-load position, the effect of this lack-of-fit would need to be included in the analysis model. The lack-of-fit may be analyzed by defining the corresponding initial strains. This does not influence the uniqueness of the analysis solution.

If the Engineer wishes to determine the forces required to erect or assemble various portions of the structure, the deflections or stresses in any components of the bridge

within a particular partially completed state, or the stability of the structure during the erection process, then an explicit simulation of the erection process is necessary to obtain accurate results. This type of analysis is addressed by Chang (2006).

Figure 3.8.3 shows a schematic of the steel erection sequence for the test bridge. The erection was accomplished in the following three main steps:

1) Girders G1 and G2 were placed on the lab floor with their webs in the plumb position. The bottom flanges of these girders were supported by closely-spaced wood blocks such that the girders were in their ideal no-load condition, including the initial camber specified in their design. Holes were then drilled within the connection plates of these girders such that the fit-up with the five cross frames connecting them is ideal, i.e., such that the cross-frames may be connected to these girders ideally without inducing any internal deformation or stress. The five cross-frames were then connected to these girders. Girders G1 and G2 were then lifted as a pair and placed on their end bearing supports.

2) Girder G3 was also placed on the lab floor in the same manner as G1 and G2. Prior to lifting G1 and G2, the holes in the connection plates for G2 and G3 were also drilled such that the five cross-frames connecting them fit within their no-load configuration without inducing any internal deformation or stress. Subsequent to the placement of girders G1 and G2 as a pair, girder G3 was lifted and positioned on its end bearings.

3) Girder G3 was held by the overhead crane used for its placement while the five cross frames were installed and the connections established between G2 and G3.

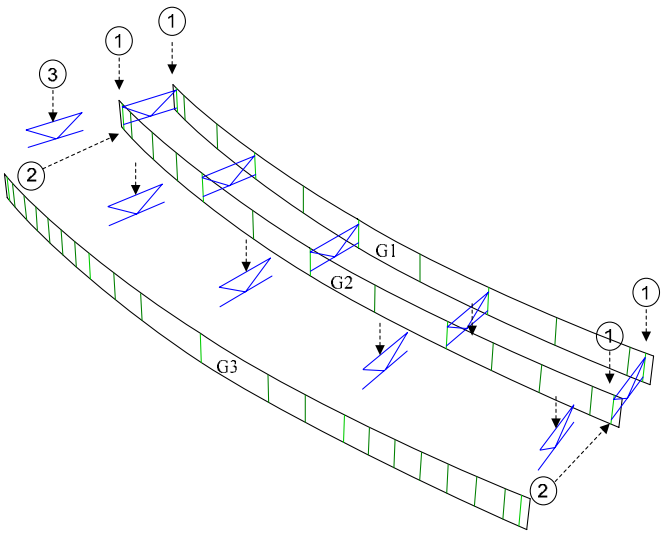

Figure 3.8.3. Schematic representation of steel erection sequence for the test bridge.

Based on the above erection procedure, ideally there was no lack-of-fit between the various components of the structure in the no-load position. Therefore, assuming zero yielding within the structure during the erection process, perfect geometry of the structure, and connections of all of the structural components at the ideal drilled locations, the only source of internal stress and deformation within the final erected structure is the self-weight of the steel superstructure itself. Since the focus of the full nonlinear FEA is on the strength behavior of the completed composite bridge, explicit simulation of the erection process is not necessary. The finite element model of the steel superstructure is established as explained in Step 1, and the self-weight of the steel is simply "turned on," as explained at the beginning of this step (i.e., Step 2).

It should be noted that the prediction of the end reactions in structures such as the test bridge is highly sensitive to minor deviations from the perfect no-load geometry. Deviations of the structural steel from its ideal geometry, minor stresses existing within the girders when they were blocked on the lab floor, and minor deviations in the bearings

from their ideal elevations can result in significant changes in the steel dead-load end reactions. That is, the end reactions are sensitive to geometric tolerances whenever the support reactions for the completed structure are statically indeterminate, which is practically always the case, and the structure is relatively stiff corresponding to displacements at the supports. Therefore, it is necessary to adjust the bridge bearings at the end of the steel erection such that the end reactions match with the ideal values determined from analysis. Once the test bridge erection was completed, minor adjustments were made at the bearings such that the dead load (DL) analysis reactions and the actual reactions matched.

Finally, it should be noted that since the I-girder webs in the test bridge were plumb in the no-load position, they must be out-of-plumb in the final erected dead-load position (since the bridge cross-section at the midspan undergoes a twist displacement due to the dead loads). This represents the approach that is used in many curved I-girder bridges, where the calculated out-of-plumbness of the girders in the final erected condition is within adequate tolerances. However, due to the initial vertical camber of the girders, the elevation of the top or bottom of the steel is ideally within a horizontal plane at completion of the slab casting (neglecting any superelevation or grade changes, which do not exist for the composite test bridge). The out-of-plumbness of the I-girder webs at the cross frames in the test bridge are essentially equal to the angle of twist of the bridge cross-section due to the loading.

Figure 3.8.4 shows a typical fabrication procedure that the AASHTO (2004b) Specifications indicate is a preferred method, when the out-of-plumbness of the I-girder webs using the above type of procedure is larger than desired. In this figure, the cross-

frames are fabricated and the connections to the I-girders are located such that the girders have to be twisted relative to their no-load geometry in order to establish the connection with the cross-frames. One can observe that in this case, some internal stresses are necessarily induced within the structural system due the initial lack-of-fit. Bridge Engineers typically assume that these induced stresses are small, and that they are relieved by the dead-load deflections of the structure. Strictly speaking, this assumption is incorrect in the sense that any initial lack-of-fit within the no-load geometry of the bridge induces internal stresses within the structure. The erection simulation procedures developed by Chang (2006) allow the Engineer to determine accurate estimates of the ideal stresses induced within the structural system due to detailing such that the components do not fit up within their no-load geometry. Chang's procedures accommodate either the direct analysis for the final dead-load stresses and deflections, or the simulation of the complete erection process.

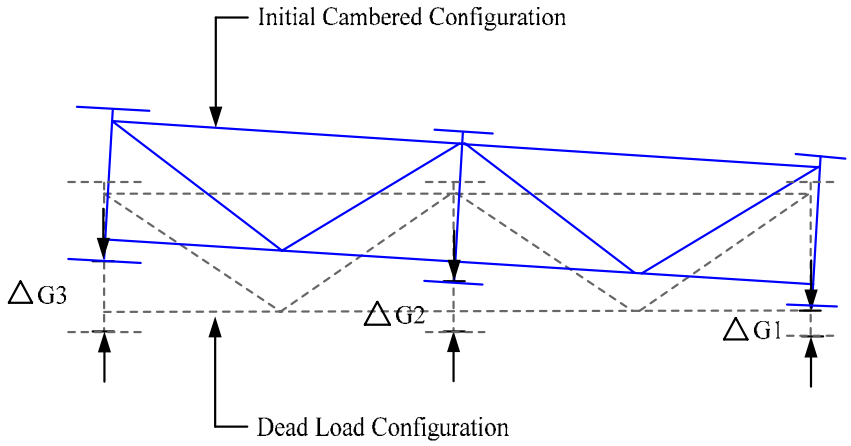

Figure 3.8.4. Initial cambered configuration and final dead-load configuration of bridge cross-section at a cross-frame location if the girders are twisted from their no-load web-plumb position to align them with the rectangular cross-frame geometry.

Step 3: Construction of the Forms for Casting of the Concrete Slab and Casting of the Concrete Slab. The slab casting operations were conducted continuously over a time period of approximately four hours, with the main door of the laboratory open for the pump truck to boom into the lab for the placement of the concrete. The ambient temperature inside of the lab was between 50 and 60 ºF during this period. Therefore, there was little set of the slab concrete during the entire casting operations. As a result, the dead-loads due to the weight of the forms and the slab concrete are modeled by applying a line load to the top flange of the I-girders in the FEA model of the steel superstructure. The full dead-load from the slab plus the forms is assumed to be taken solely by the structural steel. The eccentric bracket loads on girders G1 and G3 are modeled by applying equal and opposite radial line loads to the girder flanges. These loads are statically equivalent to the applied torsion from the brackets.

Step 4: Strength and Stiffness Gain of the Slab Concrete for Composite Action. The concrete slab was covered and allowed to cure for approximately 28 days prior to stripping of the formwork. It is expected that significant strength and stiffness gain of the concrete was achieved early within this process. This strength and stiffness gain is represented within the FEA model by using the CHANGE MODEL command in ABAQUS to reinstate the FEA representation of the concrete slab. A number of approximations are necessary at this stage due to limitations of the ABAQUS software. One difficulty in ABAQUS is that every portion of the finite element model must be defined in its initial geometry. ABAQUS does not permit the instantiation of the slab at the location of the current deformed steel geometry. Fortunately, this is not a significant problem since the slab and the centerline of the top flanges of the I-girders are ideally

horizontal and flat within the final dead-load position at the end of the slab casting. However, a more significant problem is that the slab nodes immediately above the top flange of the steel I-girders (in the no-load geometry) are tied to the flange nodes by multi-point constraints. If the beam multi-point constraint is employed, these slab nodes are subjected to displacements that are compatible with the steel I-girders during the noncomposite loading of the bridge, i.e., Steps 1 through 3. However, the other slab nodes, which are not constrained to the I-girder flange nodes by multi-point constraints, do not experience any displacements during the noncomposite loading. This produces a severe distortion of the slab finite elements immediately over the tops of the steel I-girders. This problem is alleviated by explicit definition of a multi-point constraint between the above flange and slab nodes, using the EQUATION command in ABAQUS. In this approach, the above spurious deflection of the slab nodes during the noncomposite loading of the bridge is negated such that all the slab nodes are within a horizontal plane in Step 4. The detailed derivation of this new kinematic definition is provided in Appendix E. Also, the girder vertical displacements due to the full bridge dead load are slightly different in the final full nonlinear FEA model than the predicted vertical displacements based on load estimates during the design of the test bridge. Therefore, the girder top flanges are not ideally in a horizontal plane at the end of Step 3 if the actual initial camber is used within the FEA model. To avoid the need to define the initial slab geometry in anything other than a horizontal plane, the I-girder cambers used within the FEA model are adjusted such that the centerline of the top flange in each of the I-girders is in a horizontal plane at the end of Step 3. In as such, the haunch between the I-girders and the slab is 7.6 cm (3.0 in) and the distance between the top of the slab and the top of

the steel is 27.9 cm (11.0 in) along the entire bridge when the slab is instantiated in Step 4. The slab is in a condition of zero stress at this stage, whereas the steel superstructure is subjected to the stresses due to the full noncomposite dead load.

As noted previously, there is some twisting of the I-girders due to the dead loads, and the I-girder webs are therefore not plumb within the final dead load configuration. Correspondingly, there is a radial displacement at the top flanges of all the I-girders in the final dead load configuration. The top flange nodes in this deflected position are constrained to the corresponding slab nodes that are located at the ideal position over the top of the flanges in the no-load geometry. After detailed inspection of the FEA results, it was concluded that the approximations induced by this modeling approach are acceptable. Separate FEA capabilities are developed in the research by Chang (2006) that will allow for direct instantiation of the slab on the deflected geometry of the steel superstructure.

Step 5: Removal of the Slab Forms. The removal of the slab forms from the bridge system is modeled by applying the negative of the corresponding dead load to the composite bridge model.

Step 6: Shrinkage of the Slab. The shrinkage strains measured in the slab at the beginning of the applied load testing are applied to the composite finite element model. These measured strains are approximately uniform. They are applied to the slab finite elements via the corresponding initial stresses, denoted by S11 and S22 in Figure 3.8.5.

Step 7: Application of Composite Live Loads. Lastly, the loads from the hydraulic jacks are applied to the complete bridge model.

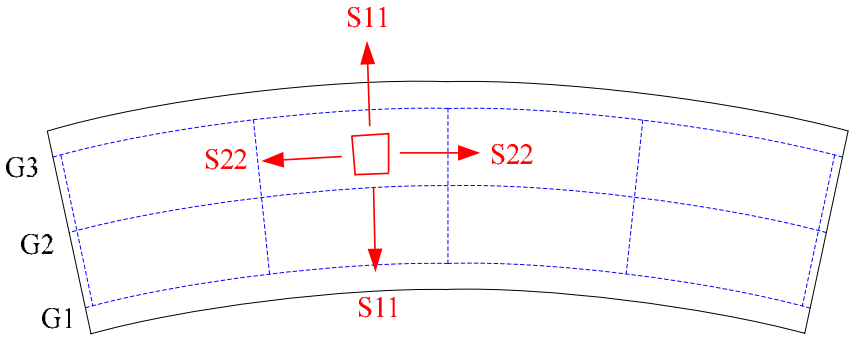

Figure 3.8.5. Introduction of compressive strain due to shrinkage into the bridge slab in the form of initial circumferential and radial stresses, S22 and S11.

CHAPTER 4

REPEATED LOADING TESTS, EXPERIMENTAL AND ANALYTICAL RESULTS

4.1 Overview

As described in Section 1.6, four major sets of experimental tests were conducted on the composite test bridge. They are labeled as Tests 1 through 3, 4a and 4b, following the testing sequence. Test 1 addressed the generation of influence surfaces by applying a concentrated load of 72 kN (16 kips) repeatedly on a number of grid points on the slab. The reader is referred to Beshah (2006) for the results of these tests. This research focuses on the last four sets of tests, which are more directly related to the strength limit states behavior of the bridge.

In Tests 2 and 3, the test bridge was subjected to a group of six loads from hydraulic jacks positioned on the test bridge slab such that they were directly above the bridge girders. These concentrated hydraulic jack loads were directly applied on G2 and G3 for Test 2, inducing the maximum flexural effects on G3, whereas they were applied on G1 and G2 for Test 3, inducing the maximum flexural effects on G1. The hydraulic jack loads were applied to the test bridge repeatedly for three times during each test. The repeated loading was intended to evaluate the stability of the load-deflection response over repeated loading cycles.

In the final two tests, Tests 4a and 4b, the test bridge was subjected to a group of nine hydraulic jack loads that were approximately equivalent to the two AASHTO design trucks plus two lane loads used for the design of the outside girder G3 in the test bridge. Test 4a involved repeated loading at several load levels defined in relation to the various

AASHTO (2004b) design requirements, and Test 4b involved the final monotonic loading of the test bridge to its ultimate capacity. The latter part of this chapter focuses on the results from Test 4a. Experimental results and corresponding FEA solutions from the final monotonic loading test, Test 4b, are presented in Chapter 5.

Since Tests 2 through 4a all involve repeated loading, they are referred to collectively as the repeated loading tests. The results from the repeated loading tests need to be investigated thoroughly for a complete assessment of their influence on the bridge behavior, including the extent that they affect the responses during the final monotonic loading test. Of particular interest are the changes in geometry (e.g., residual deflections and slip displacements at the concrete/steel interface) and material nonlinearities (e.g., steel yielding and concrete cracking) during the repeated loading tests. The repeated loading tests have a potential impact on the state of the bridge at the start of the final monotonic loading test. It is desired also to consider whether the final monotonic loading response of the composite test bridge can be predicted accurately without considering the influence of the prior repeated loading tests.

In what follows, various measured bridge responses are presented, along with the corresponding FEA solutions, to assess the state of the bridge at several stages of the construction and subsequently after each of the repeated loading tests. First, the measured no-load camber values for the three test bridge girders are presented and compared to the nominal cambers specified in the engineering drawings. Then, the bridge responses at the end of steel erection are considered, with a focus on the overall girder reactions, deflections and flange major-axis and lateral bending stresses. This is followed by a discussion of the bridge responses after placement of the slab concrete.

Next, the results of Tests 2 and 3 are considered. Finally, this chapter focuses on the bridge responses obtained from Test 4a. Emphasis is placed on the effects of these tests on the subsequent responses of the bridge.

4.2 Girder Cambered Geometries Prior to Steel Erection

The test bridge girders were cambered to offset the dead load vertical deflections such that their final constructed geometries are flat prior to the application of live loads. The target cambers for the bridge girders were obtained from an elastic noncomposite dead load analysis. Figure 4.2.1 shows the resulting target cambers specified for each of the test bridge girders. Figure 4.2.1 also shows the measured cambers. The measured cambers were obtained by using the laser scanning system shown in Figure 4.2.2. This system was not only used to measure actual cambers, but also to track the girder deformed geometries during the steel erection process. More specific details regarding the laser system measurements are reported by Fuchs (2005). The camber measurements were made on the north edge of the bottom flange of the girders, with the girders placed in their blocked positions on the laboratory floor prior to the steel erection. The G3 camber measurements were made with girder G3 sitting alone on the laboratory floor, not connected to G2 by cross-frames. Conversely, the camber readings for G1 and G2 were taken when they were blocked as a pair sitting on the laboratory floor. As noted previously, holes were drilled in the connection plates for connection of the cross-frames to the girders with the girders setting in their blocked no-load positions. Therefore, the influence of the pairing of G1 and G2 is expected to be small.

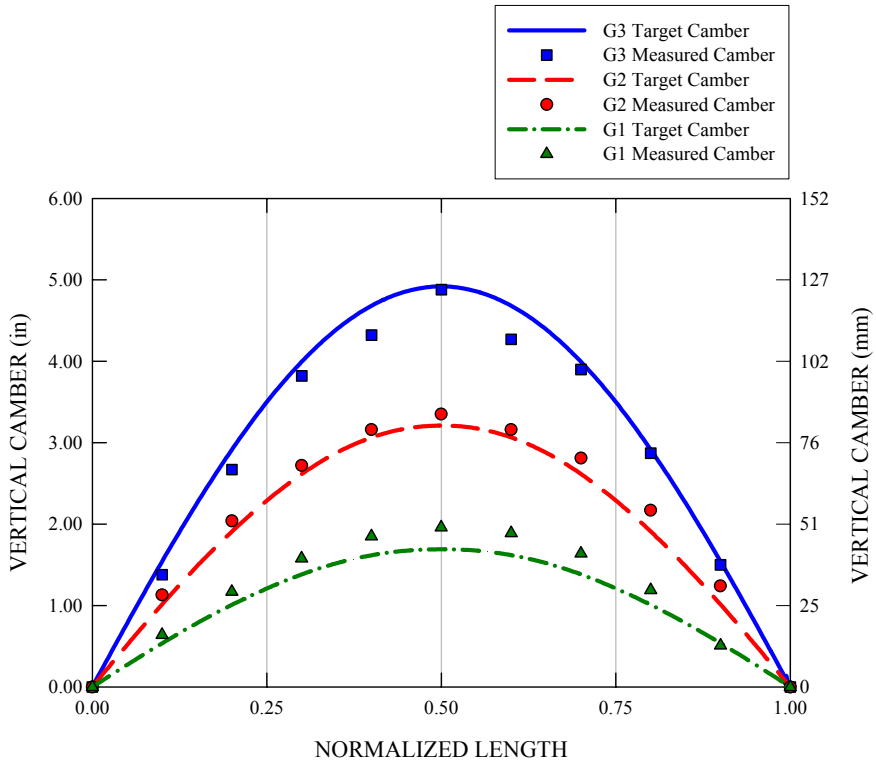

Figure 4.2.1. Targeted and measured vertical cambers of the test bridge girders along the normalized length (measured data courtesy of Fuchs (2005).

(a) (b)

Figure 4.2.2. Laser scanning system: (a) overall view of laser system setup in the laboratory (b) close-up view of the laser scanner mounted on the wall, courtesy of FHWA.

Figure 4.2.1 indicates that the targeted cambers for G3 are matched well by the measured cambers along the entire girder normalized length except at two locations along the normalized length, 0.4 and 0.6. At these locations, there are relatively large differences between the targeted and measured cambers. The measured cambers at these locations are 9.20 mm (0.362 in) and 10.46 mm (0.412 in) smaller than corresponding targeted cambers. A subsequent inspection of the G3 camber diagrams provided on the engineering drawings indicated that the source of the above discrepancy was a transposition in the specified camber values at these locations. Nevertheless, due to the fact that the connection plates were drilled in the laboratory for no-load fit, with the girders blocked in the cambered positions specified on the engineering drawings, and since these deviations were only over a short length of G3, the above deviation from the targeted cambers is judged to be inconsequential. The provisions in Section 3.5 of the AWS Bridge Welding Code (2002) require that the measured cambers for welded girders with the top flange embedded in concrete and a designed haunch shall not be smaller than the required cambers. Therefore, G3 is slightly in violation of the AWS Code.

The camber measurements for G1 and G2 provided in Figure 4.2.1 show that their comparisons to the targeted camber values are not as good as that of the G3 camber readings, neglecting the two outliers. It can be seen that the measured cambers for these two girders are slightly larger than the target cambers. The maximum deviations are + 6.83 mm (0.269 in) and + 3.56 mm (0.14 in) at mid-span for G1 and G2, respectively (the positive sign indicating that the measured camber is larger than the targeted value). However, these deviations are within the maximum camber tolerances allowed by the

AASHTO Bridge Welding Code (2002) provisions. The maximum camber tolerances stipulated in the Welding Code are +20 mm (+3/4 in) for these two girders.

4.3 Noncomposite Dead Load Bridge Responses

The accuracy and reliability of the full nonlinear FEA predictions relative to the experimental results are directly dependent on the extent to which the bridge FEA model can represent the initial state of the physical composite test bridge at zero applied load level. Therefore, the bridge responses at the end of steel erection and concrete casting are an important consideration. In the following, various bridge responses obtained from full nonlinear FEA are compared to corresponding experimental data obtained from these two stages of construction.

4.3.1. Bridge Responses at the End of the Steel Erection

Table 4.3.1 compares the measured girder reactions and the corresponding FEA predictions at the end of steel superstructure erection. It should be noted that the FEA solutions presented here are obtained from a noncomposite analysis of the test bridge where all the bare steel components are assembled simultaneously without consideration of step-by-step erection sequences, and then their gravity loads are applied to the FEA model. The fifth column of Table 4.3.1 shows that the sum of the FEA girder reactions is exactly equal to that of the measured reactions. The fourth column of Table 4.3.1 shows that the G3 FEA reaction is slightly larger than the corresponding measured reaction by 6 percent. Furthermore, it can be seen from the second and third columns of Table 4.3.1 that the predicted FEA reactions are a rather poor estimate of the G1 and G2 measured

reactions. The measured girder reaction for G1 is less than the FEA girder reaction by almost 20 percent. Conversely, the measured girder reaction for G2 is larger than the FEA prediction by 16 percent. These discrepancies are believed to be due to the sensitivity of the reactions to the precise elevation of the support bearings as well as the precise no-load geometry of the steel. Small changes in hypothetical girder no-load elevations at the bearings relative to the bearing elevations lead to large changes in the girder dead load reactions. This is due to the fact that the stiffness of the bridge corresponding to small support movements is quite large relative to the steel dead load reactions. It should be noted that the supports were adjusted at the end of the steel erection to obtain the reasonable match between the values shown in Table 4.3.1. It appears that these differences in the predictions of individual girder reactions do not have any significant adverse effects on the subsequent FEA predictions, as will be shown later in this chapter. The next section shows that the measured and FEA total dead load reactions match closely.

Table 4.3.1 Girder reaction comparisons at the end of steel superstructure erection.

Girder	G1	G2	G3	Sum Total
FEA prediction kN (kips)	26 (5.8)	78.4 (17.6)	196 (44.2)	300 (67.6)
Measured reaction kN (kips)	22 (4.9)	93.6 (21.0)	186 (41.7)	300 (67.6)
FEA/Measured	1.19	0.84	1.06	1.00

Figure 4.3.1 presents FEA vertical deflections along the normalized length for girders G1, G2 and G3 at the end of steel erection. Corresponding measured deflections are not

available at the time of completion of this study. The predicted maximum vertical deflections are 5.1 mm (0.20 in), 19 mm (0.75 in), 25 mm (1.0 in) for girders G1, G2 and G3, respectively.

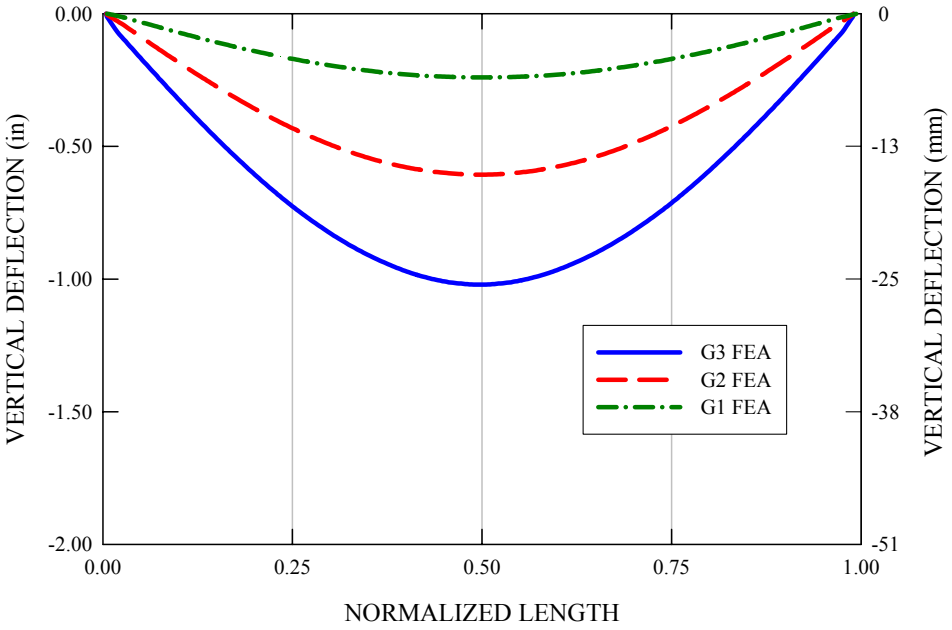

Figure 4.3.1. Predicted girder vertical deflections at the web-flange juncture along the normalized length at the end of steel superstructure erection.

Figure 4.3.2 presents the elastic major-axis and lateral bending stresses along the length of the G3 bottom flange at the end of steel erection, determined from the experimental strain measurements as well as from FEA . Except for the stresses near the normalized length of 0.75, it can be seen that experimentally based stresses (referred to subsequently as the measured values) match reasonably well with the FEA predictions. There is a better correlation between the measured and predicted values for the major-axis bending stresses than for the lateral bending stresses. The measured lateral bending stresses are approximately two times larger than the FEA predictions at one of the

quarter-span cross-frames, while they are quite small relative to the FEA predictions at the other quarter-span cross-frame location. Conversely, the measured major-axis bending stresses are 13 percent larger than the FEA values at the gage locations near the mid-span while the measured major-axis bending stresses are 40 percent smaller than the FEA values at the cross-frame location with the large measured f_ℓ.

Figure 4.3.3 provides similar stress comparisons for the G3 top flange major-axis and lateral bending stresses at the end of the steel erection. It can be observed that the correlation between the measured and FEA lateral bending stresses is better over the normalized lengths 0 to 0.25 and 0.75 to 1.0 in Figure 4.3.3 whereas it is better over the lengths 0.25 to 0.75 in Figure 4.3.2. The FEA lateral bending stress values are smaller than the measured values for the top flange. Despite these seemingly substantial differences between the measured and predicted values, it is found that they do not have significant effects on the comparisons between the results of the subsequent experimental tests and corresponding FEA predictions. This is largely because the magnitudes of the stress differences, particularly the lateral bending stresses, are significantly smaller than the flange yield strengths.

For the G2 top and bottom flange stresses provided in Appendix C, it is also found that the comparisons between the measured and predicted values are similar to those for G3. The G1 top and bottom flanges stresses provided in Appendix C are generally less than 6.9 MPa (1.0 ksi). As a result, no meaningful comparisons between the FEA predictions and the experimental values are possible for G1.

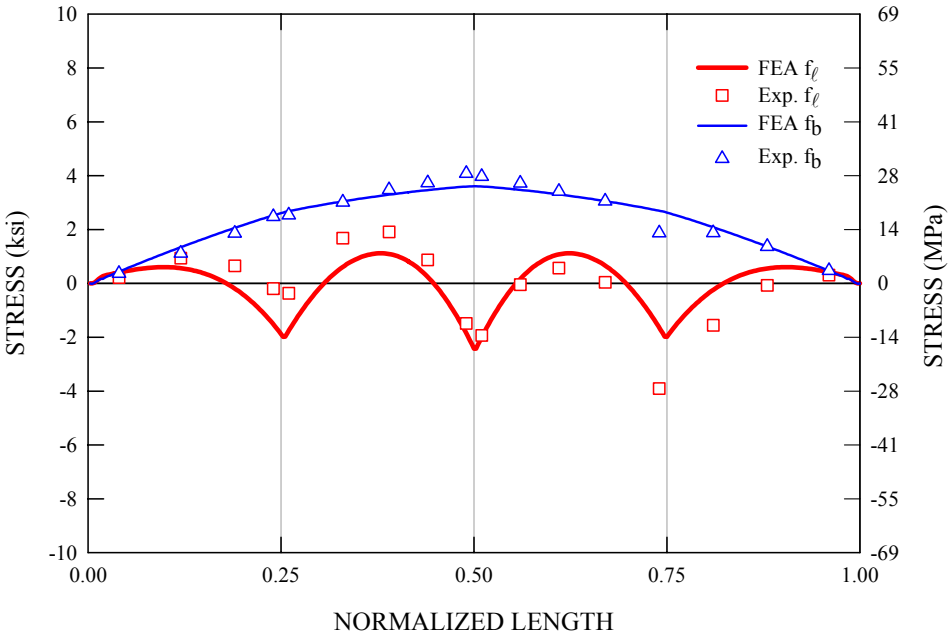

Figure 4.3.2. Measured and predicted major-axis and lateral bending stresses of the G3 bottom flange along the normalized length due to the self weight of steel superstructure.

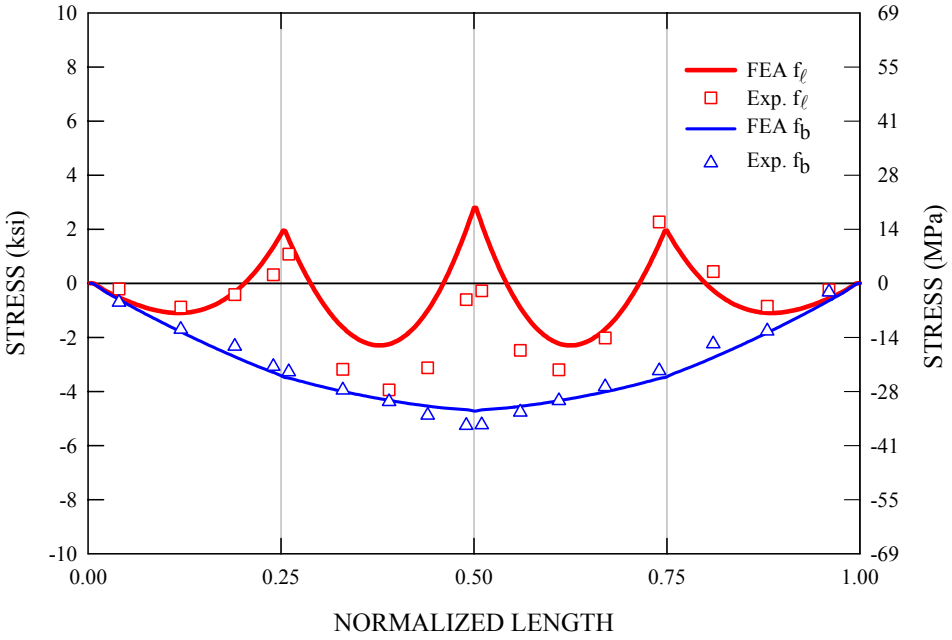

Figure 4.3.3. Measured and predicted major-axis and lateral bending stresses of the G3 top flange along the normalized length due to the self weight of steel superstructure.

4.3.2. Bridge Responses after Placement of the Slab Concrete

The slab was cast in a single continuous operation (approximately four hours), starting at one end of the bridge and working toward the opposite end. Displacements and strains were monitored throughout the bridge during the concrete casting and were sequenced with video of the casting process. The weight of the construction equipment was insignificant compared to the other dead loads. The concrete was pumped into position on the slab, and a small vibrating screed was used for placing the concrete. Also, the displacements and strains were monitored subsequently during the curing of the slab, capturing the strains in the slab and in the structural steel due to concrete shrinkage. Figure 4.3.4 shows a picture taken during the placement of the concrete.

Figure 4.3.4. Placement of the slab concrete, courtesy of FHWA.

Table 4.3.2 compares the measured girder end reactions after the placement of the concrete to the corresponding FEA predictions. It should be noted that the reactions reported in the table are total accumulated values, including the reactions due to the weight of the steel superstructure. It can be seen that the FEA predictions closely match the measured girder reactions for the individual girders as well as the sum total of the girder reactions. That is, although the measured and FEA steel dead load reactions differ somewhat, the total dead load values are a close match. Also, it is noteworthy that the measured and FEA reactions on G3 are close at the end of the steel erection.

Table 4.3.2 Total girder reactions after placement of the slab concrete.

Girder	G1	G2	G3	Sum Total
FEA reaction* kN (kips)	129.7 (29.16)	428.8 (96.39)	731.7 (164.5)	1290 (290.0)
Measured reaction* kN (kips)	130.6 (29.37)	429.4 (96.53)	732.8 (164.7)	1292 (290.6)
FEA/Measured	1.00	1.00	1.00	1.00

* The measurements presented here were made at 298 days after placement of the concrete. The FEA predictions include the influence of the concrete shrinkage at 298 days.

Figure 4.3.5 compares the measured outside tip vertical deflections of the girder bottom flanges along the normalized lengths due to the concrete dead load plus the weight of the forms to the corresponding FEA predictions. These values correspond to the state of the bridge immediately after placement of the slab concrete. The measurements were located at the three points indicated in the figure. These points are at the mid-span and approximately at the two adjacent points corresponding to subsequent

applied loadings. In general, there is a slightly better correlation between the measurements and predictions for the G3 vertical deflections than for the G1 and G2 deflections. With respect to the maximum deflection at mid-span, the measured vertical deflection for G3 is 82.0 mm (3.23 in), compared to the FEA prediction of 81.5 mm (3.21 in), while the measured deflections for G1 and G2 are 51.1 mm (2.01 in) and 26.7 mm (1.05 in). These deflections are less than the FEA predictions by 4.1 mm (0.16 in) and 5.3 mm (0.21 in), respectively.

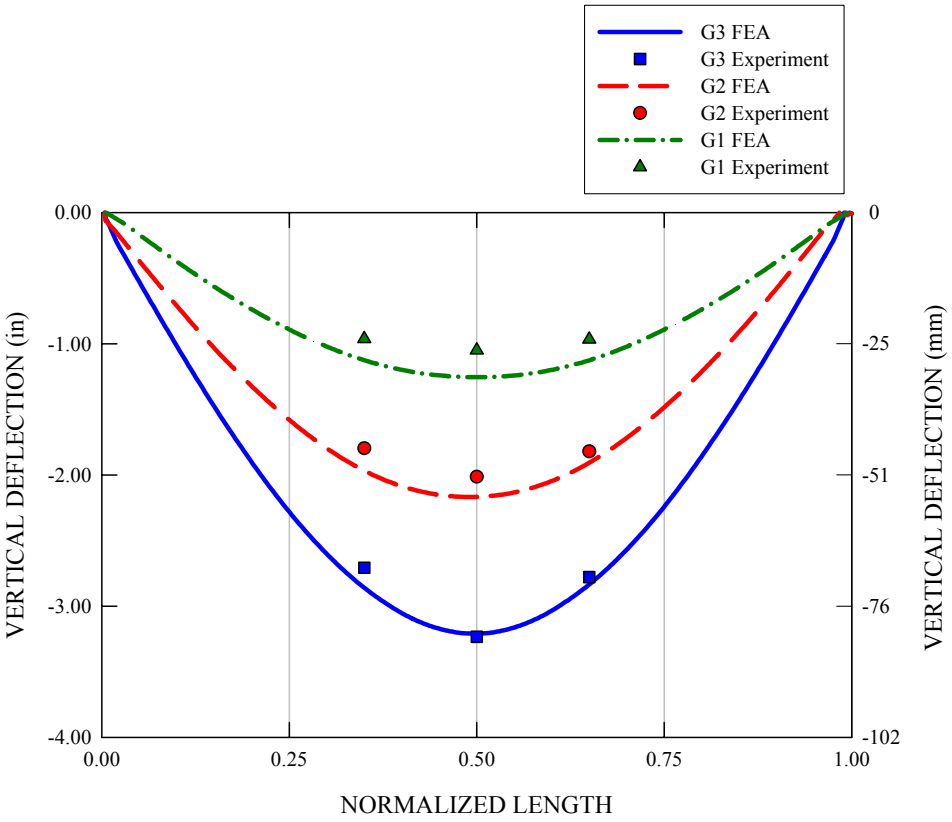

Figure 4.3.5. Outside tip vertical deflections of the girder bottom flanges along the normalized length due to the concrete dead load plus the weight of the forms (values correspond to the state immediately after placement of the slab concrete).

Figure 4.3.6 presents measured and predicted major-axis and lateral bending stresses along the length of the G3 bottom flange due to the weight of wet concrete plus the weight of the forms. In general, it can be seen that the FEA predictions and the experimental values match well for both the major-axis and lateral bending stresses, with the exception of some local deviations. With respect to the stresses measured in the vicinity of the mid-span, the major-axis bending stress is 100 MPa (14.6 ksi), which is close to the corresponding FEA prediction of 110 MPa (16.0 ksi) at the same location while the measured lateral bending stress is 52.4 MPa (7.60 ksi), which is also comparable to the corresponding FEA prediction of 54.2 MPa (7.86 ksi).

Figure 4.3.7 provides similar comparisons for the G3 top flange major-axis and lateral bending stresses at the end of the concrete placement. Similar to the comparisons of the bottom flange stresses, there is a good match between the measured and predicted values for both the major-axis and lateral bending stresses.

For the G2 top and bottom flange stresses provided in Appendix C, it is also found that the comparisons between the measured and predicted values are similar to those for the G3 flange stresses. Conversely, when it comes to the G1 flange stresses provided in Appendix C, it is found that overall comparisons between the measured and predicted values are not as good as those for the G2 and G3 flange stresses. However, the magnitude of the girder stress differences for G1 are relatively small compared to those in the other two girders. Therefore, their effects on the strength behavior of the bridge girders in the subsequent loading tests are judged to be negligible.

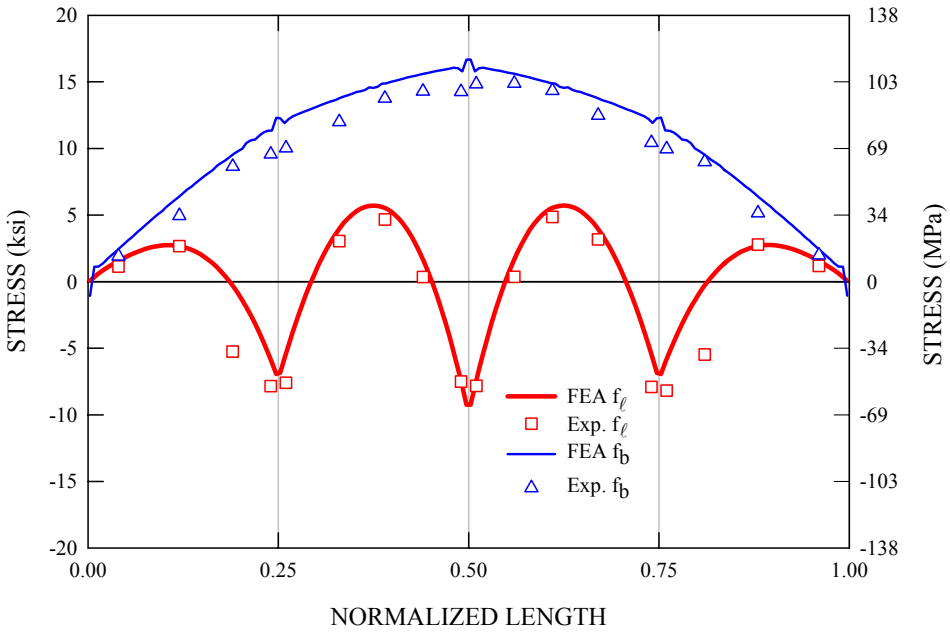

Figure 4.3.6. Measured and predicted major-axis and lateral bending stresses along the G3 bottom flange due to the concrete dead load plus the weight of the forms (values correspond to the state immediately after placement of the slab concrete).

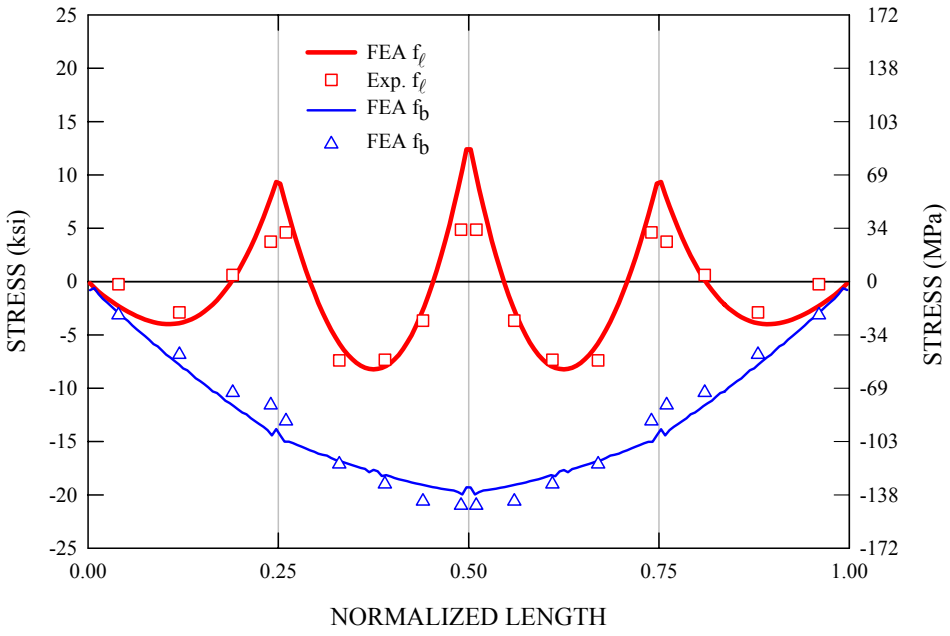

Figure 4.3.7. Measured and predicted major-axis and lateral bending stresses of the G3 top flange along the normalized length due to the concrete dead load plus the weight of the forms (values correspond to the state immediately after placement of the slab concrete).

4.4 Tests 2 and 3

4.4.1 Results of Test 2

Figure 4.4.1 shows the composite test bridge with the loading fixtures placed on the outer lane to simulate a single truck plus single lane AASHTO live load. Various bridge responses for this loading, including girder deflections and reactions obtained from the full nonlinear FEA simulations are compared to corresponding experimental values in the following. It should be noted that experimental values are only available up to a total applied load level of 1220 kN (274 kips), which is 90 percent of the total factored live load corresponding to the AASHTO design vehicle plus a lane load positioned to cause a maximum flexural effect on G3.

Figure 4.4.1. Composite test bridge with loading fixtures for Test 2, courtesy of FHWA.

The experimental loading was halted because G1 started to lift off of its bearings at this load during the experimental testing, causing a sharp increase of tensile strains on the top surface of the test bridge slab. The test bridge was not loaded beyond this stage to avoid potential damage to the slab. After the first loading cycle, the test bridge was subjected to two additional loading cycles with the peak applied loads approximately equal to 1220 kN (274 kips). In contrast to the experimental testing, the FEA simulation of Test 2 was conducted beyond the peak applied load in the experimental test to investigate the bridge responses with girder G1 lifted off of its supports (although the AASHTO (2004b) Specifications require tie downs if the design loadings are sufficient to cause such an uplift). It should be noted that under the actual factored AASHTO loading corresponding to the above, uplift does not occur at the G1 supports.

Figures 4.4.2 through 4.4.4 provide measured and predicted vertical deflections at the mid-span outside tip of the G1, G2 and G3 bottom flanges during Test 2. Since there are essentially no differences between the FEA solutions predicted by the repeated and monotonic loading analyses of the test bridge, only the results of the monotonic loading analysis are presented in these plots. In addition, only the live load displacements are shown in the plots. For all of the girders, it can be seen that the FEA predictions closely match the experimental data, and their responses are predominantly linear up to a total applied load of 1220 kN (274 kips). The measured maximum vertical deflections are 14 mm (0.54 in), 52.1 mm (2.05 in) and 95.5 mm (3.76 in) for G1, G2 and G3 at this load level, respectively, and the corresponding FEA predictions are 13 mm (0.52 in), 49.8 mm (1.96 in) and 86.9 mm (3.42 in). The slope of the FEA curve in Figure 4.4.2 increases

slightly at approximately the above load level. This is due to the lifting of G1 off of its supports.

Figures 4.4.5 through 4.4.7 provide measured and predicted radial deflections at the mid-span outside tip of the G1, G2 and G3 bottom flanges during Test 2. Similar to the vertical deflection plots, only the live load displacements are shown in these plots. Similar to the vertical deflection comparisons, it can be seen that the FEA predictions are in excellent agreement with the experimental data. At the peak experimental load level, the measured radial deflections are 24 mm (0.95 in), 24 mm (0.96 in) and 26.9 mm (1.06 in) for G1, G2 and G3, respectively, and the corresponding FEA predictions are 23 mm (0.91 in), 24 mm (0.95 in) and 25 mm (1.0 in).

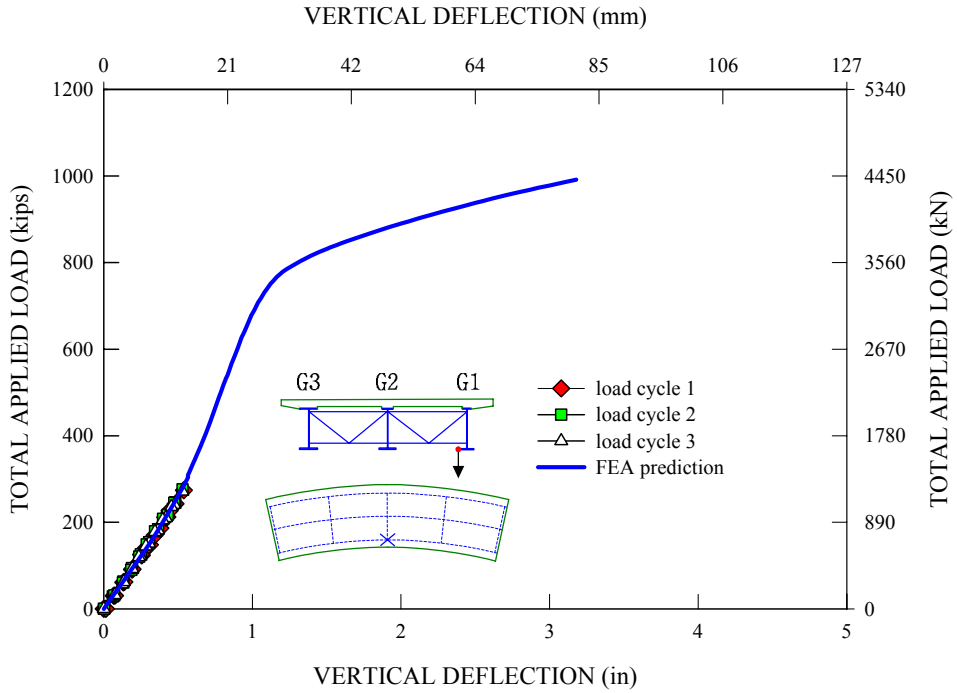

Figure 4.4.2. Measured and predicted live load vertical deflections at the mid-span outside tip of the G1 bottom flange during Test 2.

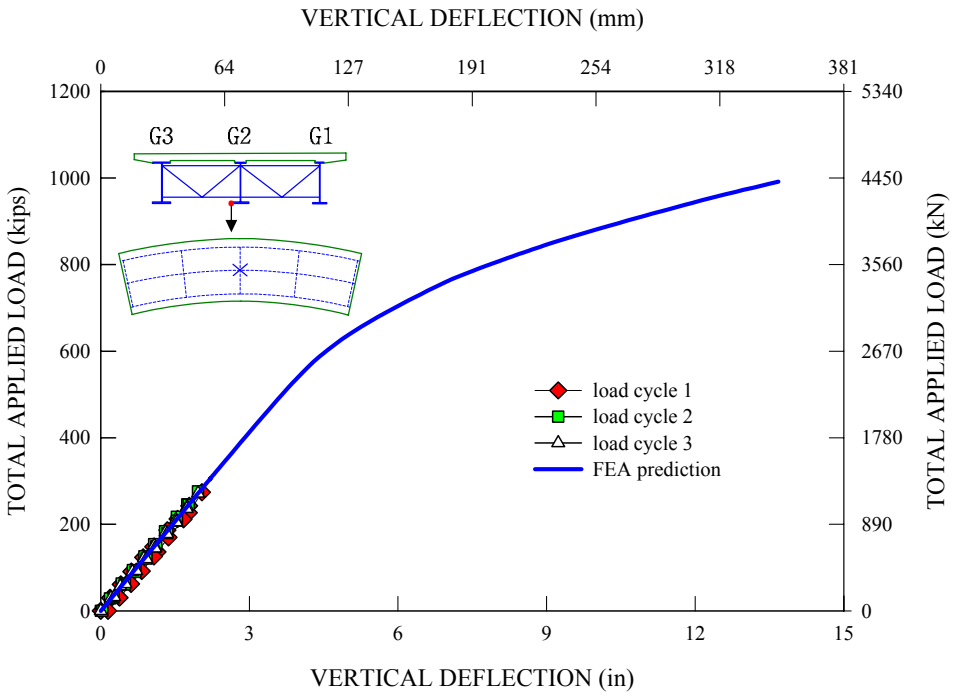

Figure 4.4.3. Measured and predicted live load vertical deflections at the mid-span outside tip of the G2 bottom flange during Test 2.

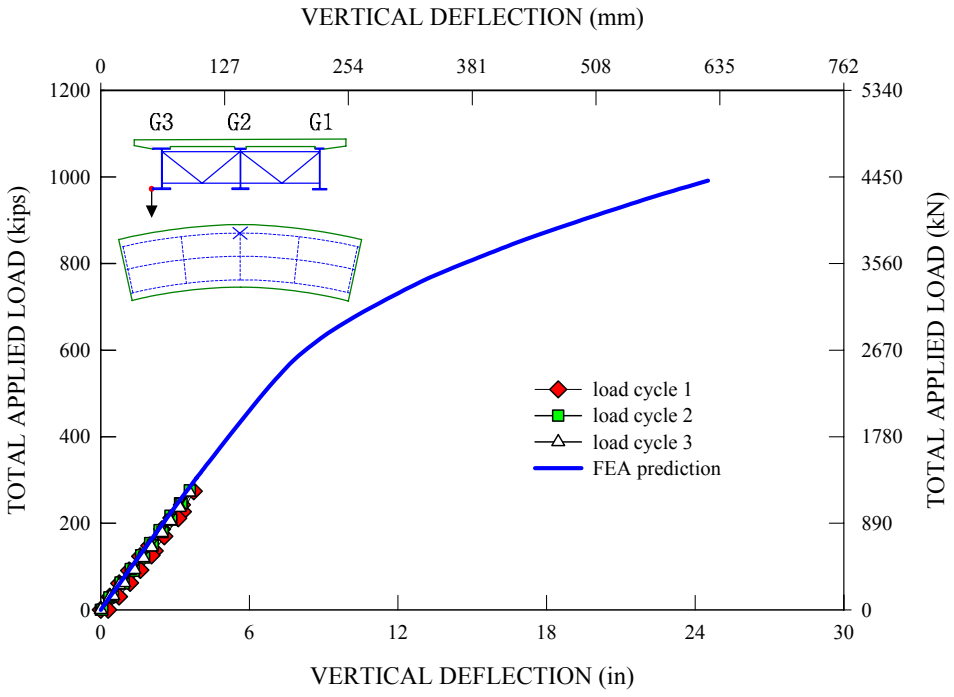

Figure 4.4.4. Measured and predicted live load vertical deflections at the mid-span outside tip of the G3 bottom flange during Test 2.

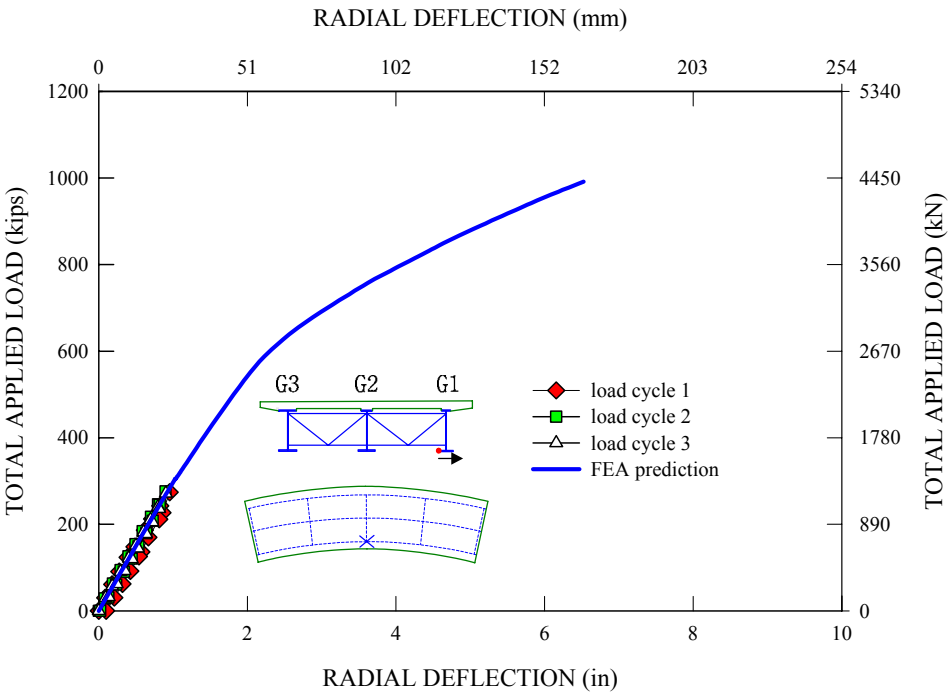

Figure 4.4.5. Measured and predicted live load radial deflections at the mid-span outside tip of the G1 bottom flange during Test 2.

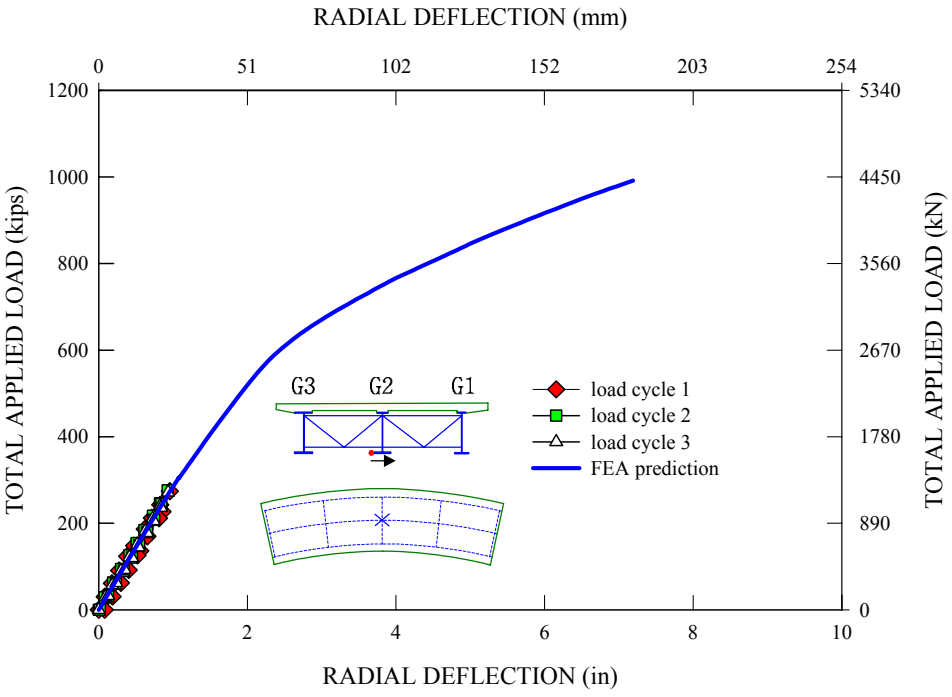

Figure 4.4.6. Measured and predicted live load radial deflections at the mid-span outside tip of the G2 bottom flange during Test 2.

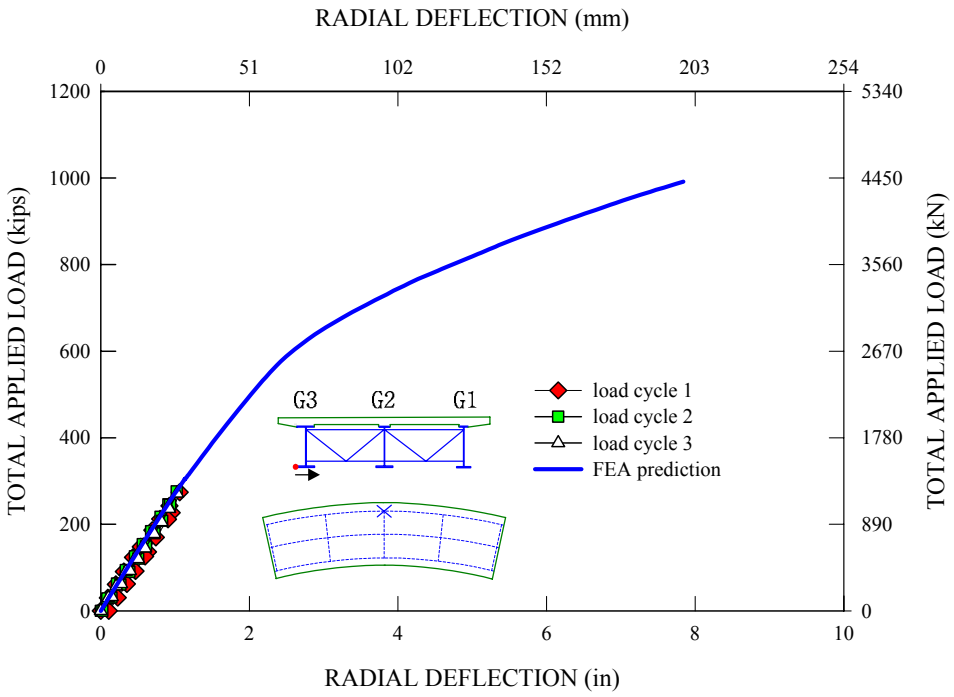

Figure 4.4.7. Measured and predicted live load radial deflections at the mid-span outside tip of the G3 bottom flange during Test 2.

Figures 4.4.8 through 4.4.10 provide the measured and predicted girder end reactions for G1, G2 and G3, respectively, during Test 2. Initial dead load reactions are included in these plots. Since the radial and longitudinal reactions are small relative to the vertical reactions, they are not presented here. For all of the reaction plots, it can be seen that measured initial dead load reactions are matched accurately by the corresponding FEA predictions. Figure 4.4.8 shows that, upon the application of the directly applied loads, the G1 reaction force is continuously reduced from the initial dead load reaction, down to zero when G1 is lifted off of its supports. Although there is a slight difference between the measured and predicted reaction forces at the time of the support lift-off, it can be seen that the FEA simulation provides a reasonably good representation of the behavior. Figure 4.4.9 shows that both the measured and predicted reactions on G2 increase

approximately in a bilinear fashion up to a point where the G1 is lifted off of its supports, although the predicted reaction is generally larger than the measured value, with a maximum difference of 67 kN (15 kips) at a loading close to the maximum applied experimental load. Subsequent to the lift-off of the G1 supports, it is interesting to note that the FEA reaction on G2 gradually reduces in a nonlinear fashion, eventually reaching a limiting value of about 534 kN (120 kips). For the G3 reactions, it can be seen in Figure 4.4.10 that there is an excellent correlation between the measured and predicted reaction forces, and the they increase predominantly in a linear fashion throughout the entire loading history. The measured reactions at the end of the experimental loading are 0.0 kN (0.0 kips), 592 kN (133 kips) and 1900 kN (427 kips) for G1, G2 and G3, respectively, and the corresponding FEA predictions are 0.0 kN (0.0 kips), 645 kN (145 kips) and 1873 kN (421 kips).

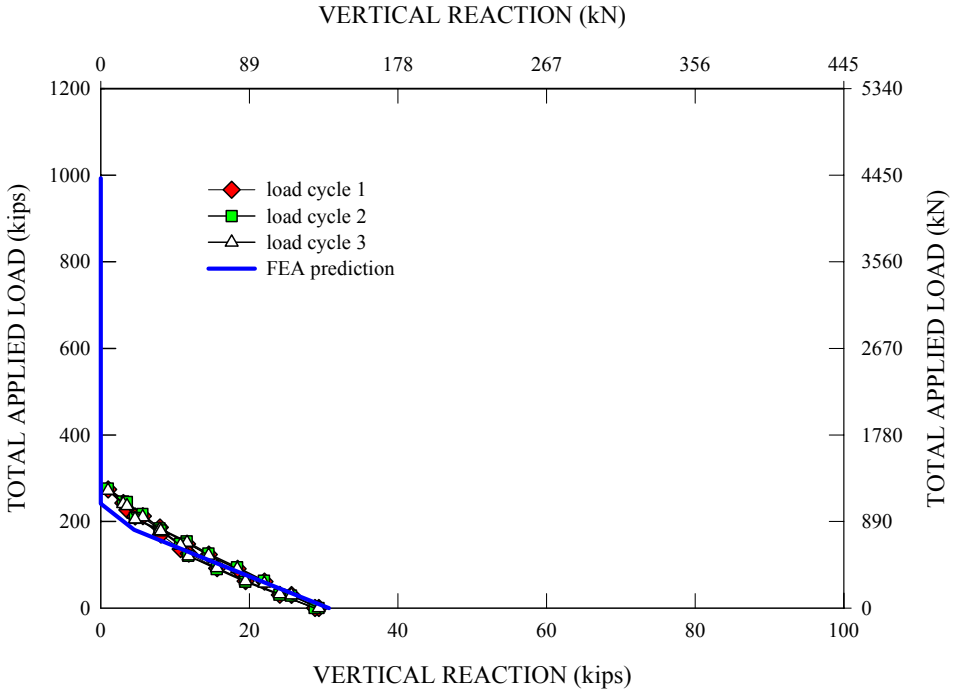

Figure 4.4.8. Measured and predicted reactions for G1 during Test 2.

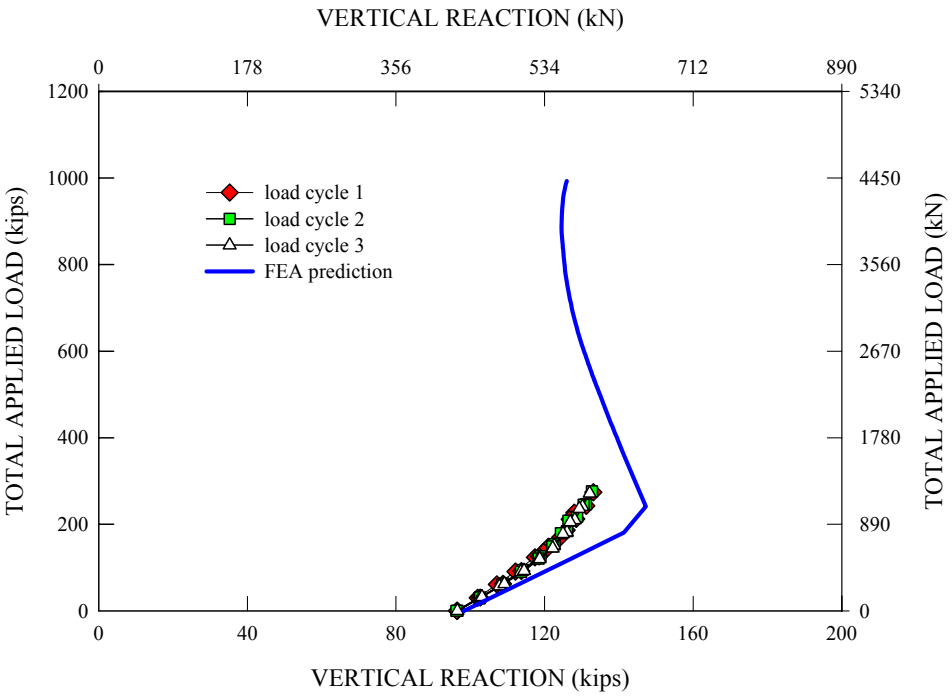

Figure 4.4.9. Measured and predicted reactions for G2 during Test 2.

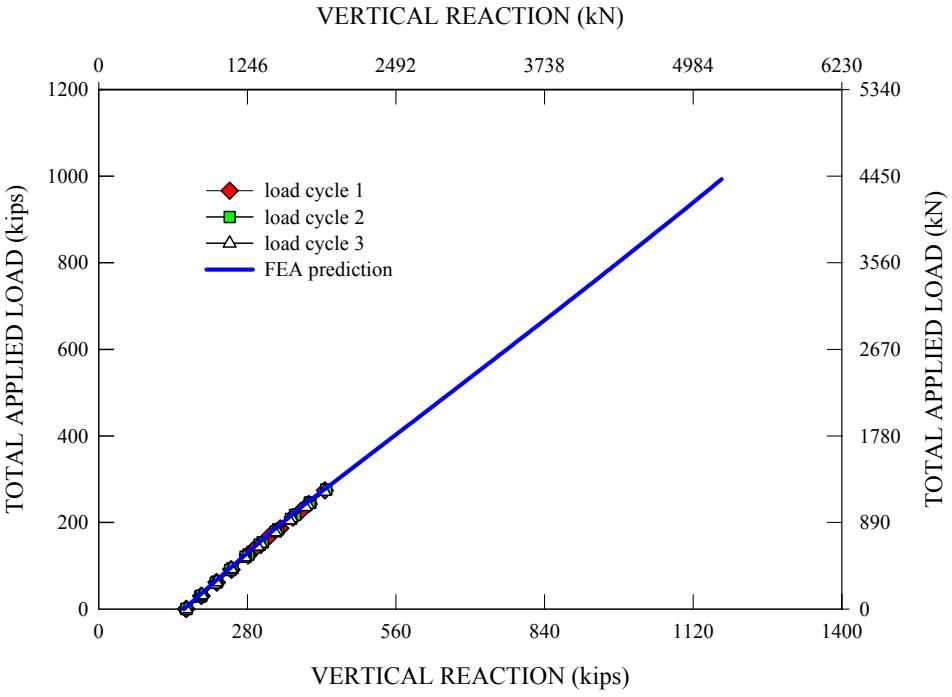

Figure 4.4.10. Measured and predicted reactions for G3 during Test 2.

Figure 4.4.11 provides the measured and predicted member axial forces in the bottom chord of the mid-span cross-frame attached to G3 during Test 2. The dead load member axial forces are included in the plot. It can be seen that the FEA predictions compare favorably to the measured data. The computed maximum axial force at a total applied load level of 1220 kN (274 kips) is − 845 kN (190 kips) (positive for tension). The corresponding experimental value is − 822 kN (185 kips).

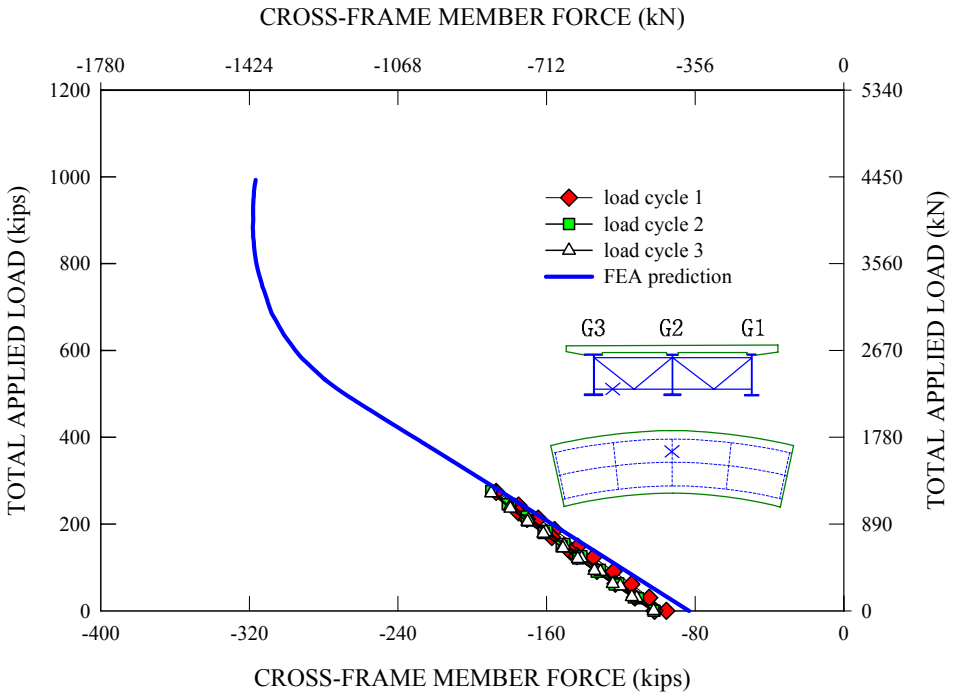

Figure 4.4.11. Measured and predicted member total axial force in the bottom chord attached to G3 of the mid-span cross-frame during Test 2 (initial dead load member forces are included).

Figures 4.4.12 and 4.4.13 provide the measured and predicted slab top surface longitudinal strain distributions near the mid-span bridge cross-section at gauge lines L9 and L10 at the total applied load level of 1201 kN (270 kips) during Test 2. It should be noted that the strains associated with concrete shrinkage are not included in the plots. It is of great interest to see that, except for minor local deviations, there is a good correlation in the overall strain patterns between the FEA predictions and experimental data. Also, one can see that the longitudinal strains vary approximately in a linear fashion across the slab, with a maximum at the outer edge of the overhang outside of G3 and a minimum at the inner edge of the overhang outside of G1. Most importantly, it should be noted that the magnitudes of these strains are within the elastic limit of the concrete stress-stain response defined in Section 3.3.3.1. This helps explain why there are no noticeable changes in the slab strains due to the repeated loading.

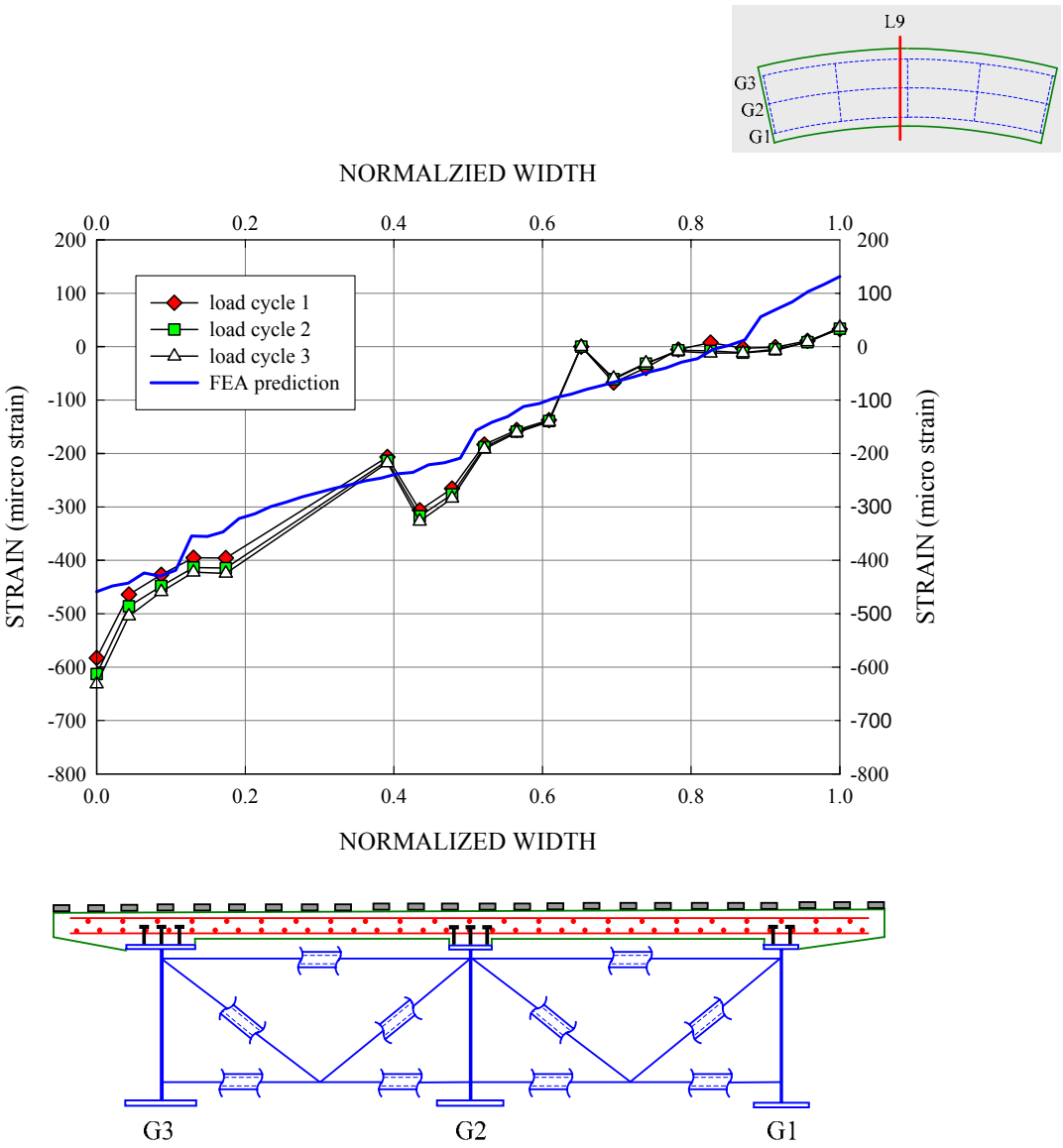

Figure 4.4.12. Slab top surface longitudinal strain distributions across the mid-span bridge cross-section for gage location L9 at a total applied load of 1201 kN (270 kips) in Test 2.

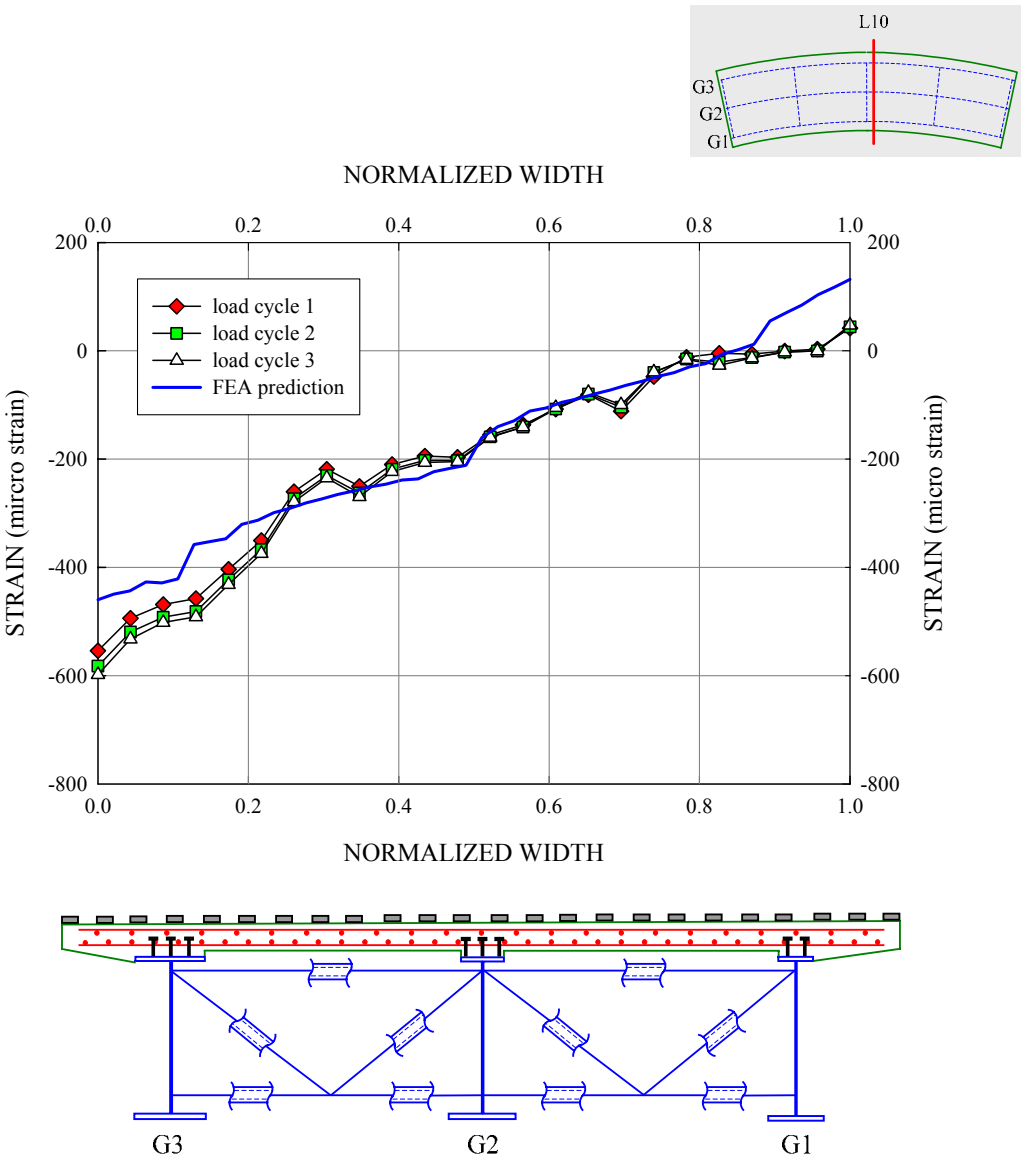

Figure 4.4.13. Slab top surface longitudinal strains across the mid-span bridge cross-section for gage location L10 at a total applied load of 1201 kN (270 kips) in Test 2.

4.4.2 Results of Test 3

Figure 4.4.14 shows the composite test bridge with loading fixtures placed on its inside lane to simulate a single truck plus single lane AASHTO live load. It should be noted that the experimental values are available only up to a total applied load of 1200 kN (270 kips), which is 90 percent of the factored AASHTO live load. This is due to the fact that the bottom flange of G1 started showing the onset of active yielding at this load level during the experimental test. The test loading was halted at this point to prevent further spread of yielding on the G1 steel section. In contrast, the FEA simulation concerning Test 3 loads the test bridge FEA model up to a significantly higher applied load.

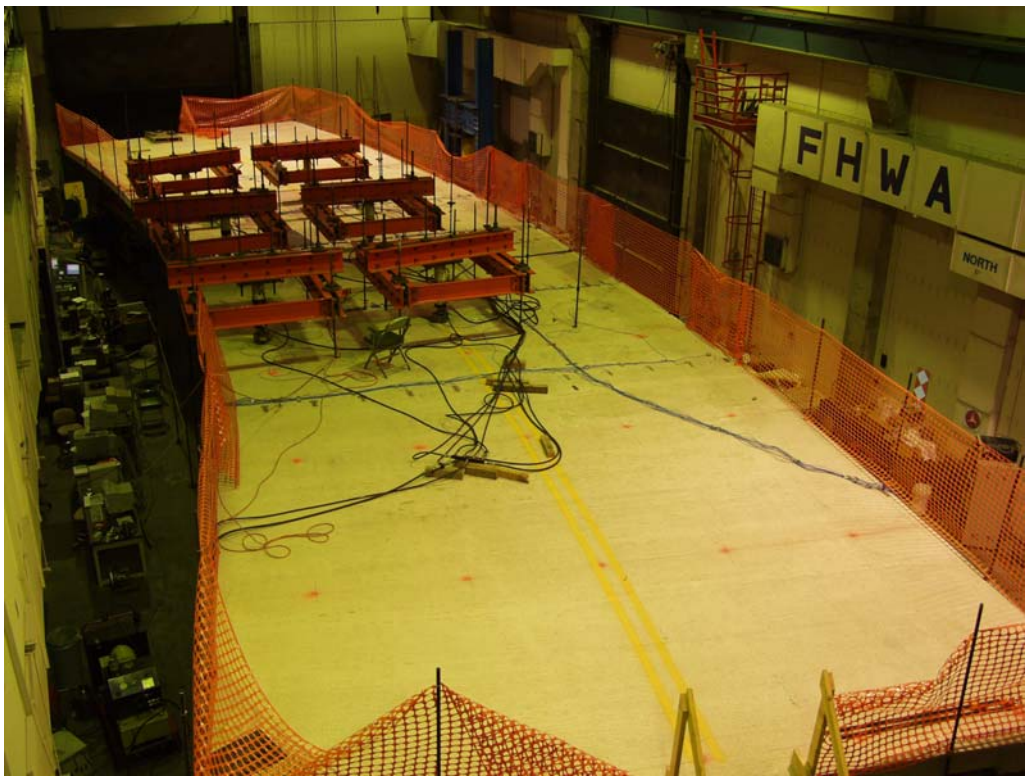

Figure 4.4.14. Composite test bridge with loading fixtures for Test 3, courtesy of FHWA.

When it comes to the full nonlinear FEA predictions, it is found that the results of the FEA solutions involving the repeated loading of the test bridge up to the maximum experimental load level are essentially identical to the result from the simple monotonic loading of the bridge. This same behavior of the FEA model was obtained for Test 2. Therefore, only the results of the monotonic loading analysis are presented here.

Figure 4.4.15 through 4.4.17 provide measured and predicted vertical deflections for the mid-span outside tip of the G1, G2 and G3 bottom flanges during Test 3. Only the live load deflections are included in these plots. With the exception of the G3 vertical deflections, it can be seen that the measured vertical deflections and corresponding FEA solutions match closely. Furthermore, it is interesting to note that the measured and predicted girder vertical deflections are predominantly linear up to 1201 kN (270 kips). The measured maximum vertical deflections at the peak applied load level are 37.3 mm (1.47 in) and 32.8 mm (1.29 in) for G1 and G2, respectively, while the corresponding FEA predictions are 37.3 mm (1.47 in) and 29.7 mm (1.17 in). For the G3 vertical deflection, the measured maximum deflection is 27.9 mm (1.1 in), which is somewhat larger than the corresponding FEA prediction of 20 mm (0.80 in).

Figures 4.4.18 through 4.4.20 provide measured and predicted radial deflections for the mid-span outside tip of the G1, G2 and G3 bottom flanges during Test 3. Only the live load displacements are included in these plots. At first glance, it may seem that the FEA predictions are significantly deviated from the measured data. However, it is important to note that the magnitude of these deflections are less than 5 mm (0.2 in). The measured maximum radial deflections at the peak applied load are 1.3 mm (0.05 in), 2.3 mm (0.09 in) and 1.5 mm (0.06 in) for G1, G2 and G3, respectively, and the

corresponding full nonlinear FEA predictions are 3.18 mm (0.125 in), 3.96 mm (0.156 in) and 3.96 mm (0.156 in).

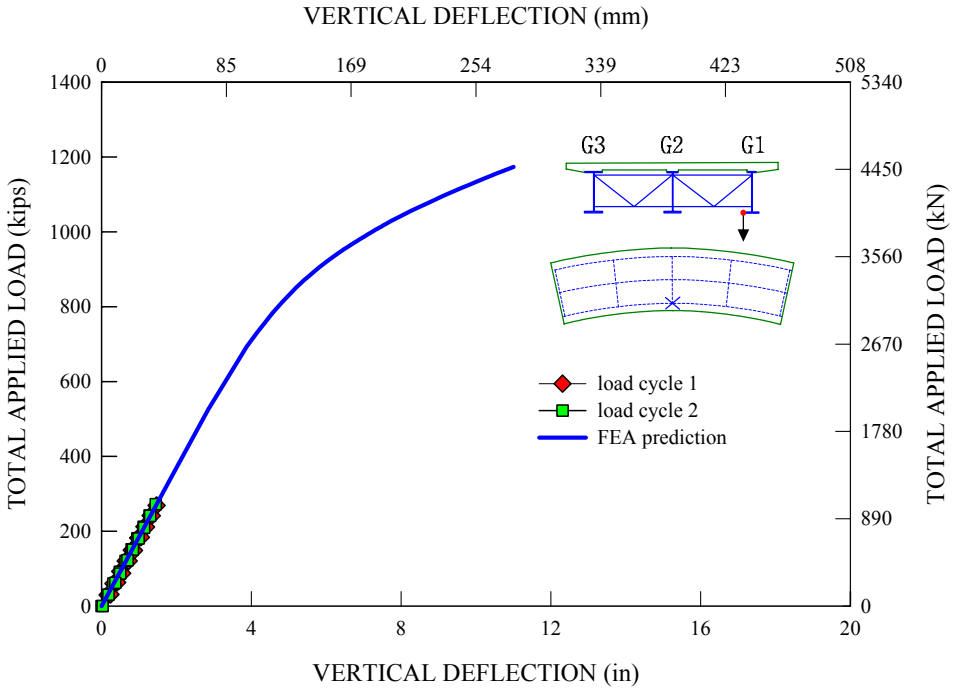

Figure 4.4.15. Measured and predicted live load vertical deflections at the mid-span outside tip of the G1 bottom flange during Test 3.

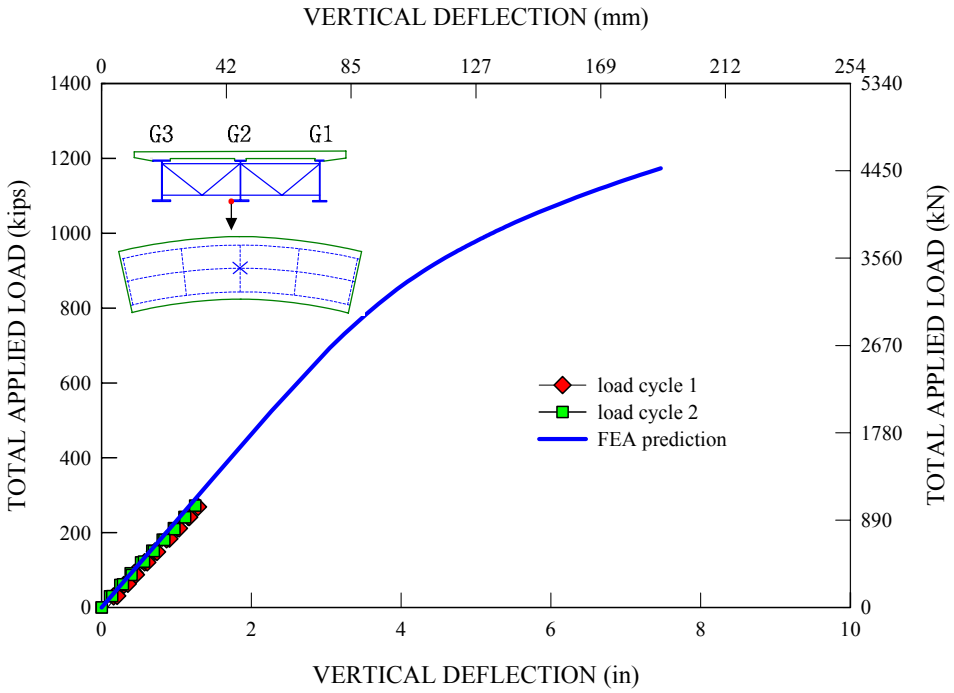

Figure 4.4.16. Measured and predicted live load vertical deflections at the mid-span outside tip of the G2 bottom flange during Test 3.

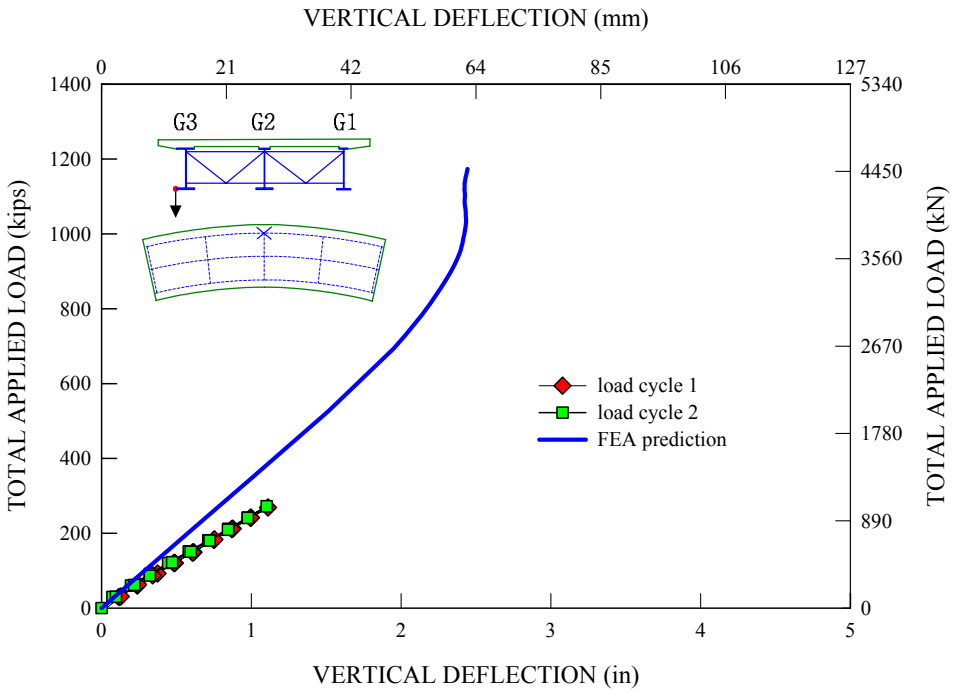

Figure 4.4.17. Measured and predicted live load vertical deflections at the mid-span outside tip of the G3 bottom flange during Test 3.

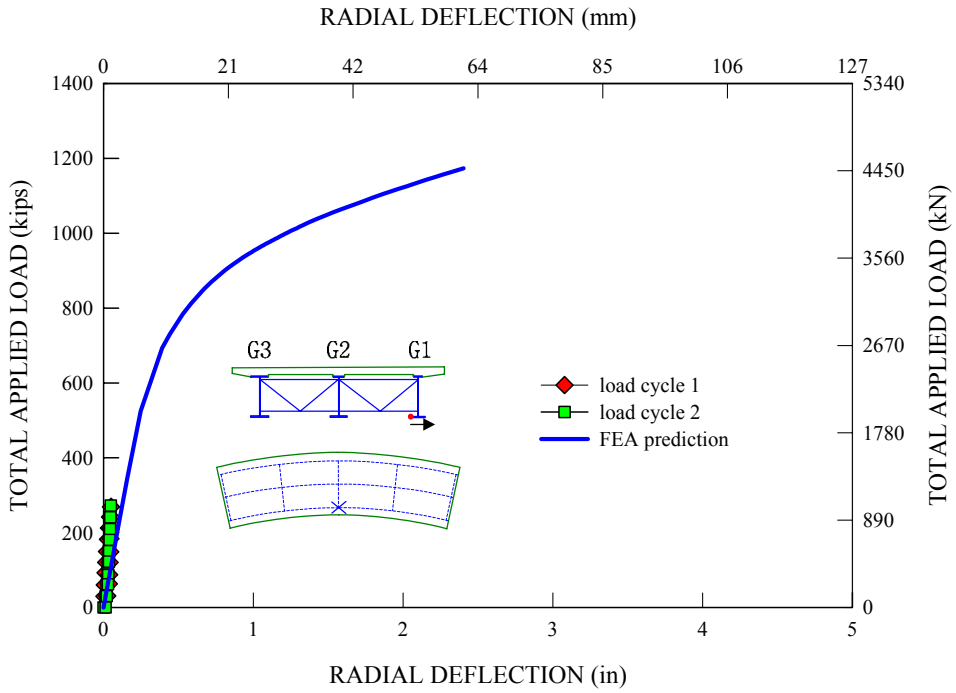

Figure 4.4.18. Measured and predicted live load radial deflections at the mid-span outside tip of the G1 bottom flange during Test 3.

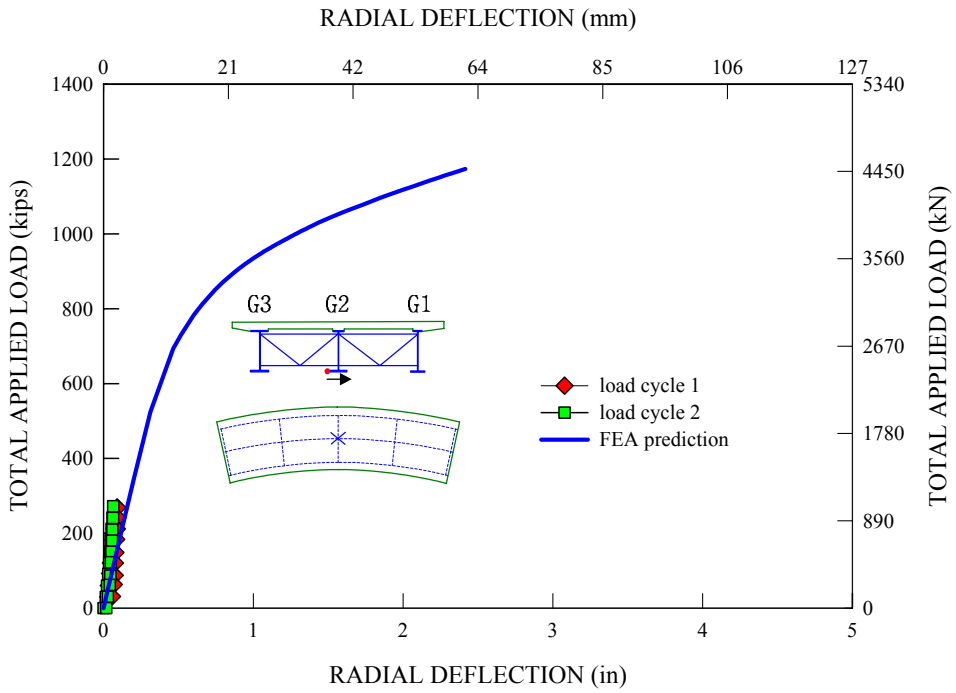

Figure 4.4.19. Measured and predicted live load radial deflections at the mid-span outside tip of the G2 bottom flange during Test 3.

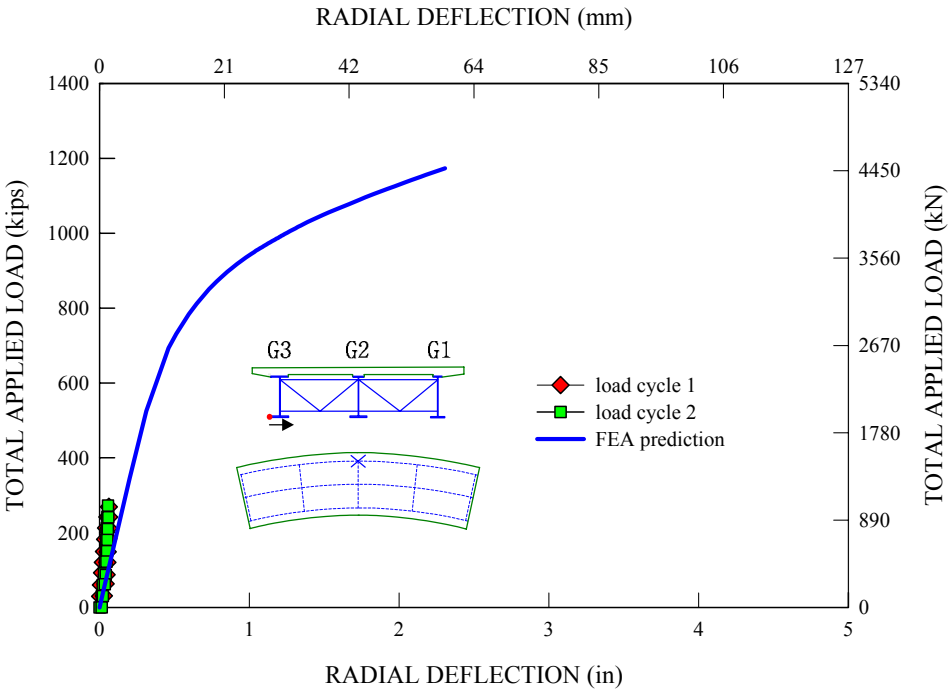

Figure 4.4.20. Measured and predicted live load radial deflections at the mid-span outside tip of the G3 bottom flange during Test 3.

Figures 4.4.21 through 4.4.23 provide measured and predicted girder end reactions for G1, G2 and G3, respectively, during Test 3. The dead load reactions are included in these plots. For all of the reaction forces, there is a good correlation between the measured and predicted values. Moreover, similar to the deflection responses, the reaction responses are also predominantly linear up to the total applied load of 1201 kN (270 kips). The measured maximum reaction forces at the peak applied load of 1201 kN (270 kips) are 512 kN (115 kips), 827 kN (186 kips) and 1165 kN (262 kips) for G1, G2 and G3, respectively, while the corresponding FEA predictions are 596 kN (134 kips), 823 kN (185 kips) and 1112 kN (250 kips).

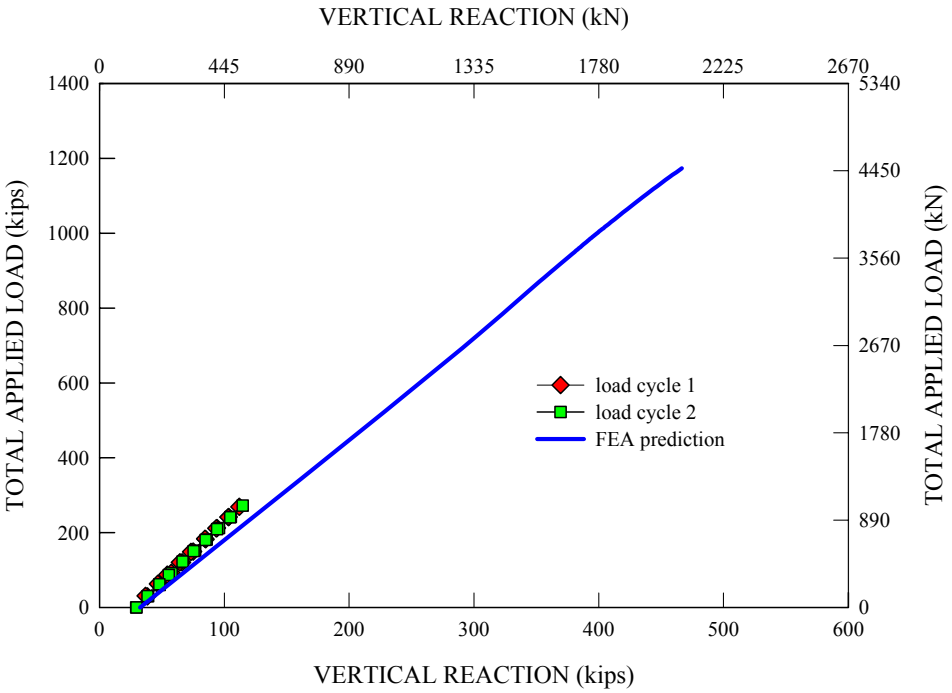

Figure 4.4.21. Measured and predicted reactions for G1 during Test 3.

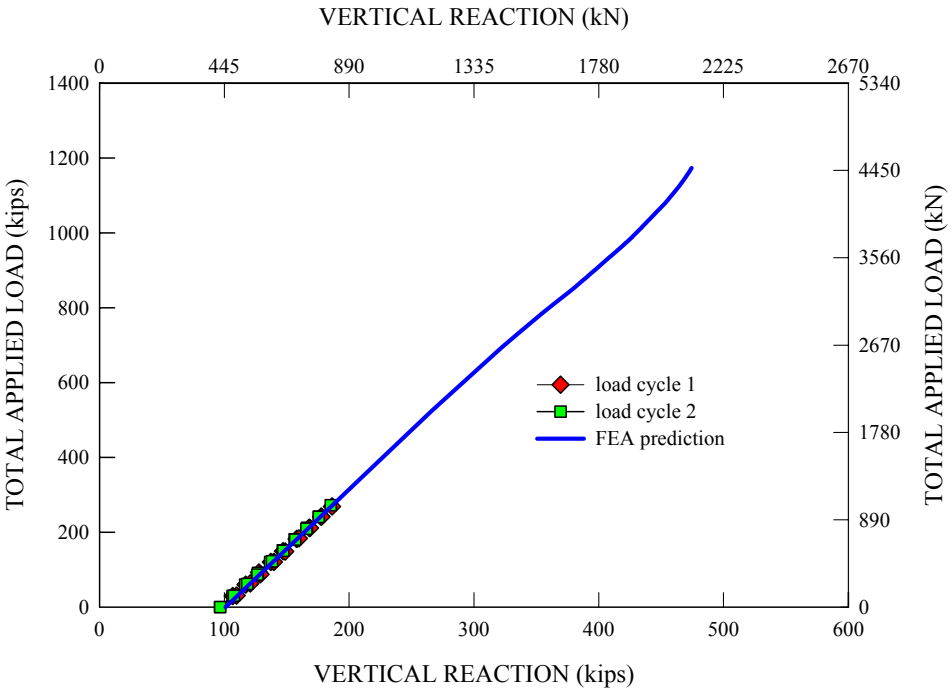

Figure 4.4.22. Measured and predicted reactions for G2 during Test 3.

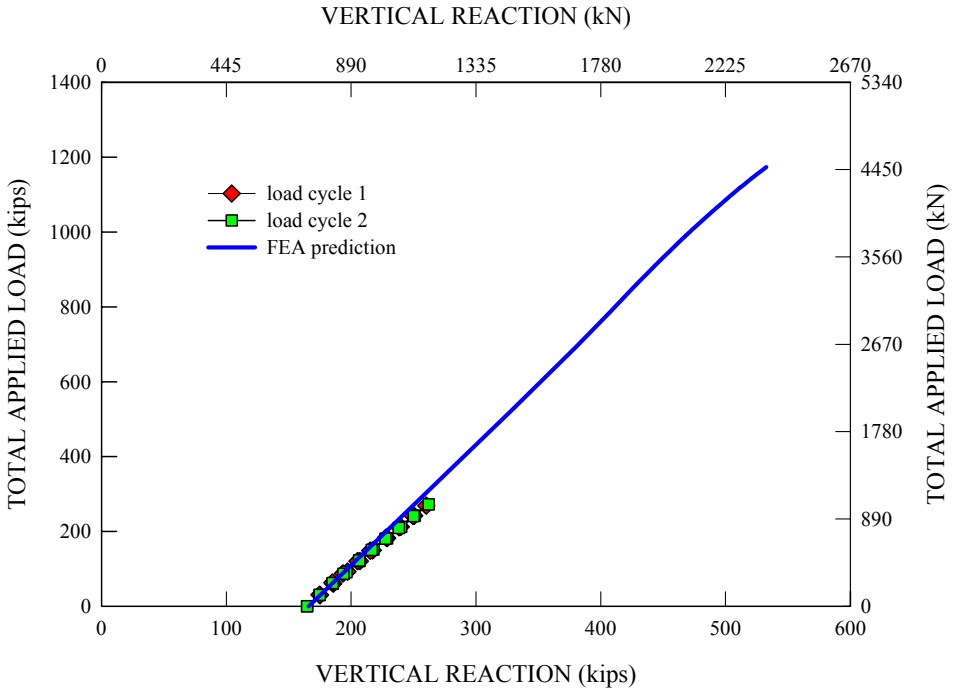

Figure 4.4.23. Measured and predicted reactions for G3 during Test 3.

Figure 4.4.24 provides the measured and predicted member total axial forces in the bottom chord of the mid-span cross-frame attached to G3 during Test 3. The dead load member forces are included. Similar to other bridge responses, it can be seen that the member forces are predominantly linear up to the total applied load of 1201 kN (270 kips) for both of the measured and predicted responses. The computed axial force at a total applied load level of 1201 kN (270 kips) is − 578 kN (130 kips) (positive for tension) while the corresponding experimental value is − 667 kN (150 kips).

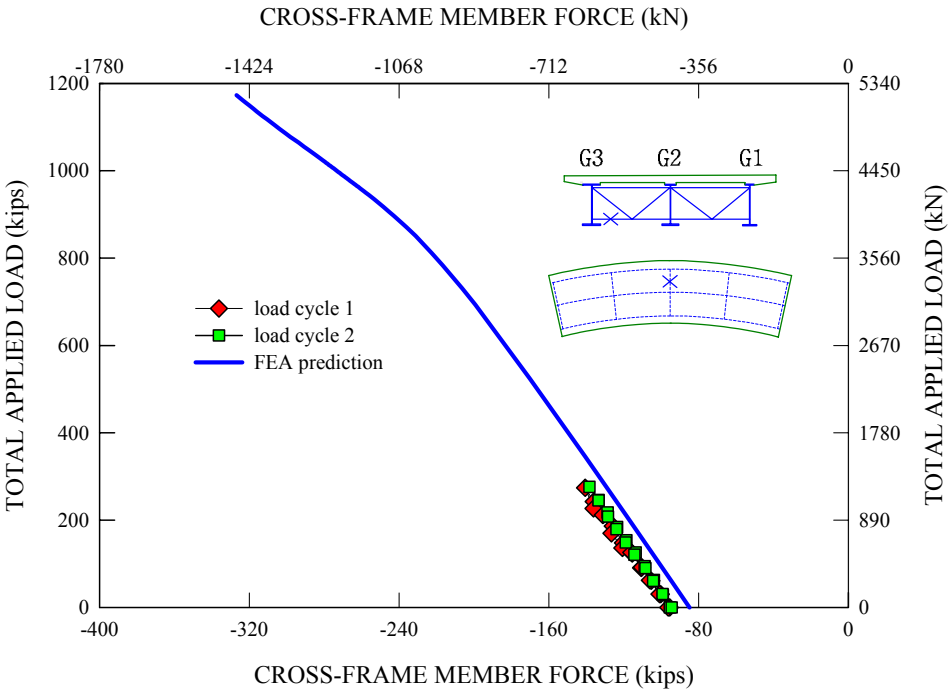

Figure 4.4.24. Measured and predicted member total axial forces in the bottom chord attached to G3 of the mid-span cross-frame during Test 3 (initial member dead load forces are included).

Figure 4.4.25 and 4.4.26 provide the measured and predicted slab top surface longitudinal strain distributions across the mid-span bridge cross-section for gauge lines L9 and L10 at the peak applied load level of 1201 kN (270 kips) during Test 3. The concrete shrinkage strains are not included in the plots. It can be seen that there is a good correlation between the overall strain patterns of the FEA predictions and experimental values. The overall strain variations are fairly constant across the bridge cross-section, with an average of 200 με for both of the measured and predicted strains. Furthermore, similar to the slab strains for Test 2, all of the strains are well within the elastic limit of the concrete stress-stain response.

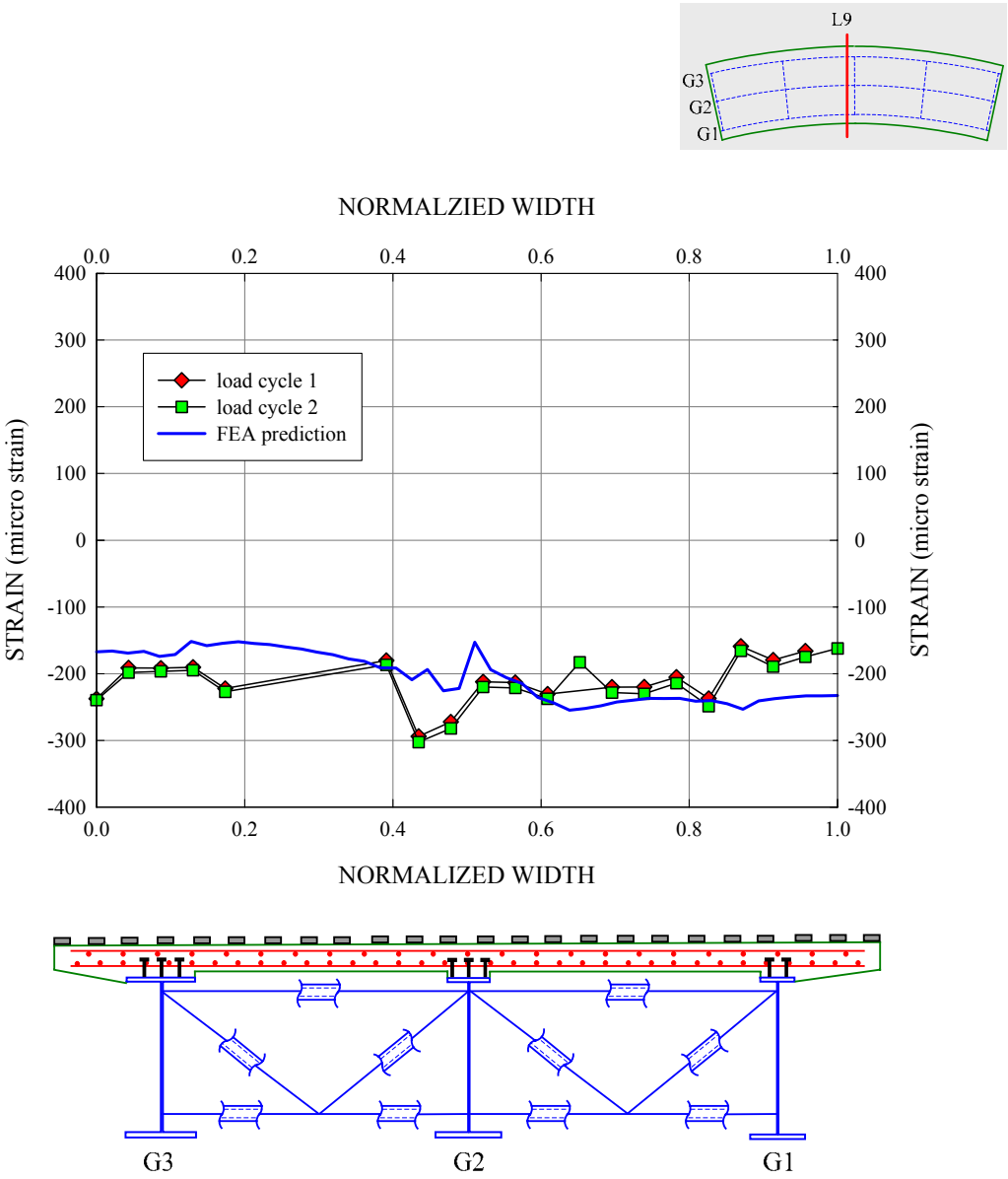

Figure 4.4.25. Slab top surface longitudinal strain variations across the mid-span bridge cross-section for gage location L9 at a total applied load level of 1201 kN (270 kips) during Test 3.

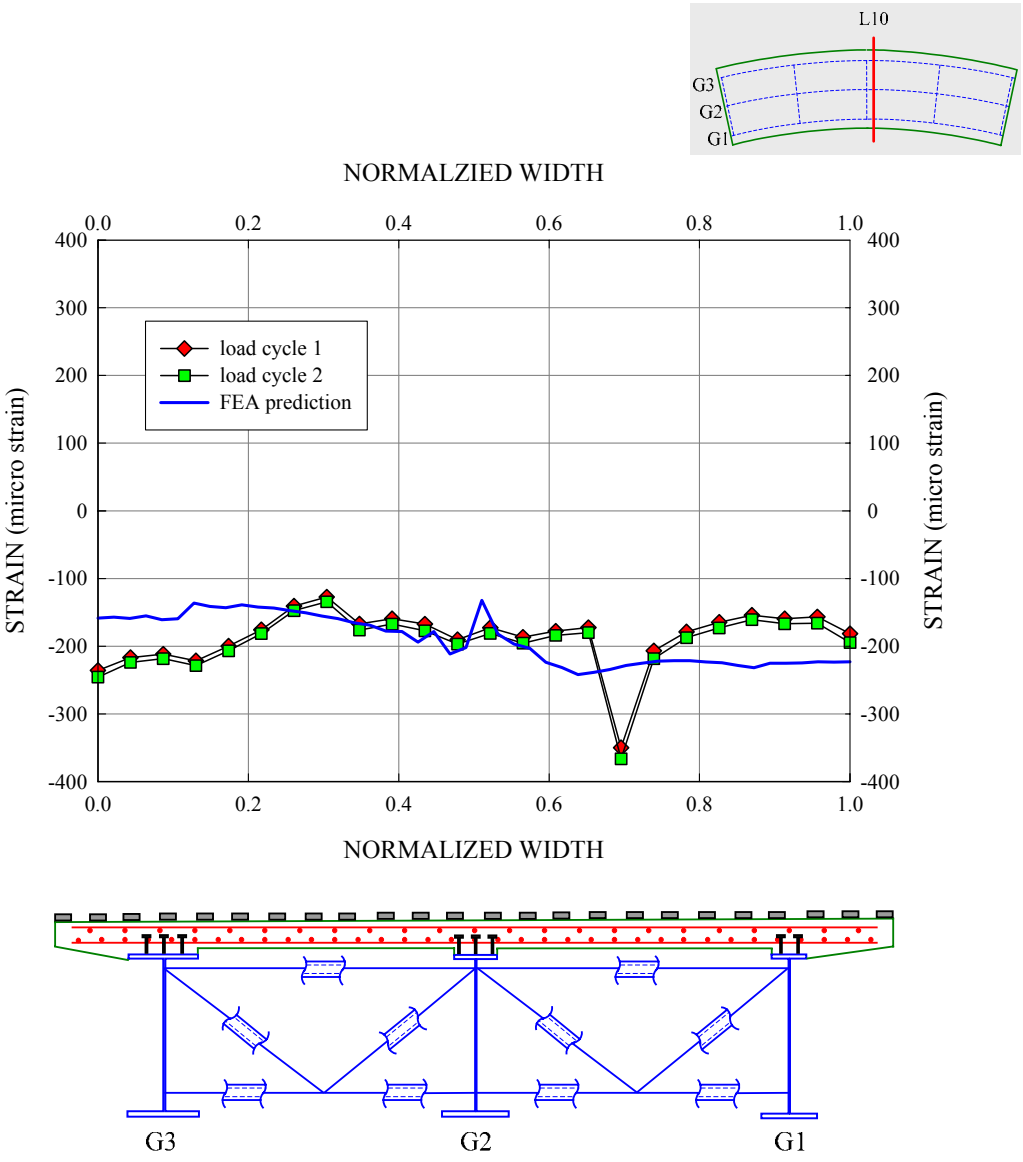

Figure 4.4.26. Slab top surface longitudinal strain variations across the mid-span bridge cross-section for gage location L10 at a total applied load level of 1201 kN (270 kips) during Test 3.

4.4.3 Overall Assessment of Tests 2 and 3

The following observations are made pertaining to the results from Tests 2 and 3:

- For Tests 2 and 3, the measured girder vertical and radial deflections increase predominantly in a linear fashion up to the peak experimental load level. There are negligible residual deflections at the end of these tests. Furthermore, these measured quantities are matched well by the FEA predictions. The FEA solutions obtained from the repeated loading analysis indicate that there are no residual deflections at the end of these tests.
- Regarding the girder stresses in Test 2, it is found that the maximum flange stress measured at the G3 flange tip, a combination of the major-axis and lateral bending stresses, is significantly less than the flange yield strength at the peak applied load. In the case of Test 3, the maximum flange stress occurring at the G1 bottom flange tip is at the flange yield strength at the peak applied load. However, the flange yielding is very minor
- Similar to the girder deflections, the girder vertical reactions also increase in a linear fashion for both of the tests, and they are comparable to corresponding FEA predictions. The radial and longitudinal reactions at the bridge bearings are found to be negligible relative to the girder vertical reactions.
- Both the predicted and measured member axial forces in the bottom chord of the mid-span cross-frame attached to G3 increase linearly for loads up to the peak applied load level. Also, it is found that incremental member residual forces at the end of each loading cycle are negligible for both of the tests, leaving essentially zero total accumulated member residual forces at the end of the tests.

- Regarding the slab top surface strains in Test 2, both the measured and predicted strains vary in an approximate linear fashion across the bridge cross-section, with the maximum strain occurring at the edge of the overhang outside G3. These strains are less than the strain associated with the elastic limit of the concrete stress-strain response at the peak applied load level. Similarly, the measured and predicted slab strains in Test 3 are within the elastic limit of the concrete response, but their distributions across the bridge cross-section are approximately constant.

Based on the above findings, it is clear that all the measured responses for Tests 2 and 3 are essentially in the linear elastic range. The test bridge system is not left with any residuals or permanent sets with the completion of the first two experimental tests conducted on the composite test bridge. Similar results are also obtained from repeated loading analyses of these tests. Therefore, in the subsequent FEA simulations concerning the repeated and monotonic loading of the test bridge conducted in Test 4a, the effects of Tests 2 and 3 are not accounted for in the assessment of strength behavior.

4.5 Test 4a: Repeated Loading Tests

Prior to the final monotonic loading of the composite test bridge for its ultimate load-carrying capacity, two sequences of repeated loadings were performed using the loading pattern for the final monotonic loading test. Figure 4.5.1 shows the composite test bridge with loading fixtures positioned for these tests. A total of nine loads from hydraulic jacks are placed directly above the girders to simulate two AASHTO design trucks plus two lane loads. It should be noted that this loading pattern produces slightly more critical girder responses than the AASHTO design live load model used in the design analysis of the test bridge.

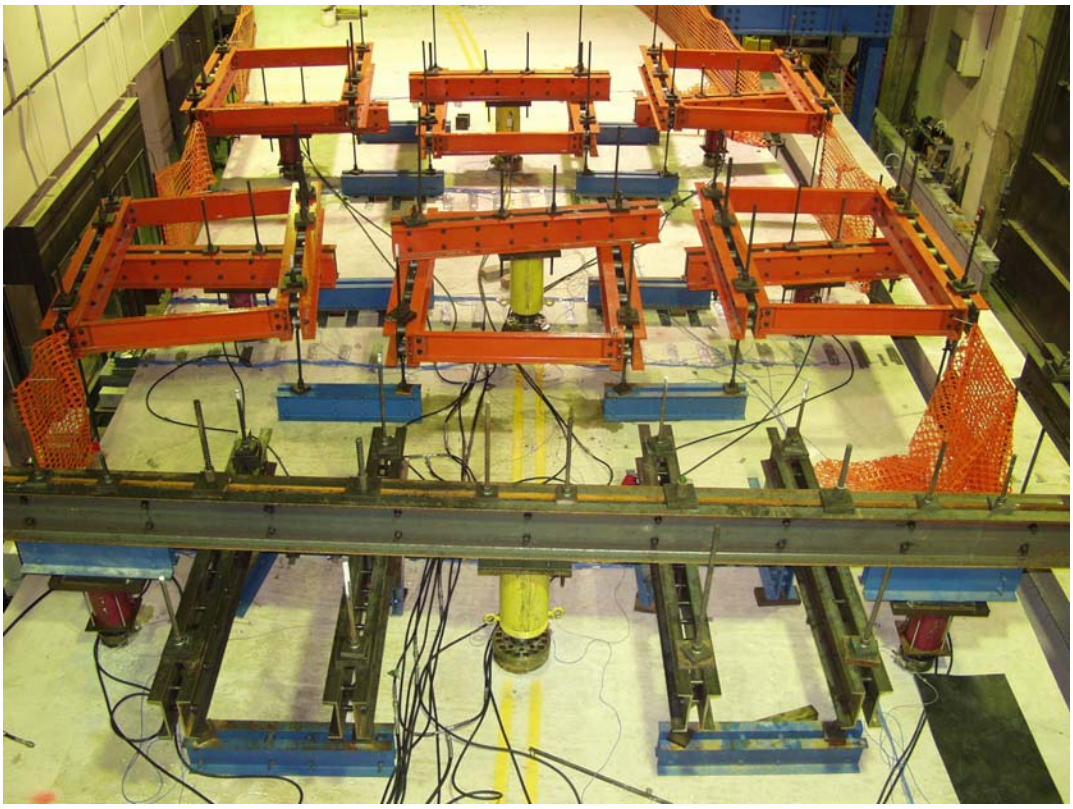

Figure 4.5.1. Composite test bridge with the Test 4a loading fixtures for the first repeated loading sequence, courtesy of FHWA.

4.5.1 Significant Load Levels

Test 4a was the first test in which the composite test bridge was loaded sufficiently to induce significant inelastic behavior in the steel members as well as in the concrete slab. A number of different load levels are of potential interest in investigating the behavior of the composite test bridge in Test 4a, and subsequently in Test 4b. One way of defining these significant load levels is to consider the following combinations of the girder stresses or moments from a linear elastic analysis that correspond either to specific AASHTO (2004b) limit states or to other conditions related to the AASHTO limit states:

- Initial yielding : $f_b + f_\ell = R_h F_{yt}$ (4.1)
- Service II condition : $f_b + f_\ell/2 = 0.95 R_h F_{yt}$ (4.2)
- Strength I condition : $f_b + f_\ell/3 = R_h F_{yt}$ (4.3)
- Plastic moment capacity *with* 1/3 reduction : $f_b S_{xt} + f_\ell/3 \, S_{xt} = M_p$ (4.4)
- Plastic moment capacity *without* 1/3 reduction : $f_b S_{xt} = M_p$ (4.5)

where f_b is the tension flange major-axis bending stress,

f_ℓ is the tension flange lateral bending stress,

S_{xt} is the elastic section modulus about the major-axis of the section to the bottom tension, taken generally as M_{yt}/F_{yt},

M_{yt} is the yield moment corresponding to the tension flange, calculated as defined in Appendix D of AASHTO (2004b) accounting for the influence of non-composite, long-term composite and short-term composite loadings,

M_p is the plastic moment capacity in the absence of any flange lateral bending, and F_{yt} is the specified minimum yield strength of the tension flange.

In the above equations, the stress terms f_b and f_ℓ are in all cases determined from a linear elastic analysis of the bridge system. If desired, Eqs. (4.1) through (4.3) may be multiplied on both sides by the elastic section modulus to the tension flange, S_{xt}, such that the applied major-axis bending term becomes a stress-resultant major-axis bending moment in each girder $M = f_b S_{xt}$ (including the contribution from the tributary area of the slab). Alternately, Eqs. (4.4) and (4.5) may be divided by S_{xt} such that the applied major-axis bending term is simply the elastic stress f_b and the corresponding moment on the right-hand side of the equation is a "pseudo-elastic" stress (greater than the yield stress of the tension flange).

AASHTO (2004b) defines the elastic section modulus in major-axis bending in general as M_{yf}/F_{yf}, where M_{yf} is the moment causing first yield in the cross-section at the flange under consideration if the flange lateral bending stresses are taken equal to zero, and F_{yf} is the specified minimum yield strength of this flange. In general, composite bridge girders are assumed to resist moment based on the three different cross-section models shown in Figure 4.5.2. The moment due to dead loads on the steel section before the concrete reaches its compressive strength is M_{D1}. The corresponding elastic stresses are obtained using the noncomposite section modulus S_{NC}. The moment due to the remainder of the dead loads (wearing surface, concrete barriers, etc.) is M_{D2} and is assumed to be resisted by the long-term composite section, which has the section modulus S_{LT} to the flange under consideration. The long term section modulus is calculated using the modular ratio 3n, where $n = E_c/E$ is the modular ratio of the section corresponding to short term loadings. This accounts approximately for the long-term effects of creep deformations in the concrete slab. The additional moment required to

cause yielding in the flange under consideration is M_{AD}. This moment is due to live load and resisted by the short-term composite section, which has the modulus S_{ST}. The moment M_{AD} can be determined from the equation

$$F_{yf} = \frac{M_{D1}}{S_{NC}} + \frac{M_{D2}}{S_{LT}} + \frac{M_{AD}}{S_{ST}} \tag{4.6}$$

and the yield moment M_{yf} is then calculated as

$$M_{yf} = M_{D1} + M_{D2} + M_{AD} \tag{4.7}$$

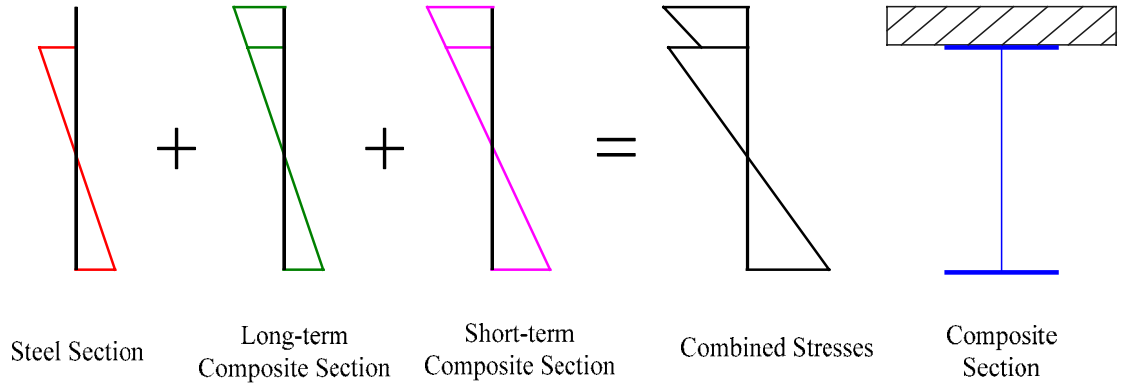

Figure 4.5.2. Flexural stresses at first yield of composite sections.

Table 4.5.1 compares the section moduli associated with the first yield moment of the composite sections for girders G1, G2 and G3 to the corresponding short-term section moduli. It can be seen that for the test bridge composite girders, these two section moduli are relatively close to one another. This is because of the relatively large flange lateral bending stress, which is accommodated in the Chapter 2 design calculations, as well as the fact that M_{D1} (or the corresponding flange stress) is based on the *actual* dead load moment in this chapter. The actual dead load moment (i.e., the moment associated with a load factor on the dead load of 1.0) is used here since the focus in this chapter is on the

response during the experimental testing. Generally, the section modulus associated with the first yield moment is slightly smaller than the short term section modulus.

Table 4.5.1 Short-term composite section moduli and section moduli associated with the first yield moment.

	G1	G2	G3
S_{ST} cm^3 (in^3)	18681 (1140)	24712 (1508)	34642 (2114)
S_{xt} (first yield) cm^3 (in^3)	18249 (1114)	23555 (1437)	32807 (2002)

One should note that the above calculation of $S_x = M_{yf}/F_{yf}$ and the usage $M = f_b S_x$ is exact only for $M = M_{yf}$. However, $M = f_b S_x$ gives a reasonable approximation of the relationship between the flange stress and the girder moment at moments in the vicinity of $M = M_{yf}$. The approximation is conservative, i.e., the value of f_b associated with a given moment is overestimated and the value of the moment associated with a given flange stress is underestimated, for moments larger than M_{yf}.

Equations (4.1) through (4.5) define several different significant load levels in terms of the elastic flange stresses caused by the applied loads at a given cross-section. Equations (4.6) and (4.7) explain the calculation of the first-yield moment employed in determining the elastic section modulus S_{xt} used in Eqs. (4.4) and (4.5). However, in the following, it is desired to determine significant load levels on the composite test bridge in terms of the total load applied by the rams shown in Figure 4.5.1 and the associated responses from Eqs. (4.1) through (4.5) on the different girders. As such, the relationships

between the total applied load and the girder stresses f_b and f_ℓ at the critical mid-span cross-section are needed. Figures 4.5.3 through 4.5.5 show these relationships. It should be noted that the initial dead load stresses, which are the intercepts for the vertical stress axis, are obtained from separate analyses of the noncomposite steel superstructure subjected to the unfactored dead loads.

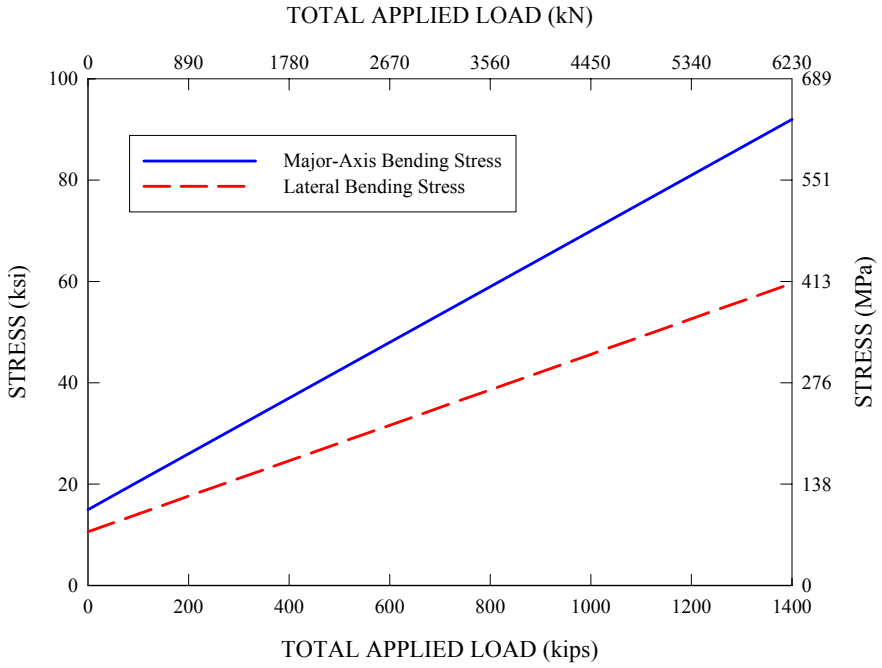

Figure 4.5.3. G3 bottom flange – total applied loads versus elastically-computed major-axis and lateral bending stresses.

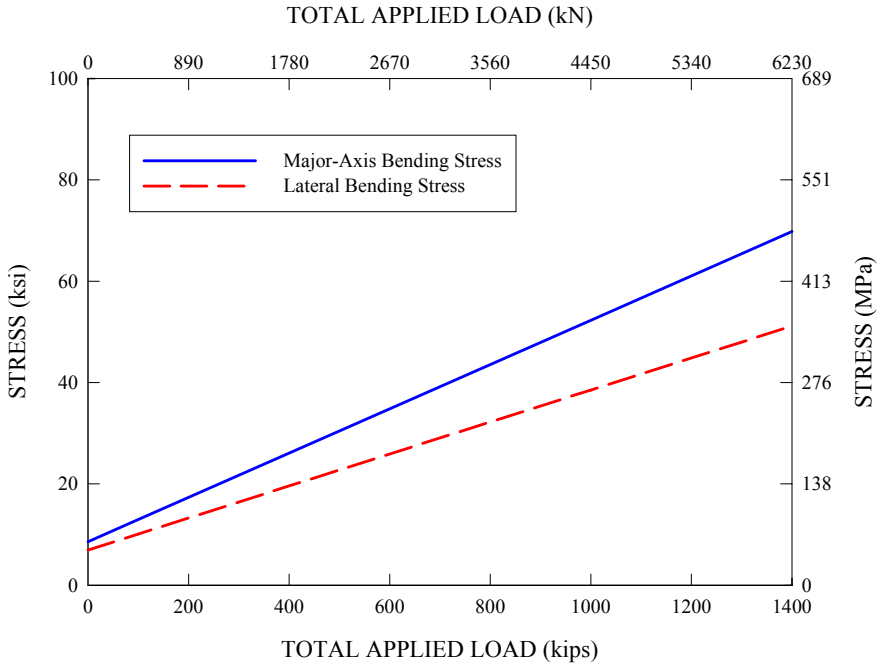

Figure 4.5.4. G2 bottom flange – total applied loads versus elastically-computed major-axis and lateral bending stresses.

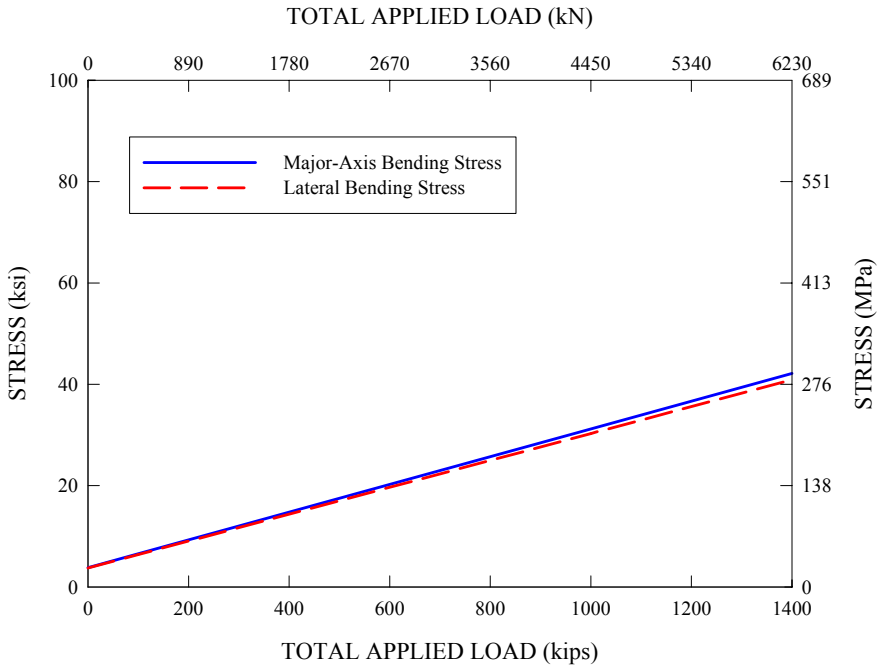

Figure 4.5.5. G1 bottom flange – total applied loads versus elastically-computed major-axis and lateral bending stresses.

As an illustration of the above calculations, consider the load level when girder G3 reaches the M_p-based 1/3 rule load level. The M_p-based 1/3 rule resistance equation is given by

$$S_{xt}f_b + \frac{1}{3}S_{xt}f_\ell = M_p$$

The elastic section modulus S_{xt} is taken as 32,807 cm^3 (2002 in^3) from Table 4.5.1. The plastic moment M_p is equal to 18850 kN-m (13860 k-ft) based on a fundamental plastic section analysis of G3 (see Table D.6.1-1 in AASHTO (2004b)). The relationships between the total applied load and the stresses f_b and f_ℓ in G3's bottom flange are shown in Figure 4.5.3. The resulting load level satisfying the above resistance equation is found to be 3964 kN (891 kips). It should be noted that this is a significant reduction from the M_p-based load level of 5075 kN (1141 kips) without any consideration of torsional effects (via the flange lateral bending term f_ℓ). Other significant load levels can be obtained in a similar fashion.

Figure 4.5.6 shows various significant load levels based on Eqs. (4.1) through (4.5) as well as several other significant load levels. These significant load levels are marked on a plot of the total applied load versus the vertical deflection of G3's bottom flange outside tip at the mid-span, obtained from a full nonlinear analysis of the test bridge. The specific significant load levels shown in Figure 4.5.6 are as follows:

1) Initial yielding on G3, total load = 2220 kN (499 kips) (obtained both from full nonlinear analysis as well as from elastic analysis using the equation $f_b + f_\ell = R_h F_{yt}$ at bottom flange).

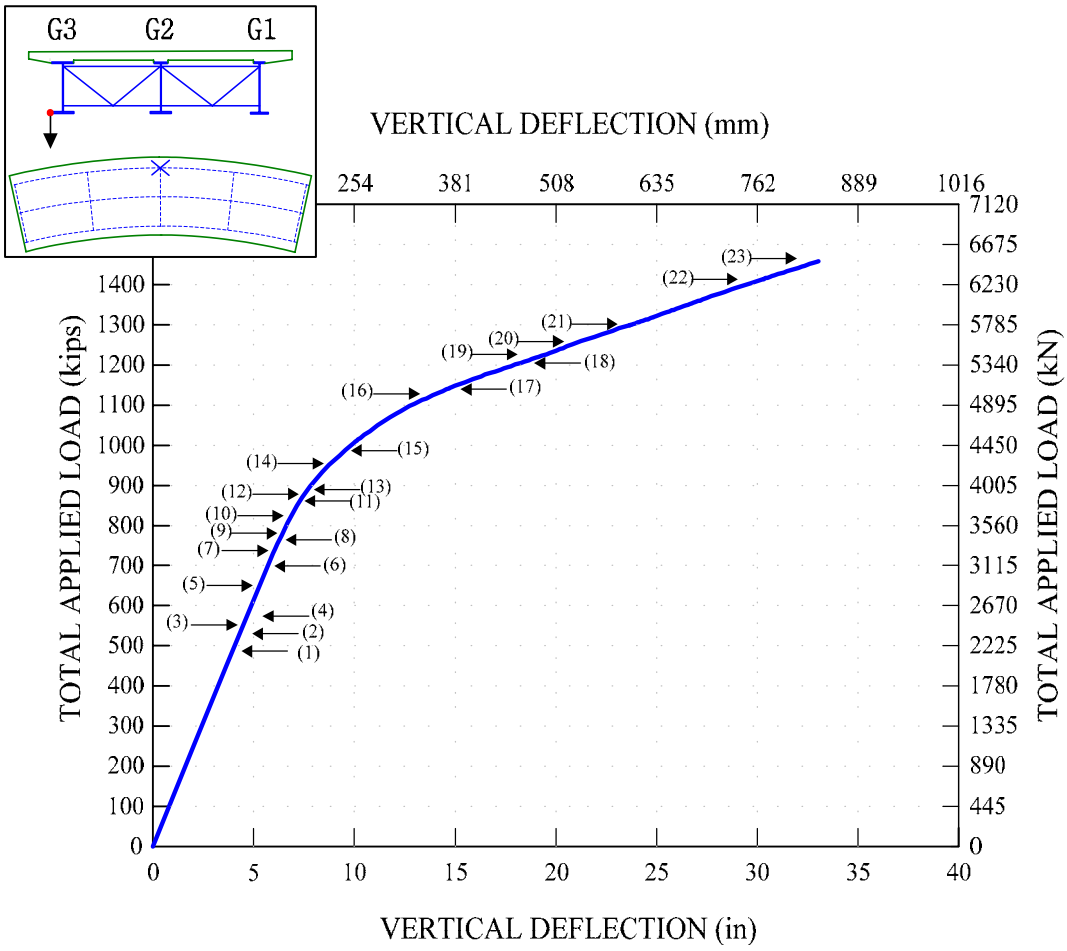

Figure 4.5.6. Total applied load versus vertical deflection of the mid-span outside tip of the G3 bottom flange, with significant load levels marked.

2) Total factored AASHTO design live load = 2398 kN (539 kips) (two trucks + two lanes, dynamic allowance factor of 1.33 on trucks, load factor of 1.75, multiple presence factor of 1.0). Note that this load level is somewhat low for the test bridge due to: (a) the difference between the actual material strengths and the nominal material strengths used in the design and (b) the use of the unfactored dead load in the calculations performed in this chapter.

3) Proportional limit reached at bottom chord of mid-span cross-frame attached on G3, total load = 2447 kN (550 kips) (from full nonlinear analysis, proportional limit =

24.1 cm^2 (3.73 in^2) * 414 MPa (60 ksi) = 1001 kN (225 kips)). Note that a number of the cross-frame members were reinforced prior to the start of Test 4b, as explained in Section 2.5.2.

4) Initial yielding on G2, total load = 2513 kN (565 kips)(from full nonlinear analysis and from elastic analysis, $f_b + f_\ell = R_h F_{yt}$ at bottom flange).
5) Service II condition reached on G3, total load = 2865 kN (644 kips) (from elastic analysis, $f_b + f_\ell/2 = 0.95 R_h F_{yt}$ at bottom flange).
6) Initial yielding in bending at top of intermediate transverse stiffeners on G3, total load = 3114 kN (700 kips) (from full nonlinear analysis).
7) Service II condition reached on G2, total load = 3221 kN (724 kips).
8) Initial yielding at the bottom of the G3 web panel at midspan, total load = 3385 kN (761 kips) (from full nonlinear analysis).
9) Strength I condition reached on G3, total load = 3470 kN (780 kips) (from elastic analysis, $f_b + f_\ell/3 = R_h F_{yt}$ at bottom flange).
10) Initial yielding in bending at top of intermediate transverse stiffeners on G2, total load = 3723 kN (837 kips) (from full nonlinear analysis).
11) Strength I condition reached on G2, total load = 3870 kN (870 kips).
12) Plastic moment capacity *with* 1/3 reduction reached on G3, total load = 3963 kN (891 kips) ($f_b S_{xt} + f_\ell/3 S_{xt} = M_p$ on bottom flange, from linear analysis).
13) Initial yielding at the bottom of G2 web panel at midspan, total load = 3981 kN (895 kips) (from full nonlinear analysis).
14) Initial yielding on G1, total load = 4124 kN (927 kips) (from elastic analysis, $f_b + f_\ell = R_h F_{yt}$ at bottom flange).

15) Initial yielding of G1, total load = 4426 kN (995 kips) (from full nonlinear analysis).

16) Plastic moment condition *with* 1/3 rule reduction reached on G2, total load = 5004 kN (1125 kips) ($M_p = f_b S_{xt} + f_\ell/3 S_{xt}$ on bottom flange, from linear analysis).

17) Plastic moment capacity *without* 1/3 rule reduction reached on G3, total load = 5102 kN (1147 kips) ($M_p = f_b S_{xt}$ on bottom flange, from linear analysis).

18) Full plastification of G2 and G3 bottom flange, total load = 5338 kN (1200 kips) (from full nonlinear analysis).

19) Service II condition reached on G1, total load = 5360 kN (1205 kips) (from elastic analysis, $f_b + f_\ell/2 = 0.95R_hF_{yt}$ at bottom flange).

20) Compressive strain of 0.003 reached on the outside edge of the slab at the midspan of the bridge, total load = 5534 kN (1244 kips) (from full nonlinear analysis).

21) Maximum member force obtained at bottom chord of mid-span cross-frame attached on G3 = 1557 kN (350 kips), total load = 5783 kN (1300 kips) (from full nonlinear analysis, required section capacity = 37.6 cm^2 (5.83 in^2) * 414 MPa (60 ksi) = 1557 kN (350 kips)).

22) Plastic moment condition *without* 1/3 reduction reached on G2, total load = 6441 kN (1448 kips) ($M_p = f_b S_{xt}$ on bottom flange, from linear analysis).

23) Strength I condition reached on G1, total load = 6446 kN (1449 kips) (from elastic analysis, $f_b + f_\ell/3 = R_hF_{yt}$ at bottom flange).

4.5.2 Loading Protocol

Of the two Test 4a sequences of repeated loadings applied to the test bridge prior to the final monotonic loading test, the first involved loading cycles at five different levels (Levels A to E), based on the average peak total applied load in each of the cycles. These load levels were 2420 kN (544 kips) for Level A, 2798 kN (629 kips) for Level B, 3376 kN (759 kips) for Level C, 3785 kN (851 kips) for Level D and 4217 kN (948 kips) for Level E. It should be noted that the peak applied load for each set of cycles corresponded approximately to one of the significant load levels defined previously in Figure 4.5.6 as listed below:

- Level A: total factored AASHTO design load, Level (2) in Figure 4.5.6.
- Level B: Service II condition on G3, Level (5) in Figure 4.5.6.
- Level C: Strength I condition on G3, Level (9) in Figure 4.5.6 (also initial yielding at the bottom of G3's web, Level (8) in Figure 4.5.6).
- Level D: Strength I condition on G2, Level (11) in Figure 4.5.6.
- Level E: Initial yielding on G1, between Levels (14) and (15) in Figure 4.5.6.

In the first sequence of the Test 4a repeated loadings, the applied load was cycled three times from zero to the above target maximum values during the first four sets of cycles up to load levels A, B, C and D. This was followed by four cycles up to load level E. Load levels higher than E were not considered in the repeated loading tests since the bridge started to exhibit significant nonlinear responses at this final load level, and also this final load level was well above the Service II condition on G3 (Level B).

In the second sequence of the Test 4a repeated loadings, the applied load was cycled from zero load, starting again at the smallest load level, Level A, then at load level C and

finally at load level D. The load was cycled three times at each of these levels. The purpose of this sequence was to gage the impact of the yielding or damage encountered at the higher load levels in the first sequence on the subsequent behavior at smaller loads.

4.5.3 Chairing of Jacks for Load Levels Exceeding Level C

The hydraulic rams used in Tests 4a and 4b did not have sufficient stroke to load the bridge beyond Level C without chairing. Figure 4.5.7 shows a schematic cross-section view of a typical loading fixture at each of the hydraulic rams used in Tests 4a and 4b. One can observe from this schematic that the loads were applied to the bridge by jacking against a top transverse spreader beam. The reactions from the top transverse spreader beam were in turn transmitted to four dywidag bars which then passed through the bridge slab and were anchored through the laboratory floor. To accomplish the chairing, two transverse tie-down beams, aligned approximately in the radial direction of the bridge, were positioned on the sides of each ram. The specific procedure for chairing of the rams was as follows:

- When the hydraulic jacks reached a certain point where chairing was required, the transverse tie-down beams were lowered into contact with the deformed slab and locked-off on the dywidag bars.
- The hydraulic jacks were retracted, thus transferring the load from the jacks to the tie-down beams.
- While the deformed bridge is held by the tie-down beams, the assemblies above the rams are lowered down, and then the heads of the hydraulic jack are positioned back into contact with the deformed slab.
- The hydraulic jacks are advanced to continue the loading of the structure.

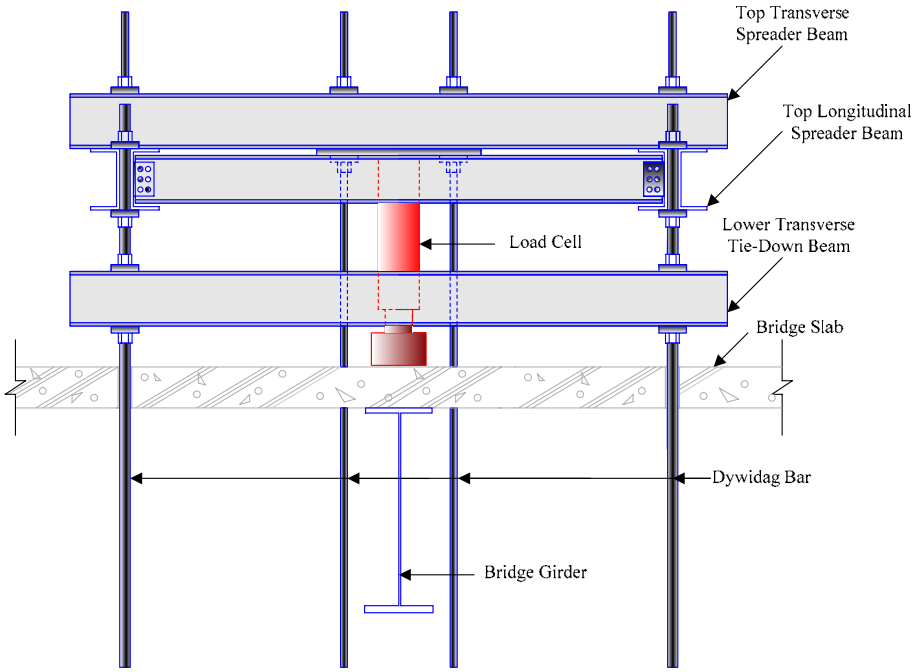

(a) Transverse view

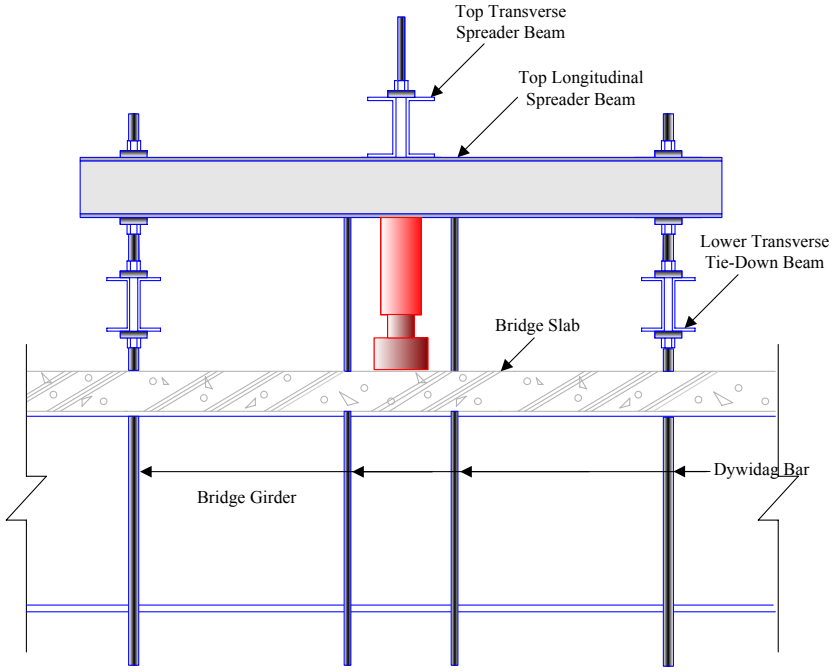

(b) Longitudinal view

Figure 4.5.7. Schematic cross-section view of typical loading fixture assemblies arranged for each of the hydraulic load cells, Test 4.

Once the peak load targeted at each loading cycle was reached, the test bridge was unloaded. During the unloading process, the chairing operation was repeated in the reverse direction. For the loading cycles up to Levels D and E, the rams were chaired at one stage during the loading and unloading. For the subsequent ultimate strength test (Test 4b), multiple chairing operations were required.

Two different types of tie-down arrangements were utilized during the experimental testing: Type 1 for the first repeated loading sequence and Type 2 for the second repeated loading sequence and the final monotonic loading test. The change from Type 1 to Type 2 was necessary because a significant increase in the slab top surface strains was observed during the Type 1 chairing operations. Figure 4.5.8 shows the Test 4a loading scheme with transverse tie-down beams of Type 1 used for the first repeated loading test, and corresponding experimental setup is shown in Figure 4.5.1. One can observe that the transverse tie-down beams are not placed at the same radial location where the rams are positioned. Instead, they are located halfway between the rams.

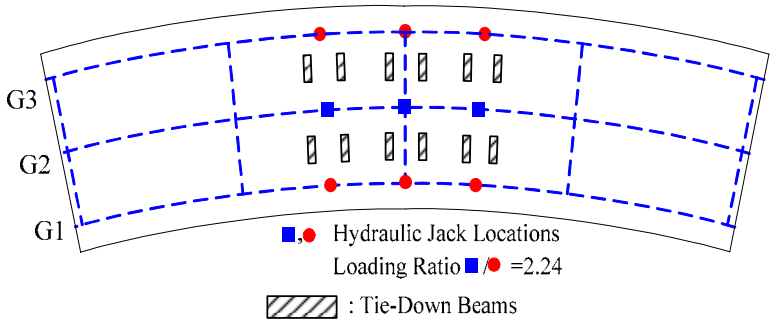

Figure 4.5.8. Test 4a loading scheme with transverse tie-down beams of Type 1 used for the first repeated loading test.

Figure 4.5.9 shows a close-up view of one of the Test 4a loading assemblies with transverse tie-down beams of Type 2 used for the second repeated loading sequence and

the final monotonic test. As opposed to Type 1 arrangement, Type 2 arrangement involves two tie-down beams placed on each side of the loading ram in parallel. Also, it can be seen in Figure 4.5.9 that bearing plates are placed below the flange bottom surface to facilitate the contact of the tie-down beams with the deformed test bridge, and they are approximately at the same radial position where the loading ram is located. Similar bearing plates are used for Type 1 arrangement.

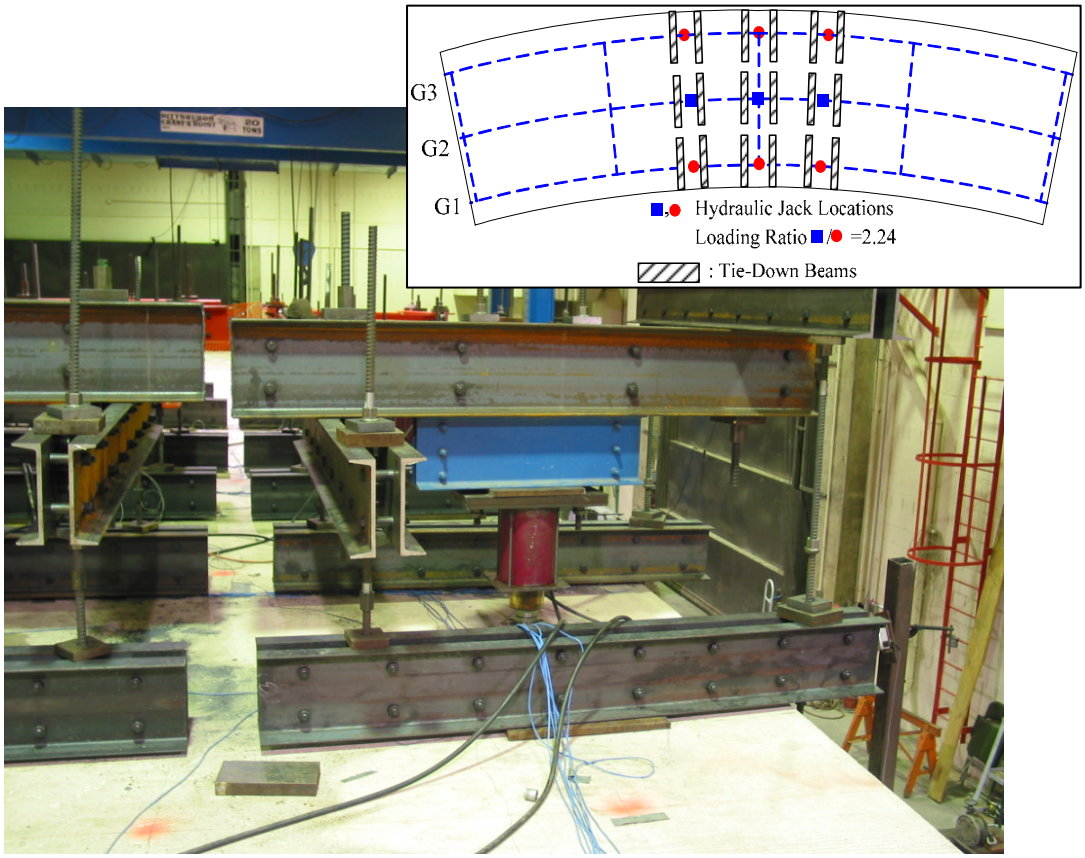

Figure 4.5.9. Close-up view of one of the Test 4a loading assemblies with transverse tie-down beams of Type 2 used for the second repeated loading test and the final monotonic test, courtesy of FHWA.

It should be noted that careful measures were taken to minimize the changes in the state of the bridge during the chairing operations. Nonetheless, as shown below, there are some small but inevitable changes in the bridge responses due to the tie-down operations.

This is in large part because the tie-down locations were not exactly the same as the loading points from the hydraulic jacks. Therefore, there is a need to assess to what extent the bridge responses change before and after the tie-down operations. To this end, detailed bridge responses are scrutinized in the following, in particular the girder end reactions and the girder deflections.

Tables 4.5.2 and 4.5.3 provide the measured girder reactions and mid-span girder deflections before and after each of the chairing operations for the *first* and the *second* sequences of Test 4a. One can observe that there are some small changes in the deflections and reactions due to the chairing. In particular, it is important to note that in many cases the distribution of the girder reactions after the chairing operations is somewhat different than before these operations. These changes in the girder reactions and their sum total indicate that the state of the bridge before and after the chairing operations are not identical. That is, the test bridge experiences a slight change in its equilibrium configuration. For example, consider Figure 4.5.10, which shows the measured mid-span vertical deflection for the outside tip of G3's bottom flange at the first loading cycle at Level D versus the total applied load. This figure illustrates the response only for the loadings in the vicinity of the chairing operation. It can be seen that the chairing is conducted at a total applied load of 2200 kN (500 kips) and a corresponding deflection 112 mm (4.40 in). When the hydraulic jacks are disengaged, and the deformed bridge configuration is held by the tie-down beams, the G3 deflection remains at 112 mm (4.40 in), but the total applied load is reduced to 2179 kN (490 kips). That is, it takes less applied loads for the test bridge held down by the tie-down beams to maintain the same deflection at G3.

Table 4.5.2 Girder reactions and deflections before and after tie-down operations for the *first* sequence of Test 4a (Beshah 2006).

Peak Load Level/ Cycle	Applied Load just prior to Chairing kN (kips)		Girder Reactions kN (kips)				Girder Vertical Deflections, mm (in)		
			G1	G2	G3	Total	G1	G2	G3
D/1	Loading at 2220(500)	before	186 (42)	625 (141)	1409 (317)	2220 (500)	48 (1.9)	78.0 (3.07)	112 (4.40)
		after	169 (38)	613 (138)	1397 (314)	2179 (490)	47.2 (1.86)	77.5 (3.05)	112 (4.40)
	Unloading at 2537 (570)	before	174 (39)	726 (163)	1637 (368)	2537 (570)	57.9 (2.28)	98.8 (3.89)	144 (5.69)
		after	181 (41)	733 (165)	1641 (369)	2555 (575)	58.4 (2.30)	98.8 (3.89)	145 (5.69)
D/2	Loading at 2102 (472)	before	177 (40)	593 (133)	1332 (299)	2102 (472)	45.7 (1.80)	74.4 (2.93)	106 (4.18)
		after	168 (38)	608 (137)	1385 (311)	2161 (486)	46.7 (1.84)	77.5 (3.05)	112 (4.39)
	Unloading at 2565 (577)	before	181 (41)	727 (163)	1657 (373)	2565 (577)	55.6 (2.19)	94.7 (3.73)	138 (5.45)
		after	186 (42)	731 (164)	1664 (374)	2581 (580)	55.9 (2.20)	95.0 (3.74)	138 (5.44)
D/3	Loading at 2220 (499)	before	186 (42)	624 (140)	1410 (317)	2220 (499)	48.0 (1.89)	78.0 (3.07)	112 (4.42)
		after	172 (39)	610 (137)	1402 (315)	2184 (491)	46.7 (1.84)	77.5 (3.05)	112 (4.42)
	Unloading at 2554 (574)	before	179 (40)	725 (163)	1650 (371)	2554 (574)	55.4 (2.18)	94.2 (3.71)	138 (5.43)
		after	184 (41)	729 (164)	1656 (372)	2569 (577)	55.9 (2.20)	94.5 (3.72)	138 (5.43)
E/1	Loading at 2786 (626)	before	229 (51)	782 (176)	1775 (399)	2786 (626)	59.9 (2.36)	98.0 (3.86)	140 (5.53)
		after	204 (46)	760 (171)	1749 (393)	2713 (610)	58.2 (2.29)	97.0 (3.82)	140 (5.53)
	Unloading at 3156 (709)	before	236 (53)	879 (197)	2041 (459)	3156 (709)	73.7 (2.90)	128 (5.07)	190 (7.47)
		after	218 (49)	806 (181)	1873 (421)	2897 (651)	68.6 (2.70)	119 (4.72)	177 (6.96)
E/2	Loading at 2813 (632)	before	227 (51)	774 (174)	1812 (407)	2813 (632)	59.2 (2.33)	96.8 (3.81)	139 (5.46)
		after	209 (47)	755 (170)	1795 (403)	2759 (620)	57.7 (2.27)	96.3 (3.79)	139 (5.46)
	Unloading at 2888 (649)	before	201 (45)	801 (180)	1886 (424)	2888 (649)	62.2 (2.45)	107 (4.22)	156 (6.16)
		after	202 (45)	803 (180)	1891 (425)	2896 (650)	62.5 (2.46)	107 (4.22)	156 (6.16)
E/3	Loading at 2780 (625)	before	232 (52)	772 (174)	1776 (399)	2780 (625)	59.2 (2.33)	97.5 (3.84)	139 (5.49)
		after	213 (48)	754 (169)	1761 (396)	2728 (613)	57.7 (2.27)	96.8 (3.81)	139 (5.49)
	Unloading at 2850 (640)	before	206 (46)	789 (177)	1855 (417)	2850 (640)	61.5 (2.42)	106 (4.19)	155 (6.11)
		after	209 (47)	792 (178)	1860 (418)	2861 (643)	61.5 (2.42)	106 (4.19)	155 (6.11)
E/4	Loading at 3316 (745)	before	275 (62)	913 (205)	2128 (478)	3316 (745)	69.3 (2.73)	115 (4.52)	165 (6.51)
		after	258 (58)	892 (201)	2113 (475)	3263 (734)	67.8 (2.67)	114 (4.50)	165 (6.51)
	Unloading at 3459 (777)	before	263 (59)	949 (213)	2247 (505)	3459 (777)	72.1 (2.84)	124 (4.90)	181 (7.13)
		after	268 (60)	953 (214)	2255 (507)	3476 (781)	72.6 (2.86)	124 (4.90)	181 (7.13)

Table 4.5.3 Girder reactions and deflections before and after tie-down operations for the *second* sequence of Test 4a (Beshah 2006).

Peak Load Level/ Cycle	Applied Load just prior to Chairing kN (kips)		Girder Reactions kN (kips)				Girder Vertical Deflections, mm (in)		
			G1	G2	G3	Total	G1	G2	G3
D/1	Loading at 2196 (494)	before	186 (42)	603 (136)	1407 (316)	2196 (494)	47.0 (1.85)	78.2 (3.08)	112 (4.43)
		after	175 (39)	600 (135)	1421 (319)	2196 (493)	47.0 (1.85)	79.0 (3.11)	114 (4.50)
	Unloading at 2544 (572)	before	184 (41)	702 (158)	1658 (373)	2544 (572)	54.9 (2.16)	94.2 (3.71)	138 (5.45)
		after	183 (41)	699 (157)	1652 (371)	2534 (569)	54.6 (2.15)	93.7 (3.69)	138 (5.43)
D/2	Loading at 2747 (618)	before	231 (52)	759 (171)	1757 (395)	2747 (618)	58.9 (2.32)	97.3 (3.83)	141 (5.53)
		after	217 (49)	750 (169)	1758 (395)	2725 (613)	58.2 (2.29)	97.3 (3.83)	142 (5.58)
	Unloading at 2854 (642)	before	210 (47)	787 (177)	1857 (418)	2854 (642)	61.0 (2.40)	104 (4.11)	153 (6.03)
		after	217 (49)	794 (179)	1861 (418)	2872 (646)	61.2 (2.41)	104 (4.11)	153 (6.02)
D/3	Loading at 2750 (618)	before	232 (52)	761 (171)	1757 (395)	2750 (618)	58.9 (2.32)	97.3 (3.83)	141 (5.53)
		after	210 (47)	740 (166)	1739 (391)	2689 (604)	57.4 (2.26)	96.8 (3.81)	141 (5.54)
	Unloading at 2850 (641)	before	209 (47)	787 (177)	1854 (417)	2850 (641)	60.7 (2.39)	104 (4.11)	153 (6.02)
		after	208 (47)	787 (177)	1856 (417)	2851 (641)	60.7 (2.39)	104 (4.10)	153 (6.02)

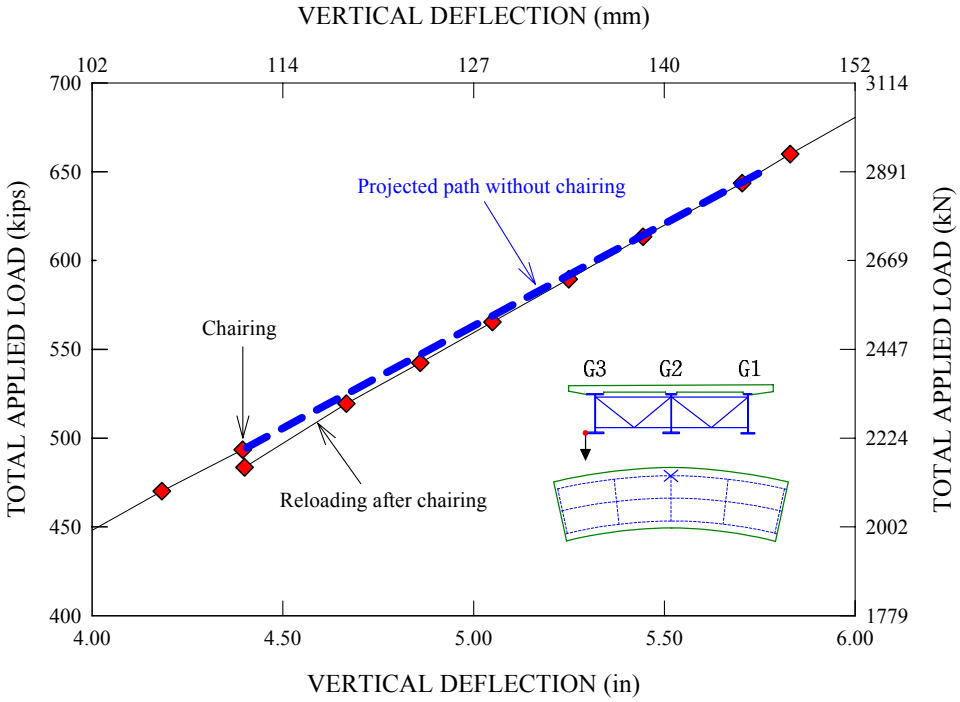

Figure 4.5.10. Vertical deflection changes of the G3 bottom flange outside tip at mid-span before and after chairing during the first loading cycle of loading at level D in the first sequence of Test 4a.

However, once the test bridge is released from the tie-down beams and re-loaded by the hydraulic jacks, it can be seen in Figure 4.5.10 that the total load versus G3 deflection curve tends to come back to the path that would be obtained otherwise by a continuous loading without chairing as shown by the dotted line in Figure 4.5.10. The reactions behave similarly. Similar observations can be made from the load-deflection and load-reaction curves for the other repeated loading tests.

Also, noticeable changes are observed in the longitudinal slip displacements at the concrete-steel interface due to the tie-down operations. Figures 4.5.11 and 4.5.12 provide measured longitudinal slips at the east end of G3 during the loading to levels D and E, respectively, in the first repeated loading sequence.

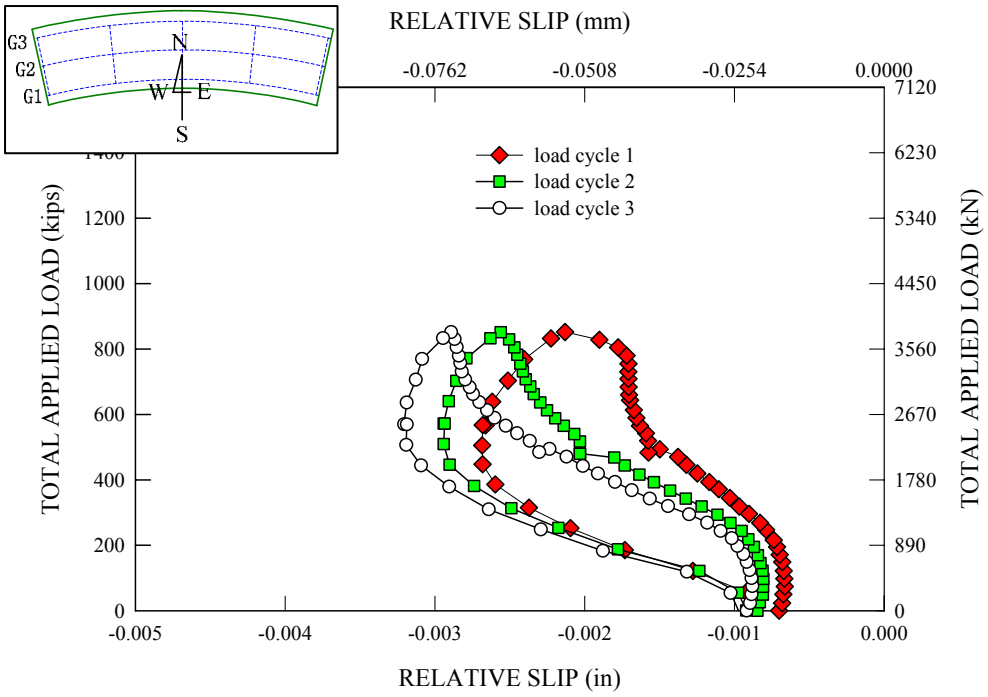

Figure 4.5.11. Longitudinal slip measurements taken at the east end of G3 for cycling to load level D during the first sequence of Test 4a (Beshah 2006).

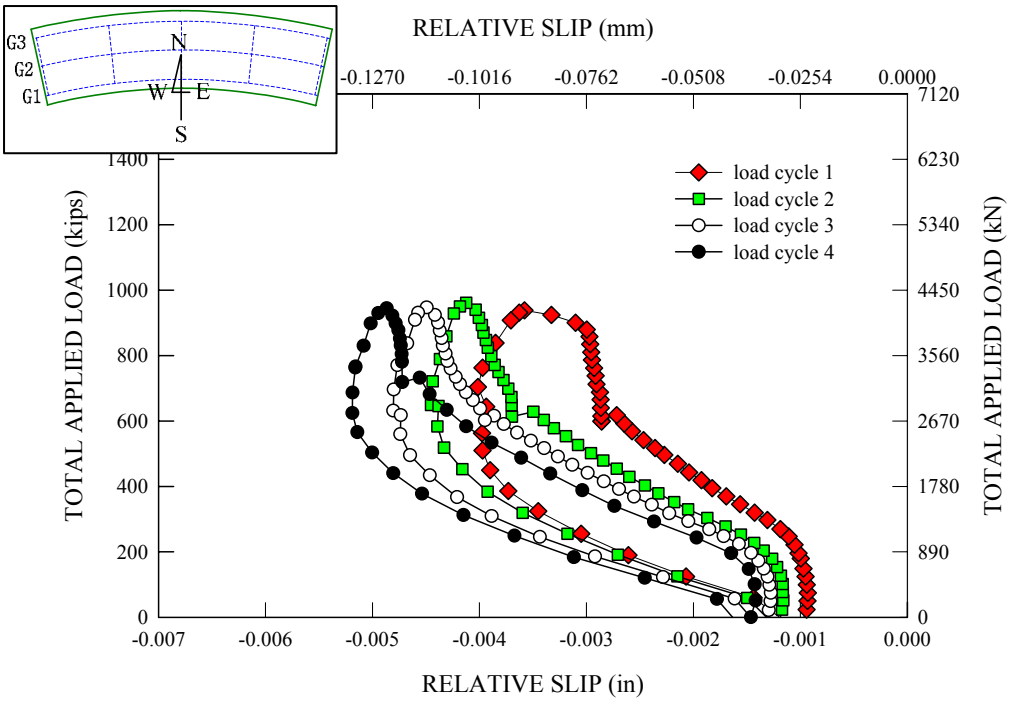

Figure 4.5.12. Longitudinal slip measurements taken at the east end of G3 for cycling to load level E during the first sequence of Test 4a (Beshah 2006).

The residual slip accumulated during the prior loading cycles (A, B and C) is 0.02 mm (0.0007 in) and is included in the plots. It can be seen in both of the plots that there is a slight increase in the slip during each chairing operation, causing a horizontal shift in the load-slip plots. This suggests that part of the residual slips accumulated during the loading sequences involving tie-down operations comes from the slips that occur during the chairing operations. However, since the horizontal shifts in the longitudinal slip are quite small, and also the residual slips are quite small, their effect on the bridge response is expected to be inconsequential. In contrast with the longitudinal slips at G3's ends, it is found that the effects of the chairing operations on the radial slips at the G3 mid-span are somewhat larger. Figures 4.5.13 and 4.5.14 show the radial slips measured at the G3 mid-span at the load levels D and E, respectively, during the first repeated loading sequence.

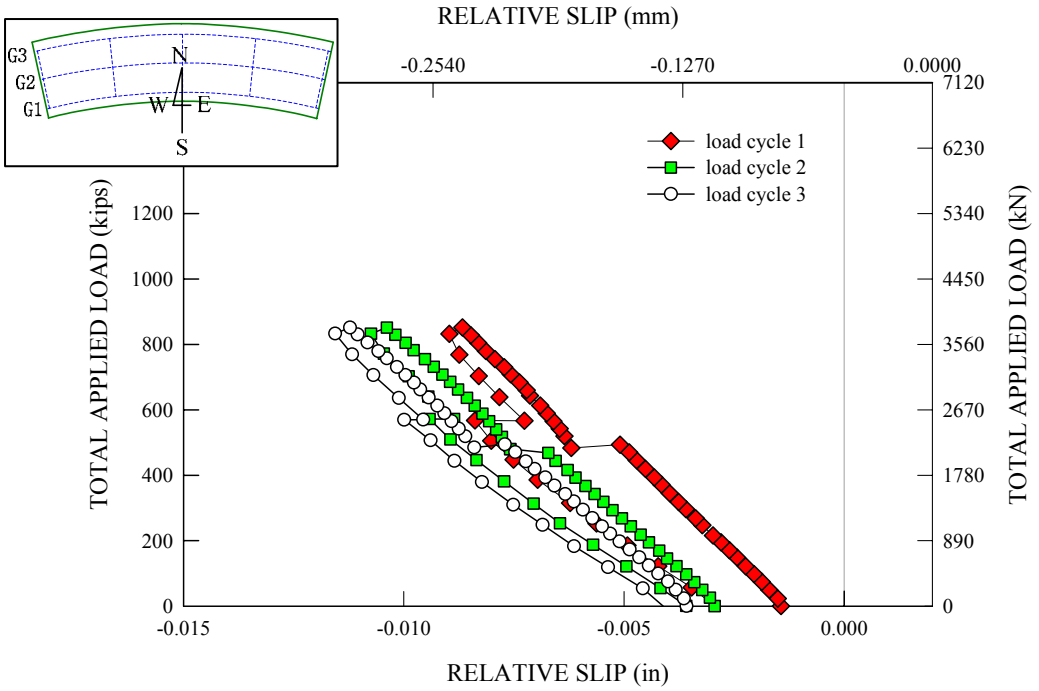

Figure 4.5.13. Radial slip measurements taken at G3 for cycling to load level D during the first sequence of Test 4a (Beshah 2006).

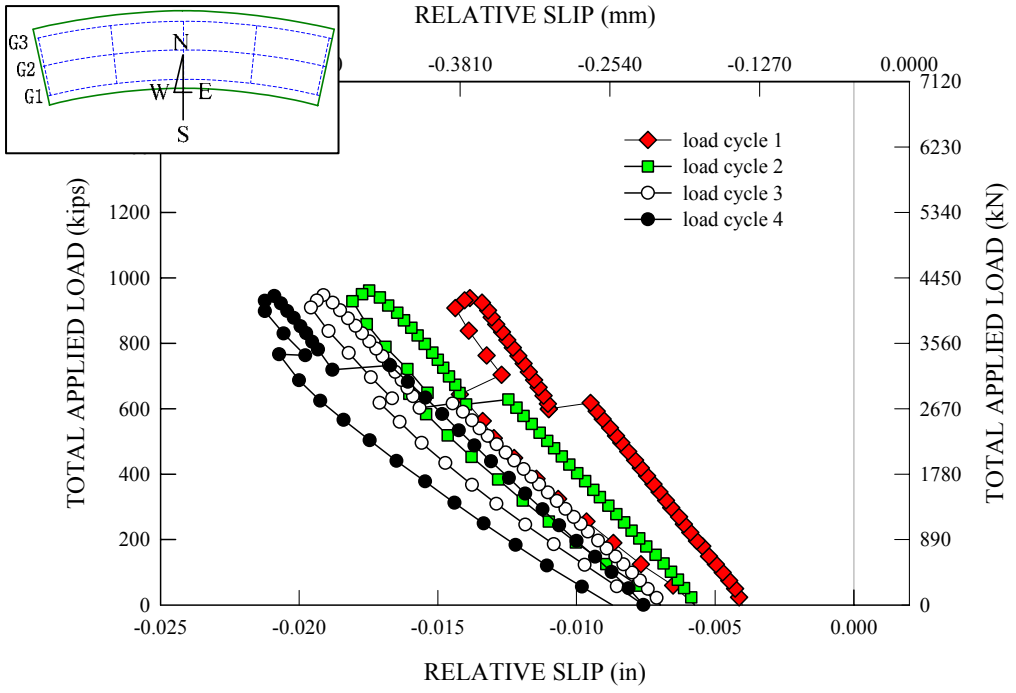

Figure 4.5.14. Radial slip measurements taken at G3 for cycling to load level E during the first sequence of Test 4a (Beshah 2006).

A residual slip of 0.0363 mm (0.00143 in) from the prior repeated loading cycles is also included in the plots. It should be noted that the magnitude of the residual radial slip at the G3 mid-span is several times larger than the corresponding longitudinal residual slip at G3's ends. Nevertheless, the maximum radial slip measured at the end of the cycles at load level E is only approximately 0.2 mm (0.009 in). Based on Figure 3.5.3, one can observe that this corresponds to a shear connector force level that is significantly smaller than the shear connector capacities. Also, this amount of residual radial slip is expected to be very local to the area in the vicinity of the cross-frame radial forces on G3 at the mid-span of the bridge. Therefore, the measured slips at the steel-concrete interface are judged to be inconsequential.

Figure 4.5.15 provides longitudinal slip measurements taken at the east end of G3 for the cycles at load level D during the second sequence of Test 4a, and Figure 4.5.16 gives a similar plot for the radial slip measurements at the G3 mid-span. The slip residuals accumulated during the prior sequence as well as the cycling at load levels A and C in the second sequence are included in both of the plots. Interestingly, it is common to both of the plots that there are essentially zero changes in the slips before and after the chairing operations. This is believed to be due potentially to a combination of (1) the change from the Type 1 to the Type 2 chairing operations and (2) the elastic response of the bridge at the smaller load levels subsequent to the cycling at load level E at the end of the first sequence of Test 4a. At the time of the completion of this research, measured concrete strains were not available during the chairing operations. However, based on the all other data available, there are no indications that other bridge responses including the slab strains were influenced by chairing operations during the repeated loading cycles.

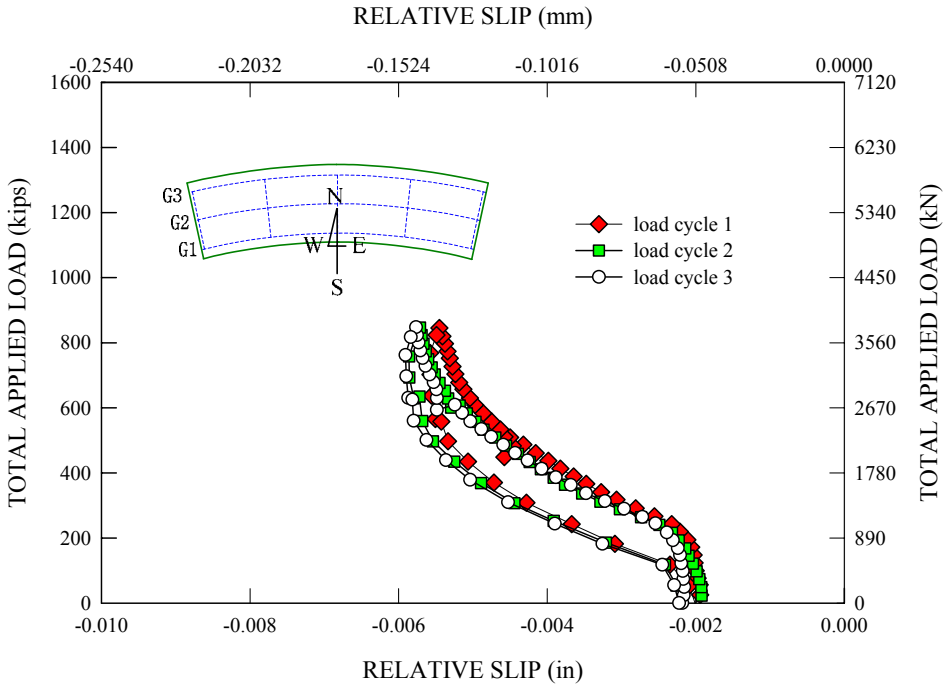

Figure 4.5.15. Longitudinal slip measurements taken at the east end of G3 for cycles to load level D in the second sequence of Test 4a (Beshah 2006).

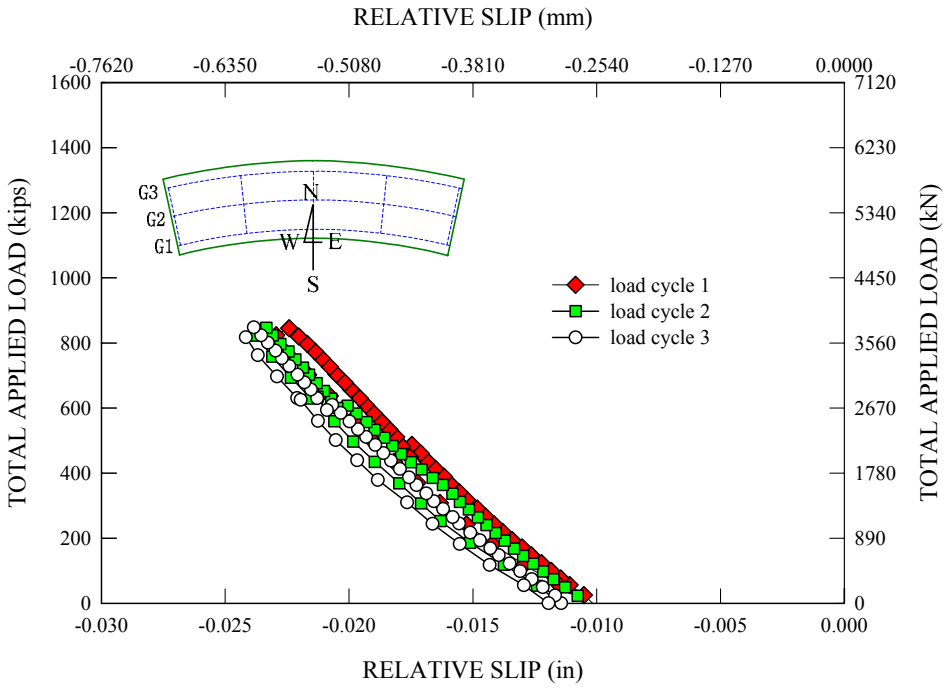

Figure 4.5.16. Radial slip measurements taken at G3 for cycles to load level D in the second sequence of Test 4a (Beshah 2006).

4.5.4 Results of Test 4a: Repeated Loading Tests

4.5.4.1 Vertical and Radial Deflections

Figure 4.5.17 shows the envelope of the maximum measured vertical deflections at the mid-span outside tip of the G3 bottom flange versus the total applied load from Test 4a. The corresponding FEA predictions are presented in Figure 4.5.17 as well. It should be noted that the FEA predictions are obtained from a full nonlinear analysis in which the test bridge model is subjected to a single monotonic loading instead of repeated loadings. This is because the full nonlinear FEA simulation involving the repeated loading of the test bridge essentially produces the same results. The effects of the repeated loadings on the subsequent final monotonic testing of the test bridge are addressed at the end of this chapter.

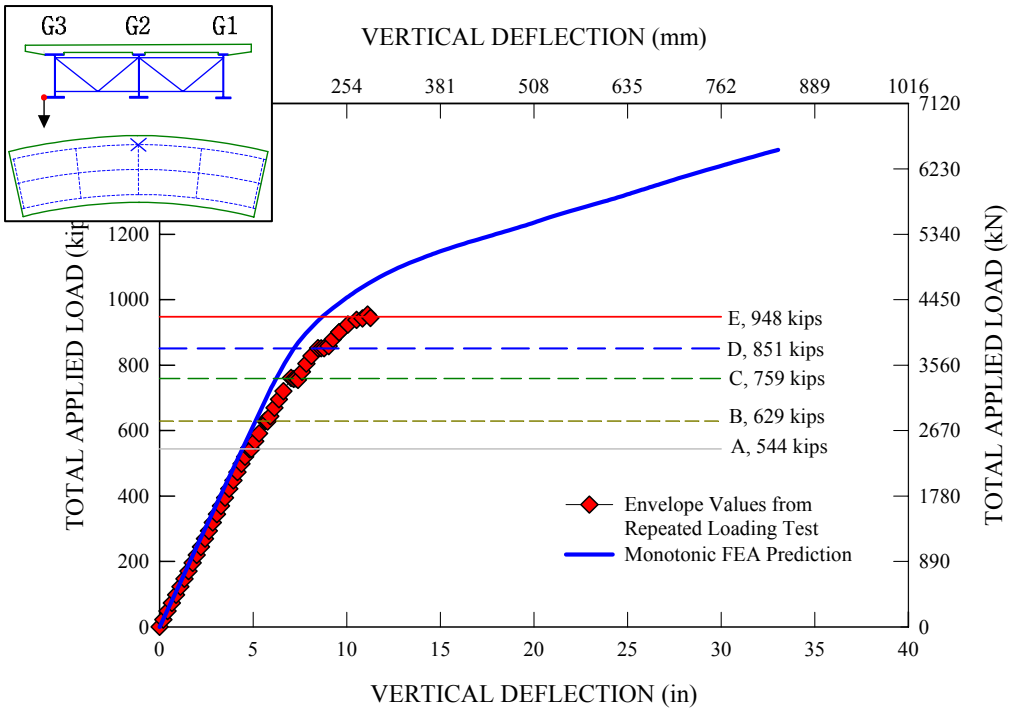

Figure 4.5.17. Envelope values of vertical deflections for the mid-span outside tip of the G3 bottom flange during the first sequence of Test 4a (initial dead load deflection is not included in the plot).

Similarly, Figure 4.5.18 shows the envelope of the radial deflections for the mid-span outside tip of the G3 bottom flange and the corresponding FEA predictions.

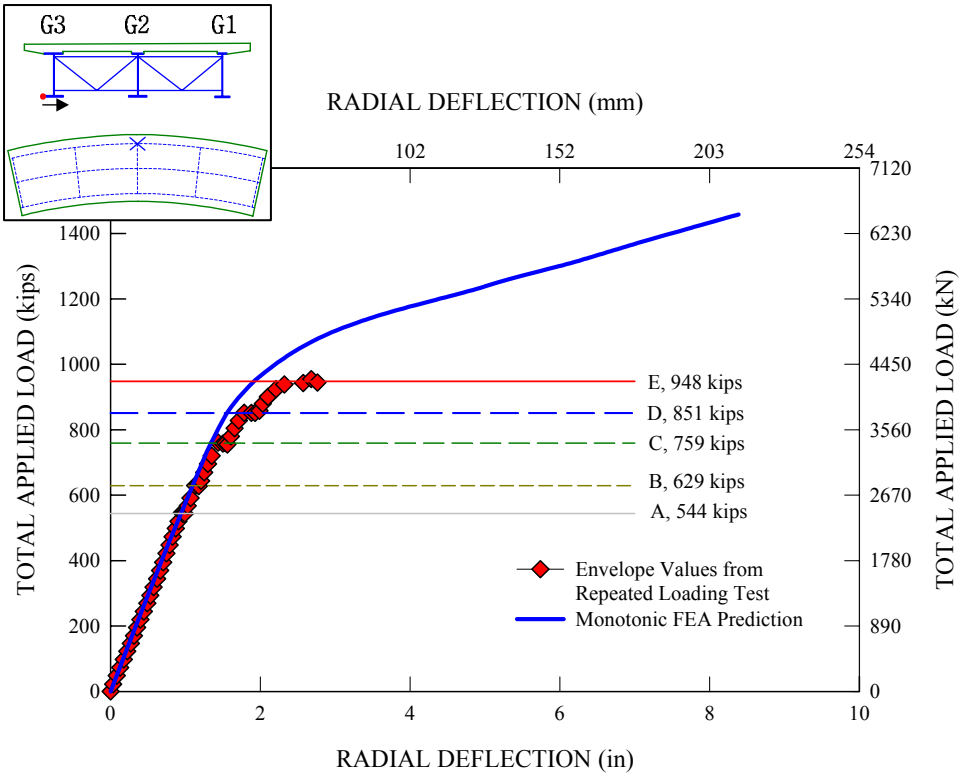

Figure 4.5.18. Envelope values of radial deflections for the mid-span outside tip of the G3 bottom flange during the first sequence of Test 4a (initial dead load deflection is not included in the plot).

As can be seen from Figures 4.5.17 and 4.5.18, there is a good correlation between the measured and predicted deflections for relatively low applied load levels, A and B. The load-deflection responses are essentially linear at these two load levels. However, as the magnitude of the load cycles is increased to levels C, D and E, the envelopes tend to drift away from the FEA predictions due to the accumulated deflections during each cycle. The initial load-deflection response during the first cycle at level C (not shown) is also essentially linear. This response becomes slightly nonlinear for the first cycle at load

level D. For the final load level E, the initial load-deflection response becomes noticeably nonlinear. The load-deflection curves are only slightly nonlinear for the repeated loading cycles at load levels C, D and E. Most of the nonlinearity at levels D and E occurs in the first cycle.

The responses at load levels A, C and D in the second sequence of Test 4a are very similar to the responses at these levels during the first sequence. This is evidenced by the peak deflections shown for each cycle in Figure 4.5.19. However, the total vertical deflections at these levels are larger during the second sequence. This is due to the residual deflections caused by the larger load cycles in sequence one.

Figure 4.5.19 shows the maximum vertical deflections at the end of each loading cycle versus the number of cycles. The first sequence of loading cycles (cycling at load levels A, B, C, D and E) is represented by the square symbols whereas the second sequence (cycling at load levels A, C and D) is represented by the triangular symbols in the figure. In general, it can be seen that there is some gradual growth in the maximum vertical deflections with each cycle at a given load level, particularly at the higher load levels of the first sequence. It is important to note that the drift of the deflection envelopes from the FEA predictions in Figures 4.5.17 and 4.5.18 is largely due to these incremental deflections during the repeated cycles at each applied load level.

Figure 4.5.20 shows the measured residual deflections at the end of each loading cycle for the mid-span outside tip of the G3 bottom flange during Test 4a. One can observe that the largest changes in the residual deflections occur in the first cycle at each of the load levels. However, there is some growth in the residual deflections during the repeated cycles, particularly at load level E.

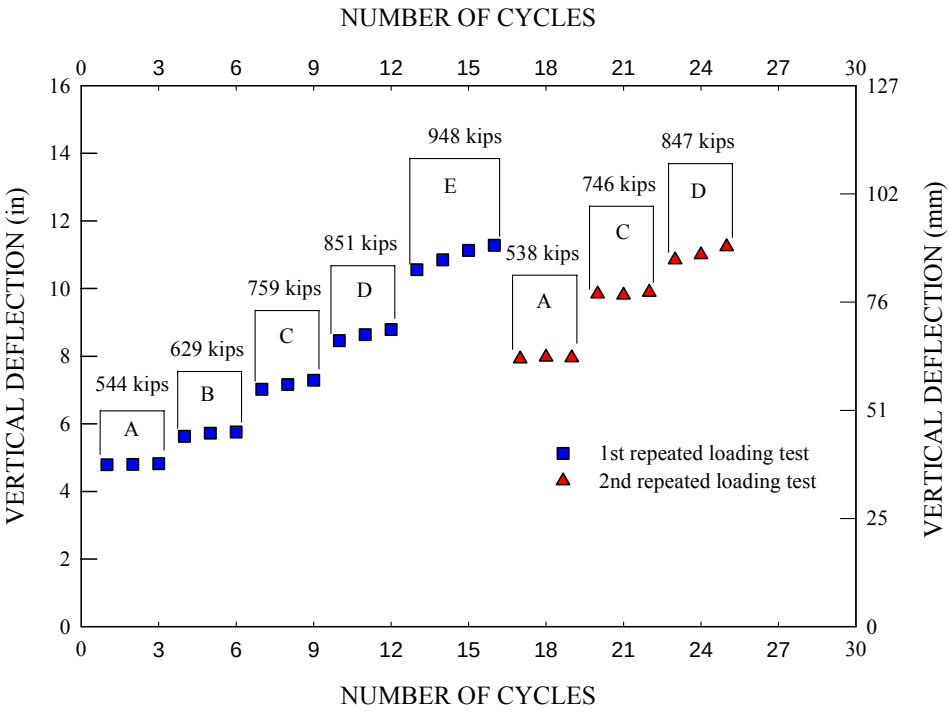

Figure 4.5.19. Measured maximum vertical deflections for the mid-span outside tip of the G3 bottom flange during the first and second sequences of Test 4a, Beshah (2006).

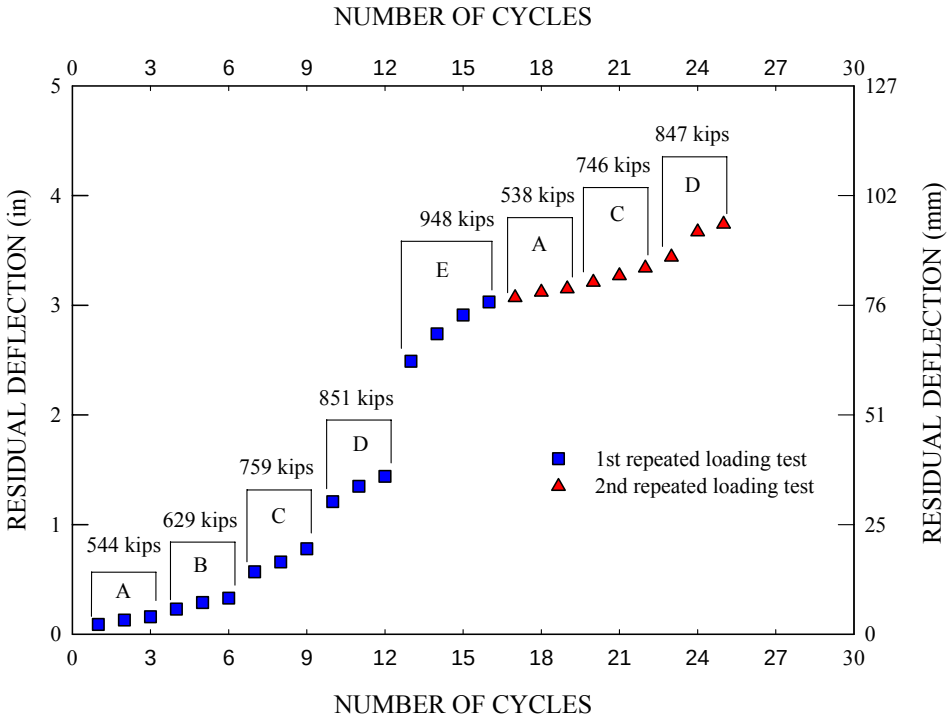

Figure 4.5.20. Measured vertical residual deflections at the G3 bottom flange mid-span outside tip during the first and second sequences of Test 4a (Beshah 2006).

Figure 4.5.20 shows that there is a permanent set of 2.5 mm (0.10 in) at the end of the first loading cycle at load level A. This permanent set increases slightly during the next two cycles, resulting in a total residual deflection of 4.1 mm (0.16 in) at the end of load level A. The total accumulated residual deflection is increased further to 8.4 mm (0.33 in) due to the cycles at load level B. For load level C, Figure 4.5.20 shows that the total accumulated residual deflection is increased to 20 mm (0.78 in), due to an additional permanent set of 6.1 mm (0.24 in) in the first loading cycle of load level C and subsequent incremental residual deflections of 2.3 mm (0.090 in) and 3.1 mm (0.12 in) for the repeated cycles at this load level. For load level D, it can be seen that there is a relatively large increase in the residual deflection of 11 mm (0.43 in) at the first loading cycle followed by smaller additional residual deflections of 3.6 mm (0.14 in) and 2.3 mm (0.09 in) in the remaining cycles. The total accumulated residual deflection is 36.6 mm (1.44 in) at the end of load level D. For load level E, Figure 4.5.20 shows that there is a relatively large increase in the residual deflections at the first loading cycle. In fact, the magnitude of the initial residual deflection increment is 26.7 mm (1.05 in), which is significantly larger than other initial residual deflections observed in the first loading cycle at other load levels. For the remaining loading cycles at level E, there is a further development of incremental residual deflections that gradually decrease from 6.4 mm (0.25 in), 4.3 mm (0.17 in) and 3.1 mm (0.12 in). The total accumulated residual deflection amounts to 77.0 mm (3.03 in) at the end of load level E.

Regarding the residual deflections for the second sequence of Test 4a, Figure 4.5.20 shows that the increase in these deflections is much smaller between levels A and C and

between levels C and D than in the first sequence. However, the increase in the residual displacements during the repeated cycles is very similar in both sequences.

If one adds up the additional residual displacements that occur after the first cycle at each of the load levels for the first sequence in Figure 4.5.20, one obtains 1.6 mm (0.06 in) at level A, 2.5 mm (0.1 in) at level B, 5.4 mm (0.21 in) at level C, 5.9 mm (0.23 in) at level D, and 13.8 mm (0.54 in) at level E. If these additional residual displacements are subtracted from the envelope curves in Figure 4.5.17, the envelope curves closely match monotonic FEA prediction.

4.5.4.2 Slip at the Steel-Concrete Interface

Figures 4.5.21 and 4.5.22 provide measured longitudinal slip residuals left at the west and east ends of the outermost girder, G3, at the end of each loading cycle. Similarly, Figure 4.5.23 presents measured radial slip residuals left at the mid-span overhang region of G3. It can be seen from Figures 4.5.21 through 4.5.23 that the radial slip residuals at mid-span are significantly larger than the longitudinal slip residuals measured at the girder ends. In fact, the maximum radial slip residual left at the end of all the loading cycles including both the first and second sequences of the repeated loading test is about 0.31 mm (0.012 in). This is over five times larger than the corresponding longitudinal slip residual of 0.0572 mm (0.00225 in) measured at the east end of G3. Nonetheless, it should be noted that the magnitude of the radial residual slip is insignificant.

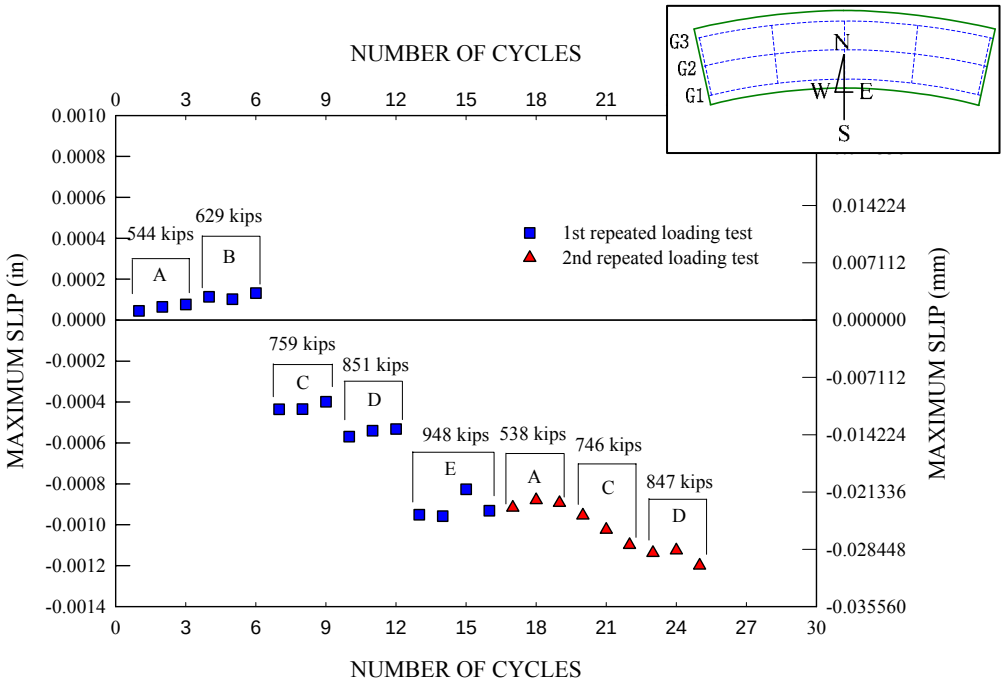

Figure 4.5.21. Measured longitudinal residual slips at G3 west end during the first and second sequences of Test 4a (Beshah 2006).

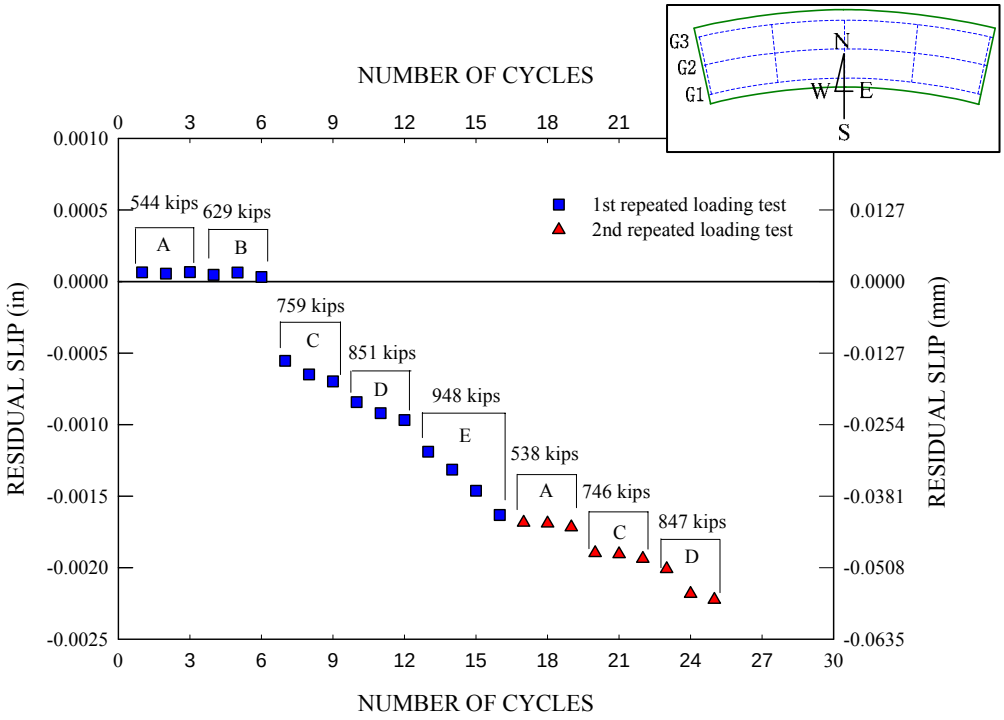

Figure 4.5.22. Measured longitudinal residual slips at G3 east end during the first and second sequences of Test 4a (Beshah 2006).

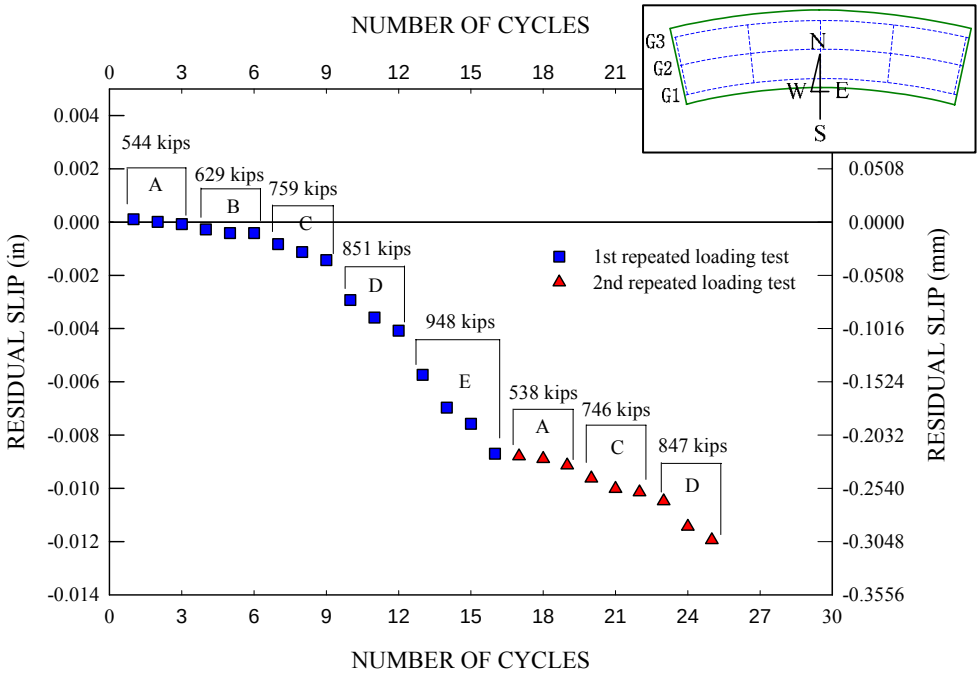

Figure 4.5.23. Measured radial residual slip at G3 mid-span during the first and second sequences of Test 4a (Beshah 2006).

4.5.4.3 Girder Reactions

Figure 4.5.24 shows envelope values of the girder end reactions obtained from the repeated loading test of Test 4, Test 4a, and corresponding FEA predictions based on a monotonic loading analysis. Initial dead load reactions are included in the plot as well. It can be seen that there is a good correlation between the measured reactions and corresponding FEA predictions for all of the three girders, including the initial dead load reactions. Furthermore, it is quite interesting to note that the girder reactions are predominantly linear throughout the entire loading history of Test 4a.

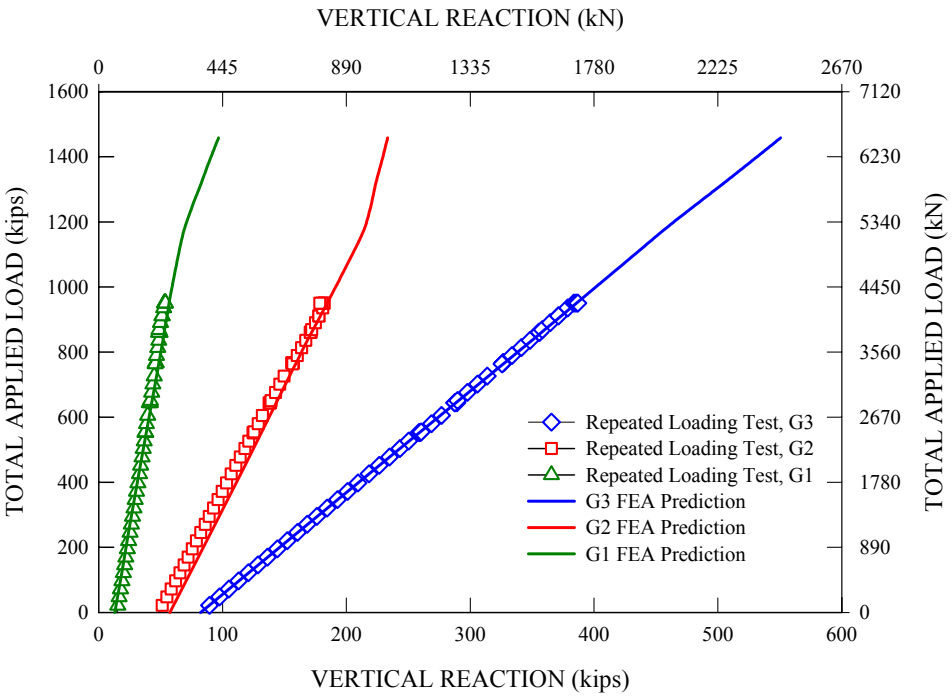

Figure 4.5.24. Envelope values of the girder end reactions obtained from the repeated loading test of Test 4, Test 4a, and corresponding FEA predictions based on a monotonic loading analysis, initial dead load reactions are included in the plot as well.

4.5.4.4 Bridge Slab Strains

Figures 4.5.25 through 4.5.29 provide measured slab longitudinal strain distributions across the mid-span bridge cross-section (gage location L10) for load levels A through E. Corresponding FEA predictions based on a monotonic loading analysis of the test bridge are also presented in the plots. Strains associated with concrete shrinkage are not included. It should be noted that the strain measurements for each loading cycle do not include residual strains from previous loading cycles. For all the load levels, it can be seen that the measured slab strains are in good agreement with the corresponding FEA predictions. Interestingly, the overall strain distribution is approximately linear across the cross-section, with the minimum occurring at the inside edge of G1 and the maximum occurring at the outside edge of G3. Furthermore, it is worthwhile noting that the slab

strains do not show any significant increase with repeated loading cycles. Most importantly, it should be noted that the measured maximum strain is slightly larger than the strain associated with the elastic limit in the measured concrete stress-strain response for all cases. At load level E, the maximum slab strain is approximately 1200 με that is above the elastic limit. However, the secant stiffness at this strain in the concrete stress-strain curve is not significantly away from the initial elastic stiffness.

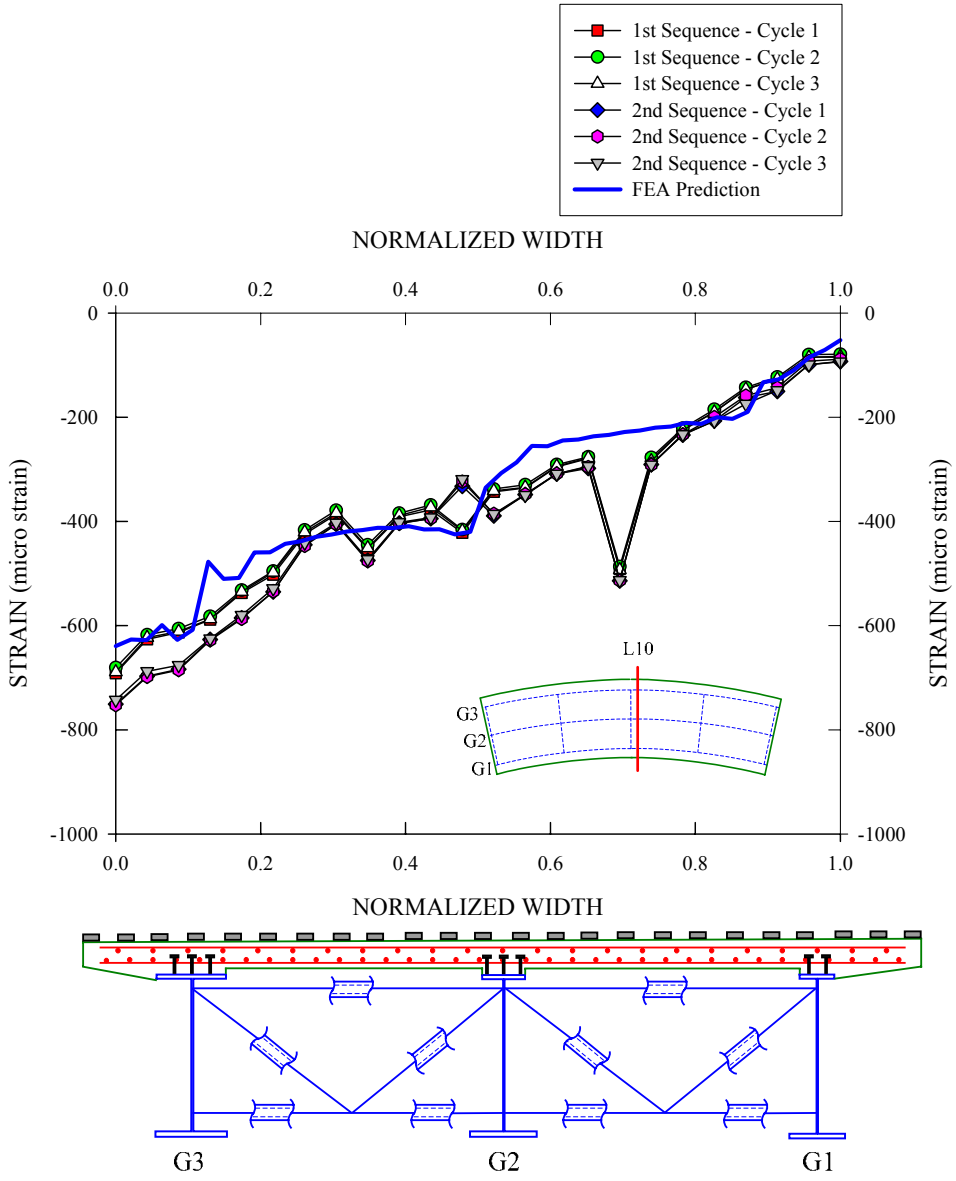

Figure 4.5.25. Slab longitudinal strain distribution for gage location L10 at load level A during the first and second sequences of Test 4a, strains associated with concrete shrinkage are not included in the plot.

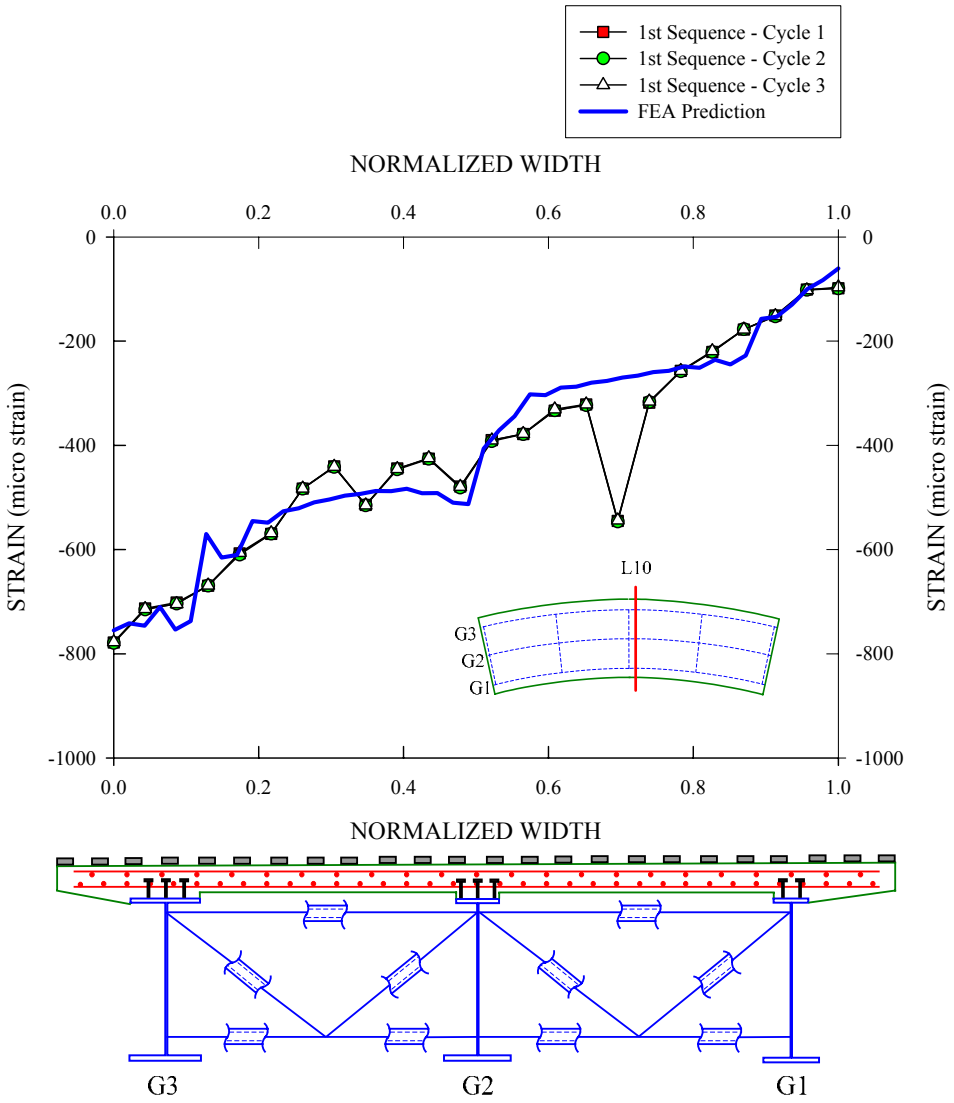

Figure 4.5.26. Slab longitudinal strain distribution for gage location L10 at load level B during the first and second sequences of Test 4a, strains associated with concrete shrinkage are not included in the plot.

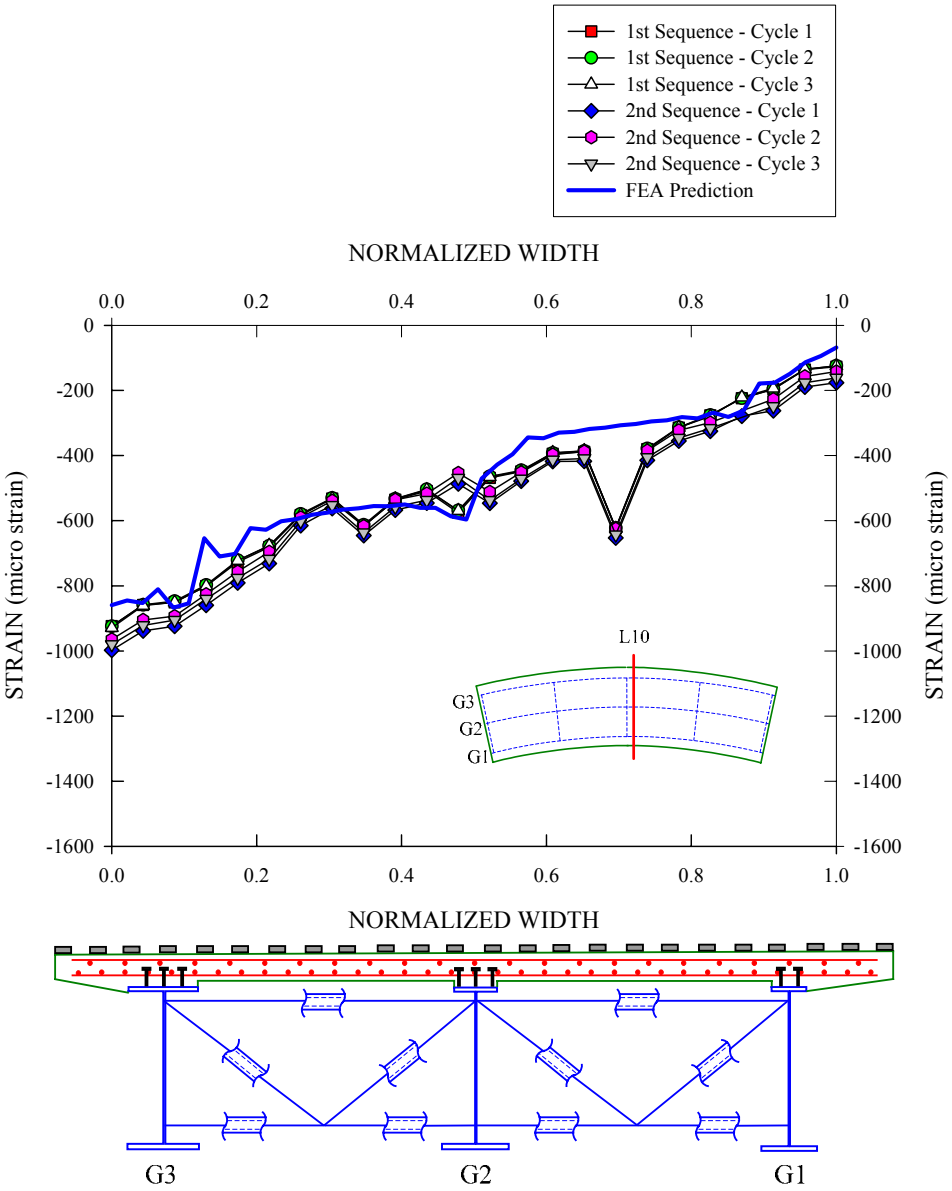

Figure 4.5.27. Slab longitudinal strain distribution for gage location L10 at load level C during the first and second sequences of Test 4a, strains associated with concrete shrinkage are not included in the plot.

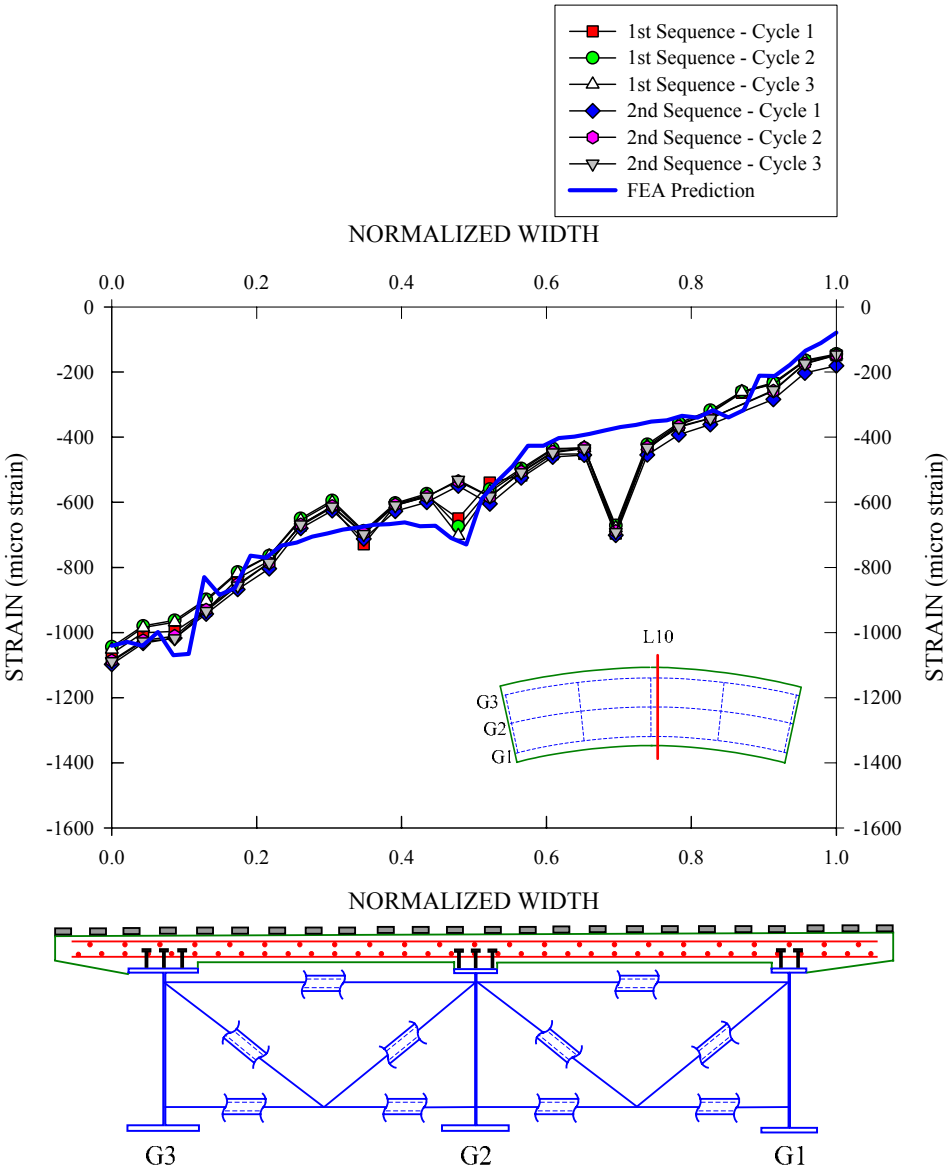

Figure 4.5.28. Slab longitudinal strain distribution for gage location L10 at load level D during the first and second sequences of Test 4a, strains associated with concrete shrinkage are not included in the plot.

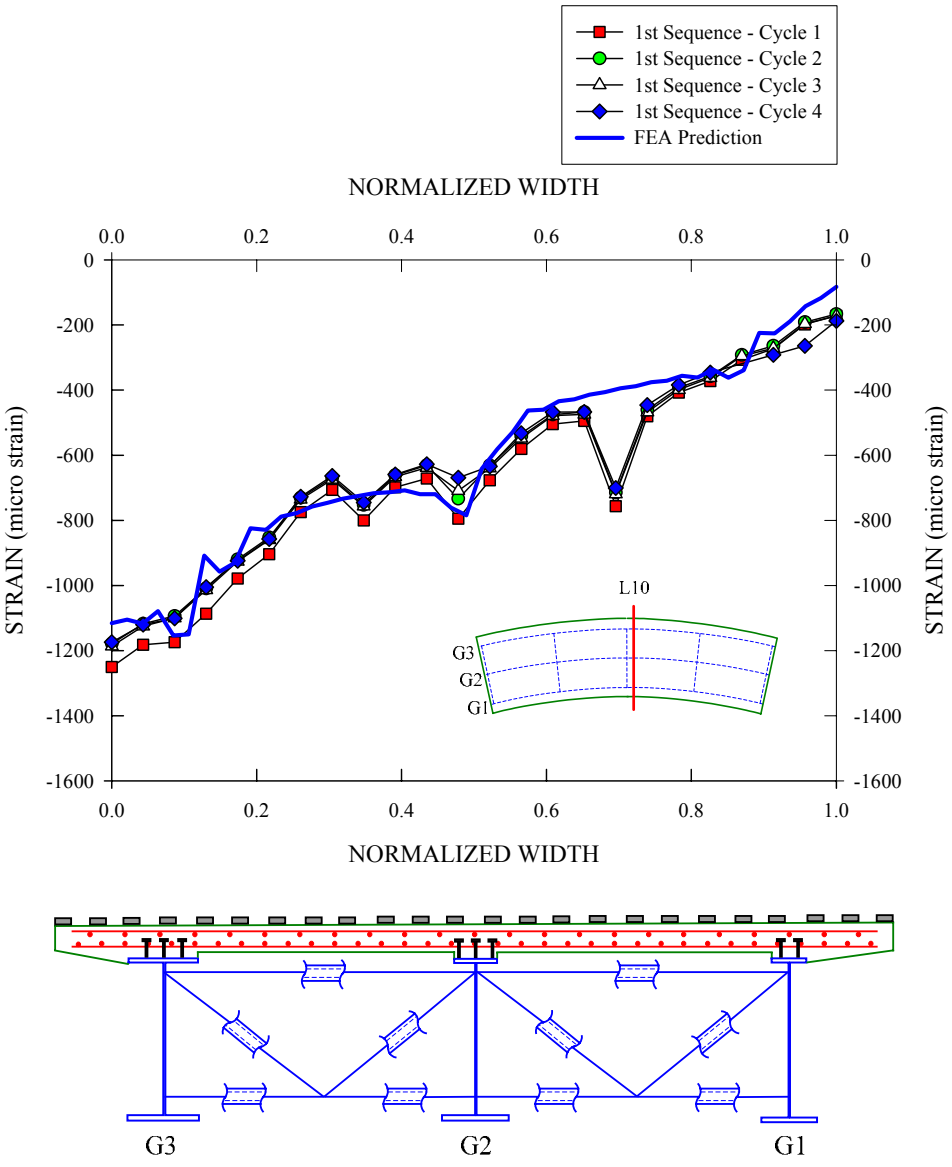

Figure 4.5.29. Slab longitudinal strain distribution for gage location L10 at load level E during the first and second sequences of Test 4a, strains associated with concrete shrinkage are not included in the plot.

4.5.4.5 Girder Bottom Flange Strains

Figures 4.5.30 and 4.5.31 provide measured major-axis and lateral bending strains along the normalized length of the G3 bottom flange for load level A, and corresponding FEA predictions based on a monotonic analysis of the test bridge are presented in the plots as well. It should be noted that the strain measurements for each loading cycle do not include residual strains from previous loading cycles. Figures 4.5.32 and 4.5.33 present similar plots for the measured and predicted major-axis and lateral bending strains for the G3 bottom flange at load level B and Figures 4.5.34 and 4.5 35 at load level C. From these figures, it can be seen that both the measured major-axis and lateral bending strains are closely matched by the corresponding FEA predictions. Also, it should be noted that the girder strains do not show noticeable changes with repeated loading cycles. In general, the majority of the bottom flange strains are less than the bottom flange yield strain for all the three load levels, with the exception of the mid-span strain. Figure 4.5.30 shows that the major-axis bending strain shows a small jump at mid-span due to the onset of yielding. As the applied load is further increased to higher load levels, B and C, the strain jump at mid-span changes to a sharp peak due to the further yielding. Similar observations are also made for the lateral bending strains. As will be presented in Chapter 5, these noticeable yielding activities are in general highly localized in close proximity to the flange outside tip region where there is a sharp strain gradient. Interestingly, much of the inside portion of the G3 bottom flange at mid-span is predominantly linear elastic, even at significantly high applied load levels.

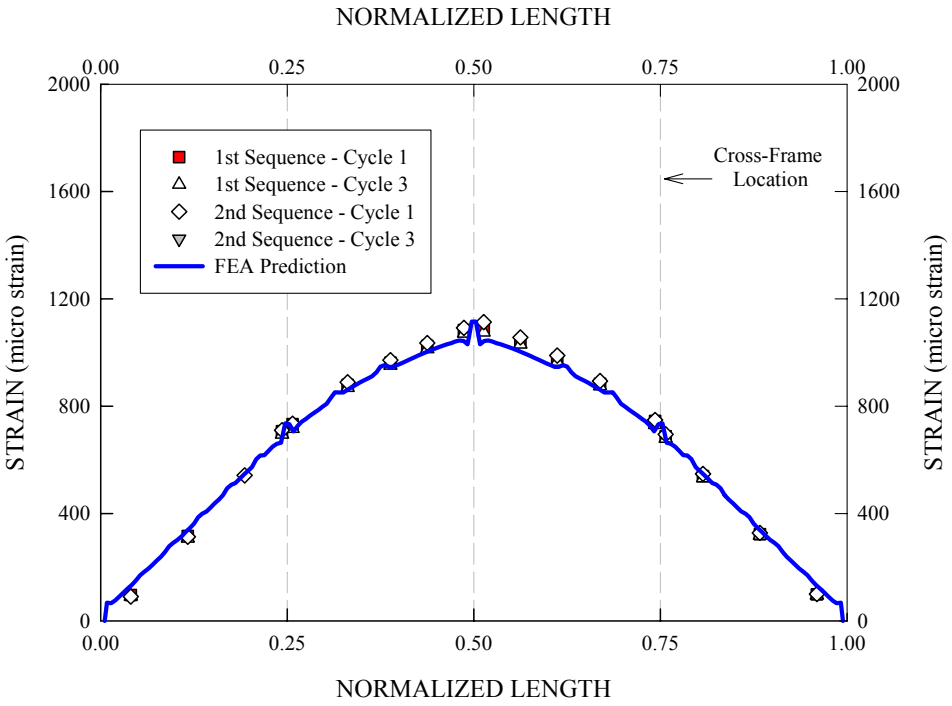

Figure 4.5.30. G3 bottom flange major-axis bending strain variations along the girder length, load level A.

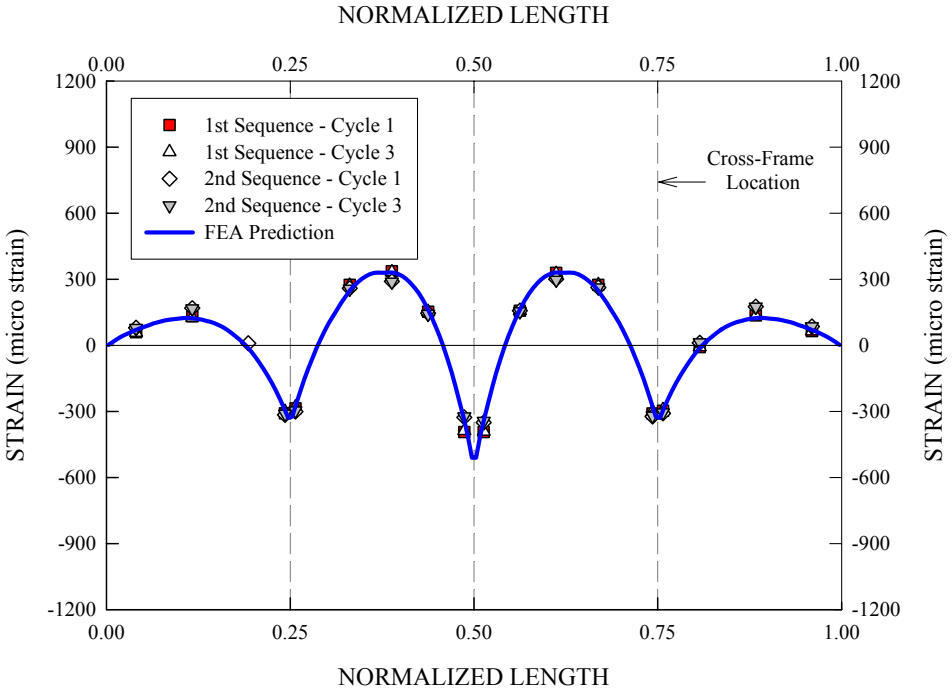

Figure 4.5.31. G3 bottom flange lateral bending strain variations along the girder length, load level A.

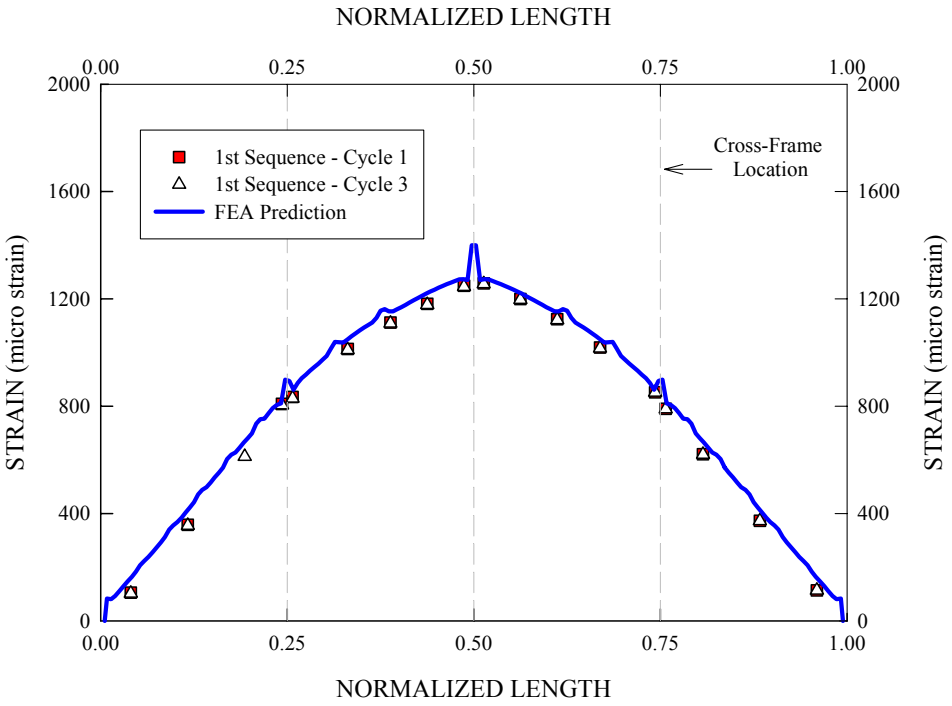

Figure 4.5.32. G3 bottom flange major-axis bending strain variations along the girder length, load level B.

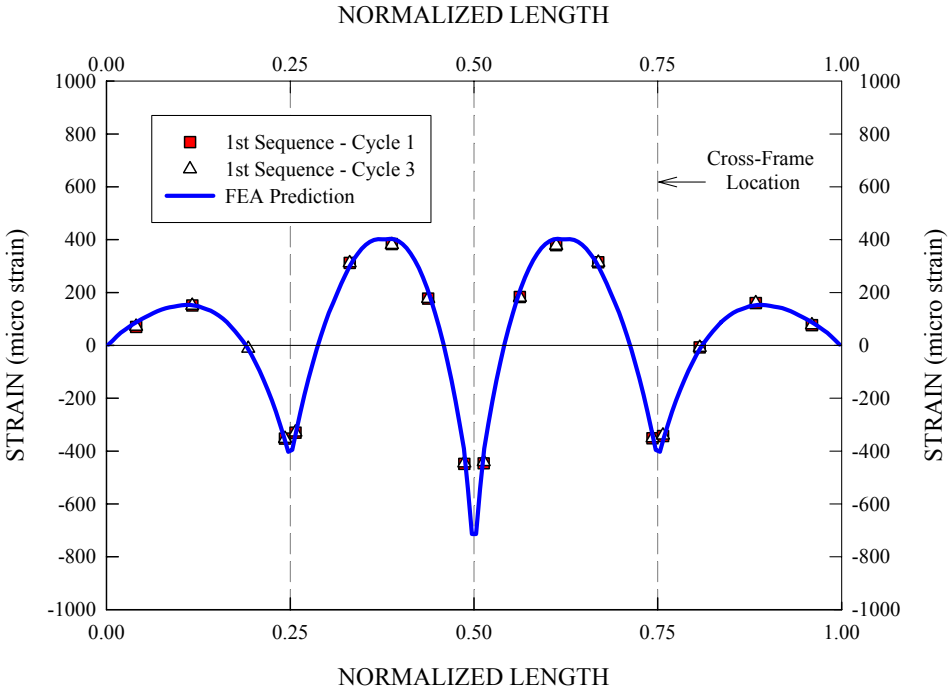

Figure 4.5.33. G3 bottom flange lateral bending strain variations along the girder length, load level B.

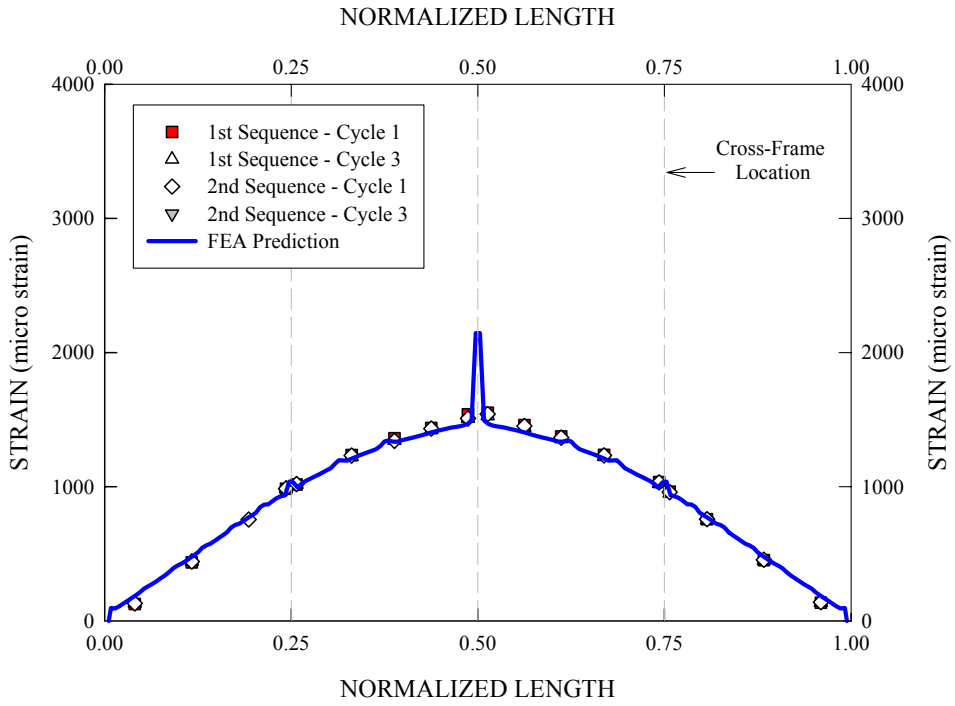

Figure 4.5.34. G3 bottom flange major-axis bending strain variations along the girder length, load level C.

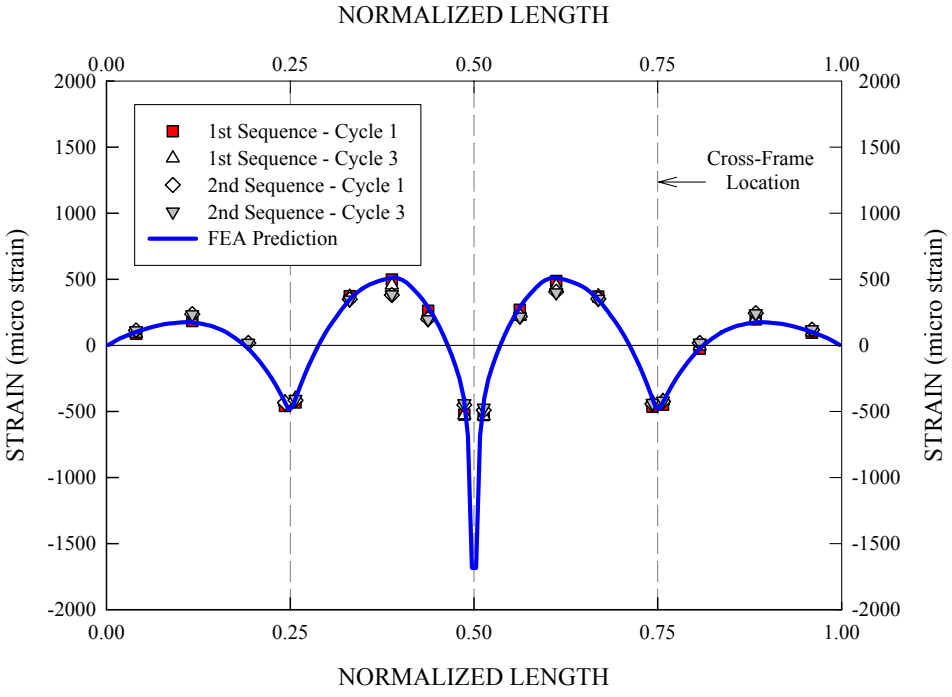

Figure 4.5.35. G3 bottom flange lateral bending strain variations along the girder length, load level C.

Figures 4.5.36 and 4.5.37 provide measured and predicted major-axis and lateral bending strains for the G3 bottom flange at load level D and Figures 4.5.38 and 4.5.39 at load level E. Similar to the prior lower applied load levels, it can be seen that the experimental values are well matched by the FEA predictions for both the load levels. It can be seen that the sharp strain peaks at the mid-span region is significantly increased in magnitude while other neighboring regions near mid-span are in general less than the flange yield strain. Another important thing to note here is that a large portion of the G3 bottom flange near the mid-length of the unbraced length on each side of the mid-span is also yielded. Interestingly, it can be seen that the FEA solutions produce more active yielding activities for this region than the measurement, which is evidenced by a relatively large strain bump in the strain predictions. As will be shown in Chapter 5, this yielding is also localized to the inside tip of the bottom flange.

When it comes to the major-axis and lateral bending strains for the G1 and G2 bottom flanges, good comparisons are also made between the measurements and predictions for all the load levels. In addition, although there is a difference in the degree of active yielding, overall yielding behavior of the G2 bottom flange is quite similar to that of the G3 bottom flange strains. In contrast, the G1 bottom flange strains are all within the linear elastic range for all the load levels. For more detailed information, interested readers are referred to Appendix B.

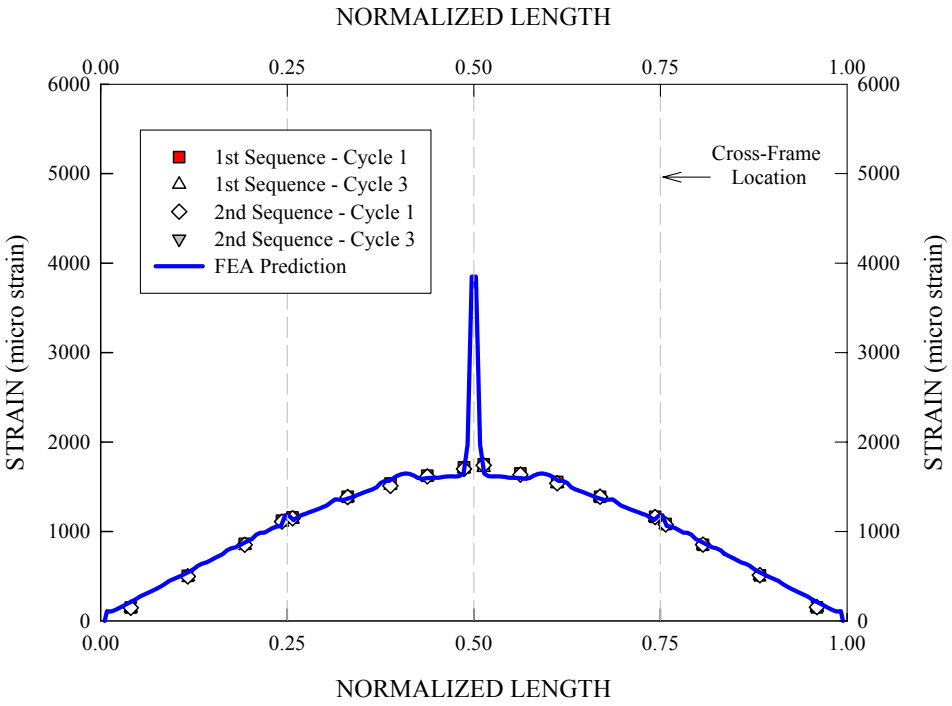

Figure 4.5.36. G3 bottom flange major-axis bending strain variations along the girder length, load level D.

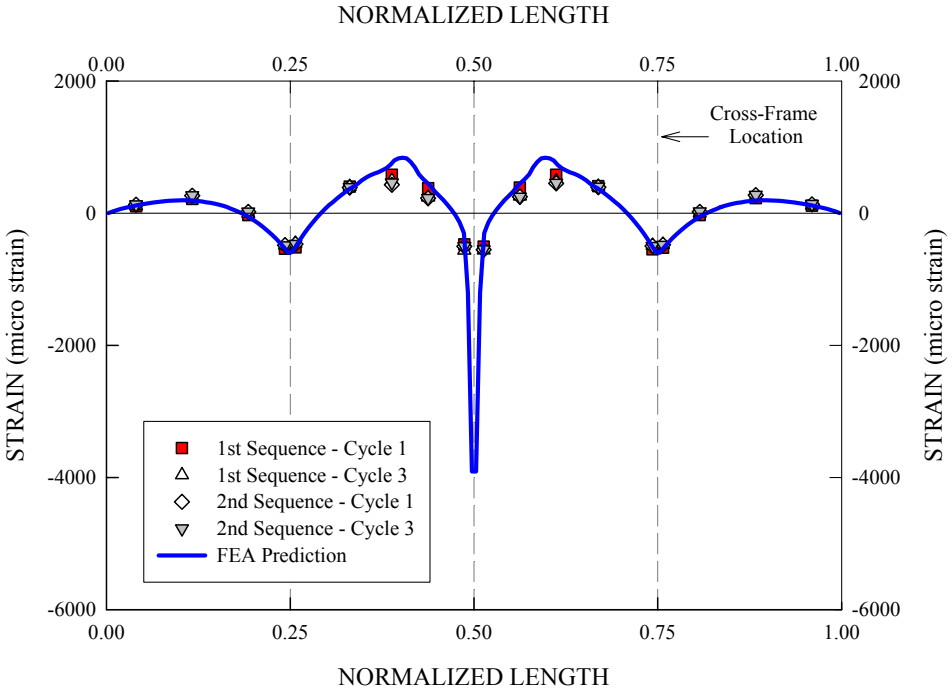

Figure 4.5.37. G3 bottom flange lateral bending strain variations along the girder length, load level D.

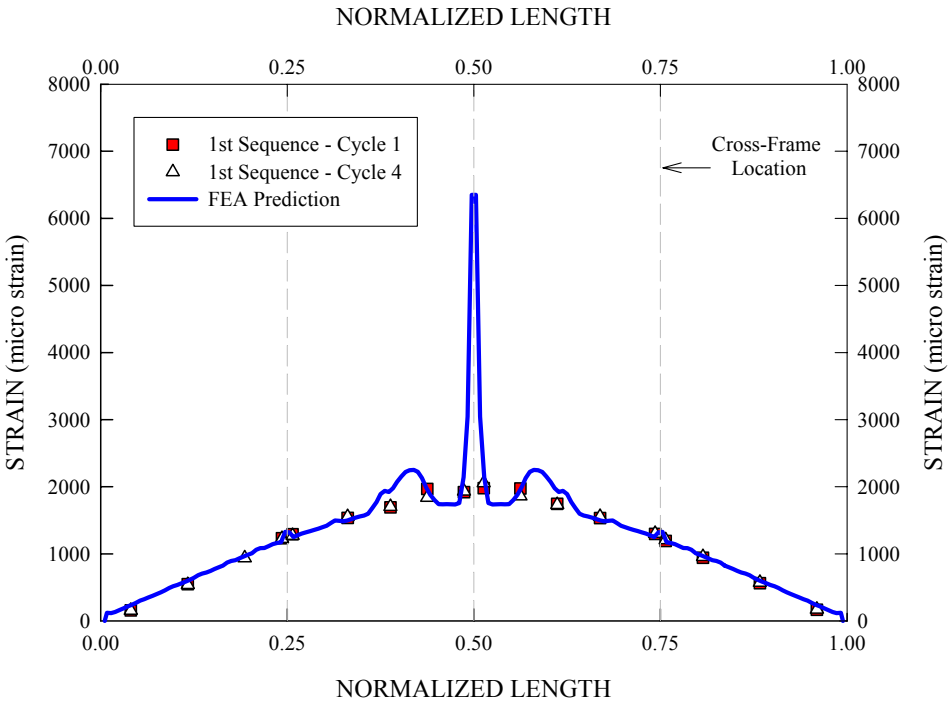

Figure 4.5.38. G3 bottom flange major-axis bending strain variations along the girder length, load level E.

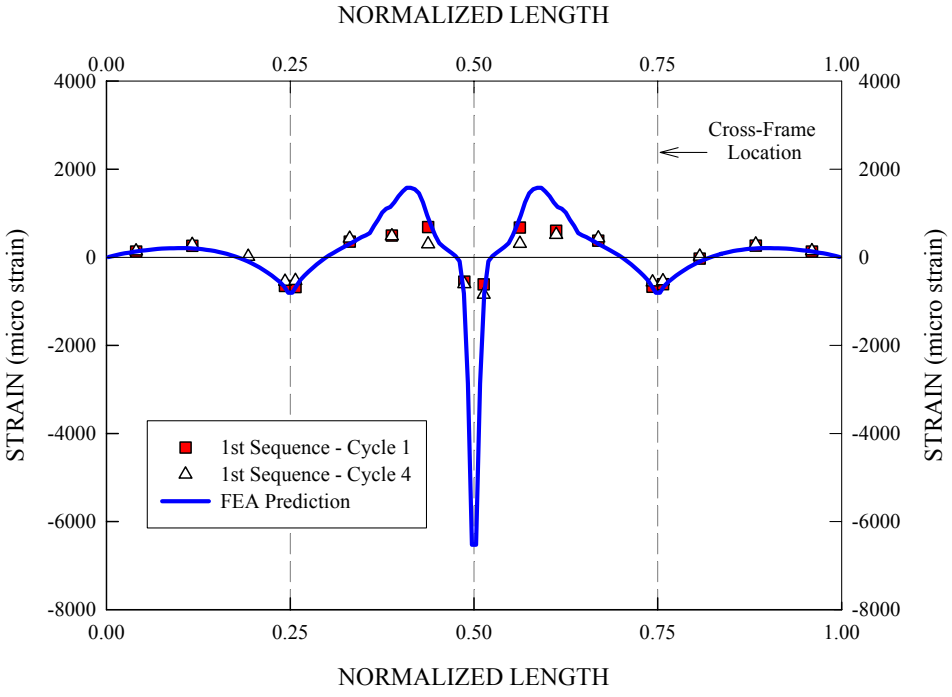

Figure 4.5.39. G3 bottom flange lateral bending strain variations along the girder length, load level E.

4.5.4.6 Cross-Frame Member Forces

Figure 4.5.40 provides envelope values of the member axial force for the bottom chord of the mid-span cross-frame attached to G3 that are obtained from repeated loading test of Test 4, Test 4a, and corresponding FEA predictions based on a monotonic loading analysis. Initial dead load member forces are included in the plot as well. Similar to other bridge responses presented earlier, it can be seen in Figure 4.5.40 that the initial member forces measured at the first loading cycle of each loading sequence are gradually increased with the subsequent repeated loading cycles. This leads to a gradual deviation of the measured data from the FEA solution.

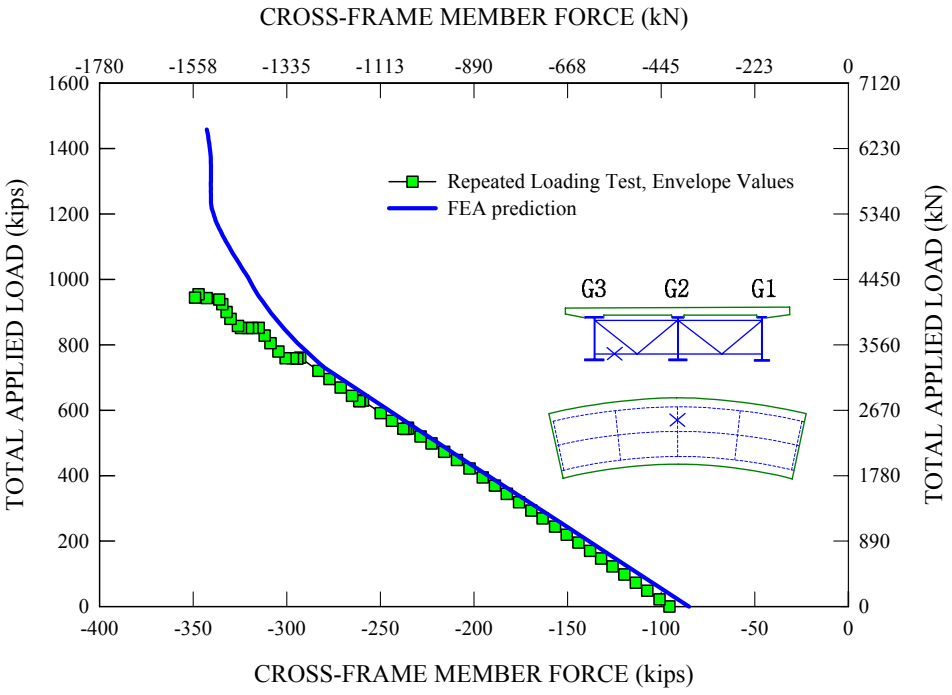

Figure 4.5.40. Envelope values of the member axial force for the bottom chord of the mid-span cross-frame attached to G3 obtained from repeated loading test of Test 4, Test 4a, and corresponding FEA predictions based on a monotonic loading analysis, initial dead load member forces are included in the plot as well.

Seemingly significant deviations for higher applied load levels are due to the fact that the measured initial deal load member force was taken before the start of Test 4a and added to the measured member force due to the directly applied loads for all the load levels. This is based on an assumption that the dead load member force for each loading cycle presumably comes back to zero upon the unloading of the test bridge system. However, the repeated loading FEA simulation indicates that there is a reduction in the cross-frame member force at the start of the loading cycles at load levels D and E. If these changes are incorporated into the measured data, the deviation between the measured and predicted values is not as far as shown in Figure 4.5.40.

4.5.5 Assessment of the Influence of the Repeated Loading Cycles

As shown in Figure 4.5.20, the total residual deflection just before the start of Test 4b is 3.75 in. This measurement was also confirmed by separate tape measurements. However, the corresponding FEA prediction obtained at the end of the repeated loading simulation is only 1.0 in. The source of significant additional residual deflections during the repeated loading tests is not clear at the time of completions of this research. The slip residuals at the concrete-steel interface were measurable both in the longitudinal and radial directions. However, their magnitudes were too small to cause the measured residual deflections. The girder vertical reactions and slab mid-span longitudinal strains were predominantly linear. There are no indications of significant additional strains due to the repeated loading cycles. In addition, the girder bottom flange strains did not show any significant changes during the repeated loading cycles. There are no indications of significant changes in the cross-frame member forces during the repeated loading cycles.

No causes of the residual deflections are apparent from the measured test data. Other potential sources are as follows:

- Friction forces may have provided some degree of horizontal restraints at the girder bearings, and nonlinear bridge behavior may have been caused by the friction restraints. However, the bridge responses are predicted accurately without the modeling of any unintended horizontal restraints. These responses are provided in Beshah (2006).
- Slab portions away from gauge locations may have experienced cracking and softening without any influence on the slab mid-span longitudinal strains. In this case, the girder bottom flange strains could have been also affected. However, the experimental data shows that they were not affected.
- Concrete may have experienced stiffness degradation associated with hysteresis within the nominally elastic range. However, the experimental data shows that there was no significant influence on the girder bottom flange strains.
- Cross-frame connections may have experienced slips. This type of behavior is known to not necessarily be an abrupt action, but rather a gradual one in terms of load versus deflection.
- Cross-frame gusset plates and connection plates may have deformed locally.
- Finally, there may have been some drifts in the experimental measurements. However, this is not likely to be a major cause since the residual deflections were confirmed to exist by the tape measurements.

Ongoing research discussed in the future work section of this work needs to address the above hypotheses. Fortunately, the repeated loadings, although increasing the inelastic vertical and radial deflection of the test bridge, do not show any significant effect on the subsequent responses.

In order to address the effects of the repeated loading tests on the test bridge responses during its ultimate loading test, two full nonlinear FEA simulations are performed. The first FEA simulation is a control case involving only the monotonic loading of the test bridge FEA model, whereas the second FEA simulation concerns the repeated loading of the test bridge following all the experimental loading sequences outlined before, as well as the final monotonic loading of the test bridge FEA model for its ultimate load capacity. It should be noted that the first FEA simulation treats the test bridge as if it were a virgin structure without any memory of the prior repeated loading cycles.

Figure 4.5.41 provides resulting load-vertical deflection curves obtained from these two analyses. Along with the FEA predictions, the experimental results obtained from the final monotonic testing of the test bridge are also presented in the plot for the comparison purposes. It is important to note that the deflections in Figure 4.5.41 are plotted relative to the position of the test bridge at the start of Test 4b. In other words, residual deflections left during the repeated loading test are not included in the plot.

In general, it can be seen that both of the FEA predictions are comparable to the experimental data over the entire loading range. The two FEA solutions produce essentially identical responses up to a total applied load of 3781 kN (850 kips).

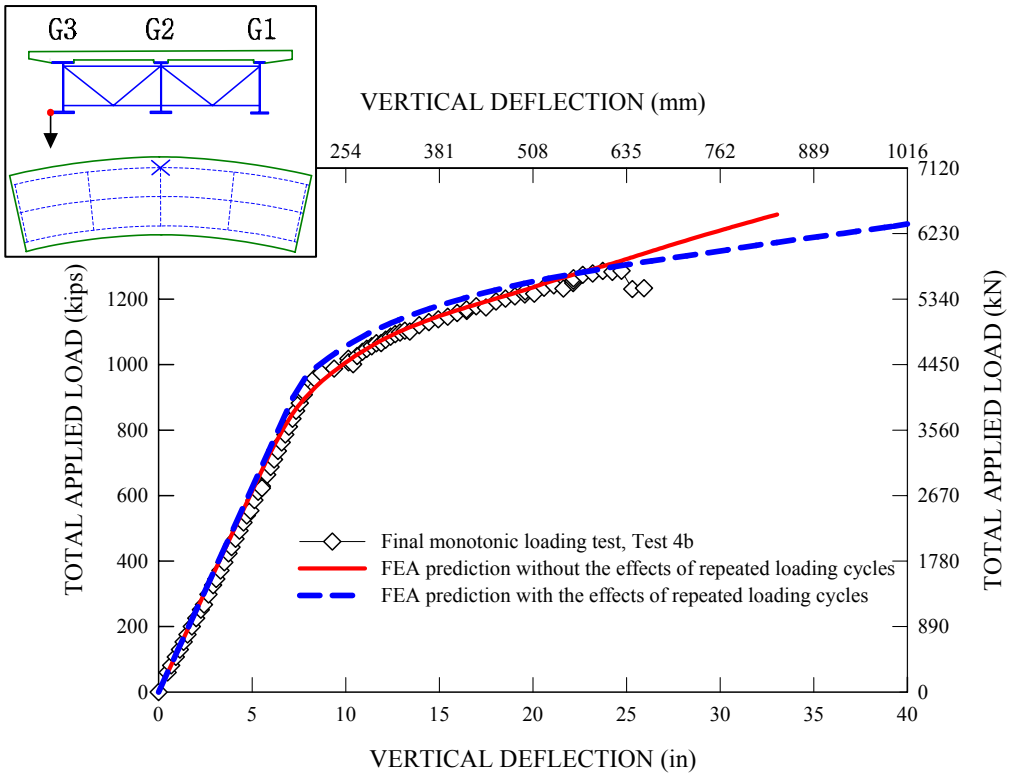

Figure 4.5.41. Measured mid-span vertical defection for the outside tip of the G3 bottom flange obtained from the final monotonic loading test of Test 4, Test 4b, versus corresponding FEA solutions with and without the effects of the previous repeated loading cycles.

However, for higher applied load levels beyond 3718 kN (850 kips), two FEA solutions start to show slight deviations from each other. In particular, one can observe that the FEA solution including the effects of the prior repeated loading cycles show a knee at a total applied load of 4226 kN (950 kips). A closer look at the experimental data also reveals that there is a knee in the plot. However, the FEA solution not including the effects of the prior repeated loading cycles does not show this knee. Instead, it shows a smooth nonlinear transition at this load level. This indicates that the test bridge system behaves in a linear fashion up to a total applied load of 4226 kN (950 kips) during the final monotonic testing, which is the peak applied load of load level E in the first loading

sequence of Test 4a. In other words, the proportional limit has been extended from a total applied load of 3559 kN (850 kips) to 4226 kN (950 kips). This behavior can be understood as follows. Figure 4.5.42 shows a general nonlinear load-displacement response for a structure subjected to loading and unloading. Once the peak target load accompanying a plastic deformation of the structure is reached, the entire structural system is unloaded. Then, the structural system is elastically unloaded (springback).

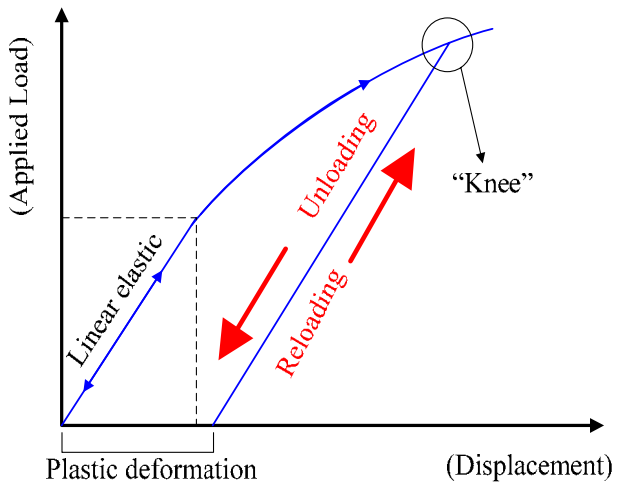

Figure. 4.5.42. General nonlinear load-displacement response of a structure subjected to loading and unloading and work-hardening phenomenon at the structural level.

For a subsequent reloading, the structural system is elastically loaded until the applied load reaches the prior peak applied load. Then, the deflection curve makes a transition from the linear elastic line to the nonlinear curve, forming the knee as illustrated in Figure 4.5.42. For further plastic deformation of the structure, there should be an increase in the applied loads. The peak applied load up to which the structure behaves elastically is gradually increased with accumulation of the plastic deformation. This is referred to as "work hardening" at the structural level in this research. It should

be noted that this definition is different than a typical definition for the work hardening that refers to an increase in strength of a material that accompanies plastic deformation. The source of the work hardening at the structural level may be due to the residual stress field left in the structural system upon the unloading of the structure. The residual stresses delay the onset of yielding until the previous peak applied load that accompanies the plastic deformation is reached. Or, inelastic force redistribution within the structural system may be responsible for the work hardening. Detailed examinations of the girder strains show that girders G2 and G3 were work-hardened during the prior repeated loading sequences, in particular at load level E. This leads to the extension of the proportional limit shown in Figure 4.5.41.

Based on the above findings, it can be seen that the full nonlinear FEA simulation including the effects of the prior repeated loading cycles is a better representation of the final monotonic testing of the composite test bridge system for its ultimate capacity. Therefore, the results of the final monotonic test presented in Chapter 5 are discussed largely in relation to the full nonlinear FEA solutions including the effects of the prior repeated loading cycles. However, the results of the FEA solutions not including the effects of the prior repeated loading cycles are also presented in Chapter 5 for reference.

CHAPTER 5

ULTIMATE MONOTONIC LOADING TEST, EXPERIMENTAL AND ANALYTICAL RESULTS

5.1 Overview

Subsequent to the repeated loading tests including Tests 2, 3 and 4a, a single monotonic loading test was conducted on the composite test bridge, using the same loading pattern as in Test 4a. This final test, referred to as Test 4b, was aimed to investigate the ultimate strength and associated behavior of the test bridge. Figure 4.5.1 shows a snapshot of the composite test bridge with the loading fixtures configured for Test 4a. The configuration for Test 4b was the same except that the tie-down beams were configured differently (see Section 4.5.3). This figure shows that the experimental loading pattern involved a total of nine hydraulic rams to simulate the AASHTO live load model of two design truck loads plus two lane loads. Figure 4.5.1 shows the Type 1 tie-down arrangement discussed in Section 4.5.3, used for chairing of the jacks. This tie-down arrangement was modified to the Type 2 arrangement shown in Figure 4.5.9 at the end of the first loading sequence of Test 4a. Test 4b involved a total of six chairing operations to load the bridge to its ultimate capacity.

Table 5.1.1 provides measured reactions at the girder end supports and vertical deflections at the midspan outside tip of the girder bottom flanges before and after the chairing operations. Similar to the findings for Test 4a, Table 5.1.1 shows that there are some changes in the total loads, the magnitude and distribution of the reactions, and the girder maximum deflections during the chairing operations. However, it should be noted that the extent of these deviations is generally small such that, upon the re-loading of the

bridge after chairing of the jacks, the altered bridge equilibrium configurations are effectively restored to the path that would have occurred if the chairing had not been required. To illustrate, Figure 5.1.1 shows a measured load-deflection curve for the midspan outside tip of the G3 bottom flange that focuses on the response before and after the second chairing operation in Table 5.1.1. It can be clearly seen that it takes a smaller total applied load to induce the same deflection due to the chairing operation, causing a slight departure in the equilibrium configuration. However, it should be noted that, upon the re-loading of the test bridge, the load-deflection curve tends to come back to the expected equilibrium path if the chairing had not been required, indicated by the dashed line.

Table 5.1.1 Measured girder reactions and vertical deflections before and after chairing operations during the final monotonic loading test (Beshah 2006).

Tie-downs	Applied Load at Chairing kN (kips)		Girder Reactions kN (kips)				Girder Vertical Deflections mm (in)		
			G1	G2	G3	Total	G1	G2	G3
1st	1139 (256)	before	107 (24)	311 (70)	721 (162)	1139 (256)	25.9 (1.02)	42.2 (1.66)	57.4 (2.26)
		after	111 (25)	329 (74)	774 (174)	1214 (267)	27.4 (1.08)	45.0 (1.77)	61.7 (2.43)
2nd	2874 (646)	before	245 (55)	792 (178)	1837 (413)	2874 (646)	61.7 (2.43)	102 (4.01)	140 (5.53)
		after	227 (51)	774 (174)	1824 (410)	2825 (635)	60.5 (2.38)	101 (3.99)	140 (5.52)
3rd	4546 (1022)	before	427 (96)	1188 (267)	2931 (659)	4546 (1022)	106 (4.18)	183 (7.22)	258 (10.2)
		after	414 (93)	1170 (263)	2940 (661)	4524 (1017)	106 (4.17)	186 (7.33)	264 (10.4)
4th	5205 (1170)	before	525 (118)	1308 (294)	3372 (758)	5205 (1170)	148 (5.84)	285 (11.22)	418 (16.5)
		after	507 (114)	1303 (293)	3394 (763)	5204 (1170)	150 (5.89)	292 (11.5)	418 (16.5)
5th	5391 (1212)	before	547 (123)	1339 (301)	3505 (788)	5391 (1212)	166 (6.52)	333 (13.1)	484 (19.0)
		after	552 (124)	1339 (301)	3519 (791)	5410 (1216)	168 (6.63)	341 (13.4)	497 (19.6)
6th	5538 (1245)	before	569 (128)	1366 (307)	3603 (810)	5538 (1245)	181 (7.14)	375 (14.8)	536 (21.1)
		after	552 (124)	1334 (300)	3581 (805)	5467 (1229)	183 (7.19)	378 (14.9)	549 (21.6)

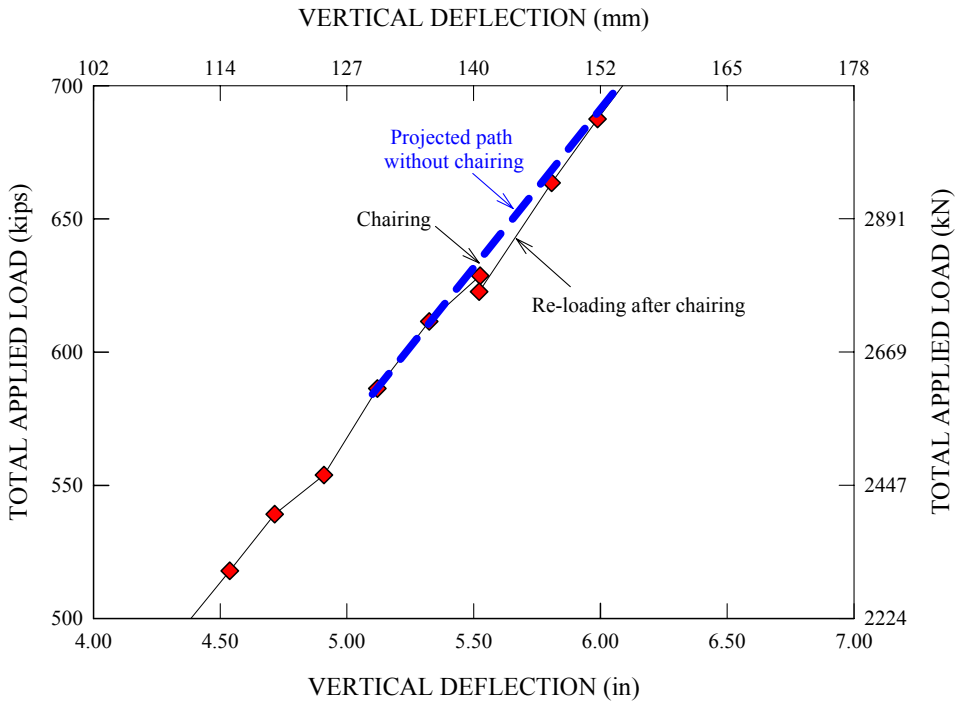

Figure 5.1.1. Measured load versus vertical deflection for the midspan outside tip of the G3 bottom flange during the ultimate load test, focusing on the response before and after the second tie-down operation at a total applied load of 2874 kN (646 kips).

Figure 5.1.2 shows radial slip measurements taken at the steel-concrete interface of the G3 midspan indicating the six load levels at which the chairing operations were carried out. It can be seen that although there are some additional slip displacements due to the tie-down operations, their magnitudes are generally small enough such that their effect on the bridge response is expected to be insignificant. Similar findings are also made for longitudinal slip measurements taken at the girder ends.

Based on the above observations, as well as other data discussed subsequently in this Chapter, it can be concluded that the chairing operations did not have any significant influence on the component and system responses of the test bridge during the ultimate load test.

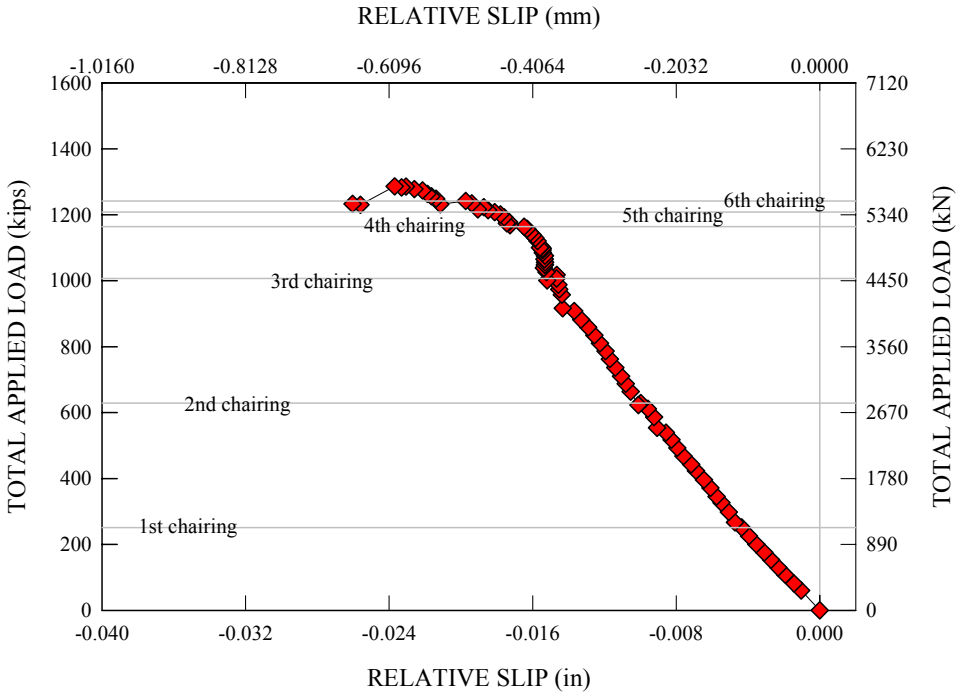

Figure 5.1.2. Radial slip measured at the midspan of G3 during the ultimate load test with the six load levels at which the tie-down operations were carried out marked on the plot (Beshah 2006).

A single important change made to the test bridge as part of the preparations for the ultimate load test is that cross-frames members anticipated to experience yielding were strengthened. These members were the bottom chords and diagonal members for the mid- and quarter-span cross-frames located between G2 and G3. Figure 5.1.3 shows a typical cross-frame with retrofitted members, and Figure 5.1.4 gives a close-up view of the retrofitted bottom chord strut where a steel tube of 54.1 cm^2 (8.39 in^2) in area encloses an existing tube of 24.1 cm^2 (3.73 in^2) in area.

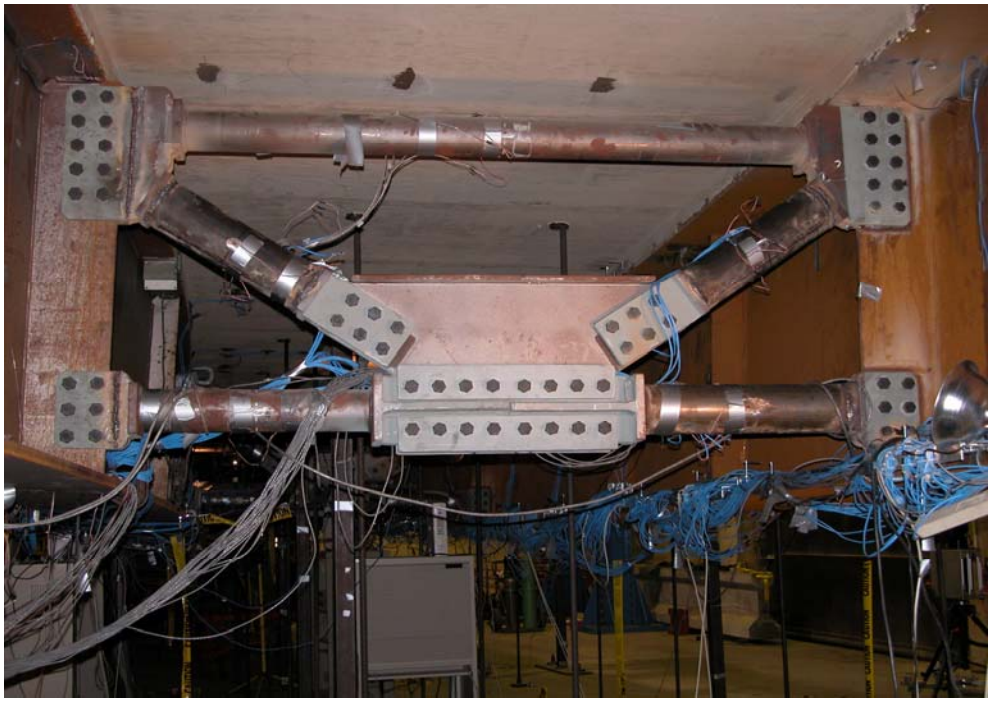

Figure 5.1.3. Typical G2-G3 cross-frame with retrofitted members for the ultimate load test, courtesy of FHWA.

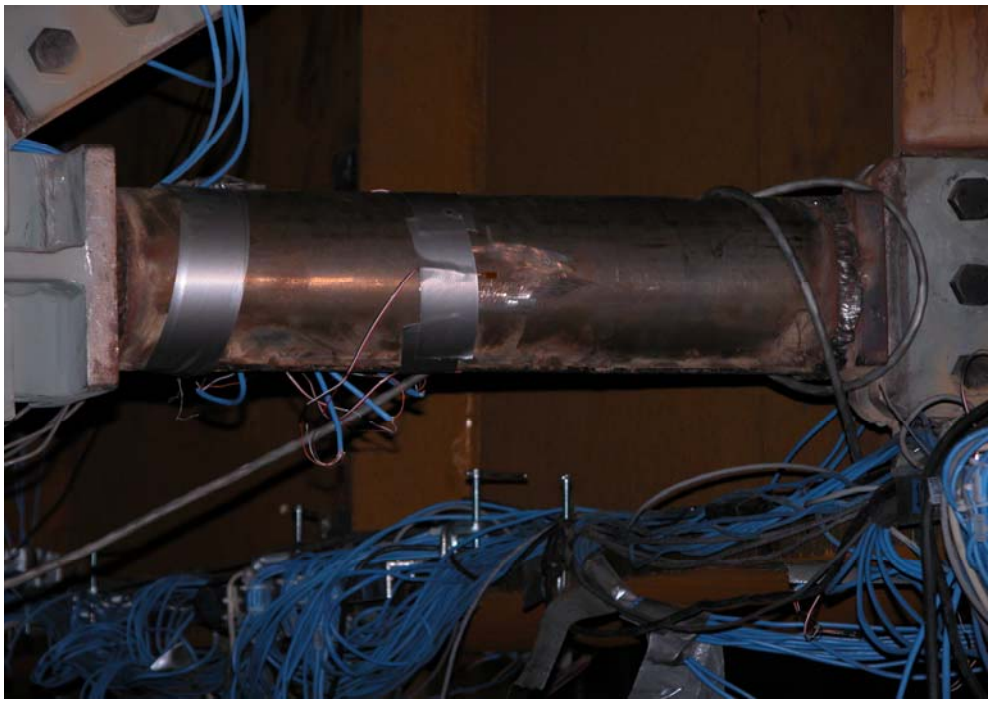

Figure 5.1.4. Retrofitted bottom chord strut, courtesy of FHWA.

In parallel with the ultimate load test, two full nonlinear FEA simulations are conducted to analytically investigate the strength behavior of the test bridge during the ultimate load test. A unique distinction between these two FEA solutions is that one includes the effects of the prior repeated loading tests while the other does not. It is clear from the discussions of the effects of the repeated loading tests in Chapter 4 that the test bridge was loaded inelastically during the cycles at load levels D and E, in the first sequence of Test 4a. As a result, the bridge experienced a noticeable increase in its permanent deflections. Therefore, the first FEA solution including the effects of the repeated loading tests is believed to be a better representation of the strength behavior of the test bridge during the final monotonic loading test. However, it should be noted that the degree of nonlinearity observed in the prior repeated loading tests is generally minor. Therefore, the latter FEA solution treating the test bridge as a virgin structure without any memory of the prior repeated loading tests also gives good estimates of the experimental measurements. Furthermore, since other types of bridge structures considered in the parametric studies of this work are only subjected to a single monotonic loading rather than repeated loadings, the FEA solution using a monotonic loading scheme needs to be evaluated as to its usefulness as a base case that the behavior of other types of bridge configurations can be evaluated against. Also, the monotonic loading analysis of the composite test bridge may be more realistic, since the levels of applied loads at levels D, E and above would correspond only to a once-in-a-life-time loading event. In this regard, various results obtained from two different FEA simulations are presented side by side along with corresponding experimental data in the remaining sections of this chapter. Emphasis is placed on the FEA simulations that include the effects of the prior repeated

loading tests, since these simulations are the most faithful representation of the actual loading history on the test bridge.

Of the various load levels defined in Chapter 4, all of the discussions in this chapter center primarily around two resistance levels related to the AASHTO (2004b) provisions: the M_y- and M_p-based 1/3 rule load levels on G3. The M_y-based 1/3 rule load level relates to the total applied loads inducing first yield moment on G3 of the composite test bridge, minus a reduction for flange lateral bending effects. This is the resistance limit for the design of horizontally curved I-girder bridge structures allowed by the newly adopted AASHTO (2004b) steel bridge design provisions. The limitations imposed on the curved bridges are mainly due to the lack of a better understanding about the strength behavior of these types of structures beyond the first yield moment, in particular the validity of elastic analysis. On the contrary, the M_p-based 1/3 rule load level relates to the resistance level that can be obtained by using the plastic moment resistance of the G3 composite section as a base design resistance, but with a reduction due to flange lateral bending associated with horizontal curvature and other effects. In particular, much of the discussions in this chapter focus on the behavior at the M_p-based 1/3 rule load level on G3.

The organization of this chapter is as follows. The chapter first describes the overall bridge responses including the overall bridge deformations, vertical and radial deflections at midspan, cross-section deformations and overall girder end reactions. This is followed by a detailed discussion of various component responses. These responses include major-axis and lateral bending strains in the steel sections, equivalent plastic strains on the steel sections, radial and longitudinal slab stresses and corresponding strains, damage

evolution in the slab concrete, crack patterns in the slab, cross-frame member forces and behavior of intermediate transverse stiffeners. The chapter then closes with an evaluation of the force transfer mechanisms among the test bridge girders for the noncomposite dead load and composite live load test bridge configurations. This is achieved by inspecting the FEA internal moment and shear force diagrams at the end of concrete casting and at a few significant load levels during the ultimate live load test, in particular the M_p-based 1/3 rule load level on G3. The main focus is on the component and system responses of the slab when the outermost girder, G3, reaches its M_p-based 1/3 rule resistance.

5.2 Overall Bridge Deformations

Figure 5.2.1 shows a snapshot of the deformed composite test bridge just before the total applied load reaches 5783 kN (1300 kips). It should be noted that this is the maximum load resisted by test bridge just before concrete spalling and crushing occurred in the G3 overhang region at its midspan.

At a first glance, it is difficult to see the level of deformation at this load level from Figure 5.2.1. However, the midspan outside tip of the G3 bottom flange has reached a total deflection of 610 mm (24 in) due to the directly applied loads (not including the prior residual displacements from Test 4a), which is half of the nominal girder depth. Furthermore, as shown in the following sections of this Chapter, the load-deflection responses are well into the nonlinear range at this load level due to extensive yielding on the steel sections and wide spread of concrete slab cracking. Nonetheless, it is important to note that the composite test bridge does not show any sign of severe structural distress at this load level, which is significantly larger than the M_y- and M_p-based 1/3 rule strength load levels on G3 of 3470 kN (780 kips) and 3959 kN (890 kips), respectively.

Figure 5.2.2 gives a perspective view of the deformed test bridge FEA model with contours of vertical deflections just before spalling and crushing of the slab concrete in the experiment, when the midspan outside tip of the G3 bottom flange reaches a deflection of 610 mm (24 in) due to a total applied load of 5783 kN (1300 kips). Figure 5.2.3 provides the same perspective view as Figure 5.2.2, but focuses on the deformed geometry of the steel superstructure alone by hiding the geometry of the slab. In both of these plots, the initial dead-load displacements are *not* included in the deflection contours; however, the predicted permanent displacements at the end of Test 4a are included. Interestingly, it can be seen that a maximum deflection of 689 mm (27.14 in) actually occurs at the midspan outer edge of the overhang outside of G3. This is due to the torsional rotation of the bridge cross-section. Detailed characteristics concerning the vertical and radial girder deflections are presented in the following sections.

Figure. 5.2.1. Picture of the deformed composite test bridge just prior to the spalling and crushing of the slab concrete at the midspan overhang region outside G3, deflection at midspan outside tip of the G3 bottom flange = 610 mm (24 in), total applied load = 5783 kN (1300 kips), courtesy of FHWA.

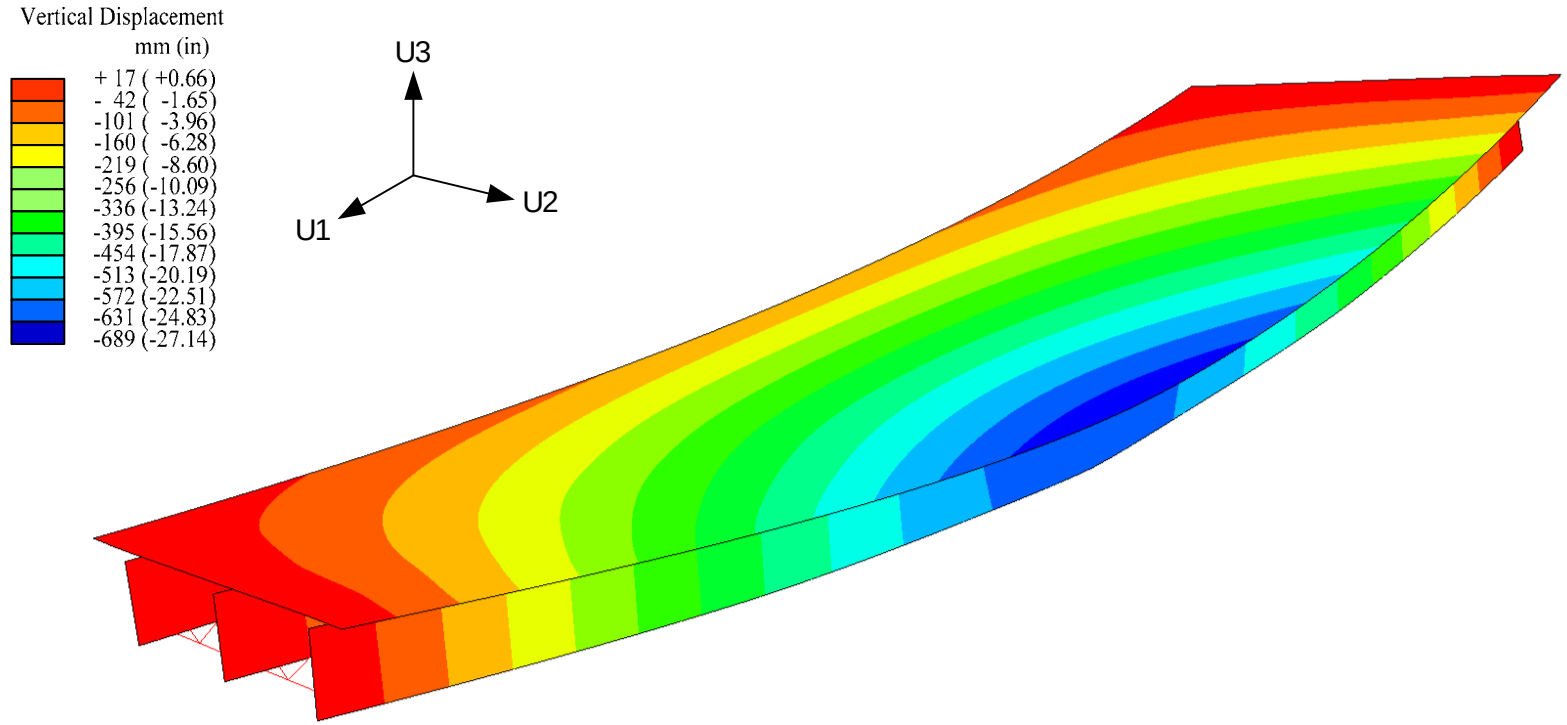

Figure. 5.2.2. Perspective view of the deformed test bridge FEA model with contours of the vertical deflections just prior to spalling and crushing of the slab concrete in the experimental test, deflection at midspan outside tip of the G3 bottom flange = 610 mm (24 in), total applied load = 5783 kN (1300 kips), initial dead-load displacements *not* included in the contours, predicted permanent displacements from Test 4a included, Displacement Scale Factor = 2.0.

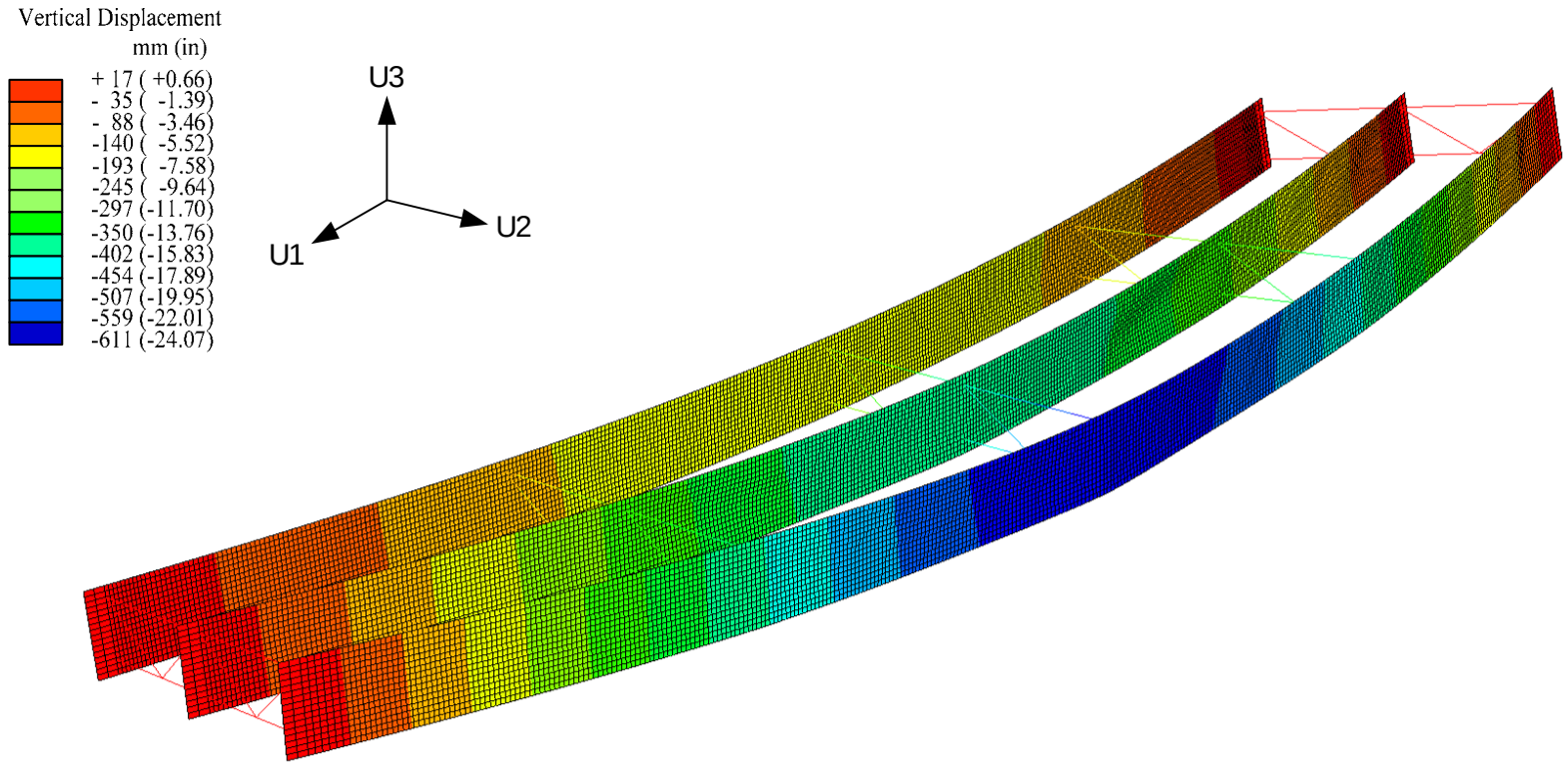

Figure. 5.2.3. Perspective view of the FEA model of the deformed steel superstructure with the contours of vertical deflections just prior to spalling and crushing of the slab concrete in the experimental test, deflection at midspan outside tip of the G3 bottom flange = 610 mm (24 in), total applied load = 5783 kN (1300 kips), initial dead-load displacements *not* included in the contours, predicted permanent displacements from Test 4a included, Displacement Scale Factor = 2.0.

5.3 Girder Vertical Deflections

Figure 5.3.1 provides measured and predicted vertical deflections for the midspan outside tip of the G1 bottom flange (i.e., the tip further from the center of curvature of the bridge). The dead-load displacements and the residual displacements prior to Test 4b are not included in these plots. Figures 5.3.2 and 5.3.3 give similar plots for the G2 and G3 bottom flanges. It can be seen that both of the FEA solutions presented in each of the plots compare reasonably well with the measured data throughout the entire loading history. However, a closer look at the plots reveals that a better correlation is obtained for the FEA solutions including the effects of the prior repeated loading tests relative to the measured data. To be more specific, the FEA solutions including the effects of the prior repeated loading tests, which are indicated by the solid line in the figures, successfully capture the extension of the proportional limit in the measured load-deflection curves due to the yielding of the steel sections during the prior repeated loading tests. Also, they do a slightly better job of capturing the ordinate and the slope of the load-deflection curves observed at the highest applied load levels.

Given the fact that the total factored design load causing the maximum bending effects for the flexural design of G3 is 2398 kN (539 kips), it can be seen that the overall load-vertical deflection responses are effectively linear for the applied loads up to approximately 1.67 times the design load level. It should be noted that this conservatism is due partly to the higher measured yield strengths compared to the nominal yield strengths used in the design, the differences between the actual and the nominal geometries, and the fact that the AASHTO Strength I load combination combines the above factored live load with 1.25 of the factored dead load. Also, the test loadings are somewhat different than the AASHTO design loadings. Therefore, it is more meaningful

to consider the responses relative to the load levels at which the M_y or M_p-based 1/3 rules are violated based on a linear elastic analysis for the test loading, using the measured material properties and cross-section geometries.

Based on the results of linear elastic analyses of the test bridge subjected to the same loading pattern as in the ultimate load test, two significant load levels are obtained and marked on the deflection plots as the M_y- and M_p-based 1/3 rule load levels on G3. It can be seen that the girder vertical deflection responses are essentially linear up to the M_p-based 1/3 rule load level of 3959 kN (890 kips) for the measured data and the FEA solutions, including the effects of the prior repeated loading tests. In contrast, it can be seen that there is a slight nonlinearity involved in the FEA solution without the effects of prior repeated loading tests at this load level. However, it is important to note that the extent of this nonlinearity is fairly minor such that the overall deflection responses still can be considered linear. More importantly, it is worthwhile to note that the M_p-based 1/3 rule load level corresponds to a point where the load/deflection curves start to show significant nonlinear behavior.

Figure 5.3.4 gives a plan view of the deformed slab with the contours of vertical deflections at the total applied load of 5783 kN (1300 kips) corresponding to spalling and crushing of the slab concrete in the experimental test. The initial dead-load displacements are *not* included in the deflection contours; however, the predicted permanent displacements at the end of Test 4a are included. The computed maximum vertical deflection is measured at the outside tip of the overhang outside G3, and its magnitude is 686 mm (27 in). This is larger than the maximum G3 bottom flange deflection by about 76 mm (3 in).

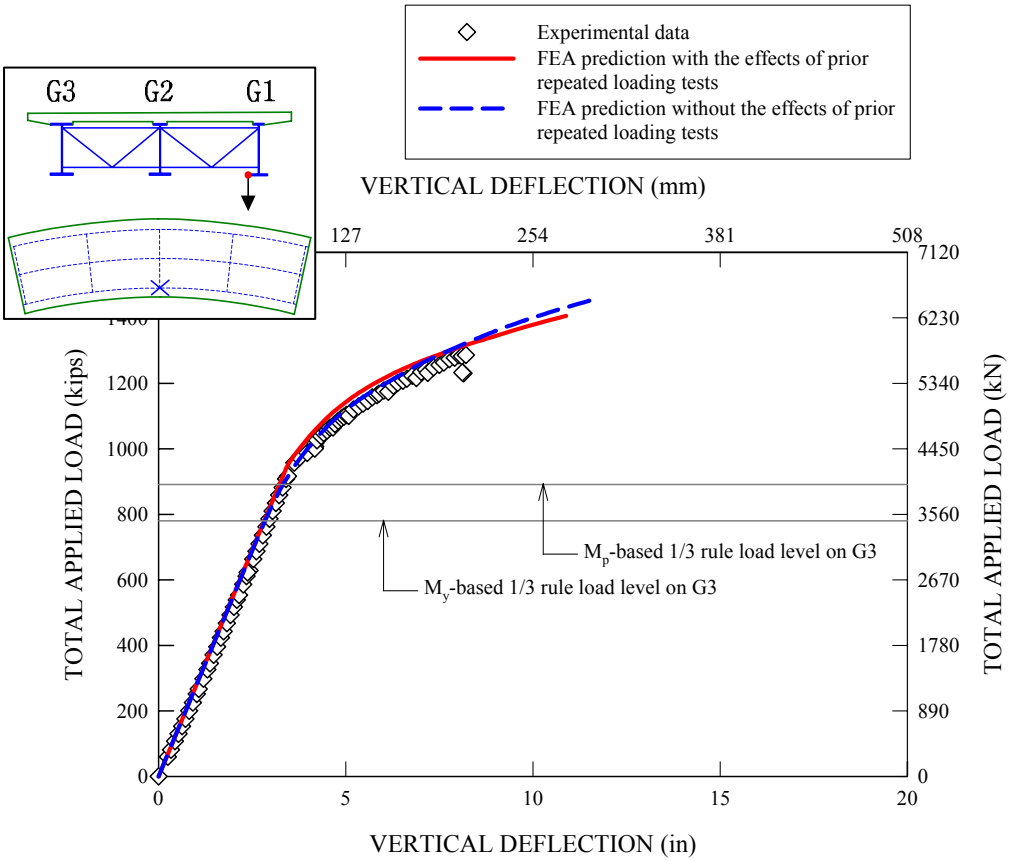

Figure 5.3.1. Load versus measured and predicted vertical deflections for the midspan outside tip of the G1 bottom flange due to the applied loads during the ultimate load test (dead load deflections and residual deflections prior to Test 4b are not included in the plot).

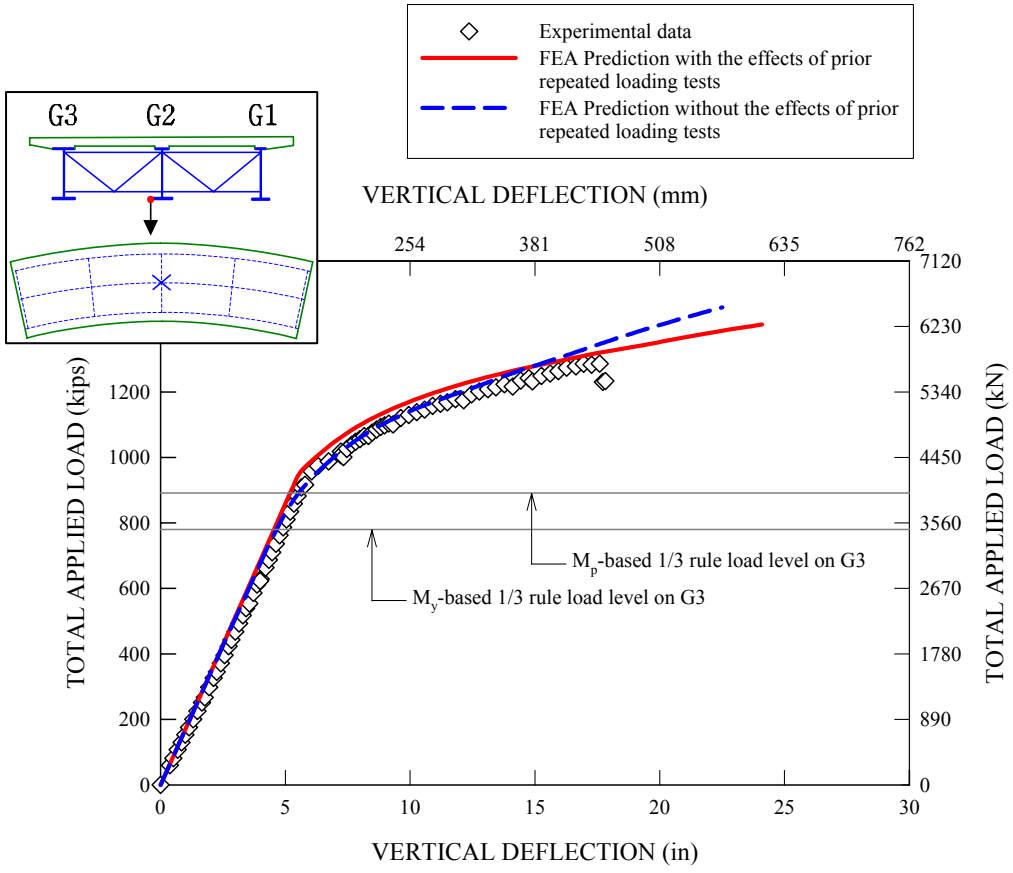

Figure 5.3.2. Load versus measured and predicted vertical deflections for the midspan outside tip of the G2 bottom flange due to the applied loads during the ultimate load test (dead load deflections and residual deflections prior to Test 4b are not included in the plot).

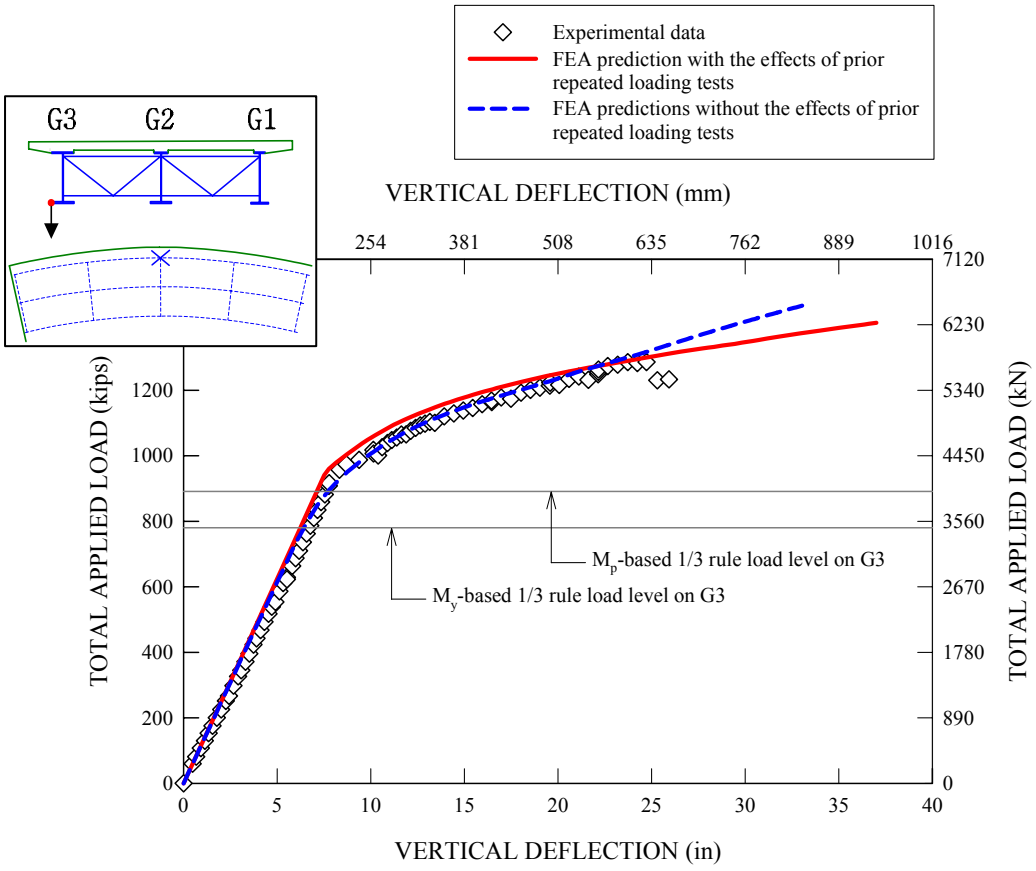

Figure 5.3.3. Load versus measured and predicted vertical deflections for the midspan outside tip of the G3 bottom flange due to the applied loads during the ultimate load test (dead load deflections and residual deflections prior to Test 4b are not included in the plot).

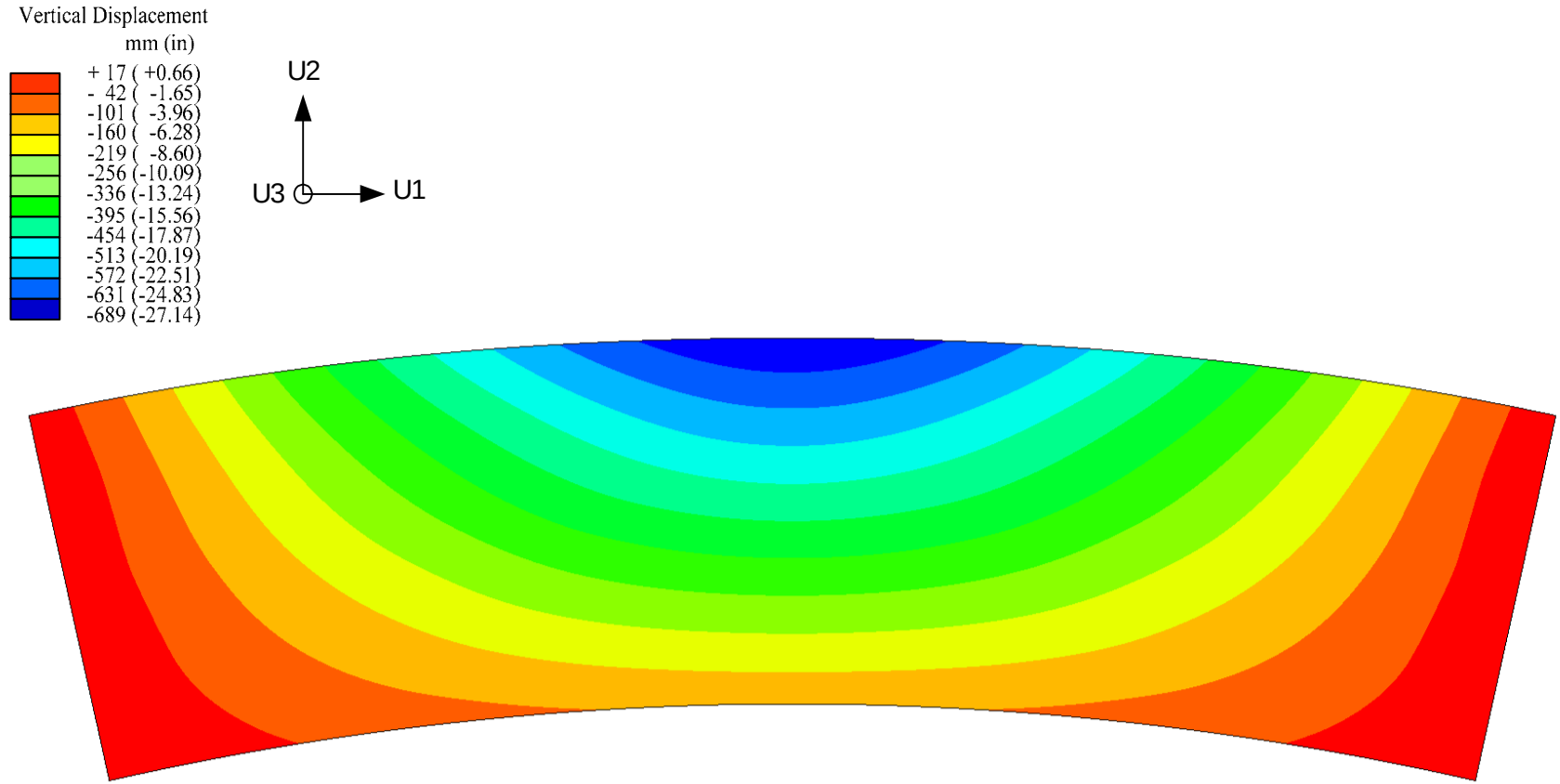

Figure 5.3.4. Plan view of the slab with contours of vertical deflections just prior to spalling and crushing of the slab concrete, deflection of midspan outside tip of the G3 bottom flange = 610 mm (24 in), total applied load = 5783 kN (1300 kips), initial dead-load displacements *not* included in the contours, predicted permanent displacements from Test 4a included, Displacement Scale Factor = 2.0.

A more meaningful way of interrogating the behavior of the test bridge girders is to plot the vertical deflections against corresponding internal moments instead of total applied loads. To this end, radial cuts are made in the FEA model at several locations of interest along the girder lengths, such as cross-frame locations and the loading points. Then, FEA internal moments and shear forces are calculated by obtaining the nodal forces in the deformed FEA model and summing them up over the undeformed cross-sections at the radial cuts. Figure 5.3.5 presents a schematic representation of the internal moment calculations for the midspan of the isolated G3 composite section. Astute readers may raise some concerns about potential errors associated with calculating internal force resultants over the undeformed cross-sections. However, the errors associated with this assumption fortunately are very small or negligible as explained in the following.

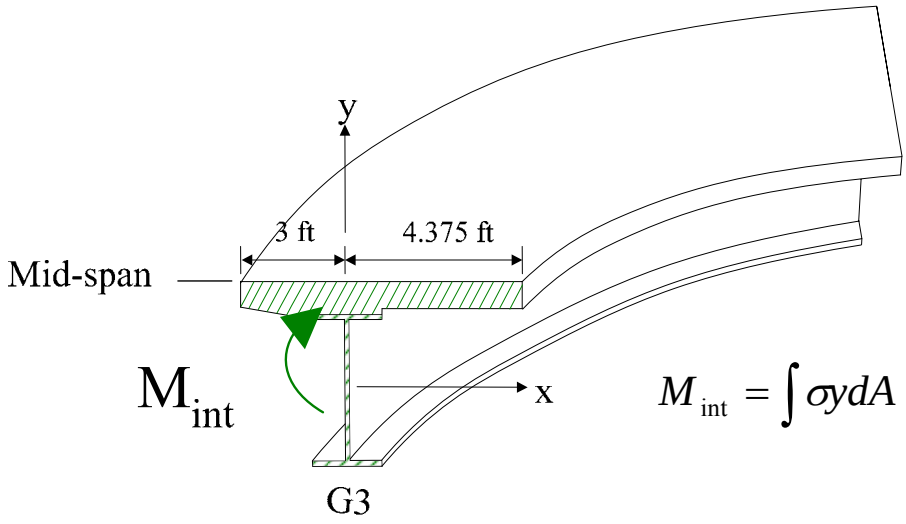

Figure 5.3.5. Schematic representation of G3 internal moment calculation at midspan.

The correctness of the above FEA internal force calculations can be checked by comparing the sum total of the individual girder FEA internal forces at a certain location

of the test bridge to corresponding simple statics solutions. In order to check if the FEA internal forces satisfy overall static equilibrium, the whole bridge system is first converted to a single equivalent beam with one degree indeterminacy as shown in Figure 5.3.6. Then, this simple beam model is analyzed to obtain the total internal forces required at the test bridge cross-section at the desired locations. For example, Figure 5.3.7 compares the midspan internal moment calculations obtained from the full nonlinear FEA analysis due to composite live loads to the corresponding statics solutions using the beam model shown in Figure 5.3.6. It can be seen that the full nonlinear FEA solution is in an excellent agreement with the statics solutions for various load levels, even at significantly high load levels where the test bridge is deformed considerably. Internal moment calculations for other locations including the other loading points (Figure 5.3.6), the quarter-span locations, and the locations halfway between the end- and quarter-span cross-frames also show similar agreement at all the load levels.

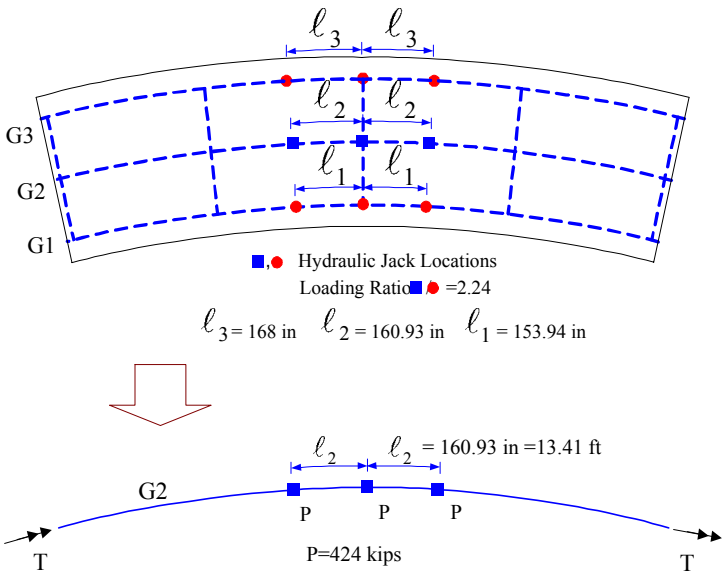

Figure 5.3.6. Schematic representation of the composite test bridge as a statically equivalent beam with one degree of indeterminacy.

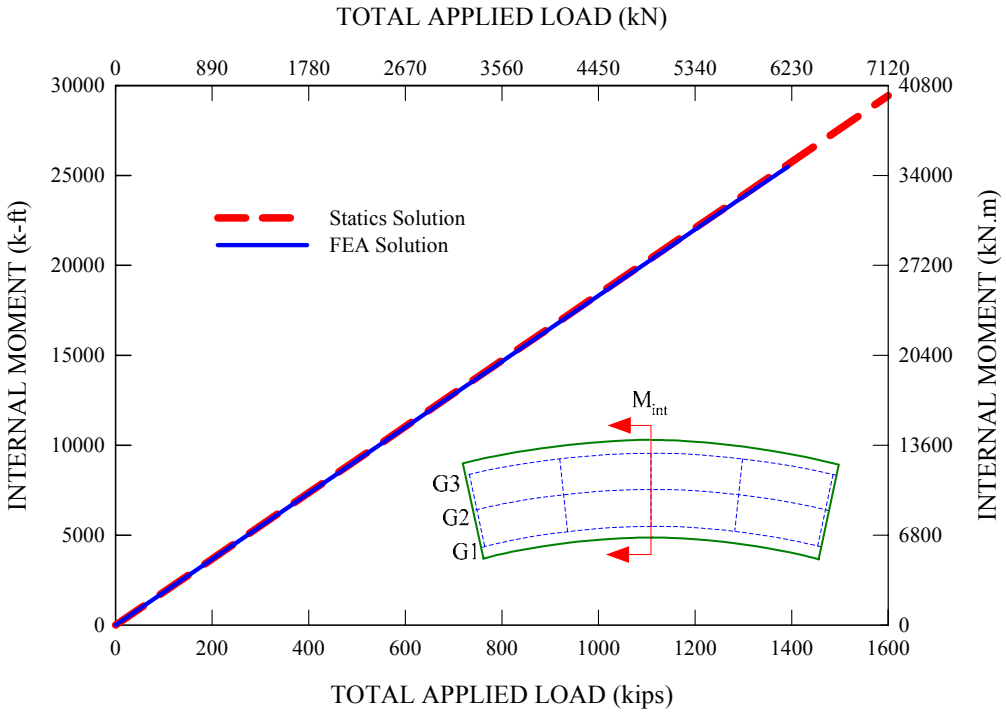

Figure 5.3.7. Comparison of internal moment calculations at midspan obtained from the full nonlinear FEA and corresponding statics solutions throughout the entire loading history.

Figure 5.3.8 compares the shear force diagram due to directly applied loads for the entire bridge cross-section along the normalized length obtained from the full nonlinear FEA solutions at total applied load levels of 3959 kN (890 kips) to the corresponding shear force diagram based on simple statics solutions. It can be seen that the full nonlinear FEA solutions are closely matched by the simple statics solutions throughout the normalized length. Similarly, good comparisons are also obtained for the shear force diagrams at different total applied load levels, even at the maximum applied load of 5783 kN (1300 kips).

Based on the above comparisons for the internal moments and shear forces, it is clear that the individual FEA internal forces presented below are good representations of

internal force state for the test bridge girders over the course of loading history during the ultimate load test.

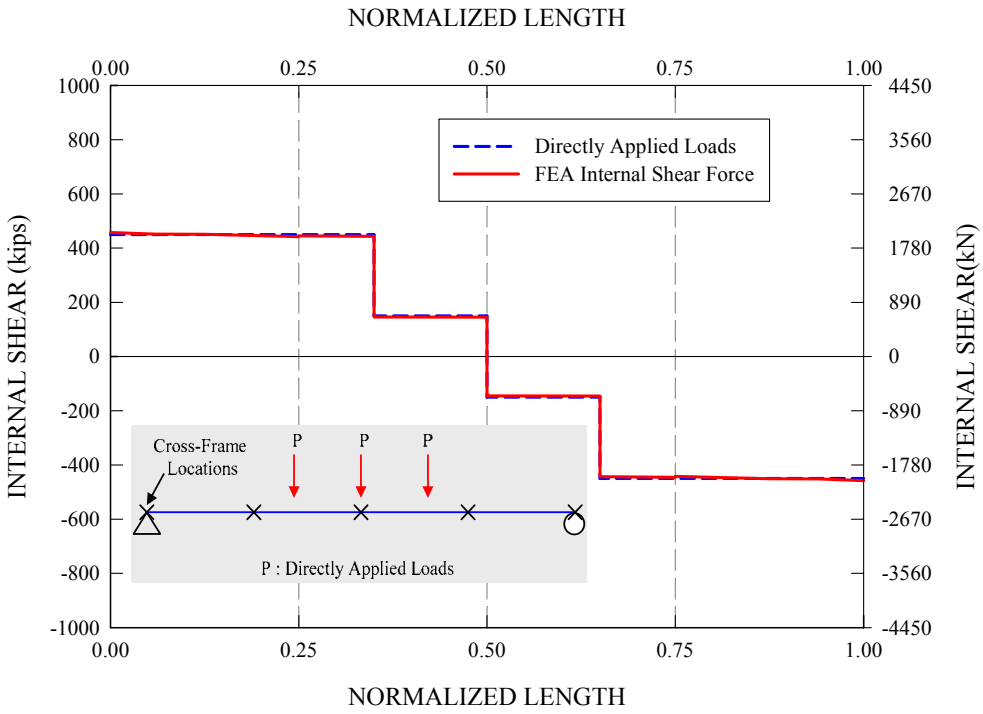

Figure 5.3.8. Comparison of internal shear force diagram computed from the full nonlinear FEA solutions and corresponding static shear force diagram at a total applied load level of 3959 kN (890 kips).

Figure 5.3.9 plots the midspan FEA internal moments throughout the entire loading history for the isolated G3 composite section versus the corresponding vertical deflections at the midspan outside tip of the G3 bottom flange. The initial dead load moments are included in the plot. Also, it should be noted that the internal moments at the M_y- and M_p-based 1/3 rule load levels on G3 are marked on the plot. Although the FEA solutions including the effects of the prior repeated loading tests show an extension of the proportional limit and more substantial nonlinear behavior at higher applied load

levels, they are reasonably close to the other FEA solution that does not include these effects. Furthermore, for both of the FEA solutions, it can be seen that internal moments are predominantly linear up to the M_p-based 1/3 rule load level, and then they become significantly nonlinear, approaching asymptotically a moment slightly less than the section plastic moment capacity M_p (the reduction below M_p is due partly to the presence of flange lateral bending stresses). In fact, it is quite interesting to see that the FEA internal moment including the effects of the prior repeated loading tests reaches a peak moment at a total deflection of 635 mm (25 in), and gradually decreases with further increases in the vertical deflection.

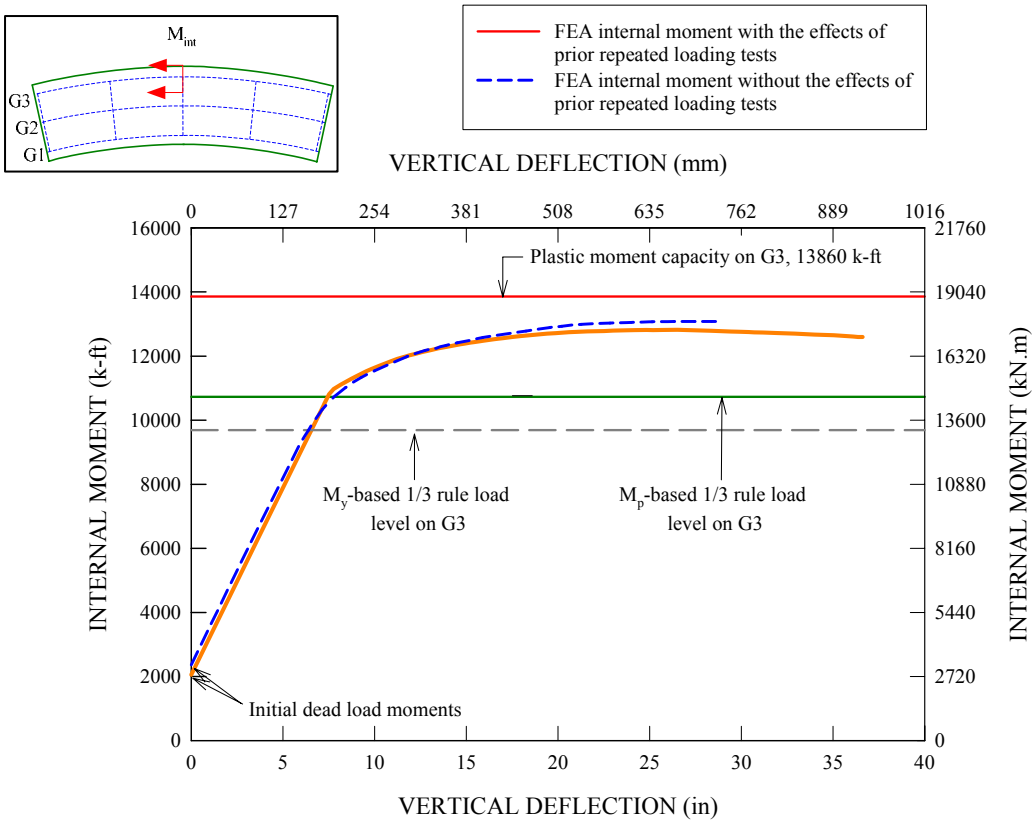

Figure 5.3.9. Midspan FEA internal moments for the isolated G3 composite section versus live load vertical deflections at the midspan outside tip of the G3 bottom flange.

Similarly, Figure 5.3.10 provides the FEA internal moment calculations at the midspan of the isolated G2 composite section. It can be seen that the two FEA solutions are quite close each other for the load levels slightly higher than the M_p-based 1/3 rule load level on G3. However, beyond this load level, the FEA solutions including the effects of the prior repeated loading tests predicts larger deflections for a given internal moment level than the other FEA solution. Nonetheless, it is important to note that both of these FEA solutions are essentially linear up to the moment levels due to the applied loads when the outermost girder reaches its M_p-based 1/3 rule resistance level. Quite interestingly, it can be seen in Figure 5.3.10 that the calculated internal FEA moments for both of the FEA solutions are well above the nominal plastic moment capacity of the G2 composite section in the absence of flange lateral bending stresses. This is largely because a large portion of the slab constituting the G2 composite section develops high biaxial compressive stresses that confine the concrete of the test slab in this region, thereby increasing the concrete compressive strength. Details of this concrete confinement are provided in Section 5.9, which discusses the slab stresses.

Figure 5.3.11 provides a similar plot showing the FEA internal moments at the midspan of the isolated G1 composite section. At a first glance, one can see that the extent of nonlinearity in the moment-deflection plots shown in this figure is not as significant as that of the previous two curves shown in Figures 5.3.9 and 5.3.10. In general, it can be seen that the FEA solutions including the effects of the prior repeated loading tests produce larger deflections for a given internal moment level than the other FEA solutions not including the effects of the prior repeated loading tests. Also, for both of the FEA solutions, it can be seen that the internal moments of the isolated G1

composite section are still significantly less than the section plastic moment capacity at the ultimate load level. Nonetheless, the most important consideration to note here is again that both of the FEA solutions increase predominantly in a linear fashion up to the moment levels corresponding to the M_p-based 1/3 rule resistance level on G3.

Based on the above linear behavior in the moment-deflection responses, it can be concluded that the nonlinear behavior associated with material yielding is generally minor at the M_p-based 1/3 rule load level on the outermost girder, G3, and the results of linear elastic analysis can be used to obtain reasonably good estimates of the girder moments and deflections for which the test bridge components can be designed.

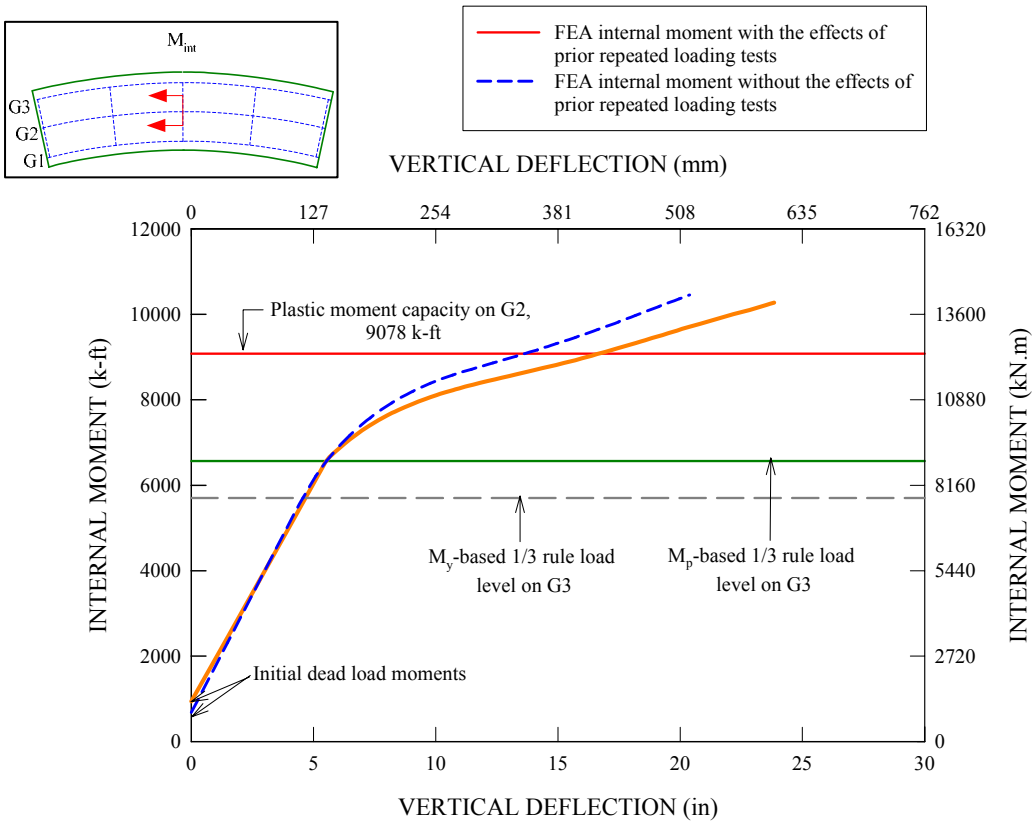

Figure 5.3.10. Midspan FEA internal moment for the isolated G2 composite section versus live load vertical deflections at the midspan outside tip of the G2 bottom flange.

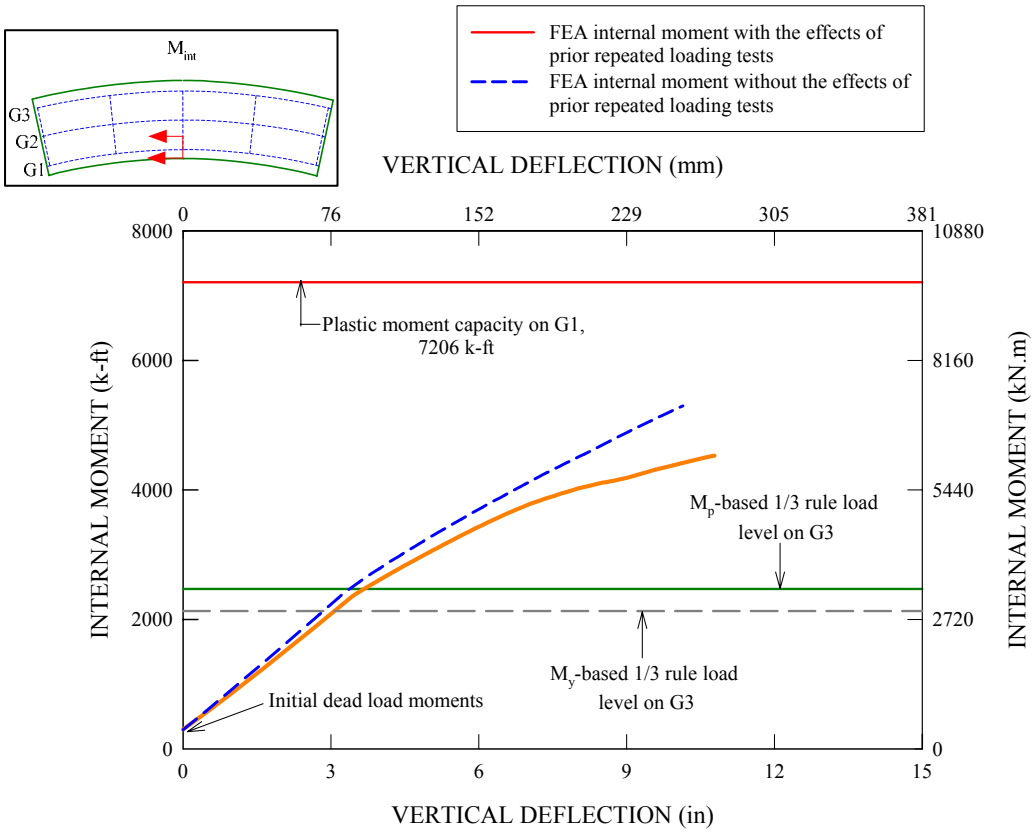

Figure 5.3.11. Midspan FEA internal moments for the isolated G1 composite section versus the live load vertical deflections at the midspan outside tip of the G1 bottom flange.

5.4 Girder Radial Deflections

Figure 5.4.1 gives a plan view of the deformed FEA slab model with contours of lateral deflections at spalling and crushing of the slab concrete in the experimental test, when the midspan outside tip of the G3 bottom flange reaches a deflection of 610 mm (24 in) due to a total applied load of 5783 kN (1300 kips). The initial dead-load displacements are *not* included in the deflection contours; however, the predicted permanent displacements at the end of Test 4a are included. Interestingly, it can be seen that the slab movements are predominantly toward the center of curvature as indicated by minus values in the legend, with the exception of the regions in close proximity to the

end supports moving away from the center of curvature. This is due to the fact that the bridge cross-section rotates about its effective shear center, which is located slightly above the bridge slab top surface as shown in Figure 1.5.1. The maximum computed radial deflection of 46.5 mm (1.83 in) is measured at the outer edge of the overhang outside G3.

Figure 5.4.2 provides measured and predicted radial deflections at the midspan outside tip of the G1 bottom flange during the ultimate load test. Initial dead load displacements and the residual displacements from Test 4a are not included in the plot. Figures 5.4.3 and 5.4.4 give similar plots for the middle and outside girders, G2 and G3, respectively. For all three of these plots, it is important to note that the radial deflections toward the center of curvature are taken as positive, since the radial movements in this direction are dominant for all of the three composite sections. This is in sharp contrast with the fact that the noncomposite bridge I-girders actually move away from the center of curvature due to noncomposite dead load deflections.

It can be seen in Figures 5.4.2 through 5.4.4 that although the FEA solutions without the effects of the prior repeated loading tests are reasonably in a good comparison with the measured data, the FEA solutions including the effects of the prior repeated loading tests provide a better comparison with the measured data, in particular in capturing the extension of proportional limit due to the prior repeated loading tests, as well as the total load magnitude and the slope of the curves near the peak applied load of 5783 kN (1300 kips). This parallels the results for the vertical deflections discussed in the previous section.

Similar to the vertical deflection responses, the measured radial deflections and the corresponding FEA predictions including the effects of the prior repeated loading tests are essentially linear up to a total applied load of approximately 4226 kN (950 kips), which is slightly higher than the M_p-based 1/3 rule load level of 3959 kN (890 kips) on G3. However, the FEA solutions without the effects of the prior repeated loading are only linear up to a load level of approximately 3559 kN (800 kips). However, the nonlinearity of the load-radial deflection curves is very minor at the M_p-based 1/3 rule load level on G3.

The load versus radial deflection behavior of the individual girders can be better understood in relation to the amount of internal moment each girder supports for a given total applied load level. Figures 5.4.5 through 5.4.7 plot the radial deflections shown in Figures 5.4.2 through 5.4.4 against the corresponding midspan FEA internal moments throughout the monotonic loading test for G3, G2 and G1, respectively. The initial deal load moments are included in the plots as well. The important thing to note for all of the plots is that the internal moments increase in a linear proportion to the corresponding radial deflections both at the M_y- and M_p-based 1/3 rule load levels on G3, although the FEA solutions without the effects of the prior repeated loading tests are slightly nonlinear at the M_p-based 1/3 rule load level.

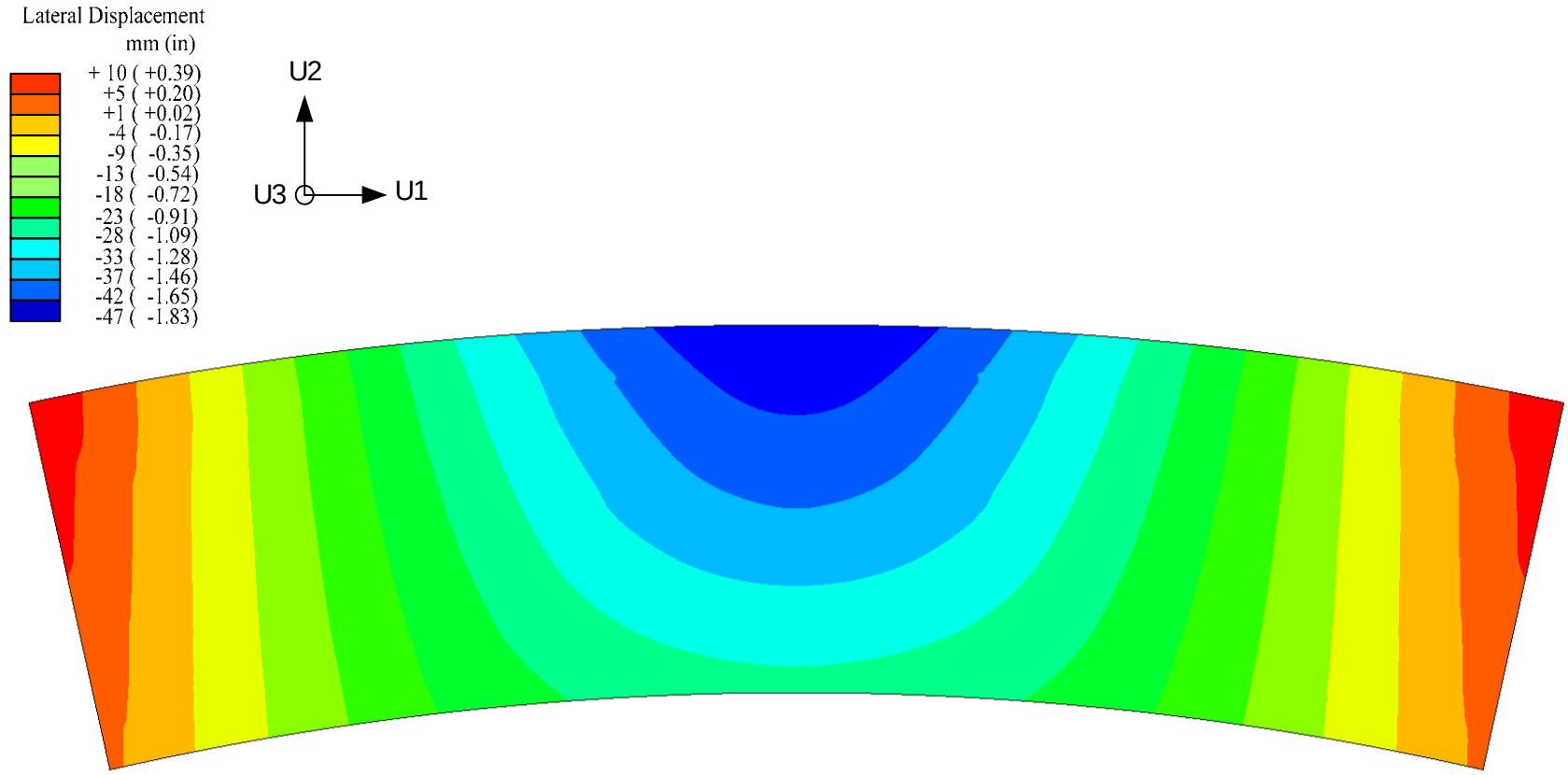

Figure 5.4.1. Plan view of the slab FEA model with contours of lateral deflections at spalling and crushing of the slab concrete in the experimental test, deflection of midspan outside tip of the G3 bottom flange = 610 mm (24 in), total applied load = 5783 kN (1300 kips), initial dead-load displacements *not* included in the contours, the predicted permanent displacements from Test 4a included.

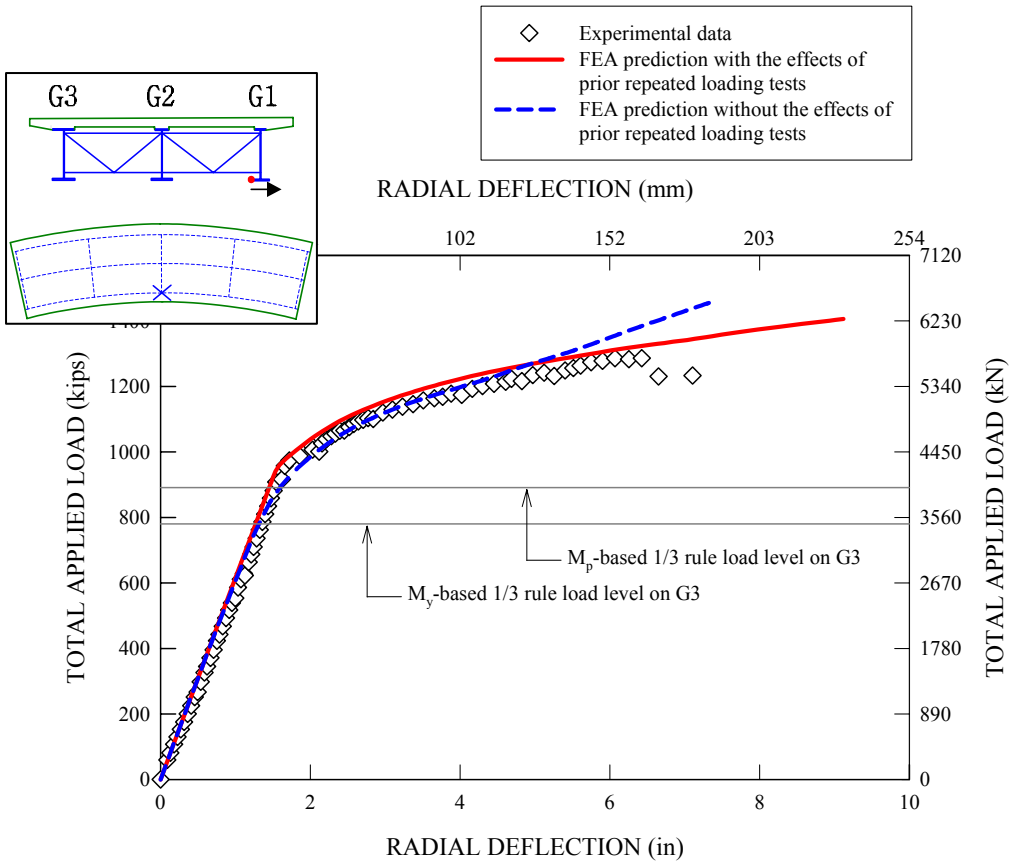

Figure 5.4.2. Load versus measured and predicted radial deflections for the midspan outside tip of the G1 bottom flange due to the applied loads during the ultimate load test (dead load deflections and residual deflections from Test 4a are not included in the plot).

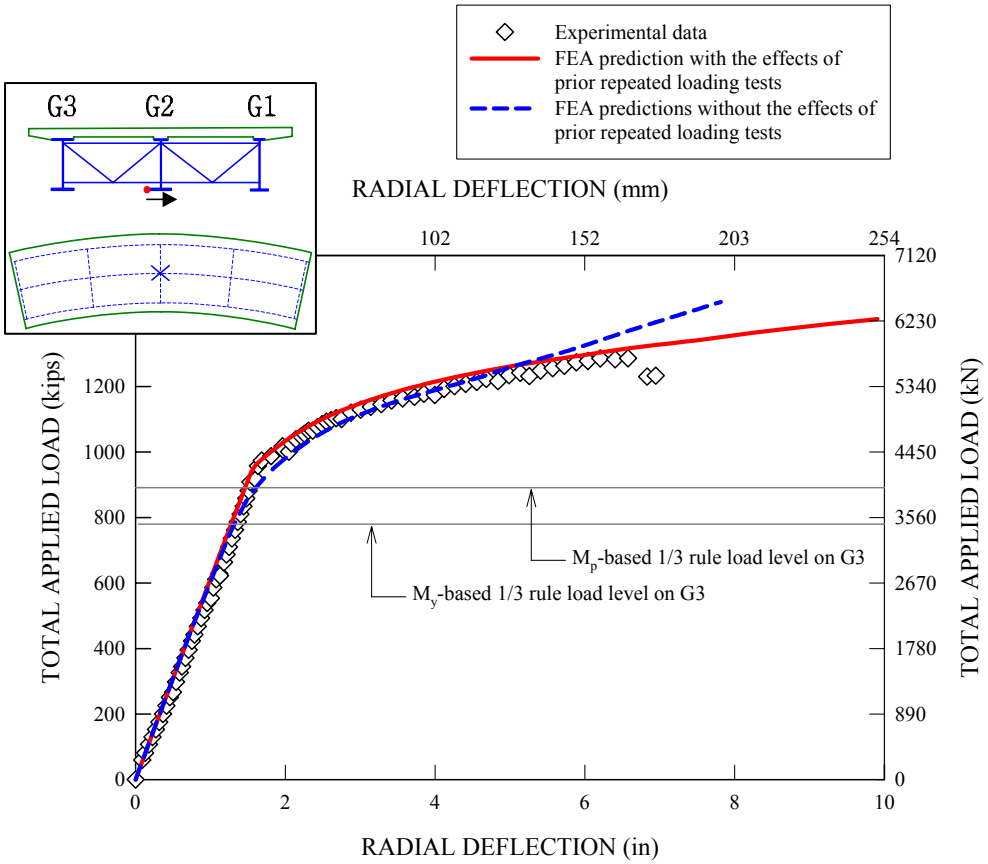

Figure 5.4.3. Load versus measured and predicted radial deflections for the midspan outside tip of the G2 bottom flange due to the applied loads during the ultimate load test (dead load deflections and residual deflections from Test 4a are not included in the plot).

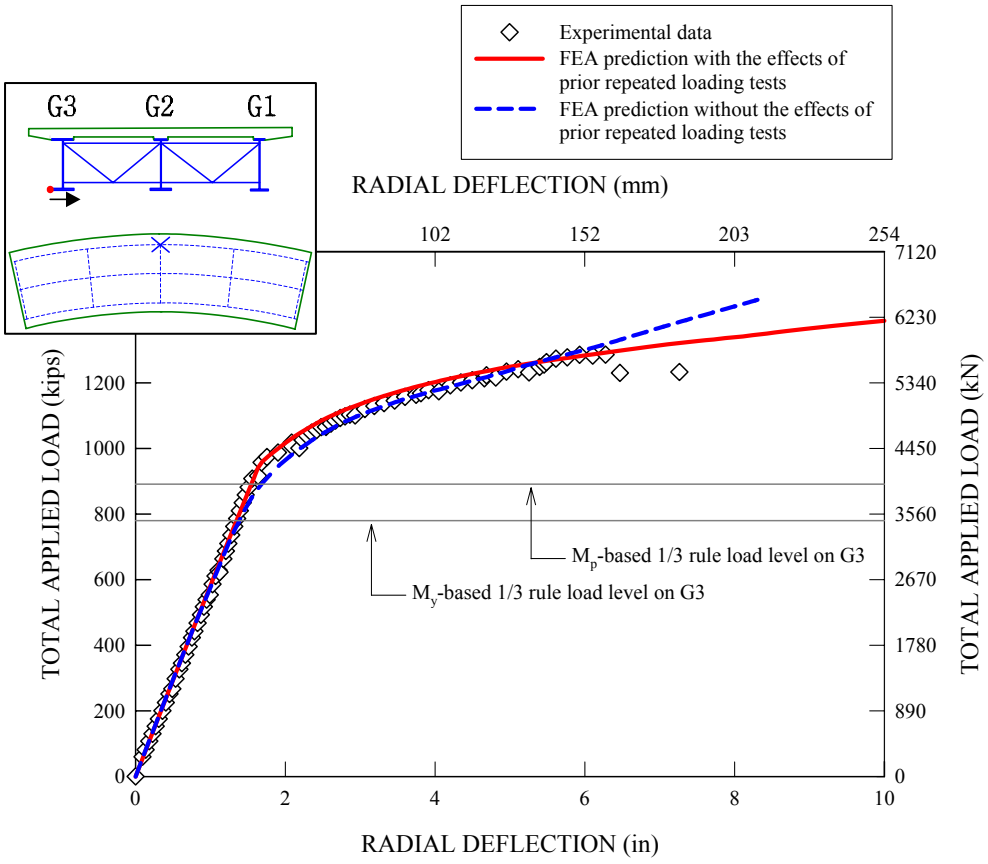

Figure 5.4.4. Load versus measured and predicted radial deflections for the midspan outside tip of the G3 bottom flange due to the applied loads during the ultimate load test (dead load deflections and residual deflections from Test 4a are not included in the plot).

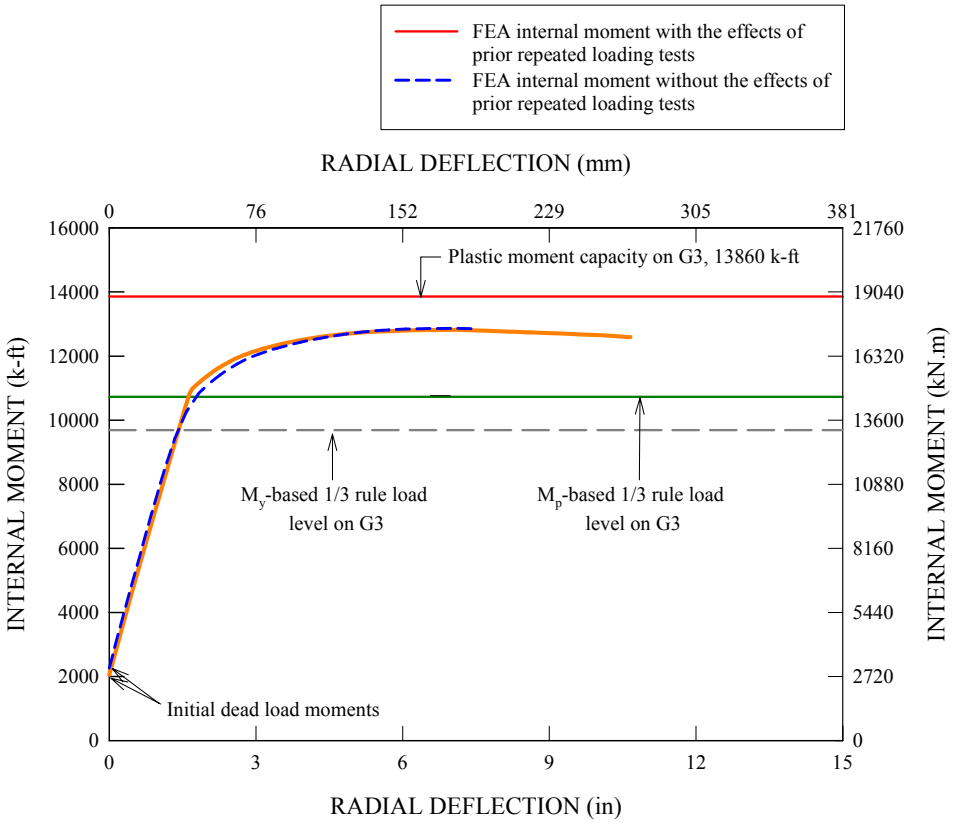

Figure 5.4.5. Midspan FEA internal moments for the isolated G3 composite section versus the live load radial deflections at the midspan outside tip of the G3 bottom flange.

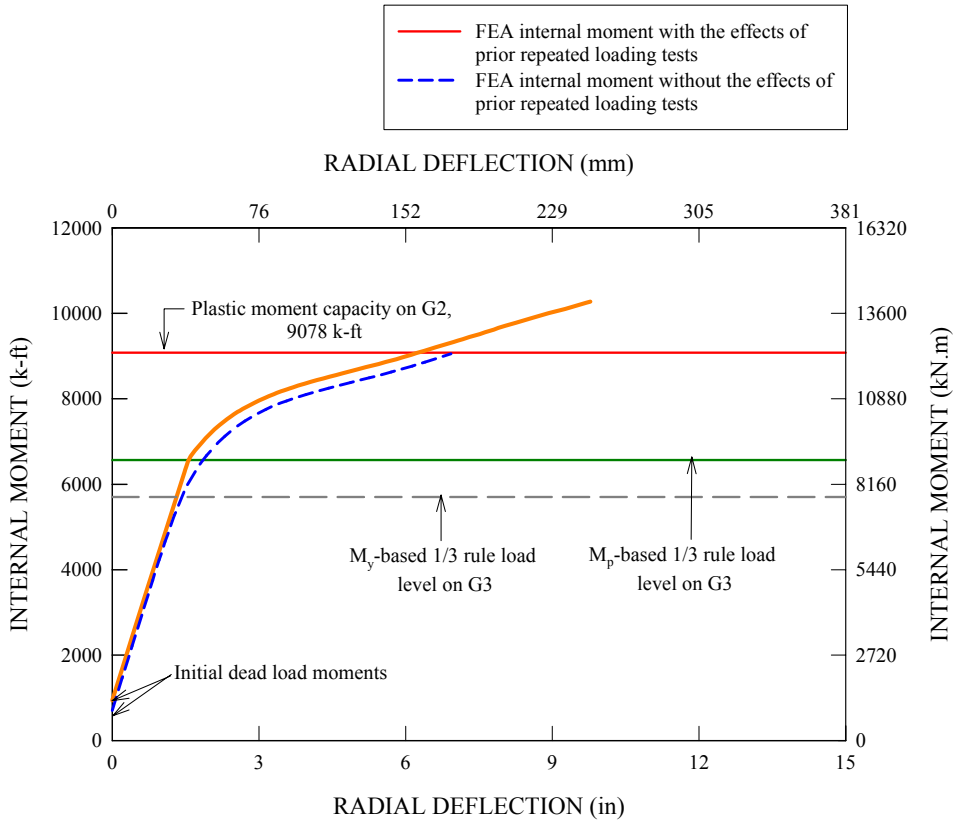

Figure 5.4.6. Midspan FEA internal moments for the isolated G2 composite section versus the live load radial deflections at the midspan outside tip of the G2 bottom flange.

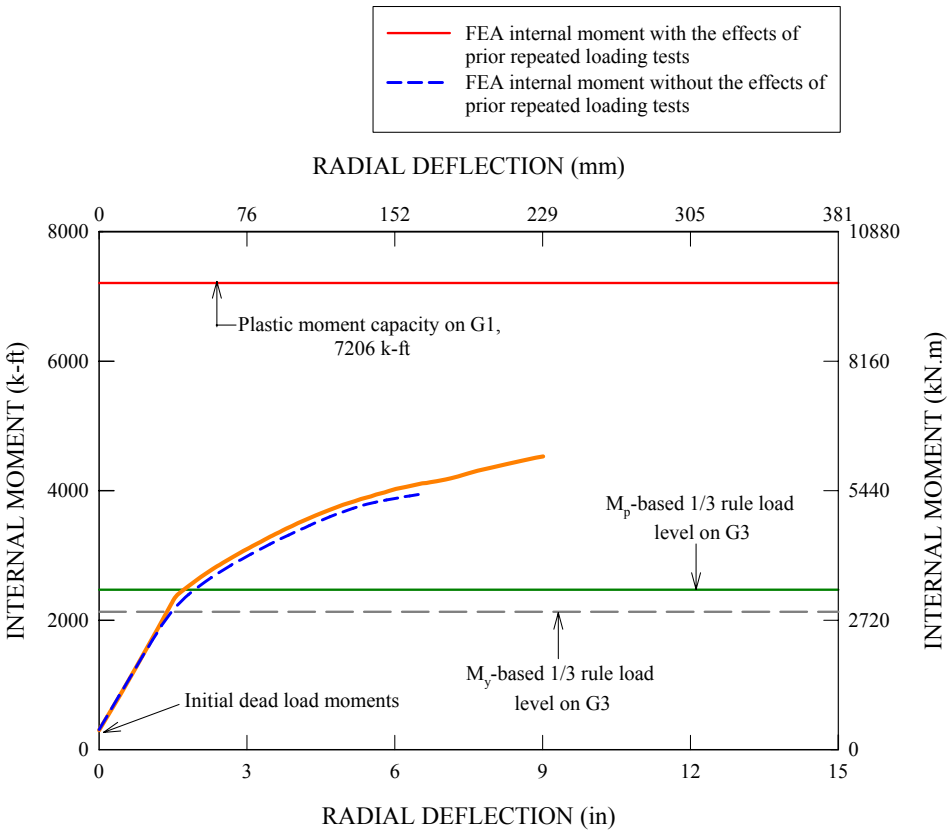

Figure 5.4.7. Midspan FEA internal moments for the isolated G1 composite section versus the live load radial deflections at the midspan outside tip of the G1 bottom flang3.

5.5 Cross-Section Distortion

Figure 5.5.1 provides a schematic that shows a typical movement of the bridge cross-section at a typical the cross-frame locations, based on the information about the vertical and radial deflections shown in the previous sections. It can be seen that the bridge cross-section not only moves in the downward direction upon the application of loading, but also moves toward the center of curvature, rotating with respect to the shear center located slightly above the top surface of the slab.

Figure 5.5.2 shows a perspective view of the FEA model of the steel superstructure with contours of the lateral deflections at spalling and crushing of the slab concrete in the experimental test, when the midspan outside tip of the G3 bottom flange reaches a deflection of 610 mm (24 in) due to a total applied load of 5783 kN (1300 kips). The initial dead-load displacements are *not* included in the deflection contours; however, the predicted permanent displacements at the end of Test 4a are included. It is interesting to note that the largest lateral movements occur on the bottom portion of the girders approximately halfway between the mid- and quarter-span cross-frame locations rather than at the midspan cross-frame. This is due to the cross-section distortion that occurs within the girders between the cross-frame locations.

In order to take a closer look at the cross-section distortions along the girder lengths, four key locations of interest are selected. Along with the mid- and quarter-span cross-frame locations, they include two additional locations where the largest lateral movement takes place within each of the unbraced lengths on one side of the midspan. Figures 5.5.3 through 5.5.5 show the resulting girder cross-section deformation profiles for G1, G2 and G3, respectively, at a total applied load of 5783 kN (1300 kips). For all of the plots, it can be seen that the cross-section rotation is larger toward the midspan of the bridge.

Furthermore, it should be noted that there is no significant bulging of the web panel caused by the effects of the horizontal curvature. In fact, the section profile is distorted very little in most cases. The webs and the top and bottom flanges appear to undergo nearly the same "rigid body" rotation, which is also the same as the slab rotation at the cross-sections. The G3 cross-section profile at 0.4375L has the most noticeable distortion, as shown in Figure 5.5.5. It can be seen at this location that the bottom flange basically slides laterally relative to the top flange, causing the web panel to deform into an S-shape. This is because there are not intermediate transverse stiffeners or connection plates in the vicinity of the web panel at 0.4375L. In contrast, it is interesting to see that the cross-section profile at the midspan, 0.5L, essentially maintains its original cross-section shape even at this high applied load level.

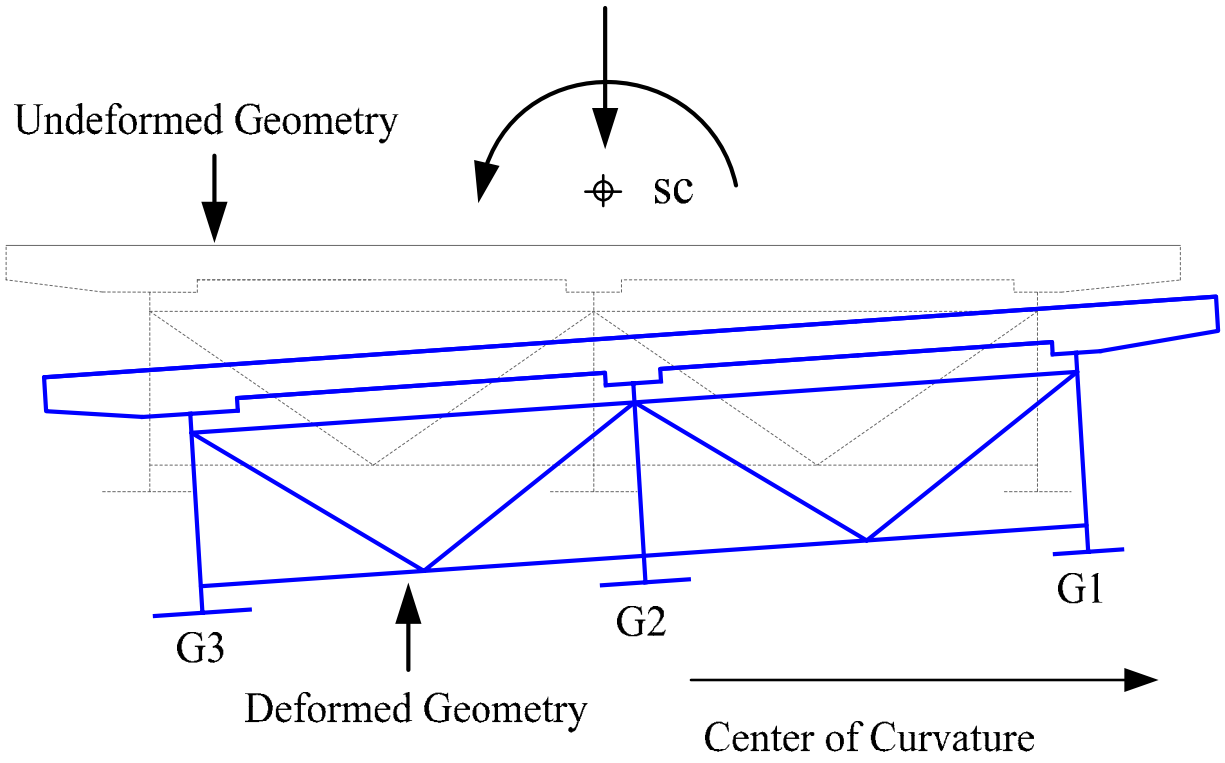

Figure 5.5.1. Schematic of showing typical overall bridge cross-section movements toward the center of curvature as well as in the downward direction.

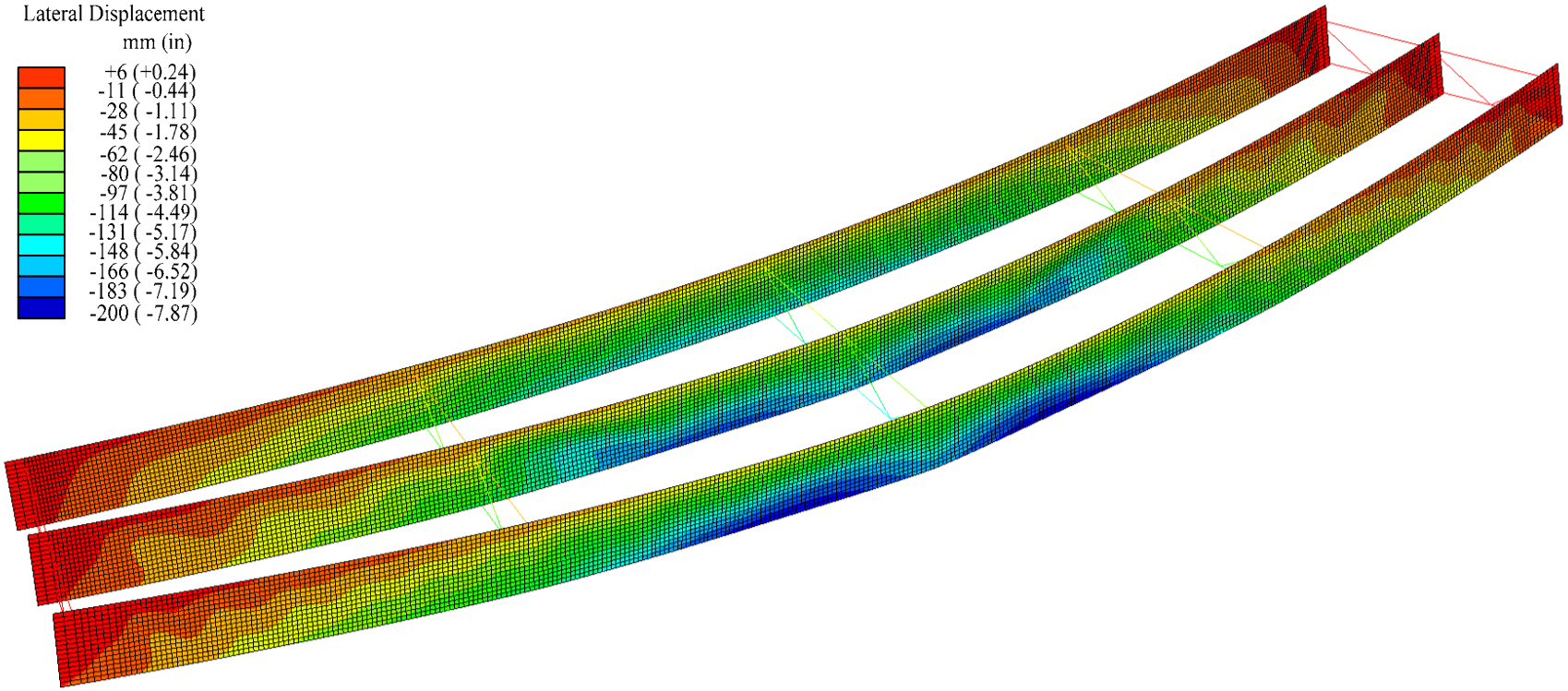

Figure 5.5.2. Perspective view of the FEA model of the steel superstructure with contours of lateral deflections just prior to spalling and crushing of the slab concrete in the experimental test, deflection of the midspan outside tip of the G3 bottom flange = 610 mm (24 in), total applied load = 5783 kN (1300 kips), the initial dead-load displacements *not* included in the contours, predicted permanent displacements from Test 4a included, Displacement Scale Factor = 2.0.

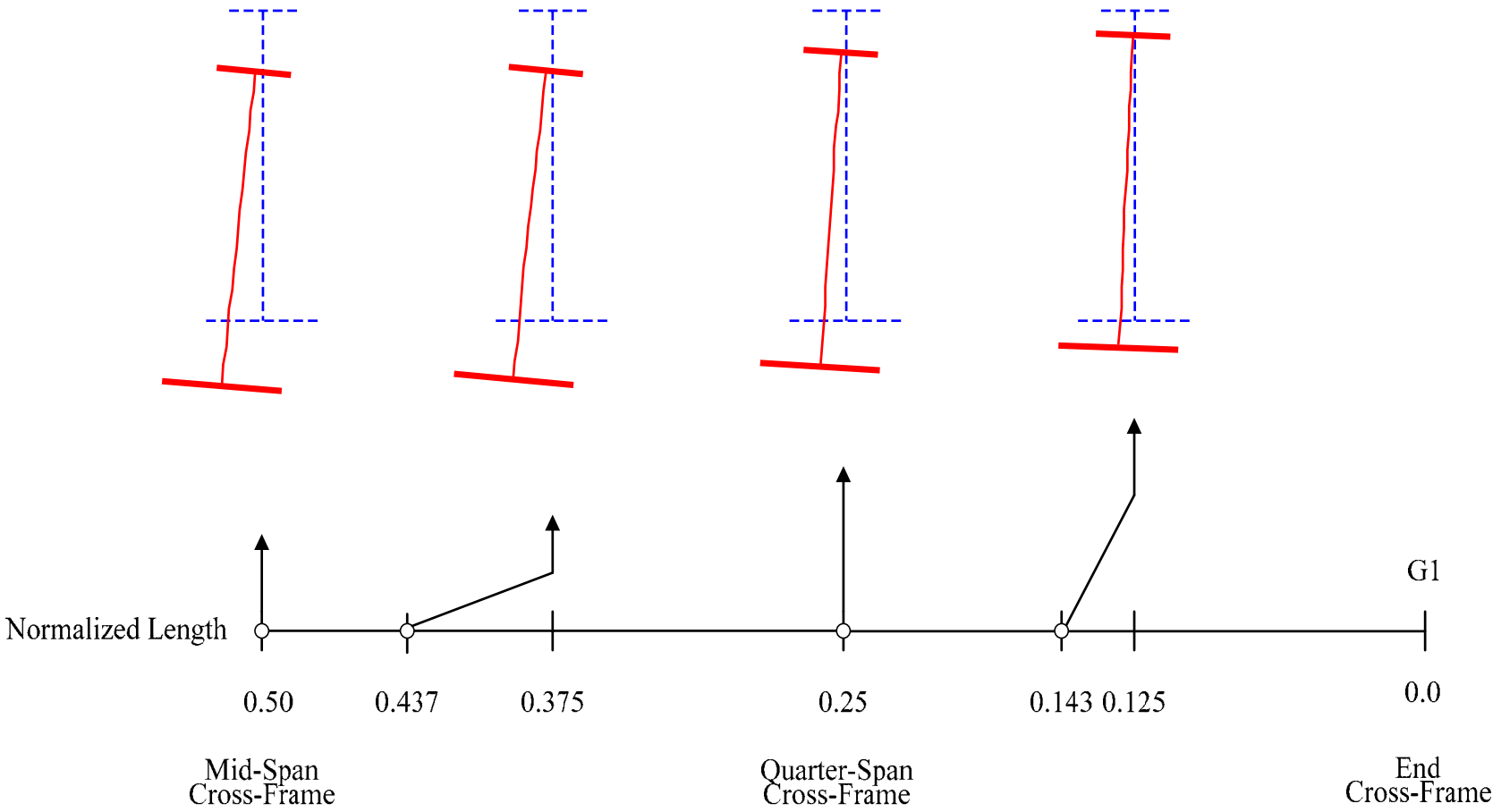

Figure 5.5.3. Cross-section deformation profiles along the length of G1 just prior to spalling and crushing of the slab concrete in the experimental test, deflection of midspan outside tip of the bottom flange = 610 mm (24 in), total applied load = 5783 kN (1300 kips), Deformation Scale Factor = 1.0.

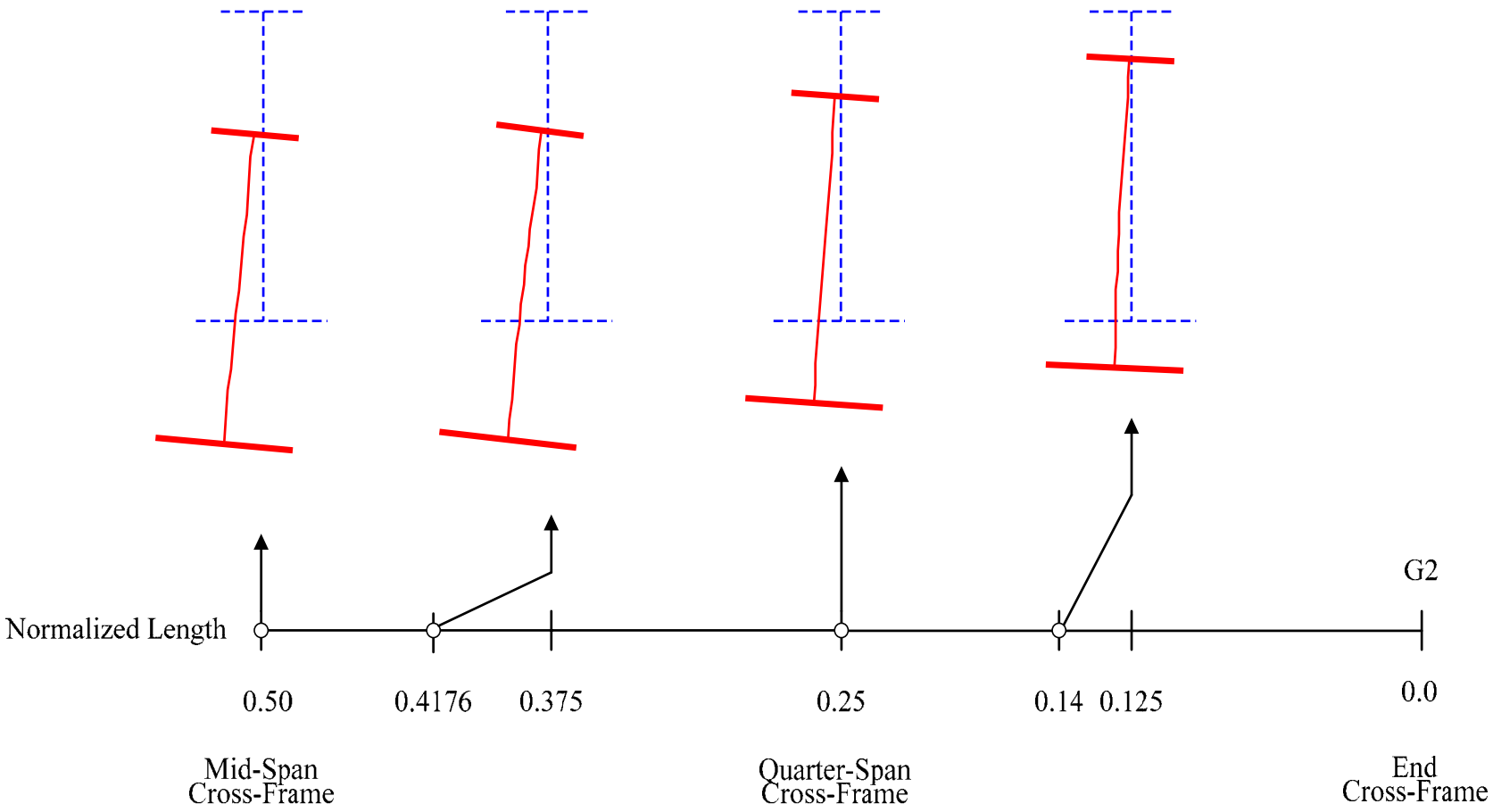

Figure 5.5.4. Cross-section deformation profiles along the length of G2 just prior to spalling and crushing of the slab concrete in the experimental test, deflection of midspan outside tip of the G3 bottom flange = 610 mm (24 in), total applied load = 5783 kN (1300 kips), Deformation Scale Factor = 1.0.

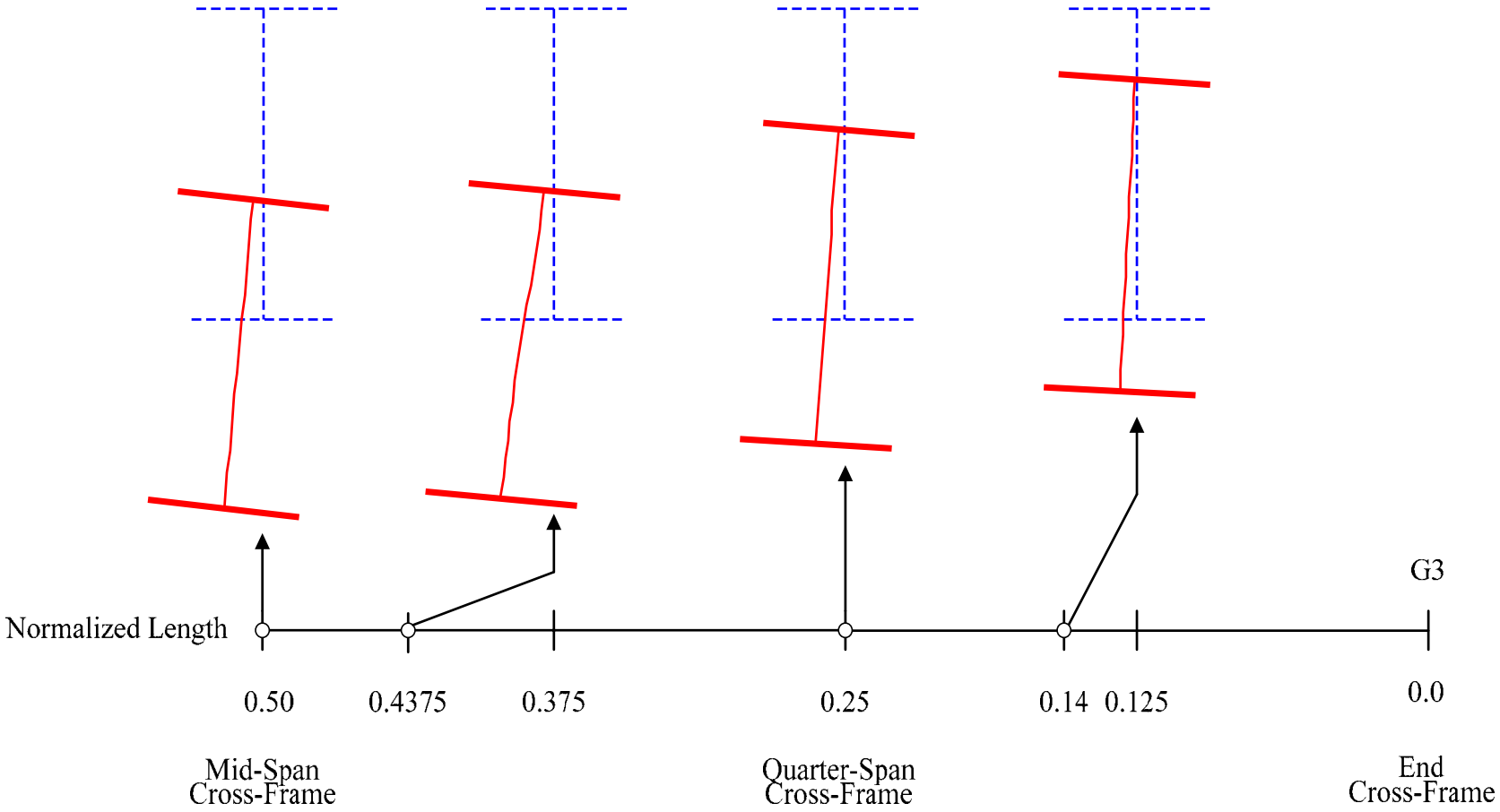

Figure 5.5.5. Cross-section deformation profiles along the length of G3 just prior to spalling and crushing of the slab concrete in the experimental test, deflection of midspan outside tip of the G3 bottom flange = 610 mm (24 in), total applied load = 5783 kN (1300 kips), Deformation Scale Factor = 1.0.

5.6 Girder End Vertical Reactions

Figure 5.6.1 provides measured and predicted ratios of individual girder vertical reactions versus the total applied loads in Test 4b. The reaction forces in the radial directions are found to be small or negligible relative to the vertical reaction forces, and thus are not reported. The predicted values in Figure 5.6.1 are obtained from the full nonlinear FEA solutions that account for the effects of the prior repeated loading tests. In contrast, Figure 5.6.2 provides the predicted ratios of the individual girder reactions to the total applied loads obtained from the other full nonlinear FEA solution without the effects of prior repeated loading tests included. Both plots show the predicted as well as the corresponding measured ratios. For both of the plots, the measured ratios are closely matched by the FEA predictions. In fact, the girder reaction ratios are almost constant over the entire loading range, indicating that the girder reactions increase linearly with increasing total applied loads. The average ratios are 0.09, 0.27 and 0.64 for G1, G2 and G3, respectively in Figure 5.6.1. However, a closer look at the plots reveals that the FEA solution including the effects of the prior repeated loading tests provides a slightly better comparison to the measured responses, particularly in capturing slight nonlinear changes in the measured reaction ratios for G1 and G2 at high load levels above 4003 kN (900 kips).

Figures 5.6.3 through 5.6.5 show more detailed reaction information by providing the measured and predicted girder end vertical reactions with total applied loads. The dead load reactions are also included in the plots. Similar to the above, it can be seen that there is a good correlation between the measured and predicted responses for all of these plots. For example, the computed maximum reaction forces at a total applied load level of 5783 kN (1300 kips) are 365 kN (82 kips), 947 kN (213 kips) and 2215 kN (498 kips)

for G1, G2 and G3, respectively. Correspondingly, the experimental values are 360 kN (81 kips), 961 kN (216 kips) and 2229 kN (501 kips). More importantly, Figure 5.6.5 shows that the measured and predicted reactions on G3 are essentially linear on G3 throughout the entire loading history, including the M_y- and M_p-based 1/3 rule load levels. This is quite interesting considering the fact that the test bridge system experiences significant inelastic deflections at high applied load levels. For the reactions on G1 and G2, Figures 5.6.3 and 5.6.4 show that the measured responses increase linearly up to a total applied load of about 4448 kN (1000 kips), which is less than the load level up to which the FEA predicted responses are linear. It can be seen in Figures 5.6.3 and 5.6.4 that the predicted responses deviate slightly from the measured values starting at a total applied load of about 4448 kN (1000 kips) and up to the peak experimental load of 5783 kN (1300 kips). Nonetheless, it is important to note that the variation in the girder reactions on G1 and G2 is predominantly linear up to the M_p-based 1/3 rule load level on G3, similar to the reaction variations on G3.

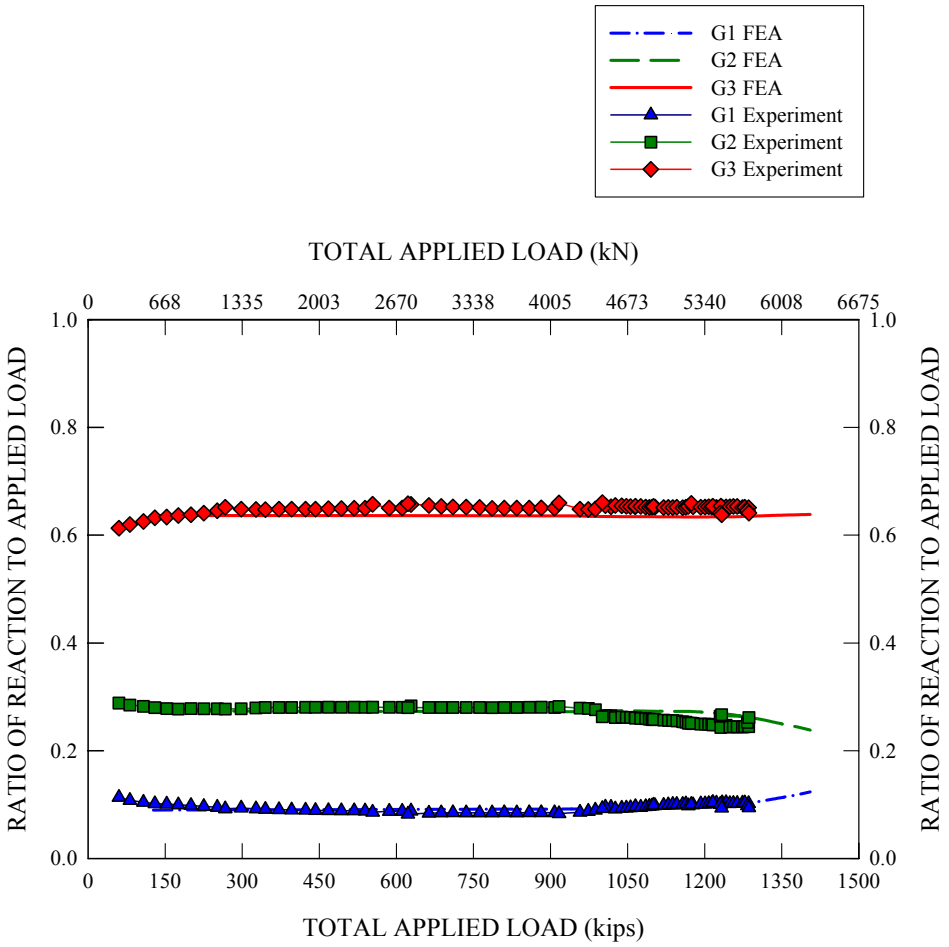

Figure 5.6.1. Measured and predicted ratios of individual girder end vertical reactions versus the total applied loads, FEA solutions including the effects of the prior repeated loading tests.

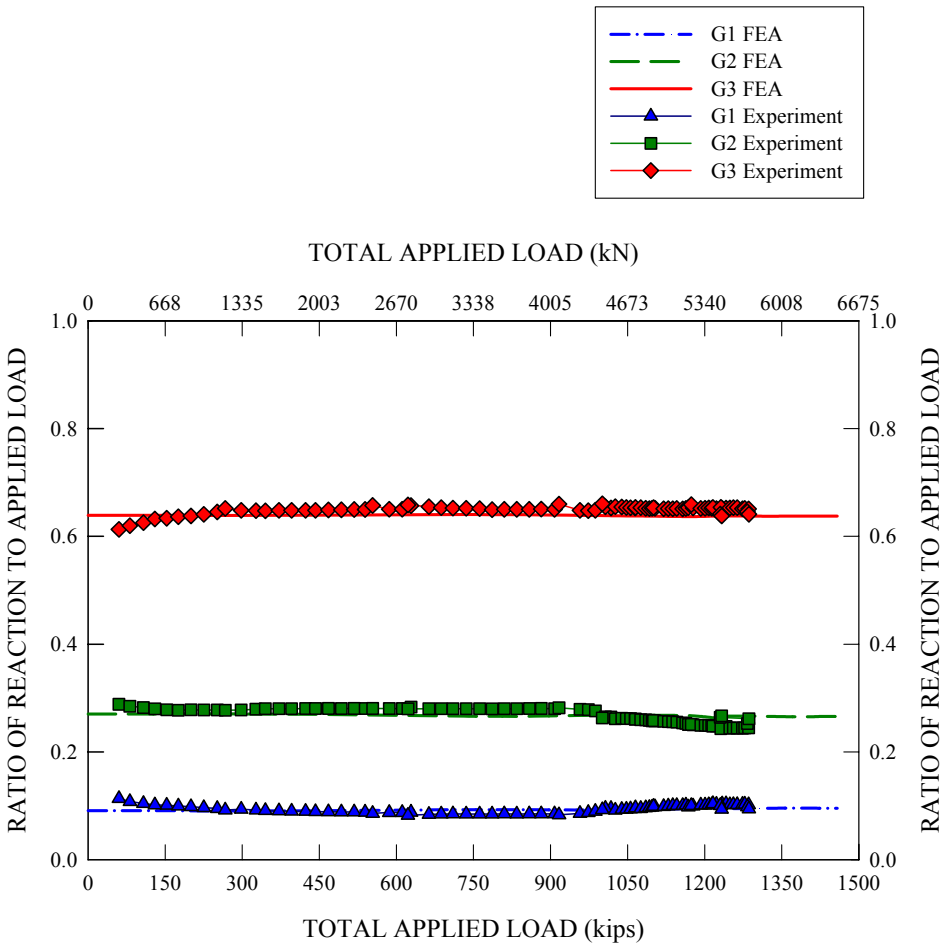

Figure 5.6.2. Measured and predicted ratios of individual girder end vertical reactions versus the total applied loads, FEA solutions not including the effects of the prior repeated loading tests.

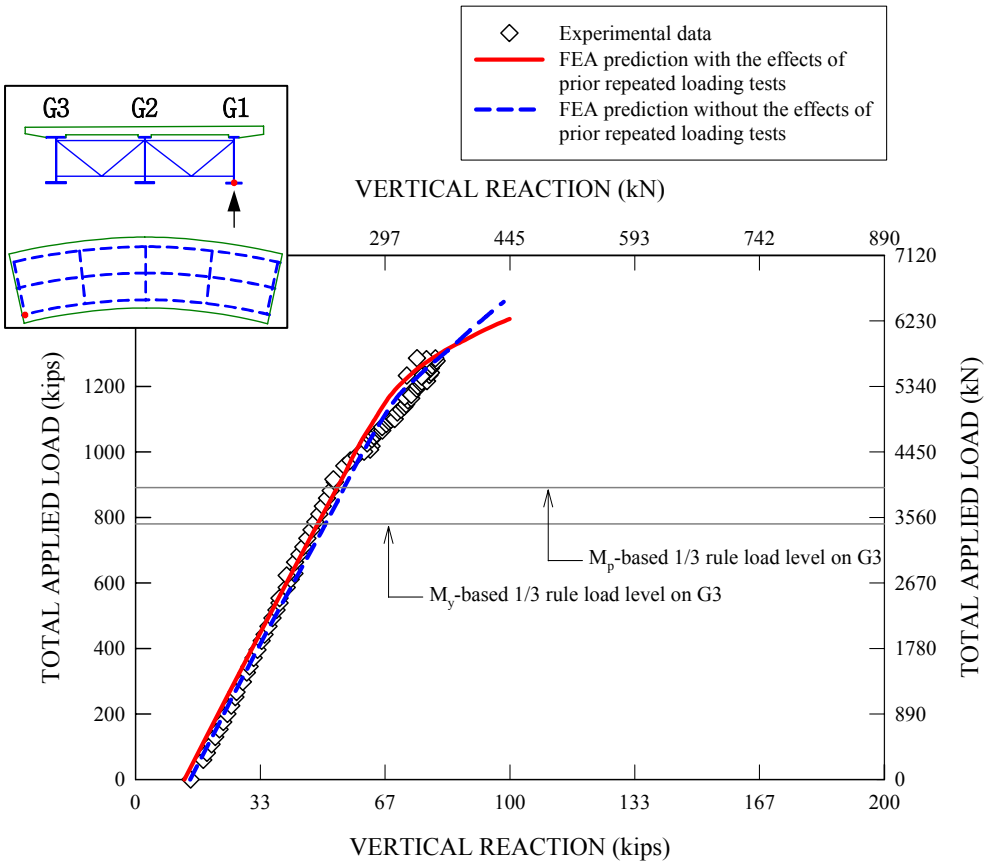

Figure 5.6.3. Applied load versus measured and predicted girder end vertical reactions for G1 during the final monotonic loading test.

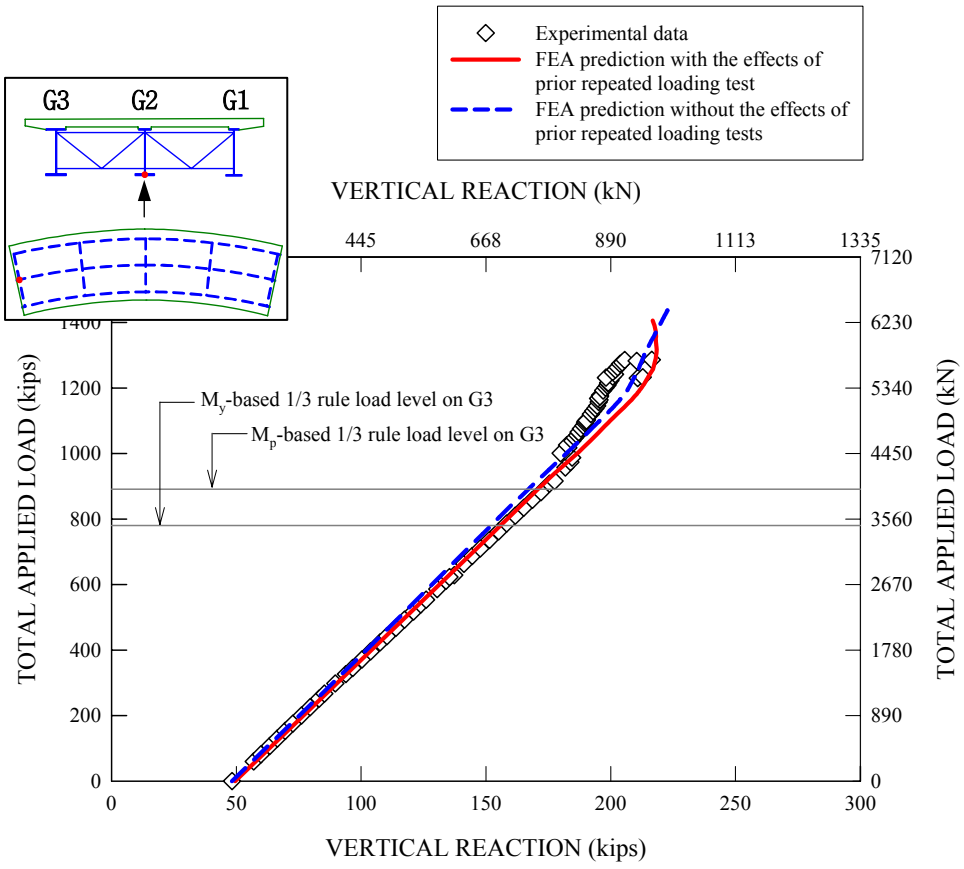

Figure 5.6.4. Applied load versus measured and predicted girder end vertical reactions for G2 during the final monotonic loading test.

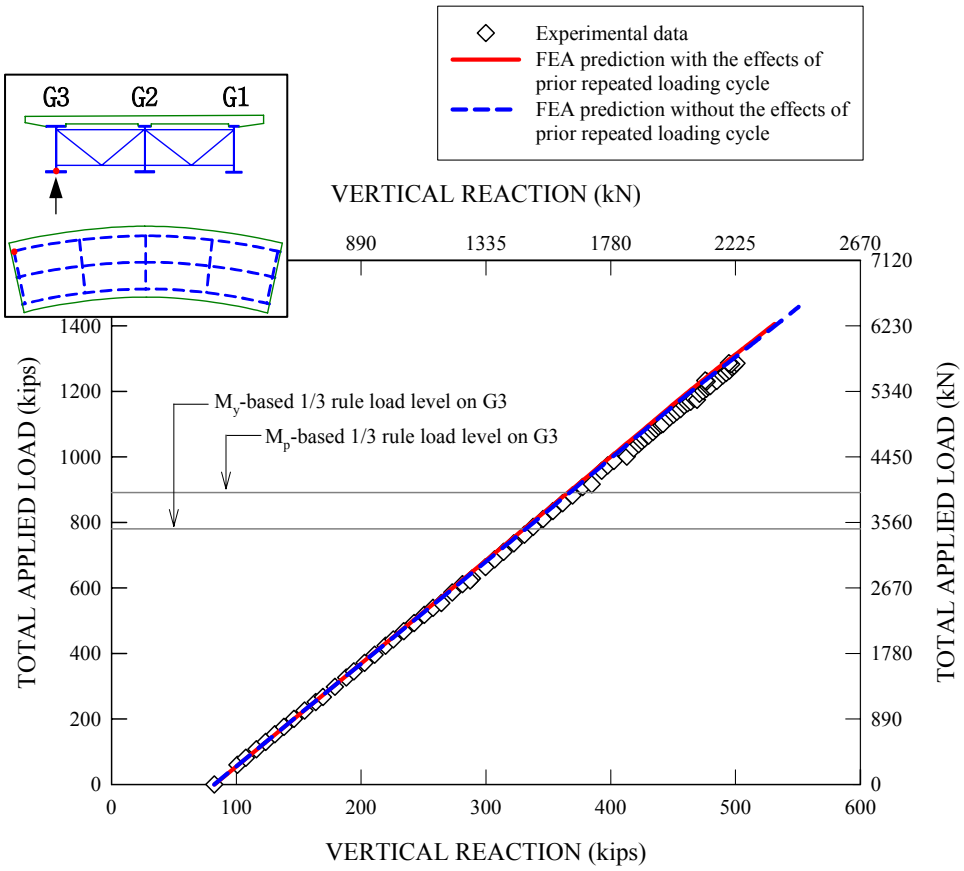

Figure 5.6.5. Applied load versus measured and predicted girder end vertical reactions for G3 during the final monotonic loading test.

5.7 Major-Axis and Lateral Bending Strains

Figure 5.7.1 provides measured major-axis and lateral bending strains for the G3 bottom flange along with corresponding FEA solutions with and without the effects of the prior repeated loading tests. These solutions are generated at a total applied load level of 3959 kN (890 kips) during the final monotonic loading test. As shown previously, this is the load level at which the M_p-based 1/3 rule is reached in a linear elastic analysis of girder G3. The initial dead load strains and the residual strains from the prior repeated loading tests are not included in this plot. This allows the plots to focus solely on the strains generated by the applied loads in Test 4b. It can be seen that the major-axis bending strain measurements are matched closely by the corresponding FEA predictions regardless of whether they include the effects of the prior repeated loading tests or not, with the exception of a local region around the midspan. However, one can observe that there is a significant difference between the two FEA predictions and between these predictions and a simple extrapolation of the measured data for the strains near the midspan of the test bridge. The maximum midspan strain from the FEA solution including the effects of the prior repeated loading tests is 4000 με, which is significantly larger than the other FEA prediction of 1000 με without the effects of the prior repeated loading tests. The FEA strains including the effects of the prior repeated loading tests are obtained by subtracting the strains at the start of Test 4a, which include the plastic strains induced during the previous repeated loading tests, from the total strains. In the case of the FEA solution including the effects of the prior repeated loading tests, the sudden jump in the major-axis bending strains at the midspan is much smaller than in the other FEA solution (and is in fact in the opposite direction from that obtained by the other solution). These spikes in the major-axis bending strains at the midspan are due to

localized yielding predicted in the FEA models. The smaller spike in the case of the FEA solution that includes the prior repeated loading tests is due to the extension of the elastic loading range in these locally yielded regions due to the prior plastic deformations that occurred during Test 4a.

When it comes to the lateral bending strains, Figure 5.7.1 shows that the measured lateral bending strains are also predicted well by the corresponding FEA solutions. Interestingly, one can observe that the FEA predictions including the effects of the prior repeated loading tests actually provide a slightly better comparison to the measured values in the proximity of the midspan. In addition, similar to the major-axis bending strains, it should be noted that a large sudden jump appears in the FEA prediction with the effects of the prior repeated loading tests not included, while only a small deviation from a simple extrapolation of the measured test data is predicted by the FEA solution with the effects of the prior repeated loading tests included.

In addition, it is worthwhile noting that some localized yielding is predicted approximately halfway between the mid- and quarter-span cross-frames in the solution that does not include the prior repeated loading tests. More details regarding the spread of yielding are presented in the next section by considering the equivalent plastic strains on the steel sections.

Figures 5.7.2 and 5.7.3 provide similar major-axis and lateral bending strain plots for G2 and G1, respectively. The behavior in these figures is very similar to that shown in Figure 5.7.1.

Figure 5.7.4 provides measured major-axis and lateral bending strains for the G3 bottom flange along with the corresponding FEA solutions with and without the effects

of the prior repeated loading tests at a total applied load of 5115 kN (1150 kips). This load level corresponds to the satisfaction of $M = M_p$ at the G3 midspan in a linear elastic analysis using the Test 4b applied loadings. Similar to Figure 5.7.3, the dead load strains and the residual strains from the prior repeated loading tests are not included. It can be seen that there is a close match between the measured and predicted values, both for the major-axis bending and lateral bending strains, particularly within the lengths somewhat removed from the midspan region. However, the comparisons tend to degrade for the strains close to the midspan of the bridge. Compared to Figure 5.7.1, it can be seen that both the measured and the FEA strains are noticeably increased at the mid- and quarter-span cross-frame locations, as well as at around 0.4L and 0.6L.

Figures 5.7.5 and 5.7.6 provide similar plots that show the measured and lateral bending strains for G2 and G1, respectively, at a total applied load level of 5115 kN (1150 kips). Similar to the strains presented in Figure 5.7.4, it can be seen in Figure 5.7.5 that there is a noticeable strain increase at the cross-frame locations relative to the strains observed in Figure 5.7.2. This is particularly the case at the midspan cross-frame. In addition, there is an increase in the strains the vicinity of 0.4L and 0.6L, except that measured lateral bending strain at 0.4L is small.

Concerning the stains for G1, Figure 5.7.6 shows that there is a good correlation between the measured and predicted values with the exception of the strains measured near the middle of the unbraced lengths adjacent to the midspan.

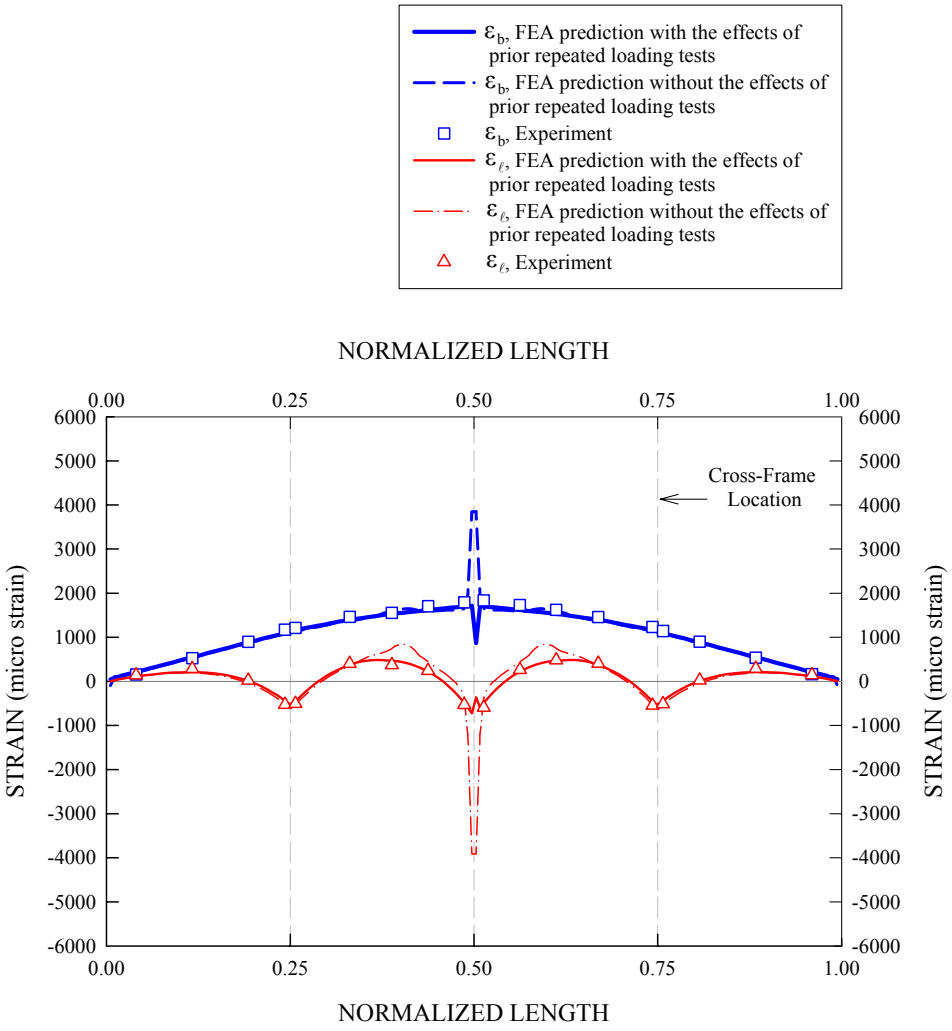

Figure 5.7.1. Measured major-axis and lateral bending strains for the G3 bottom flange along with corresponding FEA solutions with and without the effects of prior repeated loading tests at a total applied load level of 3959 kN (890 kips) during the final monotonic loading test, dead load strains and residual strains from the prior repeated loading tests are not included.

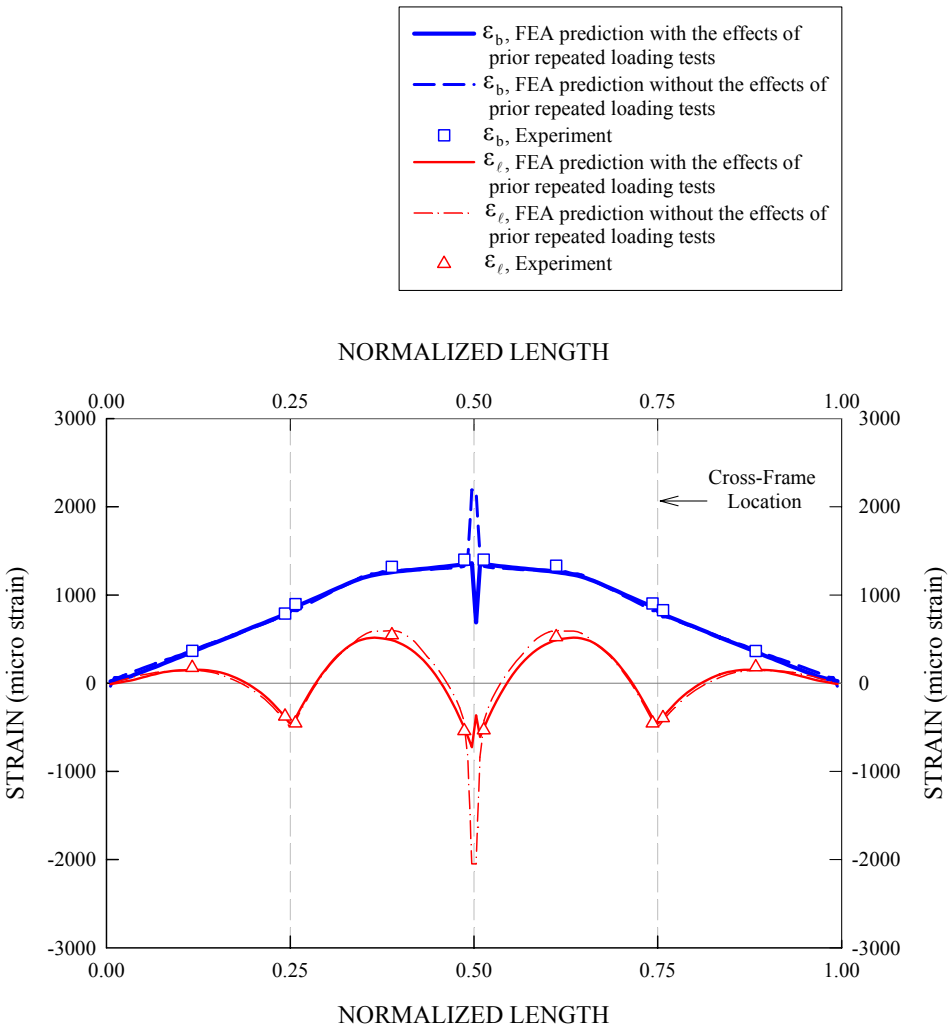

Figure 5.7.2. Measured major-axis and lateral bending strains for the G2 bottom flange along with corresponding FEA solutions with and without the effects of prior repeated loading tests at a total applied load level of 3959 kN (890 kips) during the final monotonic loading test, dead load strains and residual strains from the prior repeated loading tests are not included.

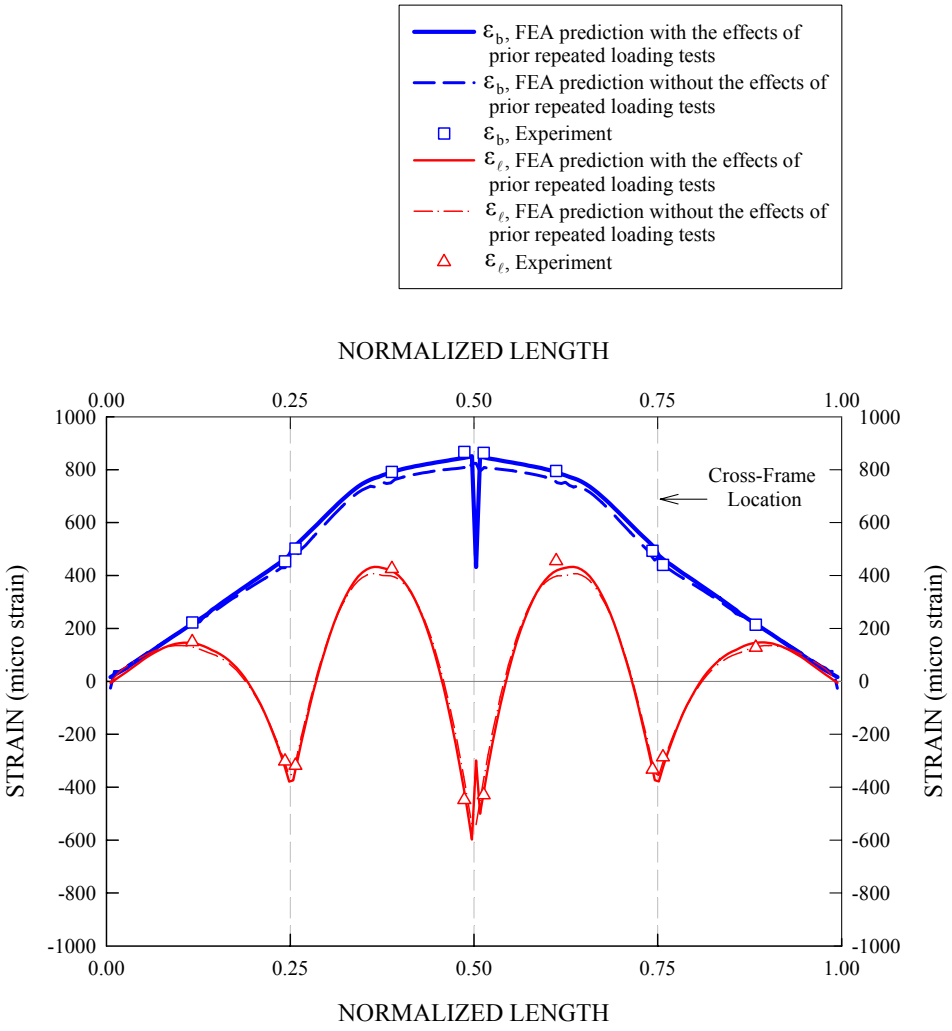

Figure 5.7.3. Measured major-axis and lateral bending strains for the G1 bottom flange along with corresponding FEA solutions with and without the effects of prior repeated loading tests at a total applied load level of 3959 kN (890 kips) during the final monotonic loading test, dead load strains and residual strains from the prior repeated loading tests are not included.

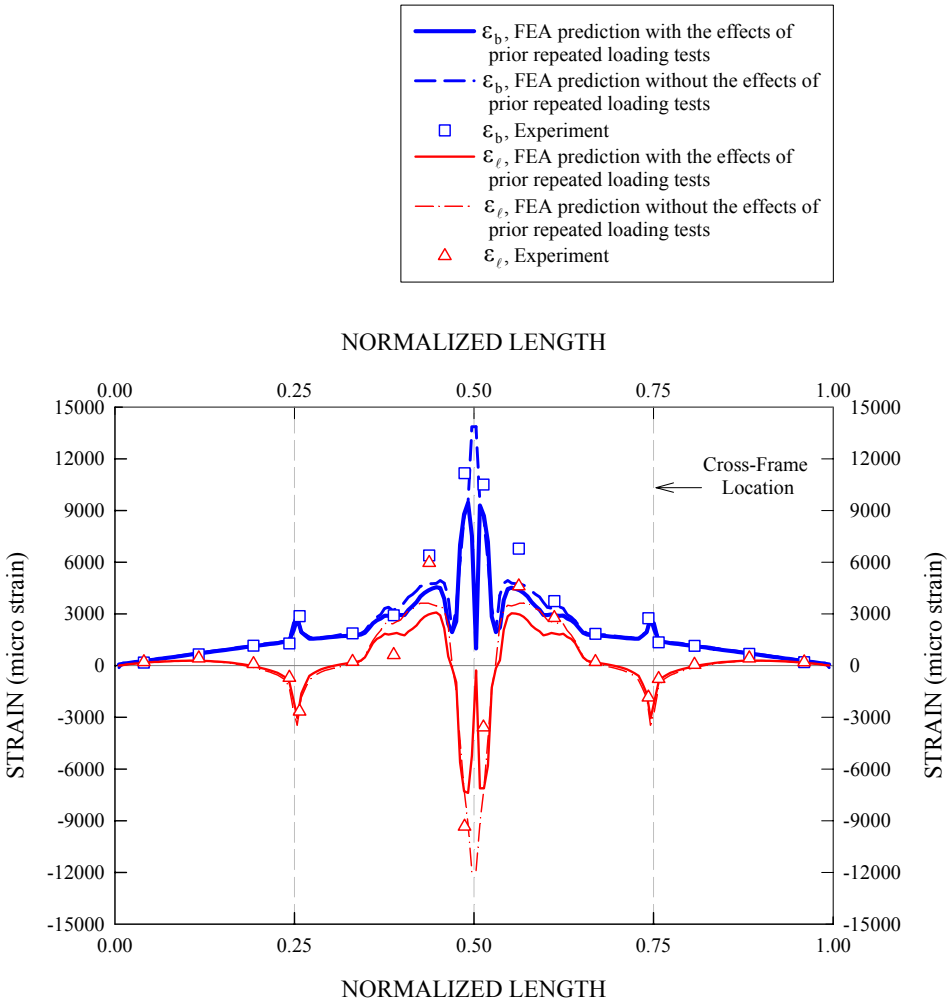

Figure 5.7.4. Measured major-axis and lateral bending strains for the G3 bottom flange along with corresponding FEA solutions with and without the effects of prior repeated loading tests at a total applied load level of 5115 kN (1150 kips) during the final monotonic loading test, dead load strains and residual strains from the prior repeated loading tests are not included.

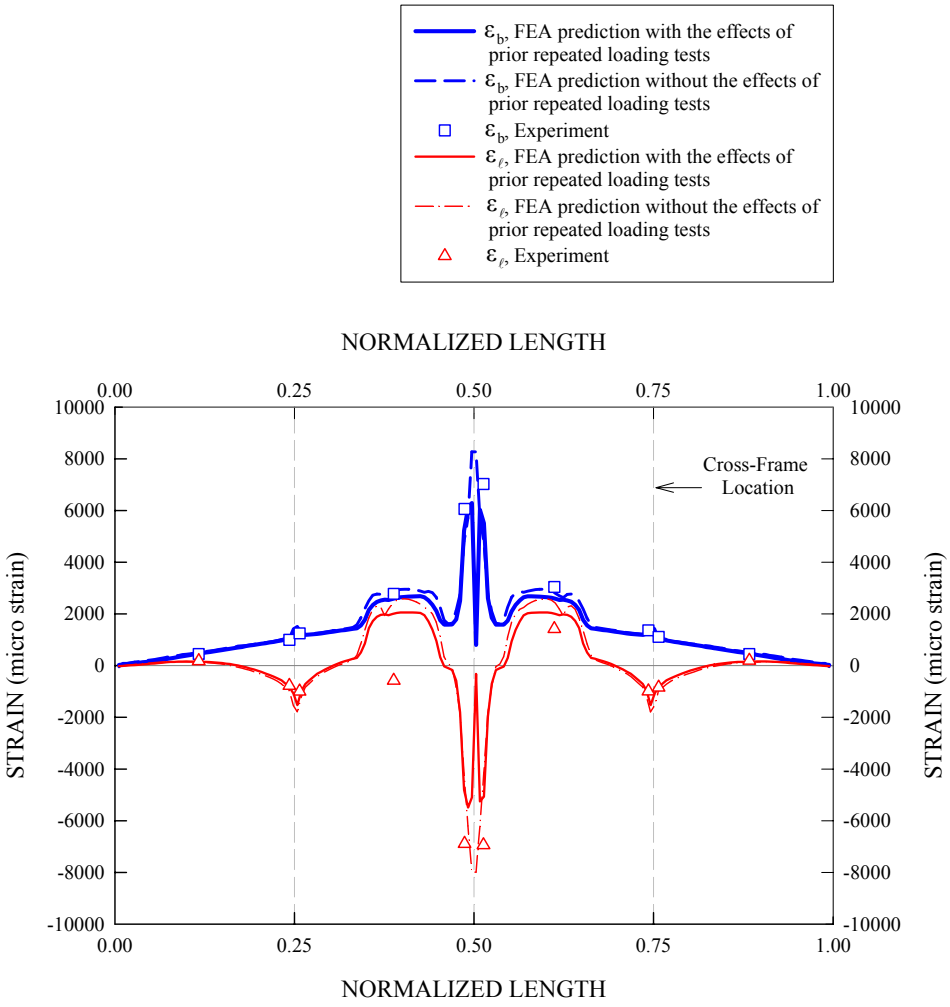

Figure 5.7.5. Measured major-axis and lateral bending strains for the G2 bottom flange along with corresponding FEA solutions with and without the effects of prior repeated loading tests at a total applied load level of 5115 kN (1150 kips) during the final monotonic loading test, dead load strains and residual strains from the prior repeated loading tests are not included.

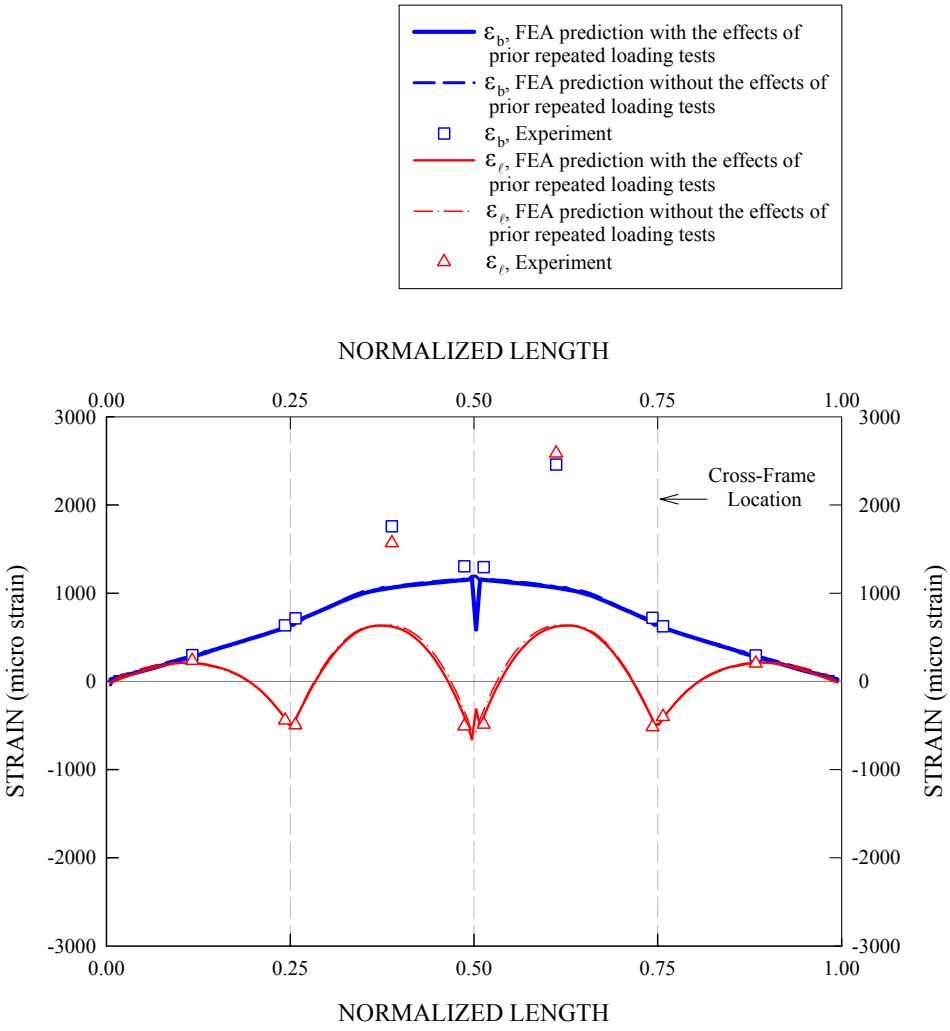

Figure 5.7.6. Measured major-axis and lateral bending strains for the G1 bottom flange along with corresponding FEA solutions with and without the effects of prior repeated loading tests at a total applied load level of 5115 kN (1150 kips) during the final monotonic loading test, dead load strains and residual strains from the prior repeated loading tests are not included.

5.8 FEA Equivalent Plastic Strains in Steel I-Girders

Although the major-axis and lateral bending strain plots offered in the previous section give useful information about the regions subjected to higher strains, they do not directly show the regions where the strains exceed the flange yield strain. Furthermore, the strains presented in the previous section do not include the dead load and residual strains that exist in the girders at the start of Test 4b. To clearly identify the yielded regions, one can consider the strains from all the sources (dead load, prior load cycling, and the monotonic loading in Test 4b) and compare resulting total to the flange yield strains (assuming that the stress-strain behavior is uniaxial in the flanges). However, a more convenient and direct way of checking the spread of yielding in the steel sections is to look at equivalent plastic strains (ε_{eq}^{p})obtained from the full nonlinear FEA solutions. The equivalent plastic strain is a scalar representation of multi-dimensional plastic strain developments at each integration point of the finite element model.

It is important to note that the test bridge was subjected to a series of repeated loading tests prior to the application of the final monotonic loading to the test bridge. It is important to note that the test bridge was loaded into the inelastic range at load levels D and E particularly in the first sequence of Test 4a. As a result, the steel sections that experienced yielding during these load levels were left with permanent strains upon removal of the Test 4a loads. Of the two FEA solutions considered in this study, the first FEA solution takes into account the residual strains at the end of Test 4a. Therefore, in this analysis, the plastic strain distributions along the girder lengths remain equal to the above residual strain distributions until the total applied load reaches a total applied load of approximately 4226 kN (950 kips), i.e., load level E from Test 4a. In other words, the

FEA solution including the effects of the prior repeated loading tests does not experience any additional plastic strains at the M_y- and M_p-based 1/3 rule load levels on G3 during the final monotonic loading test. In this light, it is also useful to investigate the equivalent plastic strain distributions from the FEA solution without the effects of the prior repeated loading tests. These strains predict how the structure would respond if the girders had not experienced any yielding prior to the final ultimate load test.

Figure 5.8.1 gives a perspective view of the FEA model of the steel superstructure with contours of equivalent plastic strains on the girder webs at the M_y-based 1/3 rule load level on G3, i.e., at total applied load of 3470 kN (780 kips). The FEA solution presented in this figure does not include the effects of the prior repeated loading tests. Also, the contours of the plastic strains are taken at the mid-surface of the shell elements used to represent the girder webs. It can be seen that, except for highly localized yielding at the bottom of the G3 web near the midspan, there is no yielding observed in the girder web panels.

When it comes to the yielding behavior of the girder flanges, the use of one-dimensional beam elements for representing the girder flanges makes it difficult to visualize the extent of yielding. Thus, separate plots showing the spread of yielding on the girder flanges are generated. Figure 5.8.2 provides a plot showing the normalized equivalent plastic strains along the normalized length for five mid-thickness locations across the width of the G3 bottom flange at the M_y-based 1/3 rule load level on G3. It should be noted that the plastic strains are obtained from the FEA solution without the effects of the prior repeated loading tests included. Figure 5.8.3 gives a similar plot for the G2 bottom flange. The corresponding plot for G1 is not presented here, since there is

no yielding developing on the bottom flange of G1 at this load level. The yield strains based on the measured F_y and E values for the bridge girders are used to the normalize the equivalent plastic strains. For both of the plots shown in Figures 5.8.2 and 5.8.3, it is of interest to note that, due to the effects of the flange lateral bending associated with horizontal curvature, there is significant yielding at the midspan outside portion of the flanges. In fact, the largest plastic strains are occurring at the outside flange tips, and their magnitudes are 1.5 and 0.63 times the corresponding flange yield strains for G3 and G2, respectively. However, there is a high strain gradient across the flange width at the midspan locations. As a result, the entire inside half-width of these flanges is elastic. In addition, Figure 5.8.2 shows that there is a minor onset of the yielding at the inside tip of the G3 bottom flange near mid-length of the unbraced length next to midspan. An important attribute to note here is that there are no signs of yielding at the inside portion of the G2 and G3 bottom flanges at midspan or at the outside portion of the G3 flange halfway between the mid- and quarter-span cross-frames as shown in Figures 5.8.2 and 5.8.3. This is due to the fact that the flange lateral bending moments reduce the tensile strains in the inner part of the bottom flanges at midspan and the outer part at the middle of the unbraced length adjacent to the midspan, thereby delaying the onset of yielding.

Figure 5.8.4 gives a perspective view of the FEA model of the steel superstructure with contours of equivalent plastic strains on the girder webs at the M_p-based 1/3 rule load level on G3, corresponding to an applied load level of 3959 kN (890 kips). It can be seen that the yielded region at the lower bottom of the G3 web panel at the midspan cross-frame has expanded relative to that shown in Figure 5.8.1. However, the web still has not yielded throughout its entire depth. In addition, localized yielding starts to appear

in the bottom of the web in the middle of the unbraced lengths adjacent to the midspan. The yielding on G2's web has just started at this load.

Figures 5.8.5 and 5.8.6 provide normalized equivalent plastic strains along the normalized length for five mid-thickness locations across the width of the G3 and G2 bottom flanges at the M_p-based 1/3 rule load level on G3, or a total applied load of 3959 kN (890 kips). For both of these plots, it can be seen that the maximum plastic strains at the tip of the bottom flanges at midspan are increased to four and 2.7 times the flange yield strain for G3 and G2 respectively. However, it is interesting to note that the inside portion of the G3 and G2 bottom flanges at the midspan is still elastic at this load level. Furthermore, it can be seen in both of the plots that there is a mild increase in the plastic strains at the mid-length of the unbraced lengths next to midspan relative to the magnitudes observed in Figures 5.8.2 and 5.8.3. Most importantly, it should be noted that only a small portion of the I-girders are yielded at this load level. In fact, it can be seen that the inside portion of the G2 and G3 bottom flanges at midspan and the outside portion of the G3 flange halfway between the mid- and quarter-span cross-frames are not yielded yet.

Figure 5.8.7 gives a perspective view of the FEA model of the steel superstructure with contours of equivalent plastic strains on the girder webs at the spalling and crushing of the slab concrete in the experimental test, when the midspan outside tip of the G3 bottom flange reaches a deflection of 610 mm (24 in) at a total applied load level of 5783 kN (1300 kips). It should be noted that the FEA solution presented in this figure *includes* the effects of the prior repeated loading tests. Unlike the previous two contour plots shown in Figures 5.8.1 and 5.8.4, it can be seen that a significant portion of the G3 web is

yielded in the unbraced length next to the midspan. A maximum equivalent plastic strain of 3.24 percent is calculated in a very local region at the bottom of the web at midspan. In addition, it should be noted that the web near midspan is essentially plastified throughout its depth. Similarly, Figure 5.8.7 also shows that the G2 is extensively yielded in the vicinity of its midspan. In contrast, it can be seen that the G1 web is essentially elastic at this high applied load level.

Figures 5.8.8 and 5.8.9 show the normalized equivalent plastic strains along the normalized length for five mid-thickness locations across the width of the G3 and G2 bottom flanges at the load level of 5783 kN (1300 kips). Consistent with Figure 5.8.7, the plastic strains are obtained from the FEA solution *including* the effects of the prior repeated loading tests in these figures. In both of these plots, it can be seen that the bottom flanges are essentially fully yielded across their entire widths at the midspan cross-section as well as between the midspan and the mid-length of both of the adjacent unbraced lengths, except for the inside tip of the flanges at the midspan. In addition, it is worthwhile to note that the outer portion of the flanges at the quarter-span cross-frames is also yielded. Figure 5.8.10 shows a comparable plot for the G1 bottom flange at this load level. It can be seen that the outside portion at midspan and the inside portion at the mid-length of the unbraced lengths next to midspan are yielded, but that there is a high strain gradient across the flange widths similar to that observed for the G3 and G2 bottom flanges at lower load levels.

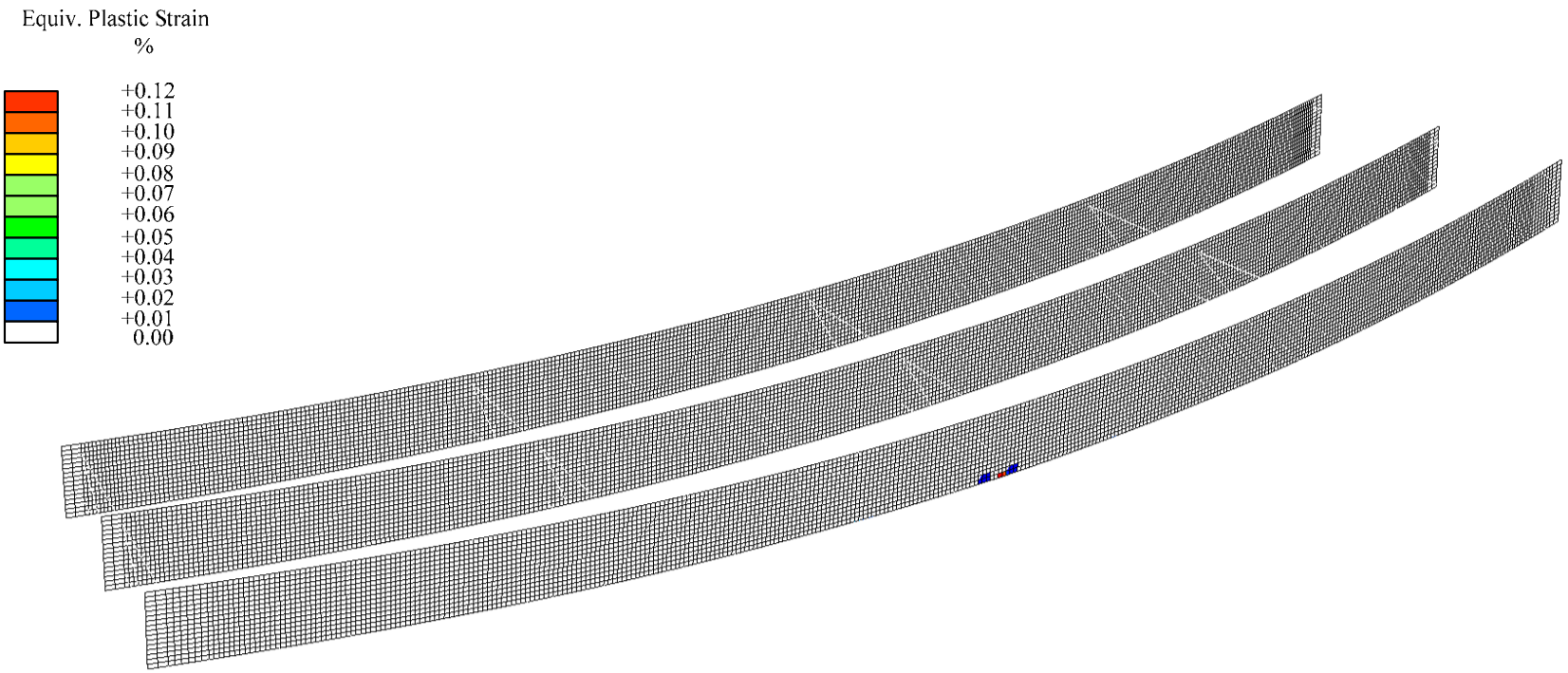

Figure 5.8.1. Perspective view of the FEA model of the steel I-girders with contours of equivalent plastic strains on the girder webs at the M_y-based 1/3 rule load level on G3, total applied load = 3470 kN (780 kips), effects of prior repeated loading tests *not* included (Displacement Scale Factor = 2.0).

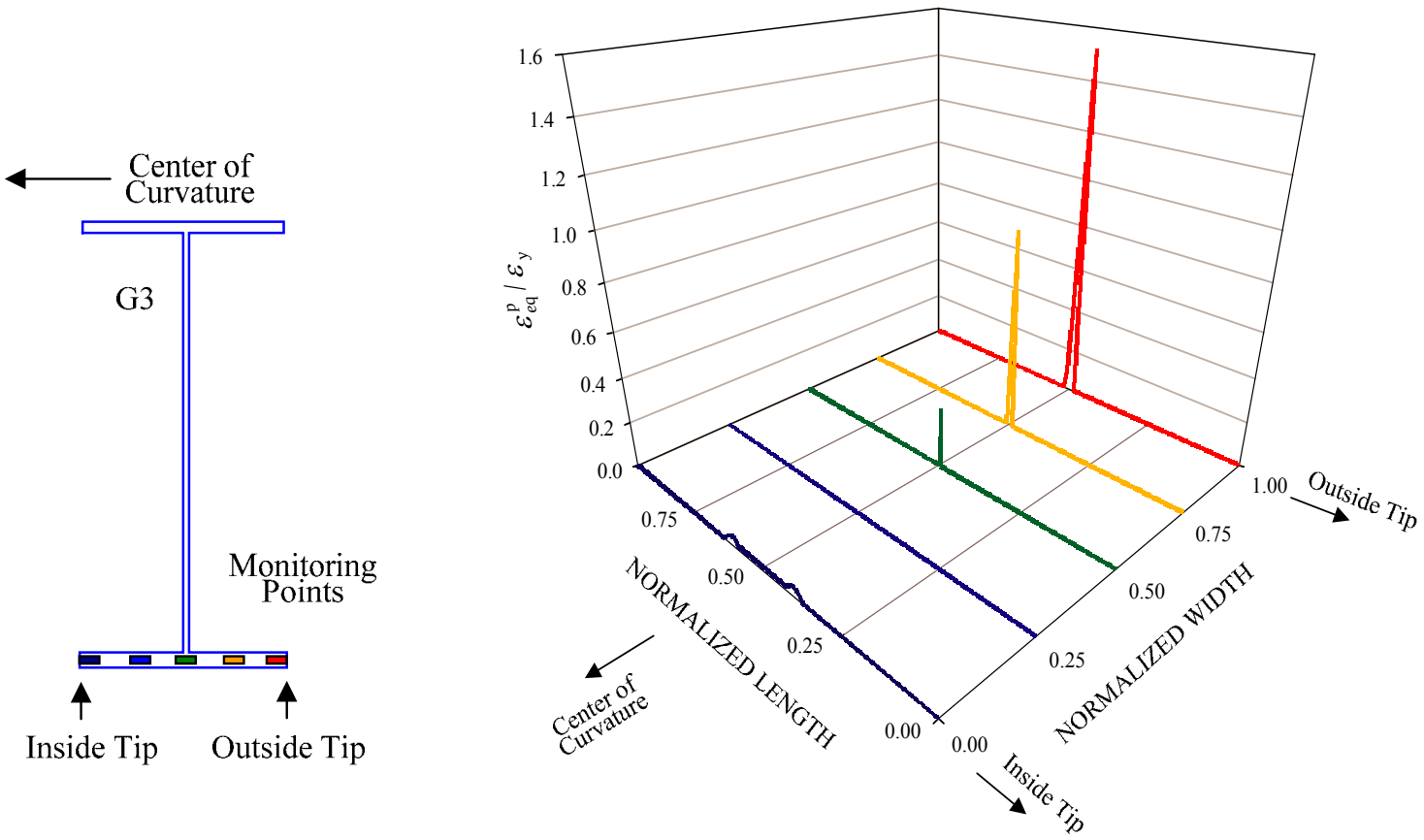

Figure 5.8.2. Normalized equivalent plastic strains along the normalized length for five mid-thickness locations through the width of the G3 bottom flange, taken at the M_y-based 1/3 rule load level on G3, 3470 kN (780 kips), effects of prior repeated loading tests *not* included.

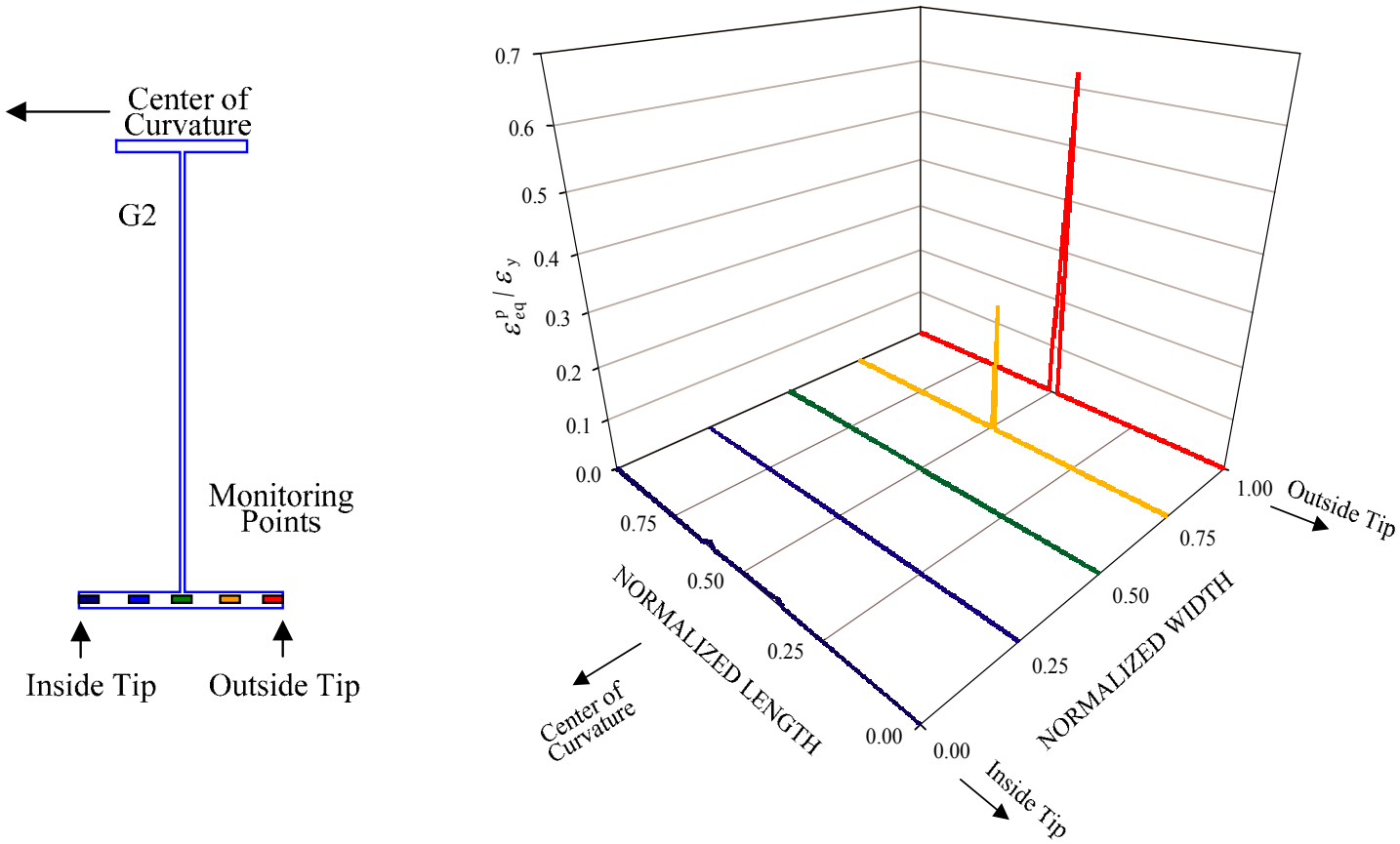

Figure 5.8.3. Normalized equivalent plastic strains along the normalized length for five mid-thickness locations through the width of the G2 bottom flange, taken at the M_y-based 1/3 rule load level on G3, 3470 kN (780 kips), effects of prior repeated loading tests *not* included.

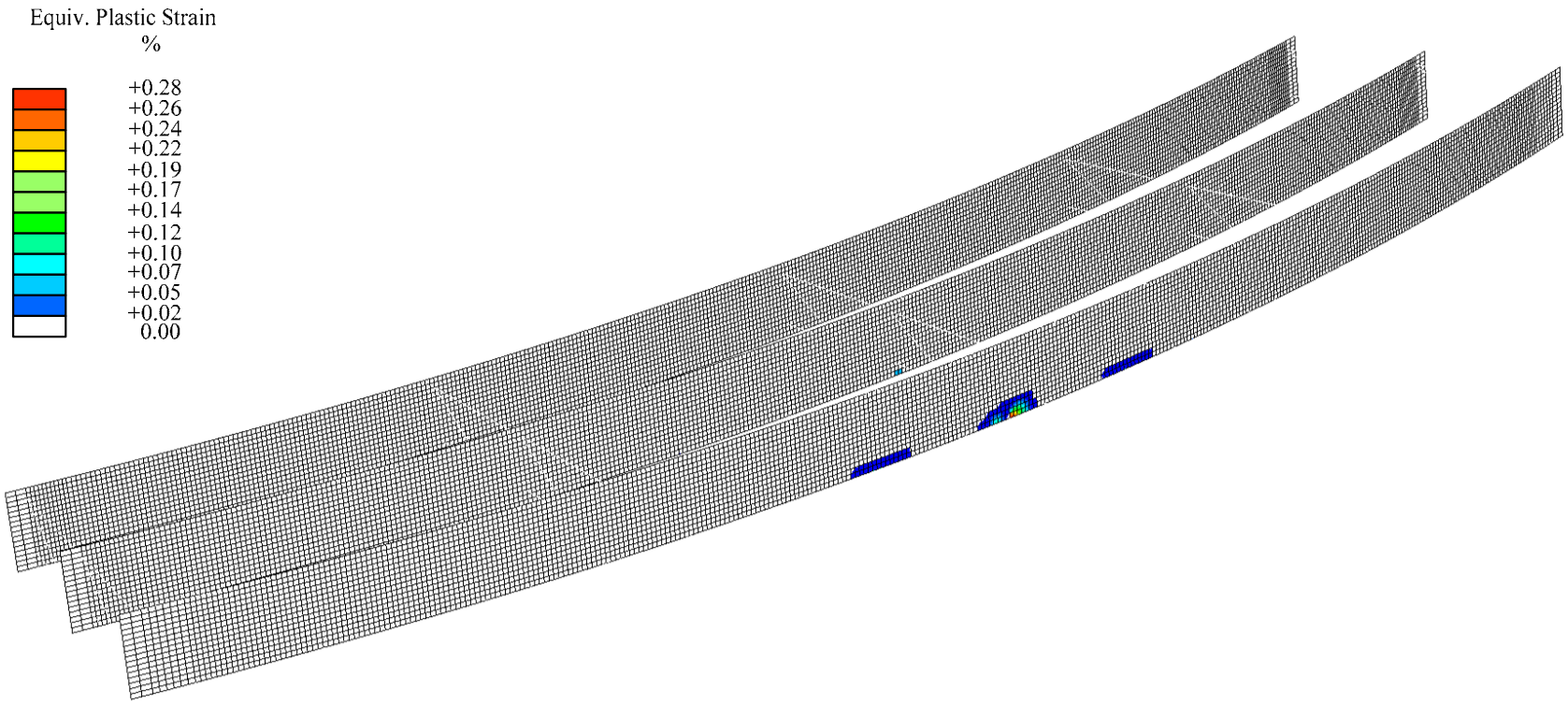

Figure 5.8.4. Perspective view of the FEA model of the steel I-girders with contours of equivalent plastic strains on the girder webs at the M_p-based 1/3 rule load level on G3, total applied load = 3959 kN (890 kips), effects of prior repeated loading tests *not* included (Displacement Scale Factor = 2.0).

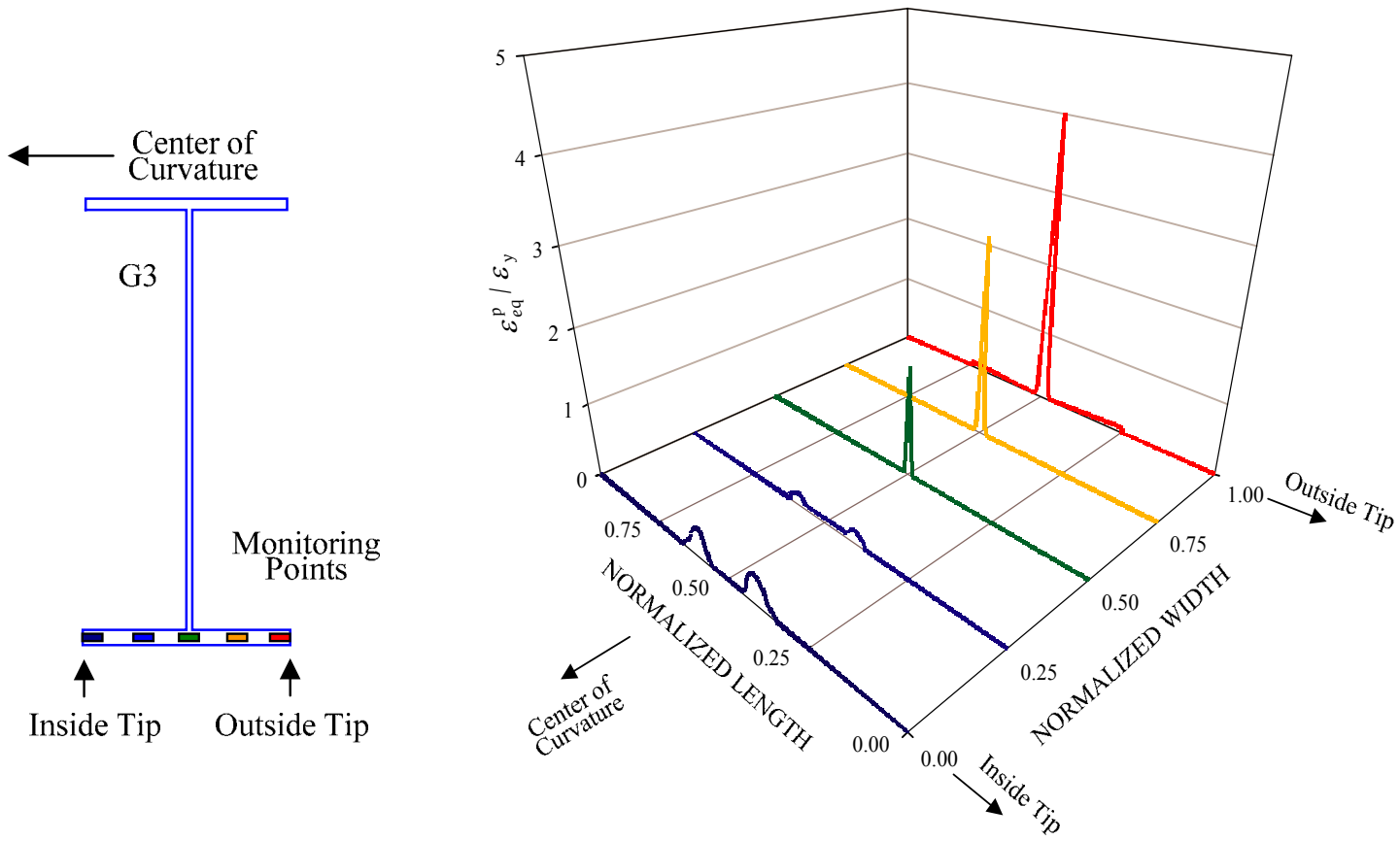

Figure 5.8.5. Normalized equivalent plastic strains along the normalized length for five mid-thickness locations through the width of the G3 bottom flange, taken at the M_p-based 1/3 rule load level on G3, 3959 kN (890 kips), effects of prior repeated loading tests *not* included.

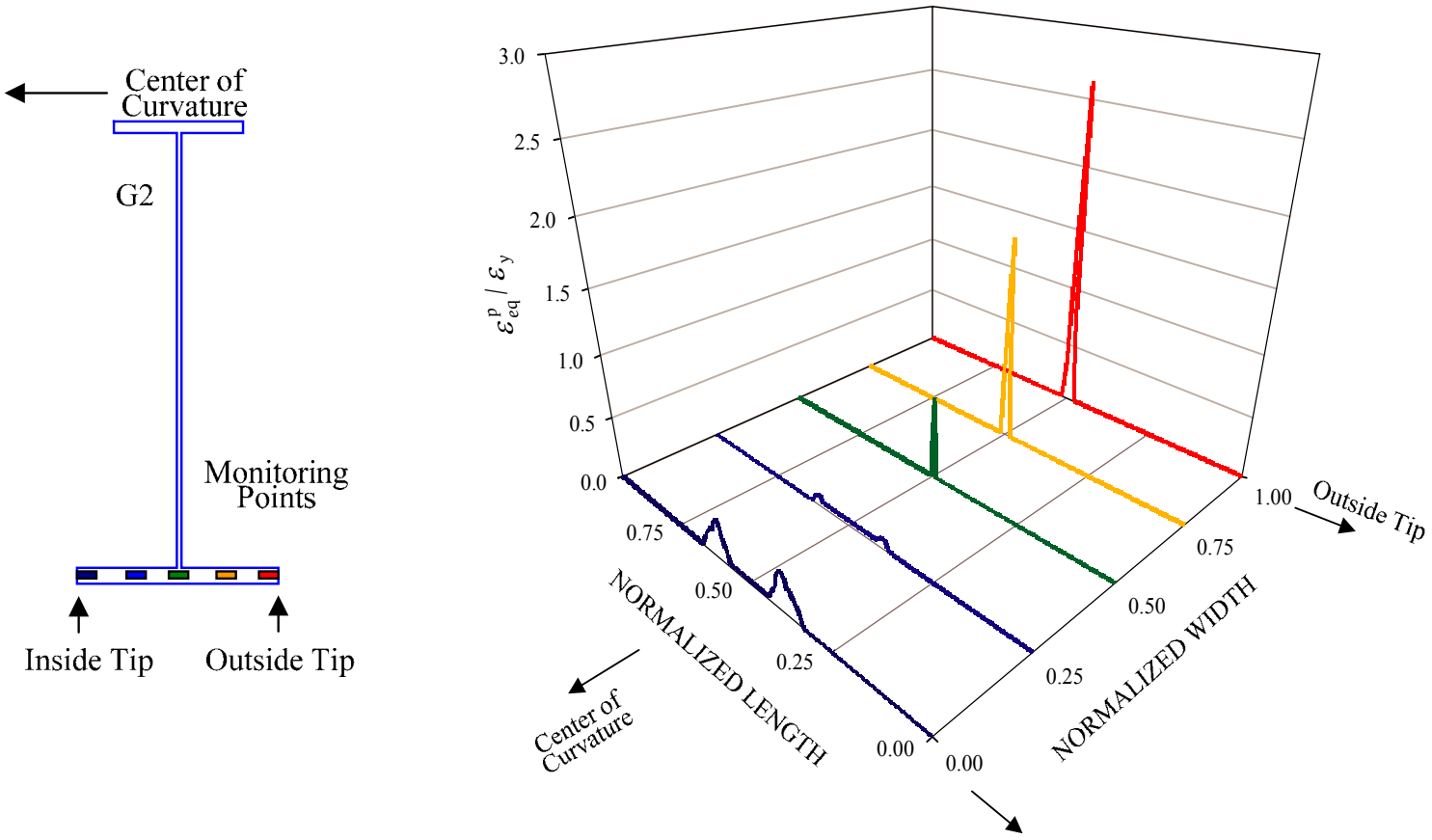

Figure 5.8.6. Normalized equivalent plastic strains along the normalized length for five mid-thickness locations through the width of the G2 bottom flange, taken at the M_p-based 1/3 rule load level on G3, 3959 kN (890 kips), effects of prior repeated loading tests *not* included.

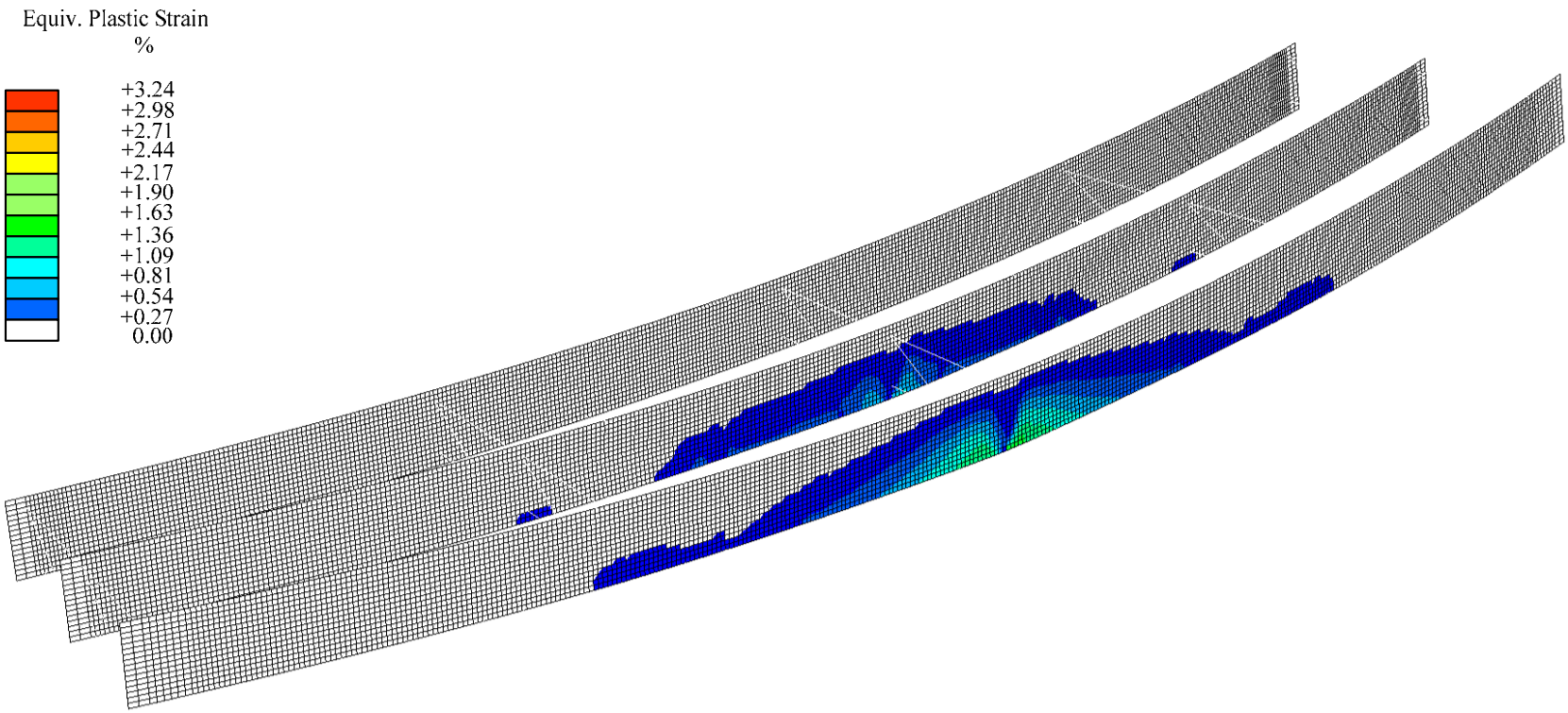

Figure 5.8.7. Perspective view of the FEA model of the steel I-girders with contours of equivalent plastic strains on the girder webs at spalling and crushing of the slab concrete during the experimental test, defection of the midspan outside tip of the G3 bottom flange = 610 mm (24 in), total applied load = 5783 kN (1300 kips), effects of prior repeated loading tests *included*, Displacement Scale Factor = 2.0.

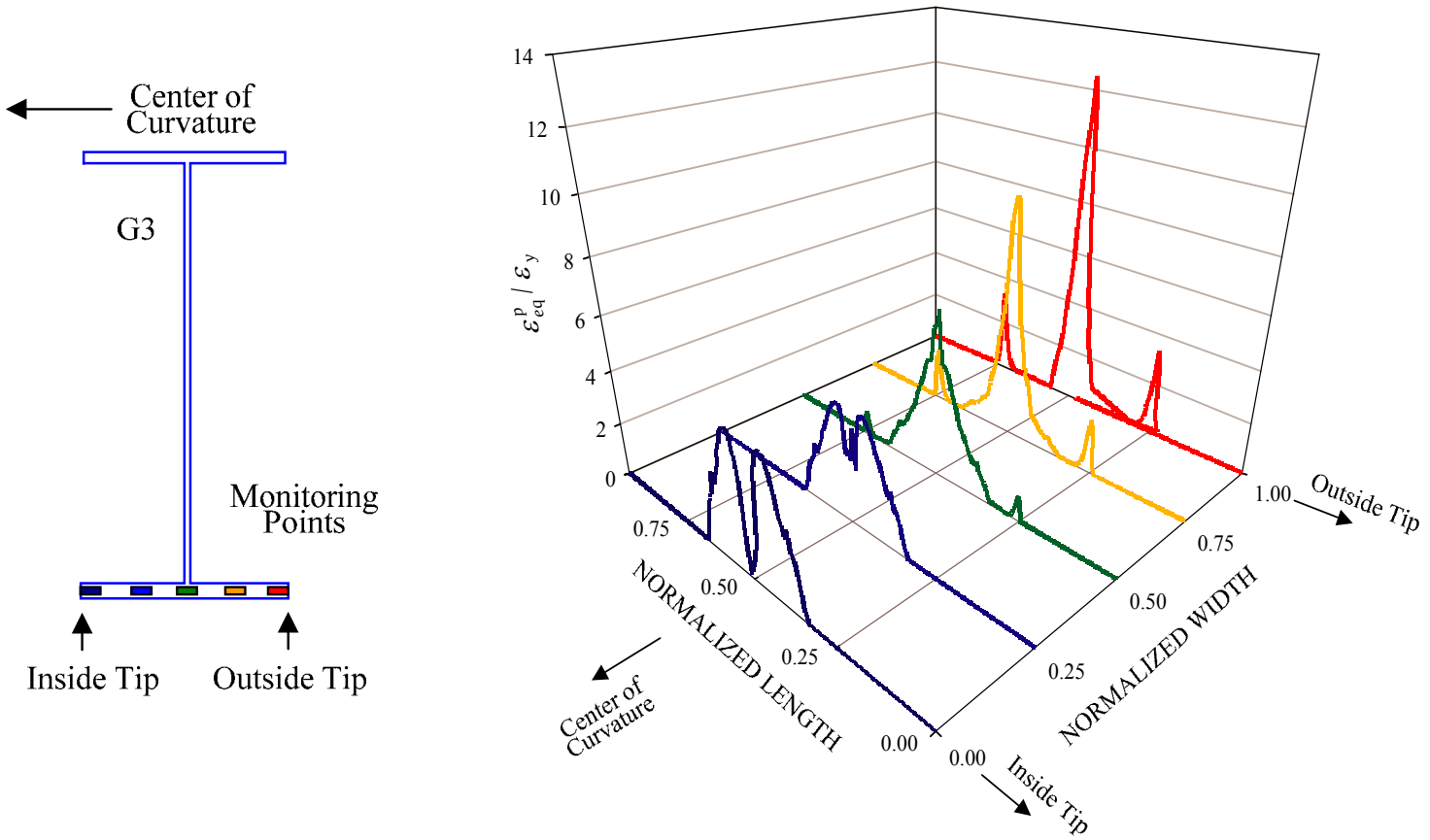

Figure 5.8.8. Normalized equivalent plastic strains along the normalized length for five mid-thickness locations through the width of the G3 bottom flange at spalling and crushing of the slab concrete in the experimental test, deflection of the midspan outside tip of the G3 bottom flange = 610 mm (24 in), total applied load = 5783 kN (1300 kips), effects of prior repeated loading tests *included*.

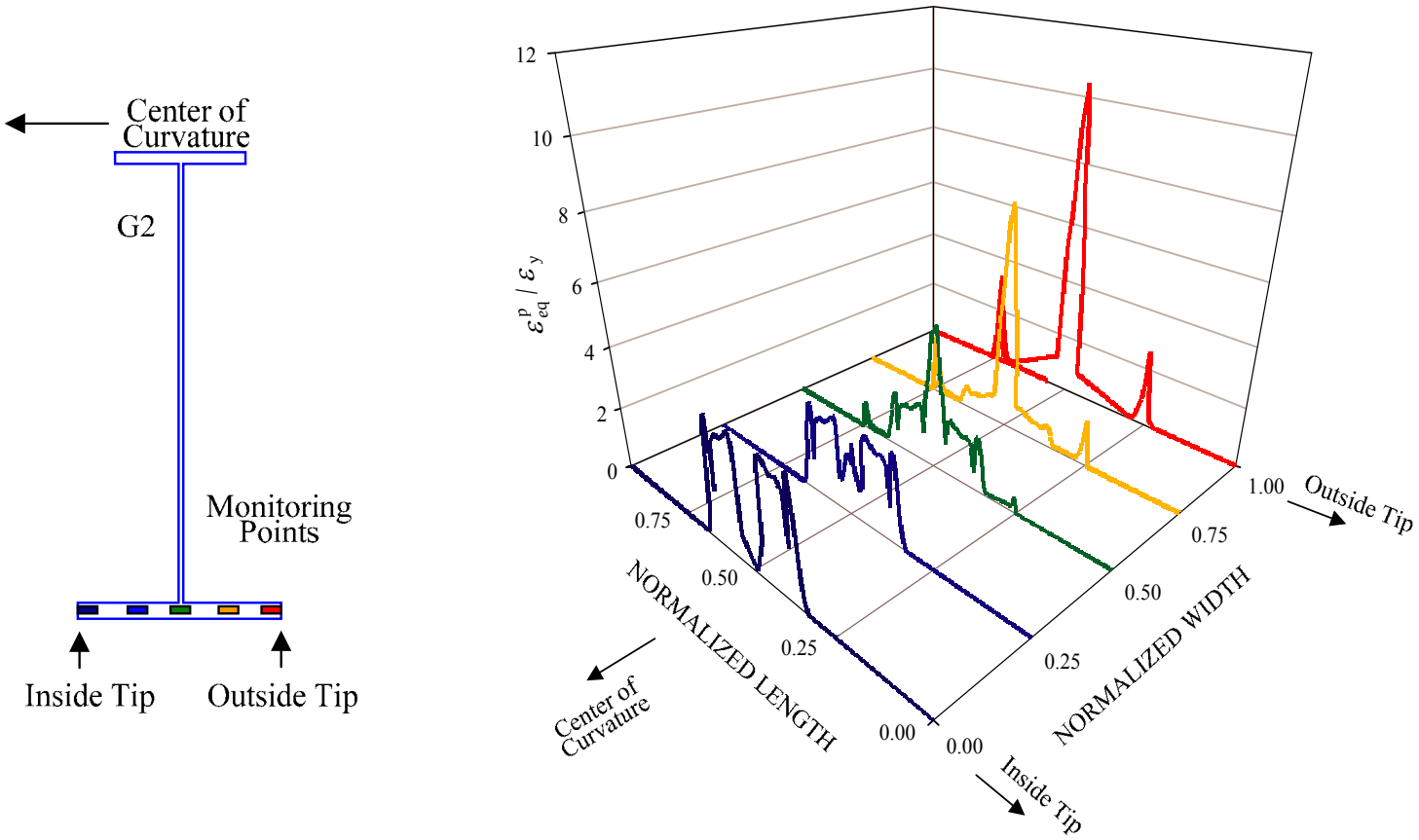

Figure 5.8.9. Normalized equivalent plastic strains along the normalized length for five mid-thickness locations through the width of the G2 bottom flange at spalling and crushing of the slab concrete in the experimental test, deflection of the midspan outside tip of the G3 bottom flange = 610 mm (24 in), total applied load = 5783 kN (1300 kips), effects of prior repeated loading tests *included*.

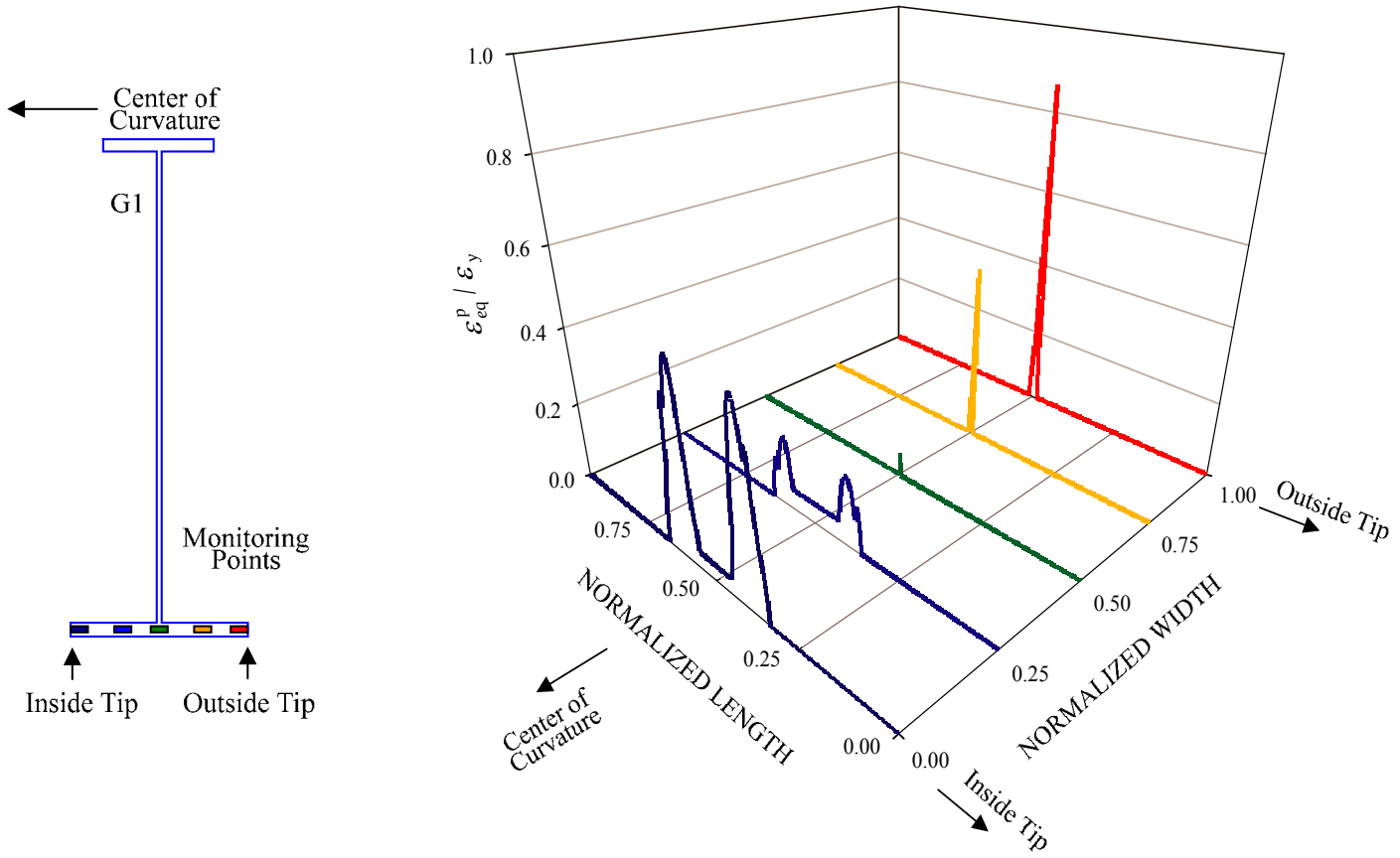

Figure 5.8.10. Normalized equivalent plastic strains along the normalized length for five mid-thickness locations through the width of the G1 bottom flange at spalling and crushing of the slab concrete during the experimental test, deflection of the midspan outside tip of the G3 bottom flange = 610 mm (24 in), total applied load = 5783 kN (1300 kips), effects of prior repeated loading tests *included*.

5.9 Slab FEA Longitudinal and Radial Stresses

Figure 5.9.1 provides a plot showing the predicted longitudinal stresses across the midspan cross-section on the top surface of slab for gage location L9 at the M_p-based 1/3 rule load level of 3959 kN (890 kips) on G3. Initial dead load stresses are not included in this plot, as well as in the other plots presented below. It can be seen that the two FEA solutions are essentially identical except for some minor local deviations. Also, it can be seen that the stresses gradually increase toward the outer edge of the overhang region outside G3 with a maximum stress slightly above 21 MPa (3.0 ksi). To provide information about the stresses in other regions of the slab, Figure 5.9.2 gives a plan view of the test bridge FEA model with longitudinal stress contours on the top surface of the slab at the M_p-based 1/3 rule load level of 3959 kN (890 kips). It is interesting to note that relatively high longitudinal stresses occur locally in the overhang region just outside of G3 at the midspan. Figure 5.9.3 shows a plan view of the test bridge FEA model with radial stress contours on the top surface of the slab at the same load level. In general, one can observe that overall radial compressive stresses on the top surface are quite small relative to the concrete compressive strength, except for several regions with highly localized stresses just outside of the girders at the midspan cross-frames. In contrast, it can be seen that tensile stresses on the top surface, in particular the slab portion just inside G3, are relatively high and are close to the concrete tensile strength.

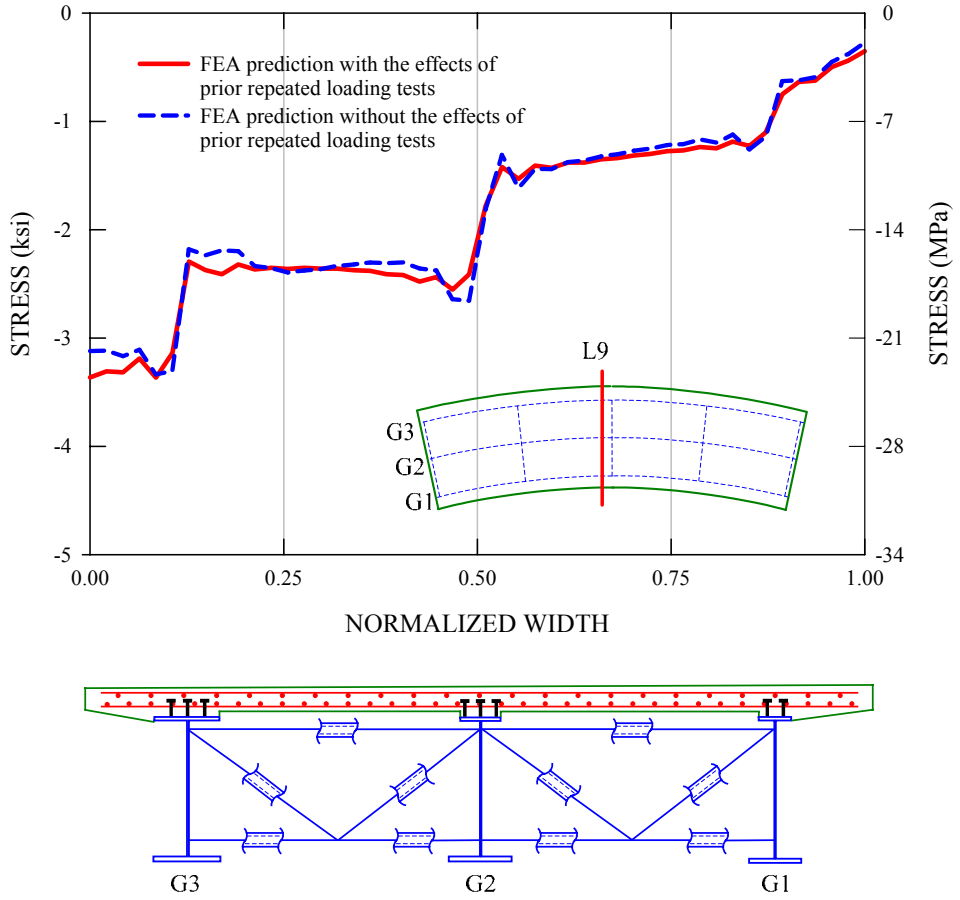

Figure 5.9.1. Predicted longitudinal stresses across the top surface of the slab for gage location L9 at the M_p-based 1/3 rule load level of 3959 kN (890 kips), initial dead load stresses *not* included.

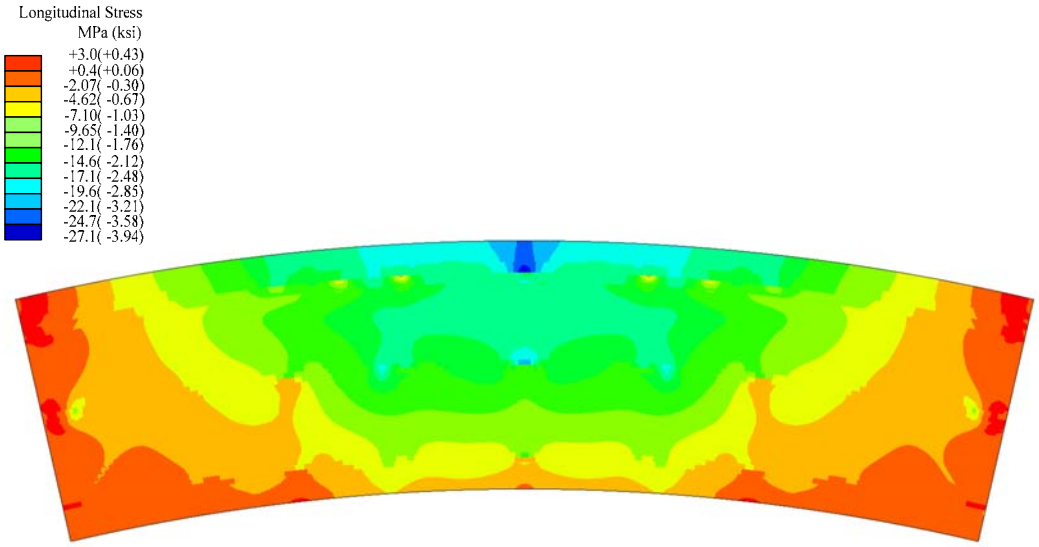

Figure 5.9.2. Plan view of the test bridge FEA model with longitudinal stress contours on the top surface of the slab at the M_p-based 1/3 rule load level of 3959 kN (890 kips). The contours do not include stresses due to dead loads.

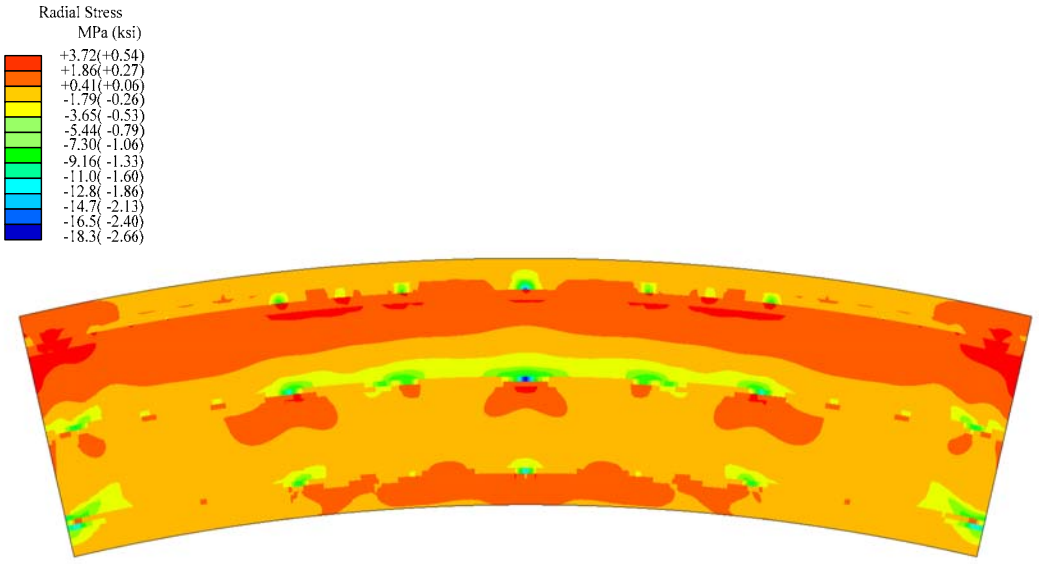

Figure 5.9.3. Plan view of the test bridge FEA model with radial stress contours on the top surface of the slab at the M_p-based 1/3 rule load level of 3959 kN (890 kips). The contours do not include stresses due to dead loads.

Figure 5.9.4 shows a plot of the predicted longitudinal stresses across the top surface of the slab for gage location L9 at a total applied load of 5783 kN (1300 kips). It can be observed that the FEA solution without the effects of the prior repeated loading tests, indicated by the dashed line, gives slightly higher overall stress predictions. Interestingly, one can see that the maximum stress now occurs at the inner region between G2 and G3 instead at the outer edge of the slab. This is largely because the concrete slab near the outer edge of the G3 overhang is in the softening (unloading) part of the concrete stress-strain curve due to the development of extensive strains, as is shown later in Section 3.3.3. Figures 5.9.5 and 5.9.6 show a plan view of the test bridge FEA model with longitudinal and radial stress contours on the top surface of the slab at the above load level. It can be seen in Figure 5.9.5 that the overhang region just outside of G3 is in a high compressive stress state, with a maximum compressive stress of 46 MPa (6.7 ksi), which is significantly higher than the concrete cylinder compressive strength of 34 MPa (4.9 ksi). This is in large part due to the fact that the strength of concrete can be increased due to confinement. In the concrete constitutive model used in the analysis, this behavior is represented by an expansion of yield and failure surfaces of the concrete constitutive model, resulting in a higher peak strength. Similarly, Figure 5.9.6 also shows that radial compressive stresses are developed at the overhang region outside G3 as well as in the region between G2 and G3 near midspan.

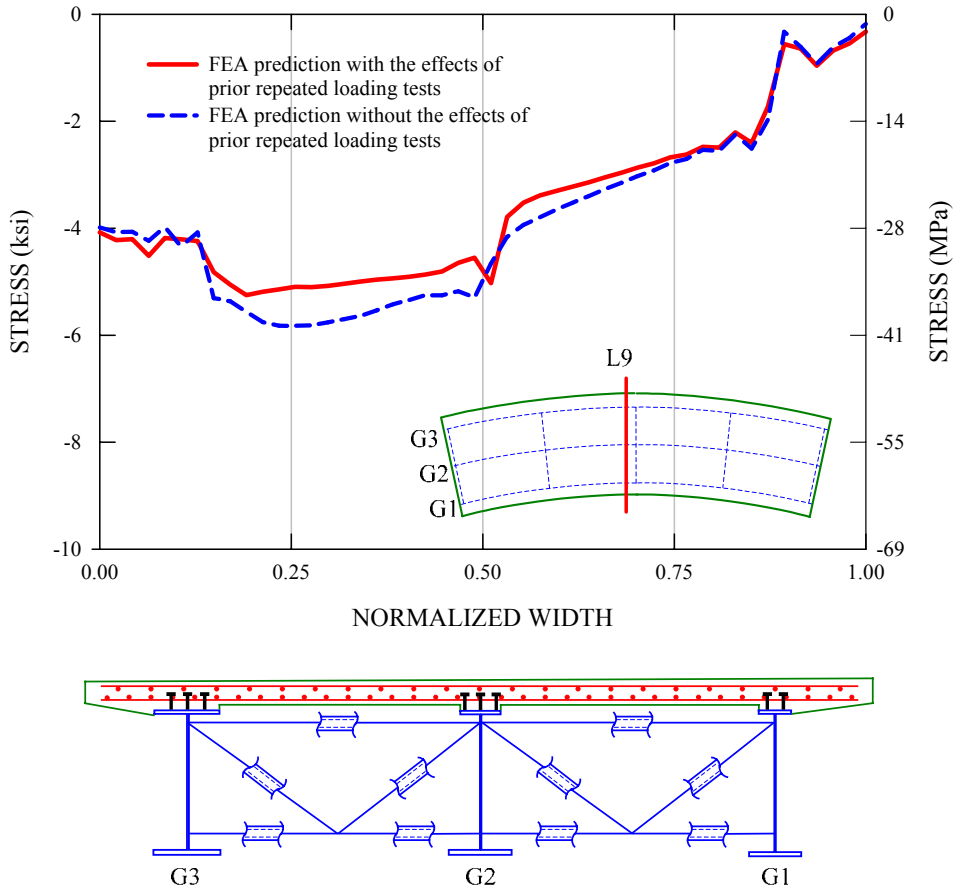

Figure 5.9.4. Predicted longitudinal stresses across the top surface of the slab for gage location L9 at spalling and crushing of the slab concrete in the experimental test, deflection of the midspan outside tip of the G3 bottom flange = 610 mm (24 in), total applied load = 5783 kN (1300 kips), initial dead load stresses *not* included.

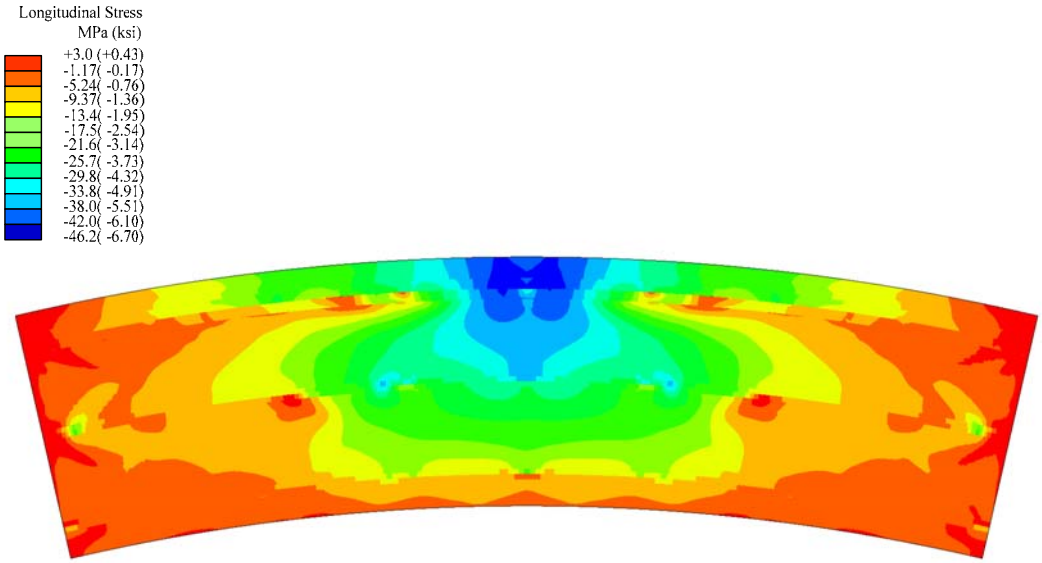

Figure 5.9.5. Plan view of the test bridge FEA model with longitudinal stress contours on the top surface of the slab at spalling and crushing of the slab concrete in the experimental test, deflection of the midspan outside tip of the G3 bottom flange = 610 mm (24 in), total applied load = 5783 kN (1300 kips), the contours do not include stresses due to dead loads.

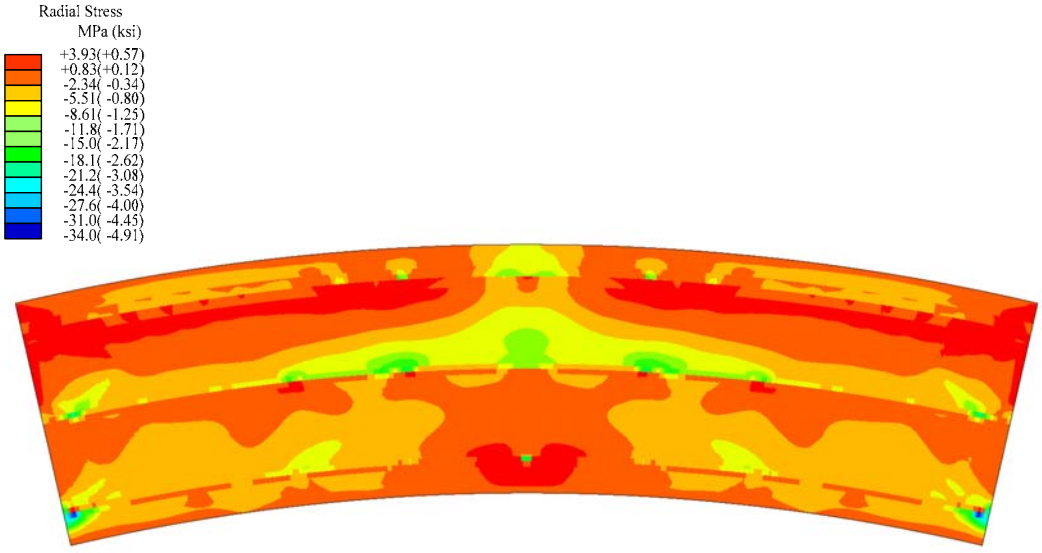

Figure 5.9.6. Plan view of the test bridge FEA model with radial stress contours on the top surface of the slab at spalling and crushing of the slab concrete in the experimental test, deflection of the midspan outside tip of the G3 bottom flange = 610 mm (24 in), total applied load = 5783 kN (1300 kips), the contours do not include stresses due to dead loads.

Figure 5.9.7 shows predicted longitudinal stresses across the midspan cross-section on the *bottom* surface of the slab for gage location L9 at the M_p-based 1/3 rule load level of 3959 kN (890 kips) on G3. It can be seen that the midspan bottom surface of the slab is in general subjected to compressive stresses that are less than 14 MPa (2 ksi). However, it should be noted that there is no clear pattern observed in the bottom surface stresses, compared to that for the top surface longitudinal stresses. Figures 5.9.8 and 5.9.9 show a plan view of the test bridge FEA model with longitudinal and radial stress contours on the bottom surface of the slab at the M_p-based 1/3 rule load level of 3959 kN (890 kips) on G3. It can be seen that the majority of the bottom surface has compressive longitudinal and radial stresses that are relatively small compared to the concrete compressive strength.

Figure 5.9.10 shows the predicted longitudinal stresses across the midspan cross-section on the bottom surface of the slab for gage location L9 at a total applied load of 5783 kN (1300 kips). It is interesting to note that the longitudinal stresses between G1 and G2 are increased relative to the corresponding values at 3959 kN (890 kips) as shown in Figure 5.9.7, whereas the stresses between G2 and G3 are actually decreased from the corresponding values at 3959 kN (890 kips). Figures 5.9.11 and 5.9.12 show a plan view of the test bridge FEA model with longitudinal and radial stress contours on the bottom surface of the slab at a total applied load of 5783 kN (1300 kips).

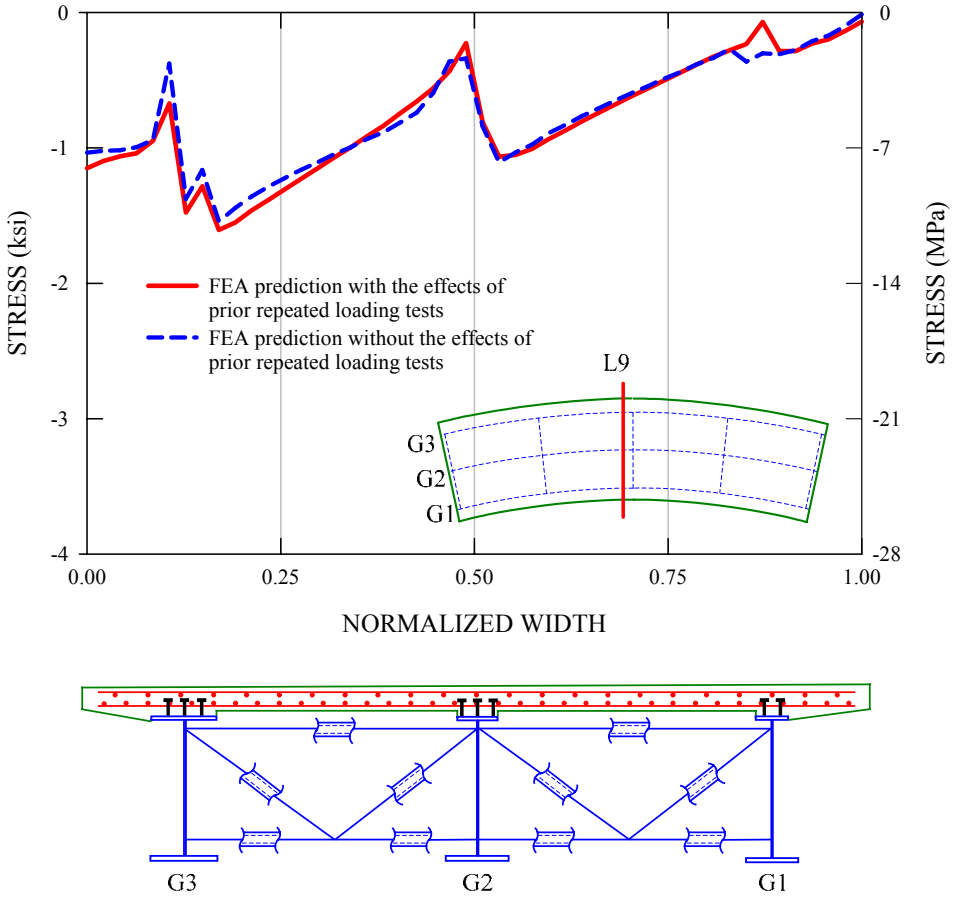

Figure 5.9.7. Predicted longitudinal stresses across the bottom surface of the slab for gage location L9 at the M_p-based 1/3 rule load level of 3959 kN (890 kips).

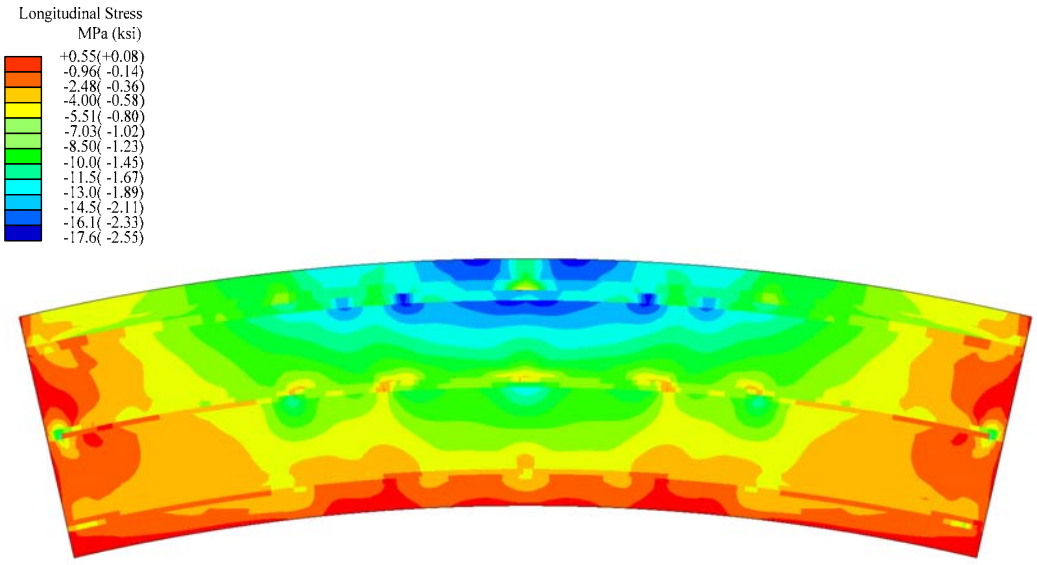

Figure 5.9.8. Plan view of the test bridge FEA model with longitudinal stress contours on the bottom surface of the slab at the M_p-based 1/3 rule load level of 3959 kN (890 kips).

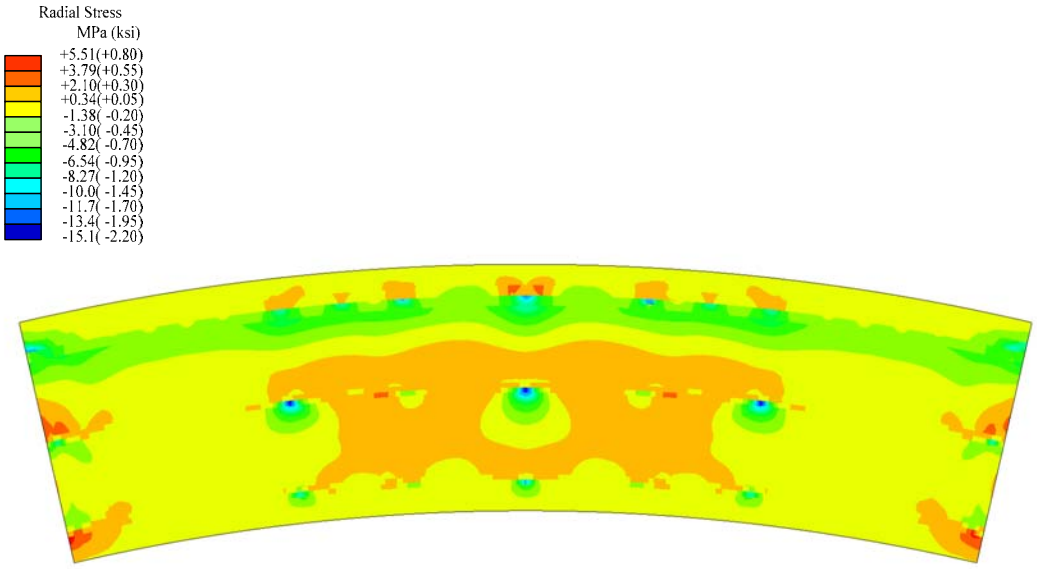

Figure 5.9.9. Plan view of the test bridge FEA model with radial stress contours on the bottom surface of the slab at the M_p-based 1/3 rule load level of 3959 kN (890 kips).

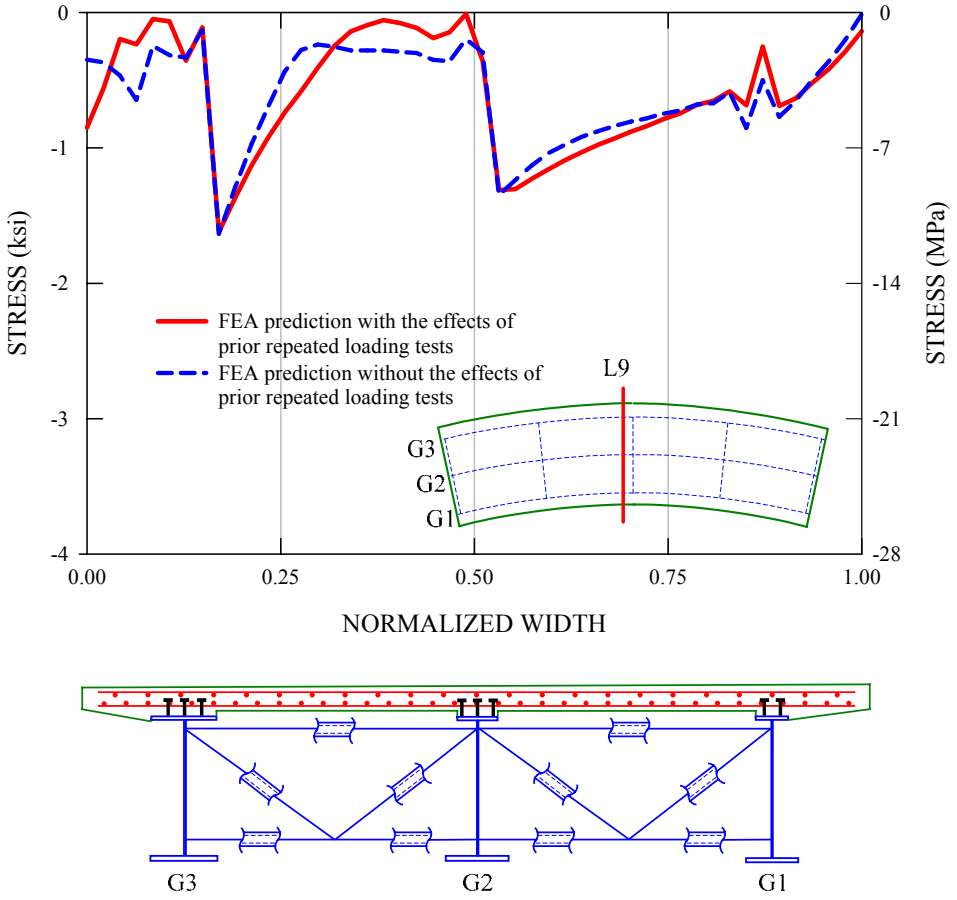

Figure 5.9.10. Predicted longitudinal stresses across the top surface of the slab for gage location L9 at spalling and crushing of the slab concrete in the experimental test, deflection of the midspan outside tip of the G3 bottom flange = 610 mm (24 in), total applied load = 5783 kN (1300 kips).

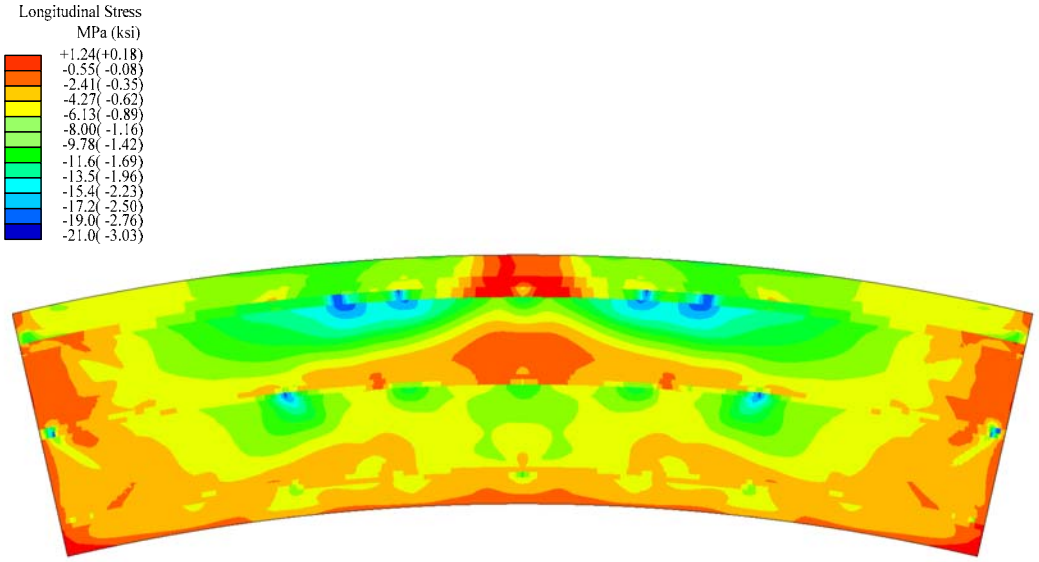

Figure 5.9.11. Plan view of the test bridge FEA model with longitudinal stress contours on the bottom surface of the slab at spalling and crushing of the slab concrete in the experimental test, deflection of the midspan outside tip of the G3 bottom flange = 610 mm (24 in), total applied load = 5783 kN (1300 kips).

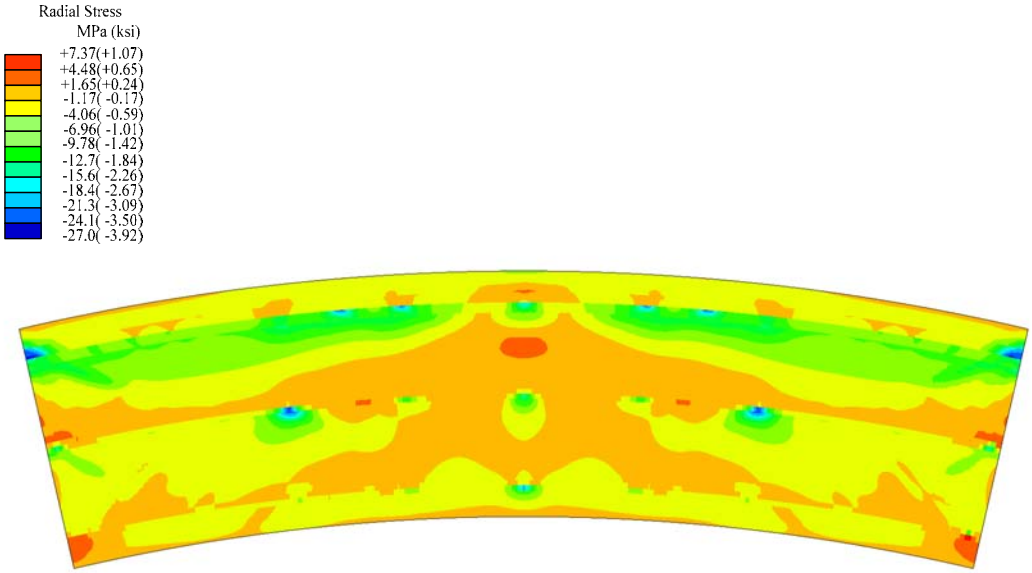

Figure 5.9.12. Plan view of the test bridge FEA model with radial stress contours on the bottom surface of the slab at spalling and crushing of the slab concrete in the experimental test, deflection of the midspan outside tip of the G3 bottom flange = 610 mm (24 in), total applied load = 5783 kN (1300 kips).

5.10 Slab Longitudinal and Radial Strains

Figures 5.10.1 and 5.10.2 show the measured and predicted longitudinal strains across the midspan cross-section on the top surface of the slab for gage locations L9 and L10, respectively, at the M_p-based 1/3 rule load level of 3959 kN (890 kips). Initial strains including dead load strains and other residual strains from the prior repeated loading tests are not included in the plots. However, the predicted slab residual strains from the prior repeated loading tests are provided as a separate curve in the plot. It can be seen that the slab residual strains directly above G3 are as large as 25 percent of the total peak strain due to the directly applied load during the final monotonic loading test. For both of the plots, it can be seen that, except for some local deviations, there is a good correlation between the measured and predicted responses. Also, one can see that the longitudinal strains across the slab width at midspan vary approximately in a linear fashion with the largest measured value of approximately 1200 με, occurring at the outer edge of the overhang outside girder G3. It is important to note that this maximum strain is slightly above the strain associated with the elastic limit of the concrete stress-strain response. Also, it is significantly less than the nominal concrete crushing strain of 0.003. For more details regarding strains throughout the slab, Figure 5.10.3 gives a plan view of the test bridge FEA model with longitudinal strain contours on the top surface of the slab at the M_p-based 1/3 rule load level. Figure 5.10.4 provides a similar plot for the radial strains. It can be seen in Figure 5.10.3 that highly localized longitudinal strains are occurring in the midspan overhang region outside G3. This is consistent with the observations made for the stress contours shown in Figure 5.9.2.

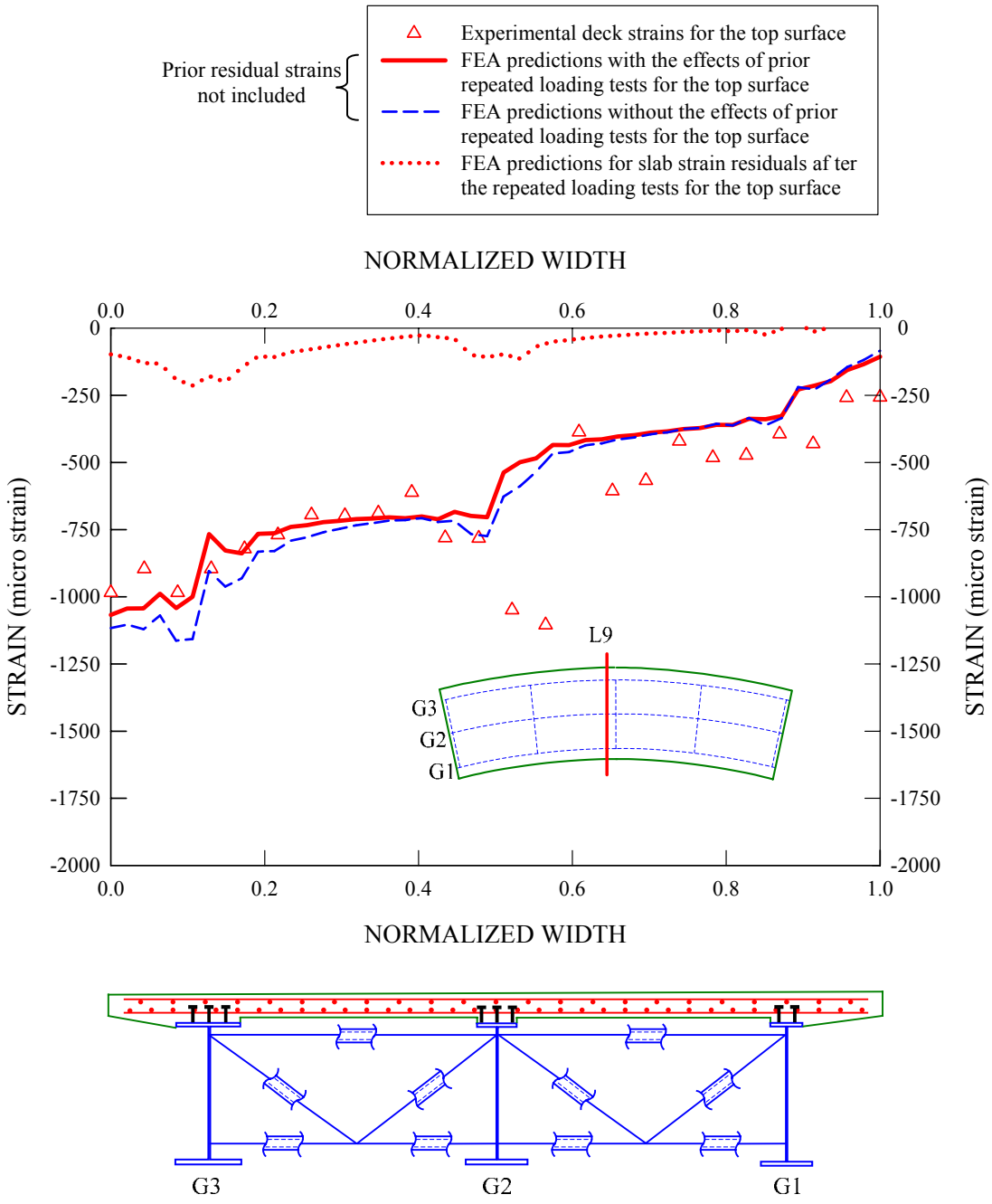

Figure 5.10.1. Measured and predicted longitudinal strains across the top surface of the slab for gage location L9 at the M_p-based 1/3 rule load level of 3959 kN (890 kips).

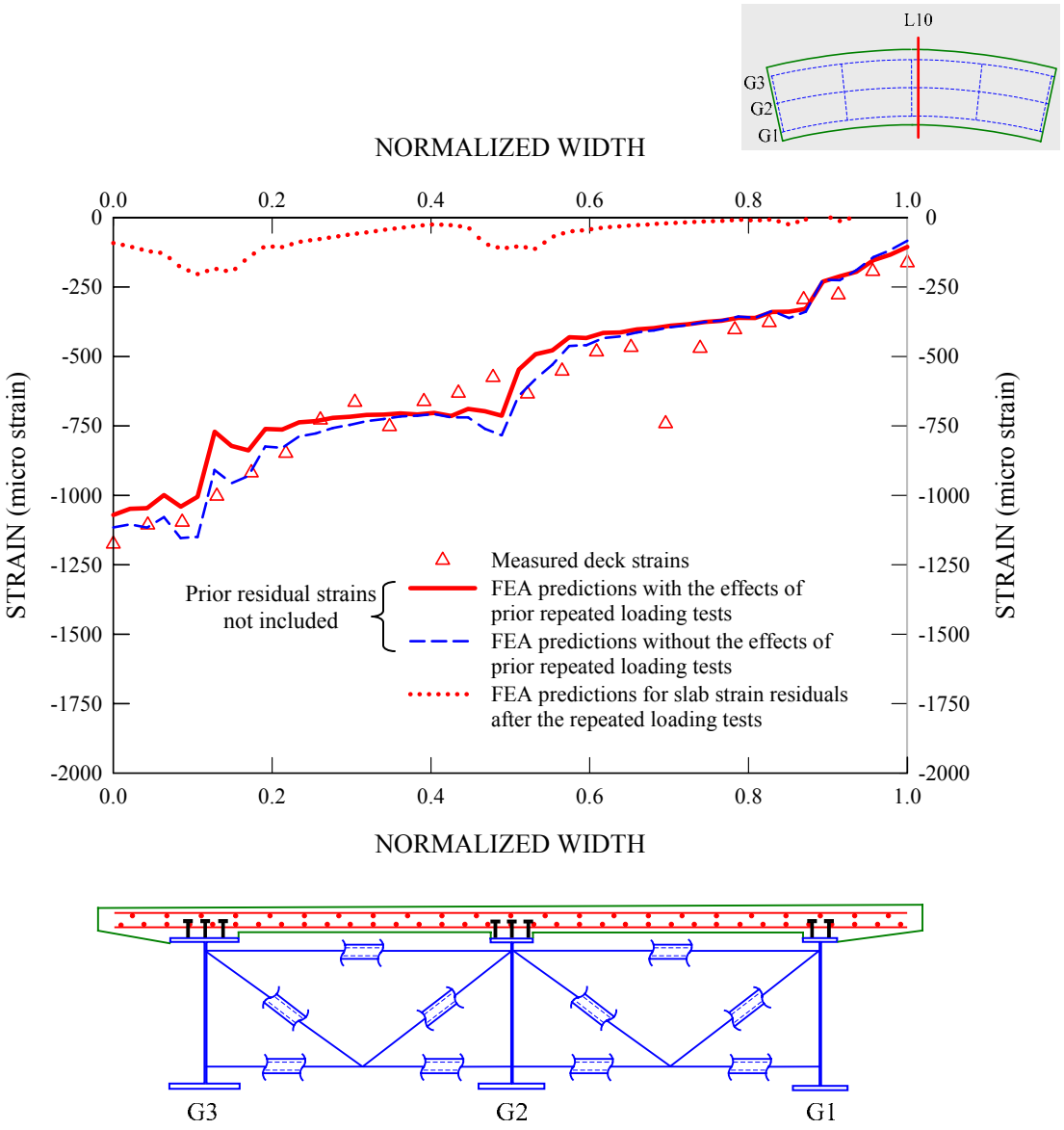

Figure 5.10.2. Measured and predicted longitudinal strains across the top surface of the slab for gage location L10 at the M_p-based 1/3 rule load level of 3959 kN (890 kips).

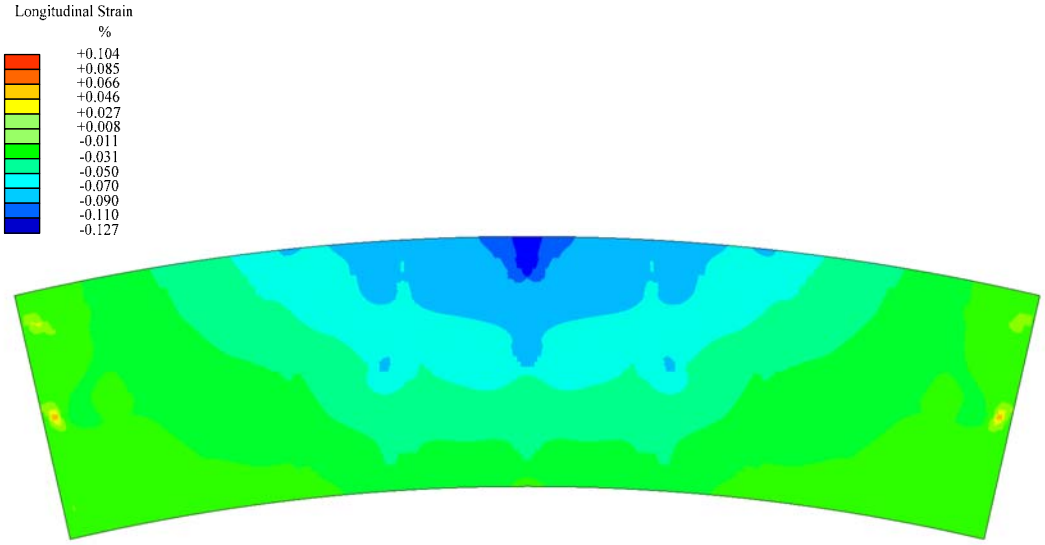

Figure 5.10.3. Plan view of the test bridge FEA model with longitudinal strain contours on the top surface of the slab at the M_p-based 1/3 rule load level of 3959 kN (890 kips).

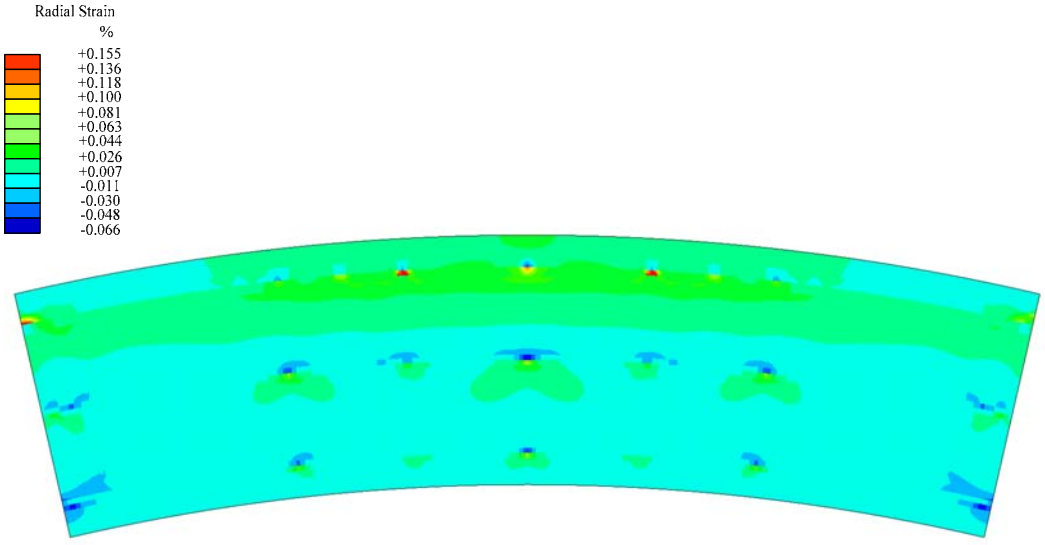

Figure 5.10.4. Plan view of the test bridge FEA model with radial strain contours on the top surface of the slab at the M_p-based 1/3 rule load level of 3959 kN (890 kips).

Figure 5.10.5 provides the predicted longitudinal strains across the midspan cross-section on the bottom surface of the slab for gage location L9 at the M_p-based 1/3 rule load level of 3959 kN (890 kips). It can be seen that the strains increase nearly in a linear fashion across the bridge cross-section, similar to the top surface longitudinal strains, but with a maximum of about 400 με that is less than half the maximum strain observed on the top surface. For other parts of the slab, Figures 5.10.6 and 5.10.7 present plan views of the test bridge FEA model with longitudinal and radial strain contours on the bottom surface of the slab at the M_p-based 1/3 rule load level of 3959 kN (890 kips).

Figures 5.10.8 and 5.10.9 provide measured and predicted longitudinal strains across the top surface of the slab for gage locations L9 and L10 at a total applied load of 5783 kN (1300 kips). As noted previously, this is the load level at which the midspan outer region of the slab experienced concrete spalling and crushing during the ultimate load test. Again, it can be seen that the measured responses compare favorably to the FEA predictions. It is important to note that the maximum strain at the overhang region outside G3 is already beyond the nominal concrete crushing strain of 0.003. Figures 5.10.10 and 5.10.11 give a plan view of the test bridge FEA model with longitudinal and radial strain contours on the top surface of the slab at a total applied load level of 5783 kN (1300 kips). It can be seen in Figure 5.10.10 that a large portion of the overhang outside G3 near midspan develops strains larger than the nominal concrete crushing strain, leading to the spalling and crushing of the concrete during the ultimate load test. Figure 5.10.12 shows a close-up snapshot of the overhang outside of G3 after the spalling and crushing of concrete at a total applied load of 5783 kN (1300 kips).

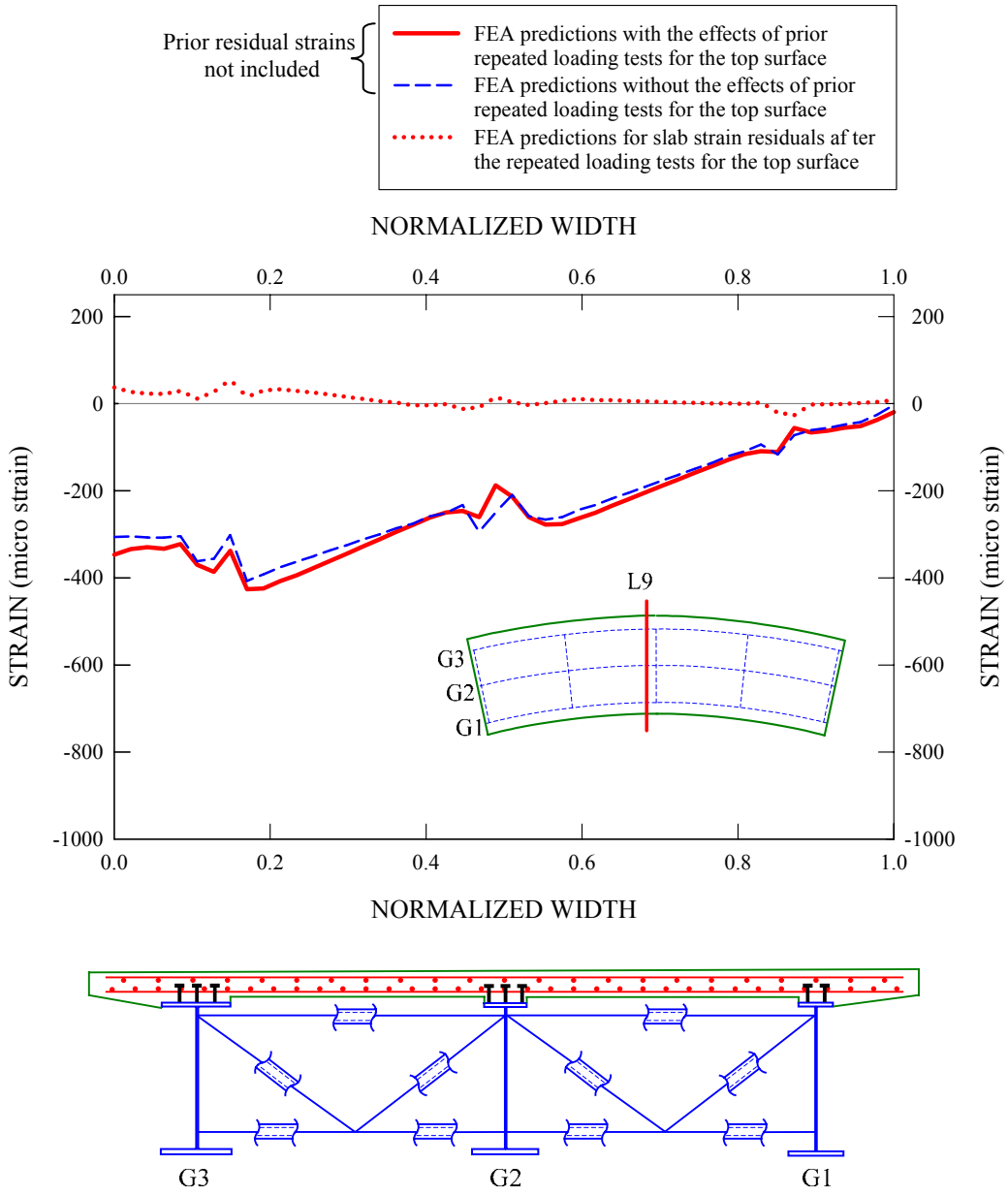

Figure 5.10.5. Predicted longitudinal strains across the bottom surface of the slab for gage location L9 at the M_p-based 1/3 rule load level of 3959 kN (890 kips).

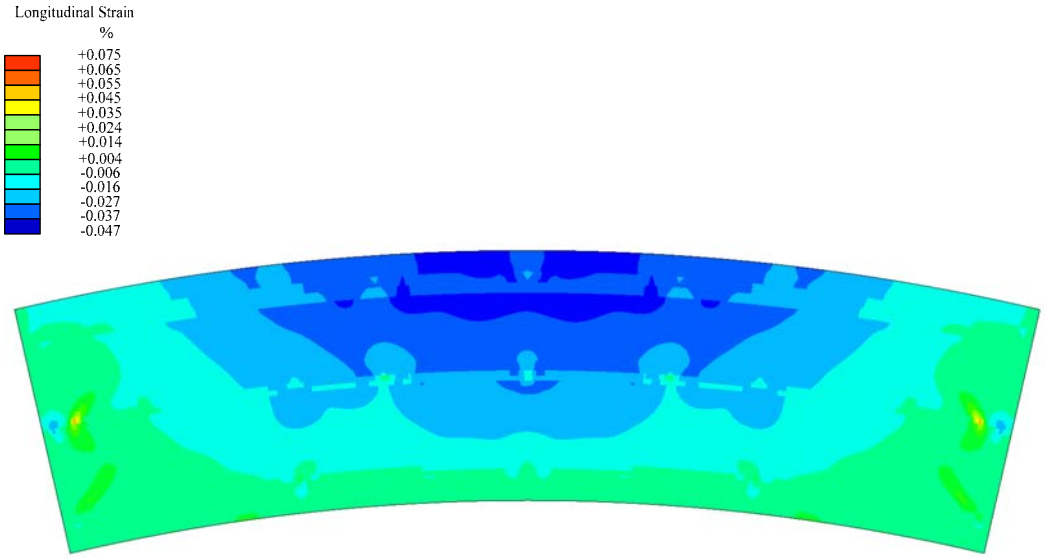

Figure 5.10.6. Plan view of the test bridge FEA model with longitudinal strain contours on the bottom surface of the slab at the M_p-based 1/3 rule load level of 3959 kN (890 kips).

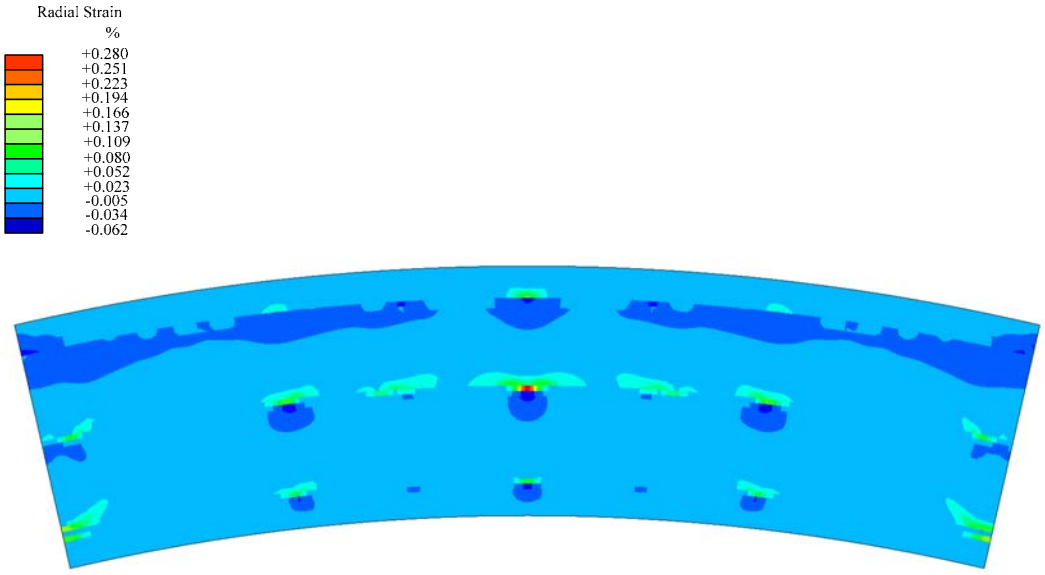

Figure 5.10.7. Plan view of the test bridge FEA model with radial strain contours on the bottom surface of the slab at the M_p-based 1/3 rule load level of 3959 kN (890 kips).

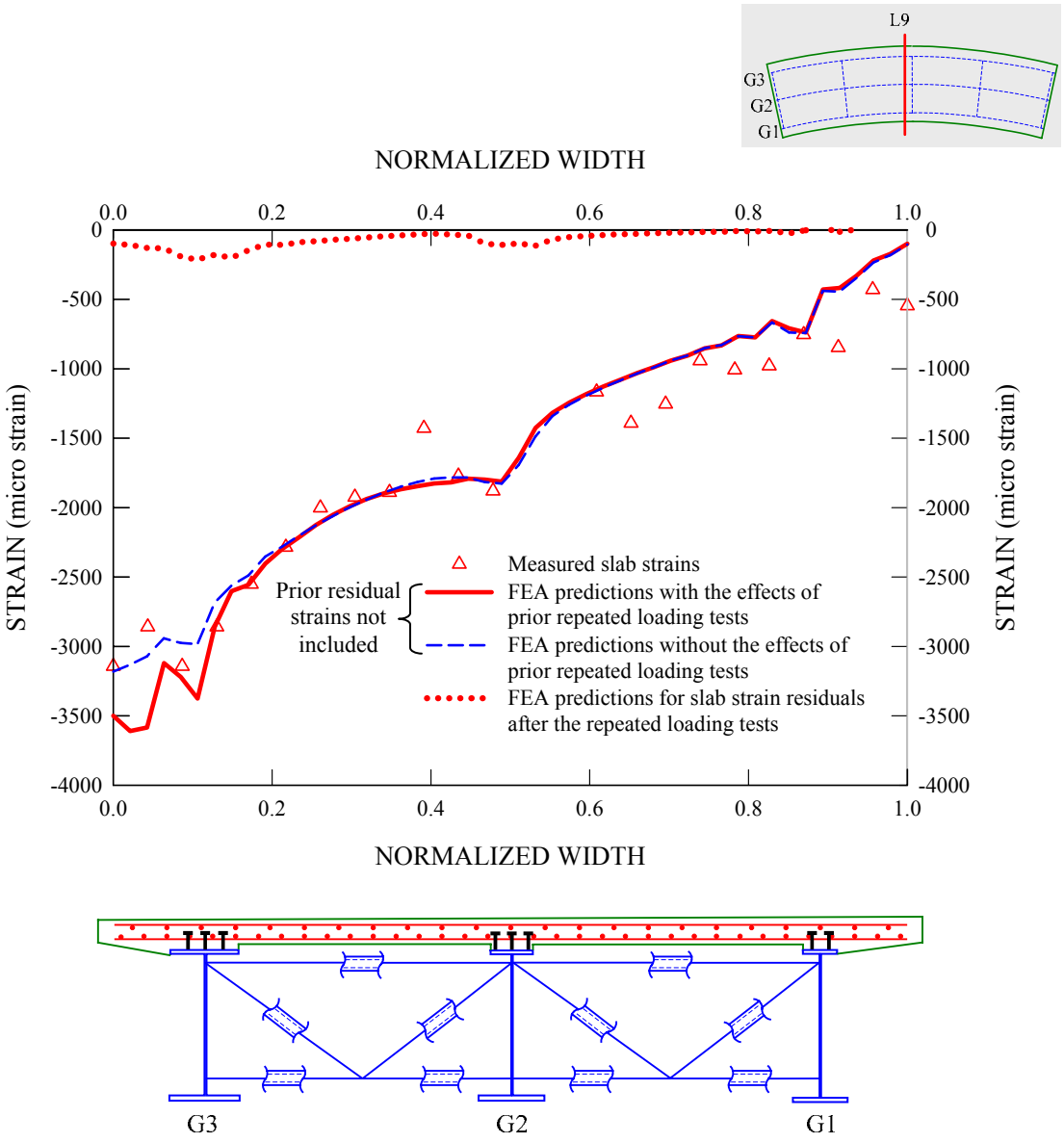

Figure 5.10.8. Measured and predicted longitudinal strains across top surface of the slab for gage location L9 at spalling and crushing of the slab concrete in the experimental test, deflection of the midspan outside tip of the G3 bottom flange = 610 mm (24 in), total applied load = 5783 kN (1300 kips).

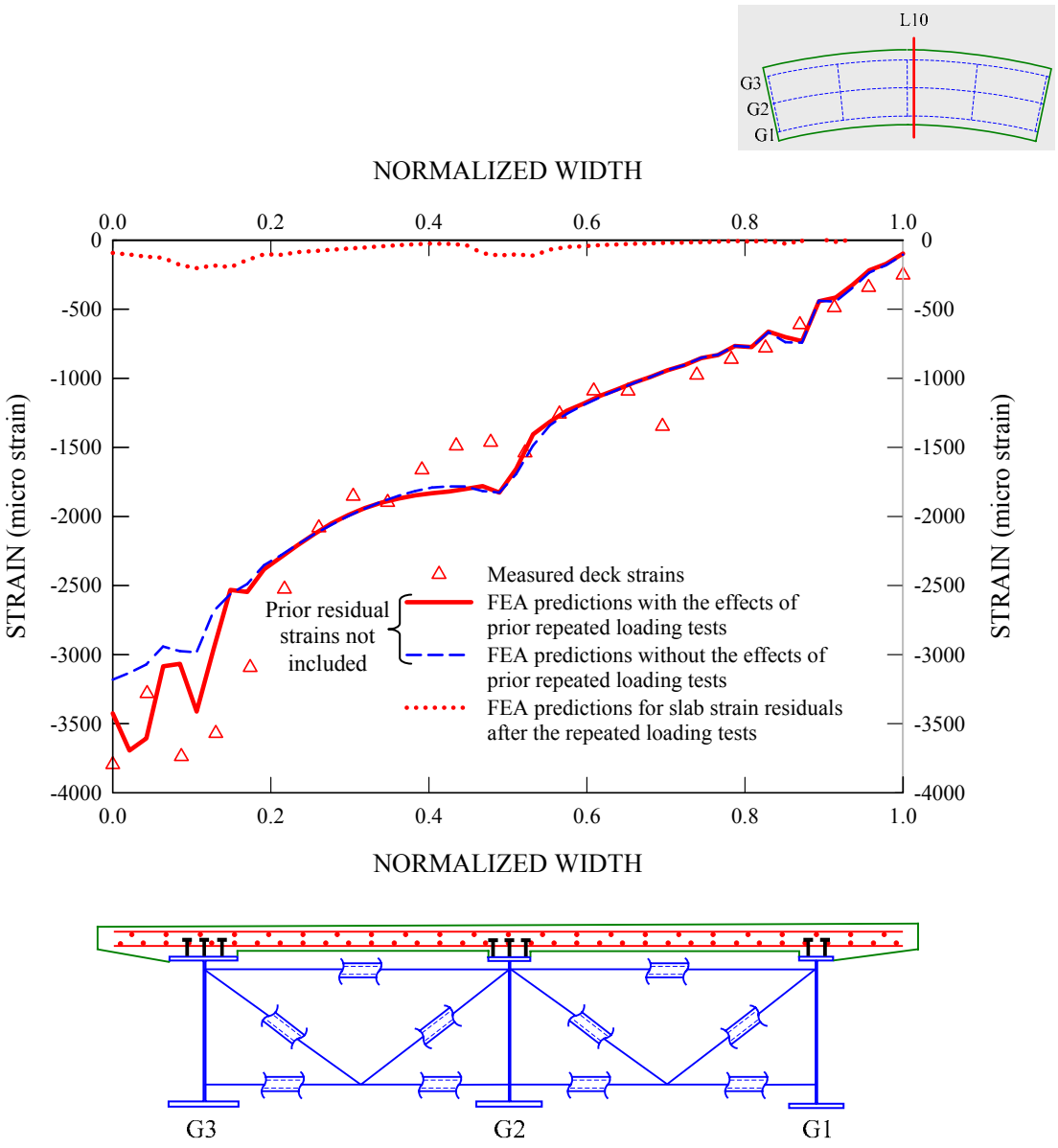

Figure 5.10.9. Measured and predicted longitudinal strains across the top surface of the slab for gage location L10 at spalling and crushing of the slab concrete in the experimental test, deflection of the midspan outside tip of the G3 bottom flange = 610 mm (24 in), total applied load = 5783 kN (1300 kips).

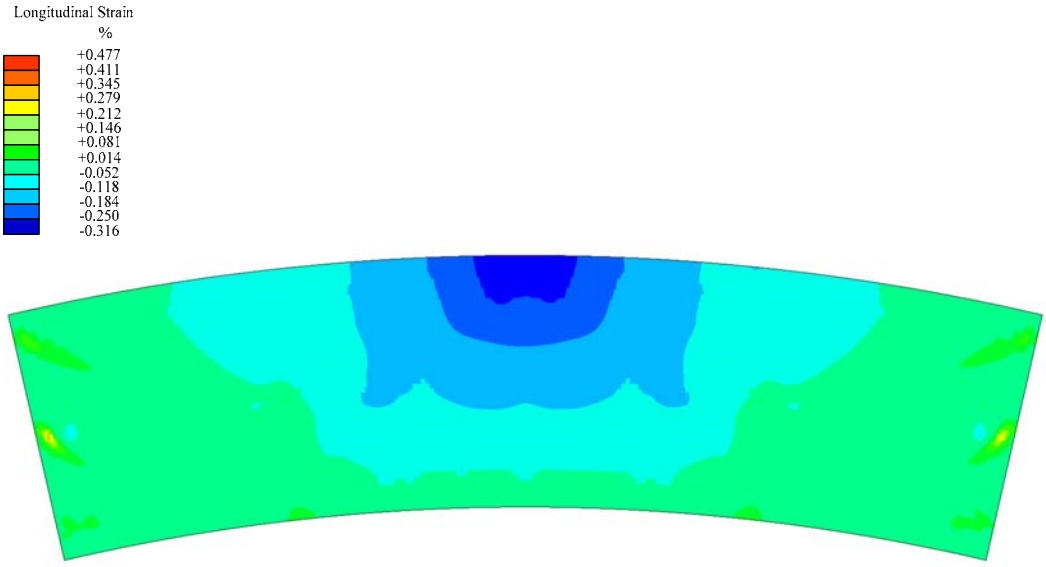

Figure 5.10.10. Plan view of the test bridge FEA model with longitudinal strain contours on the top surface of the slab at spalling and crushing of the slab concrete in the experimental test, deflection of the midspan outside tip of the G3 bottom flange = 610 mm (24 in), total applied load = 5783 kN (1300 kips).

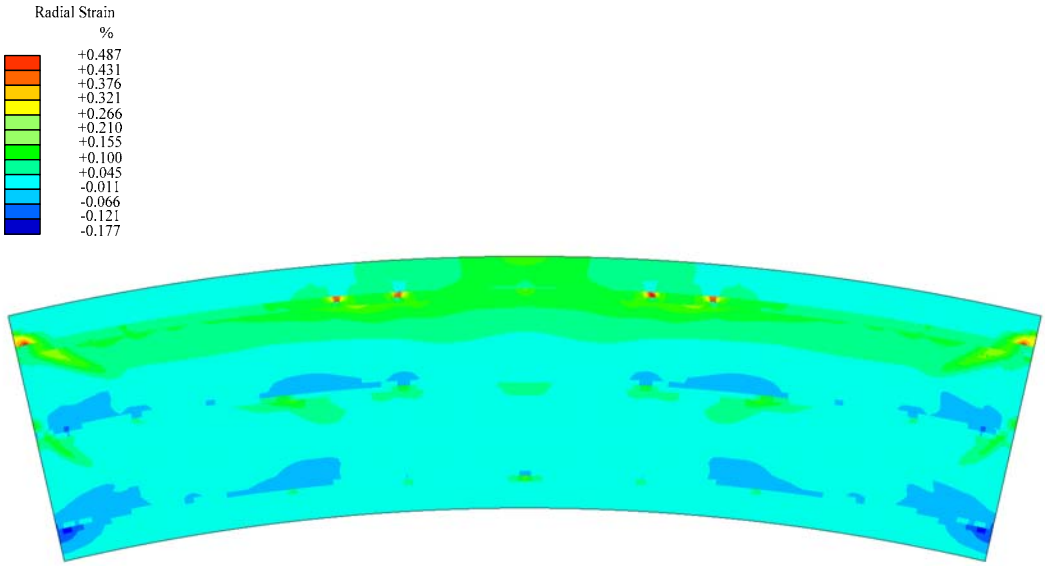

Figure 5.10.11. Plan view of the test bridge FEA model with radial strain contours on the top surface of the slab at spalling and crushing of the slab concrete in the experimental test, deflection of the midspan outside tip of the G3 bottom flange = 610 mm (24 in), total applied load = 5783 kN (1300 kips).

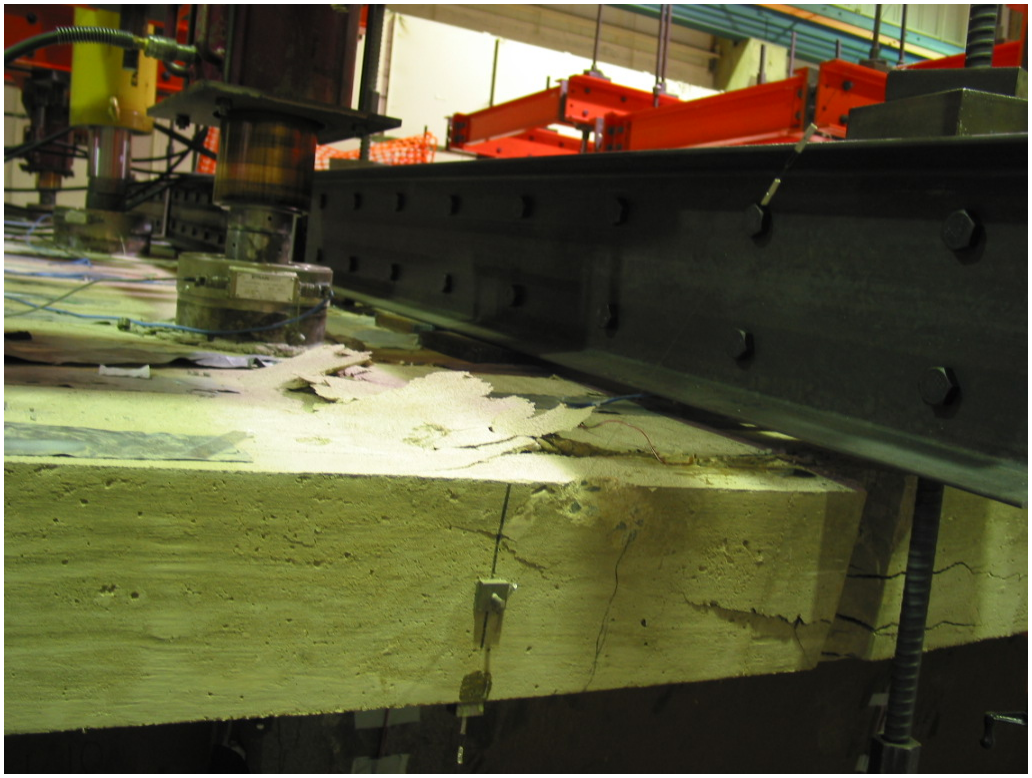

Figure 5.10.12. Close-up view of the midspan region of the overhang outside G3 after the crushing of concrete at a total applied load of 5783 kN (1300 kips), courtesy of FHWA.

Figure 5.10.13 provides predicted longitudinal strains across the midspan cross-section on the bottom surface of the test bridge for gage location L9 at the total applied load of 5783 kN (1300 kips). It is interesting to note that the strains from the inside edge of the slab at G1 toward the mid-width of the bridge cross-section are larger than the corresponding values at 3959 kN (890 kips). Conversely, it can be seen that the strains between the mid-width of the cross-section toward the outside edge of the slab at G3 are decreased from the corresponding values at 3959 kN (890 kips). Furthermore, it should be noted that there are tensile longitudinal strains developed on the bottom surface just above G2 and G3, which is in sharp contrast with large compressive longitudinal strains in these two regions at the top of the slab. Figures 5.10.14 and 5.10.15 provide a plan

view of the test bridge FEA model with longitudinal and radial strain contours on the bottom surface of the slab when the midspan outside tip of the G3 bottom flange reaches a deflection of 610 mm (24 in) due to a total applied load of 5783 kN (1300 kips).

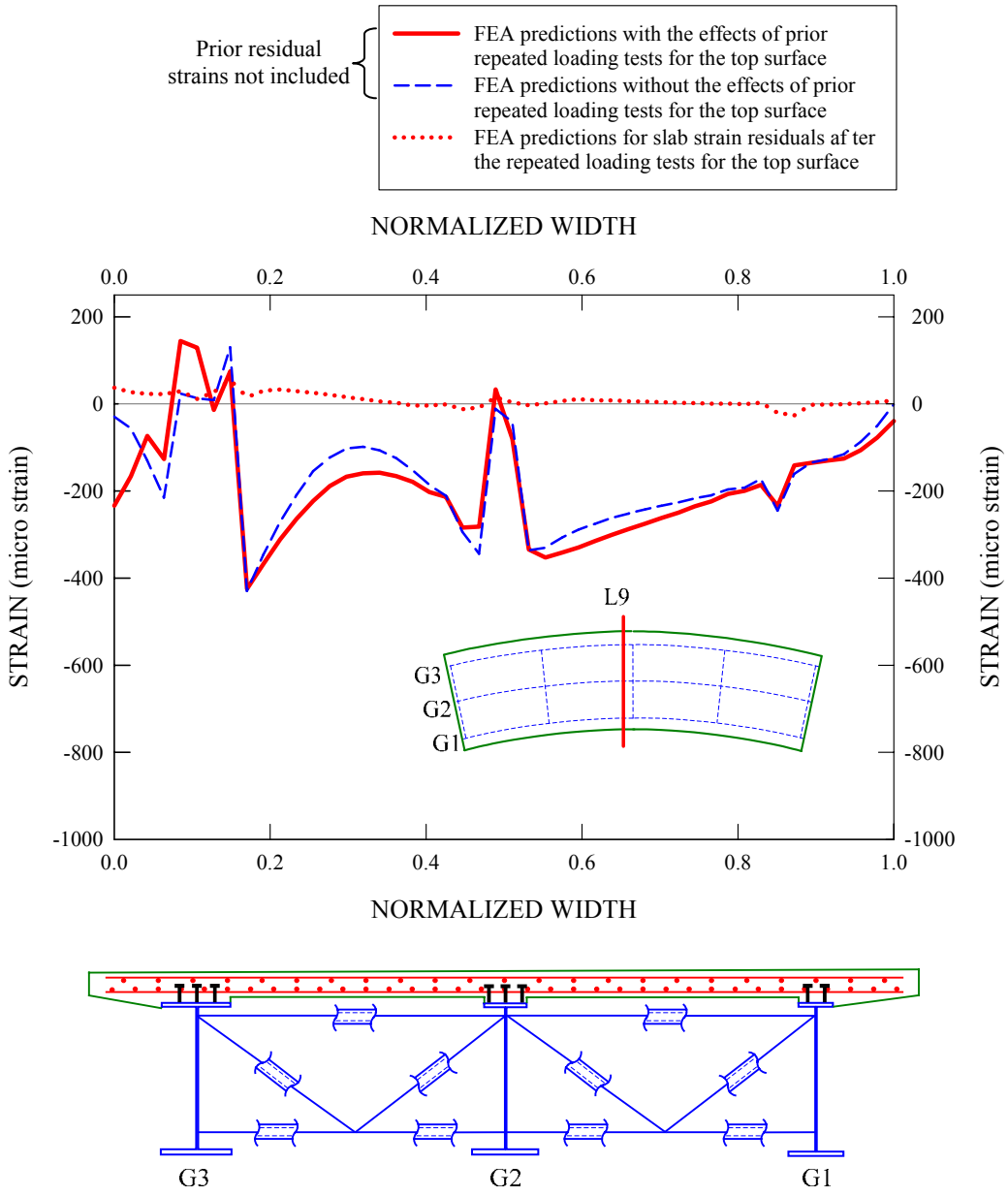

Figure 5.10.13. Predicted longitudinal strains across the midspan cross-section on the bottom surface of the slab for gage location L9 at spalling and crushing of the slab concrete in the experimental test, deflection of the midspan outside tip of the G3 bottom flange = 610 mm (24 in), total applied load = 5783 kN (1300 kips).

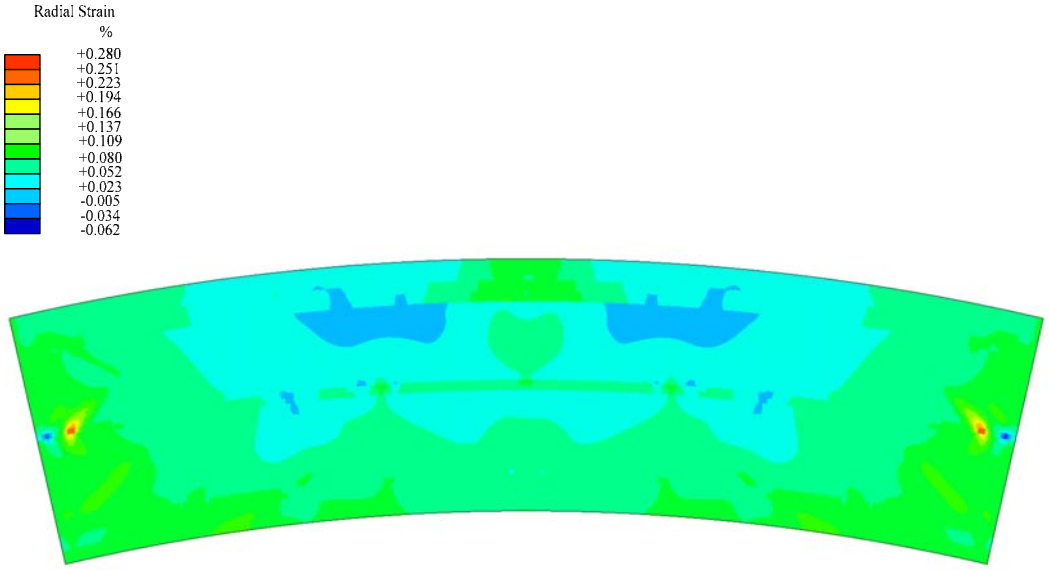

Figure 5.10.14. Plan view of the test bridge FEA model with longitudinal strain contours on the bottom surface of the slab at spalling and crushing of the slab concrete in the experimental test, deflection of the midspan outside tip of the G3 bottom flange = 610 mm (24 in), total applied load = 5783 kN (1300 kips).

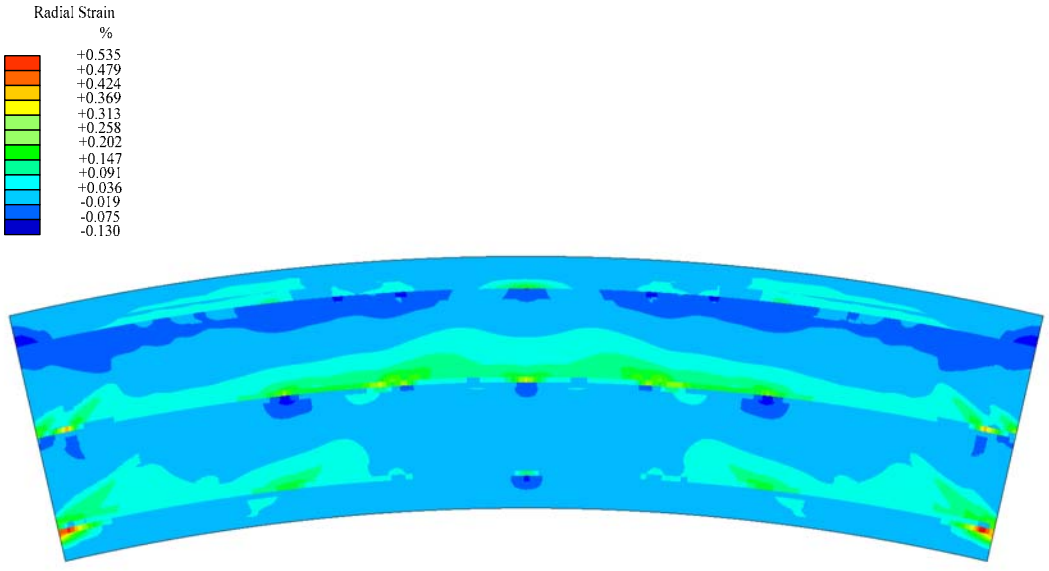

Figure 5.10.15. Plan view of the test bridge FEA model with radial strain contours on the bottom surface of the slab at spalling and crushing of the slab concrete in the experimental test, deflection of the midspan outside tip of the G3 bottom flange = 610 mm (24 in), total applied load = 5783 kN (1300 kips).

5.11 Slab FEA Damage Variable Evolution

Along with plastic strains, the coupled damage plasticity model used for the analysis of the test bridge concrete slab involves additional internal state variables to track the evolution of tensile and compressive damage in the concrete. These internal variables provide useful information regarding the extent of damage in the concrete, in particular the degree of elastic stiffness reduction, at a certain loading stages. Figures 5.11.1 and 5.11.2 show a plan view of the test bridge FEA model with contours of the compression and tension damage variables on the top surface of the slab at a total applied load of 5783 kN (1300 kips). As noted previously, this is the load level at which the slab overhang outside G3 showed spalling and crushing. It can be seen in Figure 5.11.1 that the FEA simulation predicts extensive compression damage in the overhang region outside G3 at midspan, as well as in the regions just inside G3 between the mid- and quarter-span cross-frames. Figure 5.11.2 shows that the tensile damage develops predominantly in the regions just inside each girder, particularly near the G2 and G3 girder ends. It can be seen that the dominant tension damage bands are formed at the ends of girders G3 and G2 with an inclination angle of approximately 45 and 30 degrees relative to girders respectively.

Figures 5.11.3 and 5.11.4 provide a plan view of the test bridge FEA model with contours of compression and tension damage variables on the bottom surface of the slab at the total applied load of 5783 kN (1300 kips). Interestingly, it can be seen in Figure 5.11.3 that the outside region along each girder is affected by the compression damage. Furthermore, as can be seen in Figure 5.11.4, the tensile damage is high in the regions outside of each girder. Particularly, it can be seen that severe tension damage bands are formed at the G1 and G2 girder ends. The inclination of these bands is approximately at

90 degrees to the inclination of the bands for the top surface tension damage over G2 in Figure 5.11.2.

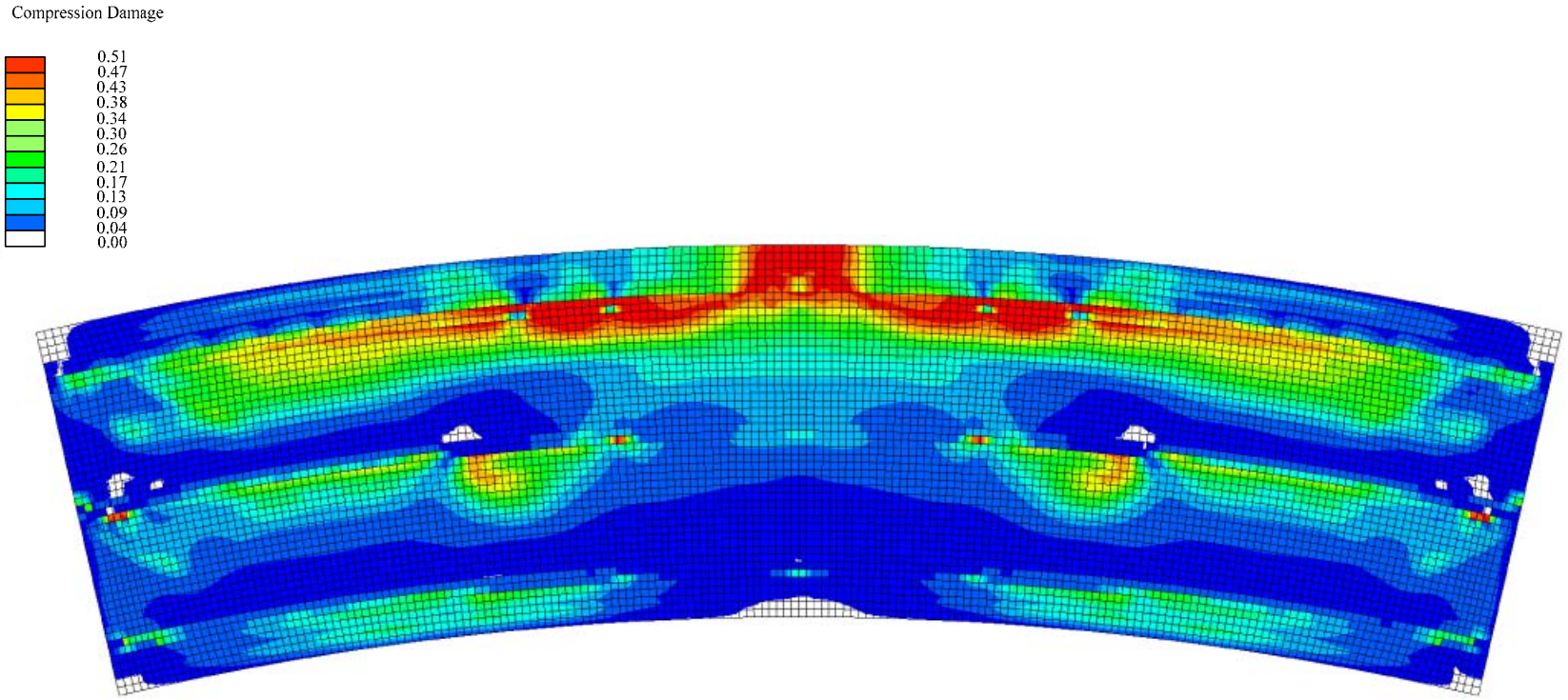

Figure 5.11.1. Plan view of the test bridge FEA model with contours of compression damage variables on the top surface of the slab at spalling and crushing of the slab concrete in the experimental test, deflection of the midspan outside tip of the G3 bottom flange = 610 mm (24 in), total applied load = 5783 kN (1300 kips).

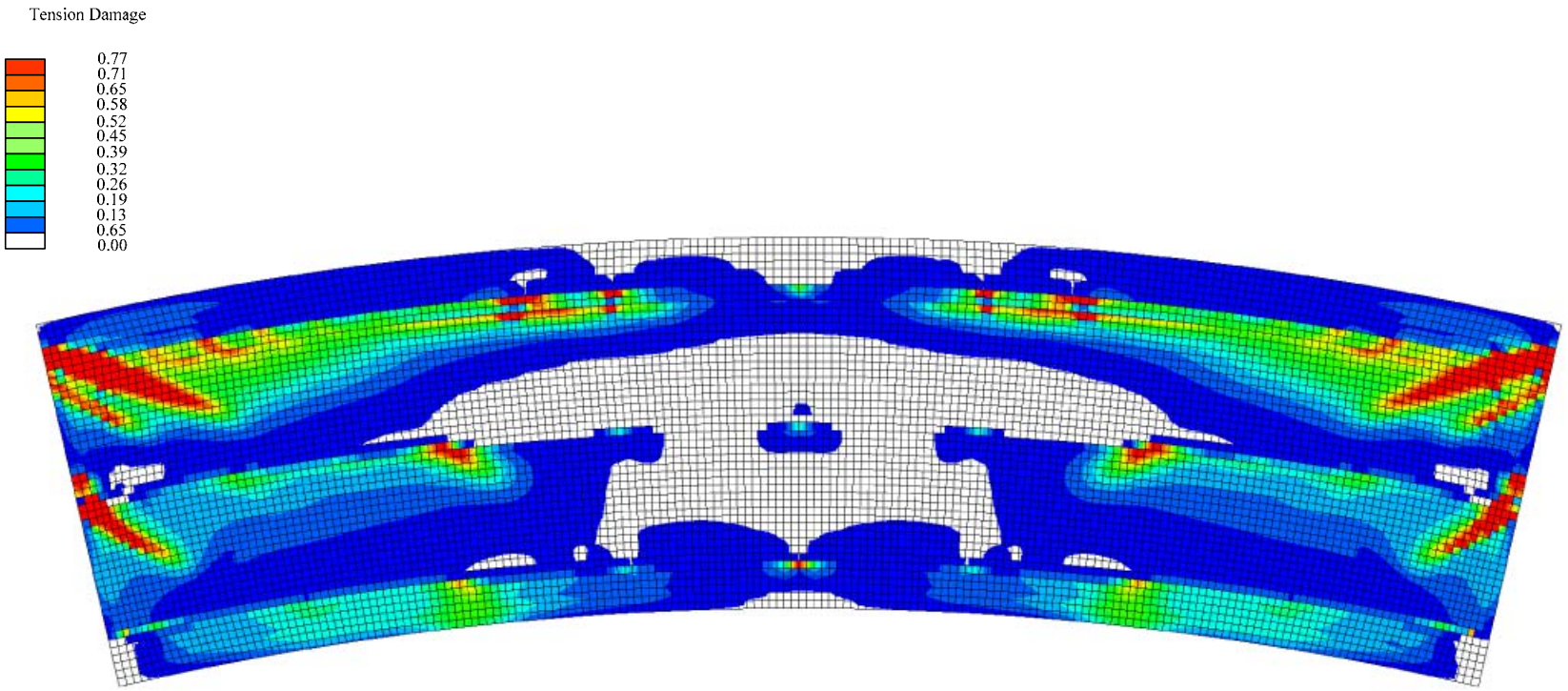

Figure 5.11.2. Plan view of the test bridge FEA model with contours of tension damage variables on the top surface of the slab at spalling and crushing of the slab concrete in the experimental test, deflection of the midspan outside tip of the G3 bottom flange = 610 mm (24 in), total applied load = 5783 kN (1300 kips).

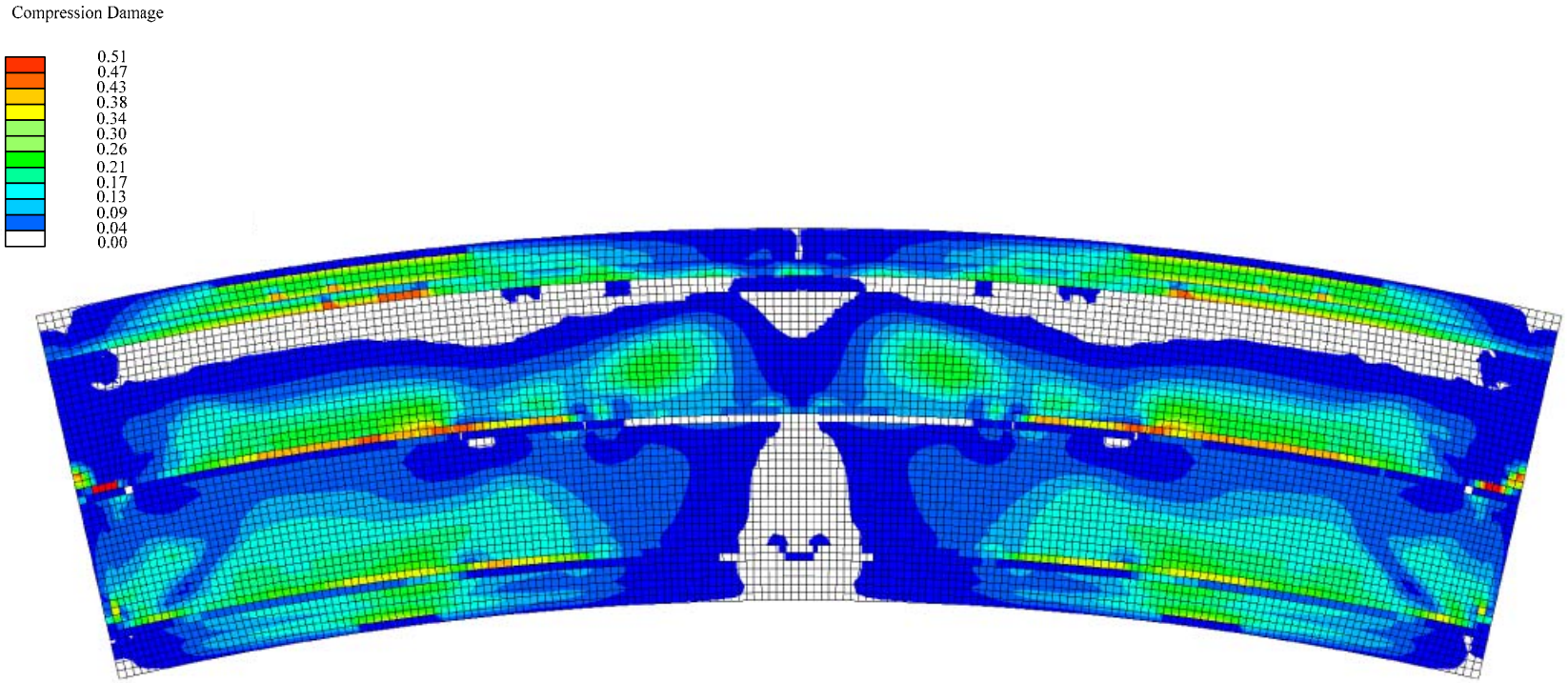

Figure 5.11.3. Plan view of the test bridge FEA model with contours of compression damage variables on the bottom surface of the slab at spalling and crushing of the slab concrete in the experimental test, deflection of the midspan outside tip of the G3 bottom flange = 610 mm (24 in), total applied load = 5783 kN (1300 kips).

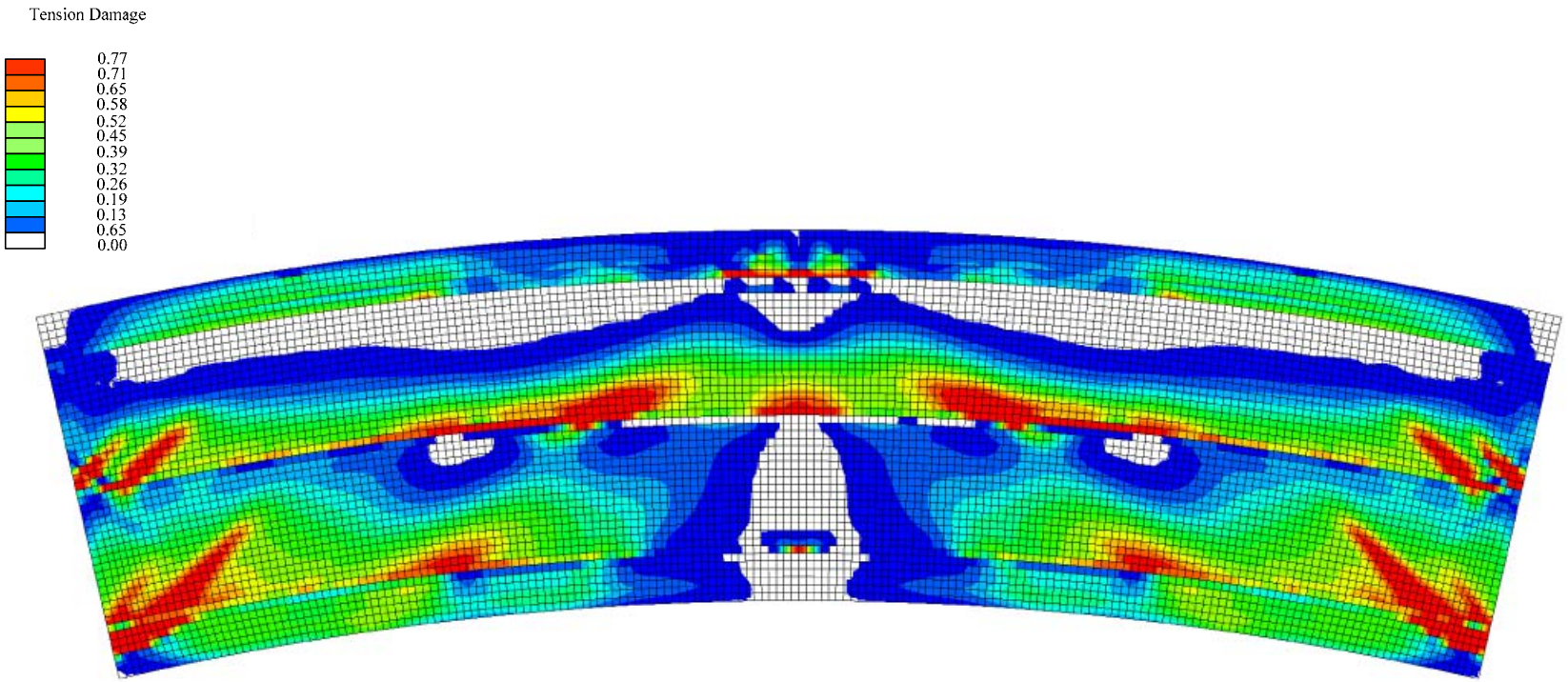

Figure 5.11.4. Plan view of the test bridge FEA model with contours of tension damage variables on the bottom surface of the slab at spalling and crushing of the slab concrete in the experimental test, deflection of the midspan outside tip of the G3 bottom flange = 610 mm (24 in), total applied load = 5783 kN (1300 kips).

5.12 Slab Crack Patterns

Although the damage variables presented in the previous section provide useful information regarding the extent of damage in the slab, they do no provide any directional information about the initiation and propagation of cracks. This is due to the fact that the coupled damage elastoplasticity model used in this study is formulated based on the assumption of isotropic damage evolution. However, principal tensile strains are often utilized to identify potential cracking in concrete structures. Not only can they be used to decide whether concrete is cracked or not by comparing them to the strain at the tensile strength, but also they provide an indication of the direction that the cracks propagate with applied loads.

Figures 5.12.1 through 5.12.3 give a plan view of the slab with the maximum principal FEA top surface strains as well as the corresponding expected crack patterns on the top surface of the slab at the M_y- and M_p-based 1/3 rule resistance levels on G3, as well as at the experimental ultimate capacity of 5783 kN (1300 kips). It should be noted that the plots only show principal tensile strains for the magnitude of which is larger than the cracking strain of the concrete (approximately 0.015 percent). Also, the strains associated with concrete shrinkage are not included in the plots. Furthermore, due to the symmetric nature of the maximum principal strain distribution on the slab, only the left half of the slab is considered.

Figure 5.12.1 shows that there are some expected surface cracks above G3 when the bridge is loaded to the M_y-based 1/3 rule level and the maximum top surface strain throughout the slab in the FEA solution is 0.05 percent (the length of the symbols representing the principal tensile strains and corresponding to 0.05 percent strain is shown in the top left corner of the figure). It is interesting to see that the expected cracks

are inclined with an angle of 45 degrees to the longitudinal axis of the test bridge between the end- and quarter-span cross-frames. On the other hand, the cracks between the quarter- and midspan cross-frames are parallel to G3. In addition to the surface cracks in the vicinity of G3, it can be seen that there are some expected inclined cracks near the end of G2 and on G1 between the end- and quarter-span cross frames.

Figure 5.12.2 shows that the expected surface cracks on G3 increase in number and size at the M_p-based 1/3 rule load level. The maximum tensile principal strain throughout the top surface of the slab is 0.06 percent at this level. In addition, there are additional inclined cracks on G2 between the end- and quarter-span cross-frames. However, there is little cracking activity near G1.

Figure 5.12.3 shows that the expected surface cracks on G3 significantly increase in size and number as the bridge approaches its ultimate load capacity. The maximum tensile principal strain throughout the top surface of the slab is increased to 0.34 percent at this load level. In addition, it can be seen that the existing cracks on G2 grow in a similar order of magnitude. Also, new parallel cracks are expected between the quarter- and mid-span cross-frames. It can be seen also that there are some inclined cracks formed on G1, particularly on the overhang region inside G1.

Figure 5.12.4 presents a plan view of the composite slab with the cracks that were observed on the top surface of the slab at the end of ultimate loading test. It can be seen that, as projected in Figure 5.12.3, there are many cracks formed between the end- and quarter-span cross-frames that are inclined at about 30 to 45 degrees to the radial lines at the girder supports pointing toward the center of curvature. Also, there are parallel cracks formed in the longitudinal direction over G2 and G3 between the quarter- and

midspan cross-frames, although these cracks are not as extensive as predicted by the FEA solutions. Also, it should be noted that there are radial cracks formed at the midspan on G3 associated with the final concrete spalling and crushing failure.

With respect to the crack patterns on the slab bottom surface, the behavior is completely different in terms of directions and locations compared to the characteristics of the top surface cracks. For example, at a total applied load of 3470 kN (780 kips), Fig 5.12.5 shows that inclined cracks are expect on G1 and G2 between the end- and quarter-span cross-frames. The maximum tensile principal strain on the bottom surface is 0.15 percent at this stage in the FEA solution. Also, some inclined cracks are expected on the overhang region outside G3. It should be noted that the directions of the bottom surface cracks are approximately perpendicular to those of the top surface cracks shown in Figure 5.2.1. When the total applied loads are increased to 3959 kN (890 kips), Figure 5.12.6 shows that the cracks on G1 and G2 grow in size and number, and that the maximum tensile principal strain throughout the bottom surface of the slab is 0.18 percent. One can observe that new inclined cracks are formed on the G2 portion of the slab between the end- and quarter-span cross-frames, and that additional parallel cracks are expected between the quarter- and midspan cross-frames.

Figure 5.12.7 shows a plan view of the slab with principal tensile strains and corresponding crack patterns on the bottom surface of the slab at the experimental ultimate load level of 5783 kN (1300 kips). It can be seen that the surface cracks on G1 and G2 between the end- and quarter-span cross-frames significantly increase in size and number. The maximum tensile principal strain throughout the bottom surface of the slab

is 0.52 percent at this load level. Also, inclined cracks are expected on G3's overhang region.

Figure 5.12.8 presents a plan view of the composite slab with the patterns of cracks observed on the bottom surface of the slab at the end of ultimate loading test. Although it is not easy to identify any dominant crack directions in some of the areas of the slab, it can be seen that, as predicted in Figure 5.12.7, there are many cracks inclined at an angle of 30 to 45 degrees to the radial lines of the girder supports between the end- and quarter-span cross-frames, pointing away from the center of curvature. It should be noted that these cracks are perpendicular to the directions of the top surface cracks. Also, the pattern of the cracks between the quarter- and midspan cross-frames is a combination of inclined and parallel cracks as projected by the FEA solutions.

Based on the above observations regarding the overall crack patterns on the top and bottom surfaces, it is believed that the overall twisting deformation of the composite test bridge is a major source of the cracking in the slab. This is evidenced in by the formation of the top and bottom surface cracks approximately in perpendicular directions to one another.

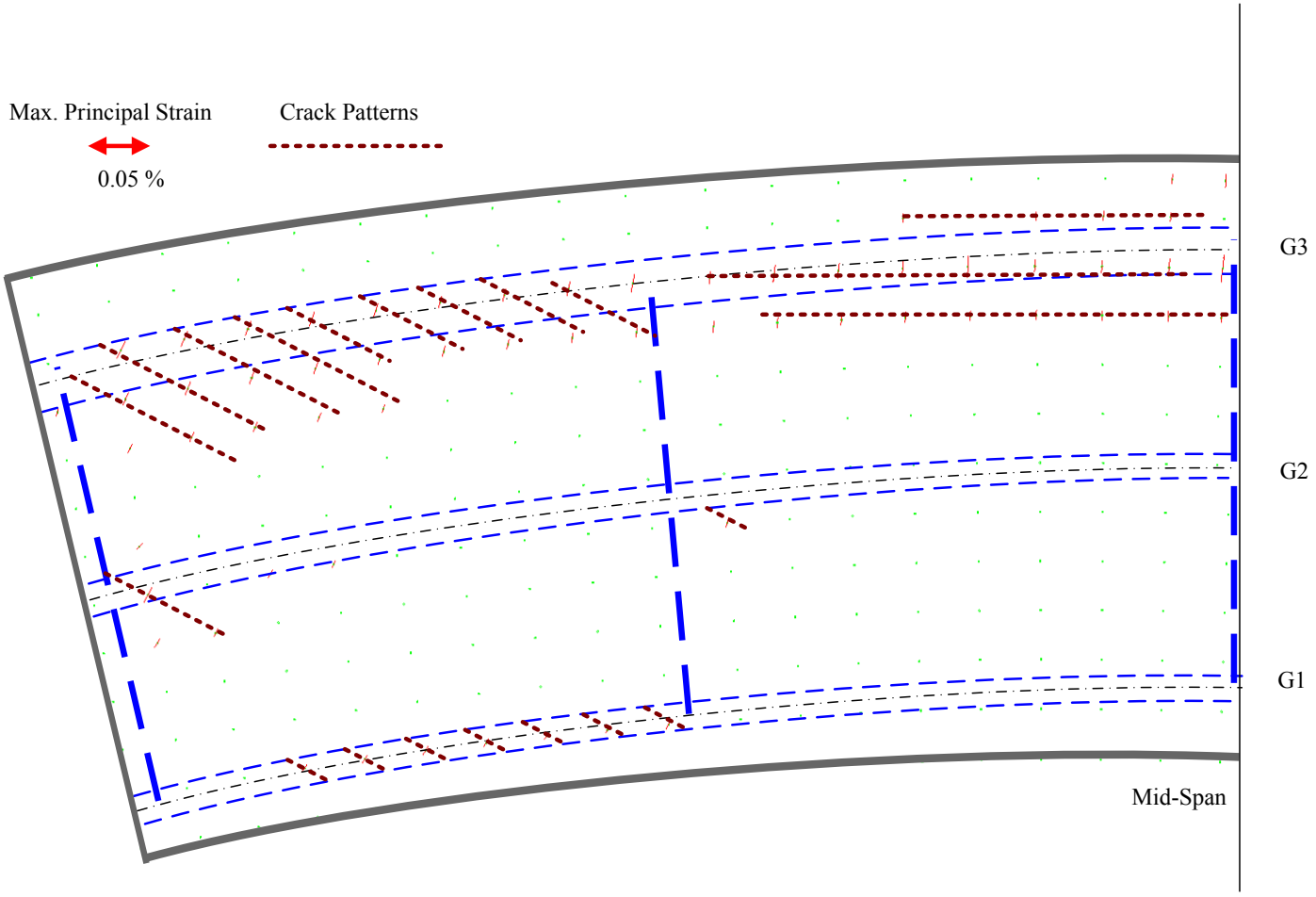

Figure 5.12.1. Plan view of the composite test bridge FEA model with computed maximum principal strains and corresponding crack patterns on the top surface of the slab at the M_y-based 1/3 rule load level, total applied load = 3470 kN (780 kips).

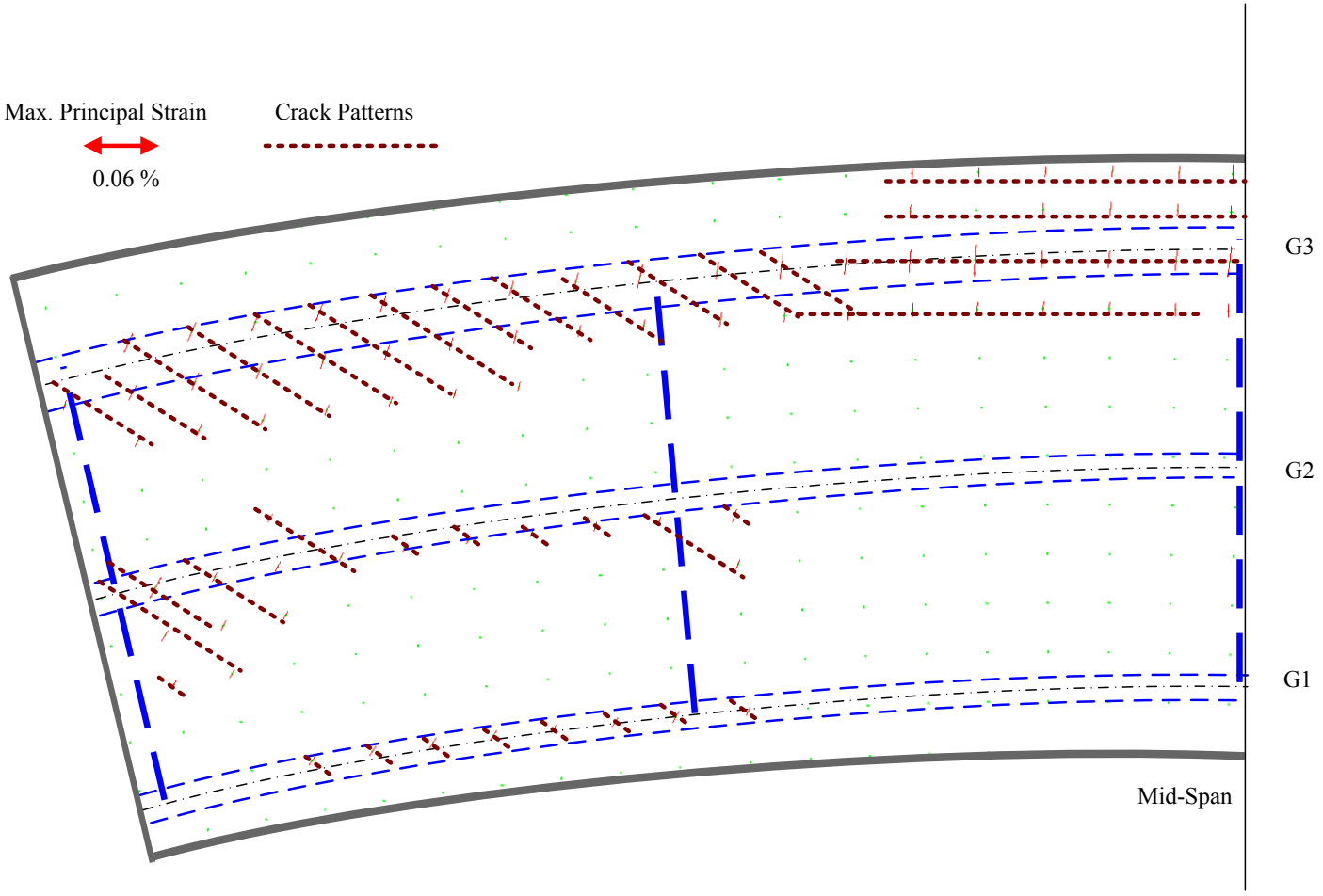

Figure 5.12.2. Plan view of the composite test bridge FEA model with computed maximum principal strains and corresponding crack patterns on the top surface of the slab at the M_p-based 1/3 rule load level, total applied load = 3959 kN (890 kips).

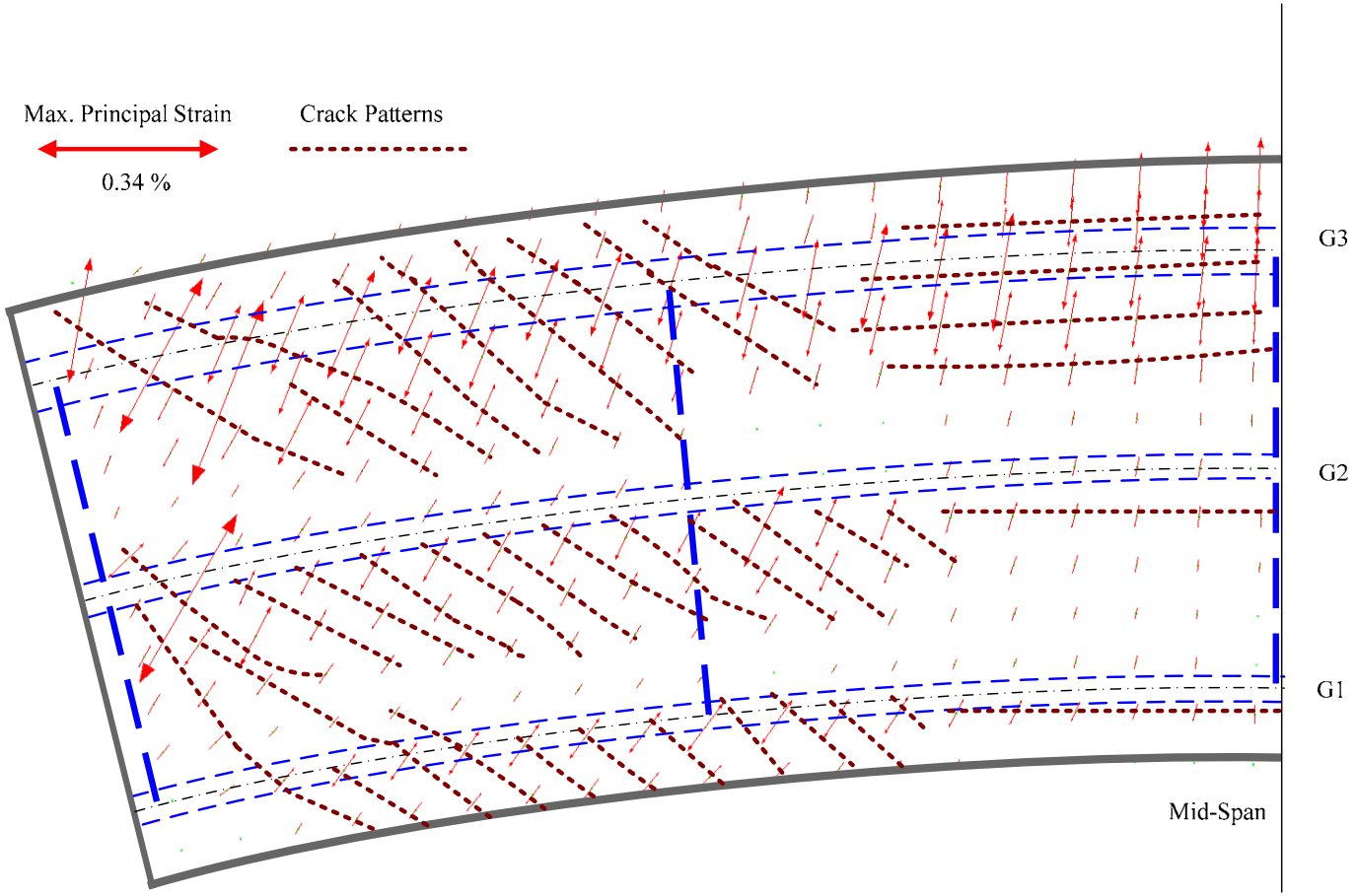

Figure 5.12.3. Plan view of the composite test bridge FEA model with computed maximum principal strains and corresponding crack patterns on the top surface of the slab at spalling and crushing of the slab concrete in the experimental test, deflection of the midspan outside tip of the G3 bottom flange = 610 mm (24 in), total applied load = 5783 kN (1300 kips).

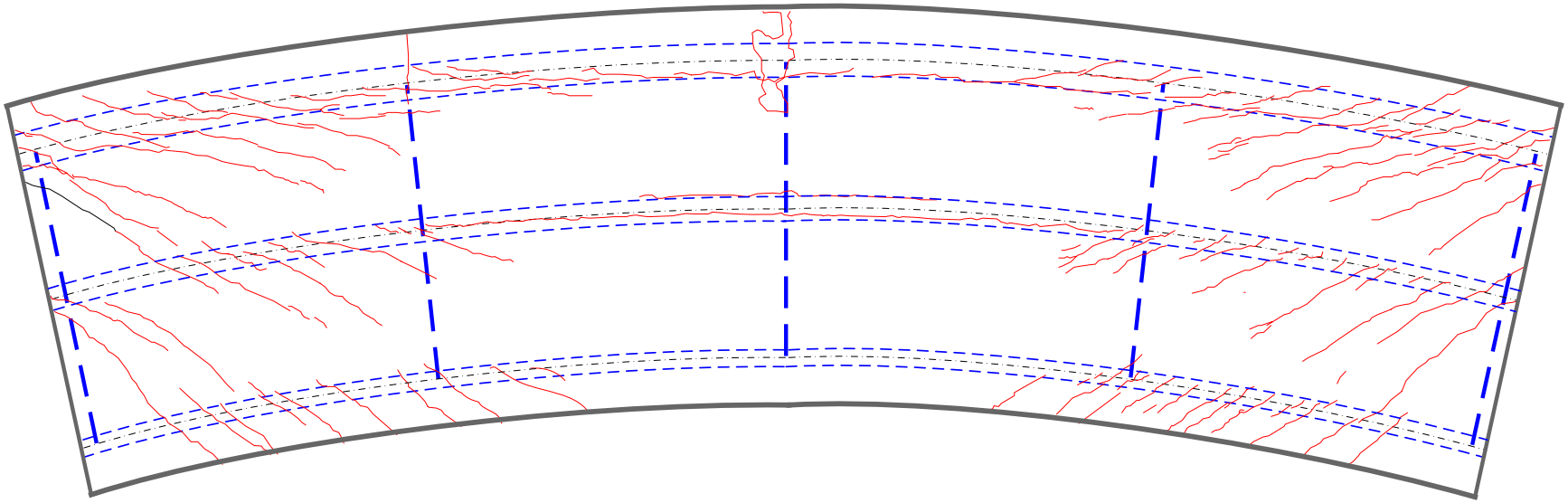

Figure 5.12.4. Plan view of the composite slab with crack patterns observed on the top surface at the end of the ultimate loading test, courtesy of FHWA.

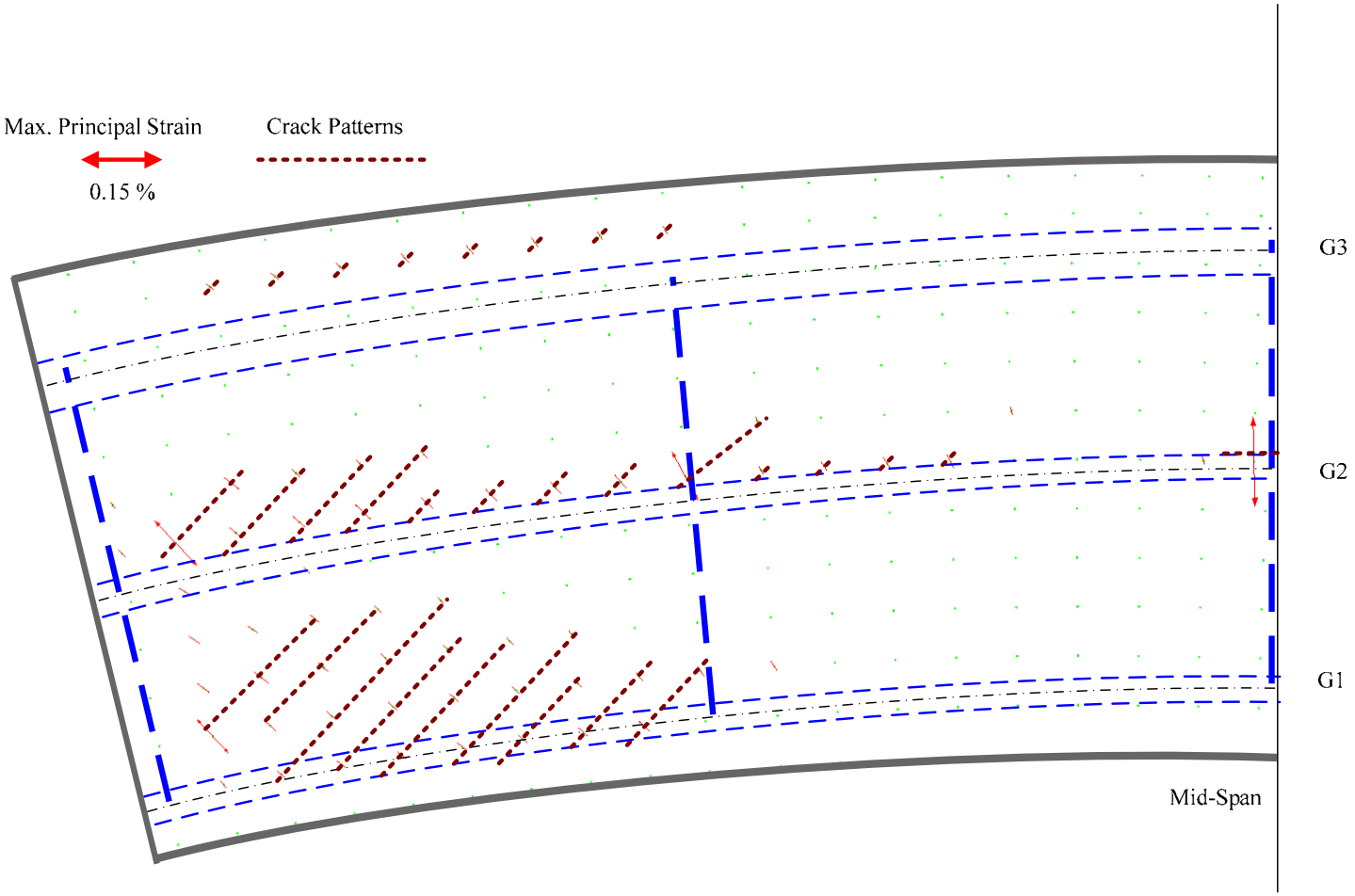

Figure 5.12.5. Plan view of the composite test bridge FEA model with computed maximum principal strains and corresponding crack patterns on the bottom surface of the slab at the M_y-based 1/3 rule load level, total applied load = 3470 kN (780 kips).

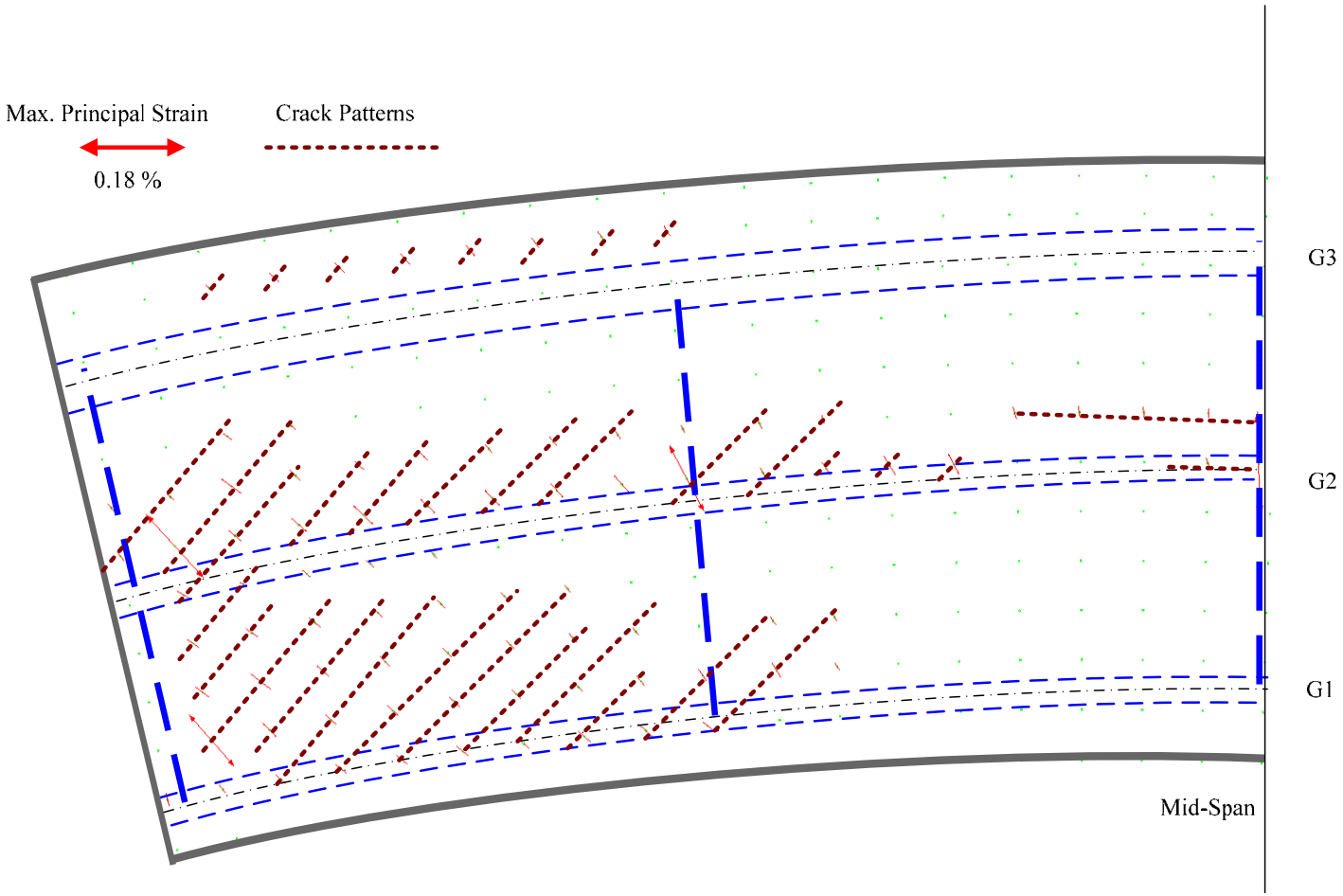

Figure 5.12.6. Plan view of the composite test bridge FEA model with computed maximum principal strains and corresponding crack patterns on the bottom surface of the slab at the M_p-based 1/3 rule load level, total applied load = 3959 kN (890 kips).

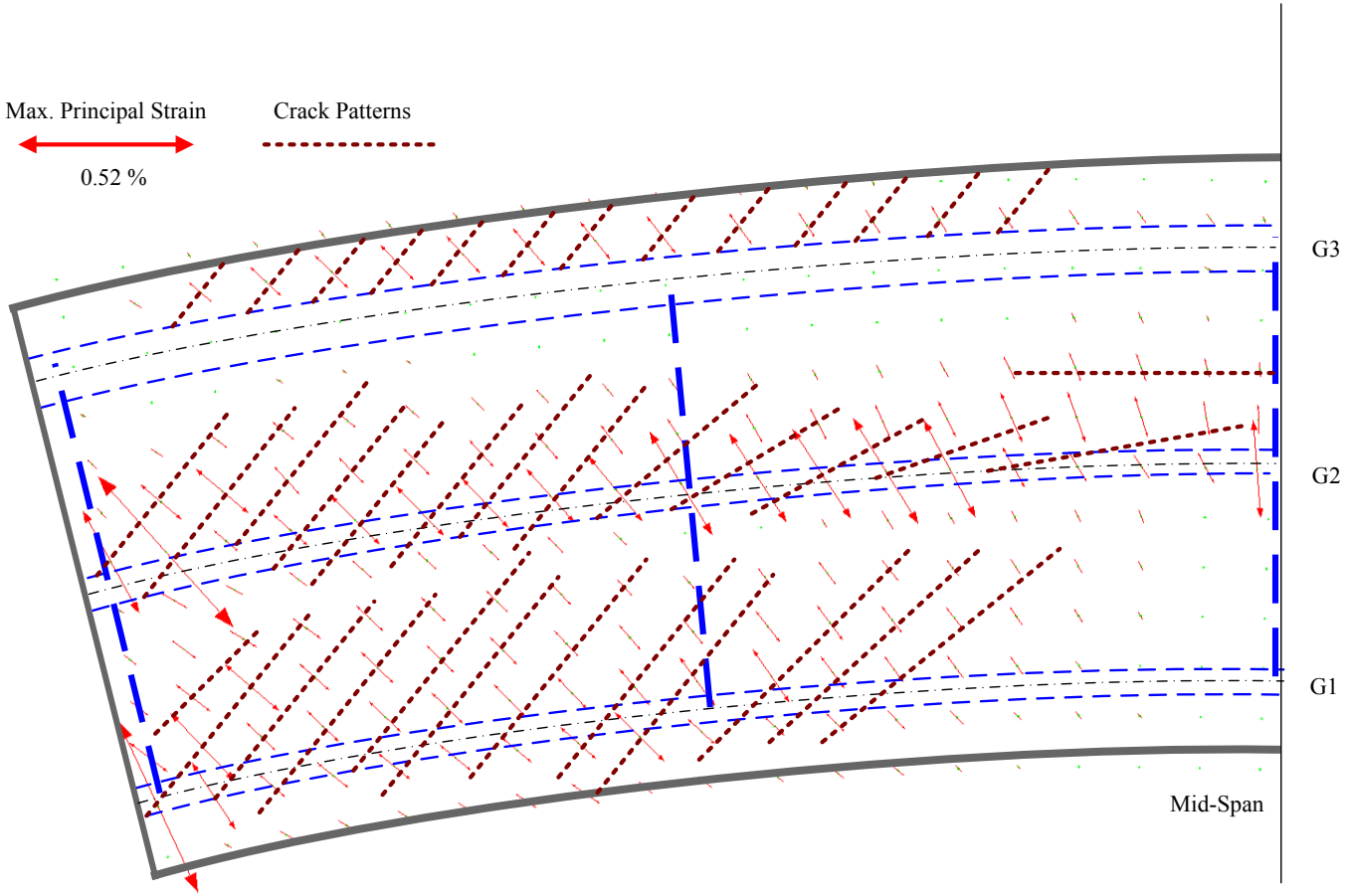

Figure 5.12.7. Plan view of the composite test bridge FEA model with computed maximum principal strains and corresponding crack patterns on the bottom surface of the slab at spalling and crushing of the slab concrete in the experimental test, deflection of the midspan outside tip of the G3 bottom flange = 610 mm (24 in), total applied load = 5783 kN (1300 kips).

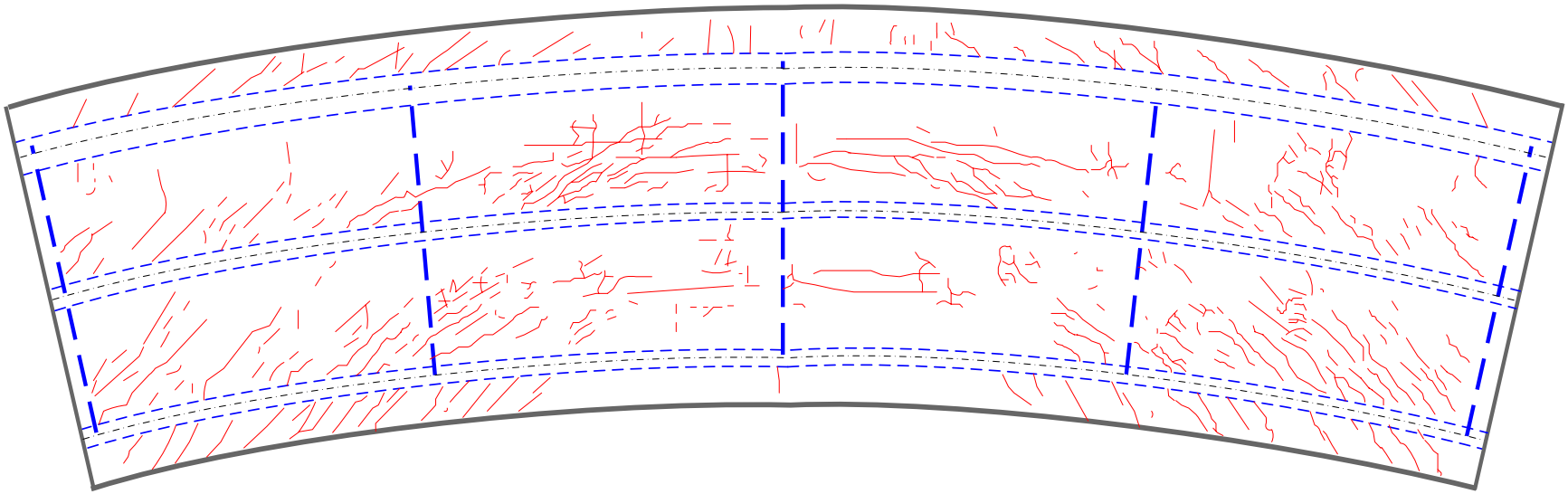

Figure 5.12.8. Plan view of the composite test bridge with crack patterns observed on the bottom surface of the slab at the end of ultimate loading test, courtesy of FHWA.

5.13 Cross-Frame Member Forces

Figure 5.13.1 provides the Test 4b measured and predicted axial forces in the bottom chord of the midspan cross-frame attached to G3. It should be noted that the initial dead load member forces are included in this plot, as well as in the other plots presented below. Also, as in the previous sections, FEA solutions are provided with and without the effects of the repeated loading cycles in Test 4a. Furthermore, it is important to note that changes due to the Test 4a loading cycles are not included in determining the measured cross-frame member forces in this and in the subsequent plots. The cross-frame member forces at zero applied load in Test 4b are based on measurements at the start of Test 4a. Values at the start of Test 4b were not available at the completion of this research. As a result, there is a closer match between the initial values from the FEA solution that does not account for the effects of the prior repeated loading tests and the initial measured values.

The prior loading cycles from Test 4a actually cause a reduction in the member axial force in Figure 5.13.1, thus shifting the corresponding FEA solution to the right in the plot. Also, it can be seen that the prior loading cycles cause an extension of the linear range of the FEA total applied load versus member force curve. This extension matches well with the linear range from the measured data. If the measured data were shifted to the right by the same amount as the predicted shift between the two FEA solutions, one can observe that there would be an excellent correlation between the measured data and the FEA solution in which the effect of the prior loading cycles is included. Nevertheless, it is important to note that all the measured and predicted responses are predominantly linear up to the M_p-based 1/3 rule load level on G3.

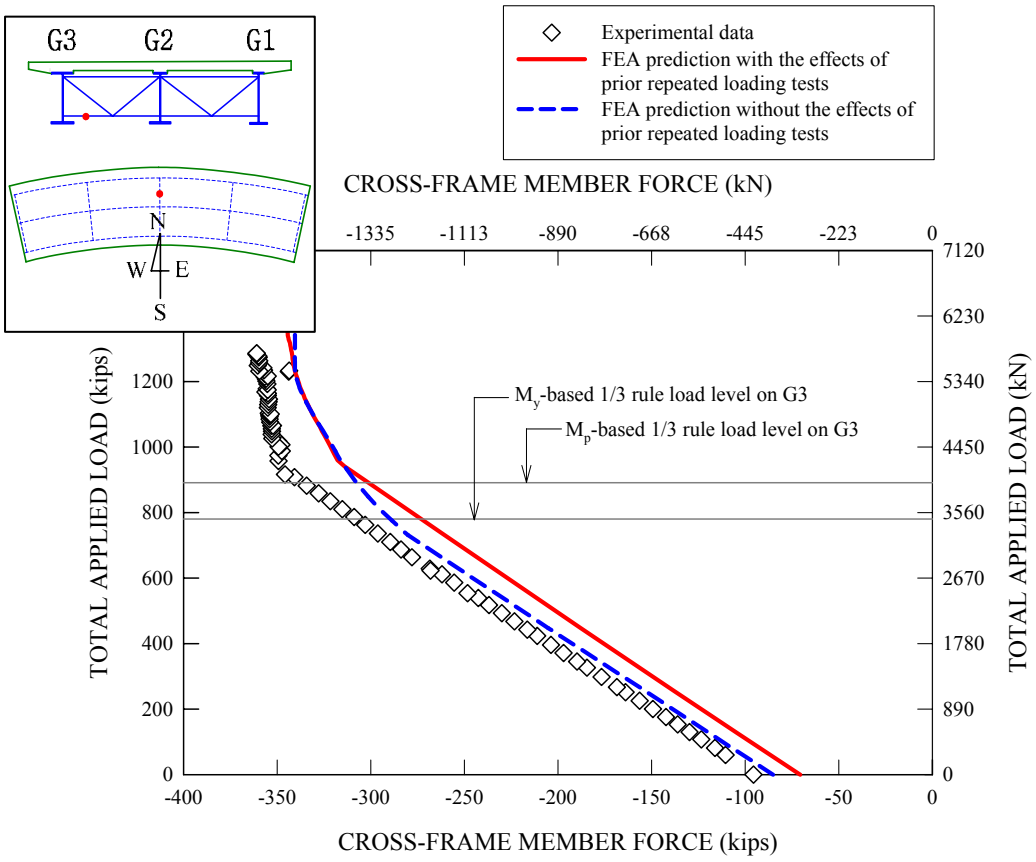

Figure 5.13.1. Measured and predicted Test4b axial forces in the bottom chord of the midspan cross-frame attached to G3, initial dead load forces are included but the measured force does not include any changes that occurred during Test 4a.

Interestingly, Figure 5.13.1 also shows that the bottom chord axial force reaches a plateau in the limit when the applied loads are close to 5783 kN (1300 kips). It should be noted that the appearance of this plateau does not have anything to do with yielding or plastification of the cross-frame members. In fact, the cross-frame members are sized (or retrofitted) such that they remain elastic during the complete testing to the ultimate capacity of the bridge, as discussed previously in Section 5.1.

To understand why the plateau appears in Figure 5.13.1, one can consider the simplified free-body diagram shown in Figure 5.13.2. In the limit when the G3 web and bottom flange are fully plastified, they tend to straighten into chords between the cross-

frame locations. Figure 5.13.2 shows a free body diagram at the midspan of G3 for a portion of the straightened web and bottom flange segments constructed by making cuts halfway between the cross-frame locations. In this extreme configuration, the sum of the axial forces in the web and the bottom flange can be expressed as $P = A_f F_{yf} + A_w F_{yw}$, where A_f and A_w are the areas of the bottom flange and the web, and F_{yf} and F_{yw} are the corresponding yield strengths. The maximum cross-frame bottom chord force can be estimated conservatively as 1753 kN (394 kips), based on the sum of the radial components of the forces P on each side of the midspan cross-frame location. The plateau in Figure 5.13.1 is due to the fact that the web and the bottom flange of G3 have become significantly yielded. This in turn limits the radial reaction on the bottom chord of the cross-frame connected to G3.

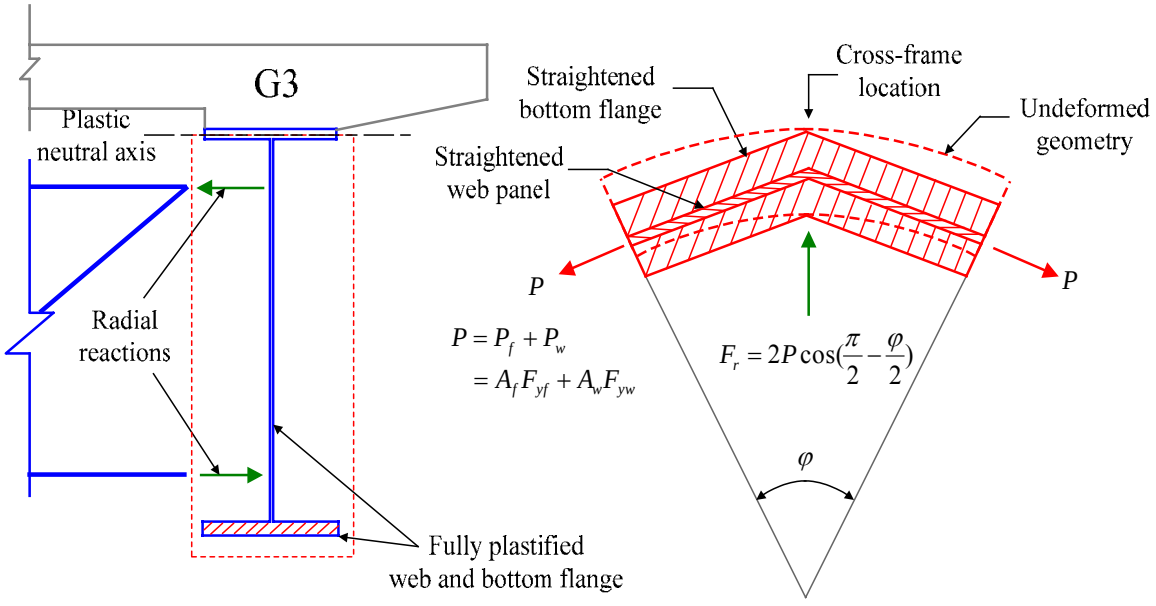

Figure 5.13.2. Cross-frame bottom chord reaction resisting the radial component from the axial forces in the fully plastified web and bottom flange of G3.

Figure 5.13.3 shows results comparable to Figure 5.13.1, but for the compression diagonal of the cross-frame attached to the midspan of G3. The previous discussions regarding the correlation between the measured and FEA solutions for the bottom chord of this cross-frame also apply to the results for the diagonal axial force. Also, again it can be observed that all of the measured and predicted responses are essentially linear up to the M_p-based 1/3 rule load level on G3.

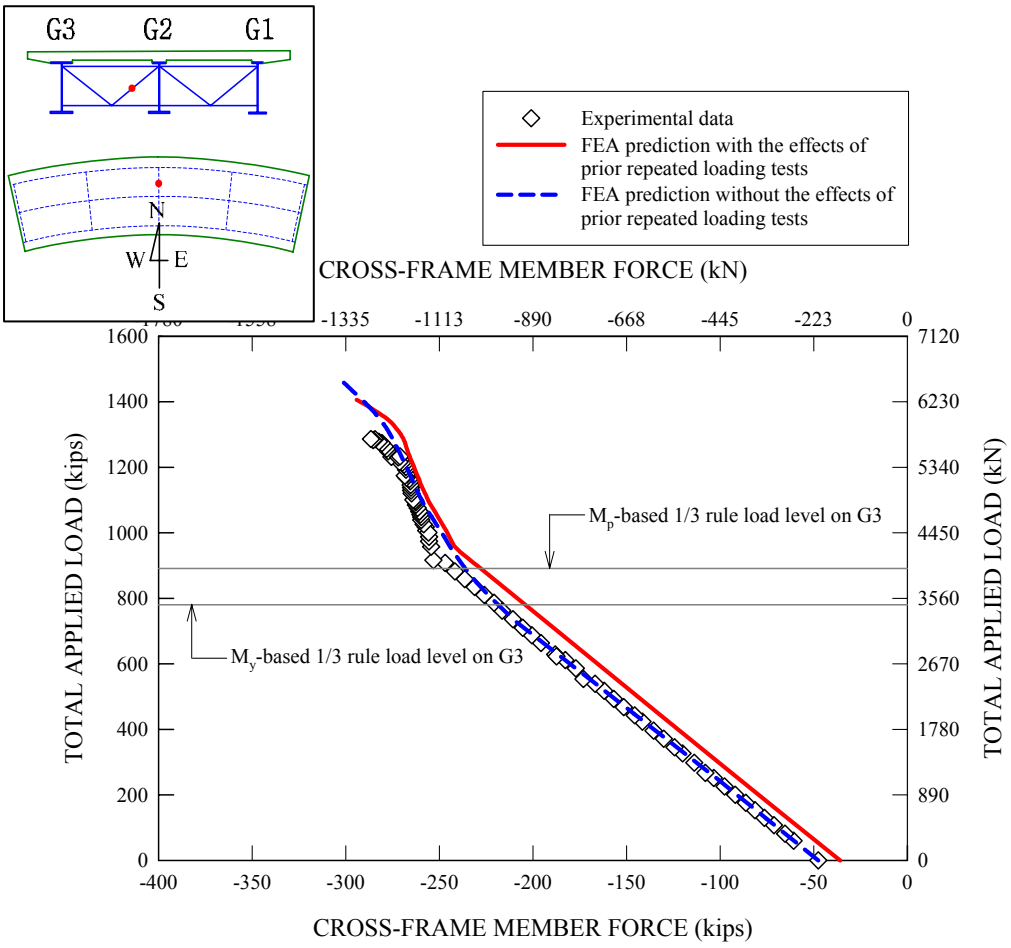

Figure 5.13.3. Measured and predicted Test4b axial forces in the compression diagonal of the cross-frame attached to G3, initial dead load forces are included but the measured force does not include any changes that occurred during Test 4a.

Figure 5.13.4 gives the measured and predicted Test 4b axial forces in the top chord of the midspan cross-frame attached to G3. One can observe that the correlation between the measured and predicted forces for the top chord is not as good as that for the other members. This appears to be largely because the FEA values are substantially smaller than the measured values for the force in the top chord at the start of Test 4a. Also, the slope on the measured top chord force versus total applied load curve during Test 4b is somewhat steeper than the slope on the corresponding FEA based curves. This indicates that possibly the top chord is taking a larger share of the axial tension transferred from G3 in the physical test compared to the FEA solutions. Nonetheless, the top chord force is still quite small compared to the bottom chord force. That is, most of the radial tension reaction at the top of G3 at the midspan is resisted by the slab. Also, it is important to note that the measured and predicted member forces are all increased in a linear fashion up to the M_p-based 1/3 rule load level on G3.

Figures 5.13.5 through 5.13.7 show the above solutions for the quarter-span cross-frames attached to G3. The member forces were measured on both the east and west quarter-span cross-frames and both sets of measured data are included in the plots. The FEA predictions are the same for both of these cross-frames due to symmetry of the FEA model. The previous discussions regarding the correlation between the measured and FEA solutions in Figure 5.13.1 also apply to the bottom chord of both quarter-span cross-frames and to the compression diagonal of the west quarter-span cross-frame. The measured data for the east quarter-span cross-frame diagonal indicates much smaller initial force at the start of Test 4a (see Figure 5.13.6). However, the diagonal in the east quarter-span cross-frame appears to pick up force more rapidly than the one in the west

cross-frame during Test 4b. As a result, this force is slightly larger and fits slightly better with the FEA predictions at high applied load levels. The measured top chord member forces are again significantly larger than the FEA values.

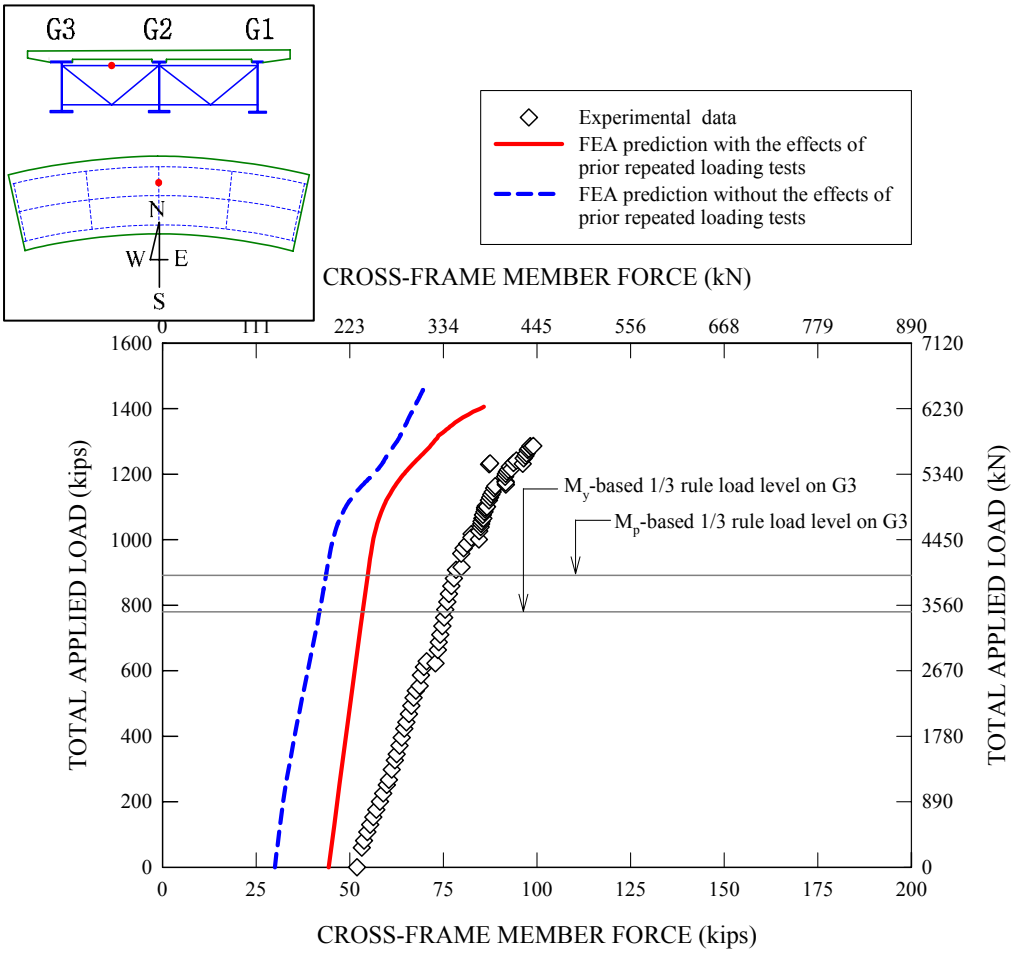

Figure 5.13.4. Measured and predicted Test 4b axial forces in the top chord of the midspan cross-frame attached to G3, initial dead load forces are included but the measured force does not include any changes that occurred during Test 4a.

Based on each of Figures 5.13.5 through 5.13.7, one can observe that the quarter-span cross-frames start to pick up an increasing amount of force at high load levels. That is, the slope of all the total applied load versus cross-frame member force curves decreases significantly at a total applied load above about 4450 kN (1000 kips). This is due to

inelastic load redistribution associated with the yielding of girders G2 and G3 at the midspan. Nevertheless, this load is significantly larger than the M_p-based 1/3 rule load level on G3. All the measured and predicted member forces vary in essentially a linear fashion up to the M_p-based 1/3 rule load level on G3.

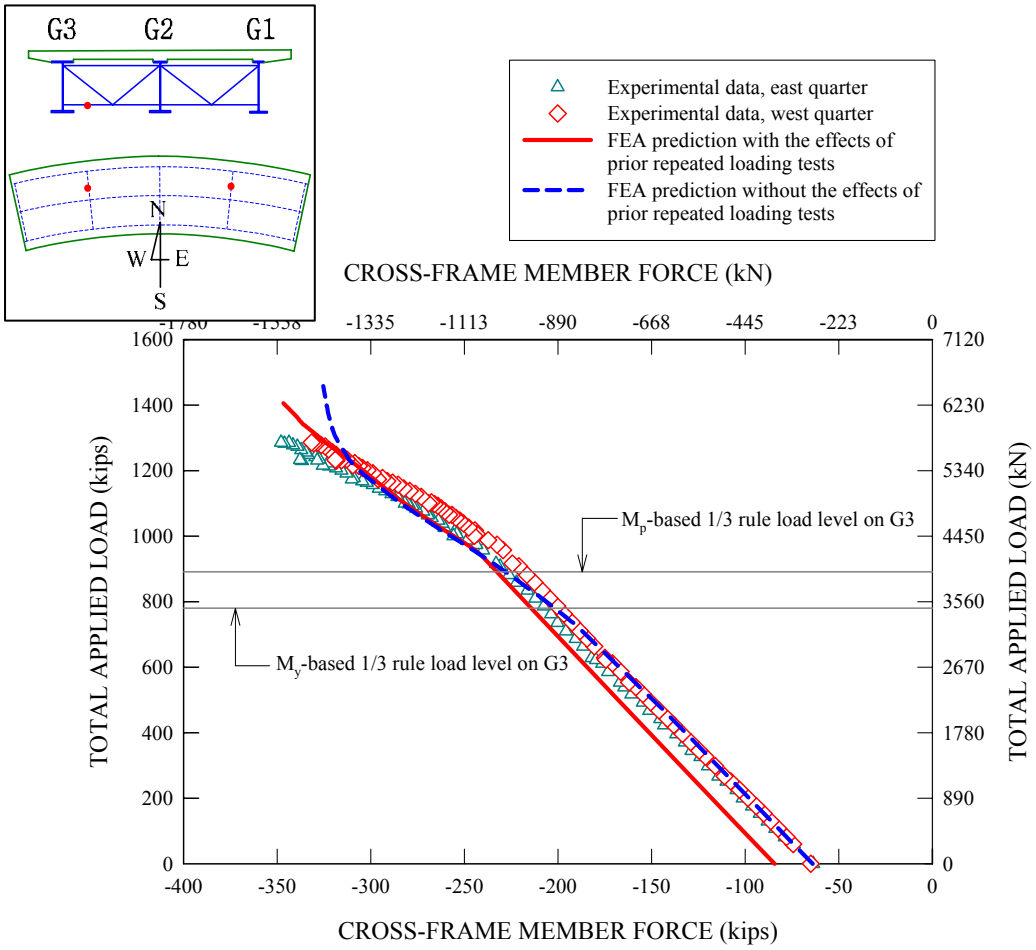

Figure 5.13.5. Measured and predicted Test 4b axial forces in the bottom chord of the quarter-span cross-frames attached to G3, initial dead load member forces are included but the measured force does not include any changes that occurred during Test 4a.

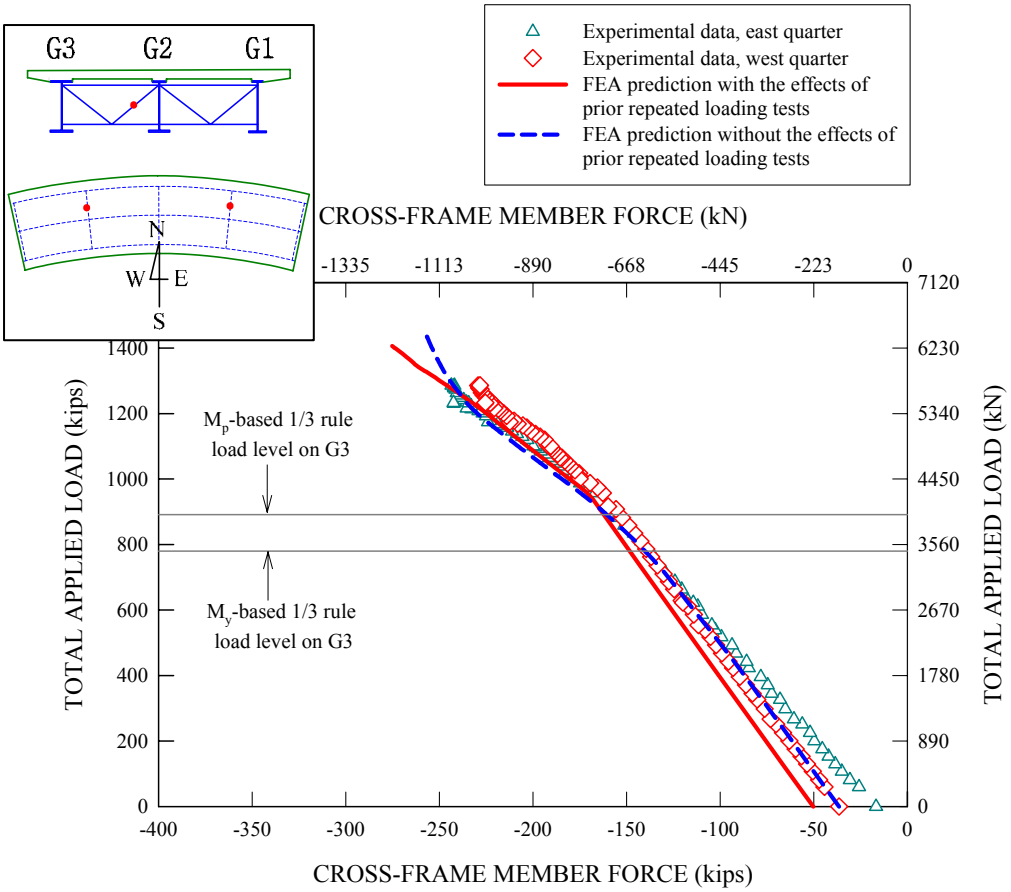

Figure 5.13.6. Measured and predicted Test 4b axial forces in the compression diagonal of the quarter-span cross-frames attached to G3, initial dead load member forces are included but the measured force does not include any changes that occurred during Test 4a.

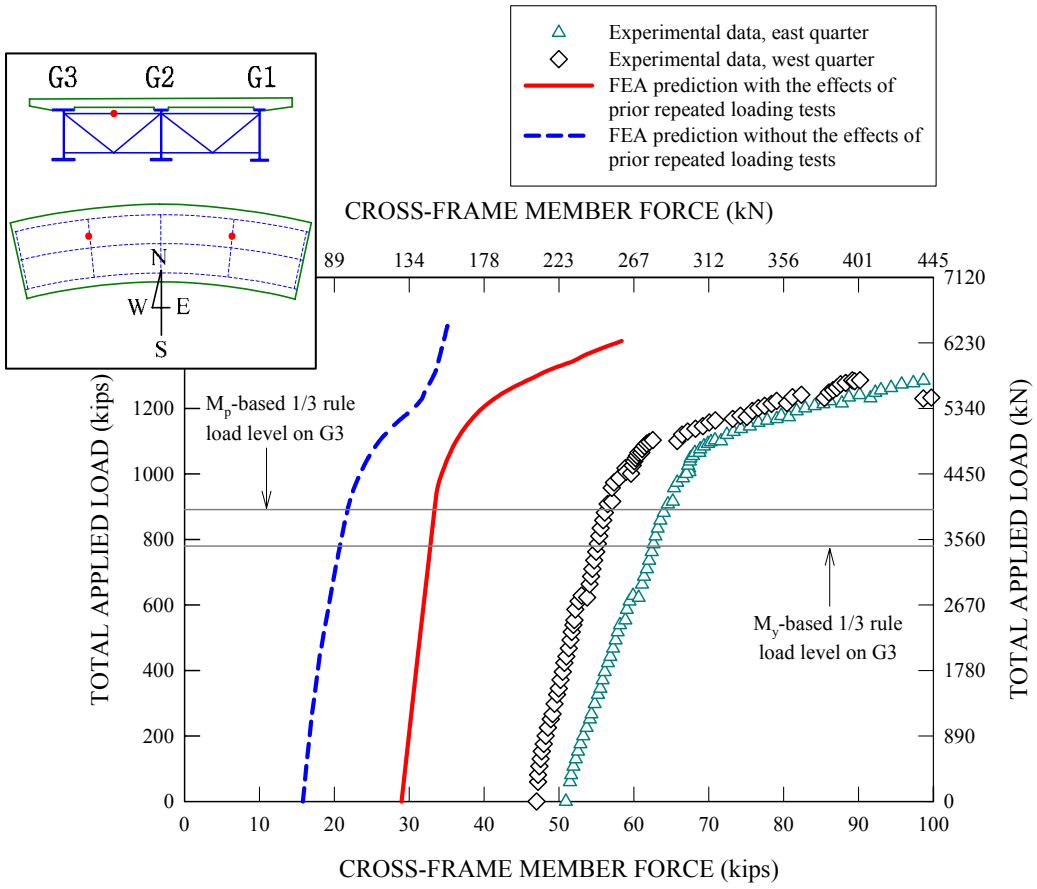

Figure 5.13.7. Measured and predicted Test 4b axial forces in the top chord of the quarter-span cross-frames attached to G3, initial dead load member forces are included but the measured force does not include any changes that occurred during Test 4a.

5.14 Behavior of Intermediate Transverse Stiffeners

5.14.1 Intermediate Transverse Stiffeners Located Close to the Midspan

Two G3 intermediate transverse stiffeners located between the midspan and the quarter-span cross-frames, labeled as G3_IST7 and G3_IST9, were instrumented to investigate detailed stiffener responses during the ultimate load test. Figure 5.14.1 shows the location of these stiffeners within the overall bridge plan layout. The intermediate transverse stiffeners on G3 are located on the side of the web toward the bridge center of curvature.

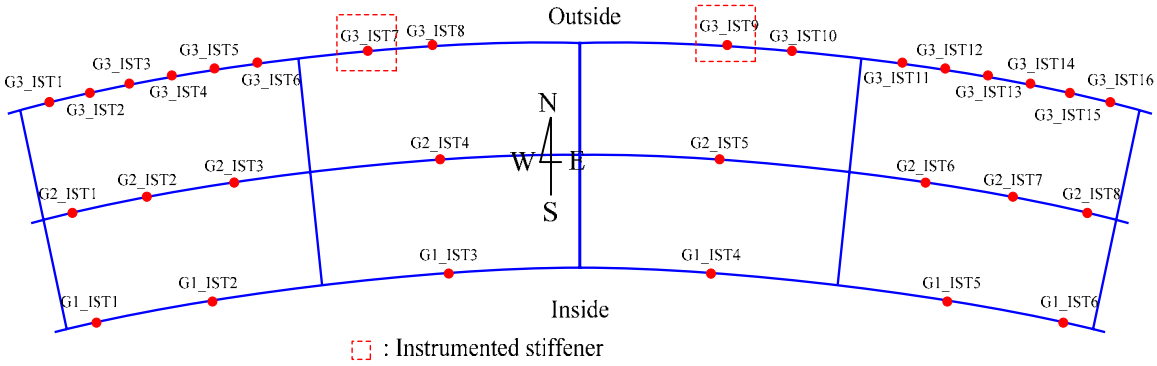

Figure 5.14.1. Locations of two G3 intermediate transverse stiffeners instrumented with strain gauges: G3_IST7 and G3_IST9.

Figure 5.14.2 shows the layout of the strain gauges on each of the stiffeners. Each stiffener was instrumented with six gauges on each side of the stiffener, two near the top, two at the mid-height and two near the bottom of the stiffener. The gauges were located at the 1/4 and 3/4 of the stiffener widths and were spaced at 76 mm (3 in) apart. The top and bottom gauges were located at 100 mm (4 in) away from the inside face of the flanges. For reference purposes, the side of the stiffeners facing the east end of the bridge is labeled E while the side facing the west end of the bridge is labeled W in the following discussions. As noted previously in Section 2.5, the stiffeners on the east side of the midspan were cut short of the bottom tension flange. This is illustrated in the sketches of G3-IST9 in Figure 5.14.2. Figure 5.14.3 gives a snapshot of the stiffener G3_IST7.

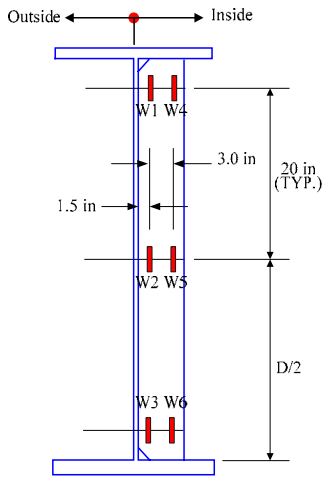

(a) G3_IST7 – W

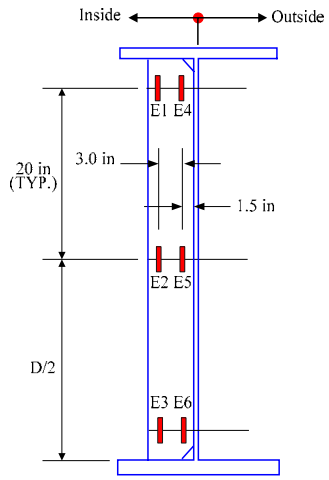

(b) G3_IST7 - E

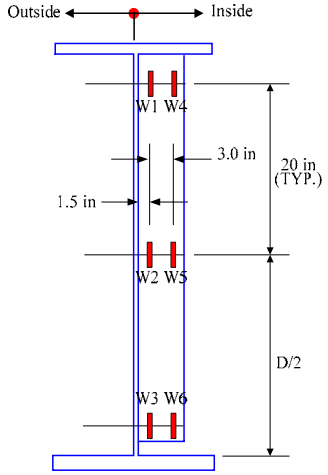

(c) G3_IST9 – W

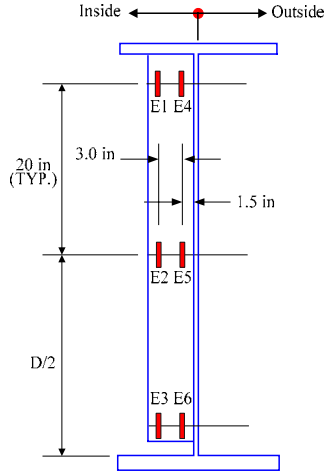

(d) G3_IST9 - E

Figure 5.14.2. Detailed instrumentation layouts on the face of each stiffener: (a) G3_IST7-W, (b) G3_IST7-E, (c) G3_IST9-W and (d) G3_IST9-E.

Figure 5.14.3. Instrumented intermediate transverse stiffener for G3_IST7, courtesy of FHWA.

Figures 5.14.4 through 5.14.9 provide the measured and predicted stiffener normal strains measured at the top, mid-height and bottom of G3_IST7. It should be noted that the normal strains presented in these plots are solely due to applied loads in Test 4b. Since beam elements are used to represent the transverse stiffeners in the full nonlinear FEA bridge model, the predicted strain variations through the thickness and through the width are linear. In addition, one can observe that the predicted normal strains on both sides of the stiffener are essentially equal each other with the exception of a small departure at high load levels. All the strain comparisons presented in Figures 5.14.4 through 5.14.9 show a good correlation between the experimental data and FEA predictions in terms of the overall trends as well as the strain magnitudes. Furthermore,

similar to other bridge component responses shown in the earlier parts of this chapter, significant nonlinearities start slightly beyond the G3 M_p-based 1/3 rule applied load level of 3959 kN (890 kips). All the strains in the stiffener increase predominantly in a linear fashion up to this level. At significantly higher loads, the top outside gauge of the stiffener experience strain levels larger than the yield strain (approximately 2000 με) as shown in Figures 5.14.4 and 5.14.5, while the strains at the other gauge locations are less than the yield strain throughout the entire loading history.

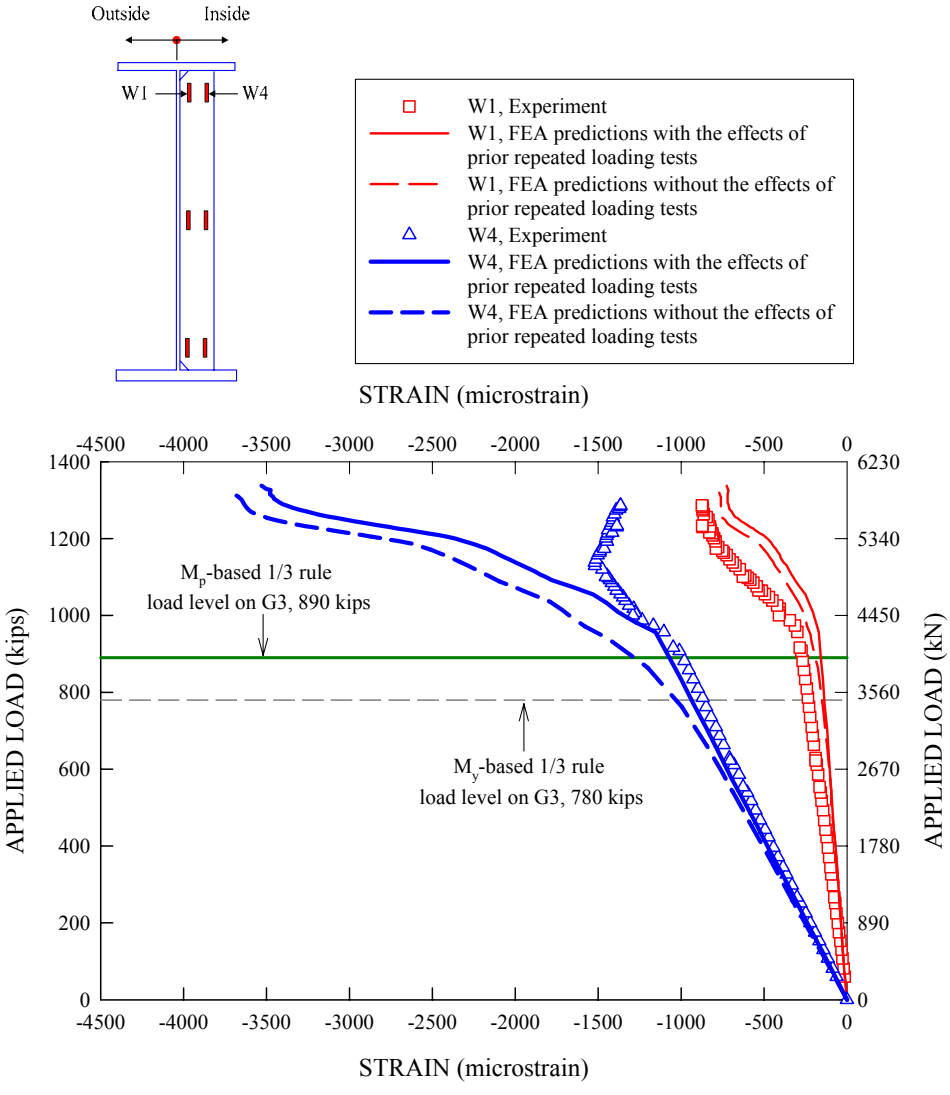

Figure 5.14.4. Measured and predicted stiffener strains for G3_IST7-W top locations.

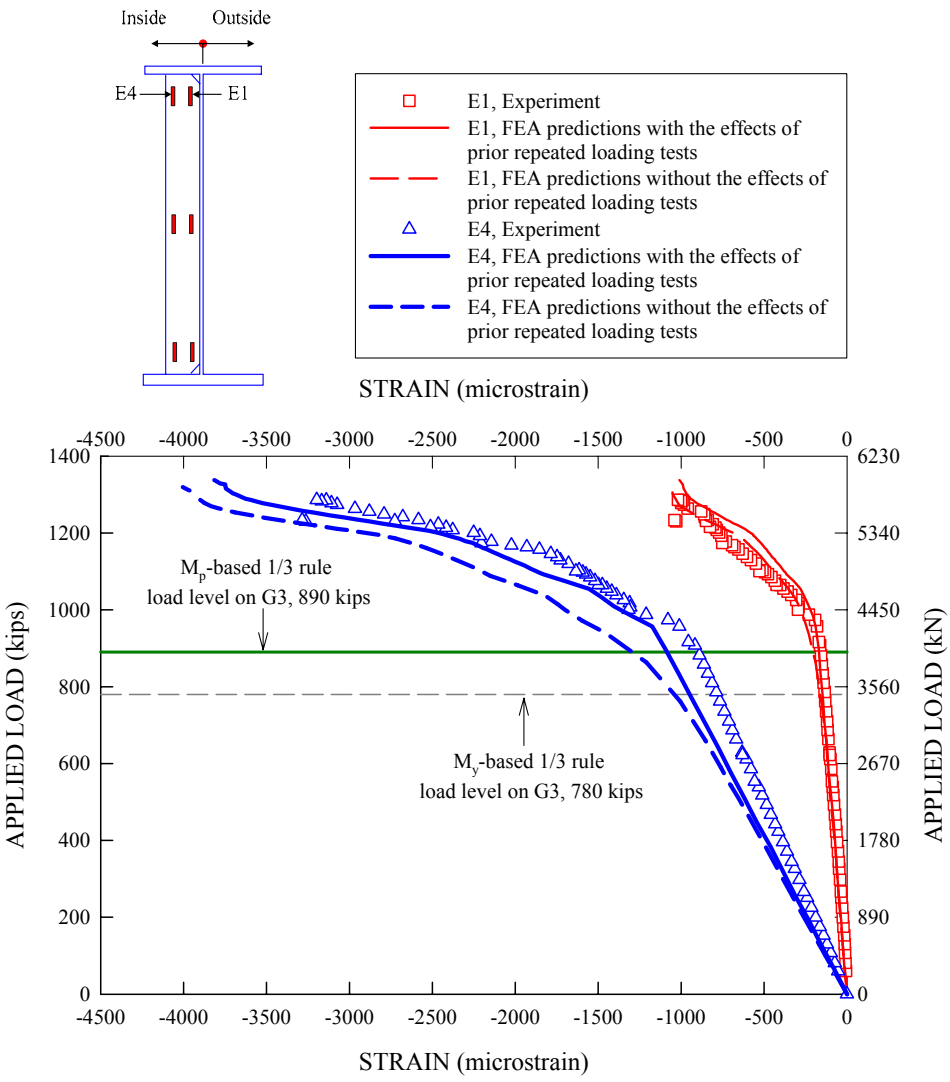

Figure 5.14.5. Measured and predicted stiffener strains for G3_IST7-E top locations.

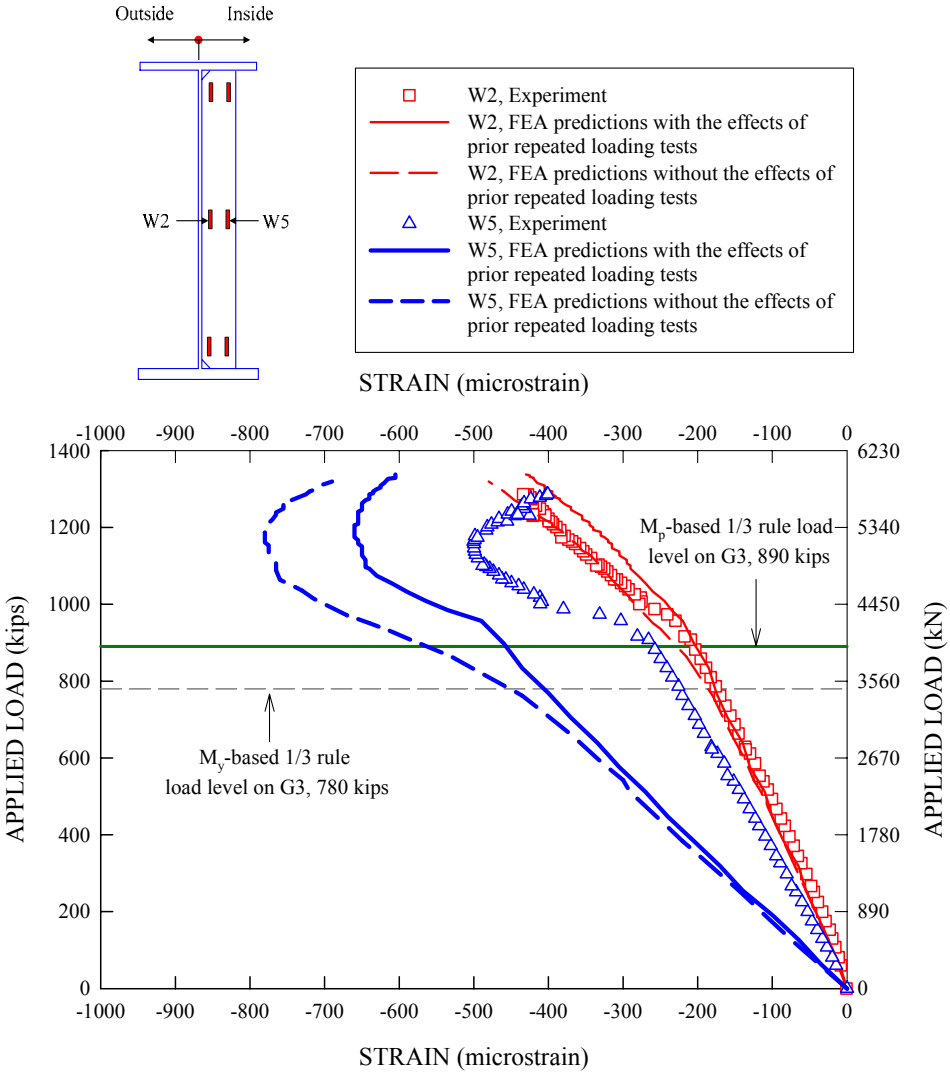

Figure 5.14.6. Measured and predicted stiffener strains for G3_IST7-W mid-height locations.

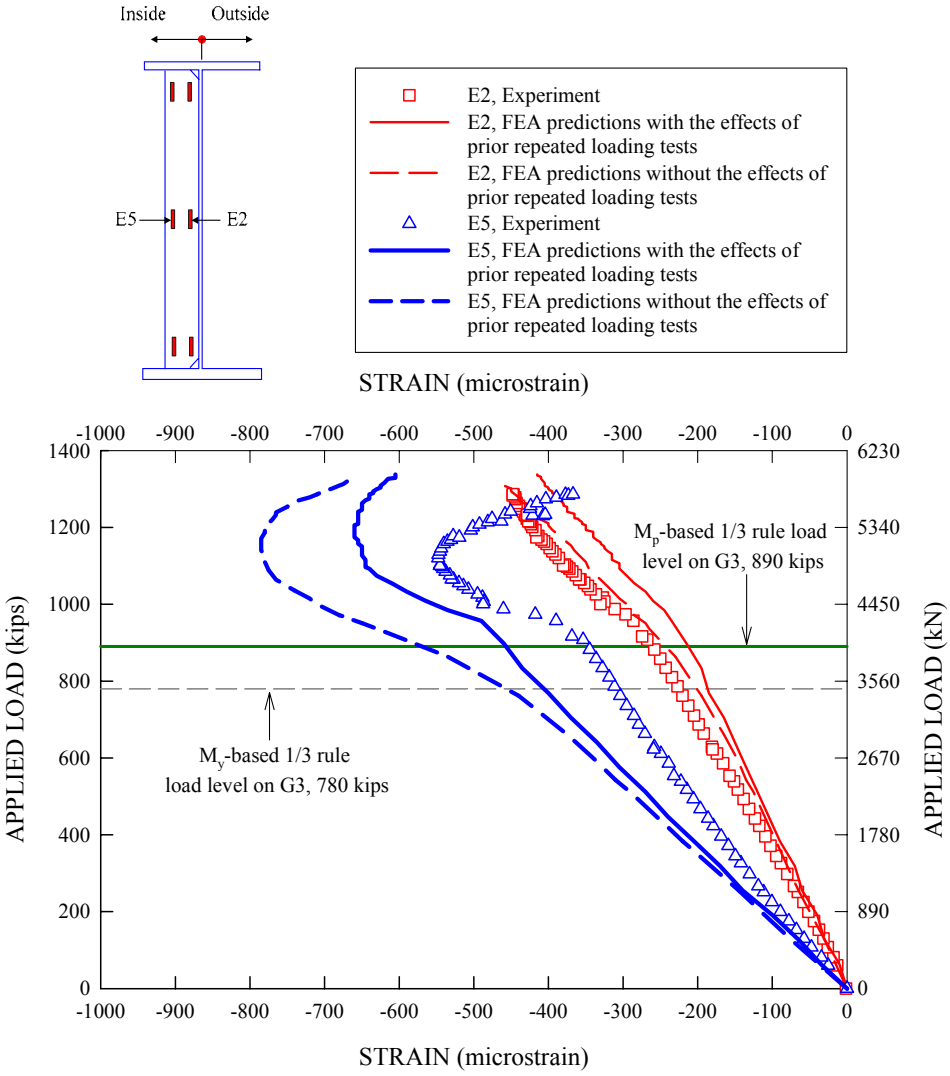

Figure 5.14.7. Measured and predicted stiffener strains for G3_IST7-E mid-height locations.

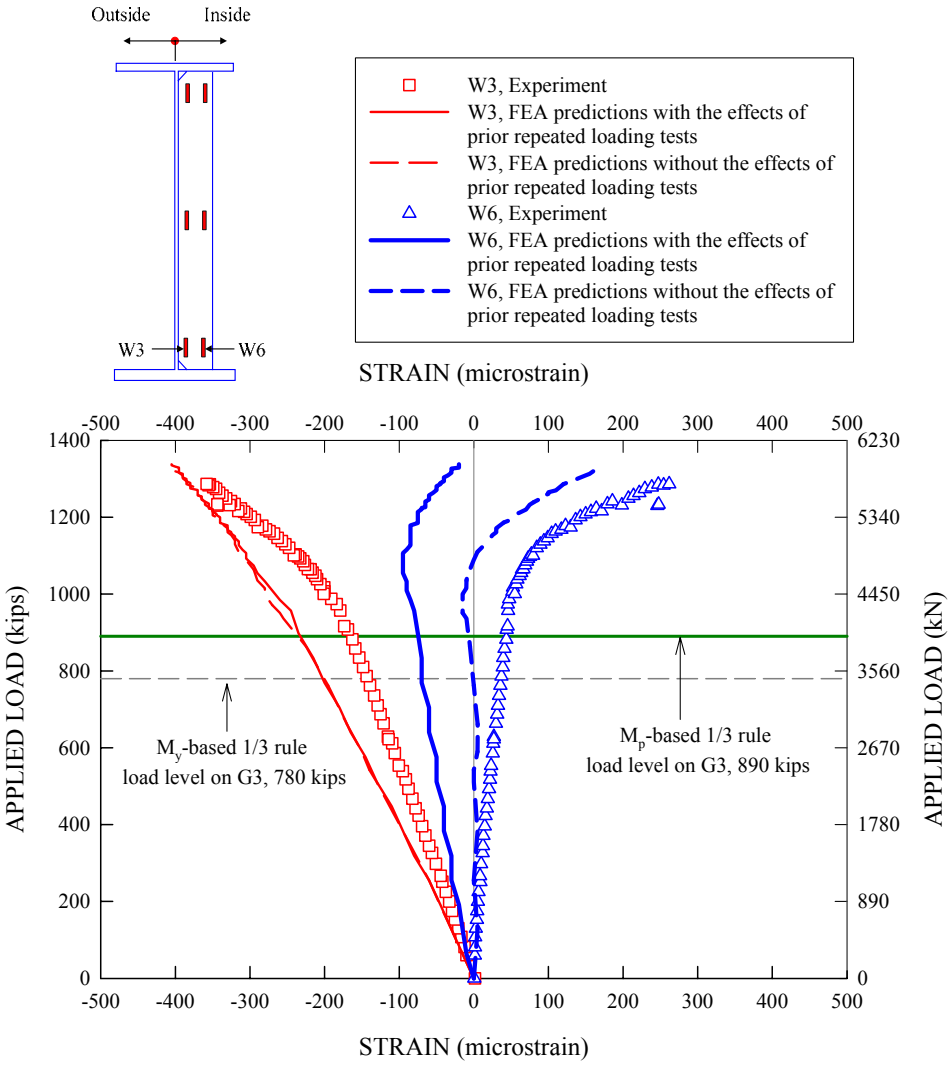

Figure 5.14.8. Measured and predicted stiffener strains for G3_IST7-W bottom locations.

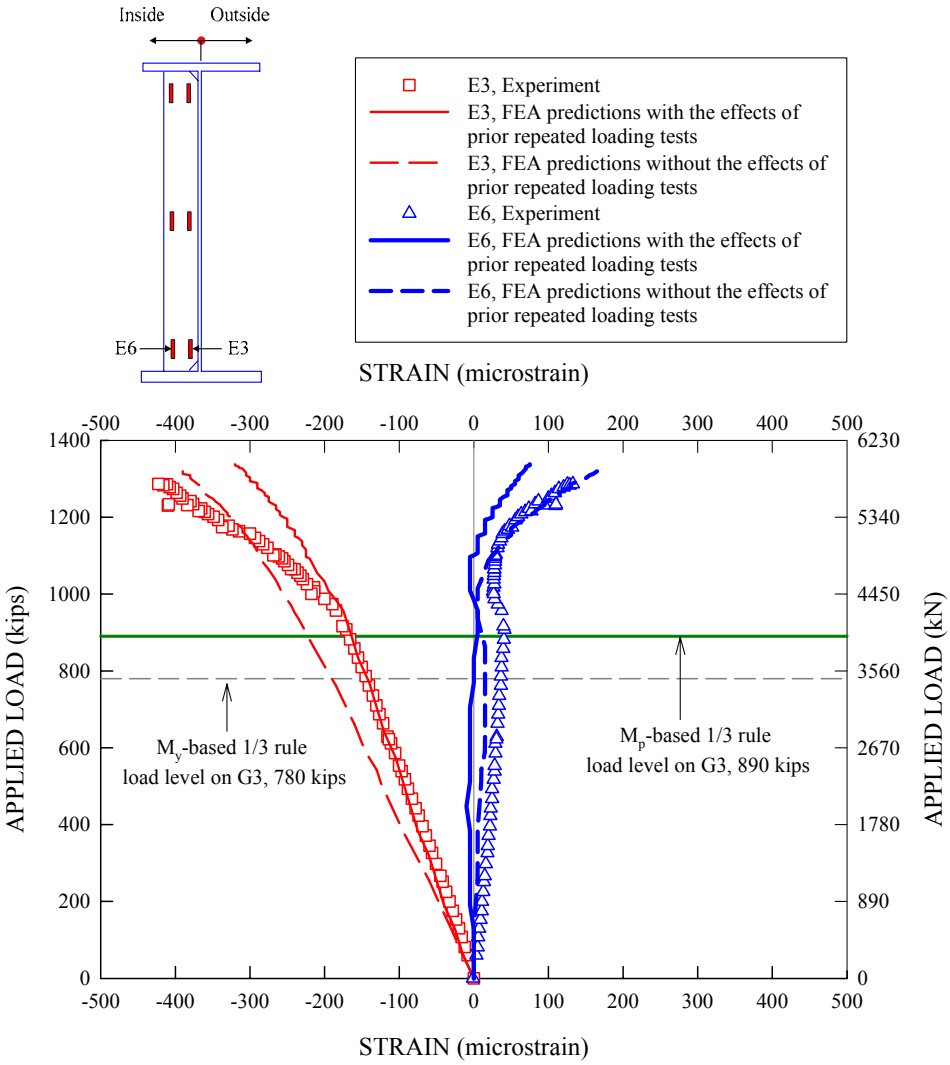

Figure 5.14.9. Measured and predicted stiffener strains for G3_IST7-E bottom locations.

Figures 5.14.10 through 5.14.15 provide the measured and predicted normal strains on G3_IST9. In contrast to the strains observed on G3_IST7, it can be seen that the strains are essentially the same on both sides of G3_IST9 at all the gauge locations throughout the entire loading history. That is, the bending of the G3_IST9 is entirely uniaxial. Again, the overall correlation between the measured and FEA strains is reasonably good. Similar to G3_IST7, the stiffener strains increase dramatically at a total applied load larger than about 4450 kN (1000 kips), which is significantly beyond the M_p-based 1/3 rule load level on G3. The most distinctive characteristic of the G3_IST9 strains is that the maximum strains measured at the top outside gauges are almost two orders of magnitude greater than the measured yield strain at the ultimate strength of the structure. This indicates that G3_IST9 performs much like a cantilever beam, with its fixed end at the top flange of G3, restraining the tendency of the web to distort laterally. The fixed end restraint is provided by the slab. However, at loads approaching the ultimate strength condition, the stiffener is not sufficient to provide this restraint and hence a plastic hinge is formed at its top. This behavior is similar for G3_IST7, although not as dramatic.

The fact that G3_IST9 is cut short of the bottom flange does not appear to be a significant factor in the behavior of the stiffener. Obviously, if stiffeners are cut short of the top flange (e.g., in the negative moment region of a continuous-span girder), the effect on the behavior may be substantial.

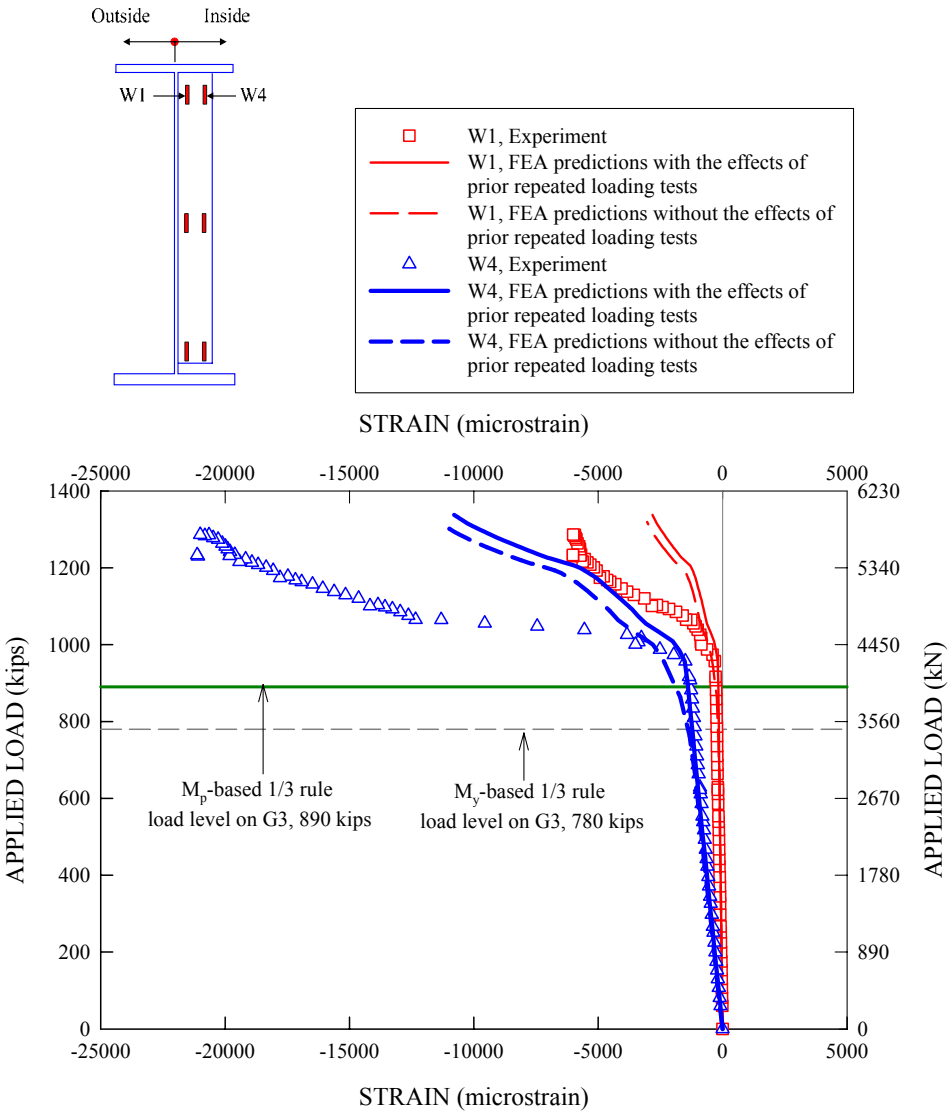

Figure 5.14.10. Measured and predicted stiffener strains for G3_IST9-W top locations.

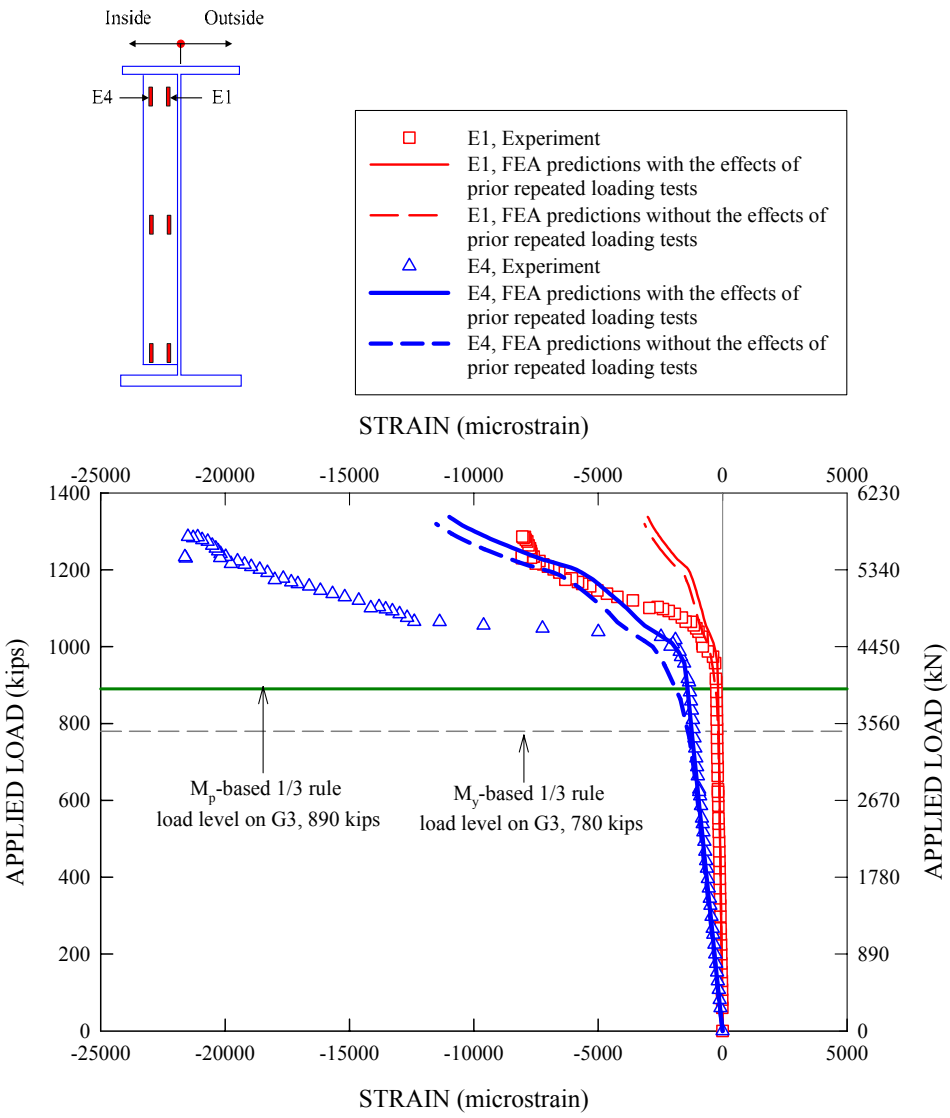

Figure 5.14.11. Measured and predicted stiffener strains for G3_IST9-E top locations.

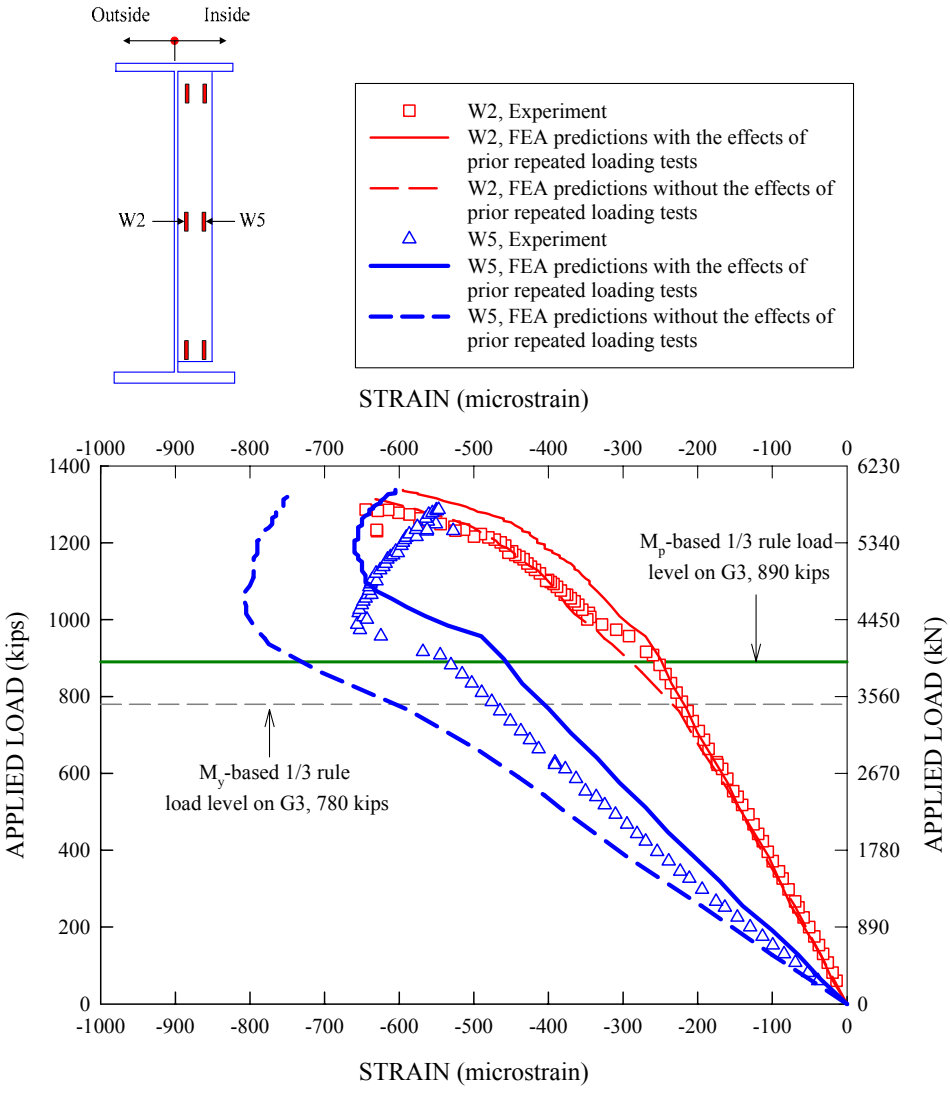

Figure 5.14.12. Measured and predicted stiffener strains for G3_IST9-W mid-height locations.

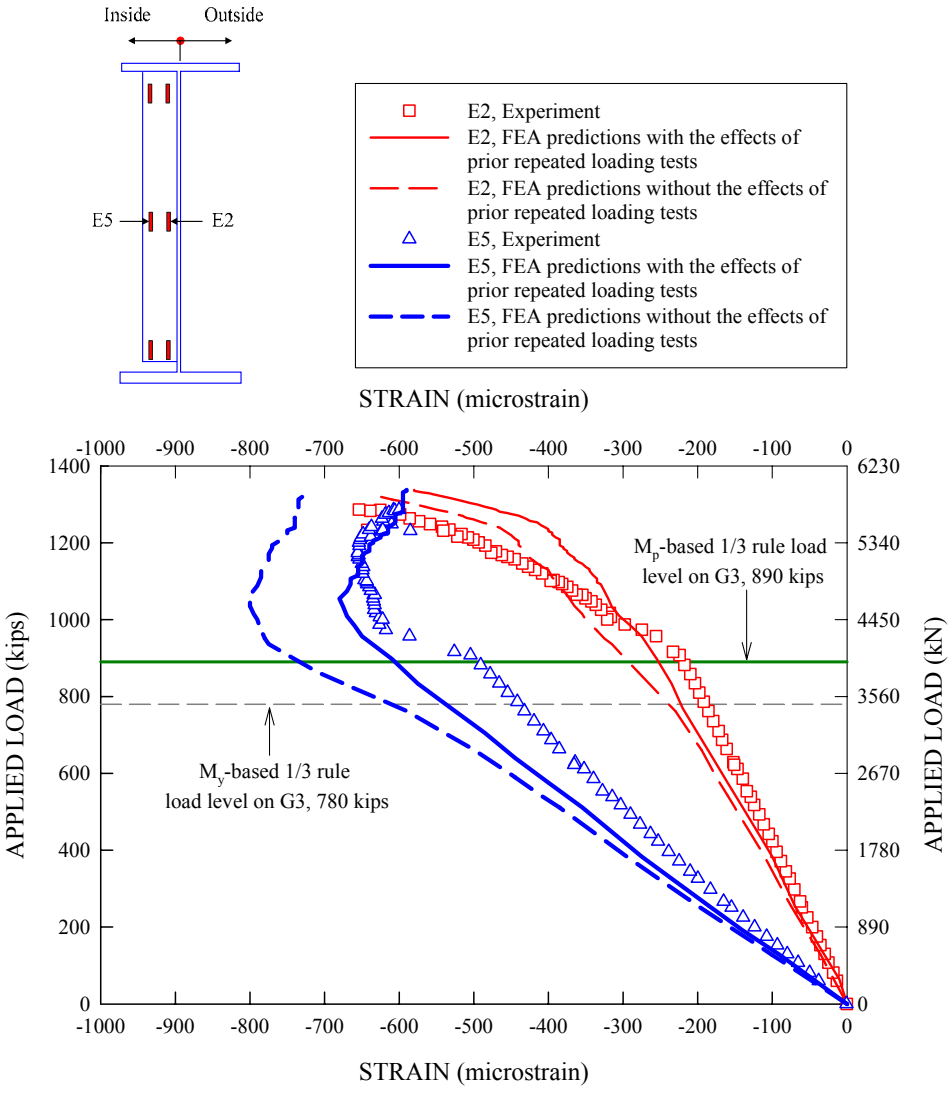

Figure 5.14.13. Measured and predicted stiffener strains for G3_IST9-E mid-height locations.

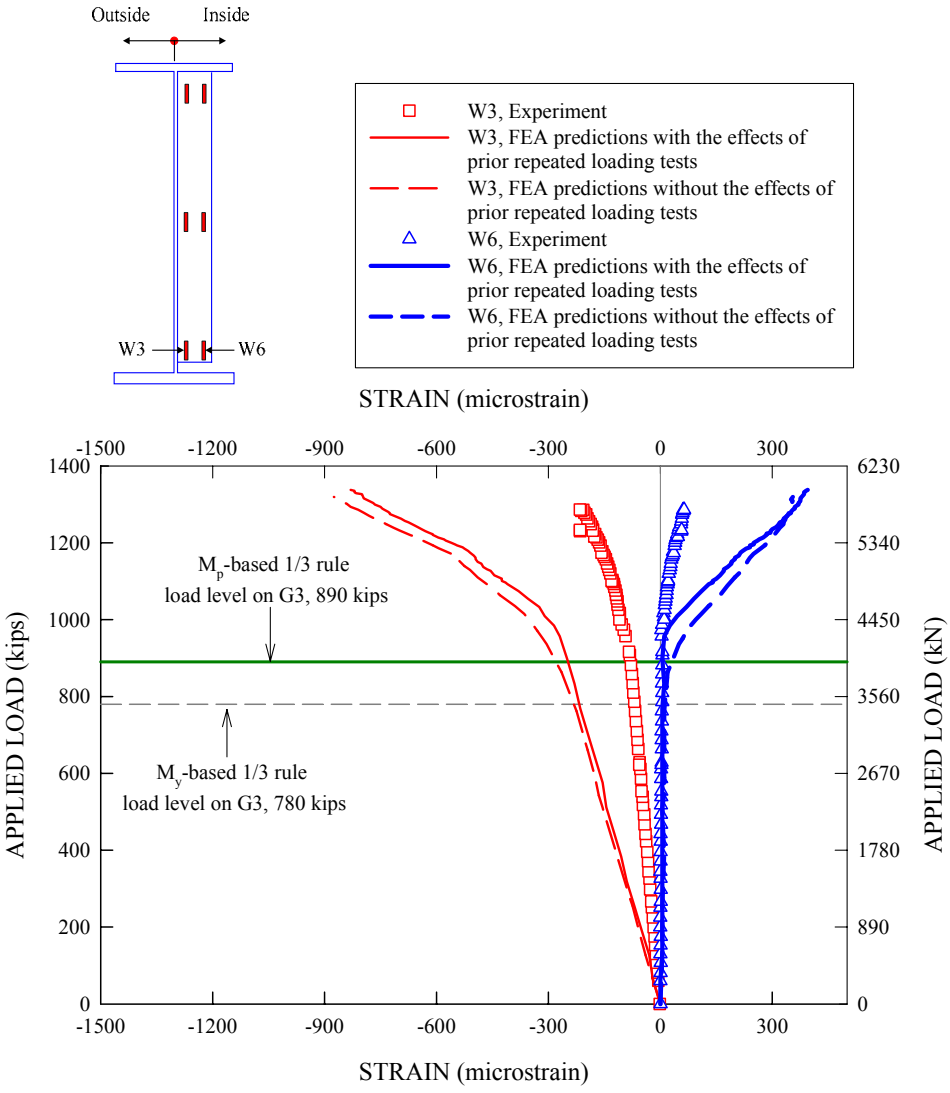

Figure 5.14.14. Measured and predicted stiffener strains for G3_IST9-W bottom locations.

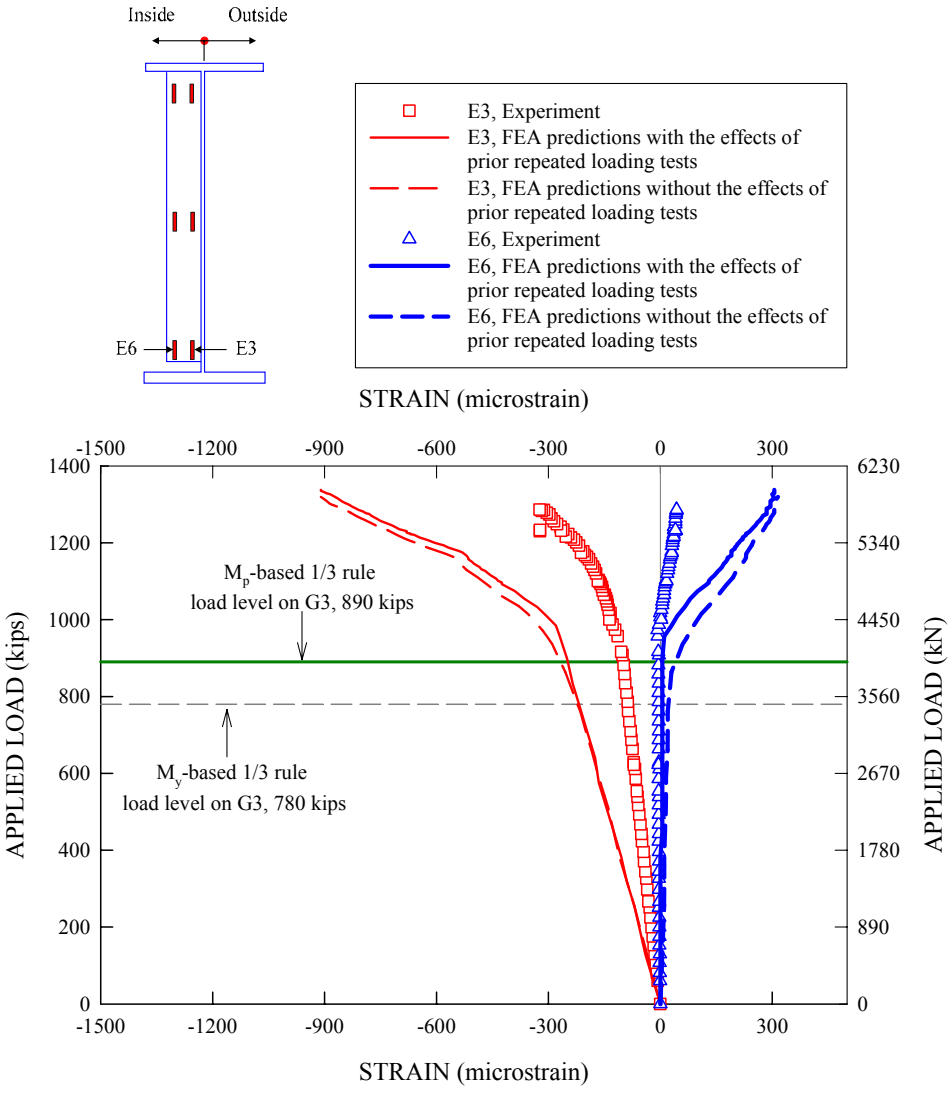

Figure 5.14.15. Measured and predicted stiffener strains for G3_IST9-E bottom locations.

To gain a better understanding of the stiffener behavior presented in Figures 5.14.4 through 5.14.15, it is useful to consider strain variations along the stiffener height. Figures 5.14.16 and 5.14.17 compare the measured stiffener normal strains along the normalized height of G3_IST7 with the corresponding full nonlinear FEA predictions at the G3 M_p-based 1/3 rule and the ultimate load levels of 3959 kN (890 kips) and 5783 kN (1300 kips). Figures 5.14.18 and 5.14.19 provide similar plots for G3_IST9. The bottom surface of the top flange is located at x/D = 1. The stiffener strains due to dead loads are not included in these plots. Their values are relatively small or negligible compared to the strains associated with directly applied loads. The experimental values reported in these plots are the average values from the gauges on each side of the stiffeners while the FEA strains are evaluated at the mid-thickness of the stiffeners. The stiffener strains in the figures are normalized by the measured yield strain ($\varepsilon_y = F_{ys}/E$, where F_{ys} = 400 MPa (58 ksi) and E = 200 GPa (29000 ksi)).

Figures 5.14.16 and 5.14.18 show that measured strains are closely matched by FEA predictions along the stiffener height for both of the stiffeners at the M_p-based 1/3 rule load level, and that the overall strain variations are predominantly linear along the stiffener height at this load level. Also, all the strains are less than the measured yield strain 2000 με throughout the height for G3_IST7 while the top part of G3_IST9 is slightly yielded. Conversely, Figures 5.14.17 and 5.14.19 show that there is significant yielding at the juncture of the stiffener and top flange at the ultimate load level, and that there is still a good correlation between the FEA predictions and experimental data, except for the strain comparison at the outside gauge line of G3_IST7. Conceptually, this behavior can be explained using the analogy of a cantilever subjected to lateral forces due

to the horizontal curvature. Eventually, there is a formation of the plastic hinge at the top of the stiffeners. However, this behavior does not occur in the test bridge until well beyond the G3 M_p-based 1/3 rule load level.

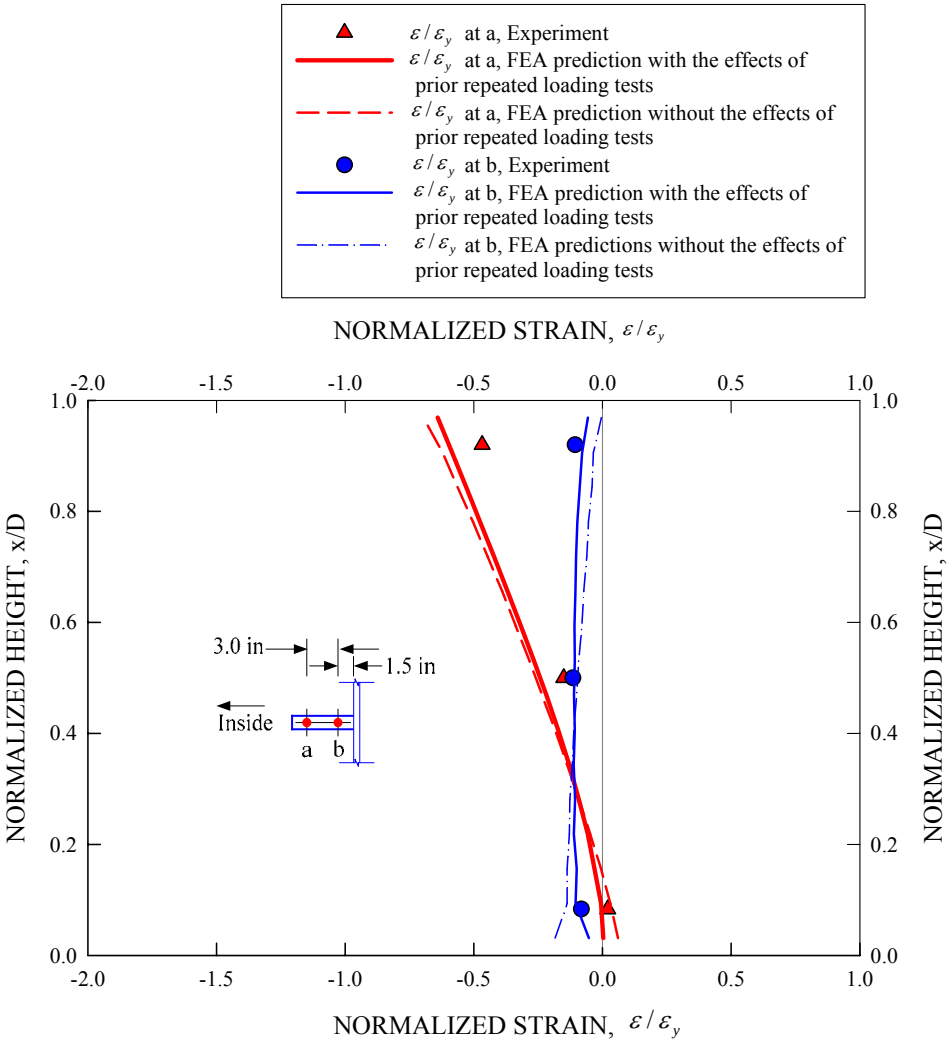

Figure 5.14.16. Stiffener strains along the normalized height for G3_IST7 at the M_p-based 1/3 rule load level of 3959 kN (890 kips).

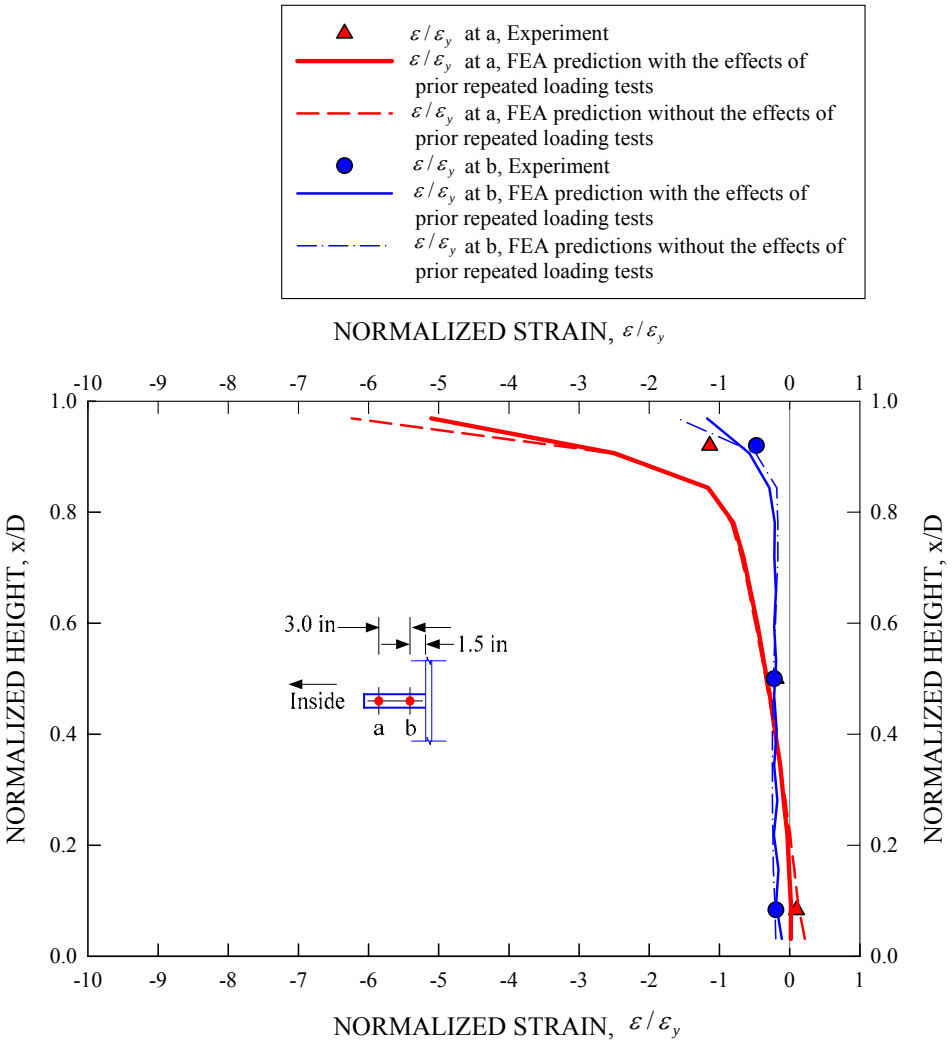

Figure 5.14.17. Stiffener strains along the normalized height for G3_IST7 at the ultimate load level of 5783 kN (1300 kips).

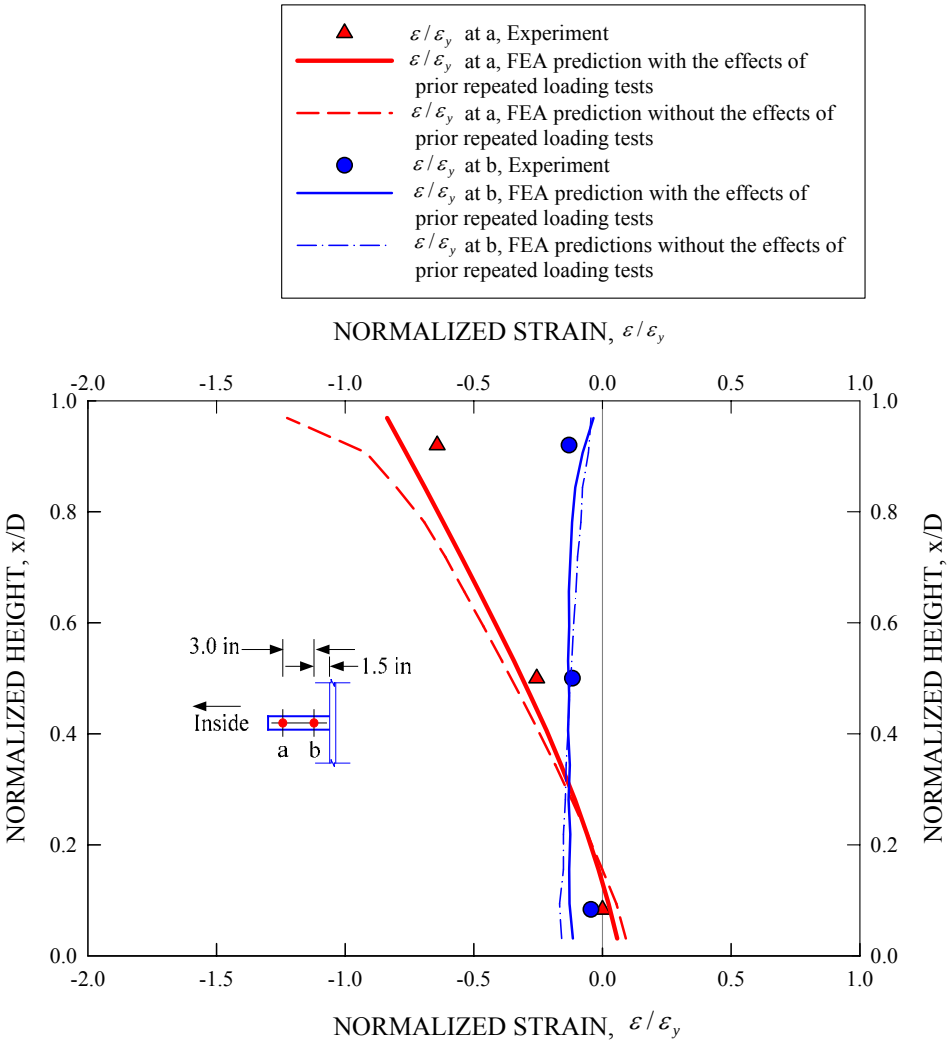

Figure 5.14.18. Stiffener strains along the normalized height of G3_IST9 at the M_p-based 1/3 rule load level of 3959 kN (890 kips).

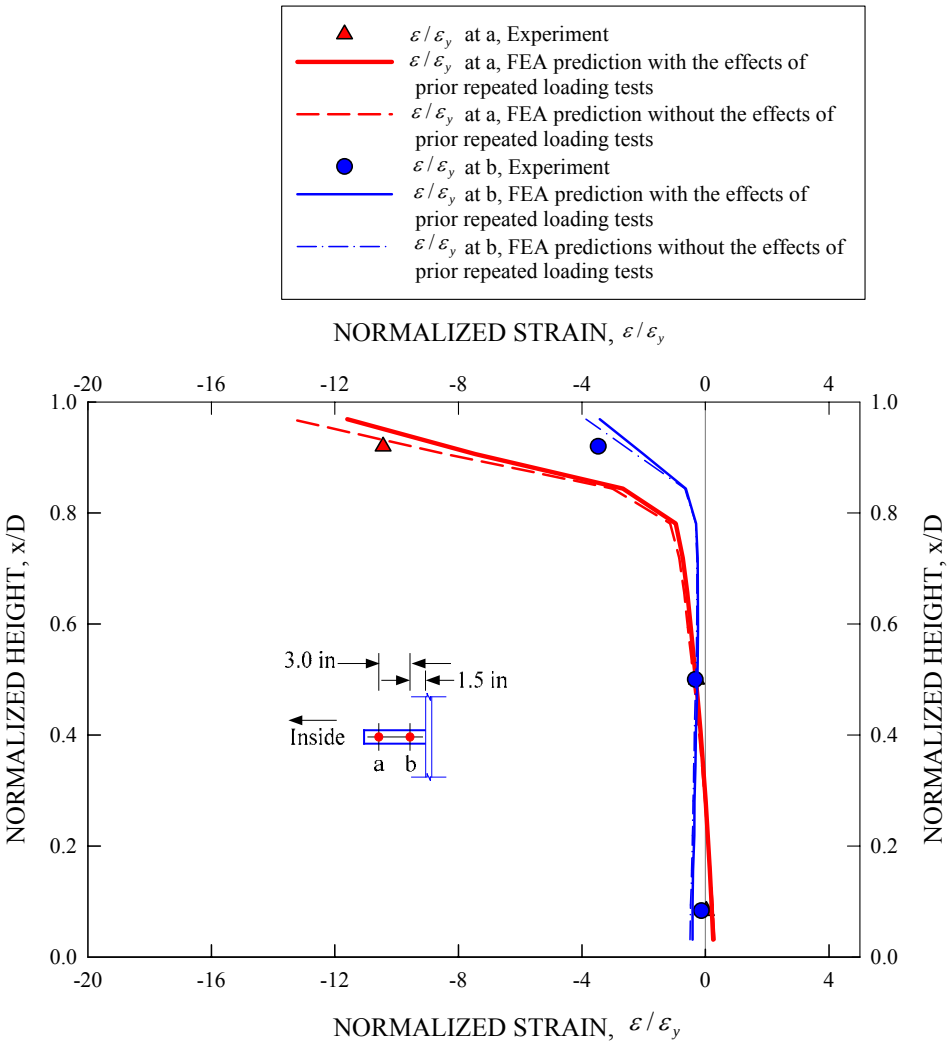

Figure 5.14.19. Stiffener strains along the normalized height of G3_IST9 at the ultimate load level of 5783 kN (1300 kips).

To gain an even more detailed understanding of the yielding behavior of the above two stiffeners, one can consider Figures 5.14.20 and 5.14.21 which show normalized moment-shear plots for the girder cross-sections where G3_IST7 and G3_IST9 are located. Figure 5.14.20 shows the moments and shears at the G3 cross-sections corresponding to these stiffeners at M_p-based 1/3 rule load level, while Figure 5.14.21 shows the moments and shears at the ultimate load level. The cross-section shear forces obtained from the full nonlinear FEA model are normalized by the AASHTO (2004) nominal shear resistance of G3, V_n. The internal moments are normalized by the major-axis resistances (denoted here by M_n^*) obtained using the M_y- and M_p-based 1/3 rules (by using the appropriate elastic f_ℓ defined by AAHSTO (2004) and subtracting the lateral bending term from both sides of Eqs. (2.1) and (2.8)).

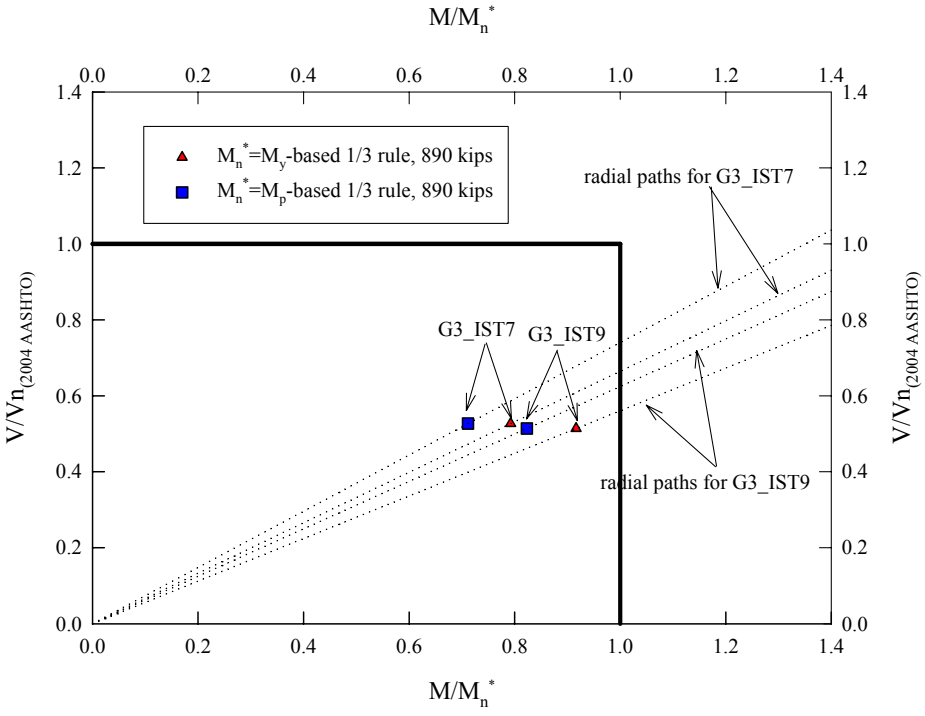

Figure 5.14.20. Normalized girder moments and shears at the G3_IST7 and G3_IST9 stiffener locations at the M_p-based 1/3 rule load level of 3959 kN (890 kips).

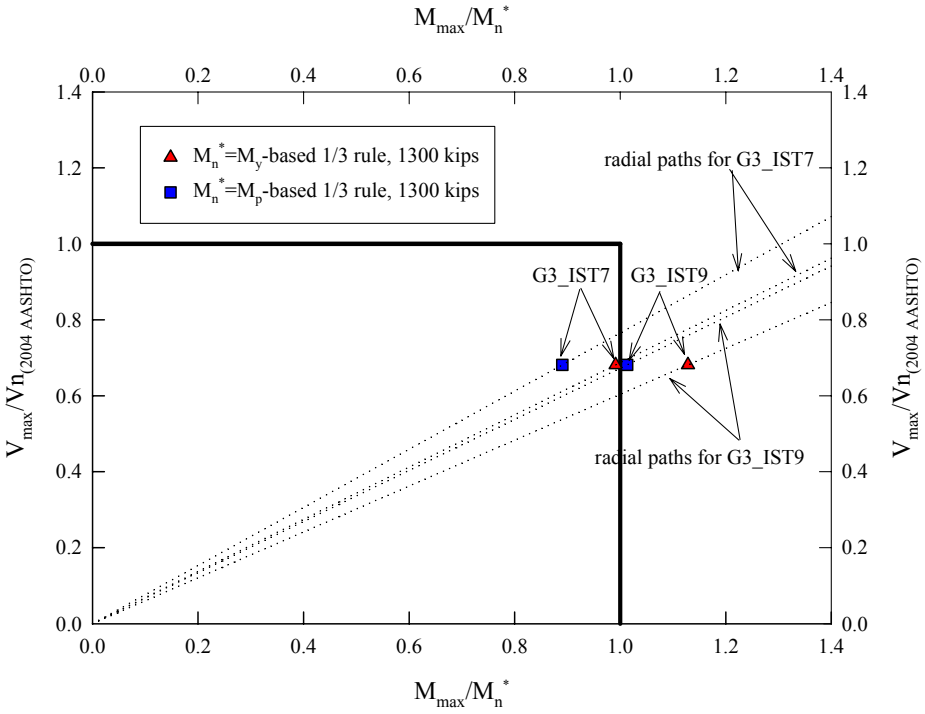

Figure 5.14.21. Normalized girder moments and shears at the G3_IST7 and G3_IST9 stiffener locations at the ultimate load level of 5783 kN (1300 kips).

One can observe that the shear force demands relative to the strength V_n are small at the above stiffener locations. Furthermore, it can be seen that the section for G3_IST9 sees a higher ratio of M/M_n^* than the section for G3_IST7. The more significant yielding at the top of G3_IST9 is believed to be due to this larger M/M_n^* value. The transverse stiffeners are provided to enhance the girder shear resistance, but they are working in the ultimate strength test help resist the tendency of the G3 web and bottom flange to deflect radially due to the horizontal curvature. This lateral restraint can be beneficial to help reduce the lateral bending effects on the bottom flanges to a certain degree until a plastic hinge is formed at the top of the stiffeners.

It is important to note that the conservatism put into the design of the transverse stiffeners in the test bridge may have ensured that they did not show any significant

yielding at the M_p-based 1/3 rule load level. As described in Section 2.5.5, the flexural rigidity of the transverse stiffeners is four times larger than the minimum moment of inertia necessary for the test bridge girders to develop their web shear post-buckling resistance associated with tension-field action. Since typical stiffener designs may not have this kind of conservatism, there is a high probability that stiffeners in other bridge configurations might experience early yielding at the top flange-stiffener juncture prior to the development of the M_y- or M_p-based 1/3 rule resistances. Therefore, it is desirable and safe to exclude the transverse stiffeners in elastic design analysis models for curved I-girders. Chang (2006) discusses appropriate beam-grillage analysis models that discount the torsional restraint to the I-girders from the slab.

The above hinging of the transverse stiffeners at the top of the girders at strength load levels is not anticipated to be of any significance as long as they are not included in the elastic design analysis. The major role of the transverse stiffeners is to enhance the shear capacity of the girder, and their proportions are sized based on the sole consideration that stiffeners have enough flexural rigidity against lateral deformation of the web panel due to shear demands.

5.14.2 Intermediate Transverse Stiffeners Located Close to the End Supports

Figures 5.14.22 through 5.14.27 provide similar stiffener strain plots for the six intermediate transverse stiffeners located on G3 between the quarter-span cross-frames and the girder end supports. These are denoted as G3_IST6 through G3_IST1 in Figure 5.14.1. The strains are plotted at the total applied load levels corresponding to satisfaction of the M_p-based 1/3 rule on G3 (3959 kN (890 kips)) and corresponding to the ultimate capacity of the bridge (5783 kN (1300 kips)). The effects of the prior repeated loading

tests are accounted for in these FEA solutions. Since only FEA solutions are available at these stiffeners, the strains are sampled at the stiffener free edge and at the juncture of the stiffener with the web.

Compared to the solutions for the two stiffeners located near midspan, the variation in the strains along the stiffener height shows more nonlinearity in the regions other than the top of the stiffeners, particularly at the ultimate capacity load level. This nonlinearity is believed to be due to restraint that the stiffeners provide to radial (out-of-plane) deflections of the web, i.e., due to a radial loading effect from the web. The strains at locations a and b differ substantially, indicating flexure of the stiffeners about an axis parallel to the web. Nevertheless, the predominant strains are still at the tops of the stiffeners. The strain patterns in the stiffeners near the middle of the bridge appear to be associated more with a restraint of lateral movement of the G3 bottom flange. The strain patterns in Figures 5.14.22 through 5.14.27 appear to have a larger effect of radial loading from the web in addition to a radial loading from the bottom flange. Furthermore, contrary to the behavior of the stiffeners near the midspan, the stiffeners near the ends of the bridge are unyielded at their tops, even at the ultimate capacity of the bridge. This behavior is believe to be due to the higher shear forces and lower major-axis bending moments near the end of G3.

.

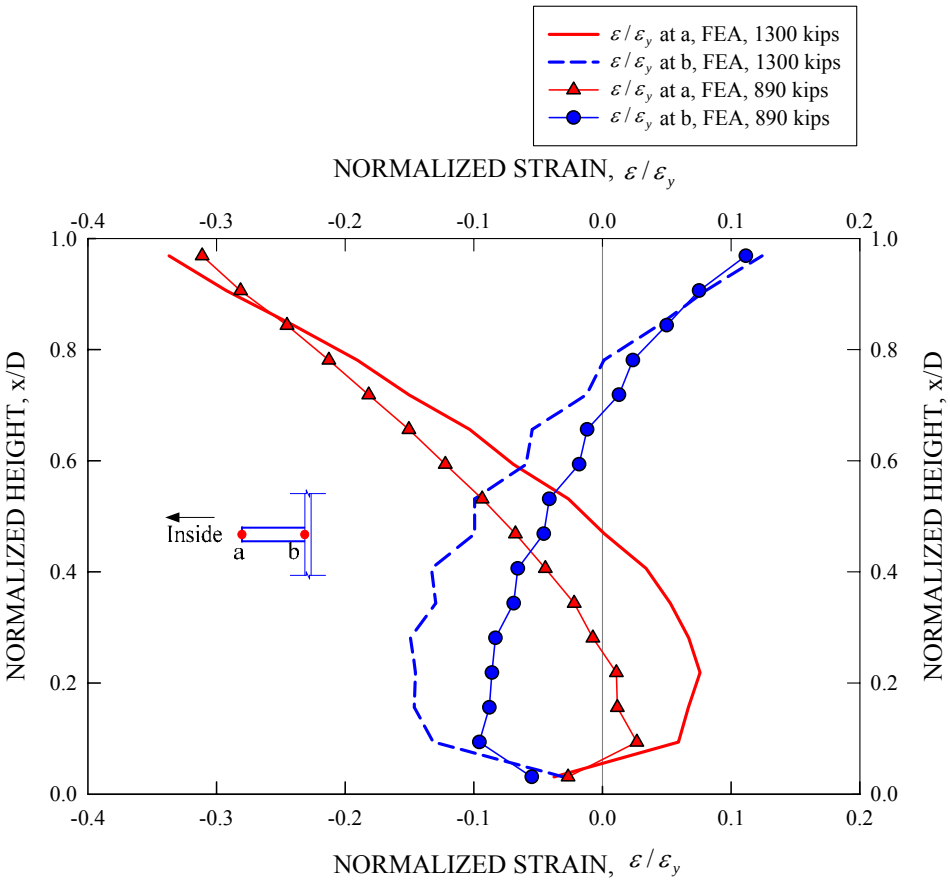

Figure 5.14.22. FEA stiffener strains along the normalized height of G3_IST6 at the M_p-based 1/3 rule load and the ultimate load levels (3959 kN (890 kips) and 5783 kN (1300 kips)), effects of prior repeated loading tests included.

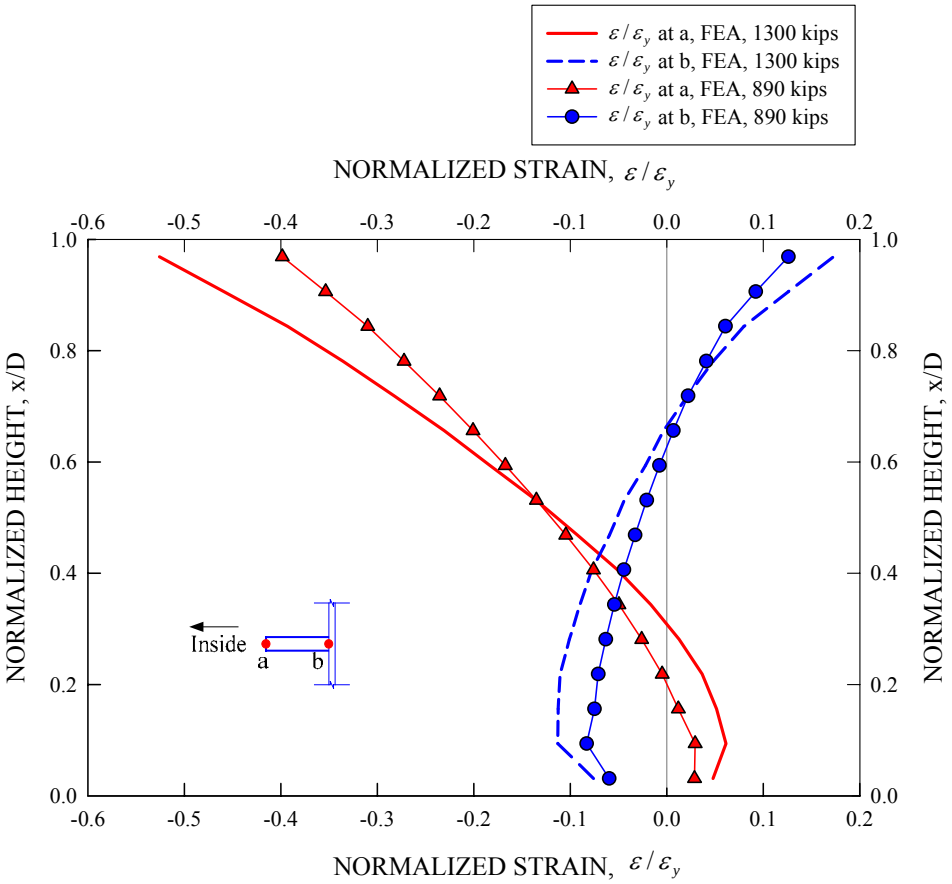

Figure 5.14.23. FEA stiffener strains along the normalized height of G3_IST5 at the M_p-based 1/3 rule load and the ultimate load levels (3959 kN (890 kips) and 5783 kN (1300 kips)), effects of prior repeated loading tests included.

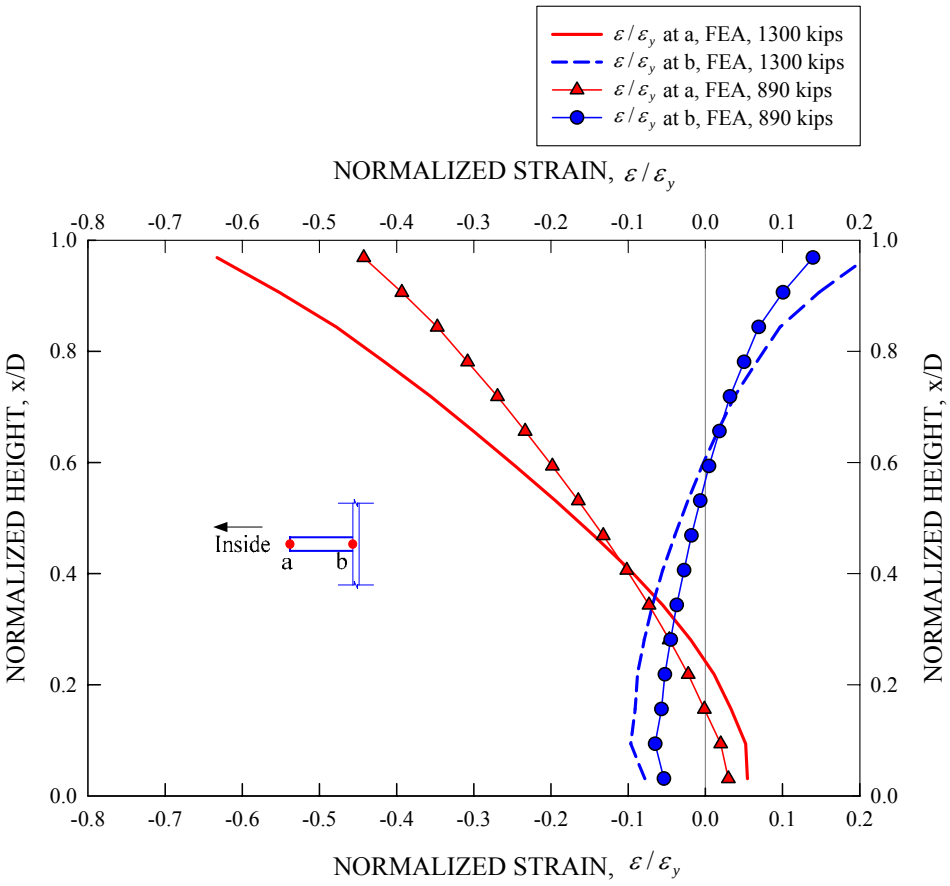

Figure 5.14.24. FEA stiffener strains along the normalized height of G3_IST4 at the M_p-based 1/3 rule load and the ultimate load levels (3959 kN (890 kips) and 5783 kN (1300 kips)), effects of prior repeated loading tests included.

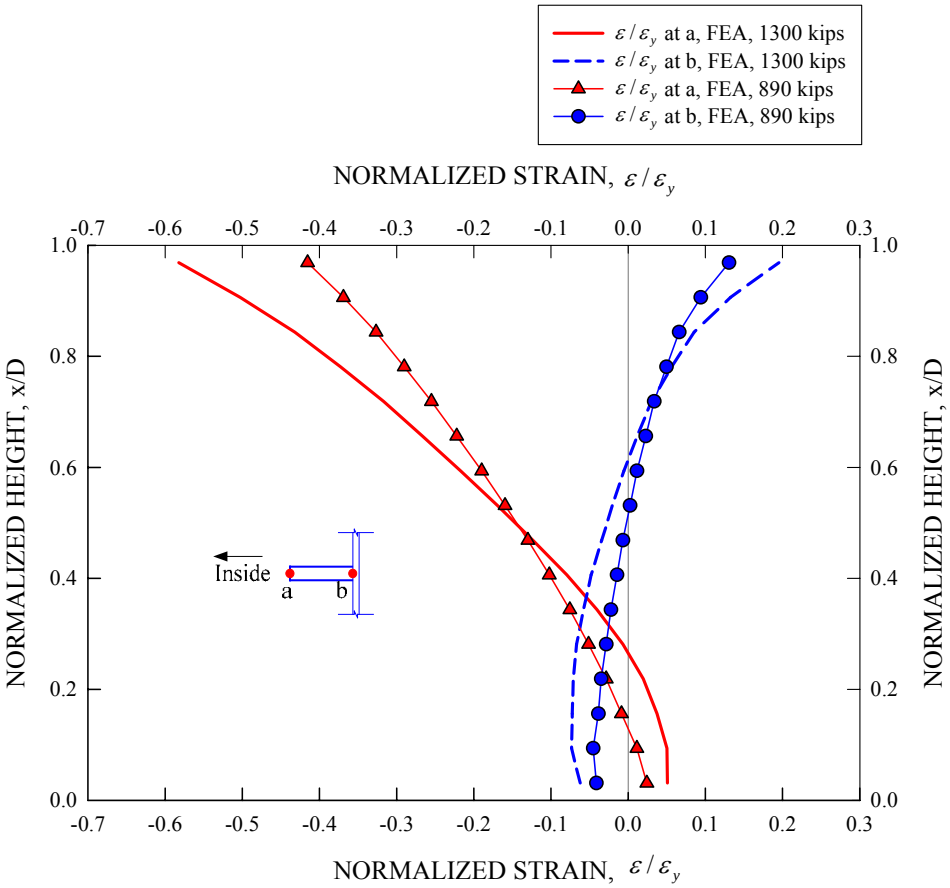

Figure 5.14.25. FEA stiffener strains along the normalized height of G3_IST3 at the M_p-based 1/3 rule load and the ultimate load levels (3959 kN (890 kips) and 5783 kN (1300 kips)), effects of prior repeated loading tests included.

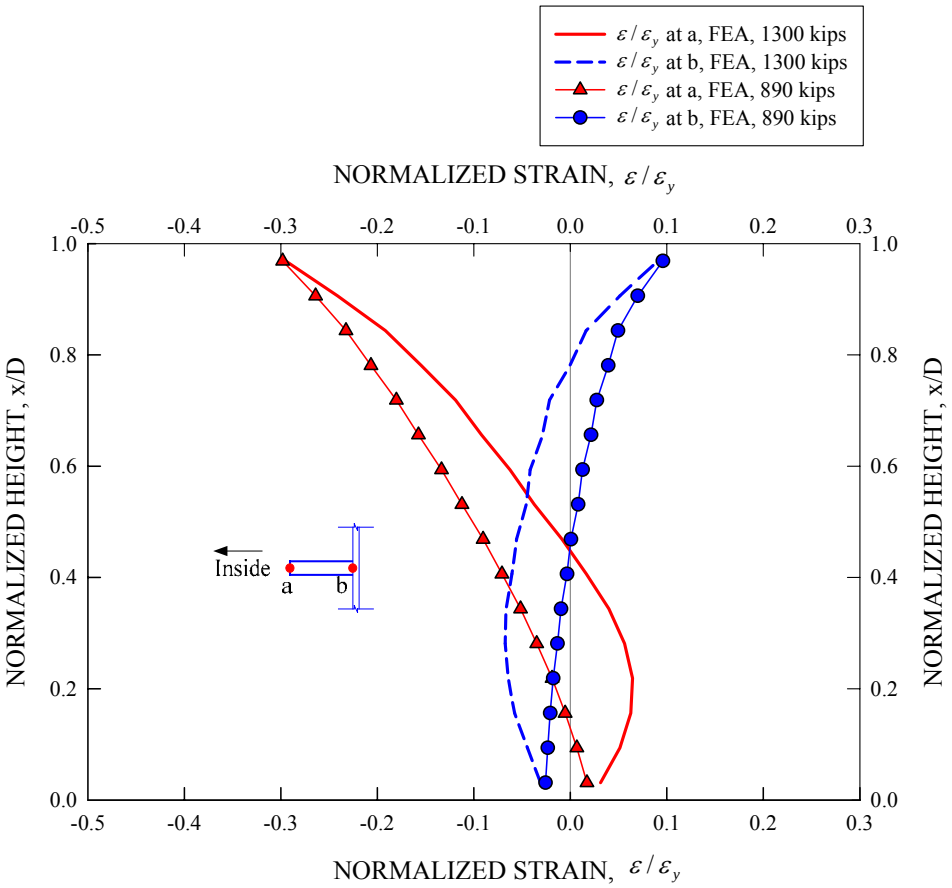

Figure 5.14.26. FEA stiffener strains along the normalized height of G3_IST2 at the M_p-based 1/3 rule load and the ultimate load levels (3959 kN (890 kips) and 5783 kN (1300 kips)), effects of prior repeated loading tests included.

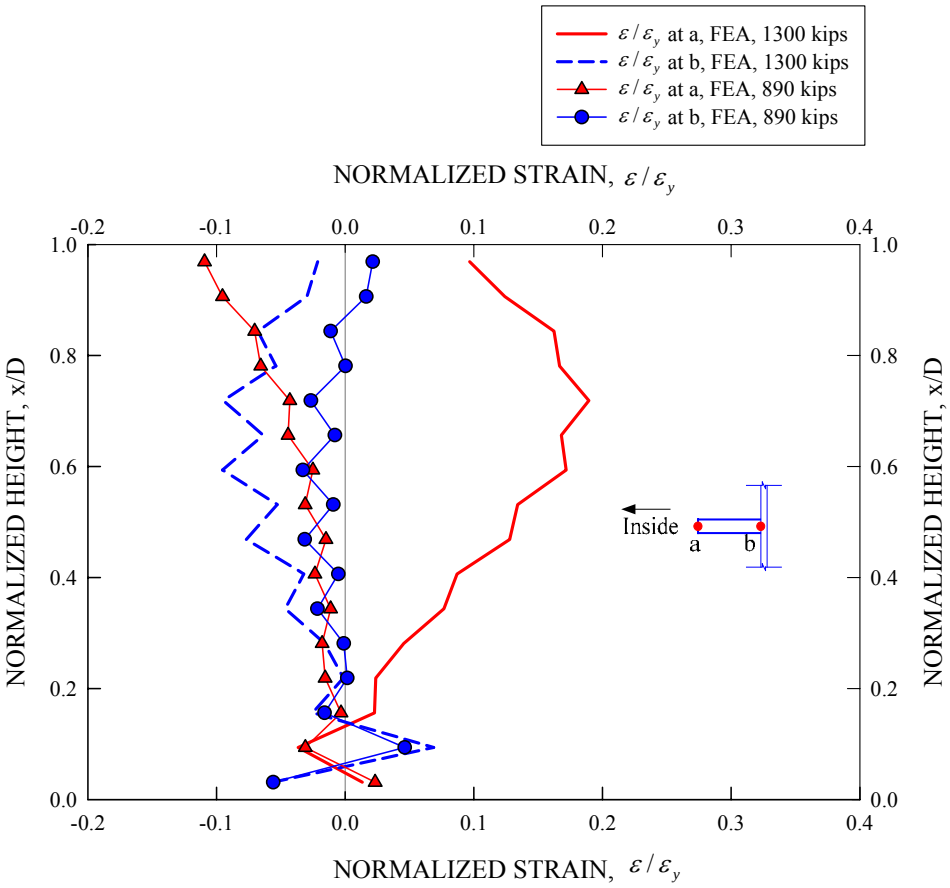

Figure 5.14.27. FEA stiffener strains along the normalized height of G3_IST1 at the M_p-based 1/3 rule load and the ultimate load levels (3959 kN (890 kips) and 5783 kN (1300 kips)), effects of prior repeated loading tests included.

Similar to Figures 5.14.20 and 5.14.21, the behavior of the stiffeners within the end unbraced length of G3 can be considered in the context of the girder moments and shears. Figures 5.14.28 and 5.14.29 provide normalized moments and shears for the cross-sections where G3_IST1 through G3_IST6 are located. These plots show the G3 moments and shears at the M_p-based 1/3 rule and ultimate load levels respectively. It can be seen that the ratio of $V/V_{n(2004\ AASHTO)}$ never exceeds 1.0 for both of these load levels; however, this ratio is also greater than M/M_n*. This implies that the behavior at these stiffeners may be dominated more by the shear response rather than by the bending response of the girders. However, the webs are still loaded somewhat below the shear limit state even at the ultimate capacity of the bridge. If the $V/V_{n(2004\ AASHTO)}$ values in these web panels were somewhat larger, the lateral bending of the stiffeners due to the restraint they provide to lateral deflections of the web panels would be more significant. Kim et al. (2006) and Kim (2004) show the results of curved I-girder shear studies that illustrate this characteristic.

The reason for the low V/V_n values in the above plots is the fact that the shear force is limited by the onset of the maximum flexural strength conditions at the midspan. The stiffener rigidity requirements imposed on these stiffeners are generally low since there is no full development of tension-field action at these load levels. Nonetheless, it is quite interesting to note that the stiffeners near the girder end exhibit noticeable flexural behavior.

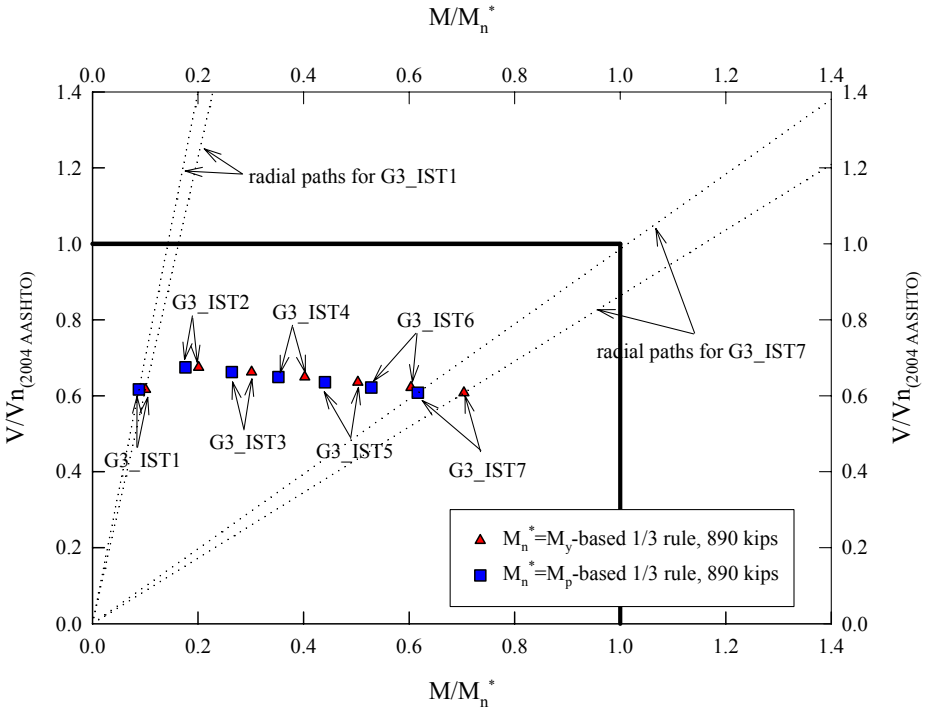

Figure 5.14.28. Normalized girder moments and shears at the stiffener locations G3_IST1 through G3_IST6 at the M_p-based 1/3 rule load level of 3959 kN (890 kips).

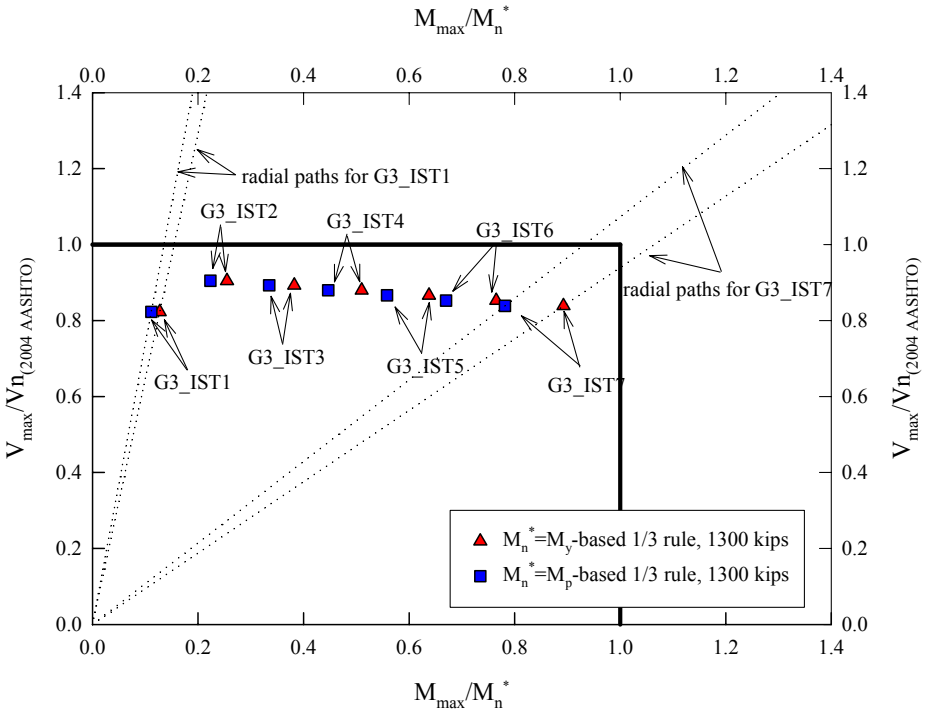

Figure 5.14.29. Normalized girder moments and shears at the stiffener locations G3_IST1 through G3_IST6 at the ultimate load level of 5783 kN (1300 kips).

Figures 5.14.30 and 5.14.31 show side views of the G3 end unbraced length containing the above stiffeners with von Mises stress contours on the inside surface of the web. Figure 5.14.30 corresponds to the M_p-base 1/3 rule load level while Figure 5.14.31 corresponds to the ultimate load level of the composite test bridge. In Figure 5.14.30, one can observe that von Mises stresses are largest at the top of the web around the quarter-span connection plate. This is due to web lateral bending effects. However, in Figure 5.14.31, large von Mises stresses are also observed in the web panels between G3_IST1 and G3_IST2 as well as GS_IST2 and GS_IST3. These large von Mises stresses indicate the onset of a diagonal tension field in the above web panels.

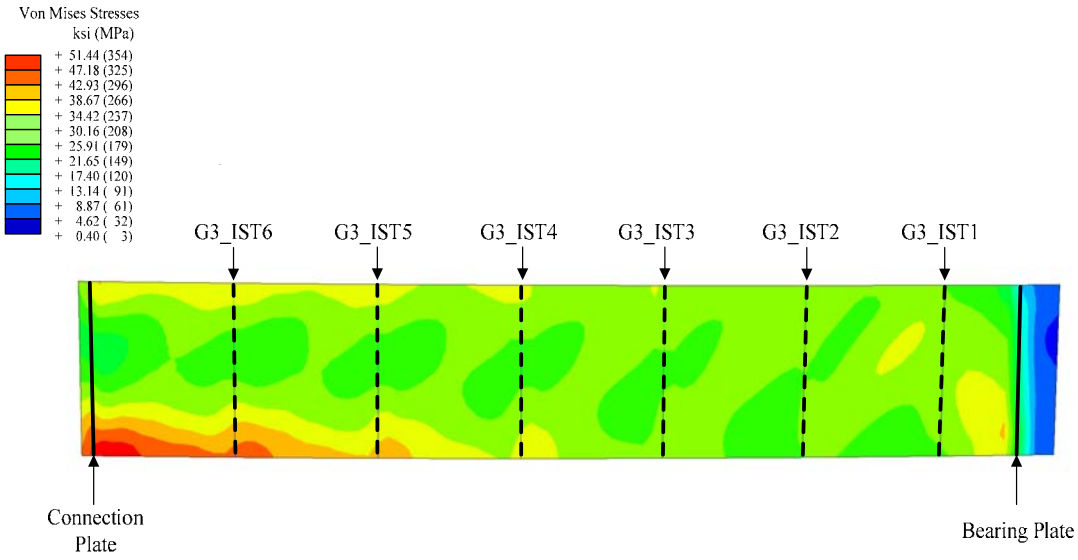

Figure 5.14.30.Side view of G3 end unbraced length with von Mises contours on the inside surface of the web panel at the M_p-based 1/3 rule load level of 3959 kN (890 kips) (Deformation Scale Factor = 1.0).

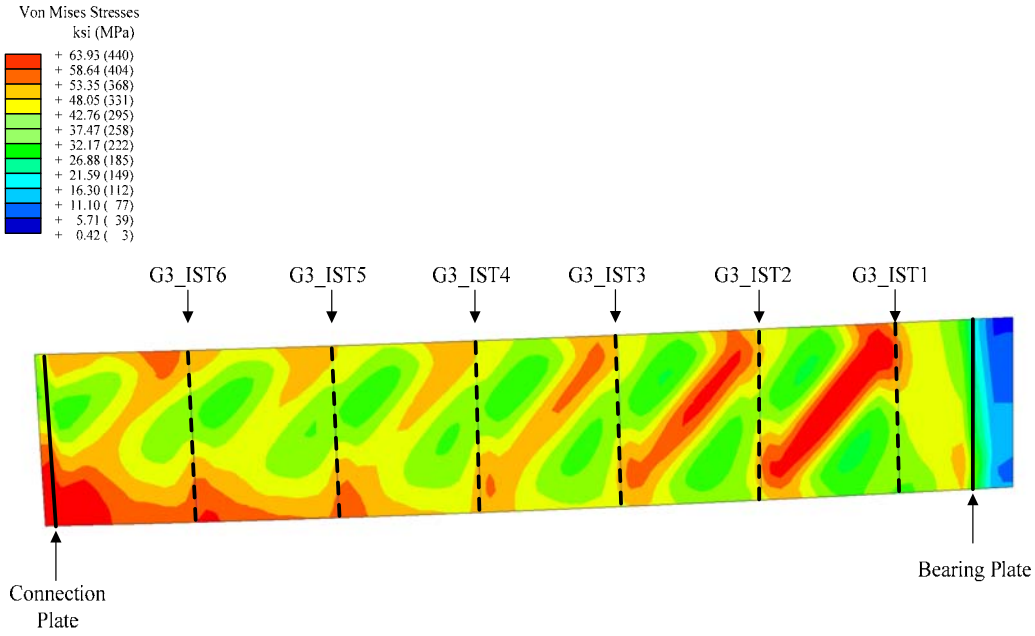

Figure 5.14.31. Side view of G3 end unbraced length with von Mises stress contours on the inside surface of the web panel at the ultimate load level of 5783 kN (1300 kips) (Deformation Scale Factor = 1.0).

5.15 Overall Force Transfer Mechanisms

5.15.1 FEA Internal Moments and Shears for Noncomposite Dead Load Configuration

Figures 5.15.1 and 5.15.2 give the FEA *dead load* moment and shear force diagrams along the normalized bridge length for the entire test bridge cross-section and for the individual girders. It can be seen in Figure 5.15.1 that a significant portion of the internal moment is carried by G3. Of the total moment on the bridge cross-section at the midspan, G3 supports approximately 70 percent (3207 kN-m (2365 k-ft)) while G2 and G1 support only 20 percent (926 kN-m (683 k-ft)) and 10 percent (400 kN-m (295 k-ft)) respectively. In other words, G3's midspan moment is much larger than the moment due to the directly applied loads on G3. The force transfer mechanisms that lead to this result can be

identified by looking at the shear force diagrams for the test bridge girders. It can be seen in Figure 5.15.2 that all the shear force diagrams vary almost linearly between the cross-frame locations. The total shear force diagram, indicated by the solid line in the plot, shows small discrete jumps at the cross-frame locations. This is due to the weight of the cross-frames. Also, for the individual girder shear force diagrams, there are discrete jumps at the cross-frame locations that substantially increase the shears on G3, slightly increase the shears on G2, and substantially decrease the shears on G1. The shear force diagram for G3 shows that it is subjected to concentrated downward forces from the cross-frames, while the shear force diagrams for G1 and G2 show that these girders are unloaded by upward concentrated cross-frame forces. This highlights the critical role of the outside girder G3 as well as the cross-frames in resisting the dead loads due to steel and concrete self weight plus the construction loads on the noncomposite structure. Figure 5.15.3 provides a schematic showing a conceptual representation of the forces acting on G3: (1) the uniformly distributed load due to its self weight, (2) the uniformly distributed loads directly applied at its top flange due to the concrete dead weight acting on the tributary slab area, (3) the torques acting due to the eccentric bracket loads from the slab overhangs, (4) the concentrated loads from the cross-frames due to the weight of the cross-frames and (5) the shears transferred from the cross-frames, required to satisfy the overall torsional equilibrium of the horizontally curved structure.

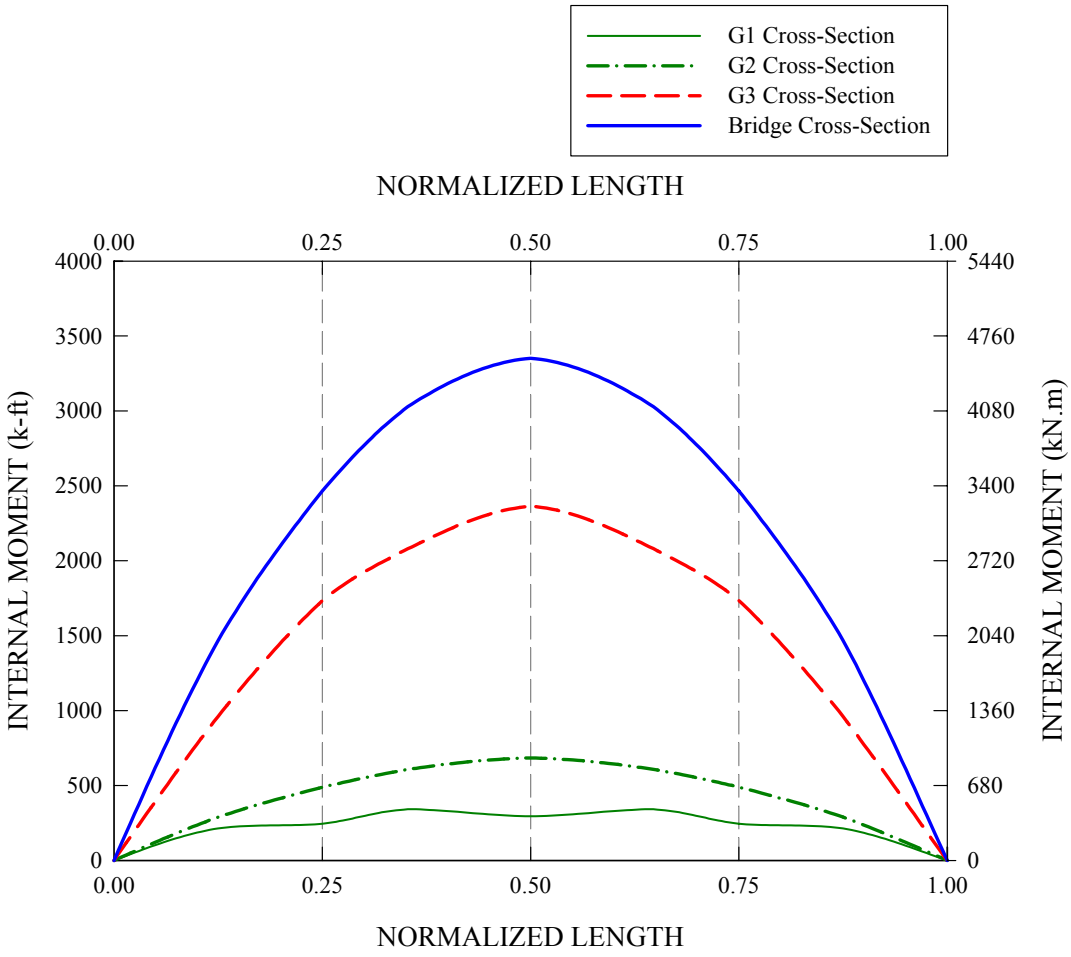

Figure 5.15.1. FEA internal moments for the entire bridge cross-section and for the individual girders along the normalized bridge length at zero applied load.

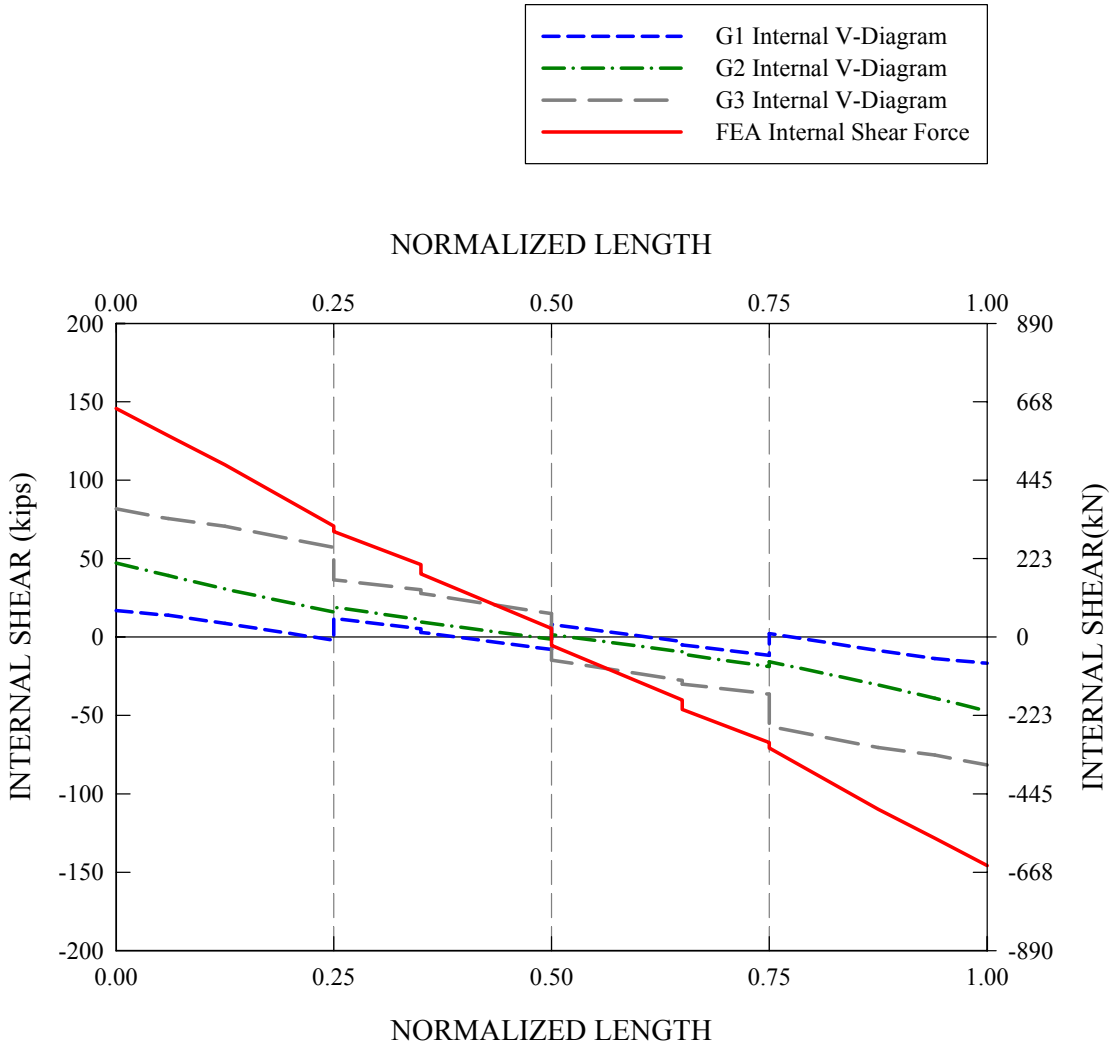

Figure 5.15.2. FEA internal shear force diagrams for the entire bridge cross-section and for the individual girders along the normalized bridge length at zero applied load.

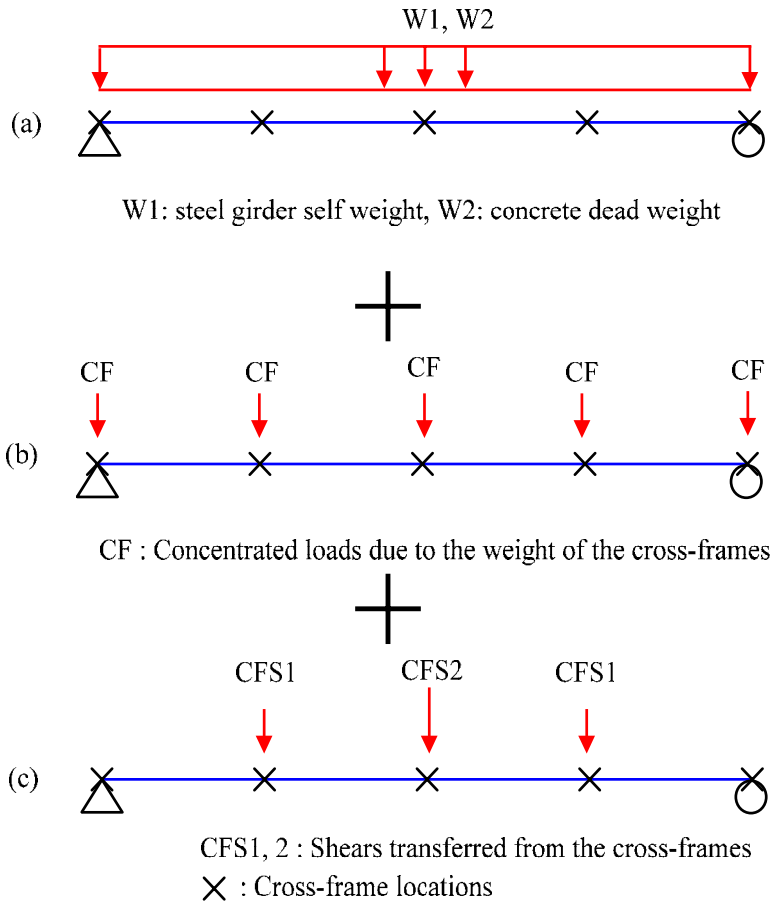

Figure 5.15.3. Internal and external vertical force components acting on girder G3, (a) uniformly distributed loads due to steel girder self weight and concrete dead weight, (b) concentrated loads due to the weight of the cross-frames, and (c) shear forces transferred from the cross-frames.

It is useful to emphasize the source of the additional downward cross-frame shear forces acting on G3. Figure 5.15.4 shows the resultant of the total dead load (W) and the resultant of the corresponding total vertical end reactions (R) for the test bridge. If the resultant reactions R are assumed to act at the middle of the bridge cross-section at the end supports, one can observe that additional resultant end torques (T) are necessary for equilibrium. These torques increase the vertical reactions on the outside girder G3 and decrease the vertical reactions on the inside girder G1.

The internal torsional resistance of the test bridge to dead and construction loads is developed predominantly via the transfer of vertical shear forces between the girders by the cross-frames as shown in Figure 5.15.5. These vertical shears, referred to traditionally as V-loads (NSBA 1996), increase the downward forces G3 and offset the downward vertical loads on G1 and G2. This increases the major-axis bending moments and end reactions on the G3 and decreases them on G1 and G2. The overall internal torque on the structure at any cross-section along the bridge length is developed predominantly by the differences in the girder shears across the width of the structure. The couples generated by the V-loads on each of the individual girder free-body diagrams of Figure 5.15.5 also resist the tendency of the I-girders to twist about their individual axes relative to the overall torsional rotation of the bridge cross-section.

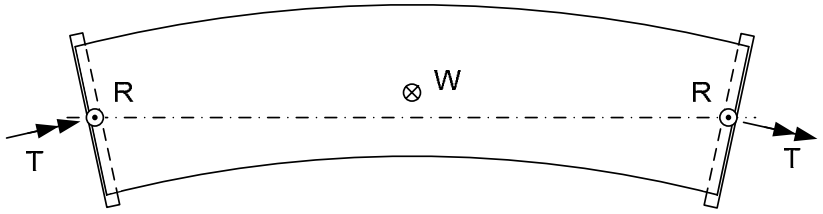

Figure 5.15.4. Plan view illustrating the required resultants for the reactions due to dead load at the ends of a simply-supported horizontally-curved bridge with radial supports.

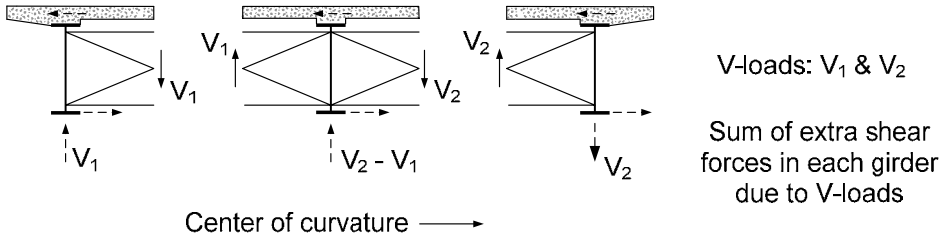

Figure 5.15.5. Transfer of vertical shear forces due to torsion (V-loads) by the cross-frames and the slab in a curved bridge.

5.15.2 FEA Internal Moments and Shears for Composite Live Load Configuration

With regard to the force transfer mechanism for the noncomposite dead load configuration of the test bridge, it is clearly shown in the previous section that the cross-frames play an important role in transferring a significant portion of the noncomposite dead loads to the outermost girder, thereby satisfying the overall torsional equilibrium associated with the horizontal curvature. However, when it comes to the force transfer mechanism for the composite live load configuration of the test bridge, the slab also can participate in distributing some of the loads to the outside girder.

As an illustration, Figure 5.15.6 shows the various vertical forces acting on G3 due to the applied loads on the bridge versus the total applied load. The separate vertical forces acting on G3 include: (1) the directly applied loads, (2) the vertical force components in the diagonal members of the quarter- and midspan cross-frames, (3) the slab shear force transferred to G3, and (4) the vertical end reactions. The slab shear forces are obtained indirectly by subtracting the sum of the directly applied loads and the cross-frame shear forces from the total reactions. The reaction force varies linearly through the loading history as shown previously. However, Figure 5.15.6 shows that the internal forces vary in a slightly nonlinear fashion. Nonetheless, the extent of nonlinearity is generally minor up to the M_p-based 1/3 rule load level of 3959 kN (890 kips). Furthermore, the error in the linear elastic FEA predictions (not shown in Figure 5.15.6) for the mid- and quarter-span cross-frame shear forces is only 3 and 6 percent unconservative relative to the corresponding experimental values. In addition, it is noteworthy that the slab carries considerable shear forces to G3 throughout the loading history. In other words, together with the cross-frames, the slab plays an important role in transferring loads to G3.

Similar to the cross-frame shear forces, the slab shear force curve indicates some minor nonlinear behavior after a total applied load of 3959 kN (890 kips).

Although Figure 5.15.6 shows an interesting role of the slab in transferring the applied loads between the test bridge girders in an overall sense, it lacks details regarding how the force transfer occurs along the length of the girder. Therefore, similar to the solutions for the noncomposite bridge configuration, detailed FEA internal moments and shear force diagrams along the length of the test bridge girders are presented in the following.

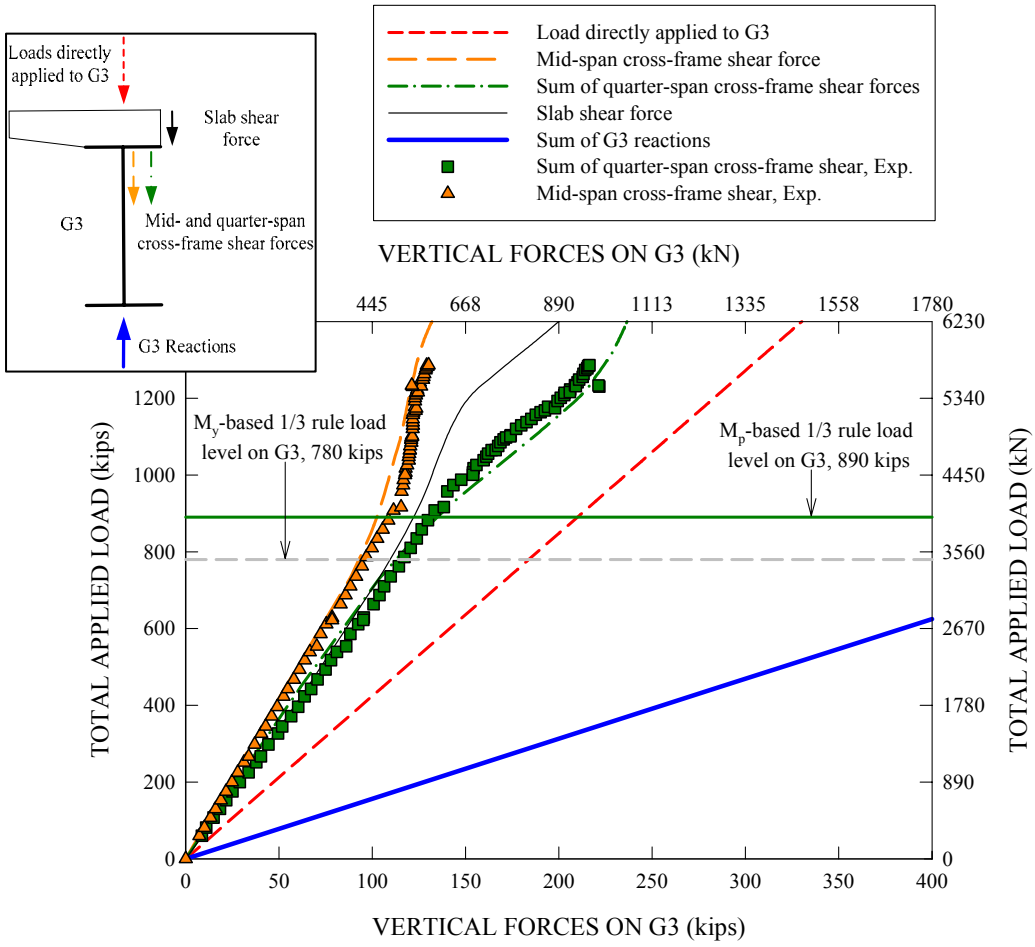

Figure 5.15.6. Total applied load versus the vertical force components acting on the isolated G3 composite section.

5.15.2.1 FEA Internal Moments and Shears on G3

Figures 5.15.7 and 5.15.8 give the total FEA internal moment and shear force along the normalized length for the entire bridge cross-section and for the individual bridge girders at a total applied load level of 3959 kN (890 kips) corresponding to the M_p-based 1/3 rule load level on G3. It should be noted that both of these plots include the initial moments and shears due to the dead loads. Of the total internal moment on the bridge cross-section at midspan, G3 carries 55 percent (14550 kN-m (10729 k-ft)) while G1 and G2 take 12 percent (3349 kN-m (2470 k-ft)) and 33 percent (8905 kN-m (6568 k-ft)) respectively.

The shear force diagram in Figure 5.15.8 shows that there are several significant jumps due to the externally applied loads and internal cross-frame forces. The first jump, located at midspan, is caused by the externally applied loads and the cross-frame forces combined together. The second jump, located at the adjacent loading points, is caused by the directly applied loads only. The third jump, located at the quarter-span cross-frame locations, is caused by the cross-frame forces only. It should be noted that all the cross-frame forces act on G3 such that its positive internal moments are increased. In other words, all the vertical internal forces applied to G3 are acting in the downward direction. Similar to the shear force diagram for G3, the shear force diagram for G2 has three jumps at the same locations as those of G3. However, the cross-frame forces acting on G2 are in the upward direction. Contrary to the shear force diagrams for G2 and G3, the shear force diagram for G1 has only jumps at the outer loading points (see Figure 5.15.8) and the quarter-span cross-frame locations. That is, there is no significant jump associated with the directly applied loads at midspan. This is because the cross-frame force at this

location is in the upward direction such that it approximately cancels the directly applied loads. Conversely, the cross-frame forces acting on G2 at the midspan of G2 do not completely cancel out the directly applied loads acting on G2.

Figures 5.15.9 and 5.15.10 provide the total FEA internal moment and shear force along the normalized length for the entire bridge cross-section and for the individual bridge girders at a total applied load level of 5783 kN (1300 kips), when the slab experienced spalling and crushing at the overhang region outside G3 during the ultimate load test. Initial dead load moments and shears are included in both of the plots. Among other things, it can be seen in Figure 5.15.9 that a fraction of the total internal moment carried by G3 is smaller than at the M_p-based 1/3 rule load level on G3 (shown in the previous set of plots) while the moments supported by the other two girders are increased. For example, of the midspan total internal moment (36830 kN-m (27167 k-ft)), G3 carries 17670 kN-m (13035 k-ft), which is now 48 percent of the total bridge cross-section moment, and G1 and G2 take 17 percent (6261 kN-m (4618 k-ft)) and 35 percent (12890 kN-m (9508 k-ft)) respectively. This force redistribution is largely associated with the fact that the G3 internal moment at this high load level is bounded by G3's major-axis bending moment capacity, which is slightly less than the section plastic moment capacity in the absence of lateral bending moments as shown previously in Section 5.3.

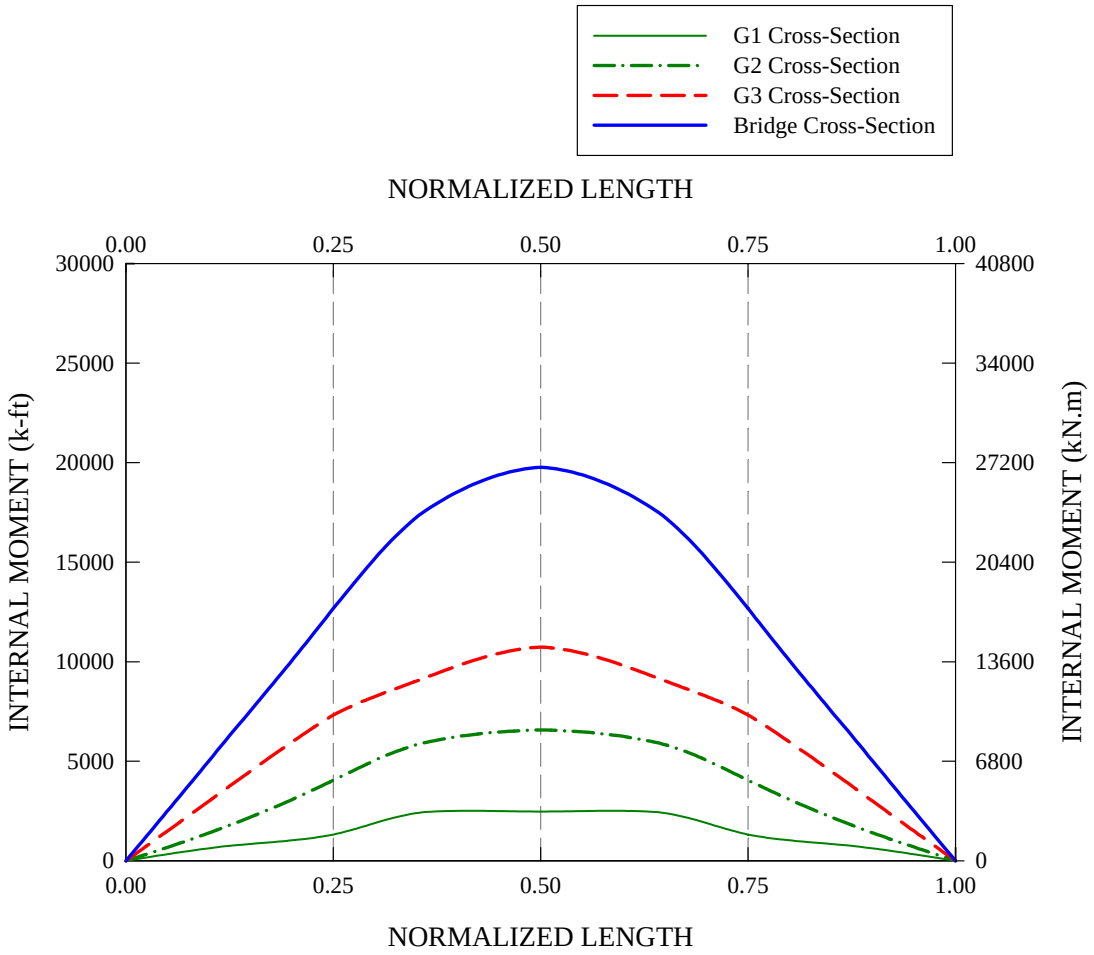

Figure 5.15.7. Live load plus dead load FEA internal moments on the total bridge and individual girder cross-sections along the normalized length at the M_p-based 1/3 rule load level on G3.

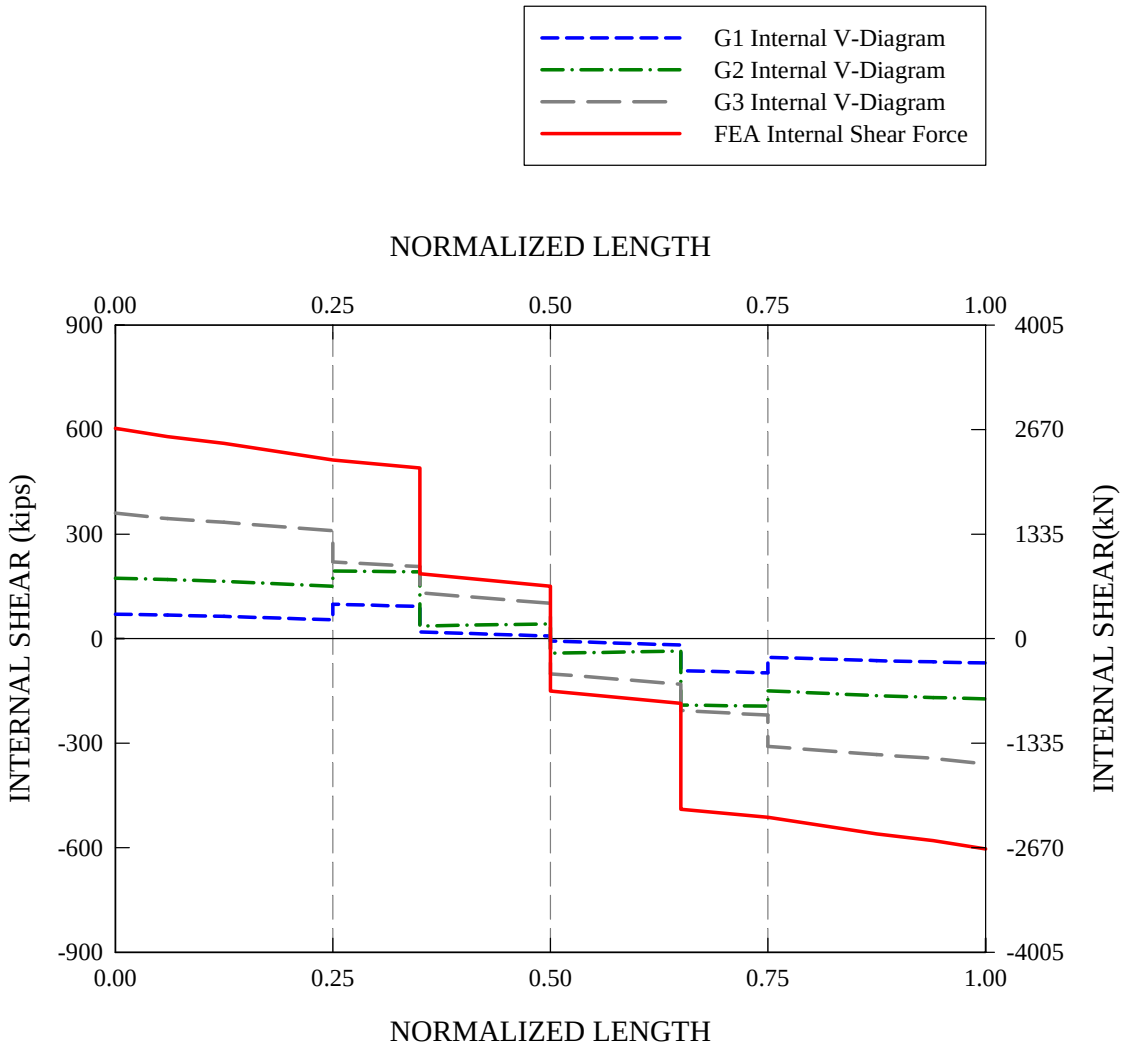

Figure 5.15.8. Live load plus dead load FEA internal shears on the total bridge and individual girder cross-sections along the normalized length at the M_p-based 1/3 rule load level on G3.

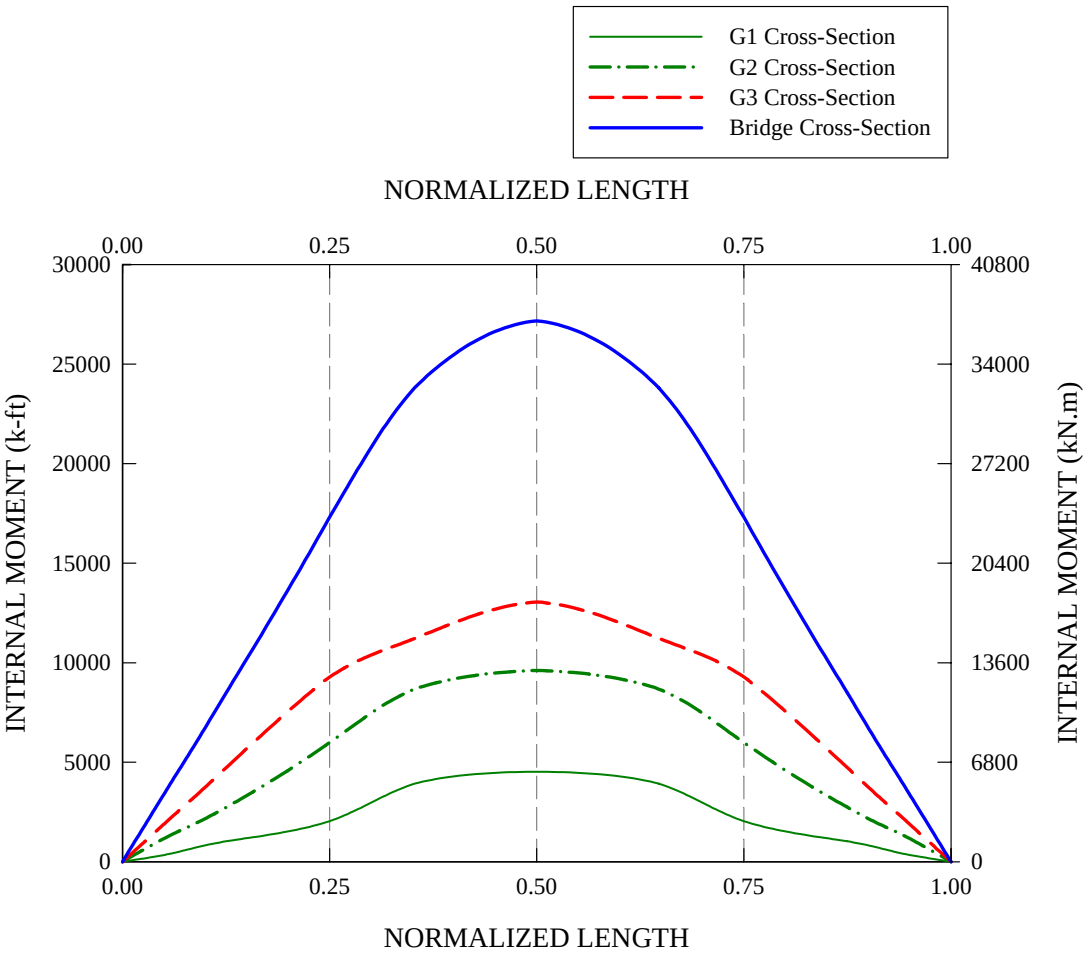

Figure 5.15.9. Internal moments on the total bridge and individual girder cross-sections along the normalized length at spalling and crushing of the slab concrete in the experimental test, deflection of the midspan outside tip of the G3 bottom flange = 610 mm (24 in), total applied load = 5783 kN (1300 kips).

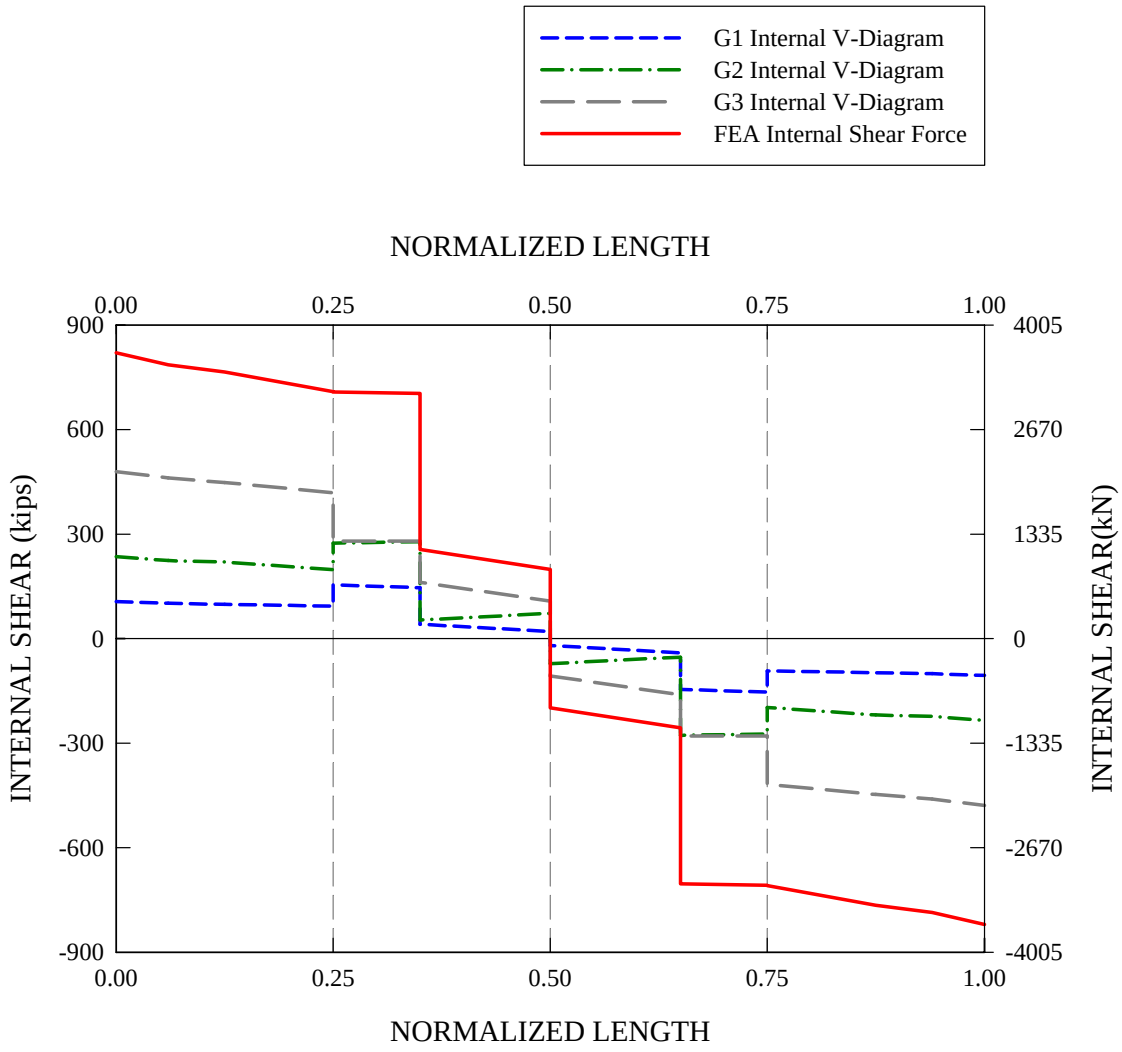

Figure 5.15.10. Internal shear force diagrams for the total bridge and individual girder cross-sections along the normalized length at spalling and crushing of the slab concrete in the experimental test, deflection of the midspan outside tip of the G3 bottom flange = 610 mm (24 in), total applied load = 5783 kN (1300 kips).

5.15.2.2 Force Transfer Mechanisms on G3

Figure 5.15.11 shows the FEA live load internal shear force diagrams for the isolated G3 composite girder at a total applied load level of 3959 kN (890 kips). This figure shows the total live load internal shear force diagram on G3, as well as the shear force diagrams due to the directly applied loads on G3, the vertical forces transferred from the cross-frames attached to G3, and the combination of the two. It is apparent that the sum of the girder internal shear forces due to the directly applied loads and the cross-frame vertical forces do not add up to the total live load internal shear force obtained from the full nonlinear FEA results. The additional portion of the total live load shear force has to come from the slab. A careful look at the difference between the total live load shear diagram and the combined shear diagram due to the directly applied load and the cross-frame vertical forces, highlighted by the hatched pattern in Figure 5.15.11, reveals that the distributed vertical forces transferred through the slab to G3 from the adjacent girders are nearly constant along the girder length except in the vicinity of G3's ends. The vertical forces transferred through the slab are slightly larger in magnitude at G3's ends (the slope of the shear diagram increases). Figure 5.15.12 presents a conceptual representation of these vertical load distributions on G3.

Figure 5.15.13 shows the FEA live load internal shear force diagrams for the isolated G3 composite girder at a total applied load level of 5783 kN (1300 kips**)**. It can be seen that the overall shape of the shear force diagrams is not exactly to the same as that of the shear forces at 3959 kN (890 kips). This is due to some minor changes in the distributed slab forces transferred to the girders as well as changes in the relative values of the shear forces transmitted by the cross-frames at the higher load level (the distributed forces from

the slab appear to be close to constant). Nonetheless, it is important to note that the force transfer mechanism presented in Figure 5.15.12 is still applicable at this load level.

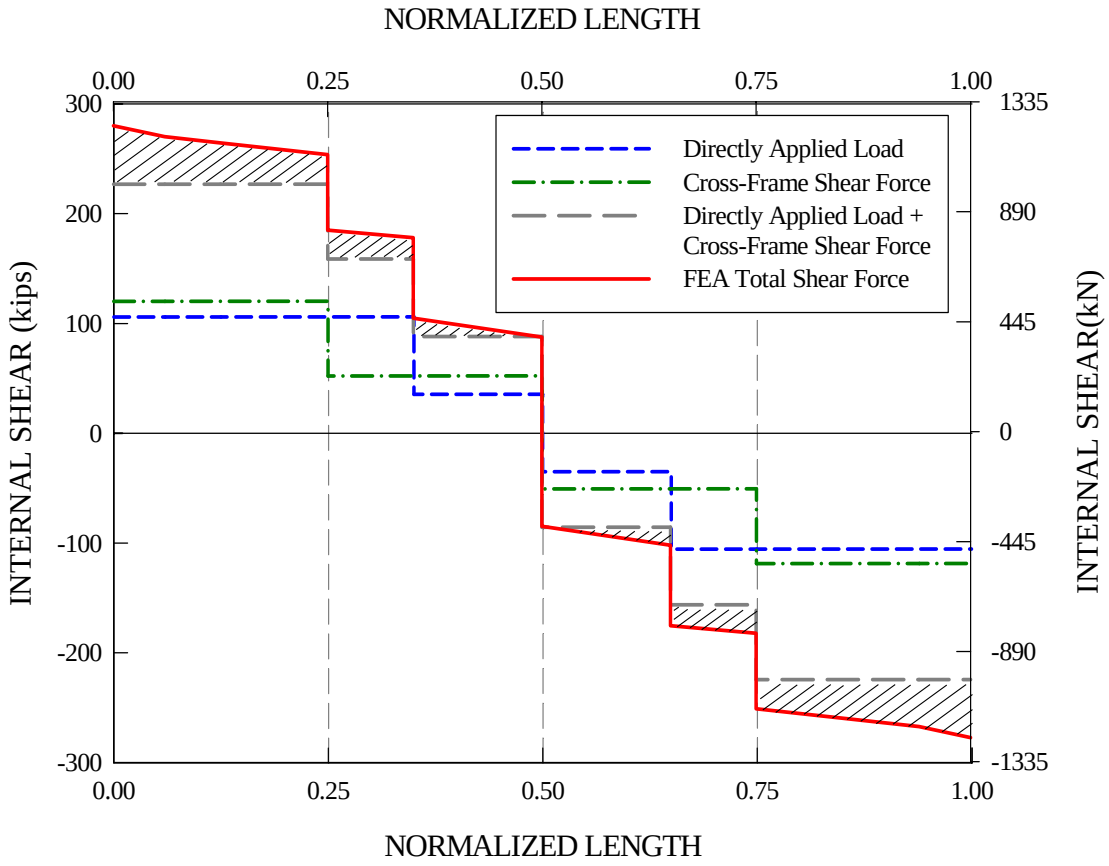

Figure 5.15.11. Calculated live load internal FEA shear force diagrams for the isolated G3 composite section along the normalized length, and shear force diagrams due to directly applied loads, cross-frame shear forces, and a combination of the two on G3 at a total applied load level of 3959 kN (890 kips).

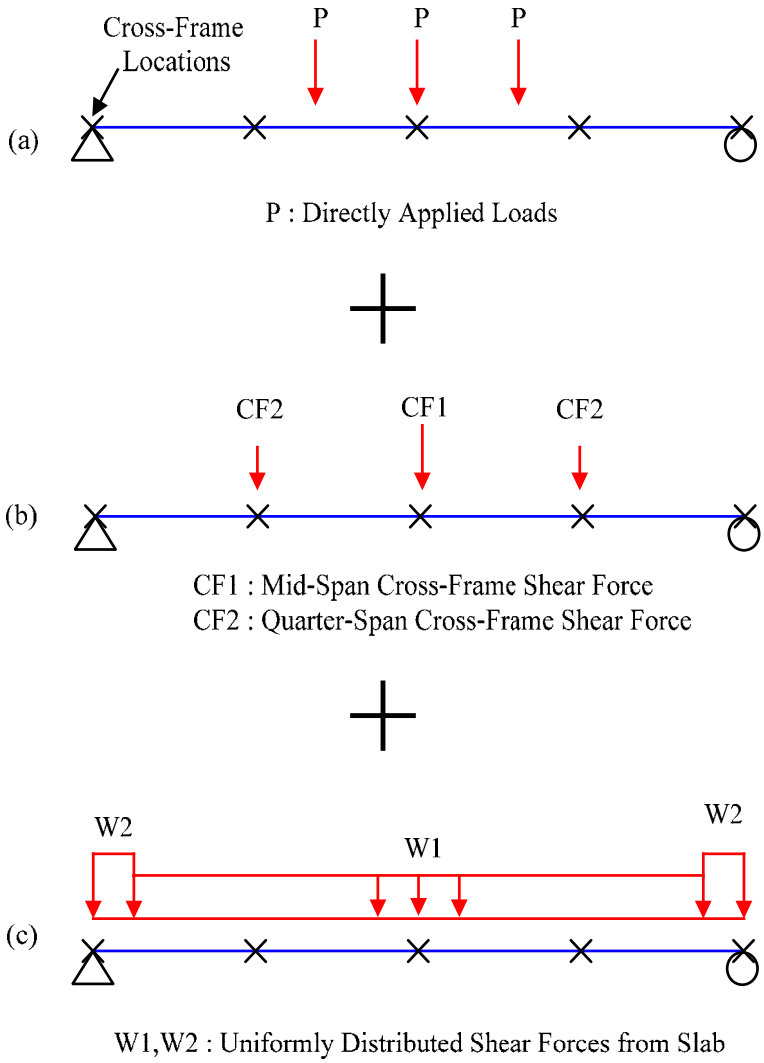

Figure 5.15.12. Internal and external vertical force components acting on girder G3, (a) directly applied loads, (b) cross-frame shear forces, and (c) uniformly distributed shear forces from slab before G3 reaches its plastic moment capacity.

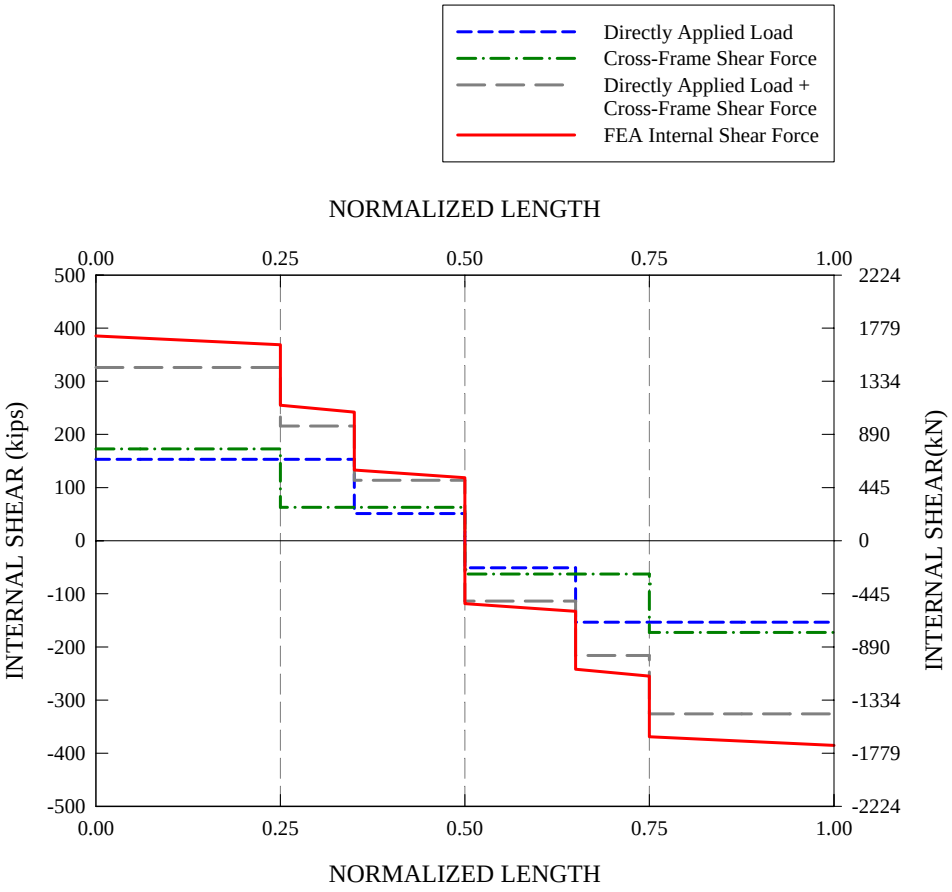

Figure 5.15.13. Calculated live load internal FEA shear force diagrams for the isolated G3 composite section along the normalized length, and shear force diagrams due to directly applied loads, cross-frame shear forces, and a combination of the two on G3 at a total applied load level of 5783 kN (1300 kips).

INELASTIC STRENGTH BEHAVIOR OF HORIZONTALLY CURVED COMPOSITE I-GIRDER BRIDGE STRUCTURAL SYSTEMS

VOLUME II

By

Se-Kwon Jung

CHAPTER 6

PARAMETRIC FEA STUDIES

6.1 Overview

The test bridge incorporates a number of key attributes pertaining to horizontally curved composite I-girder bridges and the requirements stipulated by the AASHTO (2004b) LRFD Specifications. However, one test cannot capture all the important physical attributes that may have significant influence on the strength behavior of these types of structures. Therefore, the base test bridge FEA model is utilized as a starting point for parametric FEA investigations into the strength behavior of other horizontally curved I-girder bridge systems. This is accomplished by systematically modifying selected parameters of the test bridge. In general, the parametric extensions involve specific targeted variations relative to the composite test bridge. For cases where individual girder responses obtained from updated elastic analysis and design checks significantly differ from those of the original test bridge, the bridge girders are re-designed accordingly. Otherwise, the overall bridge configuration, girder geometries and cross-frame sizes, and material properties are taken the same as the measured values for the base composite test bridge. In all cases, the geometry of the bridges, dimensions of the girders and cross-frames and material properties of the steel and concrete are the same as those of the composite test bridge unless noted otherwise. For the full nonlinear FEA solutions of the parametric study bridges, a single monotonic loading is employed for all the cases. In addition, the composite test bridge Test 4b loading pattern is employed for the full nonlinear analyses unless noted otherwise. Shrinkage strains are not included in the full nonlinear FEA solutions unless noted otherwise.

This chapter is organized as a case-by-case study of each of the parametric study examples summarized in Section 1.4.4.

6.2 Case 1: No Load Fit (NLF) vs. Total Dead Load Fit (TDLF)

In typical I-girder bridge construction, the girders are cambered to compensate for the dead load displacements. In most cases, only vertical cambers are considered. This approach works well for many straight bridges and for some curved I-girder bridges. However, for horizontally curved as well as skewed I-girder bridges, considerations other than just the vertical camber may be necessary to achieve a desired final geometry within desired tolerances. This is due to the fact that these types of bridges generally exhibit complex three dimensional movements that influence the vertical and horizontal position of the erected structure. These movements can be significant factors with regard to the roadway alignment and relative displacements at expansion joints for example. Also, the rotation capacity of bearings must either be able to accommodate the necessary torsional rotations or the bearings must be installed in a manner to ensure that their rotation capacities are not exceeded (AASHTO 2004b).

One consideration in controlling the geometry of curved girders is the web plumbness. As discussed in Section 1.1, curved I-girders undergo torsional rotations due to dead loads. These rotations make the webs out of plumb if the out-of-plumbness is not compensated for in some way. There are no specific guidelines offered in the AASHTO (2004b) Specifications about when the girder webs should be plumb. In fact, the necessary requirements can vary depending on the size and geometry of the bridge as well as the preferences of the Owner and Engineer. However, AASHTO (2004b) Article 6.7.2 suggests that “the contract documents should clearly state an intended erected

position and the condition under which that position is to be theoretically achieved." Also the commentary to the above article indicates three conditions in which the intended erected positions can be theoretically achieved:

1. the no-load condition,
2. the steel dead load condition, or
3. the full dead load condition.

The first and third of these conditions are referred to as No-Load Fit (NLF) and Total Dead Load Fit (TDLF) in this work. This nomenclature highlights the ways recommended in the AASHTO (2004b) commentary for achieving these conditions. The specific NLF and TDLF procedures are discussed in the summary of the Case 1 parametric study in Section 1.4.4. The second condition is referred to as Steel Dead Load Fit (SDLF) in this work.

As noted in Section 1.4.4, in the NLF method, the cross-frames are detailed to fit up ideally with the girders in their cambered no-load geometry. Therefore, the webs will not be plumb under the steel or total dead loads, due to the torsional rotations caused by these loads. Nevertheless, this out-of-plumbness can be inconsequential in many structures. When this is the case, this procedure would often be preferred since it is the simplest.

Also, as noted in Section 1.4.4, in the TDLF method the cross-frames are detailed to fit up with the girders in a web plumb position *after* the estimated total dead load vertical deflections are removed from the girder cambers. As such, the cross-frames and girders do not fit together in the theoretical no-load condition. Internal forces are locked into the structural system when these incompatibilities are removed by forcing the different components together. This is illustrated by Figure 6.2.1 from Chang (2006), which

shows a vertical lack-of-fit between a cross-frame and the connection workpoints on the right-hand girder of a girder pair due to a differential camber δ in the no-load geometry. This differential camber may be removed and the cross-frame may be connected to the girder on the right by theoretically twisting the girders in the no-load geometry as shown in Figure 6.2.1.

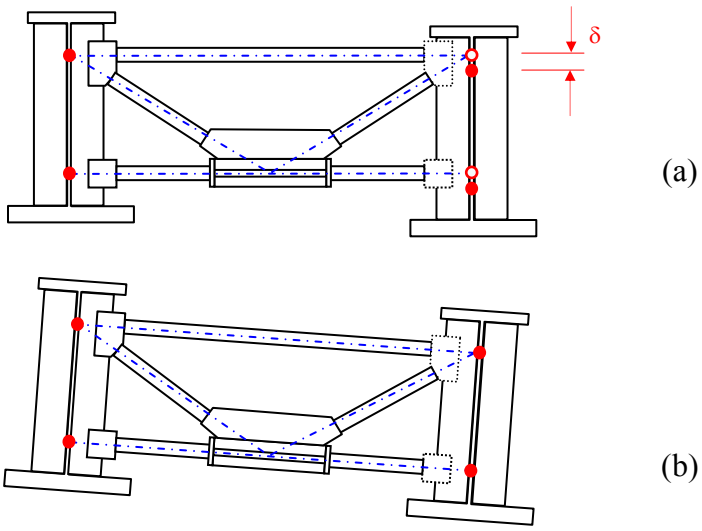

Figure 6.2.1. (a) Initial no load cambered geometry with lack of fit between the girders and cross-frames due to a differential camber deflection δ and (b) final no load configuration after establishing the compatibility between the girders and cross-frames by theoretically twisting the girders into position to connect the cross-frames (Chang 2006).

This twist offsets the twisting of the girders under the total dead load, but also changes the girder vertical displacements and locks forces and stresses into the structure. Steel Dead Load Fit (SDLF) detailing works similarly to TDLF, but the target web plumb condition is under the steel dead load and the calculations are performed only for this loading. Only the TDLF detailing is considered here, since this method results in larger compensating girder rotations and displacements as well as larger locked in stresses than

the SDLF method. The reader can find other detailed discussions regarding the above different types of detailing in Chang (2006).

Despite the advantage of the TDLF detailing method for controlling the final constructed geometry of curved I-girder bridges, one should recognize that TDLF detailing and construction leaves residual stresses within the bridge system due to the fit-up operations. These residual stresses typically are not considered in the analysis and design, although AASHTO (2004b) Article 6.7.2 states that "…the Engineer may need to consider the potential for any problematic locked-in stresses in the girder flanges or the cross-frames or diaphragms when this method of detailing is specified…". In general, these locked-in stresses may be only of minor significance in many cases. However, they may have significant effects for curved bridges with longer spans, tight radii and sharp skews. Most importantly, it is possible that these residual stresses may affect the strength behavior. In order to address the influence of TDLF detailing on the composite test bridge ultimate strength, another version of the full nonlinear FEA simulation for the composite test bridge is conducted in which TDLF detailing is utilized instead of NLF. This simulation is basically identical to the test bridge full nonlinear FEA simulation for the final ultimate load test presented earlier in this work, with the exception that the following additional analysis steps are employed:

- In a separate analysis, the test bridge is defined in its ideal initial no load geometry and then the girders are displaced vertically to their target camber positions to obtain estimates of locked-in forces in the cross-frame members due to the fit-up operations handling the lack-of-fit. It is important to note that the girder cambers are designed based on the TDLF detailing method, and resulting

camber values are shown in Figure 6.2.2. It can be seen that the maximum camber for the G3 midspan is 92.5 mm (3.7 in) as opposed to 125 mm (5 in) based on the NLF detailing method.

- In a subsequent analysis, in which the test bridge girders are initially cambered to the targeted position, the locked-in forces obtained from the above separate analysis are introduced to the cross-frame members in the form of initial stresses. This completes the steel erection simulation using the TDLF detailing.

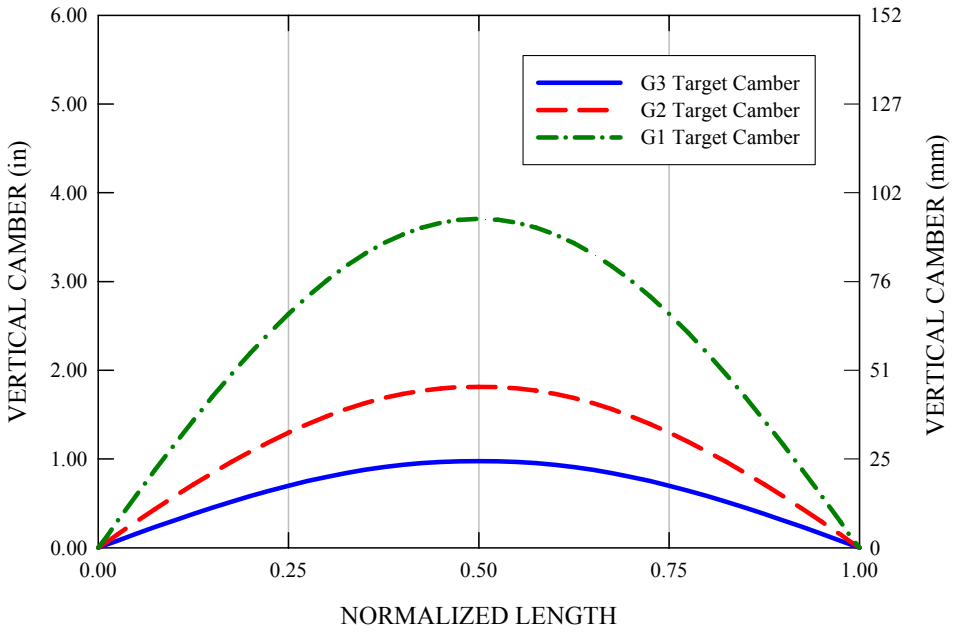

Figure 6.2.2. Targeted vertical cambers of the test bridge girders along the normalized length based on the TDLF detailing method (Chang 2006).

Subsequent to the steel erection based on the TDLF detailing scheme, the test bridge FEA model is made composite with the instantiation of the slab portion over the deformed steel geometry. It is then subjected to the ultimate strength test load pattern, which represents two lane loads plus two trucks placed side by side at the middle of the

bridge to produce the maximum flexural effects on G3. Figure 6.2.2 compares the vertical deflections at the midspan outside tip of the G3 bottom flange based on the No Load Fit (NLF) and Total Dead Load Fit (TDLF) detailing methods. It can be seen that the full nonlinear FEA solution based on the NLF detailing method produces larger ultimate capacities than the FEA solution based on the TDLF detailing method. This is due to the fact that the TDLF method introduces locked-in flange lateral bending stresses at the cross-frame locations that are additive with the lateral bending stresses due to composite live loads. The TDLF method produces locked-in flange major-axis bending stresses that cancel out the major-axis bending stresses due to composite live loads.

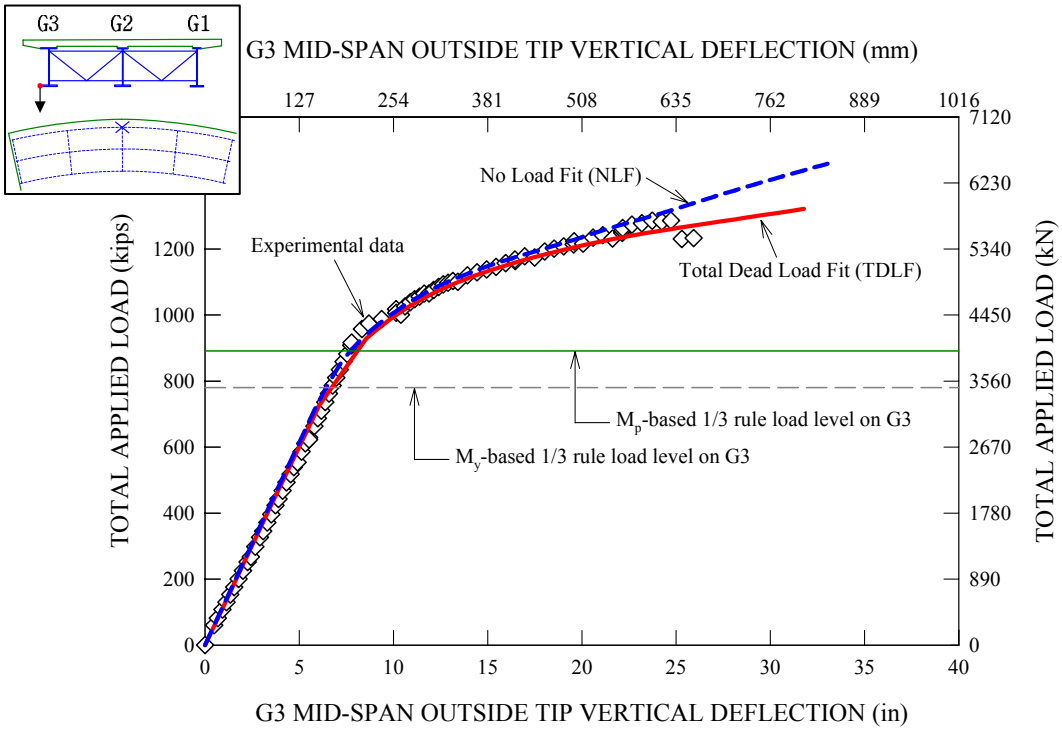

Figure 6.2.3. Applied load versus vertical deflection at the midspan outside tip of the G3 bottom flange based on No Load Fit (NLF) and Total Dead Load Fit (TDLF) detailing.

One can observe that it is not until high applied load levels well above the M_p-based 1/3 rule load level that any substantial distinction can be made between the two FEA solutions. Furthermore, it can be seen in Figure 6.2.4 that the FEA major-axis bending moments calculated for the G3 composite section at midspan are essentially identical for both of the cases throughout the entire loading range.

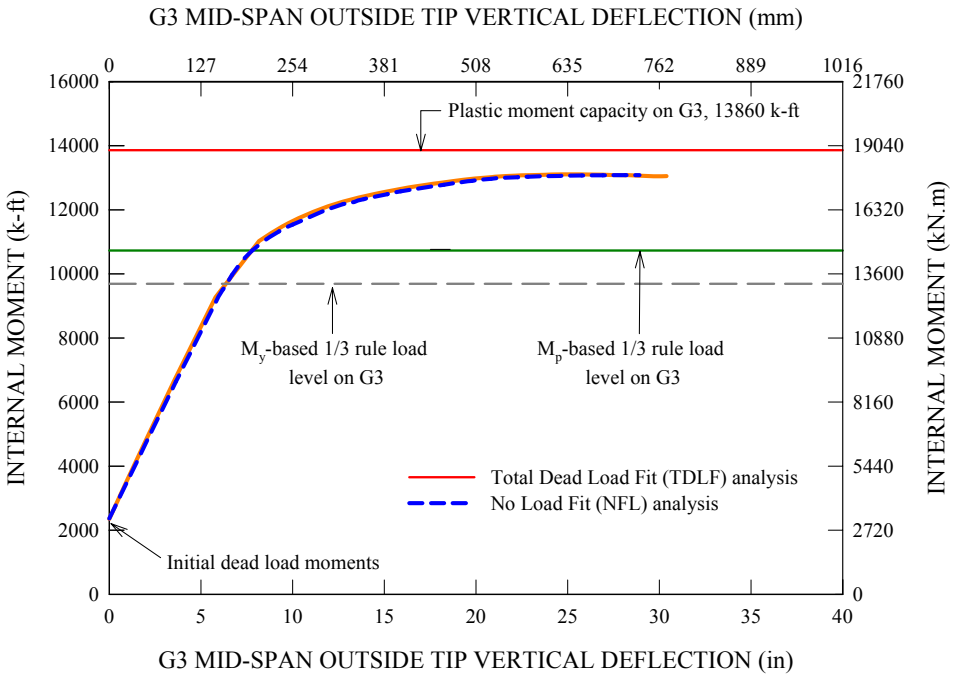

Figure 6.2.4. G3 midspan moment versus corresponding vertical deflection based on No Load Fit (NLF) and Total Dead Load Fit (TDLF) detailing.

When it comes to the predictions for the axial forces in the bottom chord of the cross-frame attached to G3 at the midspan, Figure 6.2.4 indicates that different detailing methods do not have a significant effect on the cross-frame member forces. It is important to note that for all practical purposes, the strength behavior is essentially identical regardless of the choice of detailing methods until applied loads are significantly

larger than the G3 1/3 rule strength level based on the elastically-computed major-axis and lateral bending stresses.

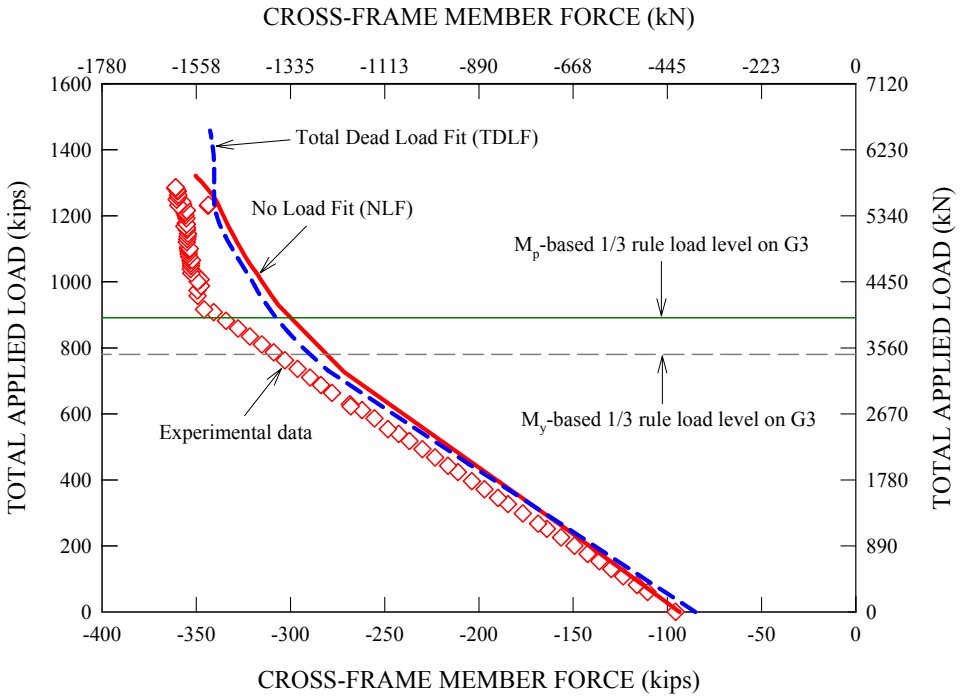

Figure 6.2.5. Applied load versus axial force in the bottom chord of the midspan cross-frame attached to G3 based on No Load Fit (NLF) and Total Dead Load Fit (TDLF) detailing.

6.3 Case 2: Homogeneous Section for the Outermost Girder, G3

In this variation on the test bridge, Grade 50 steel is used for the bottom flange of the outermost girder, G3, instead of HPS 70W. This makes G3 a homogeneous section instead of a hybrid section. Figure 6.3.1 shows the resulting modified design of the G3 cross-section. It can be seen that the width of the G3 bottom flange is 650 mm (26 in), which is increased from a nominal value of 600 mm (24 in) used for the G3 bottom flange of the base composite test bridge. This is because the flange lateral bending stress limit check, $f_l/0.6F_y$, is easily violated if Grade 50 steel is used with a G3 bottom flange width of 600 mm (24 in). The G1 and G2 cross-sections and all the other design

characteristics are the same as shown in Figure 1.5.1. The design unity checks for flexure are 0.60, 0.70 and 1.0 for the G1, G2 and G3 midspan unbraced lengths, respectively, under the Strength I loading combination. The corresponding lateral bending stress limit checks are 0.80, 0.62 and 0.75 for G1, G2 and G3, respectively.

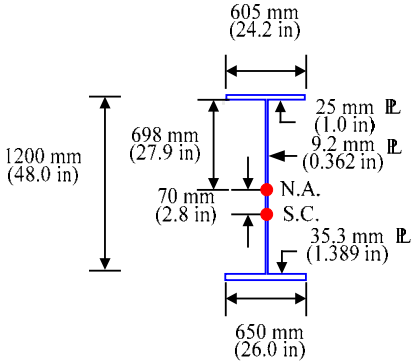

Figure 6.3.1 Case 2 G3 cross-section with Grade 50 steel used for the bottom flange instead of Grade 70.

It is noteworthy that the shape factor of M_p/M_y is larger for the homogeneous section shown in Figure 6.3.1 than for the original hybrid G3 cross-section. The shape factor of the original G3 hybrid composite section is 1.11 while it is 1.17 for the cross-section shown in Figure 6.3.1.

Figures 6.3.2 through 6.3.4 show the midspan internal moments versus the midspan vertical displacements for the G3, G2 and G1 isolated composite cross-sections throughout the applied loading history. The initial dead load moments are included in the plots (3188 kN-m (2351 k-ft) for G3, 912 kN-m (673 k-ft) for G2 and 404 kN-m (298 k-ft) for G1). All three plots indicate the moment corresponding to the M_p-based 1/3 rule load level on G3. In Figure 6.3.2, the G3 internal moment associated with the M_y-based 1/3 rule load level on G3 (10030 kN-m (7400 k-ft)) is also marked.

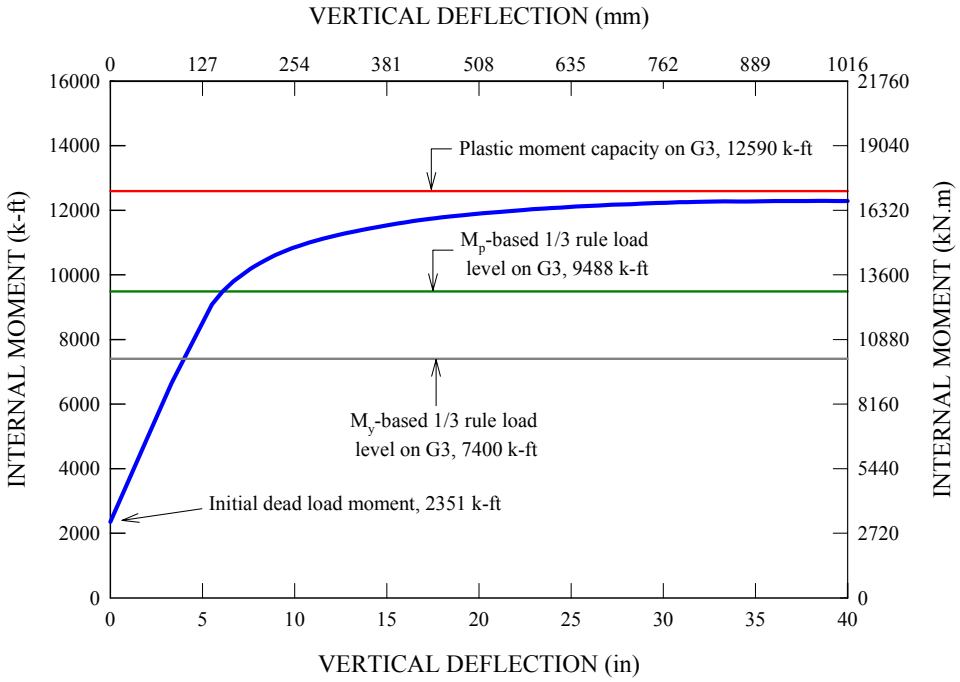

Figure 6.3.2. Case 2 G3 midspan internal moment versus corresponding vertical deflection at the web-flange juncture, initial dead load moment included.

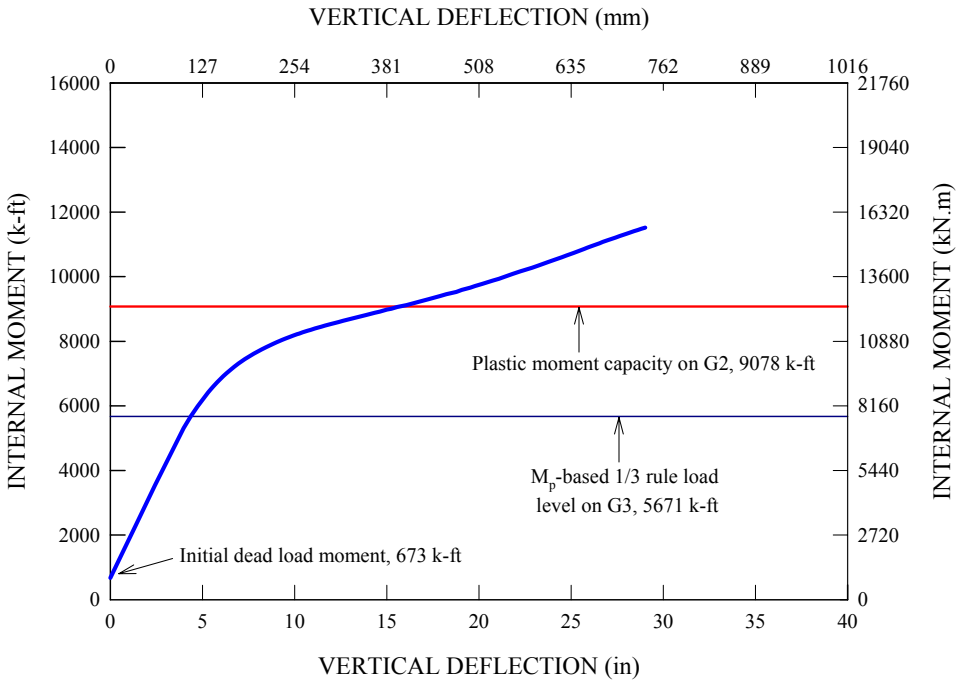

Figure 6.3.3. Case 2 G2 midspan internal moment versus corresponding vertical deflection at the web-flange juncture, initial dead load moment included.

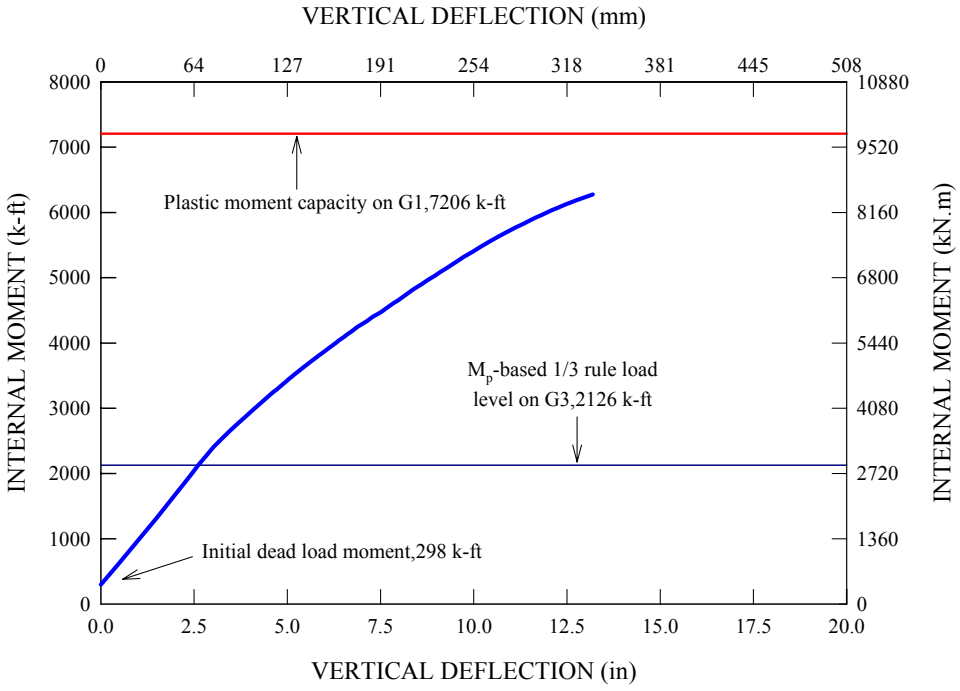

Figure 6.3.4. Case 2 G1 midspan internal moment versus corresponding vertical deflection at the web-flange juncture, initial dead load moment included.

As can be seen from Figure 6.3.2, the M_y-based 1/3 rule load level on G3 is located well below the proportional limit in the plot. For all three plots, it can be observed that the girder midspan moments increase linearly until the total applied load reaches the M_p-based 1/3 rule load level on G3.

Figure 6.3.5 shows the total applied load versus the axial force in the bottom-chord of the midspan cross-frame attached to G3. The initial dead load axial force is included in the plot. Although there is a slight departure in the axial force from the linear prediction starting at an applied load of about 3114 kN (700 kips), it can be seen that the member force variation is essentially linear up to the load levels associated with the M_y- and M_p-based 1/3 rule load levels on G3.

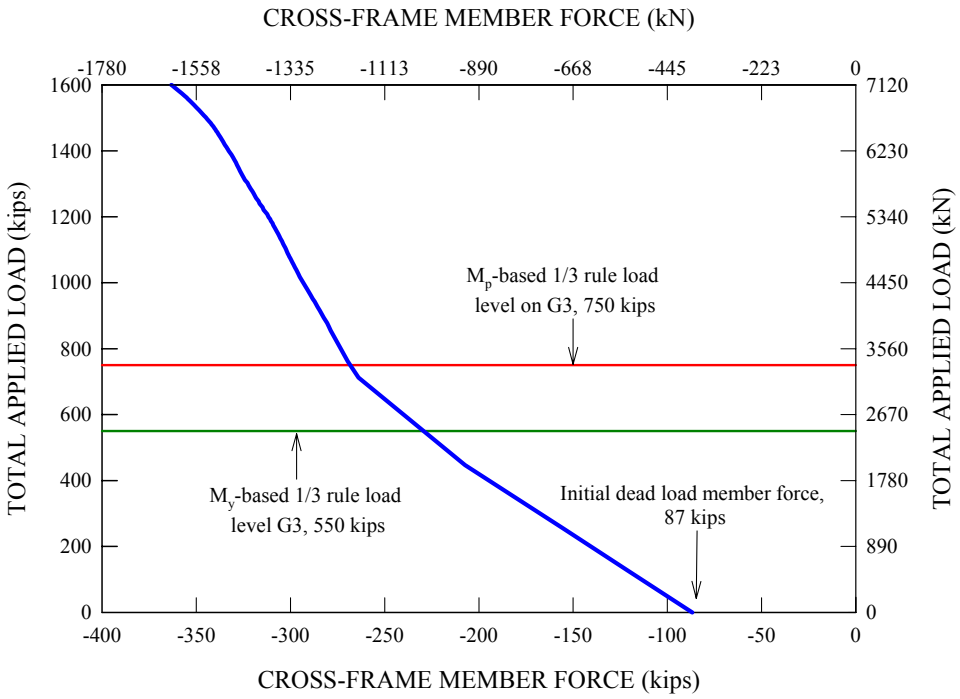

Figure 6.3.5. Case 2 applied load versus axial force in the bottom chord of the midspan cross-frame attached to G3, initial dead load force included.

Figure 6.3.6 shows the variations in the girder reactions throughout the analysis, including the initial dead load values at zero applied load. Again, similar to the original composite test bridge, all the girder reactions increase in a linear fashion throughout the entire applied loading history.

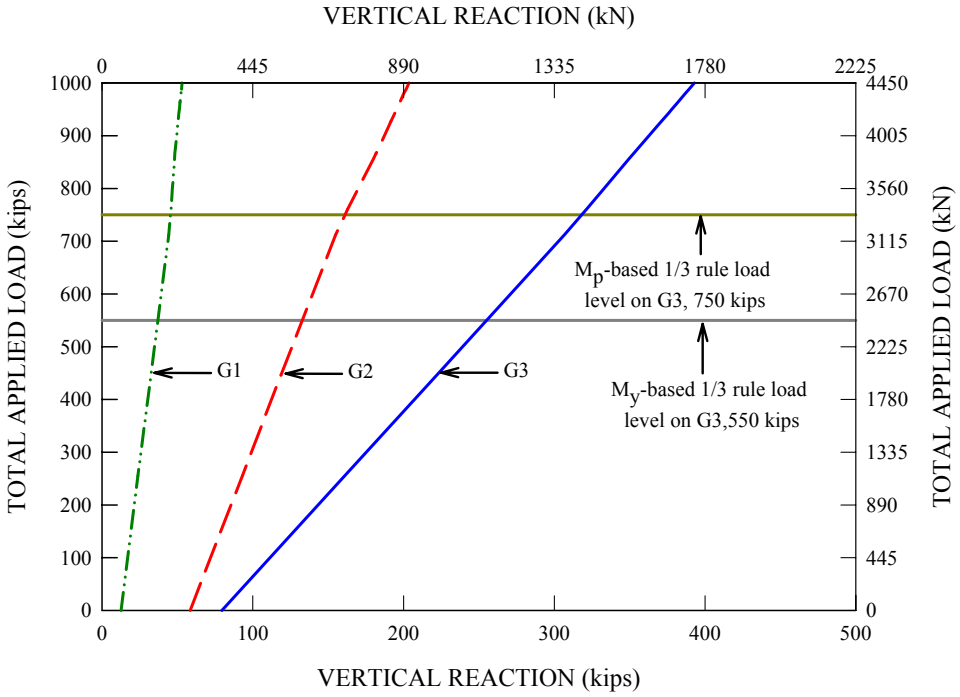

Figure 6.3.6. Case 2 applied load versus girder vertical reactions, initial dead load reactions included.

Figure 6.3.7 shows the slab top surface longitudinal strains across the midspan bridge cross-section when the total applied load reaches the M_p-based 1/3 rule load level on G3 (3336 kN (750 kips)). The longitudinal strains vary nearly in a linear fashion except for some local fluctuations near the center line of each girder. However, the maximum strain occurs near the centerline of the outermost girder, G3, rather than the outer edge of the bridge slab at the M_p-based 1/3 rule load level. The magnitude of the maximum strain is about 1060 με, which is slightly higher than the strain associated with the elastic limit of the concrete stress-strain response. However, this is significantly smaller than the nominal concrete crushing strain of 0.003. This means that the bridge slab strains vary essentially in a linear elastic fashion up to the M_p-base 1/3 rule load level.

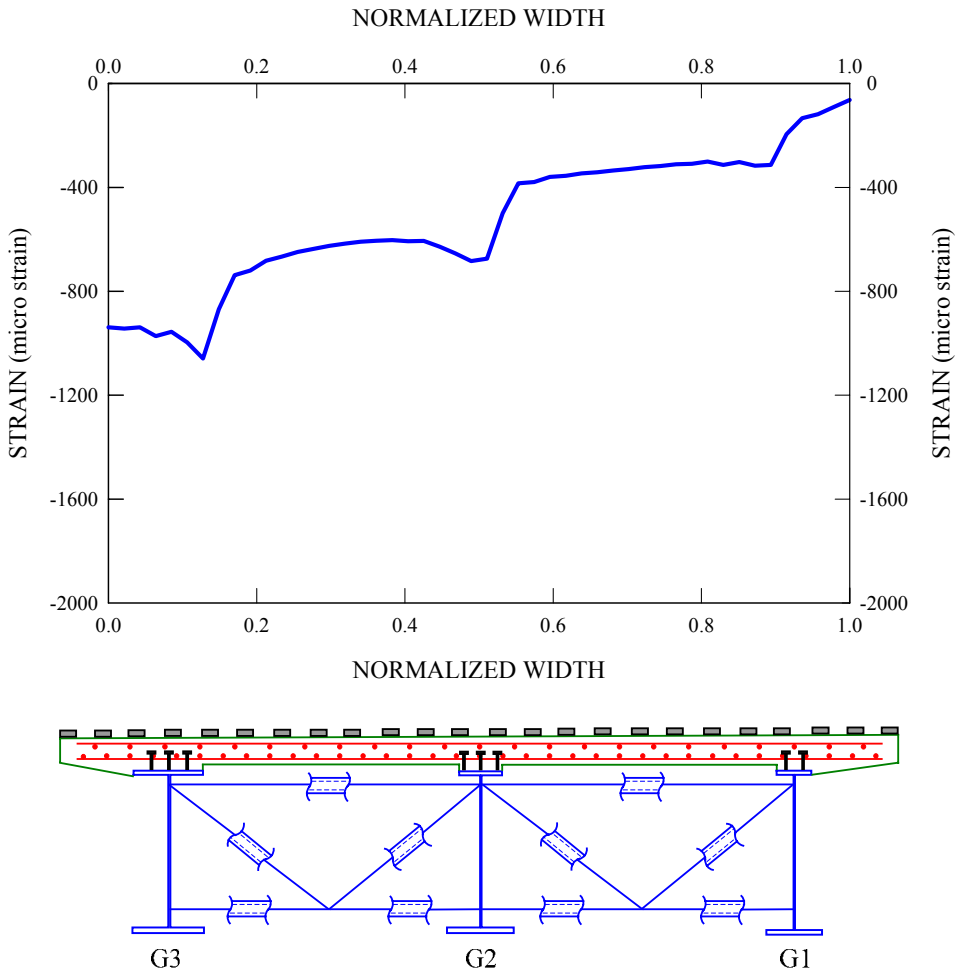

Figure 6.3.7. Case 2 slab top surface longitudinal strains across the midspan bridge cross-section at the M_p-based 1/3 rule load level on G3 (total applied load = 3336 kN (750 kips)), strains associated with shrinkage not included in the plot.

6.4 Case 3: Cross-Frame Spacing, L_b, Set to 0.075R

The cross-frame spacing in the test bridge configuration produces a subtended angle L_b/R of 0.1125 radians. This is slightly larger than the maximum limit of 0.1 radians allowed in the AASHTO (2004b) Specifications. Therefore, it is useful to investigate the strength behavior of the composite test bridge with a smaller cross-frame spacing that satisfies the AASHTO requirements. To this end, the number of intermediate cross-frames in the test bridge is increased from three to five. This sets the spacing between the cross-frames on G2 to 4.57 m (15 ft) instead of 6.75 m (22.5 ft), producing a subtended angle of 0.075 radians.

Figure 6.4.1 shows the girder cross-sections, the bridge cross-section and a plan view of the redesigned test bridge based on this reduced cross-frame spacing. All the girder plate thicknesses and the web depths are kept the same as those of the test bridge girders for purposes of simplicity in the redesign. The flange widths are varied to satisfy the design requirements. Figures 6.4.1a-c show that all the flange widths are reduced from the corresponding dimensions used for the test bridge. The insertion of the additional cross-frames does not have any important effect on the major-axis bending moments, but the flange lateral bending moments are changed significantly. This reduces the demands on the girder flange widths. The design unity checks for flexure are 0.70, 0.86 and 1.0 for the G1, G2 and G3 midspan unbraced lengths, respectively under the Strength I load combination. The corresponding lateral bending stress limit checks are 0.70, 0.57 and 0.62 for G1, G2 and G3, respectively.

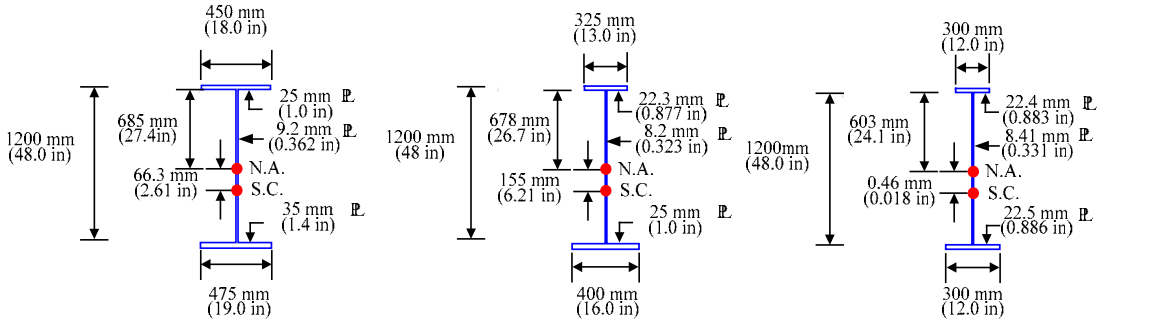

(a) G3 cross-section (b) G2 cross-section (c) G1 cross-section

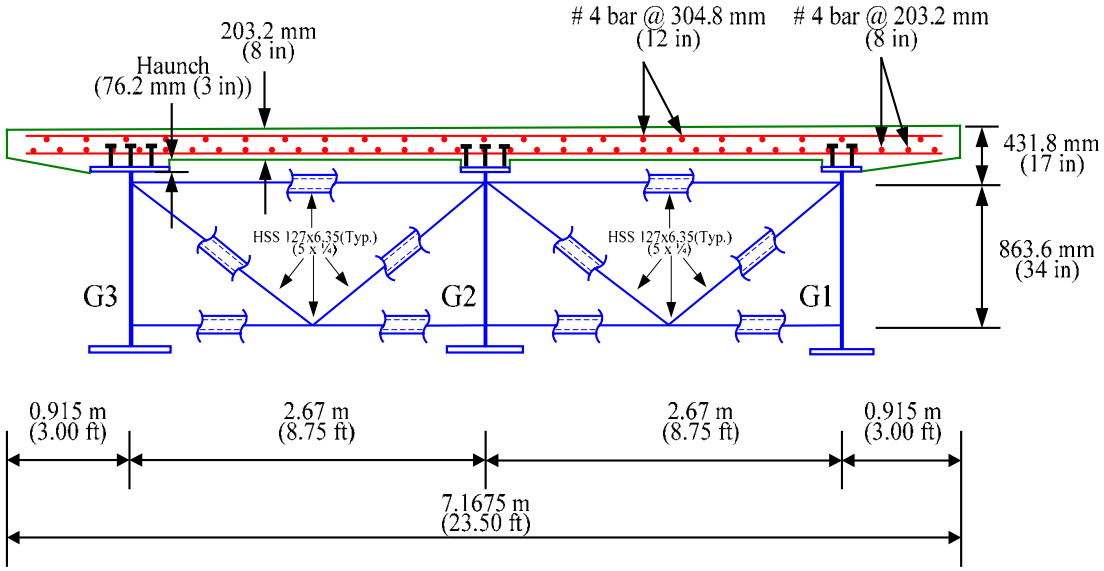

(d) Bridge cross-section

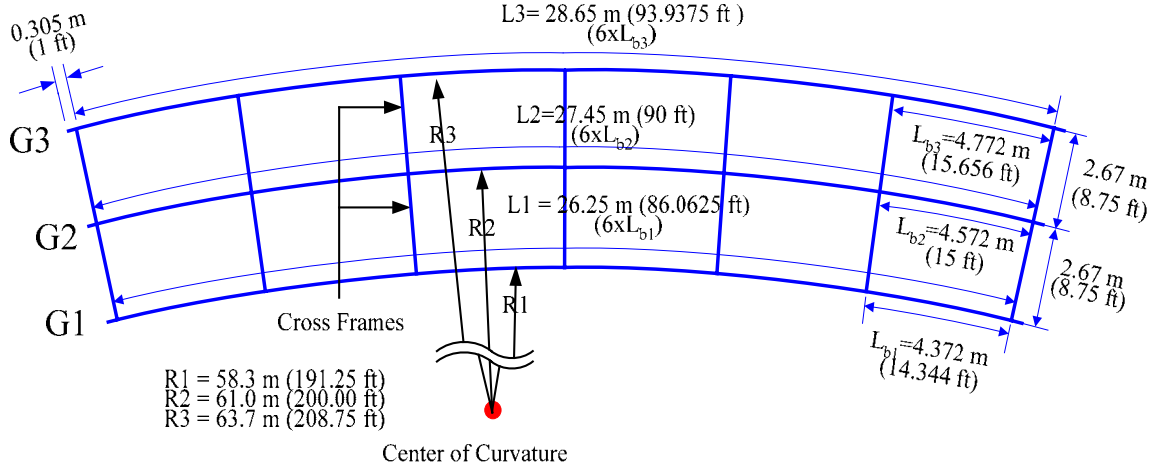

(e) Bridge plan

Figure 6.4.1. Case 3 composite test bridge geometry with L_b/R equal to 0.075.

Figures 6.4.2 through 6.4.4 show the midspan moments versus the corresponding vertical deflections at the girder bottom web-flange juncture for the G3, G2 and G1 isolated composite cross-sections. The initial dead load moments are included in the plots (2977 kN-m (2196 k-ft) for G3, 1047 kN-m (772 k-ft) for G2 and 393 kN-m (290 k-ft) for G1). All three plots show the cross-section moment associated with the M_p-based 1/3 rule level on G3. In Figure 6.4.2, the G3 internal moment associated with the M_y-based load level (10300 kN-m (7600 k-ft)) on G3 is also marked. Figure 6.4.2 shows that the G3 midspan moment associated with the M_p-based 1/3 rule load level on G3 is located at a point where there is a slight deviation relative to the linear elastic estimate. However, this deviation is minor. Therefore, it can be said that the G3 midspan moment variation is approximately linear up to the M_p-based 1/3 rule load level on G3. Similarly, Figures 6.4.3 and 6.4.4 show that the G2 and G1 midspan moments increase linearly up to the M_p-based 1/3 rule load level on G3.

Figure 6.4.5 shows the total applied load versus the axial force in the bottom chord of the midspan cross-frame attached to G3, including the initial dead load axial force. Except for a slight departure from the linear elastic estimate starting at a total applied load of 3114 kN (700 kips), it can be seen that the member force varies linearly up to the load levels associated with the M_y- and M_p-based 1/3 rule load levels on G3.

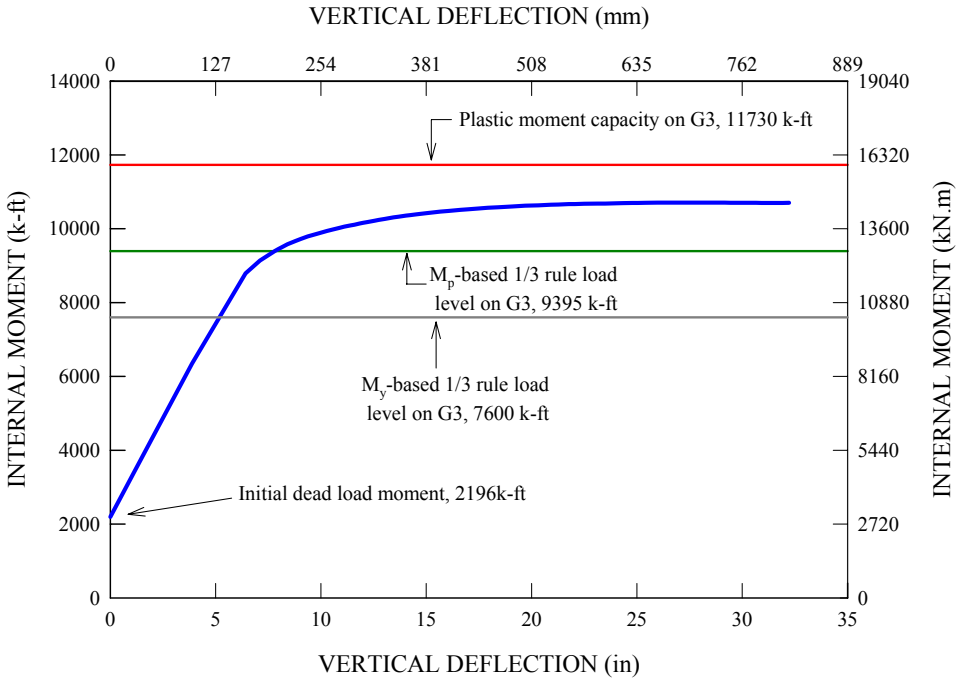

Figure 6.4.2. Case 3 G3 midspan moment versus corresponding vertical deflection at the web-flange juncture, initial dead load moment included.

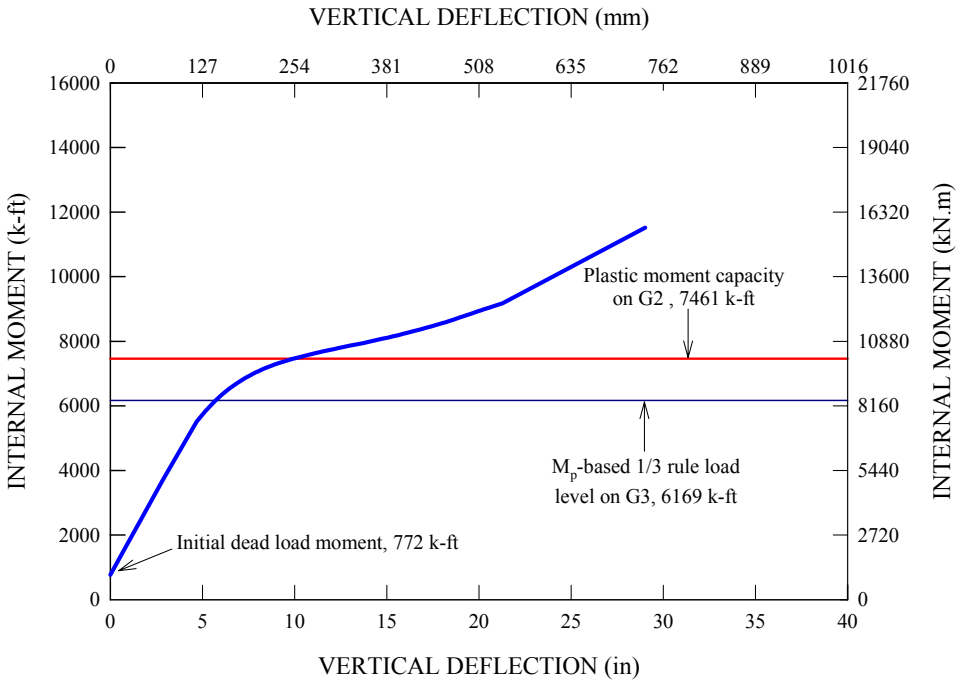

Figure 6.4.3. Case 3 G2 midspan moment versus corresponding vertical deflection at the web-flange juncture, initial dead load moment included.

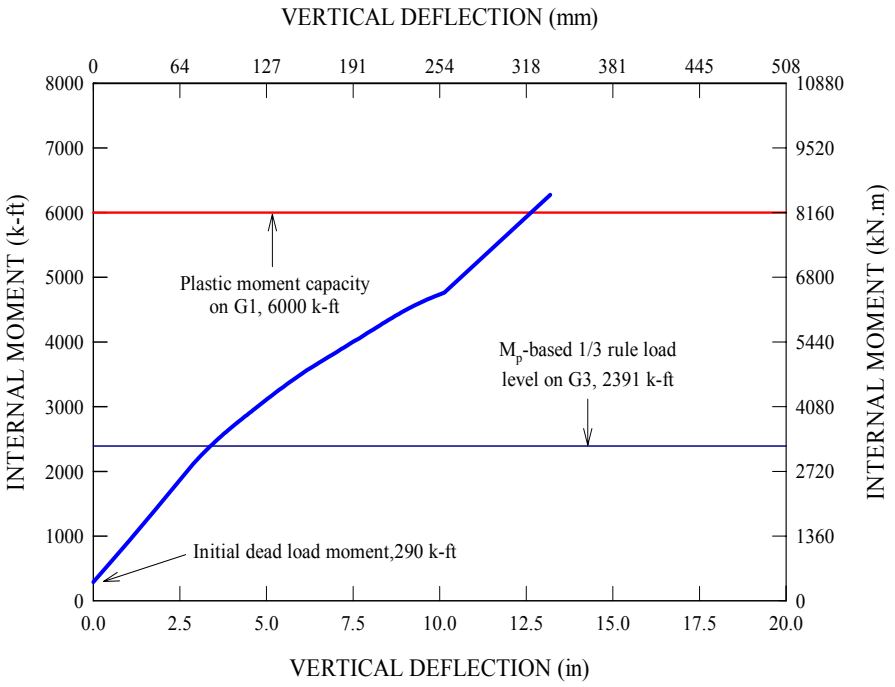

Figure 6.4.4. Case 3 G1 midspan moment versus corresponding vertical deflection at the web-flange juncture, initial dead load moment included.

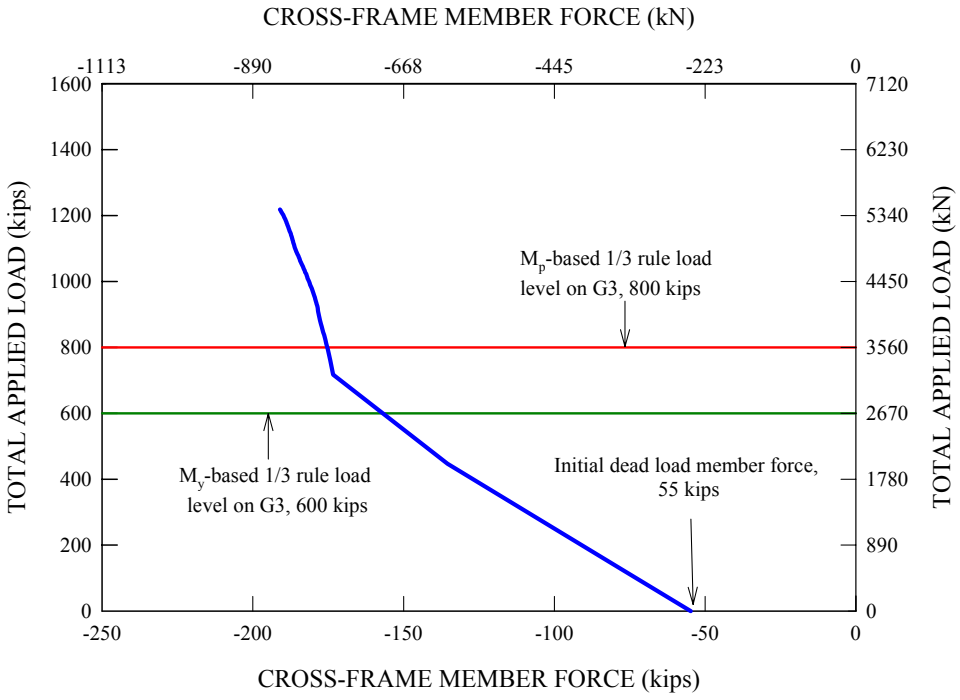

Figure 6.4.5. Case 3 applied load versus axial force in the bottom chord of the midspan cross-frame attached to G3, initial dead load axial force included.

Figure 6.4.6 shows the total applied load versus the girder reactions, including the initial dead load reactions at zero applied load for the Case 3 bridge. Similar to the behavior of the reactions for the previous bridges, it can be seen that all the girder reactions increase predominantly in a linear fashion throughout the analysis.

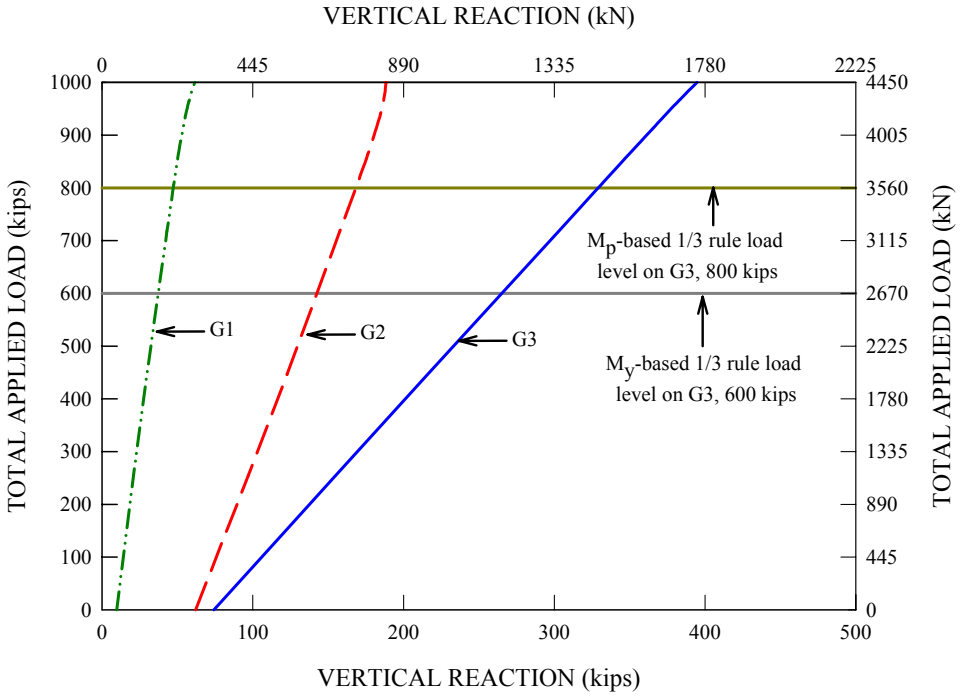

Figure 6.4.6. Case 3 applied load versus girder vertical reactions, initial dead load reactions included.

Figure 6.4.7 shows the slab top surface longitudinal strains across the midspan cross-section when the total applied load reaches the M_p-based 1/3 rule load level of 3559 kN (800 kips). Again, it can be seen that the maximum strain takes place near the centerline of the outermost girder, G3, rather than the outer edge of the bridge slab at the M_p-based 1/3 rule load level. The magnitude of the maximum strain is about 1100 με, which is slightly higher than the strain associated with the elastic limit of the concrete stress-strain

response. However, the maximum strain is still significantly lower than the nominal concrete crushing strain of 0.003, indicating the linear behavior of the bridge slab up to the M_p-base 1/3 rule load level on G3. Interestingly, the deviation in the strains from an ideal linear variation across the slab width appears to be slightly smaller in this case than in the other examples.

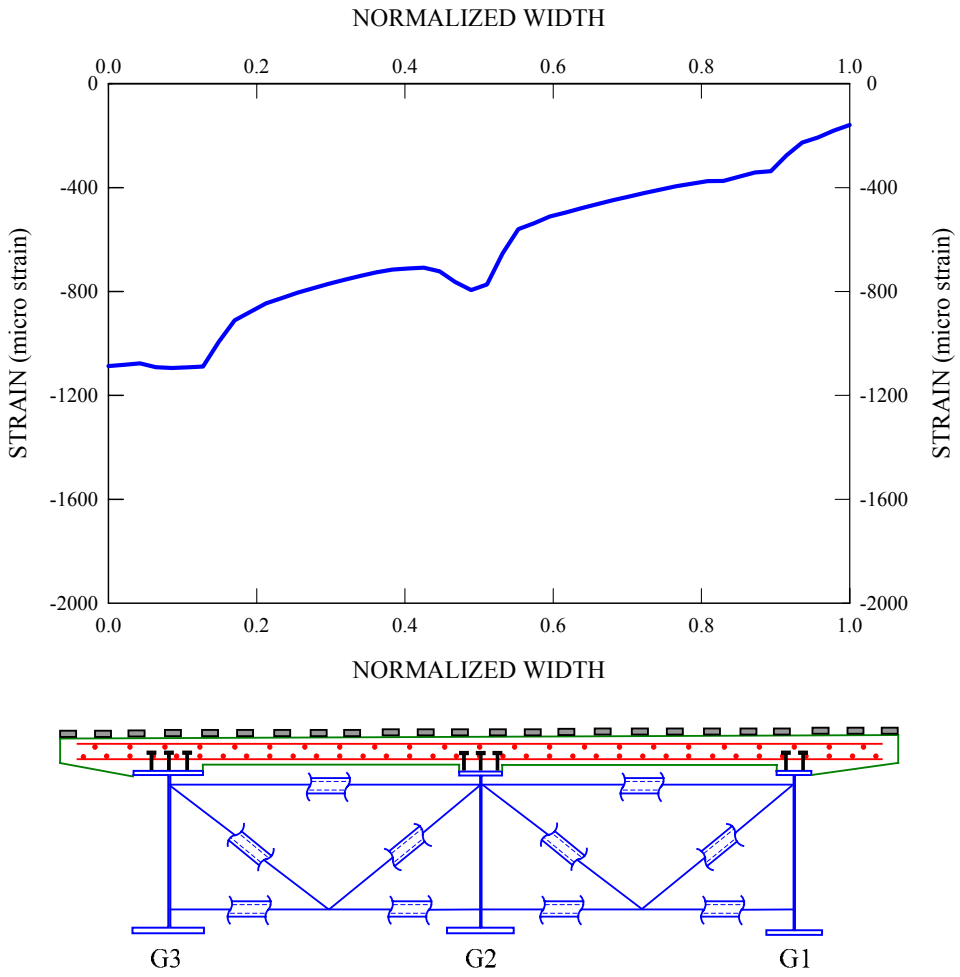

Figure 6.4.7. Case 3 slab top surface longitudinal strains across the midspan bridge cross-section at the M_p-based 1/3 rule load level on G3 (total applied load = 3559 kN (800 kips)), strains associated with shrinkage not included in the plot.

6.5 Cases 4 through 6: Skewed Bridges

Three skewed bridges are considered to investigate the effects of skew angles on the strength behavior. The first two cases have a maximum skew angle of 20 degrees specified at one of the bearing lines. The geometrical configuration of these two bridges are identical to each other except for the fact that the first case has the intermediate cross-frames placed normal to the girder axes while the second one has the cross-frames parallel to the lines of support. The skew angle of 20 degrees used for these two bridges is the limit allowed by the AASHTO (2004b) Specifications up to which intermediate cross-frames may be placed either normal to the girder axes or parallel to the girder support lines. The third case has a maximum skew angle of 60 degrees at one of the support lines. Although there is no practical limit imposed on the angle of skew in the AASHTO (2004b) Specifications, the skew angle of 60 degrees can be taken as a rather extreme case that may be encountered in bridge structures. The last case is intended to investigate the effects of extreme skew angles on the strength behavior of curved bridges.

6.5.1 Case 4: Skewed Supports (Maximum Skew Angle of 20 Degrees)

The first skewed bridge has the test bridge geometry, but the bearing lines on both sides of the bridge are parallel each other. One support line has a maximum skew angle of 20 degrees while the other has a skew angle of 5.8 degrees. The intermediate cross-frames within the bridge system are framed normal to girder axes. Figure 6.5.1 shows the plan view of this skewed bridge system. Despite the loss of symmetry due to the skew angle, the midspan cross-section is defined along the cross-frame located at the mid-length of girder G2 as shown in Figure 6.5.1. The girder dimensions are the same as those of the original test bridge. This is due to the fact that the elastic analysis and design

checks performed for this bridge indicate that the girder responses do not change dramatically with the introduction of the mild skew angles at the support lines. The design unity checks for flexure are essentially the same as shown in Table 2.5.2.

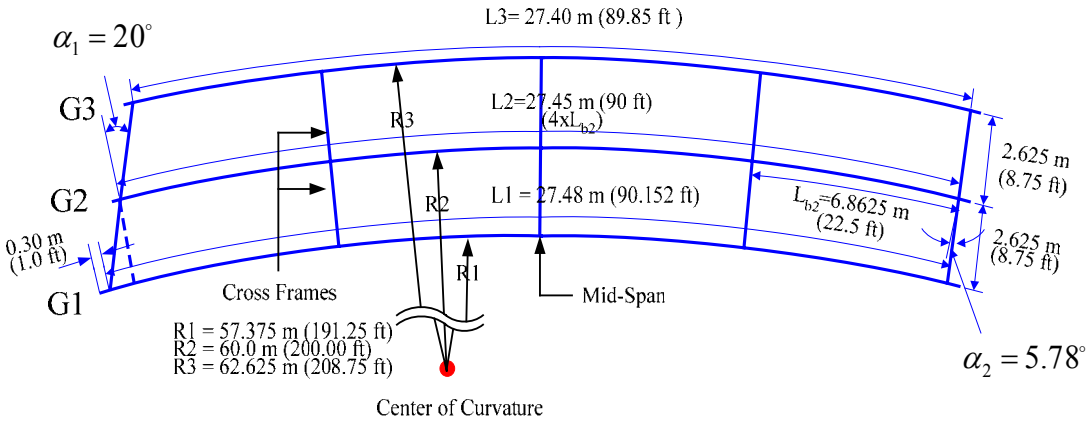

Figure 6.5.1. Plan view of Case 4 composite test bridge geometry with skew angles of 20 and 5.8 at the lines of supports and intermediate cross-frames normal to the girder axes.

Due to the skew angle, the outermost girder, G3, has the smallest length (27.0 m (89.85 ft)) of the three girders. Furthermore, as can be seen from the plan view of this skewed bridge, G3 has unequal unbraced lengths along the girder length, but the controlling unbraced length used for the sizing of the girder is still the same as that of the original test bridge, 7.0 m (23.48 ft). Conversely, the overall length of G1 is increased from 25.82 m (86.0625 ft) to 27.0 m (90.15 ft) due to the skew angle. Also, it has unequal unbraced lengths. However, contrary to G3, the controlling unbraced length used for the sizing of this girder is the end unbraced length of 7.41 m (24.7 ft), which is larger than that of G1 in the test bridge, 6.5 m (21.52 ft). This governing unbraced length has a subtended angle of 0.13 radian, which is substantially larger than the limit of 0.1 allowed in the AASHTO (2004b) Specifications. Ideally, one additional cross-frame may

be needed towards the end of the girder G1 as indicated by the dashed line Figure 6.5.1. This is to reduce this subtended angle, thereby satisfying the Specification requirement and reducing the possibility of significant increase in the lateral bending stresses. However, it is found that there is essentially no difference between the FEA solutions with and without this additional cross-frame inserted. This additional cross-frame is not needed for strength. Therefore, only three intermediate cross-frames are used in this skewed bridge configuration. The overall length for the middle girder, G2, is 27 m (90 ft), which is the same as that of the base composite test bridge.

Figures 6.5.2 through 6.5.4 show the midspan internal moments versus the bottom web-flange juncture vertical displacements for the G3, G2 and G1 isolated composite cross-sections throughout the loading history for the Case 4 skewed bridge.

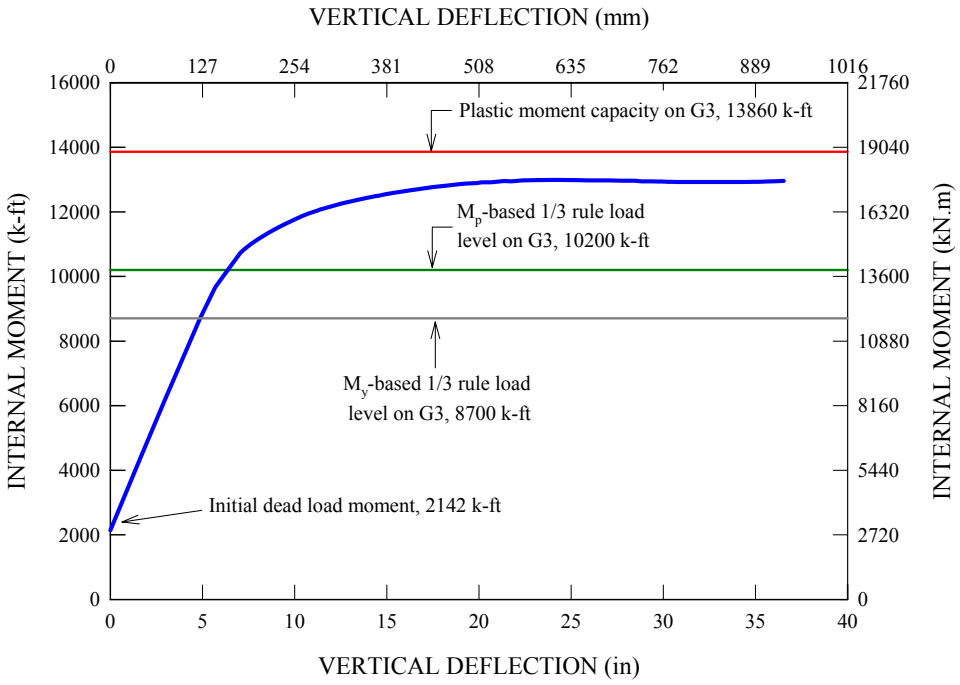

Figure 6.5.2. Case 4 G3 midspan internal moment versus corresponding vertical deflection at the web-flange juncture, initial dead load moment included.

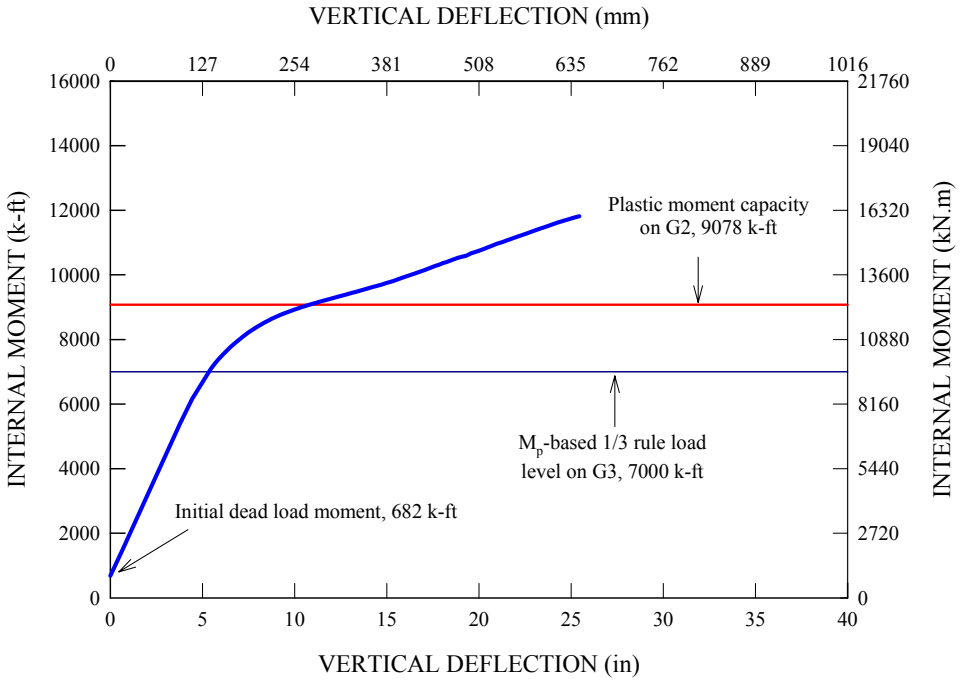

Figure 6.5.3. Case 4 G2 midspan internal moment versus corresponding vertical deflection at the web-flange juncture, initial dead load moment included.

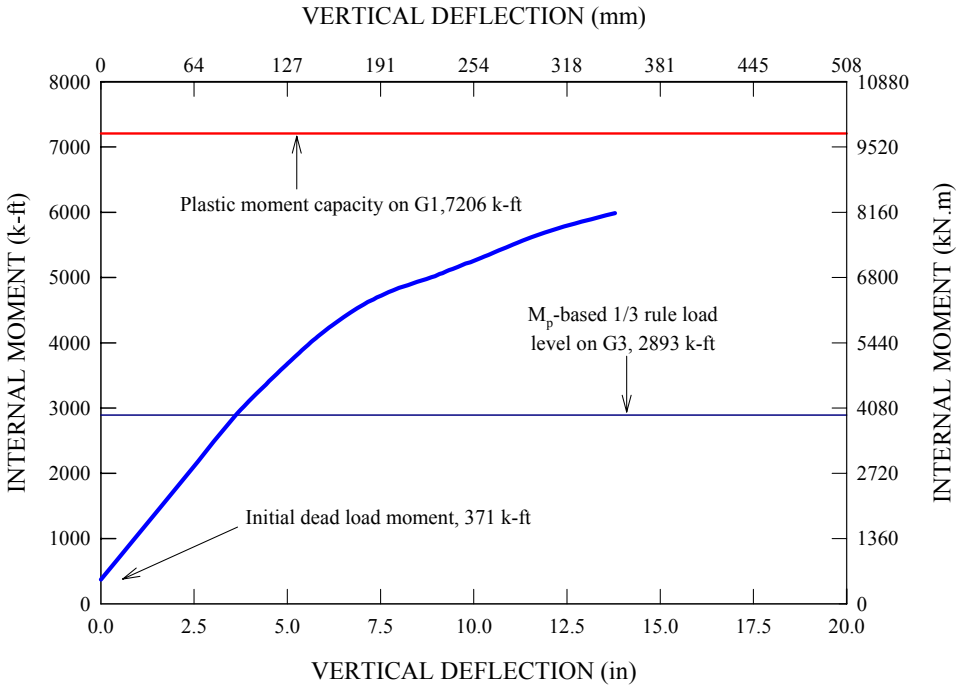

Figure 6.5.4. Case 4 G1 midspan internal moment versus corresponding vertical deflection at the web-flange juncture, initial dead load moment included.

The same simplified loading scheme used for the experimental testing of the base composite test bridge is also employed for the full nonlinear FEA simulation of this skewed bridge system. The initial dead load moments are included in the plots (2904 kN-m (2142 k-ft) for G3, 925 kN-m (682 k-ft) for G2 and 503 kN-m (371 k-ft) for G1). The M_p-based 1/3 rule and M_p-based load levels on G3 are marked on all three plots. Interestingly, the linear elastic estimates for the total applied load levels corresponding to the above limit state are 3336 kN (750 kips) and 4003 kN (900 kips) for the M_y- and M_p-based 1/3 rule load levels on G3, respectively. The corresponding estimates for the original composite test bridge are 3470 kN (780 kips) and 3959 kN (890 kips). Therefore, given the same section properties and dimensions, it can be seen that the introduction of a mild skew angle of 20 degrees or less at the support locations does not affect the response of the composite test bridge significantly. Most importantly, it can be seen from Figures 6.5.3 and 6.5.4 that the girder midspan moments increase linearly up to the M_p-based 1/3 rule load level on G3. It should be noted that the midspan cross-section for the Case 4 bridge is defined as cross-section at the middle cross-frame line.

Figure 6.5.5 shows the total applied load versus the axial force in the bottom chord of the midspan cross-frame attached to G3 throughout the loading history. The included initial dead load axial force is 347 kN (78 kips), which is reduced from 378 kN (85 kips) in the composite test bridge. Although there is a slight departure in the member force from the linear prediction starting at a total applied load of 3780 kN (850 kips), it can be seen that the member force varies essentially in a linear fashion up to the load levels associated with the M_y- and the M_p-based 1/3 rule load levels. The member force at the M_p-based 1/3 rule load level is about 1201 kN (270 kips). It should be noted that this

member force is slightly reduced from 1334 kN (300 kips) obtained from the full nonlinear FEA of the composite test bridge. It is believed that this reduction in the member force is due to the reduction in the G3 girder length, thereby reducing the total lateral forces necessary to maintain the equilibrium of this girder.

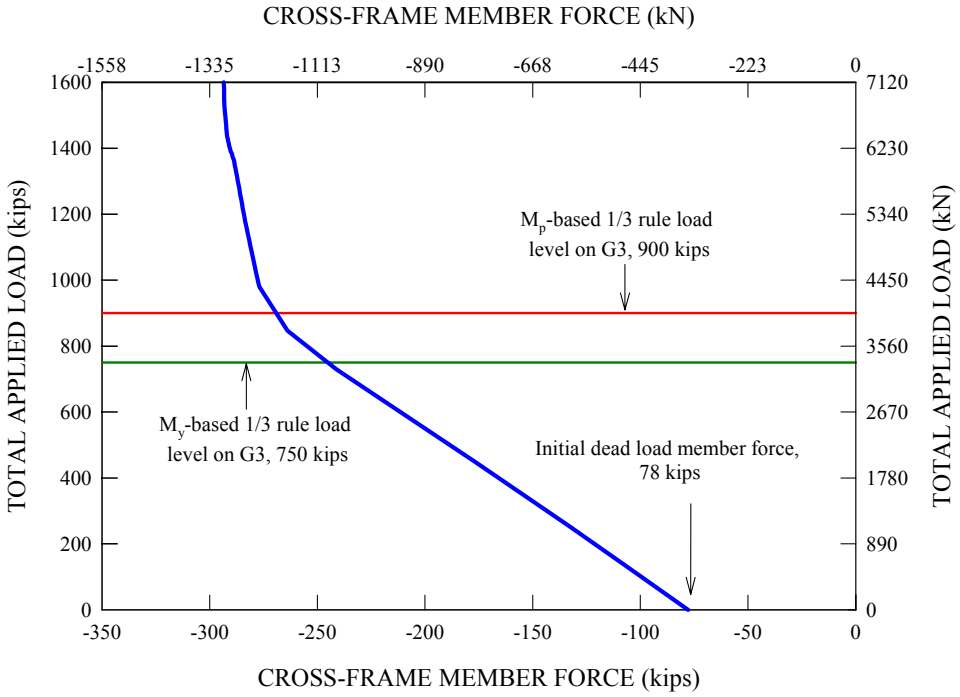

Figure 6.5.5. Case 4 applied load versus axial force in the bottom chord attached to G3 of the midspan cross-frame, initial dead load axial force included.

Figures 6.5.6 and 6.5.7 provide the girder reactions throughout the analysis for the lines of supports with a skew angle of 20 degrees (west end) and 5.8 degrees (east end), respectively. Both of the plots include initial dead load reactions at zero applied load. Similar to the girder reaction responses observed for the composite test bridge, it can be seen that all the girder reactions increase linearly throughout the entire loading range. The initial dead load reactions are 334 kN (75 kips), 258 kN (58 kips) and 58 kN (13

kips) for G3, G2 and G1, respectively, at the line of support with a skew angle of 20 degrees while they are 325 kN (73 kips), 271 kN (61 kips), and 76 kN (17 kips) at the line of support with a skew angle of 5.8 degrees. Because of skew angle, it can be seen that G3 has a larger reaction on the west side than the east side. Conversely, G1 and G2 have larger reactions on the east side than the west side. Similar observations can be made for the girder reactions due to the directly applied loads.

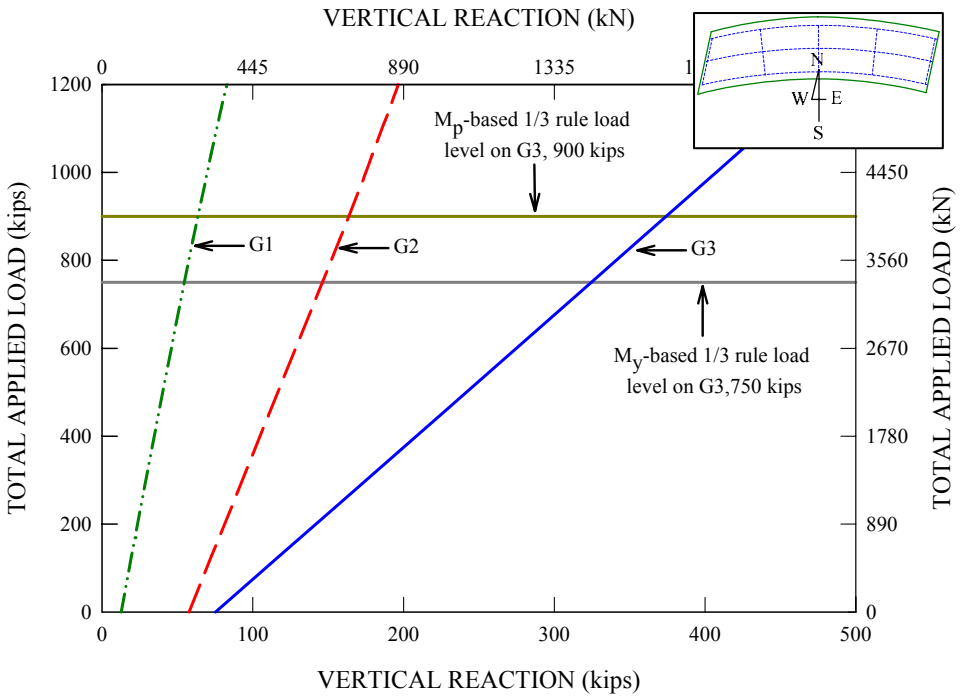

Figure 6.5.6. Case 4 applied load versus west end girder vertical reactions, initial dead load reactions included.

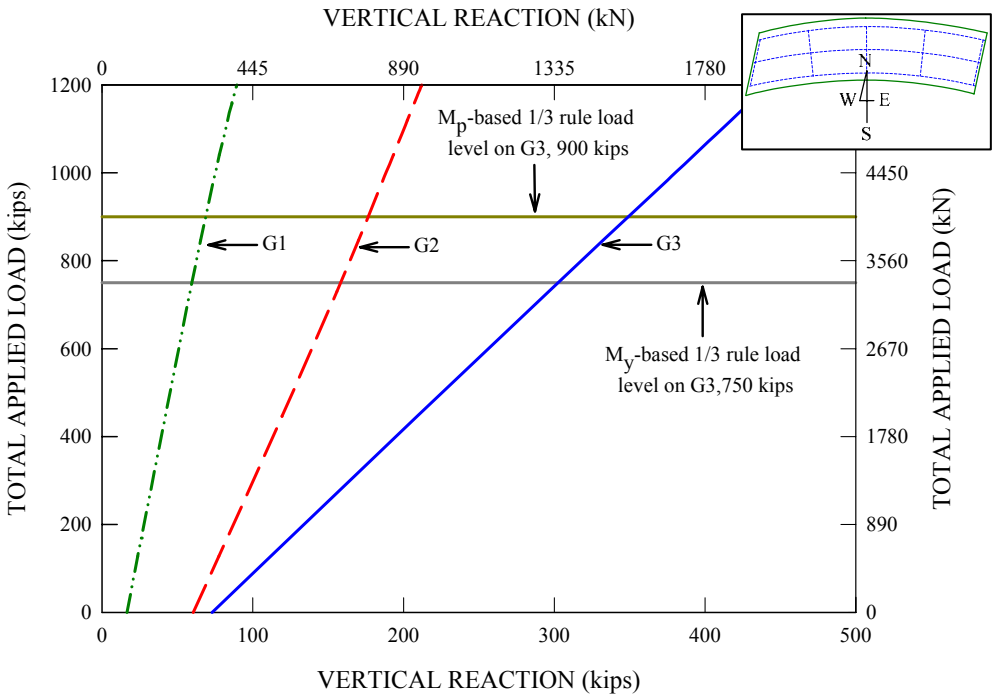

Figure 6.5.7. Case 4 applied load versus east end girder vertical reactions, initial dead load reactions included.

Moreover, the girder reactions at the M_p-based 1/3 rule load level of 4003 kN (900 kips) are 1681 kN (378 kips), 738 kN (166 kips) and 289 kN (65 kips) for G3, G2 and G1, respectively, at the line of support with a skew angle of 20 degrees while they are 1570 kN (353 kips), 792 kN (178 kips) and 311 kN (70 kips) for the line of support with a skew angle of 5.8 degrees. Although there are some minor deviations in the girder reactions between two bearing lines, the sum total of the reactions on each side reveals that the girder reactions due to the applied loads remain almost symmetric with a slightly higher reaction sum at the side with a skew angle of 20 degrees. This is because G3's support is closer to the middle of the bridge on this end. .

Figure 6.5.8 shows the slab top surface longitudinal strain distribution across the midspan bridge cross-section at the M_p-based 1/3 rule load level of 4003 kN (900 kips)

on G3. The maximum strain near the centerline of the outermost girder, G3, is about 1660 με. This value is significantly larger than the strain value of 1100 με observed for the composite test bridge and is very close to the strain associated with concrete compressive strength. However, it should be noted that this peak strain is still less than the nominal concrete crushing strain of 0.003. Also, the peak longitudinal strain is highly localized near girder G3. In fact, the majority of the bridge slab develops strains less than 1200 με at the M_p-based 1/3 rule load level.

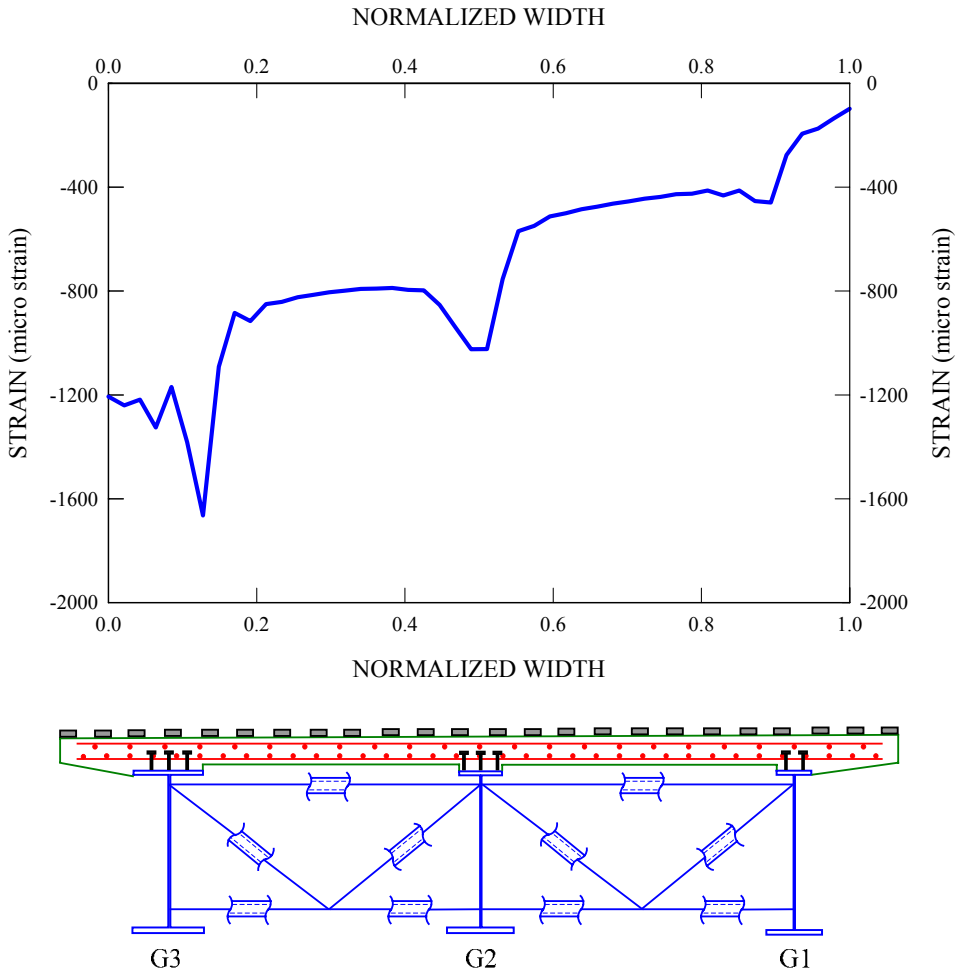

Figure 6.5.8. Case 4 slab top surface longitudinal strains across the midspan bridge cross-section at the M_p-based 1/3 rule load level on G3 (total applied load = 4003 kN (900 kips)).

6.5.2 Case 5: Skewed Cross-Frames and Supports (Maximum Skew Angle of 20 Degrees)

The second skewed bridge system also uses the original test bridge girder geometries, one line of supports at the girder ends that has a maximum skew angle of 20 degrees, a second bearing line that is parallel to the first, as in the first skewed bridge case. However, in addition, the intermediate cross-frames are also skewed so that they are in parallel with the bearing lines. Figure 6.5.9 shows the plan view of the second skewed bridge case. The midspan cross-section is defined along the cross-frame located at the mid-length of girder G2 as shown in Figure 6.5.9. Similar to the first skewed bridge case, the design unity checks for flexure are essentially the same as shown in Table 2.5.2.

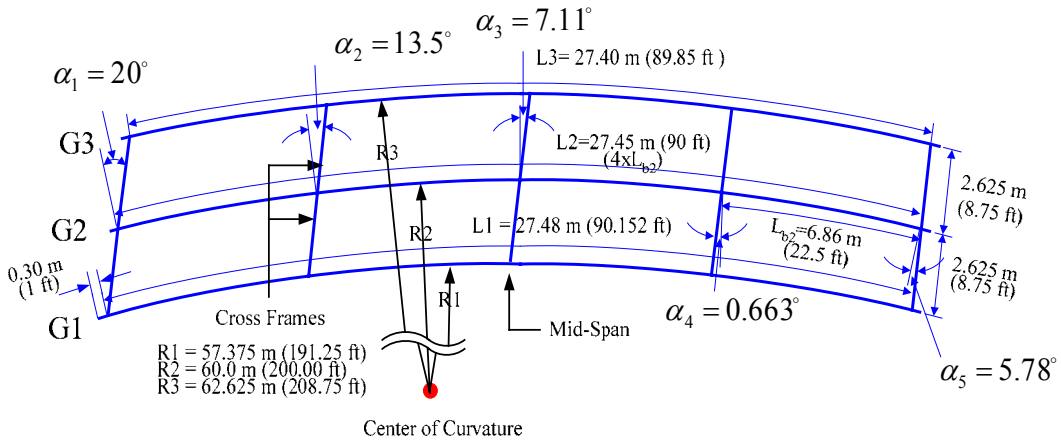

Figure 6.5.9. Plan view of Case 5 composite test bridge geometry with skew angles of 20 and 5.78 degrees at the bearing lines and intermediate cross-frames parallel to the lines of support.

Figures 6.5.10 through 6.5.12 show the midspan internal moments for the G3, G2 and G1 isolated composite cross-sections throughout the loading history. The midspan bridge cross-section is taken as a radial cut through the girders that passes through the

intersection of the middle cross-frames and girder G2. That is, the midspan cross-section is taken as the same location on the bridge as in the Case 4 example. The initial dead load moments are included in the plots (2891 kN-m (2132 k-ft) for G3, 925 kN-m (682 k-ft) for G2 and 503 kN-m (371 k-ft) for G1). There are two strength limit states calculations shown in Figure 6.5.10 (the M_y- and M_p-based 1/3 rule load levels on G3) whereas Figures 6.5.11 and 6.5.12 show the M_p-based 1/3 rule load level only. The total applied loads at the above limit state conditions are 3514 kN (790 kips) and 4226 kN (950 kips) for the M_y- and M_p-based 1/3 rule load levels on G3, respectively.

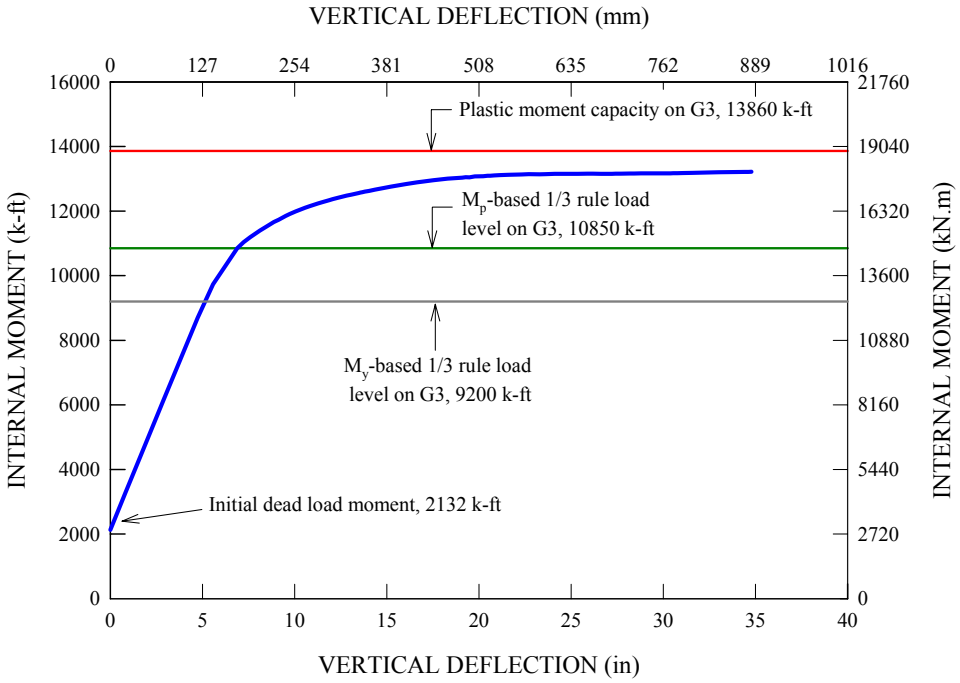

Figure 6.5.10. Case 5 G3 midspan internal moment versus corresponding vertical deflection at the web-flange juncture, initial dead load moment included.

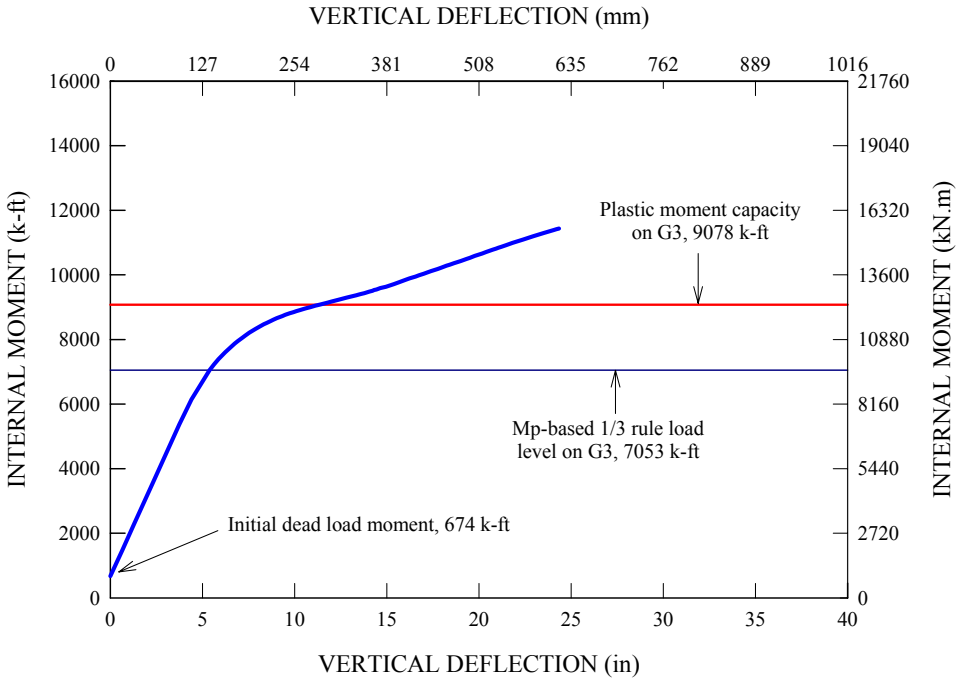

Figure 6.5.11. Case 5 G2 midspan internal moment versus corresponding vertical deflection at the web-flange juncture, initial dead load moment included.

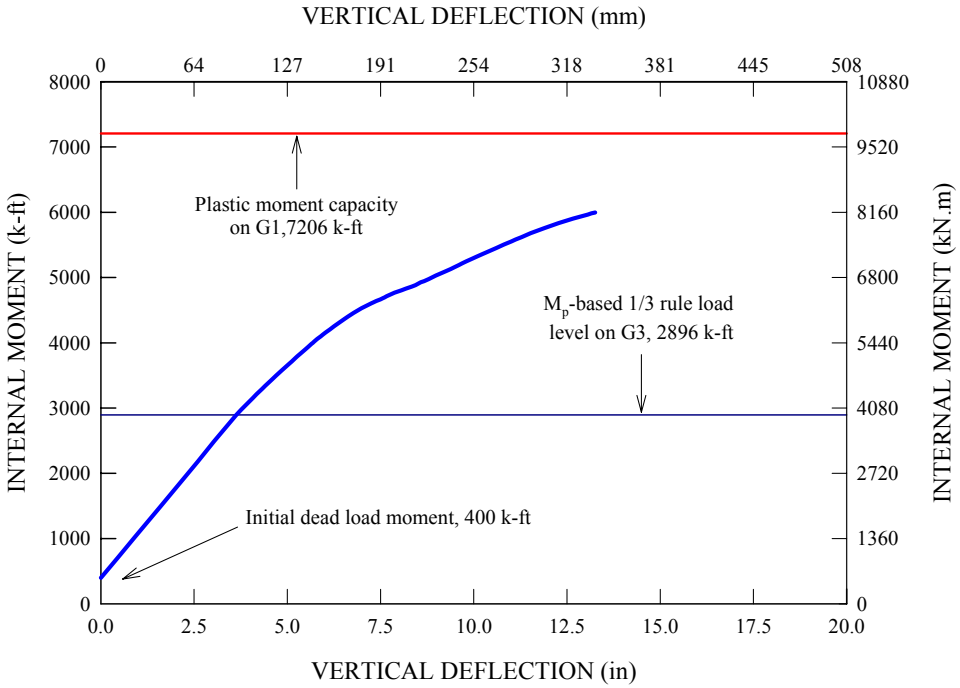

Figure 6.5.12. Case 5 G1 midspan internal moment versus corresponding vertical deflection at the web-flange juncture, initial dead load moment included.

It is quite interesting to note that the same load levels calculated for the original composite test bridge are 3470 kN (780 kips) for the first-yield moment and 3959 kN (890 kips) for the M_p-based 1/3 rule load level. In other words, given the same section properties and dimensions, it takes more load for the second skewed bridge to reach the same limit state than in the bridge without skew angles. This behavior is rather obvious, considering the fact that the second skewed bridge has the unbraced length of 6.72 m (22.4 ft) on G3 that is smaller than 7.0 m (23.48 ft), the unbraced length of its counter part in the composite test bridge. For all three plots, it is not until the total applied load reaches the M_p-based 1/3 rule load level on G3 that the girder midspan moments start to show noticeable nonlinear behavior.

Figure 6.5.13 gives axial forces in the bottom chord of the midspan cross-frame attached to G3 throughout the loading history. The included dead load axial force is 316 kN (71 kips), which is reduced from 347 kN (78 kips) in the first skewed bridge case considered in this study. Although there is a slight departure in the member force from the linear elastic estimate starting with a total applied load of 3780 kN (850 kips). It can be seen that the member force variation is essentially linear up to the load levels associated with the M_y- and the M_p-based 1/3 rule load levels on G3.

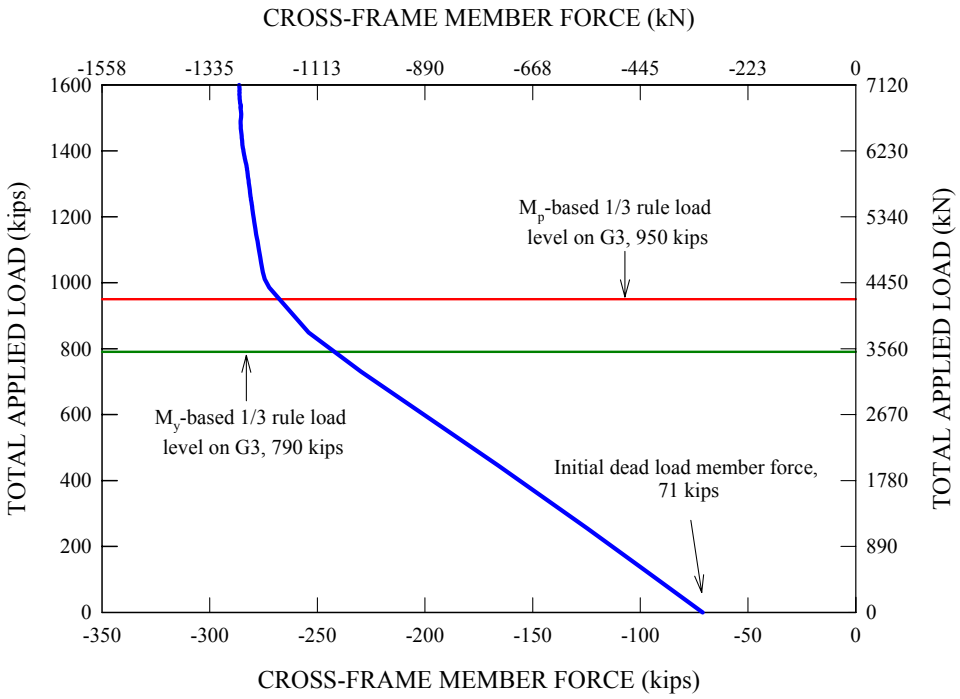

Figure 6.5.13. Case 5 applied load versus axial force in the bottom chord attached to G3 of the midspan cross-frame, initial dead load axial force included.

Figures 6.5.14 and 6.5.15 show the girder reactions throughout the analysis for the lines of supports with a skew angle of 20 degrees (west end) and 5.8 degrees (east end), respectively. The dead load reactions are also included in these plots. It can be seen that all the girder reactions increase linearly throughout the analysis. The initial dead load reactions are 334 kN (75 kips), 267 kN (60 kips) and 67 kN (15 kips) for G3, G2 and G1, respectively, at the line of support with a skew angle of 20 degrees while they are 316 kN (71 kips), 271 kN (61 kips) and 62 kN (14 kips) at the line of support with a skew angle of 5.8 degrees. That is, although the line of supports with a skew angle of 20 degrees carries slightly higher girder reactions that the other side, the magnitude of the girder reactions is essentially symmetric at a zero applied load level. However, these girder reactions are not symmetric any more for the directly applied loads. With respect to the

M_p-based 1/3 rule load level of 4226 kN (950 kips), the girder reactions are 1744 kN (392 kips), 805 kN (181 kips) and 338 kN (76 kips) for G3, G2 and G1, respectively, at the line of support with a skew angle of 20 degrees while they are 1704 kN (383 kips), 810 kN (182 kips) and 302 kN (68 kips) for the line of support with a skew angle of 5.8 degrees.

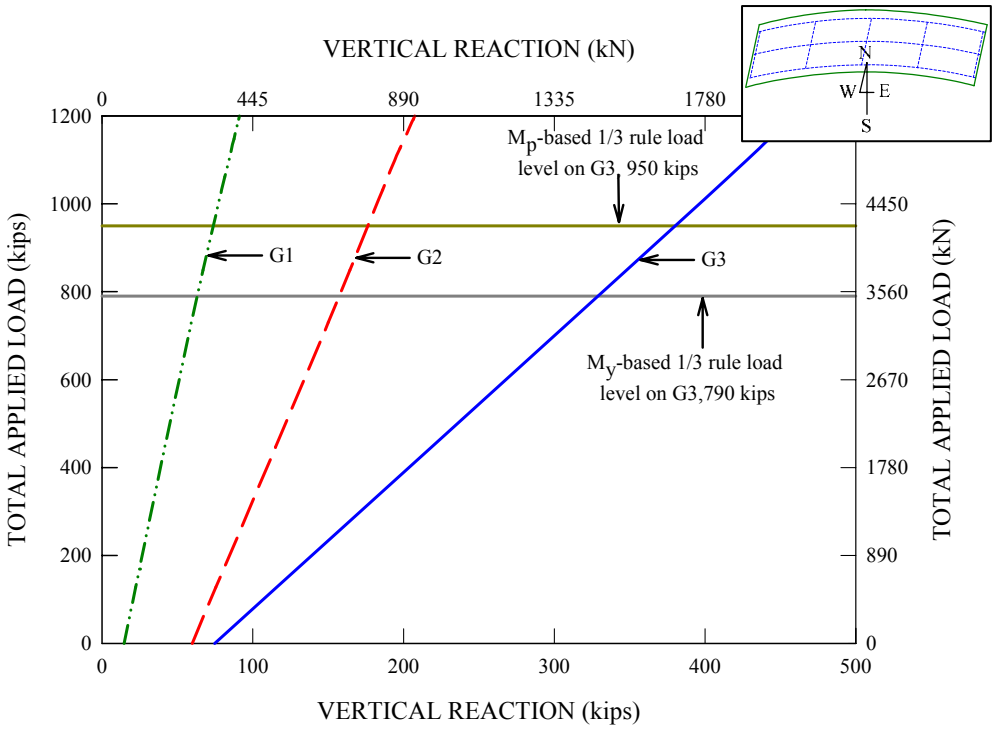

Figure 6.5.14. Case 5 applied load versus west end girder vertical reactions, initial dead load reactions included.

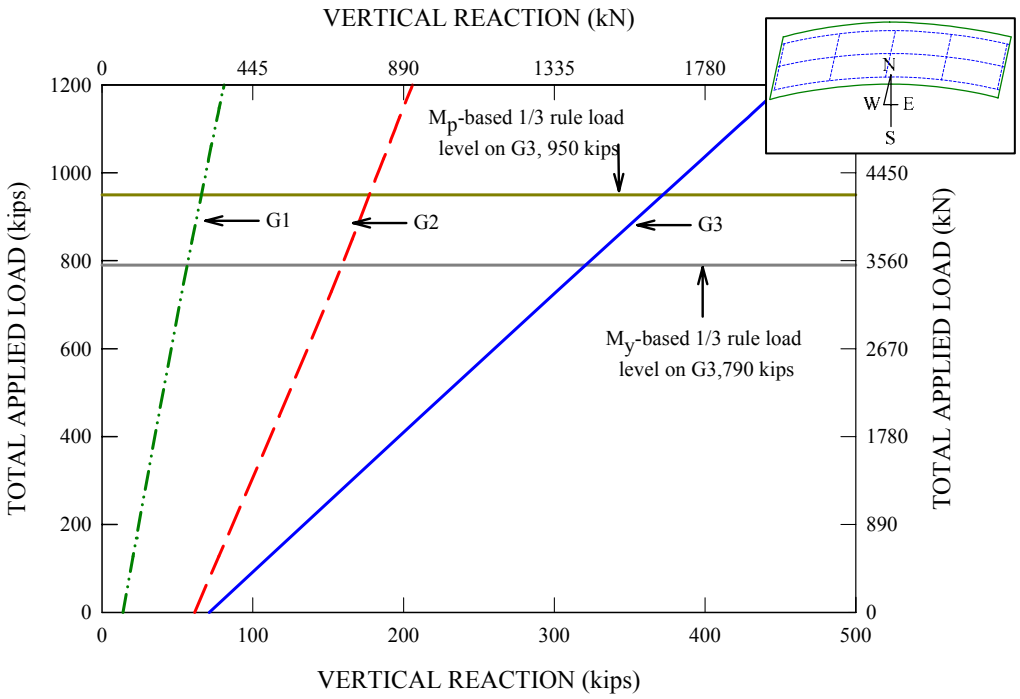

Figure 6.5.15. Case 5 applied load versus east end girder vertical reactions, initial dead load reactions included.

Figure 6.5.16 gives a plot that shows the slab top surface longitudinal strain distribution across the midspan cross-section when the total applied load reaches the M_p-based 1/3 rule load level of 4226 kN (950 kips). It can be seen that the maximum strain of 1600 με happens near the centerline of the outermost girder, G3, rather than the outer edge of the bridge slab at the M_p-based 1/3 rule load level, but it is highly localized. It is important to note that the majority of the bridge slab has strains less than 1100 με, which is the strain associated with concrete compressive strength. Also, it should be noted that the slab strains are still much less than the nominal concrete crushing strain of 0.003.

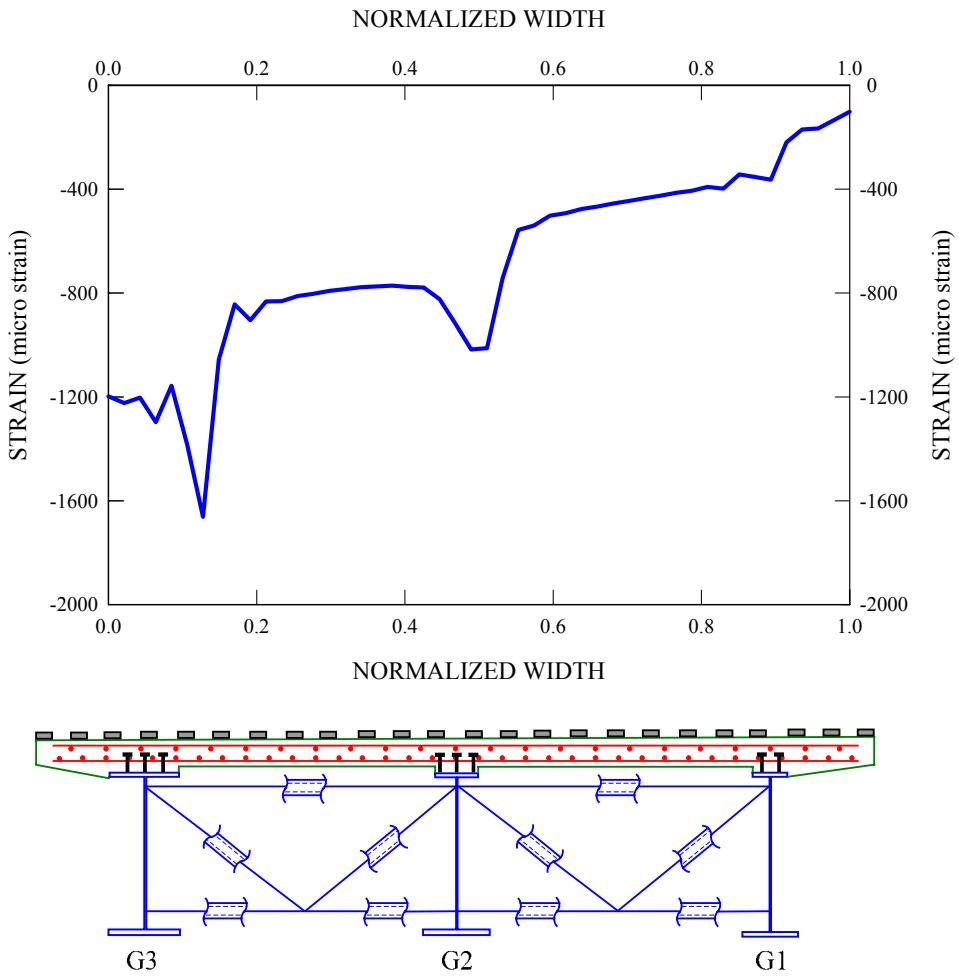

Figure 6.5.16. Case 5 slab top surface longitudinal strains across the midspan bridge cross-section at the M_p-based 1/3 rule load level on G3 (total applied load = 4226 kN (950 kips)).

6.5.3 Case 6: Skewed Supports (Maximum Skew Angle of 60 Degrees)

As opposed to the first two skewed bridges with mild skew angles, the third skewed bridge system has a rather extreme skew angle of 60 degrees at one bearing line. However, the intermediate cross-frames within this bridge system are made normal to the girder axes. This is because the AASHTO (2004b) Specifications require that intermediate cross-frames shall be normal to girder axes when the bearing lines are skewed more than 20 degrees.

Figure 6.5.17 shows the girder cross-sections, bridge cross-section and plan view of the resulting bridge. It can be seen that, in contrast with the first two skewed bridges, the configuration of this bridge is not close to that of the original composite test bridge in terms of girder lengths and cross-frame arrangements. Since the skew angles are specified by rotating the lines of supports about the middle girder, G2, the G2 girder total length and unbraced lengths remain the same. Conversely, there are significant changes in the geometries of the facia girders, G1 and G3. In fact, due to the introduction of extreme skew angles, it can be seen that G3 has one unbraced length near the more highly skewed supports that is significantly reduced to 1.85 m (6.16 ft) and an unbraced length at the other end of the bridge that is considerably increased to 9.1 m (30.28 ft). Since the subtended angle between the cross-frame locations on G3 is already higher than the AASHTO (2004b) limit of 0.10 radian, the above increase in the unbraced length leads to a significant increase in the lateral bending stresses. Similar considerations apply to girder G1. Thus, additional cross-frames are provided as shown in Figure 6.5.17e.

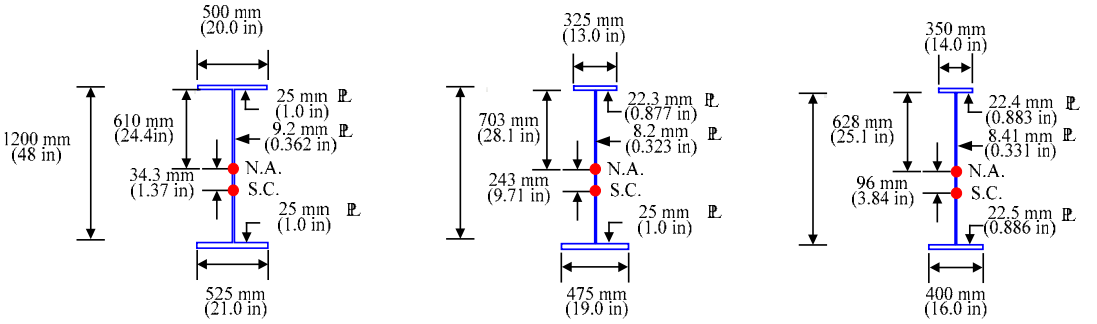

(a) G3 cross-section (b) G2 cross-section (c) G1 cross-section

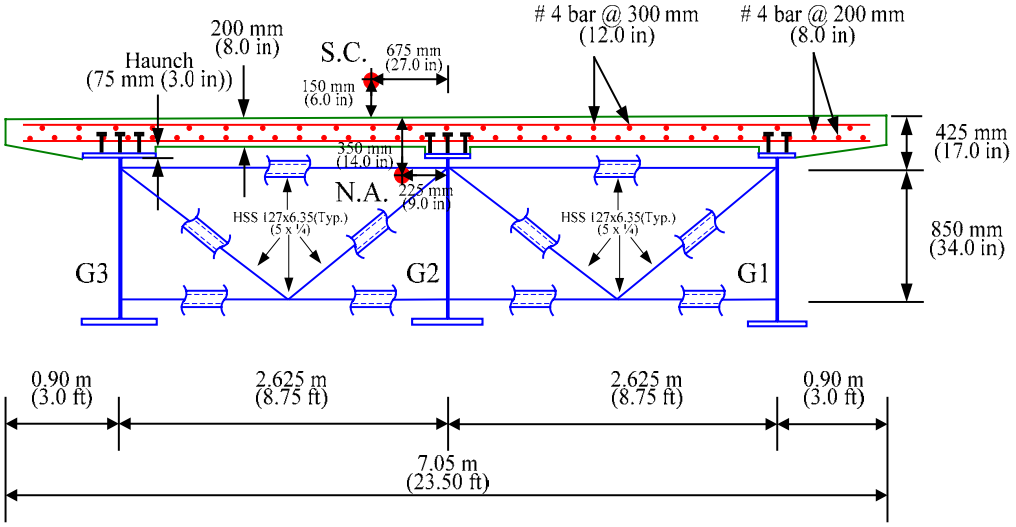

(d) Bridge cross-section

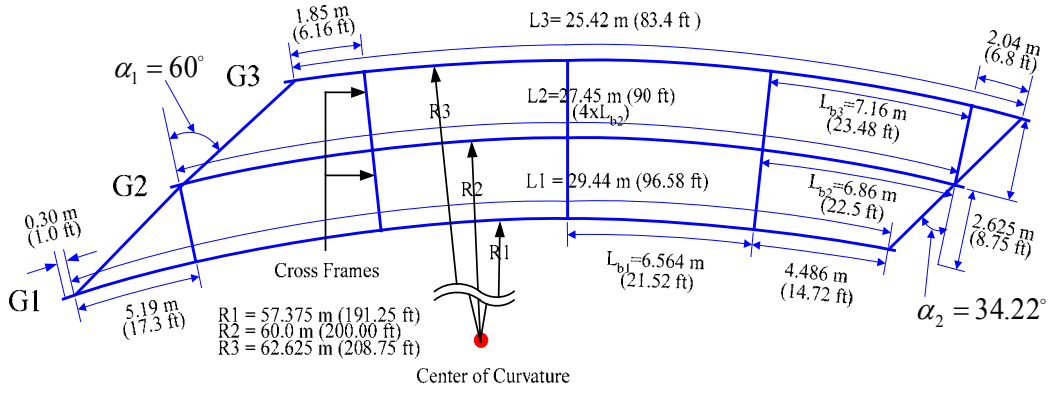

(e) Bridge plan

Figure 6.5.17. Plan view of Case 6 composite test bridge geometry with skew angles of 60 and 34.2 degrees at the lines of supports and intermediate cross-frames normal to the girder axes.

The overall length of G3 is reduced from 28.18 m (93.9375 ft) in the original composite test bridge to 25.0 m (83.4 ft) due to the above skew. The overall length of G1 is increased from 25.82 m (86.0625 ft) to 28.97 m (96.58 ft). Due to these changes in the overall lengths of G3 and G1 and the different arrangement of the cross-frames, the bridge girders need to be re-designed. It is interesting to note that the governing load case in the updated elastic analysis and design for the maximum flexural responses in G1 involves two AASHTO design truck loads plus two lane loads, rather than a single truck load plus a single lane load as in the test bridge and other previous bridge configurations. The design unity checks for flexure are 0.77, 0.80 and 0.92 for the G1, G2 and G3 midspan unbraced lengths, respectively, under the Strength I load combination. The corresponding lateral bending stress limit checks are 1.0, 0.82 and 0.96 for G1, G2 and G3, respectively. Figure 6.5.18 shows the loading scheme for the AASHTO design vehicle used for maximum flexural effects on G3 in the elastic analysis and design of the Case 6 skewed bridge.

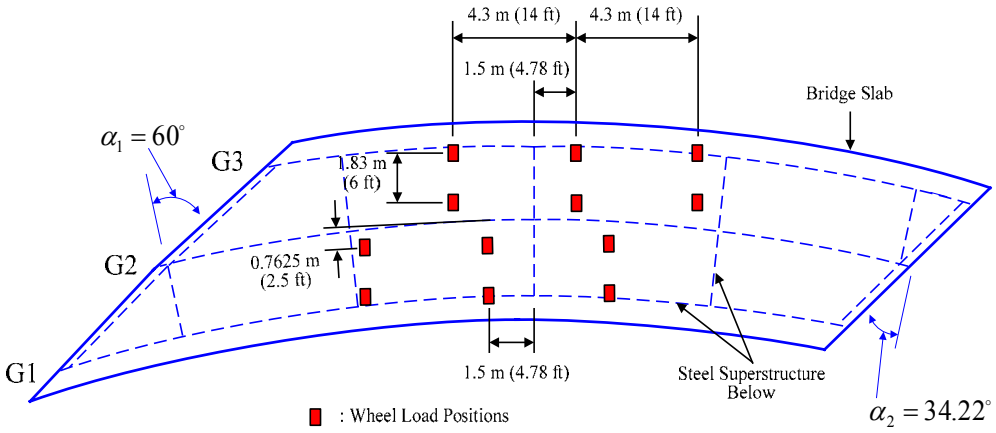

Figure 6.5.18. Two AASHTO HL-93 design truck loads positioned on the slab of the Case 6 skewed composite bridge with a maximum skew angle of 60 degrees used for the elastic design-analysis and the full nonlinear FEA simulation.

This loading pattern is applied with two lane loads similar to the lane loads described in Chapter 2 for the elastic analysis and design. Only the concentrated loads from the AASHTO design trucks are applied in the full nonlinear FEA simulation though.

As can be seen from Figure 6.5.18, the two HL-93 design trucks are positioned on the two traffic lanes with a slight offset from each other, in contrast to the side-by-side placement of the two design trucks in the composite test bridge. Since it is rather awkward and difficult to come up with a simplified loading scheme that can be used for the full nonlinear FEA, the AASHTO design truck loads shown in the Figure6.5.18 are used directly for the full nonlinear FEA. In addition, since the modified bridge is not symmetric in its geometry as well as the above loading, the bridge component responses also lose their symmetry with respect to the bridge midspan. For example, the maximum internal moment of the bridge cross-section is located 14.23 m (47.44 ft) away west end of G3 and 10.8 m (36 ft) from east end as shown in Figure 6.5.19 due to the loads shown in Figure 6.5.18.

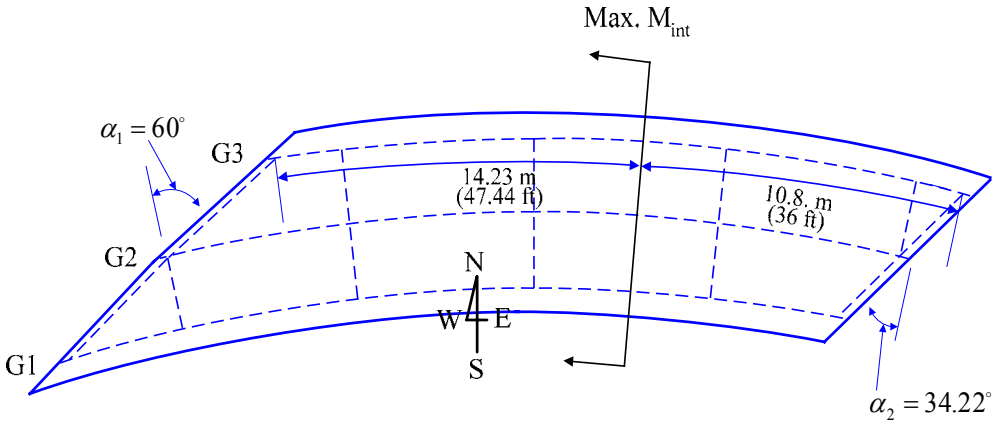

Figure 6.5.19. Plan view of the Case 6 composite bridge (maximum skew angle of 60 degrees) showing the location of the maximum FEA internal moment for both on G3 as well as for the total bridge cross-section.

Also, the locations of the maximum girder internal moments for the non-composite dead load analysis are not the same as the positions associated with the maximum girder internal moments for the composite bridge.

Figures 6.5.20 through 6.5.22 show the midspan internal moments for girders G3, G2 and G1 versus the corresponding midspan live load vertical deflections at the middle of their bottom flanges. Initial dead load moments are included in the plots (2020 kN-m (1490 k-ft) for G3, 912 kN-m (673 k-ft) for G2 and 446 kN-m (336 k-ft) for G1). The linear elastic estimates for the total applied loads corresponding to the M_y- and M_p-based 1/3 rule levels on G3 are 2535 kN (570 kips) and 3314 kN (745 kips).

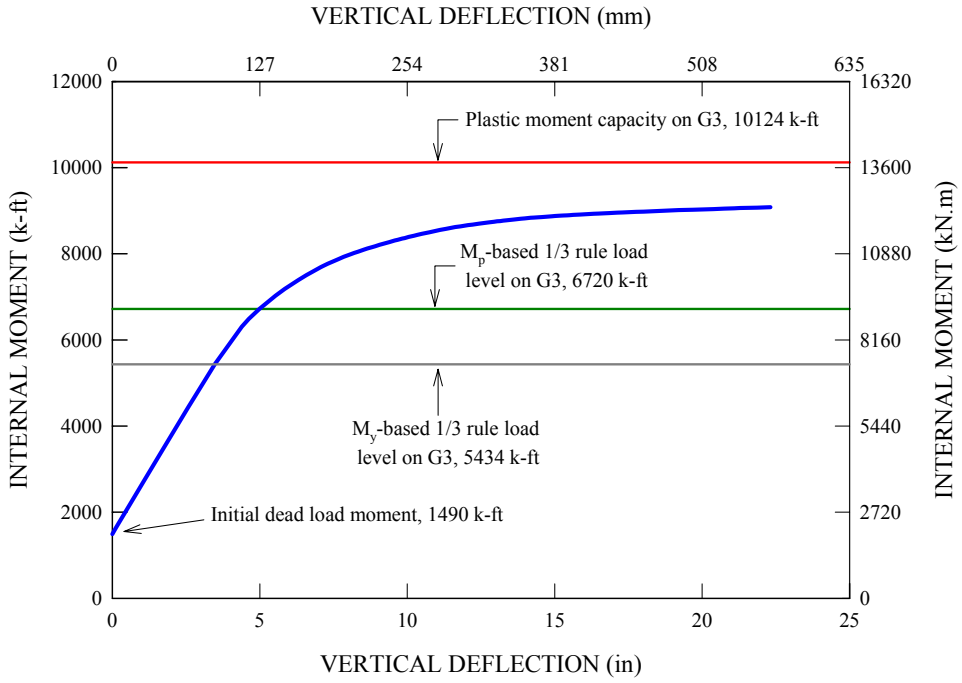

Figure 6.5.20. Case 6 G3 internal moment versus corresponding vertical deflection at the web-flange juncture for the location shown in Figure 6.5.19, initial dead load moment included.

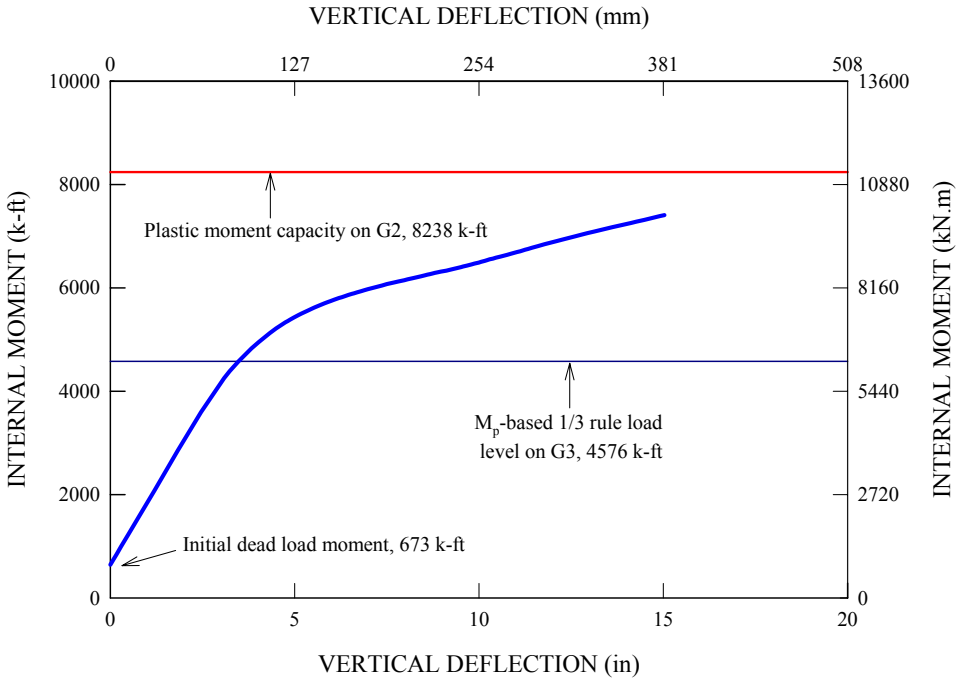

Figure 6.5.21. Case 6 G2 internal moment versus corresponding vertical deflection at the web-flange juncture for the location shown in Figure 6.5.19, initial dead load moment included.

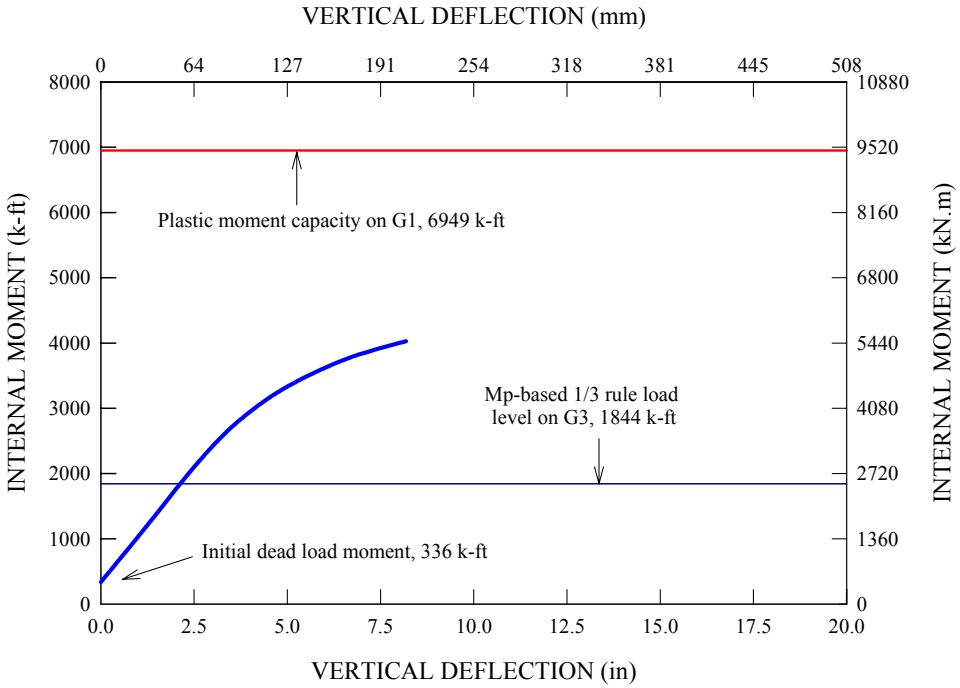

Figure 6.5.22. Case 6 G1internal moment versus corresponding vertical deflection at the web-flange juncture for the location shown in Figure 6.5.19, initial dead load moment included.

Despite the extreme skew angle of 60 degrees, it can be seen that the midspan moments are increased predominantly in a linear fashion for all three girders up to the M_p-based 1/3 rule load level on G3. The G3 moment at the M_p-based 1/3 rule load level is slightly into the nonlinear range of the response as shown in Figure 6.5.20, but its deviation from a linear prediction is minor.

Figure 6.5.23 shows the applied load versus the axial force in the bottom chord of the midspan cross-frame attached to G3, labeled as CF1. Although CF1 is not located precisely at the G3 midspan, the member force in this cross-frame turns is the largest among the cross-frame members within the bridge system for a given load level. The initial dead load axial force in the bottom chord of this cross-frame is 267 kN (60 kips). Contrary to other parametric FEA cases where the member force of the cross-frame located at midspan shows noticeable nonlinear behavior at higher applied load levels than the M_p-based 1/3 rule load level on G3, the member force variation in CF1 is predominantly linear throughout the entire loading history.

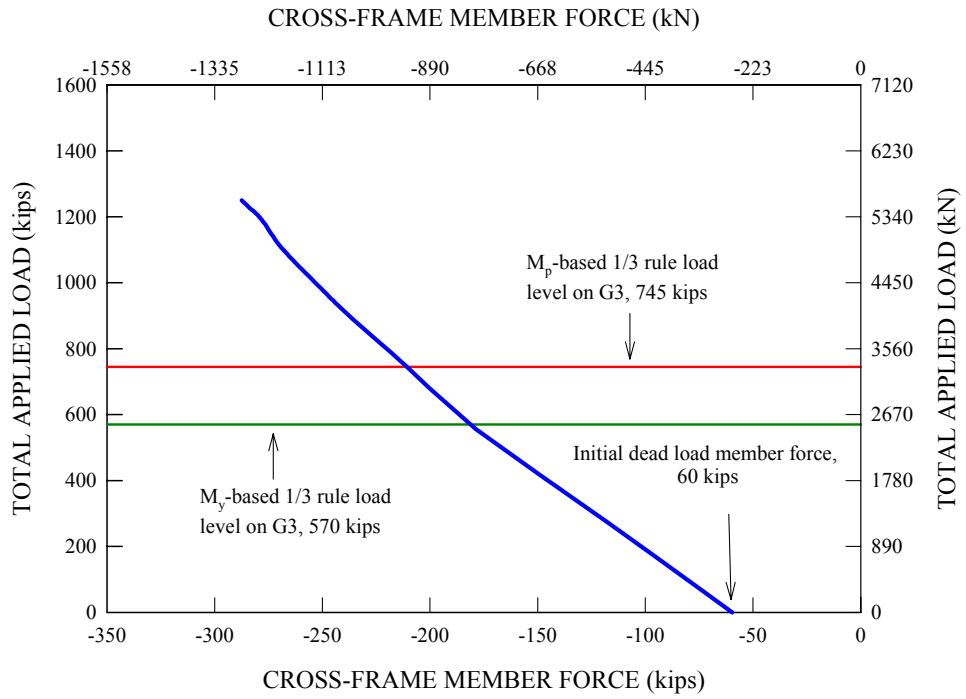

(a) Bottom chord force

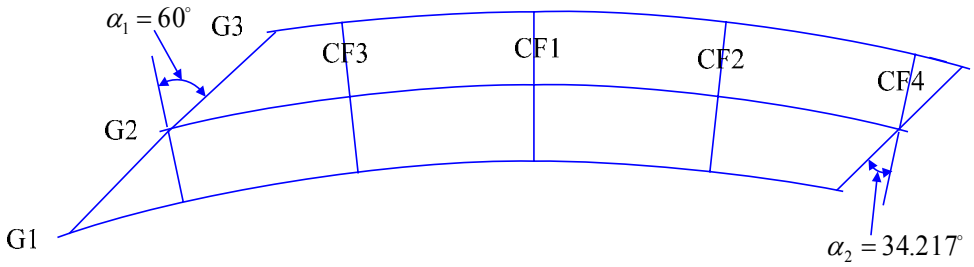

(b) Cross-frame locations

Figure 6.5.23. Case 6 applied load versus axial force in the bottom chord of the cross-frame (CF1) attached to G3, initial dead load axial force included.

Other cross-frame member forces are also checked for the possibilities of severe nonlinear behavior (from the nonlinearity of the girder responses at higher load levels), although their magnitudes are less than those of the cross-frame located at the G2 midspan. Figure 6.5.24 shows the applied load versus the axial forces in the bottom chords of the cross-frames CF2, CF3 and CF4 attached to G3. It can be seen that the member forces in these cross-frames change in a noticeably nonlinear fashion as opposed

to those for CF1. However, it should be noted that the M_p-based 1/3 rule load level on G3 is a reasonable approximate limit for the onset of the nonlinear behavior for these member forces.

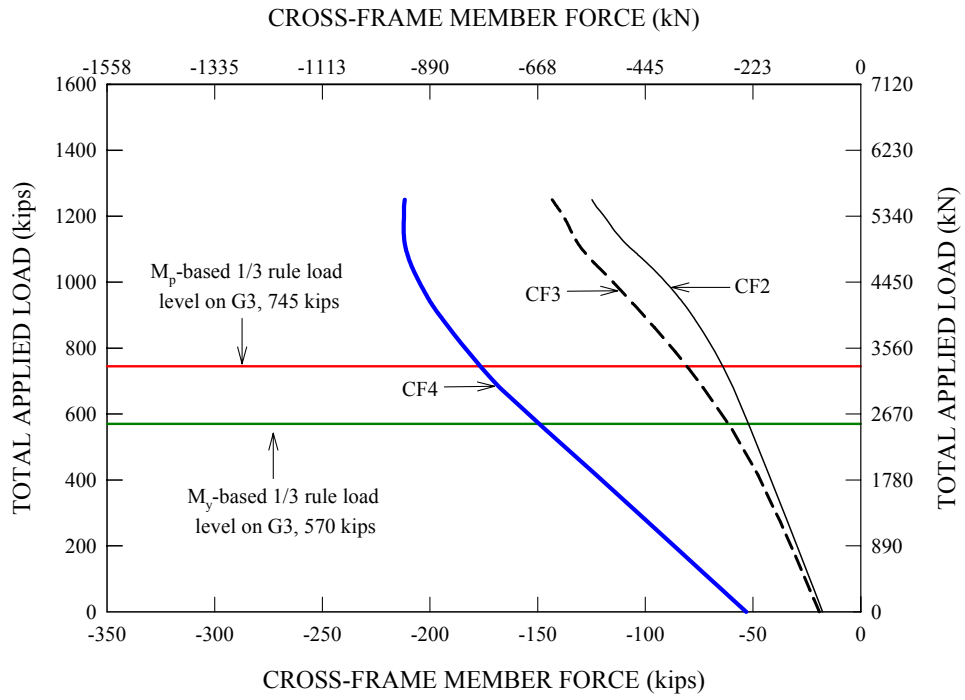

(a) Cross-frame member forces

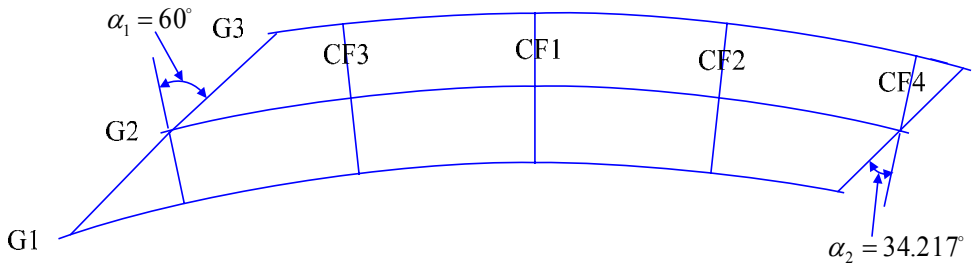

(b) Cross-frame locations

Figure 6.5.24. Case 6 applied load versus axial force in the bottom chord of the cross-frames (CF2, CF3 and CF3) attached to G3, initial dead load axial force included.

Figures 6.5.25 and 6.5.26 show the girder reactions at the two skewed bearing lines versus the total applied load. Both of the plots include initial dead load reactions at zero applied load that are 369 kN (83 kips), 196 kN (44 kips) and 133 kN (30 kips) for G3, G2 and G1, respectively, at the bearing line with the larger skew angle, while they are 276 kN (62 kips), 231 kN (52 kips) and 89 kN (20 kips) at other bearing line. It can be seen that the girder reactions on G3 increase linearly throughout the entire loading history. However, the reactions on G1 and G2 vary in a nonlinear fashion at high load levels. This is particularly the case at the west end. Nonetheless, it is important to note that the reactions on G1and G2 transition from linear behavior to nonlinear behavior after the M_p-based 1/3 rule load level of 3314 kN (745 kips) on G3 is exceeded.

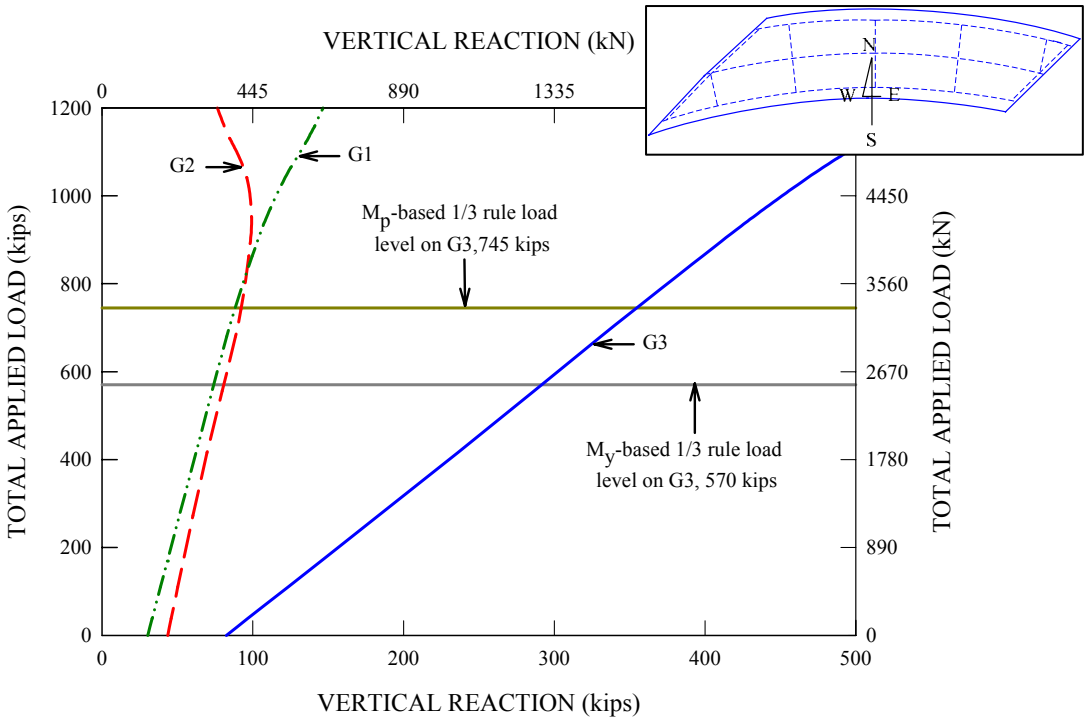

Figure 6.5.25. Case 6 applied load versus west end girder vertical reactions at the supports with a skew angle of 60 degrees, initial dead load reactions included.

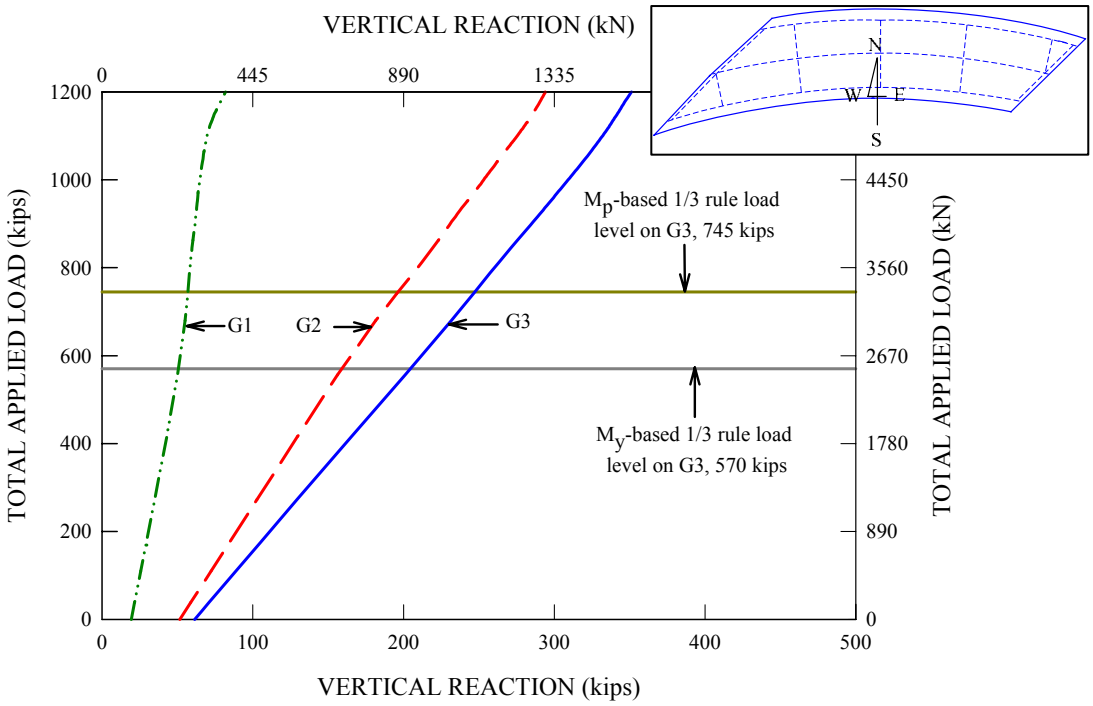

Figure 6.5.26. Case 6 applied load versus east end girder vertical reactions at the supports with a skew angle of 34.2 degrees, initial dead load reactions included.

Figure 6.5.27 provides slab top surface longitudinal strains across the "critical" bridge cross-section at the position shown in Figure 6.5.19 when the total applied load reaches the M_p-based 1/3 rule load level of 3314 kN (745 kips) on G3. The maximum strain of about 1000 με shown in the figure indicates that the concrete slab essentially remains elastic up to the M_p-based 1/3 rule load level. The strains across the bridge slab width show a substantial dip in their magnitude just to the outside of G2. However, the overall distribution is otherwise approximately linear across the bridge deck width. The dip in the strain distributions is believed to be due to localized effects from the load points.

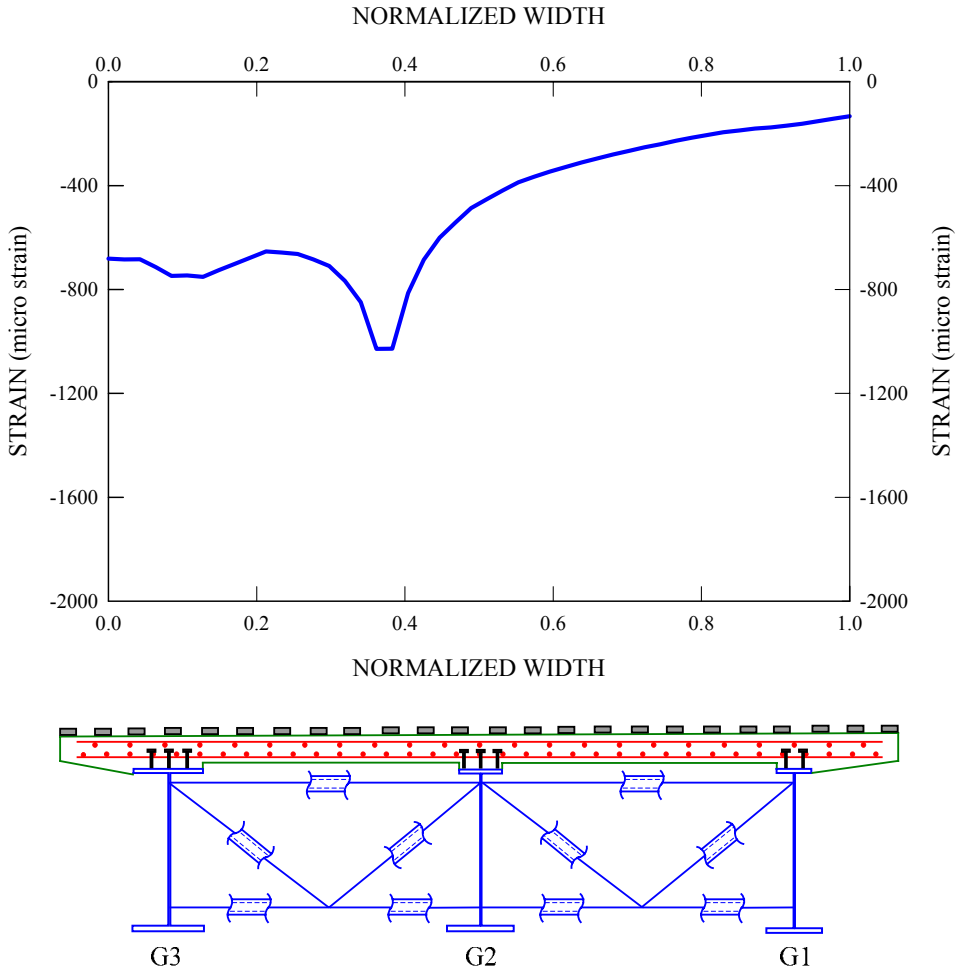

Figure 6.5.27. Case 6 slab top surface longitudinal midspan bridge cross-section at the M_p-based 1/3 rule load level on G3 (total applied load = 3314 kN (745 kips)).

Based on the findings for the above skewed bridge systems, it is clear that all the system and component responses are predominantly linear up to the total applied load level corresponding to the M_p-based 1/3 rule load level on the critical outermost girder, G3. Therefore, it appears that simply-supported horizontally curved composite I-girder bridge systems can be designed based on a linear elastic analysis up to the M_p-based 1/3 rule load level.

6.6 Case 7: Three-Lane Bridge

The base composite test bridge barely accommodates two traffic lanes. This is mainly due to the physical constraints placed on the full-scale test bridge such that it could fit within the testing laboratory. However, bridges often have more than two traffic lanes to accommodate a large traffic volume. Also, although the test bridge has only three I-girders within the system, curved bridges with wider cross-sections often have more than three girders. To extend the simple test bridge configuration to a curved bridge with more traffic lanes, one additional traffic lane is added to the base composite test bridge geometry. This addition in turn requires the use of four instead of three I-girders to achieve an efficient girder spacing.

Figure 6.6.1 shows the girder cross-sections, bridge cross-section and plan view of the resulting four girder bridge. It can be seen that this bridge system consists of four girders spaced radially at 3.0 m (10 ft) on center. The I-girders are labeled G1, G2, G3 and G4, and corresponding radius of curvature is 55.5 m (185 ft), 58.5 m (195 ft), 61.5 m (205 ft) and 64.5 m (215 ft), respectively. The design unity checks for flexure are 0.74, 0.80, 0.9 and 0.92 for the G1, G2, G3 and G4 midspan unbraced lengths, respectively, under the Strength I load combination. Corresponding lateral bending stress limit checks are 0.93, 0.94, 0.92 and 0.95 for G1, G2, G3 and G4, respectively. The overall subtended angle between the girders supports, L/R, is equal to 0.45 for all of the girders, and the subtended angle between the cross-frame locations, L_b/R, is 0.1125, as in the composite test bridge. The bridge overall cross-section width is 10.8 m (36 ft), including the two overhang regions. Each overhang is 0.9 m (3 ft) wide as in the test bridge, which leads to a small tributary slab area for the exterior girders relative to typical designs. The slab thickness is increased from 200 mm (8.0 in) to 240 mm (9.5 in).

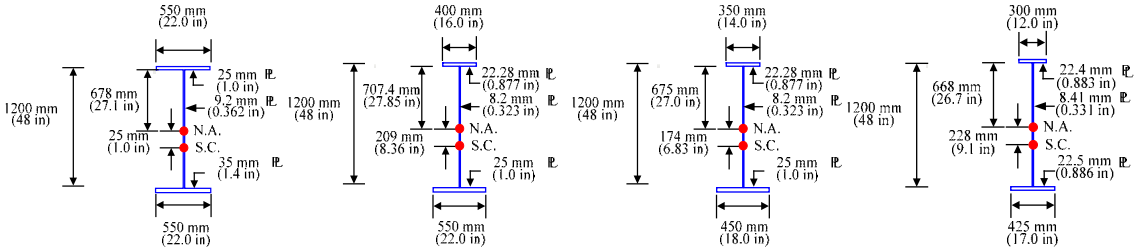

a) G4 cross-section (b) G3 cross-section (c) G2 cross-section (d) G1 cross-section

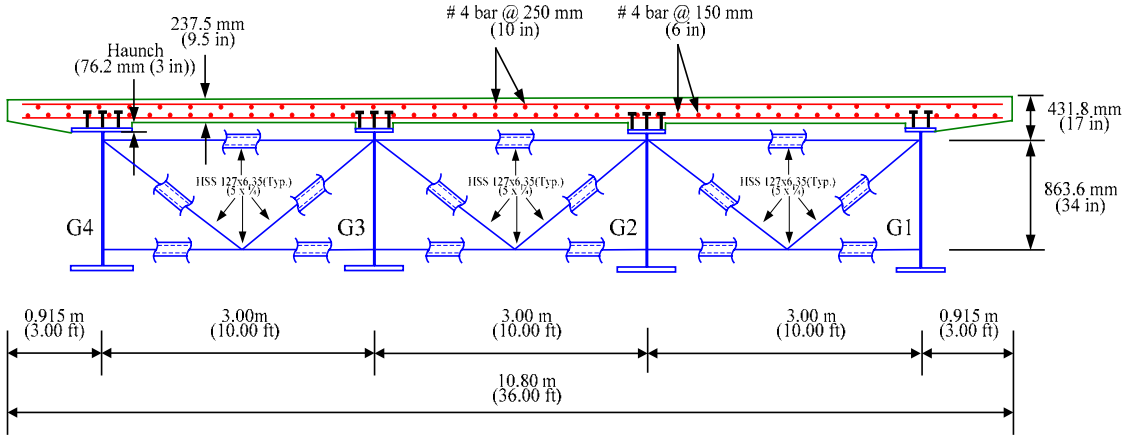

(d) Bridge cross-section

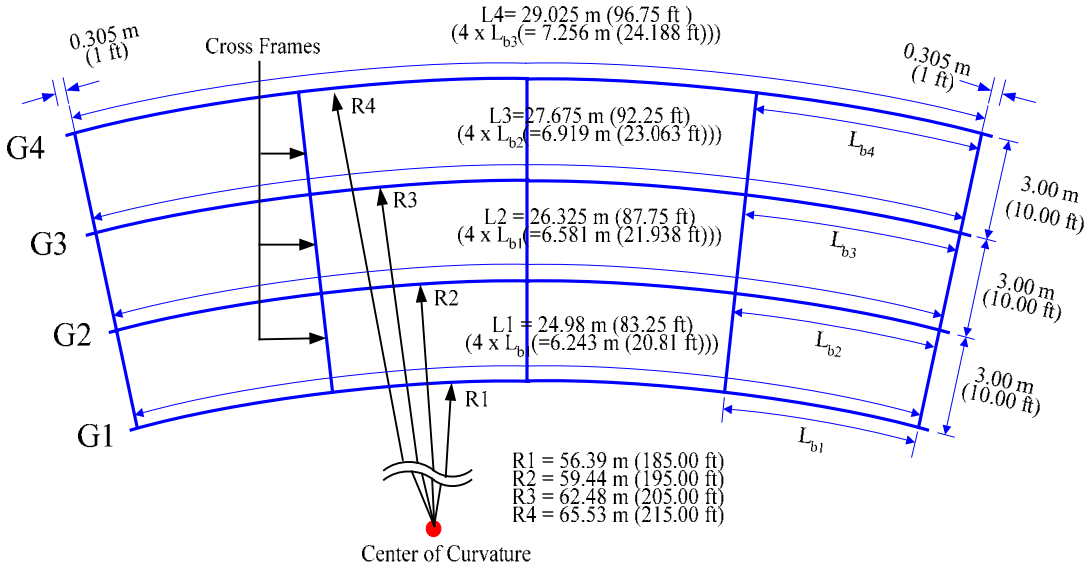

(e) Bridge plan

Figure 6.6.1. Case 7 four girder composite test bridge geometry with three traffic lanes.

This increase in the slab thickness is aimed to avoid potential considerations associated with the appropriate slab effective width, thereby allowing the use of the full tributary width of each composite girder for calculating member section properties.

Figure 6.6.2 provides a schematic showing the two AASHTO HL-93 design truck loads positioned on the slab for the elastic design-analysis to generate a maximum flexural effect on girder G4. This loading is also used (without the corresponding lane load) the full nonlinear FEA simulation of an ultimate load test for this bridge. It is important to recognize that the two truck loading scheme shown here produces the maximum flexural effects on G4 rather than a three truck loading scheme. Interestingly, it is found that the positioning of additional truck on the inside lane between G1 and G2 actually reduces the flexural effects on the outermost girder, G4.

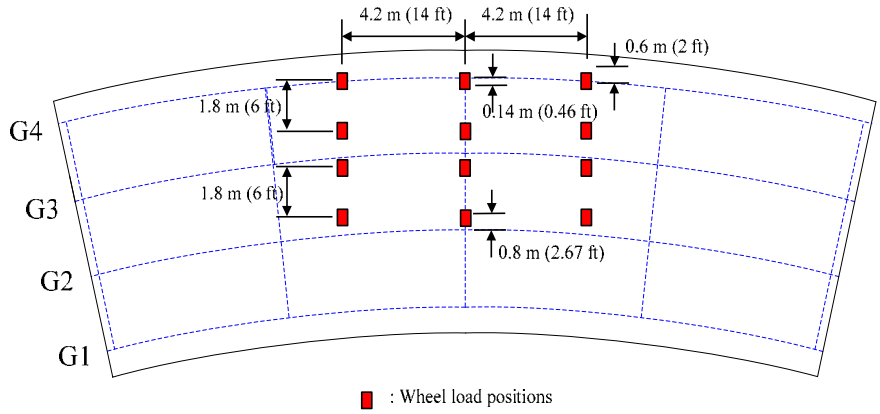

Figure 6.6.2. Case 7 AASHTO HL-93 design truck loads positioned on the slab to produce the maximum flexural effects on G4, used for the elastic design-analysis as well as the full nonlinear FEA simulation.

Figures 6.6.3 through 6.6.6 give the midspan internal moments for the girders G4, G3, G2 and G1 versus the corresponding midspan live load vertical displacements at the

middle of their bottom flanges. The initial dead load moments are included in the plots. The total applied loads corresponding to the M_y- and M_p-based 1/3 rule load levels on G4 are 2553 kN (574 kips) and 3394 kN (763 kips). It can be seen that the midspan moments are increased predominantly in a linear fashion up to the M_p-based 1/3 rule load level on G4 for the G4, G3 and G2 cross-sections. However, Figure 6.6.6 shows that the G1 midspan moment is gradually reduced from its initial positive dead load moment of 822 kN-m (606 k-ft), indicating that the G1 midspan is subjected to negative moment due to the live load. Nonetheless, it is important to note that the internal moment variations on G1 decrease in a linear fashion up to the M_p-based 1/3 rule load level on G4.

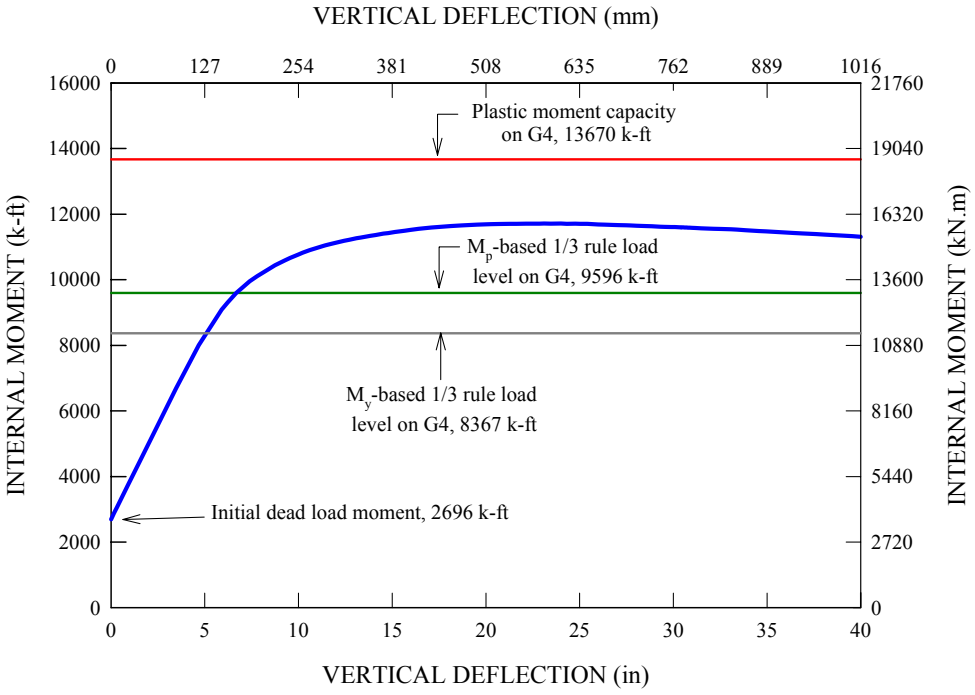

Figure 6.6.3. Case 7 G4 midspan internal moment versus corresponding vertical deflection at the web-flange juncture, initial dead load moment included.

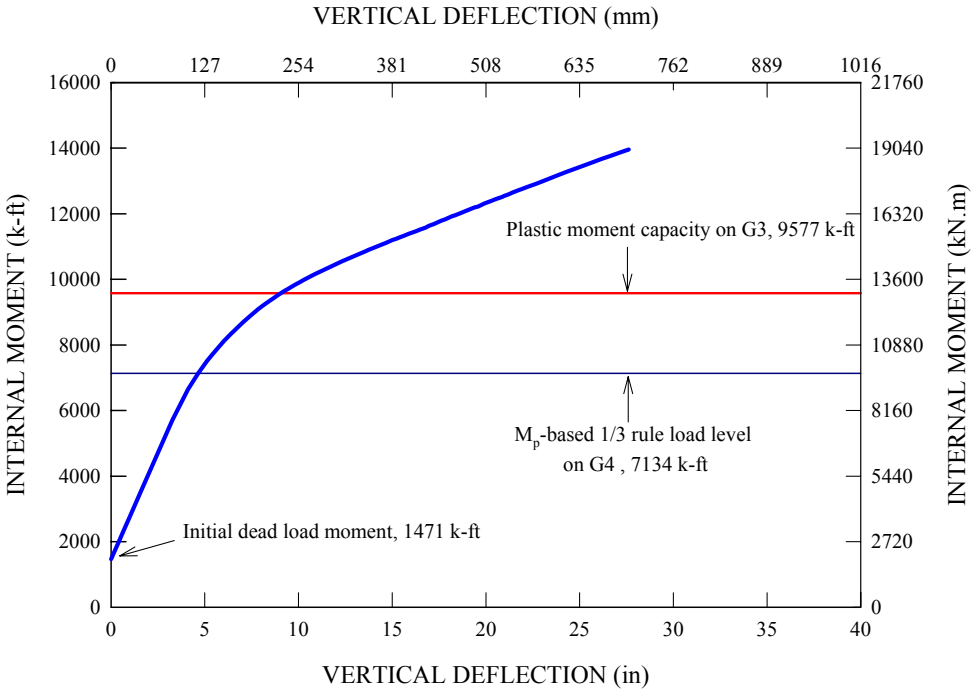

Figure 6.6.4. Case 7 G3 midspan internal moment versus corresponding vertical deflection at the web-flange juncture, initial dead load moment included.

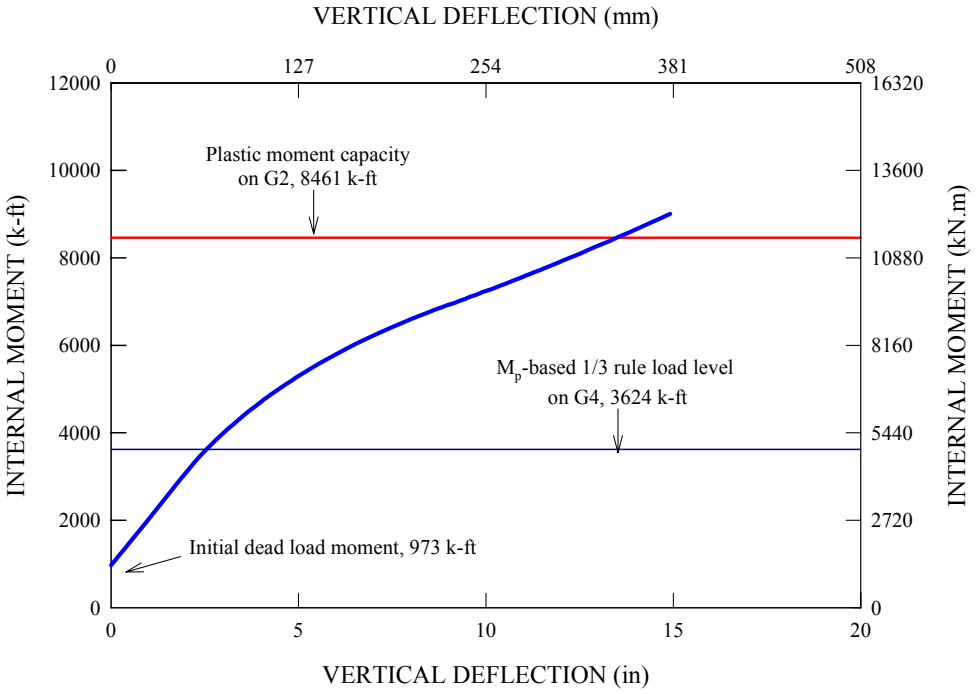

Figure 6.6.5. Case 7 G2 midspan internal moment versus corresponding vertical deflection at the web-flange juncture, initial dead load moment included.

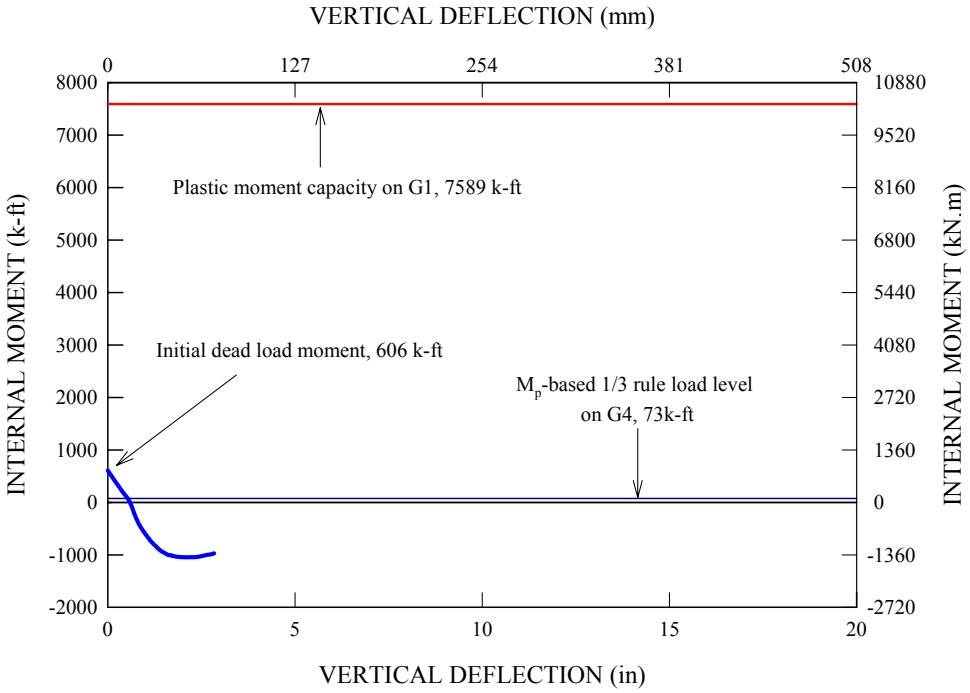

Figure 6.6.6. Case 7 G1midspan internal moment versus corresponding vertical deflection at the web-flange juncture, initial dead load moment included.

Figure 6.6.7 gives the axial force in the bottom chord of the midspan cross-frame attached to G4 throughout the loading history. It can be seen that the extent of the nonlinearity at the M_p-based 1/3 rule load level on G4 is quite minor. Interestingly, one can observe that a linear elastic analysis always produces a conservative estimate of the cross-frame member axial forces at the M_p-based 1/3 rule load level. This statement also applies to all the other cases considered so far.

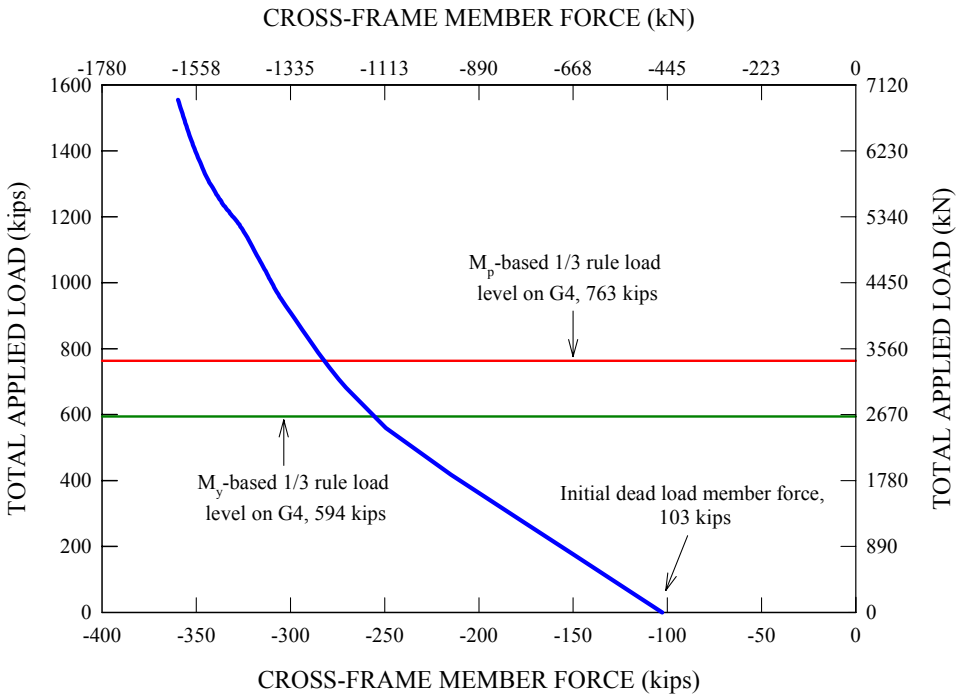

Figure 6.6.7. Case 7 applied load versus axial force in the bottom chord of the midspan cross-frame attached to G4, initial dead load axial force included.

Figures 6.6.8 and 6.6.9 provide the west and east girder reactions versus the total applied load throughout the analysis. For both of the plots, it can be seen that the girder reactions increase in a linear fashion throughout the analysis, with the exception of minor nonlinearities observed in the reactions for G1, G2 and G3. As evidenced by the G1 internal moment variation in Figure 6.6.6, it can be seen that the G1 end reactions on both sides gradually decrease from initial dead load positive reactions, and their sign changes from positive to negative eventually with increasing applied loads, indicating that G1 may be lifted off of its bearings if proper tie-down measures are not taken.

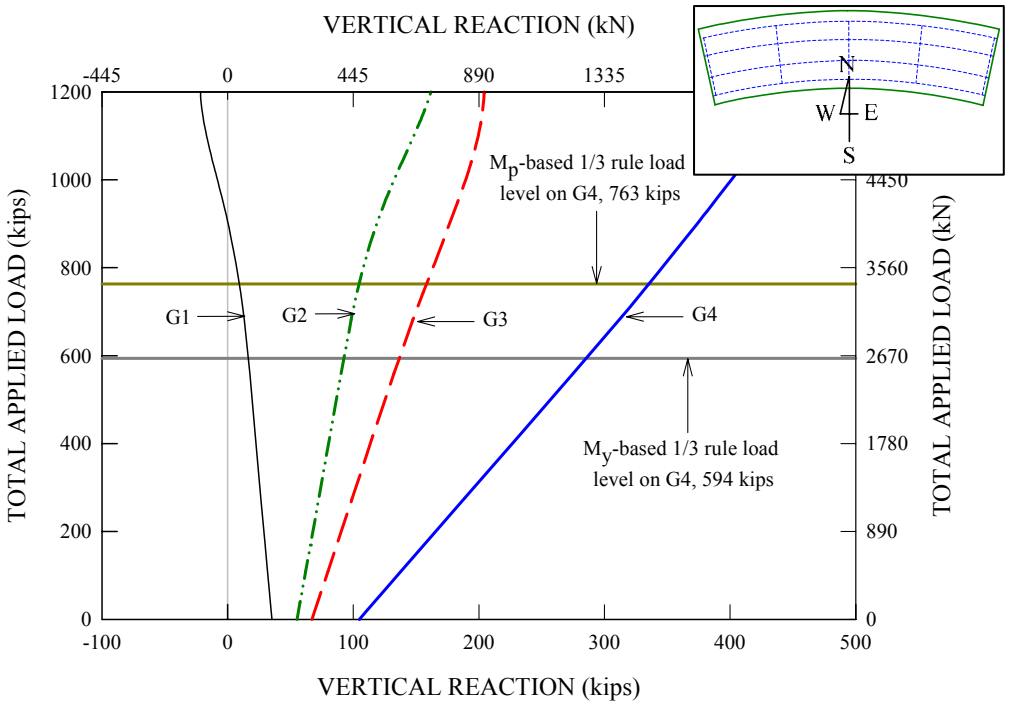

Figure 6.6.8. Case 7 applied load versus west end girder vertical reactions, initial dead load reactions included.

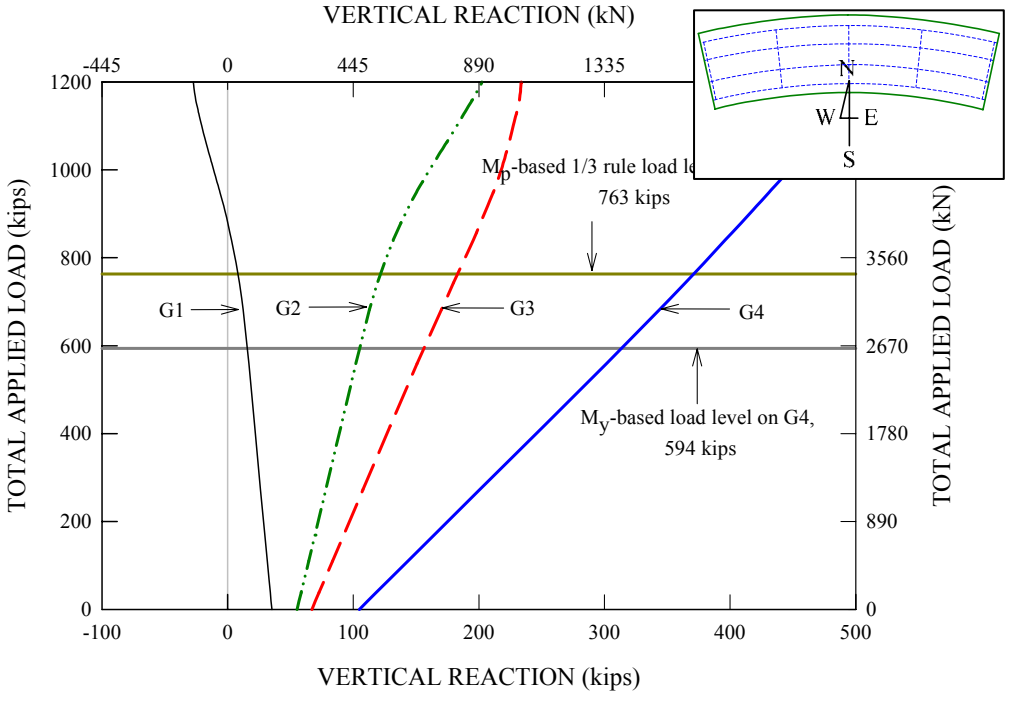

Figure 6.6.9. Case 7 applied load versus east end girder vertical reactions, initial dead load reactions included.

However, it is important to note that G1 does not lift off of its supports at the M_p-based 1/3 rule load level on G4. Therefore, the magnitude of the applied loadings that would create uplift at the G1 bearings is significantly higher than would be necessary based on the AASHTO design criteria, either at the M_y- or M_p-based 1/3 rule limit on a critical girder.

Figure 6.6.10 shows the slab top surface longitudinal strains across the midspan bridge cross-section at the M_p-based 1/3 rule load level on G4. It can be seen that the slab strains vary linearly across the bridge cross-section as in the base composite test bridge. On the other hand, it is important to note that tensile strains are developed on the slab portion of the G1 composite section with a maximum of 170 με, which is slightly less than the concrete cracking strain. Also, despite localized strain peaks, it is important to note that the maximum compressive concrete strain is never beyond 1200 με, indicating that the bridge slab strains are only slightly above the strain associated with the elastic limit in the concrete compressive stress-strain response at the above load level.

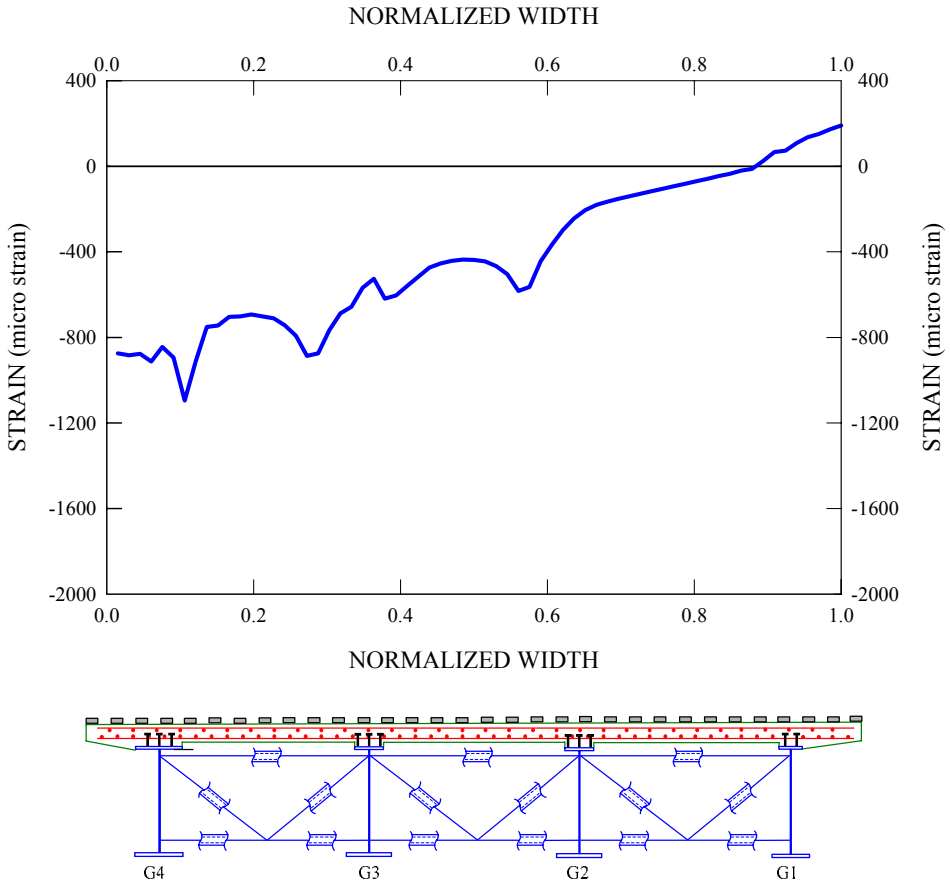

Figure 6.6.10. Case 7 slab top surface longitudinal strains across the midspan cross-section at the M_p-based 1/3 rule load level on G4 (total applied load = 3394 kN (763 kips)).

6.7 Case 8: Yielding and Failure of Critical Cross-Frame Members

The cross-frames in the composite test bridge were ensured to remain elastic during the ultimate load test by increasing the areas for members anticipated to experience yielding. The retrofitted members were the diagonals and the bottom chord members for the mid- and quarter-span cross-frames located between G2 and G3. For these members, the retrofitted areas are much larger than those required for the factored axial forces based on the design analysis. Typically, the cross-frame members are sized for the factored member forces under the most critical load combination. For stocky members

such as the test bridge cross-frame members, their nominal strength behavior can be approximated reasonably well by the yielding behavior of their cross-sections, shown by the stress-strain curve of Figure 3.3.6.

One can raise a legitimate question regarding how the test bridge system would respond to yielding of the cross-frame members. Furthermore, one can envision a rather extreme case where one of the critically-loaded cross-frame members completely loses its load-carrying capacity. Engineers typically should suspect that curved bridges may not have sufficient capabilities to redistribute released forces from a failed cross-frame member to other less critically-loaded components, potentially leading to an abrupt overall system failure instead of a ductile failure. In this regard, there is a need to consider several idealized cross-frame member failure scenarios to gain a better understanding of the effects on the system strength behavior.

Four failure scenarios are considered in this section. The first one relates to the case in which the most critically-loaded cross-frame member, the bottom chord attached to the outermost girder, G3, of the midspan cross-frame in the test bridge, reaches its yield stress shown in Figure 3.3.6 at the M_p-based 1/3 rule load level on G3. It is found that a member area of 27.4 cm^2 (4.25 in^2) is required for this scenario. Therefore, these areas are specified for the bottom chord and the diagonals of the mid- and quarter-span cross-frames located between G2 and G3. These areas are also used in the other FEA solutions outlined below. Second, the other rather extreme scenario relates to the case in which the bottom chord on the above cross-frame is effectively removed from the bridge system at the M_p-based 1/3 rule load level on G3, assuming that there is zero resistance provided from the failed member. The third scenario assumes a fracture (pseudo-statically) of the

tension diagonal of the midspan cross-frame connected to G3 at the M_p-based 1/3 rule load level on G3. Lastly, the fourth scenario assumes that the bottom chord and tension diagonal of the midspan cross-frame between G2 and G3 fail catastrophically at the M_p-based 1/3 rule load level on G3 such that they both suddenly lose all their load-carrying capacities. The M_p-based 1/3 rule load level on G3 is selected in the above scenarios since this would lead to the maximum forces in the system and the greatest required redistribution at the cross-frame member failures based (based on the suggested potential use of the M_p-based 1/3 rule as a design limit for the I-girders).

One important assumption invoked for the above failure scenarios is that the adjacent quarter-span cross-frame members respond in a ductile fashion if they yield after the failure of the compression bottom chord or/and the tension diagonal of the midspan cross-frame. Otherwise, the bridge system may not be able to withstand the critical cross-frame member failures. In what follows, analysis results for each case are presented with a focus on behavioral changes of the test bridge after either yielding or complete failure of the selected cross-frame members.

6.7.1 Case 8a: Yielding of the Bottom Compression Chord of the Midspan Cross-Frame Attached to G3

Figure 6.7.1 provides two FEA predictions of the midspan vertical deflection at the center of the G3 bottom flange due to the applied loads. The dashed line represents the FEA solution for the composite test bridge, where yielding of the cross-frame members is prevented. In contrast, the solid line shows the FEA solution if the compression bottom chord of the midspan cross-frame experiences general yielding (based on the stress-strain curve of Figure 3.3.6) starting at the M_p-based 1/3 rule load level on G3.

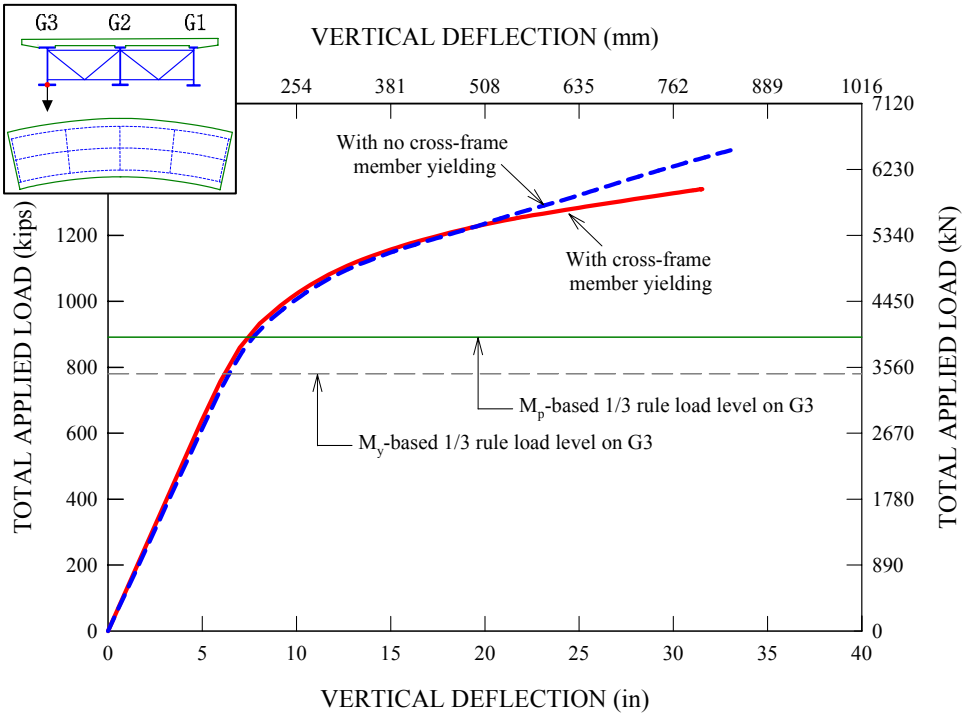

Figure 6.7.1. Applied load versus predicted midspan vertical live load deflections at the G3 bottom web-flange juncture with and without assumed general yielding of the bottom chord of the midspan cross-frame attached to G3 at its design strength limit.

Figure 6.7.1 shows that the two FEA solutions are essentially identical up to a total applied load of 5340 kN (1200 kips). At larger applied loads, the FEA solution allowing for the yielding of the bottom chord makes a noticeable departure from the base FEA solution. It can be seen that the bridge system resistance is weakened by the effect of the cross-frame member yielding. Nonetheless, it is important to note that yielding of the critical cross-frame bottom chord does not cause any sudden loss in the ability of the bridge to support greater loads.

Similarly, Figure 6.7.2 provides two different FEA solutions for the axial force variation in the bottom chord of the midspan cross-frame attached to G3. It can be seen that the FEA solution indicated by the solid line carries slightly smaller axial member

forces than the other FEA solution represented by the dashed line at small load levels. This is simply due to the fact that the former FEA solution utilizes a smaller member area as required by the member forces at the M_p-based 1/3 rule load level on G3. Also, the solid curve tends to deviate somewhat more from the dashed curve at load levels larger than load level at which the bottom chord starts to yield. Other than that, there are strong similarities between the two FEA solutions.

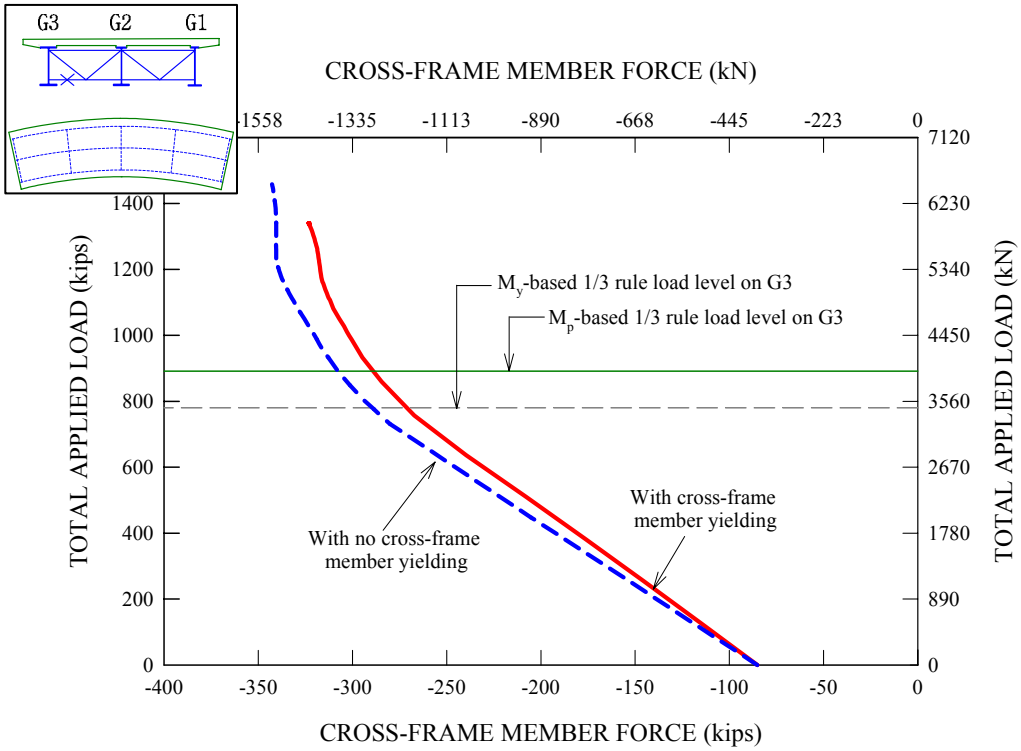

Figure 6.7.2. Applied load versus axial force in the bottom chord of the midspan cross-frame attached to G3, initial dead load axial forces included, with and without assumed general yielding of the bottom chord at the M_p-based 1/3 rule limit on G3.

The member forces reach a plateau at the ultimate load level of about 6230 kN (1400 kips) in the base FEA solution, while the member forces are smaller (due to the yielding of the chord) but still slightly increasing at this level in the modified solution. However,

a clear distinction should be made for the source of the plateau appearance between the two FEA solutions. As mentioned in Chapter 5, the appearance of the plateau for the base FEA solution due to the fact that G3 reaches its full section capacity at midspan. That is, there is no cross-frame member yielding involved in this case. However, the appearance of the plateau for the other FEA solution allowing for the member yielding is believed to be due both to the yielding of G3 and due to the cross-frame member yielding. In spite of the yielding of the cross-frame bottom chord, it is important to note that this member continues to resist axial forces as shown in Figure 6.7.2. This also shows that the yielding of the critically-loaded cross-frame member at the M_p-based 1/3 rule load level does not lead to an abrupt reduction in the overall system capacity.

6.7.2 Case 8b: Complete Loss of the Bottom Compression Chord of the Midspan Cross-Frame Attached to G3

Figure 6.7.3 provides two FEA predictions of the midspan vertical deflection at the center of the G3 bottom flange due to the applied loads.. The dashed line represents the base FEA solution that does not allow for any yielding or failure of the cross-frame members. In contrast, the solid line represents the other FEA solution accounting for the failure (removal) of the bottom chord of the midspan cross-frame attached to G3 at the M_p-based 1/3 rule load level on G3. Figure 6.7.4 shows that the axial force of 1228 kN (276 kips) in the midspan bottom chord at the M_p-based 1/3 rule load level is instantly reduced to zero upon the removal of the midspan bottom chord. It can be seen in Figure 6.7.3 that the test bridge has a corresponding dramatic increase in the midspan deflection of G3. The total deflection is instantly increased from 186 mm (7.44 in) to 234 mm (9.36 in) upon the removal of the bottom chord due to an equilibrium shift.

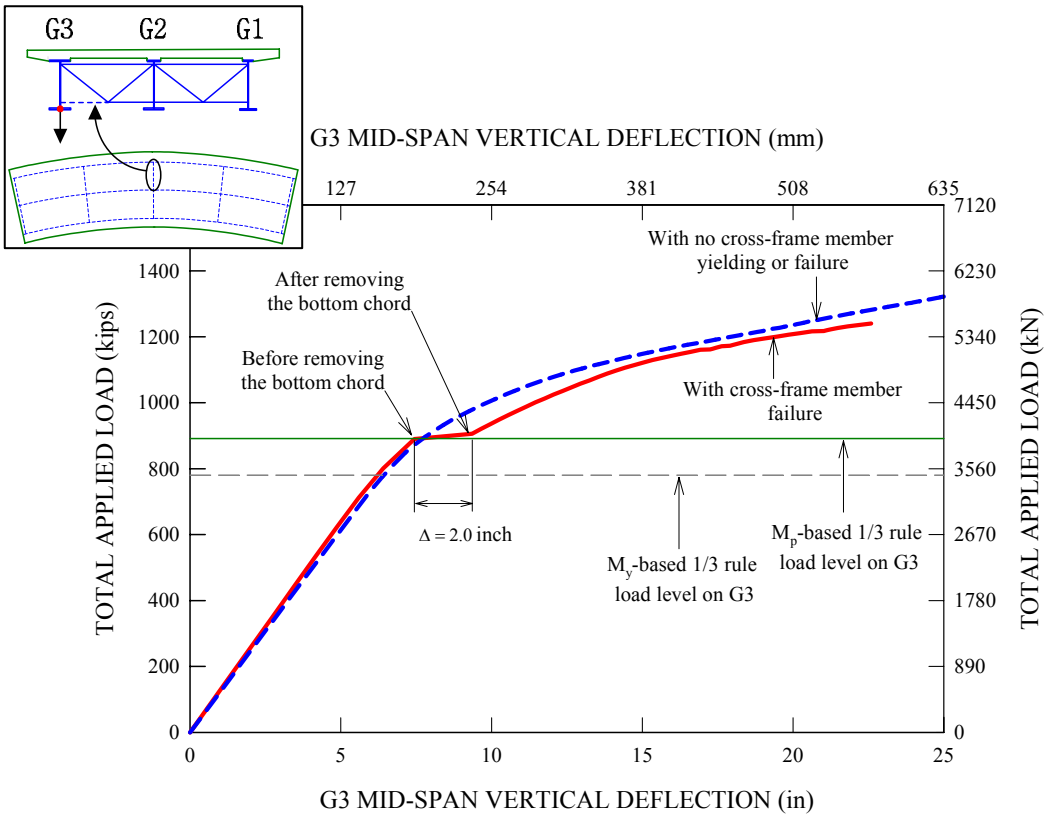

Figure 6.7.3. Applied load versus predicted midspan live load vertical deflections at the G3 bottom web-flange juncture with and without the bottom chord removed at the M_p-based 1/3 rule load level on G3 (total applied load = 3959 kN (890 kips)), dead load deflections not included in the plot.

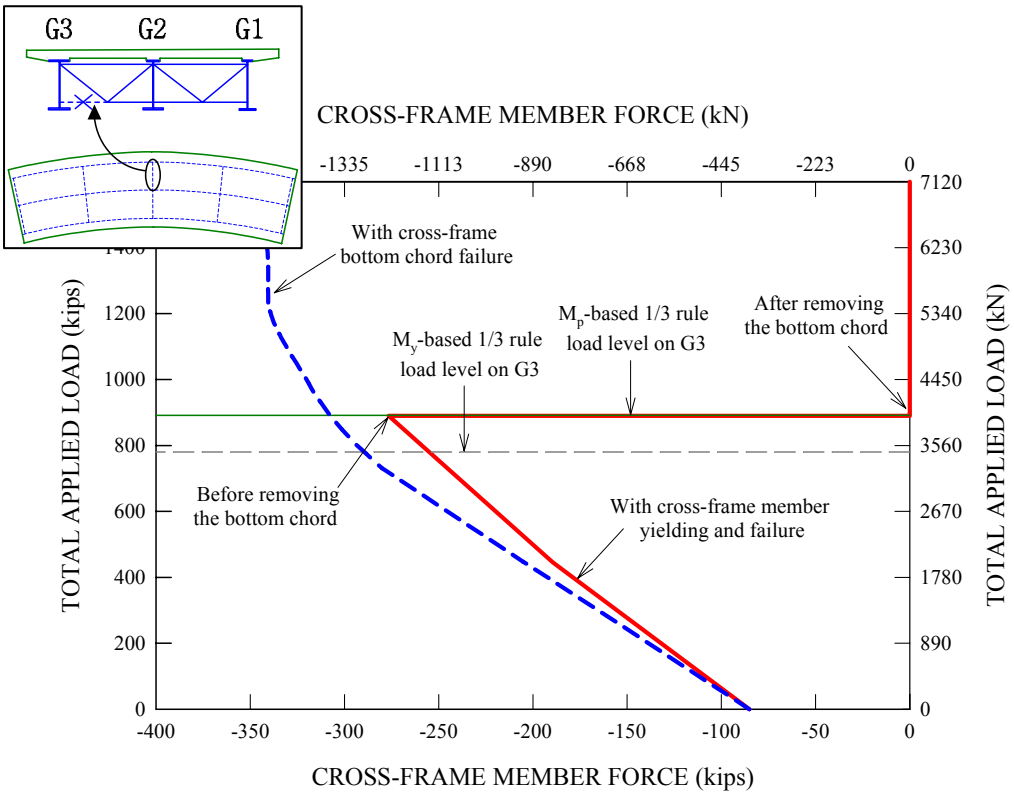

Figure 6.7.4. Applied load versus axial force in the bottom chord of the midspan cross-frame attached to G3, initial dead load axial force included, with and without the midspan bottom chord removed at the M_p-based 1/3 rule applied load level on G3 (total applied load = 3959 kN (890 kips)).

The use of the term equilibrium shift is intended to indicate that the large bottom chord axial force resisting the radial forces coming from the web and bottom flange of G3 needs to be redistributed within the modified bridge configuration missing the midspan bottom chord. With the new equilibrium reached, it is found that a significant portion of the outermost girder, G3, is yielded. Also, there is a noticeable increase in the slab top surface longitudinal strains. Nonetheless, the test bridge continues to support more applied loads, indicating that the test bridge system has greater redundancy than expected. Other component and system responses are presented in the following.

Similar to Figure 6.7.4, Figure 6.7.5 provides two FEA solutions for the axial force in the bottom chord of the quarter-span cross-frame attached to G3.

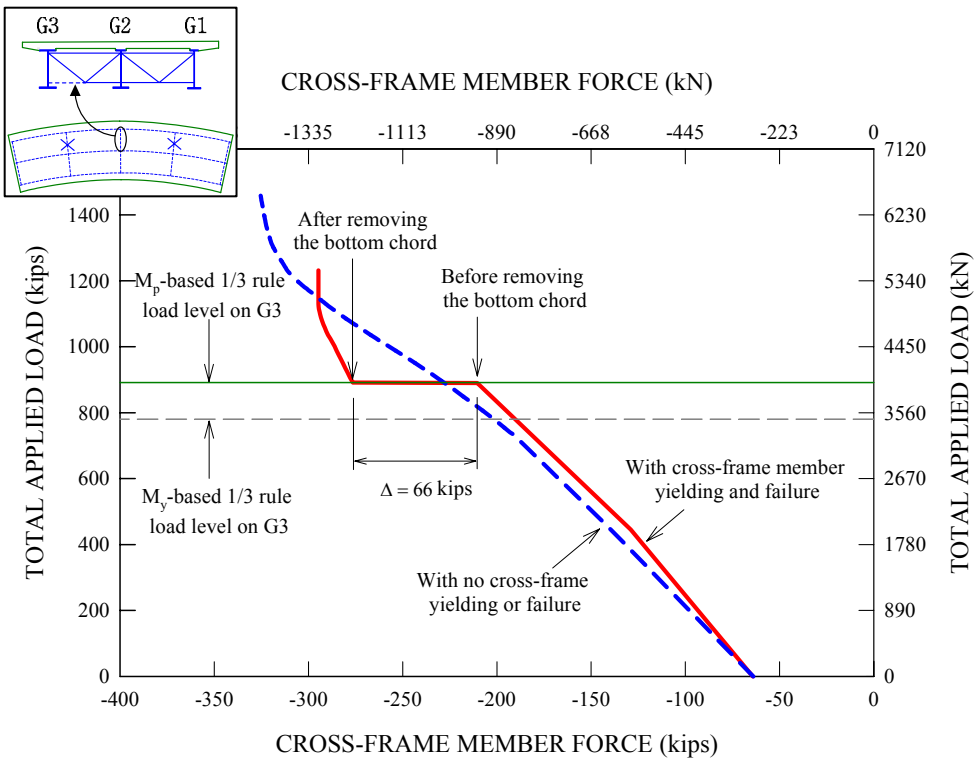

Figure 6.7.5. Applied load versus axial force in the bottom chord of the quarter-span cross-frame attached to G3, initial dead load axial force included, with and without the midspan bottom chord removed at the M_p-based 1/3 rule load level on G3 (total applied load = 3959 kN (890 kips)).

It can be seen that the axial force in the quarter-span bottom chord is instantly increased from 934 kN (210 kips) to 1228 kN (276 kips) due to the equilibrium shift. The dramatic increase of the member force yields the quarter-span bottom chords at the instant when the midspan bottom chord is removed from the bridge FEA model. As a result, one can observe from Figure 6.7.5 that further loading of the test bridge does not increase the bottom chord force significantly. It can be seen that the bottom chord axial force reaches a bounding value of 1335 kN (300 kips) in the limit.

Figure 6.7.6 shows the girder reactions versus the total applied load for the case with the bottom chord of the midspan cross-frame removed at the M_p-based 1/3 rule load level on G3. It can be seen that the girder reactions increase in a linear fashion before and after the removal of the midspan bottom chord, but with different slopes.

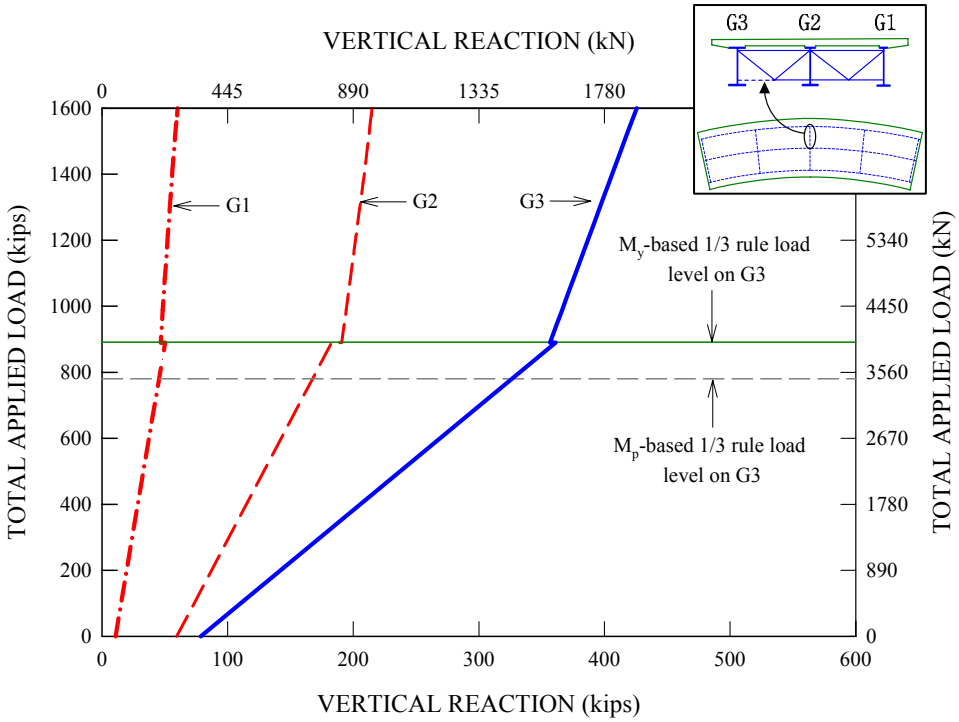

Figure 6.7.6. Case 8b applied load versus girder vertical reactions before and after the removal of the bottom chord of the midspan cross-frame attached to G3.

Unlike other responses presented above, it can be seen that there are only small changes in the girder reactions after the removal of the midspan bottom chord: small reductions for the G1 and G3 end reactions and a small increase for the G2 girder reaction. This should not come as a surprise, considering the fact that girder reactions should not change before and after the removal of the compression bottom chord in order to satisfy a global equilibrium. Equilibrium of the bridge requires a large vertical reaction on G3. In other words, although there are some changes in the force transfer mechanism among the bridge girders, the resulting girder reaction forces should not change significantly before and after the removal of the midspan bottom chord.

6.7.3 Case 8c: Fracture of Tension Diagonal in the Midspan Cross-Frame Attached to G3

Figure 6.7.7 compares the G3 midspan vertical deflection obtained from the test bridge FEA simulation involving a pseudo-static fracture of the tension diagonal in the cross-frame attached to G3 at midspan to the corresponding prediction from the base full nonlinear FEA simulation where no cross-frame member yielding or failure is allowed. Dead load deflections are not included in the plot. Similar to the failure of the bottom chord of the midspan cross-frame attached to G3, the tension diagonal attached to G3 is removed from the bridge FEA model once the model is loaded to the M_p-based 1/3 rule load level on G3 of 3959 kN (890 kips). As can be seen from Figure 6.7.7, the total vertical deflection is instantly increased from 186 mm (7.44 in) to 194 mm (7.77 in) with the total applied load fixed at 3959 kN (890 kips) upon the removal of the tension diagonal, which is a manifestation of the equilibrium shift between two different bridge configurations with and without the tension diagonal at the midspan.

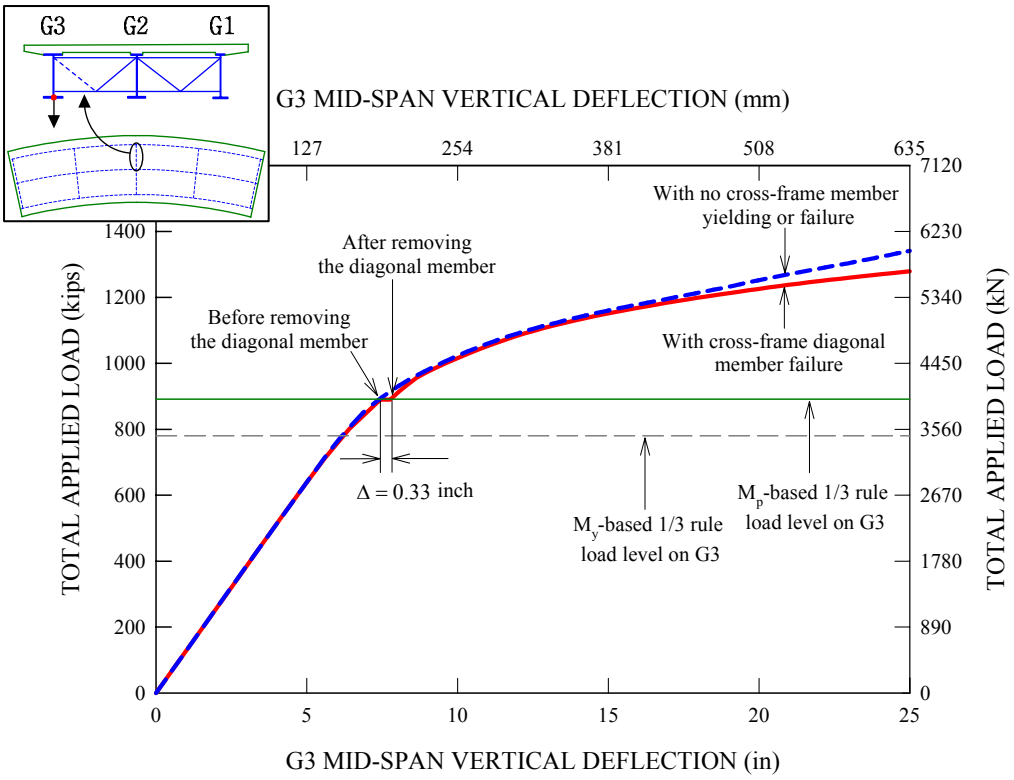

Figure 6.7.7. Applied load versus predicted midspan live load vertical deflection at the G3 bottom web-flange juncture with and without the midspan tension diagonal removed at the M_p-based 1/3 rule load level on G3 (total applied load = 3959 kN (890 kips)), dead load deflections not included in the plot.

The deflection increase of 8.3 mm (0.33 in) for this case is not as large as the deflection increase of 50 mm (2.0 in) for the previous case when the bottom chord is removed. It is believed that this small increase in the vertical deflection is mainly due to the fact that a portion of the slab adjacent to the failed diagonal member is able to effectively replace the role of the diagonal for the shear transfer, thereby limiting the change in the equilibrium configuration to a minimum. In fact, it can be seen in Figure 6.7.7 that, upon additional loading of the test bridge FEA model after the removal of the tension diagonal, the deflection curve tends to trace back to the deflection curve for the base bridge FEA simulation when there is no yielding or failure of the cross-frame

members. However, it should be noted that, for significantly high applied load levels, the nonlinearity in the deflection curve is higher for the case without the tension diagonal than for the base case in which this member remains intact. This should not come as a surprise in view of the fact that the slab concrete would experience some reduction in stiffness compared to the previously assumed elastic response of the cross-frame tension diagonal at the high applied load levels. However, in the case of the removal of the compression bottom chord, there is no alternate load path in the immediate vicinity of the removed member such as the test bridge slab for the tension diagonal. Naturally, the test bridge needs to undergo a more significant change in the equilibrium configuration in Case 8b.

Figures 6.7.8 and 6.7.9 show the applied load versus the axial force in the bottom chord of the mid- and quarter-span cross-frames attached to G3. The initial dead load member forces are included in the plots. In contrast to the small change in the girder vertical deflection, Figure 6.7.8 shows that the axial force for the bottom chord of the midspan cross-frame experiences a significant drop of 490 kN (110 kips) due to the removal of the tension diagonal. This is also in strong contrast with a mild increase of 70 kN (16 kips) in the axial force in the bottom chord of the quarter-span cross-frame.

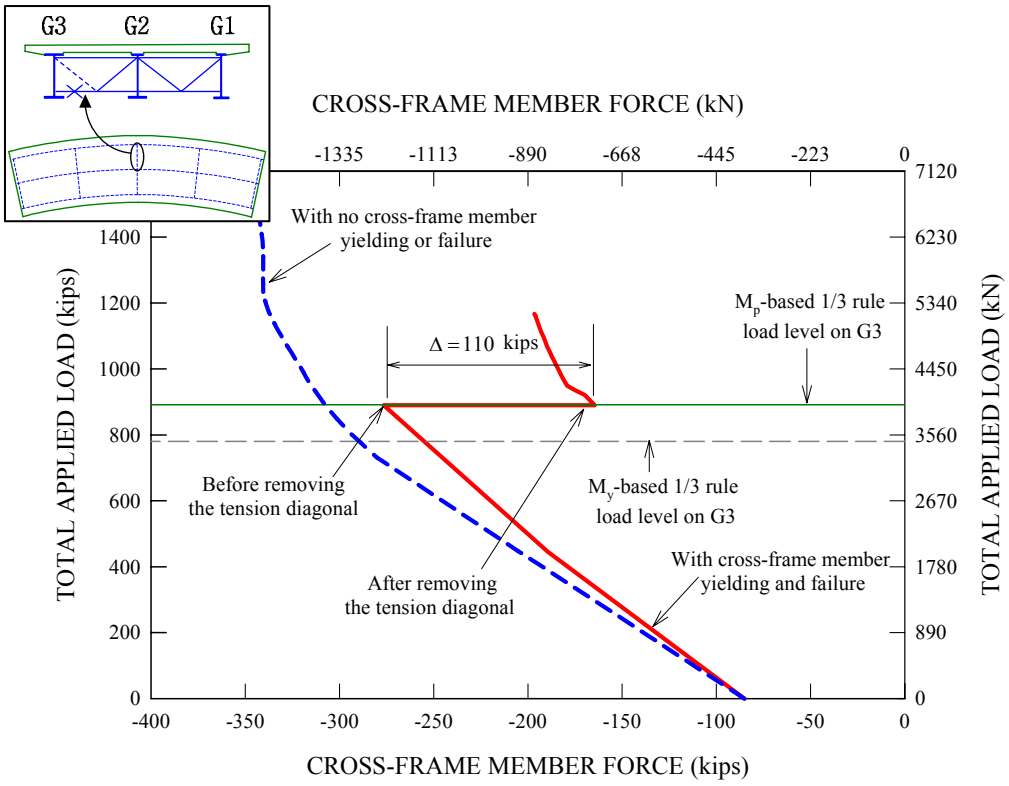

Figure 6.7.8. Applied load versus axial force in the bottom chord of the midspan cross-frame attached to G3, initial dead load axial force included, with and without the midspan tension diagonal removed at the M_p-based 1/3 rule load level on G3 (total applied load = 3959 kN (890 kips)).

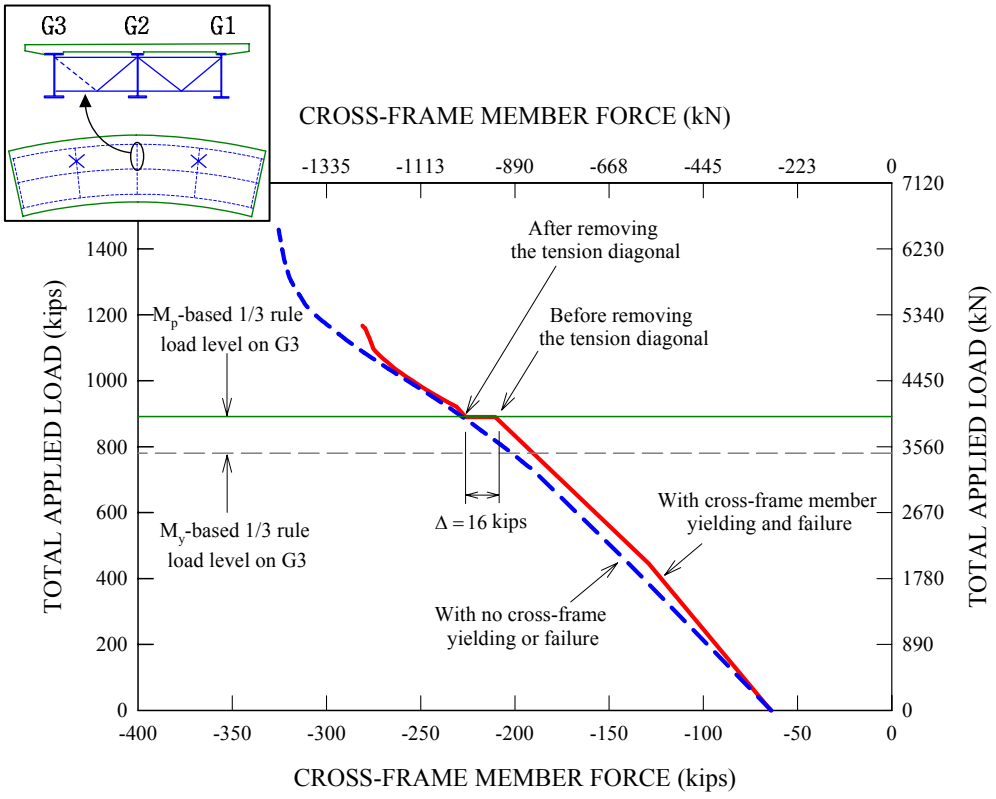

Figure 6.7.9. Applied load versus axial force in the bottom chord of the quarter-span cross-frame attached to G3, initial dead load axial force included, with and without the midspan cross-frame tension diagonal removed at the M_p-based 1/3 rule load level on G3, (total applied load = 3959 kN (890 kips)).

Figure 6.7.10 provides the girder vertical reactions before and after removing the tension diagonal of the midspan cross-frame attached to G3. It can be seen that there are small changes in the reactions at the M_p-based 1/3 rule load level when the tension diagonal is removed: a small decrease for the G2 and G3 reactions and a small increase for the G1 reaction. Nonetheless, the girder reactions continue to increase predominantly in a linear fashion without any change in the slope of the curves after the removal of the tension diagonal.

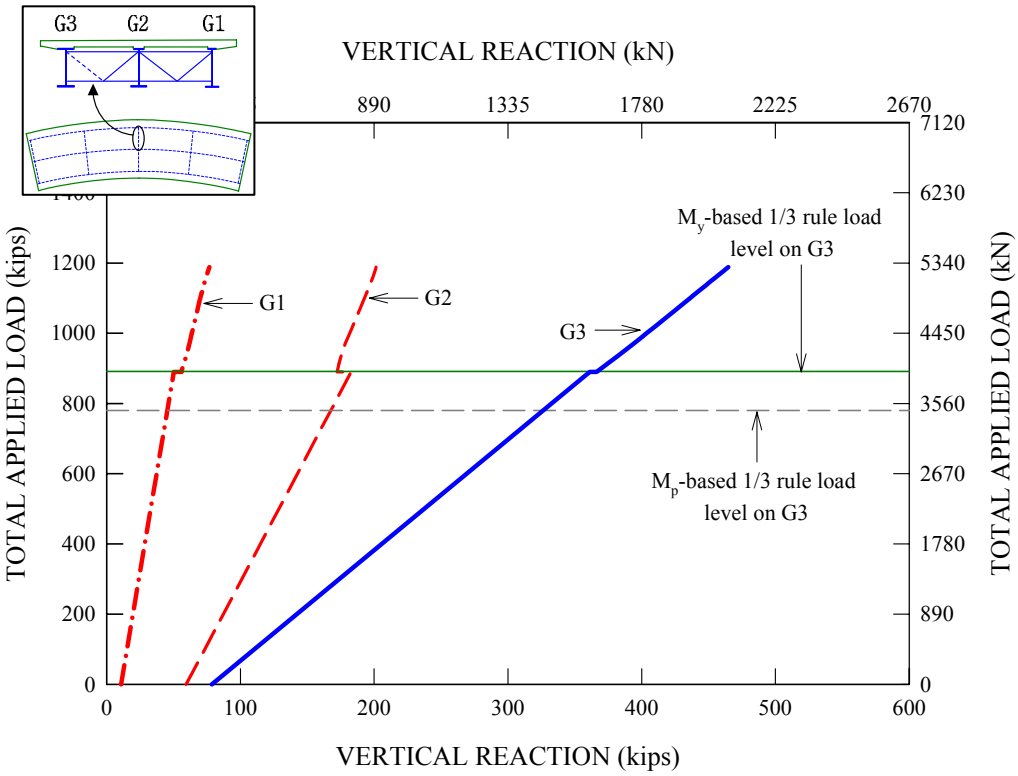

Figure 6.7.10. Case 8c applied load versus girder vertical reactions before and after removing the tension diagonal of the midspan cross-frame attached to G3.

6.7.4 Case 8d: Complete Loss of the Bottom Compression Chord as well as Fracture of the Tension Diagonal in the Midspan Cross-Frame Attached to G3

Figure 6.7.11 compares the G3 midspan vertical deflection obtained from the test bridge FEA simulation involving a combination of a complete failure of the bottom chord and a pseudo-static fracture of the tension diagonal attached to G3 at midspan to the corresponding prediction for the base full nonlinear FEA simulation where no cross-frame member yielding or failure is allowed. Dead load deflections are not included in the plot. Similar to the previous two cases involving a failure of the bottom chord or the tension diagonal, these members are instantly removed from the test bridge FEA model once the test bridge is loaded to the M_p-based 1/3 rule load level on G3 of 3959 kN (890 kips). Since this is arguably the worst case scenario considered so far, one may expect that the changes in the test bridge responses are far more drastic than those in the previous cases.

However, as can be seen from Figure 6.7.11, the vertical deflection increase on G3 upon the removal of both the bottom chord and the tension diagonal is 50 mm (2.0 in) at 3959 kN (890 kips). Quite interestingly, this deflection increase is essentially equal to that of the previous case when the bottom chord only is removed from the bridge FEA model. Furthermore, it is important to note that the deflection curve at higher applied load levels in Figure 6.7.11 is basically equal to that shown in Figure 6.7.3 when the bottom chord alone is removed.

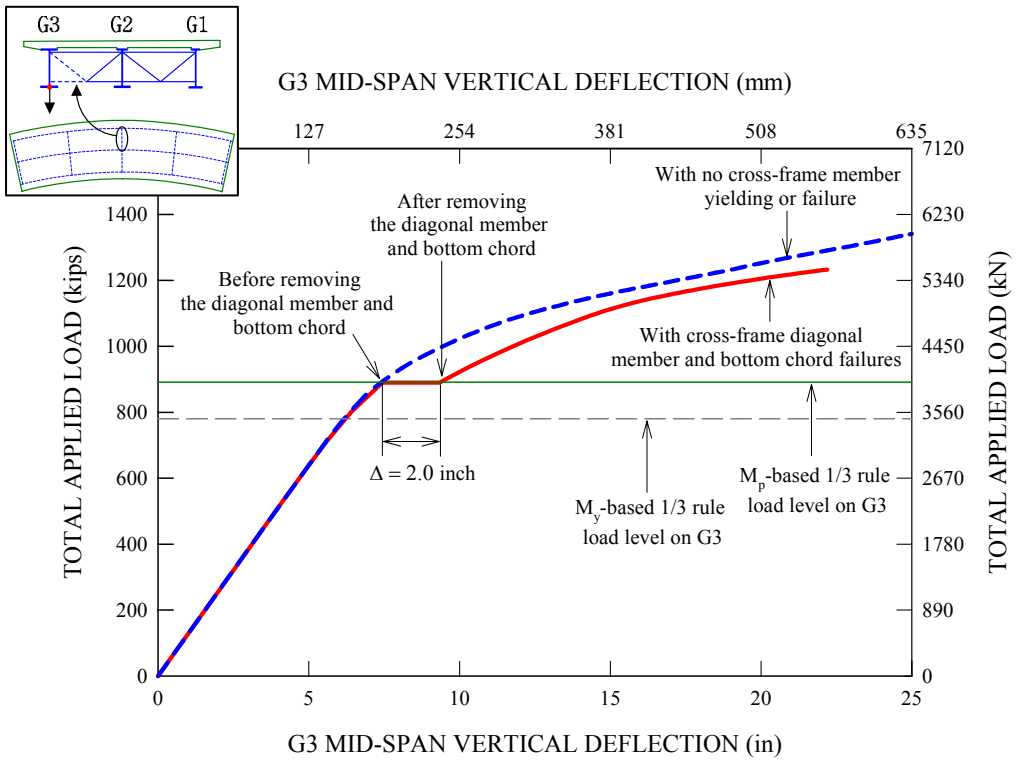

Figure 6.7.11. Applied load versus predicted midspan live load vertical deflection at the G3 bottom web-flange juncture with and without the tension diagonal and compression bottom chord of the midspan cross-frame attached to G3 removed at the M_p-based 1/3 rule load level on G3 (total applied load = 3959 kN (890 kips)), dead load deflection not included in the plot.

Figure 6.7.12 shows the total applied load versus the axial force in the bottom chord of the quarter-span cross-frame attached to G3. The initial dead load member forces are included in the plot. Similar to the deflection increase shown in Figure6.7.11, the member force increase of 294 kN (66 kips) is also equal to that for the case where the bottom chord only was removed (see Figure 6.7.5). In addition, the member force increase pattern for further loading after the removal of the bottom chord and tension diagonal is found to be quite similar to that for the case where the bottom chord only was removed.

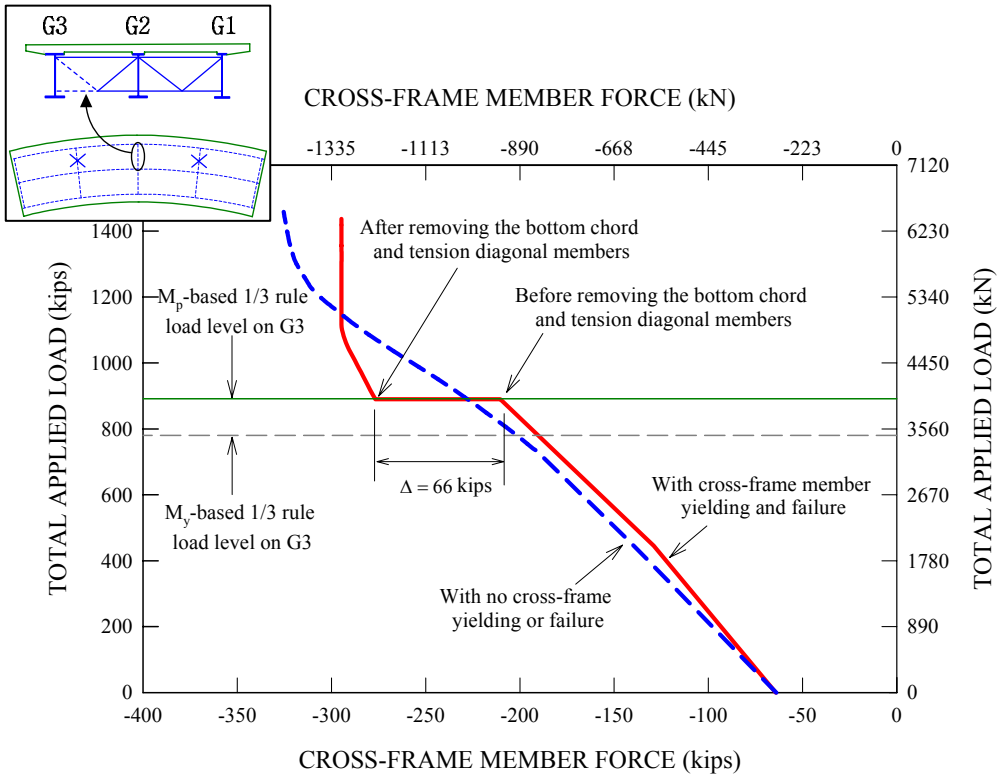

Figure 6.7.12. Applied load versus axial force in the bottom chord of the quarter-span cross-frame attached to G3, initial dead load axial force included, with and without both the tension diagonal and the bottom chord of the midspan cross-frame attached to G3 removed at the M_p-based 1/3 rule load level on G3 (total applied load = 3959 kN (890 kips)).

Figure 6.7.13 provides the girder vertical reactions before and after removing the tension diagonal and compression bottom chord of the midspan cross-frame attached to G3. Compared to the previous cases, it is noteworthy that the girder reactions remain the same before and after the removal of the bottom chord and tension diagonal, not to mention the rate of the reaction increase. The G3 reaction increases approximately in a linear fashion throughout the entire loading history whereas the reactions on G1 and G2 change nonlinearly above a total applied load of about 4005 kN (900 kips).

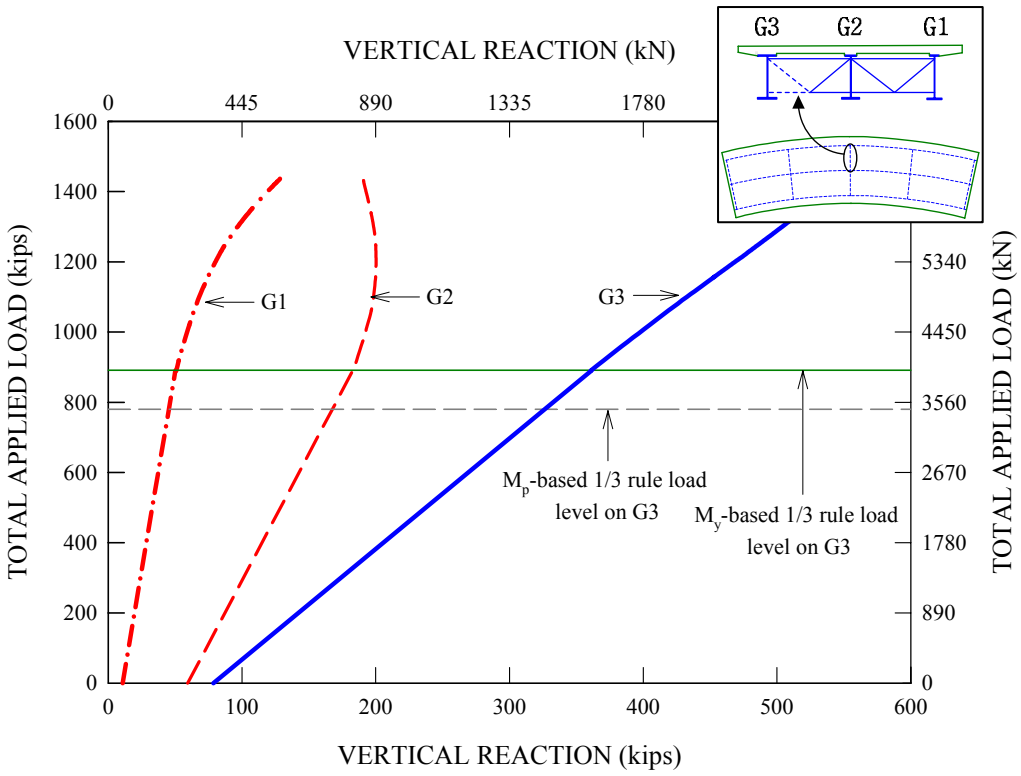

Figure 6.7.13. Case 8d applied load versus girder vertical reactions before and after removing the tension diagonal and compression bottom chord of the midspan cross-frame attached to G3.

6.8 Case 9: Fixed-End Bridge Systems

Since all the bridge structures studied so far are simply-supported, a logical and natural extension of the current research is the consideration of continuous-span bridges. A convenient way of achieving this extension, while limiting the changes to the base test bridge configuration to a minimum, is to invoke an ideal assumption that the girder ends are fully restrained. As such, two fixed-end bridges are considered in the following. The first fixed-end bridge has the test bridge geometry with prismatic girders and the same unbraced length, L_b, set to 0.1125R. The second fixed-end bridge also has the test bridge geometry, but with the unbraced length, L_b, set to 0.075R and a transition in the girder cross-sections to "optimize" the designs for the positive and negative moment regions. Although these two cases are simple pilot study cases derived from the test bridge

configuration, they allow important key attributes typical of the strength behavior of continuous-span structures to be investigated.

One should note that welded I-girders in negative bending tend to have highly noncompact or slender webs for the purpose of design economy. As such, the strength resistance equations can be simplified in terms of stresses as

$$f_{bu} + \frac{1}{3} f_{\ell} \le \phi_f F_n$$

where f_{bu} and f_{ℓ} are the elastically-computed flange major-axis and lateral bending stresses respectively, and $\phi_f F_n$ is the factored flexural resistance in terms of the flange major-axis bending stress for $f_{\ell} = 0$, which is generally less than or equal to $\phi_f F_{yf}$. For typical welded I-girders in negative bending, the use of the above equation does not involve any significant economic penalty. The AASHTO (2004b) Article 6.10 provisions recognize this fact by utilizing the above format the resistance checks of composite members in negative bending. Alternate equations are provided in Appendix A of the AASHTO Specifications that give significantly higher capacities for members that have compact or nearly compact webs. These alternate equations are particularly important for design using rolled I-section members.

6.8.1 Case 9a: Fixed-End Bridge System with Prismatic Girders and $L_b/R = 0.1125$

Figure 6.8.1 shows the girder profiles, and the bridge plan and cross-section views of a fixed-end composite bridge system with prismatic girders and $L_b/R = 0.1125$. It should be noted that the girder cross-sections shown in Figure 6.8.1 are sized based on the unbraced lengths in negative bending.

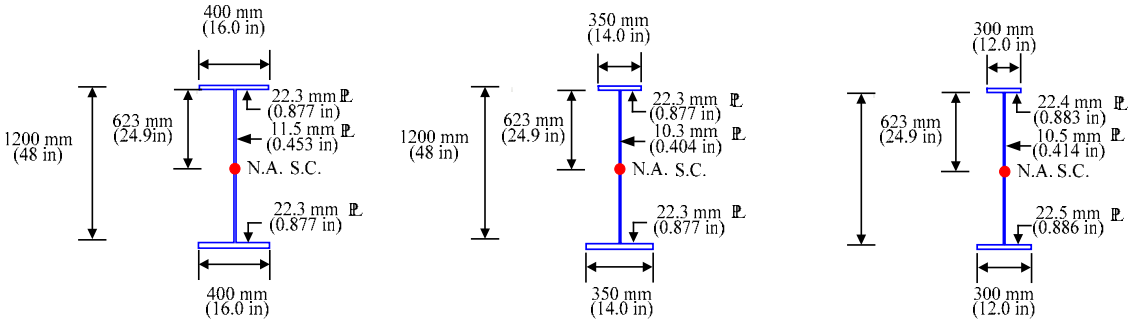

(a) G3 cross-section (b) G2 cross-section (c) G1 cross-section

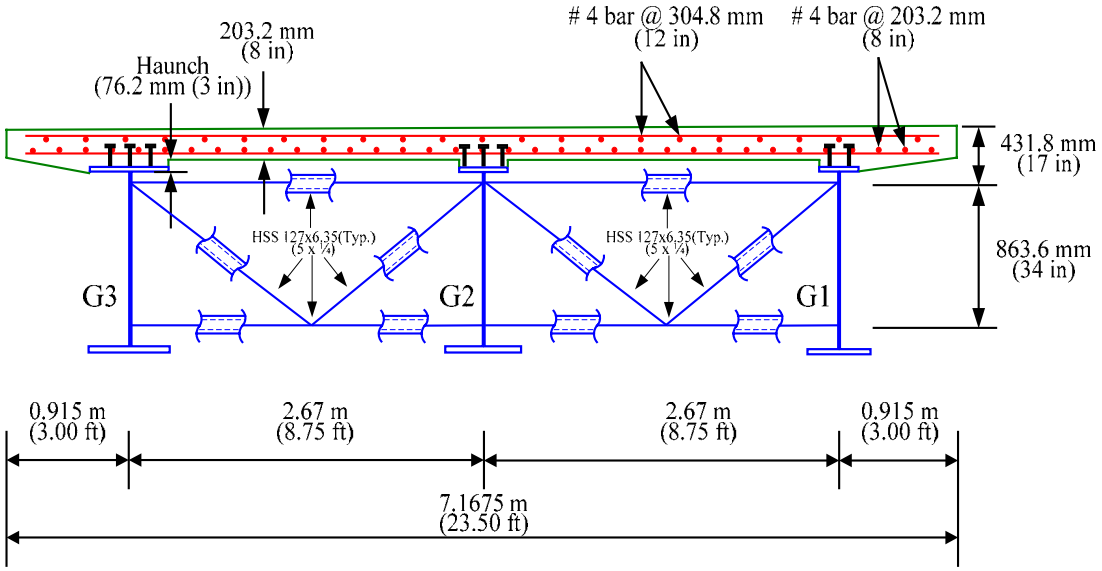

(d) Bridge cross-section at midspan

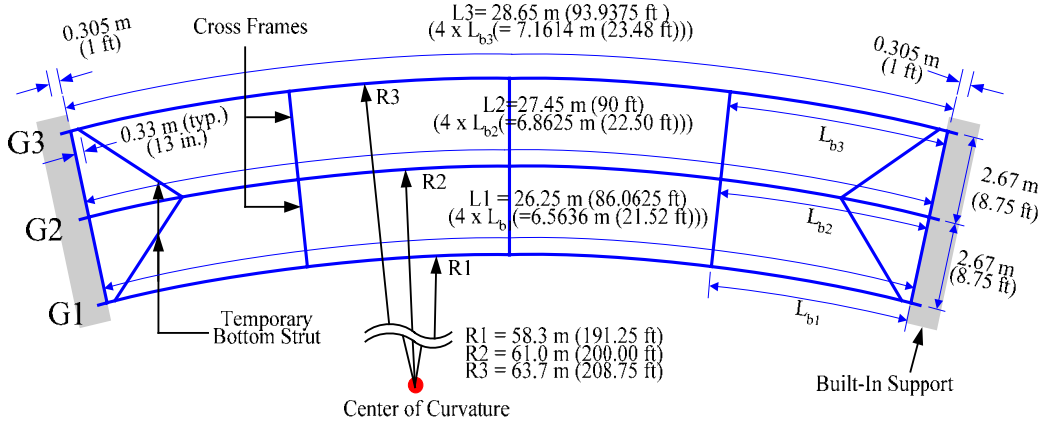

(e) Bridge plan

Figure 6.8.1. Case 9a fixed-end composite bridge with prismatic girders and L_b/R = 0.1125.

The governing flexural capacity, F_n, is the flange local buckling (FLB) resistance, which is slightly smaller than the flange yield strength, F_{yf} for the girder designs shown in the figure. The lateral-torsional buckling (LTB) resistance lies in the plateau region, i.e, $F_n = F_{yf}$, due to the moment gradient factor, C_b, which is close to 1.75 for all of the girders. The strength ratio for flexure under the Strength I loading combination is 0.93 for G3 based on FLB at the fixed ends. Conversely, the strength ratio is just 0.54 for the positive moment region, since a prismatic section is used for G3. It is also important to note that a slight conservatism in the flexural unity check for G3 is due to the increase in the G3 web thickness from 9.05 mm (0.362 in) to 11.31 mm (0.4525 in) in order to satisfy the web bend buckling check under Service II load combination. Similarly, the web thickness for the other two girders, G1 and G2, is also increased to 10.1 mm (0.404 in) and 10.4 mm (0.414 in), respectively (web thicknesses that exactly satisfy the web bend buckling limit are used rather than selecting the next largest plate thickness increment). Interestingly, despite the increases in the girder web thickness, the web slenderness for all of the girders still falls within the slender web category, limiting the base maximum major-axis bending resistance of the composite I-girders (prior to reduction by the 1/3 rule) to their first yield moment, or $F_n = F_{yf}$. For the proportioning of the G1 and G2 flanges, the recommended shipping piece limit, L/85, is used to determine their widths. It is found that this consideration actually results in small strength ratios for these girders, in particular for the flexural checks of the inside girder, G1. In addition, steel reinforcement corresponding to one percent of the gross cross-section area of the slab is specified in the negative moment regions between the end- and quarter-span cross-frame locations. This satisfies the AASHTO (2004b) design requirement for the minimum negative flexure

concrete deck reinforcement wherever the longitudinal tensile stresses in the concrete deck due to either the factored construction loads or Service II load combination exceed ϕf_r, where f_r is taken as the modulus of rupture of the concrete.

For the full nonlinear FEA simulation of the fixed-end bridges to assess the strength behavior, the same loading used for the experimental and analytical studies of the base composite test bridge is also used here. However, residual stresses due to flame cutting and welding of the flanges to the web are included, since these stresses are likely to have a significant effect on the behavior of the bridge I-girders in the negative moment regions. Correspondingly, S4R shell finite elements (HKS 2004) are utilized for the flanges to accommodate the input of the initial residual stresses (as noted previously, the B31 beam finite element in ABAQUS does not accommodate the input of initial residual stresses). Figure 6.8.2 shows the resulting Gauss point residual stresses used within the bridge FEA model in accordance with ECCS (1976). Furthermore, portions of the bridge slab model located between the end- and quarter-span cross-frames are provided with steel reinforcement corresponding to one percent of the total cross-sectional area of the concrete slab as required by Section 6.10.1.7 in the AASHTO (2004b) Specifications. Finally, the concrete tension stress-strain response is simplified such that the peak tensile stress is kept constant for strains larger than the cracking strain. This simplification is justified based on the finding that the bridge FEA solution including a refined representation of tension stiffening effects in the concrete strain-stress response essentially produces the same solution as presented below, but requires substantially higher computational overhead due to numerical troubles often caused by material instabilities in the softening region of the concrete tension stress-strain response.

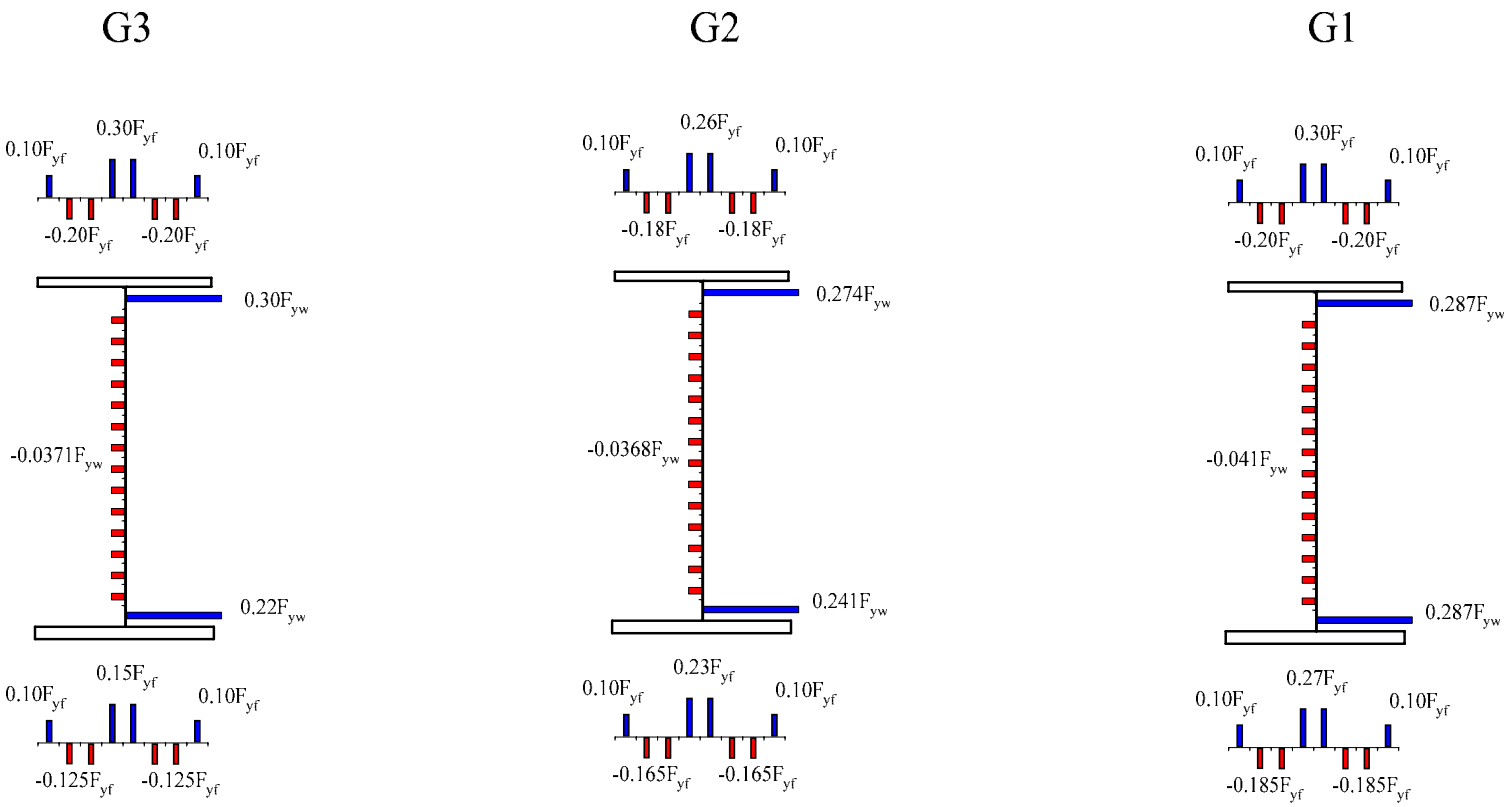

Figure 6.8.2. Gauss point residual stresses used within the bridge FEA model in accordance with ECCS (1976), based on flame cutting and consecutive placement of web-to-flange welds.

Figure 6.8.3 shows the applied load versus the midspan live load vertical deflection of the center of the G3 bottom flange for the Case 9a fixed-end bridge system. The full nonlinear FEA solution represented by the solid line starts to deviate from the linear elastic prediction represented by the dashed line at approximately 2224 kN (500 kips). An examination of the slab stresses near the fixed-end regions reveals that this is the point when the slab is effectively fully cracked (through its depth and through its width) at the fixed-end supports.

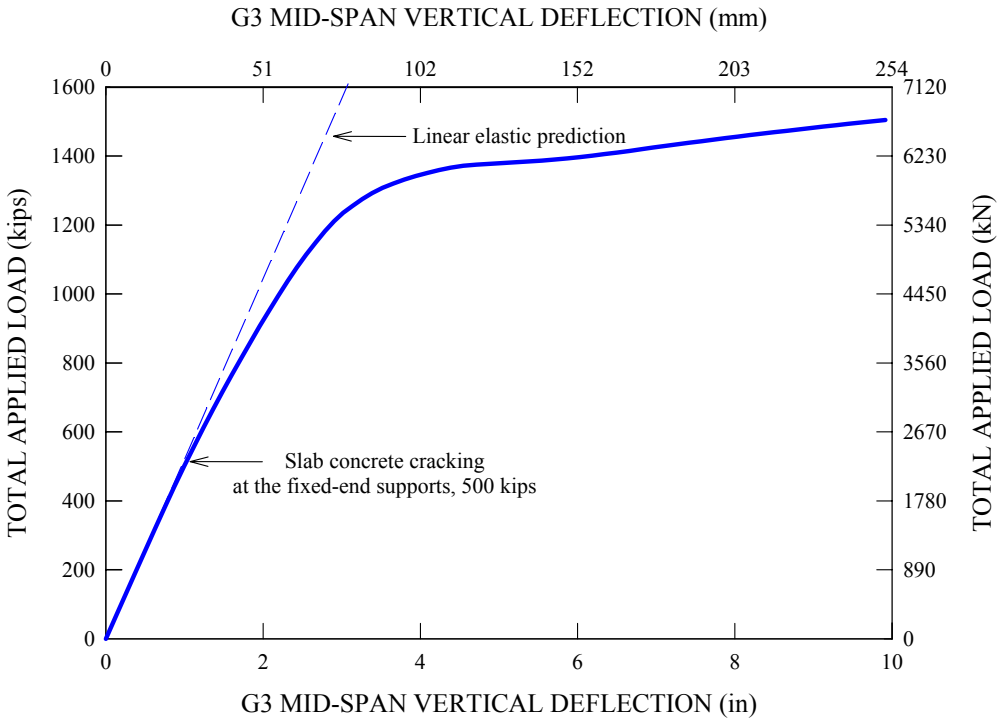

Figure 6.8.3. Case 9a applied load versus girder vertical deflection at the midspan of the G3 bottom flange.

For subsequent higher applied loads, it can be seen that vertical deflection continues to increase in a nonlinear fashion up to about 6140 kN (1380 kips) where the deflection curve levels off, resulting in a significant increase in the vertical deflection upon further loading. Interestingly, it can be seen that the bridge system exhibits an increase in its

inelastic stiffness starting at a vertical deflection of about 150 mm (6 in) after the initial appearance of the deflection plateau.

Figure 6.8.4 presents the fixed-end and midspan internal moments for the entire composite bridge cross-section throughout the loading history. The moments are calculated about the axis indicated in the inset shown on the upper left corner of Figure 6.8.4. The initial dead load moments are included in the plot. In addition, the FLB-based 1/3 rule load level on G3 is marked on the plot. This strength limit occurs at a total applied load of 4050 kN (910 kips) in the elastic analysis, when the G3 cross-section at the fixed ends reaches the flexural strength limit associated with flange local buckling (FLB) failure under proportionally increased loads beyond the Strength I load combination values.

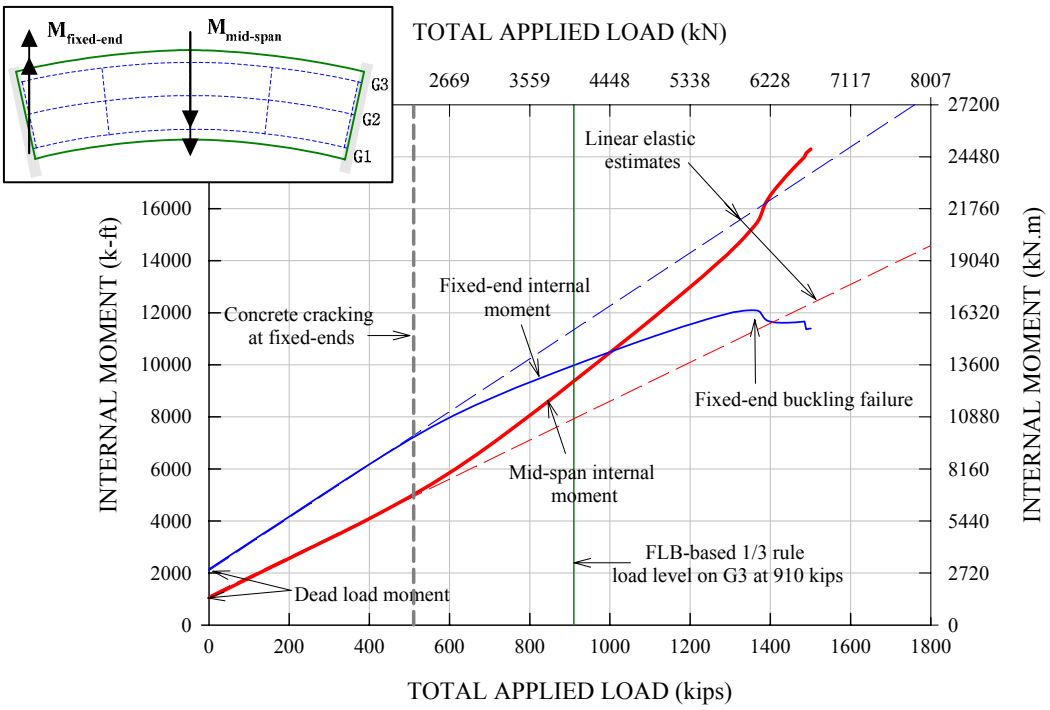

Figure 6.8.4. Case 9a applied load versus fixed-end and midspan internal moments for the entire composite bridge cross-section.

Figure 6.8.4 shows that both the fixed-end and midspan moments increase linearly up to a total applied load of 2224 kN (500 kips). As mentioned above, this is the load level at which the slab is cracked through its width and depth at the fixed-end supports. This marks the onset of some moment redistribution (relative to the elastic design-analysis solution) from the fixed-end to the midspan region. As a result, the fixed-end moment obtained from the full nonlinear FEA solution tends to be gradually reduced relative to the linear elastic estimate indicated by the dashed line. The resulting difference between the fixed-end moments obtained from the full nonlinear and linear elastic solutions is redistributed to the midspan region, leading to a gradual increase in the midspan moment relative to the corresponding linear elastic estimate. At the FLB-based 1/3 rule load level on G3, the midspan moment obtained from the full nonlinear FEA solution is 11800 kN-m (8700 k-ft), which is significantly larger than the corresponding elastic estimate of 10900 kN-m (8000 k-ft). Conversely, the linear elastic moment estimate for the bridge fixed-end moment is significantly overestimated. The fixed-end moment obtained from the full nonlinear FEA simulation at the same load level is 13600 kN-m (10000 k-ft), which is significantly less than the corresponding linear elastic estimate of 14550 kN-m (10700 k-ft). It is important to recognize that the elastic FEA model involves the use of the nominal elastic stiffness for the bridge slab concrete throughout the length of the bridge, which is the recommended approach of AASHTO (2004b) Article 6.10.1.5. That is, the moment redistribution shown in Figure 6.8.4 is not accounted for in a typical composite bridge elastic analysis. As a result, the elastic estimate of the negative moment at the strength resistance level can be much larger than the actual moment developed at the fixed-end support. As discussed subsequently, this is generally not

considered to be a problem. Among other things in Figure 6.8.4, it is interesting to note that the fixed-end moment curve shows a limit point at a total applied load of 6140 kN (1380 kips). This is due to the fact that unbraced lengths in negative bending exhibit a stability-related failure as discussed in the following. Right after the limit point is reached, it can be seen that the fixed-end moment in the post-peak range is slightly reduced from its peak value. In turn, the midspan moment exhibits a sharp increase due the moment redistribution from the fixed-end supports. The midspan moment increase allows substantial additional load to be applied to the bridge after the failure at the fixed-end supports. This may be attributed to the substantial inelastic reserve capacity in this bridge due to the small flexural design strength ratios for the girder positive moment regions in the elastic design.

Figures 6.8.5 through 6.8.7 show the detailed internal moments in girders G1, G2 and G3 at the fixed-end and the midspan throughout the entire loading history. Similar to Figure 6.8.4, the girder moments are calculated about an axis parallel to the radial direction at the midspan. The dead load internal moments are included in the figures. In general, it appears that there are many similarities between the overall bridge cross-section and the individual girder cross-section moments. All the girder internal moments at the fixed-end and midspan regions increase linearly up to the point when the slab is cracked through its width and depth at the fixed-end supports. Then, the fixed-end and midspan moments obtained from the full nonlinear FEA simulation start to deviate from corresponding linear elastic estimates indicated by the dashed lines in the figures. However, there are also some subtle differences between the overall bridge and the individual girder moments.

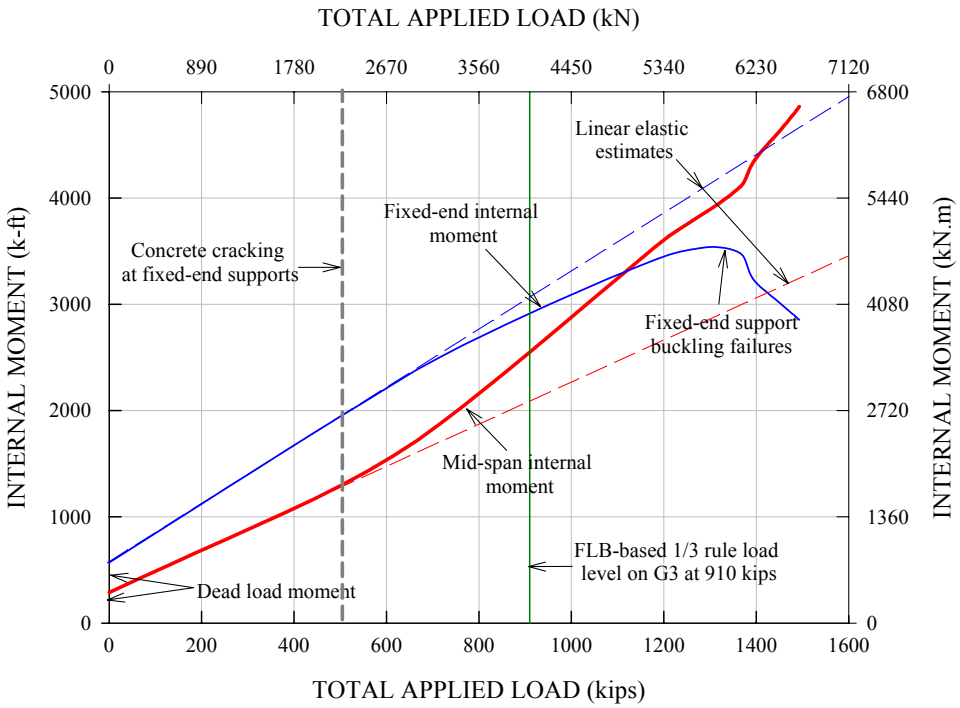

Figure 6.8.5. Case 9a applied load versus internal moments for the isolated G1 composite cross-section at the fixed-end and at the midspan.

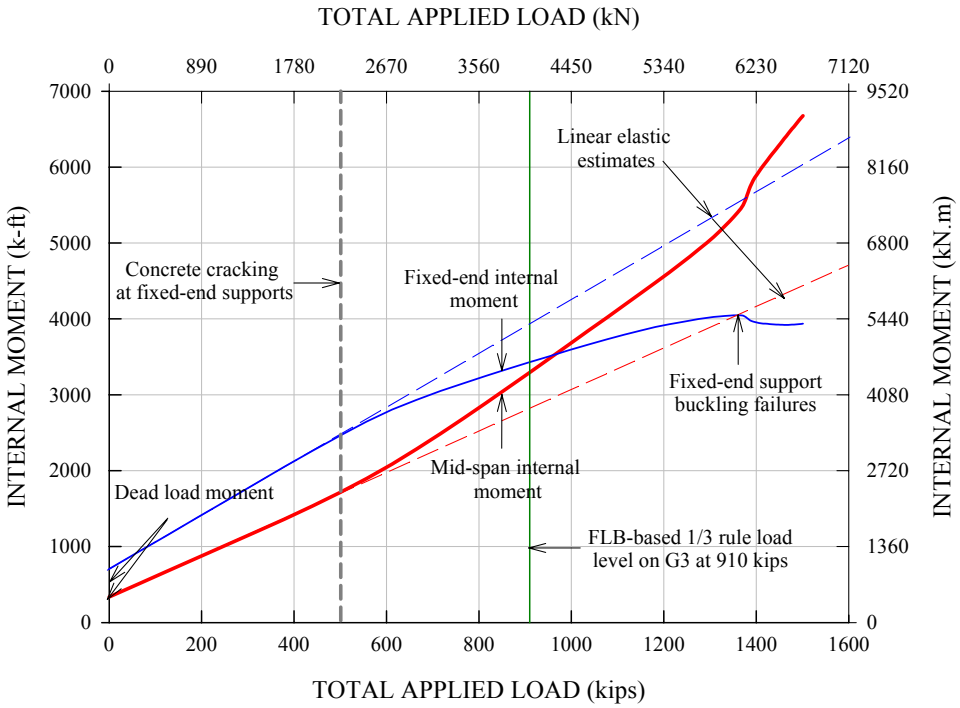

Figure 6.8.6. Case 9a applied load versus internal moments for the isolated G2 composite cross-section at the fixed-end and at the midspan.

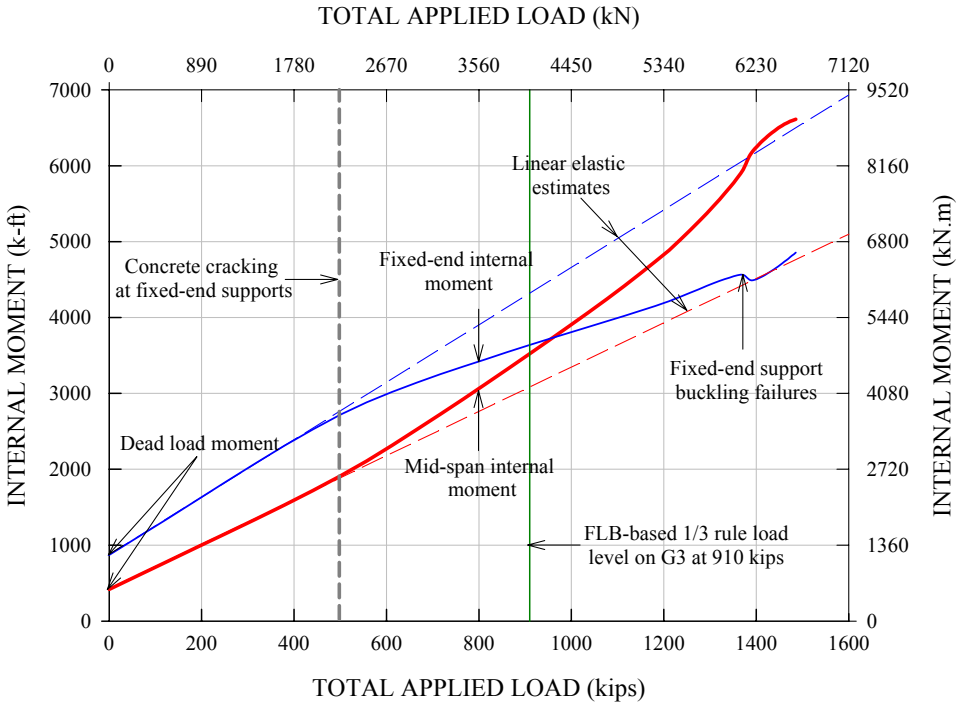

Figure 6.8.7. Case 9a applied load versus internal moments for the isolated G3 composite cross-section at the fixed-end and at the midspan.

Figure 6.8.6 shows that the G2 fixed-end moment drop from the linear elastic estimate approximately corresponds to the increase in the G2 midspan moment relative to the linear elastic estimate. However, Figure 6.8.5 shows that the redistributed G1 fixed-end moment is actually smaller than the increase in the midspan moment relative to the linear elastic estimate. Conversely, Figure 6.8.7 shows that the increase in the G3 midspan moment due to the moment redistribution from the fixed-end region is relatively small compared to its redistributed fixed-end moment. This indicates that a portion of the fixed-end moment redistributed from the G3 fixed-end support is actually taken by the G1 midspan cross-section instead of the G3 midspan cross-section.

For higher applied loads, both the fixed-end and midspan moments continue to increase in a nonlinear fashion until the fixed-end moment curves reach a peak value at a

total applied load of 6008 kN (1350 kips). It can be seen in Figure 6.8.5 that the G1 fixed-end moment curve exhibits a sharp drop at this load level followed by a steady decline in the post-peak region. This is because the G1 unbraced length in negative bending fails by a combination of flange local buckling (FLB), web bend buckling and lateral-torsional buckling (LTB) deformations. Figure 6.8.6 shows that the G2 fixed-end moment reaches a plateau at this load level. A visual inspection of the FEA deformed geometries shows that the G2 unbraced length in negative bending fails predominantly by a combination of flange local buckling (FLB) and web bend buckling deformations (i.e., the lateral displacements of the bottom flange in the negative moment region are relatively small). Figure 6.8.7 shows that the G3 fixed-end moment curve experiences a slight drop at this load level, which is related to the buckling failure in the G3 unbraced length in negative bending. Interestingly, the G3 fixed-end moment starts to increase again at 6230 kN (1400 kips) after the drop due to the buckling failure at the fixed-end support region. Figure 6.8.8 provides the predicted moment-curvature response for the G3 midspan cross-section throughout the entire loading history. It should be noted that the curvature is calculated approximately based on the average longitudinal normal strain at the integration point in the shell element at the bottom of the web and a similar value for the shell element at the top of the web. The difference between these two strains divided by the depth between these two points gives an estimate of the curvature at that location along the length. This calculation is termed the web strain-based curvature for purposes of discussion. Since the midspan strain variation through the web depth is predominantly linear for all the load levels, the curvature estimate based on this calculation is believed to be a reasonable estimate of the corresponding true curvature.

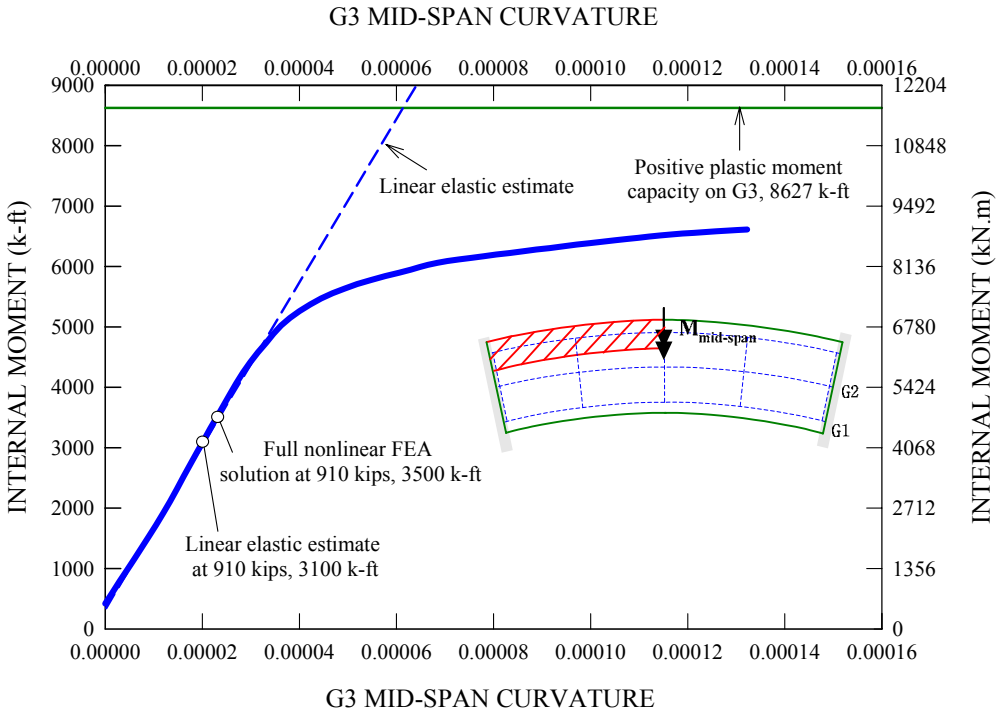

Figure 6.8.8. Case 9a G3 midspan internal moment versus corresponding curvature due to the applied loads, initial dead load moment included (the load 4048 kN of (910 kips) corresponds to the FLB-based 1/3 rule strength limit on G3 at the fixed-ends).

The G3 positive plastic moment capacity in the absence of flange lateral bending is marked on the plot in Figure 6.8.8. Figure 6.8.8 shows that the G3 midspan moment increases linearly up to approximately 6120 kN-m (4500 k-ft), and then it starts to deviate from the linear elastic estimate represented by the dashed line. With respect to the FLB-based 1/3 rule load level on G3 at 4050 kN (910 kips), the linear elastic estimate for the G3 midspan moment is 4216 kN-m (3100 k-ft), which is smaller than the corresponding full nonlinear estimate of 4760 kN-m (3500 k-ft) at this load level due to the moment redistribution from the fixed-end support region. Nonetheless, it is interesting to note that the midspan moment-curvature response is linear at the FLB-based 1/3 rule load level on G3.

Figures 6.8.9 and 6.8.10 provide similar moment-curvature responses for the isolated midspan G2 and G1 composite cross-sections. It can be seen that the moment-curvature curves obtained from the full nonlinear FEA are slightly above the linear elastic estimates for certain load levels, in particular for the G1 moment-curvature. This is believed to be due to the inherent approximations in the curvature calculation using the average normal strains in the top and bottom portions of the web panel. With respect to the FLB-based 1/3 rule load level on G3 at 4050 kN (910 kips), the linear elastic estimates for the G2 and G1 midspan moments are 3808 kN-m (2800 k-ft) and 2924 kN-m (2150 k-ft), respectively, while the corresponding full nonlinear estimates are 4488 kN-m (3300 k-ft) and 3600 kN-m (2650 k-ft).

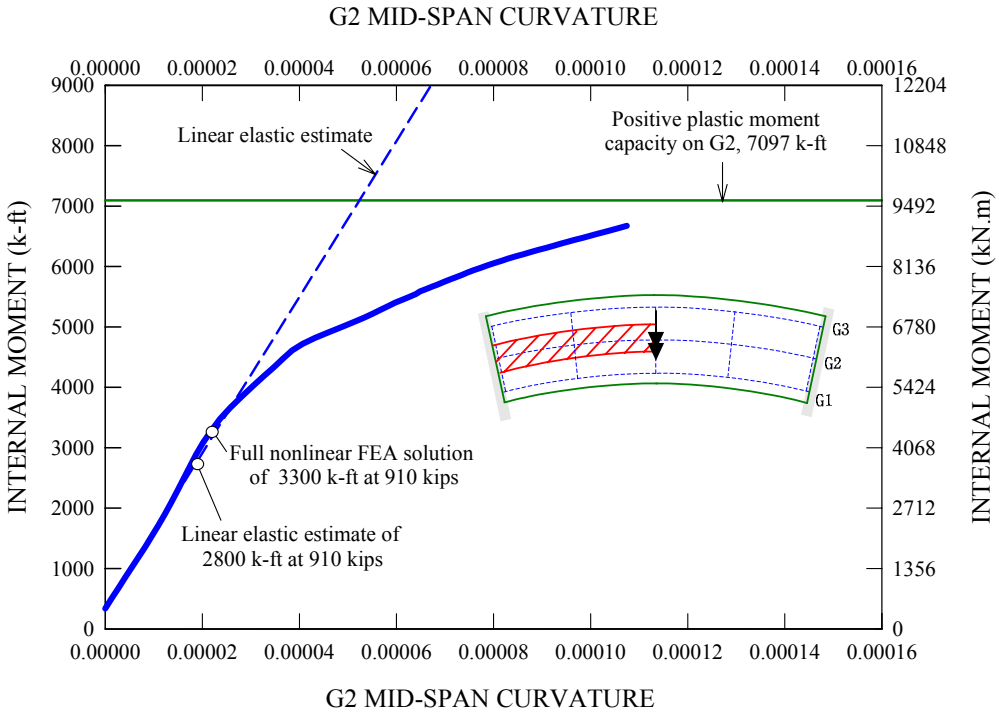

Figure 6.8.9. Case 9a G2 midspan internal moment versus corresponding curvature due to the applied loads, initial dead load moment included (the load 4048 kN of (910 kips) corresponds to the FLB-based 1/3 rule strength limit on G3 at the fixed-ends).

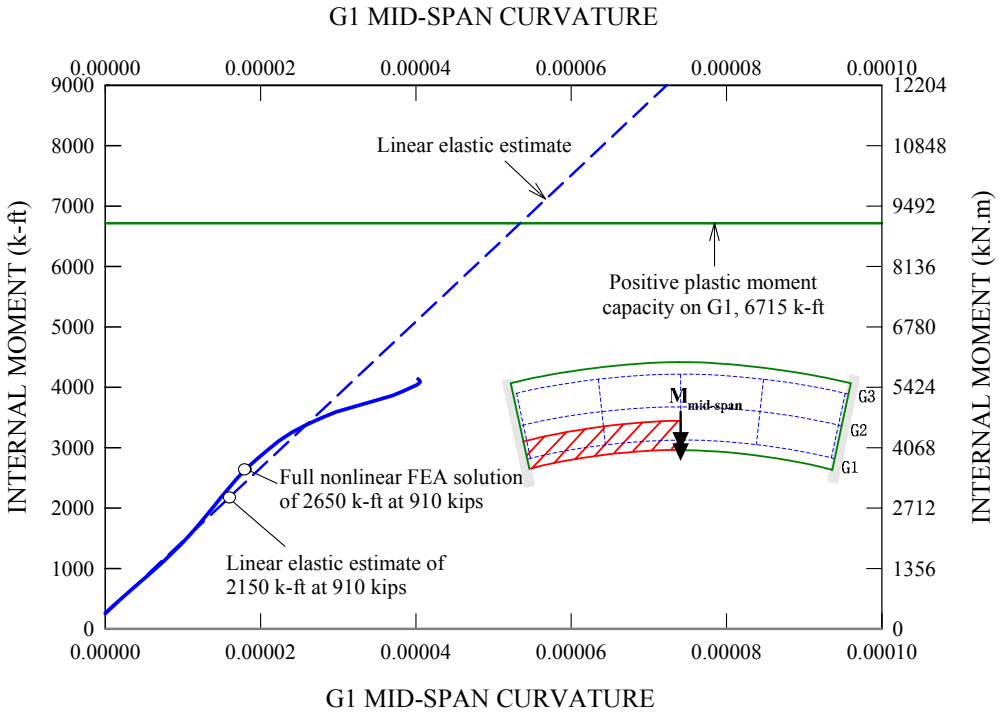

Figure 6.8.10. Case 9a G1 midspan internal moment versus corresponding curvature due to the applied loads, initial dead load moment included (the load 4048 kN of (910 kips) corresponds to the FLB-based 1/3 rule strength limit on G3 at the fixed-ends).

Figure 6.8.11 presents the moment-curvature response for the G3 fixed-end cross-section throughout the entire loading history. In addition to the web strain-based curvature described earlier, one other curvature estimate is presented in this plot. This estimate is termed the nodal displacement-based curvature. The web strain-based curvature calculation generally works well as long as the web strain distribution through the web depth remains approximately linear, which is the case for the midspan region. However, the web strain-based approach generally does not work well for the fixed-end support curvature calculation once the plate buckling distortions become significant. This is because the post-buckling web strain distribution is significantly nonlinear through the web depth. Therefore, the web strain-based curvature calculation is only

applicable prior to the buckling of the web panel. The curvature calculation by the web-strain based method is indicated by the thick solid line in Figure 6.8.11.

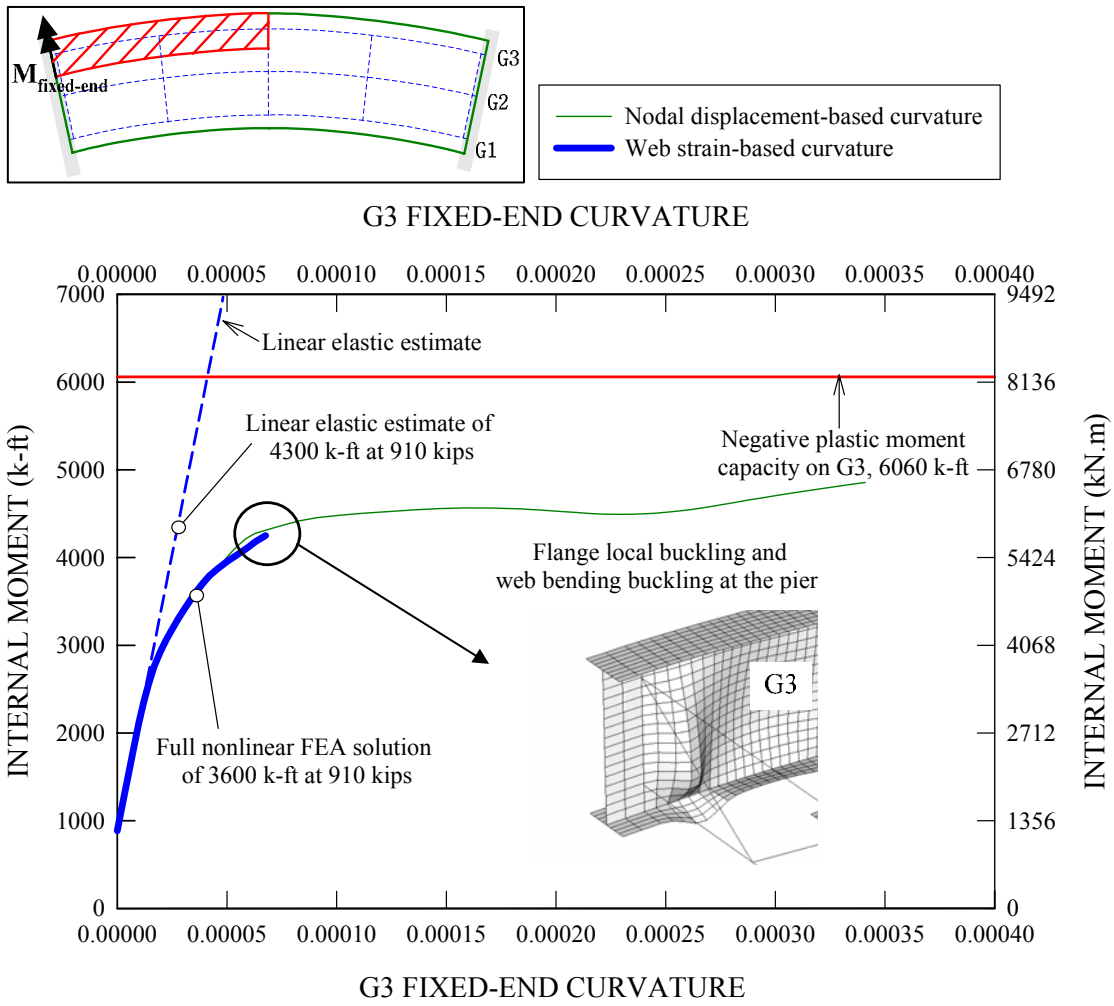

Figure 6.8.11. Case 9a G3 fixed-end internal moment versus corresponding curvature due to the applied loads, initial dead load moment included (the load 4048 kN of (910 kips) corresponds to the FLB-based 1/3 rule strength limit on G3 at the fixed-ends).

The inset located in the lower right corner of the figure shows the deformed geometry of the G3 fixed-end support region right at the incipient stage of the buckling (Deformation Scale Factor = 5.0). In order to complement the web strain-based method for calculating the post-buckling curvature, nodal displacement-based curvature is

determined as follows. First, three nodes located at the web-bottom flange juncture near the fixed-end support are chosen including the fixed-end node. The two nodes other than the fixed end node are chosen such that they are as close to the fixed-end support as possible but are not located within the local buckling wavelength. Otherwise, the curvature calculation is significantly affected by local deformed geometries resulting from the buckling distortions. The nodal displacements at these three nodes are fitted by a quadratic curve for each increment of the full nonlinear FEA solution. The second derivative of this quadratic curve, which is constant, produces an estimate for the fixed-end curvature. The resulting moment-curvature curve is represented by the thin solid line in Figure 6.8.11. Not only does the nodal displacement-based curve closely match the web strain-based curve up to the buckling point, but also it continues to show a reasonable post-buckling curvature response.

Figure 6.8.11 shows that the fixed-end moment-curvature increases in a linear fashion up to approximately 3660 kN-m (2700k-ft) when the slab concrete at the fixed-end supports is cracked through the width and depth. Then, the moment-curvature curve continues to increase nonlinearly, but shows significant deviations from the linear elastic estimate indicated by the dashed line. With respect to the FLB-based 1/3 rule load level on G3 of 4050 kN (910 kips), the G3 fixed-end moment obtained from the full nonlinear FEA simulation is 4900 kN-m (3600 k-ft). This is significantly less than the corresponding linear elastic estimate of 5848 kN-m (4300 k-ft). Therefore, the fixed-end region reaches its buckling limit state at a much higher internal moment from the linear elastic analysis than from the full nonlinear analysis at the total applied load corresponding to the FLB-based 1/3 rule load level on G3 of 4050 kN (910 kips).

Eventually the fixed-end moment curve reaches a plateau with a bounding value of 6120 kN-m (4500 k-ft). A closer look at the girder deformation shown in the inset to Figure 6.8.11 suggests that a combination of flange local buckling and web bend buckling at the fixed-end support is mainly responsible for the appearance of this plateau. It is important to note that the midspan moment-curvature response is within the linear region at this load level as shown in Figure 6.8.8, as well as further higher load levels.

Figures 6.8.12 and 6.8.13 give the corresponding moment-curvature responses for the isolated G2 and G1 fixed-end cross-sections. Similar to the G3 fixed-end moment, it can be seen that the elastic estimates for the G2 and G1 fixed-end moments are noticeably larger than the corresponding full nonlinear FEA solutions. With respect to the FLB-based 1/3 rule load level on G3, the fixed-end moments obtained from the full nonlinear FEA solutions are 3944 kN-m (2900 k-ft) and 4760 kN-m (3500 k-ft) for the G1 and G2 composite sections, respectively, whereas the corresponding linear elastic estimates are 4284 kN-m (3150 k-ft) and 5440 kN-m (4000 k-ft). Eventually the G1 and G2 fixed-end moments also reach a plateau with a bounding value of 4760 kN-m (3500 k-ft) and 5440 kN-m (4000 k-ft), respectively. However, there is a sharp distinction between the two moment-curvature curves in terms of the post-peak behavior. The G2 fixed-end moment decreases only slightly relative to the peak moment. In contrast, Figure 6.8.13 shows that the post-peak G1 fixed-end moments show a steady decline once the G1 fixed-end moment reaches a plateau. Since the sum the fixed-end moments remains fairly constant beyond 5783 kN (1300 kips) as shown in Figure 6.8.4, the reduced moment on G1 must be redistributed to the adjacent composite girders. Based on Figures 6.8.11 and 6.8.7, one can observe that G3 provides this additional moment.

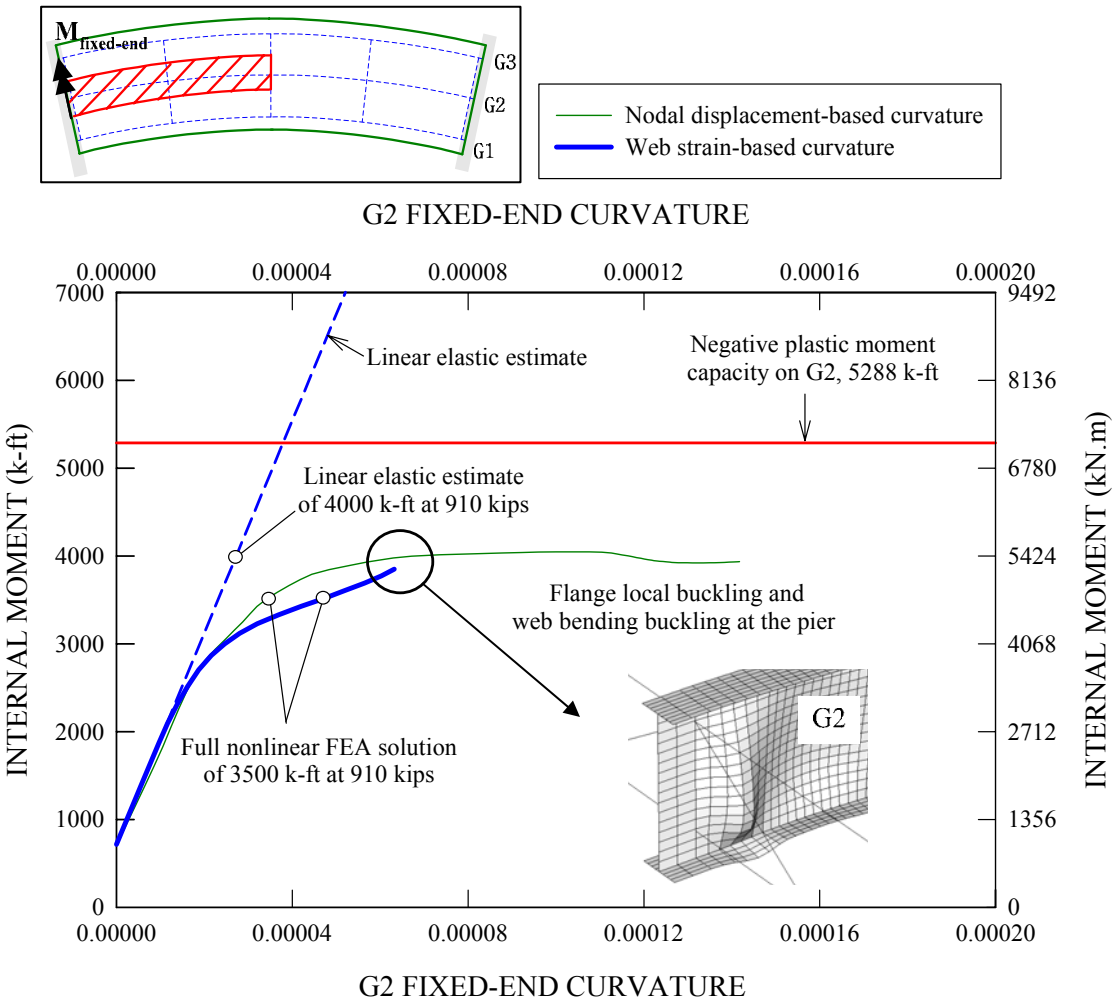

Figure 6.8.12. Case 9a G2 fixed-end internal moment versus corresponding curvature due to the applied loads, initial dead load moment included (the load 4048 kN of (910 kips) corresponds to the FLB-based 1/3 rule strength limit on G3 at the fixed-ends).

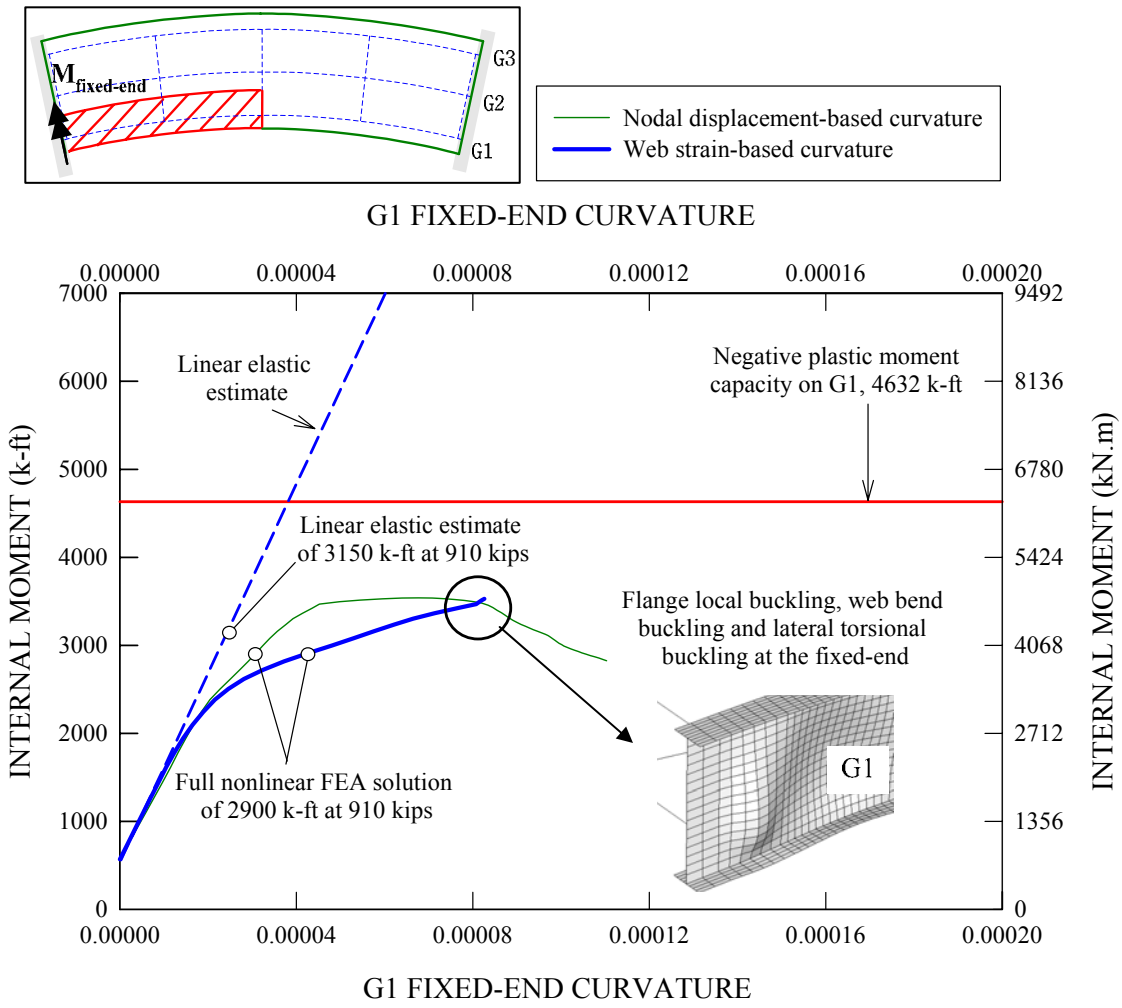

Figure 6.8.13. Case 9a G1 fixed-end internal moment versus corresponding curvature due to the applied loads, initial dead load moment included (the load 4048 kN of (910 kips) corresponds to the FLB-based 1/3 rule strength limit on G3 at the fixed-ends).

The distinct post-peak change in the G1 fixed-end moment-curvature curve can be attributed to a different failure mode exhibited by the G1 fixed-end unbraced length in negative bending. The G2 deformed geometry shown in the inset of Figure 6.8.12 suggests that the G2 fixed-end region fails by a combination of flange local buckling and web bend buckling similar to the failure of the G3 fixed-end unbraced length. By sharp contrast, a detailed examination of the G1 deformed geometry shown in the inset to Figure 6.8.13 indicates that the dominant failure mode of the G1 fixed-end unbraced length is a lateral-torsional buckling (LTB) failure accompanied by a combination of flange local buckling and web bend buckling distortions.

Figure 6.8.14 shows the applied load versus the axial forces in the bottom chords of the mid- and quarter-span cross-frames attached to G3 for the Case 9a fixed-end bridge. The dead load member forces are included in the plot. Despite the moment redistribution between the end- and midspan regions, it can be seen that the cross-frame member forces are generally linear up to the FLB-based 1/3 rule load level on G3.

Figure 6.8.15 gives the girder vertical reactions for the Case 9a fixed-end bridge system versus the total applied load. The dead load reactions are included in the plot. It can be seen that the initial dead load reactions are quite similar among the bridge girders in terms of magnitude, indicating that they share almost equally in resisting the loads. This is in contrast to the simply-supported bridge structures studied earlier, where a large percentage of the loads is supported by the G3 reactions. Although there are some minor deviations from the linear predictions, the vertical reactions increase predominantly in a linear fashion up to the FLB-based 1/3 rule load level on G3.

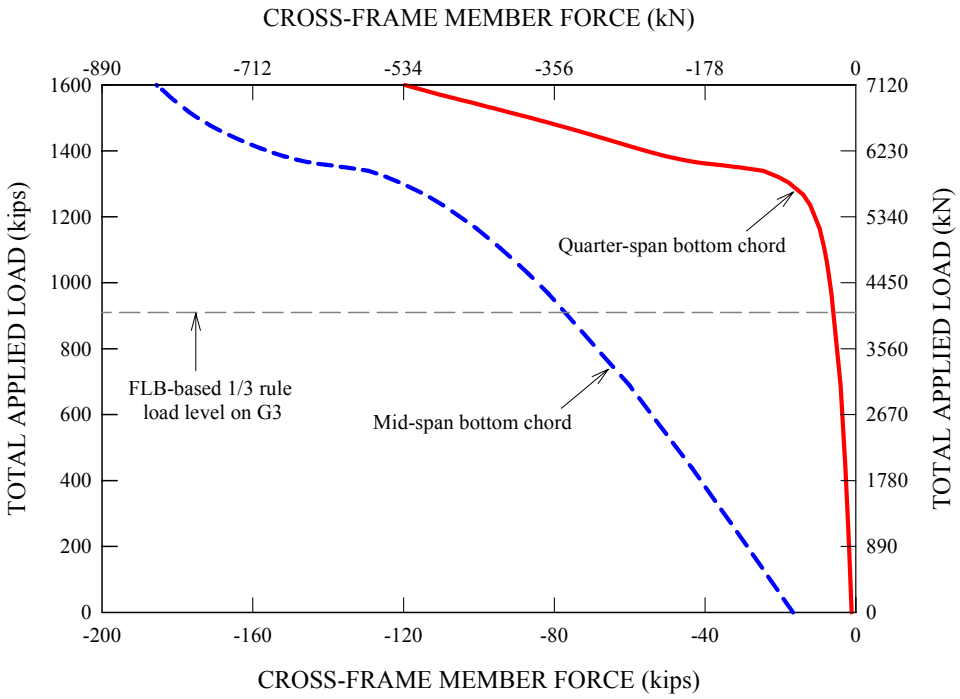

Figure 6.8.14. Case 9a applied load versus axial force in the bottom chords of the mid- and quarter-span cross-frames attached to G3, dead load member forces included.

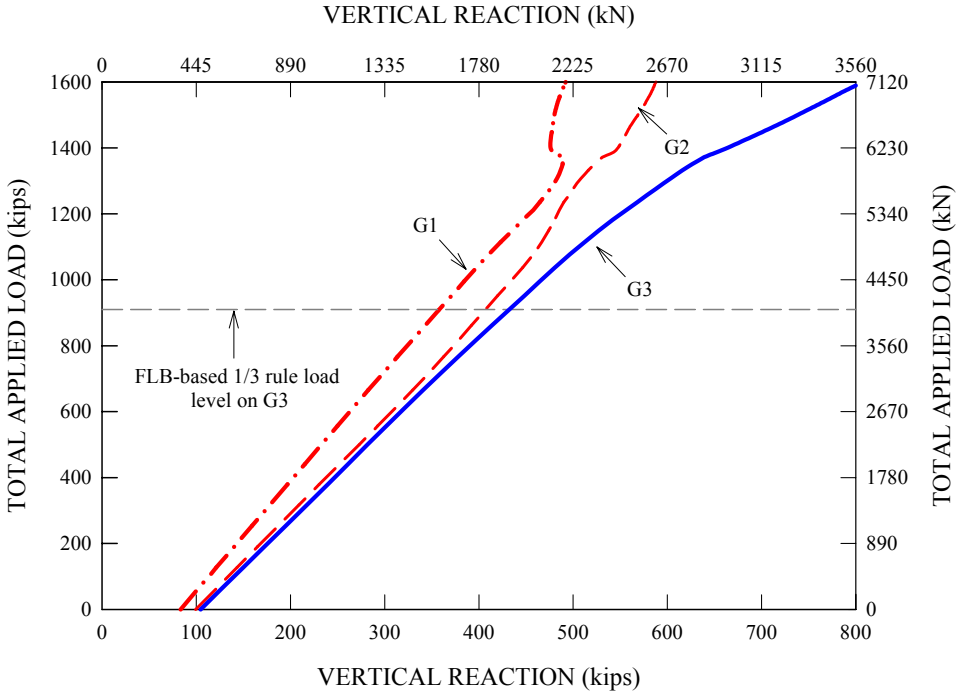

Figure 6.8.15. Case 9a applied load versus girder vertical reactions, dead load reactions included.

6.8.2 Case 9b: Fixed-End Bridge System with "Optimized" Midspan and Fixed-End Girder Cross-Sections and $L_b/R = 0.075$

Figure 6.8.16 shows the girder profiles, and the bridge plan and cross-section views for the fixed-end composite bridge system with "optimized" midspan and fixed-end girder cross-sections and $L_b/R = 0.075$. As shown in the plan view, section transitions are made at the middle of the second unbraced length from the girder end. Due to the use of prismatic sections along the girder length, the first fixed-end bridge system has low flexural unity checks in the positive moment region at the midspan. This results in substantial inelastic reserve strength that helps the first fixed-end bridge support additional loads after the capacities of the fixed-end supports are exhausted. For the second fixed-end bridge case, both the fixed-end and midspan unbraced lengths are designed to reach their corresponding strength limit states at the governing Strength I load level. This necessitates the use of section transitions along the girder lengths, as well as a reduction of the web depth from 1200 mm (48 in) to 950 mm (38 in). Also, Grade 50 steel is used for the bottom flange of girder G3 instead of Grade 70W. As shown in Figure 6.8.16e, the common cross-section shown in Figure 6.8.16c is used for all the girder cross-sections in the positive moment region.

When it comes to the design of unbraced lengths in negative bending, the governing flexural capacity, F_n, is the flange local buckling (FLB) resistance, which is slightly lower than the flange yield strength, F_{yf} for the bridge girders. Similar to the first fixed-end bridge system, the lateral-torsional buckling (LTB) resistance lies in the plateau region (i.e., $F_n = F_{yf}$) due to the moment gradient factor, C_b, which is close to 1.75 for all three girders. The design unity checks for flexure are 0.95, 0.94 and 0.98 for the G1, G2 and G3 unbraced lengths in negative bending, respectively.

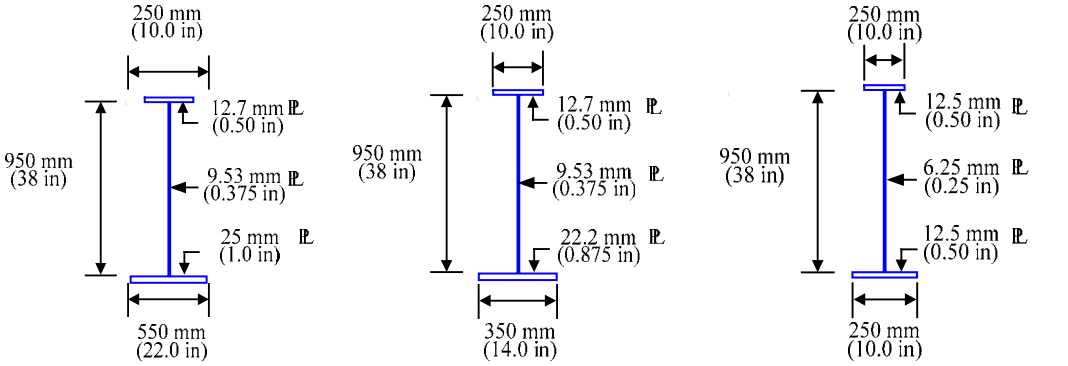

a) G3 cross-section (negative)

(b) G2 and G1 cross-sections (negative)

(c) Common cross-section (positive)

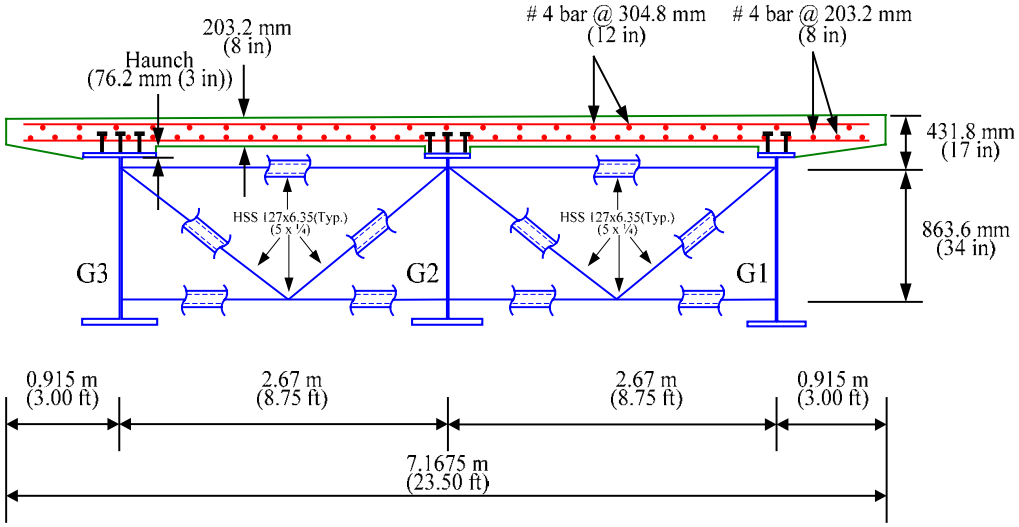

(d) Bridge cross-section at midspan

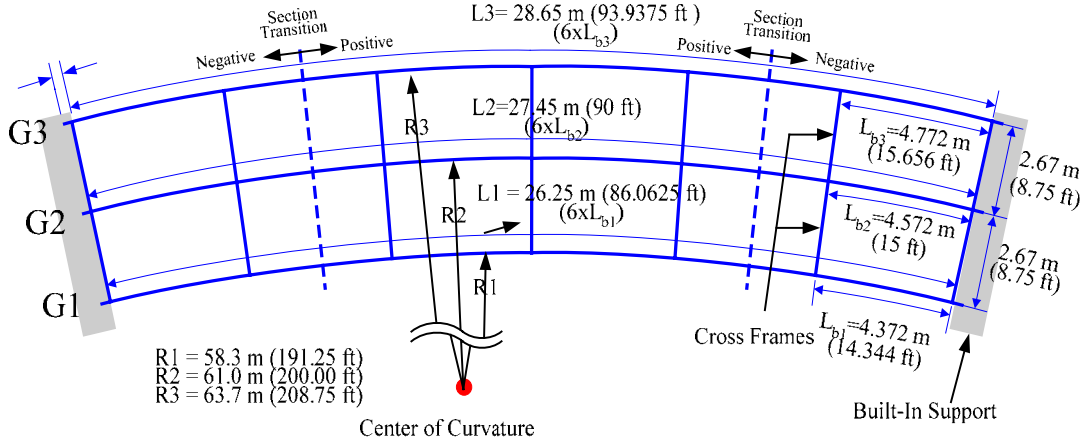

(e) Bridge plan

Figure 6.8.16. Case 9b fixed-end composite bridge with "optimized" midspan and fixed-end girder cross-sections and $L_b/R = 0.075$.

The corresponding lateral bending stress limit checks are 0.33, 0.50 and 0.40 for G1, G2 and G3, respectively. The web thickness of 9.38 mm (0.375 in) is used for all of the girder webs to satisfy the AASHTO (2004b) web bend buckling check under Service II limit state.

Regarding the design of unbraced lengths in positive bending, the design unity checks for flexure are 0.90, 0.82 and 1.0 for the G1, G2 and G3 unbraced lengths, respectively. The corresponding lateral bending stress limit checks are 0.90, 0.90 and 1.0 for G1, G2 and G3, respectively. The web thickness is set to 6.25 mm (0.25 in) for all the girder webs in the positive moment region.

It should be noted that some of the above girder dimensions are smaller than would ordinarily be employed in steel bridge design. In this regard, the second fixed-end bridge (Case 9b) may be considered as say a 2/3 scale test of a prototype bridge structure. Of course, the AASHTO design load model does not scale by 2/3, but it is believed that the estimate of the overall behavior is applicable for a larger bridge. Regarding the full nonlinear FEA simulation of the fixed-end bridge Case 9b, the same modeling assumptions and analysis considerations used as in Case 9a. Figure 6.8.17 provides updated Gauss point residual stresses patterns for the three girder cross-sections shown in Figure 6.8.16a-c.

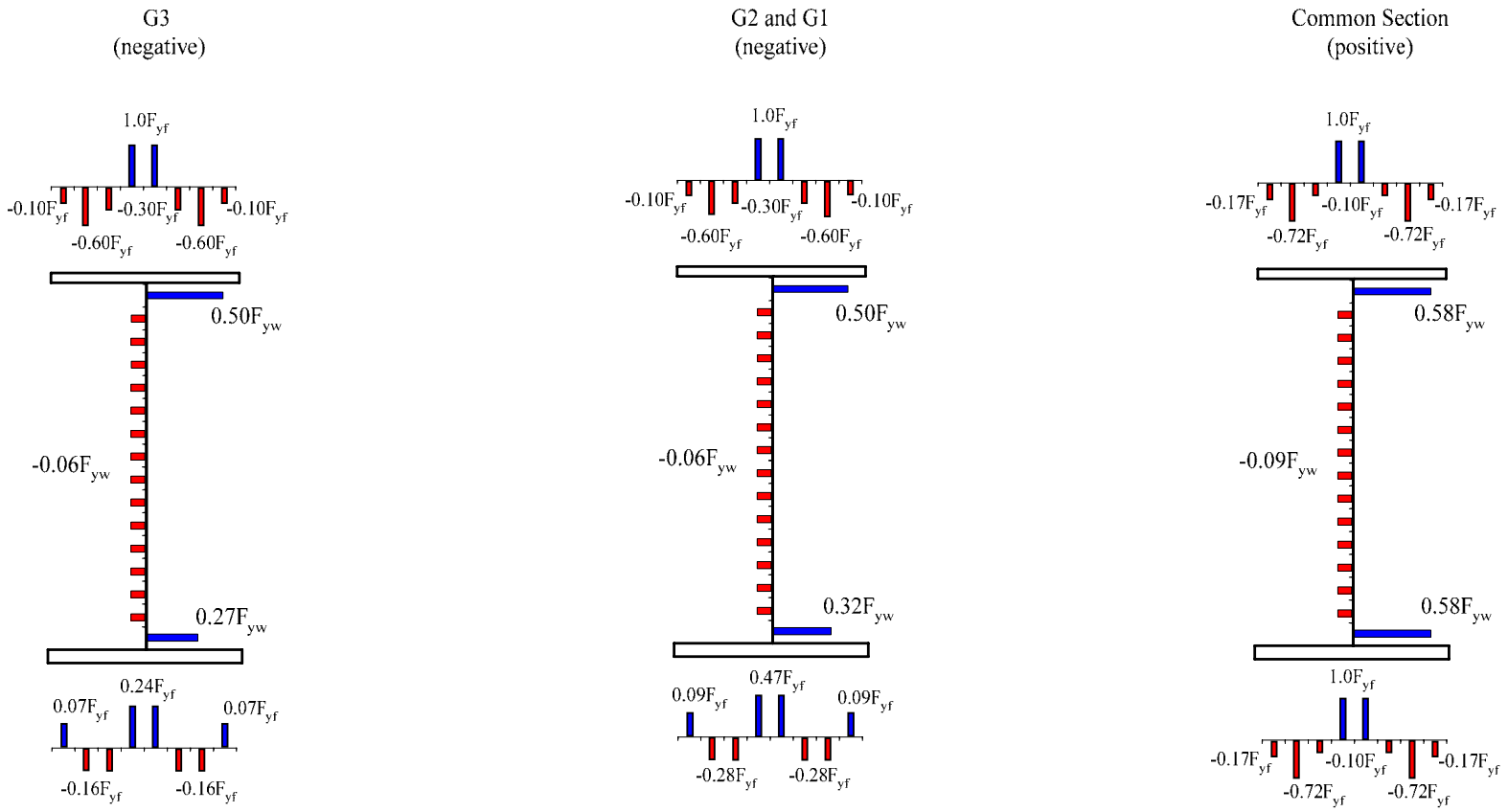

Figure 6.8.17. Case 9b gauss point residual stresses used within the bridge FEA model in accordance with ECCS(1976), based on flame cutting and consecutive placement of web-to-flange weld.

Figure 6.8.18 gives the applied load versus the midspan vertical deflection at the middle of G3's bottom flange for the Case 9b fixed-end bridge. It can be seen that the full nonlinear FEA solution represented by the solid line starts to deviate from the linear elastic prediction represented by the dashed line at about 2224 kN (500 kips) due to the cracking of the bridge slab at the fixed-end supports. For subsequent higher applied loads, the vertical deflection continues to increase in a nonlinear fashion up to 4106 kN (923 kips) where the deflection curve levels off showing a limit point. The corresponding vertical deflection is about 125 mm (4 in).

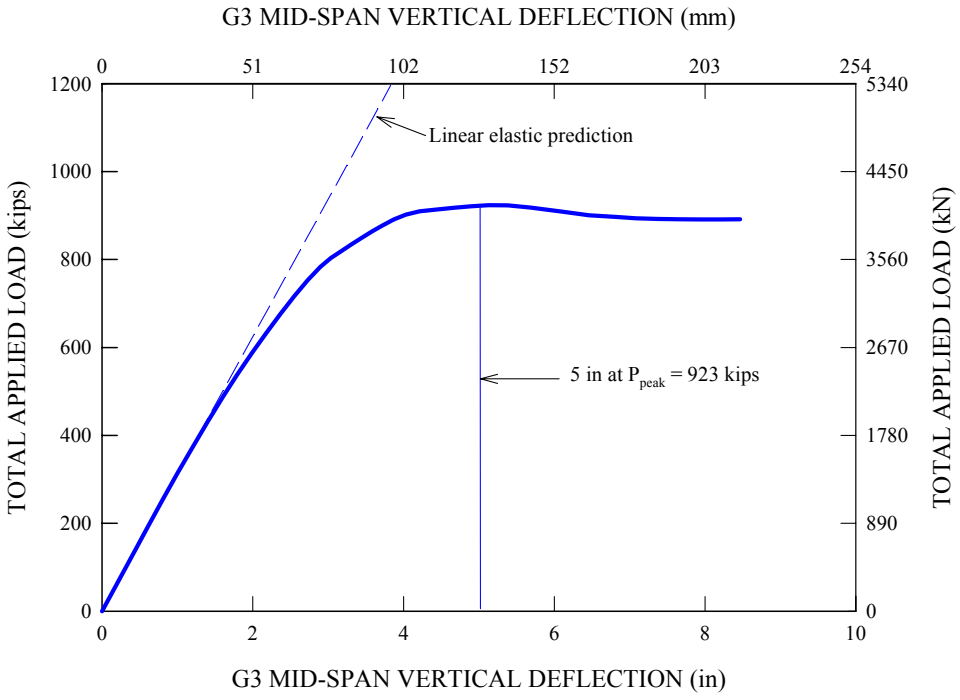

Figure 6.8.18. Case 9b applied load versus vertical deflection at the midspan of the G3 bottom flange.

As discussed for Case 9a, the onset of the full nonlinear FEA solution's departure from the linear elastic estimate is closely related to the concrete cracking near the fixed-

end supports and the resulting moment redistribution between the fixed-end and midspan regions. Figure 6.8.19 gives the fixed-end and midspan moments for the entire composite bridge cross-section throughout the applied loading history. The moments are calculated about an axis parallel to the radial direction at the midspan, as shown in the inset to Figure 6.8.19. The dead load internal moments are included in the plot. It can be seen that both the fixed-end and midspan moments are increase linearly up to a total applied load of about 2224 kN (500 kips). Again, this is the point when the bridge slab is effectively cracked through its width and depth at the fixed-end supports. As a result, moment redistribution starts to occur from the fixed-end supports to the midspan region.

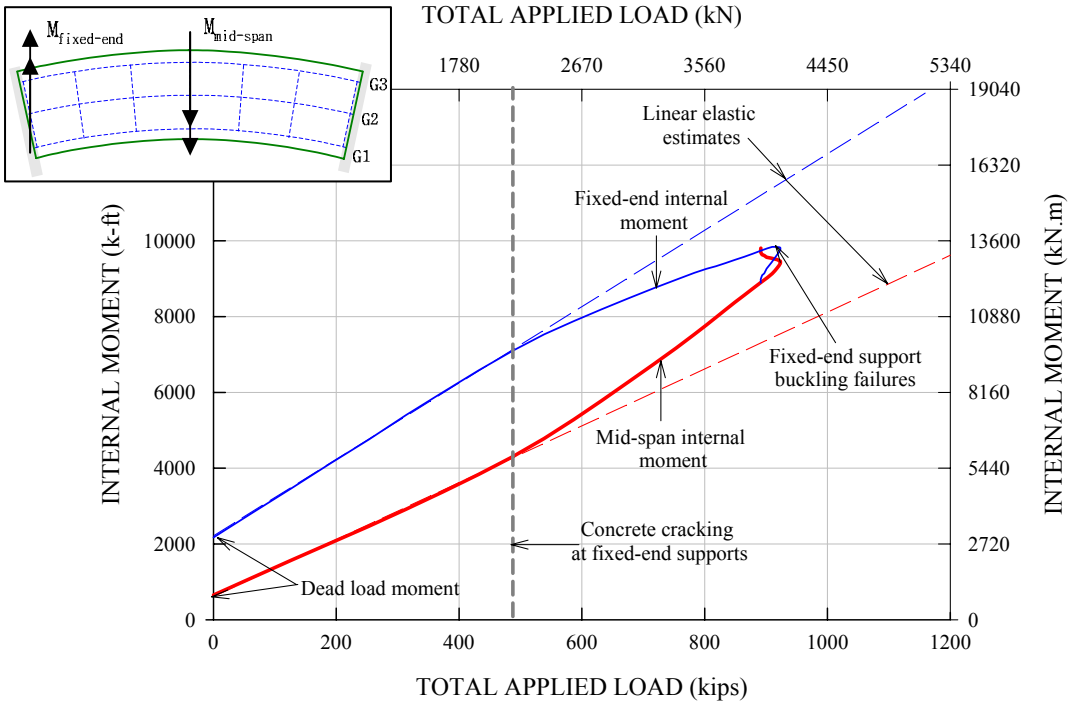

Figure 6.8.19. Case 9b applied load versus fixed-end and midspan moments for the entire composite bridge cross-section.

For loads higher than 2224 kN (500 kips), the fixed-end moment tends to be reduced relative to the linear elastic estimate indicated by the dashed line, and a portion of the fixed-end moment is redistributed to the midspan, resulting in a relative increase in the midspan moment. The moment redistribution continues to occur until the midspan section capacity is exhausted due to extensive yielding of the steel sections and nonlinear behavior of the concrete. Both the fixed-end and midspan moments increase nonlinearly relative to the total applied load until the limit point of Figure 6.8.18 is reached at a total applied load of 4106 kN (923 kips). It is important to note that the above limit point corresponds to the bridge cross-section capacity at midspan is close to fully exhausted. Otherwise, the midspan moment might have continued to increase substantially and the bridge may have supported additional load as in Case 9a.

Furthermore, it is important to note that the capacity of the fixed-end support region is reached by buckling failures at the same peak load level. In other words, both the fixed-end and midspan regions reach their ultimate capacities at the limit load of the bridge. This is in strong contrast with the previous fixed-end bridge system for which the bridge system further sustains additionally applied loads after the failure of the fixed-end support regions due to inelastic reserve capacity in the positive moment region. However, it is important to recognize that the above limit point appears well above the elastic analysis and design resistance levels considered in this research. Interestingly, it is shown subsequently that the midspan moment continues to increase slightly at applied load levels in the post-peak range of Fig 6.8.18. The fixed-end support regions fail by a combination of flange local buckling (FLB) and web bend buckling and shed a portion the fixed-end moment to the midspan in the post-peak range of the response.

Figure 6.8.20 shows the girder deformed geometries at the girder fixed-end supports when the limit point is reached at a total applied load of 4106 kN (923 kips). One should note that all three girders fail essentially by a combination of the flange local buckling (FLB) and web bending buckling at their fixed ends. Interestingly, the visual inspection of the girder deformed geometries shows that all three girders reach their strength limit states shown in Figure 6.8.12 approximately at the above limit load level. This eliminates the possibility any significant redistribution by changes in the girder end moments.

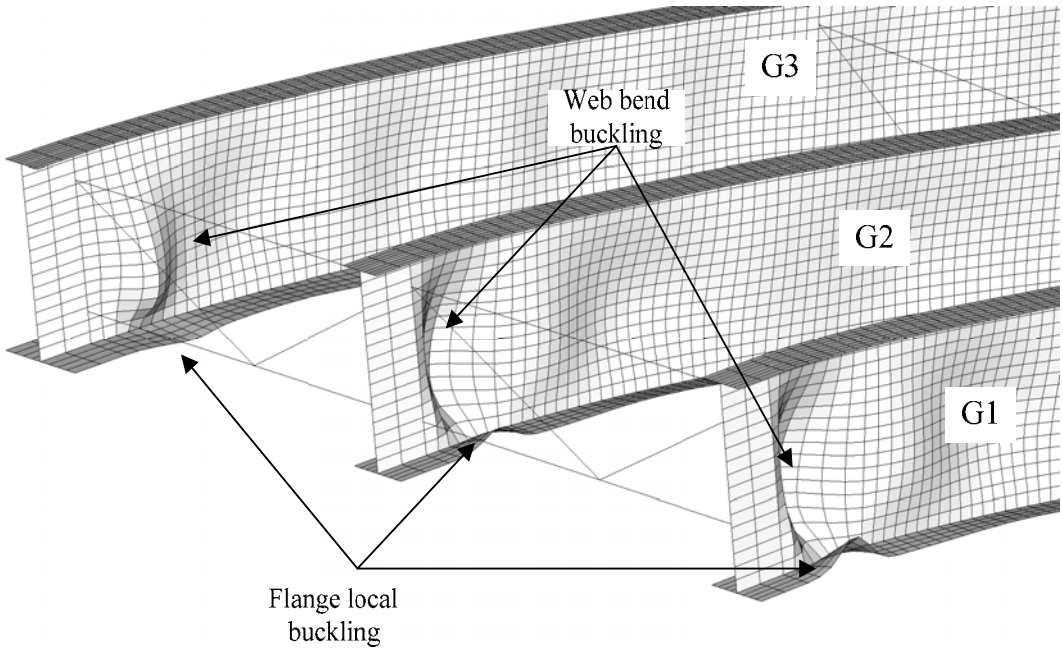

Figure 6.8.20. Case 9b girder deformed geometries at the fixed-end supports when the limit point is reached at a total applied load of 4106 kN (923 kips) (Deformation Scale Factor = 10).

Figure 6.8.21 shows the girder deformed geometries at midspan with contours of the von Mises stresses when a the bridge limit load). It should be noted that a large portion

of the midspan girder cross-sections are extensively yielded at this load level, indicating the fact that the midspan bridge cross-section is close to its ultimate capacity. As a result, the fixed-end bridge Case 9b is not able to support additional applied loads at the girder end strength limits. This is in contras to Case 9a where the midspan region has extra reserve capacity after the failure of the fixed-end support regions. In what follows, detailed component responses are discussed including the individual girder moments, cross-frame member forces and girder reactions.

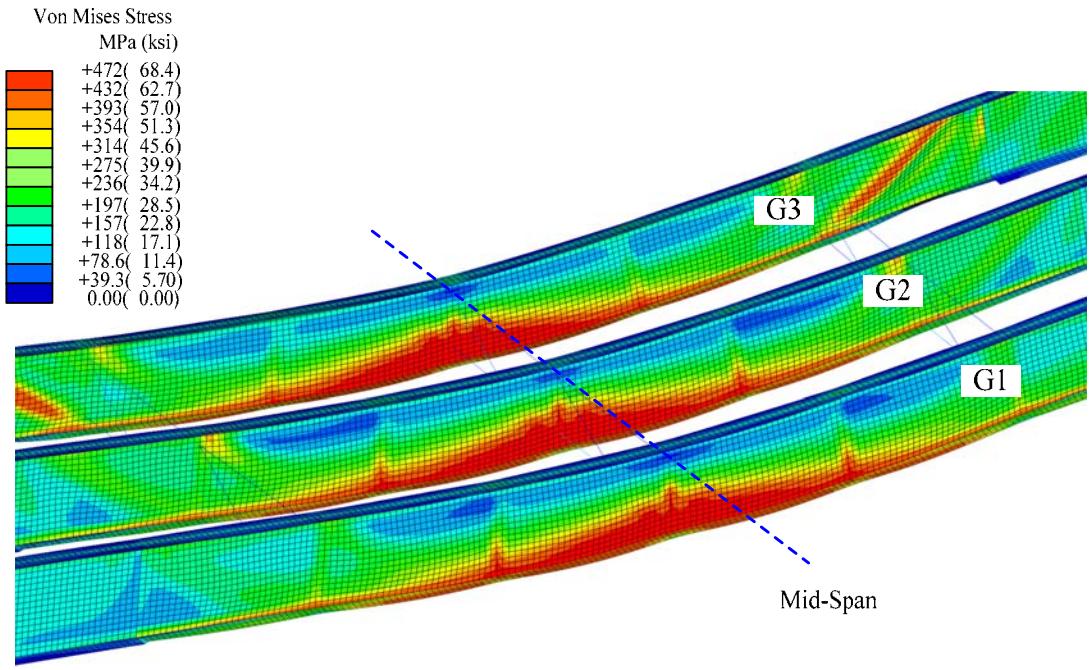

Figure 6.8.21. Case 9b girder deformed geometries at midspan with contours of von Mises stresses when the limit point is reached at a total applied load of 4106 kN (923 kips) (Deformation Scale Factor = 10).

Figures 6.8.22 through 6.8.24 show the internal moments for girders G1, G2 and G3 at the fixed-end and midspan regions throughout the applied loading history. There are two strength limit states marked on the plots: the FLB- and the $1.3M_y$-based 1/3 rule load

levels on G3. The FLB-based 1/3 rule load level on G3 relates to the total applied load level of 3203 kN (720 kips) when the G3 unbraced length in negative bending reaches the flexural strength limit state associated with the flange local buckling (FLB) failure on G3. The $1.3M_y$-based 1/3 rule load level on G3 relates to the total applied load level of 3470 kN (780 kips) when the G3 unbraced length in positive bending reaches the flexural strength limit state based on $1.3M_y$ instead of the M_p-based 1/3 rule load levels used for earlier simply-supported bridge structures. AASHTO (2004b) requires that base flexural capacity must be limited to $1.3M_y$ for straight continuous-span composite sections in positive flexure. For these types of composite sections, excessive yielding in the positive moment region can potentially lead to significant redistribution of moments to the negative moment region that are greater than those predicted by an elastic analysis (AASHTO (2004b) Section 6.10.7.1.2). That is, the limit of $1.3M_y$ essentially guards against an under-design of the negative moment regions due to moment redistribution. As discussed previously for Case 9a and also as shown in this section for Case 9b, the AASHTO (2004b) Section 6.10.1.5 assumption that the slab is fully effective throughout the bridge length also tends to protect against an under-design of the negative moment region.

One can see that all the girder internal moments at the fixed-end and midspan regions increase linearly until the point when the slab concrete is cracked essentially through its width and depth at the fixed-end supports. For higher applied loads, the fixed-end and midspan moments obtained from the full nonlinear FEA simulation deviate from corresponding linear elastic estimates indicated by the dashed lines in the figures.

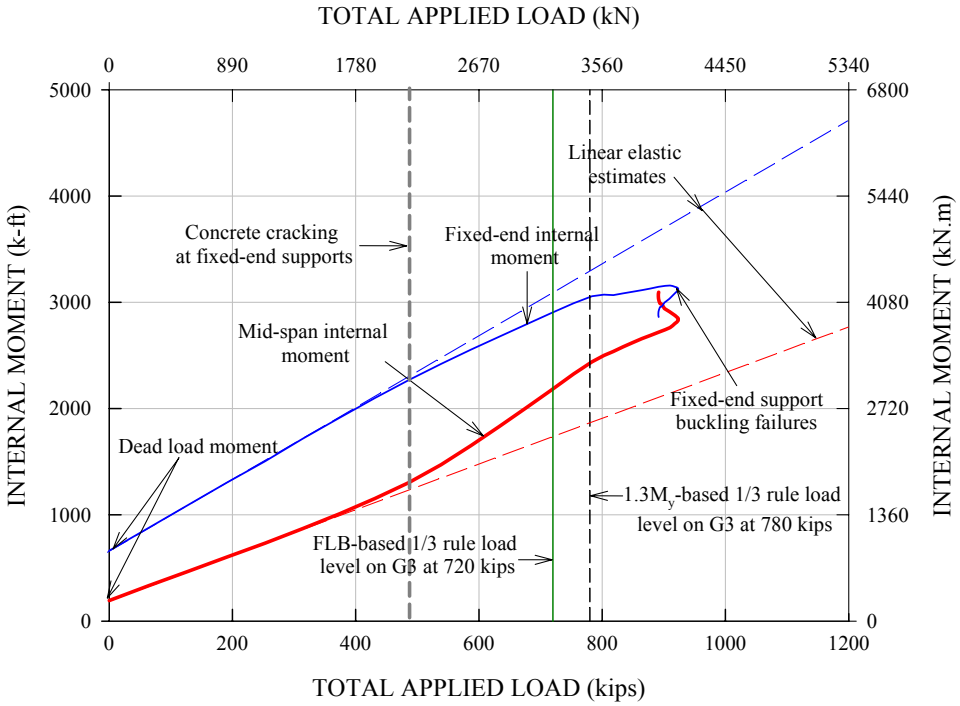

Figure 6.8.22. Case 9b applied load versus internal moments for the isolated G1 composite cross-section at the fixed-end and at the midspan.

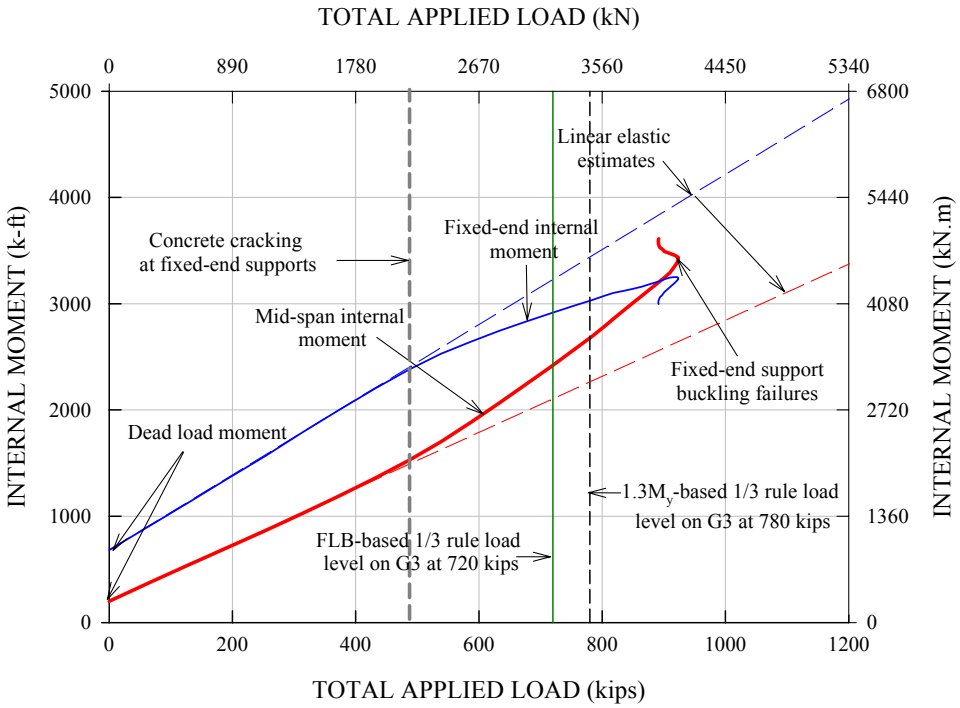

Figure 6.8.23. Case 9b applied load versus internal moments for the isolated G2 composite cross-section at the fixed-end and at the midspan.

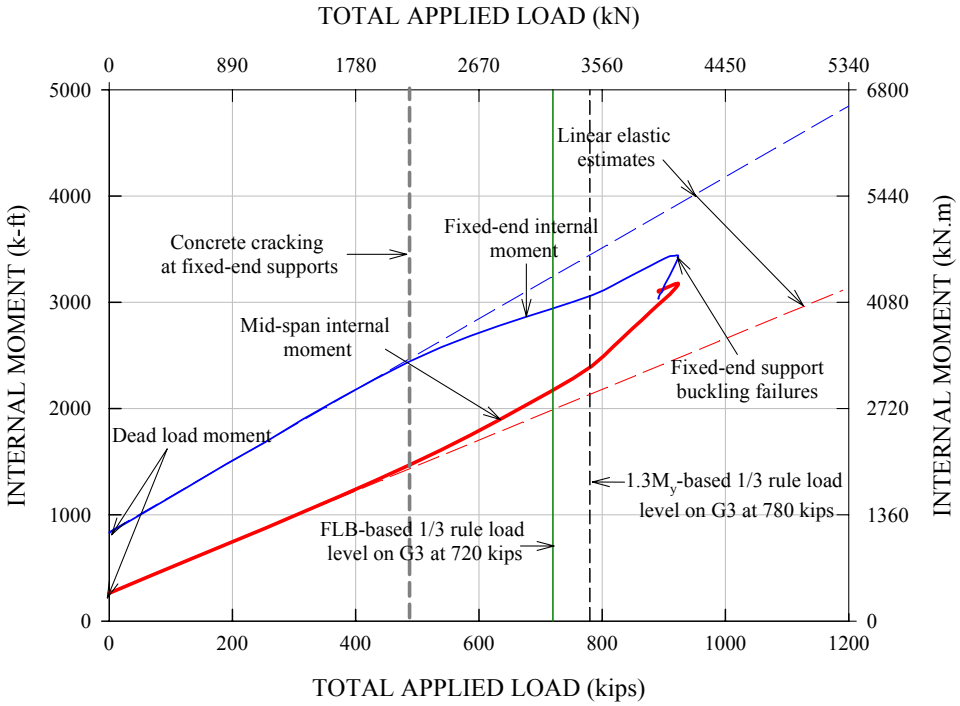

F0igure 6.8.24. Applied load versus internal moments for the isolated G3 composite cross-section at the fixed-end and midspan regions.

In case of the G2 fixed-end and midspan moments, Figure 6.8.23 shows that the fixed-end moment difference between the full nonlinear FEA and linear elastic solutions is redistributed to the positive moment region, resulting in a similar increase in the midspan moment relative to the linear elastic estimate. Interestingly, the same behavior does not occur for the G1 and G3 moments shown in Figures 6.8.22 and 6.8.24. In general, it can be seen in Figure 6.8.22 that the amount of the G1 fixed-end moment redistributed to the G1 midspan region is smaller than the moment increase at the midspan relative to the linear elastic estimate. Conversely, Figure 6.8.24 shows that the increase in the G3 midspan moment due to the moment redistribution from the fixed-end regions is smaller than the amount of the redistributed fixed-end moment. As mentioned previously for Case 9a, this implies that the fixed-end moment redistributed from G3 is

actually taken by the G1 midspan cross-section instead of the G3 midspan cross-section. However, as the total applied load nears the limit point, this kind of interplay among the girder cross-section starts to disappear, and the moment redistribution mechanism observed for the G2 cross-section moments is a better description of the incremental G1 and G3 moments.

Figures 6.8.25 through 6.8.27 give the moment-curvature responses for the G1, G2 and G3 midspan cross-sections throughout the applied loading history. For all three girders, the midspan moment increases linearly until the slab cracking moment (e.g., at about 1900 kN-m (1400 k-ft) for G3), and then it starts to deviate from the linear elastic estimate represented by the dashed line due to the slab cracking. Subsequently, the moment-curvature curve continues to increase in a nonlinear fashion. Interestingly, Figure 6.8.25 shows that the G3 midspan moment continues to increase and levels offs with a bounding internal moment of about 4204 kN-m (3100 k-ft), which is slightly larger than the section plastic moment capacity of 3932 kN-m (2900 k-ft) in the absence of lateral flange bending. With respect to the FLB-based 1/3 rule load level on G3 of 3203 kN (720 kips), the linear elastic moment estimate for the G3 midspan region is 2720 kN-m (2000 k-ft) while the corresponding full nonlinear solution is 2992 kN-m (2200 k-ft) due to the moment redistribution from the fixed-end support region. More importantly, it should be noted that the G3 full nonlinear FEA moment at this load level is located well into the nonlinear portion of the moment-curvature response. This is because the midspan cross-section must support a higher internal moment than the moment it is designed for due to the moment redistribution, thereby exhibiting early yielding. Similar observations are also made for the G1 and G2 moment-curvature responses in Figures

6.8.26 and 6.8.27. With respect to the $1.3M_y$-based 1/3 rule load level on G3 of 3470 kN (780 kips), the full nonlinear FEA solutions for the girder moments are larger than corresponding linear elastic estimates by a similar order of magnitude observed at the FLB-based 1/3 rule load level on G3. Also, it can be seen that the deviation of the full nonlinear FEA solutions from the linear elastic estimates tends to become much more significant. Despite the increased nonlinearity at this load level, it is important to note that the girder positive bending responses are quite ductile.

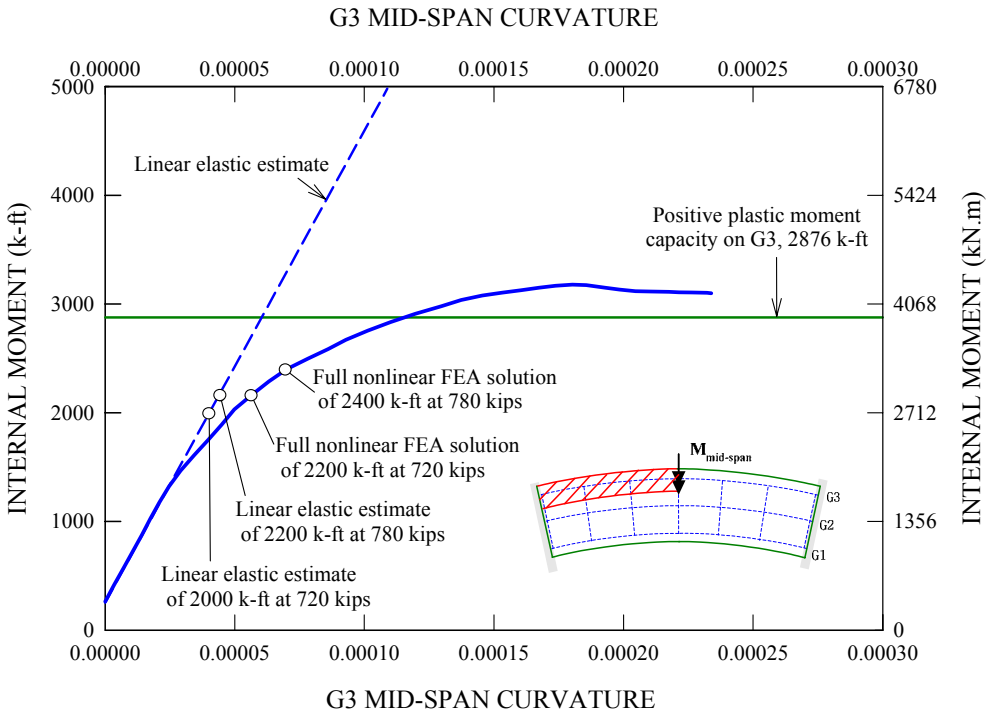

Figure 6.8.25. Case 9b G3 midspan moment versus corresponding curvature due to the applied loads, initial dead load moment included (the load of 3203 kN (720 kips) corresponds to the FLB-1/3 rule strength limit on G3 at the fixed ends and the load of 3470 kN (780 kips) corresponds to the $1.3M_y$-1/3 rule strength limit at the midspan of G3).

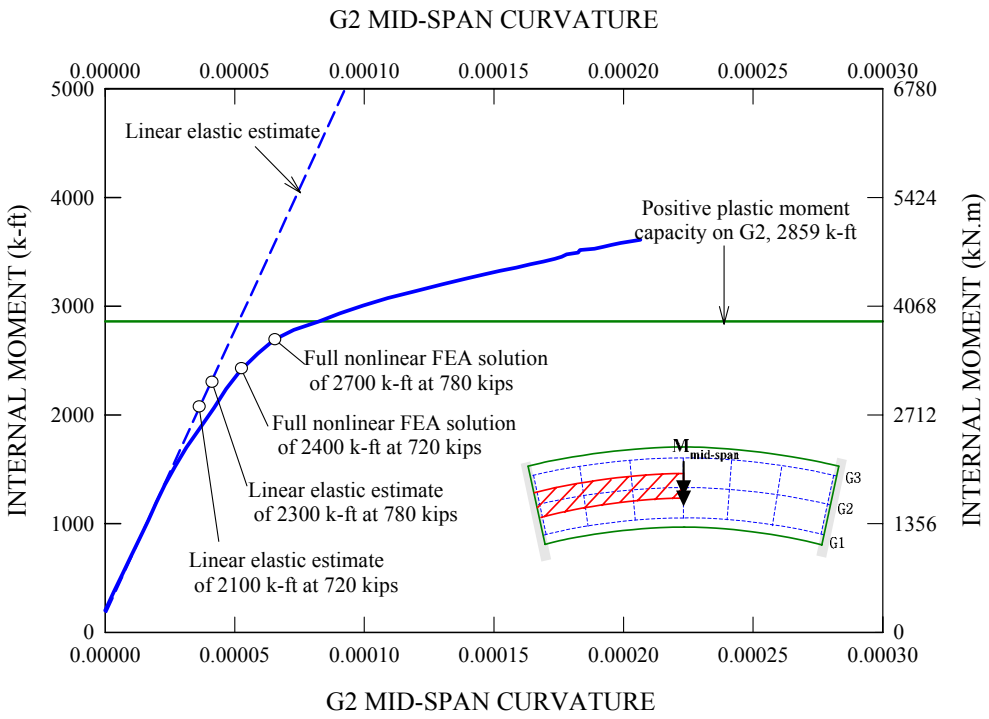

Figure 6.8.26. Case 9b G2 midspan moment versus corresponding curvature due to the applied loads, initial dead load moment included (the load of 3203 kN (720 kips) corresponds to the FLB-1/3 rule strength limit on G3 at the fixed ends and the load of 3470 kN (780 kips) corresponds to the $1.3M_y$-1/3 rule strength limit at the midspan of G3).

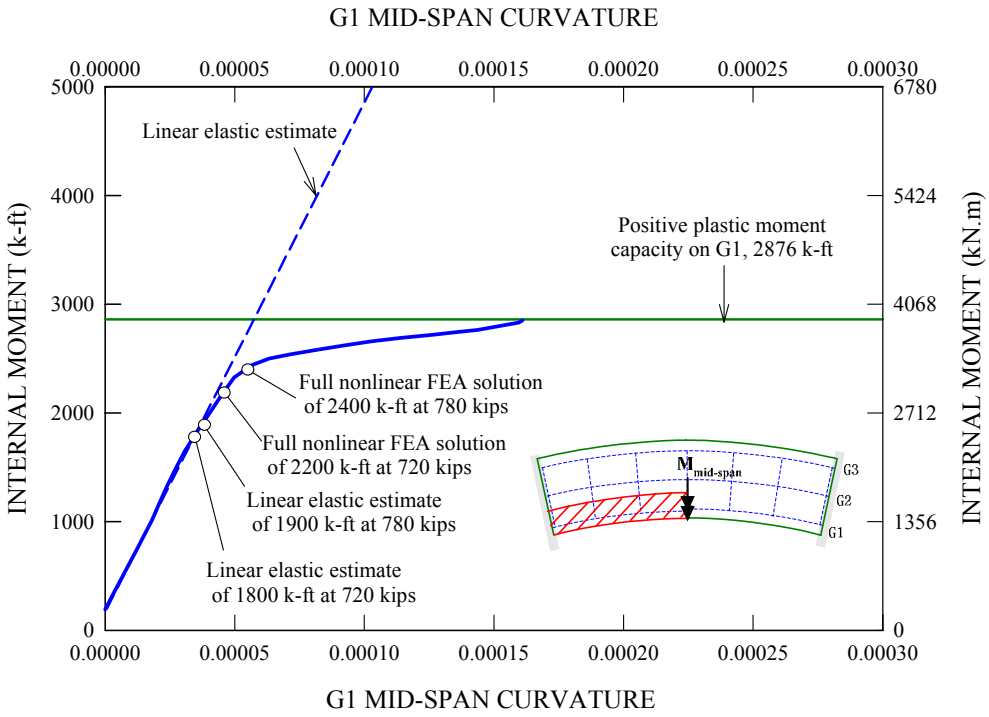

Figure 6.8.27. Case 9b G1 midspan moment versus corresponding curvature due to the applied loads, initial dead load moment included (the load of 3203 kN (720 kips) corresponds to the FLB-1/3 rule strength limit on G3 at the fixed ends and the load of 3470 kN (780 kips) corresponds to the $1.3M_y$-1/3 rule strength limit at the midspan of G3).

The above behavior is generally not a cause for concern. The positive and negative moment regions are designed for moments estimated based on the AASHTO (2004b) Article 6.10.1.5 assumptions such that the sum of all the resistances in the positive and negative bending regions is provide an equilibrium solution that balances the factored strength design loadings. Given the ductile behavior of composite I-girders in positive bending, if the positive moment regions are not sufficient to resist the calculated positive moments (because of an underestimation of these moments by the elastic analysis), redistribution to the negative moment regions will occur. This will cause the internal moments to approach the values calculated in the elastic analysis. The same cannot always be said about the negative moment regions, since a stability failure in negative bending may lead to a less ductile response.

Figures 6.8.28 through 6.8.30 present moment-curvature responses for the G1, G2 and G3 fixed-end cross-sections throughout the applied loading history. Similar to the midspan moment, the fixed-end moments increase predominantly in a linear fashion up to the point when the slab at the fixed-end regions is cracked through its width and depth. Then, the fixed-end moments continue to increase a nonlinear fashion, causing a redistribution of some of the fixed-end moments predicted by the linear elastic analysis to the midspan. It is noteworthy in the inset of Figure 6.8.28 that the G3 fixed-end region appears to fail predominantly by a combination of flange local buckling and web bend buckling distortions. This corresponds to a bounding internal moment that is slightly larger than the linear elastic estimate of the section FLB-1/3 rule based resistance (4488 kN-m (3300 k-ft)). Figures 6.8.29 and 6.8.30 show similar peak internal moments that are slightly larger than the AASHTO FLB-1/3 rule resistances of 4352 kN-m (3200 k-ft)

and 4216 kN-m (3100 k-ft) for the G2 and G1 fixed-end cross-sections, respectively. The G2 and G1 fixed-end regions also show a similar failure mode as shown in the insets to Figures 6.8.29 and 6.8.30.

With respect to the FLB- and $1.3M_y$-based 1/3 rule load levels on G3, the linear elastic moment estimate of the fixed-end moment is significantly larger than the corresponding full nonlinear FEA solution for all three girders. Therefore, the total applied load necessary to induce the failure of the fixed-end region is actually much higher than the design load level used to produce the linear elastic estimate moment at the FLB-based 1/3 rule load level. In fact, Figures 6.8.29 and 6.8.30 show that the G2 and G1 moment-curvature curves reach a plateau at the $1.3M_y$-based 1/3 rule load level of 3470 kN (780 kips) on G3 instead of the FLB-based 1/3 rule load level of 3203 kN (720 kips) on G3.

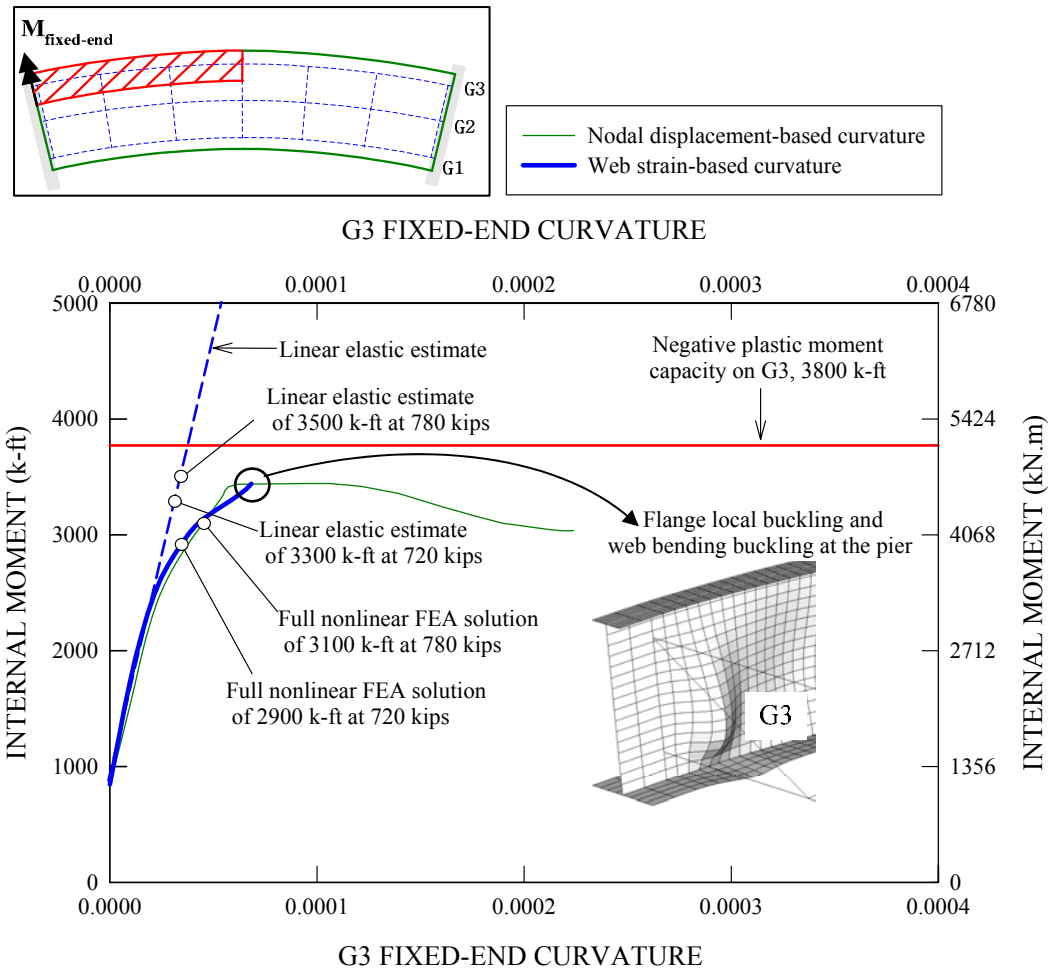

Figure 6.8.28. Case 9b G3 fixed-end moment versus corresponding curvature due to the applied loads, initial dead load moment included (the load of 3203 kN (720 kips) corresponds to the FLB-1/3 rule strength limit on G3 at the fixed ends and the load of 3470 kN (780 kips) corresponds to the $1.3M_y$-1/3 rule strength limit at the midspan of G3).

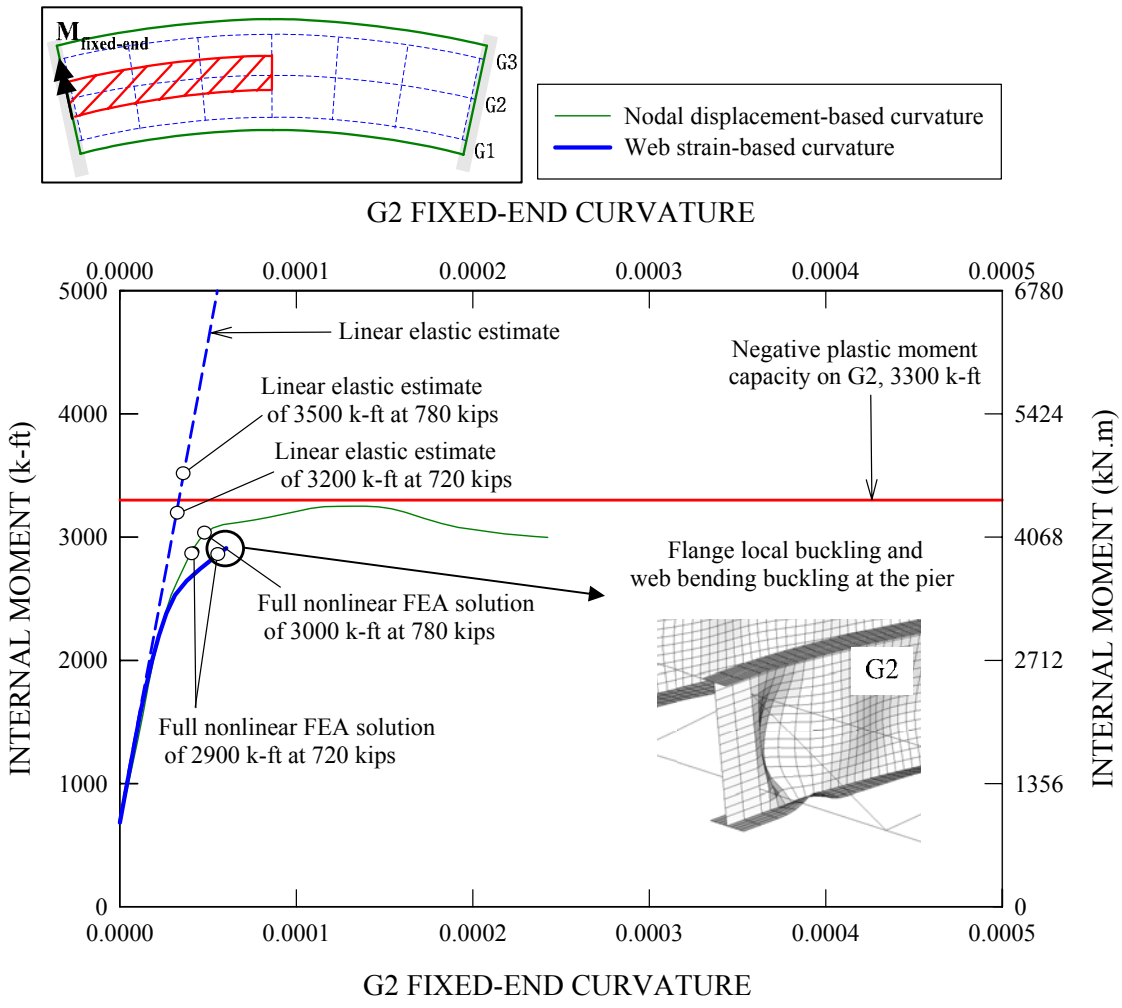

Figure 6.8.29. Case 9b G2 fixed-end moment versus corresponding curvature due to the applied loads, initial dead load moment included (the load of 3203 kN (720 kips) corresponds to the FLB-1/3 rule strength limit on G3 at the fixed ends and the load of 3470 kN (780 kips) corresponds to the $1.3M_y$-1/3 rule strength limit at the midspan of G3).

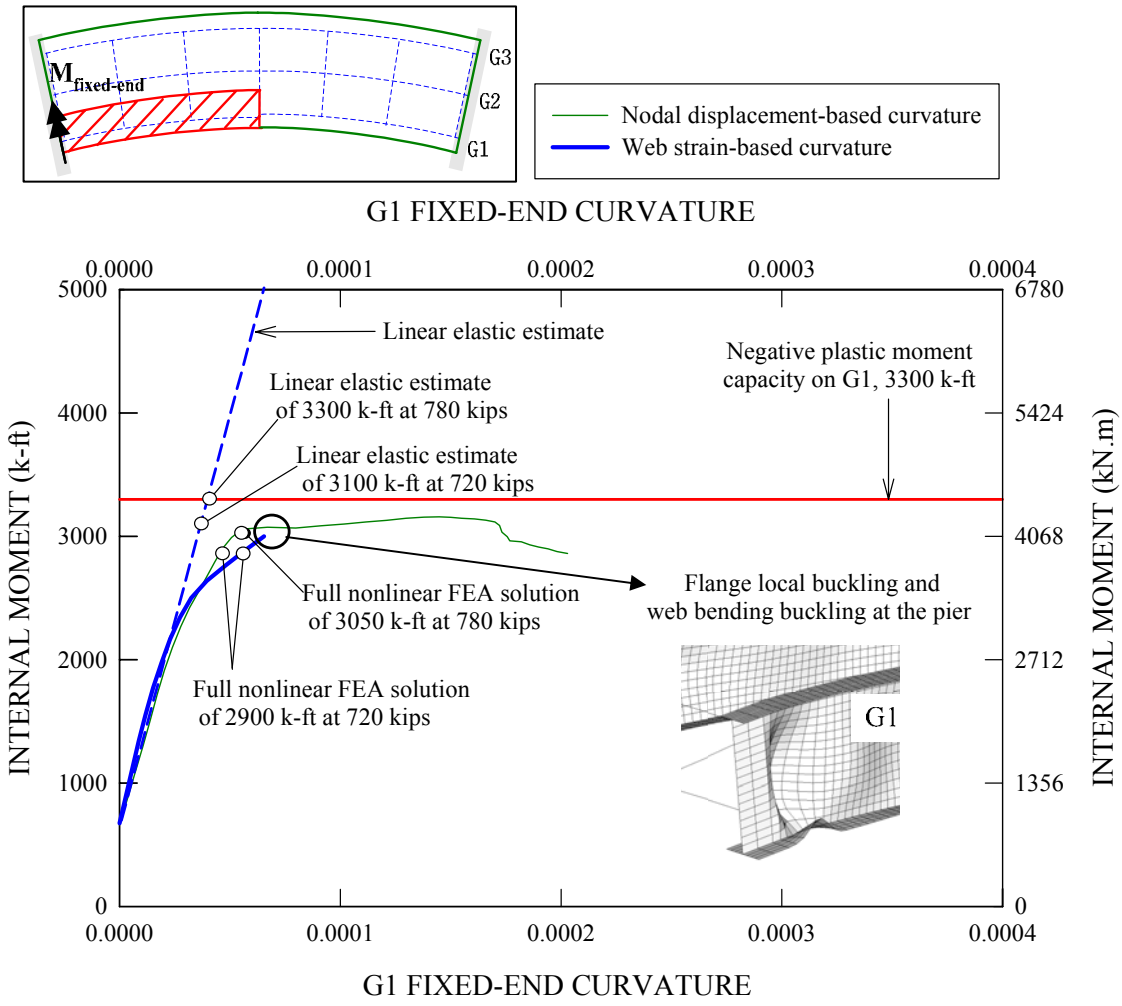

Figure 6.8.30. Case 9b G1 fixed-end moment versus corresponding curvature due to the applied loads, initial dead load moment included (the load of 3203 kN (720 kips) corresponds to the FLB-1/3 rule strength limit on G3 at the fixed ends and the load of 3470 kN (780 kips) corresponds to the $1.3M_y$-1/3 rule strength limit at the midspan of G3).

Figure 6.8.31 gives the axial forces in the bottom chords attached to G3 of the mid- and quarter-span cross-frames throughout the analysis. The initial dead load member forces are included in the plot. It can be seen that the cross-frame member forces due to applied loads increase linearly up to the FLB-based 1/3 rule load level on G3 as well as the $1.3M_y$-based 1/3 rule load level on G3.

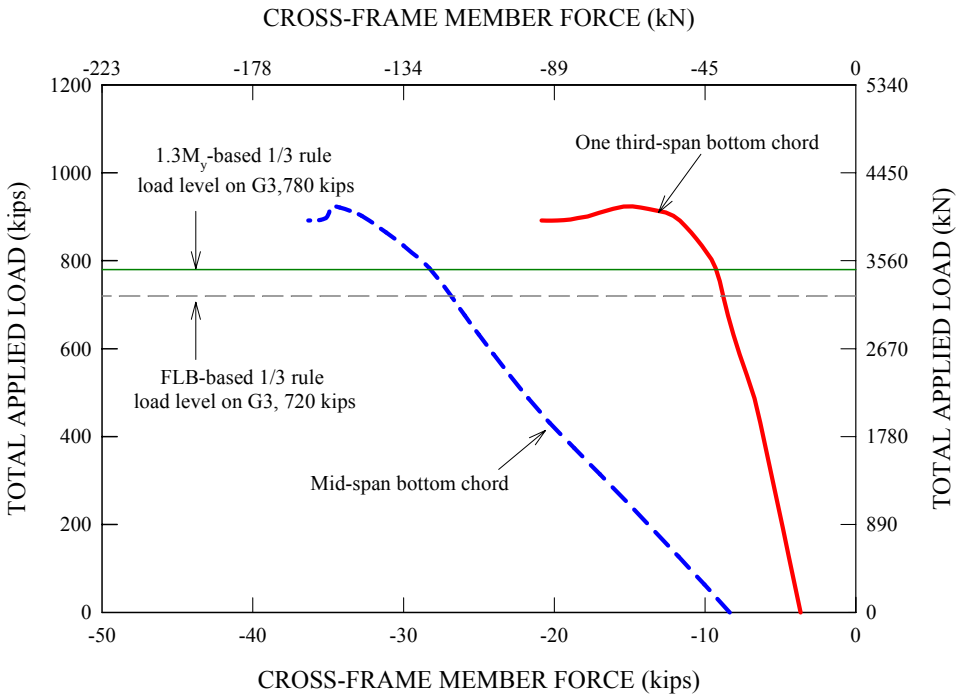

Figure 6.8.31. Case 9b applied load versus axial force in the bottom chords of the mid- and one third-span cross-frames attached to G3, dead load axial force included.

Figure 6.8.32 presents the girder vertical reactions throughout the full nonlinear FEA solution. The dead load reactions are included in the plot. It can be seen that the initial dead load reactions are quite similar among the bridge girders in terms of magnitude. The end fixity apparently results in more uniform participation of all the girders and less reliance on the outside girder G3. Furthermore, it is quite interesting to note that the

vertical reactions due to the applied loads increase in a linear fashion up to both the FLB- and 1.3M_y-based 1/3 rule load levels on G3.

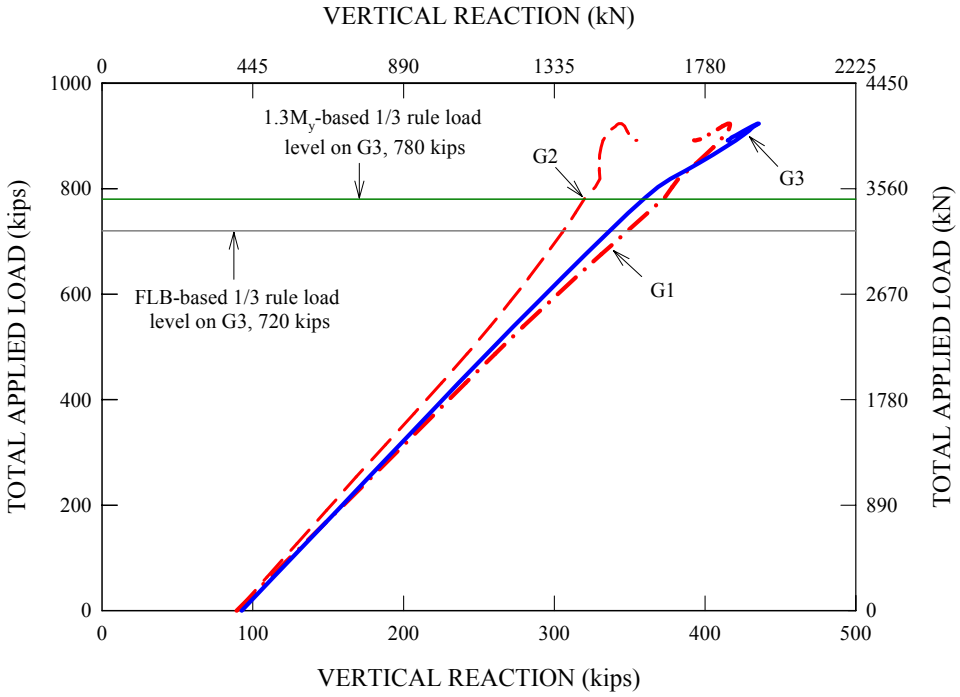

Figure 6.8.32. Case 9b applied load versus girder vertical reactions, dead load reactions included.

In summary, the ultimate capacities for simply-supported horizontally curved composite bridge structures are typically limited due to extensive yielding on steel sections. Concrete crushing is obtained ultimately at load levels substantially higher than the strength design loadings. In other words, they are not prone to non-ductile failure modes. Thus, even for horizontally curved bridge I-girders with their webs categorized as slender elements, the section plastic moment capacity of their outmost girder, with a reduction due to the effects of lateral bending moments, can be effectively used for the limit state strength resistance. This idealization is presently allowed in AASHTO

(2004b) for straight composite I-girder bridges with or without large flange lateral bending (large flange lateral bending can be caused by skew in some cases).

In the case of typical horizontally curved continuous-span bridges with highly noncompact or slender webs, their base capacities are typically smaller than the first yield moment since they are limited by stability-related limit states such as flange local buckling, lateral-torsional buckling and web bend buckling. In addition, linear elastic analysis assuming the concrete deck to be fully effective over the entire span length generally results in an overprediction of the negative bending moments and an underprediction of the positive bending moments. This is largely because of distributed cracking in the negative moment region of the slab at the strength resistance levels. Nonetheless, it is important for the engineers to recognize that this design practice is actually beneficial rather than problematic. That is, overestimated negative moments always ensure that continuous-span bridges develop their desired strength limit states, since the positive moment region generally behaves ductily when designed by the AASHTO (2004b) criteria. This is particularly true for the Case 9b fixed-end bridge system for which the fixed-end and midspan unbraced lengths are designed to reach their strength limit states at the Strength I load level.

CHAPTER 7

SUMMARY AND CONCLUSIONS

7.1 Summary

This thesis addresses the elastic design-analysis and design of a representative horizontally curved composite I-girder bridge proportioned at or above a number of maximum limits in the AASHTO (2003 and 2004b) Specifications. The test bridge was constructed at the Federal Highway Administration (FHWA) Turner-Fairbank Highway Research Center and was monitored under noncomposite dead loads, various composite live loads and a single composite ultimate loading.

Refined three-dimensional FEA models are developed and applied extensively in this research for the elastic design-analysis, as well as geometric nonlinear and full nonlinear FEA simulations of the test bridge system. The full nonlinear analysis includes the simulation of dead load effects on the intermediate noncomposite structure during construction, followed consecutively by the simulation of the effect of concrete shrinkage and then the effects of applied loads on the completed composite structure in a single continuous process.

This study provides the synthesis and scrutiny of the experimental results and corresponding full nonlinear FEA predictions for the above test bridge. Furthermore, the base test bridge FEA models, which are validated against the measured experimental responses, are extended to perform parametric FEA investigations into the strength behavior for several variations on the original test bridge.

7.2 Elastic Analysis and Design of the Test Bridge

The elastic analysis of the test bridge is performed using 3D FEA models generated within the ABAQUS 6.4-1 platform. The stresses and deflections obtained from the analysis are checked for the design limits required by the steel bridge design provisions. The composite test bridge is designed at the following extremes relative to the AASHTO (2003 and 2004b) provisions:

- There are only three internal cross frame locations, resulting in a cross-frame spacing of 6.75 m (22.5 ft) along G2 and a subtended angle between the cross-frames of $L_b/R = 0.1125$ (or 6.45^o). The maximum L_b/R permitted by AASHTO (2004b) is 0.10 for a completed bridge system. This is a practical upper limit suggested originally by McManus (1971) based on ASCE (1971). The cross-frame forces and I-girder lateral bending stresses tend to be rather large in practical configurations with L_b/R values beyond these limits.
- The nominal width of G1's top flange is 300 mm (12 in). Combined with the wide cross-frame spacing discussed above, this results in an L_b/b_f of 21.5 for this girder. The maximum value of L_b/b_f allowed for curved I-girders in AASHTO (2003) is 25. AASHTO (2004b) requires that L_b must be smaller than L_r, the smallest unbraced length at which the elastic lateral-torsional buckling equations govern the base flexural resistance. For typical I-girders, L_b/b_f is close to 25 when $L_b = L_r$. In general, members with $L_b > L_r$ tend to have larger second-order amplification of flange lateral bending stresses. The 300 mm (12 in) wide top flange on G1 also gives $L_1/b_f = 4L_b/b_f = 86$, which is close to the AASHTO (2004b) recommended maximum limit for a shipping piece.

- The slenderness ratio of the I-girder webs (D/t_w) ranges from 133 to 149. This is close to the AASHTO (2004b) limit of 150 for straight and curved transversely-stiffened web panels and exceeds limits specified for curved webs in AASHTO (2003). Also, the maximum stiffener spacing d_o is approximately 3D. This is the limit for straight and curved transversely-stiffened girders in AASHTO (2004b), and is a considerable liberalization relative to AASHTO (2003). AASHTO (2003) requires $d_o \leq D$ when the radius R is less or equal to 210 m (700 ft). The shear strength design of the girders requires a stiffener spacing of $d_o/D \cong 1$, 1.7 and 2.4 near the end supports of G3, G2 and G1 respectively, but only $d_o/D \cong 3$ near the midspan of these girders. Also, $d_o/D = 0.5$ in the end panels to anchor the shear tension field.
- The compression flange slenderness ratio $b_{fc}/2t_{fc}$, is 12.1 for G3. This is close to the maximum $b_f/2t_f$ of 12 permitted by AASHTO (2004b) for curved and straight I-girders, and is somewhat larger than the corresponding limits in AASHTO (2003). The AASHTO (2004b) limit of $b_f/2t_f = 12$ is a practical upper bound intended to ensure that the flanges will not distort excessively when welded to the web. The CSBRP studies on component behavior indicate that the resistances of straight and curved noncompact-flange I-girders are predicted accurately to conservatively and there is no significant adverse effect on the ductility by using $b_{fc}/2t_{fc}$ values up to this limit (e.g., see White and Grubb (2005)). For a given flange area, the use of larger $b_f/2t_f$ values may be more economical in some cases, since the resulting flange lateral bending section modulus is larger.

- HPS 70W material is used for the bottom flange of G3, whereas the web and top flange of G3 are composed of Grade 50 steel. AASHTO (2003) prohibits the use of hybrid construction due to the limited testing of curved hybrid girders. Conversely, the AASHTO (2004b) provisions allow curved hybrid girders based on the fact that: (1) the elastic service load stresses tend to be smaller and (2) the inelastic deformations at strength load levels are not significantly different in hybrid webs compared to webs in homogeneous girders composed of the higher-strength flange material.
- Girders G2 and G3 are sized close to the AASHTO (2004b) strength limits.

7.3 Experimental Testing and Full Nonlinear FEA of the Test Bridge

Four major sets of experimental tests were conducted on the composite test bridge. They are labeled as Tests 1 through 3, 4a and 4b, following the testing sequence. Test 1 addressed the generation of influence surfaces by applying a concentrated load of 72 kN (16 kips) repeatedly on a number of grid points on the slab. In Tests 2 and 3, the test bridge was subjected to a group of six loads from hydraulic jacks positioned on the test bridge slab such that they were directly above the bridge girders. These concentrated hydraulic jack loads were directly applied on G2 and G3 for Test 2, inducing the maximum flexural effects on G3, whereas they were applied on G1 and G2 for Test 3, inducing the maximum flexural effects on G1. In the final two tests, Tests 4a and 4b, the test bridge was subjected to a group of nine hydraulic jack loads that were approximately equivalent to the two AASHTO design trucks plus two lane loads used for the design of the outside girder G3 in the test bridge. Test 4a involved two repeated loading sequences at several load levels defined in relation to various AASHTO (2004b) design limits as

well as other limits, and Test 4b involved the final monotonic loading of the test bridge to its ultimate capacity. Of the two Test 4a sequences, the first involved loading cycles at five different levels (Levels A to E), based on the average peak total applied load in each of the cycles. These load levels corresponded to the total factored AASHTO design load for Level A, the Service II condition on G3 for Level B, the Strength I condition on G3 for Level C, the Strength I condition on G2 for Level D and the Initial yielding on G1 for Level E. In the second sequence of the Test 4a repeated loadings, the applied load was cycled from zero load, starting again at the smallest load level, Level A, then at load level C and finally at load level D.

Full nonlinear FEA simulations corresponding to each of the experimental tests 2, 3, 4a and 4b are conducted to further investigate the behavior of the composite test bridge. In what follows, key observations and findings pertaining to each of the tests are presented in the order of actual experimental tests.

7.3.1. Noncomposite Bridge Configuration and Responses

- The targeted cambers for the outermost girder, G3, are matched well by corresponding cambers measured along the entire girder length. The camber readings for the remaining two girders, G1 and G2, show that their comparisons to the targeted camber values are not as good as that of the G3 camber readings. Nonetheless, their deviations from the desired positions are within the maximum camber tolerances allowed by the AASHTO Bridge Welding Code (2002) provisions.
- Major-axis and lateral bending stresses measured at the end of the steel erection and concrete casting are all matched well by corresponding FEA predictions for all of

the girders. Similarly, good comparisons are obtained for the measured and predicted girder deflections at the midspan outside tip of the test bridge girders.

- Although the FEA solutions predict slightly different individual girder reactions relative to the measured reactions at the end of the steel erection, the total accumulated girder reactions obtained from the FEA solutions eventually equal the measured values at the end of the concrete casting operation, i.e., at the zero applied load level just prior to the application of composite live loads.

The above findings indicate that the bridge FEA model successfully represents the physical state of the composite test bridge at the zero applied load level, thereby indicating the accuracy and reliability of the full nonlinear FEA predictions relative to the experimental results at the start of the applied loadings on the test bridge.

7.3.2. Results of Tests 2 and 3

- For Tests 2 and 3, the measured girder vertical and radial deflections increase predominantly in a linear fashion up to the peak experimental loads. There are negligible residual deflections at the end of these tests. Furthermore, these measured quantities are matched well by the FEA predictions. The FEA solutions obtained from the repeated loading analysis also indicate that there are no residual deflections at the end of these tests.
- Regarding the girder stresses in Test 2, it is found that the total maximum flange stress measured at the G3 flange tip, which is a combination of the major-axis and lateral bending stresses, is significantly less than the flange yield strength at the peak applied load. In the case of Test 3, the maximum flange stress occurring at the

G1 bottom flange tip reaches the flange yield strength at the peak applied load. However, the flange yielding was very minor

- Similar to the girder deflections, the girder vertical reactions also increase in a linear fashion for both of Tests 2 and 3, and they are comparable to corresponding FEA predictions. The radial reactions at the bridge bearings are found to be quite small.
- The member axial force in the bottom chord of the midspan cross-frame attached to G3 increases linearly for both the measured and predicted quantities up to the peak applied loads. Also, it is found that incremental member residual forces at the end of each loading cycle are negligible for both of the tests, leaving essentially zero total accumulated member residual forces at the end of the tests.
- Regarding the slab top surface strains in Test 2, both the measured and predicted strains vary approximately in a linear fashion across the bridge cross-section at the peak applied load level, with the maximum strain occurring at the edge of the overhang outside G3. These strains are less than the strain associated with the elastic limit of the concrete stress-strain response. Similarly, the measured and predicted slab strains in Test 3 are also within the elastic limit of the test bridge concrete response, but their distributions across the bridge cross-section are approximately constant in magnitude.

Based on the above findings, it is clear that all the measured responses in Tests 2 and 3 are essentially in the linear elastic range. The test bridge system is not left with any residuals or permanent sets with the completion of the first two experimental tests conducted on the composite test bridge. Similar results are also obtained from the

repeated loading analyses of these two tests. Therefore, in the subsequent FEA simulations concerning the repeated and monotonic loading of the test bridge conducted in Test 4, there is no consideration of the effects of Tests 2 and 3 in them.

7.3.3 Results of Test 4a: Repeated Loading Tests

- The hydraulic rams used in Tests 4a and 4b did not have sufficient stroke to load the bridge beyond Level C without chairing. For the loading cycles up to Levels D and E, the rams were chaired at one stage during the loading and unloading. For the subsequent ultimate strength test (Test 4b), multiple chairing operations were required. Two different types of tie-down arrangements were utilized during the experimental testing: Type 1 for the first repeated loading sequence and Type 2 for the second repeated loading sequence and the final monotonic loading test. The change from Type 1 to Type 2 was necessary because a significant increase in the slab strains was observed during the Type 1 chairing operations. Based on all the available data including girder reactions, girder deflections and slip measurements at the concrete-steel interface, there are no indications that the bridge responses were significantly influenced by the chairing operations during the repeated loading cycles.
- There is a good correlation between the measured and predicted deflections for the relatively low applied load levels, A and B. The load-deflection responses are essentially linear at these two load levels. However, as the magnitude of the load cycles is increased to levels C, D and E, the envelopes for the midspan deflections tend to drift away from the FEA predictions due to accumulated deflections during the repeated cycles at each applied load level.

- The total accumulated residual deflection for the first sequence of Test 4a is 4.1 mm (0.16 in), 8.4 mm (0.33 in), 20 mm (0.78 in), 36.6 mm (1.44 in), 77.0 mm (3.03 in) at the end of load levels A, B, C, D and E, respectively. Regarding the residual deflections for the second sequence of Test 4a, the increase in these deflections is much smaller between levels A and C and between levels C and D than in the first sequence. However, the increase in the residual displacements during the repeated cycles is very similar in both sequences. The total residual deflection just before the start of Test 4b is 3.75 in. However, the corresponding FEA prediction obtained at the end of the repeated loading simulation is only 1.0 in.
- The source of significant additional residual deflections during the repeated loading tests is not clear at the time of the completion of this research. The slip residuals at the concrete-steel interface were measurable both in the longitudinal and radial directions. However, their magnitudes were too small to cause the measured residual deflections. The girder vertical reactions and slab midspan longitudinal strains were predominantly linear. There were no indications of significant additional strains at the slab strain gauges due to the repeated loading cycles. In addition, the girder bottom flange strains did not show any significant changes during the repeated loading cycles. Furthermore, there were no indications of significant changes in the cross-frame member forces during the repeated loading cycles. Despite the lack of the knowledge regarding the source of the residual deflections, it is fortunate that the repeated loadings, although increasing the inelastic vertical and radial deflections of the test bridge, did not show any significant effect on the subsequent responses.

7.3.4 Results of Test 4b: Ultimate Monotonic Loading Test

- The FEA solution including the effects of the prior repeated loading tests provides a better comparison to the experimental data by capturing the extension of the proportional limit in the measured load-deflection curves associated with the prior plastic deformation during the repeated loading tests, as well as by capturing more substantial nonlinearities at significantly high applied load levels in the ultimate load test. However, the other FEA solution without the effects of the prior repeated loading tests included also compares favorably to the measured data, since the extent of nonlinearity associated with material inelasticity during the prior repeated loading tests is minor.
- The entire bridge cross-section at midspan not only moves in the downward direction upon the application of loading, but also moves toward the center of curvature, rotating with respect to its shear center located slightly above the top surface of the slab.
- The largest lateral movements occur on the bottom portion of the girders about halfway between the mid- and quarter-span cross-frame locations rather than at the midspan.
- The cross-section deformation profile of G3 located at 0.4375L from the end of the girder shows that the bottom flange basically slides laterally relative to the top flange of the girder, thus deforming the web panel into an S-shape.
- The ratios of the individual girder reactions to the total applied loads are almost constant over the entire loading range, indicating that the girder reactions increase

in a predominantly linear fashion for increasing total applied loads. The average ratios are 0.09, 0.27 and 0.64 for G1, G2 and G3, respectively.

- The nonlinear behavior associated with material yielding is generally minor at the M_p-based 1/3 rule load level on the outermost girder, G3. The internal moment variations are predominantly linear for all of the three girders. The results of linear elastic analysis can be used to obtain good estimates of girder moments and deflections at this load level.
- The yielding on G3 at the M_p-based 1/3 rule load level is highly localized at the G3 bottom flange outside tip at the midspan, with maximum plastic strains of approximately four times the flange yield strain. In contrast, the inside portion of the bottom flange at the midspan is still elastic at this load level. At the ultimate load level close to 5783 kN (1300 kips), the G3 and G2 cross-sections near midspan are essentially fully plastified throughout the depth of the web and across the bottom flange width, indicating the development of a moment level that is close to the G3 section plastic moment. Interestingly, the FEA internal moment on G2 is slightly above its nominal section plastic moment at this load level. This is due to the substantial yielding on the steel section, as well as biaxial compressive stresses in the slab portion of G2. These biaxial stresses allow the longitudinal concrete compressive stress to significantly exceed the measured concrete compressive strength from cylinder tests.
- The test bridge slab top surface longitudinal stresses at midspan gradually increase toward the outer edge of the overhang region outside G3 with a maximum stress slightly above 21 MPa (3 ksi) at the M_p-based 1/3 rule load level on G3. At the

ultimate load level of 5783 kN (1300 kips), the overhang region just outside G3 is in a high biaxial compressive stress state, with a maximum compressive stress of 46 MPa (6.7 ksi). This stress is significantly higher than the measured concrete compressive strength of 34 MPa (4.9 ksi). This is in large part due to the fact that the concrete can develop higher strengths under a confined stress state than in an unconfined state.

- At the M_p-based 1/3 rule load level, the longitudinal strains across the slab at the midspan cross-section vary approximately in a linear fashion with the largest value of approximately 1100 με occurring at the outer edge of the overhang outside girder G3. This maximum strain is slightly above the strain associated with the elastic limit defined in the concrete stress-strain response. Also it is significantly less than the nominal concrete crushing strain of 0.003.
- The FEA simulation predicts extensive compression damage in the overhang region outside G3 at midspan, as well as in the regions just inside G3 between the mid- and quarter-span cross-frames. Extensive tensile damage generally develops in the regions just inside each girder, particularly near the G2 and G3 girder ends. The ultimate strength of the test bridge was reached at approximately 5783 kN (1300 kips) applied load when significant spalling and crushing of the concrete occurred in the above overhang region outside of G3 and just inside of G3 at the midspan. This load is 1.46 times the strength limit corresponding to the M_p-based 1/3 rule load level on G3, indicating that there is still substantial reserve strength beyond the suggested design strength limit.

- The crack patterns observed on the top surface of the test bridge slab at the end of ultimate loading test show that there are many cracks formed between the end- and quarter-span cross-frames that are inclined at about 30 to 45 degrees to the radial lines at the girder supports pointing toward the center of curvature. Conversely, it is found that the dominant direction of the cracks observed on the bottom surface of the test bridge slab is roughly perpendicular to that of the top surface cracks. The bottom surface cracks are inclined at an angle of 45 degrees to the radial lines of the girder supports between the end- and quarter-span cross-frames, pointing away from the center of curvature. Based on the overall crack patterns on the top and bottom surfaces, it is clear that the test bridge slab experienced plate twisting deformations during the ultimate load test, particularly, in the regions between the end- and quarter-span cross-frames. Similar observations are made for the crack patterns on the top and bottom surfaces of the test bridge slab based on the maximum principal strains predicted by the full nonlinear FEA simulation.
- The measured and predicted cross-frame member forces are predominantly linear up to the M_p-based 1/3 rule load level on G3. These forces reach a plateau in the limit when the applied loads are close to 5783 kN (1300 kips). The appearance of the plateau does not have anything to do with yielding or plastification of the cross-frame members. The plateau is due to the fact that the web and the bottom flange of G3 have become significantly yielded. This in turn limits the radial reaction on the bottom chord of the cross-frame connected to G3. Upper bound estimates of the cross-frame bottom chord axial force can be easily obtained based on a condition

where web and bottom flange of the outermost girder in a curved bridge are fully plastified and straighten into chords between cross-frame locations.

- The transverse stiffener strains start to show significant nonlinearity at an applied load level of 3959 kN (890 kips), which corresponds to the development of the M_p-based 1/3 rule strength resistance on the outermost girder, G3. All the strains in the stiffeners increase predominantly in a linear fashion up to the M_p-based 1/3 rule load level. Interestingly, the regions in close proximity to the juncture of the stiffener and girder top flange develop relatively high strains with further increases in the applied loads. This leads effectively to the formation of plastic hinges at the tops of the stiffeners at the ultimate load level, in particular in the transverse stiffeners closer to the bridge midspan. The transverse stiffeners are working much like cantilever beams with a fixed end at the top flange of the girders. For cases where girder web panels are represented using shell elements in an elastic design analysis, it is recommended that intermediate transverse stiffeners should not be included in analysis model. This is because transverse stiffeners can provide artificial lateral restraint to the girder bottom flanges in composite bridge FEA models that may not be sustained at the Strength load levels, resulting in underestimation of the girder bottom flange lateral bending responses.
- The shear force diagrams show that the outermost girder, G3 is subjected to uniformly distributed loads from the slab as well as by concentrated shear forces at the cross-frame locations to satisfy the overall torsional equilibrium associated with horizontal curvature.

- The cross-frames within the test bridge play an important role in transferring a significant portion of the noncomposite dead loads acting on the inside girders to the outermost girder, thereby satisfying the overall torsional equilibrium associated horizontal curvature.
- The separate vertical forces acting on G3 include: (1) the directly applied loads, (2) the vertical force components in the diagonal members of the quarter- and midspan cross-frames, (3) the slab shear force transferred to G3, and (4) the vertical end reactions. Together with the cross-frames, the test bridge slab plays an important role in transferring loads to G3.
- A careful look at the difference between the total live load shear diagram and the combined shear diagram due to the directly applied load and the cross-frame vertical forces reveals that the vertical forces transferred through the slab to G3 from the adjacent girders are nearly constant along G3.

7.4 Parametric FEA Studies

- ***No Load Fit (NLF) vs. Total Dead Load Fit (TDLF):*** It is found that the full nonlinear FEA solution based on the NLF detailing method produces larger ultimate capacities than the FEA solution based on the TDLF detailing method. This is due to the fact that the TDLF method introduces locked-in flange lateral bending stresses at the cross-frame locations that are additive with the lateral bending stresses due to composite live loads. Nonetheless, for all practical purposes, the strength behavior of the composite test bridge is essentially the same regardless of the choice of the cross-frame detailing method until the applied loads are

significantly larger than the load levels corresponding to the suggested design resistance equations.

- ***Homogeneous Section for the Outermost Girder, G3:*** With the use of Grade 50 steel for the G3 bottom flange instead of Grade 70 and a corresponding redesign of the outermost girder, the shape factor of the G3 composite section is increased from 1.11 to 1.17. Similar to the composite test bridge responses, all the component and system responses are found to behave linearly for this design up to the M_p-based 1/3 rule load level during the full nonlinear FEA simulation. Most importantly, the use of M_p-based 1/3 rule load level has a greater impact on the strength gain for the homogeneous section than for the hybrid section. The ratio of the M_p- to M_y-based 1/3 rule load level for the homogeneous case is 1.36 whereas the ratio is 1.14 for the hybrid case, indicating that substantial benefits can be gained through the relaxation of the current design provisions for homogeneous curved I-girder bridge structural systems.
- ***Cross-Frame Spacing, L_b, Set to 0.075R:*** When the intermediate cross-frames are spaced more closely, the girder flange lateral bending at the cross-frame locations is smaller, resulting in smaller flange widths compared to corresponding widths in the composite test bridge system. Also, the cross-frame member forces are reduced due to the decreased unbraced length. The component and system responses obtained from the full nonlinear FEA solutions are still predominantly linear up to the M_p-based 1/3 rule load level on G3, and can be estimated accurately based on the results of linear elastic analysis.

- ***Skewed Bridges:*** For the mildly skewed bridge cases with bearing lines skewed at or less than 20 degrees and intermediate cross-frames parallel or normal to these support lines, it is found that the overall behavior of the modified designs differs little from that of the composite test bridge. All the system and component responses are predominantly linear up to the total applied load level corresponding to the M_p-based 1/3 rule load level on the outermost girder, G3. For the case involving a rather extreme skew angle of 60 degrees and intermediate cross-frames normal to the girder axes, there are some substantial deviations relative to the test bridge response. However, it is clear that all the system and component responses increase linearly up to the total applied load corresponding to the M_p-based 1/3 rule load level on G3.
- ***Three-Lane Bridge:*** For the three-lane extension of the composite test bridge, the loading scheme involving only two design trucks placed on the outer two lanes produces the maximum flexural effects on the outermost girder, G4, instead of a three truck loading scheme. The FEA internal moments for the three outside girders, G4, G3 and G2, predominantly increase in a linear fashion up to the M_p-based 1/3 rule load level, not to mention the M_y-based 1/3 rule load level. In contrast, the internal moment on the inner most girder, G1, is gradually reduced from its initial positive dead load moment of 822 kN-m (606 k-ft) to 99 kN-m (73 k-ft) at the M_p-based 1/3 rule load level on G4, indicating that the G1 composite section is subjected to negative moment due to the composite live load. Nonetheless, it is important to note that the internal moment variation on G1 is also predominantly linear up to the M_p-based 1/3 rule load level on G4.

- ***Yielding and Failure of Critical Cross-Frame Members:*** For the case allowing the most critically loaded cross-frame member to yield at the M_p-based 1/3 rule load level on the outermost girder, G3, it is found that the test bridge system continues to carry the applied loads in spite of the yielding on the bottom chord of the midspan cross-frame. There is no abrupt reduction in the load-carrying capacity of the bridge. For the case involving the complete loss of the compression bottom chord of the midspan cross-frame attached to G3 at the M_p-based 1/3 rule load level on G3, the test bridge deformed geometry responds such that a new equilibrium configuration is reached, resulting in a substantial increase in the girder deflections and member forces of adjacent cross-frames. Nonetheless, the test bridge continues to support additional applied loads, although the overall component and system behavior becomes highly nonlinear due to widespread of yielding in the bridge girders as well as in other cross-frame members. Interestingly, the third case involving a fracture of the tension diagonal of the midspan cross-frame attached to G3, also shows a similar equilibrium shift, but the magnitude of the shift is minor. As a result, the bridge responses are only slightly different than those of the base test bridge not allowing the yielding of any cross-frame members. Finally, the results of the last case involving both the complete loss of the compression bottom chord and the fracture of tension diagonal of the midspan cross-frame attached to G3 are essentially the same as those of the case when the compression bottom chord only is removed. It should be cautioned that the second and fourth of the above cases, where the bottom chord of the cross-frame attached to G3 was removed, resulted in yielding of the bottom chord at the quarter-span cross-frames. The FEA

solution assumes that these members respond in a ductile manner. Nevertheless, the complete removal of the above bottom compression chord member represents an unlikely extreme condition.

- ***Fixed-End Bridge Systems:*** The base flexural resistance in negative bending of typical horizontally curved continuous-span bridges is limited practically to a maximum of the first yield moment, since the webs in the negative bending regions will nearly always be slender or at the upper range of slenderness for a noncompact web. Therefore, use of the AASHTO (2004b) Appendix A equations for negative moment regions of continuous-span bridges offers little practical benefits. In addition, linear elastic analysis assuming the concrete deck to be fully effective over the entire span length generally results in an overprediction of the negative bending moments and an underprediction of the positive bending moments. This is largely because of distributed cracking in the negative moment region of the slab at the strength resistance levels. It is important for engineers to recognize that this design practice is actually beneficial rather than problematic. That is, overestimated negative moments always ensure that continuous-span bridges develop their desired strength limit states, since the positive moment region generally behaves in a highly ductile fashion when designed by the AASHTO (2004b) criteria. This is particularly true for the Case 9b fixed-end bridge system for which the fixed-end and midspan unbraced lengths are designed to reach their strength limit states at the Strength I load level. The second fixed-end bridge system considered in this work shows that in spite of the underprediction of the positive moments by the AASHTO (2004b) elastic analysis procedures due to distributed cracking of the slab concrete

in negative bending, the application of the $1.3M_y$-based 1/3 rule resistance of Article 6.10.7.1 still results in a conservative estimate of the structure's ultimate capacity. The yielding in the midspan region limits the amount of moment redistribution from the negative moment regions; however, the major-axis bending moments in the negative bending regions are still overestimated by the elastic design analysis.

7.5 Conclusions

Based on the results of the horizontally curved composite I-girder bridges considered in this study, it is clear that the component and system responses are predominantly linear up to the M_p-based 1/3 rule load level, assuming that all other structural components such as the cross-frames are designed according to the AASHTO (2004b) provisions using the forces from an accurate linear elastic analysis. Therefore, the bending resistances for horizontally curved I-girder sections in positive bending may be calculated based on $M_u = \phi_f M_n - S_x f_\ell / 3$ using the Article 6.10.7.1 provisions of AASHTO (2004b) with $\phi_f M_n$ up to $\phi_f M_p$ whenever the curved members satisfy this article's requirements for straight I-sections. These provisions are applied at the present time only to straight I-girder bridges. This provides a substantial increase in the strength estimate for curved I-girder bridges relative to the current design provisions. The current provisions require composite I-section in positive bending in horizontally curved I-girder bridges to be designed using the noncompact composite section provisions of AASHTO (2004b) Article 6.10.7.2. This limits the base flexural resistance in positive bending (prior to reduction by the 1/3 rule) to a maximum of $\phi_f M_y$ (or $\phi_f F_{yf}$ for the corresponding flange stress).

The AASHTO (2004b) requirements for continuous-span bridges, which assume the concrete deck to be fully effective over the entire span length for the purposes of the analysis, tend to overpredict the negative bending moments and an underpredict the positive bending moments in continuous-span bridges. This is due to the distributed cracking that occurs in the slab in the negative moment regions as the strength load levels are approached. This practice helps protect against any potential nonductile strength limit states that could potentially result due to underestimation of the negative bending moments. The idealized fixed-end bridge studies conducted in this work indicate that the ultimate capacity of continuous-span bridges is predicted conservatively using the above procedures.

7.6 Recommendations for Further Research

The present research has conducted a reasonably comprehensive assessment of the strength and inelastic behavior of horizontally curved composite I-girder bridge systems, with a primary focus on investigating the implications of potential use of the straight bridge design provisions in the context of curved bridges. However, there are still other areas worthy of further research to provide a more complete understanding of the inelastic strength behavior of horizontally curved composite I-girder bridges. Some of the most promising potential areas for further study are as follows:

- The concrete shrinkage behavior for the composite test bridge is handled by directly specifying initial strains on the test bridge slab, since the detailed time-dependent variations of the concrete creep and shrinkage strains are not a major concern in this study. In some cases in practice (e.g., cases with strict requirements on the geometry of the structure during its service life), it may be useful for engineers to

be able to determine a refined estimate of creep and shrinkage effects in composite bridge structures. Therefore, there is a need for pursuing more refined rheological models to simulate the concrete creep and shrinkage behavior. It would be quite interesting to compare the creep and shrinkage strain predictions made by refined rheologocal models to the current practical but simplified handling of creep and shrinkage in the AASHTO provisions and to experimental measurements.

- Ideally, shell elements used to represent the bridge slab in unshored bridge construction should be dynamically instantiated over the deformed bare steel girder structure as stress-free elements (at the time that the concrete is assumed to become effective). However, due to the limited analysis capabilities in the ABAQUS system, the slab shell elements have to be defined at the desired positions at the beginning of the analysis (prior to calculation of the deformed geometry). They can not be generated dynamically following the updated deformed geometry of the steel superstructure at the time that the concrete is assumed to become effective. Therefore, in this work, complicated efforts were required to pre-compute the desired deflected geometry of the slab at the time that it becomes effective. It would be useful to have an analysis engine that can handle the insertion of new elements within the deformed model of the structure in a better way. It is believed that, along with the new concrete rheological model described in the previous item, new analysis tools will provide a better understanding of the behavior of composite steel-concrete structures during and after construction.
- Except for the fixed-end bridge systems considered in the parametric studies, all the bridge configurations studied in this work are simply supported structures. For

these types of structures, the effects attributes such as residual stresses and initial imperfections are generally minor. Although some understanding about the strength behavior of curved composite structures in the negative moment region is gained through the fixed-end bridge cases, further studies of the strength behavior of various continuous span structures would be useful. The findings from these studies should provide further information on the inelastic redistribution behavior in curved I-girder bridges due to distributed cracking of the slab regions loaded in tension and due to the general yielding and stability limit states response of the structural steel.

- The commentary of Section 6.10.4.2 states that for continuous-span flexural members in straight I-girder bridges that satisfy the provisions of Article B6.2, the procedures of either Article B6.3 or B6.6 may be used to calculate the redistribution moments at the service limit state. However, it states that there has been no research conducted to extend the provisions of Appendix B in the AASHTO (2004b) Specifications to horizontally curved I-girder bridges. Proper accounting for the inelastic redistribution from negative moment regions in continuous-span curved (and skewed) I-girder bridges should result in benefits for these types of structures similar to those for straight continuous-span non-skewed I-girder bridges designed based on AASHTO (2004b) Appendix B. These advantages include a reduction in the number of section transitions along the girder lengths without incurring economic penalties, thus reducing the number of details with lower fatigue resistance and potentially reducing fabrication costs.

- At the time of completion of this study, there are no dominant causes of the residual deflections apparent from the measured test data for the composite test bridge. Other potential sources listed in Section 4.5.5 need to be further investigated.

APPENDIX A

RESULTS OF ELASTIC ANALYSIS

This appendix presents detailed results of elastic analysis of the noncomposite and composite test bridge configurations, with focus on girder major-axis and lateral bending stresses. The organization of this appendix is as follows. Section A.1 provides the first- and second-order major-axis and lateral bending stresses for the top and bottom flanges of the three test bridge girders from the noncomposite load analysis. In addition, eccentric bracket loads associated with noncomposite constructions loads acting on overhang regions of the composite test bridge are included in the analysis models whenever the analysis models with these bracket loads included cause the maximum flexural effects for the test bridge girders. Thus, Section A.1.1 provides the girder stresses for the middle and outside girders, G2 and G3, when these bracket loads are included in the analysis models. However, Section A.1.2 gives the girder stresses for the inside girder, G1, when there are no eccentric bracket loads included in the analysis models. Section A.2 provides the first-order girder stresses from the composite live load analysis. Centrifugal forces are included in the analysis models whenever the analysis models with theses forces included produce more critical girder responses. Interestingly, it turns out that only the outside girder responses are made more critical by including the effects of centrifugal forces with respect to the girder responses without those effects. A two truck AASHTO live load model consisting of two lane loads plus two HL-93 trucks is used in getting the maximum flexural girder responses for the middle and outside girders, G2 and G3, while a single truck live load model consisting of one lane load plus a single HL-93 truck is used for the inside girder, G1. Section A.2.1 provides the results

for the middle and outside girders, G2 and G3 when the two truck AASHTO live model is employed in the analysis models. Section A.2.2 gives the results for the inside girder, G1, when the single truck live model is used in the analysis models.

A.1. Noncomposite Load Analysis

A.1.1 Maximum Effects on G2 and G3

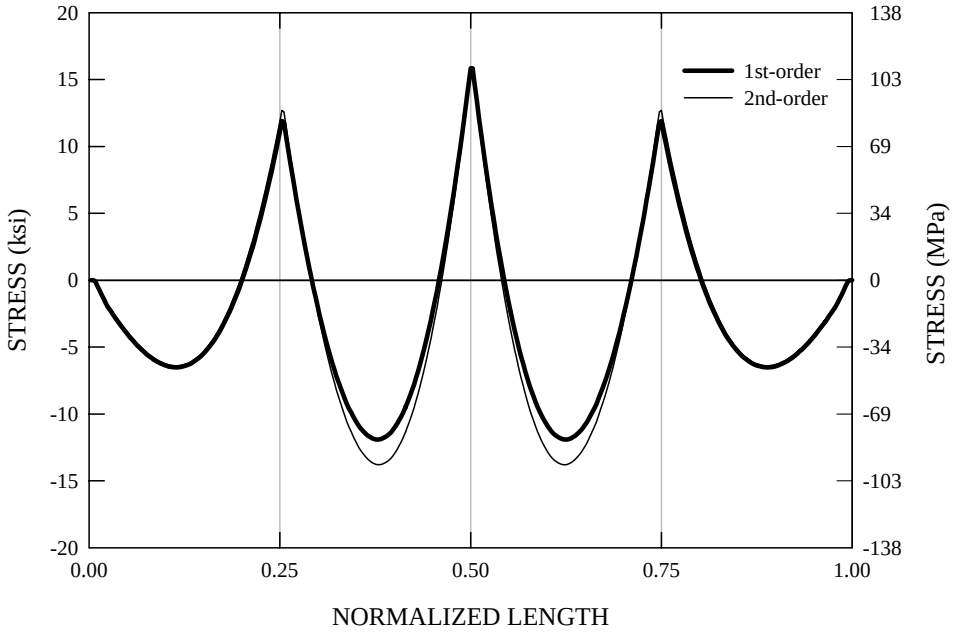

Figure A.1.1.1. Top (compression) flange lateral bending stresses in G3 due to factored construction loads (self weight + forms + slab), load factor = 1.25 (STRENGTH I).

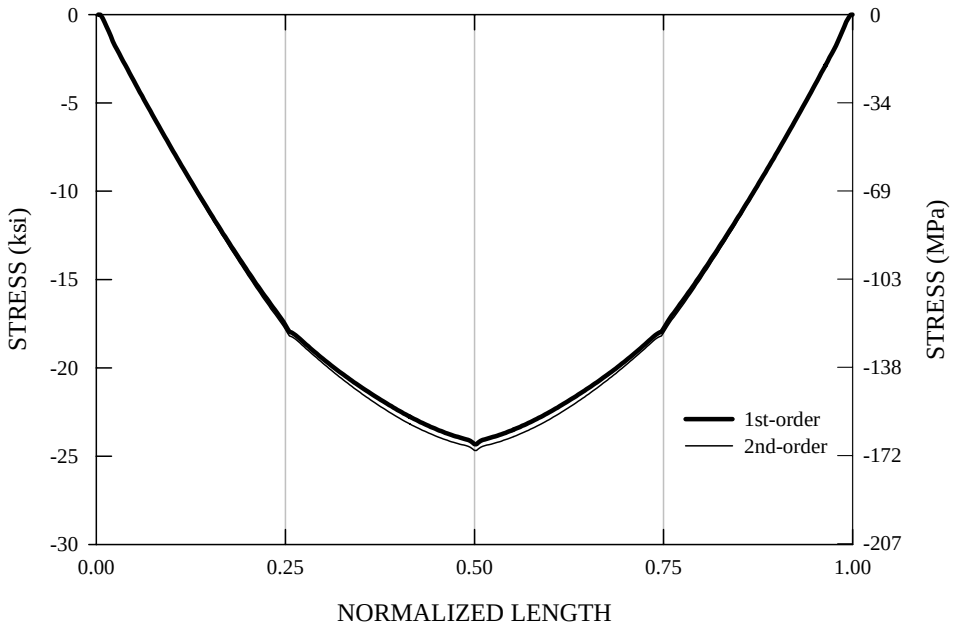

Figure A.1.1.2. Top (compression) flange major-axis bending stresses in G3 due to factored construction loads (self weight + forms + slab), load factor = 1.25 (STRENGTH I).

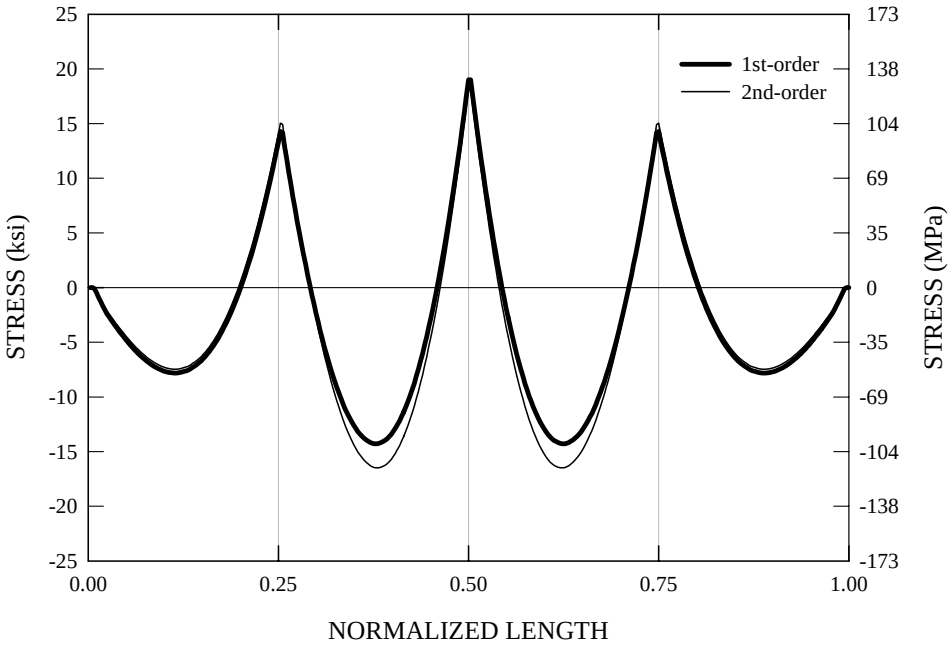

Figure A.1.1.3. Top (compression) flange lateral bending stresses in G3 due to factored construction loads (self weight + forms + slab), load factor = 1.5 (STRENGTH IV).

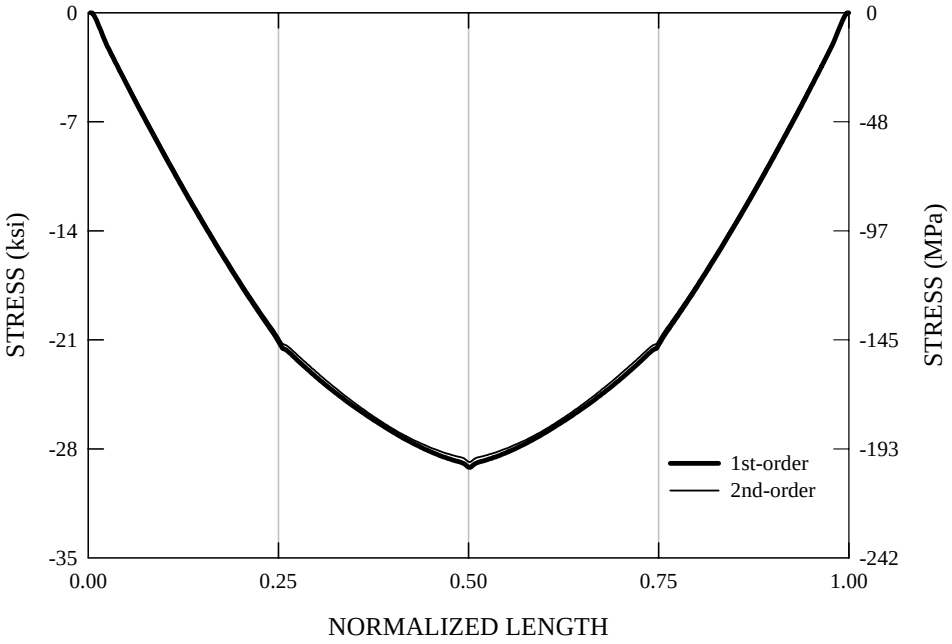

Figure A.1.1.4. Top (compression) flange major-axis bending stresses in G3 due to factored construction loads (self weight + forms + slab), load factor = 1.5 (STRENGTH IV).

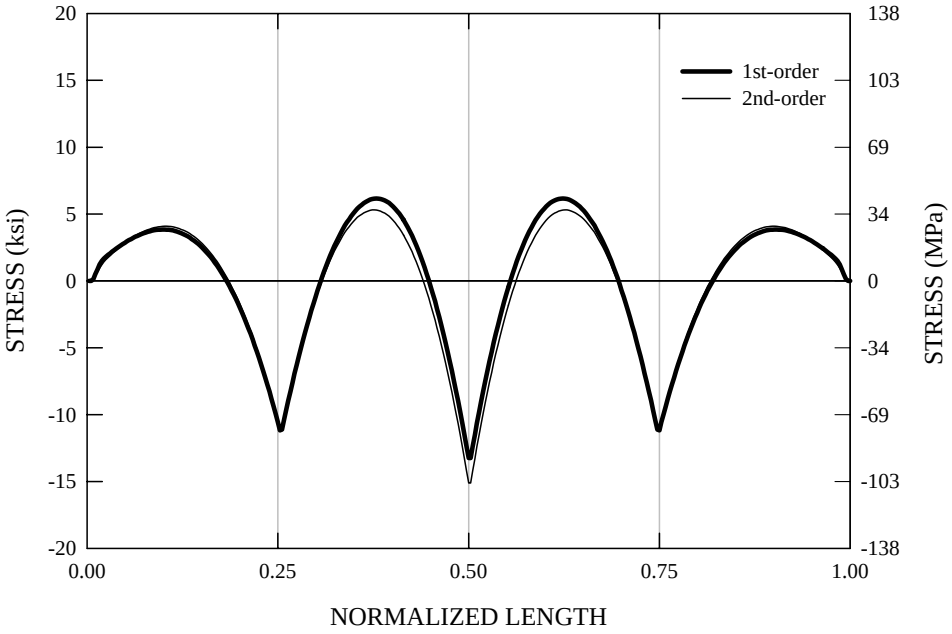

Figure A.1.1.5. Bottom (tension) flange lateral bending stresses in G3 due to factored construction loads (self weight + forms + slab), load factor = 1.25 (STRENGTH I).

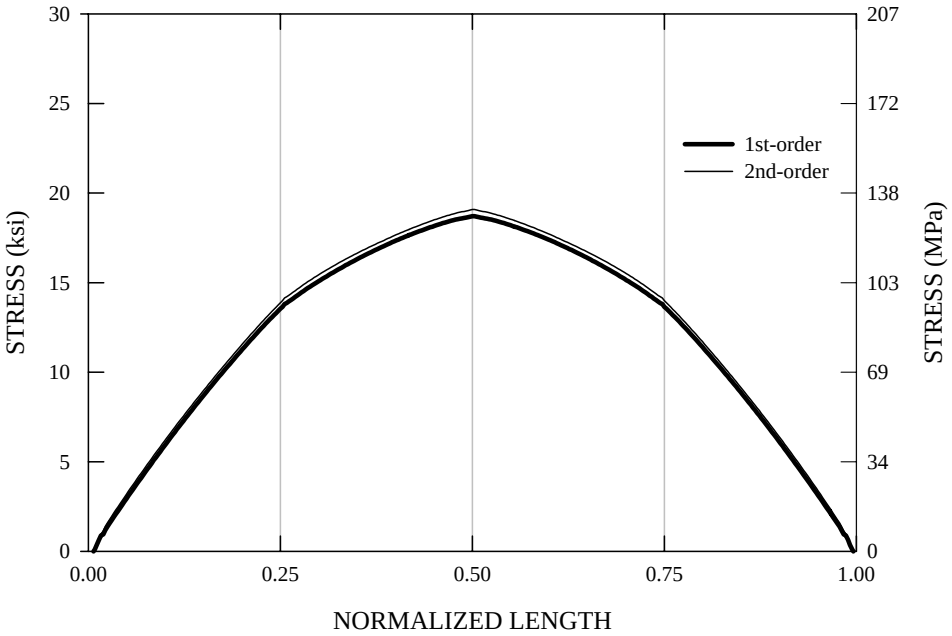

Figure A.1.1.6. Bottom (tension) flange major-axis bending stresses in G3 due to factored construction loads (self weight + forms + slab), load factor = 1.25 (STRENGTH I).

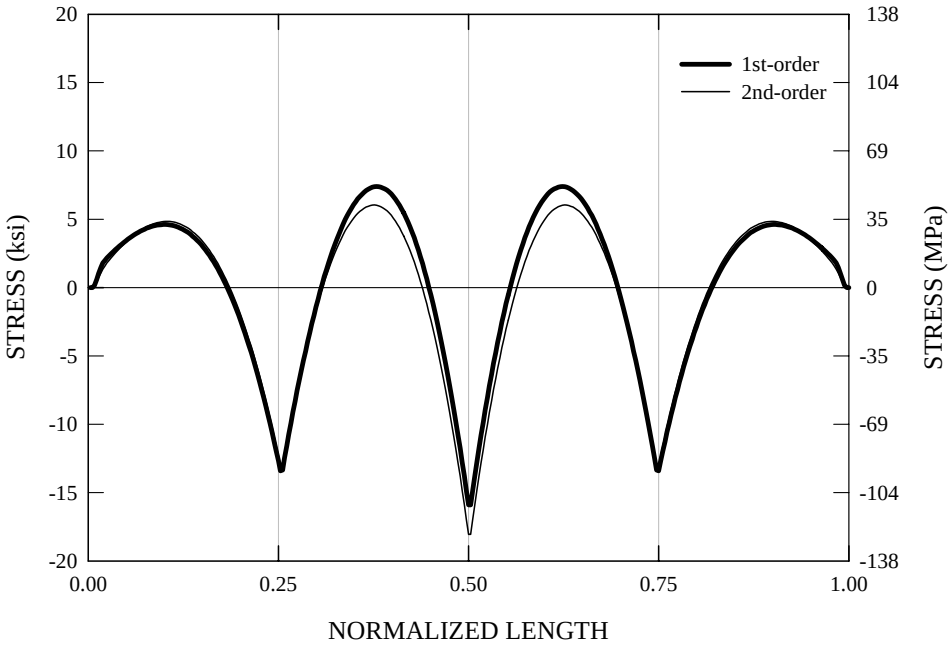

Figure A.1.1.7. Bottom (tension) flange lateral bending stresses in G3 due to factored construction loads (self weight + forms + slab), load factor = 1.5 (STRENGTH IV).

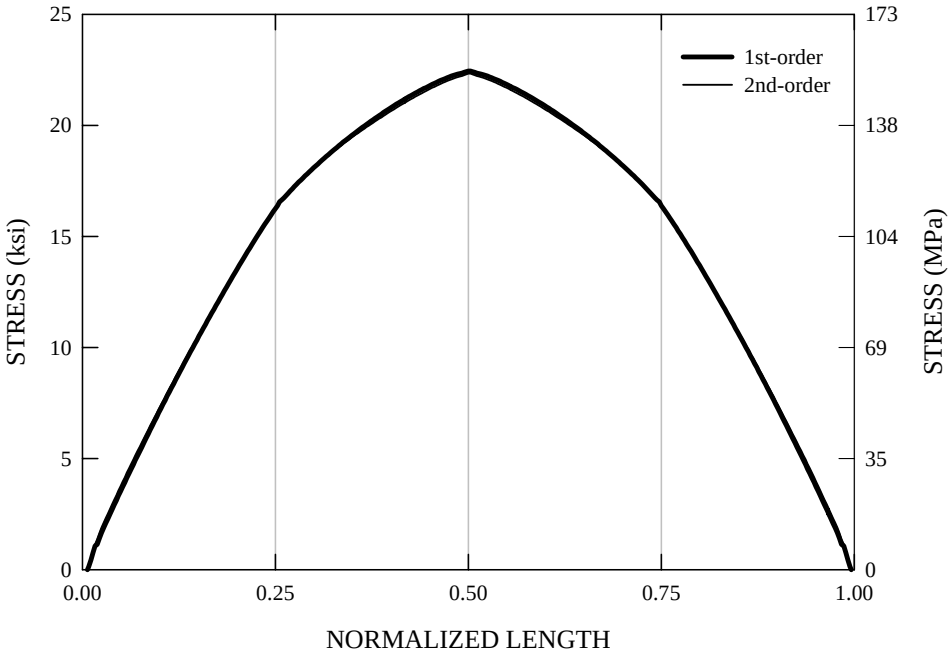

Figure A.1.1.8. Bottom (tension) flange major-axis bending stresses in G3 due to factored construction loads (self weight + forms + slab), load factor = 1.5 (STRENGTH IV).

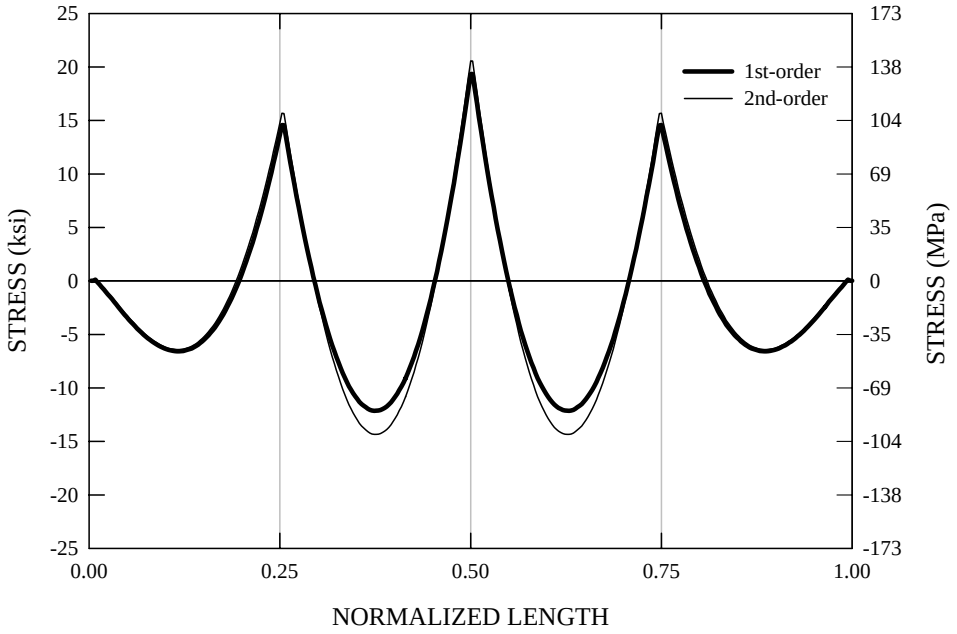

Figure A.1.1.9. Top (compression) flange lateral bending stresses in G2 due to factored construction loads (self weight + forms + slab), load factor = 1.25(STRENGTH I).

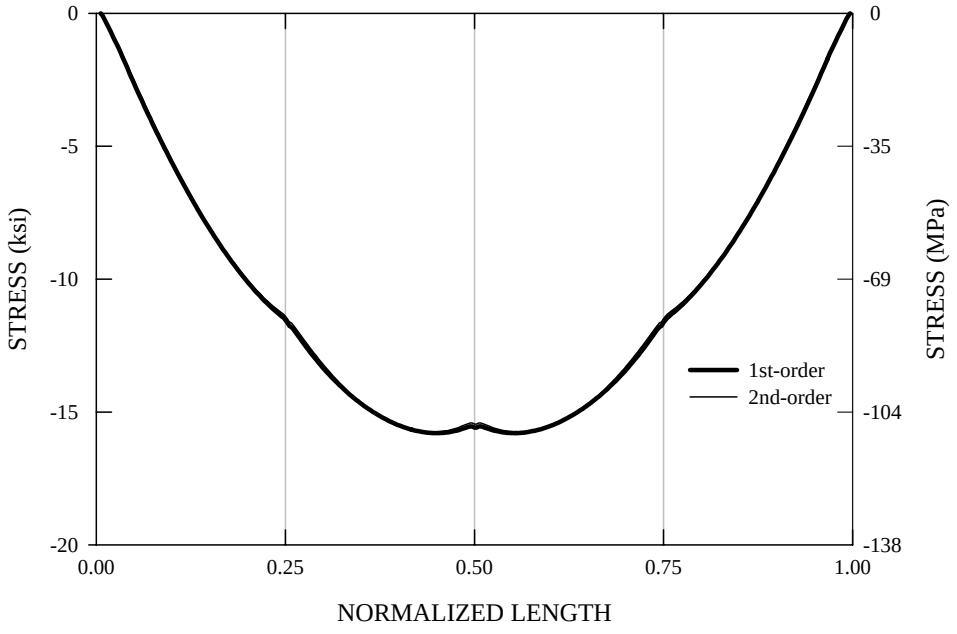

Figure A.1.1.10. Top (compression) flange major-axis bending stresses in G2 due to factored construction loads (self weight + forms + slab), load factor = 1.25 (STRENGTH I).

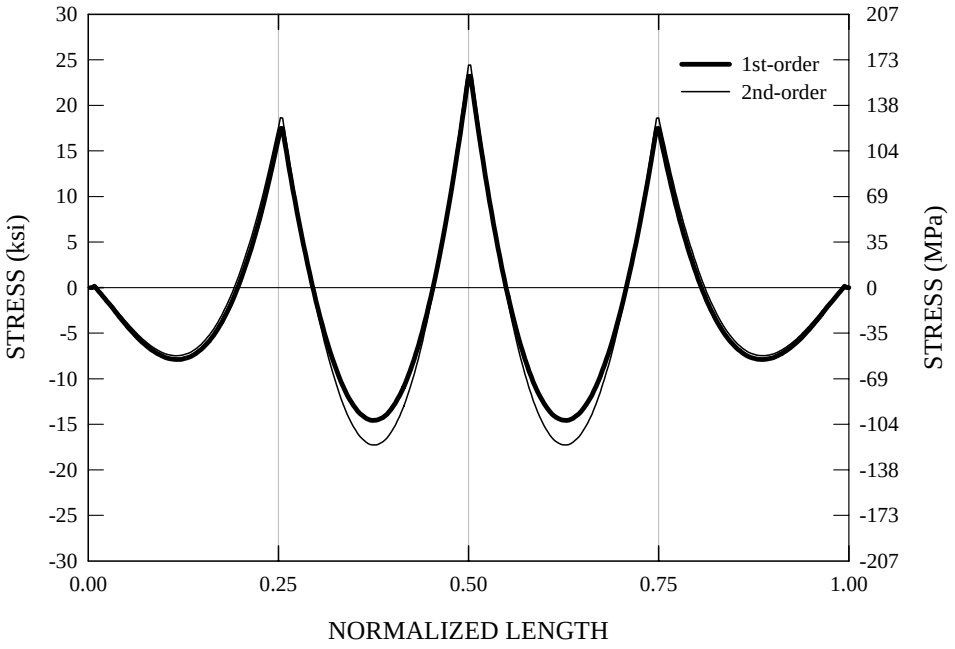

Figure A.1.1.11. Top (compression) flange lateral bending stresses in G2 due to factored construction loads (self weight + forms + slab), load factor = 1.5(STRENGTH IV).

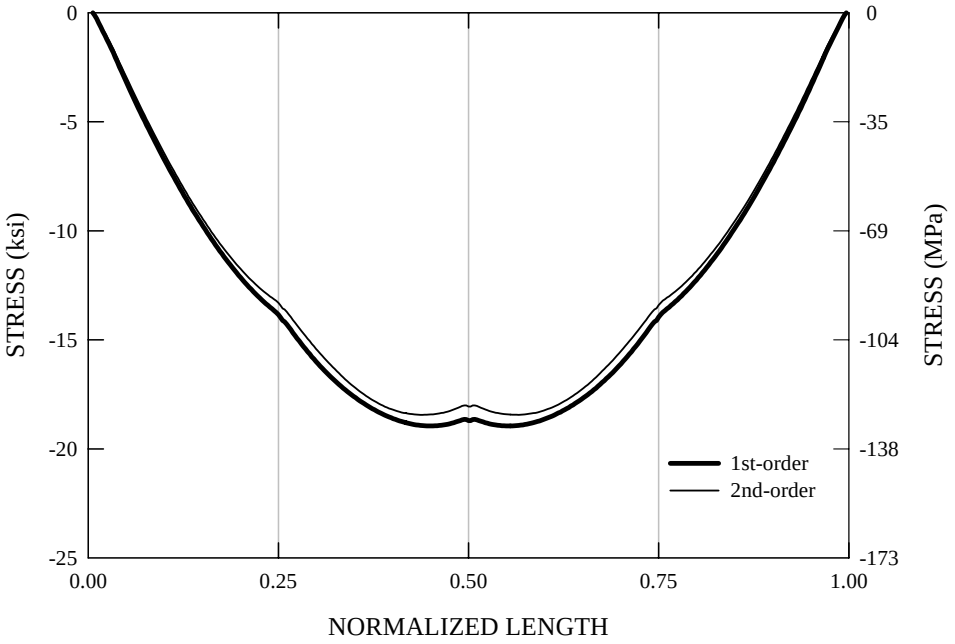

Figure A.1.1.12. Top (compression) flange major-axis bending stresses in G2 due to factored construction loads (self weight + forms + slab), load factor = 1.5 (STRENGTH IV).

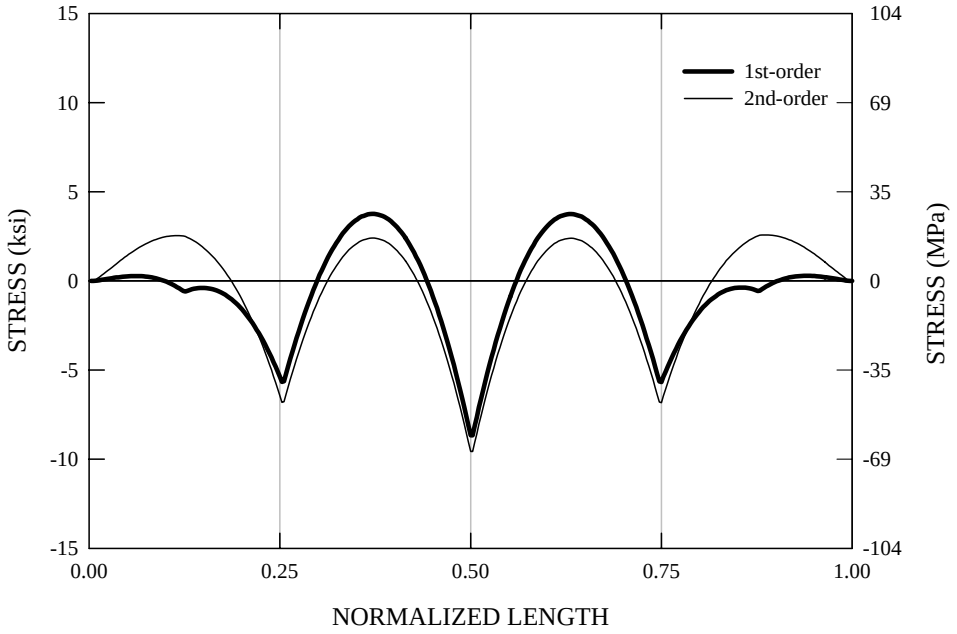

Figure A.1.1.13. Bottom (tension) flange lateral bending stresses in G2 due to factored construction loads (self weight + forms + slab), load factor = 1.25(STRENGTH I).

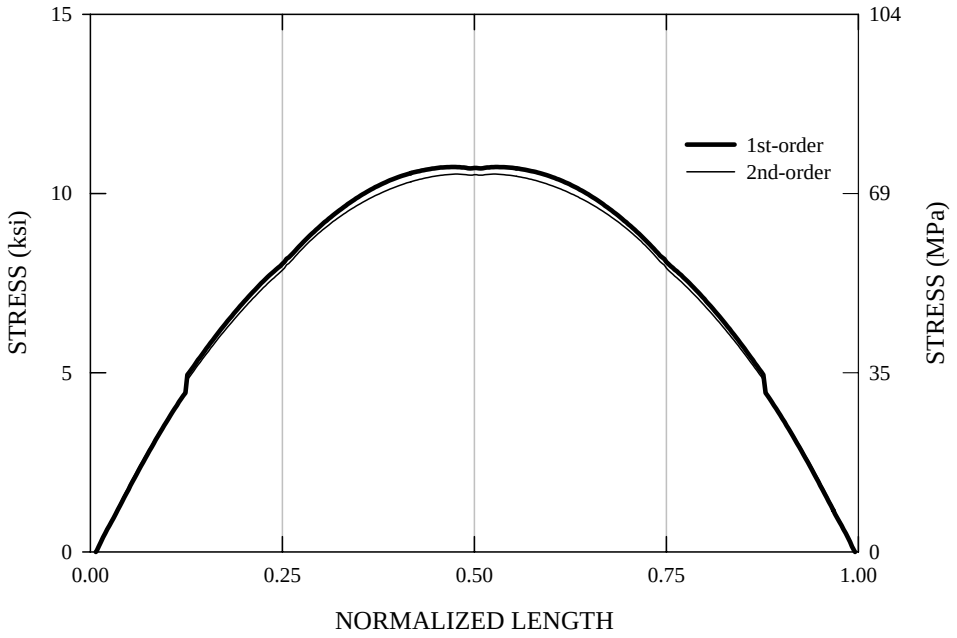

Figure A.1.1.14. Bottom (tension) flange major-axis bending stresses in G2 due to factored construction loads (self weight + forms + slab), load factor = 1.25 (STRENGTH I).

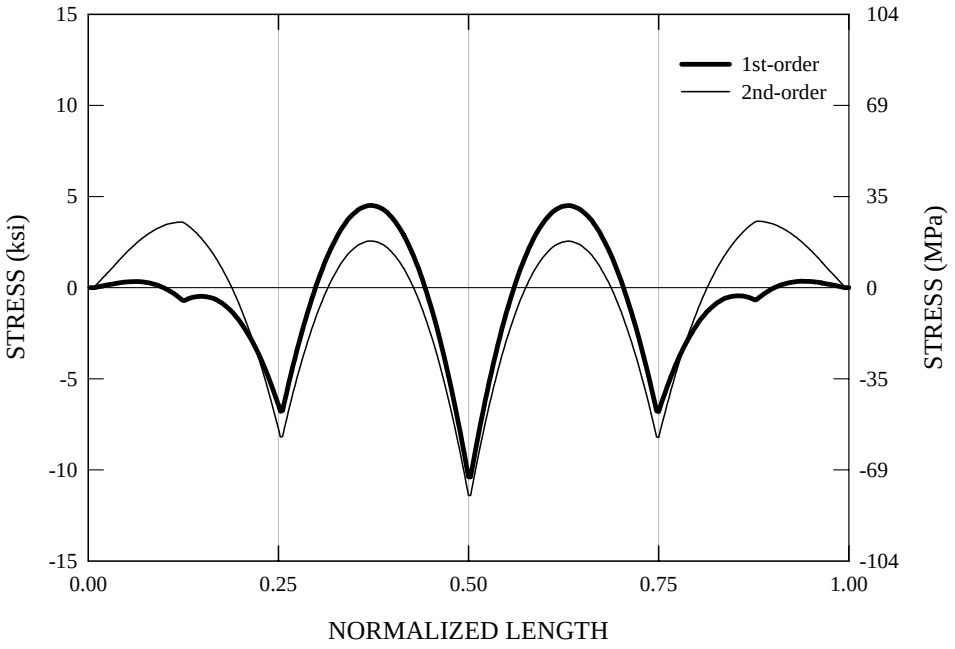

Figure A.1.1.15. Bottom (tension) flange lateral bending stresses in G2 due to factored construction loads (self weight + forms + slab), load factor = 1.5(STRENGTH IV).

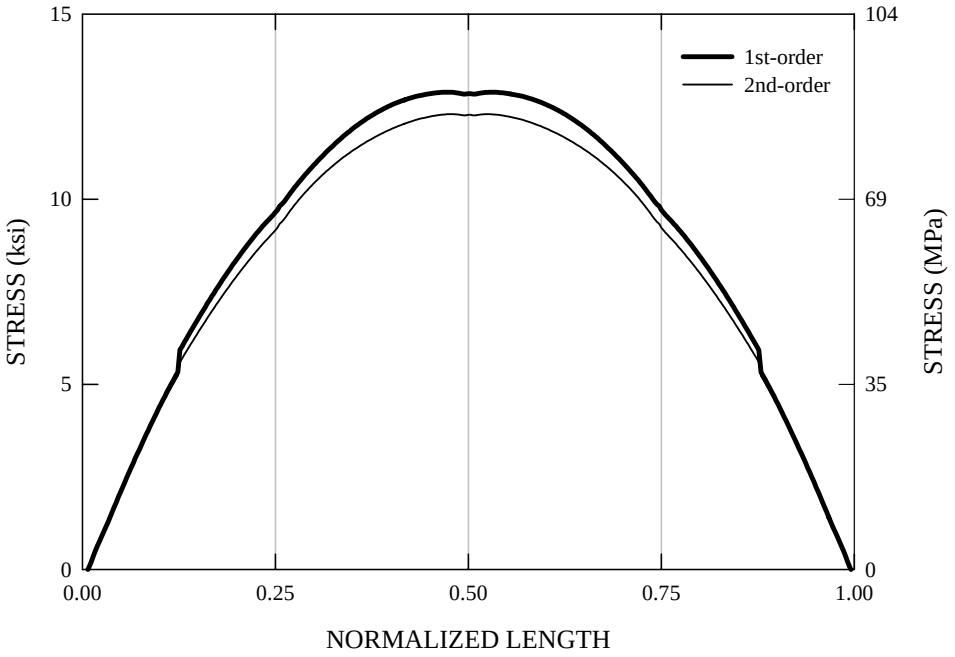

Figure A.1.1.16. Bottom (tension) flange major-axis bending stresses in G2 due to factored construction loads (self weight + forms + slab), load factor = 1.5 (STRENGTH IV).

A.1.2. Maximum Effects on G1

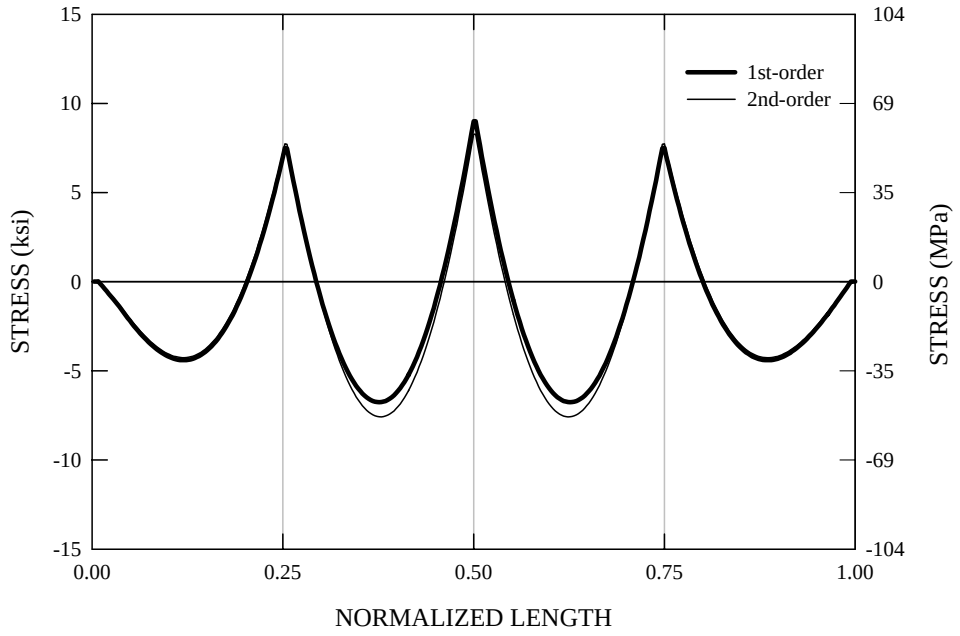

Figure A.1.2.1. Top (compression) flange lateral bending stresses in G1 due to factored construction loads (self weight + forms + slab), load factor = 1.25 (STRENGTH I), eccentric bracket loads are neglected conservatively in analysis to obtain the G1 stresses (torsion from the overhangs is included in the analysis for the stresses in G2 and G3).

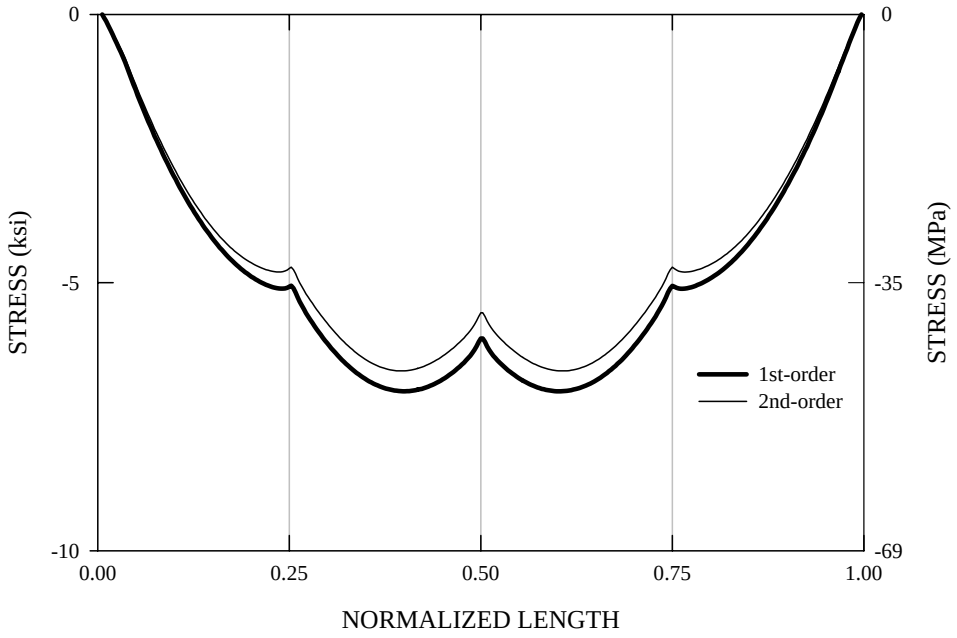

Figure A.1.2.2. Top (compression) flange major-axis bending stresses in G1 due to factored construction loads (self weight + forms + slab), load factor = 1.25 (STRENGTH I) , eccentric bracket loads are neglected conservatively in analysis to obtain the G1 stresses (torsion from the overhangs is included in the analysis for the stresses in G2 and G3).

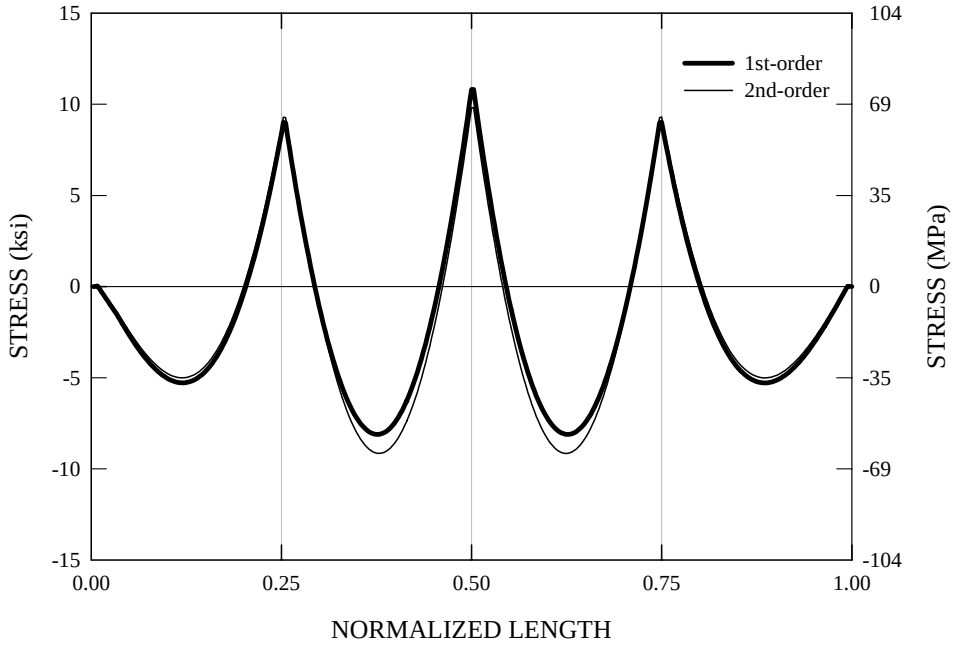

Figure A.1.2.3. Top (compression) flange lateral bending stresses in G1 due to factored construction loads (self weight + forms + slab), load factor = 1.5 (STRENGTH IV), eccentric bracket loads are neglected conservatively in analysis to obtain the G1 stresses (torsion from the overhangs is included in the analysis for the stresses in G2 and G3).

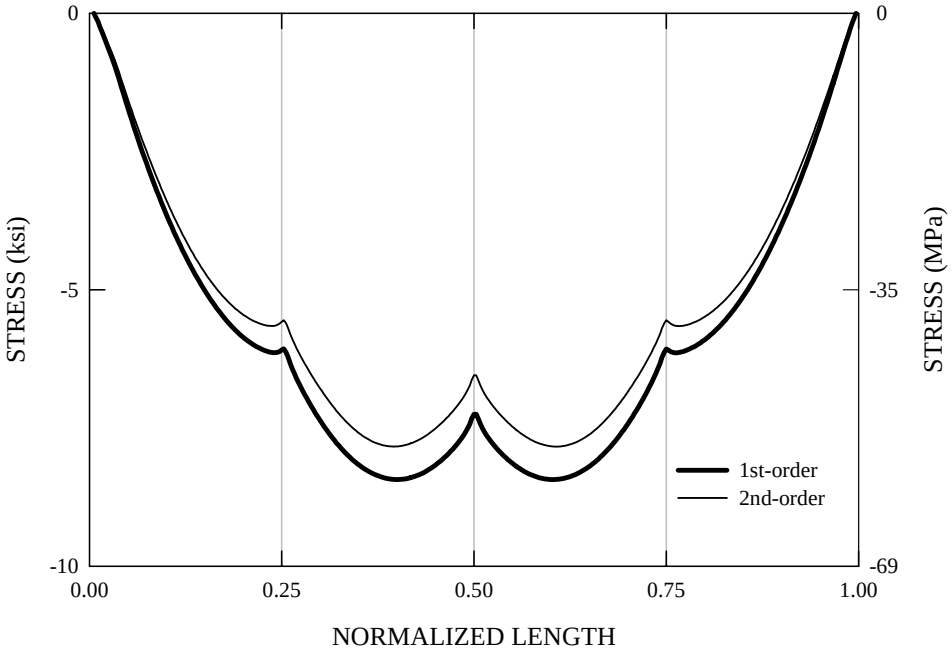

Figure A.1.2.4. Top (compression) flange major-axis bending stresses in G1 due to factored construction loads (self weight + forms + slab), load factor = 1.5 (STRENGTH IV), eccentric bracket loads are neglected conservatively in analysis to obtain the G1 stresses (torsion from the overhangs is included in the analysis for the stresses in G2 and G3).

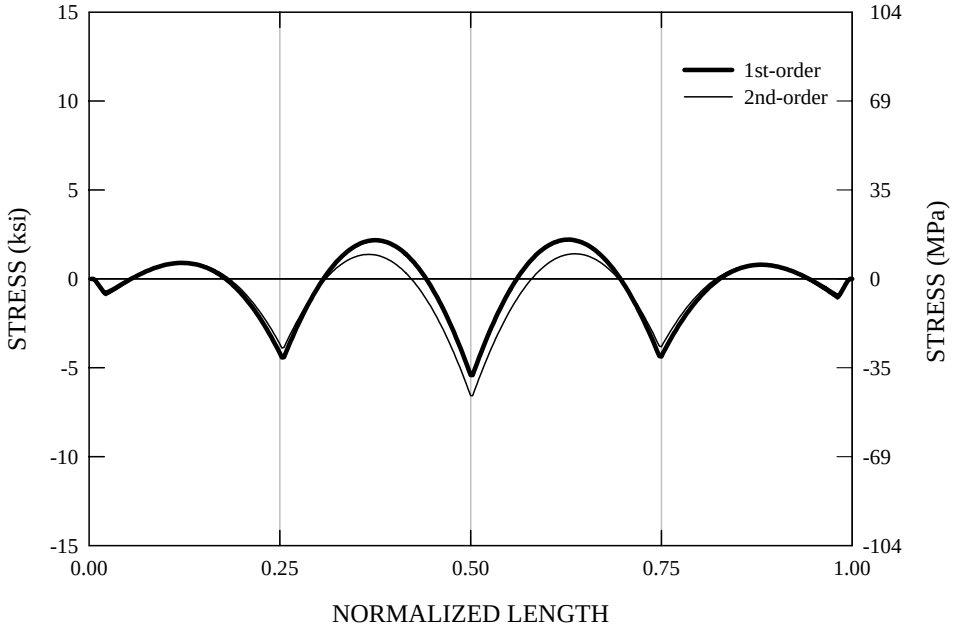

Figure A.1.2.5. Bottom (tension) flange lateral bending stresses in G1 due to factored construction loads (self weight + forms + slab), load factor = 1.25 (STRENGTH I), eccentric bracket loads are neglected conservatively in analysis to obtain the G1 stresses (torsion from the overhangs is included in the analysis for the stresses in G2 and G3), factored maximum bottom (tension) flange stresses used for combination with live load stresses.

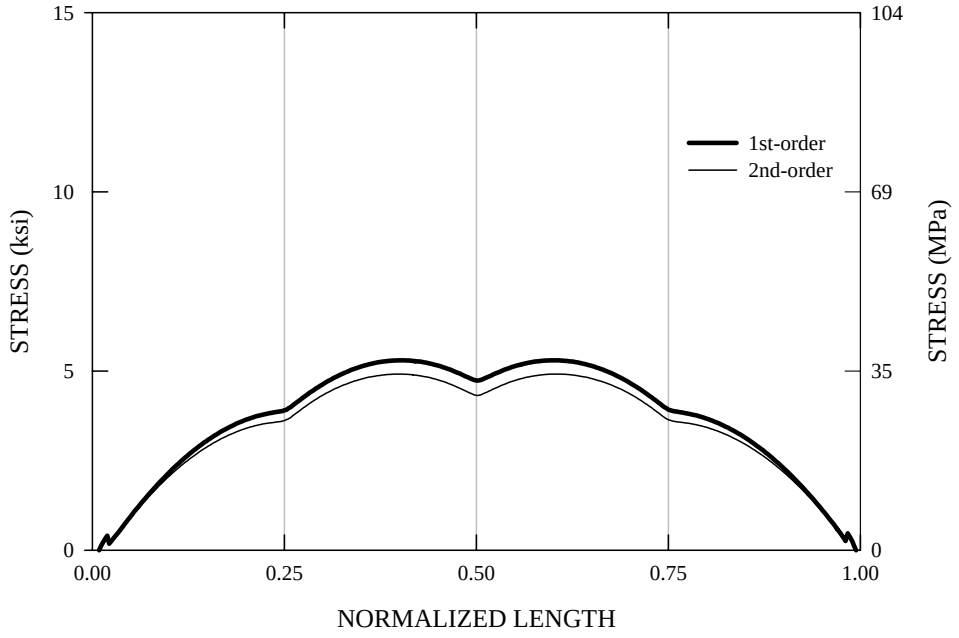

Figure A.1.2.6. Bottom (tension) flange major-axis bending stresses in G1 due to factored construction loads (self weight + forms + slab), load factor = 1.25 (STRENGTH I), eccentric bracket loads are neglected conservatively in analysis to obtain the G1 stresses (torsion from the overhangs is included in the analysis for the stresses in G2 and G3), factored maximum bottom (tension) flange stresses used for combination with live load stresses.

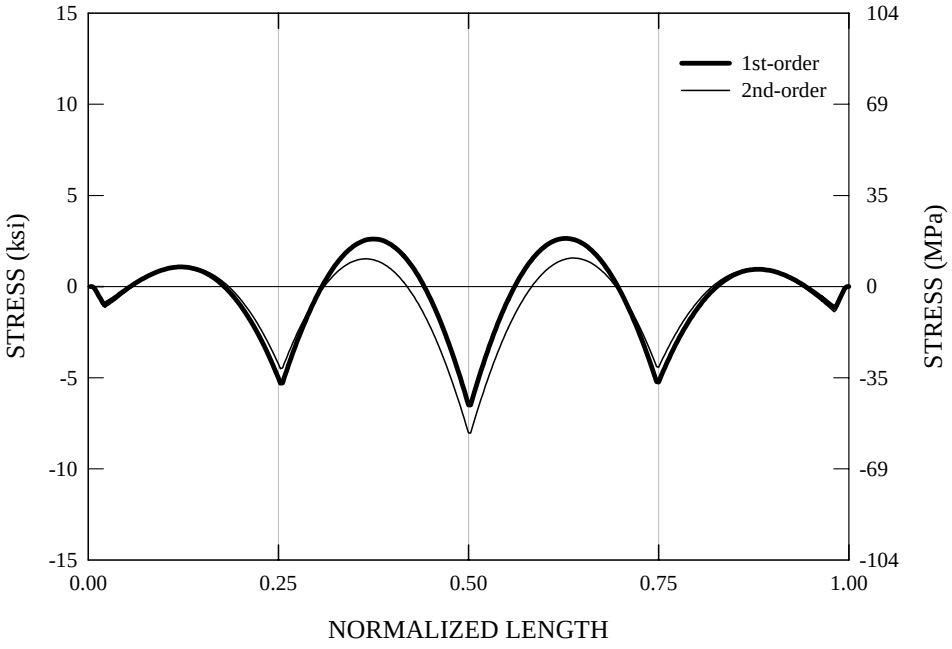

Figure A.1.2.7. Bottom (tension) flange lateral bending stresses in G1 due to factored construction loads (self weight + forms + slab), load factor = 1.5 (STRENGTH IV), eccentric bracket loads are neglected conservatively in analysis to obtain the G1 stresses (torsion from the overhangs is included in the analysis for the stresses in G2 and G3).

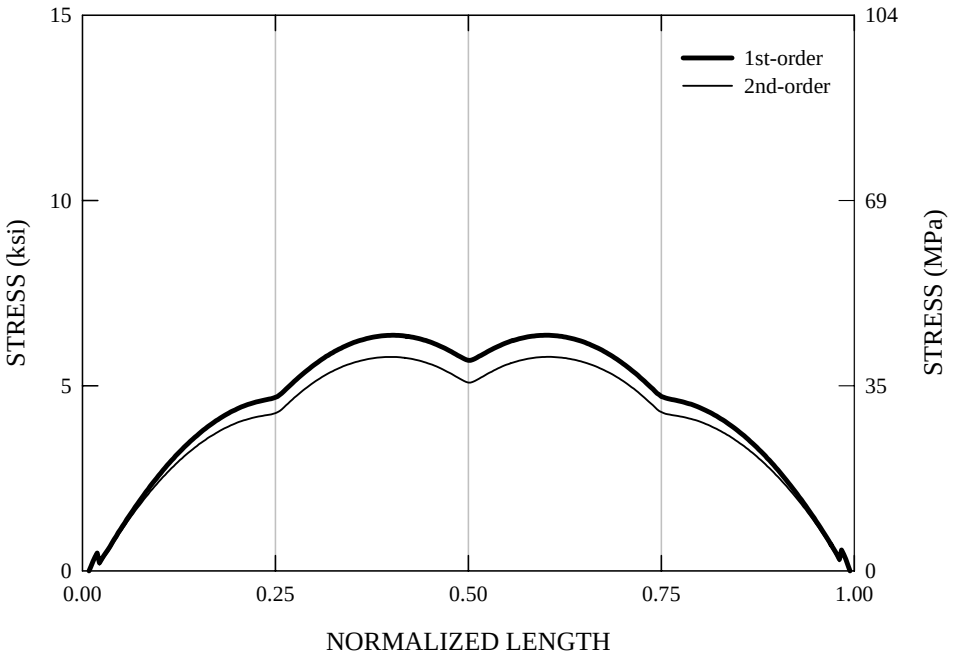

Figure A.1.2.8. Bottom (tension) flange major-axis bending stresses in G1 due to factored construction loads (self weight + forms + slab), load factor = 1.5 (STRENGTH IV), eccentric bracket loads are neglected conservatively in analysis to obtain the G1 stresses (torsion from the overhangs is included in the analysis for the stresses in G2 and G3).

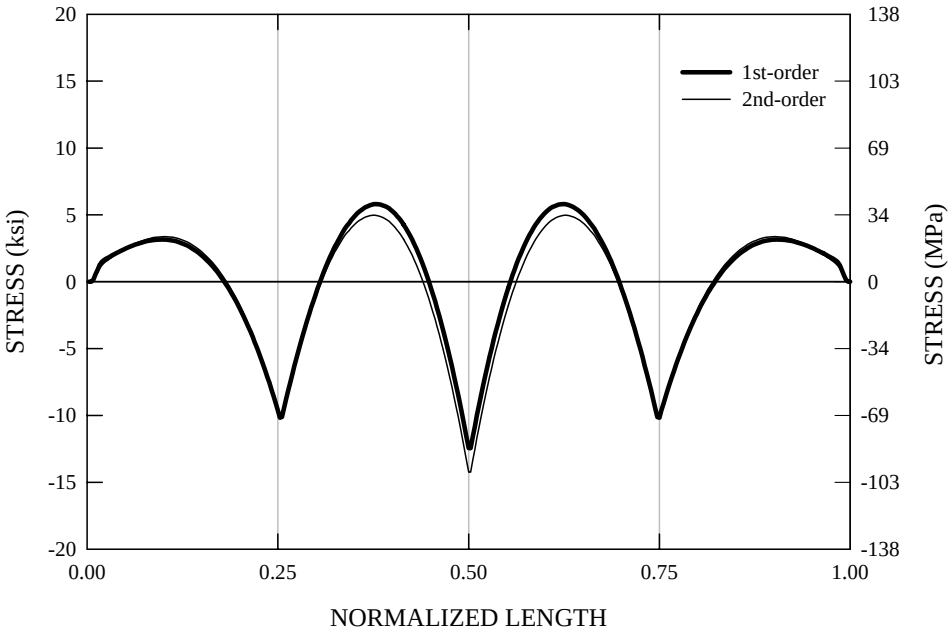

Figure A.1.2.9. Factored maximum bottom (tension) flange lateral bending stresses used for combination with live load stresses (torsion on exterior girders from overhangs not included, construction load factor = 1.25), G3.

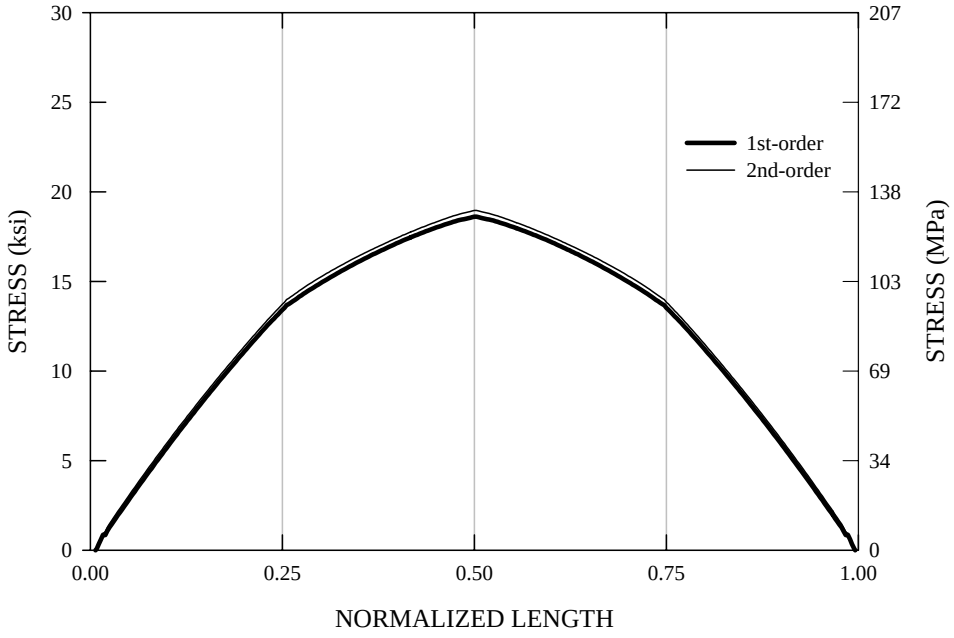

Figure A.1.2.10. Factored maximum bottom (tension) flange major-axis bending stresses used for combination with live load stresses (torsion on exterior girders from overhangs not included, construction load factor = 1.25), G3.

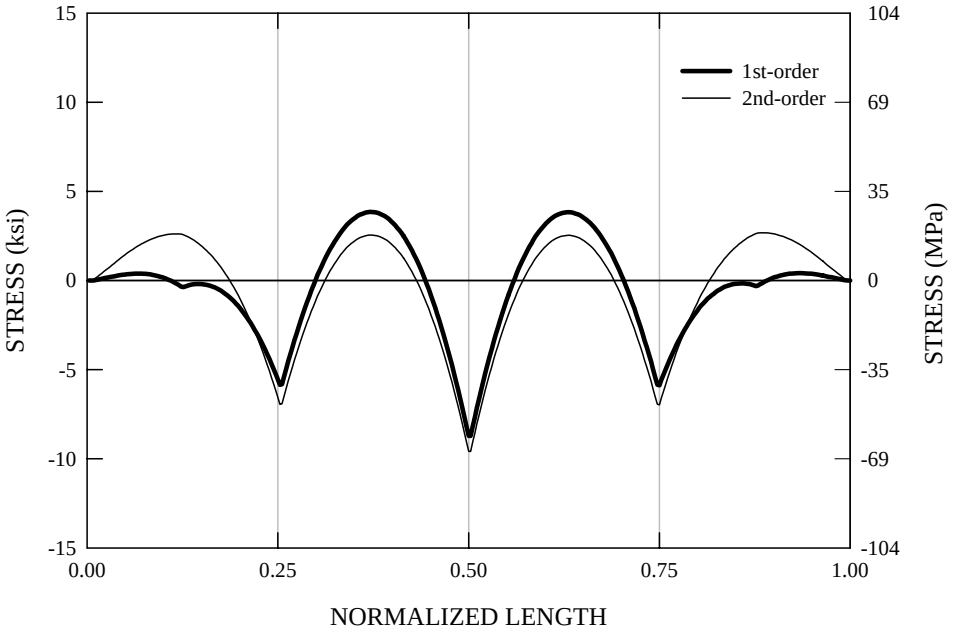

Figure A.1.2.11. Factored maximum bottom (tension) flange lateral bending stresses used for combination with live load stresses (torsion on exterior girders from overhangs not included, construction load factor = 1.25), G2.

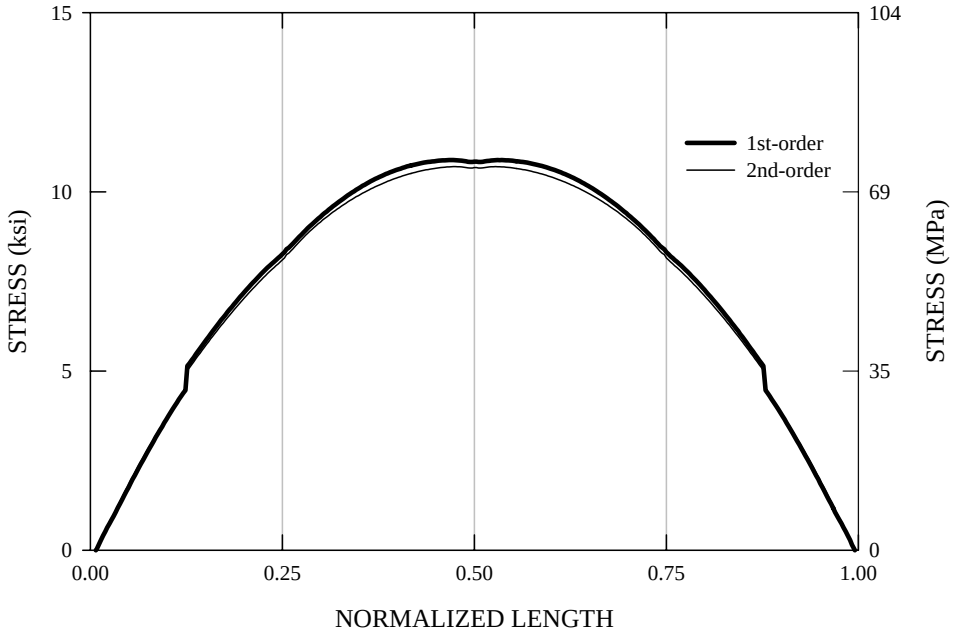

Figure A.1.2.12. Factored maximum bottom (tension) flange major-axis bending stresses used for combination with live load stresses (torsion on exterior girders from overhangs not included, construction load factor = 1.25), G2.

A.2. Composite Live Load Analysis

A.2.1 Maximum Effects on G2 and G3 Due to Design Truck Load

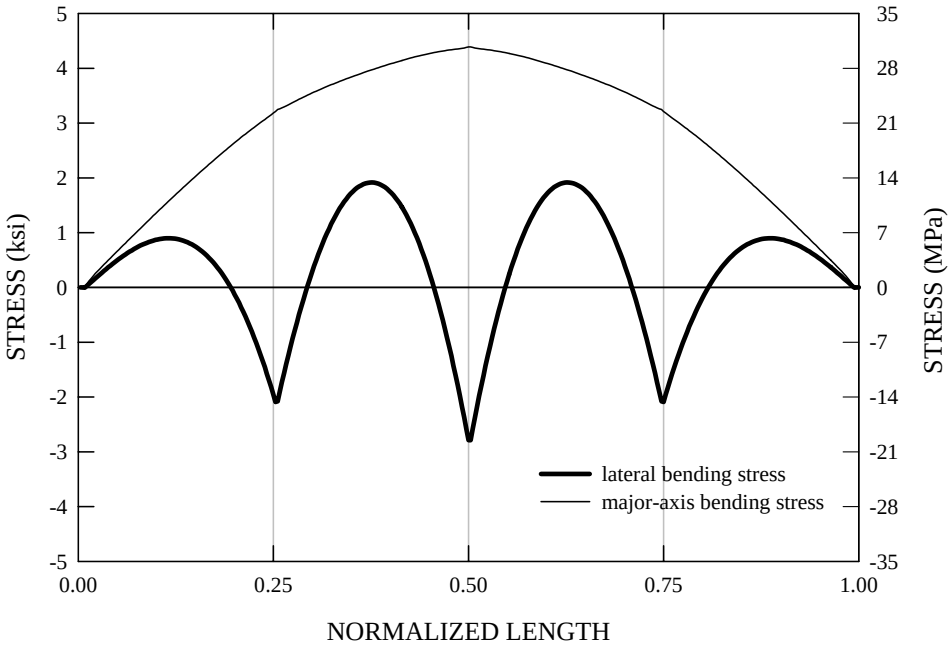

Figure A.2.1.1. First-order bottom flange stresses in G3 due to two lanes loaded by nominal (unfactored) distributed lane loads for maximum effect on G3.

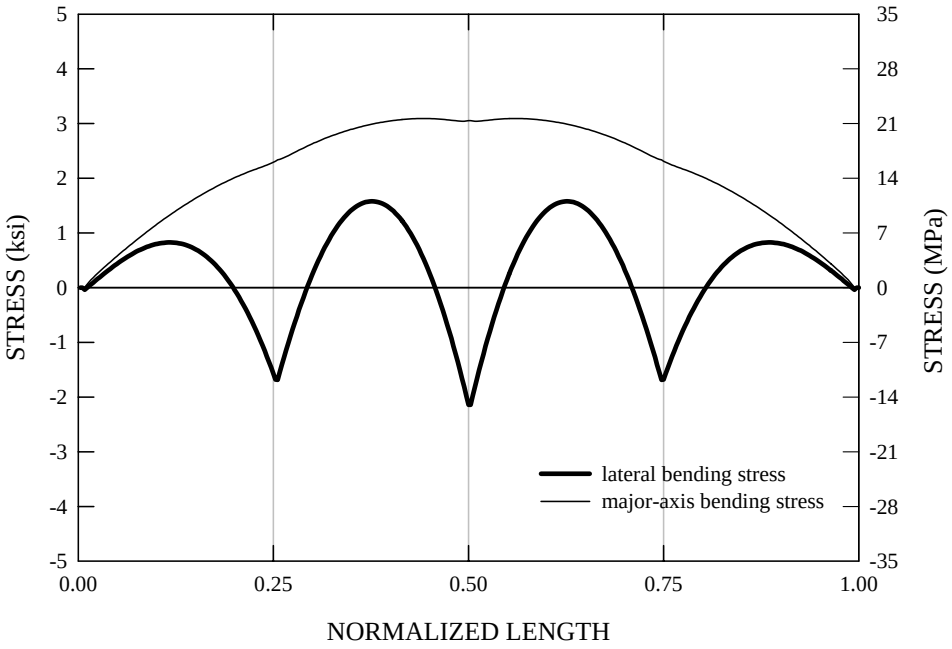

Figure A.2.1.2. First-order bottom flange stresses in G2 due to two lanes loaded by nominal (unfactored) distributed lane loads for maximum effect on G3.

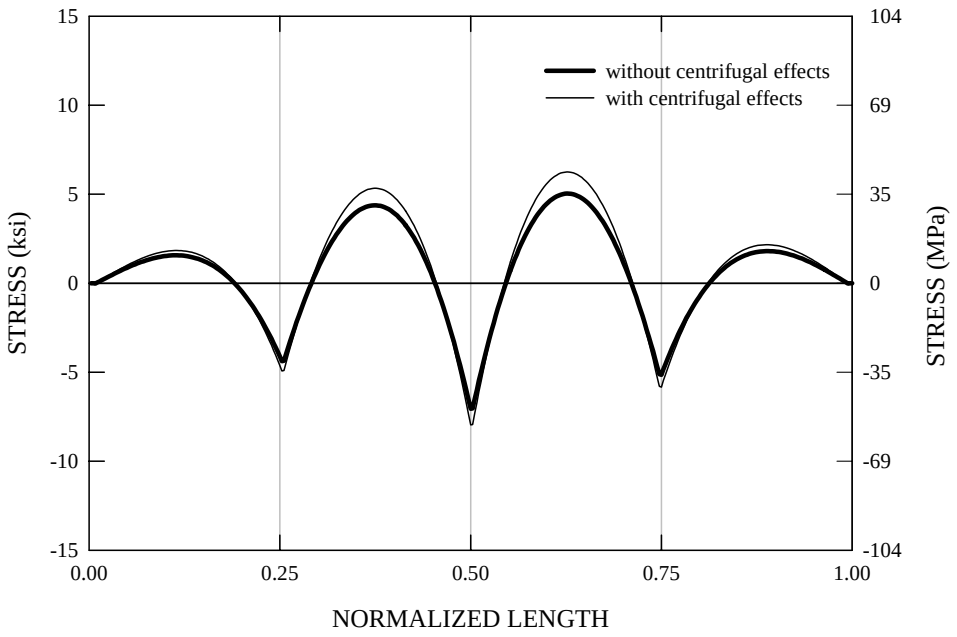

Figure A.2.1.3. First-order bottom flange lateral bending stresses in G3 due to two HL-93 AASHTO design trucks (nominal loads with dynamic allowance of 1.33 included), positioned side-by-side, for maximum effect on G3.

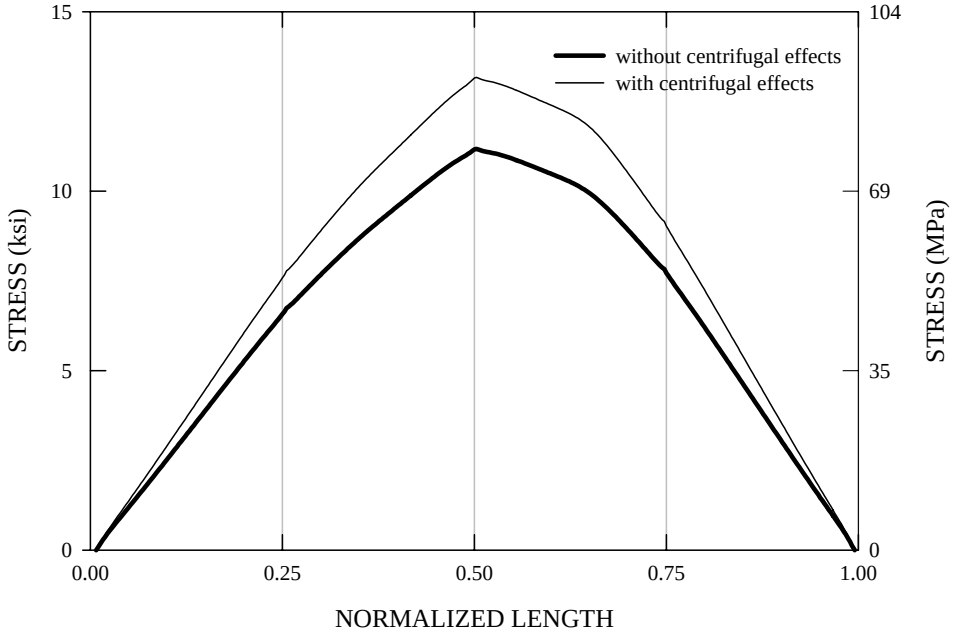

Figure A.2.1.4. First-order bottom flange major-axis bending stresses in G3 due to two HL-93 AASHTO design trucks (nominal loads with dynamic allowance of 1.33 included), positioned side-by-side, for maximum effect on G3.

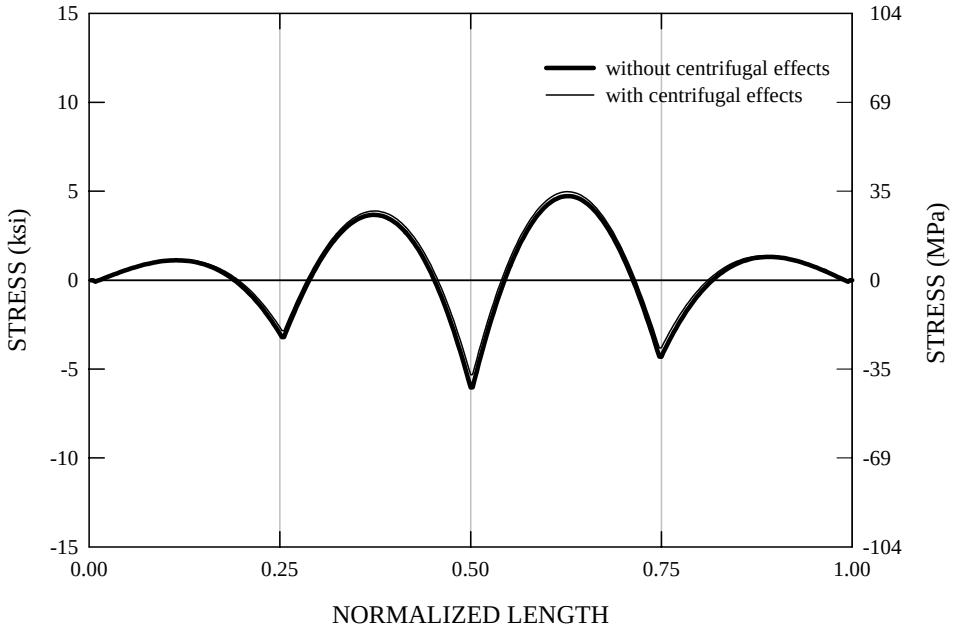

Figure A.2.1.5. First-order bottom flange lateral bending stresses in G2 due to two HL-93 AASHTO design trucks (nominal loads with dynamic allowance of 1.33 included), positioned side-by-side, for maximum effect on G3.

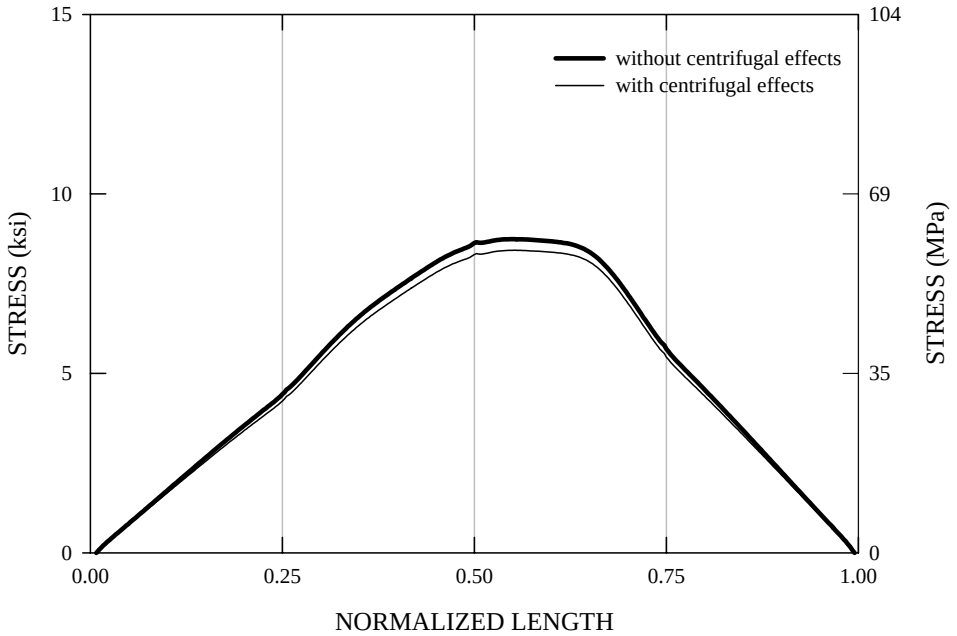

Figure A.2.1.6. First-order bottom flange major-axis bending stresses in G2 due to two HL-93 AASHTO design trucks (nominal loads with dynamic allowance of 1.33 included), positioned side-by-side, for maximum effect on G3, with the effects of centrifugal force included.

A.2.2 Maximum Effects on G1 Due to Design Truck Load

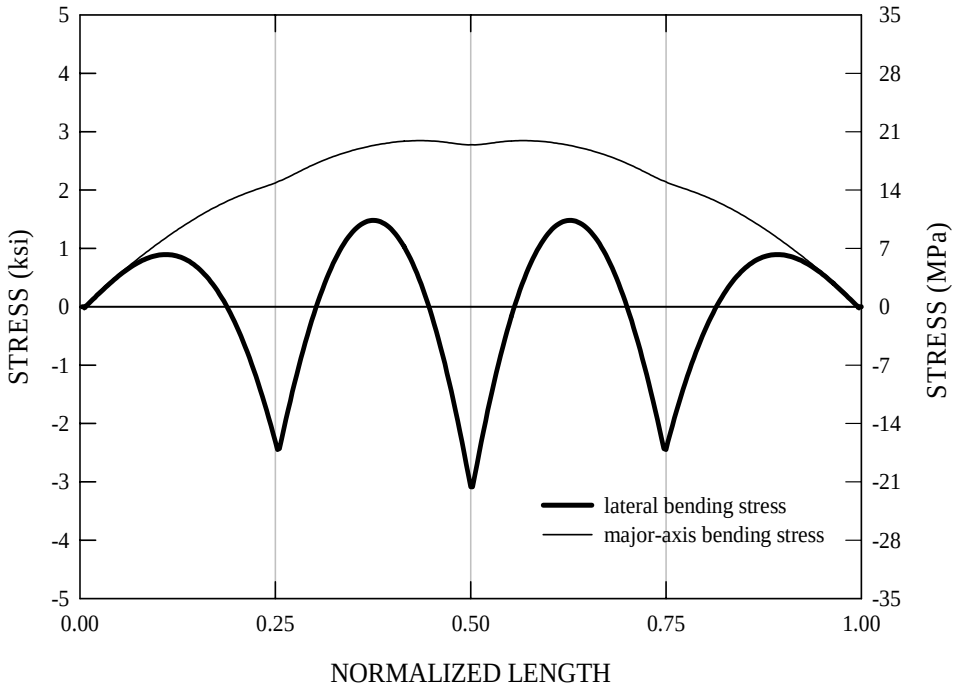

Figure A.2.2.1. First-order bottom flange stresses in G1 due to a single lane loaded by nominal (unfactored) distributed lane load (including multiple presence factor of 1.2) for the maximum effects on G1.

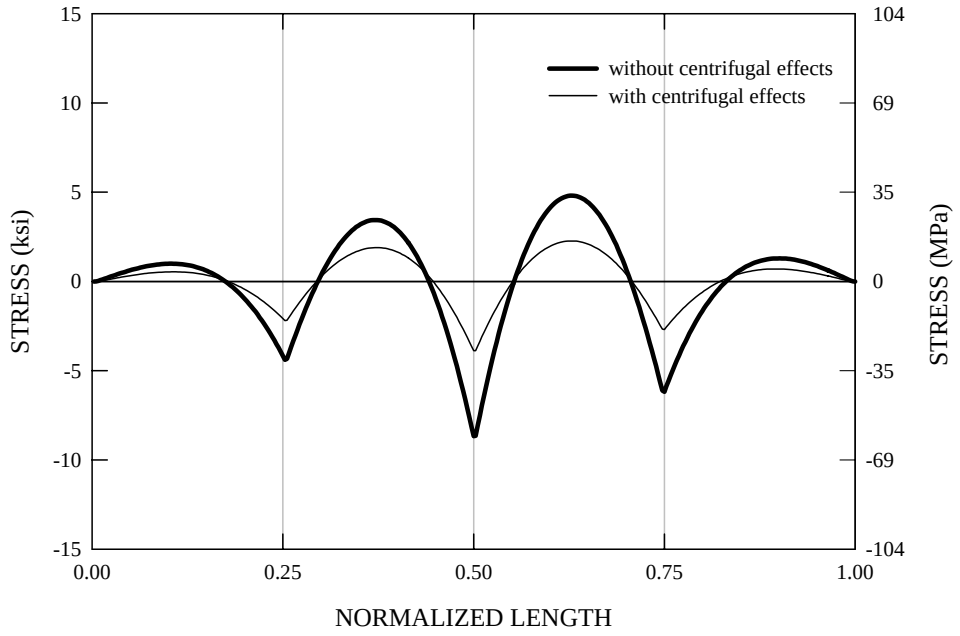

Figure A.2.2.2. First-order bottom flange lateral bending stresses in G1 due to a single HL-93 AASHTO design truck (nominal load with dynamic allowance of 1.33 included, multiple presence factor of 1.2 included), positioned for maximum effect on G1.

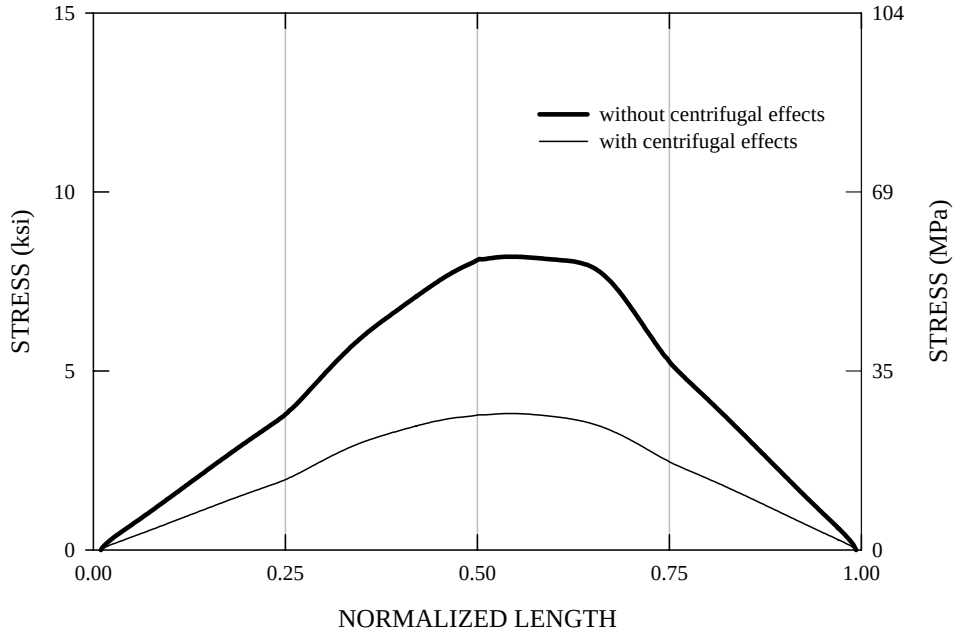

Figure A.2.2.3. First-order bottom flange major-axis bending stresses in G1 due to a single HL-93 AASHTO design truck (nominal load with dynamic allowance of 1.33 included, multiple presence factor of 1.2 included), positioned for maximum effect on G1.

APPENDIX B

TEST BRIDGE COMPONENT DESIGN

This appendix presents detailed step-by-step procedures for girder flexural design, girder web shear design, bearing stiffener design, connection plate design, cross-frame member design and shear connector design. Considering the iterative nature of a typical bridge design process, standard design templates are generated for each of the above component design using Mathcad (2001) program and used repeatedly to the extent possible where the same or similar design rules are applied. Otherwise, the design spreadsheets are updated by including relevant changes necessary to accommodate unique design requirements and used until girder proportions are obtained as reported in this section. In general, the design spreadsheets provide practical design considerations put into the sizing of the test bridge girder components in the context of the AASTHO (2004b) design provisions, as well as reasonable design assumptions made where there are no specific guidelines afforded in the AASHTO (2004b) Specifications. Furthermore, each set of the design spreadsheets dealing with the design of the test bridge girder component gives extensive step-by-step design procedures concerning the checking of girder responses obtained from the elastic design-analysis results relative to the AASHTO (2004b) Specifications. More importantly, all the design checks for the test bridge components reported in the spreadsheets were initially based on the nominal section dimensions and material properties, but they were updated using the measured material properties and test bridge geometry measurements afterwards. Therefore, it may be felt that the reported design check ratios in the spreadsheets do not seem to be as good as they are supposed to be in view of optimum design approach. But this is largely

because the measured material strengths are generally higher than the nominal material properties assumed in the initial design, and the measured section dimensions are larger than the nominal section dimensions.

The organization of this appendix is as follows. Sections B.1 through B.3 give a set of the design spreadsheets for the flexural design of the test bridge girders in the order of G1, G2 and G3. Section B.4 concerns the web shear design of the test bridge girders. Next, Section B.5 presents a set of design spreadsheet concerning the design of bearing stiffeners, connection plates and cross-frame member design. This is followed by Section B.6 which details the shear connector design. Finally, Section B.7 summarizes the flexural design of the test bridge girders by highlighting the key design checks.

B.1 G1 Positive Moment Flexural Design

Material Properties:

- Steel Properties:

$F_{yc} := 57.56\,ksi$; $F_{yw} := 63.28\,ksi$; $F_{yt} := 58.07\,ksi$; $F_{yr} := 60\,ksi$; $E := 2.9 \cdot 10^4\,ksi$

- Concrete Properties:

$f_c := 4.9\,ksi$; $E_c := 4034.4\,ksi$; $n := \frac{E}{E_c}$; $n = 7.189$ $W_{conc} := 150\,\frac{lbf}{ft^3}$

Plate Girder Dimensions:

GIRDER LENGTH:

$L := 86.0625\,ft$ $L_b := \frac{L}{4}$ $L_b = 21.516\,ft$

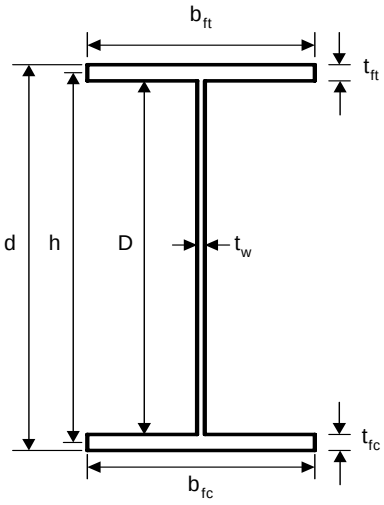

TOP FLANGE:

$b_{fc} := 12.188\,in$

$t_{fc} := 0.883\,in$

$\frac{b_{fc}}{2 t_{fc}} = 6.901$

BOTTOM FLANGE:

$b_{ft} := 17.266\,in$

$t_{ft} := 0.886\,in$

$\frac{b_{ft}}{2 \cdot t_{ft}} = 9.74$

WEB:

$D := 48.102\,in$ $t_w := 0.331\,in$ $\frac{D}{t_w} = 145.323$

$d := D + t_{ft} + t_{fc}$ $d = 49.871\,in$

$h := D + \frac{t_{ft} + t_{fc}}{2}$ $h = 48.986\,in$

Cross-section Proportion Limits :

- Web proportion checks for webs without longitudinal stiffeners

$Web\_Proportion\_Check := \begin{cases} \text{"OK"} & \text{if } \frac{D}{t_w} \le 150 \\ \text{"NG"} & \text{otherwise} \end{cases}$ $Web\_Proportion\_Check = \text{"OK"}$

$a_w := \frac{D \cdot t_w}{b_{fc} \cdot t_{fc}}$ $a_w = 1.479$

$Prevent\_Vertical\_Flange\_Buckling\_Check := \begin{cases} \text{"OK"} & \text{if } \frac{D}{t_w} \le 0.6 \cdot \sqrt{a_w} \cdot \frac{E}{F_{yc}} \\ \text{"NG"} & \text{otherwise} \end{cases}$ $0.6 \cdot \sqrt{a_w} \cdot \frac{E}{F_{yc}} = 368$

$Prevent\_Vertical\_Flange\_Buckling\_Check = \text{"OK"}$

- Flange proportion checks

$I_{yc} := \frac{t_{fc} \cdot b_{fc}^3}{12}$ $I_{yt} := \frac{t_{ft} \cdot b_{ft}^3}{12}$ $\frac{I_{yc}}{I_{yt}} = 0.351$

$$Compression\_Flange\_Check := \begin{cases} \text{"OK"} & \text{if } \frac{b_{fc}}{2 \cdot t_{fc}} \le 12.0 \wedge b_{fc} \ge \frac{D}{6} \wedge t_{fc} \ge 1.1 \cdot t_w \wedge 0.1 \le \frac{I_{yc}}{I_{yt}} \le 10 \\ \text{"NG"} & \text{otherwise} \end{cases}$$

Compression_Flange_Check = "OK"

$$Tension\_Flange\_Check := \begin{cases} \text{"OK"} & \text{if } \frac{b_{ft}}{2 \cdot t_{ft}} \le 12.0 \wedge b_{ft} \ge \frac{D}{6} \wedge t_{ft} \ge 1.1 \cdot t_w \\ \text{"NG"} & \text{otherwise} \end{cases}$$

Tension_Flange_Check = "OK"

Non-Composite Section Properties:

Top flange area :

$A_{fc} := b_{fc} \cdot t_{fc}$ $A_{fc} = 10.762 in^2$

Bottom flange area:

$A_{ft} := b_{ft} \cdot t_{ft}$ $A_{ft} = 15.298 in^2$

Web area:

$A_{web} := D \cdot t_w$ $A_{web} = 15.922 in^2$

Total section area :

$A_{girder} := A_{fc} + A_{ft} + A_{web}$ $A_{girder} = 41.981 in^2$

Neutral axis :

$D_c := \frac{A_{fc} \cdot \left(\frac{t_{fc}}{2} \right) + A_{ft} \cdot \left(d - \frac{t_{ft}}{2} \right) + A_{web} \cdot \left(\frac{D}{2} + t_{fc} \right)}{A_{girder}} - t_{fc}$ $D_c = 26.698 in$ $\frac{D_c}{D} = 0.555$

Note: Neutral axis measured from the lower surface of the top flange.

Shear center : $h_u := D_c + \frac{t_{fc}}{2}$ $h_l := D - D_c + \frac{t_{ft}}{2}$

$e := \frac{I_{yc} \cdot h_u - I_{yt} \cdot h_l}{I_{yc} + I_{yt}}$ $e = -9.132 in$ (offset distance from the neutral axis)

Moment of inertia with respect to a neutral axis :

$$I_{girder} := \frac{b_{fc} \cdot t_{fc}^3}{12} + \left[A_{fc} \cdot \left(D_c + t_{fc} - \frac{t_{fc}}{2} \right)^2 \right] \ldots + \frac{b_{ft} \cdot t_{ft}^3}{12} + \left[A_{ft} \cdot \left[d - \left(D_c + t_{fc} \right) - \frac{t_{ft}}{2} \right]^2 \right] \ldots + \frac{t_w \cdot D^3}{12} + A_{web} \cdot \left(D_c + t_{fc} - \frac{D}{2} - t_{fc} \right)^2 \qquad I_{girder} = 1.841 \times 10^4 \, in^4$$

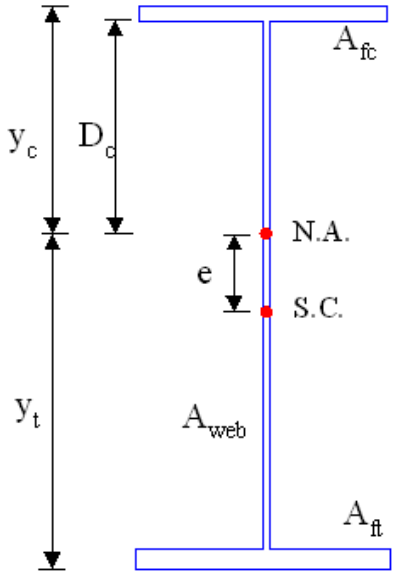

Section modulus to the compression flange :

$y_c := D_c + t_{fc}$ $\quad y_c = 27.581 in$

$S_c := \frac{I_{girder}}{y_c}$ $\quad S_c = 667.549 in^3$

Section modulus of the tension flange :

$y_t := d - y_c$ $\quad y_t = 22.29 in$

$S_t := \frac{I_{girder}}{y_t}$ $\quad S_t = 825.986 in^3$ $\quad \frac{A_{ft}}{A_{fc}} = 1.421$

- Web Bend-buckling Resistance

$\frac{D_c}{D} = 0.555$ $\quad \frac{2D_c}{t_w} = 161.315$

bend-buckling coeffient :

$k := \frac{9}{\left(\frac{D_c}{D} \right)^2}$ $\quad k = 29.216$ $\quad F_{crw} := 0.9 \cdot E \cdot \frac{k}{\left(\frac{D}{t_w} \right)^2}$ $\quad F_{crw} = 36.11 ksi$

- Yield Moment

$M_{yt\_noncomp} := S_t \cdot F_{yt}$ $\quad M_{yt\_noncomp} = 3.997 \times 10^3 \, kips \cdot ft$

$M_{yc\_noncomp} := S_c \cdot F_{yc}$ $\quad M_{yc\_noncomp} = 3.202 \times 10^3 \, kips \cdot ft$

$M_{y\_noncomp} := \begin{cases} M_{yt\_noncomp} & \text{if } M_{yt\_noncomp} \le M_{yc\_noncomp} \\ M_{yc\_noncomp} & \text{otherwise} \end{cases}$ $\quad M_{y\_noncomp} = 3.202 \times 10^3 \, kips \cdot ft$

- Radius of Gyration for LTB Check

$r_t := \frac{b_{fc}}{\sqrt{12 \cdot \left(\frac{h}{d} + \frac{D_c \cdot t_w \cdot D^2}{3 \cdot b_{fc} \cdot t_{fc} \cdot h \cdot d} \right)}}$ $\quad r_t = 3.158 in$

Note: The exact r_t equation is used in the above .

- Flange-Strength Reduction Factors (Noncomposite Girder) :

Hybrid Factor : $R_{h\_noncomp} := 1$ **since section is homogeneous**

Web Load-Shedding Factor :

$D_c = 26.698in$

$a_{wc} := \frac{2 \cdot D_c \cdot t_w}{A_{fc}}$ $a_{wc} = 1.642$

$\lambda_{rw} := 5.7\sqrt{\frac{E}{F_{yc}}}$ $\lambda_{rw} = 127.942$

$$R_{b\_noncomp} := \begin{cases} 1.0 \text{ if } \frac{2 \cdot D_c}{t_w} \le \lambda_{rw} \\ \text{otherwise} \\ \quad \begin{cases} 1 - \left(\frac{a_{wc}}{1200 + 300 \cdot a_{wc}}\right) \cdot \left(\frac{2 \cdot D_c}{t_w} - \lambda_{rw}\right) \text{ if } 1 - \left(\frac{a_{wc}}{1200 + 300 \cdot a_{wc}}\right) \cdot \left(\frac{2 \cdot D_c}{t_w} - \lambda_{rw}\right) \le 1.0 \\ 1.0 \text{ otherwise} \end{cases} \end{cases}$$

$R_{b\_noncomp} = 0.968$

Composite Section Properties :

Effective Width of Slab

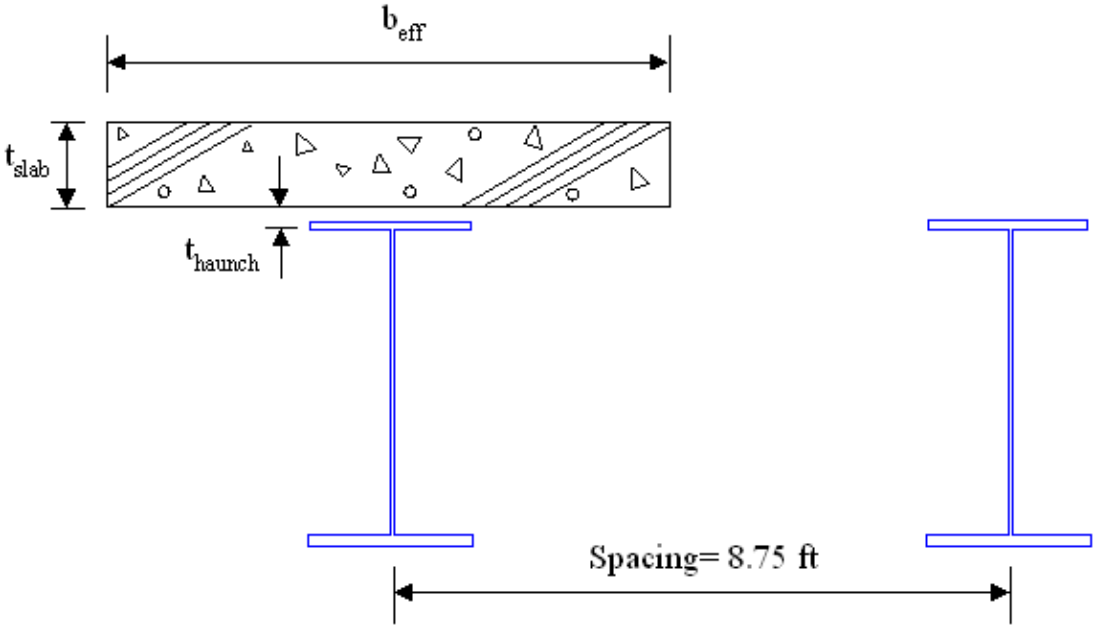

< Composite Section >

$t_{haunch} := 3in$ $b_{eff\_int} := 8.583ft$ $t_{slab} := 8in$

$$b_{eff\_ext} := \min\left(\left(\begin{array}{c}\frac{L}{8}\\ 6\cdot t_{slab} + \frac{b_{fc}}{4}\\ 3.0ft\end{array}\right)\right) + \frac{b_{eff\_int}}{2} \qquad b_{eff\_ext} = 7.292ft$$

NOTE: the full tributary width for each girder is used in the design.

$b_{slab} := 7.375ft$ $b_{s\_3n} := \frac{b_{slab}}{3n}$

Reinforcement:

Average top reinforcing steel area : $A_{top\_rebar} := \frac{0.18in\cdot b_{slab}}{12}$ $A_{top\_rebar} = 1.327in^2$

Average bottom reinforcing steel area : $A_{bottom\_rebar} := \frac{0.27in\cdot b_{slab}}{12}$ $A_{bottom\_rebar} = 1.991in^2$

Location of top reinforcing steel : $y_{rt} := 3.25in$

Location of bottom reinforcing steel : $y_{rb} := 6.25in$

Long Term Composite Section Properties(3n) :

$A_{con\_3n} := b_{s\_3n}\cdot t_{slab}$ $A_{con\_3n} = 32.828in^2$

$A_{total\_3n} := A_{girder} + A_{con\_3n}$ $A_{total\_3n} = 74.81in^2$

$$NA_{3n} := \frac{A_{fc}\cdot\left(t_{slab} + t_{haunch} - \frac{t_{fc}}{2}\right) + A_{ft}\cdot\left(D + t_{slab} + t_{haunch} + \frac{t_{ft}}{2}\right) + A_{web}\cdot\left(\frac{D}{2} + t_{slab} + t_{haunch}\right) + A_{con\_3n}\cdot\frac{t_{slab}}{2}}{A_{total\_3n}}$$

Note: Neutral axis is measured from the top of concrete slab

$NA_{3n} = 22.91in$

$$I_{3n} := \frac{b_{fc}\cdot t_{fc}^3}{12} + \left[A_{fc}\cdot\left(NA_{3n} - t_{slab} - t_{haunch} + \frac{t_{fc}}{2}\right)^2\right] \ldots + \frac{b_{ft}\cdot t_{ft}^3}{12} + \left[A_{ft}\cdot\left(t_{slab} + t_{haunch} + D + t_{ft} - NA_{3n} - \frac{t_{ft}}{2}\right)^2\right] \ldots + \frac{t_w\cdot D^3}{12} + A_{web}\cdot\left(NA_{3n} - t_{slab} - t_{haunch} - \frac{D}{2}\right)^2 + \frac{b_{s\_3n}\cdot t_{slab}^3}{12} + A_{con\_3n}\cdot\left(NA_{3n} - \frac{t_{slab}}{2}\right)^2$$

$I_{3n} = 3.951\times 10^4 in^4$

Section Moduli:

$S_{slab\_3n} := \frac{I_{3n}}{NA_{3n}}$ $S_{slab\_3n} = 1.724\times 10^{3}\,in^{3}$

$y_{c\_3n} := NA_{3n} - t_{slab} - t_{haunch} + t_{fc}$ $y_{c\_3n} = 12.793in$

$S_{c\_3n} := \frac{I_{3n}}{y_{c\_3n}}$ $S_{c\_3n} = 3.088\times 10^{3}\,in^{3}$

$y_{t\_3n} := d - y_{c\_3n}$ $y_{t\_3n} = 37.078in$

$S_{t\_3n} := \frac{I_{3n}}{y_{t\_3n}}$ $S_{t\_3n} = 1.065\times 10^{3}\,in^{3}$

$D_{c\_3n} := y_{c\_3n} - t_{fc}$ $D_{c\_3n} = 11.91in$

$\frac{D_{c\_3n}}{D} = 0.248$ $\frac{2D_{c\_3n}}{t_w} = 71.966$

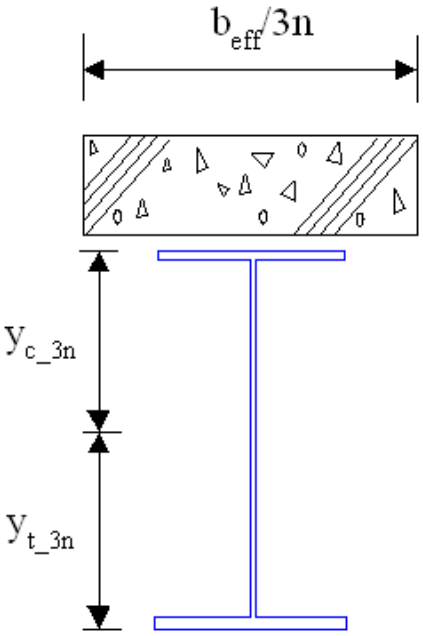

- Yield Moment (Long-term, Shored Construction) :

$M_{yt\_longterm} := S_{t\_3n}\cdot F_{yt}$ $M_{yt\_longterm} = 5.156\times 10^{3}\,kips\cdot ft$

$M_{yc\_longterm} := S_{c\_3n}\cdot F_{yc}$ $M_{yc\_longterm} = 1.481\times 10^{4}\,kips\cdot ft$

$M_{y\_longterm} := \begin{cases} M_{yt\_longterm} & \text{if } M_{yt\_longterm} \le M_{yc\_longterm} \\ M_{yc\_longterm} & \text{otherwise} \end{cases}$ $M_{y\_longterm} = 5.156\times 10^{3}\,kips\cdot ft$

- Concrete Stress at $M_{y\text{-Long Term (shored construction)}}$

$f_{c\_3n} := \frac{M_{y\_longterm}\cdot NA_{3n}}{I_{3n}\cdot 3n}$ $f_{c\_3n} = 1.664ksi$ $\frac{f_{c\_3n}}{f_c} = 0.34$

Short Term Composite Section Properties (n):

Effective Flange Width

$b_{s\_n} := \frac{b_{slab}}{n}$

$A_{con\_n} := b_{s\_n}\cdot t_{slab}$ $A_{con\_n} = 98.485in^{2}$

$A_{total\_n} := A_{girder} + A_{con\_n}$ $A_{total\_n} = 140.467in^{2}$

$$NA_n := \frac{A_{fc}\cdot\left(t_{slab} + t_{haunch} - \frac{t_{fc}}{2}\right) + A_{ft}\cdot\left(D + t_{slab} + t_{haunch} + \frac{t_{ft}}{2}\right) + A_{web}\cdot\left(\frac{D}{2} + t_{slab} + t_{haunch}\right) + A_{con\_n}\cdot\frac{t_{slab}}{2}}{A_{total\_n}}$$

Note: Neutral is axis measured from the top of concrete slab

$NA_n = 14.071in$

$$I_n := \frac{b_{fc}\cdot t_{fc}^3}{12} + \left[A_{fc}\cdot\left(NA_n - t_{slab} - t_{haunch} + \frac{t_{fc}}{2}\right)^2\right] \ldots$$
$$+ \frac{b_{ft}\cdot t_{ft}^3}{12} + \left[A_{ft}\cdot\left(t_{slab} + t_{haunch} + D + t_{ft} - NA_n - \frac{t_{ft}}{2}\right)^2\right] \ldots$$
$$+ \frac{t_w\cdot D^3}{12} + A_{web}\cdot\left(NA_n - t_{slab} - t_{haunch} - \frac{D}{2}\right)^2 + \frac{b_{s\_n}\cdot t_{slab}^3}{12} + A_{con\_n}\cdot\left(NA_n - \frac{t_{slab}}{2}\right)^2 \qquad I_n = 5.236\times 10^4\ in^4$$

Section Moduli :

$$S_{slab\_n} := \frac{I_n}{NA_n} \qquad S_{slab\_n} = 3.721\times 10^3\ in^3$$

$$y_{c\_n} := NA_n - t_{slab} - t_{haunch} + t_{fc} \qquad y_{c\_n} = 3.954in$$

$$S_{c\_n} := \frac{I_n}{y_{c\_n}} \qquad S_{c\_n} = 1.324\times 10^4\ in^3$$

$$y_{t\_n} := d - y_{c\_n} \qquad y_{t\_n} = 45.917in$$

$$S_{t\_n} := \frac{I_n}{y_{t\_n}} \qquad S_{t\_n} = 1.14\times 10^3\ in^3$$

$$D_{c\_n} := y_{c\_n} - t_{fc} \qquad D_{c\_n} = 3.071in$$

$$\frac{D_{c\_n}}{D} = 0.064 \qquad \frac{2D_{c\_n}}{t_w} = 18.558$$

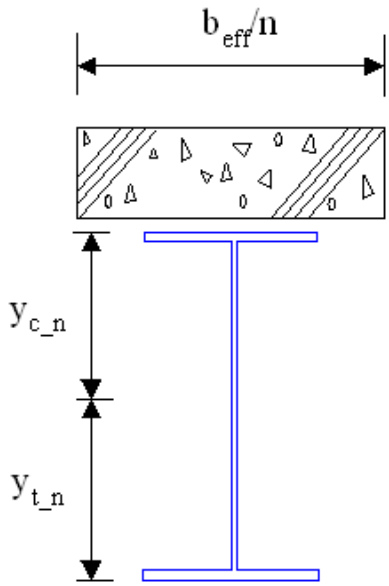

- Yield Moment (Short-term, Shored Construction) :

$$M_{yt\_shortterm} := S_{t\_n}\cdot F_{yt} \qquad M_{yt\_shortterm} = 5.518\times 10^3\ kips\cdot ft$$

$$M_{yc\_shortterm} := S_{c\_n}\cdot F_{yc} \qquad M_{yc\_shortterm} = 6.352\times 10^4\ kips\cdot ft$$

$$M_{y\_shortterm} := \begin{cases} M_{yt\_shortterm} & \text{if } M_{yt\_shortterm} \le M_{yc\_shortterm} \\ M_{yc\_shortterm} & \text{otherwise} \end{cases} \qquad M_{y\_shortterm} = 5.518\times 10^3\ kips\cdot ft$$

- Concrete Stress at M $_{y\text{-Short Term (shored construction)}}$

$$f_{c\_n} := \frac{M_{y\_shortterm}\cdot NA_n}{I_n\, n} \qquad f_{c\_n} = 2.475ksi \qquad \frac{f_{c\_n}}{f_c} = 0.505$$

Plastic Moment Capacity (Composite Section) :

NOTE: The plastic moment capacity is computed here only for reference purposes.
The design strengths are based on slender web member capacity equations

$P_{rb} := F_{yr} \cdot A_{bottom\_rebar}$ $P_{rb} = 119.475\text{kips}$

$P_{rt} := F_{yr} \cdot A_{top\_rebar}$ $P_{rt} = 79.65\text{kips}$

$P_s := 0.85 f_c \cdot b_{slab} \cdot t_{slab}$ $P_s = 2.949 \times 10^3\ \text{kips}$

$P_c := F_{yc} \cdot A_{fc}$ $P_c = 619.461\text{kips}$

$P_t := F_{yt} \cdot A_{ft}$ $P_t = 888.336\text{kips}$

$P_w := F_{yw} \cdot A_{web}$ $P_w = 1.008 \times 10^3\ \text{kips}$

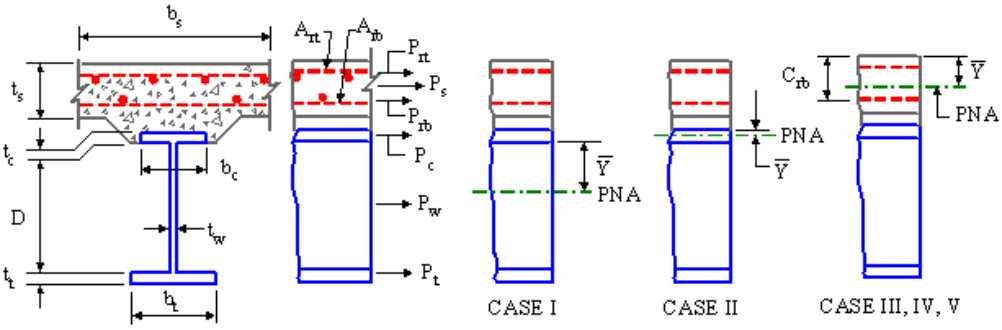

Computation of Plastic-Moment Capacity(Positive Flexure)

Location_of_PNA :=
- "In Web (Case I) " if $P_t + P_w \geq P_c + P_s + P_{rb} + P_{rt}$
- otherwise
  - "In Top Flange (Case II) " if $P_t + P_w + P_c \geq P_s + P_{rb} + P_{rt}$
  - otherwise
    - "Slab, Below Prb (Case III)" if $P_t + P_w + P_c \geq \frac{y_{rb}}{t_{slab}} \cdot P_s + P_{rb} + P_{rt}$
    - otherwise
      - "Slab,at Prb (Case IV)" if $P_t + P_w + P_c + P_{rb} \geq \frac{y_{rb}}{t_{slab}} \cdot P_s + P_{rt}$
      - "Slab, Above Prb (Case V) " otherwise

Location_of_PNA = "Slab, Below Prb (Case III)"

$$Y_{bar} := \begin{cases} \frac{D}{2}\cdot\left(\frac{P_t - P_c - P_s - P_{rt} - P_{rb}}{P_w} + 1\right) & \text{if } P_t + P_w \geq P_c + P_s + P_{rb} + P_{rt} \\ \text{otherwise} \\ \quad \begin{cases} \frac{t_{fc}}{2}\cdot\left(\frac{P_w + P_t - P_s - P_{rt} - P_{rb}}{P_c} + 1\right) & \text{if } P_t + P_w + P_c \geq P_s + P_{rb} + P_{rt} \\ \text{otherwise} \\ \quad \begin{cases} t_{slab}\cdot\frac{P_c + P_w + P_t - P_{rt} - P_{rb}}{P_s} & \text{if } P_t + P_w + P_c \geq \frac{y_{rb}}{t_{slab}}\cdot P_s + P_{rb} + P_{rt} \\ \text{otherwise} \\ \quad \begin{cases} y_{rb} & \text{if } P_t + P_w + P_c + P_{rb} \geq \frac{y_{rb}}{t_{slab}}\cdot P_s + P_{rt} \\ t_{slab}\cdot\frac{P_{rb} + P_c + P_w + P_t - P_{rt}}{P_s} & \text{otherwise} \end{cases} \end{cases} \end{cases} \end{cases}$$

$Y_{bar} = 6.284in$

$$d_s := \begin{cases} \frac{t_{slab}}{2} + t_{haunch} + Y_{bar} & \text{if } P_t + P_w \geq P_c + P_s + P_{rb} + P_{rt} \\ \text{otherwise} \\ \quad \begin{cases} \frac{t_{slab}}{2} + t_{haunch} - t_{fc} + Y_{bar} & \text{if } P_t + P_w + P_c \geq P_s + P_{rb} + P_{rt} \\ \text{"Not necessary for calculating Mp"} & \text{otherwise} \end{cases} \end{cases}$$

$d_s = \text{"Not necessary for calculating Mp"}$ in

$$d_{rt} := \begin{cases} t_{slab} - y_{rt} + t_{haunch} + Y_{bar} & \text{if } P_t + P_w \geq P_c + P_s + P_{rb} + P_{rt} \\ \text{otherwise} \\ \quad \begin{cases} t_{slab} - y_{rt} + t_{haunch} - t_{fc} + Y_{bar} & \text{if } P_t + P_w + P_c \geq P_s + P_{rb} + P_{rt} \\ Y_{bar} - y_{rt} & \text{otherwise} \end{cases} \end{cases}$$

$d_{rt} = 3.034in$

$$d_{rb} := \begin{cases} t_{slab} - y_{rb} + t_{haunch} + Y_{bar} & \text{if } P_t + P_w \geq P_c + P_s + P_{rb} + P_{rt} \\ \text{otherwise} \\ \quad \begin{cases} t_{slab} - y_{rb} + t_{haunch} - t_{fc} + Y_{bar} & \text{if } P_t + P_w + P_c \geq P_s + P_{rb} + P_{rt} \\ \text{otherwise} \\ \quad \begin{cases} Y_{bar} - y_{rb} & \text{if } P_t + P_w + P_c \geq \frac{y_{rb}}{t_{slab}}\cdot P_s + P_{rb} + P_{rt} \\ \text{otherwise} \\ \quad \begin{cases} \text{"Not necessary for calculating Mp"} & \text{if } P_t + P_w + P_c + P_{rb} \geq \frac{y_{rb}}{t_{slab}}\cdot P_s + P_{rt} \\ y_{rb} - Y_{bar} & \text{otherwise} \end{cases} \end{cases} \end{cases} \end{cases}$$

$d_{rb} = 0.034in$

$$d_c := \begin{cases} Y_{bar} - \frac{t_{fc}}{2} & \text{if } P_t + P_w \geq P_c + P_s + P_{rb} + P_{rt} \\ \text{otherwise} \\ \quad \begin{cases} \text{"Not necessary for calculating Mp"} & \text{if } P_t + P_w + P_c \geq P_s + P_{rb} + P_{rt} \\ t_{slab} + t_{haunch} - \frac{t_{fc}}{2} - Y_{bar} & \text{otherwise} \end{cases} \end{cases} \qquad d_c = 0.356\,\text{ft}$$

$$d_w := \begin{cases} \text{"Not necessary for calculating Mp"} & \text{if } P_t + P_w \geq P_c + P_s + P_{rb} + P_{rt} \\ \text{otherwise} \\ \quad \begin{cases} \frac{D}{2} + t_{fc} - Y_{bar} & \text{if } P_t + P_w + P_c \geq P_s + P_{rb} + P_{rt} \\ t_{slab} + t_{haunch} - Y_{bar} + \frac{D}{2} & \text{otherwise} \end{cases} \end{cases} \qquad d_w = 28.767\text{in}$$

$$d_t := \begin{cases} D - Y_{bar} + \frac{t_{ft}}{2} & \text{if } P_t + P_w \geq P_c + P_s + P_{rb} + P_{rt} \\ \text{otherwise} \\ \quad \begin{cases} D + t_{fc} - Y_{bar} + \frac{t_{ft}}{2} & \text{if } P_t + P_w + P_c \geq P_s + P_{rb} + P_{rt} \\ t_{slab} + t_{haunch} - Y_{bar} + D + \frac{t_{ft}}{2} & \text{otherwise} \end{cases} \end{cases} \qquad d_t = 53.261\text{in}$$

$$M_p := \begin{cases} \frac{P_w}{2 \cdot D} \cdot \left[Y_{bar}^{\,2} + \left(D - Y_{bar}\right)^2 \right] + P_s \cdot d_s + P_{rt} \cdot d_{rt} + P_{rb} \cdot d_{rb} + P_c \cdot d_c + P_t \cdot d_t & \text{if } P_t + P_w \geq P_c + P_s + P_{rb} + P_{rt} \\ \text{otherwise} \\ \quad \begin{cases} \frac{P_c}{2 \cdot t_{fc}} \cdot \left[Y_{bar}^{\,2} + \left(t_{fc} - Y_{bar}\right)^2 \right] + P_s \cdot d_s + P_{rt} \cdot d_{rt} + P_{rb} \cdot d_{rb} + P_w \cdot d_w + P_t \cdot d_t & \text{if } P_t + P_w + P_c \geq P_s + P_{rb} + P_{rt} \\ \text{otherwise} \\ \quad \begin{cases} \frac{Y_{bar}^{\,2} \cdot P_s}{2 \cdot t_{slab}} + P_{rt} \cdot d_{rt} + P_{rb} \cdot d_{rb} + P_c \cdot d_c + P_w \cdot d_w + P_t \cdot d_t & \text{if } P_t + P_w + P_c \geq \frac{y_{rb}}{t_{slab}} \cdot P_s + P_{rb} + P_{rt} \\ \text{otherwise} \\ \quad \begin{cases} \frac{Y_{bar}^{\,2} \cdot P_s}{2 \cdot t_{slab}} + P_{rt} \cdot d_{rt} + P_c \cdot d_c + P_w \cdot d_w + P_t \cdot d_t & \text{if } P_t + P_w + P_c + P_{rb} \geq \frac{y_{rb}}{t_{slab}} \cdot P_s + P_{rt} \\ \frac{Y_{bar}^{\,2} \cdot P_s}{2 \cdot t_{slab}} + P_{rt} \cdot d_{rt} + P_{rb} \cdot d_{rb} + P_c \cdot d_c + P_w \cdot d_w + P_t \cdot d_t & \text{otherwise} \end{cases} \end{cases} \end{cases} \qquad M_p = 7.206 \times 10^3\,\text{kips}\cdot\text{ft}$$

Unshored Composite Section Properties :

Yield Moment (unshored) associated with STRENGTH I

Read analysis results of factored flanges stresses.

$f_{tf\_si} :=$ $f_{bf\_si} :=$

$length := f_{tf\_si}^{\langle cols(f_{tf\_si})-3\rangle}$

$fb_{tf} := f_{tf\_si}^{\langle cols(f_{tf\_si})-2\rangle}$ $fl_{tf} := f_{tf\_si}^{\langle cols(f_{tf\_si})-1\rangle}$

$fb_{bf} := f_{bf\_si}^{\langle cols(f_{bf\_si})-2\rangle}$ $fl_{bf} := f_{bf\_si}^{\langle cols(f_{bf\_si})-1\rangle}$

Top flange stresses along the entire normalized length (psi):

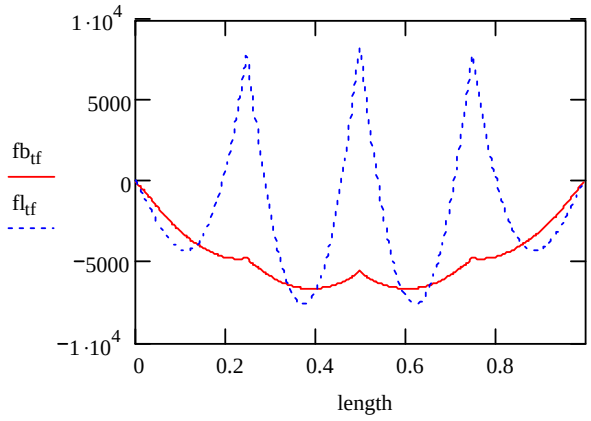

Bottom flange stresses along the entire normalized length (psi):

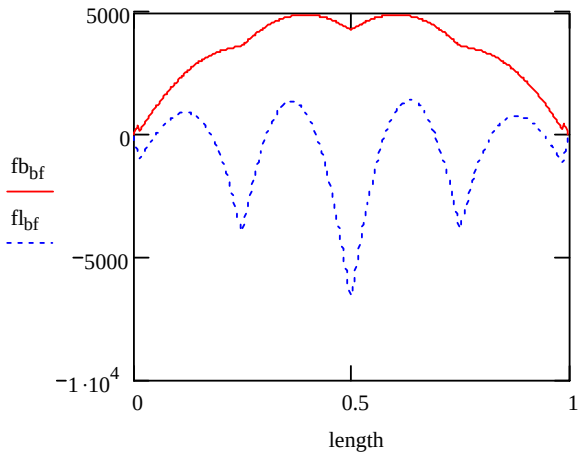

Girder stresses (psi) within the unbraced length adjacent to mid-span:

$i := 180.. 269$

$fb\_Lb\_length_i := length_i$ $fb_{tf\_Lb_i} := fb_{tf_i}$ $fl_{tf\_Lb_i} := fl_{tf_i}$

Top flange stresses within the unbraced length adjacent to mid-span:

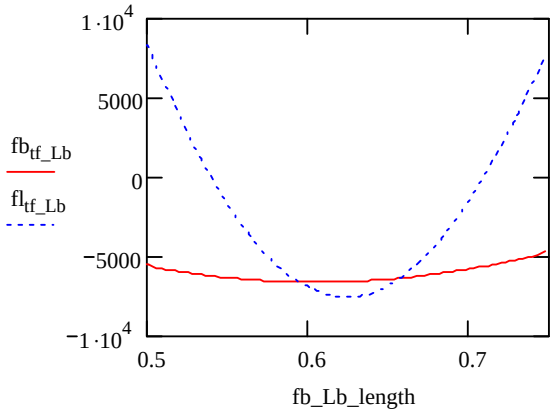

$f_{D1c} := \min(fb_{tf\_Lb})$ $f_{D1c} = -6.65 \times 10^3$

$fb_{bf\_Lb_i} := fb_{bf_i}$ $fl_{bf\_Lb_i} := fl_{bf_i}$

Bottom flange stresses within the unbraced length adjacent to mid-span:

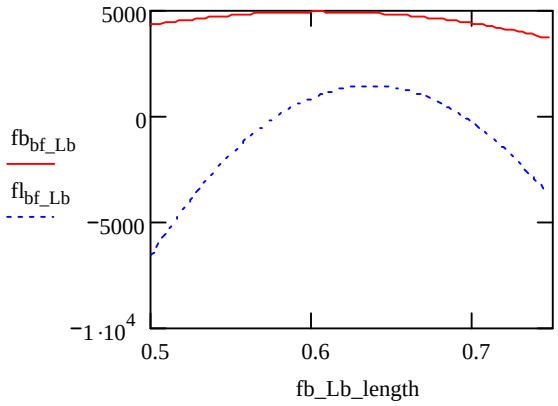

$f_{D1t} := \max(fb_{bf\_Lb})$ $f_{D1t} = 4.92 \times 10^3$

$f_{D1t} := \frac{|f_{D1t}|}{1000}\,ksi$ $f_{D1c} := \frac{|f_{D1c}|}{1000}\,ksi$ $M_{D2} := 0kips \cdot ft$

$f_{D1t} = 4.92ksi$ $f_{D1c} = 6.65ksi$

$M_{D1t} := f_{D1t} \cdot S_t$ $M_{D1c} := f_{D1c} \cdot S_c$

$M_{D1t} = 338.654kips \cdot ft$ $M_{D1c} = 369.933kips \cdot ft$

Tension Flange :

$M_{ADt} := \left(F_{yt} - \frac{M_{D1t}}{S_t} - \frac{M_{D2}}{S_{t\_3n}} \right) \cdot S_{t\_n}$ $\quad M_{ADt} = 5.051 \times 10^3 \text{ kips·ft}$

$M_{yt} := M_{D1t} + M_{D2} + M_{ADt}$ $\quad M_{yt} = 5.389 \times 10^3 \text{ kips·ft}$

Compression Flange :

$M_{ADc} := \left(F_{yc} - \frac{M_{D1c}}{S_c} - \frac{M_{D2}}{S_{c\_3n}} \right) \cdot S_{c\_n}$ $\quad M_{ADc} = 5.618 \times 10^4 \text{ kips·ft}$

$M_{yc} := M_{D1c} + M_{D2} + M_{ADc}$ $\quad M_{yc} = 5.655 \times 10^4 \text{ kips·ft}$

$M_{AD} := \min(M_{ADt}, M_{ADc})$ $\quad M_{AD} = 5.051 \times 10^3 \text{ kips·ft}$

$M_{y\_unshored} := \min(M_{yt}, M_{yc})$ $\quad M_{y\_unshored} = 5.389 \times 10^3 \text{ kips·ft}$

Concrete Stress at First Yield (unshored)

$f_{conc\_composite\_unshored\_at\_My} := \left(\frac{M_{D2}}{S_{slab\_3n} \cdot 3n} + \frac{M_{AD}}{S_{slab\_n} \cdot n} \right)$ $\quad f_{conc\_composite\_unshored\_at\_My} = 2.266 \text{ksi}$

$\frac{f_{conc\_composite\_unshored\_at\_My}}{f_c} = 0.462$

Shape Factor :

$\frac{M_p}{M_{y\_unshored}} = 1.337$ $\qquad \frac{M_p}{M_{y\_shortterm}} = 1.306$ $\qquad \frac{M_p}{M_{y\_longterm}} = 1.398$

Flange Hybrid Strength Reduction Factor (Composite Girder) :

$R_{h\_comp} := 1$ **since the girder is homogeneous**

Constructibility Check, Noncomposite Girder(STREGNTH IV)

Construction load stresses are factored, load factor = 1.5

G1 top flange

$\phi_f := 1.0$ $\quad R_b := 1$ **since bend buckling is prevented when checking constructibility**

$f_{tf\_siv\_1st} :=$ $\qquad f_{tf\_siv\_2nd} :=$

$length := f_{tf\_siv\_1st}^{\langle cols(f_{tf\_siv\_1st})-3 \rangle}$ $\qquad fb_{tf\_1st} := f_{tf\_siv\_1st}^{\langle cols(f_{tf\_siv\_1st})-2 \rangle}$ $\qquad fl_{tf\_1st} := f_{tf\_siv\_1st}^{\langle cols(f_{tf\_siv\_1st})-1 \rangle}$

$fb_{tf\_2nd} := f_{tf\_siv\_2nd}^{\langle cols(f_{tf\_siv\_2nd})-2 \rangle}$ $\qquad fl_{tf\_2nd} := f_{tf\_siv\_2nd}^{\langle cols(f_{tf\_siv\_2nd})-1 \rangle}$

Top flange stresses (psi) along the nomralized length :

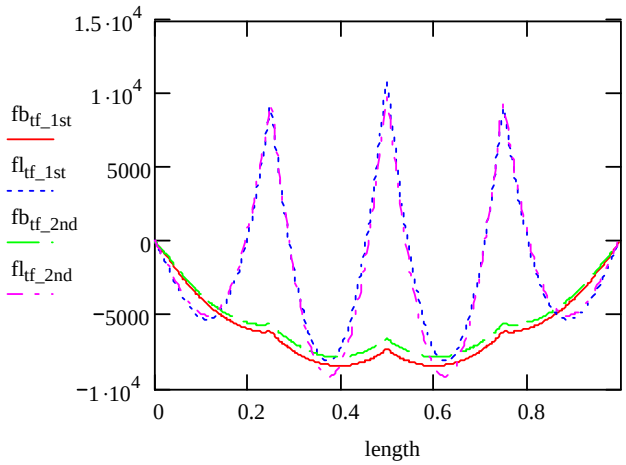

Girder stresses within the unbraced length adjacent to mid-span:

$i := 180..269$ $\quad fb_{tf\_1st\_Lb_i} := fb_{tf\_1st_i}$ $\quad fl_{tf\_1st\_Lb_i} := fl_{tf\_1st_i}$

$fb_{tf\_2nd\_Lb_i} := fb_{tf\_2nd_i}$ $\quad fl_{tf\_2nd\_Lb_i} := fl_{tf\_2nd_i}$

Top flange stresses (psi) within the unbraced length:

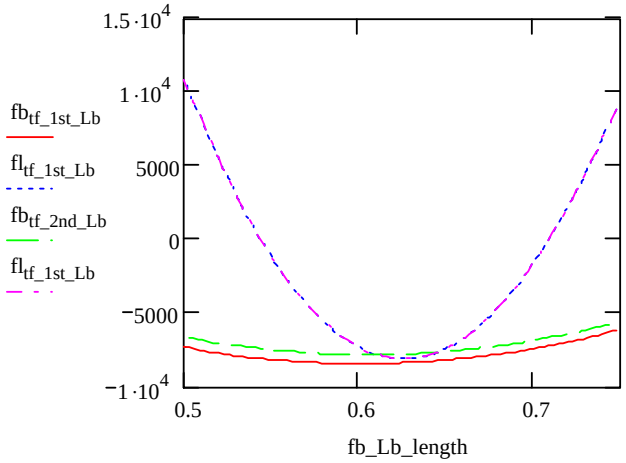

Moment Gradient Modifier for LTB(Cb) :

$f_1 := |-7.25|\ ksi$ $\quad f_2 := \frac{|\min(fb_{tf\_1st\_Lb})|}{1000}\ ksi$

$f_1 = 7.25ksi$ $\quad f_2 = 8.43ksi$

$$C_b := \begin{cases} 1.75 - 1.05\left(\frac{f_1}{f_2}\right) + 0.3\left(\frac{f_1}{f_2}\right)^2 & \text{if } 1.75 - 1.05\left(\frac{f_1}{f_2}\right) + 0.3\left(\frac{f_1}{f_2}\right)^2 \le 2.3 \\ 2.3 & \text{otherwise} \end{cases}$$

$C_b = 1.069$

Estimation of Flange Second Order Lateral Bending Stress:

$f_{b1} := \frac{\left|\min\left(fb_{tf\_1st\_Lb}\right)\right|}{1000}\cdot ksi$ $f_{l1} := \frac{\left|\max\left(fl_{tf\_1st\_Lb}\right)\right|}{1000}\cdot ksi$ $f_{b1} = 8.43ksi$ $f_{l1} = 10.8ksi$

i) Based on k=1.0 $k := 1.0$

$\lambda := \frac{k\cdot L_b}{r_t}$ $\lambda = 81.765$

$F_{cr} := \frac{C_b\cdot R_b\cdot \pi^2\cdot E}{\lambda^2}$ $F_{cr} = 45.76ksi$ $\frac{1}{1-\frac{f_{b1}}{F_{cr}}} = 1.226$ $\frac{f_{l1}}{1-\frac{f_{b1}}{F_{cr}}} = 13.24ksi$

ii) Based on k=0.5 $k := 0.5$

$\lambda := \frac{k\cdot L_b}{r_t}$ $\lambda = 40.882$

$F_{cr0.5} := \frac{C_b\cdot R_b\cdot \pi^2\cdot E}{\lambda^2}$ $F_{cr0.5} = 183.04ksi$ $\frac{1}{1-\frac{f_{b1}}{F_{cr0.5}}} = 1.048$ $\frac{f_{l1}}{1-\frac{f_{b1}}{F_{cr0.5}}} = 11.321ksi$

$f_{b2} := \frac{\left|\min\left(fb_{tf\_2nd\_Lb}\right)\right|}{1000}\cdot ksi$ $f_{l2} := \frac{\left|\max\left(fl_{tf\_2nd\_Lb}\right)\right|}{1000}\cdot ksi$

$f_{b2} = 7.84ksi$ $f_{l2} = 9.81ksi$ Actual second-order amplification: $\frac{f_{l2}}{f_{l1}} = 0.908$

Maximum Lateral Bending Stress Limit

$f_{l2} = 9.81ksi$ $\frac{F_{yc}}{1.67} = 34.467ksi$

$Lateral\_bending\_stress\_ratio := \frac{f_{l2}}{\frac{F_{yc}}{1.67}}$ $Lateral\_bending\_stress\_ratio = 0.285$

Yielding Limit

$f_{b2} + f_{l2} = 17.65ksi$ $\phi_f\cdot R_{h\_noncomp}\cdot F_{yc} = 57.56ksi$

$Yielding\_ratio := \frac{f_{b2} + f_{l2}}{\phi_f\cdot R_{h\_noncomp}\cdot F_{yc}}$ $Yielding\_ratio = 0.307$

Strength Limit

Local Buckling Resistance :

$F_{yr} := 0.7\cdot F_{yc}$

$\lambda_f := \frac{b_{fc}}{2\cdot t_{fc}}$ $\lambda_{pf} := 0.38\sqrt{\frac{E}{F_{yc}}}$ $\lambda_{rf} := 0.56\sqrt{\frac{E}{F_{yr}}}$

$$F_{nc\_FLB} := \begin{cases} R_b \cdot R_{h\_noncomp} \cdot F_{yc} & \text{if } \lambda_f \le \lambda_{pf} \\ \left[1 - \left(1 - \frac{F_{yr}}{R_{h\_noncomp} \cdot F_{yc}}\right) \cdot \left(\frac{\lambda_f - \lambda_{pf}}{\lambda_{rf} - \lambda_{pf}}\right)\right] \cdot R_b \cdot R_{h\_noncomp} \cdot F_{yc} & \text{if } \lambda_{pf} < \lambda_f \le \lambda_{rf} \\ \frac{0.36 \cdot R_b \cdot E}{\left(\frac{b_{fc}}{2 \cdot t_{fc}}\right)^2} & \text{otherwise} \end{cases}$$

$F_{nc\_FLB} = 57.56\text{ksi}$

Lateral Torsional Buckling Resistance :

$$L_p := 1.0 \cdot r_t \cdot \sqrt{\frac{E}{F_{yc}}} \qquad L_r := \pi \cdot r_t \cdot \sqrt{\frac{E}{F_{yr}}}$$

$$F_{nc\_LTB} := \begin{cases} R_b \cdot R_{h\_noncomp} \cdot F_{yc} & \text{if } L_b \le L_p \\ \min\left[C_b \cdot \left[1 - \left(1 - \frac{F_{yr}}{R_{h\_noncomp} \cdot F_{yc}}\right) \cdot \left(\frac{L_b - L_p}{L_r - L_p}\right)\right] \cdot R_b \cdot R_{h\_noncomp} \cdot F_{yc}, R_b \cdot R_{h\_noncomp} \cdot F_{yc}\right] & \text{if } L_p < L_b \le L_r \\ \text{otherwise} \\ \quad \begin{cases} F_{cr} & \text{if } F_{cr} \le R_b \cdot R_{h\_noncomp} \cdot F_{yc} \\ R_b \cdot R_{h\_noncomp} \cdot F_{yc} & \text{otherwise} \end{cases} \end{cases}$$

$F_{nc\_LTB} = 43.818\text{ksi}$

$$\text{Controling\_Strength} := \begin{cases} \text{"Flange Local Buckling"} & \text{if } F_{nc\_FLB} \le F_{nc\_LTB} \\ \text{"Lateral Torsional Buckling"} & \text{otherwise} \end{cases}$$

Controling_Strength = "Lateral Torsional Buckling"

$f_{b2} + \frac{f_{l2}}{3} = 11.11\text{ksi}$ $\quad F_{nc} := \min\left(F_{nc\_LTB}, F_{nc\_FLB}\right)$ $\quad \phi_f \cdot F_{nc} = 43.82\text{ksi}$

$$\text{Strength\_ratio} := \frac{f_{b2} + \frac{f_{l2}}{3}}{\phi_f \cdot F_{nc}}$$

Strength_ratio = 0.254

Web bend buckling limit

$$k := \frac{9}{\left(\frac{D_c}{D}\right)^2} \qquad k = 29.216 \qquad F_{crw} := 0.9 \cdot E \cdot \frac{k}{\left(\frac{D}{t_w}\right)^2} \qquad \phi_f \cdot F_{crw} = 36.11\text{ksi} \qquad f_{b2} = 7.84\text{ksi}$$

$$\text{Web\_bend\_buckling\_ratio} := \frac{f_{b2}}{\phi_f \cdot F_{crw}}$$

Web_bend_buckling_ratio = 0.22

G1 bottom flange

$f_{bf\_siv\_2nd} :=$

$length := f_{bf\_siv\_2nd}^{\langle cols(f_{bf\_siv\_2nd})-3\rangle}$ $fb_{bf\_2nd} := f_{bf\_siv\_2nd}^{\langle cols(f_{bf\_siv\_2nd})-2\rangle}$ $fl_{bf\_2nd} := f_{bf\_siv\_2nd}^{\langle cols(f_{bf\_siv\_2nd})-1\rangle}$

Bottom flange stresses (psi) along the normalized length:

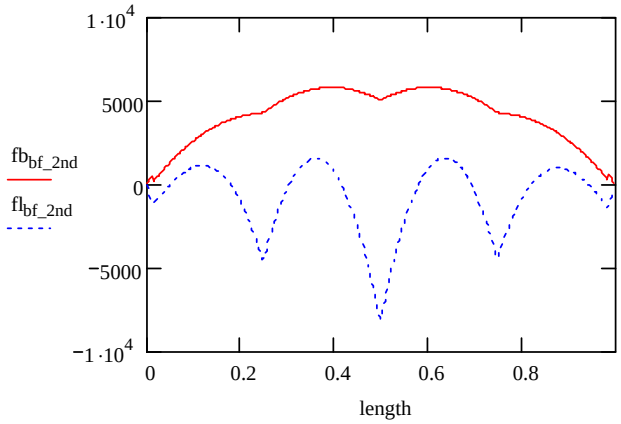

Girder stresses along the unbraced length adjacent to mid-span:

$fb\_Lb\_length_i := length_i$ $fb_{bf\_2nd\_Lb_i} := fb_{bf\_2nd_i}$ $fl_{bf\_2nd\_Lb_i} := fl_{bf\_2nd_i}$

Bottom flange stresses (psi) within the unbraced length:

$$f_{b2} := \frac{|\max(fb_{bf\_2nd\_Lb})|}{1000}\cdot ksi$$

$f_{b2} = 5.78ksi$

$$f_{l2} := \frac{|\min(fl_{bf\_2nd\_Lb})|}{1000}\cdot ksi$$

$f_{l2} = 8.03ksi$

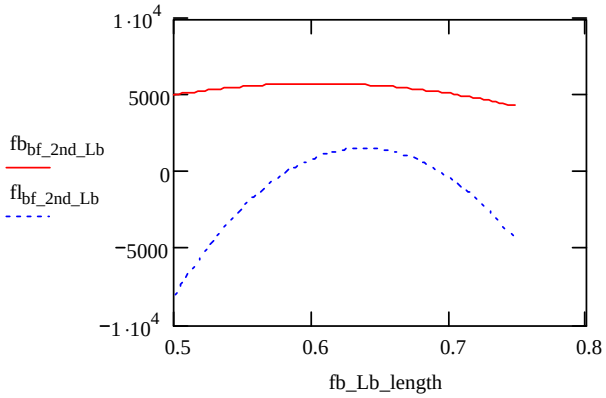

Maximum Lateral Bending Stress Limit

$f_{l2} = 8.03ksi$ $\frac{F_{yt}}{1.67} = 34.772ksi$

$$Lateral\_bending\_stress\_ratio := \frac{f_{l2}}{\frac{F_{yt}}{1.67}}$$

$Lateral\_bending\_stress\_ratio = 0.231$

Yielding Limit

$f_{b2} + f_{l2} = 13.81ksi$ $\phi_f \cdot R_{h\_noncomp} \cdot F_{yt} = 58.07ksi$

$$Yielding\_ratio := \frac{f_{b2} + f_{l2}}{\phi_f \cdot R_{h\_noncomp} \cdot F_{yt}}$$

$Yielding\_ratio = 0.238$

Strength I Check

Construction stresses are based on factored construction loads, load factor = 1.25
Lane and truck load stresses are unfactored, but the dynamic allowance of 1.33 is included in the calcuation of the truck load stresses

G1 Bottom flange

$fb_{bf\_noncomp} := f_{bf\_si}^{\langle cols(f_{bf\_si})-2\rangle}$ $fl_{bf\_noncomp} := f_{bf\_si}^{\langle cols(f_{bf\_si})-1\rangle}$

Factored noncomposite stresses along the entire normalized length:

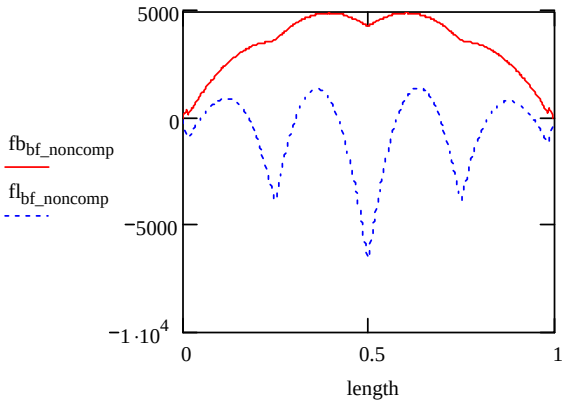

Read analysis results of unfactored composite stresses:

$f_{bf\_lane} :=$ $f_{bf\_truck} :=$

$length := f_{bf\_lane}^{\langle cols(f_{bf\_lane})-3\rangle}$ $fb_{bf\_lane} := f_{bf\_lane}^{\langle cols(f_{bf\_lane})-2\rangle}$ $fl_{bf\_lane} := f_{bf\_lane}^{\langle cols(f_{bf\_lane})-1\rangle}$

$fb_{bf\_truck} := f_{bf\_truck}^{\langle cols(f_{bf\_truck})-2\rangle}$ $fl_{bf\_truck} := f_{bf\_truck}^{\langle cols(f_{bf\_truck})-1\rangle}$

Bottom flange stresses along the entire normalized length:

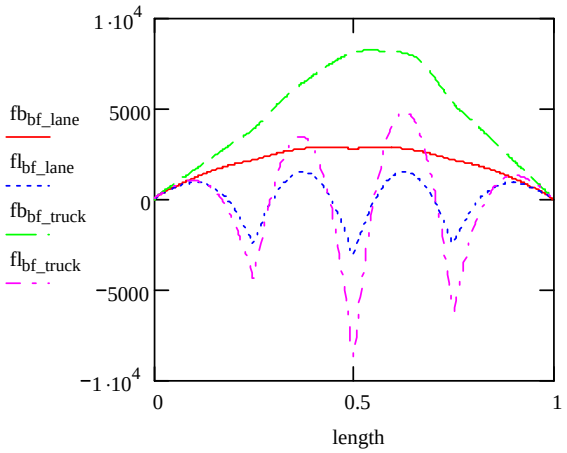

Factored bottom flange stresses relating to Strength I load combination:

$fb_{bf} := fb_{bf\_noncomp} + 1.75 \cdot (fb_{bf\_lane} + fb_{bf\_truck})$ $fl_{bf} := fl_{bf\_noncomp} + 1.75 \cdot (fl_{bf\_lane} + fl_{bf\_truck})$

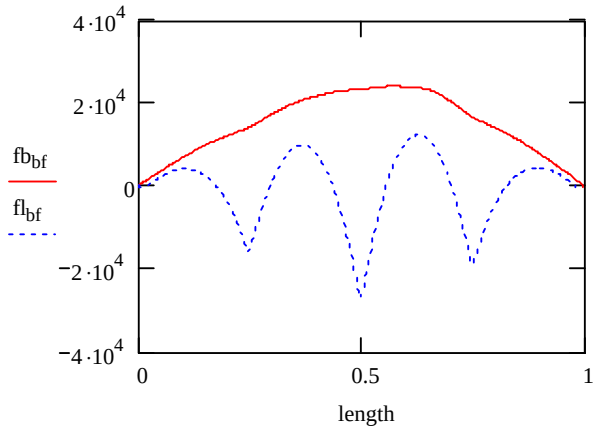

Bottom flange stresses within the unbraced length adjacent o mid-span

$fb\_Lb\_length_i := length_i$ $fb_{bf\_Lb_i} := fb_{bf_i}$ $fl_{bf\_Lb_i} := fl_{bf_i}$

Maximum major-axis and lateral bending stresses within the unbraced length

$$f_b := \frac{|\max(fb_{bf\_Lb})|}{1000} \cdot ksi$$

$f_b = 24.128ksi$

$$f_l := \frac{|\min(fl_{bf\_Lb})|}{1000} \cdot ksi$$

$f_l = 27.098ksi$

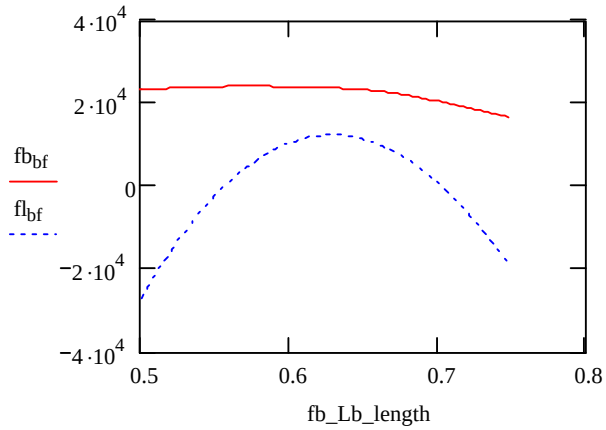

Lateral Bending Stress Limit

$f_l = 27.1ksi$

$\frac{F_{yt}}{1.67} = 34.772ksi$

$Lateral\_bending\_stress\_ratio := \frac{f_l}{\frac{F_{yt}}{1.67}}$

$Lateral\_bending\_stress\_ratio = 0.78$

Strength Limit

$f_b + \frac{f_l}{3} = 33.16ksi$

$\phi_f \cdot R_{h\_comp} \cdot F_{yt} = 58.07ksi$

$$Strength\_ratio := \frac{f_b + \frac{f_l}{3}}{\phi_f \cdot R_{h\_comp} \cdot F_{yt}}$$

$Strength\_ratio = 0.571$

G1 Top flange

Factored noncomposite stresses (psi) along the entire normalized length:

$fb_{tf\_noncomp} := f_{tf\_si}^{\langle cols(f_{tf\_si})-2 \rangle}$ $fl_{tf\_noncomp} := f_{tf\_si}^{\langle cols(f_{tf\_si})-1 \rangle}$

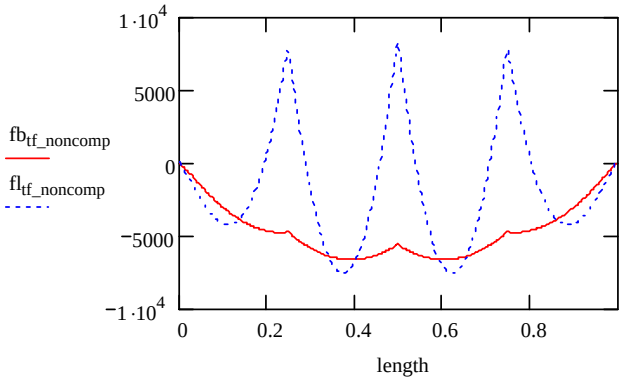

Read analysis results of unfactored composite stresses:

$f_{tf\_lane} :=$ $f_{tf\_truck} :=$

$length := f_{tf\_lane}^{\langle cols(f_{tf\_lane})-3 \rangle}$

$fb_{tf\_lane} := f_{tf\_lane}^{\langle cols(f_{tf\_lane})-2 \rangle}$ $fl_{tf\_lane} := f_{tf\_lane}^{\langle cols(f_{tf\_lane})-1 \rangle}$

$fb_{tf\_truck} := f_{tf\_truck}^{\langle cols(f_{tf\_truck})-2 \rangle}$ $fl_{tf\_truck} := f_{tf\_truck}^{\langle cols(f_{tf\_truck})-1 \rangle}$

Unfactored top flange stresses (psi) along the entire normalized length:

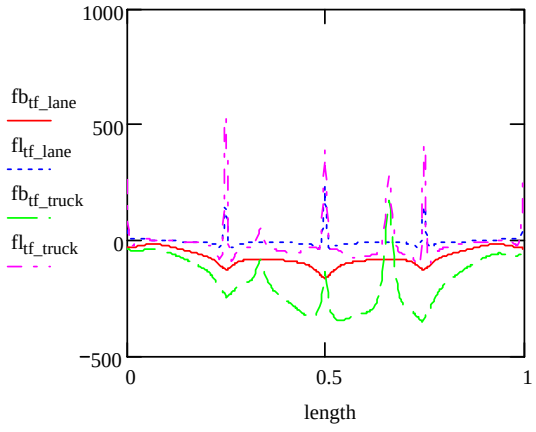

Factored top flange stresses relating to Strength I load combination:

$fb_{tf} := fb_{tf\_noncomp} + 1.75\left(fb_{tf\_lane} + fb_{tf\_truck}\right)$ $fl_{tf} := fl_{tf\_noncomp} + 1.75\left(fl_{tf\_lane} + fl_{tf\_truck}\right)$

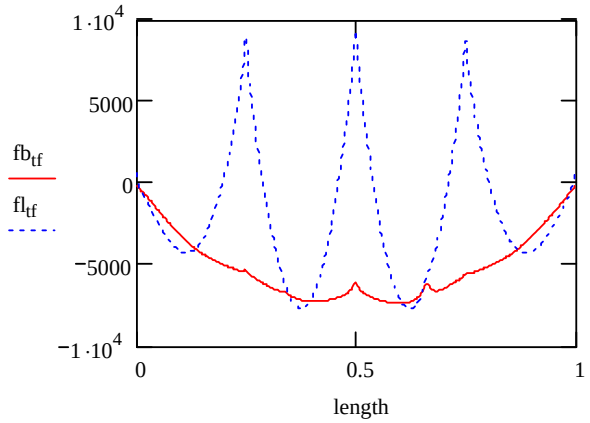

Factored top fflange stresses within the unbraced length adjacent to mid-span

$fb\_Lb\_length_i := length_i$ $fb_{tf\_Lb_i} := fb_{tf_i}$ $fl_{tf\_Lb_i} := fl_{tf_i}$

Maximum major-axis and lateral bending stresses within the unbraced length

$$f_b := \frac{\left|\min\left(fb_{tf\_Lb}\right)\right|}{1000}\cdot ksi$$

$f_b = 7.35ksi$

$$f_l := \frac{\left|\max\left(fl_{tf\_Lb}\right)\right|}{1000}\cdot ksi$$

$f_l = 9.347ksi$

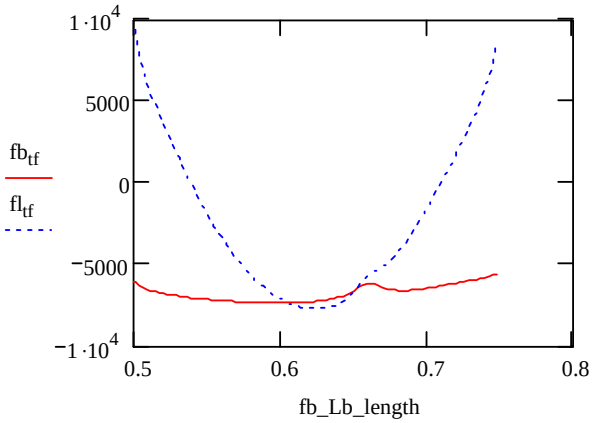

Strength Limit

$f_b = 7.35ksi$ $\phi_f \cdot R_{h\_comp} \cdot F_{yc} = 57.56ksi$

$$Strength\_ratio := \frac{f_b}{\phi_f \cdot R_{h\_comp} \cdot F_{yc}}$$

$Strength\_ratio = 0.128$

Service II Check

G1 Bottom flange

Factored bottom flange stresses relating to Serive I load combination:

$fb_{bf} := fb_{bf\_noncomp} \cdot 0.8 + 1.30 \cdot (fb_{bf\_lane} + fb_{bf\_truck})$ $fl_{bf} := fl_{bf\_noncomp} \cdot 0.8 + 1.30 \cdot (fl_{bf\_lane} + fl_{bf\_truck})$

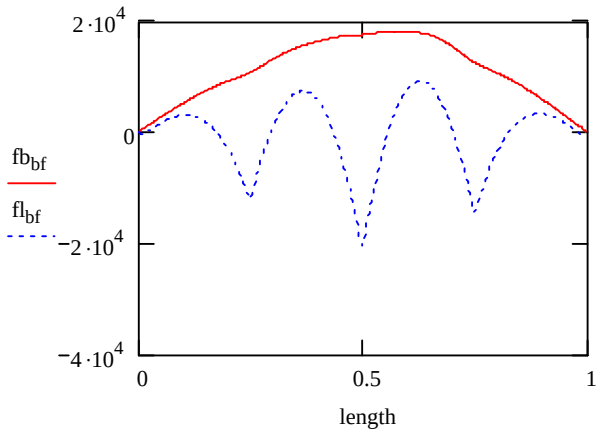

Bottom flange stresses within the unbraced length adjacent o mid-span

$fb\_Lb\_length_i := length_i$ $fb_{bf\_Lb_i} := fb_{bf_i}$ $fl_{bf\_Lb_i} := fl_{bf_i}$

Maximum major-axis and lateral bending stresses within the unbraced length

$$f_b := \frac{|\max(fb_{bf\_Lb})|}{1000} \cdot ksi$$

$f_b = 18.201ksi$

$$f_l := \frac{|\min(fl_{bf\_Lb})|}{1000} \cdot ksi$$

$f_l = 20.505ksi$

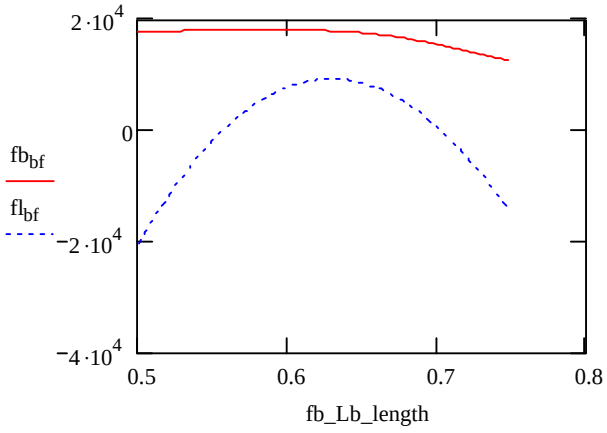

$0.95 \cdot F_{yt} = 55.166ksi$

$$Permanent\_deformation\_ratio := \frac{f_b}{0.95 \cdot F_{yt}}$$

$Permanent\_deformation\_ratio = 0.33$

G1 Top flange

Factored top flange stresses relating to Serive I load combination:

$fb_{tf} := fb_{tf\_noncomp} \cdot 0.8 + 1.30 \cdot (fb_{tf\_lane} + fb_{tf\_truck})$ $fl_{tf} := fl_{tf\_noncomp} \cdot 0.8 + 1.30 \cdot (fl_{tf\_lane} + fl_{tf\_truck})$

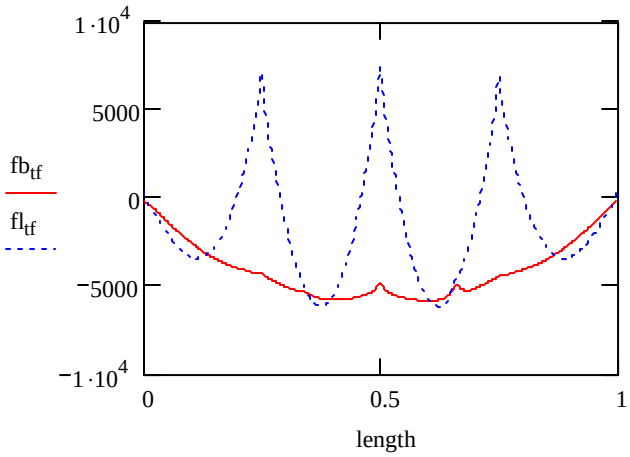

Bottom flange stresses within the unbraced length adjacent o mid-span

$fb\_Lb\_length_i := length_i$ $fb_{tf\_Lb_i} := fb_{tf_i}$ $fl_{tf\_Lb_i} := fl_{tf_i}$

Maximum major-axis and lateral bending stresses within the unbraced length

$$f_b := \frac{|\min(fb_{tf\_Lb})|}{1000} \cdot ksi$$

$f_b = 5.84ksi$

$$f_l := \frac{|\min(fl_{bf\_Lb})|}{1000} \cdot ksi$$

$f_l = 20.505ksi$

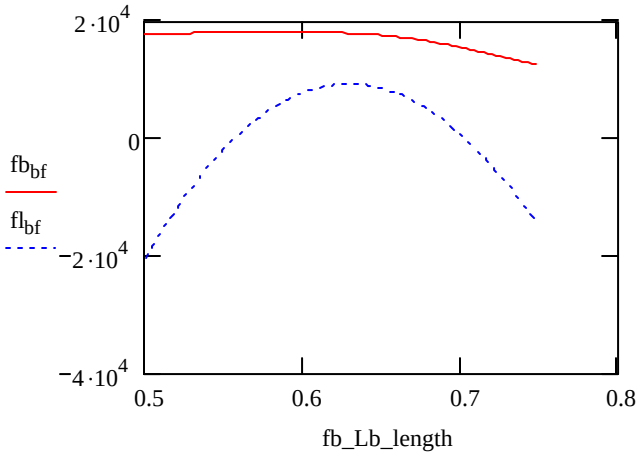

$0.95 \cdot F_{yc} = 54.682ksi$

$$Permanent\_deformation\_ratio := \frac{f_b}{0.95 \cdot F_{yc}}$$ $Permanent\_deformation\_ratio = 0.107$

B.2 G2 Positive Moment Flexural Design

Material Properties:

- Steel Properties:

$F_{yc} := 57.56\,ksi$; $F_{yw} := 63.28\,ksi$; $F_{yt} := 58.07\,ksi$; $F_{yr} := 60\,ksi$; $E := 2.9 \cdot 10^4\,ksi$

- Concrete Properties:

$f_c := 4.9\,ksi$; $E_c := 4034\,ksi$; $n := \frac{E}{E_c}$; $n = 7.189$ $W_{conc} := 150\,\frac{lbf}{ft^3}$

Plate Girder Dimensions:

GIRDER LENGTH:

$L := 90\,ft$ $L_b := \frac{L}{4}$ $L_b = 22.5\,ft$

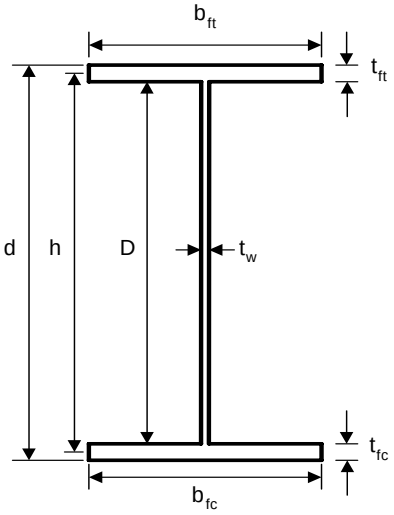

TOP FLANGE:

$b_{fc} := 14.188\,in$

$t_{fc} := 0.877\,in$

$\frac{b_{fc}}{2t_{fc}} = 8.089$

BOTTOM FLANGE:

$b_{ft} := 22.168\,in$

$t_{ft} := 1.002\,in$

$\frac{b_{ft}}{2 \cdot t_{ft}} = 11.06$

WEB:

$D := 48.057\,in$ $t_w := 0.323\,in$ $\frac{D}{t_w} = 148.783$

$d := D + t_{ft} + t_{fc}$ $d = 49.936\,in$

$h := D + \frac{t_{ft} + t_{fc}}{2}$ $h = 48.997\,in$

Cross-section Proportion Limits :

- Web proportion checks for webs without longitudinal stiffeners

$$Web\_Proportion\_Check := \begin{cases} \text{"OK"} & \text{if } \frac{D}{t_w} \le 150 \\ \text{"NG"} & \text{otherwise} \end{cases}$$

Web_Proportion_Check = "OK"

$a_w := \frac{D \cdot t_w}{b_{fc} \cdot t_{fc}}$ $a_w = 1.247$

$$Prevent\_Vertical\_Flange\_Buckling\_Check := \begin{cases} \text{"OK"} & \text{if } \frac{D}{t_w} \le 0.6 \cdot \sqrt{a_w} \cdot \frac{E}{F_{yc}} \\ \text{"NG"} & \text{otherwise} \end{cases}$$

$0.6 \cdot \sqrt{a_w} \cdot \frac{E}{F_{yc}} = 338$

Prevent_Vertical_Flange_Buckling_Check = "OK"

- Flange proportion checks

$I_{yc} := \frac{t_{fc} \cdot b_{fc}^3}{12}$ $I_{yt} := \frac{t_{ft} \cdot b_{ft}^3}{12}$ $\frac{I_{yc}}{I_{yt}} = 0.229$

$$Compression\_Flange\_Check := \begin{cases} \text{"OK"} & \text{if } \frac{b_{fc}}{2 \cdot t_{fc}} \le 12.0 \wedge b_{fc} \ge \frac{D}{6} \wedge t_{fc} \ge 1.1 \cdot t_w \wedge 0.1 \le \frac{I_{yc}}{I_{yt}} \le 10 \\ \text{"NG"} & \text{otherwise} \end{cases}$$

Compression_Flange_Check = "OK"

$$Tension\_Flange\_Check := \begin{cases} \text{"OK"} & \text{if } \frac{b_{ft}}{2 \cdot t_{ft}} \le 12.0 \wedge b_{ft} \ge \frac{D}{6} \wedge t_{ft} \ge 1.1 \cdot t_w \\ \text{"NG"} & \text{otherwise} \end{cases}$$

Tension_Flange_Check = "OK"

Non-Composite Section Properties:

Top flange area :

$A_{fc} := b_{fc} \cdot t_{fc}$ $A_{fc} = 12.443 in^2$

Bottom flange area:

$A_{ft} := b_{ft} \cdot t_{ft}$ $A_{ft} = 22.212 in^2$

Web area:

$A_{web} := D \cdot t_w$ $A_{web} = 15.522 in^2$

Total section area :

$A_{girder} := A_{fc} + A_{ft} + A_{web}$ $A_{girder} = 50.178 in^2$

Neutral axis :

$$D_c := \frac{A_{fc} \cdot \left(\frac{t_{fc}}{2} \right) + A_{ft} \cdot \left(d - \frac{t_{ft}}{2} \right) + A_{web} \cdot \left(\frac{D}{2} + t_{fc} \right)}{A_{girder}} - t_{fc}$$ $D_c = 28.82 in$ $\frac{D_c}{D} = 0.6$

Note: Neutral axis measured from the lower surface of the top flange.

Shear center : $h_u := D_c + \frac{t_{fc}}{2}$ $h_l := D - D_c + \frac{t_{ft}}{2}$

$e := \frac{I_{yc} \cdot h_u - I_{yt} \cdot h_l}{I_{yc} + I_{yt}}$ $e = -10.594 in$ (offset distance from the neutral axis)

Moment of inertia with respect to a neutral axis :

$$I_{girder} := \frac{b_{fc} \cdot t_{fc}^3}{12} + \left[A_{fc} \cdot \left(D_c + t_{fc} - \frac{t_{fc}}{2} \right)^2 \right] \ldots + \frac{b_{ft} \cdot t_{ft}^3}{12} + \left[A_{ft} \cdot \left[d - \left(D_c + t_{fc} \right) - \frac{t_{ft}}{2} \right]^2 \right] \ldots + \frac{t_w \cdot D^3}{12} + A_{web} \cdot \left(D_c + t_{fc} - \frac{D}{2} - t_{fc} \right)^2 \qquad I_{girder} = 2.265 \times 10^4 \, in^4$$

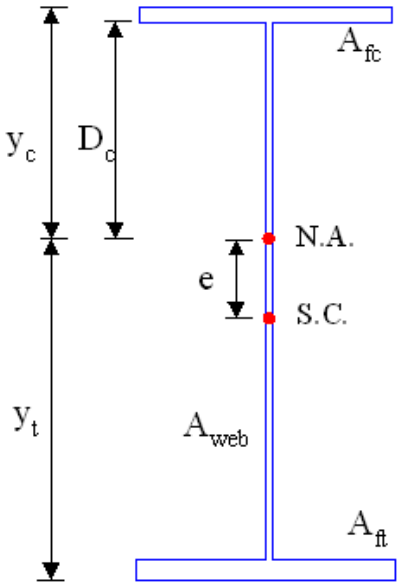

Section modulus to the compression flange :

$y_c := D_c + t_{fc}$ $\quad y_c = 29.697 in$

$S_c := \frac{I_{girder}}{y_c}$ $\quad S_c = 762.773 in^3$

Section modulus of the tension flange :

$y_t := d - y_c$ $\quad y_t = 20.239 in$

$S_t := \frac{I_{girder}}{y_t}$ $\quad S_t = 1.119 \times 10^3 \, in^3$ $\quad \frac{A_{ft}}{A_{fc}} = 1.785$

- Web Bend-buckling Resistance

$\frac{D_c}{D} = 0.6$ $\quad \frac{2D_c}{t_w} = 178.451$

bend-buckling coeffient :

$k := \frac{9}{\left(\frac{D_c}{D} \right)^2}$ $\quad k = 25.025$ $\quad F_{crw} := 0.9 \cdot E \cdot \frac{k}{\left(\frac{D}{t_w} \right)^2}$ $\quad F_{crw} = 29.51 ksi$

- Yield Moment

$M_{yt\_noncomp} := S_t \cdot F_{yt}$ $\quad M_{yt\_noncomp} = 5.416 \times 10^3 \, kips \cdot ft$

$M_{yc\_noncomp} := S_c \cdot F_{yc}$ $\quad M_{yc\_noncomp} = 3.659 \times 10^3 \, kips \cdot ft$

$M_{y\_noncomp} := \begin{cases} M_{yt\_noncomp} & \text{if } M_{yt\_noncomp} \le M_{yc\_noncomp} \\ M_{yc\_noncomp} & \text{otherwise} \end{cases}$ $\quad M_{y\_noncomp} = 3.659 \times 10^3 \, kips \cdot ft$

- Radius of Gyration for LTB Check

$r_t := \frac{b_{fc}}{\sqrt{12 \cdot \left(\frac{h}{d} + \frac{D_c \cdot t_w \cdot D^2}{3 \cdot b_{fc} \cdot t_{fc} \cdot h \cdot d} \right)}}$ $\quad r_t = 3.713 in$

Note: The exact r_t equation is used in the above .

- Flange-Strength Reduction Factors (Noncomposite Girder) :

Hybrid Factor :

$R_{h\_noncomp} := 1$ **since section is homogeneous**

Web Load-Shedding Factor :

$D_c = 28.82\text{in}$

$a_{wc} := \frac{2 \cdot D_c \cdot t_w}{A_{fc}}$ $a_{wc} = 1.496$

$\lambda_{rw} := 5.7\sqrt{\frac{E}{F_{yc}}}$ $\lambda_{rw} = 127.942$

$$R_{b\_noncomp} := \begin{cases} 1.0 & \text{if } \frac{2 \cdot D_c}{t_w} \le \lambda_{rw} \\ \text{otherwise} & \\ \quad \begin{cases} 1 - \left(\frac{a_{wc}}{1200 + 300 \cdot a_{wc}}\right) \cdot \left(\frac{2 \cdot D_c}{t_w} - \lambda_{rw}\right) & \text{if } 1 - \left(\frac{a_{wc}}{1200 + 300 \cdot a_{wc}}\right) \cdot \left(\frac{2 \cdot D_c}{t_w} - \lambda_{rw}\right) \le 1.0 \\ 1.0 & \text{otherwise} \end{cases} \end{cases}$$

$R_{b\_noncomp} = 0.954$

Composite Section Properties :

Effective Width of Slab

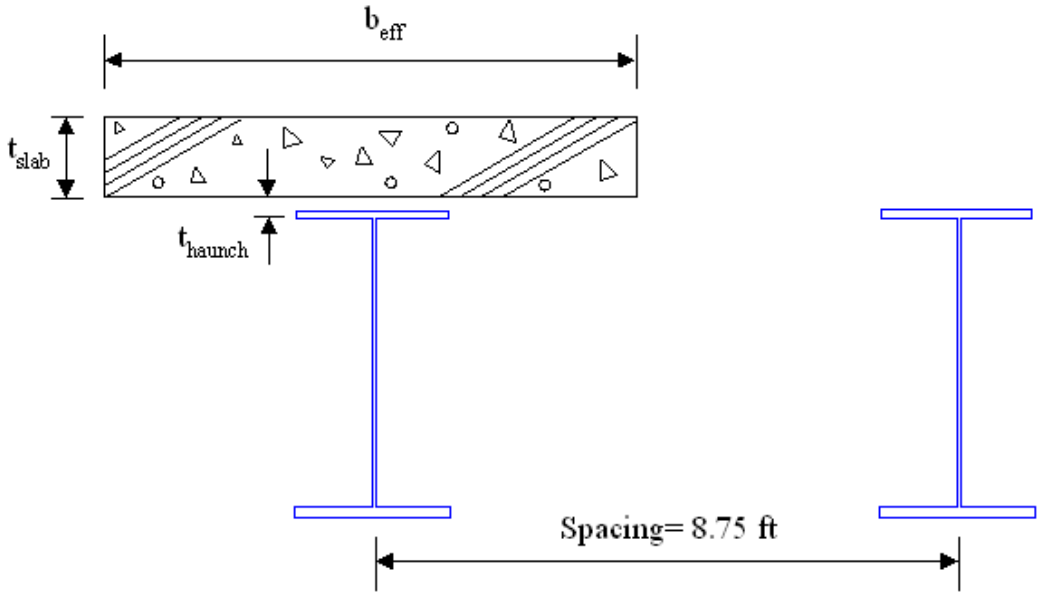

< Composite Section >

$t_{haunch} := 3in$ $b_{int} := 8.75ft$ $t_{slab} := 8in$

$$b_{eff\_int} := \min\left(\begin{pmatrix} \frac{L}{4} \\ 12 \cdot t_{slab} + \frac{b_{fc}}{2} \\ b_{int} \end{pmatrix}\right) \qquad b_{eff\_int} = 8.591ft$$

NOTE: the full tributary width for each girder is used in the design.

$b_{slab} := 8.75ft$ $b_{s\_3n} := \frac{b_{slab}}{3n}$

Reinforcement:

Average top reinforcing steel area : $A_{top\_rebar} := \frac{0.18in \cdot b_{slab}}{12}$ $A_{top\_rebar} = 1.575in^2$

Average bottom reinforcing steel area : $A_{bottom\_rebar} := \frac{0.27in \cdot b_{slab}}{12}$ $A_{bottom\_rebar} = 2.363in^2$

Location of top reinforcing steel : $y_{rt} := 3.25in$

Location of bottom reinforcing steel : $y_{rb} := 6.25in$

Long Term Composite Section Properties(3n) :

$A_{con\_3n} := b_{s\_3n} \cdot t_{slab}$ $A_{con\_3n} = 38.949in^2$

$A_{total\_3n} := A_{girder} + A_{con\_3n}$ $A_{total\_3n} = 89.127in^2$

$$NA_{3n} := \frac{A_{fc}\cdot\left(t_{slab} + t_{haunch} - \frac{t_{fc}}{2}\right) + A_{ft}\cdot\left(D + t_{slab} + t_{haunch} + \frac{t_{ft}}{2}\right) + A_{web}\cdot\left(\frac{D}{2} + t_{slab} + t_{haunch}\right) + A_{con\_3n}\cdot\frac{t_{slab}}{2}}{A_{total\_3n}}$$

Note: Neutral axis is measured from the top of concrete slab

$NA_{3n} = 24.166in$

$$I_{3n} := \frac{b_{fc}\cdot t_{fc}^3}{12} + \left[A_{fc}\cdot\left(NA_{3n} - t_{slab} - t_{haunch} + \frac{t_{fc}}{2}\right)^2\right] \ldots + \frac{b_{ft}\cdot t_{ft}^3}{12} + \left[A_{ft}\cdot\left(t_{slab} + t_{haunch} + D + t_{ft} - NA_{3n} - \frac{t_{ft}}{2}\right)^2\right] \ldots + \frac{t_w\cdot D^3}{12} + A_{web}\cdot\left(NA_{3n} - t_{slab} - t_{haunch} - \frac{D}{2}\right)^2 + \frac{b_{s\_3n}\cdot t_{slab}^3}{12} + A_{con\_3n}\cdot\left(NA_{3n} - \frac{t_{slab}}{2}\right)^2$$

$I_{3n} = 5.099 \times 10^4 in^4$

Section Moduli:

$S_{slab\_3n} := \frac{I_{3n}}{NA_{3n}}$ $S_{slab\_3n} = 2.11\times 10^{3}\,in^{3}$

$y_{c\_3n} := NA_{3n} - t_{slab} - t_{haunch} + t_{fc}$ $y_{c\_3n} = 14.043in$

$S_{c\_3n} := \frac{I_{3n}}{y_{c\_3n}}$ $S_{c\_3n} = 3.631\times 10^{3}\,in^{3}$

$y_{t\_3n} := d - y_{c\_3n}$ $y_{t\_3n} = 35.893in$

$S_{t\_3n} := \frac{I_{3n}}{y_{t\_3n}}$ $S_{t\_3n} = 1.421\times 10^{3}\,in^{3}$

$D_{c\_3n} := y_{c\_3n} - t_{fc}$ $D_{c\_3n} = 13.166in$

$\frac{D_{c\_3n}}{D} = 0.274$ $\frac{2D_{c\_3n}}{t_w} = 81.525$

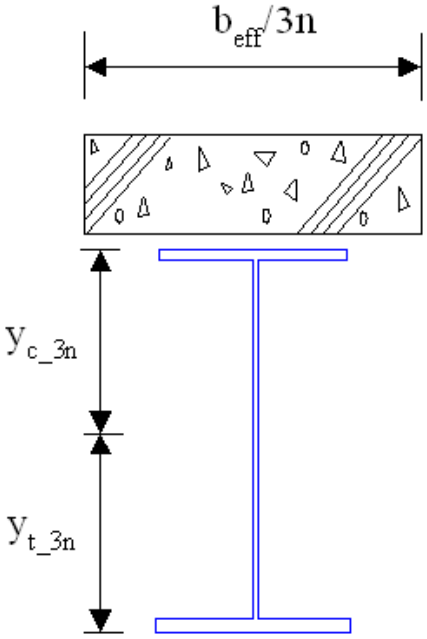

- Yield Moment (Long-term, Shored Construction) :

$M_{yt\_longterm} := S_{t\_3n}\cdot F_{yt}$ $M_{yt\_longterm} = 6.875\times 10^{3}\,kips\cdot ft$

$M_{yc\_longterm} := S_{c\_3n}\cdot F_{yc}$ $M_{yc\_longterm} = 1.742\times 10^{4}\,kips\cdot ft$

$M_{y\_longterm} := \begin{cases} M_{yt\_longterm} & \text{if } M_{yt\_longterm} \le M_{yc\_longterm} \\ M_{yc\_longterm} & \text{otherwise} \end{cases}$ $M_{y\_longterm} = 6.875\times 10^{3}\,kips\cdot ft$

- Concrete Stress at $M_{y\text{-Long Term (shored construction)}}$

$f_{c\_3n} := \frac{M_{y\_longterm}\cdot NA_{3n}}{I_{3n}\cdot 3n}$ $f_{c\_3n} = 1.813ksi$ $\frac{f_{c\_3n}}{f_c} = 0.37$

Short Term Composite Section Properties (n):

Effective Flange Width

$b_{s\_n} := \frac{b_{slab}}{n}$

$A_{con\_n} := b_{s\_n}\cdot t_{slab}$ $A_{con\_n} = 116.847in^{2}$

$A_{total\_n} := A_{girder} + A_{con\_n}$ $A_{total\_n} = 167.025in^{2}$

$$NA_n := \frac{A_{fc}\cdot\left(t_{slab} + t_{haunch} - \frac{t_{fc}}{2}\right) + A_{ft}\cdot\left(D + t_{slab} + t_{haunch} + \frac{t_{ft}}{2}\right) + A_{web}\cdot\left(\frac{D}{2} + t_{slab} + t_{haunch}\right) + A_{con\_n}\cdot\frac{t_{slab}}{2}}{A_{total\_n}}$$

$NA_n = 14.761in$

Note: Neutral is axis measured from the top of concrete slab

$$I_n := \frac{b_{fc}\cdot t_{fc}^3}{12} + \left[A_{fc}\cdot\left(NA_n - t_{slab} - t_{haunch} + \frac{t_{fc}}{2}\right)^2\right] \ldots$$
$$+ \frac{b_{ft}\cdot t_{ft}^3}{12} + \left[A_{ft}\cdot\left(t_{slab} + t_{haunch} + D + t_{ft} - NA_n - \frac{t_{ft}}{2}\right)^2\right] \ldots$$
$$+ \frac{t_w\cdot D^3}{12} + A_{web}\cdot\left(NA_n - t_{slab} - t_{haunch} - \frac{D}{2}\right)^2 + \frac{b_{s\_n}\cdot t_{slab}^3}{12} + A_{con\_n}\cdot\left(NA_n - \frac{t_{slab}}{2}\right)^2 \qquad I_n = 6.831\times 10^4\ in^4$$

Section Moduli :

$$S_{slab\_n} := \frac{I_n}{NA_n} \qquad S_{slab\_n} = 4.628\times 10^3\ in^3$$

$$y_{c\_n} := NA_n - t_{slab} - t_{haunch} + t_{fc} \qquad y_{c\_n} = 4.638in$$

$$S_{c\_n} := \frac{I_n}{y_{c\_n}} \qquad S_{c\_n} = 1.473\times 10^4\ in^3$$

$$y_{t\_n} := d - y_{c\_n} \qquad y_{t\_n} = 45.298in$$

$$S_{t\_n} := \frac{I_n}{y_{t\_n}} \qquad S_{t\_n} = 1.508\times 10^3\ in^3$$

$$D_{c\_n} := y_{c\_n} - t_{fc} \qquad D_{c\_n} = 3.761in$$

$$\frac{D_{c\_n}}{D} = 0.078 \qquad \frac{2D_{c\_n}}{t_w} = 23.288$$

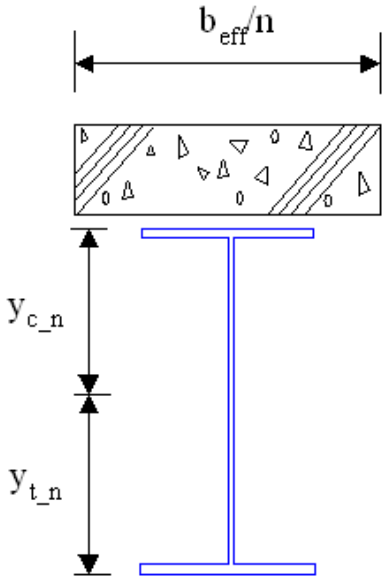

- Yield Moment (Short-term, Shored Construction) :

$$M_{yt\_shortterm} := S_{t\_n}\cdot F_{yt} \qquad M_{yt\_shortterm} = 7.298\times 10^3\ kips\cdot ft$$

$$M_{yc\_shortterm} := S_{c\_n}\cdot F_{yc} \qquad M_{yc\_shortterm} = 7.065\times 10^4\ kips\cdot ft$$

$$M_{y\_shortterm} := \begin{cases} M_{yt\_shortterm} & \text{if } M_{yt\_shortterm} \le M_{yc\_shortterm} \\ M_{yc\_shortterm} & \text{otherwise} \end{cases} \qquad M_{y\_shortterm} = 7.298\times 10^3\ kips\cdot ft$$

- Concrete Stress at $M_{y\text{-Short Term (shored construction)}}$

$$f_{c\_n} := \frac{M_{y\_shortterm}\cdot NA_n}{I_n\, n} \qquad f_{c\_n} = 2.632ksi \qquad \frac{f_{c\_n}}{f_c} = 0.537$$

Plastic Moment Capacity (Composite Section) :

NOTE: The plastic moment capacity is computed here only for reference purposes.
The design strengths are based on slender web member capacity equations

$P_{rb} := F_{yr} \cdot A_{bottom\_rebar}$ $P_{rb} = 141.75\text{kips}$

$P_{rt} := F_{yr} \cdot A_{top\_rebar}$ $P_{rt} = 94.5\text{kips}$

$P_s := 0.85 f_c \cdot b_{slab} \cdot t_{slab}$ $P_s = 3.499 \times 10^3 \text{ kips}$

$P_c := F_{yc} \cdot A_{fc}$ $P_c = 716.212\text{kips}$

$P_t := F_{yt} \cdot A_{ft}$ $P_t = 1.29 \times 10^3 \text{ kips}$

$P_w := F_{yw} \cdot A_{web}$ $P_w = 982.258\text{kips}$

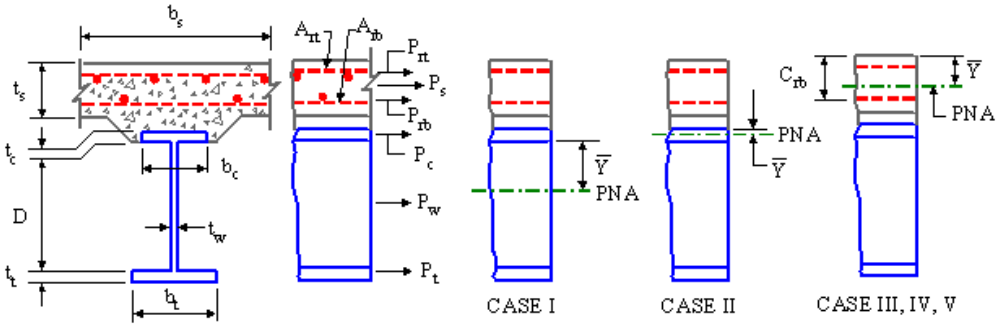

Computation of Plastic-Moment Capacity(Positive Flexure)

Location_of_PNA :=
- "In Web (Case I) " if $P_t + P_w \geq P_c + P_s + P_{rb} + P_{rt}$
- otherwise
  - "In Top Flange (Case II) " if $P_t + P_w + P_c \geq P_s + P_{rb} + P_{rt}$
  - otherwise
    - "Slab, Below Prb (Case III)" if $P_t + P_w + P_c \geq \frac{y_{rb}}{t_{slab}} \cdot P_s + P_{rb} + P_{rt}$
    - otherwise
      - "Slab,at Prb (Case IV)" if $P_t + P_w + P_c + P_{rb} \geq \frac{y_{rb}}{t_{slab}} \cdot P_s + P_{rt}$
      - "Slab, Above Prb (Case V) " otherwise

Location_of_PNA = "Slab, Below Prb (Case III)"

$$Y_{bar} := \begin{cases} \frac{D}{2}\cdot\left(\frac{P_t - P_c - P_s - P_{rt} - P_{rb}}{P_w} + 1\right) & \text{if } P_t + P_w \geq P_c + P_s + P_{rb} + P_{rt} \\ \text{otherwise} \\ \quad \begin{cases} \frac{t_{fc}}{2}\cdot\left(\frac{P_w + P_t - P_s - P_{rt} - P_{rb}}{P_c} + 1\right) & \text{if } P_t + P_w + P_c \geq P_s + P_{rb} + P_{rt} \\ \text{otherwise} \\ \quad \begin{cases} t_{slab}\cdot\frac{P_c + P_w + P_t - P_{rt} - P_{rb}}{P_s} & \text{if } P_t + P_w + P_c \geq \frac{y_{rb}}{t_{slab}}\cdot P_s + P_{rb} + P_{rt} \\ \text{otherwise} \\ \quad \begin{cases} y_{rb} & \text{if } P_t + P_w + P_c + P_{rb} \geq \frac{y_{rb}}{t_{slab}}\cdot P_s + P_{rt} \\ t_{slab}\cdot\frac{P_{rb} + P_c + P_w + P_t - P_{rt}}{P_s} & \text{otherwise} \end{cases} \end{cases} \end{cases} \end{cases}$$

$Y_{bar} = 6.293\text{in}$

$$d_s := \begin{cases} \frac{t_{slab}}{2} + t_{haunch} + Y_{bar} & \text{if } P_t + P_w \geq P_c + P_s + P_{rb} + P_{rt} \\ \text{otherwise} \\ \quad \begin{cases} \frac{t_{slab}}{2} + t_{haunch} - t_{fc} + Y_{bar} & \text{if } P_t + P_w + P_c \geq P_s + P_{rb} + P_{rt} \\ \text{"Not necessary for calculating Mp"} & \text{otherwise} \end{cases} \end{cases}$$

$d_s = \text{"Not necessary for calculating Mp"}$ in

$$d_{rt} := \begin{cases} t_{slab} - y_{rt} + t_{haunch} + Y_{bar} & \text{if } P_t + P_w \geq P_c + P_s + P_{rb} + P_{rt} \\ \text{otherwise} \\ \quad \begin{cases} t_{slab} - y_{rt} + t_{haunch} - t_{fc} + Y_{bar} & \text{if } P_t + P_w + P_c \geq P_s + P_{rb} + P_{rt} \\ Y_{bar} - y_{rt} & \text{otherwise} \end{cases} \end{cases}$$

$d_{rt} = 3.043\text{in}$

$$d_{rb} := \begin{cases} t_{slab} - y_{rb} + t_{haunch} + Y_{bar} & \text{if } P_t + P_w \geq P_c + P_s + P_{rb} + P_{rt} \\ \text{otherwise} \\ \quad \begin{cases} t_{slab} - y_{rb} + t_{haunch} - t_{fc} + Y_{bar} & \text{if } P_t + P_w + P_c \geq P_s + P_{rb} + P_{rt} \\ \text{otherwise} \\ \quad \begin{cases} Y_{bar} - y_{rb} & \text{if } P_t + P_w + P_c \geq \frac{y_{rb}}{t_{slab}}\cdot P_s + P_{rb} + P_{rt} \\ \text{otherwise} \\ \quad \begin{cases} \text{"Not necessary for calculating Mp"} & \text{if } P_t + P_w + P_c + P_{rb} \geq \frac{y_{rb}}{t_{slab}}\cdot P_s + P_{rt} \\ y_{rb} - Y_{bar} & \text{otherwise} \end{cases} \end{cases} \end{cases} \end{cases}$$

$d_{rb} = 0.043\text{in}$

$$d_c := \begin{cases} Y_{bar} - \frac{t_{fc}}{2} & \text{if } P_t + P_w \geq P_c + P_s + P_{rb} + P_{rt} \\ \text{otherwise} \\ \quad \begin{cases} \text{"Not necessary for calculating Mp"} & \text{if } P_t + P_w + P_c \geq P_s + P_{rb} + P_{rt} \\ t_{slab} + t_{haunch} - \frac{t_{fc}}{2} - Y_{bar} & \text{otherwise} \end{cases} \end{cases}$$

$d_c = 0.356\,\text{ft}$

$$d_w := \begin{cases} \text{"Not necessary for calculating Mp"} & \text{if } P_t + P_w \geq P_c + P_s + P_{rb} + P_{rt} \\ \text{otherwise} \\ \quad \begin{cases} \frac{D}{2} + t_{fc} - Y_{bar} & \text{if } P_t + P_w + P_c \geq P_s + P_{rb} + P_{rt} \\ t_{slab} + t_{haunch} - Y_{bar} + \frac{D}{2} & \text{otherwise} \end{cases} \end{cases}$$

$d_w = 28.735\text{in}$

$$d_t := \begin{cases} D - Y_{bar} + \frac{t_{ft}}{2} & \text{if } P_t + P_w \geq P_c + P_s + P_{rb} + P_{rt} \\ \text{otherwise} \\ \quad \begin{cases} D + t_{fc} - Y_{bar} + \frac{t_{ft}}{2} & \text{if } P_t + P_w + P_c \geq P_s + P_{rb} + P_{rt} \\ t_{slab} + t_{haunch} - Y_{bar} + D + \frac{t_{ft}}{2} & \text{otherwise} \end{cases} \end{cases}$$

$d_t = 53.265\text{in}$

$$M_p := \begin{cases} \frac{P_w}{2 \cdot D} \cdot \left[Y_{bar}^{\,2} + \left(D - Y_{bar} \right)^2 \right] + P_s \cdot d_s + P_{rt} \cdot d_{rt} + P_{rb} \cdot d_{rb} + P_c \cdot d_c + P_t \cdot d_t & \text{if } P_t + P_w \geq P_c + P_s + P_{rb} + P_{rt} \\ \text{otherwise} \\ \quad \begin{cases} \frac{P_c}{2 \cdot t_{fc}} \cdot \left[Y_{bar}^{\,2} + \left(t_{fc} - Y_{bar} \right)^2 \right] + P_s \cdot d_s + P_{rt} \cdot d_{rt} + P_{rb} \cdot d_{rb} + P_w \cdot d_w + P_t \cdot d_t & \text{if } P_t + P_w + P_c \geq P_s + P_{rb} + P_{rt} \\ \text{otherwise} \\ \quad \begin{cases} \frac{Y_{bar}^{\,2} \cdot P_s}{2 \cdot t_{slab}} + P_{rt} \cdot d_{rt} + P_{rb} \cdot d_{rb} + P_c \cdot d_c + P_w \cdot d_w + P_t \cdot d_t & \text{if } P_t + P_w + P_c \geq \frac{y_{rb}}{t_{slab}} \cdot P_s + P_{rb} + P_{rt} \\ \text{otherwise} \\ \quad \begin{cases} \frac{Y_{bar}^{\,2} \cdot P_s}{2 \cdot t_{slab}} + P_{rt} \cdot d_{rt} + P_c \cdot d_c + P_w \cdot d_w + P_t \cdot d_t & \text{if } P_t + P_w + P_c + P_{rb} \geq \frac{y_{rb}}{t_{slab}} \cdot P_s + P_{rt} \\ \frac{Y_{bar}^{\,2} \cdot P_s}{2 \cdot t_{slab}} + P_{rt} \cdot d_{rt} + P_{rb} \cdot d_{rb} + P_c \cdot d_c + P_w \cdot d_w + P_t \cdot d_t & \text{otherwise} \end{cases} \end{cases} \end{cases}$$

$M_p = 9.078 \times 10^3\,\text{kips}\cdot\text{ft}$

Unshored Composite Section Properties :

Yield Moment (unshored) associated with STRENGTH I

Read analysis results of factored flanges stresses.

$f_{tf\_si} :=$ $f_{bf\_si} :=$

$length := f_{tf\_si}^{\langle cols(f_{tf\_si})-3 \rangle}$

$fb_{tf} := f_{tf\_si}^{\langle cols(f_{tf\_si})-2 \rangle}$ $fl_{tf} := f_{tf\_si}^{\langle cols(f_{tf\_si})-1 \rangle}$

$fb_{bf} := f_{bf\_si}^{\langle cols(f_{bf\_si})-2 \rangle}$ $fl_{bf} := f_{bf\_si}^{\langle cols(f_{bf\_si})-1 \rangle}$

Top flange stresses along the entire normalized length (psi):

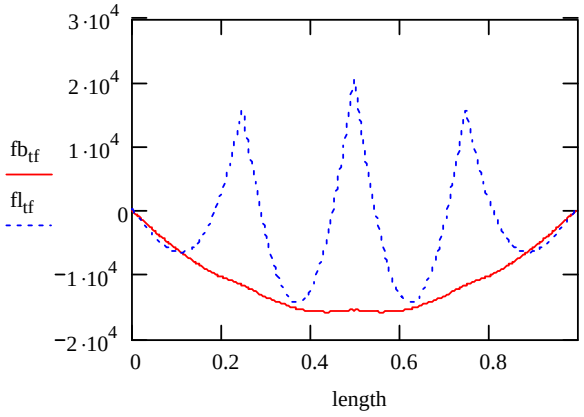

Bottom flange stresses along the entire normalized length (psi):

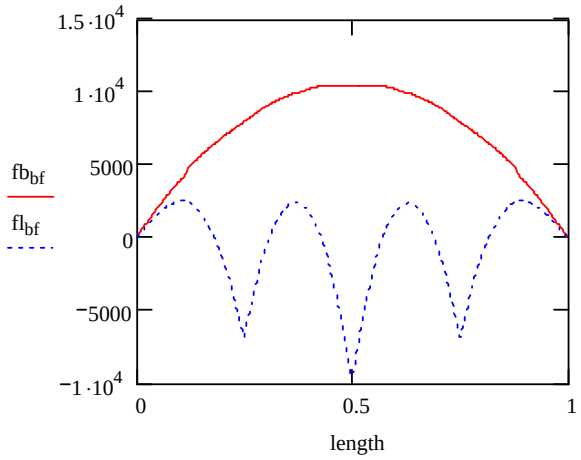

Girder stresses (psi) within the unbraced length adjacent to mid-span:

$i := 180.. 269$

$fb\_Lb\_length_i := length_i$ $\quad fb_{tf\_Lb_i} := fb_{tf_i}$ $\quad fl_{tf\_Lb_i} := fl_{tf_i}$

Top flange stresses within the unbraced length adjacent to mid-span:

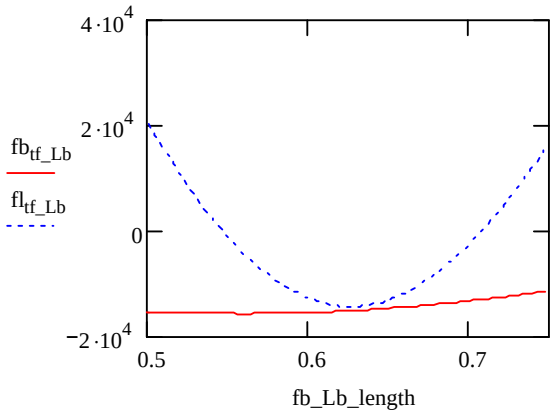

$f_{D1c} := \min(fb_{tf\_Lb})$ $\quad f_{D1c} = -1.58 \times 10^4$

$fb_{bf\_Lb_i} := fb_{bf_i}$ $\quad fl_{bf\_Lb_i} := fl_{bf_i}$

Bottom flange stresses within the unbraced length adjacent to mid-span:

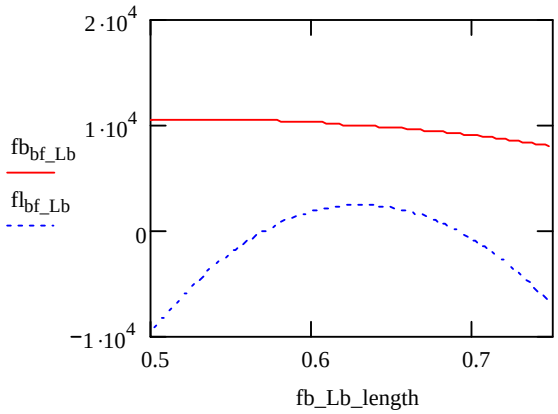

$f_{D1t} := \max(fb_{bf\_Lb})$ $\quad f_{D1t} = 1.05 \times 10^4$

$f_{D1t} := \frac{|f_{D1t}|}{1000}\,ksi$ $\quad f_{D1c} := \frac{|f_{D1c}|}{1000}\,ksi$ $\quad M_{D2} := 0kips \cdot ft$

$f_{D1t} = 10.5ksi$ $\quad f_{D1c} = 15.8ksi$

$M_{D1t} := f_{D1t} \cdot S_t$ $\quad M_{D1c} := f_{D1c} \cdot S_c$

$M_{D1t} = 979.311 \text{kips}\cdot\text{ft}$ $M_{D1c} = 1.004\times 10^{3} \text{kips}\cdot\text{ft}$

Tension Flange :

$M_{ADt} := \left(F_{yt} - \frac{M_{D1t}}{S_t} - \frac{M_{D2}}{S_{t\_3n}} \right) \cdot S_{t\_n}$ $M_{ADt} = 5.978\times 10^{3} \text{kips}\cdot\text{ft}$

$M_{yt} := M_{D1t} + M_{D2} + M_{ADt}$ $M_{yt} = 6.958\times 10^{3} \text{kips}\cdot\text{ft}$

Compression Flange :

$M_{ADc} := \left(F_{yc} - \frac{M_{D1c}}{S_c} - \frac{M_{D2}}{S_{c\_3n}} \right) \cdot S_{c\_n}$ $M_{ADc} = 5.126\times 10^{4} \text{kips}\cdot\text{ft}$

$M_{yc} := M_{D1c} + M_{D2} + M_{ADc}$ $M_{yc} = 5.226\times 10^{4} \text{kips}\cdot\text{ft}$

$M_{AD} := \min(M_{ADt}, M_{ADc})$ $M_{AD} = 5.978\times 10^{3} \text{kips}\cdot\text{ft}$

$M_{y\_unshored} := \min(M_{yt}, M_{yc})$ $M_{y\_unshored} = 6.958\times 10^{3} \text{kips}\cdot\text{ft}$

Concrete Stress at First Yield (unshored)

$f_{conc\_composite\_unshored\_at\_My} := \left(\frac{M_{D2}}{S_{slab\_3n}\cdot 3n} + \frac{M_{AD}}{S_{slab\_n}\cdot n} \right)$ $f_{conc\_composite\_unshored\_at\_My} = 2.156\text{ksi}$

$\frac{f_{conc\_composite\_unshored\_at\_My}}{f_c} = 0.44$

Shape Factor :

$\frac{M_p}{M_{y\_unshored}} = 1.305$ $\frac{M_p}{M_{y\_shortterm}} = 1.244$ $\frac{M_p}{M_{y\_longterm}} = 1.32$

Flange Hybrid Strength Reduction Factor (Composite Girder) :

$R_{h\_comp} := 1$ **since the girder is homogeneous**

Constructibility Check, Noncomposite Girder(STREGNTH IV)

Construction load stresses are factored, load factor = 1.5

G2 top flange

$\phi_f := 1.0$ $R_b := 1$ **since bend buckling is prevented when checking constructibility**

$f_{tf\_siv\_1st} :=$ $f_{tf\_siv\_2nd} :=$

$length := f_{tf\_siv\_1st}^{\langle \text{cols}(f_{tf\_siv\_1st})-3 \rangle}$ $fb_{tf\_1st} := f_{tf\_siv\_1st}^{\langle \text{cols}(f_{tf\_siv\_1st})-2 \rangle}$ $fl_{tf\_1st} := f_{tf\_siv\_1st}^{\langle \text{cols}(f_{tf\_siv\_1st})-1 \rangle}$

$fb_{tf\_2nd} := f_{tf\_siv\_2nd}^{\langle \text{cols}(f_{tf\_siv\_2nd})-2 \rangle}$ $fl_{tf\_2nd} := f_{tf\_siv\_2nd}^{\langle \text{cols}(f_{tf\_siv\_2nd})-1 \rangle}$

Top flange stresses (psi) along the nomralized length :

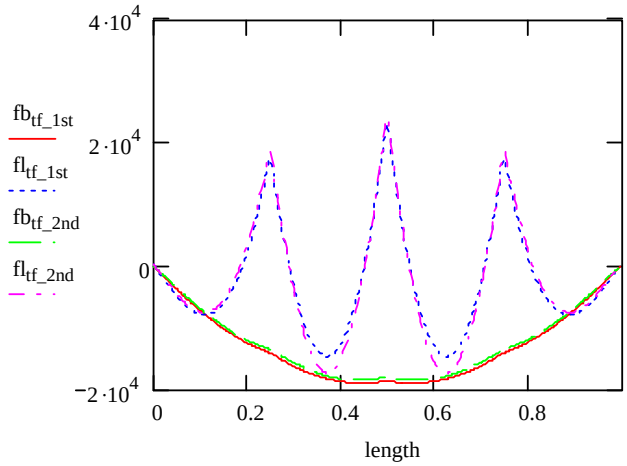

Girder stresses within the unbraced length adjacent to mid-span:

$i := 180..269$ $\quad fb_{tf\_1st\_Lb_i} := fb_{tf\_1st_i}$ $\quad fl_{tf\_1st\_Lb_i} := fl_{tf\_1st_i}$

$fb_{tf\_2nd\_Lb_i} := fb_{tf\_2nd_i}$ $\quad fl_{tf\_2nd\_Lb_i} := fl_{tf\_2nd_i}$

Top flange stresses (psi) within the unbraced length:

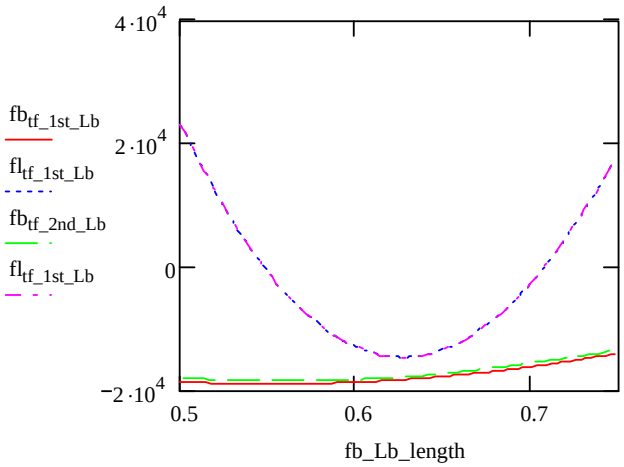

Moment Gradient Modifier for LTB(Cb) :

$f_1 := |-14.1|\ ksi$ $\quad f_2 := \frac{|\min(fb_{tf\_1st\_Lb})|}{1000} ksi$

$f_1 = 14.1ksi$ $\quad f_2 = 19ksi$

$$C_b := \begin{cases} 1.75 - 1.05\left(\frac{f_1}{f_2}\right) + 0.3\left(\frac{f_1}{f_2}\right)^2 & \text{if } 1.75 - 1.05\left(\frac{f_1}{f_2}\right) + 0.3\left(\frac{f_1}{f_2}\right)^2 \le 2.3 \\ 2.3 & \text{otherwise} \end{cases}$$

$C_b = 1.136$

Estimation of Flange Second Order Lateral Bending Stress:

$f_{b1} := \frac{\left|\min\left(fb_{tf\_1st\_Lb}\right)\right|}{1000}\cdot ksi$ $f_{l1} := \frac{\left|\max\left(fl_{tf\_1st\_Lb}\right)\right|}{1000}\cdot ksi$ $f_{b1} = 19\,ksi$ $f_{l1} = 23.2ksi$

i) Based on k=1.0 $k := 1.0$

$\lambda := \frac{k\cdot L_b}{r_t}$ $\lambda = 72.711$

$F_{cr} := \frac{C_b\cdot R_b\cdot \pi^2\cdot E}{\lambda^2}$ $F_{cr} = 61.5ksi$ $\frac{1}{1-\frac{f_{b1}}{F_{cr}}} = 1.447$ $\frac{f_{l1}}{1-\frac{f_{b1}}{F_{cr}}} = 33.57ksi$

ii) Based on k=0.5 $k := 0.5$

$\lambda := \frac{k\cdot L_b}{r_t}$ $\lambda = 36.356$

$F_{cr0.5} := \frac{C_b\cdot R_b\cdot \pi^2\cdot E}{\lambda^2}$ $F_{cr0.5} = 246ksi$ $\frac{1}{1-\frac{f_{b1}}{F_{cr0.5}}} = 1.084$ $\frac{f_{l1}}{1-\frac{f_{b1}}{F_{cr0.5}}} = 25.142ksi$

$f_{b2} := \frac{\left|\min\left(fb_{tf\_2nd\_Lb}\right)\right|}{1000}\cdot ksi$ $f_{l2} := \frac{\left|\max\left(fl_{tf\_2nd\_Lb}\right)\right|}{1000}\cdot ksi$

$f_{b2} = 18.4ksi$ $f_{l2} = 24.4ksi$ Actual second-order amplification: $\frac{f_{l2}}{f_{l1}} = 1.052$

Maximum Lateral Bending Stress Limit

$f_{l2} = 24.4ksi$ $\frac{F_{yc}}{1.67} = 34.467ksi$

$Lateral\_bending\_stress\_ratio := \frac{f_{l2}}{\frac{F_{yc}}{1.67}}$ $Lateral\_bending\_stress\_ratio = 0.708$

Yielding Limit

$f_{b2} + f_{l2} = 42.8ksi$ $\phi_f\cdot R_{h\_noncomp}\cdot F_{yc} = 57.56ksi$

$Yielding\_ratio := \frac{f_{b2}+f_{l2}}{\phi_f\cdot R_{h\_noncomp}\cdot F_{yc}}$ $Yielding\_ratio = 0.744$

Strength Limit

Local Buckling Resistance :

$F_{yr} := 0.7\cdot F_{yc}$

$\lambda_f := \frac{b_{fc}}{2\cdot t_{fc}}$ $\lambda_{pf} := 0.38\sqrt{\frac{E}{F_{yc}}}$ $\lambda_{rf} := 0.56\sqrt{\frac{E}{F_{yr}}}$

$$F_{nc\_FLB} := \begin{cases} R_b \cdot R_{h\_noncomp} \cdot F_{yc} & \text{if } \lambda_f \le \lambda_{pf} \\ \left[1 - \left(1 - \frac{F_{yr}}{R_{h\_noncomp} \cdot F_{yc}}\right) \cdot \left(\frac{\lambda_f - \lambda_{pf}}{\lambda_{rf} - \lambda_{pf}}\right)\right] \cdot R_b \cdot R_{h\_noncomp} \cdot F_{yc} & \text{if } \lambda_{pf} < \lambda_f \le \lambda_{rf} \\ \frac{0.36 \cdot R_b \cdot E}{\left(\frac{b_{fc}}{2 \cdot t_{fc}}\right)^2} & \text{otherwise} \end{cases}$$

$F_{nc\_FLB} = 57.56\text{ksi}$

Lateral Torsional Buckling Resistance :

$$L_p := 1.0 \cdot r_t \cdot \sqrt{\frac{E}{F_{yc}}} \qquad L_r := \pi \cdot r_t \cdot \sqrt{\frac{E}{F_{yr}}}$$

$$F_{nc\_LTB} := \begin{cases} R_b \cdot R_{h\_noncomp} \cdot F_{yc} & \text{if } L_b \le L_p \\ \min\left[C_b \cdot \left[1 - \left(1 - \frac{F_{yr}}{R_{h\_noncomp} \cdot F_{yc}}\right) \cdot \left(\frac{L_b - L_p}{L_r - L_p}\right)\right] \cdot R_b \cdot R_{h\_noncomp} \cdot F_{yc}, R_b \cdot R_{h\_noncomp} \cdot F_{yc}\right] & \text{if } L_p < L_b \le L_r \\ \begin{cases} F_{cr} & \text{if } F_{cr} \le R_b \cdot R_{h\_noncomp} \cdot F_{yc} \\ R_b \cdot R_{h\_noncomp} \cdot F_{yc} & \text{otherwise} \end{cases} & \text{otherwise} \end{cases}$$

$F_{nc\_LTB} = 49.443\text{ksi}$

$$Controling\_Strength := \begin{cases} \text{"Flange Local Buckling"} & \text{if } F_{nc\_FLB} \le F_{nc\_LTB} \\ \text{"Lateral Torsional Buckling"} & \text{otherwise} \end{cases}$$

$Controling\_Strength = \text{"Lateral Torsional Buckling"}$

$f_{b2} + \frac{f_{l2}}{3} = 26.53\text{ksi}$ $\quad F_{nc} := \min\left(F_{nc\_LTB}, F_{nc\_FLB}\right)$ $\quad \phi_f \cdot F_{nc} = 49.44\text{ksi}$

$$Strength\_ratio := \frac{f_{b2} + \frac{f_{l2}}{3}}{\phi_f \cdot F_{nc}}$$

$Strength\_ratio = 0.537$

Web bend buckling limit

$$k := \frac{9}{\left(\frac{D_c}{D}\right)^2} \qquad k = 25.025 \qquad F_{crw} := 0.9 \cdot E \cdot \frac{k}{\left(\frac{D}{t_w}\right)^2} \qquad \phi_f \cdot F_{crw} = 29.51\text{ksi} \qquad f_{b2} = 18.4\text{ksi}$$

$$Web\_bend\_buckling\_ratio := \frac{f_{b2}}{\phi_f \cdot F_{crw}}$$

$Web\_bend\_buckling\_ratio = 0.62$

G2 bottom flange

$f_{bf\_siv\_2nd} :=$

$$length := f_{bf\_siv\_2nd}^{\langle cols(f_{bf\_siv\_2nd}) - 3 \rangle} \qquad fb_{bf\_2nd} := f_{bf\_siv\_2nd}^{\langle cols(f_{bf\_siv\_2nd}) - 2 \rangle} \qquad fl_{bf\_2nd} := f_{bf\_siv\_2nd}^{\langle cols(f_{bf\_siv\_2nd}) - 1 \rangle}$$

Bottom flange stresses (psi) along the normalized length:

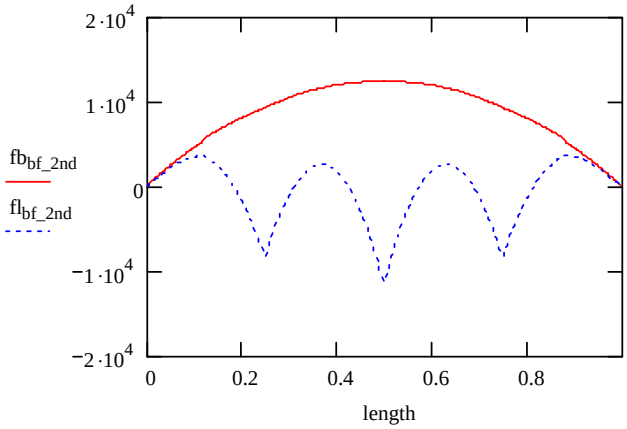

Girder stresses along the unbraced length adjacent to mid-span:

$fb\_Lb\_length_i := length_i$ $\quad fb_{bf\_2nd\_Lb_i} := fb_{bf\_2nd_i}$ $\quad fl_{bf\_2nd\_Lb_i} := fl_{bf\_2nd_i}$

Bottom flange stresses (psi) within the unbraced length:

$$f_{b2} := \frac{\left|\max\left(fb_{bf\_2nd\_Lb}\right)\right|}{1000}\cdot ksi$$

$f_{b2} = 12.3ksi$

$$f_{l2} := \frac{\left|\min\left(fl_{bf\_2nd\_Lb}\right)\right|}{1000}\cdot ksi$$

$f_{l2} = 11.4ksi$

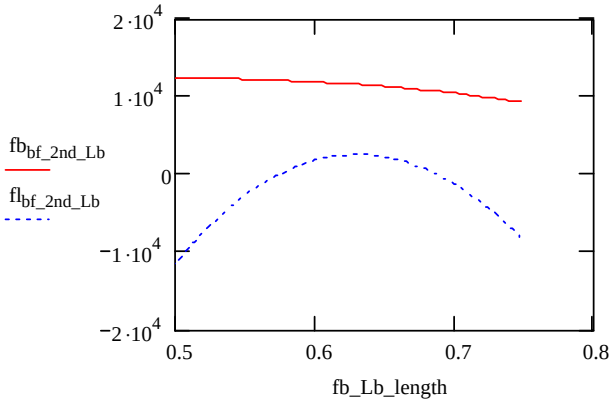

Maximum Lateral Bending Stress Limit

$f_{l2} = 11.4ksi$ $\quad \frac{F_{yt}}{1.67} = 34.772ksi$

$$Lateral\_bending\_stress\_ratio := \frac{f_{l2}}{\frac{F_{yt}}{1.67}}$$

$Lateral\_bending\_stress\_ratio = 0.328$

Yielding Limit

$f_{b2} + f_{l2} = 23.7ksi$ $\quad \phi_f \cdot R_{h\_noncomp} \cdot F_{yt} = 58.07ksi$

$$Yielding\_ratio := \frac{f_{b2} + f_{l2}}{\phi_f \cdot R_{h\_noncomp} \cdot F_{yt}}$$

$Yielding\_ratio = 0.408$

Strength I Check

Construction stresses are based on factored construction loads, load factor = 1.25
Lane and truck load stresses are unfactored, but the dynamic allowance of 1.33 is included in the calcuation of the truck load stresses

G2 Bottom flange

$fb_{bf\_noncomp} := f_{bf\_si}^{\langle cols(f_{bf\_si})-2\rangle}$ $fl_{bf\_noncomp} := f_{bf\_si}^{\langle cols(f_{bf\_si})-1\rangle}$

Factored noncomposite stresses
along the entire normalized length:

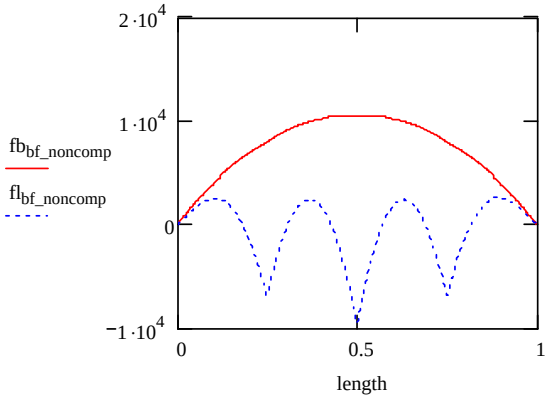

Read analysis results of unfactored composite stresses:

$f_{bf\_lane} :=$ $f_{bf\_truck} :=$

$length := f_{bf\_lane}^{\langle cols(f_{bf\_lane})-3\rangle}$ $fb_{bf\_lane} := f_{bf\_lane}^{\langle cols(f_{bf\_lane})-2\rangle}$ $fl_{bf\_lane} := f_{bf\_lane}^{\langle cols(f_{bf\_lane})-1\rangle}$

$fb_{bf\_truck} := f_{bf\_truck}^{\langle cols(f_{bf\_truck})-2\rangle}$ $fl_{bf\_truck} := f_{bf\_truck}^{\langle cols(f_{bf\_truck})-1\rangle}$

Bottom flange stresses along the entire
normalized length:

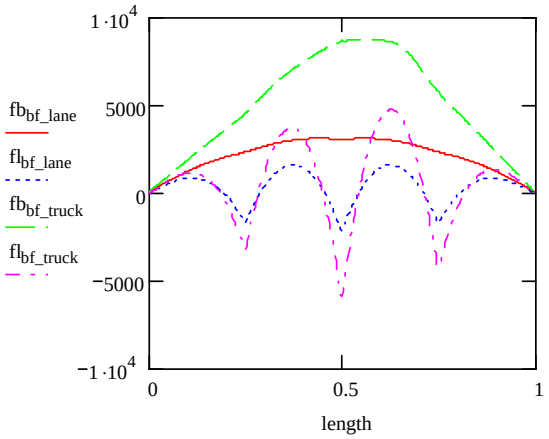

Factored bottom flange stresses relating to Strength I load combination:

$fb_{bf} := fb_{bf\_noncomp} + 1.75 \cdot (fb_{bf\_lane} + fb_{bf\_truck})$ $fl_{bf} := fl_{bf\_noncomp} + 1.75 \cdot (fl_{bf\_lane} + fl_{bf\_truck})$

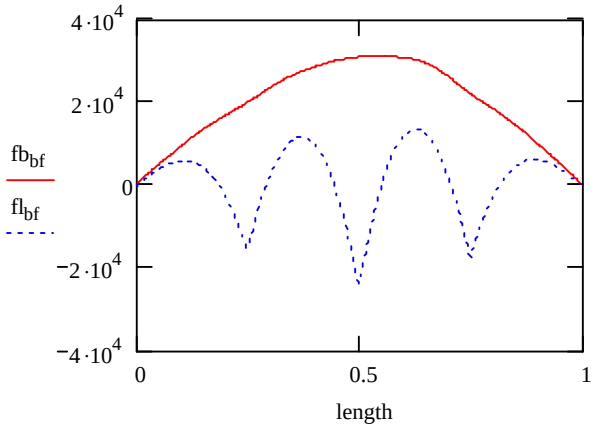

Bottom flange stresses within the unbraced length adjacent o mid-span

$fb\_Lb\_length_i := length_i$ $\quad fb_{bf\_Lb_i} := fb_{bf_i}$ $\quad fl_{bf\_Lb_i} := fl_{bf_i}$

Maximum major-axis and lateral bending stresses within the unbraced length

$$f_b := \frac{\left|\max\left(fb_{bf\_Lb}\right)\right|}{1000}\cdot ksi$$

$f_b = 31.203ksi$

$$f_l := \frac{\left|\min\left(fl_{bf\_Lb}\right)\right|}{1000}\cdot ksi$$

$f_l = 23.867ksi$

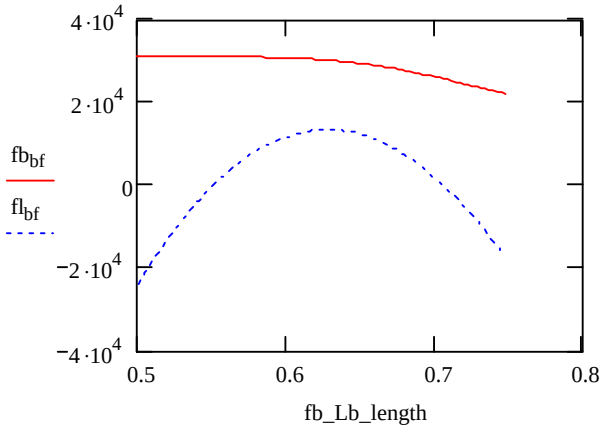

Lateral Bending Stress Limit

$f_l = 23.87ksi$

$\frac{F_{yt}}{1.67} = 34.772ksi$

$$Lateral\_bending\_stress\_ratio := \frac{f_l}{\frac{F_{yt}}{1.67}}$$

$Lateral\_bending\_stress\_ratio = 0.69$

Strength Limit

$f_b + \frac{f_l}{3} = 39.16ksi$

$\phi_f \cdot R_{h\_comp} \cdot F_{yt} = 58.07ksi$

$$Strength\_ratio := \frac{f_b + \frac{f_l}{3}}{\phi_f \cdot R_{h\_comp} \cdot F_{yt}}$$

$Strength\_ratio = 0.674$

G2 Top flange

Factored noncomposite stresses (psi) along the entire normalized length:

$fb_{tf\_noncomp} := f_{tf\_si}^{\langle cols(f_{tf\_si})-2\rangle}$ $fl_{tf\_noncomp} := f_{tf\_si}^{\langle cols(f_{tf\_si})-1\rangle}$

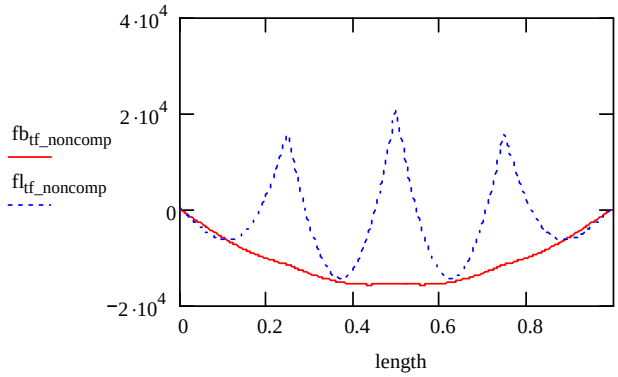

Read analysis results of unfactored composite stresses:

$f_{tf\_lane} :=$ $f_{tf\_truck} :=$

$length := f_{tf\_lane}^{\langle cols(f_{tf\_lane})-3\rangle}$ $fb_{tf\_lane} := f_{tf\_lane}^{\langle cols(f_{tf\_lane})-2\rangle}$ $fl_{tf\_lane} := f_{tf\_lane}^{\langle cols(f_{tf\_lane})-1\rangle}$

$fb_{tf\_truck} := f_{tf\_truck}^{\langle cols(f_{tf\_truck})-2\rangle}$ $fl_{tf\_truck} := f_{tf\_truck}^{\langle cols(f_{tf\_truck})-1\rangle}$

Unfactored top flange stresses (psi) along the entire normalized length:

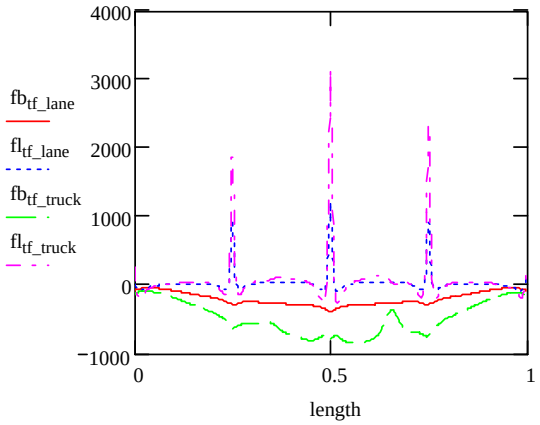

Factored top flange stresses relating to Strength I load combination:

$fb_{tf} := fb_{tf\_noncomp} + 1.75 \cdot (fb_{tf\_lane} + fb_{tf\_truck})$ $fl_{tf} := fl_{tf\_noncomp} + 1.75 \cdot (fl_{tf\_lane} + fl_{tf\_truck})$

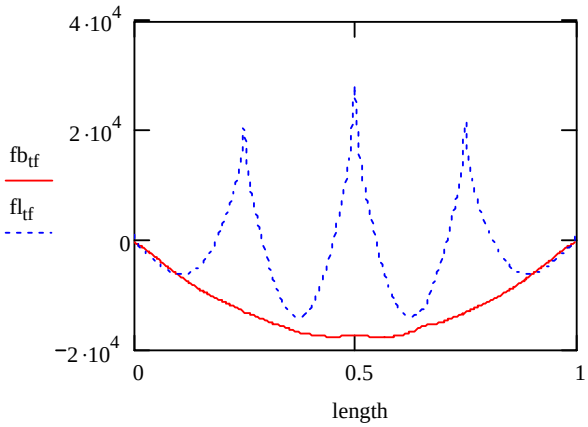

Factored top fflange stresses within the unbraced length adjacent to mid-span

$fb\_Lb\_length_i := length_i$ $\quad fb_{tf\_Lb_i} := fb_{tf_i}$ $\quad fl_{tf\_Lb_i} := fl_{tf_i}$

Maximum major-axis and lateral bending stresses within the unbraced length

$$f_b := \frac{\left|\min\left(fb_{tf\_Lb}\right)\right|}{1000}\cdot ksi$$

$f_b = 17.789ksi$

$$f_l := \frac{\left|\max\left(fl_{tf\_Lb}\right)\right|}{1000}\cdot ksi$$

$f_l = 28.233ksi$

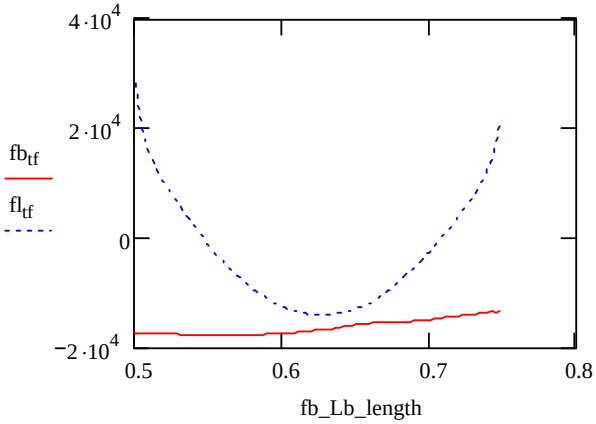

Strength Limit

$f_b = 17.789ksi$ $\quad \phi_f \cdot R_{h\_comp} \cdot F_{yc} = 57.56ksi$

$$Strength\_ratio := \frac{f_b}{\phi_f \cdot R_{h\_comp} \cdot F_{yc}}$$

$Strength\_ratio = 0.309$

Service II Check

G2 Bottom flange

Factored bottom flange stresses relating to Serive I load combination:

$fb_{bf} := fb_{bf\_noncomp} \cdot 0.8 + 1.30 \cdot (fb_{bf\_lane} + fb_{bf\_truck})$ $fl_{bf} := fl_{bf\_noncomp} \cdot 0.8 + 1.30 \cdot (fl_{bf\_lane} + fl_{bf\_truck})$

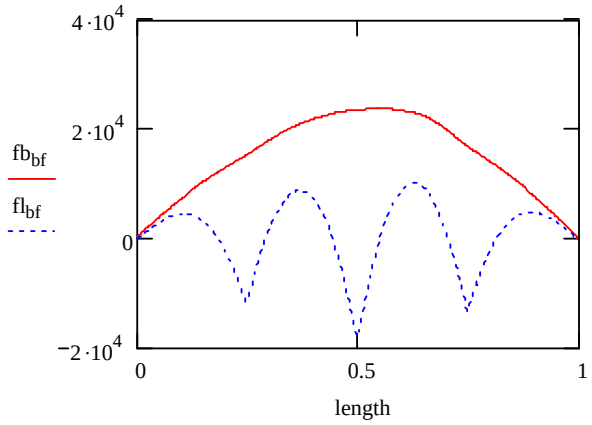

Bottom flange stresses within the unbraced length adjacent o mid-span

$fb\_Lb\_length_i := length_i$ $fb_{bf\_Lb_i} := fb_{bf_i}$ $fl_{bf\_Lb_i} := fl_{bf_i}$

Maximum major-axis and lateral bending stresses within the unbraced length

$$f_b := \frac{|\max(fb_{bf\_Lb})|}{1000} \cdot ksi$$

$f_b = 23.779 ksi$

$$f_l := \frac{|\min(fl_{bf\_Lb})|}{1000} \cdot ksi$$

$f_l = 18.277 ksi$

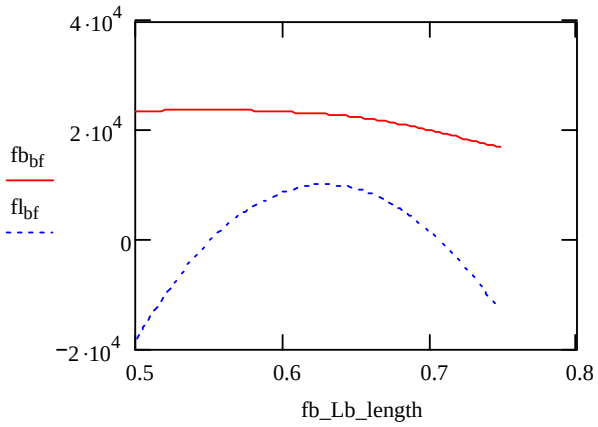

$0.95 \cdot F_{yt} = 55.166 ksi$

$$Permanent\_deformation\_ratio := \frac{f_b}{0.95 \cdot F_{yt}}$$ $Permanent\_deformation\_ratio = 0.431$

G2 Top flange

Factored top flange stresses relating to Serive I load combination:

$fb_{tf} := fb_{tf\_noncomp} \cdot 0.8 + 1.30 \cdot \left(fb_{tf\_lane} + fb_{tf\_truck} \right)$ $fl_{tf} := fl_{tf\_noncomp} \cdot 0.8 + 1.30 \cdot \left(fl_{tf\_lane} + fl_{tf\_truck} \right)$

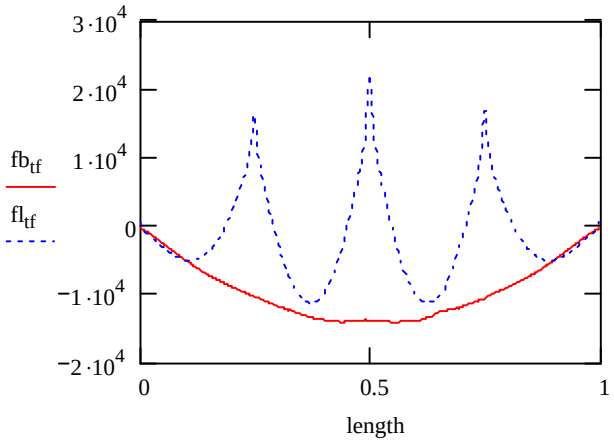

Bottom flange stresses within the unbraced length adjacent o mid-span

$fb\_Lb\_length_i := length_i$ $fb_{tf\_Lb_i} := fb_{tf_i}$ $fl_{tf\_Lb_i} := fl_{tf_i}$

Maximum major-axis and lateral bending stresses within the unbraced length

$$f_b := \frac{\left| \min\left(fb_{tf\_Lb} \right) \right|}{1000} \cdot ksi$$

$f_b = 14.118 ksi$

$$f_l := \frac{\left| \min\left(fl_{bf\_Lb} \right) \right|}{1000} \cdot ksi$$

$f_l = 18.277 ksi$

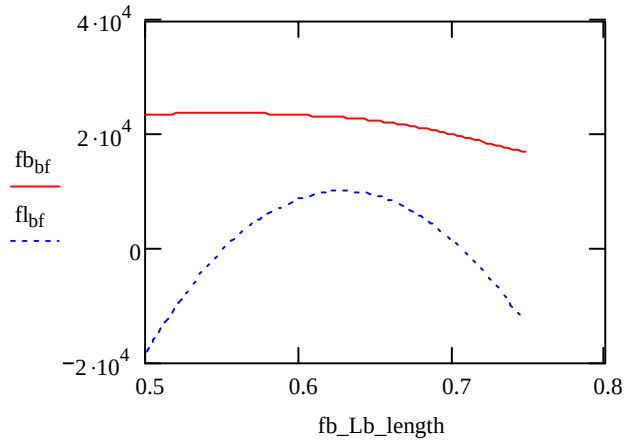

$0.95 \cdot F_{yc} = 54.682 ksi$

$$Permanent\_deformation\_ratio := \frac{f_b}{0.95 \cdot F_{yc}}$$

$Permanent\_deformation\_ratio = 0.258$

B.3 G3 Positive Moment Flexural Design

Material Properties:

- Steel Properties:

$F_{yc} := 58.07\,ksi$; $F_{yw} := 63.63\,ksi$; $F_{yt} := 71.63\,ksi$; $F_{yr} := 60\,ksi$; $E := 2.9 \cdot 10^4\,ksi$

- Concrete Properties:

$f_c := 4.9\,ksi$; $E_c := 4034\,ksi$; $n := \frac{E}{E_c}$; $n = 7.189$ $W_{conc} := 150\,\frac{lbf}{ft^3}$

Plate Girder Dimensions:

GIRDER LENGTH:

$L := 93.9375\,ft$ $L_b := \frac{L}{4}$ $L_b = 23.484\,ft$

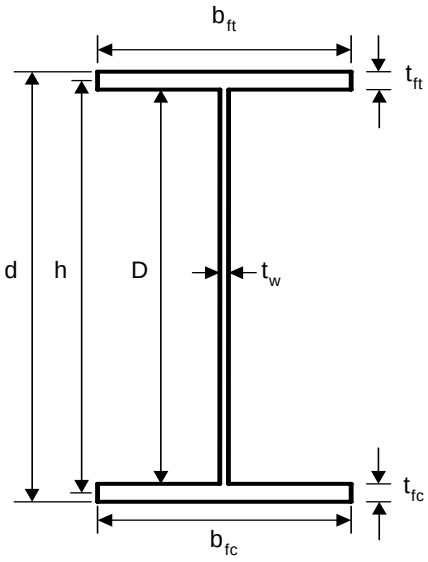

TOP FLANGE:

$b_{fc} := 24.185\,in$

$t_{fc} := 1\,in$

$\frac{b_{fc}}{2 t_{fc}} = 12.092$

BOTTOM FLANGE:

$b_{ft} := 24.185\,in$

$t_{ft} := 1.389\,in$

$\frac{b_{ft}}{2 \cdot t_{ft}} = 8.71$

WEB:

$D := 48.062\,in$ $t_w := 0.362\,in$ $\frac{D}{t_w} = 132.768$

$d := D + t_{ft} + t_{fc}$ $d = 50.451\,in$

$h := D + \frac{t_{ft} + t_{fc}}{2}$ $h = 49.256\,in$

Cross-section Proportion Limits :

- Web proportion checks for webs without longitudinal stiffeners

$$Web\_Proportion\_Check := \begin{cases} \text{"OK"} & \text{if } \frac{D}{t_w} \le 150 \\ \text{"NG"} & \text{otherwise} \end{cases}$$

$Web\_Proportion\_Check = \text{"OK"}$

$a_w := \frac{D \cdot t_w}{b_{fc} \cdot t_{fc}}$ $a_w = 0.719$

$\text{Prevent\_Vertical\_Flange\_Buckling\_Check} := \begin{cases} \text{"OK"} & \text{if } \frac{D}{t_w} \le 0.6 \cdot \sqrt{a_w} \cdot \frac{E}{F_{yc}} \\ \text{"NG"} & \text{otherwise} \end{cases}$ $0.6 \cdot \sqrt{a_w} \cdot \frac{E}{F_{yc}} = 254$

Prevent_Vertical_Flange_Buckling_Check = "OK"

- Flange proportion checks

$I_{yc} := \frac{t_{fc} \cdot b_{fc}^3}{12}$ $I_{yt} := \frac{t_{ft} \cdot b_{ft}^3}{12}$ $\frac{I_{yc}}{I_{yt}} = 0.72$

$\text{Compression\_Flange\_Check} := \begin{cases} \text{"OK"} & \text{if } \frac{b_{fc}}{2 \cdot t_{fc}} \le 12.0 \wedge b_{fc} \ge \frac{D}{6} \wedge t_{fc} \ge 1.1 \cdot t_w \wedge 0.1 \le \frac{I_{yc}}{I_{yt}} \le 10 \\ \text{"NG"} & \text{otherwise} \end{cases}$

Compression_Flange_Check = "NG"

NOTE: flange proportion is slightly beyond the limit, but is considered acceptable for the design

$\text{Tension\_Flange\_Check} := \begin{cases} \text{"OK"} & \text{if } \frac{b_{ft}}{2 \cdot t_{ft}} \le 12.0 \wedge b_{ft} \ge \frac{D}{6} \wedge t_{ft} \ge 1.1 \cdot t_w \\ \text{"NG"} & \text{otherwise} \end{cases}$

Tension_Flange_Check = "OK"

Non-Composite Section Properties:

Top flange area :

$A_{fc} := b_{fc} \cdot t_{fc}$ $A_{fc} = 24.185 \text{in}^2$

Bottom flange area:

$A_{ft} := b_{ft} \cdot t_{ft}$ $A_{ft} = 33.593 \text{in}^2$

Web area:

$A_{web} := D \cdot t_w$ $A_{web} = 17.398 \text{in}^2$

Total section area :

$A_{girder} := A_{fc} + A_{ft} + A_{web}$ $A_{girder} = 75.176 \text{in}^2$

Neutral axis :

$D_c := \frac{A_{fc} \cdot \left(\frac{t_{fc}}{2}\right) + A_{ft} \cdot \left(d - \frac{t_{ft}}{2}\right) + A_{web} \cdot \left(\frac{D}{2} + t_{fc}\right)}{A_{girder}} - t_{fc}$ $D_c = 27.188 \text{in}$ $\frac{D_c}{D} = 0.566$

Note: Neutral axis measured from the lower surface of the top flange.

Shear center : $h_u := D_c + \frac{t_{fc}}{2}$ $h_l := D - D_c + \frac{t_{ft}}{2}$

$e := \frac{I_{yc} \cdot h_u - I_{yt} \cdot h_l}{I_{yc} + I_{yt}}$ $e = -0.951\text{in}$ (offset distance from the neutral axis)

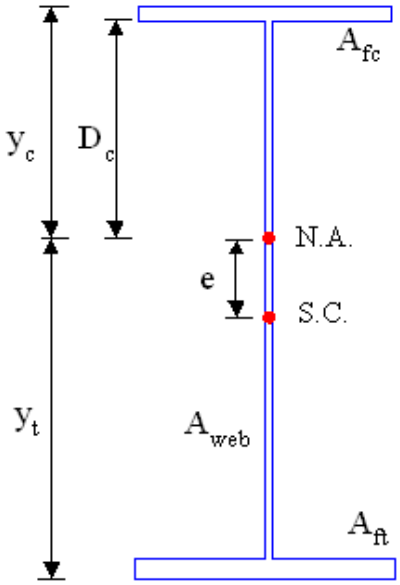

Moment of inertia with respect to a neutral axis :

$$I_{girder} := \frac{b_{fc} \cdot t_{fc}^3}{12} + \left[A_{fc} \cdot \left(D_c + t_{fc} - \frac{t_{fc}}{2} \right)^2 \right] ... + \frac{b_{ft} \cdot t_{ft}^3}{12} + \left[A_{ft} \cdot \left[d - \left(D_c + t_{fc} \right) - \frac{t_{ft}}{2} \right]^2 \right] ... + \frac{t_w \cdot D^3}{12} + A_{web} \cdot \left(D_c + t_{fc} - \frac{D}{2} - t_{fc} \right)^2$$

$I_{girder} = 3.77 \times 10^4 \text{in}^4$

Section modulus to the compression flange :

$y_c := D_c + t_{fc}$ $y_c = 28.188\text{in}$

$S_c := \frac{I_{girder}}{y_c}$ $S_c = 1.337 \times 10^3 \text{in}^3$

Section modulus of the tension flange :

$y_t := d - y_c$ $y_t = 22.263\text{in}$

$S_t := \frac{I_{girder}}{y_t}$ $S_t = 1.693 \times 10^3 \text{in}^3$ $\frac{A_{ft}}{A_{fc}} = 1.389$

- Web Bend-buckling Resistance

$\frac{D_c}{D} = 0.566$ $\frac{2D_c}{t_w} = 150.209$

bend-buckling coeffient :

$k := \frac{9}{\left(\frac{D_c}{D} \right)^2}$ $k = 28.125$ $F_{crw} := 0.9 \cdot E \cdot \frac{k}{\left(\frac{D}{t_w} \right)^2}$ $F_{crw} = 41.64\text{ksi}$

- Yield Moment

$M_{yt\_noncomp} := S_t \cdot F_{yt}$ $\quad M_{yt\_noncomp} = 1.011 \times 10^4 \text{ kips} \cdot \text{ft}$

$M_{yc\_noncomp} := S_c \cdot F_{yc}$ $\quad M_{yc\_noncomp} = 6.472 \times 10^3 \text{ kips} \cdot \text{ft}$

$M_{y\_noncomp} := \begin{cases} M_{yt\_noncomp} & \text{if } M_{yt\_noncomp} \le M_{yc\_noncomp} \\ M_{yc\_noncomp} & \text{otherwise} \end{cases}$ $\quad M_{y\_noncomp} = 6.472 \times 10^3 \text{ kips} \cdot \text{ft}$

- Radius of Gyration for LTB Check

$$r_t := \frac{b_{fc}}{\sqrt{12 \cdot \left(\frac{h}{d} + \frac{D_c \cdot t_w \cdot D^2}{3 \cdot b_{fc} \cdot t_{fc} \cdot h \cdot d} \right)}} \qquad r_t = 6.649\text{in}$$

Note: The exact r_t equation is used in the above .

- Flange-Strength Reduction Factors (Noncomposite Girder) :

Hybrid Factor :

$D_n := \max(D - D_c, D_c)$ $\quad D_n = 27.188\text{in}$

$First\_Yield\_at := \begin{cases} \text{"Bottom Flange"} & \text{if } M_{yt\_noncomp} < M_{yc\_noncomp} \\ \text{"Top Flange"} & \text{otherwise} \end{cases}$ $\quad First\_Yield\_at = \text{"Top Flange"}$

$f_n := F_{yc}$ $\quad f_n = 58.07\text{ksi}$

NOTE: The above calculation of f_n applies only to Girder G3

$$\rho := \min\left(\frac{F_{yw}}{f_n}, 1.0 \right) \qquad \rho = 1$$

$A_{fn} := A_{fc}$

$$\beta := \frac{2 \cdot D_n \cdot t_w}{A_{fn}} \qquad \beta = 0.814$$

$$R_{h\_noncomp} := \frac{12 + \beta \cdot \left(3 \cdot \rho - \rho^3\right)}{12 + 2 \cdot \beta} \qquad R_{h\_noncomp} = 1$$ **since yielding is governed by Grade 50 top flange**

Web Load-Shedding Factor :

$D_c = 27.188\text{in}$

$a_{wc} := \frac{2 \cdot D_c \cdot t_w}{A_{fc}}$ $a_{wc} = 0.814$

$\lambda_{rw} := 5.7\sqrt{\frac{E}{F_{yc}}}$ $\lambda_{rw} = 127.379$

$$R_{b\_noncomp} := \begin{cases} 1.0 & \text{if } \frac{2 \cdot D_c}{t_w} \le \lambda_{rw} \\ \text{otherwise} & \\ \quad \begin{cases} 1 - \left(\frac{a_{wc}}{1200 + 300 \cdot a_{wc}}\right) \cdot \left(\frac{2 \cdot D_c}{t_w} - \lambda_{rw}\right) & \text{if } 1 - \left(\frac{a_{wc}}{1200 + 300 \cdot a_{wc}}\right) \cdot \left(\frac{2 \cdot D_c}{t_w} - \lambda_{rw}\right) \le 1.0 \\ 1.0 & \text{otherwise} \end{cases} \end{cases}$$

$R_{b\_noncomp} = 0.987$

Composite Section Properties :

Effective Width of Slab

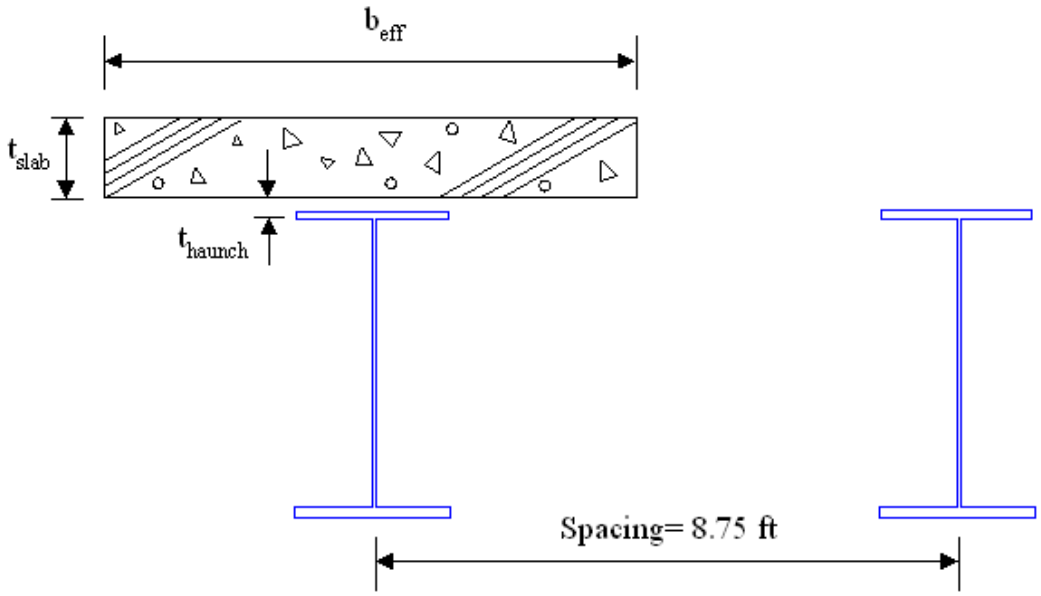

< Composite Section >

$t_{haunch} := 3\text{in}$ $b_{eff\_int} := 8.5833\text{ft}$

$t_{slab} := 8\text{in}$

$$b_{eff\_ext} := \min\left(\left(\frac{L}{8}\right), \left(6 \cdot t_{slab} + \frac{b_{fc}}{4}\right), 3.0\,ft\right) + \frac{b_{eff\_int}}{2} \qquad b_{eff\_ext} = 7.292\,ft$$

NOTE: the full tributary width for each girder is used in the design.

$b_{slab} := 7.375\,ft$ $\qquad b_{s\_3n} := \frac{b_{slab}}{3n}$

Reinforcement:

Average top reinforcing steel area : $\qquad A_{top\_rebar} := \frac{0.18\,in \cdot b_{slab}}{12} \qquad A_{top\_rebar} = 1.327\,in^2$

Average bottom reinforcing steel area : $\qquad A_{bottom\_rebar} := \frac{0.27\,in \cdot b_{slab}}{12} \qquad A_{bottom\_rebar} = 1.991\,in^2$

Location of top reinforcing steel : $\qquad y_{rt} := 3.25\,in$

Location of bottom reinforcing steel : $\qquad y_{rb} := 6.25\,in$

Long Term Composite Section Properties(3n) :

$A_{con\_3n} := b_{s\_3n} \cdot t_{slab} \qquad A_{con\_3n} = 32.828\,in^2$

$A_{total\_3n} := A_{girder} + A_{con\_3n} \qquad A_{total\_3n} = 108.005\,in^2$

$$NA_{3n} := \frac{A_{fc}\left(t_{slab} + t_{haunch} - \frac{t_{fc}}{2}\right) + A_{ft}\left(D + t_{slab} + t_{haunch} + \frac{t_{ft}}{2}\right) + A_{web}\left(\frac{D}{2} + t_{slab} + t_{haunch}\right) + A_{con\_3n}\cdot\frac{t_{slab}}{2}}{A_{total\_3n}}$$

Note: Neutral axis is measured from the top of concrete slab

$NA_{3n} = 27.796\,in$

$$I_{3n} := \frac{b_{fc}\cdot t_{fc}^3}{12} + \left[A_{fc}\cdot\left(NA_{3n} - t_{slab} - t_{haunch} + \frac{t_{fc}}{2}\right)^2\right] \ldots + \frac{b_{ft}\cdot t_{ft}^3}{12} + \left[A_{ft}\cdot\left(t_{slab} + t_{haunch} + D + t_{ft} - NA_{3n} - \frac{t_{ft}}{2}\right)^2\right] \ldots + \frac{t_w\cdot D^3}{12} + A_{web}\cdot\left(NA_{3n} - t_{slab} - t_{haunch} - \frac{D}{2}\right)^2 + \frac{b_{s\_3n}\cdot t_{slab}^3}{12} + A_{con\_3n}\cdot\left(NA_{3n} - \frac{t_{slab}}{2}\right)^2$$

$I_{3n} = 6.458 \times 10^4\,in^4$

Section Moduli:

$S_{slab\_3n} := \frac{I_{3n}}{NA_{3n}}$ $S_{slab\_3n} = 2.323\times 10^{3}\,in^{3}$

$y_{c\_3n} := NA_{3n} - t_{slab} - t_{haunch} + t_{fc}$ $y_{c\_3n} = 17.796in$

$S_{c\_3n} := \frac{I_{3n}}{y_{c\_3n}}$ $S_{c\_3n} = 3.629\times 10^{3}\,in^{3}$

$y_{t\_3n} := d - y_{c\_3n}$ $y_{t\_3n} = 32.655in$

$S_{t\_3n} := \frac{I_{3n}}{y_{t\_3n}}$ $S_{t\_3n} = 1.978\times 10^{3}\,in^{3}$

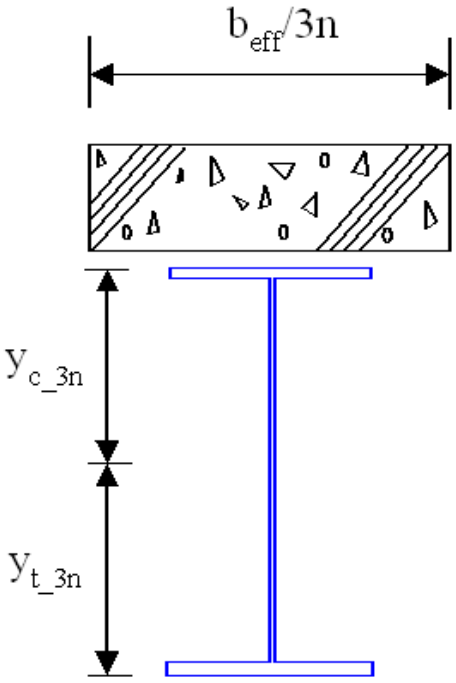

$D_{c\_3n} := y_{c\_3n} - t_{fc}$ $D_{c\_3n} = 16.796in$

$\frac{D_{c\_3n}}{D} = 0.349$ $\frac{2D_{c\_3n}}{t_w} = 92.797$

- Yield Moment (Long-term, Shored Construction) :

$M_{yt\_longterm} := S_{t\_3n}\cdot F_{yt}$ $M_{yt\_longterm} = 1.181\times 10^{4}\,kips\cdot ft$

$M_{yc\_longterm} := S_{c\_3n}\cdot F_{yc}$ $M_{yc\_longterm} = 1.756\times 10^{4}\,kips\cdot ft$

$M_{y\_longterm} := \begin{cases} M_{yt\_longterm} & \text{if } M_{yt\_longterm} \le M_{yc\_longterm} \\ M_{yc\_longterm} & \text{otherwise} \end{cases}$ $M_{y\_longterm} = 1.181\times 10^{4}\,kips\cdot ft$

- Concrete Stress at $M_{y\text{-Long Term (shored construction)}}$

$f_{c\_3n} := \frac{M_{y\_longterm}\cdot NA_{3n}}{I_{3n}\cdot 3n}$ $f_{c\_3n} = 2.827ksi$ $\frac{f_{c\_3n}}{f_c} = 0.577$

Short Term Composite Section Properties (n):

Effective Flange Width

$b_{s\_n} := \frac{b_{slab}}{n}$

$A_{con\_n} := b_{s\_n} \cdot t_{slab}$ $A_{con\_n} = 98.485 in^2$

$A_{total\_n} := A_{girder} + A_{con\_n}$ $A_{total\_n} = 173.662 in^2$

$$NA_n := \frac{A_{fc}\cdot\left(t_{slab} + t_{haunch} - \frac{t_{fc}}{2}\right) + A_{ft}\cdot\left(D + t_{slab} + t_{haunch} + \frac{t_{ft}}{2}\right) + A_{web}\cdot\left(\frac{D}{2} + t_{slab} + t_{haunch}\right) + A_{con\_n}\cdot\frac{t_{slab}}{2}}{A_{total\_n}}$$

$NA_n = 18.8 in$

Note: Neutral is axis measured from the top of concrete slab

$$I_n := \frac{b_{fc}\cdot t_{fc}^3}{12} + \left[A_{fc}\cdot\left(NA_n - t_{slab} - t_{haunch} + \frac{t_{fc}}{2}\right)^2\right] \ldots$$
$$+ \frac{b_{ft}\cdot t_{ft}^3}{12} + \left[A_{ft}\cdot\left(t_{slab} + t_{haunch} + D + t_{ft} - NA_n - \frac{t_{ft}}{2}\right)^2\right] \ldots$$
$$+ \frac{t_w\cdot D^3}{12} + A_{web}\cdot\left(NA_n - t_{slab} - t_{haunch} - \frac{D}{2}\right)^2 + \frac{b_{s\_n}\cdot t_{slab}^3}{12} + A_{con\_n}\cdot\left(NA_n - \frac{t_{slab}}{2}\right)^2$$

$I_n = 8.805 \times 10^4 in^4$

Section Moduli :

$S_{slab\_n} := \frac{I_n}{NA_n}$ $S_{slab\_n} = 4.684 \times 10^3 in^3$

$y_{c\_n} := NA_n - t_{slab} - t_{haunch} + t_{fc}$ $y_{c\_n} = 8.8 in$

$S_{c\_n} := \frac{I_n}{y_{c\_n}}$ $S_{c\_n} = 1.001 \times 10^4 in^3$

$y_{t\_n} := d - y_{c\_n}$ $y_{t\_n} = 41.651 in$

$S_{t\_n} := \frac{I_n}{y_{t\_n}}$ $S_{t\_n} = 2.114 \times 10^3 in^3$

$D_{c\_n} := y_{c\_n} - t_{fc}$ $D_{c\_n} = 7.8 in$

$\frac{D_{c\_n}}{D} = 0.162$ $\frac{2D_{c\_n}}{t_w} = 43.092$

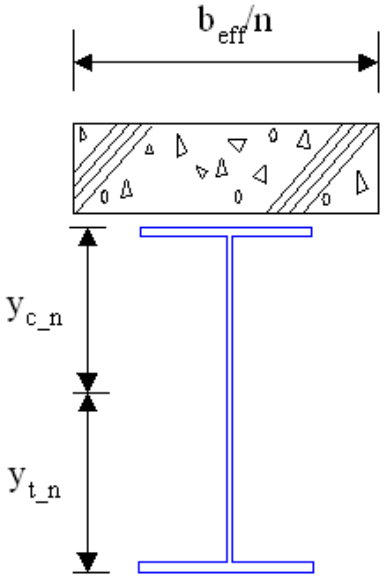

- Yield Moment (Short-term, Shored Construction) :

$M_{yt\_shortterm} := S_{t\_n} \cdot F_{yt}$ $\quad M_{yt\_shortterm} = 1.262 \times 10^4 \text{ kips} \cdot \text{ft}$

$M_{yc\_shortterm} := S_{c\_n} \cdot F_{yc}$ $\quad M_{yc\_shortterm} = 4.842 \times 10^4 \text{ kips} \cdot \text{ft}$

$$M_{y\_shortterm} := \begin{cases} M_{yt\_shortterm} & \text{if } M_{yt\_shortterm} \le M_{yc\_shortterm} \\ M_{yc\_shortterm} & \text{otherwise} \end{cases} \qquad M_{y\_shortterm} = 1.262 \times 10^4 \text{ kips} \cdot \text{ft}$$

- Concrete Stress at $M_{y\text{-Short Term (shored construction)}}$

$$f_{c\_n} := \frac{M_{y\_shortterm} \cdot NA_n}{I_n \, n} \qquad f_{c\_n} = 4.497 \text{ksi} \qquad \frac{f_{c\_n}}{f_c} = 0.918$$

Plastic Moment Capacity (Composite Section) :

NOTE: The plastic moment capacity is computed here only for reference purposes.
The design strengths are based on slender web member capacity equations

$P_{rb} := F_{yr} \cdot A_{bottom\_rebar}$ $\quad P_{rb} = 119.475 \text{kips}$

$P_{rt} := F_{yr} \cdot A_{top\_rebar}$ $\quad P_{rt} = 79.65 \text{kips}$

$P_s := 0.85 \cdot f_c \cdot b_{slab} \cdot t_{slab}$ $\quad P_s = 2.949 \times 10^3 \text{ kips}$

$P_c := F_{yc} \cdot A_{fc}$ $\quad P_c = 1.404 \times 10^3 \text{ kips}$

$P_t := F_{yt} \cdot A_{ft}$ $\quad P_t = 2.406 \times 10^3 \text{ kips}$

$P_w := F_{yw} \cdot A_{web}$ $\quad P_w = 1.107 \times 10^3 \text{ kips}$

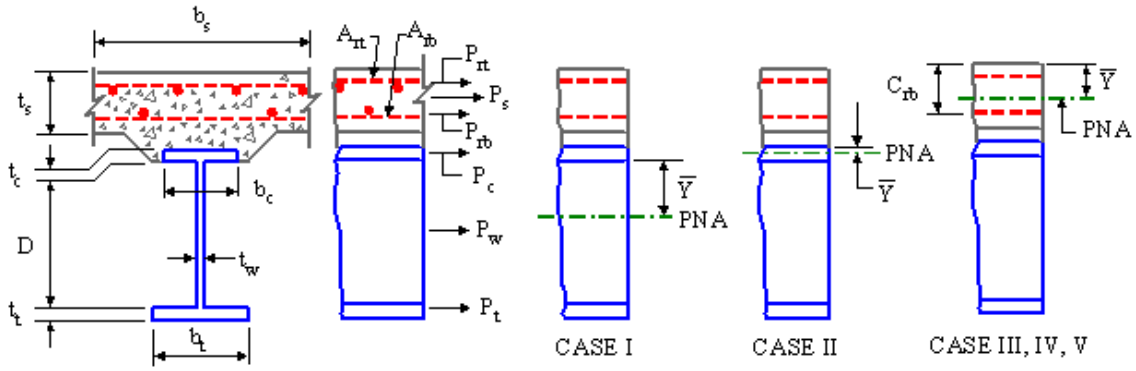

Computation of Plastic-Moment Capacity(Positive Flexure)

$$\text{Location\_of\_PNA} := \begin{cases} \text{"In Web (Case I) "} & \text{if } P_t + P_w \geq P_c + P_s + P_{rb} + P_{rt} \\ \text{otherwise} & \\ \quad \begin{cases} \text{"In Top Flange (Case II) "} & \text{if } P_t + P_w + P_c \geq P_s + P_{rb} + P_{rt} \\ \text{otherwise} & \\ \quad \begin{cases} \text{"Slab, Below Prb (Case III)"} & \text{if } P_t + P_w + P_c \geq \frac{y_{rb}}{t_{slab}} \cdot P_s + P_{rb} + P_{rt} \\ \text{otherwise} & \\ \quad \begin{cases} \text{"Slab,at Prb (Case IV)"} & \text{if } P_t + P_w + P_c + P_{rb} \geq \frac{y_{rb}}{t_{slab}} \cdot P_s + P_{rt} \\ \text{"Slab, Above Prb (Case V) "} & \text{otherwise} \end{cases} \end{cases} \end{cases} \end{cases}$$

$$\text{Location\_of\_PNA} = \text{"In Top Flange (Case II) "}$$

$$Y_{bar} := \begin{cases} \frac{D}{2} \cdot \left(\frac{P_t - P_c - P_s - P_{rt} - P_{rb}}{P_w} + 1 \right) & \text{if } P_t + P_w \geq P_c + P_s + P_{rb} + P_{rt} \\ \text{otherwise} & \\ \quad \begin{cases} \frac{t_{fc}}{2} \cdot \left(\frac{P_w + P_t - P_s - P_{rt} - P_{rb}}{P_c} + 1 \right) & \text{if } P_t + P_w + P_c \geq P_s + P_{rb} + P_{rt} \\ \text{otherwise} & \\ \quad \begin{cases} t_{slab} \cdot \frac{P_c + P_w + P_t - P_{rt} - P_{rb}}{P_s} & \text{if } P_t + P_w + P_c \geq \frac{y_{rb}}{t_{slab}} \cdot P_s + P_{rb} + P_{rt} \\ \text{otherwise} & \\ \quad \begin{cases} y_{rb} & \text{if } P_t + P_w + P_c + P_{rb} \geq \frac{y_{rb}}{t_{slab}} \cdot P_s + P_{rt} \\ t_{slab} \cdot \frac{P_{rb} + P_c + P_w + P_t - P_{rt}}{P_s} & \text{otherwise} \end{cases} \end{cases} \end{cases} \end{cases}$$

$$Y_{bar} = 0.63\text{in}$$

$$d_s := \begin{cases} \frac{t_{slab}}{2} + t_{haunch} + Y_{bar} & \text{if } P_t + P_w \geq P_c + P_s + P_{rb} + P_{rt} \\ \text{otherwise} & \\ \quad \begin{cases} \frac{t_{slab}}{2} + t_{haunch} - t_{fc} + Y_{bar} & \text{if } P_t + P_w + P_c \geq P_s + P_{rb} + P_{rt} \\ \text{"Not necessary for calculating Mp"} & \text{otherwise} \end{cases} \end{cases}$$

$$d_s = 6.63\text{in}$$

$$d_{rt} := \begin{cases} t_{slab} - y_{rt} + t_{haunch} + Y_{bar} & \text{if } P_t + P_w \geq P_c + P_s + P_{rb} + P_{rt} \\ \text{otherwise} & \\ \quad \begin{cases} t_{slab} - y_{rt} + t_{haunch} - t_{fc} + Y_{bar} & \text{if } P_t + P_w + P_c \geq P_s + P_{rb} + P_{rt} \\ Y_{bar} - y_{rt} & \text{otherwise} \end{cases} \end{cases}$$

$$d_{rt} = 7.38\text{in}$$

$$d_{rb} := \begin{cases} t_{slab} - y_{rb} + t_{haunch} + Y_{bar} & \text{if } P_t + P_w \geq P_c + P_s + P_{rb} + P_{rt} \\ \text{otherwise} \\ \quad \begin{cases} t_{slab} - y_{rb} + t_{haunch} - t_{fc} + Y_{bar} & \text{if } P_t + P_w + P_c \geq P_s + P_{rb} + P_{rt} \\ \text{otherwise} \\ \quad \begin{cases} Y_{bar} - y_{rb} & \text{if } P_t + P_w + P_c \geq \frac{y_{rb}}{t_{slab}} \cdot P_s + P_{rb} + P_{rt} \\ \text{otherwise} \\ \quad \begin{cases} \text{"Not necessary for calculating Mp"} & \text{if } P_t + P_w + P_c + P_{rb} \geq \frac{y_{rb}}{t_{slab}} \cdot P_s + P_{rt} \\ y_{rb} - Y_{bar} & \text{otherwise} \end{cases} \end{cases} \end{cases} \end{cases}$$

$d_{rb} = 4.38\text{in}$

$$d_c := \begin{cases} Y_{bar} - \frac{t_{fc}}{2} & \text{if } P_t + P_w \geq P_c + P_s + P_{rb} + P_{rt} \\ \text{otherwise} \\ \quad \begin{cases} \text{"Not necessary for calculating Mp"} & \text{if } P_t + P_w + P_c \geq P_s + P_{rb} + P_{rt} \\ t_{slab} + t_{haunch} - \frac{t_{fc}}{2} - Y_{bar} & \text{otherwise} \end{cases} \end{cases}$$

$d_c = \text{"Not necessary for calculating Mp"}$

$$d_w := \begin{cases} \text{"Not necessary for calculating Mp"} & \text{if } P_t + P_w \geq P_c + P_s + P_{rb} + P_{rt} \\ \text{otherwise} \\ \quad \begin{cases} \frac{D}{2} + t_{fc} - Y_{bar} & \text{if } P_t + P_w + P_c \geq P_s + P_{rb} + P_{rt} \\ t_{slab} + t_{haunch} - Y_{bar} + \frac{D}{2} & \text{otherwise} \end{cases} \end{cases}$$

$d_w = 24.401\text{in}$

$$d_t := \begin{cases} D - Y_{bar} + \frac{t_{ft}}{2} & \text{if } P_t + P_w \geq P_c + P_s + P_{rb} + P_{rt} \\ \text{otherwise} \\ \quad \begin{cases} D + t_{fc} - Y_{bar} + \frac{t_{ft}}{2} & \text{if } P_t + P_w + P_c \geq P_s + P_{rb} + P_{rt} \\ t_{slab} + t_{haunch} - Y_{bar} + D + \frac{t_{ft}}{2} & \text{otherwise} \end{cases} \end{cases}$$

$d_t = 49.126\text{in}$

$$M_p := \begin{cases} \frac{P_w}{2\cdot D}\cdot\left[Y_{bar}^{\,2} + (D - Y_{bar})^2\right] + P_s\cdot d_s + P_{rt}\cdot d_{rt} + P_{rb}\cdot d_{rb} + P_c\cdot d_c + P_t\cdot d_t & \text{if } P_t + P_w \geq P_c + P_s + P_{rb} + P_{rt} \\ \text{otherwise} \\ \quad \frac{P_c}{2\cdot t_{fc}}\cdot\left[Y_{bar}^{\,2} + (t_{fc} - Y_{bar})^2\right] + P_s\cdot d_s + P_{rt}\cdot d_{rt} + P_{rb}\cdot d_{rb} + P_w\cdot d_w + P_t\cdot d_t & \text{if } P_t + P_w + P_c \geq P_s + P_{rb} + P_{rt} \\ \quad \text{otherwise} \\ \quad\quad \frac{Y_{bar}^{\,2}\cdot P_s}{2\cdot t_{slab}} + P_{rt}\cdot d_{rt} + P_{rb}\cdot d_{rb} + P_c\cdot d_c + P_w\cdot d_w + P_t\cdot d_t & \text{if } P_t + P_w + P_c \geq \frac{y_{rb}}{t_{slab}}\cdot P_s + P_{rb} + P_{rt} \\ \quad\quad \text{otherwise} \\ \quad\quad\quad \frac{Y_{bar}^{\,2}\cdot P_s}{2\cdot t_{slab}} + P_{rt}\cdot d_{rt} + P_c\cdot d_c + P_w\cdot d_w + P_t\cdot d_t & \text{if } P_t + P_w + P_c + P_{rb} \geq \frac{y_{rb}}{t_{slab}}\cdot P_s + P_{rt} \\ \quad\quad\quad \frac{Y_{bar}^{\,2}\cdot P_s}{2\cdot t_{slab}} + P_{rt}\cdot d_{rt} + P_{rb}\cdot d_{rb} + P_c\cdot d_c + P_w\cdot d_w + P_t\cdot d_t & \text{otherwise} \end{cases}$$

$M_p = 1.386\times 10^4$ kips·ft

Unshored Composite Section Properties :

Yield Moment (unshored) associated with STRENGTH I

Read analysis results of factored flanges stresses.

$f_{tf\_si} :=$ $f_{bf\_si} :=$

$\text{length} := f_{tf\_si}^{\langle \text{cols}(f_{tf\_si})-3\rangle}$

$fb_{tf} := f_{tf\_si}^{\langle \text{cols}(f_{tf\_si})-2\rangle}$ $fl_{tf} := f_{tf\_si}^{\langle \text{cols}(f_{tf\_si})-1\rangle}$

$fb_{bf} := f_{bf\_si}^{\langle \text{cols}(f_{bf\_si})-2\rangle}$ $fl_{bf} := f_{bf\_si}^{\langle \text{cols}(f_{bf\_si})-1\rangle}$

Top flange stresses along the entire normalized length (psi):

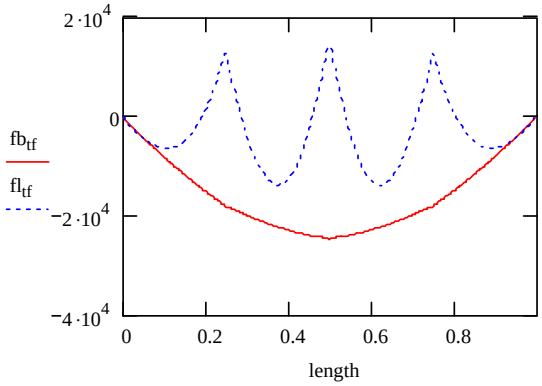

Bottom flange stresses along the entire normalized length (psi):

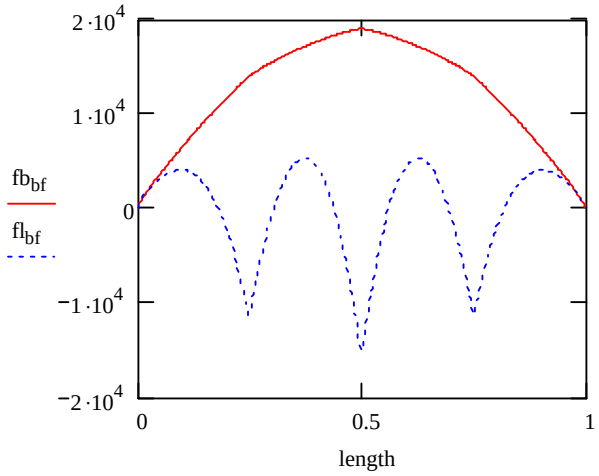

$i := 180..269$

Girder stresses (psi) within the unbraced length adjacent to mid-span:

$fb\_Lb\_length_i := length_i$ $\quad fb_{tf\_Lb_i} := fb_{tf_i}$ $\quad fl_{tf\_Lb_i} := fl_{tf_i}$

Top flange stresses within the unbraced length adjacent to mid-span:

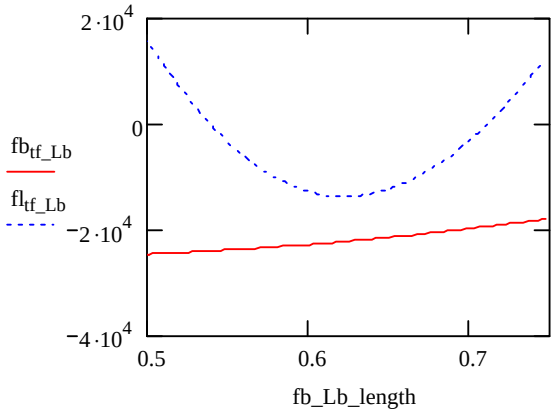

$f_{D1c} := \min(fb_{tf\_Lb})$ $\quad f_{D1c} = -2.47 \times 10^4$

$fb_{bf\_Lb_i} := fb_{bf_i}$ $\quad fl_{bf\_Lb_i} := fl_{bf_i}$

Bottom flange stresses within the unbraced length adjacent to mid-span:

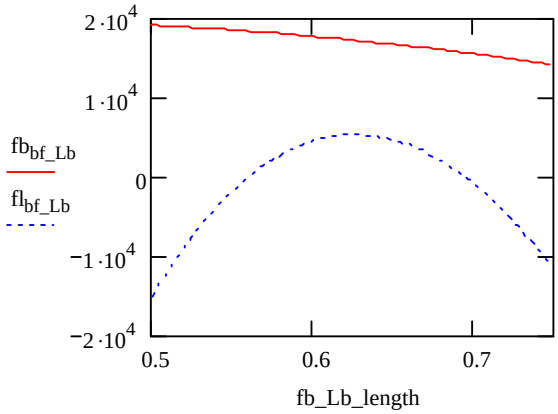

$f_{D1t} := \max(fb_{bf\_Lb})$ $\quad f_{D1t} = 1.91 \times 10^4$

$f_{D1t} := \frac{|f_{D1t}|}{1000}\,ksi$ $f_{D1c} := \frac{|f_{D1c}|}{1000}\,ksi$ $M_{D2} := 0\,kips\cdot ft$

$f_{D1t} = 19.1\,ksi$ $f_{D1c} = 24.7\,ksi$

$M_{D1t} := f_{D1t}\cdot S_t$ $M_{D1c} := f_{D1c}\cdot S_c$

$M_{D1t} = 2.695\times 10^3\,kips\cdot ft$ $M_{D1c} = 2.753\times 10^3\,kips\cdot ft$

Tension Flange :

$M_{ADt} := \left(F_{yt} - \frac{M_{D1t}}{S_t} - \frac{M_{D2}}{S_{t\_3n}}\right)\cdot S_{t\_n}$ $M_{ADt} = 9.254\times 10^3\,kips\cdot ft$

$M_{yt} := M_{D1t} + M_{D2} + M_{ADt}$ $M_{yt} = 1.195\times 10^4\,kips\cdot ft$

Compression Flange :

$M_{ADc} := \left(F_{yc} - \frac{M_{D1c}}{S_c} - \frac{M_{D2}}{S_{c\_3n}}\right)\cdot S_{c\_n}$ $M_{ADc} = 2.783\times 10^4\,kips\cdot ft$

$M_{yc} := M_{D1c} + M_{D2} + M_{ADc}$ $M_{yc} = 3.058\times 10^4\,kips\cdot ft$

$M_{AD} := \min(M_{ADt}, M_{ADc})$ $M_{AD} = 9.254\times 10^3\,kips\cdot ft$

$M_{y\_unshored} := \min(M_{yt}, M_{yc})$ $M_{y\_unshored} = 1.195\times 10^4\,kips\cdot ft$

Concrete Stress at First Yield (unshored)

$f_{conc\_composite\_unshored\_at\_My} := \left(\frac{M_{D2}}{S_{slab\_3n}\cdot 3n} + \frac{M_{AD}}{S_{slab\_n}\cdot n}\right)$ $f_{conc\_composite\_unshored\_at\_My} = 3.298\,ksi$

$\frac{f_{conc\_composite\_unshored\_at\_My}}{f_c} = 0.673$

Shape Factor :

$\frac{M_p}{M_{y\_unshored}} = 1.159$ $\frac{M_p}{M_{y\_shortterm}} = 1.098$ $\frac{M_p}{M_{y\_longterm}} = 1.174$

Flange Hybrid Strength Reduction Factor (Composite Girder) :

NOTE: The NA is assumed to be located in the web and is assumed to be closest to the top flange

$f_{c\_composite\_unshored\_at\_My} := \left(\frac{M_{D2}}{S_{c\_3n}} + \frac{M_{AD}}{S_{c\_n}} + \frac{M_{D1c}}{S_c}\right)$ $f_{c\_composite\_unshored\_at\_My} = 35.8\,ksi$

$f_{t\_composite\_unshored\_at\_My} := \left(\frac{M_{D2}}{S_{t\_3n}} + \frac{M_{AD}}{S_{t\_n}} + \frac{M_{D1t}}{S_t}\right)$ $f_{t\_composite\_unshored\_at\_My} = 71.63\,ksi$

$D_{c\_yield} := d\cdot\frac{f_{c\_composite\_unshored\_at\_My}}{f_{c\_composite\_unshored\_at\_My} + f_{t\_composite\_unshored\_at\_My}} - t_{fc}$ $D_{c\_yield} = 15.812\,in$

$D_{n\_yield} := \max(D - D_{c\_yield}, D_{c\_yield})$ $D_{n\_yield} = 32.25in$ $\frac{D_{c\_yield}}{D} = 0.329$ $\frac{2D_{c\_yield}}{t_w} = 87.357$

First_Yield_at := "Bottom Flange" if $M_{yt} < M_{yc}$ "Top Flange" otherwise First_Yield_at = "Bottom Flange"

$f_n := F_{yt}$ $f_n = 71.63ksi$

$\rho := \min\left(\frac{F_{yw}}{f_n}, 1.0\right)$ $\rho = 0.888$ $A_{fn} := A_{ft}$

$\beta := \frac{2 \cdot D_{n\_yield} \cdot t_w}{A_{fn}}$ $\beta = 0.695$

$R_{h\_comp} := \frac{12 + \beta \cdot (3 \cdot \rho - \rho^3)}{12 + 2 \cdot \beta}$ $R_{h\_comp} = 0.9981$

Constructibility Check, Noncomposite Girder(STREGNTH IV)

Construction load stresses are factored, load factor = 1.5

G3 top flange

$\phi_f := 1.0$ $R_b := 1$ **since bend buckling is prevented when checking constructibility**

$f_{tf\_siv\_1st} :=$ $f_{tf\_siv\_2nd} :=$

$length := f_{tf\_siv\_1st}^{\langle cols(f_{tf\_siv\_1st})-3 \rangle}$ $fb_{tf\_1st} := f_{tf\_siv\_1st}^{\langle cols(f_{tf\_siv\_1st})-2 \rangle}$ $fl_{tf\_1st} := f_{tf\_siv\_1st}^{\langle cols(f_{tf\_siv\_1st})-1 \rangle}$

$fb_{tf\_2nd} := f_{tf\_siv\_2nd}^{\langle cols(f_{tf\_siv\_2nd})-2 \rangle}$ $fl_{tf\_2nd} := f_{tf\_siv\_2nd}^{\langle cols(f_{tf\_siv\_2nd})-1 \rangle}$

Top flange stresses (psi) along the nomralized length :

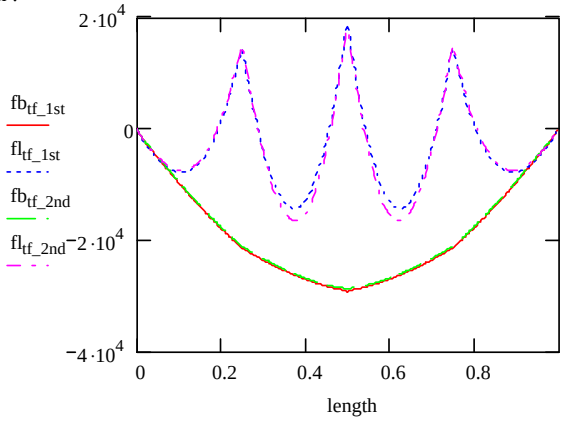

Girder stresses within the unbraced length adjacent to mid-span:

$i := 180..269$ $\quad fb_{tf\_1st\_Lb_i} := fb_{tf\_1st_i}$ $\quad fl_{tf\_1st\_Lb_i} := fl_{tf\_1st_i}$

$fb_{tf\_2nd\_Lb_i} := fb_{tf\_2nd_i}$ $\quad fl_{tf\_2nd\_Lb_i} := fl_{tf\_2nd_i}$

Top flange stresses (psi) within the unbraced length:

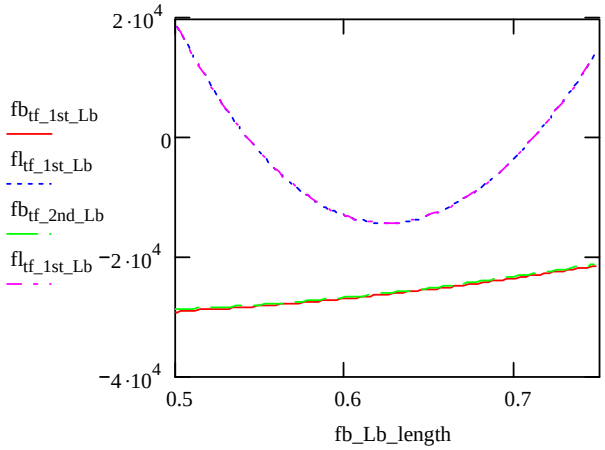

Moment Gradient Modifier for LTB(Cb) :

$f_1 := |-21.5|\ ksi$ $\quad f_2 := \frac{|\min(fb_{tf\_1st\_Lb})|}{1000} ksi$

$f_1 = 21.5ksi$ $\quad f_2 = 29.2ksi$

$$C_b := \begin{cases} 1.75 - 1.05\left(\frac{f_1}{f_2}\right) + 0.3\left(\frac{f_1}{f_2}\right)^2 & \text{if } 1.75 - 1.05\left(\frac{f_1}{f_2}\right) + 0.3\left(\frac{f_1}{f_2}\right)^2 \le 2.3 \\ 2.3 & \text{otherwise} \end{cases}$$

$C_b = 1.14$

Estimation of Flange Second Order Lateral Bending Stress:

$f_{b1} := \frac{|\min(fb_{tf\_1st\_Lb})|}{1000} \cdot ksi$ $\quad f_{l1} := \frac{|\max(fl_{tf\_1st\_Lb})|}{1000} \cdot ksi$ $\quad f_{b1} = 29.2ksi$ $\quad f_{l1} = 19ksi$

i) Based on k=1.0 $\quad k := 1.0$

$\lambda := \frac{k \cdot L_b}{r_t}$ $\quad \lambda = 42.382$

$F_{cr} := \frac{C_b \cdot R_b \cdot \pi^2 \cdot E}{\lambda^2}$ $\quad F_{cr} = 181.58ksi$ $\quad \frac{1}{1 - \frac{f_{b1}}{F_{cr}}} = 1.192$ $\quad \frac{f_{l1}}{1 - \frac{f_{b1}}{F_{cr}}} = 22.64ksi$

ii) Based on k=0.5 $\quad k := 0.5$

$\lambda := \frac{k \cdot L_b}{r_t}$ $\quad \lambda = 21.191$

$F_{cr0.5} := \frac{C_b \cdot R_b \cdot \pi^2 \cdot E}{\lambda^2}$ $\quad F_{cr0.5} = 726.32ksi$ $\quad \frac{1}{1 - \frac{f_{b1}}{F_{cr0.5}}} = 1.042$ $\quad \frac{f_{l1}}{1 - \frac{f_{b1}}{F_{cr0.5}}} = 19.796ksi$

$f_{b2} := \frac{\left|\min\left(fb_{tf\_2nd\_Lb}\right)\right|}{1000}\cdot ksi$ $f_{l2} := \frac{\left|\max\left(fl_{tf\_2nd\_Lb}\right)\right|}{1000}\cdot ksi$

$f_{b2} = 28.8ksi$ $f_{l2} = 18.1ksi$ Actual second-order amplification: $\frac{f_{l2}}{f_{l1}} = 0.953$

Maximum Lateral Bending Stress Limit

$f_{l2} = 18.1ksi$ $\frac{F_{yc}}{1.67} = 34.772ksi$

$Lateral\_bending\_stress\_ratio := \frac{f_{l2}}{\frac{F_{yc}}{1.67}}$ $Lateral\_bending\_stress\_ratio = 0.521$

Yielding Limit

$f_{b2} + f_{l2} = 46.9ksi$ $\phi_f \cdot R_{h\_noncomp} \cdot F_{yc} = 58.07ksi$

$Yielding\_ratio := \frac{f_{b2} + f_{l2}}{\phi_f \cdot R_{h\_noncomp} \cdot F_{yc}}$ $Yielding\_ratio = 0.808$

Strength Limit

Local Buckling Resistance :

$F_{yr} := 0.7 \cdot F_{yc}$

$\lambda_f := \frac{b_{fc}}{2 \cdot t_{fc}}$ $\lambda_{pf} := 0.38 \cdot \sqrt{\frac{E}{F_{yc}}}$ $\lambda_{rf} := 0.56 \cdot \sqrt{\frac{E}{F_{yr}}}$

$$F_{nc\_FLB} := \begin{cases} R_b \cdot R_{h\_noncomp} \cdot F_{yc} & \text{if } \lambda_f \le \lambda_{pf} \\ \left[1 - \left(1 - \frac{F_{yr}}{R_{h\_noncomp} \cdot F_{yc}}\right) \cdot \left(\frac{\lambda_f - \lambda_{pf}}{\lambda_{rf} - \lambda_{pf}}\right)\right] \cdot R_b \cdot R_{h\_noncomp} \cdot F_{yc} & \text{if } \lambda_{pf} < \lambda_f \le \lambda_{rf} \\ \frac{0.36 \cdot R_b \cdot E}{\left(\frac{b_{fc}}{2 \cdot t_{fc}}\right)^2} & \text{otherwise} \end{cases}$$

$F_{nc\_FLB} = 48.37ksi$

Lateral Torsional Buckling Resistance :

$L_p := 1.0 \cdot r_t \cdot \sqrt{\frac{E}{F_{yc}}}$ $L_r := \pi \cdot r_t \cdot \sqrt{\frac{E}{F_{yr}}}$

$$F_{nc\_LTB} := \begin{cases} R_b \cdot R_{h\_noncomp} \cdot F_{yc} & \text{if } L_b \le L_p \\ \min\left[C_b \cdot \left[1 - \left(1 - \frac{F_{yr}}{R_{h\_noncomp} \cdot F_{yc}}\right) \cdot \left(\frac{L_b - L_p}{L_r - L_p}\right)\right] \cdot R_b \cdot R_{h\_noncomp} \cdot F_{yc}, R_b \cdot R_{h\_noncomp} \cdot F_{yc}\right] & \text{if } L_p < L_b \le L_r \\ \text{otherwise} \\ \quad \begin{cases} F_{cr} & \text{if } F_{cr} \le R_b \cdot R_{h\_noncomp} \cdot F_{yc} \\ R_b \cdot R_{h\_noncomp} \cdot F_{yc} & \text{otherwise} \end{cases} \end{cases}$$

$F_{nc\_LTB} = 58.07ksi$

$$\text{Controling\_Strength} := \begin{cases} \text{"Flange Local Buckling"} & \text{if } F_{nc\_FLB} \le F_{nc\_LTB} \\ \text{"Lateral Torsional Buckling"} & \text{otherwise} \end{cases}$$

$\text{Controling\_Strength} = \text{"Flange Local Buckling"}$

$f_{b2} + \frac{f_{l2}}{3} = 34.83\text{ksi}$ $\quad F_{nc} := \min\left(F_{nc\_LTB}, F_{nc\_FLB}\right)$ $\quad \phi_f \cdot F_{nc} = 48.37\text{ksi}$

$$\text{Strength\_ratio} := \frac{f_{b2} + \frac{f_{l2}}{3}}{\phi_f \cdot F_{nc}} \qquad \text{Strength\_ratio} = 0.72$$

Web bend buckling limit

$k := \frac{9}{\left(\frac{D_c}{D}\right)^2}$ $\quad k = 28.125$ $\quad F_{crw} := 0.9 \cdot E \cdot \frac{k}{\left(\frac{D}{t_w}\right)^2}$ $\quad \phi_f \cdot F_{crw} = 41.64\text{ksi}$ $\quad f_{b2} = 28.8\text{ksi}$

$$\text{Web\_bend\_buckling\_ratio} := \frac{f_{b2}}{\phi_f \cdot F_{crw}} \qquad \text{Web\_bend\_buckling\_ratio} = 0.69$$

G3 bottom flange

$f_{bf\_siv\_2nd} :=$

$\text{length} := f_{bf\_siv\_2nd}^{\langle \text{cols}(f_{bf\_siv\_2nd})-3 \rangle}$ $\quad fb_{bf\_2nd} := f_{bf\_siv\_2nd}^{\langle \text{cols}(f_{bf\_siv\_2nd})-2 \rangle}$ $\quad fl_{bf\_2nd} := f_{bf\_siv\_2nd}^{\langle \text{cols}(f_{bf\_siv\_2nd})-1 \rangle}$

Bottom flange stresses (psi) along the normalized length:

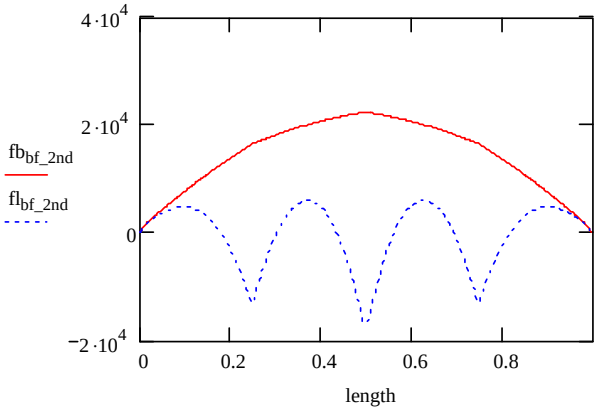

Girder stresses along the unbraced length adjacent to mid-span:

$fb\_Lb\_length_i := \text{length}_i$ $\quad fb_{bf\_2nd\_Lb_i} := fb_{bf\_2nd_i}$ $\quad fl_{bf\_2nd\_Lb_i} := fl_{bf\_2nd_i}$

Bottom flange stresses (psi) within the unbraced length:

$$f_{b2} := \frac{\left|\max\left(fb_{bf\_2nd\_Lb}\right)\right|}{1000}\cdot ksi$$

$f_{b2} = 22.3ksi$

$$f_{l2} := \frac{\left|\min\left(fl_{bf\_2nd\_Lb}\right)\right|}{1000}\cdot ksi$$

$f_{l2} = 18ksi$

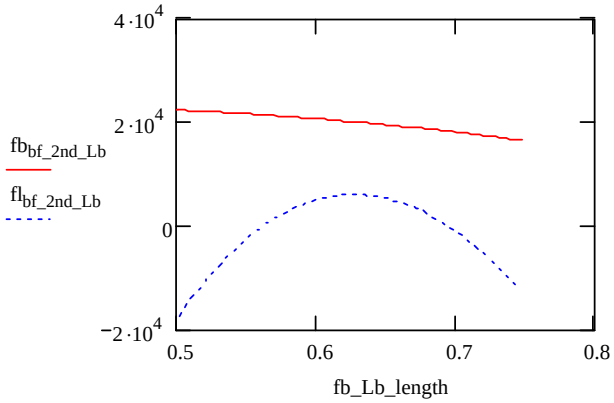

Maximum Lateral Bending Stress Limit

$f_{l2} = 18ksi$ $\qquad \frac{F_{yt}}{1.67} = 42.892ksi$

$$Lateral\_bending\_stress\_ratio := \frac{f_{l2}}{\frac{F_{yt}}{1.67}}$$

$Lateral\_bending\_stress\_ratio = 0.42$

Yielding Limit

$f_{b2} + f_{l2} = 40.3ksi$ $\qquad \phi_f \cdot R_{h\_noncomp} \cdot F_{yt} = 71.63ksi$

$$Yielding\_ratio := \frac{f_{b2} + f_{l2}}{\phi_f \cdot R_{h\_noncomp} \cdot F_{yt}}$$

$Yielding\_ratio = 0.563$

Strength I Check

Construction stresses are based on factored construction loads, load factor = 1.25
Lane and truck load stresses are unfactored, but the dynamic allowance of 1.33 is included in the calcuation of the truck load stresses

G3 Bottom flange

$$fb_{bf\_noncomp} := f_{bf\_si}^{\langle cols(f_{bf\_si})-2\rangle} \qquad fl_{bf\_noncomp} := f_{bf\_si}^{\langle cols(f_{bf\_si})-1\rangle}$$

Factored noncomposite stresses along the entire normalized length:

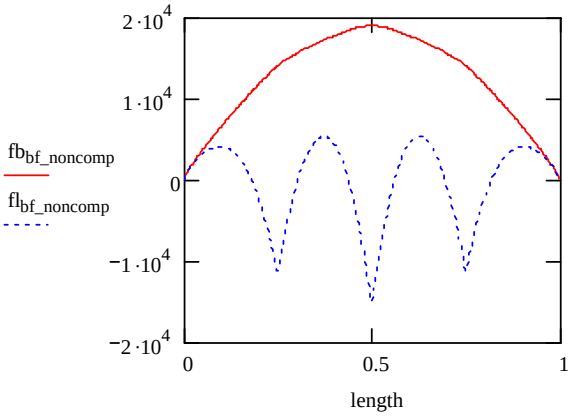

Read analysis results of unfactored composite stresses:

$f_{bf\_lane} :=$ $f_{bf\_truck} :=$

$length := f_{bf\_lane}^{\langle cols(f_{bf\_lane})-3 \rangle}$ $fb_{bf\_lane} := f_{bf\_lane}^{\langle cols(f_{bf\_lane})-2 \rangle}$ $fl_{bf\_lane} := f_{bf\_lane}^{\langle cols(f_{bf\_lane})-1 \rangle}$

$fb_{bf\_truck} := f_{bf\_truck}^{\langle cols(f_{bf\_truck})-2 \rangle}$ $fl_{bf\_truck} := f_{bf\_truck}^{\langle cols(f_{bf\_truck})-1 \rangle}$

Bottom flange stresses along the entire normalized length:

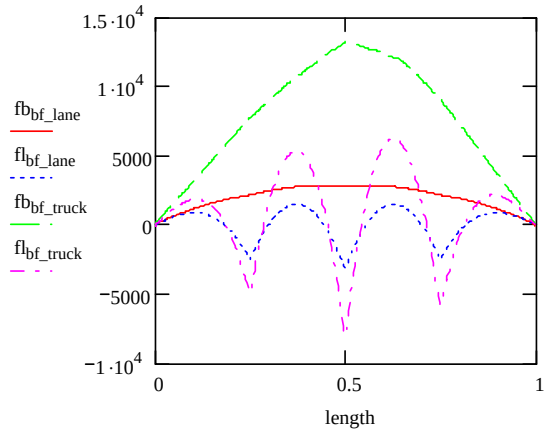

Factored bottom flange stresses relating to Strength I load combination:

$fb_{bf} := fb_{bf\_noncomp} + 1.75 \left(fb_{bf\_lane} + fb_{bf\_truck} \right)$ $fl_{bf} := fl_{bf\_noncomp} + 1.75 \left(fl_{bf\_lane} + fl_{bf\_truck} \right)$

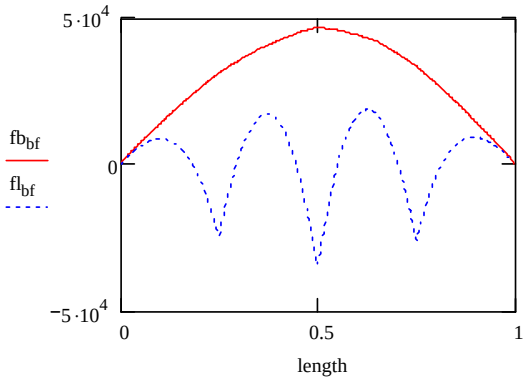

Bottom flange stresses within the unbraced length adjacent o mid-span

$fb\_Lb\_length_i := length_i$ $fb_{bf\_Lb_i} := fb_{bf_i}$ $fl_{bf\_Lb_i} := fl_{bf_i}$

Maximum major-axis and lateral bending stresses within the unbraced length

Maximum major-axis and lateral bending stresses within the unbraced length

$$f_b := \frac{\left|\max\left(fb_{bf\_Lb}\right)\right|}{1000}\cdot ksi$$

$f_b = 47.065ksi$

$$f_l := \frac{\left|\min\left(fl_{bf\_Lb}\right)\right|}{1000}\cdot ksi$$

$f_l = 34.403ksi$

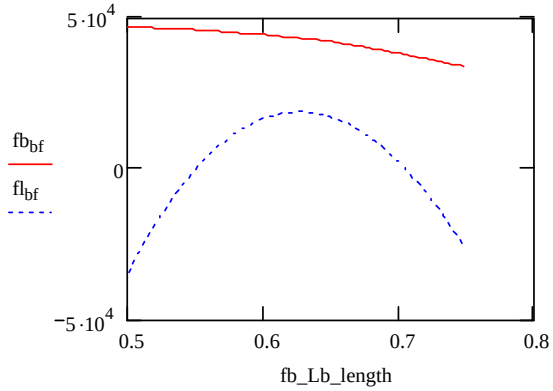

Lateral Bending Stress Limit

$f_l = 34.4ksi$

$$\frac{F_{yt}}{1.67} = 42.892ksi$$

$$Lateral\_bending\_stress\_ratio := \frac{f_l}{\frac{F_{yt}}{1.67}}$$

$Lateral\_bending\_stress\_ratio = 0.8$

Strength Limit

$$f_b + \frac{f_l}{3} = 58.53ksi$$

$$\phi_f \cdot R_{h\_comp} \cdot F_{yt} = 71.5ksi$$

$$Strength\_ratio := \frac{f_b + \frac{f_l}{3}}{\phi_f \cdot R_{h\_comp} \cdot F_{yt}}$$

$Strength\_ratio = 0.819$

G3 Top flange

Factored noncomposite stresses (psi) along the entire normalized length:

$$fb_{tf\_noncomp} := f_{tf\_si}^{\langle cols(f_{tf\_si})-2\rangle} \qquad fl_{tf\_noncomp} := f_{tf\_si}^{\langle cols(f_{tf\_si})-1\rangle}$$

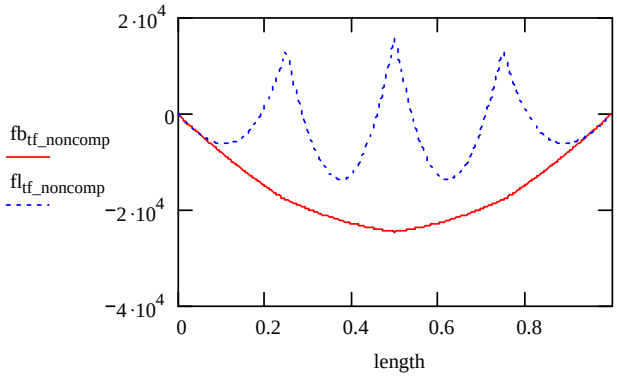

Read analysis results of
unfactored composite stresses:

$f_{tf\_lane} :=$

$f_{tf\_truck} :=$

$$length := f_{tf\_lane}^{\langle cols(f_{tf\_lane})-3\rangle}$$

$$fb_{tf\_lane} := f_{tf\_lane}^{\langle cols(f_{tf\_lane})-2\rangle} \qquad fl_{tf\_lane} := f_{tf\_lane}^{\langle cols(f_{tf\_lane})-1\rangle}$$

$$fb_{tf\_truck} := f_{tf\_truck}^{\langle cols(f_{tf\_truck})-2\rangle} \qquad fl_{tf\_truck} := f_{tf\_truck}^{\langle cols(f_{tf\_truck})-1\rangle}$$

Unfactored top flange stresses (psi) along the entire normalized length:

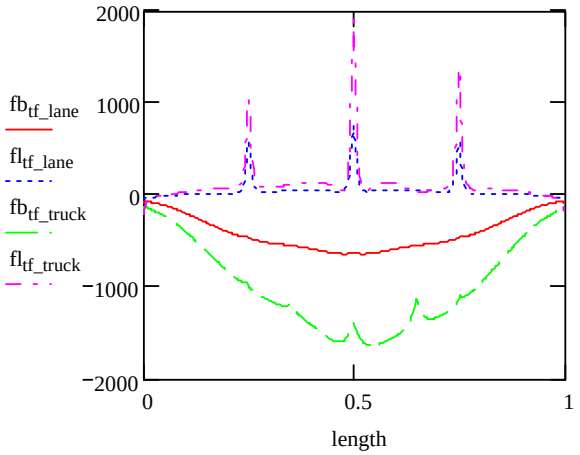

Factored top flange stresses relating to Strength I load combination:

$fb_{tf} := fb_{tf\_noncomp} + 1.75 \cdot (fb_{tf\_lane} + fb_{tf\_truck})$ $fl_{tf} := fl_{tf\_noncomp} + 1.75 \cdot (fl_{tf\_lane} + fl_{tf\_truck})$

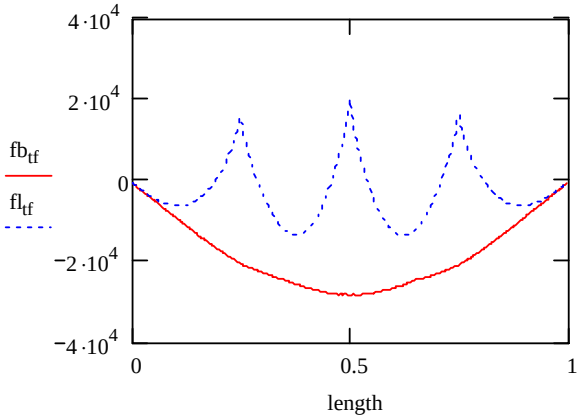

Factored top fflange stresses within the unbraced length adjacent to mid-span

$fb\_Lb\_length_i := length_i$ $fb_{tf\_Lb_i} := fb_{tf_i}$ $fl_{tf\_Lb_i} := fl_{tf_i}$

Maximum major-axis and lateral bending stresses within the unbraced length

$$f_b := \frac{|\min(fb_{tf\_Lb})|}{1000} \cdot ksi$$

$f_b = 28.264 ksi$

$$f_l := \frac{|\max(fl_{tf\_Lb})|}{1000} \cdot ksi$$

$f_l = 20.159 ksi$

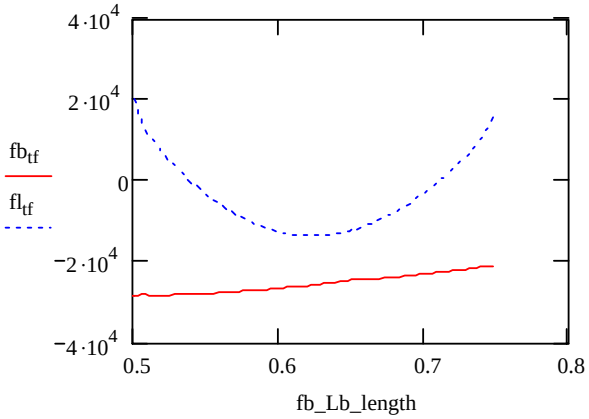

Strength Limit

$f_b = 28.264\text{ksi}$ $\phi_f \cdot R_{h\_comp} \cdot F_{yc} = 57.961\text{ksi}$

$$Strength\_ratio := \frac{f_b}{\phi_f \cdot R_{h\_comp} \cdot F_{yc}}$$ $Strength\_ratio = 0.488$

Service II Check

G3 Bottom flange

Factored bottom flange stresses relating to Serive I load combination:

$fb_{bf} := fb_{bf\_noncomp} \cdot 0.8 + 1.30 \cdot (fb_{bf\_lane} + fb_{bf\_truck})$ $fl_{bf} := fl_{bf\_noncomp} \cdot 0.8 + 1.30 \cdot (fl_{bf\_lane} + fl_{bf\_truck})$

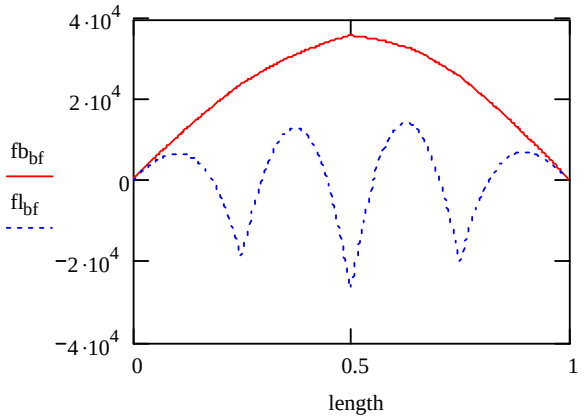

Bottom flange stresses within the unbraced length adjacent o mid-span

$fb\_Lb\_length_i := length_i$ $fb_{bf\_Lb_i} := fb_{bf_i}$ $fl_{bf\_Lb_i} := fl_{bf_i}$

Maximum major-axis and lateral bending stresses within the unbraced length

$$f_b := \frac{|\max(fb_{bf\_Lb})|}{1000} \cdot \text{ksi}$$

$f_b = 36.054\text{ksi}$

$$f_l := \frac{|\min(fl_{bf\_Lb})|}{1000} \cdot \text{ksi}$$

$f_l = 26.419\text{ksi}$

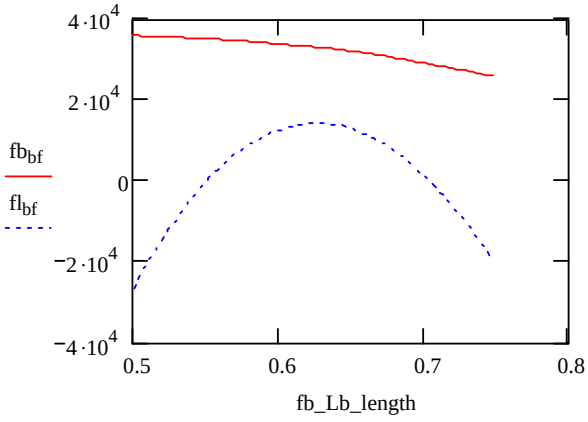

$0.95 \cdot F_{yt} = 68.048\text{ksi}$

$$Permanent\_deformation\_ratio := \frac{f_b}{0.95 \cdot F_{yt}}$$ $Permanent\_deformation\_ratio = 0.53$

G3 Top flange

Factored top flange stresses relating to Serive I load combination:

$fb_{tf} := fb_{tf\_noncomp} \cdot 0.8 + 1.30 \cdot (fb_{tf\_lane} + fb_{tf\_truck})$ $fl_{tf} := fl_{tf\_noncomp} \cdot 0.8 + 1.30 \cdot (fl_{tf\_lane} + fl_{tf\_truck})$

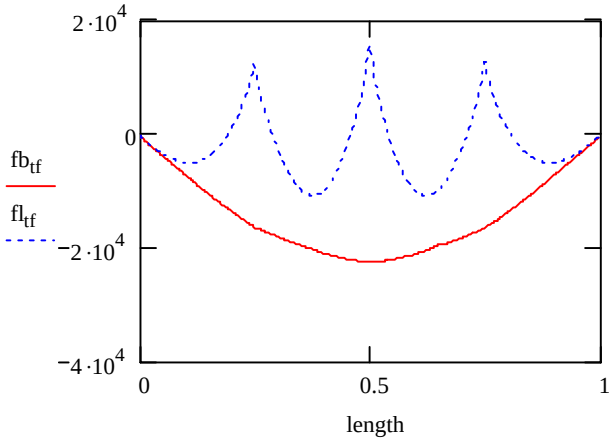

Bottom flange stresses within the unbraced length adjacent o mid-span

$fb\_Lb\_length_i := length_i$ $fb_{tf\_Lb_i} := fb_{tf_i}$ $fl_{tf\_Lb_i} := fl_{tf_i}$

Maximum major-axis and lateral bending stresses within the unbraced length

$$f_b := \frac{|\min(fb_{tf\_Lb})|}{1000} \cdot ksi$$

$f_b = 22.408 ksi$

$$f_l := \frac{|\min(fl_{bf\_Lb})|}{1000} \cdot ksi$$

$f_l = 26.419 ksi$

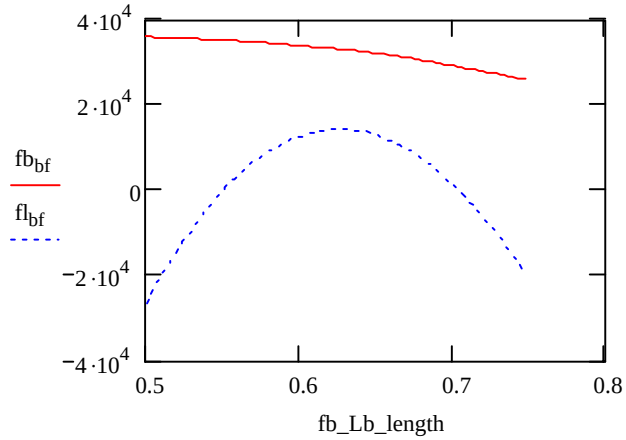

$0.95 \cdot F_{yc} = 55.166 ksi$

$$Permanent\_deformation\_ratio := \frac{f_b}{0.95 \cdot F_{yc}}$$ $Permanent\_deformation\_ratio = 0.406$

B.4 Girder Web Shear Design

Material Properties:

$F_{yw} := 50\,ksi$ $\quad E := 2.9 \cdot 10^4\,ksi$ $\quad \nu := 0.3$

Girder Dimensions:

$D := 48\,in$ $\quad t_w := 0.3125\,in$ $\quad \frac{D}{t_w} = 153.6$

$V_p := 0.58 \cdot F_{yw} \cdot D \cdot t_w$ $\quad V_p = 435\,kips$

Shear Buckling Coefficients and Elastic Shear Buckling Strength:

$$k_s(\alpha) := \begin{cases} 5 + \frac{5}{\alpha^2} & \text{if } \alpha \le 3 \\ 5 & \text{otherwise} \end{cases}$$

$$V_{cr}(\alpha) := \frac{\pi^2 \cdot E \cdot k_s(\alpha)}{12 \cdot \left(1 - \nu^2\right) \cdot \left(\frac{D}{t_w}\right)^2} \cdot D \cdot t_w$$

$$k_{ss}(\alpha) := \begin{cases} 4 + \frac{5.34}{\alpha^2} & \text{if } \alpha < 1 \\ 5.34 + \frac{4}{\alpha^2} & \text{otherwise} \end{cases}$$

$$k_{sf}(\alpha) := \begin{cases} \frac{5.34}{\alpha^2} + \frac{2.31}{\alpha} - 3.44 + 8.39 \cdot \alpha & \text{if } \alpha < 1 \\ 8.98 + \frac{5.61}{\alpha^2} - \frac{1.99}{\alpha^3} & \text{otherwise} \end{cases}$$

Shear Buckling Parameter C and Postbuckling Shear Strength V_n

$$C(\alpha) := \begin{cases} \frac{1.119}{\frac{D}{t_w}} \cdot \sqrt{E \cdot \frac{k_s(\alpha)}{F_{yw}}} & \text{if } \frac{D}{t_w} \le 1.39886 \sqrt{\frac{E \cdot k_s(\alpha)}{F_{yw}}} \\ 1 & \text{if } \frac{D}{t_w} \le 1.119 \sqrt{\frac{E \cdot k_s(\alpha)}{F_{yw}}} \\ \frac{1.5654}{\left(\frac{D}{t_w}\right)^2} \cdot \frac{E \cdot k_s(\alpha)}{F_{yw}} & \text{otherwise} \end{cases}$$

$$V_n(\alpha) := V_p \cdot \left[C(\alpha) + \frac{0.87 \cdot (1 - C(\alpha))}{\sqrt{1 + \alpha^2}} \right]$$

Plots: $\alpha := 0.35, 0.351 .. 4$ **$\alpha = d_o/D$**

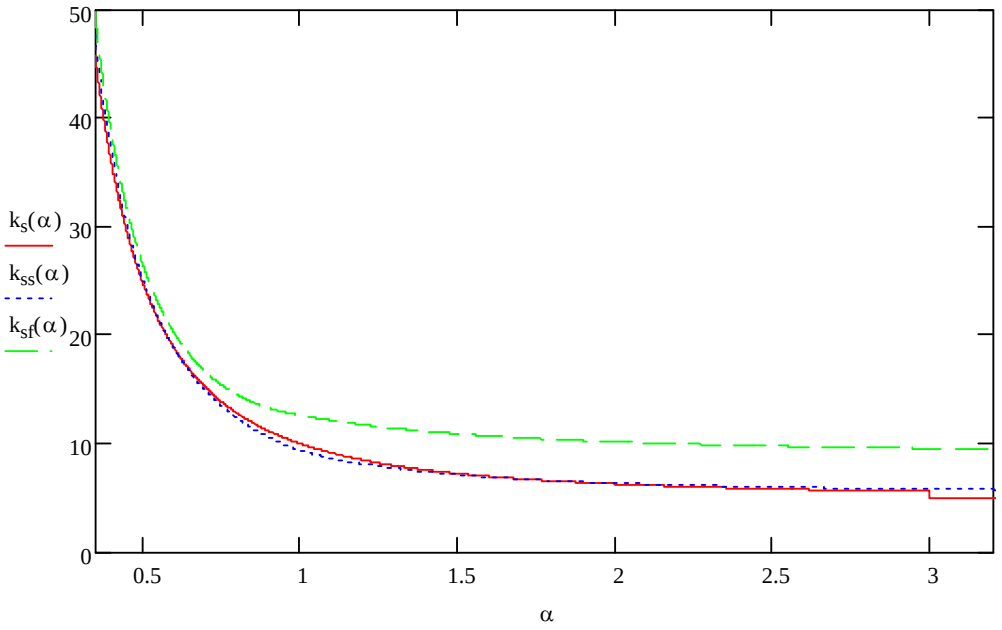

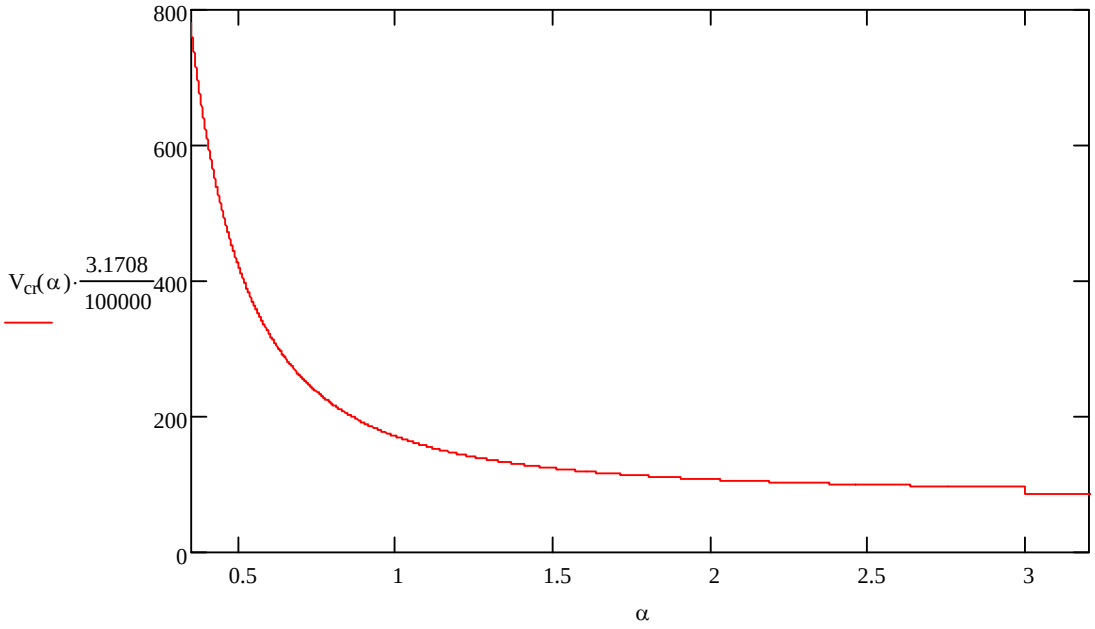

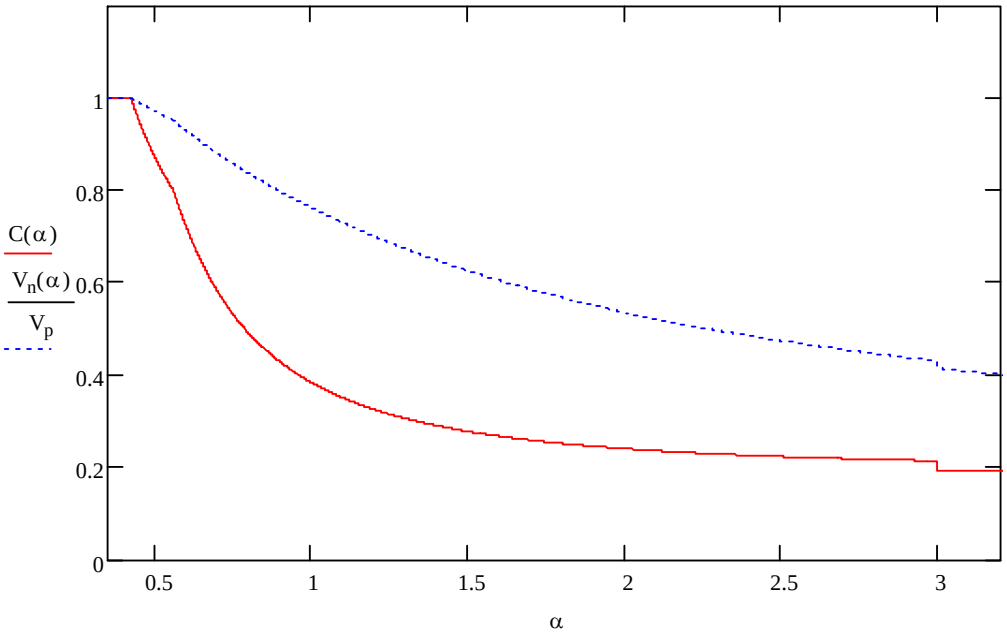
C(α)
Vn(α)
Vp
1
0.8
0.6
0.4
0.2
0
0.5
1
1.5
2
2.5
3
α

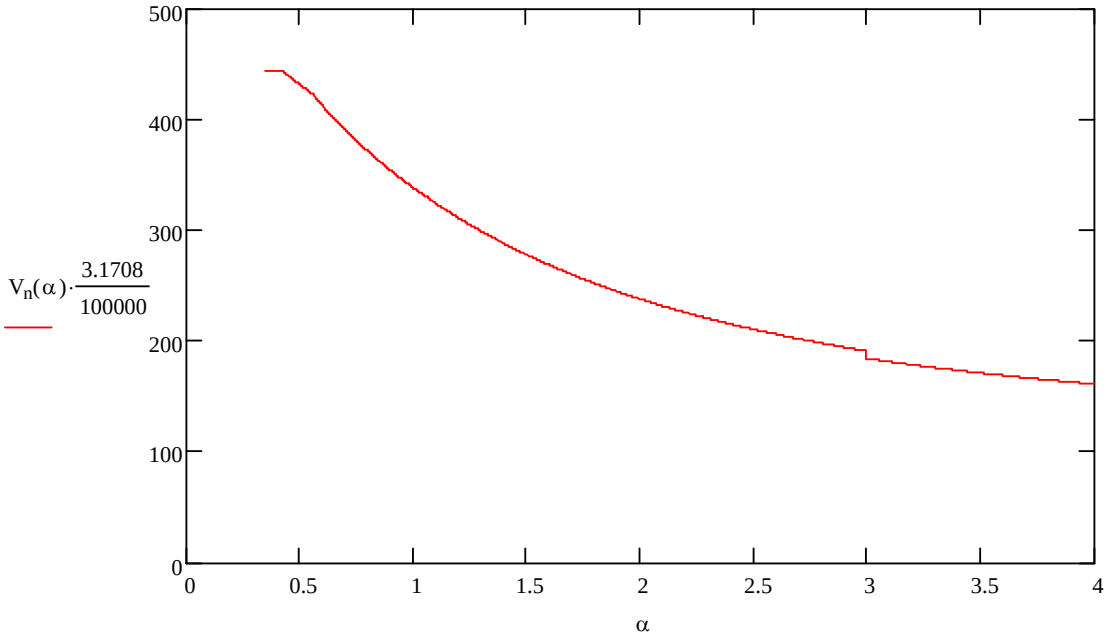
Vn(α)·3.1708/100000
500
400
300
200
100
0
0
0.5
1
1.5
2
2.5
3
3.5
4
α

Girder G3:

Estimated maximum end shears, Strength I (outside truck located at end of bridge with outside wheels over G3, inside truck located just on the midspan side of the first internal cross-frame, front axle of both trucks placed closest to the midspan, 14 ft rear axle spacing)

$V_{D1} := 98.98\,kips$

$V_{two\_lanes} := 32.28\,kips$

Influence coefficients for maximum end shear on G3 estimated at each juncture of the cross-frames and the main girders based on static equilibrium and assuming that the end torsion is resisted by a couple between G1 and G3. (G3end, G2end, G1end, G3intermed, G2intermed, G1intermed, G3mid, G2mid G1mid) = (1, 0, 0, 0.81, 0.42, 0.03, 0.57, 0.32, -0.05). Influence coefficients for wheel load positions obtained by linear interpolation between these values.

$$V_{two\_trucks} := 16\cdot kips\cdot\left(1 + 0.88 + \frac{0.75}{4} + 0.31 + 0.46 + \frac{0.51}{4} + 0.33 + 0.28 + \frac{0.23}{4} + 0.06 + 0 + 0\right)$$

$V_{two\_trucks} = 59.08\,kips$

$V_r := 1.25\cdot V_{D1} + 1.75\cdot V_{two\_lanes} + 1.75\cdot 1.33 V_{two\_trucks}$ $\quad V_r = 317.724\,kips$

Assume maximum shear at 1/4 span is 0.75 of maximum end shear $\quad 0.75\cdot V_r = 238.293\,kips$

Assume maximum shear at midspan is 0.5 of maximum end shear $\quad 0.5\cdot V_r = 158.862\,kips$

These are reasonable conservative assumptions for the Strength I shear envelope

Stiffener spacing: 1 @ 2 ft, 6 @ 3.58 ft, 2 @ 5.87 ft, 1 @ 11.74 ft $\quad \alpha = 0.5, 0.895, 1.47, 2.94$

$V_{n\_unstiffened} := C(0.5)\cdot V_p$ $\quad V_{n\_unstiffened} = 381.603\,kips$ vs 318

$V_n(0.895) = 348.192\,kips$ vs 318

$V_n(1.47) = 275.387\,kips$ vs 238

$V_n(2.94) = 189.09\,kips$ vs 199

It is expected that the maximum shear estimate used here is somewhat conservative; also, 189 is greater than the estimated shear at the middle of the panel. Therefore, the wide stiffener spacing at the middle of G3 should be ok

An upper-bound estimate for the required shear capacity at the midspan of G3 can be obtained based on the flexural capacity Mp, divided by the half-span length

$\frac{12580}{45} = 279.556$ $\qquad \frac{189}{280} = 0.675$

A more realistic estimate of the required shear capacity at the midspan on G3 can be obtained based on the V-load shear from the middle cross-frame, with three equal loads spaced at 14 ft apart applied at the middle of the bridge

$$\frac{60.5}{\frac{8.75 \cdot 2}{0.1125}} = 0.389$$

Based on this estimate, G3 sees loads of 1.0P at the outside applied positions and 1.389P at the midspan load position. After also deducting MD1 from Mp and adding the maximum D1 shear, the resulting shear in the web panel next to the midspan is

$$\frac{12580 - 2279}{62.25} \cdot 0.6945 + 98.98 (0.08 + 0.25 \cdot 0.92) = 145.608 \qquad \frac{189}{146} = 1.295 \longrightarrow \textbf{OK}$$

The resulting maximum shear in the panels with do/D = 1.47 is

$$\frac{12580 - 2279}{62.25} \cdot 1.6945 + 98.98 (0.08 + 0.5 \cdot 0.92) = 333.852 \qquad \frac{275}{334} = 0.823$$

If we assume that the majority of the outside loads are distributed to G3 at the intermediate cross-frame position the required maximum shear capacity in the panels with do/D = 1.47 is

$$\frac{12580 - 2279}{53.75} \cdot 0.6945 + 98.98 (0.08 + 0.5 \cdot 0.92) = 186.548 \qquad \frac{275}{187} = 1.471 \longrightarrow \textbf{OK}$$

The maximum required shear capacity in the panels with do/D = 0.895 is approximately

$$\frac{12580 - 2279}{62.25} \cdot 1.6945 + 98.98 = 379.382 \qquad \frac{348}{379} = 0.918$$

$$\frac{12580 - 2279}{53.75} \cdot 1.6945 + 98.98 = 423.725 \qquad \frac{348}{424} = 0.821$$

Note: The loading state toward the outside of the middle unbraced segments will likely involve combined high moment and high shear at the limit of the flexural capacity of G3; also, the end shear in G3 may approach the shear capacity of this girder as the bridge flexural capacity is appraoched. The corresponding distortions in the web of G3 should be monitored during the maximum strength test, and if a shear strength limit is apparent, additional transverse stiffeners should be bolted onto the web to increase the capacity of the bridge.

Factors that will influence whether shear or flexure controls in G3 include:

- Fyw vs Fyc, Fyt, f'c.
- tw vs other geometry
- the reduction in the maximum flexural capacity due to lateral bending of the bottom flange
- the extent of the slab that is actually effective in resisting flexure with the steel cross-section of G3
- the extent that the concrete slab acts as a large flange to increase the shear capacity of the girder
- the distribution of transverse shears from the cross-frames and the slab to G3 (note that as the G3 yields at the midspan, the transverse shears distributed to G3 will likely increase in the regions toward the ends of the girder while these transverse shears will decrease close to the midspan; this will tend to increase the internal shear at the ends of G3)

Check web shear buckling under the fatigue truck loading

Maximum end shear

$V_{fatigue\_truck} := 16 \cdot kips \cdot \left(1 + 0.73 + \frac{0.57}{4} + 0.31 + 0.50 + \frac{0.40}{4} \right)$ $V_{fatigue\_truck} = 44.52 kips$

$V_r := 98.98 kips + 0.75 \cdot 1.15 \cdot V_{fatigue\_truck}$ $V_r = 137.379 kips$

$C(0.895) \cdot V_p = 188.193 kips$ vs 137 kips → **OK**

Assume that the required shear strength at the midspan is 0.5 of that at the ends. This is expected to be a reasonable conservative approximation.

$C(1.47) \cdot V_p = 122.435 kips$ vs $0.75 \cdot V_r = 103.034 kips$ → **OK**

$C(2.94) \cdot V_p = 93.384 kips$ vs $0.5 \cdot V_r = 68.689 kips$ → **OK**

Note: bend buckling of the G3 web under the fatigue truck loading is ok by inspection since the loading is small relative to Strength I and the web is completely in tension due to the composite live load

Girder G2:

Estimated maximum end shears, Strength I, two trucks placed at the end of the bridge with wheels at 2 ft from G2 on each side of the girder, larger axles positioned toward the ends of the bridge)

$V_{D1} := 41.95 kips$

$V_{two\_lanes} := 20.09 kips$

Influence coefficients for maximum end shear on G2 estimated at each juncture of the cross-frames and the main girders based on static equilibrium and assuming that the end torsion is resisted by a couple between G1 and G3. (G3end, G2end, G1end, G3intermed, G2intermed, G1intermed, G3mid, G2mid G1mid) = (0, 1, 0, 0.25, 0.25, 0.25, 0.17, 0.17, 0.17). Influence coefficients for wheel load positions obtained by linear interpolation between these values.

$V_{two\_trucks} := 16 \cdot kips \cdot (2 \cdot 0.77 + 2 \cdot 0.09 + 2 \cdot 0.44 + 2 \cdot 0.19 + 4 \cdot 0.23)$

$V_{two\_trucks} = 62.4 kips$

$V_r := 1.25 \cdot V_{D1} + 1.75 \cdot V_{two\_lanes} + 1.75 \cdot 1.33 V_{two\_trucks}$ $V_r = 232.831 kips$

Assume maximum shear at 1/4 span is 0.75 of maximum end shear $0.75 \cdot V_r = 174.623 kips$

Assume maximum shear at midspan is 0.5 of maximum end shear $0.5 \cdot V_r = 116.415 kips$

Stiffener spacing: 1 @ 2 ft, 3 @ 6.83 ft, 2 @ 11.25 ft α = 0.5, 1.71, 2.81

$V_{n\_unstiffened} := C(0.5) \cdot V_p$ $V_{n\_unstiffened} = 381.603\,kips$ vs 233

$V_n(1.71) = 254.04\,kips$ vs 233

$V_n(2.81) = 193.679\,kips$ vs 175

Girder G1:

Estimated maximum end shears, Strength I, one truck placed with inside wheels over G1, larger axle loads positioned closer to the end of the bridge, multiple presence factor of 1.2 included

$V_{D1} := 25.31 \cdot kips$

$V_{lane} := 15.72 \cdot kips$

$V_{truck} := 16 \cdot kips \cdot (1 + 0.33 + 0.45 + 0.31 + 0.14 + 0.06)$

$V_{truck} = 36.64\,kips$

Influence coefficients for maximum end shear on G1 estimated at each juncture of the cross-frames and the main girders based on static equilibrium and assuming that the end torsion is resisted by a couple between G1 and G3. (G3end, G2end, G1end, G3intermed, G2intermed, G1intermed, G3mid, G2mid G1mid) = (0, 0, 1, -0.30, 0.08, 0.47, -0.24, -0.02, 0.38). Influence coefficients for wheel load positions obtained by linear interpolation between these values.

$V_r := 1.25 \cdot V_{D1} + 1.75 \cdot V_{lane} + 1.75 \cdot 1.33 \times 1.2 V_{truck}$ $V_r = 161.483\,kips$

Assume maximum shear at 1/4 span is 0.75 of maximum end shear $0.75 \cdot V_r = 121.112\,kips$

Assume maximum shear at midspan is 0.5 of maximum end shear $0.5 \cdot V_r = 80.742\,kips$

Stiffener spacing: 1 @ 2 ft, 2 @ 9.76 ft, 2 @ 10.76 ft α = 0.5, 2.44, 2.69

$V_{n\_unstiffened} := C(0.5) \cdot V_p$ $V_{n\_unstiffened} = 381.603\,kips$ vs 161

$V_n(2.44) = 209.024\,kips$ vs 161

$V_n(2.69) = 198.258\,kips$ vs 81

Design of Transverse Stiffeners

Use t = 5/8 in for all transverse stiffeners $t_p := 0.625\,in$

Design criterion: provide a flexural rigidity of 6x that required in the current AASTHO LRFD provisions

$$J(\alpha) := \max\left(\frac{2.5}{\alpha^2} - 2.0, 0.5\right)$$

$$I_{t\_req}(\alpha) := 6\cdot\alpha\cdot D\cdot t_w^{\,3}\cdot J(\alpha)$$

Required stiffener width based on t = 5/8 in and $I_t = tb^3/3$

$$b_{req}(\alpha) := \sqrt[3]{I_{t\_req}(\alpha)\cdot\frac{3}{t_p}}$$

$\alpha := 0.35, 0.351.. 4$ $\alpha = d_o/D$

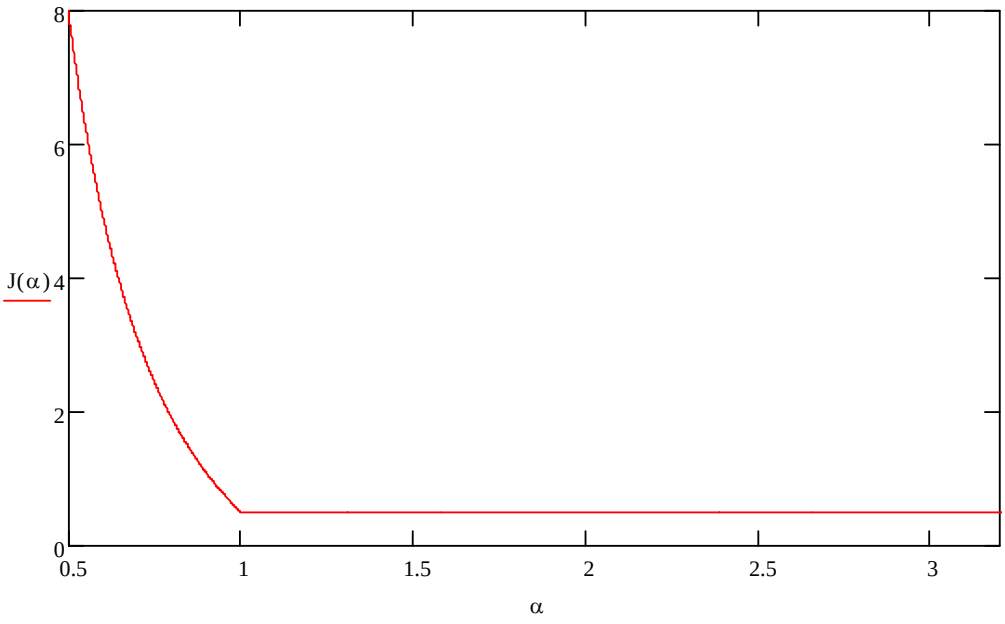

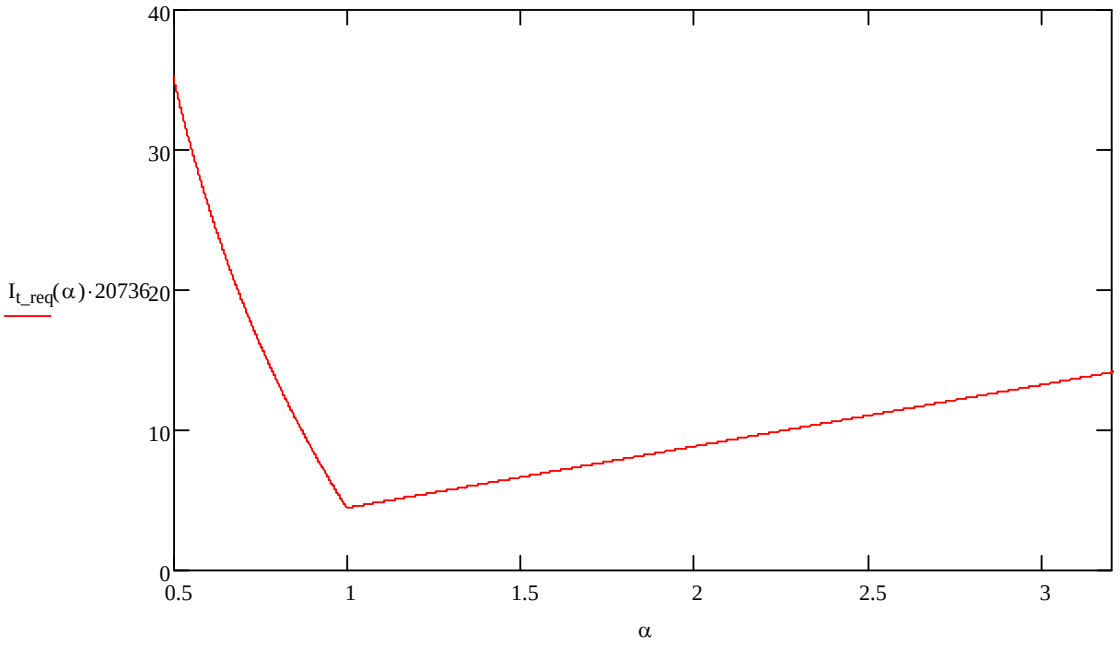
40
30
20
10
0
$I_{t\_req}(\alpha) \cdot 20736$
0.5
1
1.5
2
2.5
3
α

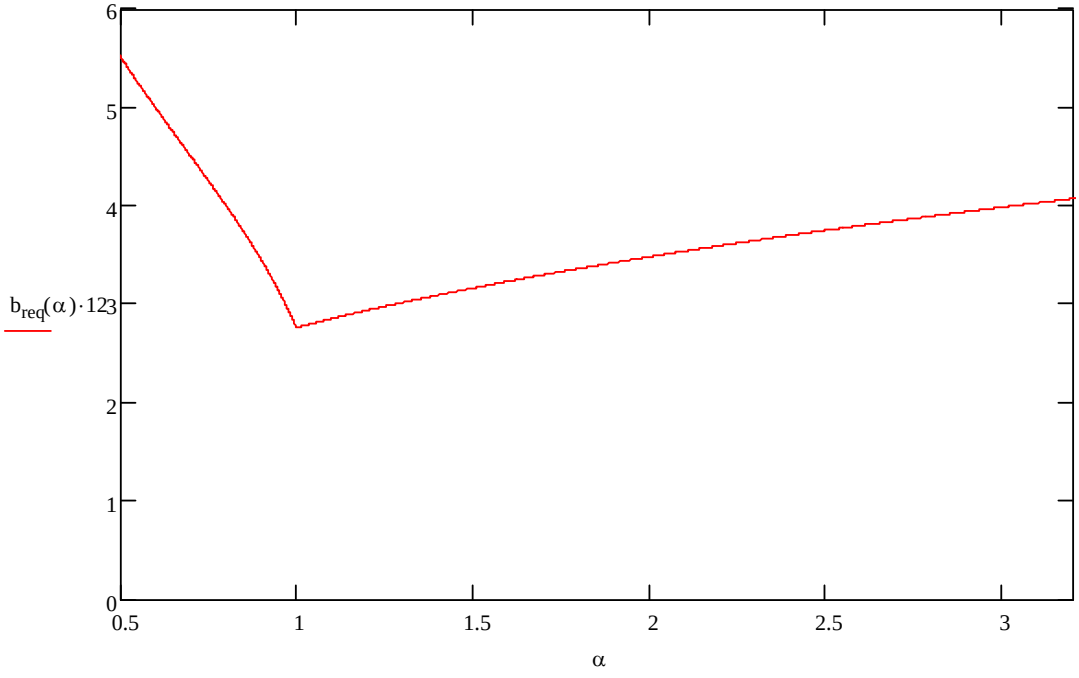
6
5
4
3
2
1
0
$b_{req}(\alpha) \cdot 123$
0.5
1
1.5
2
2.5
3
α

G3: $b_t := \max\left(b_{req}(0.5), 2.0\cdot in + \frac{D}{30}, \frac{24\cdot in}{4}\right)$ $b_t = 6\,in$

$b_{compact} := 0.48\cdot t_p\cdot\sqrt{\frac{E}{50\cdot ksi}}$ $b_{compact} = 7.225in$

It is preferred that the transverse stiffeners be compact under uniform compression, although AASHTO LRFD does not require this

→ **USE** $b_t = 6.0\ in$

G2: $b_t := \max\left(b_{req}(0.5), 2.0\cdot in + \frac{D}{30}, \frac{22\cdot in}{4}\right)$ $b_t = 5.526in$

$b_{max} := \frac{14\cdot in}{2} - 1\cdot in$ $b_{max} = 6\,in$

→ **USE** $b_t = 5.5\ in$

G1: $b_t := \max\left(b_{req}(0.5), 2.0\cdot in + \frac{D}{30}, \frac{17\cdot in}{4}\right)$ $b_t = 5.526in$

$b_{max} := \frac{12\cdot in}{2} - 1\cdot in$ $b_{max} = 5\,in$

The stiffness requirement on G1 violates the maximum width limit associated with the bottom flange. Note that the requirement of 6x the current AASHTO rigidity requirement is needed only to ensure postbuckling resistance. Check the end panel vs the current AASHTO requirement and the most critical spacing for 6x the AASHTO requirement.

$b_t := \max\left(\frac{b_{req}(0.5)}{\sqrt[3]{6}}, 2.0\cdot in + \frac{D}{30}, \frac{17\cdot in}{4}\right)$ $b_t = 4.25in$

$b_t := \max\left(b_{req}(2.69), 2.0\cdot in + \frac{D}{30}, \frac{17\cdot in}{4}\right)$ $b_t = 4.25in$

→ **USE** $b_t = 4.5\ in$

Note: the necessary stiffener requirements for adequate postbuckling strength of curved webs are unknown. It is assumed that stiffeners sized based on 6x the current AASTHO limits will be sufficient. Based on the application of this rigidity limit to all the panels that require postbuckling strength, $b_t = 4$ in should be adequate in all cases for this bridge. Therefore, for G3, the transverse stiffeners satisfy more than 20 x the current AASHTO rigidity requirement

Check the AASHTO LRFD area requirement, assuming full tension-field strength is required, just for kicks

$b_{req} := \left[0.15\cdot 2.4\cdot\frac{D}{t_w}\cdot(1 - C(2.94)) - 18\right]\cdot\frac{F_{yw}}{50\cdot ksi}\cdot\frac{t_w^2}{t_p}$ $b_{req} = 3.973in$

B.5 Bearing Stiffener, Connection Plates and Cross-Frame Designs

Material Properties:

$F_y := 50ksi$ $E := 2.9 \cdot 10^4 ksi$ $\nu := 0.3$

Girder Dimensions:

$D := 48in$ $t_w := 0.3125in$ $\frac{D}{t_w} = 153.6$

The same bearing stiffeners as in the bending component test frame are used with the exception of the exterior face of G1, to facilitate the re-use of the existing cross-frames. The bearing stiffener dimensions are:

- 1 x 9 in (G3) both sides of web
- 1 x 9 in (G2) both sides of web
- 0.75 x 7 in (G1) interior, 0.75 x 5 in (G1) facia

G2 and G3 bearing stiffeners:

For G2 and G3, which both have the same size bearing stiffeners, the maximum Strength I reaction is 317.7 kips (from the web shear design calculations)

Based on the calculated web shear strength, the reaction could be as large as 348 kips

Based on the most conservative estimate of the required shear capacity at the end of G3, to develop the full flexural strength of the girder (from the web shear design calculations), the reaction could be as large as 410 kips

The load cell allowable at the G3 bearings is 300 kips, with a maximum limit of 450 kips

Compactness limit check: $0.48\sqrt{\frac{E}{F_y}} = 11.56 > 9/1 = 9$ → **OK**

Bearing resistance check: $2 \cdot 1.4 \cdot (9 \cdot in - 1 \cdot in) \cdot 1 \cdot in \cdot F_y = 1.12 \times 10^3 kips$ → **OK**

Axial resistance check:

$$r := \frac{9in + 9 \cdot in + \frac{5}{16} \cdot in}{\sqrt{12}}$$

$$\lambda := \left(\frac{0.75 \cdot D}{r \cdot \pi}\right)^2 \cdot \frac{F_y}{E} \qquad \lambda = 8.101 \times 10^{-3}$$

$$P_n := \begin{cases} 0.66^{\lambda} \cdot F_y \cdot \left(9 \cdot in + 9 \cdot in + \frac{5}{16} \cdot in\right) \cdot 1 \cdot in & \text{if } \lambda \le 2.25 \\ \frac{0.88}{\lambda} \cdot F_y \cdot \left[\left(9 \cdot in + 9 \cdot in + \frac{5}{16} \cdot in\right) \cdot 1 \cdot in\right] & \text{otherwise} \end{cases}$$

$0.9 \cdot P_n = 821.293 kips$ → **OK**

G1 bearing stiffeners:

The maximum Strength I reaction on G1 is 161.5 kips (determined in the web shear design calculations)

Compactness limit check: $0.48 \sqrt{\frac{E}{F_y}} = 11.56 > \frac{7}{0.75} = 9.333$ → **OK**

Bearing resistance check: $1.4 \cdot (7 \cdot in - 1 \cdot in + 5 \cdot in - 1 \cdot in) \cdot 0.75 \cdot in \cdot F_y = 525 kips$ → **OK**

Axial resistance check: $r := \frac{7in + 5 \cdot in + \frac{5}{16} \cdot in}{\sqrt{12}}$

$\lambda := \left(\frac{0.75 \cdot D}{r \cdot \pi}\right)^2 \cdot \frac{F_y}{E}$ $\lambda = 0.018$

$$P_n := \begin{cases} 0.66^{\lambda} \cdot F_y \cdot \left(9 \cdot in + 9 \cdot in + \frac{5}{16} \cdot in\right) \cdot 1 \cdot in & \text{if } \lambda \le 2.25 \\ \frac{0.88}{\lambda} \cdot \left[F_y \cdot \left(9 \cdot in + 9 \cdot in + \frac{5}{16} \cdot in\right) \cdot 1 \cdot in\right] & \text{otherwise} \end{cases}$$

$0.9 \cdot P_n = 817.949 kips$ → **OK**

Connection Plates and Cross-Frames:

The same connection plates as in the bending component test frame are used except on the facia of G1. The dimensions of these plates are:

- 9 in x 13/16 in both sides (G3 and G2)
- 7 in x 5/8 in on inside (G1), 5 in x 5/8 in on outside of G1

The sizes of these plates are likely to be controlled by the transfer of a radial component of the bottom flange force + the web force below the bottom chord of the cross-frame up to the bottom chord; check the connection plates on G3 at the midspan for development of the full yield force in the section below the bottom chord.

G3:

$H_f := 0.1125\,70\cdot ksi\cdot 24\cdot in\cdot 1.375\,in$ $\quad H_f = 259.875 kips$

$H_{w1} := 0.1125\,50\cdot ksi\cdot \frac{5}{16}\cdot in\cdot 8\cdot in$ $\quad H_{w1} = 14.062 kips$

$M := H_f\cdot\left(8\cdot in + \frac{1.375\,in}{2}\right) + H_{w1}\cdot 4\cdot in$ $\quad M = 192.826 ft\cdot kips$

$S := \frac{\left(9\cdot in + 9\cdot in + \frac{5}{16}\cdot in\right)^2\cdot\frac{13}{16}\cdot in}{6}$ $\quad S = 45.412 in^3$

$f := \frac{M}{S}$ $\quad f = 50.954 ksi$ ⟶ **Marginally OK**

Check the connection plate for transfer of the required bottom chord brace force associated with the development of M_p at the midspan of G3

The PNA is located within the top flange of G3. Assume that the connection plate spans as a simply-supported element between the two chords of the cross-frame in transferring a radial force component from the web to the bottom chord.

$H_{w2} := 0.1125\,50\cdot ksi\cdot \frac{5}{16}\cdot in\cdot \frac{34\cdot in}{2}$ $\quad H_{w2} = 29.883 kips$

$H_{G3} := H_f + H_{w1} + H_{w2}$ $\quad H_{G3} = 303.82 kips$

Note: The actual brace force may be smaller than the above due to:

- Torsional restraint from the slab + the top chord of the cross-frame, plus some small moment restraint from the bottom chord of the cross-frame
- Straightening of the bottom flange under the flexural tension
- Reduction in the total tension force within the bottom portion of the cross-section due to lateral flange bending
- Moment gradient in G3

Strain hardening will tend to increase the above force. Therefore, the above force is taken as a reasonable maximum that must be developed in the bottom chord of the cross-frame at G3

Bearing resistance, 6 - 7/8 in diam fasteners (13/16 in plate assumed to govern the bearing resistance in these calculations, the cross-frame gusset plates need to be checked separately)

$\phi R := 6 \cdot 0.75 \cdot 2.4 \cdot \frac{7}{8} \cdot in \cdot \frac{13}{16} \cdot in \cdot 65 \cdot ksi$ $\phi R = 499.078 kips$ → **OK**

Shear resistance, 6 - 7/8 in diam A490 fasteners, double shear, threads excluded from the shear plane

$\phi R := 6 \cdot 0.8 \cdot 0.5 \cdot \frac{\pi}{4} \cdot \left(\frac{7}{8} \cdot in \right)^2 \cdot 120 \cdot ksi \cdot 2$ $\phi R = 346.361 kips$ → **OK**

Shear resistance, 6 - 7/8 in diam fasteners, double-shear, threads included in the shear plane

$\phi R := 6 \cdot 0.8 \cdot 0.4 \cdot \frac{\pi}{4} \cdot \left(\frac{7}{8} \cdot in \right)^2 \cdot 120 \cdot ksi \cdot 2$ $\phi R = 277.088 kips$ → **NG**

Note: for 6 - 7/8 in A490 bolts to work per the AASHTO provisions, they must be used in double shear and the threads must be excluded from the shear plane

Slip resistance, 6 - 7/8 in diam fasteners, double shear, Class A surface conditions

$\phi R := 6 \cdot 0.8 \cdot 1.0 \cdot 0.33 \cdot 2 \cdot 49 \cdot kips$ $\phi R = 155.232 kips$ → **NG**

Slip resistance, 6 - 7/8 in diam fasteners, double shear, Class B surface conditions

$\phi R := 6 \cdot 0.8 \cdot 1.0 \cdot 0.5 \cdot 2 \cdot 49 \cdot kips$ $\phi R = 235.2 kips$ → **NG**

Shear resistance, 6 - 1 in diam fasteners, double-shear, threads included in the shear plan e

$\phi R := 6 \cdot 0.8 \cdot 0.4 \cdot \frac{\pi}{4} \cdot (1 \cdot in)^2 \cdot 120 \cdot ksi \cdot 2$ $\phi R = 361.911 kips$ → **OK**

Slip resistance, 6 - 7/8 in diam fasteners, double shear, Class B surface conditions

$\phi R := 6 \cdot 0.8 \cdot 1.0 \cdot 0.5 \cdot 2 \cdot 64 \cdot kips$ $\phi R = 307.2 kips$ → **OK**

Note: 6 - 1 in diam fasteners in double-shear with Class B surface conditions are required for the AASHTO design slip resistance to be greater than the estimated bottom chord brace force at the midspan of G3. Alternatively, the connection may be welded to transfer the larger force necessary at the maximum strength level of the bridge .

Bottom Chord Stress Adjacent to G3:

$f := \frac{H_{G3}}{\frac{\pi}{4} \cdot \left[(5 \cdot in)^2 - (4.5 \cdot in)^2 \right]}$ $f = 81.439 ksi$ $> F_y = 60$ ksi → **NG**

The bottom chord strut adjacent to G3 will need to be reinforced or replaced prior to testing the bridge to failure

Radial force from the G2 flange

$H_f := 0.112550 \cdot ksi \cdot 22 \cdot in \cdot 1 \cdot in$ $H_f = 123.75 kips$

$H_{w1} := 0.112550 \cdot ksi \cdot \frac{5}{16} \cdot in \cdot 8 \cdot in$ $H_{w1} = 14.062 kips$

$H_{w2} := 0.112550 \cdot ksi \cdot \frac{5}{16} \cdot in \cdot \frac{34 \cdot in}{2}$ $H_{w2} = 29.883 kips$

$H_{G2} := H_f + H_{w1} + H_{w2}$ $H_{G2} = 167.695 kips$

Note: the G2 connection plate is ok for transfer of Hf + Hw1 to the bottom chord by inspection

G1 :

$H_f := 0.112550 \cdot ksi \cdot 17 \cdot in \cdot \frac{7}{8} \cdot in$ $H_f = 83.672 kips$

$H_{w1} := 0.112550 \cdot ksi \cdot \frac{5}{16} \cdot in \cdot 8 \cdot in$ $H_{w1} = 14.062 kips$

$M := H_f \cdot \left(8 \cdot in + \frac{7}{8 \cdot 2} \cdot in \right) + H_{w1} \cdot 4 \cdot in$ $M = 63.519 ft \cdot kips$

$S := \frac{\left(5 \cdot in + 7 \cdot in + \frac{5}{16} \cdot in \right)^2 \cdot \frac{5}{8} \cdot in}{6}$ $S = 15.791 in^3$

$f := \frac{M}{S}$ $f = 48.269 ksi$ → **OK**

$H_{w2} := 0.112550 \cdot ksi \cdot \frac{5}{16} \cdot in \cdot \frac{34 \cdot in}{2}$ $H_{w2} = 29.883 kips$

$H_{G1} := H_f + H_{w1} + H_{w2}$ $H_{G1} = 127.617 kips$

Estimate the shear transferred from the midspan cross-frame to G3 at the maximum capacity of the bridge

$H_{tot} := H_{G3} + H_{G2} + H_{G1}$ $H_{tot} = 599.133 kips$

$V := H_{tot} \cdot \frac{D + 3 \cdot in + 4 \cdot in}{17.5 \cdot ft}$ $V = 156.916 kips$

It is likely that the bridge will not be able to develop this shear in G1 unless the ends of G1 are held down. It is suggested that it is most appropriate not to hold down the ends of G1. Therefore, the prediction of the shear based on the above assumptions is invalid.

A better approximation might be obtained by assuming negligible contribution from G1 to the bottom flange radial forces at the middle of the bridge

$H_{tot} := H_{G3} + H_{G2}$ $\quad H_{tot} = 471.516\,kips$

$V := H_{tot} \cdot \frac{D + 3 \cdot in + 4 \cdot in}{17.5 \cdot ft}$ $\quad V = 123.492\,kips$

The only way to predict the cross-frame and connection plate forces at the strength limit in the components other than the bottom strut connected to the midspan of G3 is to conduct a refined nonlinear analysis of the bridge

It is likely that some of the cross-frame forces will increase dramatically as yielding develops in the system and G1 begins to lift off of its supports.

Based on the cross-frame forces calculated for the Strength I loadings for maximum flexural effects on girders G1, G2 and G3, it is expected that all the cross-frame components are adequate for loading of the bridge to its maximum strength, with the exception of the bottom struts connected to G3 at the midspan and intermediate cross-frame locations. Other load combinations may produce larger forces in some of the cross-frame components than those in the critical cross-frame connected to the midspan of G3. However, it is expected that the forces will be less than the strength of the components.

B.6 Shear Connector Design

Stud Proportions

Terminate the studs at approximately the mid-thickness of the slab. This places them well within the limits for cover and penetration specified in Article 6.10.7.4.1d and will also clear the reinforcing steel.

Stud Height: $\frac{8 \cdot in}{2} + 3 \cdot in - 1.375 \cdot in = 5.625 in$ → **USE** $h := 6 \cdot in$

Bottom of longitudinal bars is at 3.5 in below the top of the slab. The top of the studs is 3.625 in below the top of the slab.

The diameter of the studs is determined from Article 6.10.7.4.1a: h/d > 4, therefore d < h/4 = 1.5 in

→ **USE** $d := 0.75 \cdot in$

Use three studs per cross-section, spaced at 6 in transversely on G2 and G3, two studs per cross-section spaced at 6 in transversely on G1

Pitch, based on Fatigue

$n := 1$ Simple span girder with span length > 40 ft, Table 6.6.1.2.5-2

$p := 1$ Fracton of truck traffic in a single lane, for number of lanes available to trucks = 1, Table 3.5.1.4.2-1

$ADTT := 2000$ Number of trucks per day in one direction, averaged over the design life (assumed to be 2000 in this design)

$ADTT_{SL} := ADTT \cdot p$

$N := 365 \cdot 75 \cdot n \cdot ADTT_{SL}$ $N = 5.475 \times 10^{7}$

$\alpha := 34.5 \cdot ksi - 4.28 \cdot ksi \cdot \log(N)$ $\alpha = 1.38 ksi$

$Z_r := \max\left(\alpha, \frac{5.5}{2} \cdot ksi\right) \cdot d^2$ $Z_r = 1.547 kips$

$n := 3$ number of shear connectors in a cross-section

G3:

$V_f := 44.52\,kips$ end shear range from p. 6 of web shear design calculations

$I := 84800\,in^4$ $Q := 94.262\,in^2 \cdot \left(18.788\,in - \frac{8 \cdot in}{2}\right)$ $Q = 116.162\,ft\,in^2$

$V_{sr} := \frac{V_f \cdot Q}{I}$ $V_{sr} = 0.732\,\frac{kips}{in}$

$p := \frac{n \cdot Z_r}{V_{sr}}$ $p = 6.341\,in$

Assume a longitudinal shear range at midspan and at the 1/4 span of 80% of the shear range at the end of the girder. Consider the vector sum of this force with the radial shear range at the midspan asssociated with an estimated maximum flexural stress at the midspan of G3 of 5.3 ksi for the factored fatigue truck loading

$V_{sr} := \sqrt{\left(\frac{0.8 \cdot V_f \cdot Q}{I}\right)^2 + \left(\frac{24 \cdot in \cdot 1.375 \cdot in \cdot 5.3\,ksi \cdot 0.1125}{48 \cdot in}\right)^2}$ $V_{sr} = 0.715\,\frac{kips}{in}$

$p := \frac{n \cdot Z_r}{V_{sr}}$ $p = 6.493\,in$

Use 3 - 7/8 in diam 6 in high shear studs within each cross-section, spaced at 6 in transversely
Use p = 6 in
Total number of studs, end support to midspan = 95*3 = 285

G2:

$V_f := 0.75 \cdot 1.15 \cdot 32 \cdot kips \cdot (1 + 0.22 + 0.17)$ $V_f = 38.364\,kips$

$I := 66820\,in^4$ $Q := 111.836\,in^2 \cdot \left(14.966\,in - \frac{8 \cdot in}{2}\right)$ $Q = 102.199\,ft\,in^2$

$V_{sr} := \frac{V_f \cdot Q}{I}$ $V_{sr} = 0.704\,\frac{kips}{in}$

$p := \frac{n \cdot Z_r}{V_{sr}}$ $p = 6.591\,in$

Assume a longitudinal shear range at midspan and at the 1/4 span of 80% of the shear range at the end of the girder. Consider the vector sum of this force with the radial shear range at the midspan asssociated with an estimated maximum flexural stress at the midspan of G2 of 3.8 ksi for the factored fatigue truck loading

$$V_{sr} := \sqrt{\left(\frac{0.8 \cdot V_f \cdot Q}{I}\right)^2 + \left(\frac{22 \cdot in \cdot 1.0 \cdot in \cdot 3.8 ksi \cdot 0.1125}{48 \cdot in}\right)^2} \qquad V_{sr} = 0.596 \frac{kips}{in}$$

$$p := \frac{n \cdot Z_r}{V_{sr}} \qquad p = 7.781 in$$

Use 3 - 7/8 in diam 6 in high shear studs within each cross-section, spaced at 6 in transversely
Use p = 6 in
Total number of studs, end support to midspan = 91*3 = 273

G1:

$n := 2$ number of shear connectors in a cross-section

$$V_f := 0.75 \cdot 1.15 \cdot 16 \cdot kips \cdot (1 + 0.44 + 0.38 + 0.31 + 0.17 + 0.11) \qquad V_f = 33.258 kips$$

$$I := 66820 in^4 \qquad Q := 94.262 in^2 \cdot \left(14.09 in - \frac{8 \cdot in}{2}\right) \qquad Q = 79.259 ft\, in^2$$

$$V_{sr} := \frac{V_f \cdot Q}{I} \qquad V_{sr} = 0.473 \frac{kips}{in}$$

$$p := \frac{n \cdot Z_r}{V_{sr}} \qquad p = 6.535 in$$

Assume a longitudinal shear range at midspan and at the 1/4 span of 80% of the shear range at the end of the girder. Consider the vector sum of this force with the radial shear range at the midspan asssociated with an estimated maximum flexural stress at the midspan of G1 of 4.1 ksi for the factored fatigue truck loading

$$V_{sr} := \sqrt{\left(\frac{0.8 \cdot V_f \cdot Q}{I}\right)^2 + \left(\frac{17 \cdot in \cdot 0.875 in \cdot 4.1 ksi \cdot 0.1125}{48 \cdot in}\right)^2} \qquad V_{sr} = 0.405 \frac{kips}{in}$$

$$p := \frac{n \cdot Z_r}{V_{sr}} \qquad p = 7.643 in$$

Use 2 - 7/8 in diam 6 in high shear studs within each cross-section, spaced at 6 in transversely
Use p = 6 in
Total number of shear connectors, end supports to midspan = 87*2 = 174

Check strength

G3:

$$P_p := \min\left[0.85 \cdot 4.5 \cdot ksi \cdot (48 \cdot in \cdot 9.5 \cdot in + 40.5 \cdot in \cdot 8 \cdot in), \left(24 \cdot in \cdot 1 \cdot in \cdot 50 \cdot ksi + 48 \cdot in \cdot \frac{5}{16} \cdot in \cdot 50 \cdot ksi + 24 \cdot in \cdot 1.375 \, in \cdot 70 \cdot ksi\right)\right]$$

$P_p = 2.983 \times 10^3 \, kips$

$F_p := P_p \cdot 0.1125$ $\quad F_p = 335.644 kips$

$P := \sqrt{P_p^{\,2} + F_p^{\,2}}$ $\quad P = 3.002 \times 10^3 \, kips$

$Q_r := \frac{P}{285}$ $\quad Q_r = 10.534 kips$

$A_{sc} := \frac{\pi}{4} \cdot d^2$ $\quad A_{sc} = 0.442 in^2$

$E_c := 3860 \cdot ksi$ $\quad f_c := 4.5 \cdot ksi$

$F_u := 58 \cdot ksi$

$\phi Q_n := 0.85 \cdot \min\left(0.5 \cdot A_{sc} \cdot \sqrt{f_c \cdot E_c}, A_{sc} \cdot F_u\right)$ $\quad \phi Q_n = 21.78 kips$ $\longrightarrow$ **OK**

G2:

$$P_p := \min\left[0.85 \cdot 4.5 \cdot ksi \cdot (8 \cdot in \cdot 105 \cdot in), 50 \cdot ksi \cdot \left(14 \cdot in \cdot 0.875 \, in + 48 \cdot in \cdot \frac{5}{16} \cdot in + 22 \cdot in \cdot 1 \cdot in\right)\right]$$

$P_p = 2.462 \times 10^3 \, kips$

$F_p := P_p \cdot 0.1125$ $\quad F_p = 277.031 kips$

$P := \sqrt{P_p^{\,2} + F_p^{\,2}}$ $\quad P = 2.478 \times 10^3 \, kips$

$Q_r := \frac{P}{273}$ $\quad Q_r = 9.077 kips$

$A_{sc} := \frac{\pi}{4} \cdot d^2$ $\quad A_{sc} = 0.442 in^2$

$E_c := 3860 \, ksi$ $\quad f_c := 4.5 \cdot ksi$

$F_u := 58 \cdot ksi$

$\phi Q_n := 0.85 \cdot \min\left(0.5 \cdot A_{sc} \cdot \sqrt{f_c \cdot E_c}, A_{sc} \cdot F_u\right)$ $\quad \phi Q_n = 21.78 kips$ $\longrightarrow$ **OK**

G1:

$$P_p := \min\left[0.85 \cdot 4.5 \cdot ksi \cdot (8 \cdot in \cdot 46.5 \cdot in + 9.5 \cdot in \cdot 42 \cdot in),\ 50 \cdot ksi \cdot \left(12 \cdot in \cdot 0.875 \cdot in + 48 \cdot in \cdot \frac{5}{16} \cdot in + 17 \cdot in \cdot 0.875 \cdot in\right)\right]$$

$P_p = 2.019 \times 10^3\ kips$

$F_p := P_p \cdot 0.1125$ $\quad F_p = 227.109\ kips$

$P := \sqrt{P_p^2 + F_p^2}$ $\quad P = 2.031 \times 10^3\ kips$

$Q_r := \frac{P}{174}$ $\quad Q_r = 11.675\ kips$

$A_{sc} := \frac{\pi}{4} \cdot d^2$ $\quad A_{sc} = 0.442\ in^2$

$E_c := 3860 \cdot ksi$ $\quad f_c := 4.5 \cdot ksi$

$F_u := 58 \cdot ksi$

$\phi Q_n := 0.85 \cdot \min\left(0.5 \cdot A_{sc} \cdot \sqrt{f_c \cdot E_c},\ A_{sc} \cdot F_u\right)$ $\quad \phi Q_n = 21.78\ kips$ $\quad \longrightarrow$ **OK**

B.7 Summary of Key Design Checks

Girder G3

Constructability (STRENGTH IV) – Noncomposite Section

$R_h = 1$, yielding governed by Grade 50 top flange

Top Flange:

$f_{bc} = 28.84$ ksi, $f_{\ell c} = 18.14$ ksi

Lateral bending stress limit: $[f_{\ell c} = 18.14 \text{ ksi}] < [0.6F_{yc} = 34.77 \text{ ksi}]$ **ratio = 0.52**

Yielding limit: $[f_{bc} + f_{\ell c} = 46.98 \text{ ksi}] < [\phi_f R_h F_{yc} = 58.07 \text{ ksi}]$ **ratio = 0.81**

Strength limit: $[f_{bc} + f_{\ell c}/3 = 34.89 \text{ ksi}] < [\phi_f F_{nc} = 49.74 \text{ ksi}]$ **ratio = 0.72**

Web bend buckling limit: $[f_{bc} = 28.84 \text{ ksi}] < [\phi_f F_{crw} = 41.64 \text{ ksi}]$ **ratio = 0.69**

Bottom Flange:

$f_{bt} = 22.33$ ksi, $f_{\ell t} = 18.05$ ksi

Lateral bending stress limit: $[f_{\ell t} = 18.05 \text{ ksi}] < [0.6F_{yt} = 42.89 \text{ ksi}]$ **ratio = 0.42**

Yielding limit: $[f_{bt} + f_{\ell t} = 40.38 \text{ ksi}] < [\phi_f R_h F_{yt} = 71.63 \text{ ksi}]$ **ratio = 0.56**

Strength I – Composite Section

$R_h = 0.9900$, yielding governed by HPS 70W bottom flange

Bottom Flange:

$f_{bt} = 47.065$ ksi

$f_{\ell t} = 34.403$ ksi

Lateral bending stress limit: $[f_{\ell t} = 34.403 \text{ ksi}] < [0.6F_{yt} = 42.892 \text{ ksi}]$ **ratio = 0.80**

Strength limit: $[f_{bt} + f_{\ell t}/3 = 47.065 + 34.403/3 = 58.53 \text{ ksi}] < [\phi_f R_h F_{yc} = 71.5 \text{ ksi}]$

ratio = 0.82

Top Flange:
f_{bc} = 28.264 ksi

Strength limit: [f_{bc} = 28.264 ksi] < [$\phi_f R_h F_{yc}$ = 57.961 ksi] **ratio = 0.49**

Service II

Bottom Flange:

f_{bt} ≅ 36.564 ksi

Permanent deformation limit: [f_{bt} = 36.564 ksi] < [$0.95R_hF_{yt}$ = 68.05 ksi] **ratio = 0.53**

Top Flange:

f_{bc} ≅ 22.408 ksi

Permanent deformation limit: [f_{bt} = 22.408 ksi] < [$0.95F_{yt}$ = 55.16 ksi] **ratio = 0.41**

Live Load Deflection

Maximum deflection due to two AASHTO design trucks, side-by-side, positioned for maximum effect on G3 (including dynamic allowance of 1.33) = 1.76 in

L/800 = (93.9375 ft) (12) / 800 = 1.41 in **ratio = 1.25**

Girder G2

Constructibility (STRENGTH IV) – Noncomposite Section

Top Flange:

f_{bc} = 18.44 ksi, $f_{\ell c}$ = 24.43 ksi

Max lateral bending stress limit:[$f_{\ell c}$ = 24.43 ksi] < [$0.6F_{yc}$ = 34.467 ksi] **ratio = 0.71**

Yielding limit:[$f_{bc} + f_{\ell c}$ = 42.87 ksi] < [$\phi_f R_h F_{yc}$ = 57.56 ksi] **ratio = 0.75**

Strength limit: [$f_{bc} + f_{\ell c}/3$ = 26.58 ksi] < [$\phi_f F_{nc}$ = 49.581 ksi] **ratio = 0.54**

Web bend buckling limit: [f_{bc} = 18.44 ksi] < [$\phi_f F_{crw}$ = 29.51 ksi] **ratio = 0.62**

Bottom Flange:

f_{bt} = 12.30 ksi, $f_{\ell t}$ = 11.41 ksi

Max lateral bending stress limit:[$f_{\ell t}$ = 11.41 ksi] < [$0.6F_{yt}$ = 34.77 ksi] **ratio = 0.33**

Yielding limit:[$f_{bc} + f_{\ell t}$ = 23.71 ksi] < [$\phi_f R_h F_{yt}$ = 58.07 ksi] **ratio = 0.41**

Strength I – Composite Section

Bottom Flange:

f_{bt} = 32.20 ksi

$f_{\ell t}$ = 23.87 ksi

Max lateral bending stress limit:[$f_{\ell t}$ =23.87 ksi] < [$0.6F_{yt}$ = 34.77 ksi] **ratio = 0.69**

Strength limit: [$f_{bt} + f_{\ell t}/3$ = 32.20 + 23.87/3 = 39.20 ksi] < [$\phi_f R_h F_{yt}$ = 58.07 ksi]

ratio = 0.68

Top Flange:

f_{bc} = 17.80 ksi

Strength limit: [f_{bc} = 17.80 ksi] < [$\phi_f R_h F_{yc}$ = 57.56 ksi] **ratio = 0.31**

Service II

Bottom Flange:

f_{bt} ≅ 23.80 ksi

Permanent deformation limit: [f_{bt} = 23.80 ksi] < [$0.95F_{yt}$ = 55.17 ksi] **ratio = 0.43**

Top Flange:

$\mathbf{f_{bc}}$ ≅ 14.12 ksi

Permanent deformation limit: [f_{bt} = 14.12 ksi] < [$0.95F_{yt}$ = 54.68 ksi] **ratio = 0.26**

Girder G1

Constructibility

Top Flange:

f_{bc} = 7.84 ksi, $f_{\ell c}$ = 9.81 ksi (from geometric nonlinear analysis)

Max lateral bending stress limit:[$f_{\ell c}$ = 9.81 ksi] < [0.6F_{yc} = 34.47 ksi] **ratio = 0.29**

Yielding limit: [$f_{bc} + f_{\ell c}$ = 17.65 ksi] < [$\phi_f R_h F_{yc}$ = 57.56 ksi] **ratio = 0.31**

Strength limit: [$f_{bc} + f_{\ell c}/3$ = 11.11 ksi] < [$\phi_f F_{nc}$ = 41.02 ksi] **ratio = 0.25**

Web bend buckling limit: [f_{bc} = 7.84 ksi] < [$\phi_f F_{crw}$ = 36.11 ksi] **ratio = 0.22**

Width of top flange based on length of shipping piece:
[b_{fc} = 12.188 in] ≅ [L/85 = 12.15 in] **ratio = 1.00**

Bottom Flange:

f_{bt} = 5.78 ksi, $f_{\ell t}$ = 8.03 ksi

Max lateral bending stress limit: [$f_{\ell t}$ = 8.03 ksi] < [0.6F_{yt}= 34.77 ksi] **ratio = 0.23**

Yielding limit: [$f_{bc} + f_{\ell t}$ = 13.81 ksi] < [$\phi_f R_h F_{yt}$ = 58.07 ksi] **ratio = 0.24**

Strength I – Composite Section

Bottom Flange:

f_{bt} = 24.13 ksi

$f_{\ell t}$ = 27.10 ksi

Max lateral bending stress limit: [$f_{\ell t}$ = 27.10 ksi] < [0.6F_{yt} = 34.77 ksi] **ratio = 0.78**

Strength limit: [$f_{bt} + f_{\ell t}/3$ = 24.13 + 27.10/3 = 33.28 ksi] < [$\phi_f R_h F_{yt}$ = 58.07 ksi]
ratio = 0.57

Top Flange:

f_{bc} = 7.35 ksi

Strength limit: [f_{bc} = 7.35 ksi] < [$\phi_f R_h F_{yc}$ = 57.56 ksi] **ratio = 0.13**

Service II

Bottom Flange:

f_{bt} ≅ 18.20 ksi

Permanent deformation limit: [f_{bt} = 18.20 ksi] < [0.95F_{yt} = 55.17 ksi] **ratio = 0.33**

Top Flange:

f_{bc} ≅ 5.84 ksi

Permanent deformation limit: [f_{bt} = 5.84 ksi] < [0.95F_{yt} = 54.68 ksi] **ratio = 0.11**

APPENDIX C

TEST 4a: REPEATED LOADING TESTS

This appendix presents additional detailed results of the repeated loading studies from Test 4a not shown in Chapter 4. First, the measured and predicted slab top surface longitudinal strains across the mid-span bridge cross-section for gage location L9 are presented. This is followed by the measured major-axis and lateral bending strains for G1 and G2, along with their comparisons to the corresponding full nonlinear FEA predictions. Then, this appendix presents detailed relative slip displacements measured at the ends of the composite girders for the longitudinal direction and the radial slip displacements measured at the midspan of G3.

C.1 Slab Midspan Longitudinal Strains

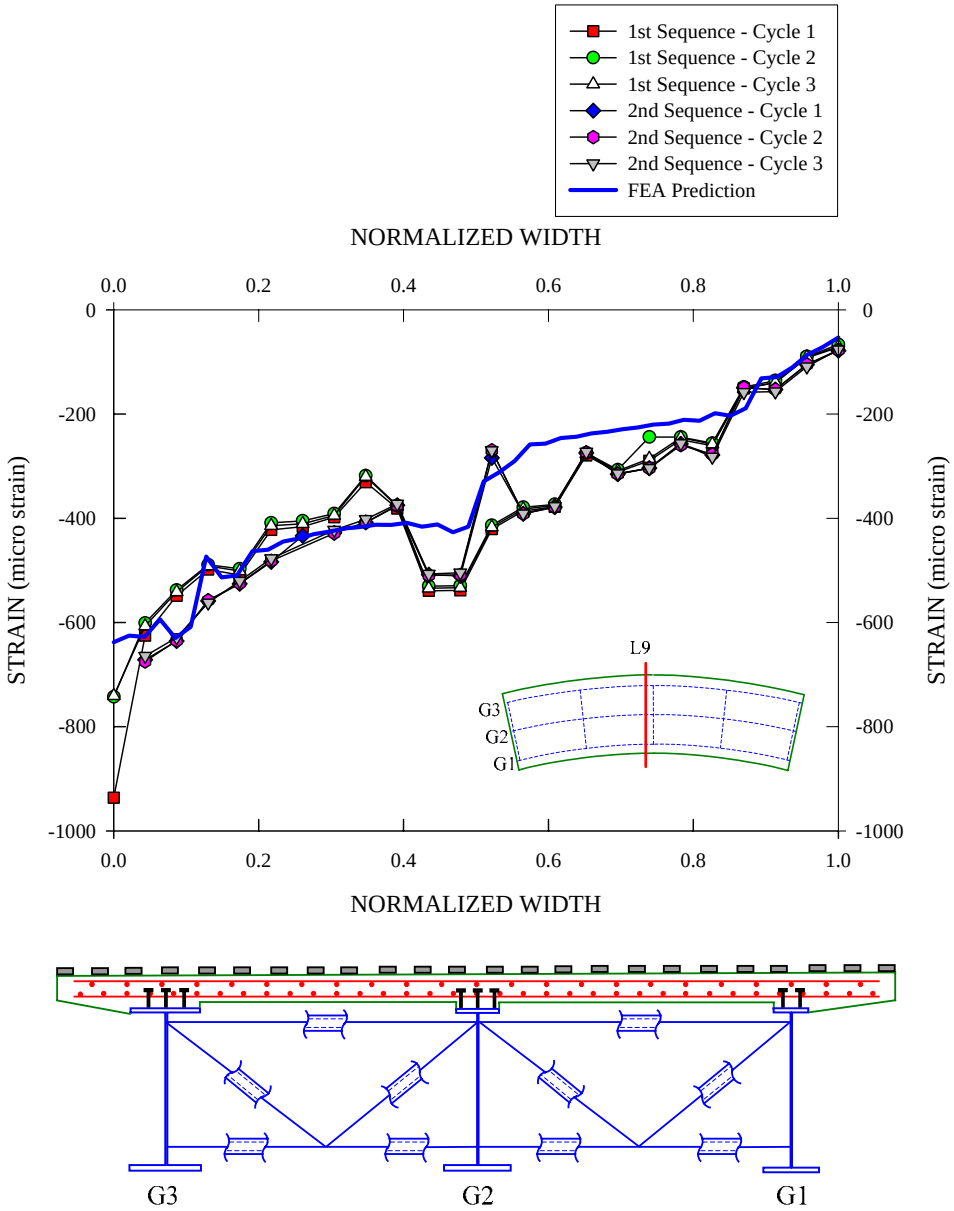

Figure C.1.1. Slab longitudinal strain distribution for gage location L9 at load level A during the first and second sequences of Test 4a, strains associated with concrete shrinkage are not included in the plot.

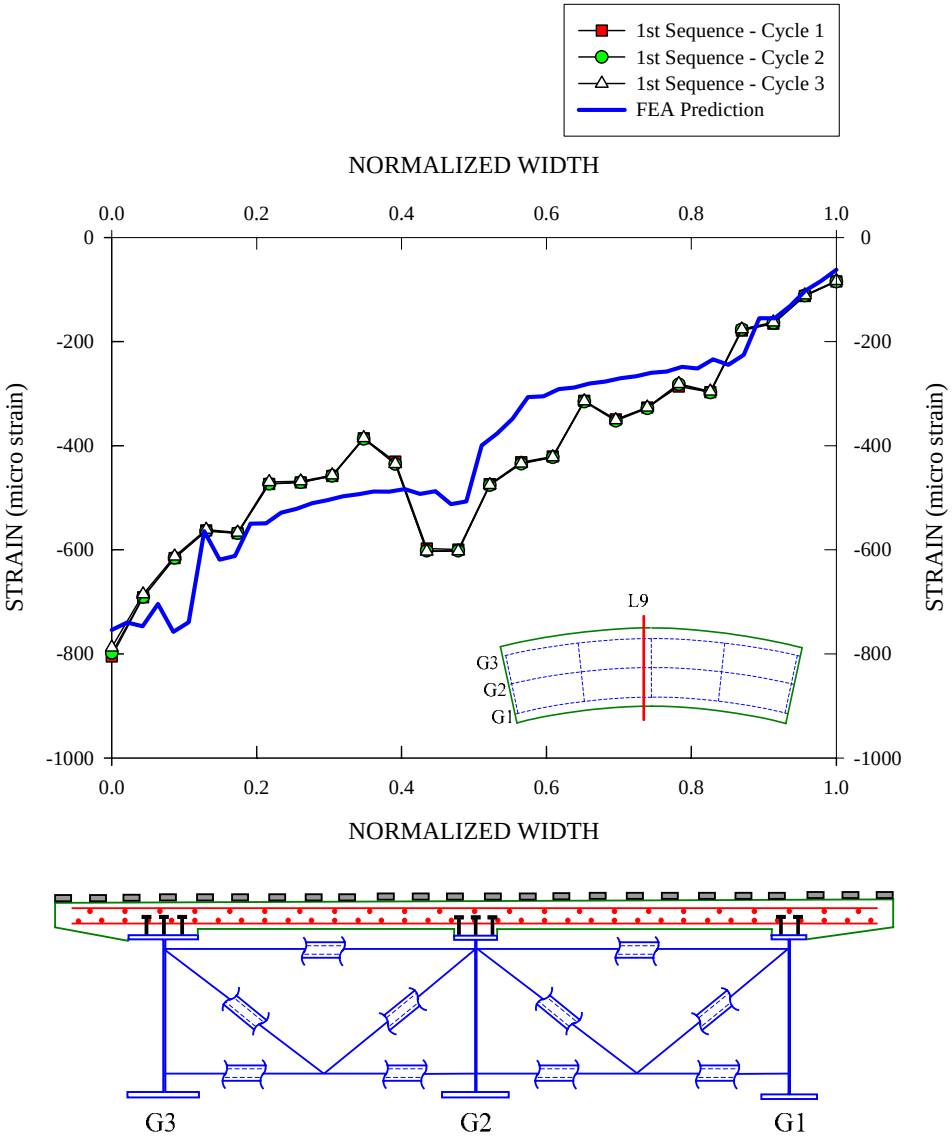

Figure C.1.2. Slab longitudinal strain distribution for gage location L9 at load level B during the first sequence of Test 4a, strains associated with concrete shrinkage are not included in the plot.

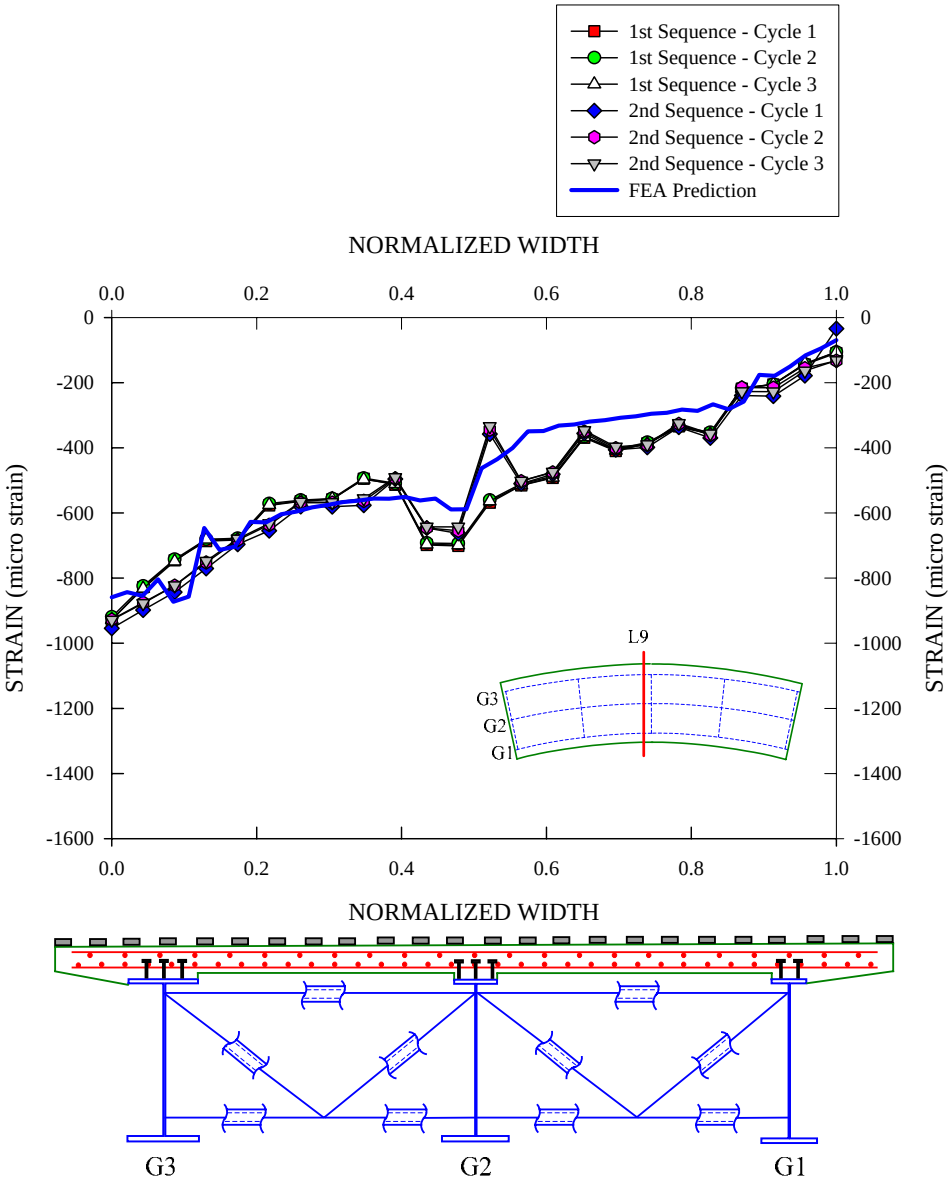

Figure C.1.3. Slab longitudinal strain distribution for gage location L9 at load level C during the first and second sequences of Test 4a, strains associated with concrete shrinkage are not included in the plot.

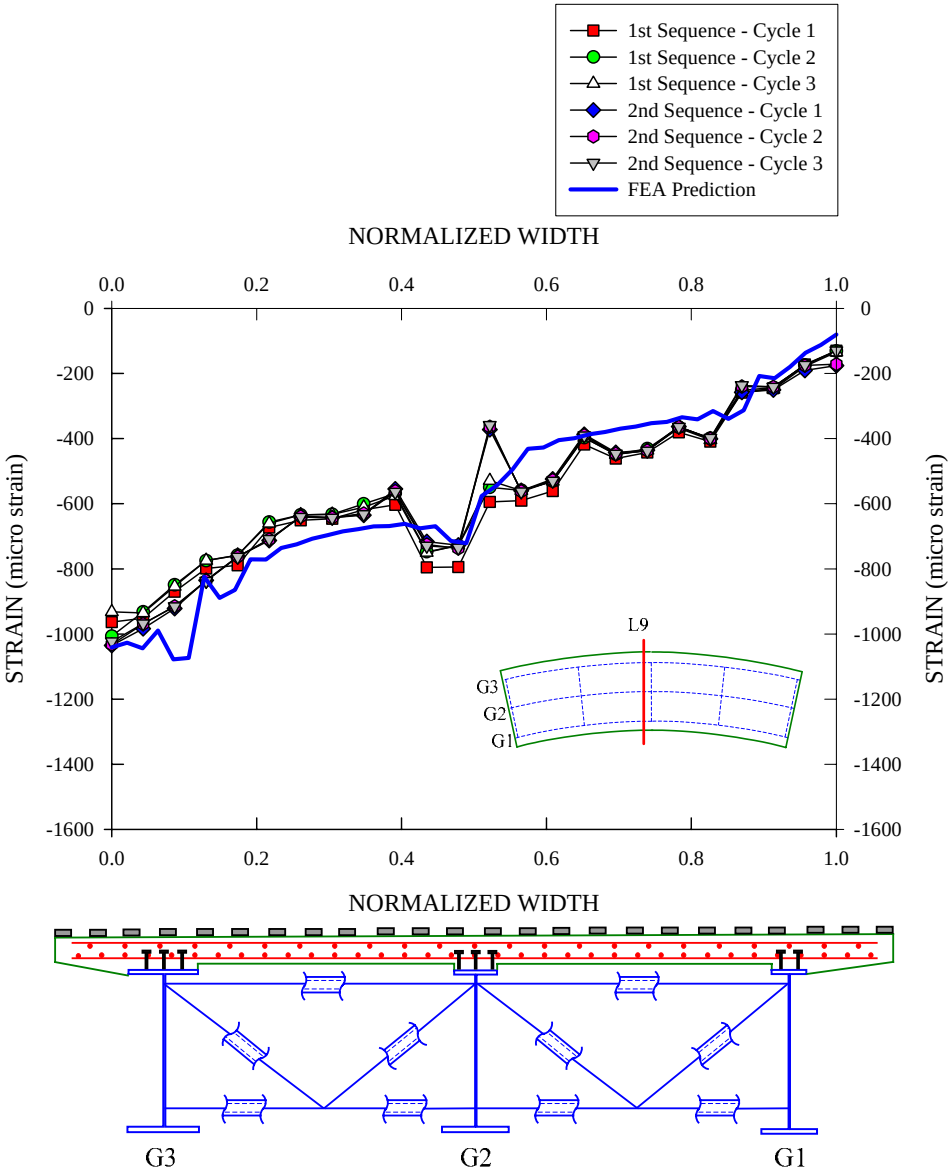

Figure C.1.4. Slab longitudinal strain distribution for gage location L9 at load level D during the first and second sequences of Test 4a, strains associated with concrete shrinkage are not included in the plot.

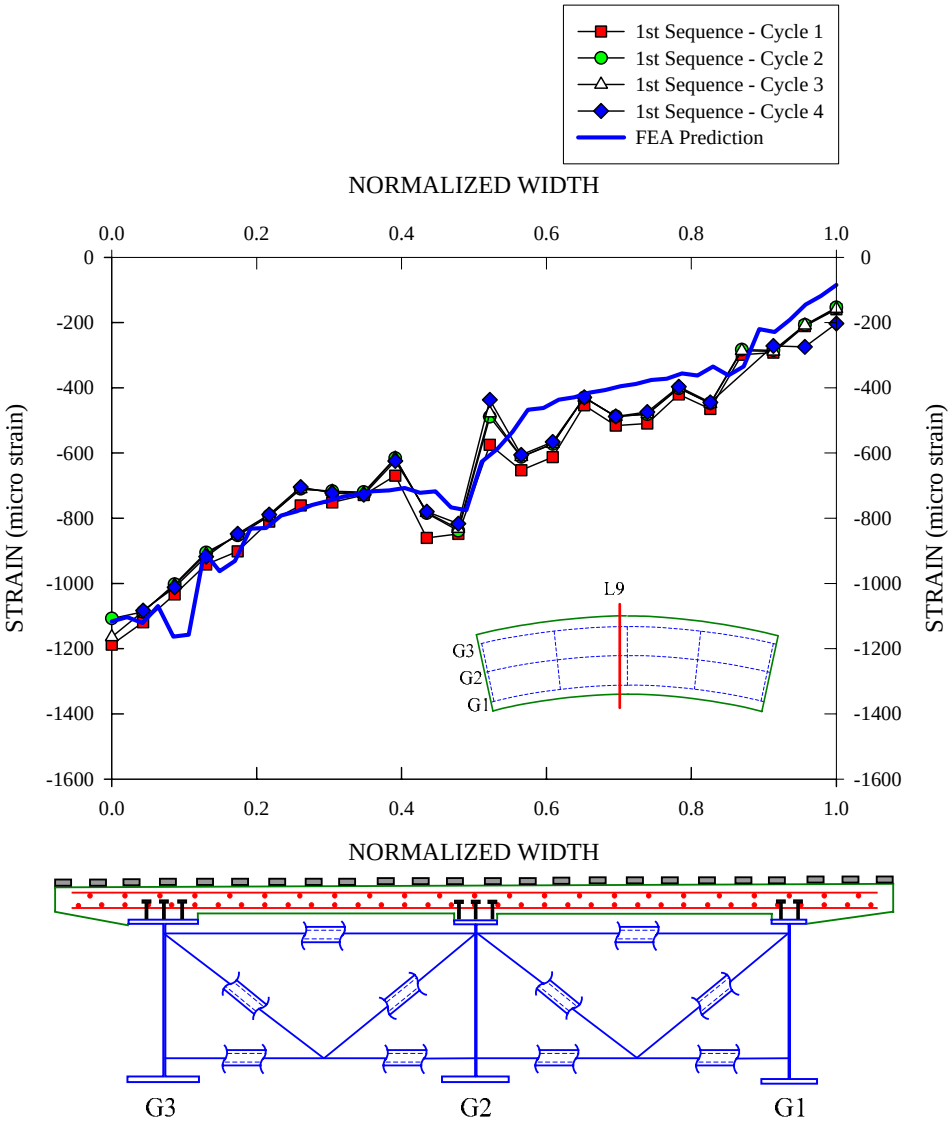

Figure C.1.5. Slab longitudinal strain distribution for gage location L9 at load level E during the first sequence of Test 4a, strains associated with concrete shrinkage are not included in the plot.

C.2 Girder Major-Axis and Lateral Bending Strains

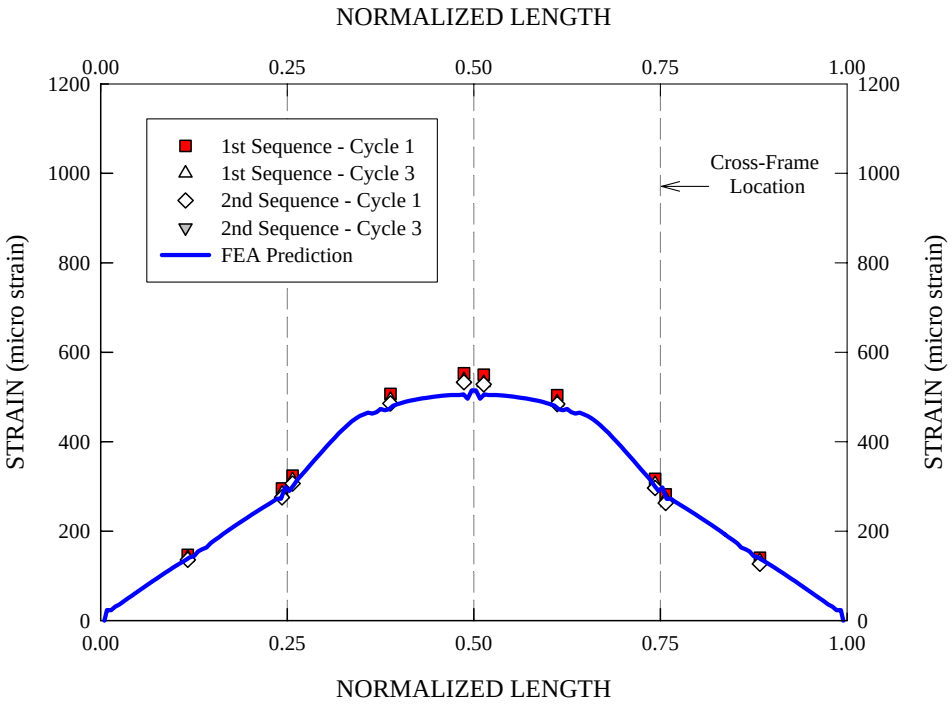

Figure C.2.1. G1 bottom flange major-axis bending strain variations along the girder length, load level A.

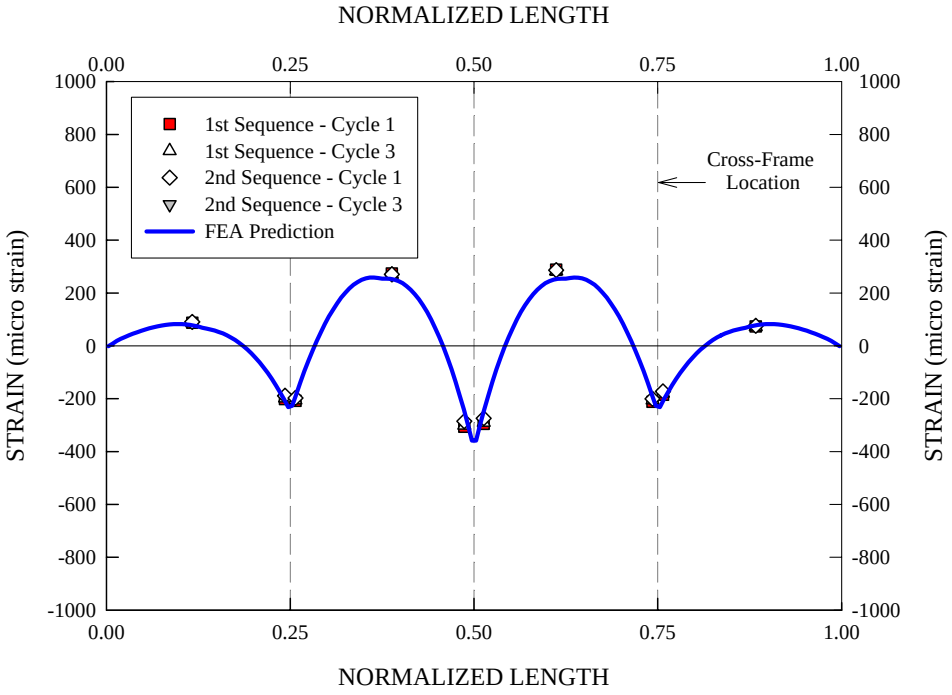

Figure C.2.2. G1 bottom flange lateral bending strain variations along the girder length, load level A.

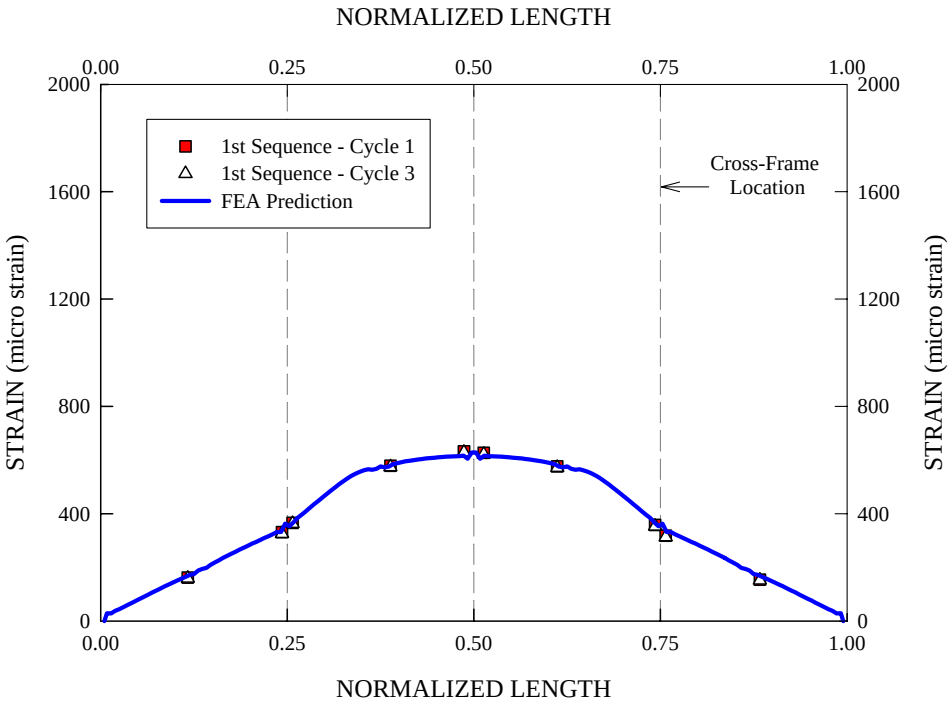

Figure C.2.3. G1 bottom flange major-axis bending strain variations along the girder length, load level B.

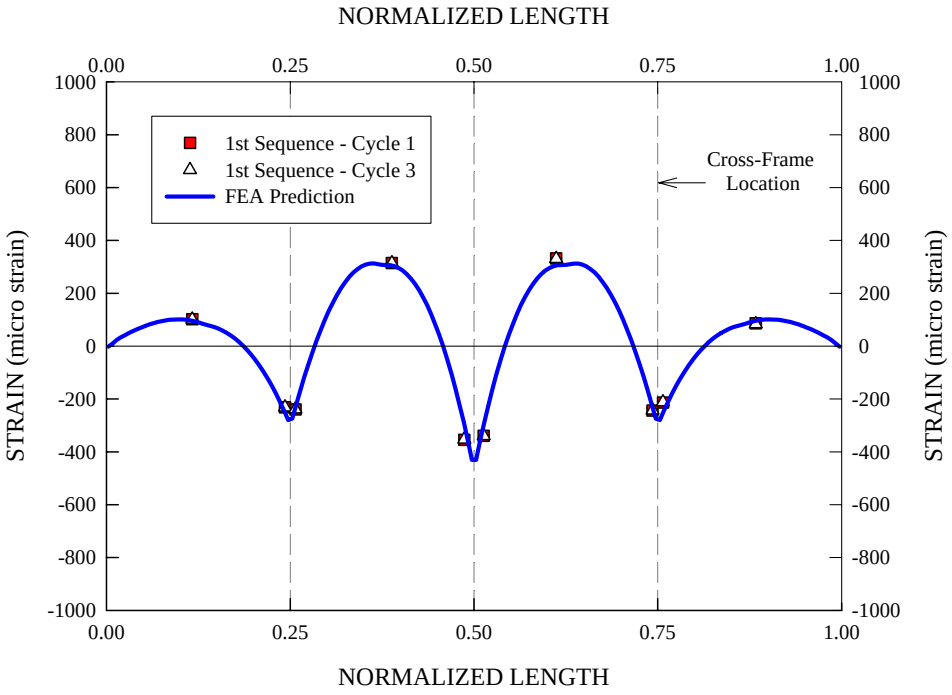

Figure C.2.4. G1 bottom flange lateral bending strain variations along the girder length, load level B.

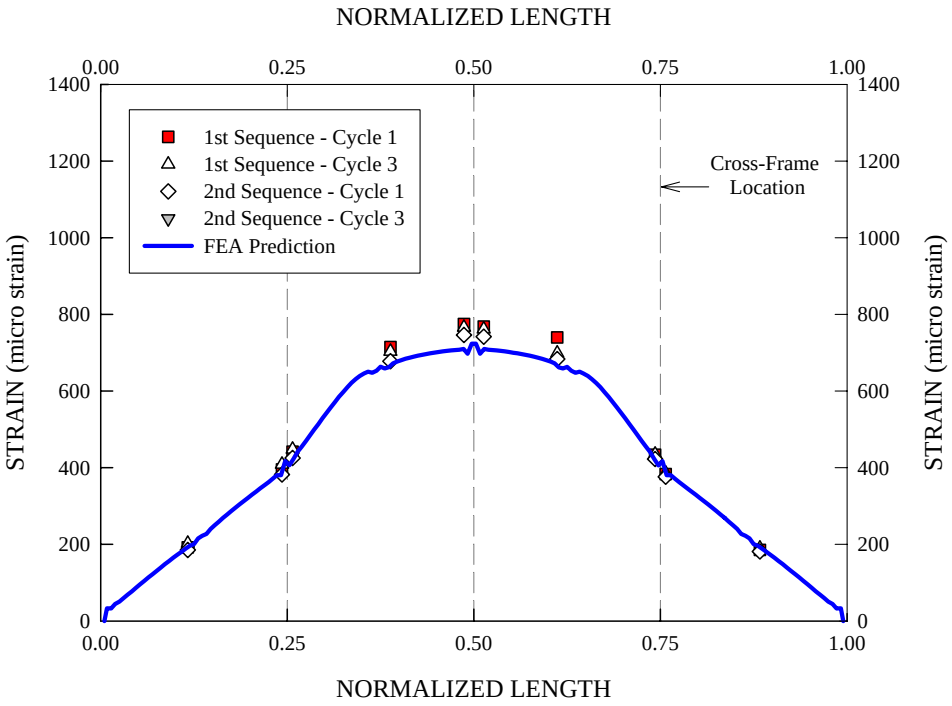

Figure C.2.5. G1 bottom flange major-axis bending strain variations along the girder length, load level C.

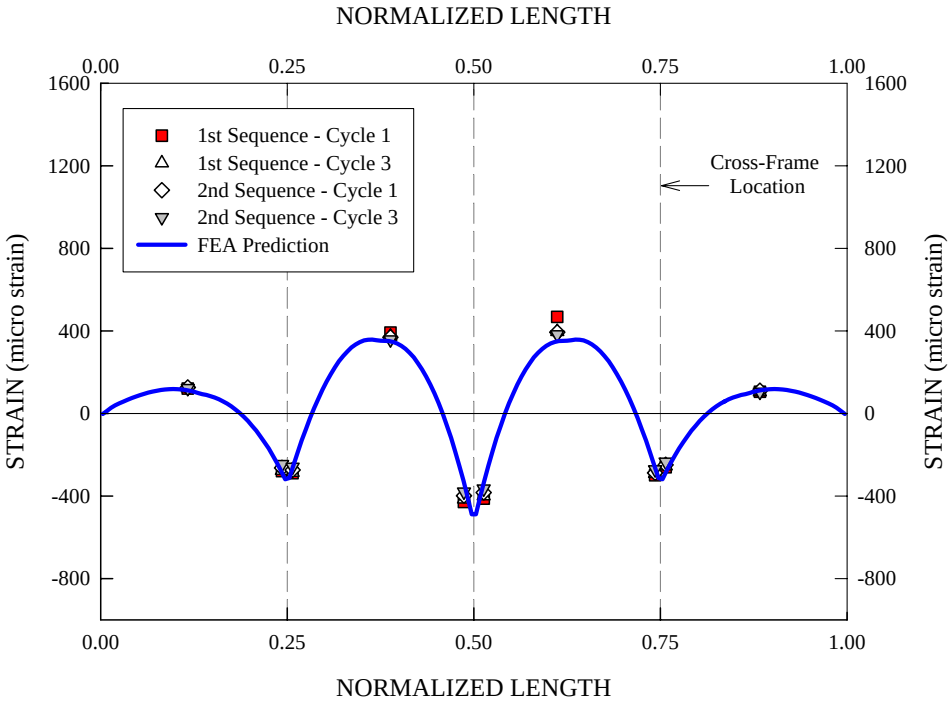

Figure C.2.6. G1 bottom flange lateral bending strain variations along the girder length, load level C.

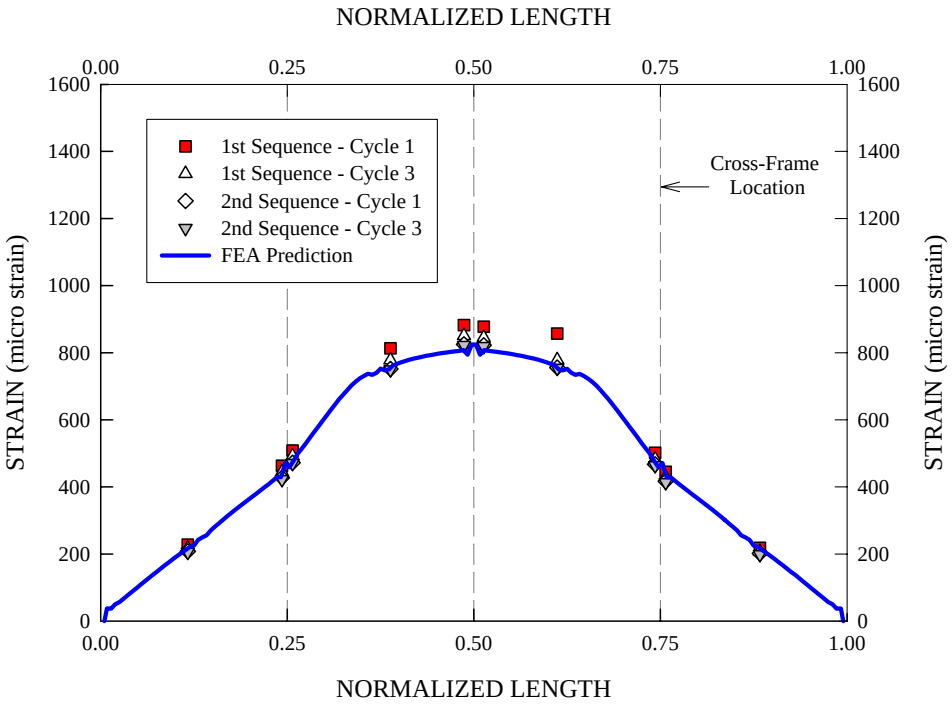

Figure C.2.7. G1 bottom flange major-axis bending strain variations along the girder length, load level D.

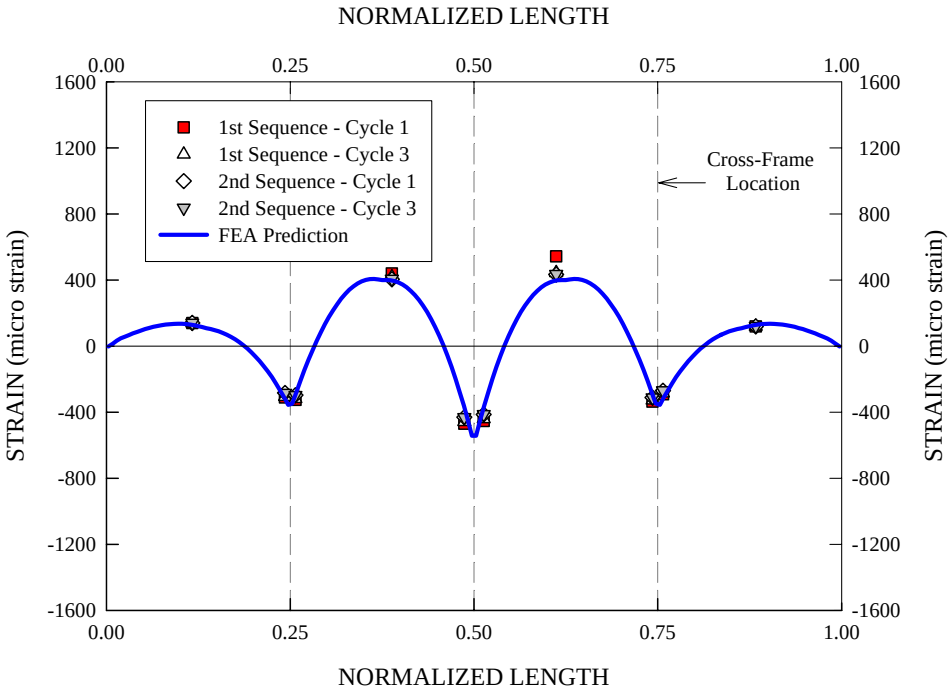

Figure C.2.8. G1 bottom flange lateral bending strain variations along the girder length, load level D.

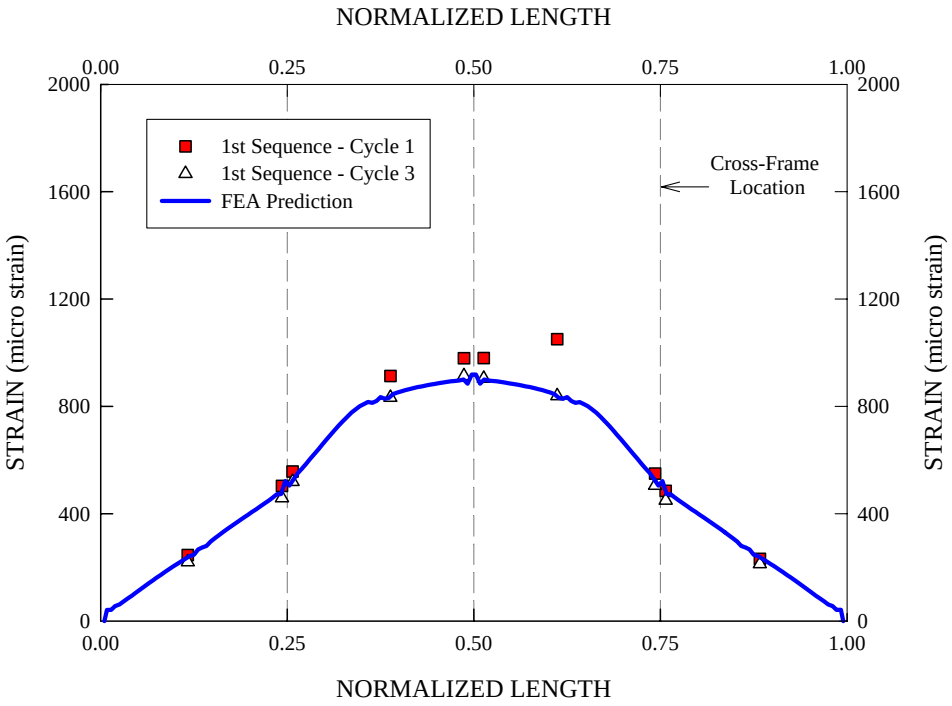

Figure C.2.9. G1 bottom flange major-axis bending strain variations along the girder length, load level E.

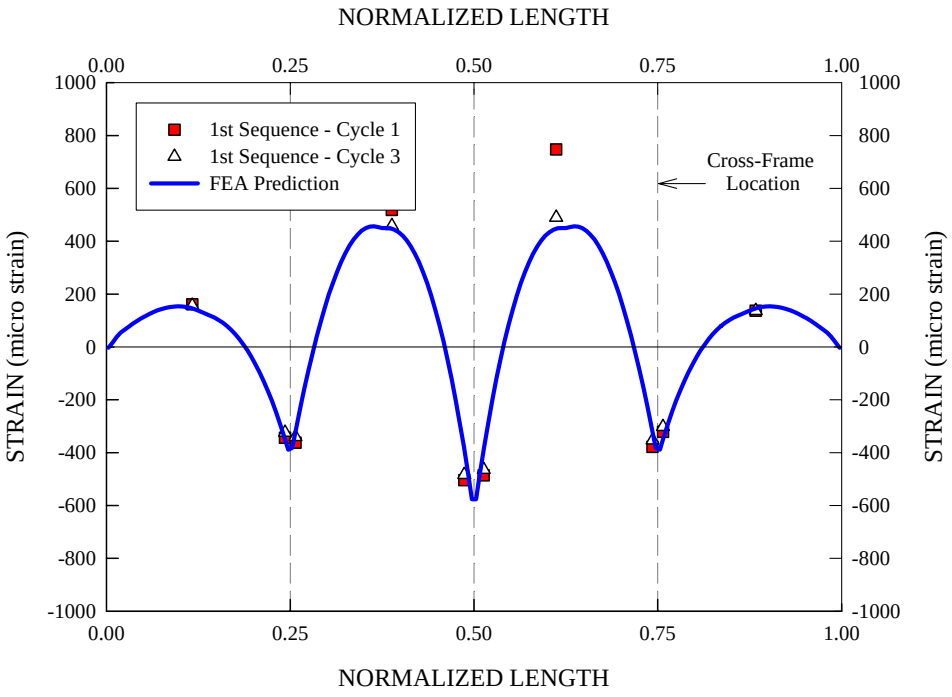

Figure C.2.10. G1 bottom flange lateral bending strain variations along the girder length, load level E.

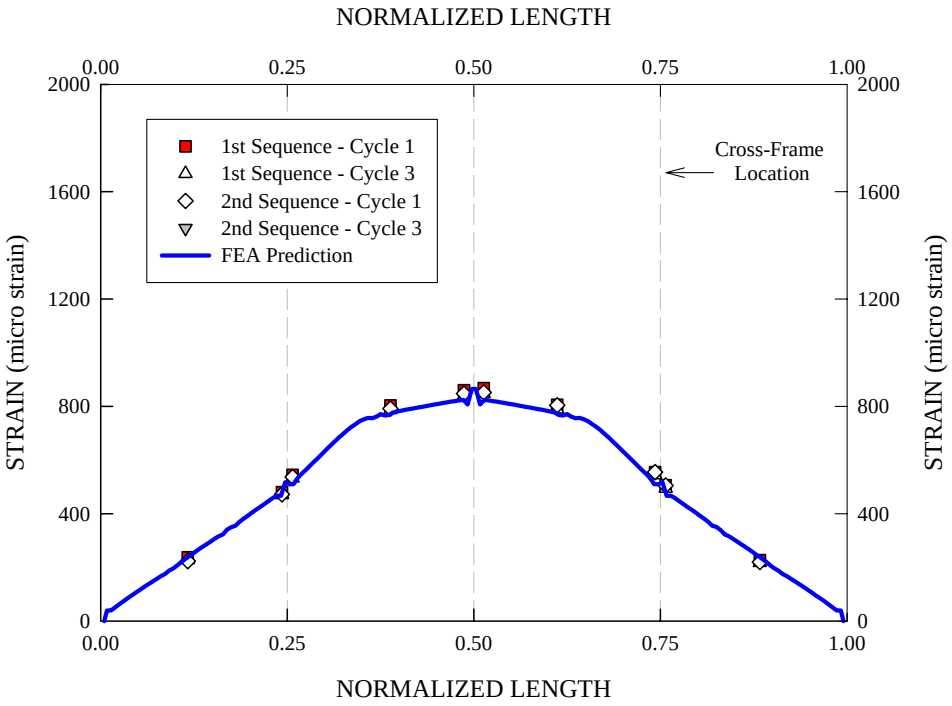

Figure C.2.11. G2 bottom flange major-axis bending strain variations along the girder length, load level A.

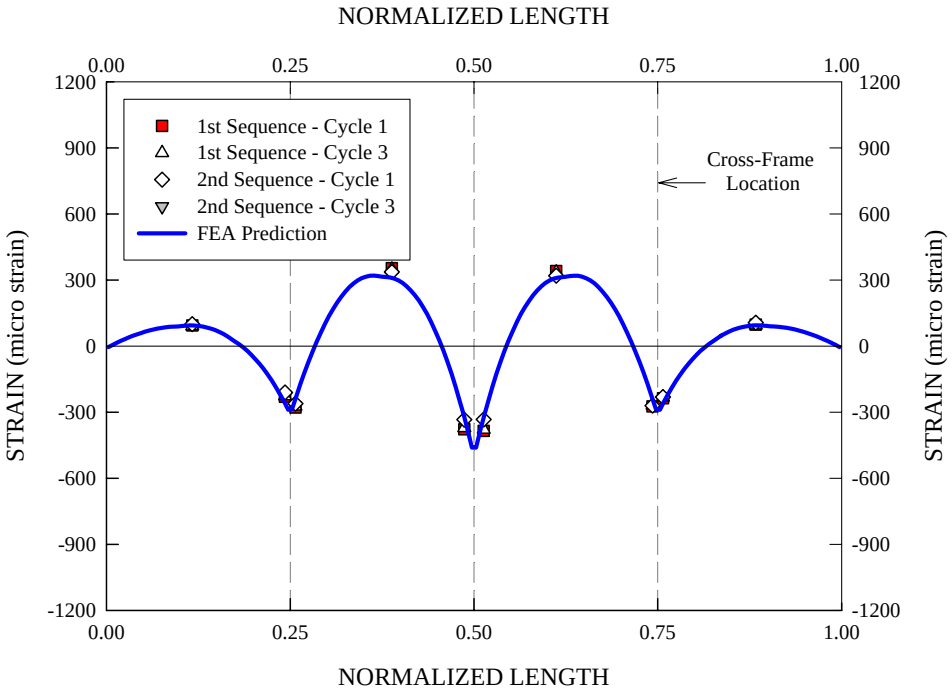

Figure C.2.12. G2 bottom flange lateral bending strain variations along the girder length, load level A.

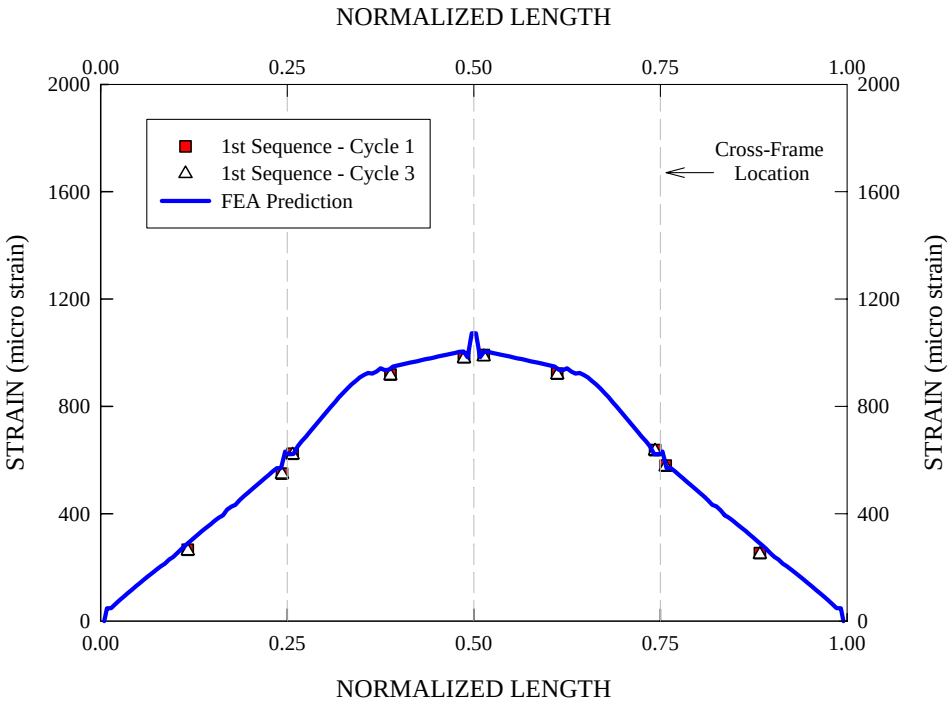

Figure C.2.13. G2 bottom flange major-axis bending strain variations along the girder length, load level B.

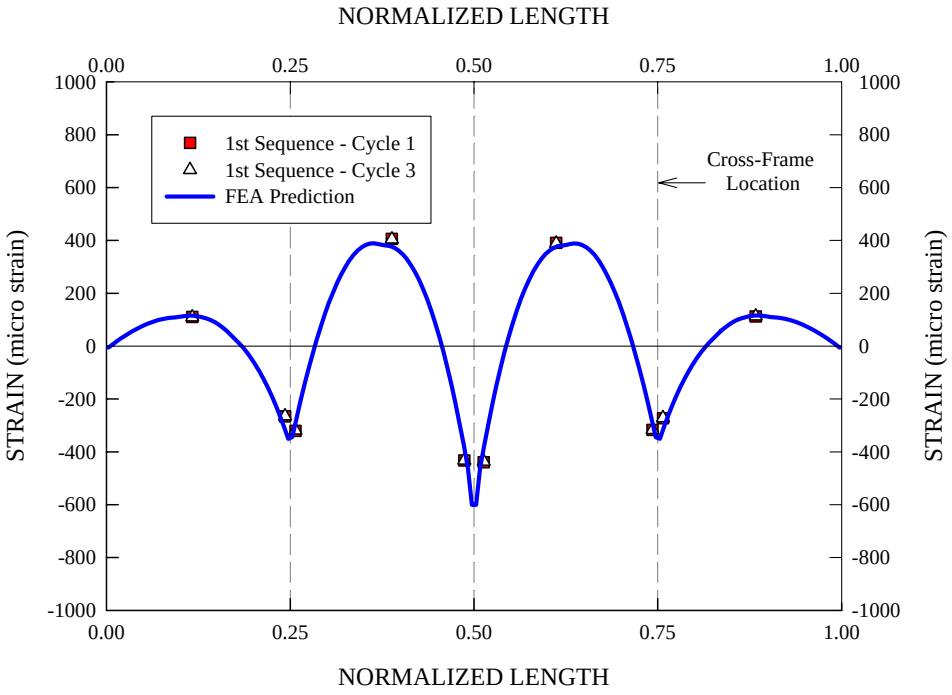

Figure C.2.14. G2 bottom flange lateral bending strain variations along the girder length, load level B.

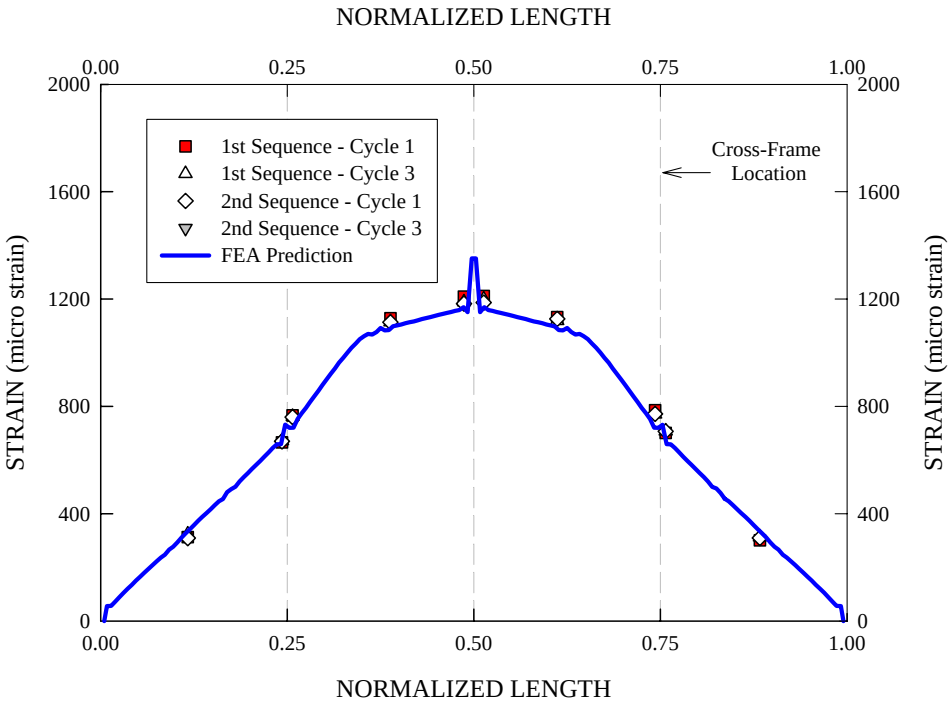

Figure C.2.15. G2 bottom flange major-axis bending strain variations along the girder length, load level C.

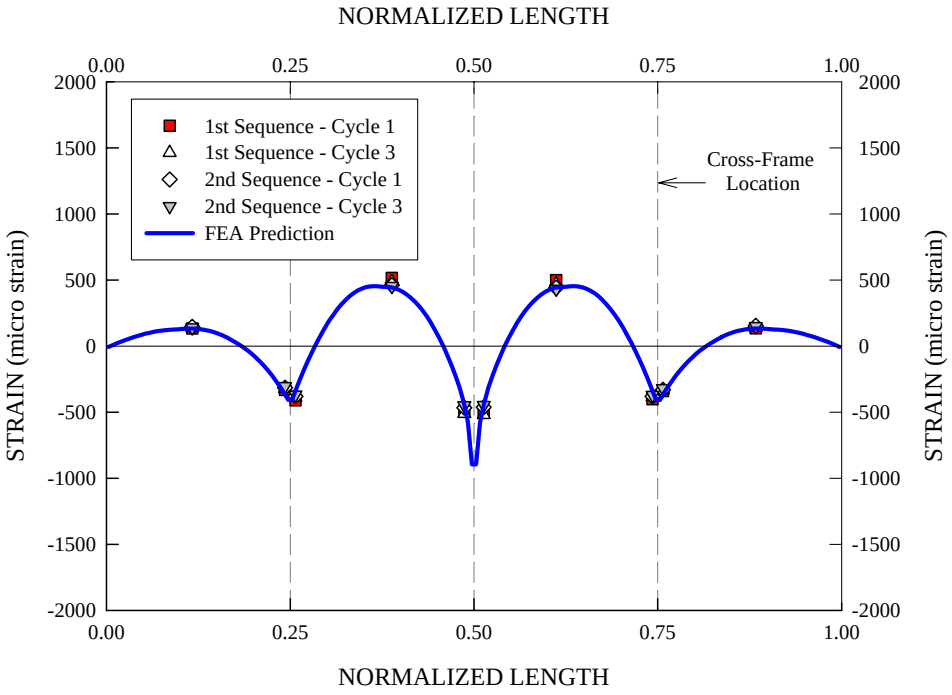

Figure C.2.16. G2 bottom flange lateral bending strain variations along the girder length, load level C.

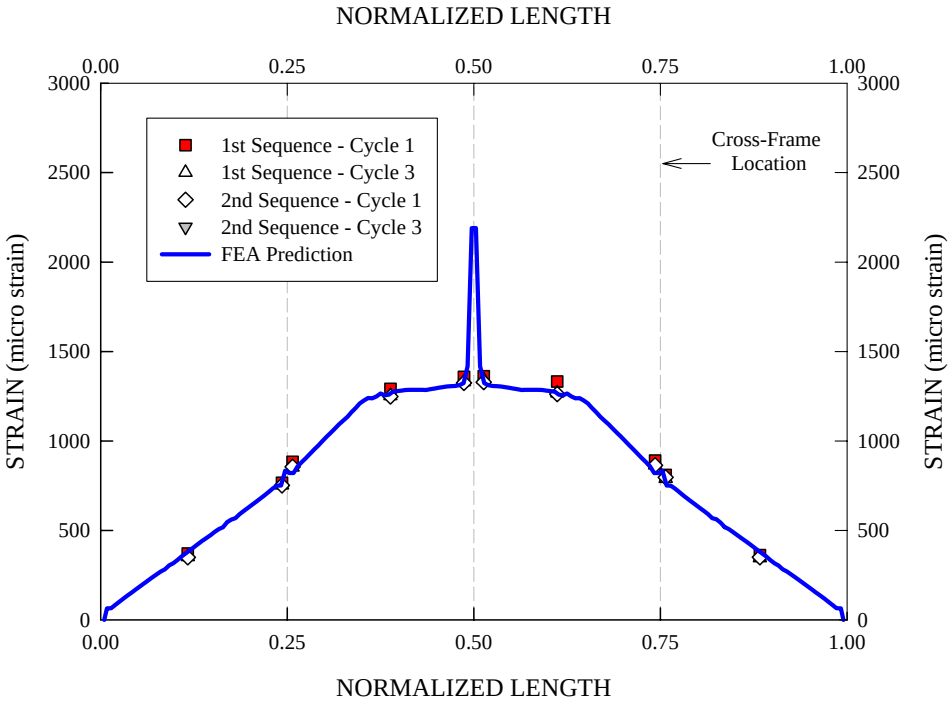

Figure C.2.17. G2 bottom flange major-axis bending strain variations along the girder length, load level D.

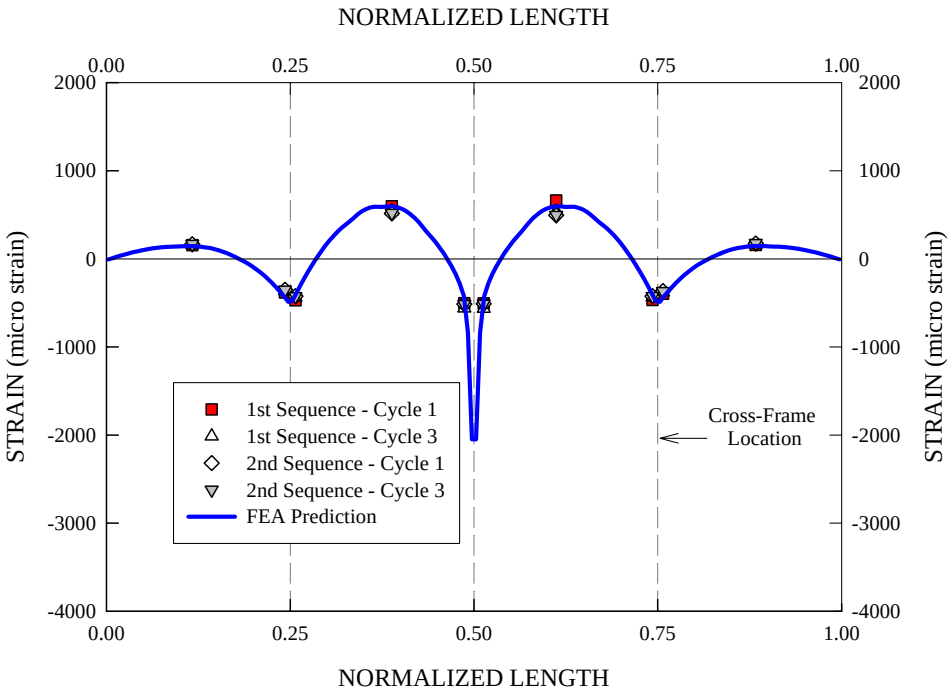

Figure C.2.18. G2 bottom flange lateral bending strain variations along the girder length, load level D.

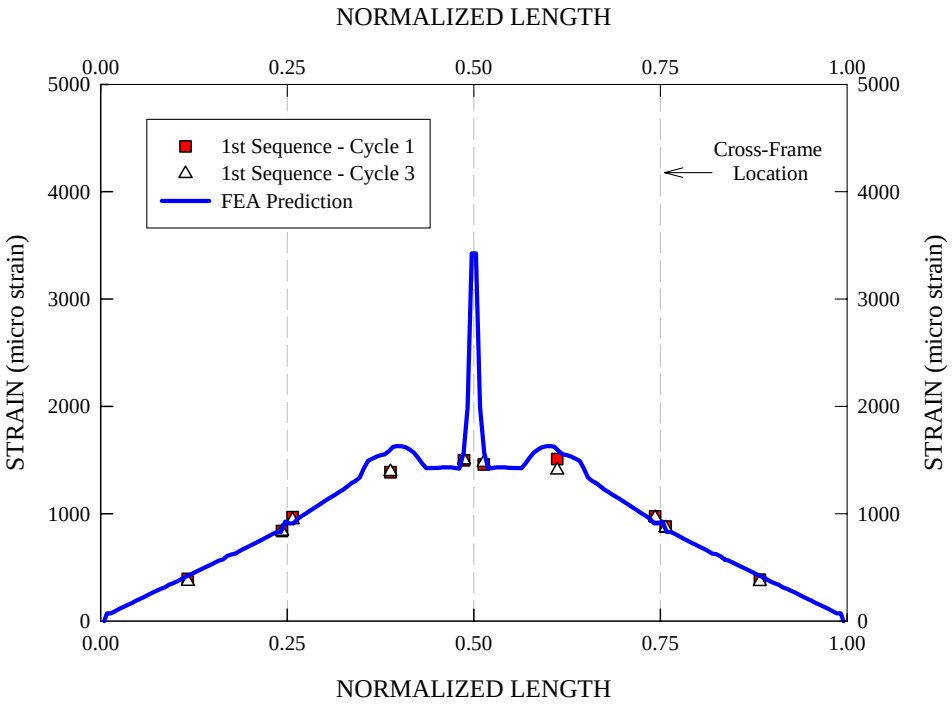

Figure C.2.19. G2 bottom flange major-axis bending strain variations along the girder length, load level E.

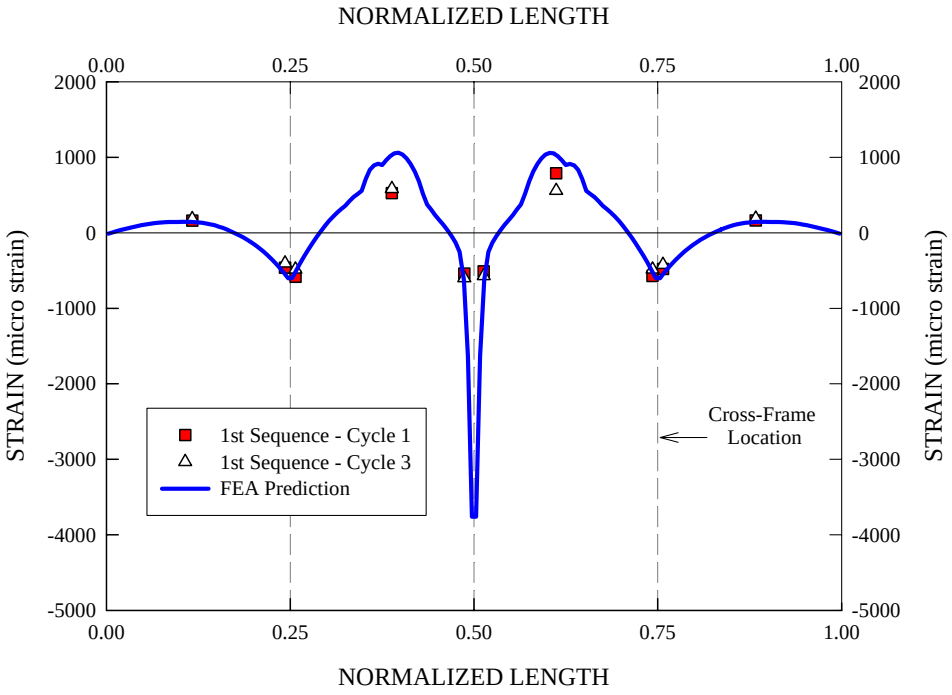

Figure C.2.20. G2 bottom flange lateral bending strain variations along the girder length, load level E.

C.3 G3 Slip Measurements

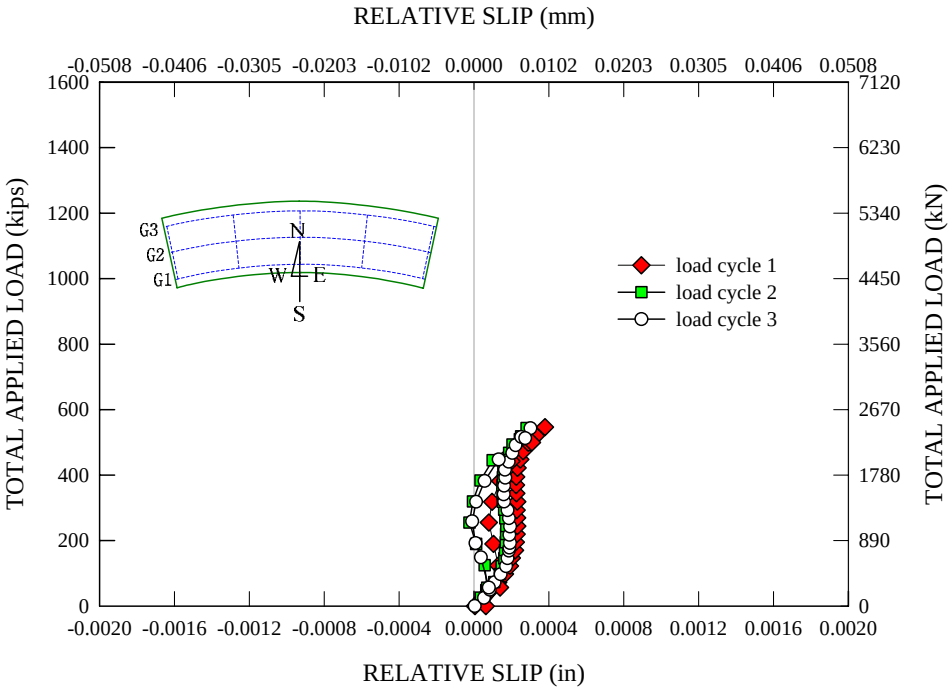

Figure C.3.1. G3 - Total applied load vs. east end relative longitudinal slip deformation at the concrete-steel interface at load level A during the first sequence of Test 4a.

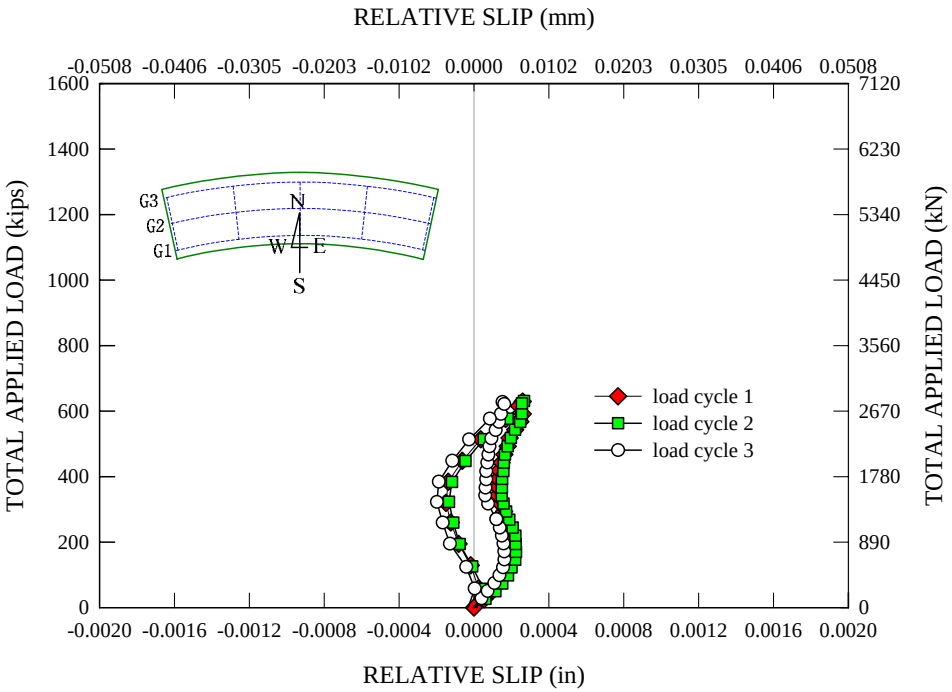

Figure C.3.2. G3 - Total applied load vs. east end relative longitudinal slip deformation at the concrete-steel interface at load level B during the first sequence of Test 4a.

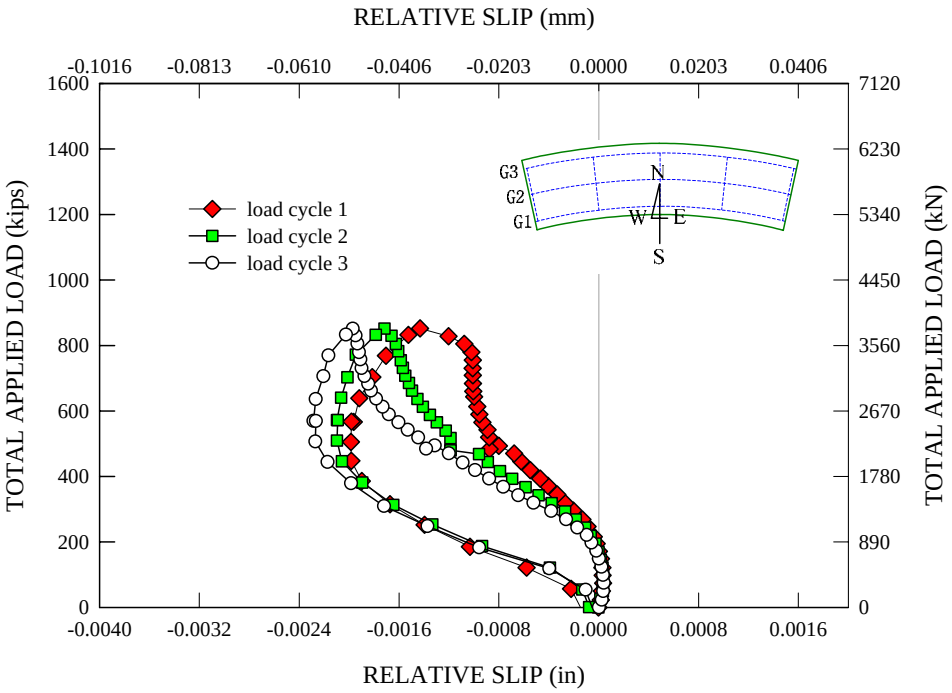

Figure C.3.3. G3 - Total applied load vs. east end relative longitudinal slip deformation at the concrete-steel interface at load level C during the first sequence of Test 4a.

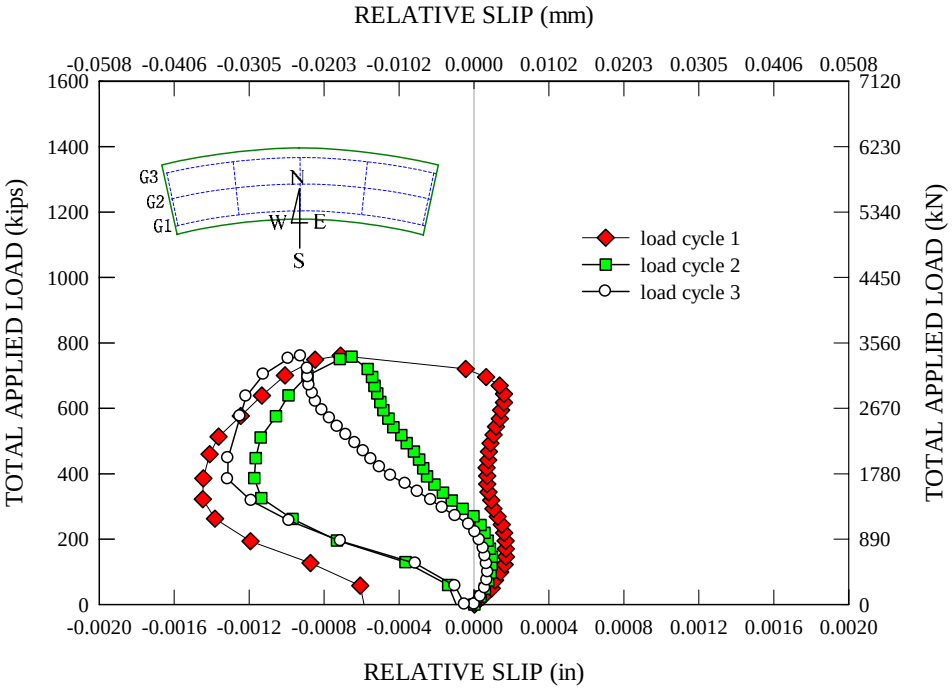

Figure C.3.4. G3 - Total applied load vs. east end relative longitudinal slip deformation at the concrete-steel interface at load level D during the first sequence of Test 4a.

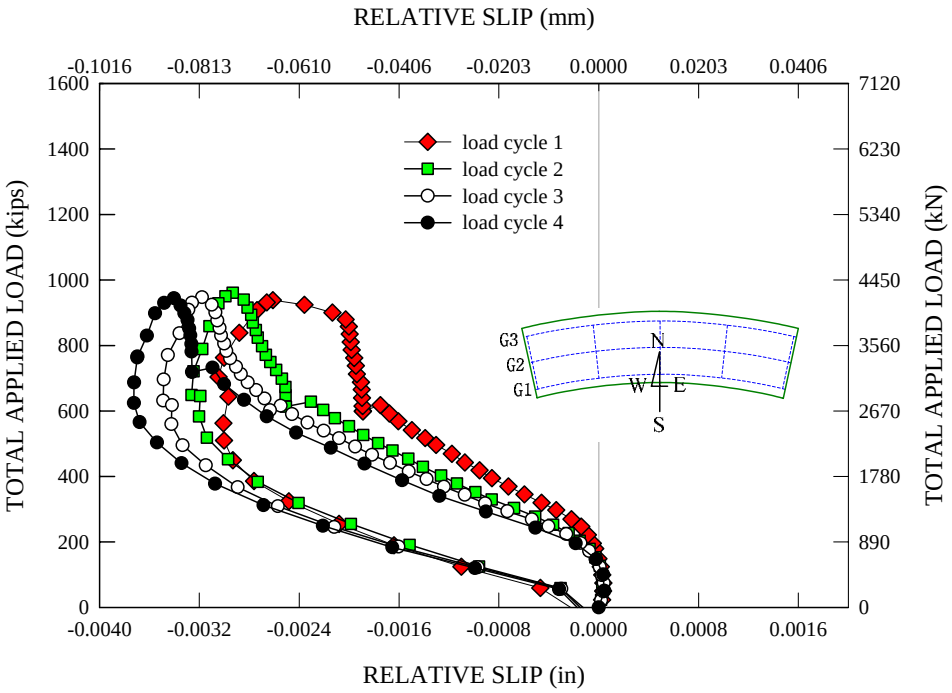

Figure C.3.5. G3 - Total applied load vs. east end relative longitudinal slip deformation at the concrete-steel interface at load level E during the first sequence of Test 4a.

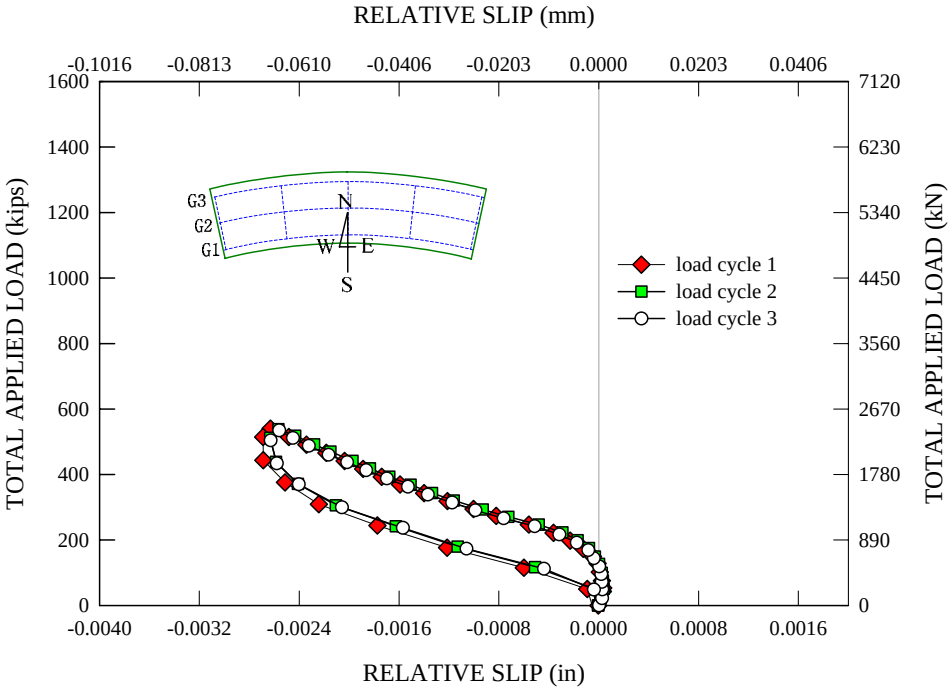

Figure C.3.6. G3 - Total applied load vs. east end relative longitudinal slip deformation at the concrete-steel interface at load level A during the second sequence of Test 4a.

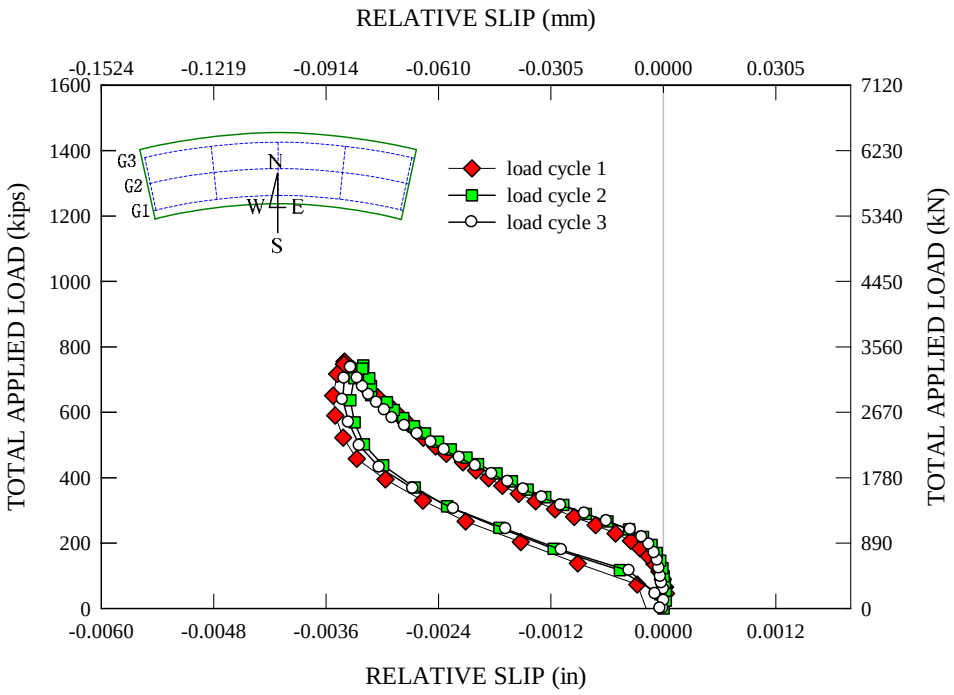

Figure C.3.7. G3 - Total applied load vs. east end relative longitudinal slip deformation at the concrete-steel interface at load level C during the second sequence of Test 4a.

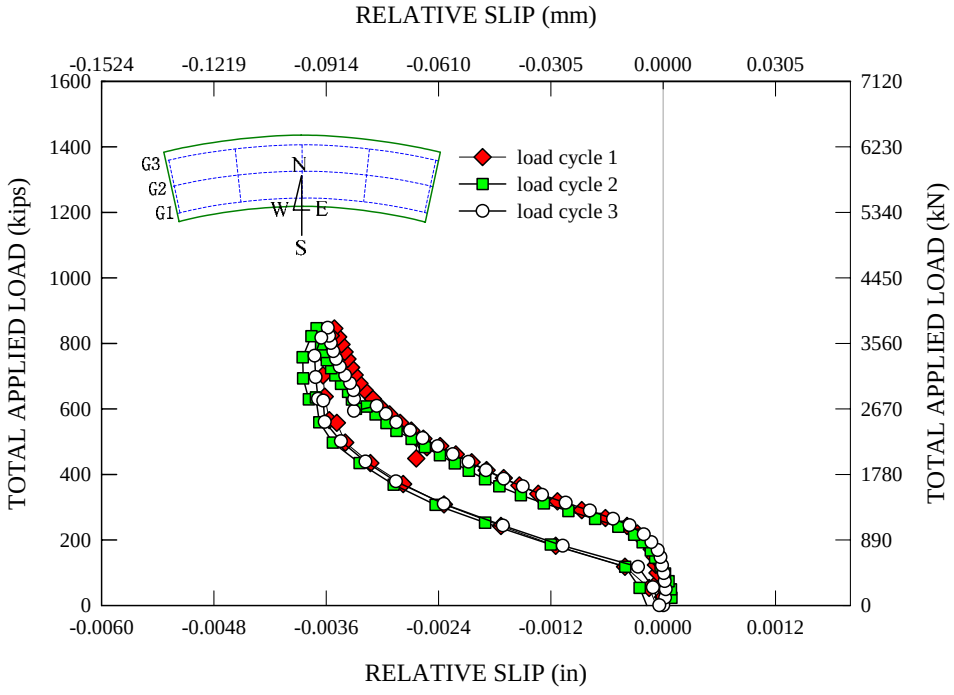

Figure C.3.8. G3 - Total applied load vs. east end relative longitudinal slip deformation at the concrete-steel interface at load level D during the second sequence of Test 4a.

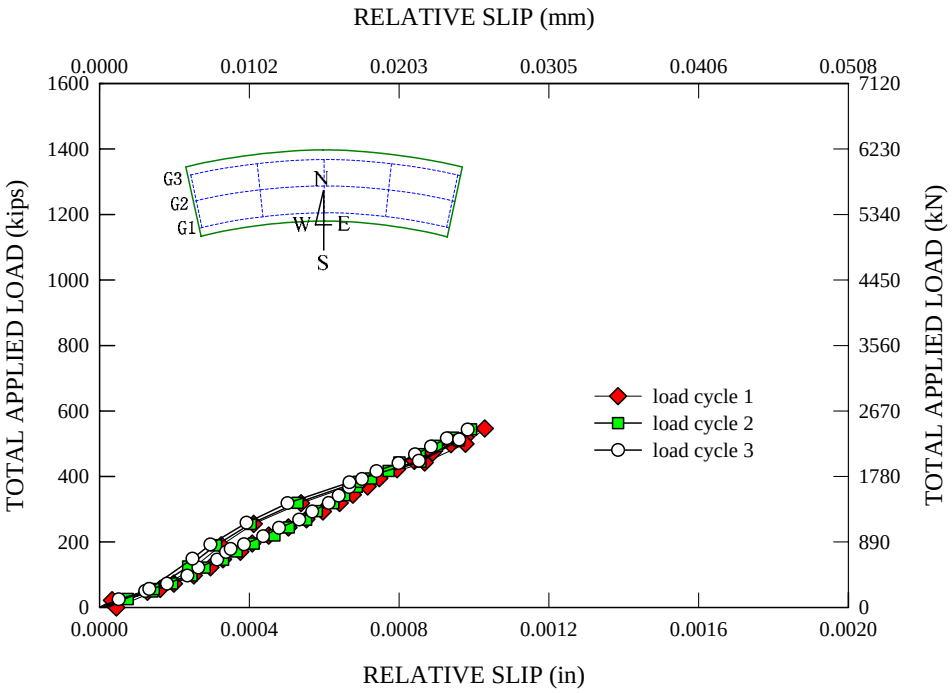

Figure C.3.9. G3 - Total applied load vs. west end relative longitudinal slip deformation at the concrete-steel interface at load level A during the first sequence of Test 4a.

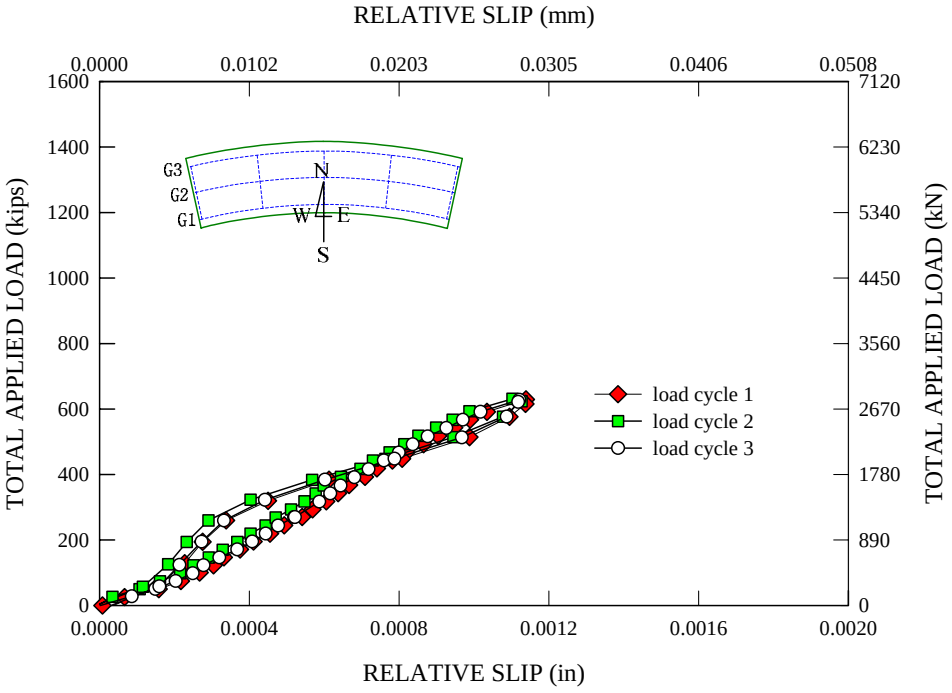

Figure C.3.10. G3 - Total applied load vs. west end relative longitudinal slip deformation at the concrete-steel interface at load level B during the first sequence of Test 4a.

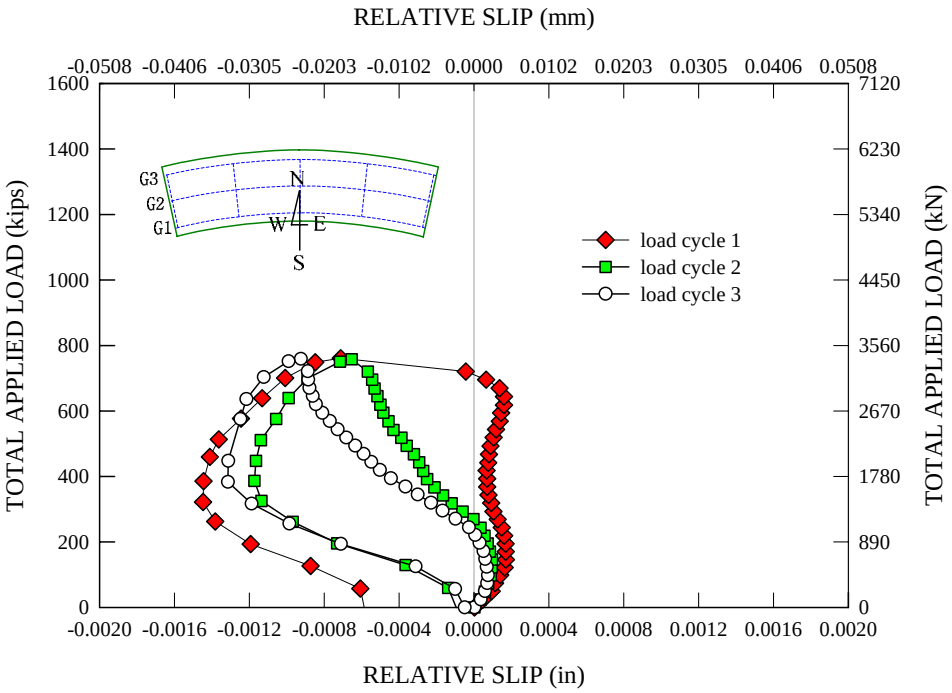

Figure C.3.11. G3 - Total applied load vs. west end relative longitudinal slip deformation at the concrete-steel interface at load level C during the first sequence of Test 4a.

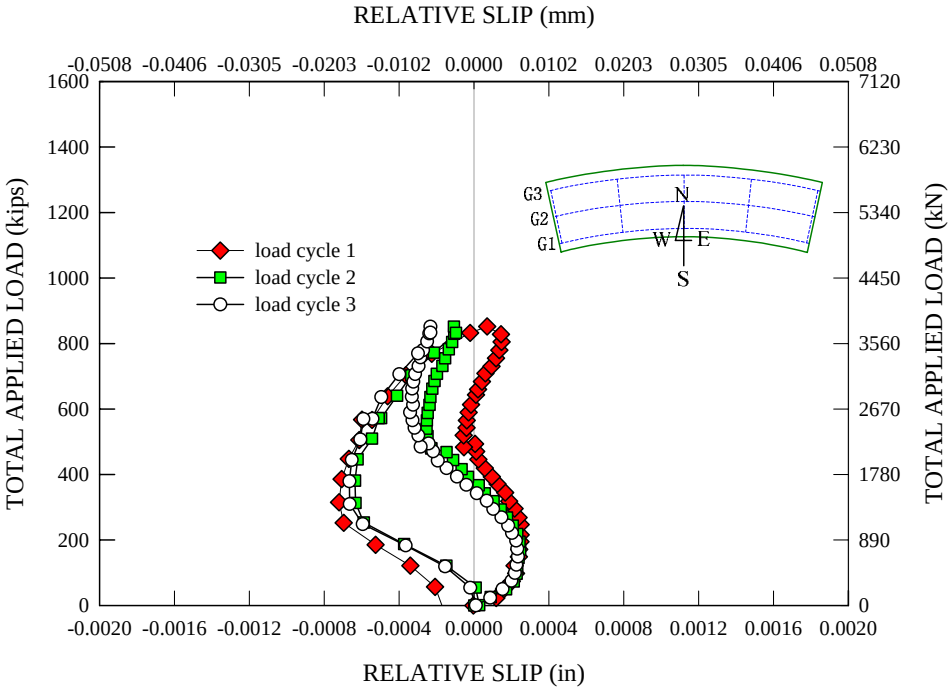

Figure C.3.12. G3 - Total applied load vs. west end relative longitudinal slip deformation at the concrete-steel interface at load level D during the first sequence of Test 4a.

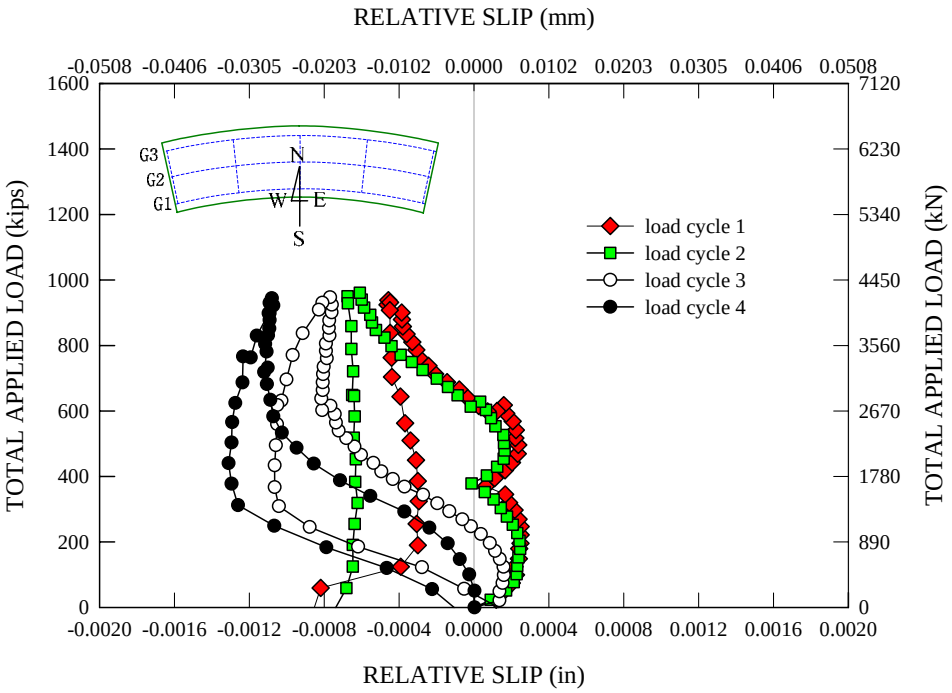

Figure C.3.13. G3 - Total applied load vs. west end relative longitudinal slip deformation at the concrete-steel interface at load level E during the first sequence of Test 4a.

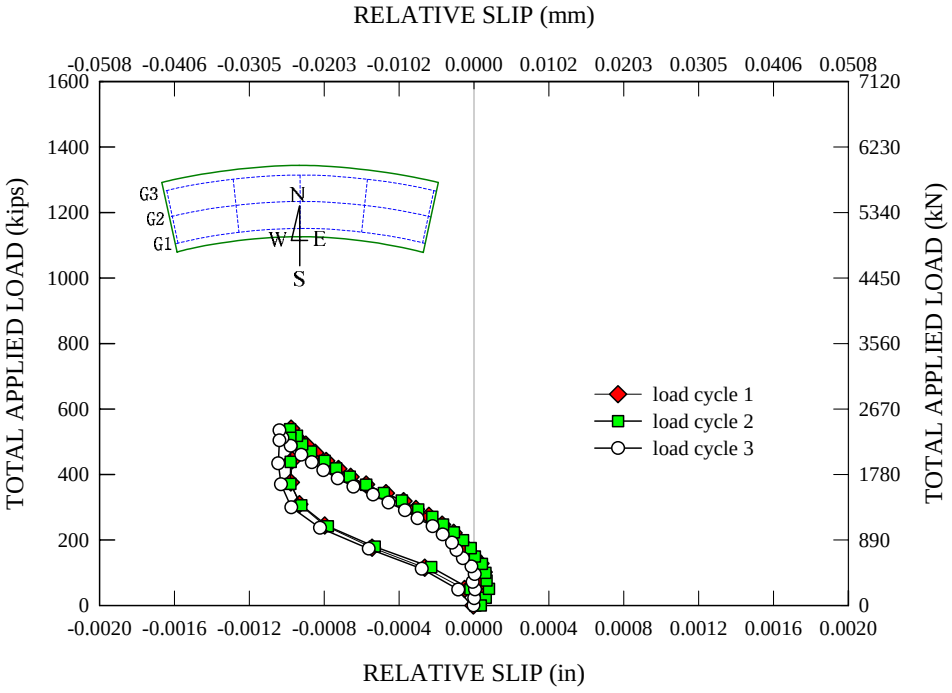

Figure C.3.14. G3 - Total applied load vs. west end relative longitudinal slip deformation at the concrete-steel interface at load level A during the second sequence of Test 4a.

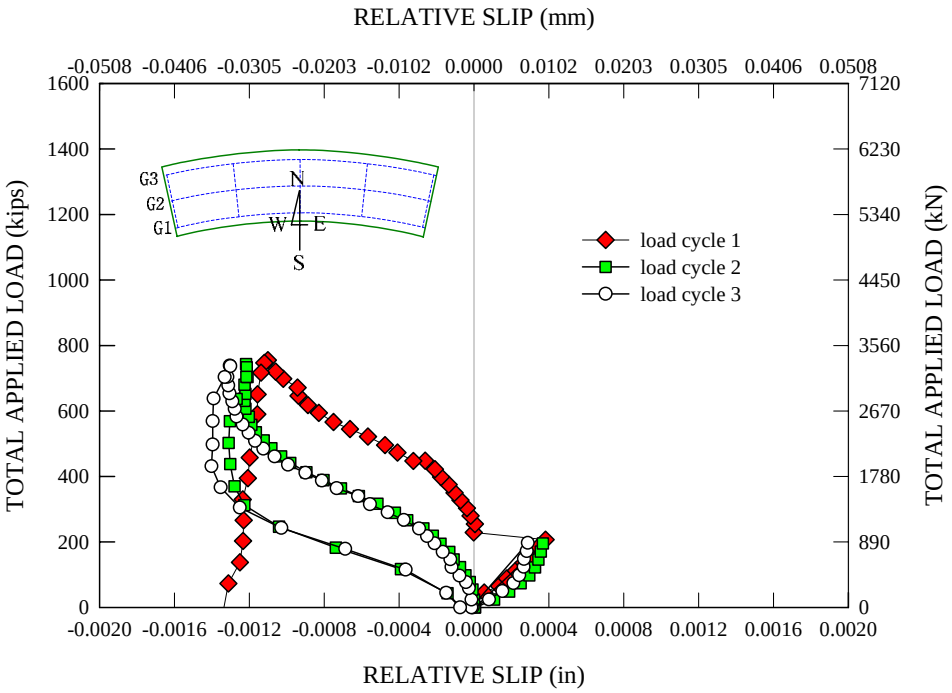

Figure C.3.15. G3 - Total applied load vs. west end relative longitudinal slip deformation at the concrete-steel interface at load level C during the second sequence of Test 4a.

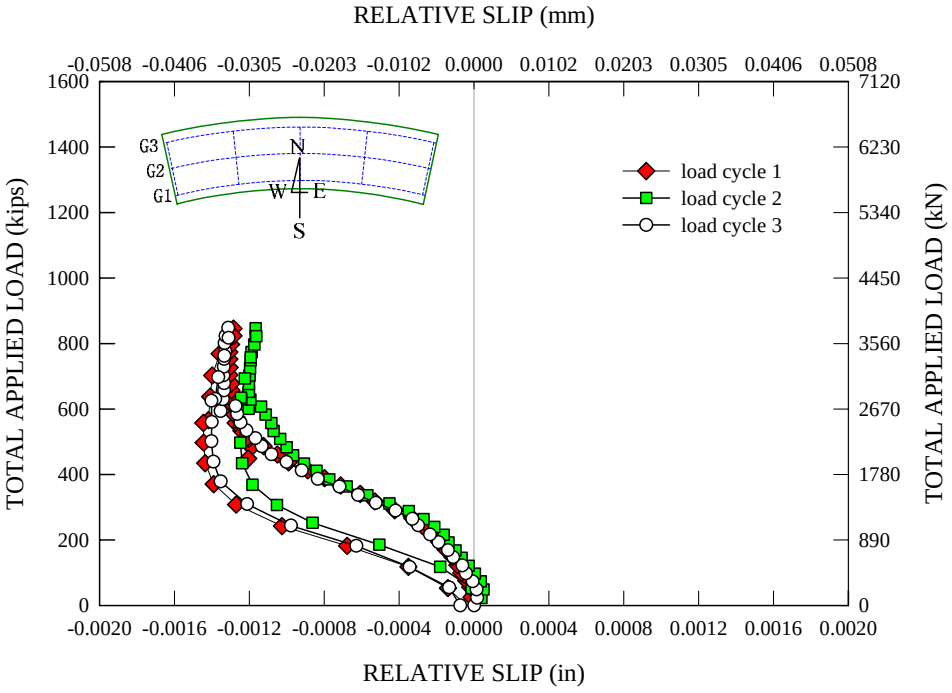

Figure C.3.16. G3 - Total applied load vs. west end relative longitudinal slip deformation at the concrete-steel interface at load level D during the second sequence of Test 4a.

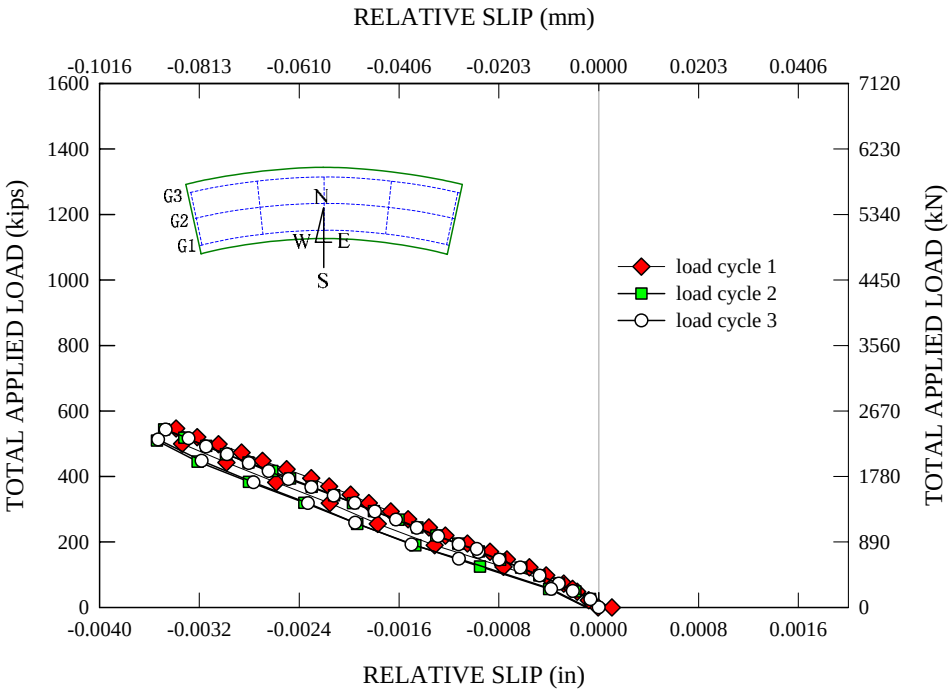

Figure C.3.17. G3 - Total applied load vs. relative radial slip deformation at the concrete-steel interface at load level A during the first sequence of Test 4a.

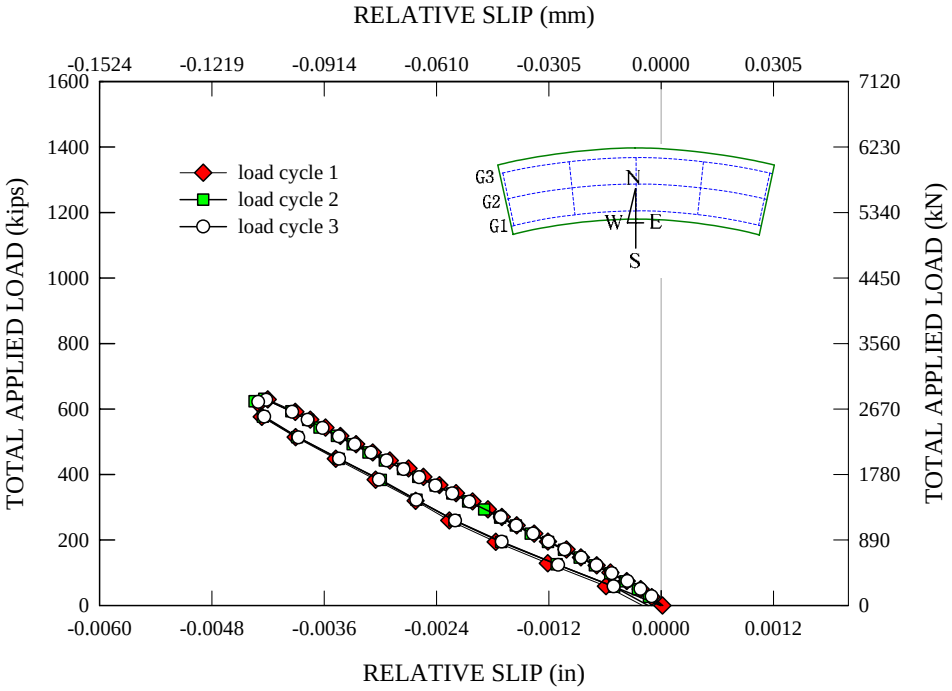

Figure C.3.18. G3 - Total applied load vs. relative radial slip deformation at the concrete-steel interface at load level B during the first sequence of Test 4a.

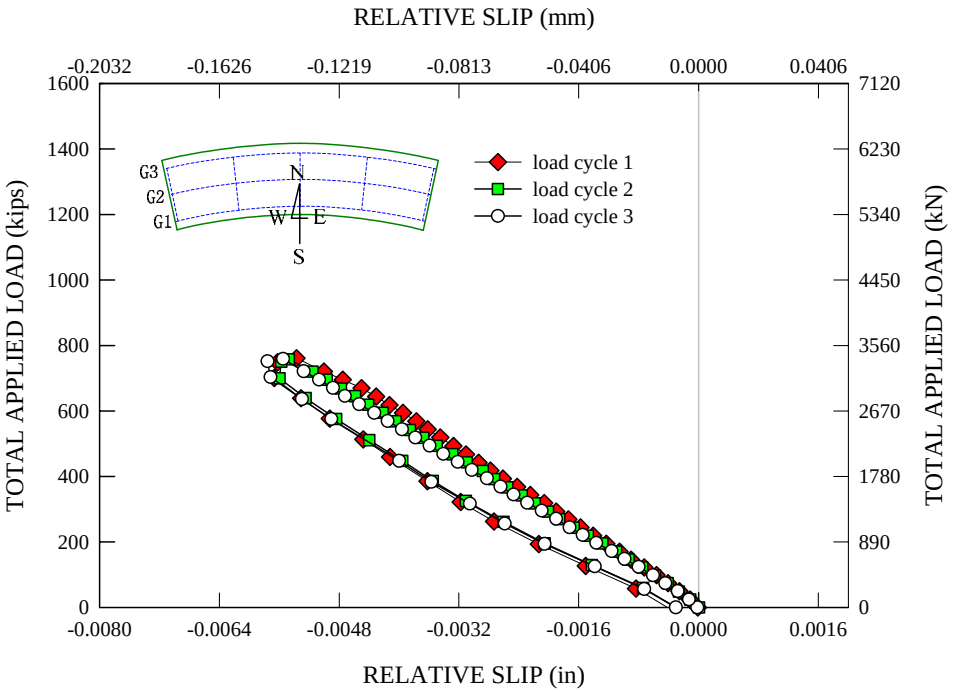

Figure C.3.19. G3 - Total applied load vs. relative radial slip deformation at the concrete-steel interface at load level C during the first sequence of Test 4a.

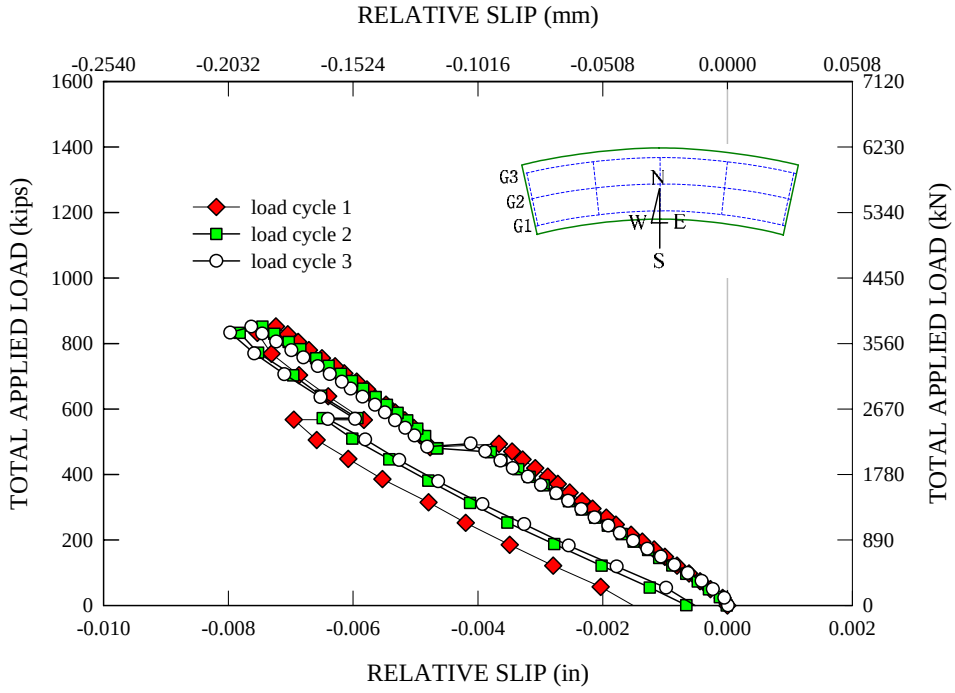

Figure C.3.20. G3 - Total applied load vs. relative radial slip deformation at the concrete-steel interface at load level D during the first sequence of Test 4a.

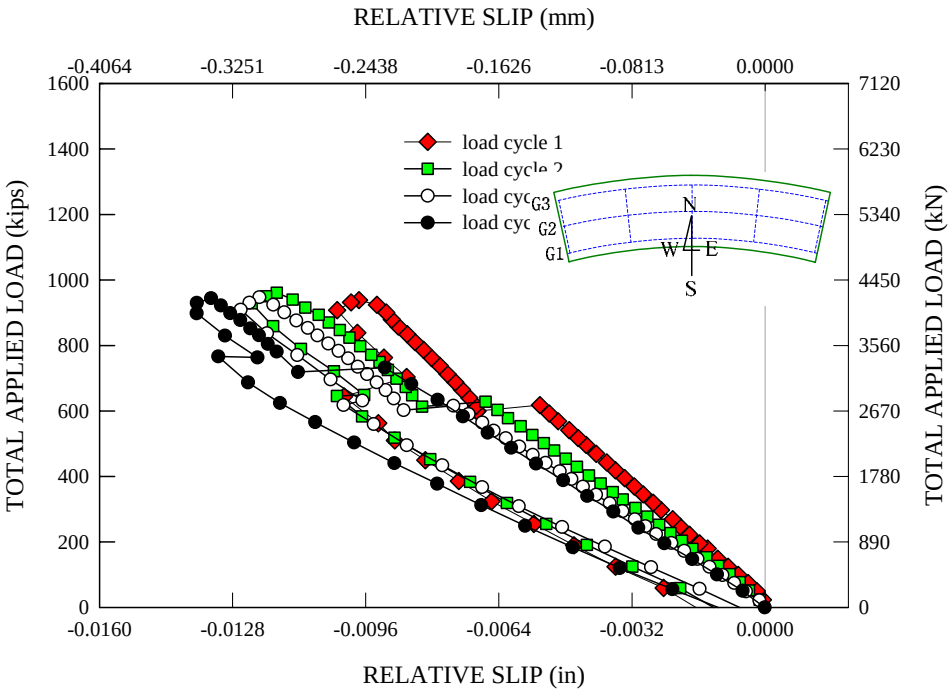

Figure C.3.21. G3 - Total applied load vs. relative radial slip deformation at the concrete-steel interface at load level E during the first sequence of Test 4a.

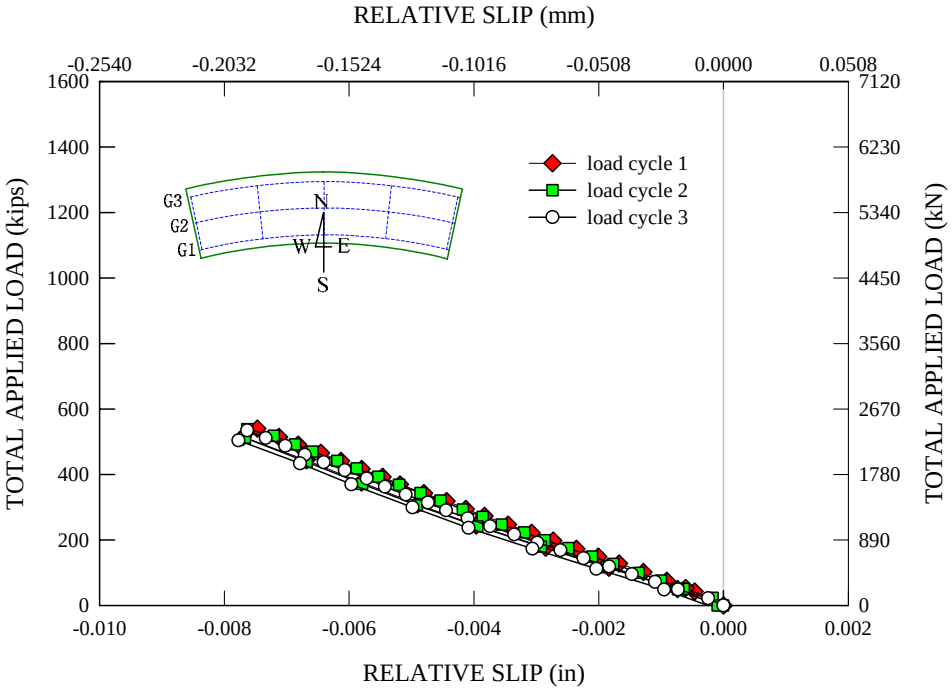

Figure C.3.22. G3 - Total applied load vs. relative radial slip deformation at the concrete-steel interface at load level A during the second sequence of Test 4a.

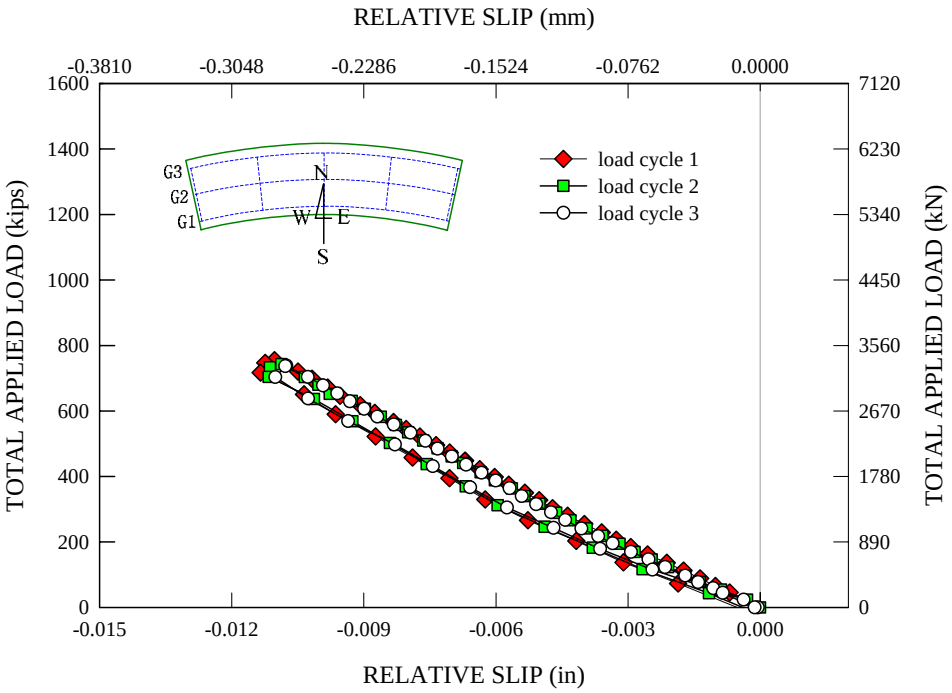

Figure C.3.23. G3 - Total applied load vs. relative radial slip deformation at the concrete-steel interface at load level C during the second sequence of Test 4a.

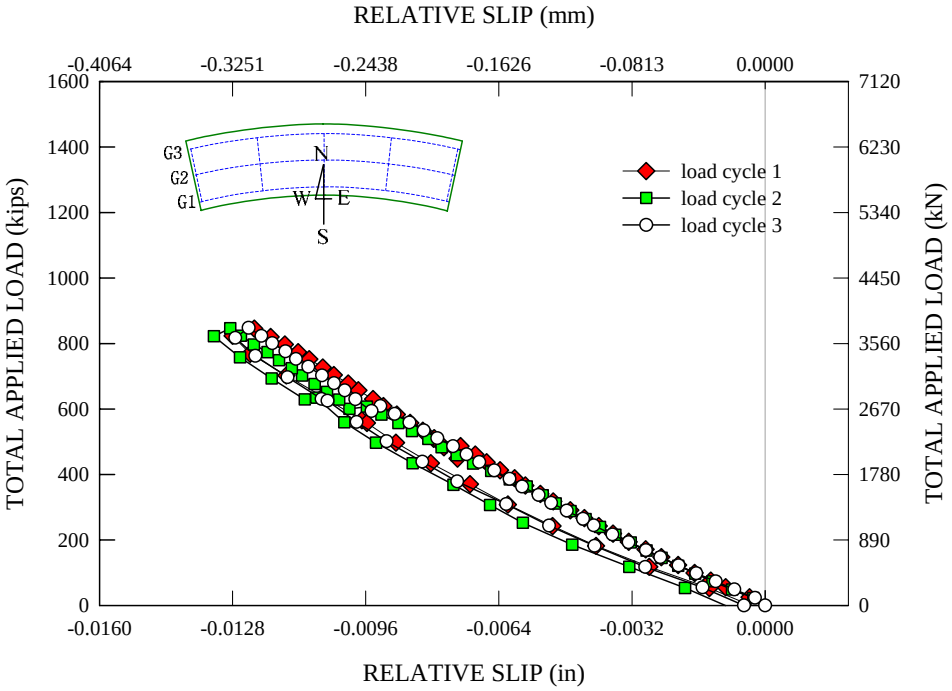

Figure C.3.24. G3 - Total applied load vs. relative radial slip deformation at the concrete-steel interface at load level D during the second sequence of Test 4a.

C.4 G2 Slip Measurements

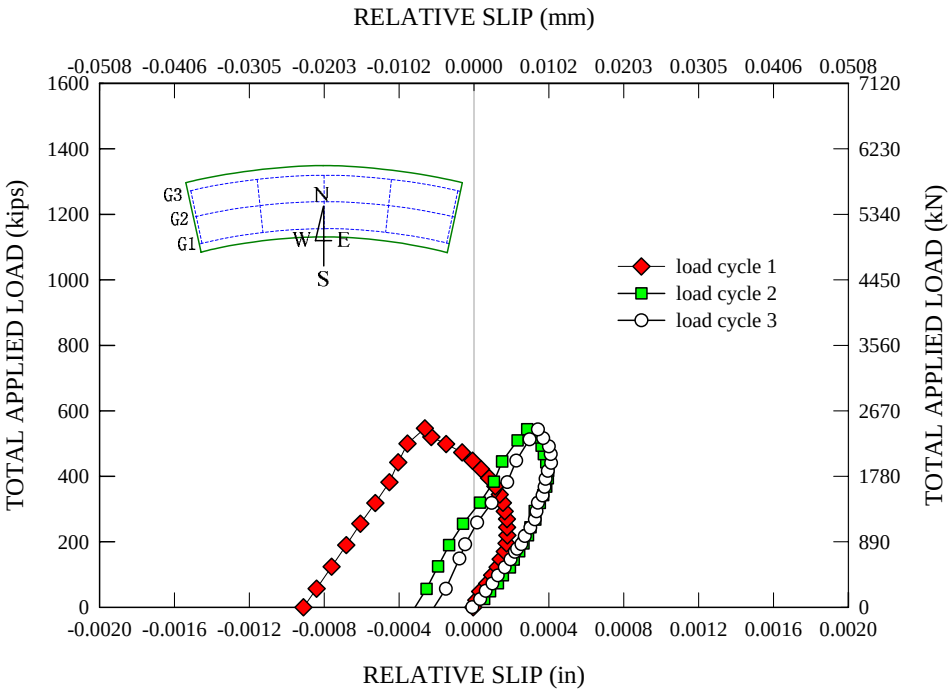

Figure C.4.1. G2 - Total applied load vs. east end relative longitudinal slip deformation at the concrete-steel interface at load level A during the first sequence of Test 4a.

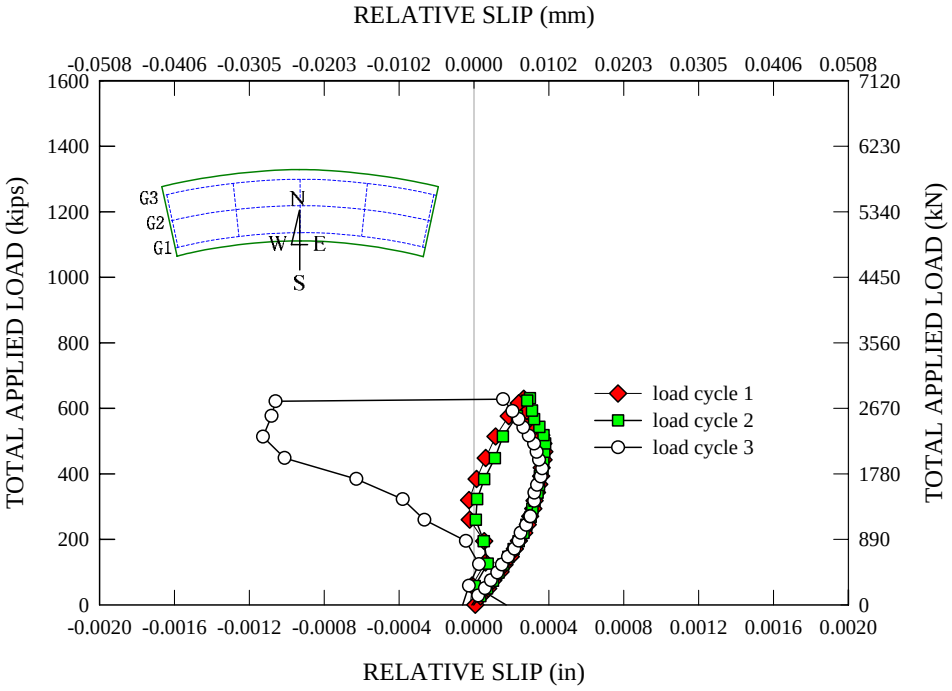

Figure C.4.2. G2 - Total applied load vs. east end relative longitudinal slip deformation at the concrete-steel interface at load level B during the first sequence of Test 4a.

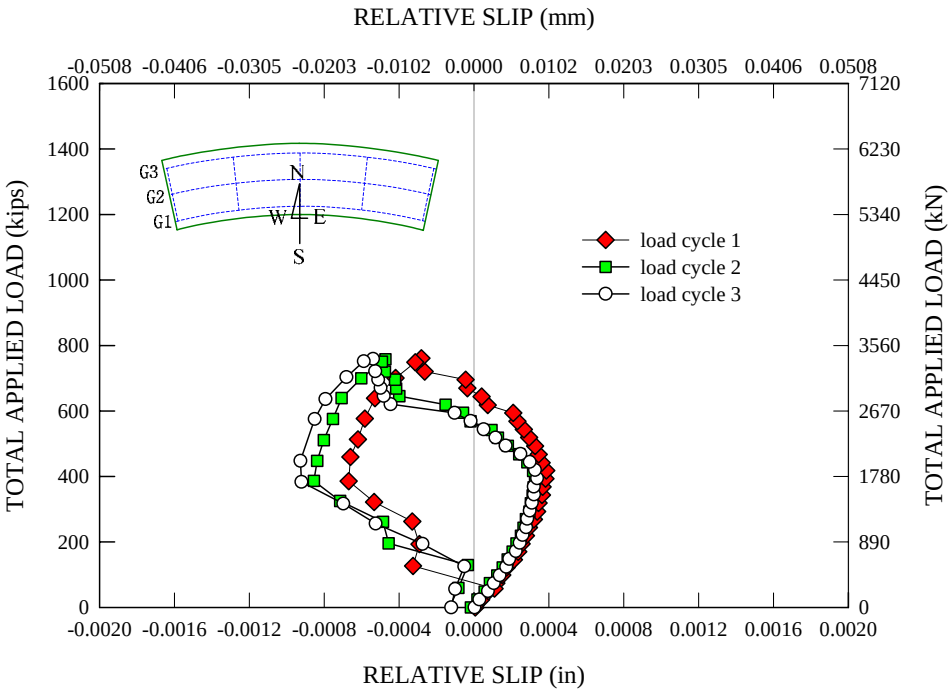

Figure C.4.3. G2 - Total applied load vs. east end relative longitudinal slip deformation at the concrete-steel interface at load level C during the first sequence of Test 4a.

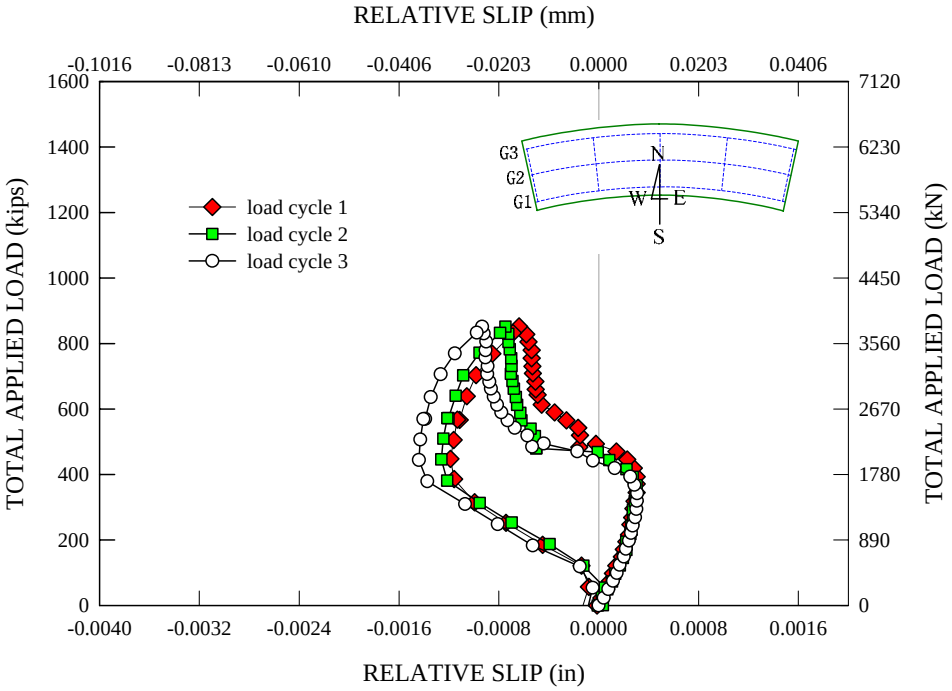

Figure C.4.4. G2 - Total applied load vs. east end relative longitudinal slip deformation at the concrete-steel interface at load level D during the first sequence of Test 4a.

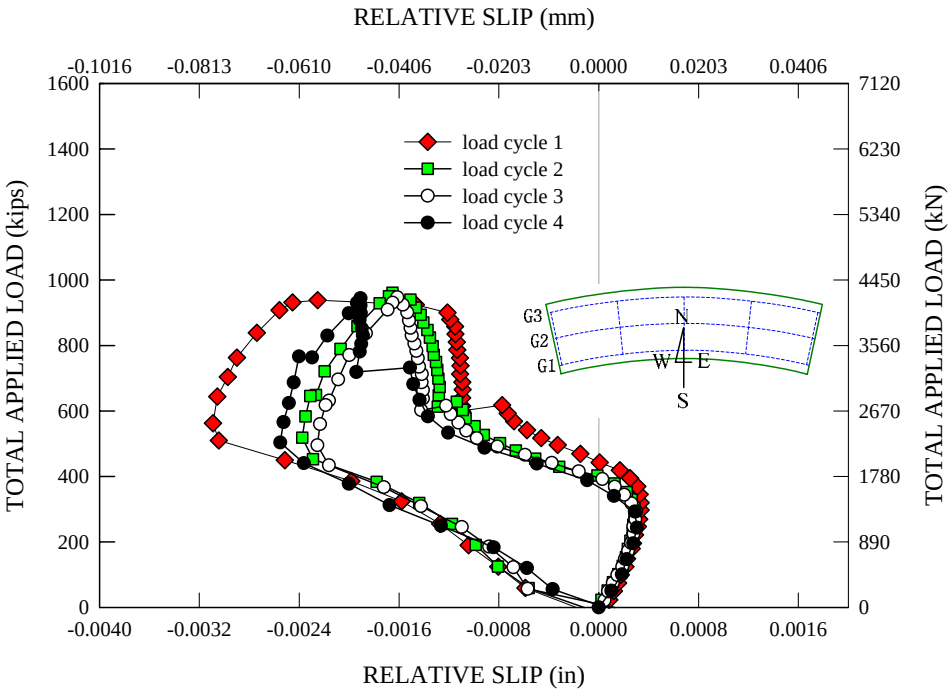

Figure C.4.5. G2 - Total applied load vs. east end relative longitudinal slip deformation at the concrete-steel interface at load level E during the first sequence of Test 4a.

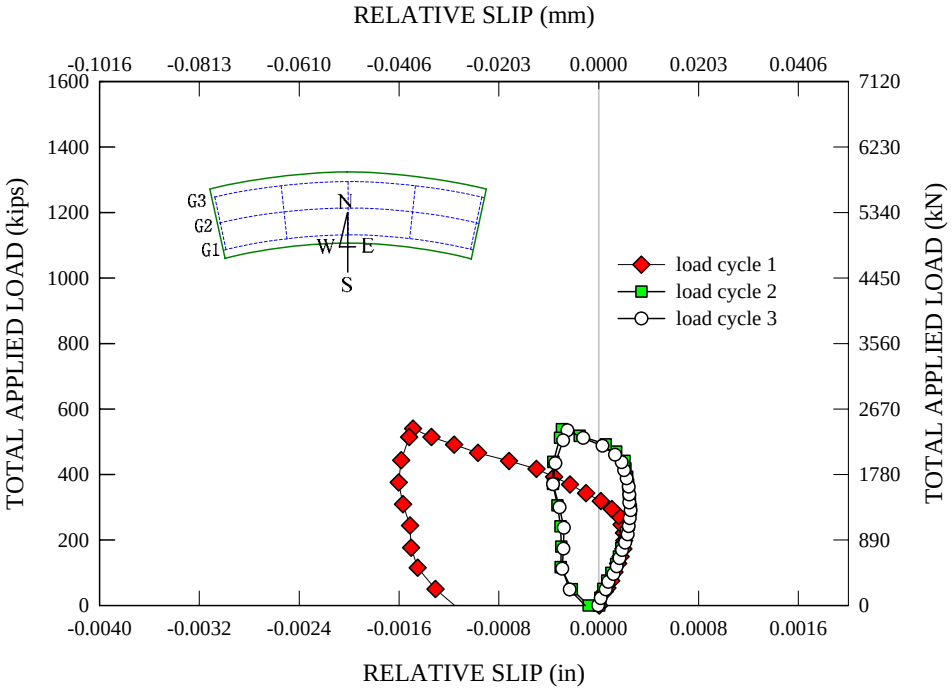

Figure C.4.6. G2 - Total applied load vs. east end relative longitudinal slip deformation at the concrete-steel interface at load level A during the second sequence of Test 4a.

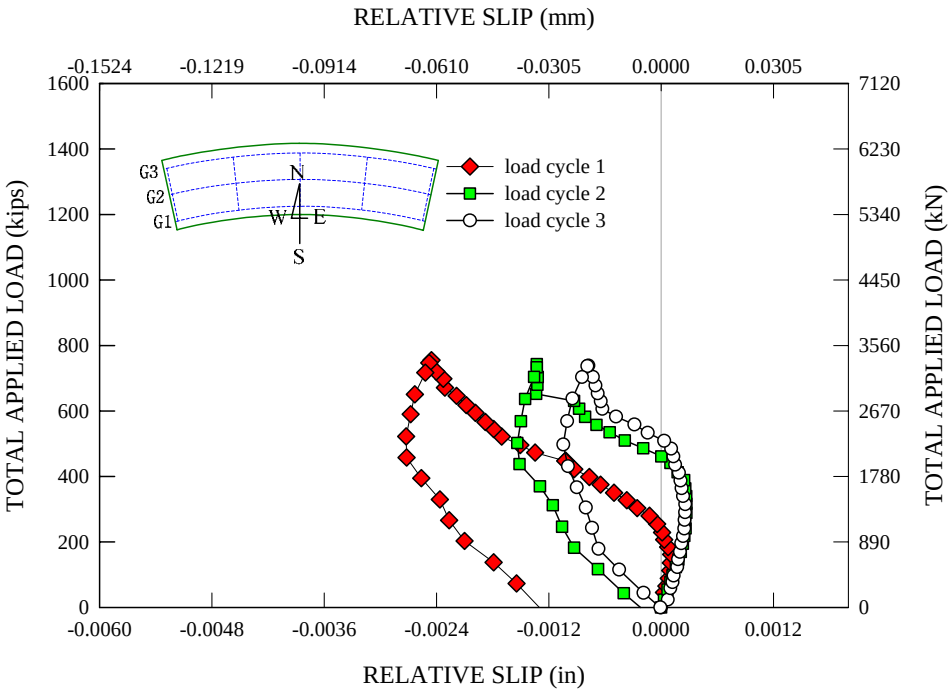

Figure C.4.7. G2 - Total applied load vs. east end relative longitudinal slip deformation at the concrete-steel interface at load level C during the second sequence of Test 4a.

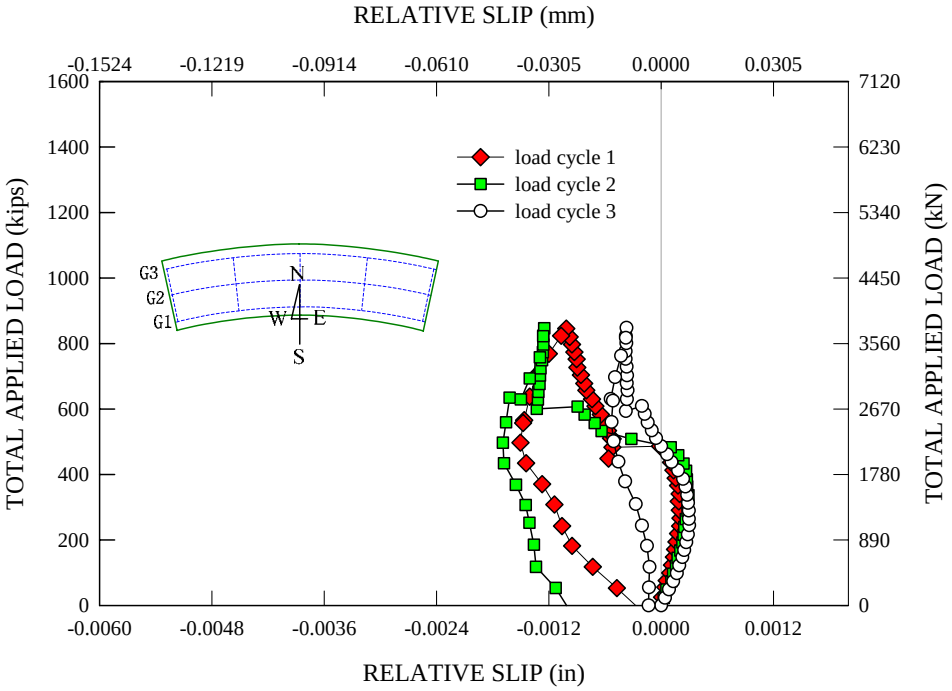

Figure C.4.8. G2 - Total applied load vs. east end relative longitudinal slip deformation at the concrete-steel interface at load level D during the second sequence of Test 4a.

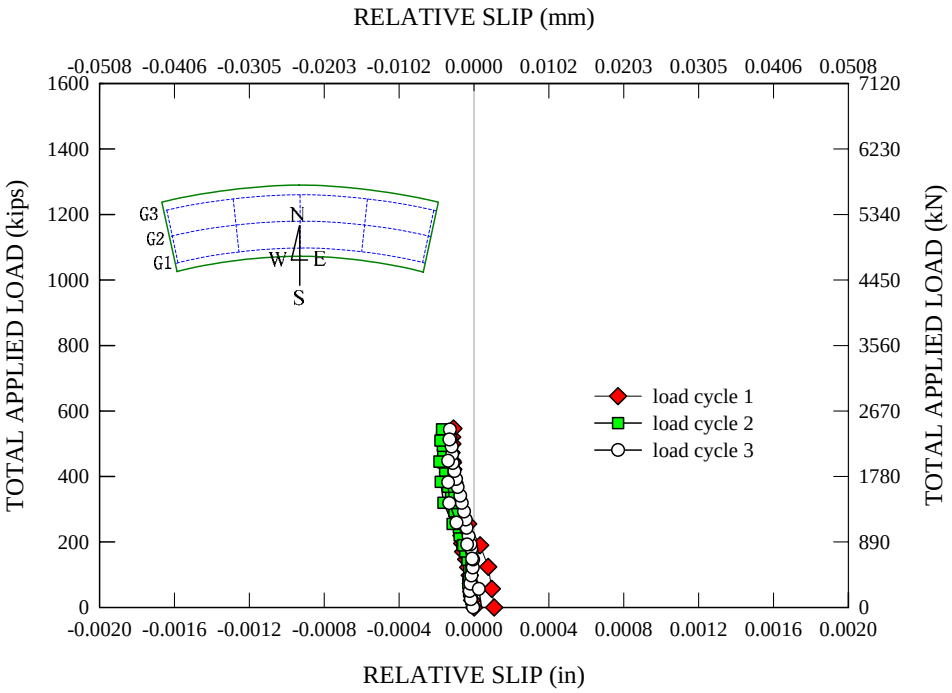

Figure C.4.9. G2 - Total applied load vs. west end relative longitudinal slip deformation at the concrete-steel interface at load level A during the first sequence of Test 4a.

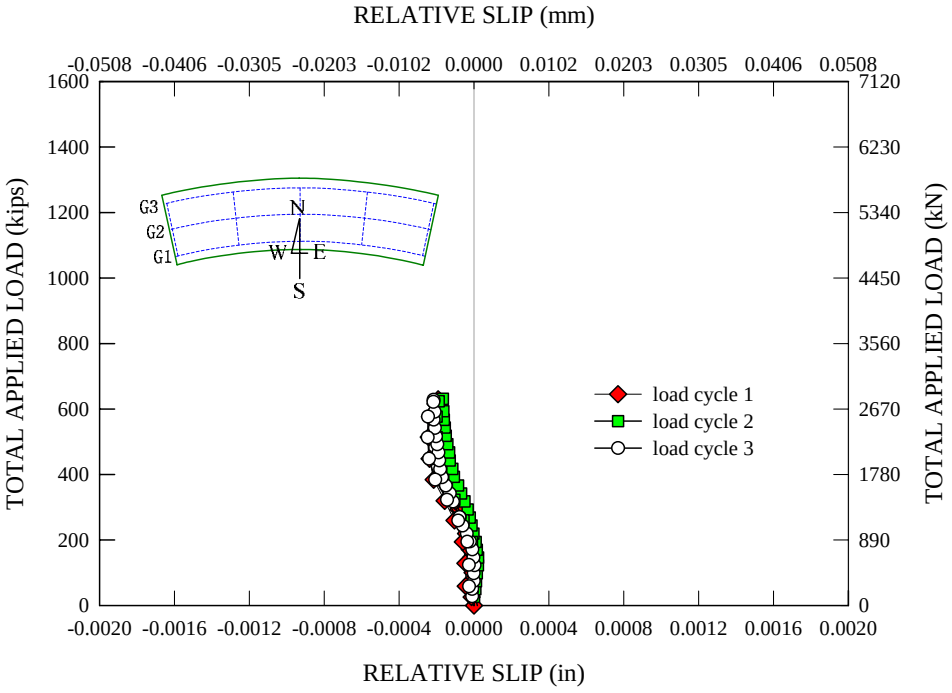

Figure C.4.10. G2 - Total applied load vs. west end relative longitudinal slip deformation at the concrete-steel interface at load level B during the first sequence of Test 4a.

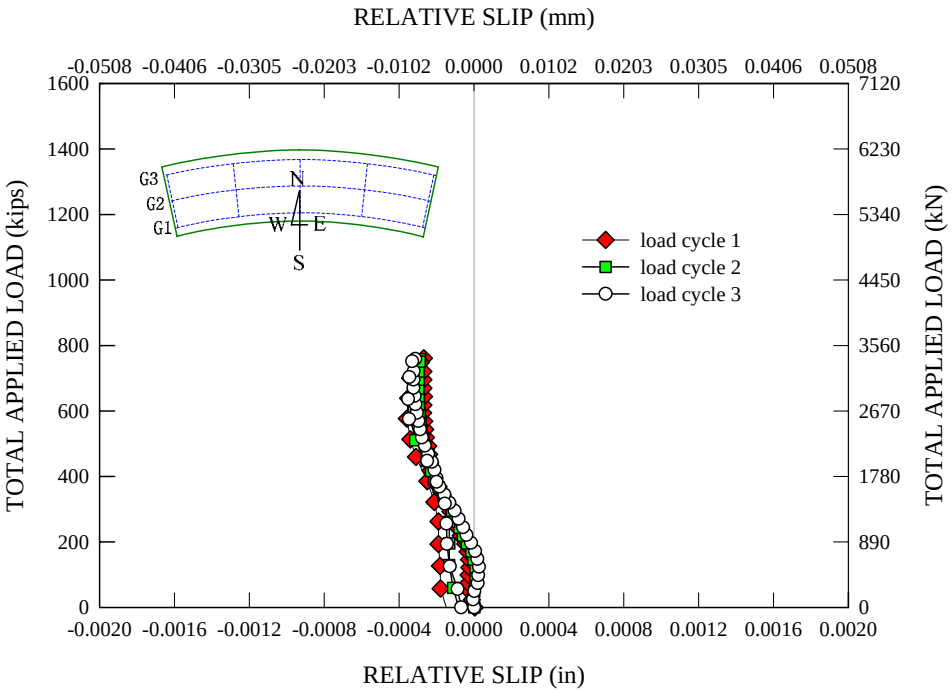

Figure C.4.11. G2 - Total applied load vs. west end relative longitudinal slip deformation at the concrete-steel interface at load level C during the first sequence of Test 4a.

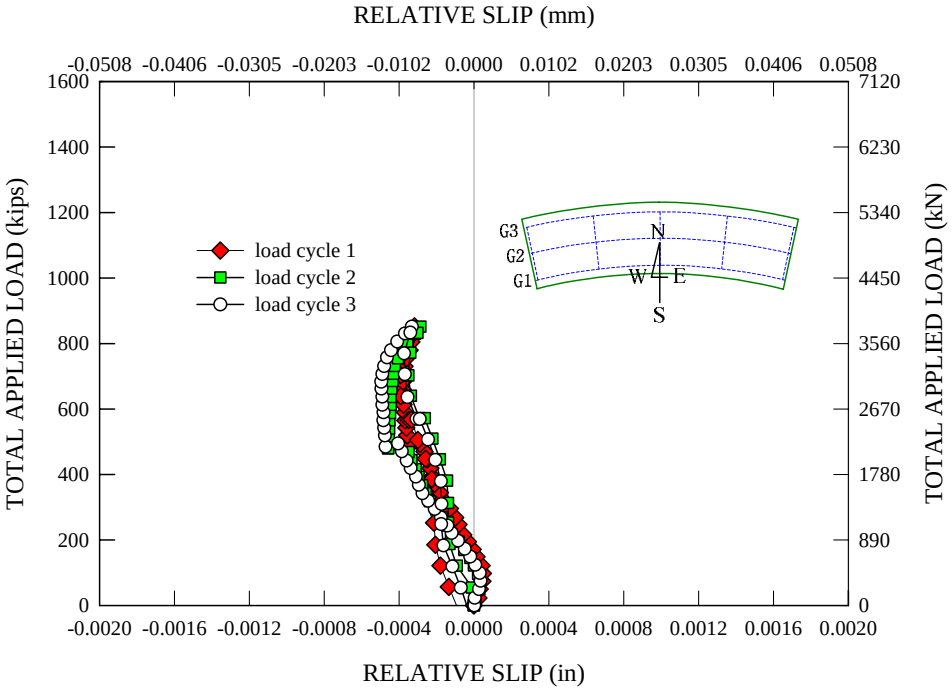

Figure C.4.12. G2 - Total applied load vs. west end relative longitudinal slip deformation at the concrete-steel interface at load level D during the first sequence of Test 4a.

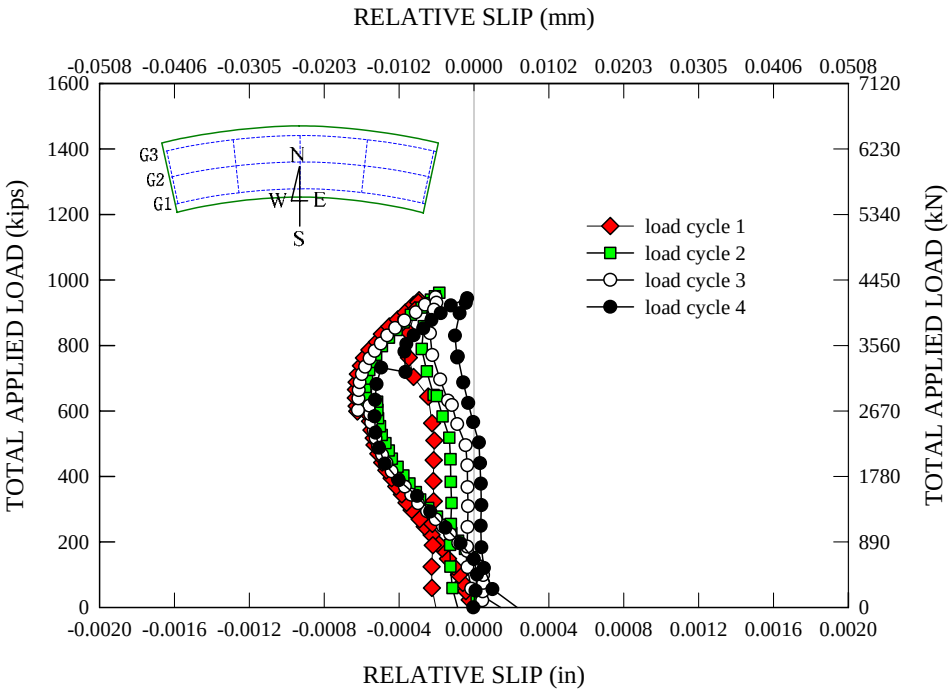

Figure C.4.13. G2 - Total applied load vs. west end relative longitudinal slip deformation at the concrete-steel interface at load level E during the first sequence of Test 4a.

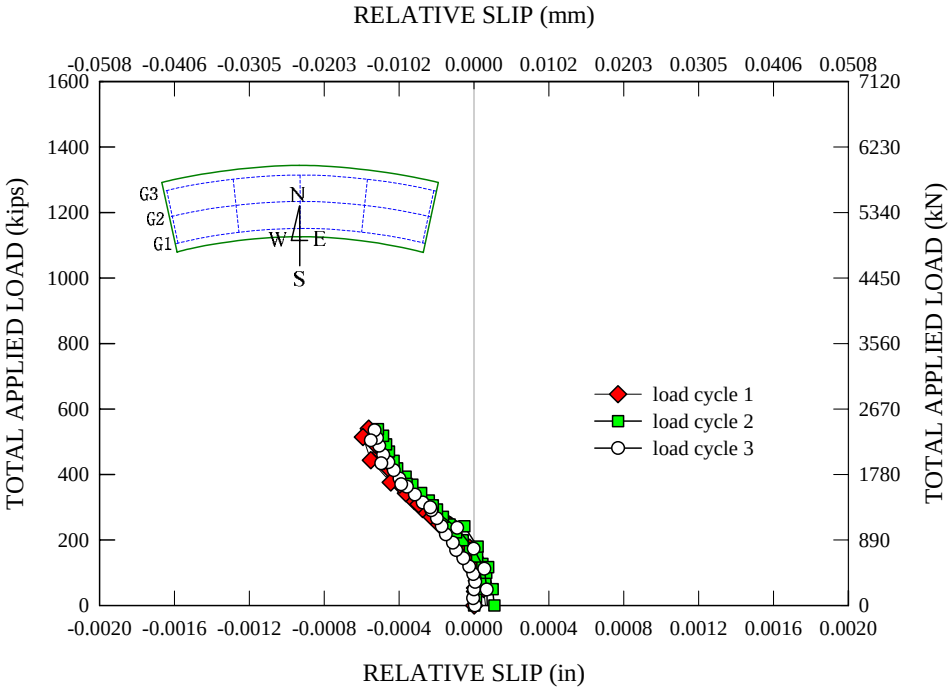

Figure C.4.14. G2 - Total applied load vs. west end relative longitudinal slip deformation at the concrete-steel interface at load level A during the second sequence of Test 4a.

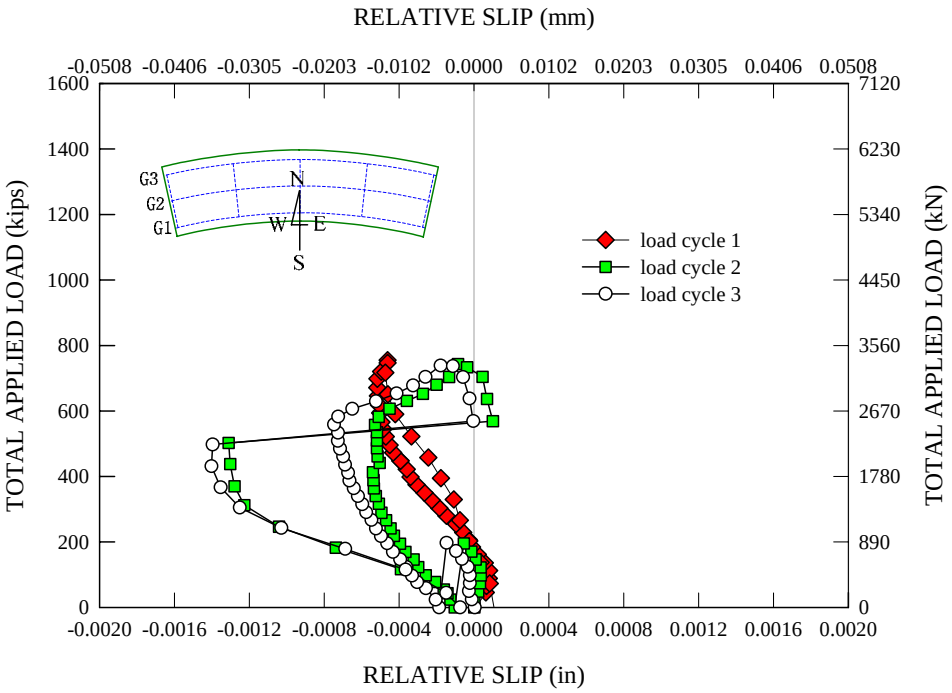

Figure C.4.15. G2 - Total applied load vs. west end relative longitudinal slip deformation at the concrete-steel interface at load level C during the second sequence of Test 4a.

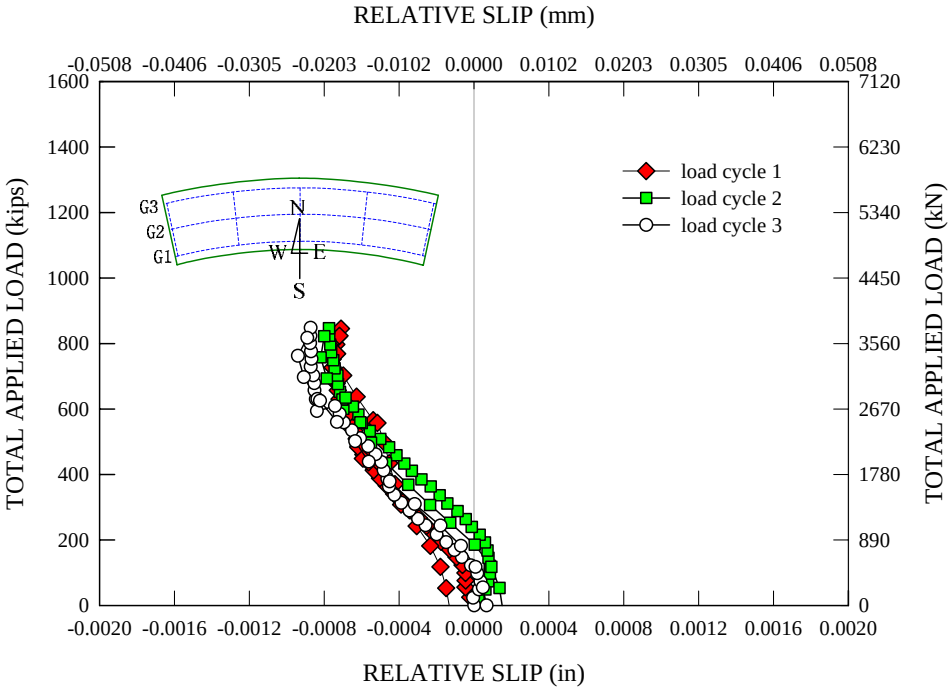

Figure C.4.16. G2 - Total applied load vs. west end relative longitudinal slip deformation at the concrete-steel interface at load level D during the second sequence of Test 4a.

C.5 G1 Slip Measurements

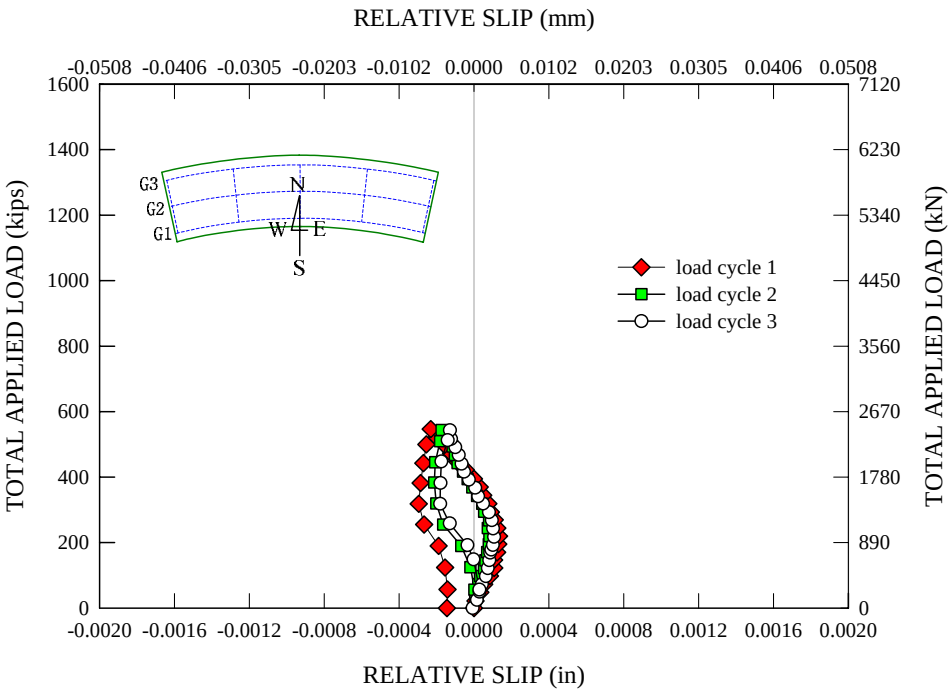

Figure C.5.1. G1 - Total applied load vs. east end relative longitudinal slip deformation at the concrete-steel interface at load level A during the first sequence of Test 4a.

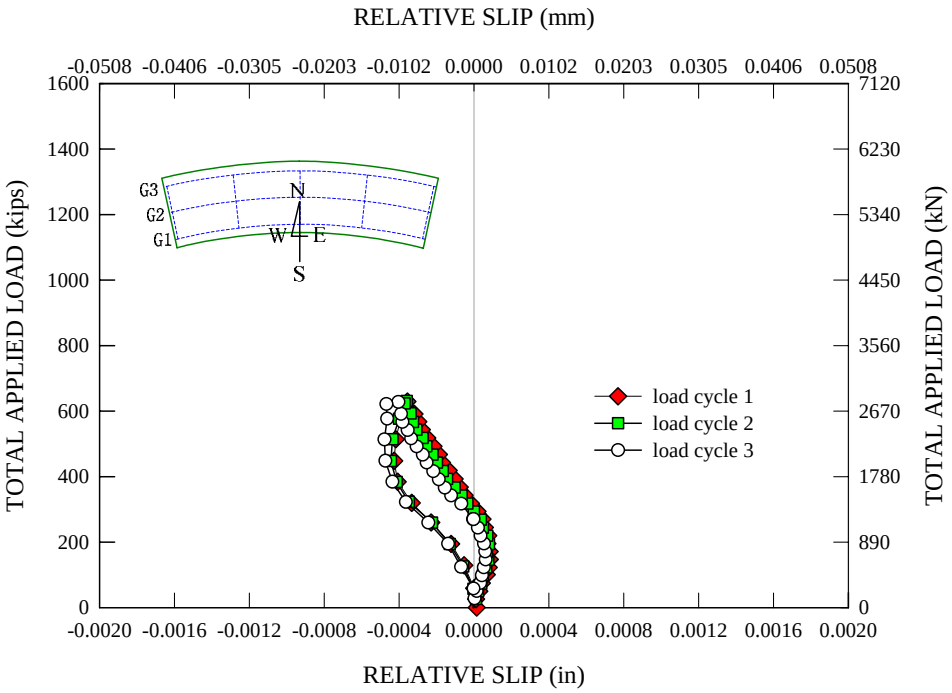

Figure C.5.2. G1 - Total applied load vs. east end relative longitudinal slip deformation at the concrete-steel interface at load level B during the first sequence of Test 4a.

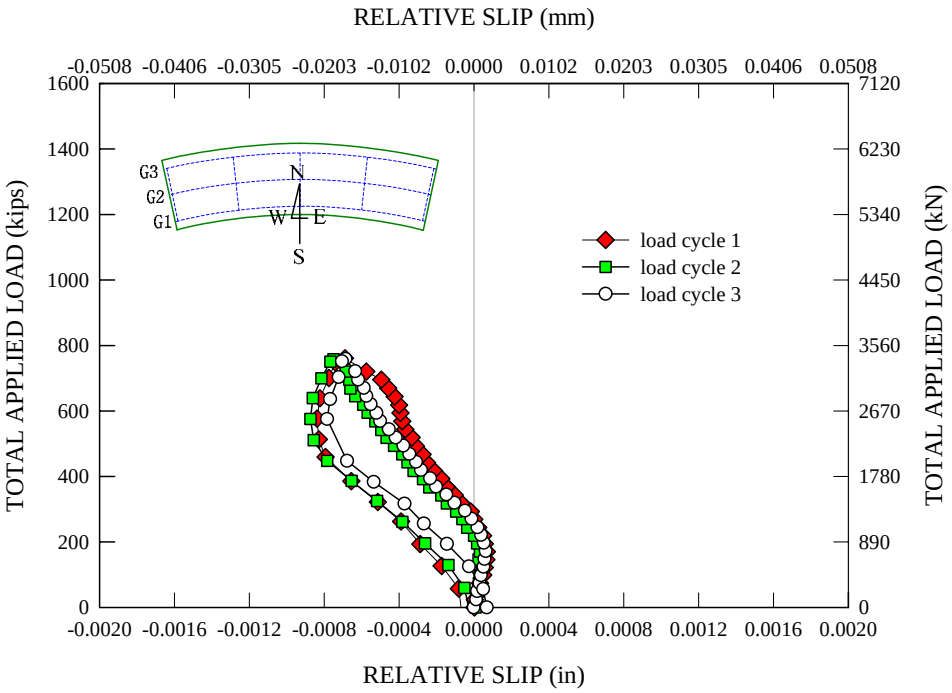

Figure C.5.3. G1 - Total applied load vs. east end relative longitudinal slip deformation at the concrete-steel interface at load level C during the first sequence of Test 4a.

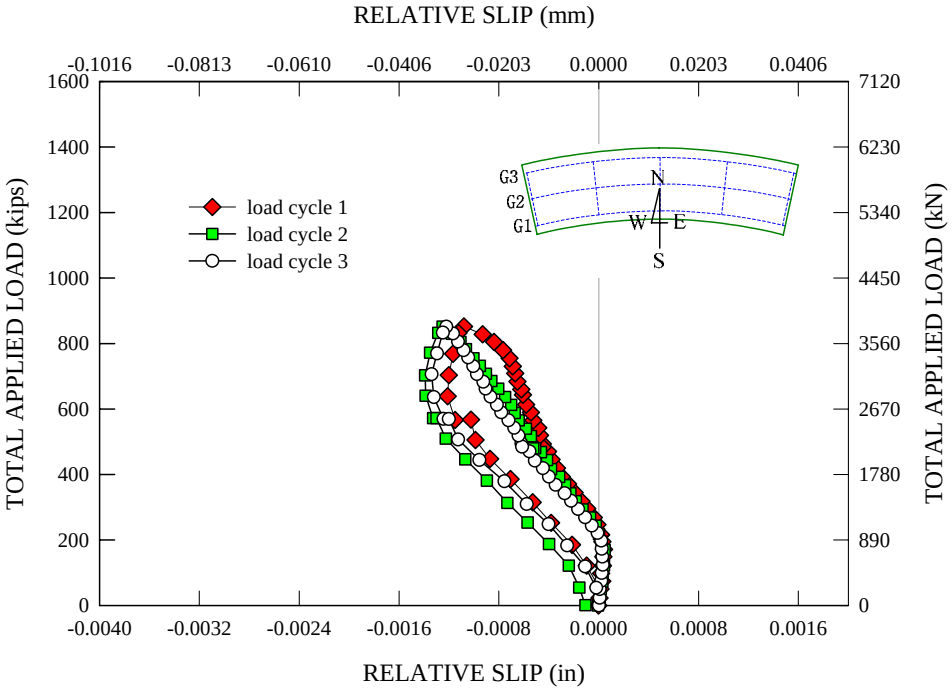

Figure C.5.4. G1 - Total applied load vs. east end relative longitudinal slip deformation at the concrete-steel interface at load level D during the first sequence of Test 4a.

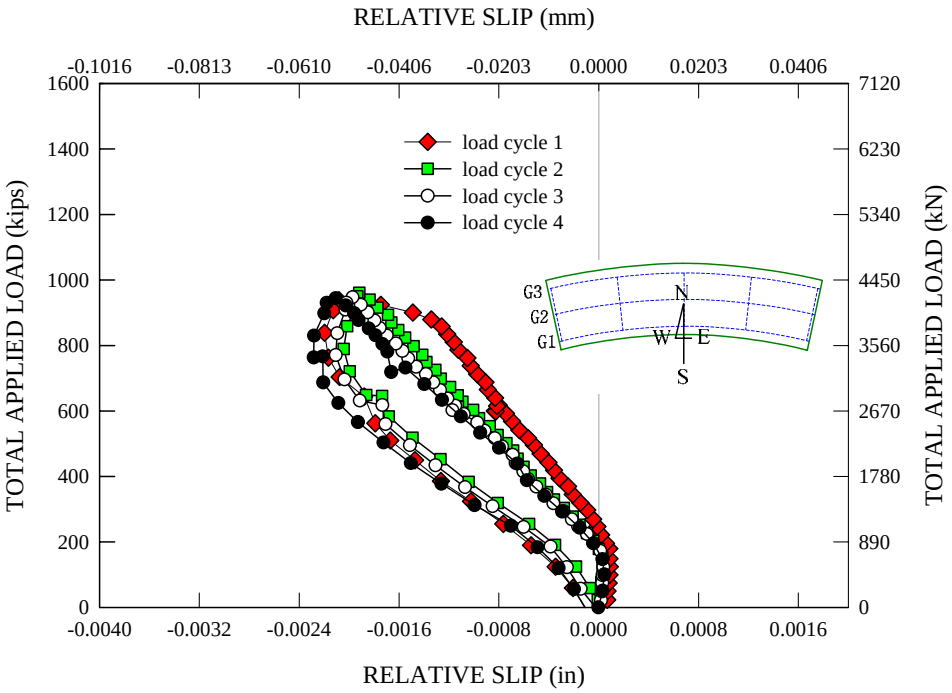

Figure C.5.5. G1 - Total applied load vs. east end relative longitudinal slip deformation at the concrete-steel interface at load level E during the first sequence of Test 4a.

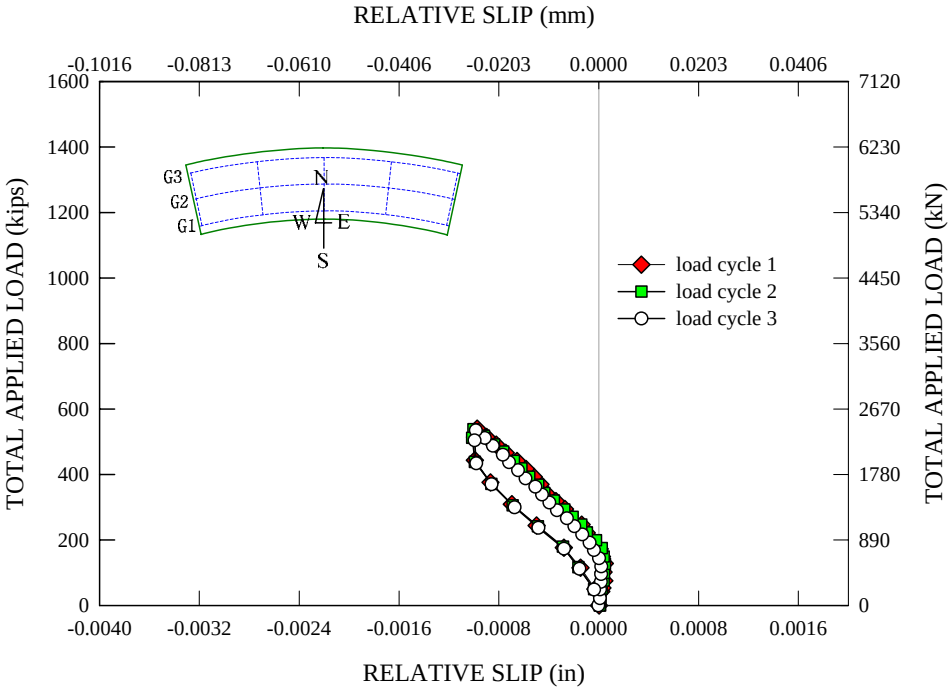

Figure C.5.6. G1 - Total applied load vs. east end relative longitudinal slip deformation at the concrete-steel interface at load level A during the second sequence of Test 4a.

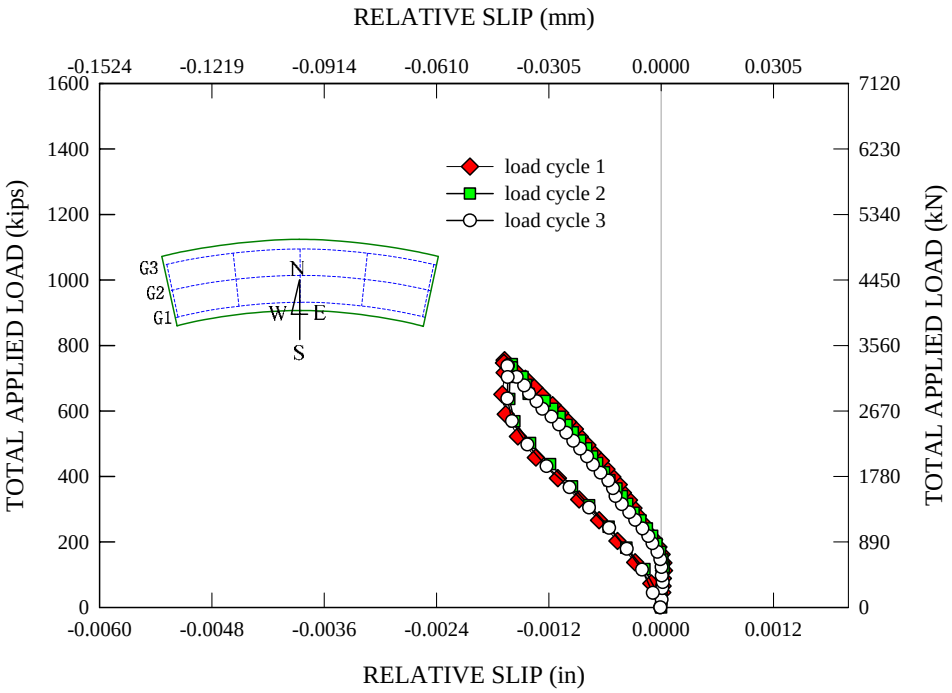

Figure C.5.7. G1 - Total applied load vs. east end relative longitudinal slip deformation at the concrete-steel interface at load level C during the second sequence of Test 4a.

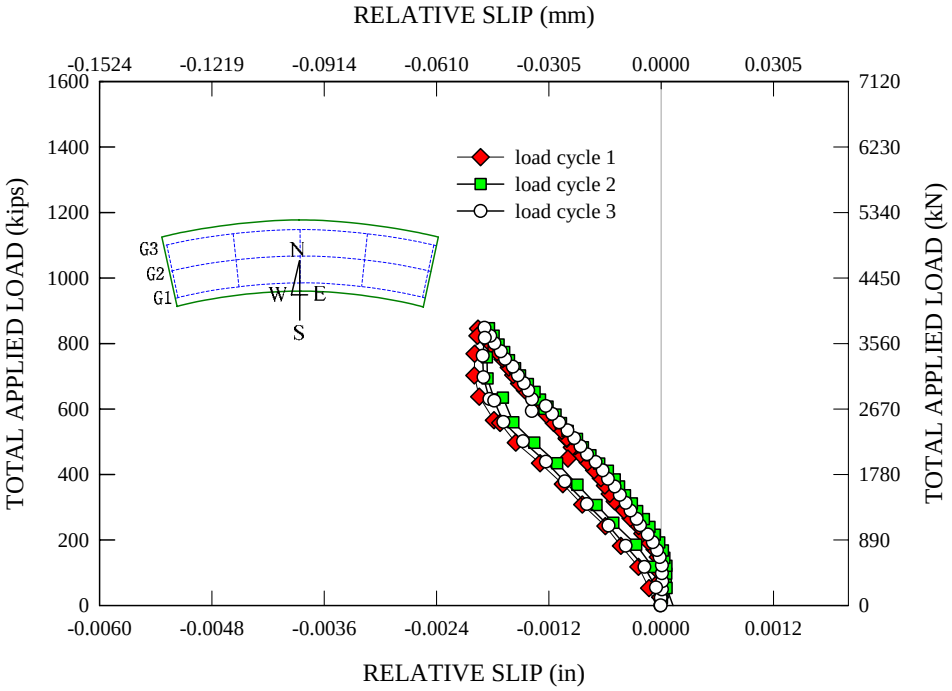

Figure C.5.8. G1 - Total applied load vs. east end relative longitudinal slip deformation at the concrete-steel interface at load level D during the second sequence of Test 4a.

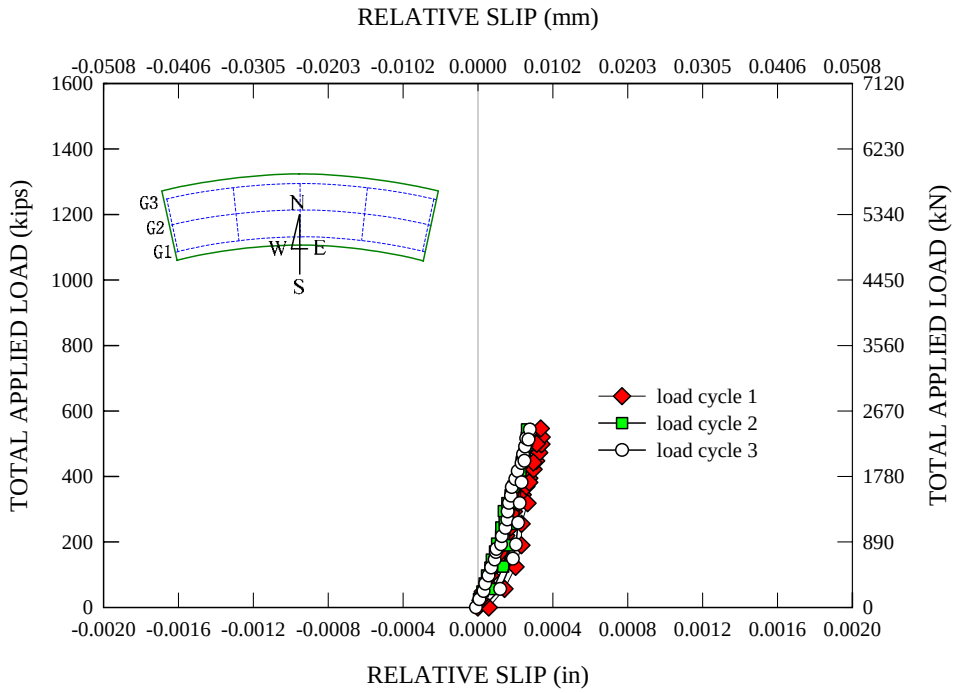

Figure C.5.9. G1 - Total applied load vs. west end relative longitudinal slip deformation at the concrete-steel interface at load level A during the first sequence of Test 4a.

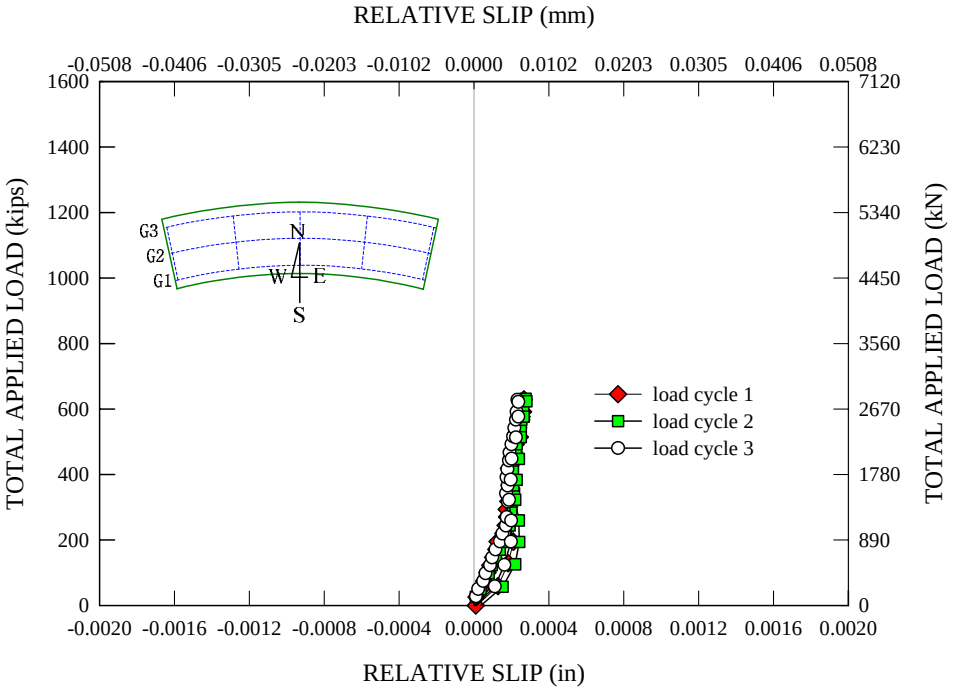

Figure C.5.10. G1 - Total applied load vs. west end relative longitudinal slip deformation at the concrete-steel interface at load level B during the first sequence of Test 4a.

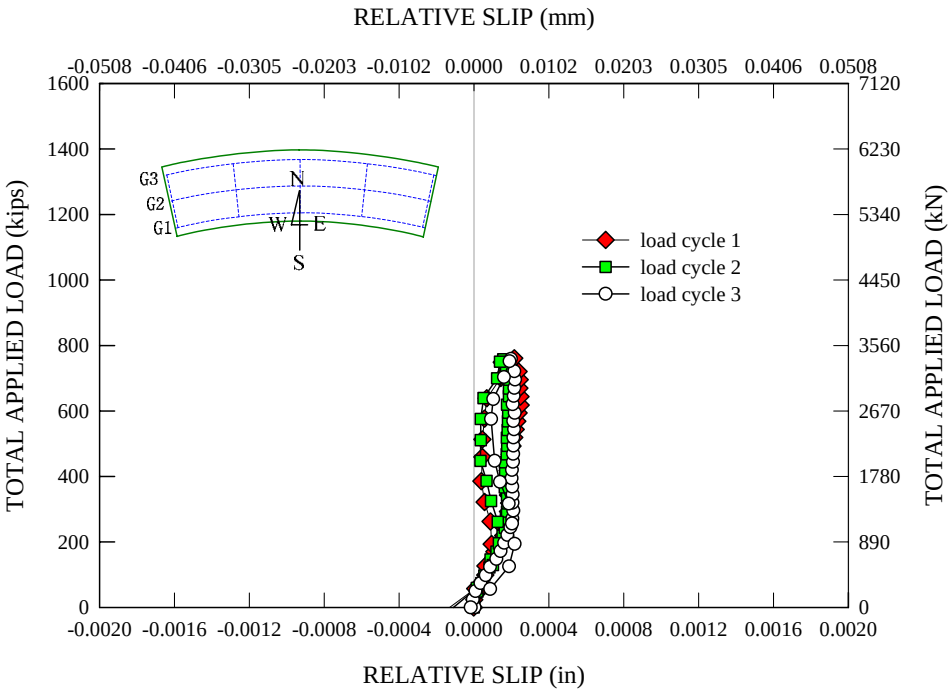

Figure C.5.11. G1 - Total applied load vs. west end relative longitudinal slip deformation at the concrete-steel interface at load level C during the first sequence of Test 4a.

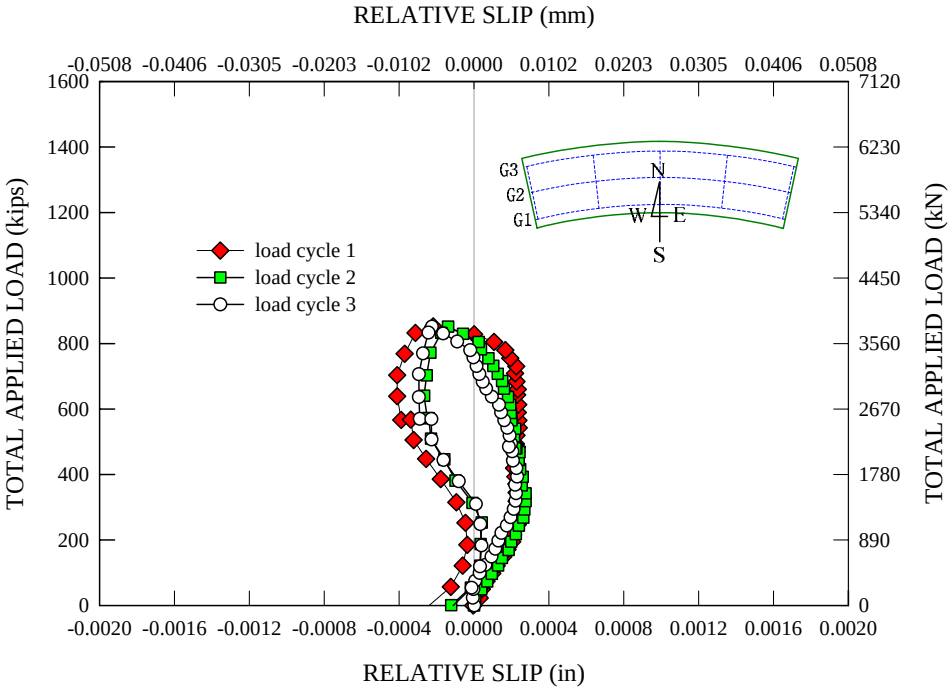

Figure C.5.12. G1 - Total applied load vs. west end relative longitudinal slip deformation at the concrete-steel interface at load level D during the first sequence of Test 4a.

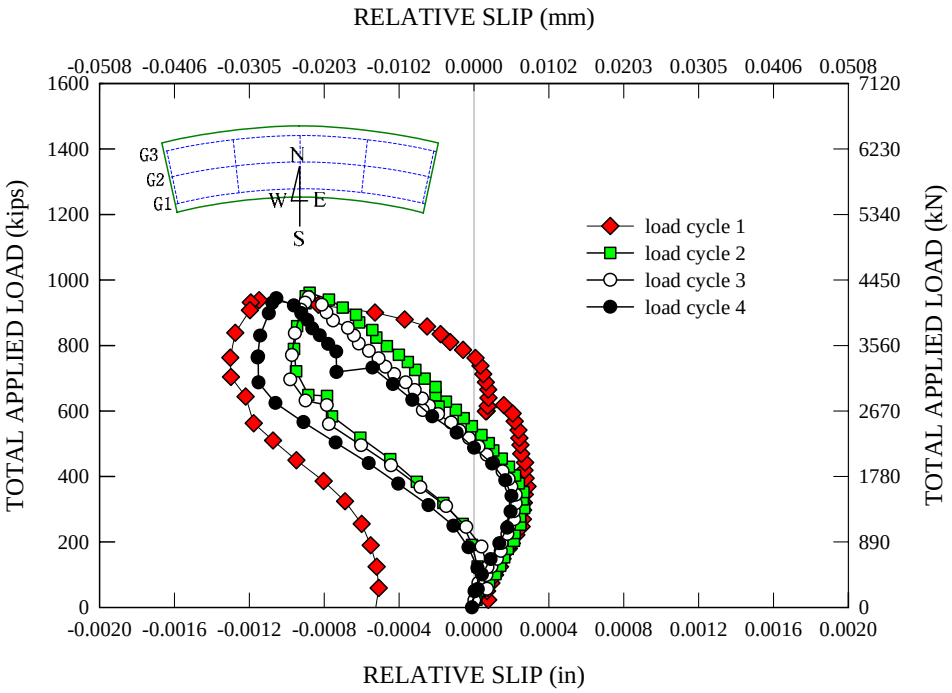

Figure C.5.13. G1 - Total applied load vs. west end relative longitudinal slip deformation at the concrete-steel interface at load level E during the first sequence of Test 4a.

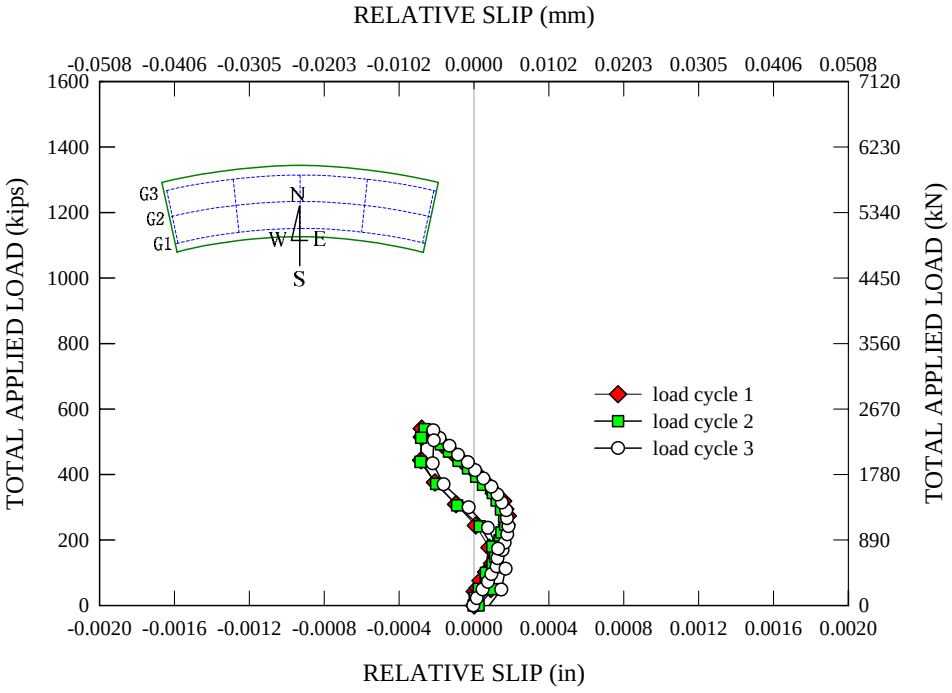

Figure C.5.14. G1 - Total applied load vs. west end relative longitudinal slip deformation at the concrete-steel interface at load level A during the second sequence of Test 4a.

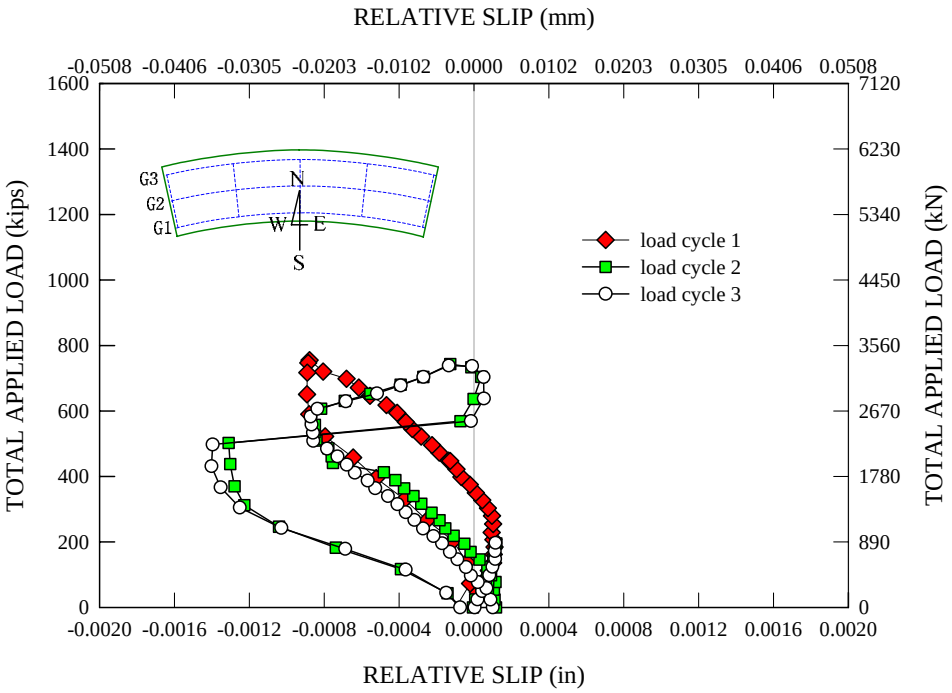

Figure C.5.15. G1 - Total applied load vs. west end relative longitudinal slip deformation at the concrete-steel interface at load level C during the second sequence of Test 4a.

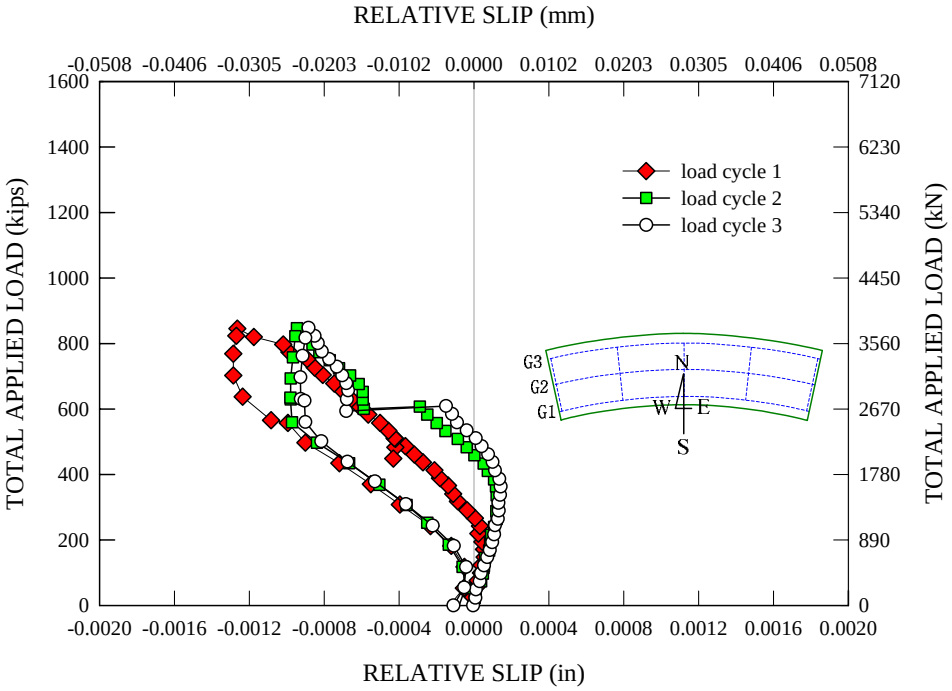

Figure C.5.16. G1 - Total applied load vs. west end relative longitudinal slip deformation at the concrete-steel interface at load level D during the second sequence of Test 4a.

APPENDIX D

TEST 4b: ULTIMATE MONOTONIC LOADING TEST

This appendix presents additional detailed results of the final monotonic loading test of Test 4b not shown in Chapter 5. First, this appendix provides the measured and predicted member axial forces in the bottom chord, diagonal member and top chord of each cross-frame. Two different FEA solutions with and without the effects of prior repeated loading cycles are compared to the measured cross-frame member axial forces. This is followed by detailed relative slip displacements measured at the ends of the composite girders for the longitudinal direction and the radial slip displacements measured at the midspan of G3.

D.1 Cross-Frame Member Forces

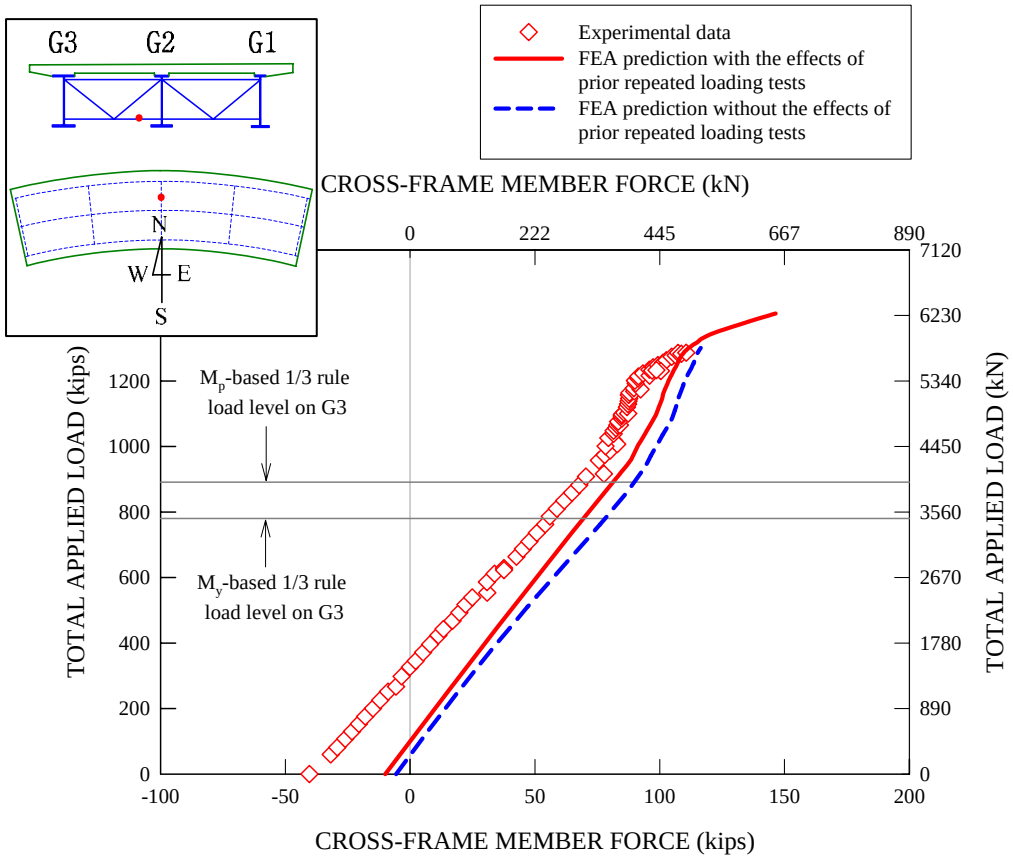

Figure D.1.1. Measured and predicted axial member forces for the bottom chord attached to G2 of the mid-span cross-frame located between G2 and G3 during the final monotonic loading test of Test 4b, initial dead load member forces are included in the plot as well, but the measured initial dead load member force is taken just before the start of the repeated loading tests of Test 4a.

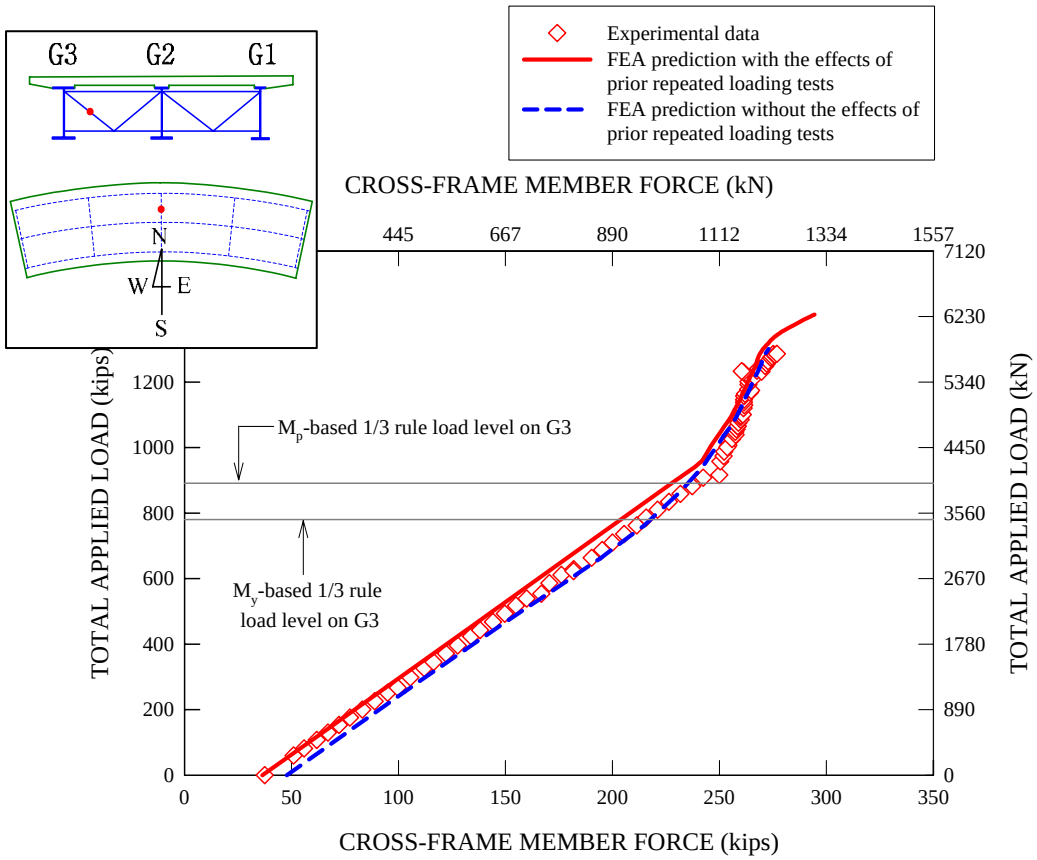

Figure D.1.2. Measured and predicted axial member forces for the diagonal member attached to G3 of the mid-span cross-frame located between G2 and G3 during the final monotonic loading test of Test 4b, initial dead load member forces are included in the plot as well, but the measured initial dead load member force is taken just before the start of the repeated loading tests of Test 4a.

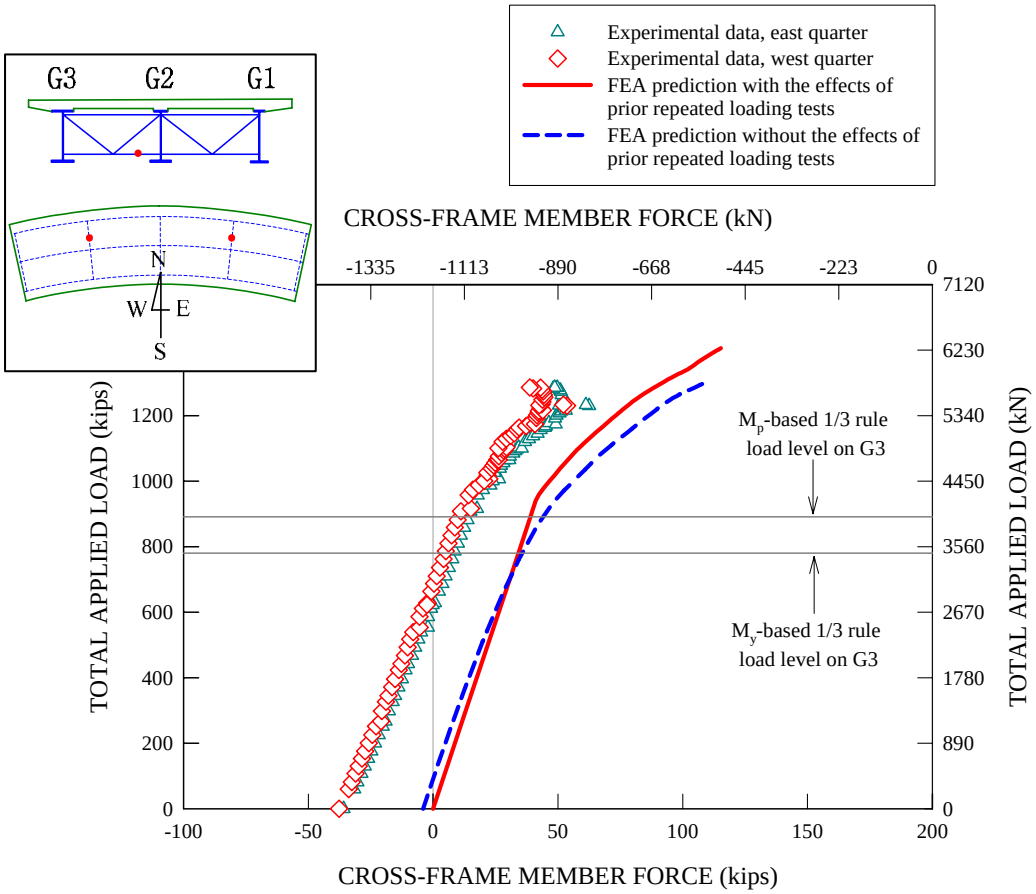

Figure D.1.3. Measured and predicted axial member forces for the bottom chords attached to G2 of the quarter-span cross-frames located between G2 and G3 during the final monotonic loading test of Test 4b, initial dead load member forces are included in the plot as well, but the measured initial dead load member forces are taken just before the start of the repeated loading tests of Test 4a.

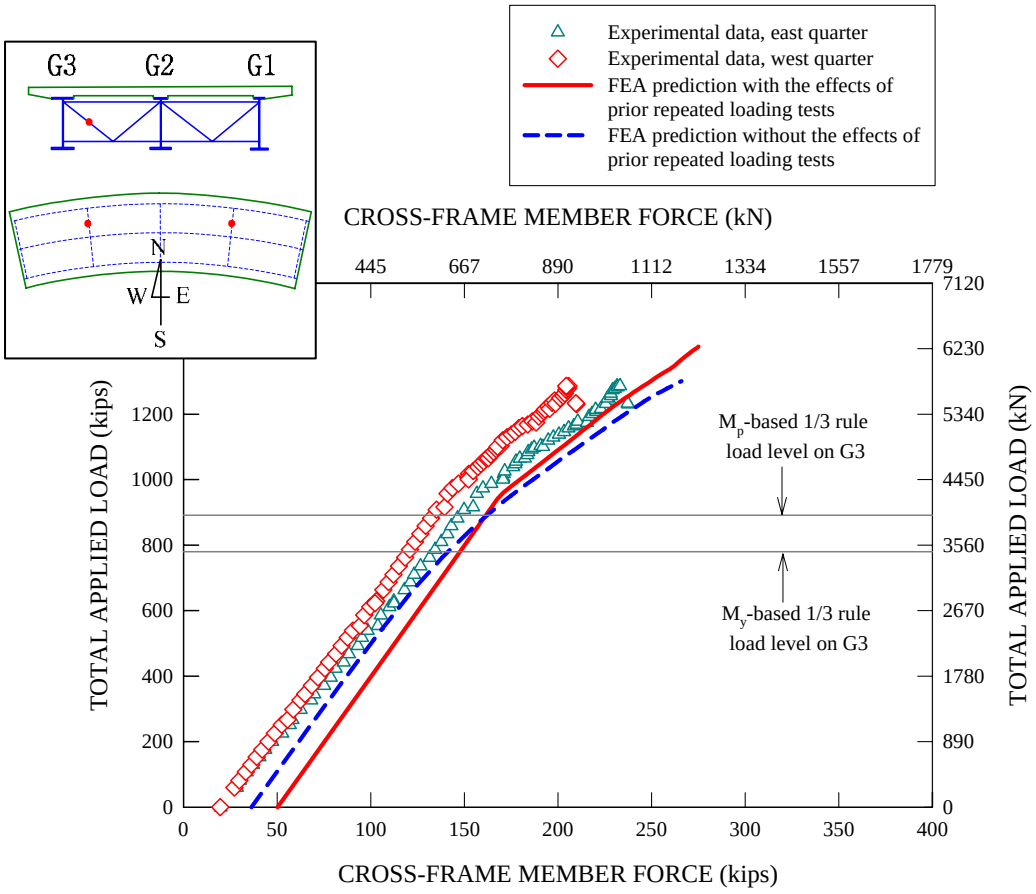

Figure D.1.4. Measured and predicted axial member forces for the diagonal members attached to G3 of the quarter-span cross-frames located between G2 and G3 during the final monotonic loading test of Test 4b, initial dead load member forces are included in the plot as well, but the measured initial dead load member forces are taken just before the start of the repeated loading tests of Test 4a.

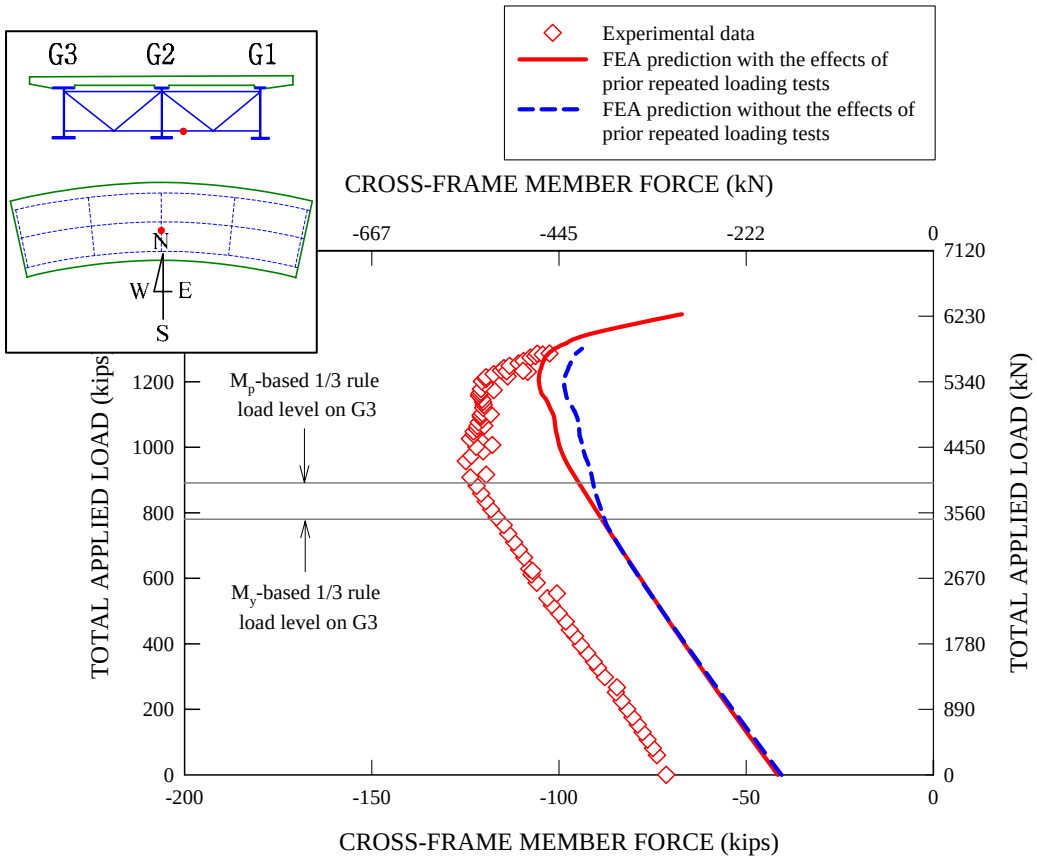

Figure D.1.5. Measured and predicted axial member forces for the bottom chord attached to G2 of the mid-span cross-frame located between G1 and G2 during the final monotonic loading test of Test 4b, initial dead load member forces are included in the plot as well, but the measured initial dead load member force is taken just before the start of the repeated loading tests of Test 4a.

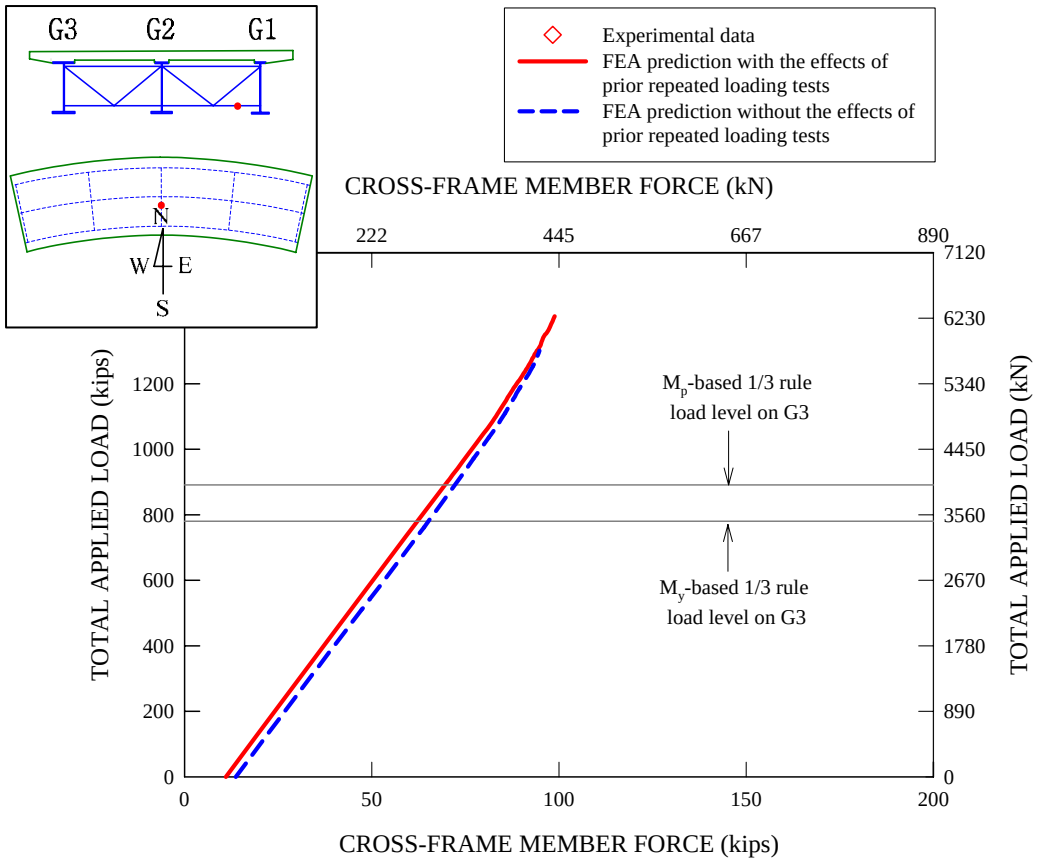

Figure D.1.6. Measured and predicted axial member forces for the bottom chord attached to G1 of the mid-span cross-frame located between G1 and G2 during the final monotonic loading test of Test 4b, initial dead load member forces are included in the plot as well, but the measured initial dead load member force is taken just before the start of the repeated loading tests of Test 4a.

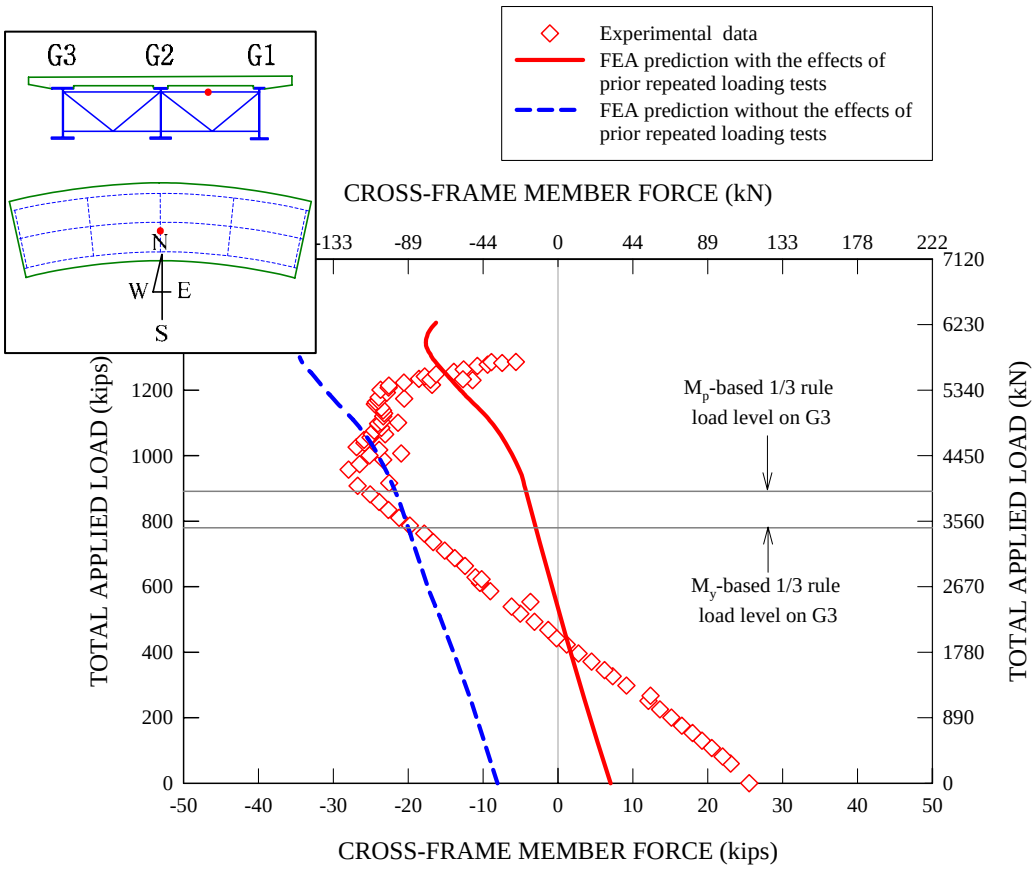

Figure D.1.7. Measured and predicted axial member forces for the top chord of the mid-span cross-frame located between G1 and G2 during the final monotonic loading test of Test 4b, initial dead load member forces are included in the plot as well, but the measured initial dead load member force is taken just before the start of the repeated loading tests of Test 4a.

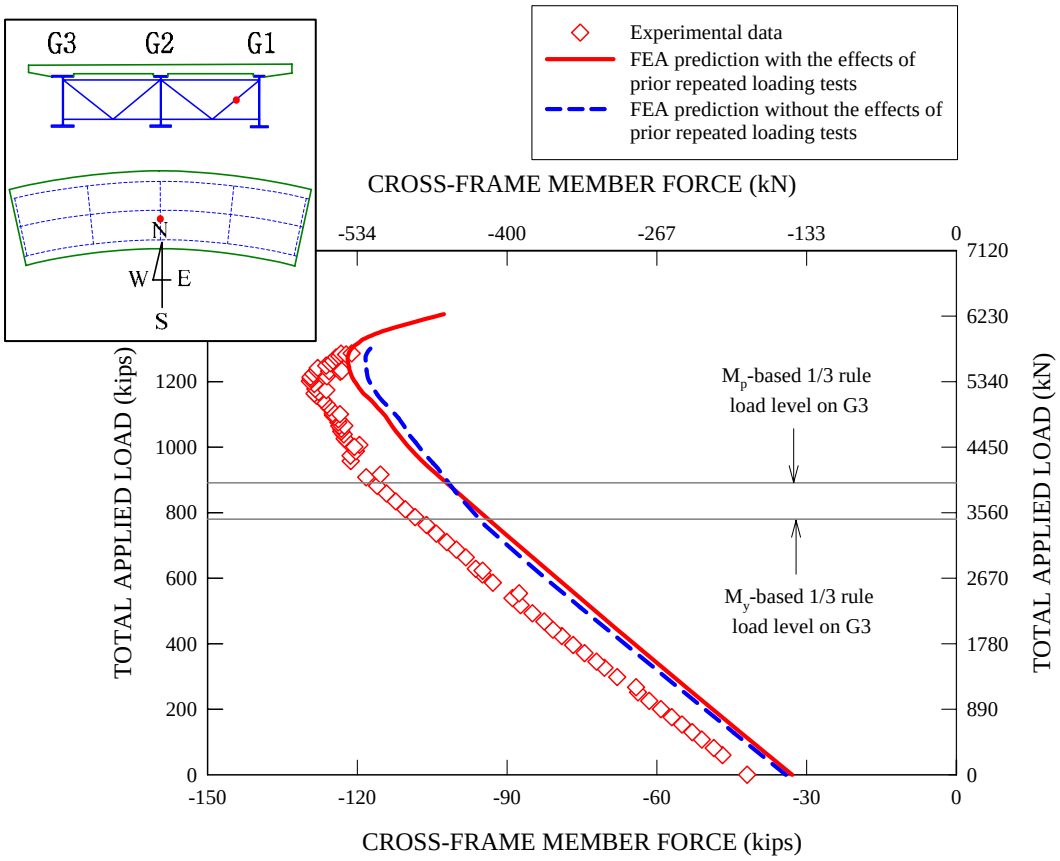

Figure D.1.8. Measured and predicted axial member forces for the diagonal member attached to G1 of the mid-span cross-frame located between G1 and G2 during the final monotonic loading test of Test 4b, initial dead load member forces are included in the plot as well, but the measured initial dead load member force is taken just before the start of the repeated loading tests of Test 4a.

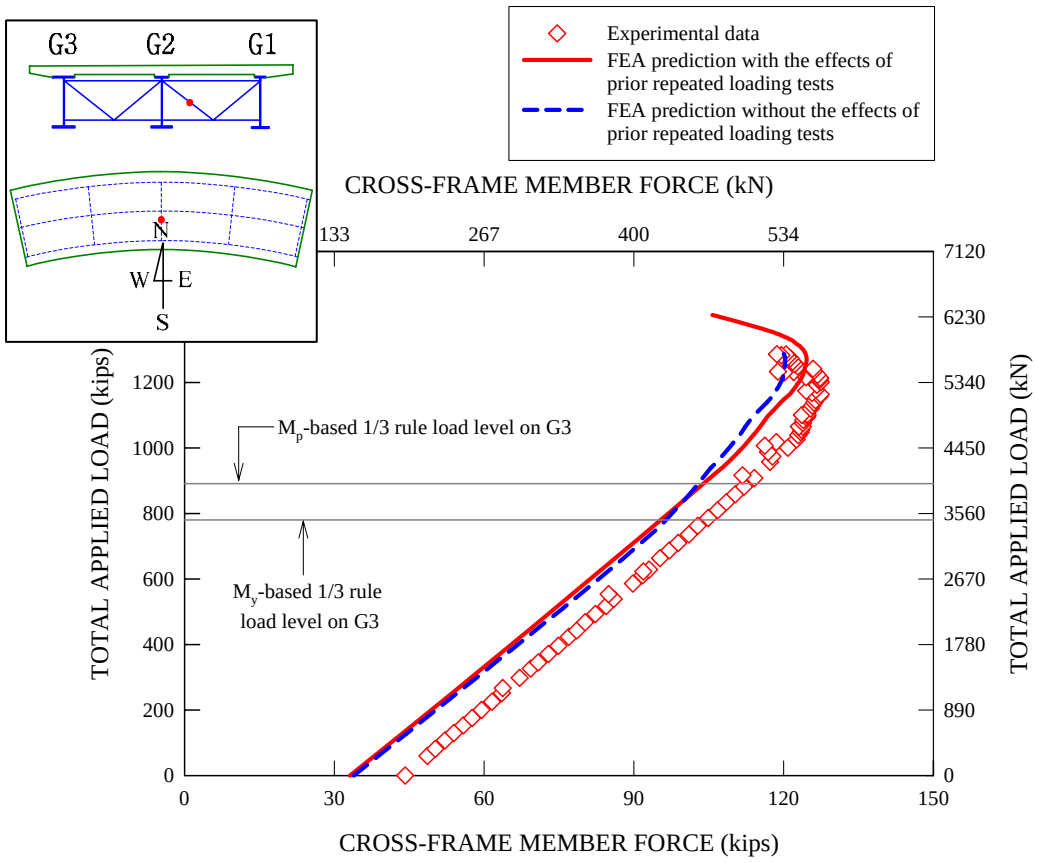

Figure D.1.9. Measured and predicted axial member forces for the diagonal member attached to G2 of the mid-span cross-frame between G1 and G2 during the final monotonic loading test of Test 4b, initial dead load member forces are included in the plot as well, but the measured initial dead load member force is taken just before the start of the repeated loading tests of Test 4a.

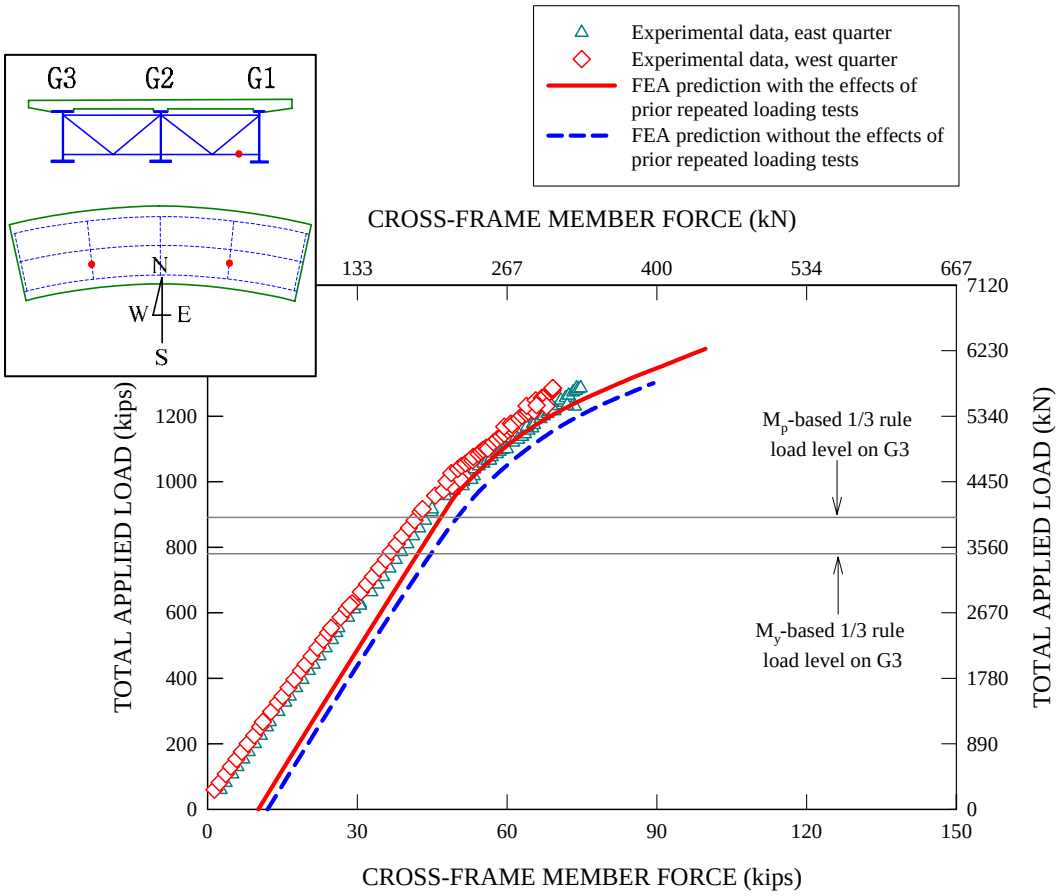

Figure D.1.10. Measured and predicted axial member forces for the bottom chords attached to G1 of the quarter-span cross-frames between G1 and G2 during the final monotonic loading test of Test 4b, initial dead load member forces are included in the plot as well, but the measured initial dead load member forces are taken just before the start of the repeated loading tests of Test 4a.

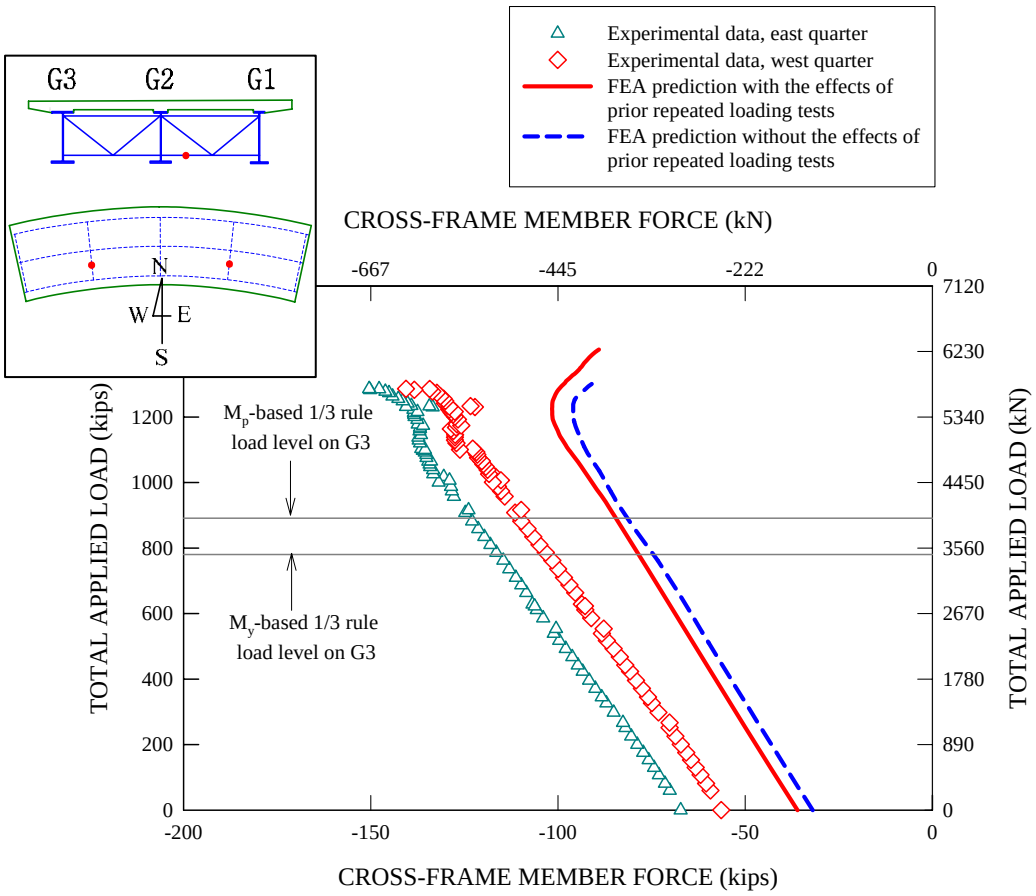

Figure D.1.11. Measured and predicted axial member forces for the bottom chords attached to G2 of the quarter-span cross-frames between G1 and G2 during the final monotonic loading test of Test 4b, initial dead load member forces are included in the plot as well, but the measured initial dead load member forces are taken just before the start of the repeated loading tests of Test 4a.

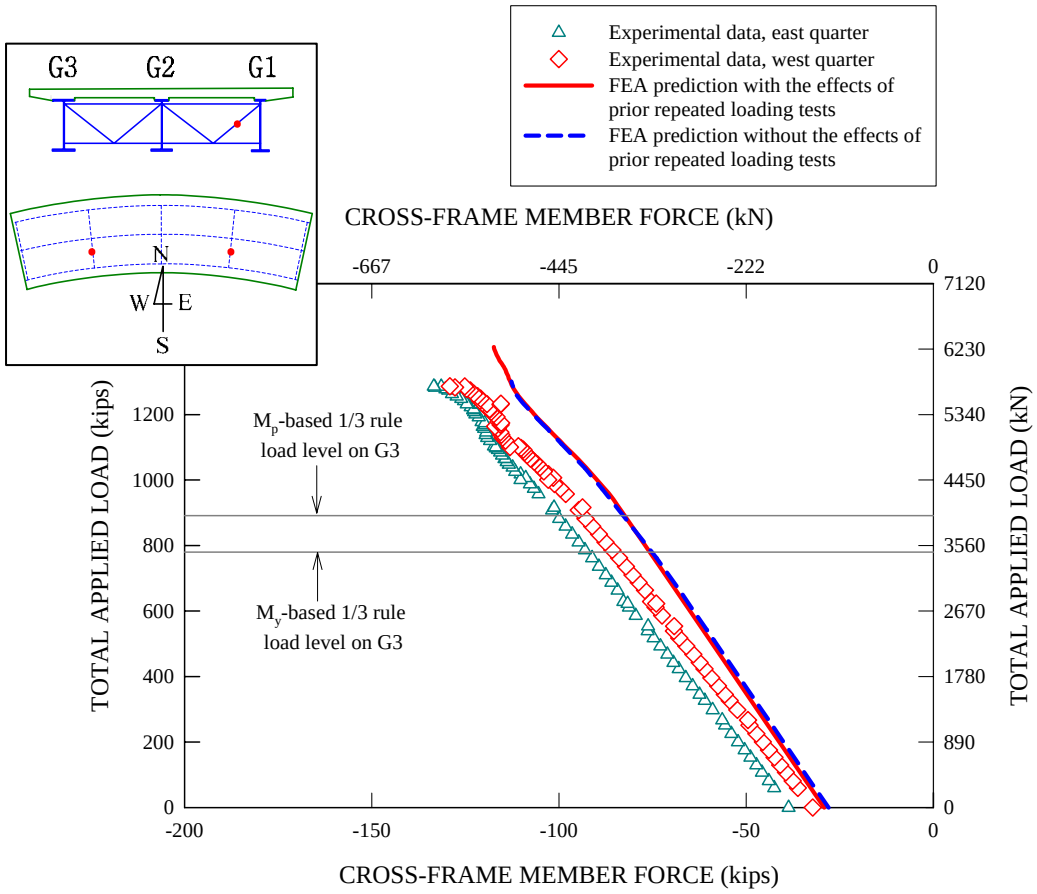

Figure D.1.12. Measured and predicted axial member forces for the diagonal members attached to G1 of the quarter-span cross-frames between G1 and G2 during the final monotonic loading test of Test 4b, initial dead load member forces are included in the plot as well, and the measured initial dead load member forces are taken just before the start of the repeated loading tests of Test 4a.

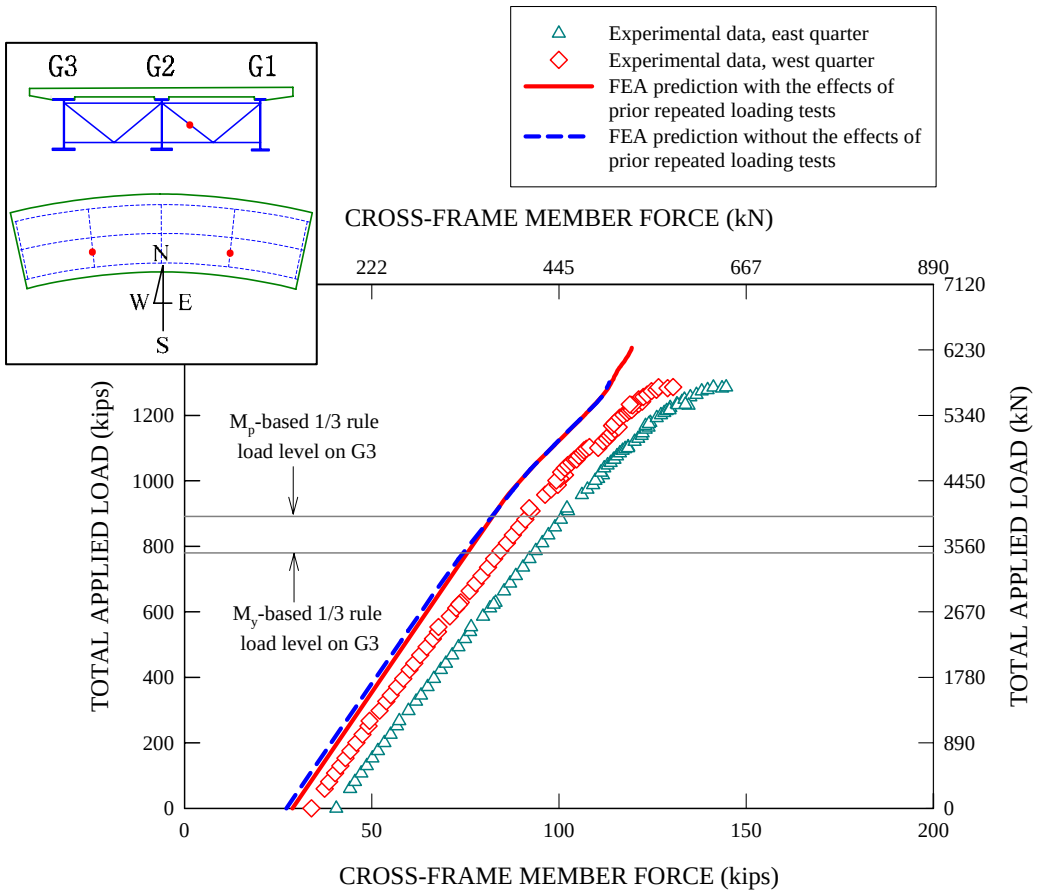

Figure D.1.13. Measured and predicted axial member forces for the diagonal members attached to G2 of the quarter-span cross-frames between G1 and G2 during the final monotonic loading test of Test 4b, initial dead load member forces are included in the plot as well, but the measured initial dead load member forces are taken just before the start of the repeated loading tests of Test 4a.

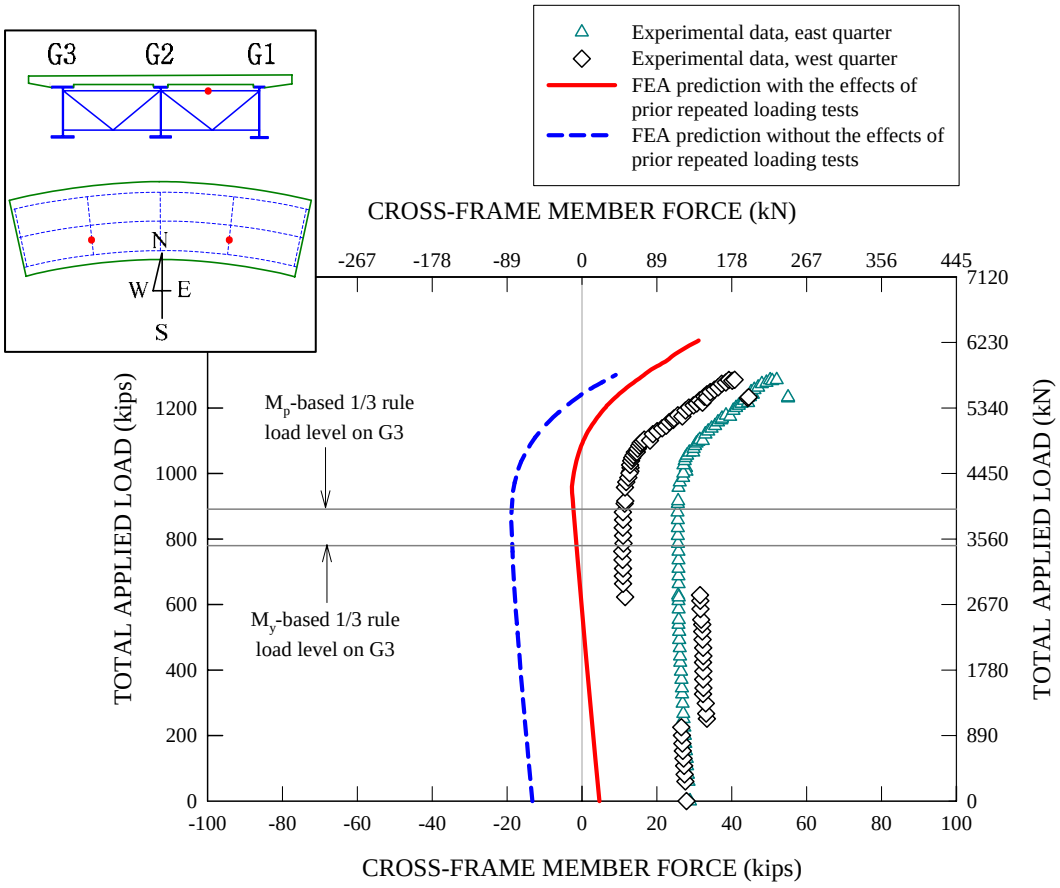

Figure D.1.14. Measured and predicted axial member forces for the top chords of the quarter-span cross-frames between G1 and G2 during the final monotonic loading test of Test 4b, initial dead load member forces are included in the plot as well, but the measured initial dead load member forces are taken just before the start of the repeated loading tests of Test 4a.

D.2 G3 Slip Measurements

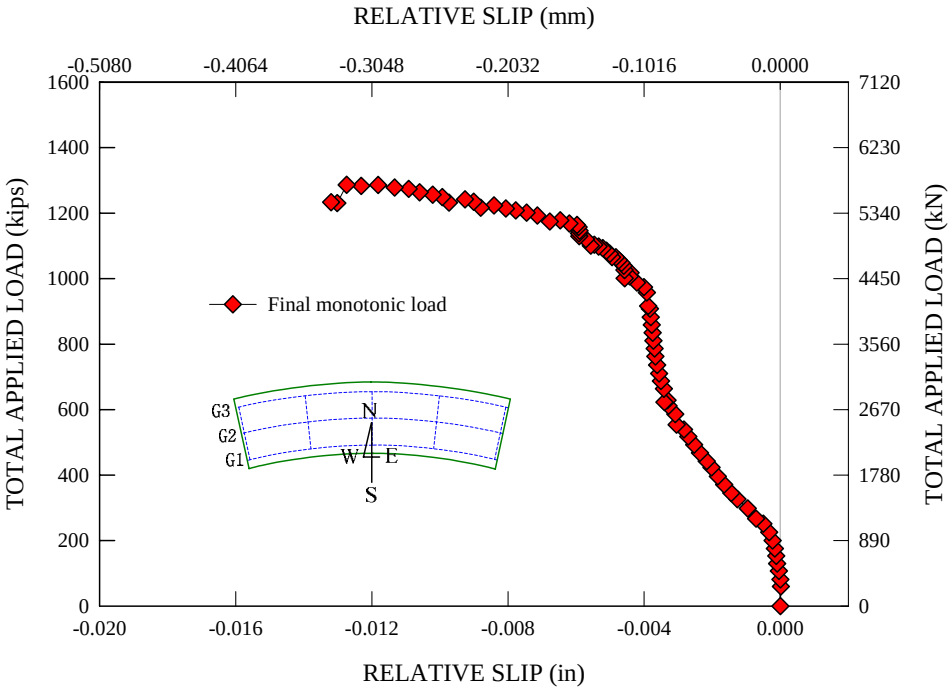

Figure D.2.1. G3 - Total applied load vs. east end relative longitudinal slip deformation at the concrete-steel interface during Test 4b.

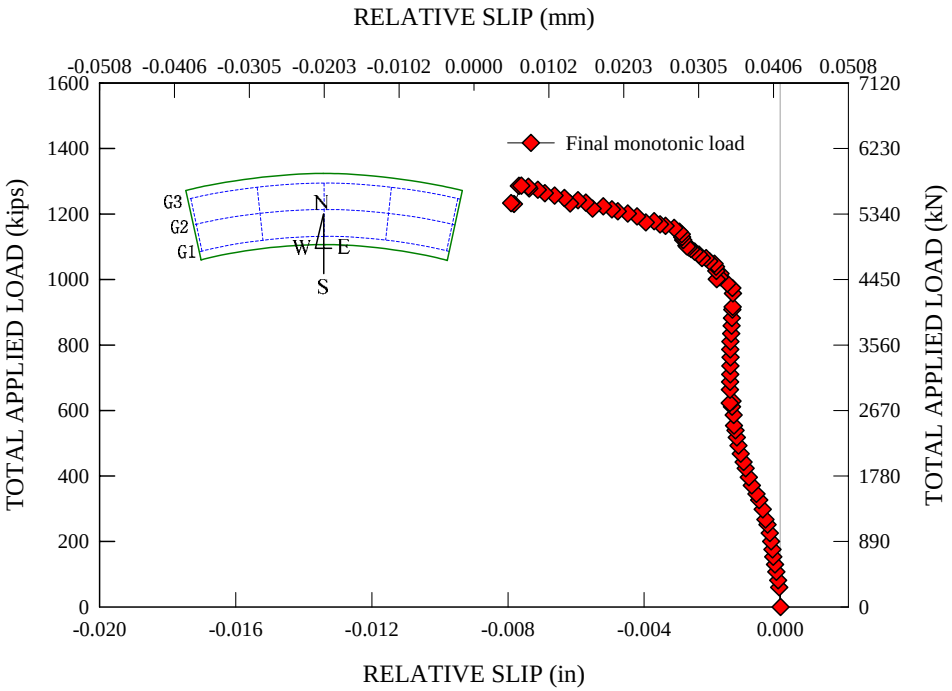

Figure D.2.2. G3 - Total applied load vs. west end relative longitudinal slip deformation at the concrete-steel interface during Test 4b.

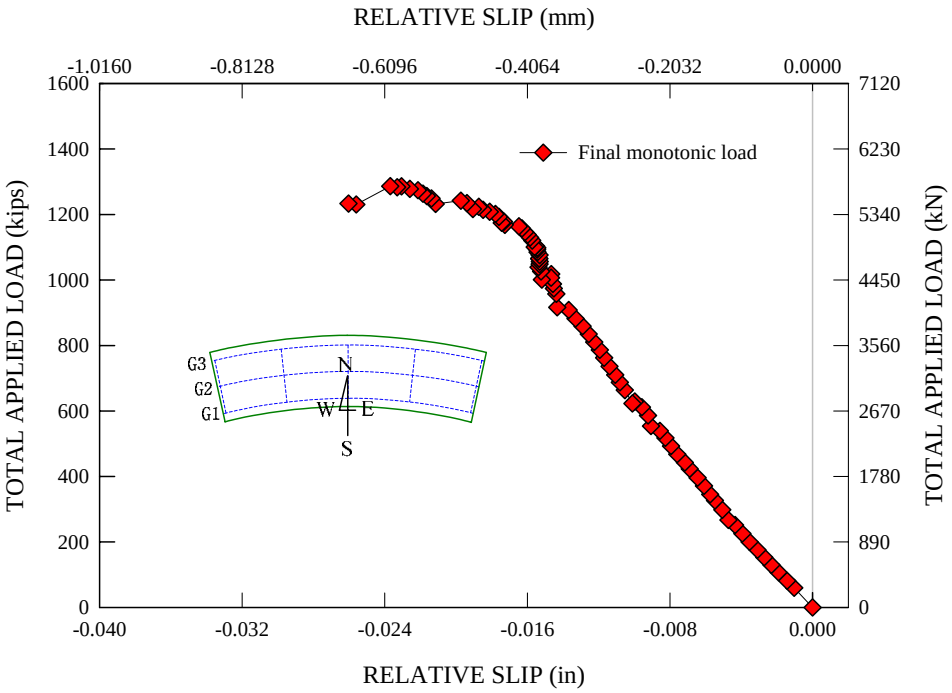

Figure D.2.3. G3 - Total applied load vs. relative radial slip deformation at the concrete-steel interface during Test 4b.

D.3 G2 Slip Measurements

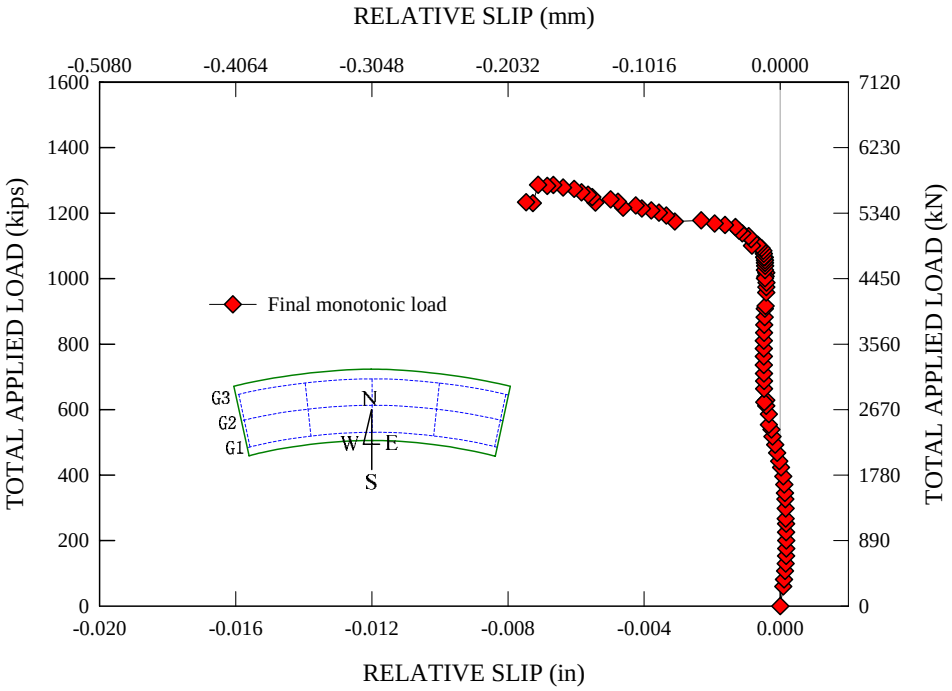

Figure D.3.1. G2 - Total applied load vs. east end relative longitudinal slip deformation at the concrete-steel interface during Test 4b.

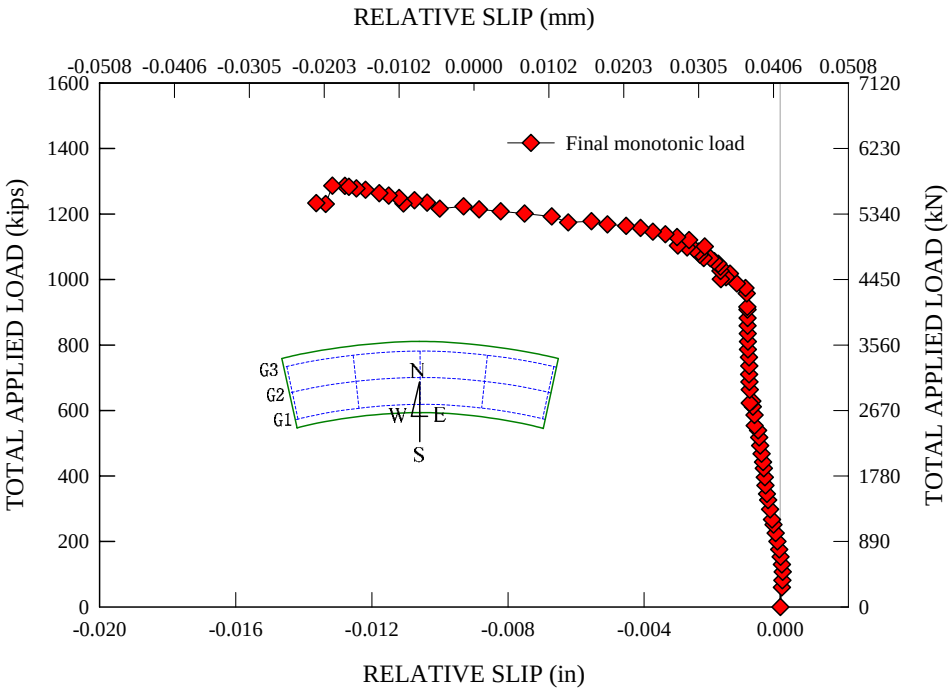

Figure D.3.2. G2 - Total applied load vs. west end relative longitudinal slip deformation at the concrete-steel interface during Test 4b.

D.4 G1 Slip Measurements

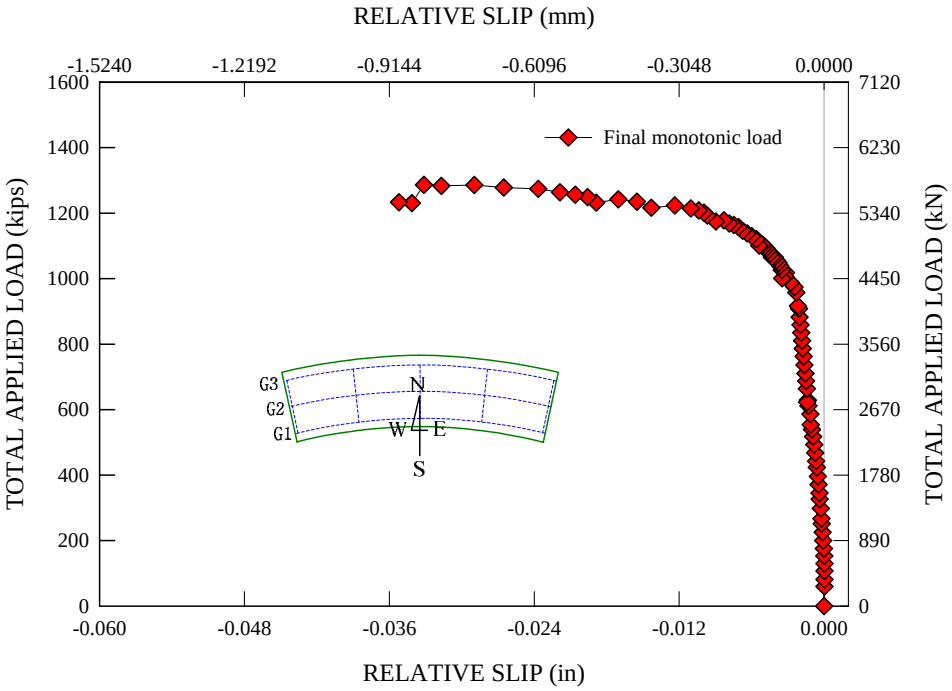

Figure D.4.1. G1 - Total applied load vs. east end relative longitudinal slip deformation at the concrete-steel interface during Test 4b.

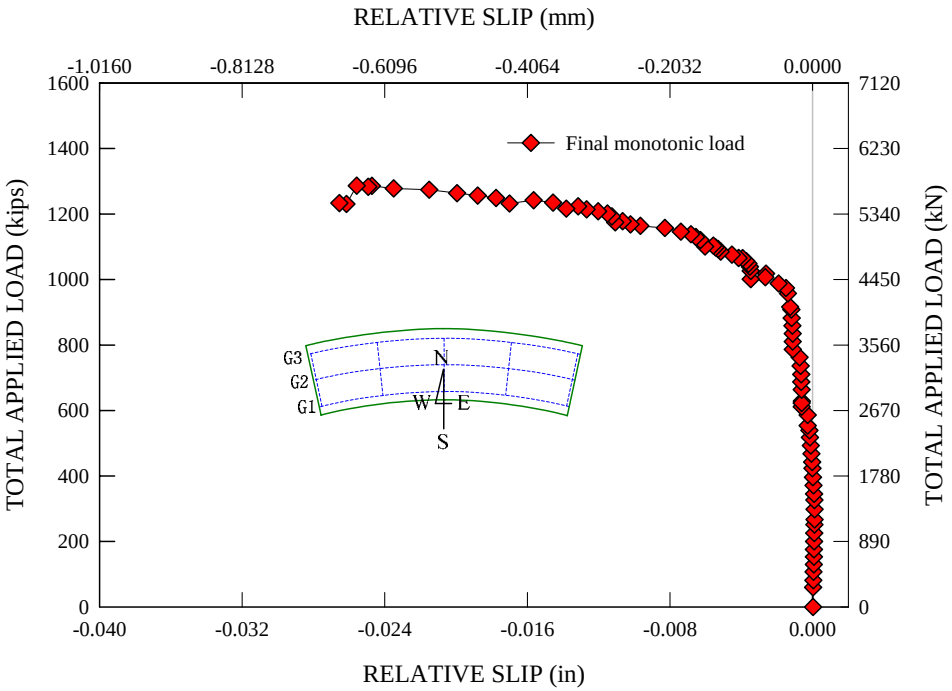

Figure D.4.2. G1 - Total applied load vs. west end relative longitudinal slip deformation at the concrete-steel interface during Test 4b.

APPENDIX E

NONLINEAR BEAM MULTI-POINT CONSTRAINT

The version of the EQUATION command used in this study is identical to the nonlinear version of the beam MPC that considers the effects of large rotation kinematics. Figure E.1 shows the conceptual representation of this beam MPC. The aim of this beam MPC is to express the displacements at node *i* in terms of the displacements at node *p*. The three rotation degrees of freedom at node *p* are equal to those at node *i* in a straightforward fashion. However, the three translation degrees of freedom at node *i* need to be expressed as a function of the translation displacements at node *p*, as well as translational contributions from the nodal rotations at node *p*. In matrix notation, the rotations at node *i* can be expressed as

$$\vec{\theta}_i = \vec{\theta}_p \tag{E.1}$$

where θ_i is a vector containing rotations at node *i* and θ_p is a vector representation of the rotations variables at node *p*. Similarly, the total translational displacement at node *i* can be expressed as

$$\vec{u}_i = \vec{u}_p + \Delta\vec{r} \tag{E.2}$$

where u_i is a total translations displacement matrix at node i, u_p is a translation displacement matrix ad node *p*, Δr is a matrix containing translational contributions from the rotation degree of freedom at node *p*.

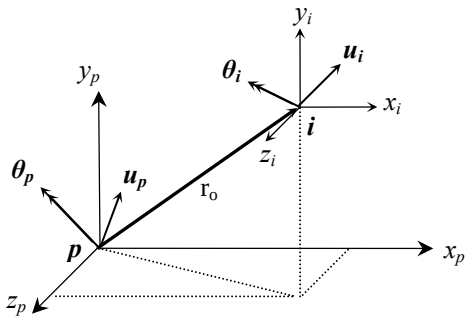

Figure E.1. Nonlinear beam multi-point constraint (MPC) (translation of axis).

for the expression for Δr needs to account for the influence of finite rotations. Consider Fig. 3.5.8 where there is a relative large rotation between the master node *p* and the slave node *i*. From Fig. E.2b, the incremental displacement vector due to the large rotation can be expressed as

$$\begin{aligned}
\Delta\vec{r} &= \Delta\vec{a} + \Delta\vec{b} \\
&= \frac{1-\cos\theta}{\theta^2}(\vec{\theta}\times(\vec{\theta}\times\vec{r})) + \frac{\sin\theta}{\theta}(\vec{\theta}\times\vec{r}) \\
&= -\frac{1-\cos\theta}{\theta^2}(\vec{\theta}\times(\vec{r}\times\vec{\theta})) - \frac{\sin\theta}{\theta}(\vec{r}\times\vec{\theta}) \\
&= \left\{-\frac{1-\cos\theta}{\theta^2}S(\vec{\theta})\cdot S(\vec{r}) - \frac{\sin\theta}{\theta}S(\vec{r})\right\}\cdot\vec{\theta} \\
&= \underline{C}\cdot\vec{\theta}
\end{aligned} \tag{E.3a}$$

$$\vec{\theta} = \theta_1 e_1 + \theta_2 e_2 + \theta_3 e_3 = \theta\vec{e} \qquad \theta = \|\theta\| = \sqrt{\theta_1^{\,2} + \theta_2^{\,2} + \theta_3^{\,2}} \tag{E.3b}$$

$$S(\vec{\theta}) = \begin{bmatrix} 0 & -\theta_3 & \theta_2 \\ \theta_3 & 0 & -\theta_1 \\ -\theta_2 & \theta_1 & 0 \end{bmatrix} \tag{E.3c}$$

$$\vec{r}_o = r_1 e_1 + r_2 e_2 + r_3 e_3 = (x_i - x_p)e_1 + (y_i - y_p)e_2 + (z_i - z_p)e_3 \tag{E.3d}$$

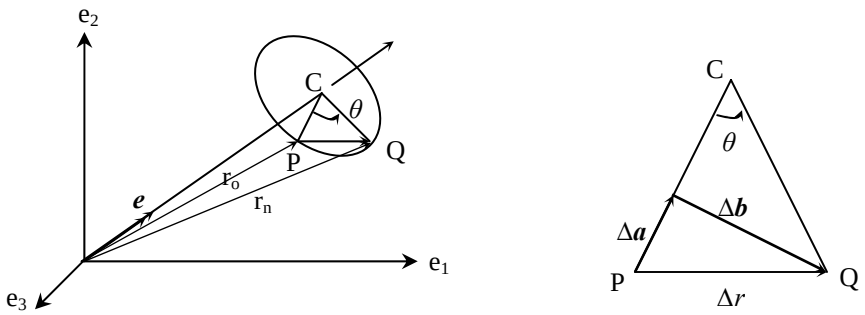

(a) (b)

Figure E.2. Three-dimensional rotation, (a) rotation about OC and (b) detail (Crisfield 1997).

Therefore, based on Eq. (E.3a), the total displacement vector at node *i* can be expressed as

$$\vec{u}_i = \vec{u}_p + \Delta\vec{r} = \vec{u}_p + \underline{C}_{ip} \cdot \vec{\theta}_p \tag{E.2}$$

Finally the translation and rotation at node *i* can be expressed in a combined compact form as

$$\begin{Bmatrix} \vec{u}_i \\ \vec{\theta}_i \end{Bmatrix} = \begin{bmatrix} I & \underline{C}_{ip} \\ 0 & I \end{bmatrix} \cdot \begin{Bmatrix} \vec{u}_p \\ \vec{\theta}_p \end{Bmatrix} \quad \text{or} \quad D_{\mathrm{i}} = T_{ip} \cdot D_p \tag{E.4}$$

This is a general expression for the nonlinear beam multi-point constraint. It should be noted that the matrix C contains the position vector r that needs to be updated in each increment of nonlinear solutions. However, this update procedure is not possible with the EQUATION command in ABAQUS, since the EQUATION command resides in the input files. Nonetheless, the matrix C can be approximated in a way such that it does not depend on the change of the position vectors, thereby still making the nonlinear FEA solutions independent of the positions vectors. First, based on the linearized rotation field for a given current configuration, the matrix C may be modified as

$$
\begin{aligned}
C &= -\frac{1-\cos\theta}{\theta^2} S(\vec{\theta}) \cdot S(\vec{r}) - \frac{\sin\theta}{\theta} S(\vec{r}) \\
&\approx -S(\vec{r}) \\
&= -\begin{pmatrix} 0 & -r_3 & r_2 \\ r_3 & 0 & -r_1 \\ -r_2 & r_1 & 0 \end{pmatrix}
\end{aligned}
\tag{E.5}
$$

where r_1, r_2 and r_3 are the components of the position vector as expressed in Eq. (E.3d). Next, based on preliminary analyses that the position vectors for the rigid links between the top flange nodes and slab nodes do not show any significant departures from the initial position vectors that are pointed in the upward direction and expressed as {0, 0, r_3}, the rotation matrix can be further simplified into the matrix with constants component as

$$
C = -\begin{pmatrix} 0 & -r_3 & 0 \\ r_3 & 0 & 0 \\ 0 & 0 & 0 \end{pmatrix}
\tag{E.5a}
$$

Therefore, the translation and rotation at node *i* can be expressed in a matrix form as

$$
\begin{Bmatrix} \vec{u}_i \\ \vec{\theta}_i \end{Bmatrix} = \begin{bmatrix} I & \underline{C}_{ip} \\ 0 & I \end{bmatrix} \cdot \begin{Bmatrix} \vec{u}_p \\ \vec{\theta}_p \end{Bmatrix} = \begin{pmatrix} 1 & 0 & 0 & 0 & r_3 & 0 \\ 0 & 1 & 0 & -r_3 & 0 & 0 \\ 0 & 0 & 1 & 0 & 0 & 0 \\ 0 & 0 & 0 & 1 & 0 & 0 \\ 0 & 0 & 0 & 0 & 1 & 0 \\ 0 & 0 & 0 & 0 & 0 & 1 \end{pmatrix} \begin{Bmatrix} u_1^p \\ u_2^p \\ u_3^p \\ \theta_1^p \\ \theta_2^p \\ \theta_3^p \end{Bmatrix} = \begin{Bmatrix} u_1^i \\ u_2^i \\ u_3^i \\ \theta_1^i \\ \theta_2^i \\ \theta_3^i \end{Bmatrix}
\tag{E.4a}
$$

$$
\begin{aligned}
u_1^i &= u_1^p + r_3 \times \theta_2^p \\
u_2^i &= u_2^p - r_3 \times \theta_1^p \\
u_3^i &= u_3^p \\
\theta_1^i &= \theta_1^p \\
\theta_2^i &= \theta_2^p \\
\theta_3^i &= \theta_3^p
\end{aligned}
$$

Note that the r_3 is taken as the length of the rigid link between the lower top flange nodes and the upper slab shell element nodes. The above relationships are implemented in the EQUATION command within the ABAQUS input files.

REFERENCES

AASHTO (1998). *AASHTO LRFD Bridge Design Specifications 2*nd Edition with 1999, 2000 and 2001 Interims, American Association of State and Highway Transportation Officials, Washington D.C.

AASHTO (2003). *Guide Specifications for Horizontally Curved Steel Girder Highway Bridges with Design Examples for I-Girder and Box-Girder Bridges*, American Association of State and Highway Transportation Officials, Washington D.C.

AASHTO (2004a). *AASHTO LRFD Bridge Design Specifications, 3rd Edition*, American Association of State and Highway Transportation Officials, Washington D.C.

AASHTO (2004b). *AASHTO LRFD Bridge Design Specifications, 3rd Edition* with 2005 Interims, American Association of State and Highway Transportation Officials, Washington D.C.

AASHTO (2004c). *A Policy on Geometric Design of Highways and Streets*, American Association of State and Highway Transportation Officials, Washington D.C.

ACI 318 and 318R (2002). *Building Code Requirements for Structural Concrete(ACI 318) and Commentary (ACI-318R),* American Concrete Institute, Farmington Hills, MI, 442 pp.

AISC (1999). *Load and Resistance Factor Design Specification for Structural Steel Buildings*, American Institute of Steel Construction, Chicago, IL, 292 pp.

ASCE (1971). "Survey of Curved Girder Bridges," committee correspondence, ASCE Task Committee on Flexural Members, Subcommittee on Curved Girders, June 17.

ASCE-WRC (1971). *Plastic Design in Steel: A Guide and Commentary (2nd Edition*, Joint Committee of American Society of Civil Engineers and Welding Research Council ASCE Manual and Reports on Engineering Practice No. 41, New York, 336 pp.

AWS (2000). *Structural Welding Code–Steel*, AWS D1.1:2000, 17th ed., prepared by AWS Committee on Structural Welding, 450 pp.

AWS (1966). *Specifications for Welded Highway and Railroad Bridges,* American Welding Society.

Barker, M.G., Bergson, P.M., French, C.E., Leon, R.T., Galambos, T.V. and Klaiber, F.W. (1996). "Shakedown Tests of One-Third-Scale Composite Bridge," *Journal of Bridgl Engineering,* ASCE, 1(), 2-9.

Baskar, K., Shanmugam, N.E., and Thevendran, V. (2002). “Finite-Element Analysis of Steel-Concrete Composite Plate Girder,” *Journal of Structural Engineering*, ASCE, 128(9), 1158-1168.

Baskar, K. and Shanmugam (2002). “Steel-Concrete Composite Plate Girders Subject to Combined Shear and Bending,” *Journal of Constructional Steel Research*, 59, 531-557.

Beshah, F. (2006). “Testing of Composite Bridge,” Volume 9, Curved Steel Bridge Research Project, Federal Highway Administration, Nov. 2006

Crisfield M.A. (1997). *Non-linear Finite Element Analysis of Solids and Structures*. New York: John Wiley & Sons, Inc., 494 ppp.

Clarke, C.B. (1966). “Testing of Model Curved Steel Girder Bridge,” *Engineering Journal*, AISC, 106-112.

Bradford, M.A. (1992). “Lateral-Distortional Buckling of Steel I-Section Members,” *Journal of Constructional Steel Research*, 23, 97-116.

Bradford, M.A. (1989). “Buckling Strength of Partially Restrained I-Beams,” *Journal of Structural Engineering*, ASCE, 115(5), 1272-1276.

Bradford, M.A. (1988). “Buckling Strength of Deformable Monosymmetric I-Beams,” *Journal of Constructional Steel Research*, 10, 167-173.

Bradford, M.A. (1985). “Distortional Buckling of Monosymmetric I-Beams,” *Journal of Constructional Steel Research*, 5, 123-136.

Bradford, M.A. and Gao, Z. (1992). “Distortional Buckling Solutions for Continuous Composite Beams,” *Journal of Structural Engineering*, ASCE, 118(1), 73-89.

Bradford, M.A. and Waters, S.W. (1988). “Distortional Instability of Fabricated Monosymmetric I-Beams,” *Computers and Structures*, 29(4), 715-724.

Bradford, M.A. and Johnson, R.P. (1987). “Inelastic Buckling of Composite Bridge Girders Near Internal Supports,” *Proceedings of the Institution of Civil Engineers*, Part 2, 83, March, 143-159.

Bradford, M.A. and Trahair, N.S. (1983). “Lateral Stability of Beams on Seats,” *Journal of Structural Engineering*, ASCE, 109(9), 2212-2215.

Bradford, M.A. and Trahair, N.S. (1981). “Distortional Buckling of I-Beams,” *Journal of the Structural Division*, ASCE, 107(ST2), 355-370.

Brennan, P.J. and Mandel, J.A. (1979). “Curved Girder Bridge Model Analysis and Testing,” *Proceedings*, IABSE, P-19/78, 1-20.

Chang, C.-J. (2006). "Construction Simulation for Curved Steel I-Girder Bridges," Ph.D. dissertation, Georgia Institute of Technology, Atlanta GA.

Civjan S.A. and Singh, P. (2003). "Behavior of Shear Studs Subjected to Fully Reversed Cyclic Loading," *Journal of Structural Engineering*, ASCE, 129(11), 1466-1474.

Domalik, D.E., Shura, J.F. and Linzell, D.G., (2005). "Design and Field Monitoring of Horizontally Curved Steel Plate Girder Bridge," *Journal of the Transportation Research Board*, Transportation Research Record, 1928, 83-91.

ECCS-Committee 8-Stability (1976). "Manual on Stability of Steel Structures 2nd Edition," European Convention for Constructional Steelwork, Publication No. 22, 328pp.

Fuchs, P.A. (2005). "Curved Girder Bridge Erection Tests – Laser System Measurements," Fuchs Consulting, Inc, Leesburg, VA.

Galambos, T.V., Hajjar, J.F., Leon, R.T., Huang, W.-H., Pulver, B.E., and Rudie, B.J. (1996). "Stresses in Steel Curved Girder Bridges," Minnesota Dept. of Trans. Report No. MN/RC-96/28, August.

Galambos, T.V., Hajjar, J.F., Huang, W.-H., Pulver, B.E., Leon, R.T., and Rudie, B.J. (2000). "Comparison of Measured and Computed Stresses in A Steel Curved Girder Bridge," *Journal of Bridge Engineering*, ASCE, 5(3), 191-199.

Goodier, J.N. and Barton, M.V. (1944). "The Effects of Web Deformation on the Torsion of I Beams," *Journal of Applied Mechanics*, March, A-35 to A-40.

Grubb, M.A. and Hall, D.H. (2001). "Chapter 2- Philosophy and Design of the I-Girder Bending Component Tests," Volume II-I-Girder Bending Component Tests, FHWA Curved Steel Bridge Research Project.

Hall, D.H., Grubb, M.A. and Yoo, C.H. (1999). "Improved Design Specifications for Horizontally Curved Steel Girder Highway Bridges," Report No. 424, NCHRP Project 12-38 Final Report, Transportation Research Board, NRC, Washington, D.C.

Hancock, G.J. (1978). "Local, Distortional, and Lateral Buckling of I-Beams," *Journal of Structural Division*, ASCE, 104(ST11),1787-1799.

Hancock, G.J., Bradford, M.A. and Trahair, N.S. (1980). "Web Distortion and Flexural-Torsional Buckling," *Journal of Structural Division*, ASCE, 106(ST7),1557-1571.

HKS (2004), *ABAQUS/Standard Version 6.4-1*, Hibbitt, Karlsson & Sorensen, Inc., Pawtucket, RI.

Horne, M.R. and Grayson, W.R. (1983). “Parametric Finite Element Study of Transverse Stiffeners for Webs in Shear,” Instability and Plastic Collapse of Steel Structures, Proceedings of the Michael R. Horne Conference, L.J.Morris (ed.), Granada Publishing, London, 329-341.

Kim, Y.D., Jung, S.K. and White, D.W. (2004). “Transverse Stiffener Requirements in Straight and Horizontally Curved Steel I-Girders,” Structural Engineering Report No. 36, School of Civil and Environmental Engineering, Georgia Institute of Technology, Atlanta, GA.

Karsan, I.D. and Jirsa, J.O., (1969), “Behavior of Concrete under Compressive Loadings,” *Journal of the Structural Division*, ASCE, 95(12), 2543-2563.

Kim, Y.D., Jung, S.K. and White, D.W. (2004). “Transverse Stiffener Requirements in Straight and Horizontally Curved Steel I-Girders,” Structural Engineering Report No. 36, School of Civil and Environmental Engineering, Georgia Institute of Technology, Atlanta, GA.

Kissane, R.J. and Beal, D.B. (1972). “Field Testing of Horizontally Curved Steel Girder Bridges,” Report No. 8, Engineering Research and Development Bureau, New York State Department of Transportation, Albany, New York.

Krzmarzick, D.P. and Hajjar, J.F. (2006). “Load Rating of Curved Composite Steel I-girder Bridges through Load Testing with Heavy Trucks,” *Proceedings of Structures Congress*.

Lam, D. and El-Lobody, E. (2005). “Behavior of Headed Stud Shear Connectors in Composite Beam,” *Journal of Structural Engineering*, ASCE, 131(1), 96-107.

Lee, J. and Fenves, G.L. (1998). “Plastic-Damage Model for Cyclic Loading of Concrete Structures,” *Journal of Engineering Mechanics*, ASCE, 124(8),892-900.

Lee, S.C., Yoo C.H. and Yoon D.Y. (2002). “Behavior of Intermediate Transverse Stiffeners Attached on Web Panels,” *Journal of Structural Engineering*, ASCE, 128(3), 337-345.

Lee, S.C., Yoo C.H. and Yoon D.Y. (2003). “New Design Rule for Intermediate Transverse Stiffeners Attached on Web Panels,” *Journal of Structural Engineering*, ASCE, 129(12), 1607-1614.

Lin, J.J., Fafard, M., Beaulieu, D., and Massicotte, B. (1991). “Nonlinear Analysis of Composite Bridges by The Finite Element Method,” *Computers and Structures*, 40(5), 1151-1167.

Linzell, D.G. (1999). “Studies of a Full-Scale Horizontally Curved Steel I-Girder Bridge System Under Self-Weight,” Doctoral dissertation, Georgia Institute of Technology, Atlanta, GA.

Mariani, N., Mozer J.D., Dym, C.L. and Culver, C.G. (1973). "Transverse Stiffener Requirements for Curved Webs," *Journal of Structural Division*, ASCE, 99(ST4), 757-771.

McEleney (2004), *Personal Communication*

McElwain, B.A. and Laman, J.A. (2000). "Experimental Verification of Horizontally Curved I-Girder Bridge Behavior," *Journal of Bridge Engineering*, ASCE, 5(4),284-292.

McManus, P.F. (1971). "Lateral Buckling of Curved Plate Girders," Ph.D. dissertation, Carnegie-Mellon University, Pittsburgh, PA, 189 pp.

Nakai, H., Kitada, T. and Ohminami R. (1985). "A Proposition for Designing Transverse Stiffeners in Web Plate of Horizontally Curved Girders," Proceeding of JSCE, 362(I-4), October, 249-257.

Jorgen G. Ollgaard, Roger G. Slutter and John W. Fisher. (1971) " Shear Strength of Stud Connectors in Lightweight and Normal-weight Concrete," Engineering Journal, AISC, 8, 2, 55-64

Okamoto, S., Shiomi, S. and Yamabe, K., (1976), "Earthquake Resistance of Prestressed Concrete Structures," *Proceedings*, Annual Convention, AIJ, 1251-1252.

Phoawanich, N. (2001). "Development of Unified Equations for Design of Curved and Straight Steel I Girders," Doctoral dissertation, Georgia Institute of Technology, Atlanta, GA.

Roberts, T.M. and Jhita, P.S. (1983). "Lateral, Local and Distortional Buckling of I-Beams," *Thin-Walled Structures*, 1,289-308.

Rahal, K.N. and Harding, J.E. (1990a). "Transversely Stiffened Girder Webs Subjected to Shear Loading – Part 1: Behaviour," *Proceedings of the Institution of Civil Engineers*, Part 2, 89, March, 47-65.

Rahal, K.N. and Harding, J.E. (1990b). "Transversely Stiffened Girder Webs Subjected to Shear Loading – Part 2: Stiffener Design," *Proceedings of the Institution of Civil Engineers*, Part 2, 89, March, 67-87.

Rahal, K.N. and Harding, J.E. (1991). "Transversely Stiffened Girder Webs Subjected to Combined In-Plane Loading," *Proceedings of the Institution of Civil Engineers*, Part 2, 91, June, 237-258.

Rockey, K.C., Valtinat, G. and Tang, K.H. (1981). "The Design of Transverse Stiffeners on Webs Loaded in Shear – An Ultimate Load Approach," *Proceedings of the Institution of Civil Engineers*, Part 2, 71, December, 2425-2441.

Shanmugam, N.E., and Baskar, K. (2003). "Steel-Concrete Composite Plate Girders Subject to Shear Loading," *Journal of Structural Engineering*, ASCE, 129(9), 1230-1242.

Faella, C., Martinelli, E. and Nigro E. (2003), "Shear Connection Nonlinearity and Deflections of Steel-Concrete Composite Beams: A Simplified Method," *Journal of Structural Engineering*, ASCE, 129(1), 12-20.

Fabbrocino, G., Manfredi, G. and Cosenza E. (2000), "Analysis of Continuous Composite Beams Including Partial Interaction and Bond," *Journal of Structural Engineering*, ASCE, 129(11), 1288-1294.

Salmon, C.G. and Johnson, J.E. (1996). *Steel Structures: Design and Behavior 4th Edition.* New York: HarperCollins College Publishers 1996, 1024 ppp.

Sebastian, W.M. and McConnel, R.E. (2000), "Nonlinear FE Analysis of Steel-Concrete Composite Structures," *Journal of Structural Engineering*, ASCE, 126(6), 662-674.

Sinha, B.P., Gerstle, K.H. and Tulin, L.G. (1964), "Stress-Strain Relations for Concrete under Cyclic Loading," *Journal of the American Concrete Institute*, 61(2), 195-211.

Slutter, R.G., and Driscoll, G.C. (1965), "Flexural Strength of Steel-Concrete Composite Beams," *Journal of Structural Division*, ASCE, ST2, 71-99.

SSRC (1998). *Guide to Stability Design Criteria for Metal Structures 5th* Edition. Structural Stability Research Council, T.V. Galambos (ed.), McGraw-Hill, New York, 910 pp.

Stanway, G.S., Chapman, J.C. and Dowling, P.J. (1993). "Behaviour of a Web Plate in Shear with an Intermediate Stiffener," *Proceedings of the Institution of Civil Engineers, Structures and Buildings*, 99, August, 327-344.

Stanway, G.S., Chapman, J.C. and Dowling, P.J. (1996). "A Design Model for Intermediate Web Stiffeners," *Proceedings of the Institution of Civil Engineers, Structures and Buildings*, 116, February, 54-68.

Tanigawa, Y. and Uchida, Y., (1979), "Hysteretic Characteristics of Concrete in the Domain of High Compressive Strain," *Proceedings*, Annual Convention, AIJ, 449-450.

Thevendran, V., Shanmugam, N.E., Chen, S., and Richard Liew, J.Y. (2000). "Experimental Study on Steel-Concrete Composite Beams Curved in Plan," *Engineering Structures*, 22, 877-889.

Timoshenko, S.P., and Gere, J.M. (1961). *Theory of Elastic Stability 2nd Edition.* Singapore: McGraw-Hill Book Company, Inc 1961, 541 ppp.

Topkaya, C., and Williamson, E.B. (2003). "Development of computational software for analysis of curved girders under construction loads," *Computers and Structures*, 81, 2087-2098.

Topkaya, C., Yura, J.A. and Williamson, E.B. (2004). "Composite Shear Stud Strength at Early Concrete Ages," *Journal of Structural Engineering*, 130(6), 952-960

White, D.W., and Jung, S.-K. (2005). "Effect of Web Distortion on the Buckling Strength of Noncomposite Discretely-Braced I-Beams," Structural Engineering, Mechanics and Materials Report No. 24c, School of Civil and Environmental Engineering, Georgia Institute of Technology, Atlanta, GA

White, D.W., Zureick, A.H., Phoawanich, N. and Jung, S.-K. (2001). *Development of Unified Equations for Design of Curved and Straight Steel Bridge I Girders*, Final Report to American Iron and Steel Institute Transportation and Infrastructure Committee, Professional Services Industries, Inc., and Federal Highway Administration, School of Civil and Environmental Engineering, Georgia Institute of Technology, Atlanta, GA, October, 551 pp.

White, D.W. and Grubb, M.A. (2004). "Comprehensive Update to AASHTO LRFD Provisions for Flexural Design of Bridge I-Girders," *Proceedings*, Structures Congress, ASCE, 8pp.

Womack, K.C. and Halling, M.W. (2001). "Static and Dynamic Testing of a Curved, Steel Girder Bridge in Salt Lake City, Utah," Report No. UT-00.13, Utah Department of Transportation, Salt Lake City, Utah.

Wright, W. and Beshah, F. (2006). "Construction of Test Bridge," Volume 8, Curved Steel Bridge Research Project, Federal Highway Administration, Nov. 2006

Xie, M. (2000). "Behavior and Design of Transversely Stiffened Plates Subject to Combined Shear and Direct In-Plane Loading," PhD Thesis, Department of Civil and Environmental Engineering, Imperial College, London.

Ynakelevsky, D.Z. and Reinhardt, H.W. (1987a). "Model for Cyclic Compressive Behavior of Concrete," *Journal of Structural Engineering*, 113(2), 228-240

Ynakelevsky, D.Z. and Reinhardt, H.W. (1987b). "Response of Plain Concrete to Cyclic Tension," *ACI Materials Journal*, 84(5), 365-373

Yura, J.A. (1993). "Fundamentals of Beam Bracing," *Conference*, SSRC, 1-2.

Zureick, A., Linzell, D., Leon, R.T., and Burrell, J. (2000). "Curved Steel I-girder Bridges: Experimental and Analytical Studies," *Engineering Structures*, 22, 180-190.

Zureick, A. and Naqib, R. (1999). "Horizontally Curved Steel I-Girders State-of-the-Art Analysis Methods," *Journal of Bridge Engineering*, 4(1), 38-47.

VITA

SE-KWON JUNG

Se-Kwon Jung was born on August 3, 1971 in Yeosu, Korea. He received his Bachelor of Science in Architectural Engineering from Yonsei University, Seoul, Korea in 1997. He has two Master of Science degrees. One is in the field of Architectural Engineering from Yonsei University, Seoul, Korea in 1999, and the other is in the field of Civil Engineering from Georgia Institute of Technology (Georgia Tech), Atlanta, Georgia in 2004. He worked as a structural engineer with Hyundai Engineering and Construction in Seoul, Korea from 1999 to 2001, where he performed design and analysis of various types of commercial and industrial structures. He joined the School of Civil and Environmental Engineering at Georgia Tech to pursue a doctorate in Structural Engineering in 2001.

His research interests include structural stability, limit state design and behavior of steel and composite (steel/concrete) bridge structures, full nonlinear finite element analysis of large-scale structures coupled with testing of large-scale structural systems, and computational mechanics (numerical modeling of materials within the thermodynamic framework and handling of large rotation kinematics in finite element computation).